CODEN: JASMAN

ISSN: 0001-4966

The Journal of the Acoustical Society of America

Vol. 111, No. 6 June 2002

(Continued)

THE JOURNAL OF THE ACOUSTICAL SOCIETY OF AMERICA VOL. 111, NO. 6, JUNE 2002

CONTENTS—*Continued from preceding page*

(Continued)

THE JOURNAL OF THE ACOUSTICAL SOCIETY OF AMERICA VOL. 111, NO. 6, JUNE 2002

CONTENTS—*Continued from preceding page*

(Continued)

THE JOURNAL OF THE ACOUSTICAL SOCIETY OF AMERICA VOL. 111, NO. 6, JUNE 2002

CONTENTS—*Continued from preceding page*

ERRATA

INDEX TO VOLUME 111

ACOUSTICAL NEWS—USA

Elaine Moran
Acoustical Society of America, Suite 1NO1, 2 Huntington Quadrangle, Melville, NY 11747-4502

Editor's Note: *Readers of this Journal are encouraged to submit news items on awards, appointments, and other activities about themselves or their colleagues. Deadline dates for news items and notices are 2 months prior to publication.*

New Fellows of the Acoustical Society of America

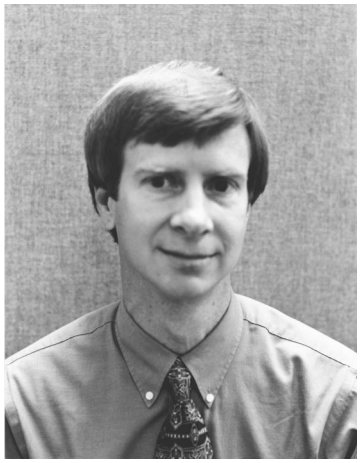

Kerry W. Commander—For contributions to ocean bubble acoustics and sonar systems development.

Peter H. Dahl—For contributions to scattering by ocean waves and bubbles.

Brian H. Houston—For contributions to acoustic scattering and radiation from structures.

Andrzej Rakowski—For contributions to music perception and education.

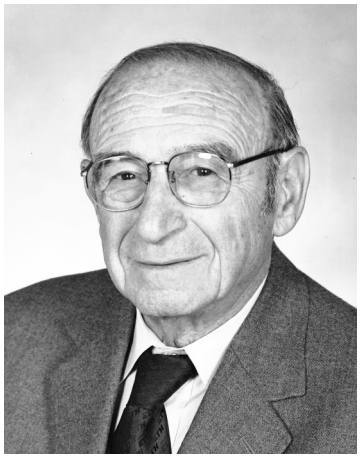

Nicholas Rott—For pioneering work in thermoacoustics.

Leon H. Sibul—For contributions to underwater acoustic signal processing.

ASA member Jan F. Lindberg receives IEEE award

ASA member Jan F. Lindberg was awarded the 2001 IEEE-USA Electrotechnology Transfer Award. This award honors individuals whose contributions in key government or civilian roles led efforts to effectively transfer/apply federal or state sponsored developments in advancing electrical, electronic, and computer technologies to successful commercial sector opportunities. Mr. Lindberg was selected because of his innovative transducer concepts that have advanced the art and science of underwater acoustic technology.

Jan Lindberg is a Fellow of the Acoustical Society of America and has recently served as a member of the Technical Committee on Engineering Acoustics.

The award was presented at the 2001 IEEE-USA Awards Ceremony held at the IEEE-USA Workshop in Richardson, Texas, on 13 April 2002.

 0001-4966/2002/111(6)/2519/2/$19.00

USA Meetings Calendar

Listed below is a summary of meetings related to acoustics to be held in the U.S. in the near future. The month/year notation refers to the issue in which a complete meeting announcement appeared.

2002

19–21 Aug. INTER-NOISE 2002, Dearborn, MI [INTER-NOISE 02 Secretariat, The Ohio State University, Department of Mechanical Engineering, 206 West 18th Ave., Columbus, OH 43210-1107; E-mail: hp @internoise2002.org].

2–6 Dec. Joint Meeting: 144th Meeting of the Acoustical Society of America, 3rd Iberoamerican Congress of Acoustics, and 9th Mexican Congress on Acoustics, Cancun, Mexico [Acoustical Society of America, Suite 1NO1, 2 Huntington Quadrangle, Melville, NY 11747-4502; Tel.: 516-576-2360; Fax: 516-576-2377; E-mail: asa@aip.org; WWW: asa.aip.org/cancun.html].

2003

28 April–2 May 145th Meeting of the Acoustical Society of America, Nashville, TN [Acoustical Society of America, Suite 1NO1, 2 Huntington Quadrangle, Melville, NY 11747-4502; Tel.: 516-576-2360; Fax: 516-576-2377; E-mail: asa@aip.org; WWW: asa.aip.org].

16–20 Sept. 7th International Conference on Spoken Language Processing (ICSLP 2002), Interspeech 2002, Denver, CO [ICSLP 2002, Centennial Conferences, 801 Main St., Suite 010, Louisville, CO 80027; Tel.: 303-499-2299; Fax: 303-499-2599; E-mail: icslp@centennialconferences.com; www: www.icslp2002.org].

10–14 Nov. 146th Meeting of the Acoustical Society of America, Austin, TX [Acoustical Society of America, Suite 1NO1, 2 Huntington Quadrangle, Melville, NY 11747-4502; Tel.: 516-576-2360; Fax: 516-576-2377; E-mail: asa@aip.org; WWW: asa.aip.org].

2004

24–28 May 75th Anniversary Meeting (147th Meeting) of the Acoustical Society of America, New York, NY [Acoustical Society of America, Suite 1NO1, 2 Huntington Quadrangle, Melville, NY 11747-4502; Tel.: 516-576-2360; Fax: 516-576-2377; E-mail: asa@aip.org; WWW: asa.aip.org].

29 Nov.–3 Dec. 148th Meeting of the Acoustical Society of America, San Diego, CA [Acoustical Society of America, Suite 1NO1, 2 Huntington Quadrangle, Melville, NY 11747-4502; Tel.: 516-576-2360; Fax: 516-576-2377; E-mail: asa@aip.org; WWW: asa.aip.org].

Cumulative Indexes to the *Journal of the Acoustical Society of America*

Ordering information: Orders must be paid by check or money order in U.S. funds drawn on a U.S. bank or by Mastercard, Visa, or American Express credit cards. Send orders to Circulation and Fulfillment Division, American Institute of Physics, Suite 1NO1, 2 Huntington Quadrangle, Melville, NY 11747-4502; Tel.: 516-576-2270. Non-U.S. orders add $11 per index.

Some indexes are out of print as noted below.

Volumes 1–10, 1929–1938: JASA and Contemporary Literature, 1937–1939. Classified by subject and indexed by author. Pp. 131. Price: ASA members $5; Nonmembers $10.

Volumes 11–20, 1939–1948: JASA, Contemporary Literature, and Patents. Classified by subject and indexed by author and inventor. Pp. 395. Out of Print.

Volumes 21–30, 1949–1958: JASA, Contemporary Literature, and Patents. Classified by subject and indexed by author and inventor. Pp. 952. Price: ASA members $20; Nonmembers $75.

Volumes 31–35, 1959–1963: JASA, Contemporary Literature, and Patents. Classified by subject and indexed by author and inventor. Pp. 1140. Price: ASA members $20; Nonmembers $90.

Volumes 36–44, 1964–1968: JASA and Patents. Classified by subject and indexed by author and inventor. Pp. 485. Out of Print.

Volumes 36–44, 1964–1968: Contemporary Literature. Classified by subject and indexed by author. Pp. 1060. Out of Print.

Volumes 45–54, 1969–1973: JASA and Patents. Classified by subject and indexed by author and inventor. Pp. 540. Price: $20 (paperbound); ASA members $25 (clothbound); Nonmembers $60 (clothbound).

Volumes 55–64, 1974–1978: JASA and Patents. Classified by subject and indexed by author and inventor. Pp. 816. Price: $20 (paperbound); ASA members $25 (clothbound); Nonmembers $60 (clothbound).

Volumes 65–74, 1979–1983: JASA and Patents. Classified by subject and indexed by author and inventor. Pp. 624. Price: ASA members $25 (paperbound); Nonmembers $75 (clothbound).

Volumes 75–84, 1984–1988: JASA and Patents. Classified by subject and indexed by author and inventor. Pp. 625. Price: ASA members $30 (paperbound); Nonmembers $80 (clothbound).

Volumes 85–94, 1989–1993: JASA and Patents. Classified by subject and indexed by author and inventor. Pp. 736. Price: ASA members $30 (paperbound); Nonmembers $80 (clothbound).

Volumes 95–104, 1994–1998: JASA and Patents. Classified by subject and indexed by author and inventor. Pp. 632. Price: ASA members $40 (paperbound); Nonmembers $90 (clothbound).

ACOUSTICAL NEWS—INTERNATIONAL

Walter G. Mayer
Physics Department, Georgetown University, Washington, DC 20057

New Books and Monographs

The French magazine *Pour la Science*, which is a French edition of *Scientific American*, has published a special issue on Acoustics (*Pour la Science*, Dossier No. 32—Juillet/Octobre 2001). The 128 pages of the magazine contain 27 articles, ranging from two to eight pages each, covering some fascinating aspects of acoustics:

The world of sounds, by J. Kergomard
The human voice, by R. Sataloff
The songs of the Touvas, by T. Levin and M. Edgerton
The sounds of whales and dolphins, by B. Woodward
Sources of noise in the ocean, by J. Potter
The sonic boom, by F. Coulouvrat
The tuning fork, by R. Lehoucq and E. Kierlik
Sand noise, by F. Nori, P. Sholtz, and M. Bretz
The acoustic laser (or ''saser''), by J.-Y. Prieur, J. Joffrin, and M. Devaud
Biomedical ultrasonic imaging, by C. Sohn
Mapping the ocean floor, by X. Lurton, J.-M. Augustin, and M. Voisset
Underwater acoustical imaging, by M. Buckingham, J. Potter, and C. Epifanio
Underwater detection of seismic activity, by P.-F. Piserchia, F. Schindelé, and O. Hyvernaud
Atmospheric infrasounds, by A. Le Pichon
Wave propagation in the earth crust, by J.-P. Massot
Wave propagation in the sun, by R. Garcia and S. Couvidat
Picosecond acoustics, by H. Maris
Aeroacoustics, by D. Juvé and C. Bailly
Human hearing, by R. Pujol
The sonar of the bats, by N. Suga
Time reversal, by M. Fink
Shock wave and lithotripsy, by D. Cathignol
Sonoluminescence, by S. Putterman
Thermoacoustic refrigeration, by S. Garrett and S. Backhaus
Active wall materials in architectural acoustics, by H. Lissek and X. Meynial
Source localization and virtual sources, by J. Martin
Outdoor sound propagation, by J. Defrance and E. Premat.

This special issue has broad appeal. Anyone with an inquisitive mind and with some basic French reading skills will tremendously enjoy reading it.

YVES H. BERTHELOT
Mechanical Engineering Department
Georgia Institute of Technology
Atlanta, Georgia 30332-0405

International Meetings Calendar

Below are announcements of meetings to be held abroad. Entries preceded by an * are new or updated listings with full contact addresses given in parentheses. *Month/year* listings following other entries refer to meeting announcements, with full contact addresses, which were published in previous issues of the *Journal*.

June 2002

1–3 **AES 21st International Conference on Architectural Acoustics and Sound Reinforcement**, St. Petersburg. (Fax: +7 812 316 1559; Web: http://www.aes.org/events/21) *4/02*

4–6 **6th International Symposium on Transport Noise and Vibration**, St. Petersburg. (Fax: +7 812 127 9323; Web: webcenter/ru/~eeaa/tn/eng/tn2002) *2/01*

12–14 ***29th National Meeting of the Italian Acoustical Association**, Ferrara, Italy. (Fax: +39 532 73 56 66; Web: acustica.ing.unife.it/aia2002)

10–14 **Acoustics in Fisheries and Aquatic Ecology**, Montpellier. (Web: www.ices.dk/symposia) *12/00*

24–27 **6th European Conference on Underwater Acoustics**, Gdańsk. (Fax: +48 58 347 1535; Web: www.ecua2002.gda.pl/) *10/01*

24–28 **11th Symposium of the International Society for Acoustic Remote Sensing**, Rome. (Fax: +39 06 20660291; Web: ISARS2002.ifa.rm.cnr.it/) *10/01*

24–28 **11th International Symposium on Nondestructive Characterization of Materials**, Berlin. (Fax: +49 30 678 07129; Web: www.cnde.com) *2/02*

24–26 ***Dynamics of Speech Production and Perception (NATO ASI)**, Il Ciocco/Lucca, Italy. (e-mail: pdivenyi@ebire.org)

July 2002

2–5 ***8th International Conference on Auditory Display**, Kyoto, Japan. (ICAD2002, ATR Media Integration and Communication Laboratories, 2-2-2 Hikaridai, Seika-cho, Kyoto 619-0288, Japan; Fax: +81 774 95 1408; Web: www.mic.atr.co.jp/icad2002/page/welcome.html)

2–7 **ClarinetFest 2002**, Stockholm. (e-mail: kkoons@pegasus.cc.ucf.edu) *10/01*

15–17 **International Symposium on Active Control of Sound & Vibration (Active 2002)**, Southampton. (Fax: +44 23 8059 3190; Web: http://www.isvr.soton.ac.uk/active2002) *10/01*

17–21 **7th International Conference on Music Perception and Cognition (7th ICMPC)**, Sydney. (Fax: +61 2 9772 6736; Web: www.uws.edu.au/marcs/icmpc7) *2/02*

19–21 ***Auditorium Acoustics: historical and contemporary design and performance [cosponsored by ASA]**, London, UK. (Institute of Acoustics, 77A St. Peter's Street, St. Albans, Hertfortshire AL1 3BN, UK; Fax: +44 1727 850553; Web: www.ioa.org.uk/aa2002)

August 2002

19–23 **16th International Symposium on Nonlinear Acoustics (ISNA16)**, Moscow. (Fax: +7 095 126 8411; Web: acs366b.phys.msu.su/isna16/) *12/00*

26–28 **2nd Biot Conference on Poromechanics**, Grenoble. (Web: geo.hmg.inpg.fr/biot2001) *8/01*

26–28 **Joint Baltic-Nordic Acoustical Meeting 2002**, Lyngby. (Fax: +45 45 88 05 77; Web: www.dat.dtu.dk/~b-nam) *10/01*

September 2002

10–12 **32nd International Acoustical Conference—EAA Symposium**, Banská Štiavnica. (Fax: +421 45 532 1811; Web: http://alpha.tuzvo.sk/skas/acoustics) *4/02*

11 **Dutch and Belgian Acoustical Societies Joint Meeting**, Utrecht. (e-mail: info@nag-acoustics.nl) *4/02*

11–13 **10th International Meeting on Low Frequency Noise and Vibration**, York. (Fax: +44 1277 223 453; Web: http://www.lowfrequency2002.org.uk) *12/01*

16–18 **International Conference on Noise and Vibration Engineering**, Leuven. (Fax: +32 1632 2987; Web: www.isma.isaac.be) *2/02*

 0001-4966/2002/111(6)/2521/2/$19.00

16–21 **Forum Acusticum 2002 (Joint EAA-SEA-ASJ Meeting)**, Sevilla. (Fax: +34 91 411 7651; Web: www.cica.es/aliens/forum2002) *2/00*

26–28 **Autumn Meeting of the Acoustical Society of Japan**, Akita. (Fax: +81 3 5256 1022; Web: http://wwwsoc.nii.ac.jp/asj/index-e.html) *12/01*

October 2002

9–11 **Acoustics Week in Canada**, Charlottetown, PE. (Fax: +1 902 628 4359; Web: http://caa-aca.ca/PEI-2002.html) *4/02*

26–28 **6th National Congress of the Turkish Acoustical Society**, Kars. (Fax: +90 212 261 0549; Web: http://www.takder.org/kongre-2002/kongre2002.html) *4/02*

November 2002

13–15 ***Australian Acoustical Society Conference 2002**, Adelaide, Australia. (AAS 2002 Conference Secretariat, Department of Mechanical Engineering, Adelaide University, SA 5005, Australia; Fax: +61 8 303 4367; Web: www.mecheng.adelaide.edu.au/aasconf)

15–17 ***Reproduced Sound 18: Perception, Reception, Deception**, Stratford-upon-Avon, UK. (Institute of Acoustics, 77A St. Peter's Street, St. Albans, Herts AL1 3BN, UK; Fax: +44 1727 850553; Web: www.ioa.org.uk)

21–22 **New Zealand Acoustical Society 16th Biennial Conference**, Auckland. (e-mail: graham@marshallday.co.nz) *2/04*

30–6 **Joint Meeting: 9th Mexican Congress on Acoustics, 144th Meeting of the Acoustical Society of America, and 3rd Iberoamerican Congress on Acoustics**, Cancún. (Web: asa.aip.org/cancun.html) *10/00*

December 2002

9–13 **International Symposium on Musical Acoustics (ISMA Mexico City)**, Mexico City. (Fax: +52 55 5601 3210; Web: http://www.unam.mx/enmusica/ismamexico.html) *2/02*

March 2003

17–20 **German Acoustical Society Meeting (DAGA2003),** Aachen. (Fax: +49 441 798 3698; e-mail: dega@akuphysik.uni-oldenburg.de) *2/02*

18–20 ***Spring Meeting of the Acoustical Society of Japan,** Tokyo, Japan. (Acoustical Society of Japan, Nakaura 5th-Bldg., 2-18-20 Sotokanda, Chiyoda-ku, Tokyo 101-0021, Japan; Fax: +81 3 5256 1022; Web: http://wwwsoc.nii.ac.jp/asj/index-e.html)

April 2003

7–9 **WESPAC8,** Melbourne, Australia. (Web: www.wespac8.com) *10/01*

June 2003

8–13 **XVIII International Evoked Response Audiometry Study Group Symposium**, Puerto de la Cruz. (Web: www.ierasg-2003.org) *8/01*

16–18 **Acoustics—Modeling & Experimental Measurements**, Cadiz. (Fax: +44 238 029 2853; Web: www.wessex.ac.uk/conference/2003/acoustics/index.html) *4/02*

29–3 **8th Conference on Noise as a Public Health Problem**, Amsterdam-Rotterdam. (Fax: +31 24 360 1159; e-mail: office.nw@prompt.nl) *4/02*

July 2003

7–10 **10th International Congress on Sound and Vibration**, Stockholm. (Fax: +46 88 661 9125; Web: www.congex.com/icsv10) *4/02*

14–16 ***8th International Conference on Recent Advances in Structural Dynamics**, Southampton, UK. (Web: www.isvr.soton.ac.uk/sd2003)

August 2003

6–9 **Stockholm Music Acoustics Conference 2003 (SMAC03)**, Stockholm. (Web: http://www.speech.kth.se/music/smac03)

25–27 **Inter-Noise 2003**, Jeju Island, Korea. (Fax: +82 42 869 8220; Web: www.icjeju.co.kr) *4/02*

September 2003

1–4 **Eurospeech 2003**, Geneva. (Web: www.symporg.ch/eurospeech2003) *8/01*

7–10 ***World Congress on Ultrasonics**, Paris, France. (P. Laugier, Laboratoire d'Image Paramétrique, Université Paris 6, 15 rue de l'Ecole de Médecine, 75006 Paris, France; Fax: +33 1 46 33 56 73; Web: http://www.sfa.asso.fr/wcu2003)

October 2003

15–17 ***34th Spanish Congress on Acoustics**, Bilbao, Spain. (Sociedad Española de Acústica, Serrano 144, 28006 Madrid, Spain; Fax: +34 91 411 7651; Web: www.ia.csic.es/sea/index.html)

March 2004

22–26 ***Joint Congress of the French and German Acoustical Societies (SFA-DEGA)**, Strasbourg, France. (Société Française d'Acoustique, 23 avenue Brunetière, 75017 Paris, France; Fax: +49 441 798 3698; e-mail: sfa4@wanadoo.fr)

April 2004

5–9 **18th International Congress on Acoustics (ICA2004)**, Kyoto. (Web: http://www.ica2004.or.jp) *4/01*

September 2004

13–17 ***4th Iberoamerican Congress on Acoustics, 4th Iberian Congress on Acoustics, 35th Spanish Congress on Acoustics**, Guimarães, Portugal. (Sociedade Portuguesa de Acústica, Laboratório Nacional de Engenharia Civil, Avenida do Brasil 101, 1700-066 Lisboa, Portugal; Fax: +351 21 844 3028; e-mail: dsilva@lnec.pt)

ADVANCED-DEGREE DISSERTATIONS IN ACOUSTICS

Editor's Note: *Abstracts of Doctoral and Master's theses will be welcomed at all times. Please note that they must be limited to 200 words, must include the appropriate PACS classification numbers, and formatted as shown below. If sent by postal mail, note that they must be double spaced. The address for obtaining a copy of the thesis is helpful. Submit abstracts to: Acoustical Society of America, Thesis Abstracts, Suite 1N01, 2 Huntington Quadrangle, Melville, NY 11747-4502, e-mail: asa@aip.org*

Subjective evaluation of temporal fluctuation of sound source and sound field [43.55.Hy]—Junko Atagi, *Graduate School of Science and Technology, Kobe University, Kobe, Japan, September 2001 (Ph.D.).* Physical properties and subjective evaluation of the time-variant sound field were investigated. Physical properties were analyzed by the autocorrelation function (ACF). Three temporal factors are extracted from the ACF: (i) effective duration, τ_e, which is ten-percentile delay of the envelope of the ACF; (ii) the delay of the first peak of the ACF, τ_1; and (iii) its amplitude, ϕ_1. The results showed that the physical properties of the time-variant sound field are identified by τ_e and the envelope of the ACF of the sound field. Paired-comparison tests on subjective preference and perception of echo in the time-variant sound field were also conducted. It was found that the subjective preference and the perception of echo in time-variant sound field can be described by τ_e and the envelope of the ACF of the sound field. In the second part, physical properties and subjective annoyance of traffic noise were investigated. It was found that the physical properties are identified by the temporal factors τ_1 and τ_e of the traffic noise. Paired-comparison tests on subjective annoyance of the traffic noise were also conducted. It was found that the subjective annoyance is associated with the temporal factors τ_1 and τ_e of the traffic noise.

Thesis advisor: Yoichi Ando

Copies of this thesis written in English can be obtained from Junko Atagi, 6813 Mosonou, Saijo-cho, Higashi-Hiroshima 739-0024, Japan. E-mail address: atagi@urban.ne.jp.

Duration sensation in relation to the autocorrelation function of sound stimuli [43.66.Mk, 43.66.Lj]—Kazi Saifuddin, *Graduate School of Science and Technology, Kobe University, Kobe, Japan, September 2001 (Ph.D.).* Relationships were investigated between subjective judgment of physical duration and the factors extracted from the autocorrelation function (ACF) of sound stimuli. Factors of ACF were changed by using different properties of pure-tone, complex-tone, white noise and bandpass-noise stimuli. Experiments by paired-comparison method were conducted in the sound proof chamber except for one in a concert hall. Sound stimuli were selected on the basis of the measured factors of ACF as parameters. Subjects were asked to compare the durations of two stimuli in the pair. Subjective durations were obtained in the psychometric function and were interpreted as duration sensation (DS) on the basis of the auditory-brain model and the theory of primary sensation. Results ($p<0.05$) are shown as below. (1) DSs are longer with larger τ_1 (being time delay of first peak of ACF corresponding to pitch. (2) DSs are longer with higher $\Phi_{(0)}$ (being energy at the beginning of ACF). (3) DSs are longer with smaller ϕ_m (being constant amplitude of all peaks of ACF). (4) DSs are similar for pure-tone and complex-tone stimuli with same pitch.

Thesis advisor: Yoichi Ando

Copies of this thesis written in English can be obtained from Kazi Saifuddin. E-mail address: ''Kazi Saifuddin'' kazi64@hotmail.com

Perception and psychological evaluation for visual and auditory environment based on the correlation mechanisms [43.10.Nq, 43.66.Lj, 43.50.Rq]—Kenji Fujii, *Graduate School of Science and Technology, Kobe University, Kobe, Japan, March 2002 (Ph.D.).* In this dissertation, the correlation mechanism in modeling the process in the visual perception is introduced. It has been well described that the correlation mechanism is effective for describing subjective attributes in auditory perception. The main result is that it is possible to apply the correlation mechanism to the process in temporal vision and spatial vision, as well as in audition. (1) The psychophysical experiment was performed on subjective flicker rates for complex waveforms. A remarkable result is that the phenomenon of missing fundamental is found in temporal vision as analogous to the auditory pitch perception. This implies the existence of correlation mechanism in visual system. (2) For spatial vision, the autocorrelation analysis provides useful measures for describing three primary perceptual properties of visual texture: contrast, coarseness, and regularity. Another experiment showed that the degree of regularity is a salient cue for texture preference judgment. (3) In addition, the autocorrelation function (ACF) and inter-aural cross-correlation function (IACF) were applied for analysis of the temporal and spatial properties of environmental noise. It was confirmed that the acoustical properties of aircraft noise and traffic noise are well described. These analyses provided useful parameters extracted from the ACF and the IACF in assessing the subjective annoyance for noise.

Thesis advisor: Yoichi Ando

Copies of this thesis written in English can be obtained from Yoichi Ando, Graduate School of Science and Technology, Kobe University, Rokkodai, Nada, Kobe 657-8501, Japan. Phone/Fax: +81-78-803-6038. E-mail address: andoy@kobe-u.ac.jp.

Dynamic analysis, psychological and physiological evaluations of the visual environment [43.64.Bt, 43.75.Cd]—Yoshiharu Soeta, *Graduate School of Science and Technology, Kobe University, Kobe, Japan, March 2002 (Ph.D.).* Attempts are made to apply preference theory for sound fields to visual fields. To investigate how the periodical flicker and movements in vertical and horizontal directions are preferred, preference judgments were conducted by paired-comparison tests. Results show that each stimulus has each preference period. The scale value of preference is formulated approximately in terms of the $\frac{3}{2}$ power of the normalized period of stimulus. It is interesting that this formulation corresponds to that of temporal factors in sound fields. Next, relationships between the subjective preference and the factors extracted from the autocorrelation function (ACF) and the cross-correlation (CCF) of the EEG and MEG alpha waves were investigated. Remarkably, preferred stimulus shows a significantly longer effective duration of the ACF, τ_e, of the alpha waves than that of less preferred stimulus. This tendency was also found in previous studies that varied the delay time of a single sound reflection and the reverberation time of a music sound field. Also, the preferred stimulus shows a significantly greater magnitude of the CCF between the alpha waves from different locations on the brain. Thus, a similar rhythm repeats over a wider range of the brain, in both space and time, under a preferred condition.

Thesis advisor: Yoichi Ando

Copies of this thesis written in English can be obtained from Yoshiharu Soeta, Graduate School of Science and Technology, Kobe University, Rokkodai, Nada, Kobe 657-8501, Japan. E-mail address: soetay@anet.ne.jp

BOOK REVIEWS

P. L. Marston
Physics Department, Washington State University, Pullman, Washington 99164

These reviews of books and other forms of information express the opinions of the individual reviewers and are not necessarily endorsed by the Editorial Board of this Journal.

Editorial Policy: *If there is a negative review, the author of the book will be given a chance to respond to the review in this section of the Journal and the reviewer will be allowed to respond to the author's comments. [See "Book Reviews Editor's Note," J. Acoust. Soc. Am.* ***81****, 1651 (May 1987).]*

Handbook of Neural Network Signal Processing

Yu Hen Hu and Jeng-Neng Hwang, Editors

CRC Press, Boca Raton. 2001.
408 pp. Price: $129.95 (hardcover) ISBN: 0849323592.

Neural Networks have found application in solving a wide variety of signal processing problems. *Handbook of Neural Network Signal Processing* edited by Hu and Hwang aptly demonstrates the effectiveness and wide scope of the neural network paradigm for signal processing. The editors have brought together many leading experts in the neural network and signal processing fields to cover a wide variety of topics and recent developments. While many texts exist describing neural network algorithms, this book is unique in its solid coverage of neural network concepts, approaches to signal processing problems, and applications. The book consists of three parts. The first part of the book describes the various neural network paradigms. The different neural network approaches are described clearly and recent developments outlined. The second part of the book covers neural network approaches to some important signal processing problems. The final part of the book examines some successful neural network based applications and systems.

The book begins with an introductory chapter by Hu and Hwang. This chapter is well written and familiarizes the reader with the basic concepts on which the remainder of the book is built. This chapter begins with neural network architectures and theory such as the McCulloch and Pitts' neuron, Multi-Layer Perceptrons, Radial Basis Networks, Competitive Learning Networks, Committee Machines, and Support Vector Machines. Code written for MATLAB is available for download from the publisher to allow readers to experiment with the various types of neural network, and useful references to publicly available software are given. The remainder of the chapter provides background on the various problems to signal processing examined by the book and concludes with an overview of the material in each chapter.

Chapter 2 is written by Manry, Chandrasekaran, and Hsieh and describes signal processing using Multi-Layer Perceptrons (MLPs). A major consideration when implementing MLPs is how to choose the best network topology and estimate the error on unseen test data based on the performance on training data. Efficient algorithms are presented in this chapter to train MLPs as well as estimate the optimal topology of a MLP for any particular problem and bound the error expected for new test data. The algorithms presented are tested by designing and training a MLP to estimate mechanical loads on a helicopter during flight based on cockpit measurements.

In Chap. 3, Andrew Back describes Radial Basis Function (RBF) networks and presents recent advances. The chapter begins with an overview of RBF networks and then describes the theoretical capabilities. Like MLPs, RBF networks have been shown to be able to approximate any smooth nonlinear function to any desired degree of accuracy when enough neurons are used. Algorithms are presented to train RBF networks and select the most effective number of hidden units. Finally, an indication of the capabilities of RBF networks is given by examining a number of real-world applications.

In the next chapter Müller, Mika, Rätsch, Tsuda, and Schölkopf present the theory of Kernel-Based Algorithms. After describing the Vapnik-Chervonekis Theory and kernel feature spaces, the chapter moves on to supervised and unsupervised learning using Support Vector Machines (SVMs), Kernel Fisher Discriminants, and Kernel Principal Component Analysis. The choice of kernel for particular applications is examined and the chapter concludes with some applications of this class of algorithm to signal processing.

Chapter 5 is written by Volker Tresp and presents the theory behind committee machines. By merging the results of many classifiers, a committee machine can achieve performances exceeding any of its component classifiers. Tresp examines the various methods for constructing committee machines and presents in detail two examples, the Mixture of Experts and the Bayesian Committee Machine.

Jose Principe has contributed the first chapter in part two of the book. This chapter looks at how Dynamic Neural Networks can be applied to the problem of optimal signal processing. The chapter begins by formulating the problem in terms of the more general problem of function approximation and then examines how the uniform approximation properties of Dynamic Neural Networks allow them to be applied to this problem. The chapter concludes by presenting a class of generalized delay operators for optimal filtering.

Scott Douglas presents the difficult problem of Blind Source Separation and Blind Signal Deconvolution in Chap. 7. This chapter covers the basic theory, recent advances, and important applications in a manner that is both clear and interesting. The chapter concludes with a discussion of open issues.

In Chap. 8 Konstantinos Diamantaras examines various neural network architectures designed to perform Principal Component Analysis (PCA). The basic theory is presented as well as application examples and the benefits and disadvantages of the various approaches. The neural network models are then expanded to perform nonlinear PCA and applications such as blind image separation are showcased.

Chapter 9 is written by Liao, Moody, and Wu and examines the problem of predicting a complex time series using neural networks. The chapter starts with an overview of the problem and traditional approaches. The authors then describe how the time delay neural networks and recurrent neural networks have been developed to solve this problem. Recent research is presented showing how committee machines and regularization schemes for recurrent networks can improve the accuracy of the results obtained. Finally, a case study involving the prediction of economic indicators using the proposed methods is studied in detail.

The final part of the book deals with real-world application of neural networks in signal processing. The first topic considered is speech recognition. Shigeru Katagiri describes the fundamentals of the speech recognition problem before examining four approaches that remain the subject of continued research. Generalized Probabilistic Descent is examined before sections on recurrent neural networks and Support Vector Machines. The chapter concludes with a discussion of signal separation theory, essential to developing speech recognition technologies to function in noisy general environments.

Chapter 11 was contributed by Muneesawang, Wong, Lay, and Guan and describes a successful application of a radial basis function network to the problem of content-based image retrieval.

In Chap. 12, Adali, Wang, and Li look at various applications of neural networks to the field of biomedical image analysis. The chapter begins by examining the methods by which neural networks may be used for image characterization. This field is concerned with identifying and measuring different tissue types and structures in medical imagery. The second half of the

 0001-4966/2002/111(6)/2525/2/$19.00

chapter describes the problem of computer-aided diagnosis and examines neural network approaches to identifying tumors in x-ray imagery. In each section, real-world applications and results are shown to validate the theory presented.

The final chapter in the book was contributed by Taur, Kung, and Lin and introduces a decision-based neural network with application to pattern classification. The decision-based network merges concepts from modular neural networks and fuzzy logic. Numerous applications from image processing are also examined.

This book is an excellent resource for anyone interested in neural networks, both in general and the applications to signal processing. The book covers both basic theory and advanced concepts and so will be useful to the experienced and inexperienced researcher alike. The division of the book into methods, problems, and applications seems to work well and the fact that most chapters are well stocked with application examples helps greatly to understand the material. Most applications in the book revolve around image processing, however, there is sufficient material on signal separation and speech recognition to interest acousticians. In addition, much of the material in the first part of the book is relevant to many applications.

The fact that the editors have brought together many experienced researchers in the field means that most chapters are easy to read and yet the mathematical fundamentals of the methods, problems, and applications are well covered. The breadth and depth of the material covered in this book has made it difficult to adequately describe each chapter in this review. In conclusion, the label of ''Handbook'' as referred to in the title seems well deserved, as I would recommend this book to anyone interested in neural networks.

STUART W. PERRY
Aeronautical and Maritime Research Laboratory
Defence Science and Technology Organisation
PO Box 44, Pyrmont, New South Wales
Australia 2009

BOOKS RECEIVED

Computational Atmospheric Acoustics. Erik M. Salomons. Kluwer Academic, Boston, 2001. 348 pp. $109.00 *hc*. ISBN 0792371616.

Inverse Problems and Inverse Scattering of Plane Waves. Dilip N. Ghosh Roy and L. S. Couchman. Academic Press, New York, 2001. 320 pp. $75.00 *hc*. ISBN 0122818652.

Acoustic Characterization of Contrast Agents for Medical Ultrasound Imaging. Lars Hoff. Kluwer Academic, Dordrecht, The Netherlands, 2001. 230 pp. $74.00 *hc*. ISBN 1402001444.

Auditory Sound Transmission: An Autobiographical Perspective. Jozel J. Zwislocki. Erlbaum, Hillsdale, NJ, 2002. 419 pp. $99.95 *hc*. ISBN 0805806792.

Higher Order Numerical Methods for Transient Wave Equations. Gary C. Cohen. Springer, New York, 2001. 348 pp. $69.95 *hc*. ISBN 354041598X.

Transient Aeroelasticity of Spherical Bodies. A. G. Gorshkov and D. V. Tarlakovskii. Springer, New York, 2001. 250 pp. $99.00 *hc*. ISBN 3540421513.

Environmental Urban Noise. Amando Garcia, Editor. Wit, Boston, 2001. 225 pp. $136.00 *hc*. ISBN 1853127523.

Duct Aeroacoustics: From Technological Applications to the Flute. Sylvia Dequand. Technische Universiteit-Eindhoven, Eindhoven, 2000. 203 pp. Price not available. ISBN 90-386-1889-1 *pb*.

Design of Knock Sensors and Piezoaccelerometers. Alexander A. Bazhenov and Valery I. Yarovikov. Futurepast, Inc., Arlington, VA, 2002. 176 pp. $115.00 *hc*. ISBN 0971046409.

The Intelligent Ear. Reinier Plomp. Erlbaum, Hillsdale, NJ, 2001. 174 pp. $39.95 *hc*. ISBN 0805838678.

Listening to Nineteenth-Century America. Mark M. Smith. University of North Carolina Press, Chapel Hill, NC, 2001. 368 pp. $55.00 *hc*. ($19.95 *pb*.). ISBN 080782657X *hc*. (0807849820 *pb*.).

The Virtual Score: Representation, Retrieval, Restoration. Walter B. Hewlett and Eleanor Selfridge-Field, Editors. MIT Press, Cambridge, MA, 2001. 291 pp. $28.00 *pb*. ISBN 0262582090.

Advanced Signal Processing Handbook. Stergios Stergiopoulos, Editor. CRC Press, New York, 2000. 752 pp. $99.95 *hc*. ISBN 0849336910.

Statistical Quality Control. M. Jeya Chandra. CRC Press, Boca Raton, FL, 2001. 284 pp. $89.95 *hc*. ISBN 0849323479.

Handbook of Multisensor Data Fusion. David L. Hall and James Llinas, Editors. CRC Press, Boca Raton, FL, 2001. 568 pp. $159.95 *hc*. ISBN 0849323797.

Continuous Signals and Systems with MATLAB. Taan S. Elali and Mohammad A. Karim. CRC Press, Boca Raton, FL, 2001. 544 pp. $89.95 *hc*. ISBN 0849303214.

Filter Design with Time Domain Mask Constraints: Theory and Applications. Ba-Ngu Vo, Antonio Cantoni, and Kok Lay Teo. Kluwer Academic, Boston, 2001. 350 pp. $136.00 *hc*. ISBN 0792371380.

Handbook of Neural Network Signal Processing. Yu Hen Hu and Jeng-Neng Hwang, Editors. CRC Press, New York, 2001. 408 pp. $129.95 *hc*. ISBN 0849323592.

Wavelets in Signal and Image Analysis: From Theory to Practice. Arthur A. Petrosian and Francois G. Meyer, Editors. Kluwer Academic, Dordrecht, The Netherlands, 2001. 543 pp. $143.00 *hc*. ISBN 1402000537.

REVIEWS OF ACOUSTICAL PATENTS

Lloyd Rice
11222 Flatiron Drive, Lafayette, Colorado 80026

The purpose of these acoustical patent reviews is to provide enough information for a Journal reader to decide whether to seek more information from the patent itself. Any opinions expressed here are those of reviewers as individuals and are not legal opinions. Printed copies of United States Patents may be ordered at $3.00 each from the Commissioner of Patents and Trademarks, Washington, DC 20231. Patents are available via the Internet at http://www.uspto.gov.

Reviewers for this issue:

GEORGE L. AUGSPURGER, *Perception, Incorporated, Box 39536, Los Angeles, California 90039*
MARK KAHRS, *Department of Electrical Engineering, University of Pittsburgh, 348 Benedum Hall, Pittsburgh, Pennsylvania 15261*
DAVID PREVES, *4 Deerfield Drive, Princeton Junction, New Jersey 08550*
DANIEL R. RAICHEL, *2727 Moore Lane, Fort Collins, Colorado 80526*
CARL J. ROSENBERG, *Acentech, Incorporated, 33 Moulton Street, Cambridge, Massachusetts 02138*
KEVIN P. SHEPHERD, *Mail Stop 463, NASA Langley Research Center, Hampton, Virginia 23681*
WILLIAM THOMPSON, JR., *Pennsylvania State University, University Park, Pennsylvania 16802*
ERIC E. UNGAR, *Acentech, Incorporated, 33 Moulton Street, Cambridge, Massachusetts 02138*

6,317,388

43.30.Nb THERMOACOUSTIC BI-STATIC SONAR SYSTEM

Harvey C. Woodsum *et al.*, assignors to Lockheed Martin Corporation
13 November 2001 (Class 367/131); filed 28 June 1982

A laser or particle accelerator **13** mounted in aircraft **11** produces a pulsed electromagnetic or ion beam **14** directed at the surface of the water **15**. Sound **17** is produced in the water either by thermal expansion or explosive vaporization of the small volume of water upon which the beam is incident. Echoes **16** from a target are subsequently received by a series of sonabouys **19**.—WT

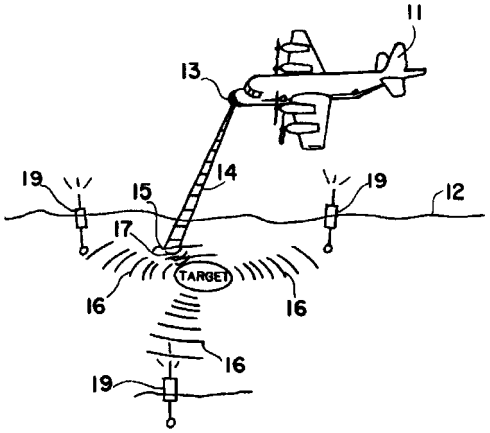

6,327,220

43.30.Tg SONAR LOCATION MONITOR

Benjamin K. Miller, Jr. *et al.*, assignors to Johnson Engineering Corporation
4 December 2001 (Class 367/134); filed 15 September 1999

The object of this patent is to provide a system for detecting and quickly locating swimmers who are at risk of drowning in, for example, a pool, lake, or water park, based on preset limits of such factors as time and depth. Each such swimmer wears a small electronic package that assesses the extent of danger and emits an ultrasonic alarm signal when these preset limits are exceeded. Thereupon, an audible or visual alarm is activated at the water's surface. The swimmer's location is tracked in real time and displayed on monitors by processing the ultrasonic alarm signal as received at a series of hydrophones positioned around the periphery of the swimming area.—WT

6,314,811

43.30.Yj ACOUSTIC SENSOR MODULE DESIGN AND FABRICATION PROCESS

Eric Lee Goldner and Joseph Scott Salinas, assignors to Litton Systems, Incorporated
13 November 2001 (Class 73/570); filed 24 January 2000

This patent describes the design of a sensor module and an associated two-part rubber shell that sandwiches several of the sensor modules so as to create a blanket structure for mounting on the hull of a surface ship or submarine. The inner details of sensor module **20** are not described. Items **110** and **120** are rubber sheets with molded bosses **130** and **140** as well as shoulder boss **140′**, all of whose positions are determined with high-dimensional precision in order to accurately locate the sensors **20**. The

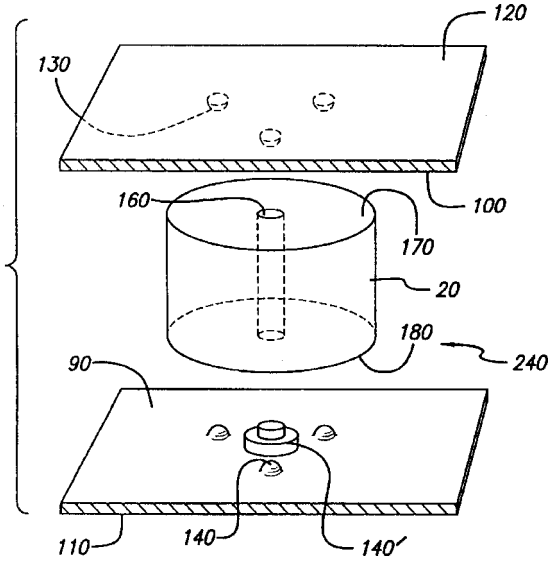

 0001-4966/2002/111(6)/2527/13/$19.00

shoulder boss **140′** is shaped to join with opening **160** in each sensor module. The upper and lower annular faces **170** and **180** of each sensor module may contain hemispherical depressions to mate with the bosses **130** and **140**. The space between the rubber sheets not occupied by sensor modules is filled with an acoustically transparent urethane. The telemetry connections between the sensor modules are accomplished within that space prior to the urethane encapsulation.—WT

6,322,527

43.35.Wa APPARATUS FOR ULTRASONIC BONE TREATMENT

Roger J. Talish, assignor to Exogen, Incorporated
27 November 2001 (Class 601/2); filed 18 April 1997

This apparatus is a portable ''strap-on'' device intended for therapeutic treatment of injuries through ultrasound application. It includes a transducer

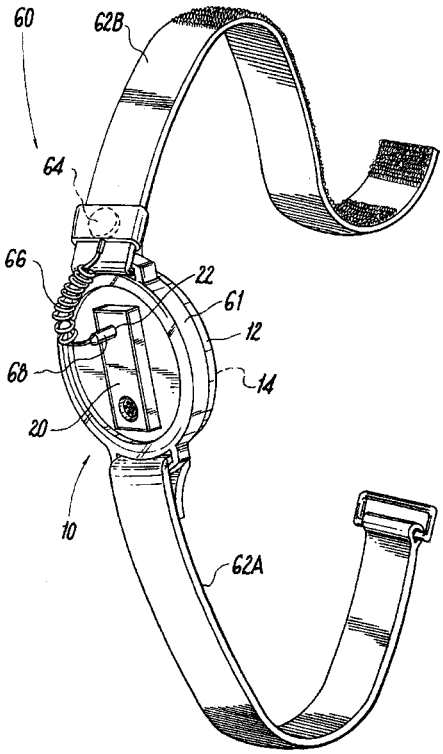

and an integrated circuit unit which generates a driving signal for the transducer. During operation, the signal generator drives the transducer to emit therapeutic ultrasound.—DRR

6,311,558

43.35.Yb ULTRASONIC STRAIN GAGE USING A MOTORIZED ELECTROMAGNETIC ACOUSTIC TRANSDUCER

Alfred V. Clark *et al.*, assignors to the United States of America as represented by the Secretary of Commerce
6 November 2001 (Class 73/643); filed 23 March 1998

This strain gage is intended for the measurement of plane stress in such metallic components as rolled plates of steel or aluminum. In such components the velocities of SH-waves polarized in the direction of rolling generally exceed that of such waves polarized in the transverse direction. The characteristics of these waves change as stress is applied, and the changes are used to evaluate the stress. The device described in this patent consists of a small-aperture electro-magnetic acoustic transducer (EMAT) that is rotated automatically about an axis perpendicular to the plate being investigated. The birefringence of the induced waves is measured as a function of the angle of rotation, and the resulting data are used to determine the strain.—EEU

6,315,731

43.35.Yb ULTRASONIC DIAGNOSTIC APPARATUS CAPABLE OF FUNCTIONAL ADDITION

Yoshiyuki Okuno and Masahiko Gondoh, assignors to Olympus Optical Company, Limited
13 November 2001 (Class 600/459); filed in Japan 31 March 1999

This ultrasonic diagnostic apparatus obtains a biogenic tomogram by irradiating an ultrasonic pulse *in vivo* and receiving a reflecting wave from a biogenic tissue. The mechanical scanning system consists of an ultrasonic transducer unit and a personal computer. The computer controls a motor-driving circuit which rotates the ultrasonic transducer, controls the transmitting/receiving module, and performs digital signal processing of the ultrasonic echo signal.—DRR

6,315,741

43.35.Yb METHOD AND APPARATUS FOR MEDICAL PROCEDURES USING HIGH-INTENSITY FOCUSED ULTRASOUND

Roy W. Martin, Seattle, Washington *et al.*
13 November 2001 (Class 601/3); filed 31 October 1997

The purpose of this apparatus is to enable substantially bloodless surgery and for stemming hemorrhaging. High-intensity focused ultrasound (HIFU) is used to form cauterized tissue regions prior to surgical incision, e.g., forming a cauterized tissue shell around a tumor to be removed. This procedure is referred to as ''presurgical volume cauterization.'' For one embodiment, this method is supposed to be particularly effective for use in surgical lesion removal or resection of tissue having a highly vascularized constitution, such as the liver or spleen, which have a high propensity for hemorrhaging. In other embodiments, the methods and apparatus for hemostasis using HIFU should be useful for surgical, presurgical, and medical emergency situations. In an apparatus embodiment, a telescoping acoustic coupling provides for an adjustable depth of focus of the HIFU energy. Yet other embodiments include apparatus designed for portability, useful for emergency medical situations.—DRR

6,319,204

43.35.Yb ULTRASONIC METHOD FOR INDICATING A RATE OF PERFUSION

George A. Brock-Fisher and Mckee D. Poland, both of Andover, Massachusetts
20 November 2001 (Class 600/458); filed 26 January 2000

This method for control of an ultrasonic system produces images to indicate the rate of perfusion in a region of interest (ROI) of an anatomical area. A contrast agent introduced into the ROI provides an ultrasonic image for a specific instant. That image is processed to identify regions of the ROI that include the contrast agent. Thereafter, an attribute, such as a color, is assigned to the region of the ROI which includes the contrast agent. The ROI is imaged again after a discrete time interval and a second color is assigned to identify regions of the ROI that include the contrast agent but have not previously been assigned a color. This process is repeated a number of times, with each successive region of the ROI that manifests the presence of the contrast agent being assigned a still different color. An image of the ROI is then displayed, enabling the user to determine from the progression of the colors across the image the rate and type of perfusion that occurs in the ROI.—DRR

6,322,505

43.35.Yb MEDICAL DIAGNOSTIC ULTRASOUND SYSTEM AND METHOD FOR POST PROCESSING

John A. Hossack *et al.*, assignors to Acuson Corporation
27 November 2001 (Class 600/437); filed 8 June 1999

In this system ultrasonic data is generated by a receive beamformer. An ultrasound image is computed by a process in which some of the steps may be reversed. For example, persistence processing may be reversed to obtain ultrasound data associated with data prior to persistence processing. This recovered data may be used to generate an image showing no persistence effects or the data may be reprocessed with a different amount of persistence. Other processes that may be reversed to recover ultrasound data include focal and depth gain compensation, dynamic range compression, intensity or color mapping, and various filtering, such as spatial or persistence filtering.—DRR

6,322,507

43.35.Yb ULTRASONIC APPARATUS AND METHOD FOR EVALUATION OF BONE TISSUE

Garri Passi *et al.*, assignors to Medson Limited
27 November 2001 (Class 600/437); filed 25 October 1998

This system for ultrasonic imaging of bone tissue uses a wide-band scanning crystal that emits an ultrasonic signal with multiple full waves into the bone tissue and a second wide-scanning receiver crystal. The transmission frequency is progressively decreased until the number of full waves in the received signal equals that of the transmitted signal, defining an upper frequency limit. The number of full waves in the transmitted signal is then gradually increased until the received signal contains at least two consecutive full waves of equal amplitude, defining a lower frequency limit. The resultant transmission signal is then used to measure signal attenuation and velocity in bone tissue, in terms of standard bone imaging techniques. Bone tissue images are derived from ultrasonic frequency spectra and the difference between upper and lower frequency limits.—DRR

6,322,509

43.35.Yb METHOD AND APPARATUS FOR AUTOMATIC SETTING OF SAMPLE GATE IN PULSED DOPPLER ULTRASOUND IMAGING

Lihong Pan *et al.*, assignors to GE Medical Systems Global Technology Company, LLC
27 November 2001 (Class 600/443); filed 1 May 2000

This patent relates to the methods for positioning the gate or sample volume in medical diagnostic ultrasound imaging. Here the apparatus automatically initializes and adjusts the Doppler sample gate position and size settings based on actual vessel data. A vessel segment search method employs an object search technique based solely on geometric and morphological information in a digitized vessel image obtained from either B-mode or color flow image data. The morphologically best or nearest vessel segment within a search region in the two-dimensional image is found. The sample gate is placed at or near the center of the targeted vessel segment. The sample gate size is adjusted relative to the vessel size, and then the optimum available steering angle that minimizes the Doppler angle is selected.—DRR

6,315,727

43.35.Yb METHOD AND APPARATUS FOR ULTRASOUND CORNEAL SCANNING

D. Jackson Coleman *et al.*, assignors to Cornell Research Foundation, Incorporated
13 November 2001 (Class 600/452); filed 29 September 1999

The objective of this apparatus is to provide high-frequency ultrasonic scanning of the human cornea while immersed in a liquid transmission medium (e.g., a balanced saline solution). Prior devices required the patient to lie supine while a dam to retain the solution was attached around the eyes. This approach has the subject sit and lean forward over the device. The eye

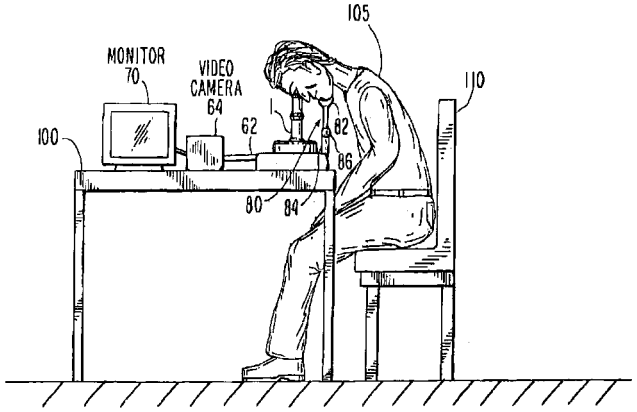

is positioned downward into a cup of solution which contains the ultrasound scanner and a video camera to monitor for correct alignment. Ultrasound waves are transmitted through the liquid medium to achieve the corneal scan. It is intended that the setup of the apparatus would be more comfortable and less stressful for the patient.—DRR

6,315,728

43.35.Yb ULTRASOUND COLOR FLOW ADAPTIVE SCANNING TECHNIQUES

David John Muzilla and Theodore Lauer Rhyne, assignors to General Electric Company
13 November 2001 (Class 600/454); filed 21 December 1999

The preferred embodiment for this fluid flow evaluation technique is designed to lessen the amount of processing and digital memory that are required to produce a color flow image of an entire range of interest. The typical ultrasound system usually interleaves B-mode imaging with color flow imaging. Flow vectors formed over the entire region of interest (ROI) for every acoustic frame are incorporated in several interleaved groups

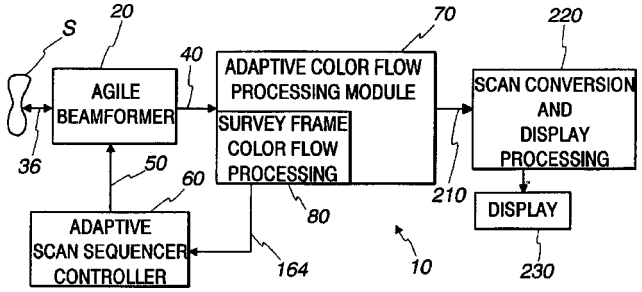

across the ROI. Each vector position in the color field of the ROI is displayed. In this embodiment, an ultrasound survey frame determines the portions representing fluid flow. A beam source again rescans only the portions in which fluid flow occurs. Target frames then are created from the rescan and provide a color flow image restricted to the portions of the survey frame in which fluid flow exists.—DRR

6,318,179

43.35.Yb ULTRASOUND BASED QUANTITATIVE MOTION MEASUREMENT USING SPECKLE SIZE ESTIMATION

James D. Hamilton *et al.*, assignors to GE Medical Systems Global Technology Company, LLC
20 November 2001 (Class 73/606); filed 20 June 2000

This measurement procedure determines the relative movement in a ''first direction'' **F1** of one material, such as blood flow **R1**, and another material, e.g., an arterial wall **8**, in a subject **S** under study. A beam of ultrasonic waves defining a plurality of beam positions and beam axes is

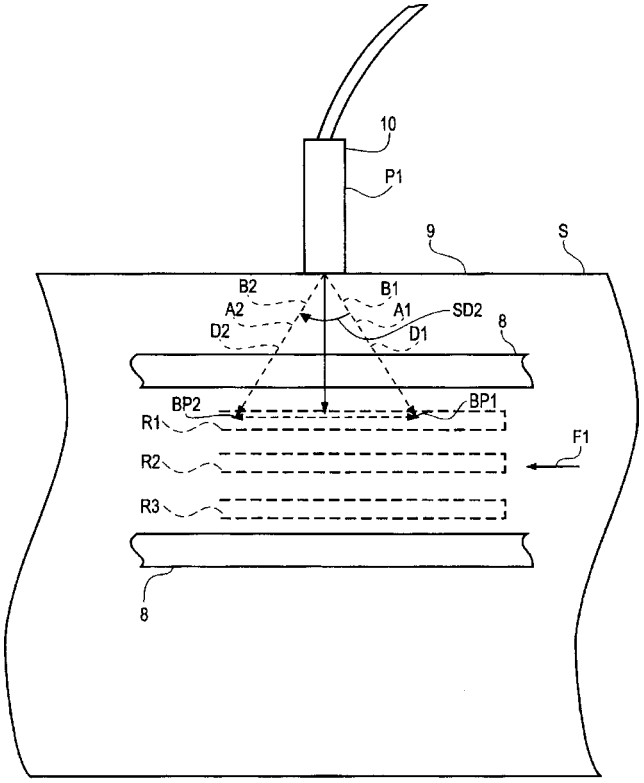

moved in scan directions having components parallel to direction **F1**. Blocks of data representing the two materials are generated. A speckle-size analysis of the first data set and an analysis of the second data set yield a measurement of the relative movement of the two materials.—DRR

6,322,506

43.35.Yb INCLINATION ANGLE DETECTING DEVICE FOR AN ULTRASOUND PROBE

Hiroshi Nagai *et al.*, assignors to Nihon Kohden Corporation
27 November 2001 (Class 600/437); filed in Japan 16 July 1998

This device provides a means of positioning an ultrasound probe to obtain three-dimensional images. To detect the probe's inclination angle, a rotating reference arm **6** is attached near the contact area **1a**. The reference arm can be pressed in a direction away from the probe and a detection unit

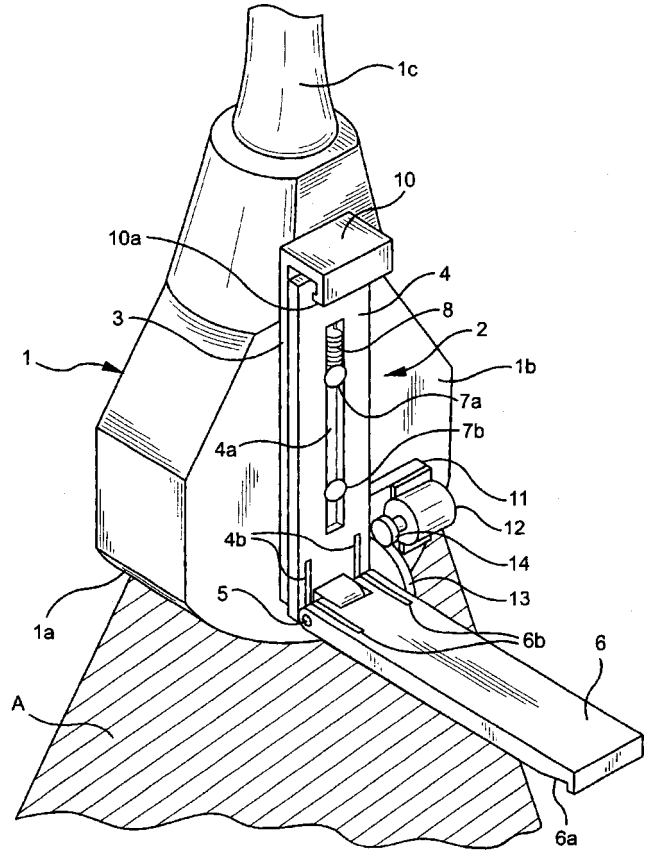

12 measures the rotation of the arm. Placing the probe against the surface of the body causes the arm to be rotated and pressed into close contact with the surface of the body. The amount of rotation indicates the inclination angle.—DRR

6,324,289

43.35.Yb PICK-UP HEAD FOR AN ELECTRONIC STETHOSCOPE

Birger Orten, assignor to Meditron A/S
27 November 2001 (Class 381/67); filed in Norway 16 November 1995

This stethoscope pick-up head incorporates an acousto-electric transducer that converts sound vibrations into electrical signals and a sound-shaping bell arranged around a slim peg bonded directly to the transducer.

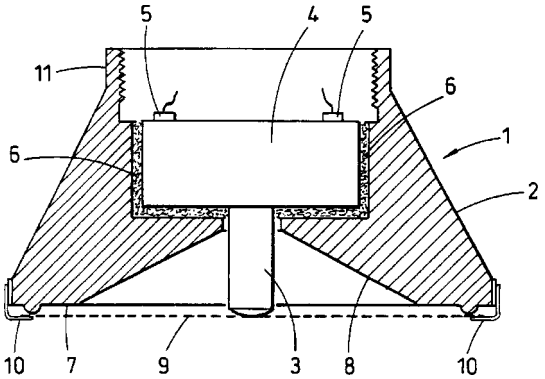

The sound-influencing bell delimits a listening area on the body surface and, by a combination of internal reflection and/or absorption, affects the direct sound picked up by the peg. The bell is acoustically decoupled from the center peg.—DRR

6,310,429

43.38.Ar ACOUSTIC WAVE TRANSDUCER DEVICE

Andre John Van Schyndel, assignor to Nortel Networks Limited
30 October 2001 (Class 310/367); filed 18 May 1998

The transducer described in this patent consists of a strip of a material, such as polyvinylide fluoride (PVDF), which responds electrically to acoustic waves. The width of the strip varies along its length, so that the voltage signal produced by this sheet represents a convolution of the incident acoustic wave and the strip's width function. A signal processor, in whose memory the width function is stored, deconvolves the voltage signal to retrieve the acoustic signal. This device is claimed to provide better signal-to-noise and directional characteristics than more conventional transducers.—EEU

6,304,434

43.38.Ja PORTABLE COMPUTER WITH BOTH DYNAMIC AND PIEZOELECTRIC TRANSDUCERS

Mitchell A. Markow, assignor to Compaq Computer Corporation
16 October 2001 (Class 361/683); filed 28 May 1998

For enhanced stereo sound from a laptop computer, piezoelectric drivers vibrate the display shell to generate rear-directed sound. These can be augmented by a second pair of electrodynamic speakers to provide front image localization.—GLA

6,304,661

43.38.Ja LOUDSPEAKERS COMPRISING PANEL-FORM ACOUSTIC RADIATING ELEMENTS

Henry Azima *et al.*, assignors to New Transducers Limited
16 October 2001 (Class 381/152); filed in the United Kingdom 2 September 1995

It is common commercial practice to mount a panel form loudspeaker in a rectangular frame and support its edges with a resilient suspension. In this case, the concept is applied to a particular kind of panel form speaker already covered by several earlier patents. Whatever novelty the design possesses is buried in impenetrable legal phrases such as ''...selected values of certain physical parameters.''—GLA

6,310,958

43.38.Ja SOUND-PRODUCING ARRANGEMENT FOR A MOTOR VEHICLE

Viktor Eisner, assignor to Volkswagen AG
30 October 2001 (Class 381/86); filed in Germany 24 April 1997

Automobile manufacturers try to utilize every square inch of passenger space. Even a miniaturized subwoofer requires volume that could otherwise be used for more important things like cup holders or map lights. There may be unused space outside the trunk or passenger compartment, but it is ''wet'' space. The patent suggests that the loudspeaker can be mounted in a waterproof compartment which transmits sound to the passenger area through watertight tubes. ''In an especially advantageous arrangement, the bass speaker is located in a bumper...since bumpers have a relatively large unused volume.''—GLA

6,307,947

43.38.Ja LOW PROFILE SPEAKER ENCLOSURE

David Wiener, Park City, Utah
23 October 2001 (Class 381/386); filed 1 March 2000

Loudspeaker **14** is mounted in shallow box **10** which includes relatively long vent **42**. That's it. Twenty-two patent claims were granted.—GLA

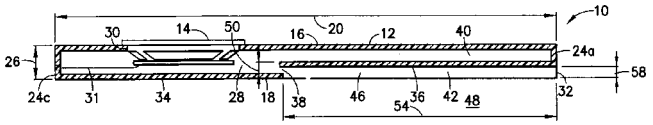

6,310,959

43.38.Ja TUNED ORDER CROSSOVER NETWORK FOR ELECTRO-ACOUSTIC LOUDSPEAKERS

Eric Alexander, assignor to Diaural, LLC
30 October 2001 (Class 381/99); filed 24 August 1999

This circuit merits the Wishful Wizard award for 2002. Tweeter **52** and woofer **54** are simply connected in parallel across the output of network **48**.

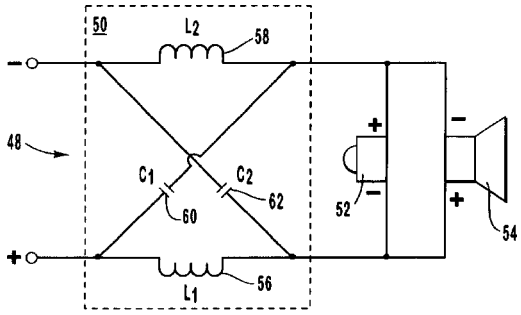

''Such parallel coupling enables both transducers to retain commonality and phase with the specific signals passing therethrough.''—GLA

6,314,191

43.38.Ja FIREPLACE ACCESSORY

Mignon J. Smith, Mesa, Arizona
6 November 2001 (Class 381/160); filed 20 July 2000

Think of a winter fire: the sizzling and popping of the wood, the smell of the pine...But what to do if you have a gas or electric fire? The patent proposes putting a sound chip in an artificial log and reflecting the sound off the fireplace back. The device also dispenses pine scent.—MK

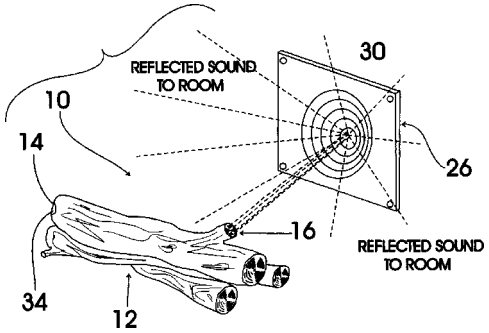

6,307,942

43.38.Kb PANEL-FORM MICROPHONES

Henry Azima *et al.*, assignors to New Transducers Limited
23 October 2001 (Class 381/152); filed in the United Kingdom 2 September 1995

A multi-resonant panel, when fitted with one or more vibration pick-ups, can function as a microphone. The patent is clearly written and includes useful information about the construction of such a device.—GLA

6,263,154

43.38.Md MULTIPLE USER RECORDING SYSTEM

Robert G. Scheffler, assignor to Broadbus Technologies, Incorporated
17 July 2001 (Class 386/96); filed 6 January 1987

Although originally filed in 1987, this patent was not issued until last year. It describes a re-recording system for producing custom recordings from a library of existing recordings. The technology described was standard for the early 1980s but is of little use in a current design.—MK

6,292,854

43.38.Md METHOD AND APPARATUS FOR PROVIDING HIGH QUALITY AUDIO IN A COMPUTER SYSTEM

Curtis Priem, assignor to Nvidia Corporation
18 September 2001 (Class 710/22); filed 14 April 1995

One reason for the creation of the cache in the IBM 360/85 circa 1965 was to reduce traffic on the main computer bus. Well, if you put a cache on a sound card, you can achieve the same result!—MK

6,286,973

43.38.Md COMBINATION FLASHLIGHT AND AUDIO RECORDER ASSEMBLY

Wallace Jackson Thrower, Pinehurst, North Carolina
11 September 2001 (Class 362/86); filed 28 February 2000

Police on the beat might need a combination audio recorder and a

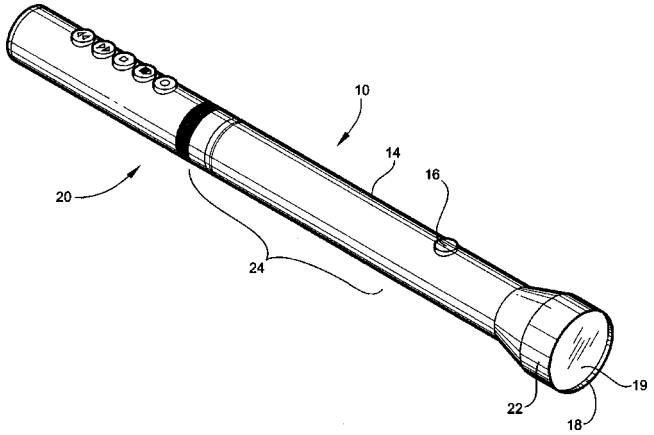

flashlight. As such, this patent exactly fits that bill. Microphone placement at the opposite end of the light might not be optimal.—MK

6,269,065

43.38.Ne RECORDING MEDIUM AND RECORDING/REPRODUCTION APPARATUS THEREOF

Yasuhiro Ogura and Ayataka Nishio, assignors to Sony Corporation
31 July 2001 (Class 369/94); filed in Japan 9 August 1995

Sony and Philips teamed up to create the Compact Disk. Now, they have collaborated to create the Super Audio Compact Disk (SACD) for storage of the Direct Stream Digital (DSD) format. The DSD format is the

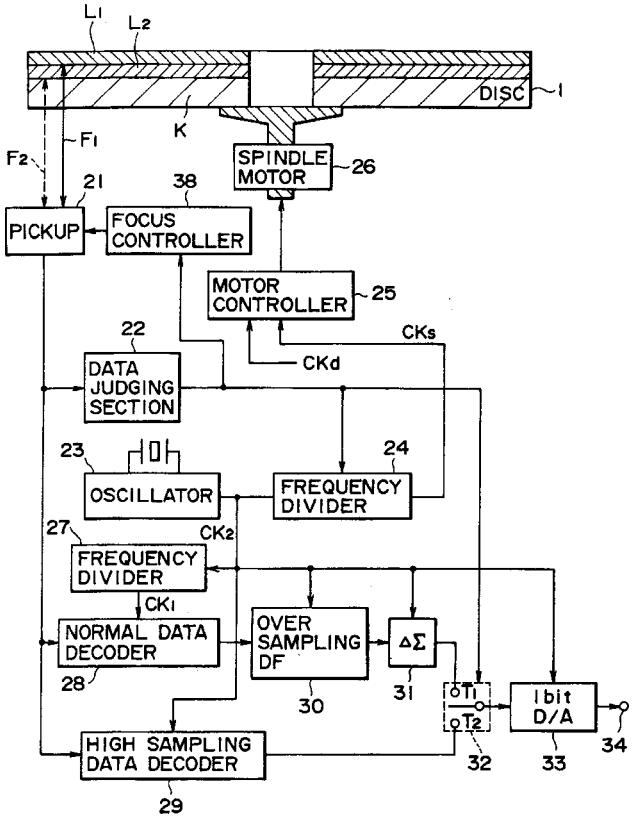

delta-sigma bit stream, stored at 2.824 Mhz. This patent describes the SACD disk, with particular attention to the compatability with existing CD players. Compatability is maintained by addition of a second layer that is not read by existing CD players.—MK

6,320,821

43.38.Pf FLUIDBORNE SOUND PROJECTOR

Jeffrey S. Goldring *et al.*, assignors to the United States of America as represented by the Secretary of the Navy
20 November 2001 (Class 367/143); filed 27 April 2000

A projector assembly for generating fluidborne acoustical waves within a tubular waveguide is described. An electromechanical shaker unit longitudinally vibrates a piston located at one end of the tubular waveguide. The piston is housed within a pressure-sealed chamber to which gas and liquid are applied or vented, on opposite faces of the piston, to automatically balance pressures and regulate the piston position. The maximum displacement of the piston is also mechanically limited by snubbers to prevent damage.—WT

6,317,389

43.38.Rh ULTRASOUND-SIGNAL RADIATING DEVICE

Kohji Toda, Yokosuka, Japan
13 November 2001 (Class 367/164); filed 21 April 2000

A SAW device features two sets of interdigital electrodes **2** and **3** on one face of a piezoelectric substrate **1** that function as input terminals and another set **4** that functions only as an output terminal. The region on the opposite face of the substrate near terminal sets **2** and **4** is shielded from the water medium in contact with that face by cap **5** that encloses a volume of air. An input electrical signal to electrode set **2** generates a wave in the substrate which is nonradiative because of the cap. However, this wave is detected by output terminal set **4**. The output signal is amplified and a part

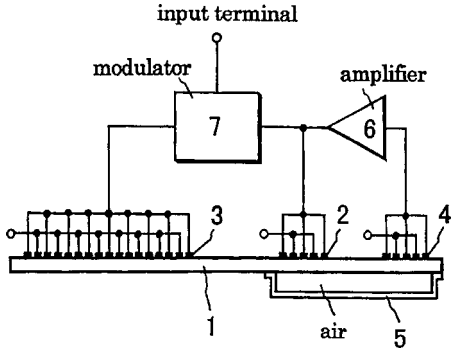

of it is fed back to input terminals **2** and the rest to a modulator **7** which amplitude modulates this original carrier signal by some other signal applied at the indicated input terminal. This AM signal is then input to the second set of output electrodes **3** wherein a second wave is excited in the piezoelectric substrate which does effectively radiate into the medium in contact with this portion of the substrate. The possibility of a second set of output interdigital electrodes near input set **3** (not shown) that would respond to echoes generated by scatterers in the medium is discussed.—WT

6,307,943

43.38.Si ELECTRO-ACOUSTIC TRANSDUCER AND HOUSING

Makoto Yamagishi, assignor to Sony Corporation
23 October 2001 (Class 381/312); filed in Japan 30 September 1989

The device is a kind of two-way semi-phone that not only produces sound from a source **2** close to the user's ear but also conducts sound into

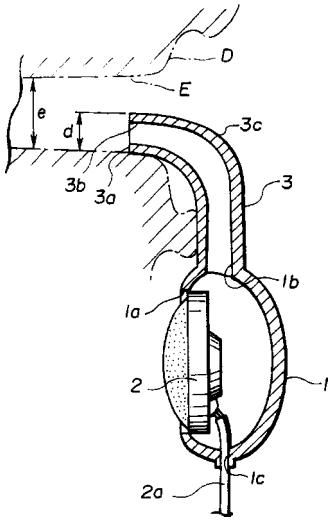

the ear through tube **3**. The sound conducting tube is smaller than the ear canal so that it does not block external sounds.—GLA

6,307,941

43.38.Vk SYSTEM AND METHOD FOR LOCALIZATION OF VIRTUAL SOUND

Theodore Calhoun Tanner, Jr. and James Patrick Lester III, assignors to Desper Products, Incorporated
23 October 2001 (Class 381/17); filed 15 July 1997

Interaural crosstalk cancellation has previously been used to improve the stereo imaging of two-channel program material reproduced by two separated loudspeakers. The technique has the unfortunate side effect of making a restricted sweet spot even smaller. The patent describes a method of ''modulating'' crosstalk cancellation to provide improved virtual sound images.—GL

6,301,968

43.40.Yq VIBRATION MEASUREMENT METHOD AND APPARATUS

Tetsuro Maruyama and Akiyoshi Ohno, assignors to Suzuki Motor Corporation
16 October 2001 (Class 73/657); filed in Japan 30 October 1998

A laser beam of a first wavelength is applied to the object whose vibration is to be measured. A beat wave is generated between a beam from a second laser with a different wavelength and the return beam from the first laser. The beat wave then is processed to provide the desired vibration information.—EEU

6,311,557

43.40.Yq MAGNETICALLY TUNABLE RESONANCE FREQUENCY BEAM UTILIZING A STRESS-SENSITIVE FILM

J. Kenneth Davis *et al.*, assignors to UT-Battelle, LLC
6 November 2001 (Class 73/514.31); filed 24 September 1999

An array of cantilever ferro-magnetic beam elements is used to measure vibrations at the resonant frequencies of these elements. In order to make these elements tunable, so that different frequencies can be measured, the beam elements are provided with a coating whose stiffness varies with the stress to which they are subjected. An adjustable magnetic field is used to deflect the beam elements statically, thus changing their effective stiffnesses, and correspondingly their natural frequencies. It is claimed that appropriate arrays may be made by micro-machining or semiconductor manufacturing methods.—EEU

6,311,559

43.40.Yq VIBRATION MEASUREMENT METHOD AND APPARATUS

Tetsuro Maruyama and Akiyoshi Ohno, assignors to Suzuki Motor Corporation
6 November 2001 (Class 73/655); filed in Japan 31 March 1998

This patent pertains to a laser Doppler velocimeter. The accuracy of the measurements is improved by processing the data by use of various alternative algorithms so as to define more precisely the point at which the slopes of the observed waves change sign.—EEU

6,275,590

43.50.Ed ENGINE NOISE SIMULATING NOVELTY DEVICE

Robert S. Prus, Seabrook, Texas
14 August 2001 (Class 381/61); filed 17 September 1998

As if it weren't noisy enough inside a vehicle, this patent proposes adding additional engine noise for different models. Now you too can have the roar of a Ferrari inside your compact car without having to imagine it.—MK

6,290,557

43.50.Gf EXHAUST SYSTEM FOR JET PROPULSION BOAT

Noboru Yokoya, assignor to Honda Giken Kogyo Kabushiki Kaisha
18 September 2001 (Class 440/89); filed in Japan 29 March 1999

An exhaust system for a jet propulsion boat (a jet ski) consists of two mufflers, arranged in series, which connect to the water jet nozzle. In contrast to a conventional design, this geometrical arrangement prevents water from entering the muffler, thus avoiding a resultant reduction in volume and subsequent degradation of acoustical performance.—KPS

6,296,074

43.50.Gf NOISE REDUCING EXHAUST SYSTEM AND METHOD

Charles W. Ridlen, Decatur, Illinois
2 October 2001 (Class 181/272); filed 19 November 1998

A ''time warp'' method of reducing exhaust noise from an internal combustion engine consists of splitting the gas stream **21** into two equal

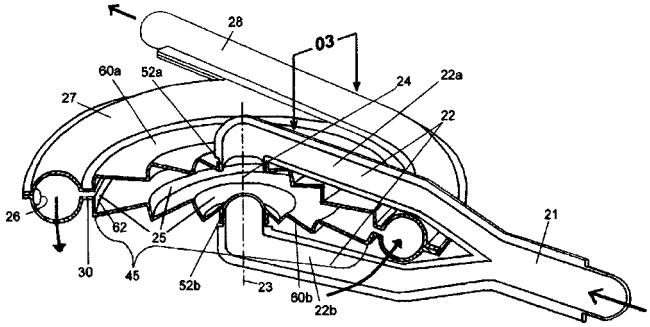

parts **22a** and **22b**. Parabolic reflectors **25** serve to reflect the acoustic disturbances toward point **24**, where destructive interference is supposed to occur. A combination of these reflectors and path length differences for the two exhaust streams is said to reduce radiated noise while minimizing backpressure.—KPS

6,302,235

43.50.Gf HIGH-PERFORMANCE MUFFLER

Carson J. Matherne, Pierre Part, Louisiana
16 October 2001 (Class 181/268); filed 3 March 2000

An automobile muffler has inlet **4** and exhaust **10** and various baffles.

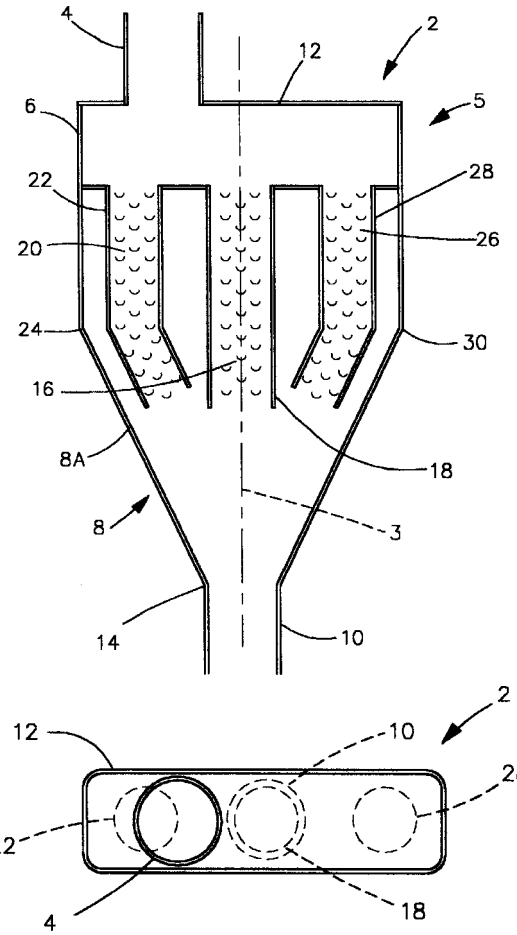

This tapered design is said to reduce heat transmission to the engine and provide a ''pleasant, deep sound.''—KPS

6,308,799

43.50.Gf INTEGRATED MUFFLER-BUMPER SYSTEM

George A. Konstantakopoulos, assignor to DaimlerChrysler Corporation
30 October 2001 (Class 181/282); filed 18 May 2000

An integrated muffler and rear bumper for an automobile consists of inlet **16** and multiple flow paths and connected cavities running the length of the bumper. Provision is also made for incorporation of sound-absorbing

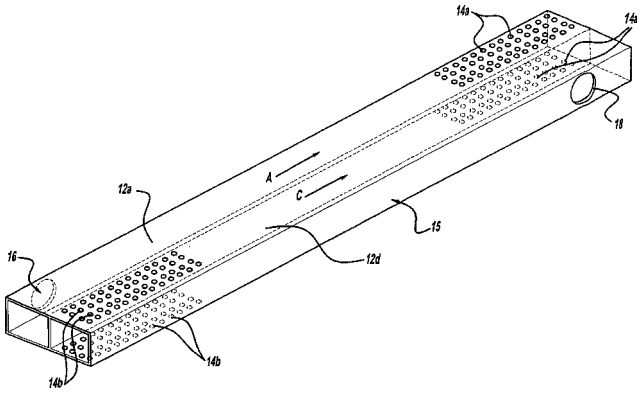

material and active control techniques. The primary motivation for this design appears to be reduction of parts count and ease of automobile assembly, but potential acoustical benefits would seem to be significant.—KPS

6,312,650

43.50.Gf SILENCER

Svend Frederiksen *et al.*, assignors to Silentor Holding A/S
6 November 2001 (Class 422/180); filed in Denmark 15 May 1996

A combination muffler/catalytic converter primarily aimed at diesel engines consists of two parallel flow paths. Exhaust gases flow through filters **5**, reverse flow direction into annulus **7**, and flow through diffuser **9**

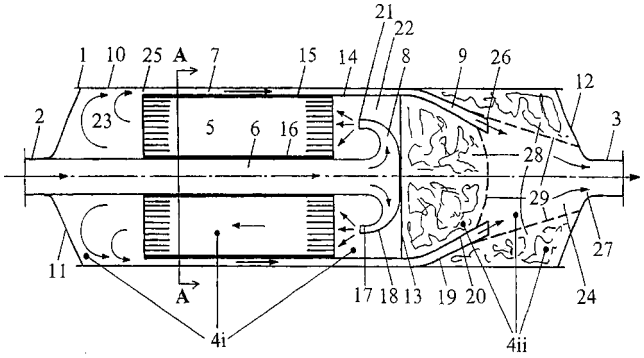

adjacent to sound absorbing material **28**. The subvolumes of this muffler configuration, along with long lengths obtained though flow reversals, allow for a relatively compact design. Extensive construction details are provided as well as several alternative geometrical variations.—KPS

6,296,202

43.50.Nm AIRCRAFT WEAPONS BAY ACOUSTIC SUPPRESSION APPARATUS

Michael J. Stanek, assignor to the United States of America as represented by the Secretary of the Air Force
2 October 2001 (Class 244/1 N); filed 9 February 2000

Flow-induced cavity resonances can yield high-amplitude acoustic oscillations that can damage the contents of the cavity, an example being a military aircraft's weapons bay. A method that seeks to control this acoustic resonance consists of a plate **12** which is placed close to the leading edge of

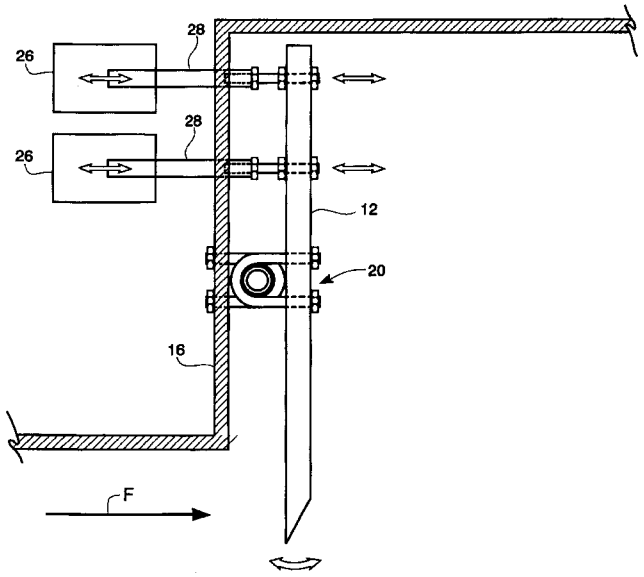

the cavity **16**. Electromagnetic actuators **26** drive the plate in order to generate large-amplitude, high-frequency disturbances that interfere with flow instabilities in the shear layer near the cavity's leading edge. Several geometrical arrangements are described, but little information is provided on selection of appropriate control signals.—KPS

6,290,022

43.55.Ev SOUND ABSORBER FOR SOUND WAVES

Franz Josef Wolf *et al.*, assignors to Woco Franz-Josef Wolf & Company
18 September 2001 (Class 181/292); filed in Germany 5 February 1998

This sheet absorber has cavities to absorb sound in the manner of Helmholtz resonators, for use in motor vehicle construction. The particular design uses differently tuned chambers on one side of the panel so as to obtain a broadband absorptive performance.—CJR

6,297,176

43.55.Ev NON-FIBERGLASS SOUND ABSORBING MOLDABLE THERMOPLASTIC STRUCTURE

John M. North and Michael P. Albert, assignors to Harodite Industries, Incorporated
2 October 2001 (Class 442/120); filed 15 July 1998

As a moldable headliner for use in motor vehicles, this product uses a laminate of fibrous batts and stiffening mats that are made of mono-filament polyester (not a glass fiber).—CJR

6,305,495

43.55.Ev SURFACING PANELS FOR ACOUSTICAL CEILING SYSTEMS

Terence M. Keegan, assignor to Capaul Corporation
23 October 2001 (Class 181/290); filed 2 November 1999

This panel is used to provide a new decorative face over older damaged acoustical tiles. The surface is made of a flexible porous mat.—CJR

6,290,021

43.55.Rg METHOD OF MANUFACTURING A SANDWICH BOARD AND A SOUND INSULATING STRUCTURE

Christian Strandgaard, assignor to Sika AG, vorm. Kaspar Winkler & Company
18 September 2001 (Class 181/290); filed 9 October 1997

This sandwich construction has a core of an elastic vibration deadening mass that joins the outer parallel plates. At least one through opening is provided in each of the outer plates with the purposes of permitting escape of any trapped air and of permitting inspection of the space between the structural layers.—CJR

6,263,620

43.55.Ti SOUNDPROOF HANGAR FOR AIRPLANES

Thomas J. Meyer, assignor to G+H Montage GmbH
24 July 2001 (Class 52/64); filed in Germany 13 August 1996

This invention concerns a soundproof hangar for airplanes. To provide noise reduction at the open side, there is a series of adjustable deflecting angled surfaces. These deflecting surfaces have sound-absorbing properties.—CJR

6,297,818

43.58.Jq GRAPHICAL USER INTERFACE HAVING SOUND EFFECTS FOR OPERATING CONTROL ELEMENTS AND DRAGGING OBJECTS

Robert Ulrich and Arlo Rose, assignors to Apple Computer, Incorporated
2 October 2001 (Class 345/326); filed 8 May 1998

Why not annoy the computer user by creating sounds when you drag and drop with the mouse? Unfortunately, the patent doesn't mention how to turn it off.—MK

6,298,990

43.58.Wc CONTAINER WITH SOUND CHIP

Barbara J. Amrod *et al.*, assignors to Kraft Foods Holdings, Incorporated; Graphic Packaging Corporation
9 October 2001 (Class 206/459.1); filed 6 September 2000

Those minds at Kraft Foods won't stop at making junk food—they

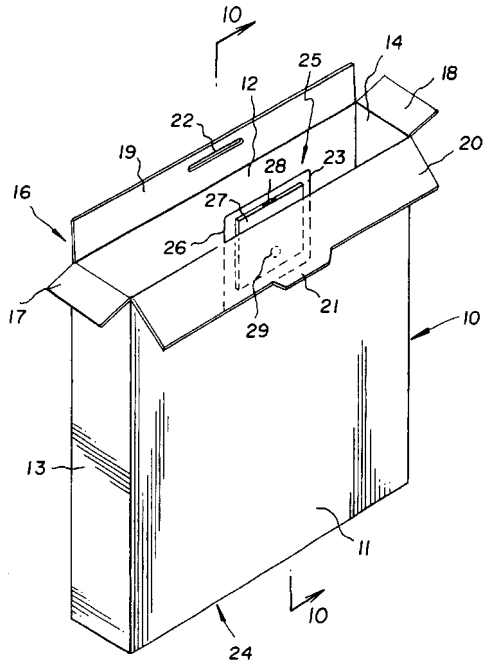

want sound effects when you open the box. Maybe it'll replace the sound of the cookie jar top?—MK

6,308,114

43.60.Bf ROBOT APPARATUS FOR DETECTING DIRECTION OF SOUND SOURCE TO MOVE TO SOUND SOURCE AND METHOD FOR OPERATING THE SAME

In-Kwang Kim and Dongjak-Ku, Seoul, the Republic of Korea
23 October 2001 (Class 700/245); filed in the Republic of Korea 20 April 1999

An illustrative example of the subject of this patent might be a robotic household appliance, such as a vacuum cleaner, which could find a charging station and move to it. A sound signal generator that has a specific pattern is provided at the position to be approached. The robot is fitted with three or more sound receivers and a unit that detects phase differences between the received signals. A controller uses this information to determine the location of the sound source and to cause the robot to move toward it.—EEU

6,317,703

43.60.Cg SEPARATION OF A MIXTURE OF ACOUSTIC SOURCES INTO ITS COMPONENTS

Ralph Linsker, assignor to International Business Machines Corporation
13 November 2001 (Class 702/190); filed 12 November 1996

This system for the isolation of the acoustic signal from a particular, single source out of a composite acoustic signal makes use of the direction-of-arrival information as recovered from an array of microphones. Each microphone signal is processed by a bank of filters, such as Gaussian log-Gabor filters. The kurtosis of the filter outputs tends to characterize the independent sources, from which source-specific properties, such as phase, delay interval, and gain, are recovered. This information is processed by a ''comparison unit,'' which recovers a selected acoustic source signal.—DLR

6,320,969

43.66.Ts HEARING AID WITH AUDIBLE ALARM

Mead C. Killion, assignor to Etymotic Research, Incorporated
20 November 2001 (Class 381/323); filed 29 September 1989

A low battery detection circuit generates an audible output signal from a hearing aid when the battery voltage falls below a predetermined level. Once initiated, the audible signal progressively increases in level and in frequency as the battery voltage continues to fall. The circuitry is said to require a minimal amount of additional size and current drain from the battery.—DAP

6,327,370

43.66.Ts HEARING AID HAVING PLURAL MICROPHONES AND A MICROPHONE SWITCHING SYSTEM

Mead Killion *et al.*, assignors to Etymotic Research, Incorporated
4 December 2001 (Class 381/313); filed 13 April 1993

A first-order or second-order directional microphone system is described in which the wearer may manually switch or the circuit automatically switches between omnidirectional and directional operating modes. Automatic switching from omnidirectional to a first-order directional mode occurs when the ambient noise exceeds a moderate preset level, and may optionally switch to a second-order directional mode if the ambient noise level exceeds a high preset level. Automatic switching is made gradual via a fader circuit resulting in an output containing the summed signals from up to three microphones. The low frequency gain loss due to directionality is at least partially compensated for by equalization circuitry.—DAP

6,324,291

43.66.Ts HEAD-WORN HEARING AID WITH SUPPRESSION OF OSCILLATIONS AFFECTING THE AMPLIFIER AND TRANSMISSION STAGE

Tom Weidner, assignor to Siemens Audiologische Technik GmbH
27 November 2001 (Class 381/322); filed in Germany 10 June 1998

A formed elastic material lies against the hearing aid amplifier assembly and fills the remaining interior space in a behind-the-ear hearing aid case assembly. The elastic material holds the amplifier assembly and other com-

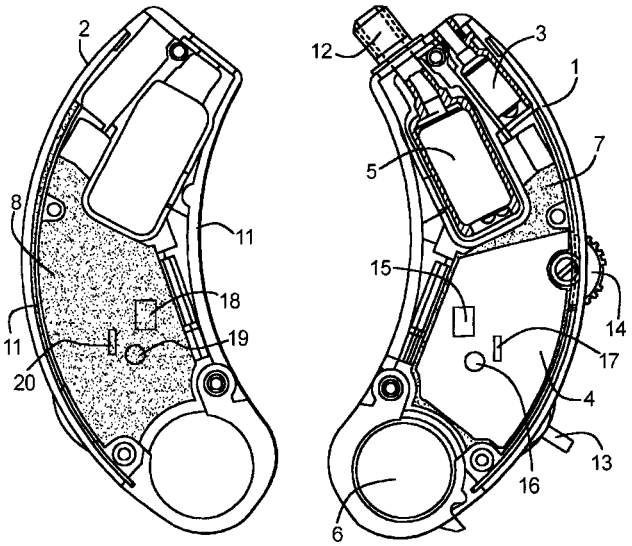

ponents in place so as to prevent them from producing self-resonant or externally excited vibrations which can result in distortion of the hearing aid signal processing.—DAP

6,319,207

43.66.Yw INTERNET PLATFORM WITH SCREENING TEST FOR HEARING LOSS AND FOR PROVIDING RELATED HEALTH SERVICES

Sharmala Naidoo, Bern, Switzerland
20 November 2001 (Class 600/559); filed 13 March 2000

Hearing loss screening is implemented over the internet by using short duration level differences, frequency differences, or duration differences. Calibration is achieved by utilizing the differences in abilities between persons with normal-hearing and persons with hearing loss to detect small level differences, small frequency differences, and small duration differences. For example, one such test is based on the theory that persons with normal hearing may not be able to detect a short-duration 1-dB increase in intensity, whereas persons with sensorineural hearing loss will be able to detect this change.—DAP

6,322,521

43.66.Yw METHOD AND SYSTEM FOR ON-LINE HEARING EXAMINATION AND CORRECTION

Zezhang Hou, assignor to Audia Technology, Incorporated
27 November 2001 (Class 600/559); filed 24 January 2000

Testing for hearing loss, sound customization for hearing loss, and simulation of hearing loss are done on-line. Calibration for hearing loss testing is accomplished by obtaining reference levels using a reference subject with normal hearing or with known hearing loss. Compensation for hearing loss and hearing loss simulation are done by manipulating an audio sound file at a remote site or at the local computer.—DAP

6,324,337

43.72.Ew AUDIO SPEED SEARCH

Eric P. Goldwasser, Yorktown Heights, New York
27 November 2001 (Class 386/75); filed 1 August 1997

Using audio time compression (not specified), you can search an audio/video steam during fast forward. Therefore, ''the listener can listen for key words that will identify the subject matter while listening to the audio at many times the normal rate.''—MK

6,314,401

43.72.Fx MOBILE VOICE VERIFICATION SYSTEM

Stephen T. Abbe *et al.*, assignors to New York State Technology Enterprise Corporation
6 November 2001 (Class 704/273); filed 29 May 1998

This voice verification system would be used at a border-crossing check station to allow rapid acceptance of preapproved travelers. The user would speak into a special handset and then aim the unit at an infrared

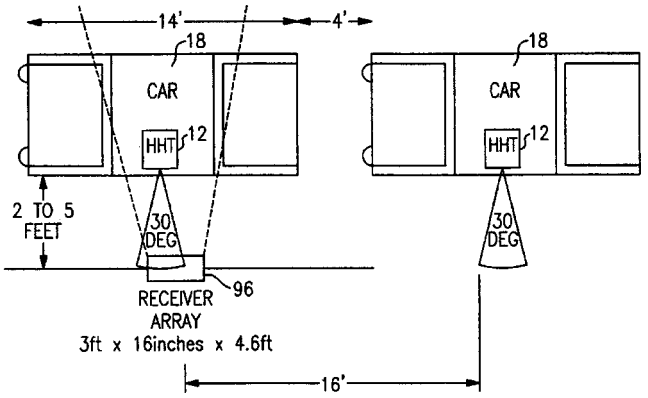

collector at the border station. In the figure, ''HHT'' is the hand-held infrared transmitter. The patent is almost entirely concerned with the mechanics of transmitting the signal and barely mentions the voice verification technology.—DLR

6,313,765

43.72.Gy METHOD FOR SAMPLE RATE CONVERSION OF DIGITAL DATA

Lyndon M. Keefer, assignor to L-3 Communications Corporation
6 November 2001 (Class 341/61); filed 10 October 1997

It seems that some modern would-be inventors (or maybe the patent examiners) have not studied mathematics. The 18th-century technique known as first-order Lagrangian interpolation describes this sample rate conversion method. Following the interpolation, the new samples are compressed according to standard mu-law principles.—DLR

6,308,156

43.72.Ja MICROSEGMENT-BASED SPEECH-SYNTHESIS PROCESS

William Barry *et al.*, assignors to G Data Software GmbH
23 October 2001 (Class 704/268); filed in Germany 14 March 1996

This speech synthesizer constructs the output signal by concatenation of stored microsegments, meaning relatively small portions of the phonetic units of speech. The argument is made, for example, that the transition into a consonant closure is relatively independent of the manner of articulation, being primarily dependent on the place of articulation. The center portions of consonants are generally kept intact. Vowels are represented by vowel halves and semivowel halves along with various quasi-stationary units which may be inserted as needed. The general principle is that a microsegment can be reused in a variety of contexts. The method is said to reduce the memory for a given language to less than one megabyte.—DLR

6,315,631

43.72.Ja METHOD OF GENERATING DUAL TRACK SOUNDS FOR AN ELECTRONIC TOY

Ralph Beckman *et al.*, assignors to Design Lab, LLC
13 November 2001 (Class 446/297); filed 18 June 1999

One problem with mechanical toys is that they don't know when to be quiet. Even if you clamp the mouth, they'll soldier on. This patent proposes the use of force feedback, which induces the sound generator to hum instead of sing when the mouth is closed.—MK

6,282,154

43.72.Ne PORTABLE HANDS-FREE DIGITAL VOICE RECORDING AND TRANSCRIPTION DEVICE

Howarlene S. Webb, Wakefield, Rhode Island
28 August 2001 (Class 369/25); filed 2 November 1998

Many professions require transcription. This patent proposes a dictation machine that can be offloaded to another machine for automatic speech recognition (ASR). No details are provided for either the recorder or the ASR algorithms.—MK

6,296,489

43.72.Ne SYSTEM FOR SOUND FILE RECORDING, ANALYSIS, AND ARCHIVING VIA THE INTERNET FOR LANGUAGE TRAINING AND OTHER APPLICATIONS

Laurie J. Blass and Pamela H. Elder, assignors to Heuristix
2 October 2001 (Class 434/185); filed 23 June 1999

The patent proposes a system for language learning by recording and comparing student responses against a master. While this seems like a reasonable concept, no details are given about the critical comparison algorithm.—MK

6,326,532

43.75.Tv HARMONICA HAVING REED VIBRATION CONVERSION CAPABILITY AND ASSOCIATED RETROFITTING METHOD

James F. Antaki, Pittsburgh, Pennsylvania
4 December 2001 (Class 84/377); filed 2 December 1999

Why not use the diatonic harmonica as an electronic instrument? Just

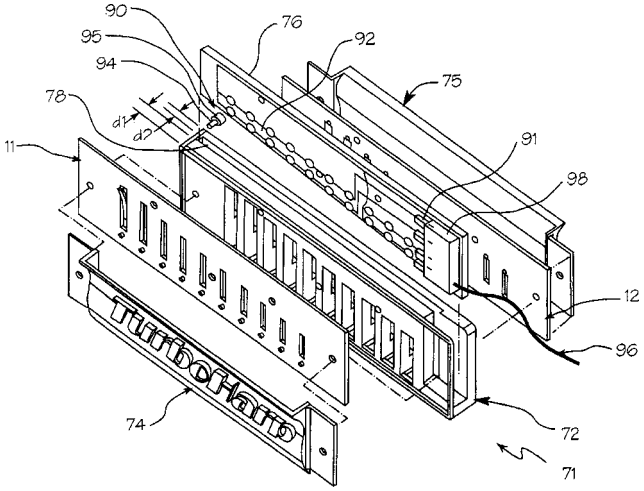

install the new circuit board with sensors **76** and away you go!—MK

6,259,015

43.75.Wx ACOUSTIC SIGNAL PRODUCING APPARATUS

Makoto Takahashi *et al.*, assignors to Yamaha Corporation
10 July 2001 (Class 84/626); filed in Japan 10 August 1994

This patent gives a vague description of a digital karaoke machine. No algorithms are given and the hardware and software architecture are sketched.—MK

6,281,423

43.75.Wx TONE GENERATION METHOD BASED ON COMBINATION OF WAVE PARTS AND TONE-GENERATING-DATA RECORDING METHOD AND APPARATUS

Masahiro Shimizu and Hideo Suzuki, assignors to Yamaha Corporation
28 August 2001 (Class 84/622); filed in Japan 27 September 1999

A sound can be decomposed into the time domain waveform, pitch, amplitude, and frequency. These waveforms can be stored and edited and the patent describes the details of doing so. Synthesis algorithms are not included.—MK

6,284,965

43.75.Wx PHYSICAL MODEL MUSICAL TONE SYNTHESIS SYSTEM EMPLOYING TRUNCATED RECURSIVE FILTERS

Julius O. Smith III and Maarten Van Walstijn, assignors to Staccato Systems, Incorporated
4 September 2001 (Class 84/661); filed 19 May 1998

In waveguide modeling an acoustic instrument with a conical bell, the scattering junction will result in an unstable pole. This can be modeled with a long FIR filter, but the computation time is excessive. The patent describes the use of a truncated IIR filter for the bell. The patent also describes a state switching method to avoid unstable behavior due to roundoff. The patent includes detailed C++ code.—MK

6,292,791

43.75.Wx METHOD AND APPARATUS OF SYNTHESIZING PLUCKED STRING INSTRUMENTS USING RECURRENT NEURAL NETWORKS

Wen-yu Su *et al.*, assignors to Industrial Technology Research Institute
18 September 2001 (Class 706/23); filed 27 February 1998

Given a digital waveguide filter of a musical instrument, one question is how to set the scattering parameters at the waveguide junctions. This patent proposes using trainable neural networks to set these parameters.—MK

6,313,388

43.75.Wx DEVICE FOR ADDING FLUCTUATION AND METHOD FOR ADDING FLUCTUATION TO AN ELECTRONIC SOUND APPARATUS

Takashi Suzuki, assignor to Kawai Musical Instruments Manufacturing Company, Limited
6 November 2001 (Class 84/622); filed in Japan 25 December 1998

Adding AM (tremolo) and FM (vibrato) to stored samples should be a well-described art by now. This patent manages 37 claims to the contrary.—MK

6,325,020

43.80.Ev FISH SIZING SONAR SYSTEM

Jacques Y. Guigne and Thomas J. McKeever, assignors to Guigne International, Limited
4 December 2001 (Class 119/215); filed 28 October 1999

A narrow beam of high-frequency (100 to 600 kHz) acoustic energy insonifies a fish tank. The resulting echoes are analyzed to provide an estimate of the size (length and thickness) of the fish.—WT

Articulation index predictions for hearing-impaired listeners with and without cochlear dead regions[a] (L)

Christine M. Rankovic[b]
Articulation Incorporated, 36 Hampshire Street, 2nd Floor, Cambridge, Massachusetts 02139

(Received 19 October 2001; accepted for publication 19 March 2002)

Vickers, Moore, and Baer [J. Acoust. Soc. Am. **110**, 1164–1175 (2001)] reported that hearing-impaired subjects with cochlear ''dead regions'' benefited from amplification of frequencies up to an octave above the estimated edge frequency of the dead region, but not beyond, whereas hearing-impaired subjects without dead regions did show benefit beyond this boundary. Dead regions are thought to have no functioning inner hair cells. Vickers *et al.* indicated that a clinical test for detecting dead regions would provide supplementary information that is important for hearing aid fitting. Furthermore, they suggested that the articulation index (AI) may overestimate the potential benefit of amplification for listeners with dead regions because the AI does not account for the presence of dead regions. To evaluate their claims, we conducted an AI analysis [H. Fletcher, *Speech and Hearing in Communication* (Van Nostrand, New York, 1953); H. Fletcher and R. H. Galt, J. Acoust. Soc. Am. **22**, 89–151 (1950)]. Results show that the AI is generally accurate in predicting the consonant recognition test scores of Vickers *et al.*'s subjects irrespective of the presence/absence of dead regions. This suggests that audiogram differences account for the observed performance differences; it was not necessary to invoke dead regions to explain the speech test results. The results of the AI analysis are sufficiently accurate to call in to question whether a clinical test for dead regions would offer additional predictive information. [DOI: 10.1121/1.1476922]

PACS numbers: 43.66.Ba, 43.66.Ts, 43.71.Ky [MRL]

I. INTRODUCTION

In their recent report, Vickers *et al.* (2001) warn that commonly used versions of the articulation index (AI) may overestimate the benefit to intelligibility from hearing aids for individuals with sensorineural hearing loss who show evidence of cochlear ''dead regions.'' Dead regions are defined as regions without functioning inner hair cells. Their presence and location are deduced from psychoacoustical tests such as those described by Moore *et al.* (2000). Vickers *et al.*'s caution about AI usage is based on the idea that audiometric pure-tone thresholds (the input to the AI calculation) do not reflect the limited ability of dead regions to process suprathreshold speech components.

To exploit the AI for hearing aid fitting and design, it is important to determine whether listeners who exhibit dead regions constitute an exceptional case and, if so, attempt to repair the AI calculation. The AI framework is worth maintaining because it predicts performance on speech recognition tests from the audiogram taken together with a physical description of the listening channel (speech intensity, frequency-gain characteristics, noise spectrum); no other tool has this capability. The purpose of this letter is to analyze Vickers *et al.*'s data using the Fletcher AI (Fletcher, 1953; Fletcher and Galt, 1950). The Fletcher AI calculation differs from less complicated, more familiar versions in that it accounts for short- and long-term average speech intensity-level effects, loudness, spectral imbalance, and other factors that contribute significantly to speech sound recognition. Rankovic (1997, 1998) reported that the Fletcher AI resolves prediction errors noted by researchers who used simpler versions of the calculation. This preliminary success motivated the choice of the Fletcher AI over other versions for the present analysis.

II. METHODS

Two groups of subjects with high-frequency sensorineural hearing loss participated in the Vickers *et al.* study: a group of seven subjects who exhibited dead regions and a group of three subjects who did not exhibit dead regions. Vickers *et al.* presented subjects with lists of vowel–consonant–vowel nonsense disyllables (VCVs) that were low-pass filtered with various cutoff frequencies. Prior to low-pass filtering, the VCVs were amplified uniquely for each subject according to the ''Cambridge'' formula (Moore and Glasberg, 1998) in an effort to provide audible speech across the entire speech spectrum (up to 7.5 kHz). Filter cutoff frequencies were selected to introduce incremental amounts of the amplified high-frequency speech spectrum into the dead region. For subjects *with* dead regions, Vickers *et al.* found that VCV test scores increased with cutoff frequency until the cutoff exceeded the dead region boundary by a factor of ''about 1.7'' [see Vickers *et al.* (2001), p. 1168] at which point further increases were minimal or lacking. In contrast, subjects *without* dead regions showed progressively increasing scores with increasing speech spectrum bandwidth. Based on this performance difference, they concluded that a special clinical test is necessary to identify listeners

[a]Submitted as Letter to the Editor.
[b]Electronic mail: rankovic@world.std.com

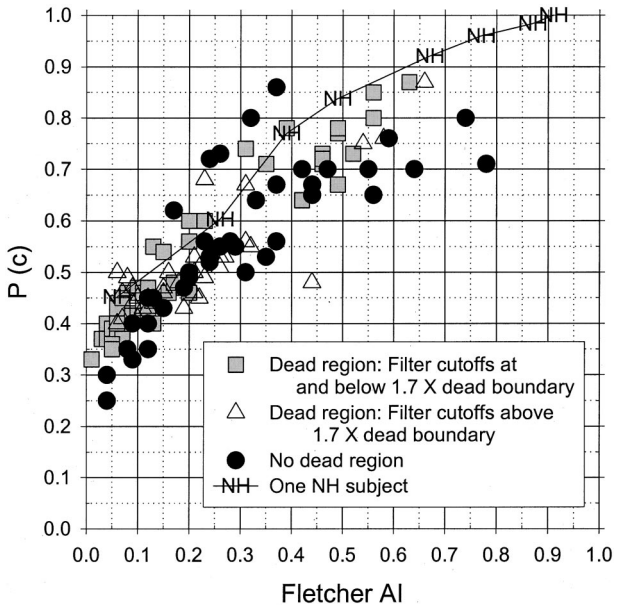

FIG. 1. Consonant recognition test scores $[P(c)]$ and AIs for all test conditions for the two hearing-impaired subject groups, and for one normal-hearing subject. Across-subject variability for $P(c)$'s is similar to that reported by Rankovic (1997, 1998). The normal-hearing subject was tested with speech at the nominal level that was then low-pass filtered with cutoff frequencies ranging from 0.5 to 7.5 kHz.

with dead regions in order to avoid superfluous high-frequency hearing aid amplification that may drive hearing aids to distortion, cause acoustic feedback, or otherwise reduce speech intelligibility.

Vickers *et al.* provide enough experimental detail to derive input values for an AI analysis. These values are the audiogram, the nominal speech intensity level, and the frequency-gain characteristic. Here, AIs are calculated for all conditions for all of their subjects. Hearing thresholds that exceeded audiometer limits were assigned a value 5 dB higher than the upper limits of a typical audiometer. As in other studies by this author (Rankovic, 1997, 1998), Fletcher's calculation was not modified in any way to account for peculiarities that have been associated with sensorineural hearing loss in psychoacoustical experiments [see Moore (1995) for a review of these phenomena].

III. RESULTS AND DISCUSSION

Figure 1 provides the AIs and consonant recognition scores [plotted as proportion correct, $P(c)$] for Vickers *et al.*'s data. There are no clear differences in the accuracy of predictions for the two hearing-impaired subject groups. For listeners *with* dead regions, data points from conditions with filter cutoffs above 1.7 times the dead region boundary (triangles) do not distinguish themselves from the rest of the data.

In Fig. 1, a slope of roughly 1.0 describes how $P(c)$ increases with AI for the VCV speech test materials. Vickers *et al.* provided us with the $P(c)$'s collected from one normal-hearing listener, and those data, too, exhibit a slope of roughly 1.0 over the AI range of interest. The slope of 1.0 indicates that any change in AI should be associated with a

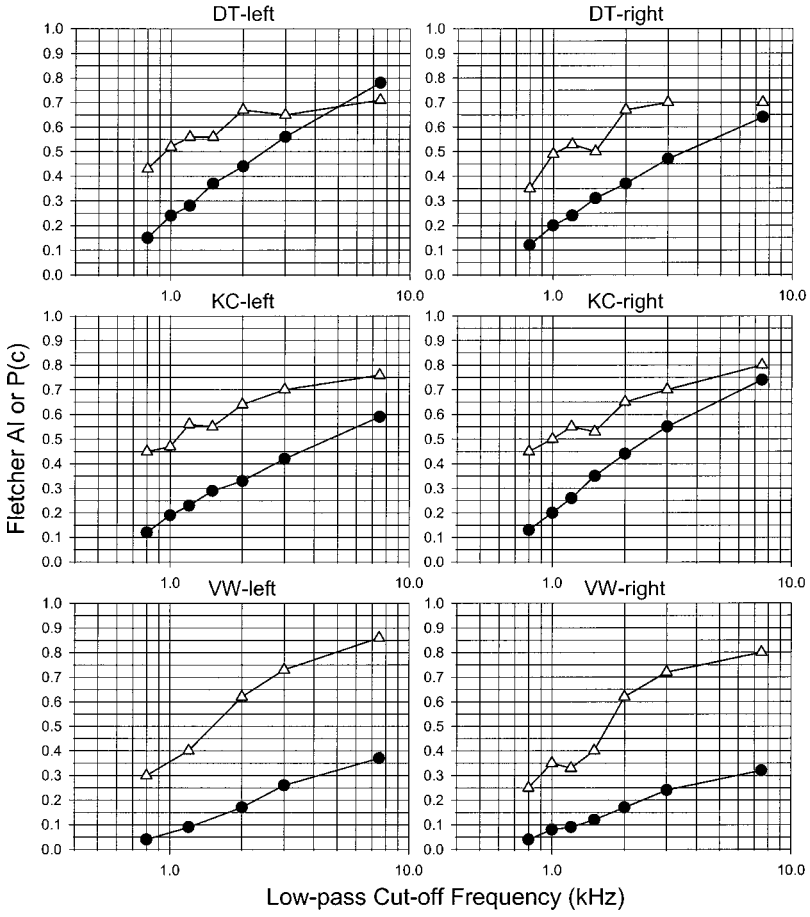

FIG. 2. Results for six ears *without* dead regions. Triangles indicate $P(c)$'s. Circles indicate AIs for corresponding conditions.

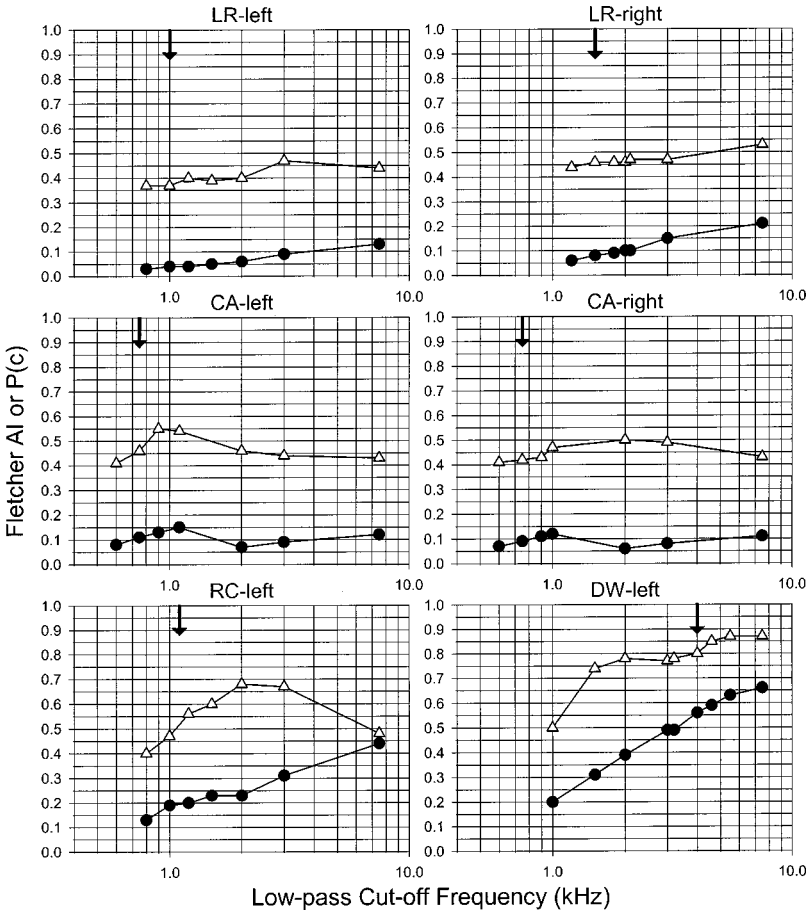

FIG. 3. Results for six ears *with* dead regions. As for Fig. 2. Arrows indicate dead region boundaries.

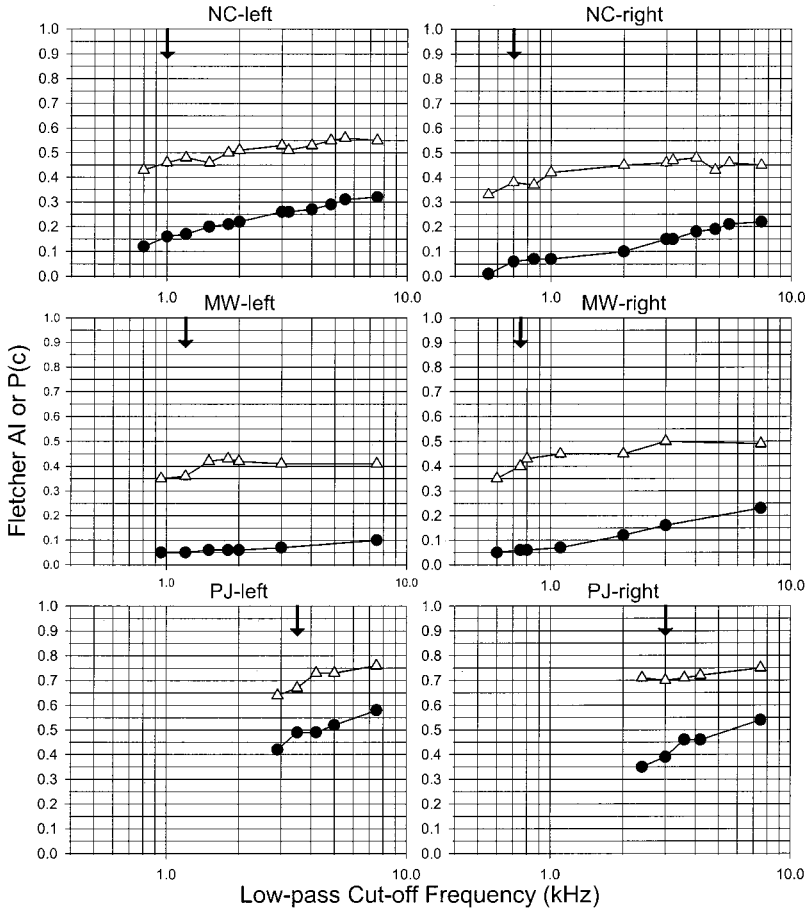

FIG. 4. Results for six more ears *with* dead regions. As for Fig. 3.

similar change in $P(c)$ as long as the variability associated with the $P(c)$ is sufficiently low. For the purposes of this analysis, it is fortunate that Vickers *et al.* tried to minimize this variability by collecting additional scores whenever the first two scores were substantially different from one another.

Results for individual subjects appear in Fig. 2 for subjects *without* dead regions and in Figs. 3 and 4 for subjects *with* dead regions. There is one panel for each test ear and each panel contains two curves. The curves with triangles show $P(c)$ plotted as a function of low-pass filter cutoff frequency, and were taken directly from Vickers *et al.*'s Figs. 1–3. The curves with circles provide AIs calculated for those conditions. Curves on the same panel share the ordinate to facilitate comparing AIs to $P(c)$'s. When displayed this way, the vertical distance between AI and $P(c)$ curves reflects the AI transformation depicted in Fig. 1.

The graphs show the AI curves are similar in form to their respective $P(c)$ curves, with few exceptions. That is, the AI predicts the general direction and size of the change in $P(c)$ with increasing cutoff frequency. For the subjects *without* dead regions (Fig. 2), both AIs and $P(c)$'s increase with increasing cutoff frequency, with few exceptions. For most subjects *with* dead regions (LR, CA, NC, MW, and PJ in Figs. 3 and 4), there is little or no AI change with increasing low-pass filter cutoff frequency, particularly at cutoffs within the dead regions. Subject RC-left (Fig. 3) has a single roll-over point for the full band condition (7.5-kHz cutoff) that the AI did not predict. Overall, the AI predicts the $P(c)$ curves reasonably well for subjects *with* and *without* dead regions.

IV. CONCLUSIONS

The Fletcher AI predicts—with reasonable accuracy—the limited benefit or lack of benefit derived from high-frequency amplification by the subjects with cochlear dead regions evaluated by Vickers *et al.* (2001). This finding implies that the audiogram characterizes the functionality of dead regions. It also highlights a confounding factor in the Vickers *et al.* study: that their subjects *with* dead regions had more high-frequency hearing loss than did their subjects *without* dead regions (see Vickers *et al.*'s Table I).

Based on the AI analysis, it seems premature to introduce a clinical test for identifying dead regions because it is not clear what information is gained beyond what is obtainable by calculating the AI.

Fletcher, H. (**1953**). *Speech and Hearing in Communication* (Van Nostrand, New York).

Fletcher, H., and Galt, R. H., (**1950**). ''The perception of speech and its relation to telephony,'' J. Acoust. Soc. Am. **22**, 89–151.

Moore, B. C. J. (**1995**). *Perceptual Consequences of Cochlear Damage* (Oxford U. P., New York).

Moore, B. C. J., and Glasberg, B. R. (**1998**). ''Use of a loudness model for hearing aid fitting. I. Linear hearing aids,'' Br. J. Audiol. **32**, 301–319.

Moore, B. C. J., Huss, M., Vickers, D. A., Glasberg, B. R., and Alcántara, J. I. (**2000**). ''A test for the diagnosis of dead regions in the cochlea,'' Br. J. Audiol. **34**, 205–224.

Rankovic, C. M. (**1997**). ''Prediction of speech reception for listeners with sensorineural hearing loss,'' in *Modeling Sensorineural Hearing Loss*, edited by W. Jesteadt (Erlbaum, Mahwah, NJ).

Rankovic, C. M. (**1998**). ''Factors governing speech reception benefits of adaptive linear filtering for listeners with sensorineural hearing loss,'' J. Acoust. Soc. Am. **103**, 1043–1057.

Vickers, D. A., Moore, B. C. J., and Baer, T. (**2001**). ''Effects of low-pass filtering on the intelligibility of speech in quiet for people with and without dead regions at high frequencies,'' J. Acoust. Soc. Am. **110**, 1164–1175.

Response to "Articulation index predictions for hearing-impaired listeners with and without cochlear dead regions" [J. Acoust. Soc. Am. 111, 2545–2548 (2002)] (L)

Brian C. J. Moore
Department of Experimental Psychology, University of Cambridge, Downing Street, Cambridge CB2 3EB, England

(Received 4 March 2002; revised 11 March 2002; accepted 19 March 2002)

Rankovic [J. Acoust. Soc. Am. **111**, 2545–2548 (2002)] argues that the AI, calculated according to Fletcher's method, gives good predictions of speech intelligibility for subjects with high-frequency hearing loss listening to amplified speech, regardless of the presence or absence of dead regions. She suggests further that "...it seems premature to introduce a clinical test for identifying dead regions because it is not clear what information is gained beyond what is obtainable by calculating the AI." I argue that, in fact, the AI is not accurate in predicting the *incremental* benefit of amplifying frequencies well above the estimated edge frequency (*Fe*) of a dead region. For five out of nine cases, application of the AI leads to the prediction that amplification of frequencies well above *Fe* would improve speech scores by 10%–15%; in fact, the largest improvement was 7%.
 [DOI: 10.1121/1.1476923]

PACS numbers: 43.66.Ba, 43.66.Ts, 43.71.Ky [MRL]

Rankovic (2002) presents a convincing case that the AI calculated according to Fletcher's (1953) method does a reasonable job in predicting most of the speech intelligibility data from the study of Vicker's *et al.* (2001), obtained using vowel–consonant–vowel (VCV) stimuli that were amplified individually for each subject (Moore and Glasberg, 1998) and then low-pass filtered with various cutoff frequencies. These data cover a wide range of conditions. However, close inspection of the data and predictions indicates that the AI does not predict accurately the *incremental* benefit of amplifying frequencies well above the estimated edge frequency (*Fe*) of a dead region. The data of Vickers *et al.* suggest that, for subjects with dead regions at high frequencies, there is some benefit for speech intelligibility of amplifying frequencies up to about 1.7 times *Fe*. However, there appears to be no benefit of amplifying frequencies beyond that limit. For subjects without dead regions, in contrast, intelligibility improves with increasing bandwidth over a wide frequency range. Vickers *et al.* proposed that a test for the diagnosis of dead regions, such as the TEN test (Moore *et al.*, 2000), might be useful in deciding on an appropriate amplification strategy for people with high-frequency hearing loss: when a dead region is identified, amplification should not be applied for frequencies above $1.7Fe$; when a dead region is not identified, amplification should be provided over the widest frequency range possible.

Rankovic correctly points out that, in the study of Vickers *et al.*, the subjects with dead regions tended to have greater hearing losses than those without. This is what allows the AI to predict the general form of the results. Rankovic concludes "...it seems premature to introduce a clinical test for identifying dead regions because it is not clear what information is gained beyond what is obtainable by calculating the AI." To assess this conclusion, I calculated, for each subject with a high-frequency dead region starting below 3 kHz, the percent correct identification score for stimuli low-pass filtered at $1.7Fe$ (interpolating where necessary) and the percent correct score for the widest bandwidth used. The difference (latter minus former) is a measure of the benefit (or penalty if negative) of increasing the cutoff frequency beyond $1.7Fe$. I also extracted, from the figures presented by Rankovic, the AI at $1.7Fe$ and the AI for the widest bandwidth used. The difference in AI gives a measure of the benefit predicted from the AI of increasing the cutoff frequency beyond $1.7Fe$. A scatter plot of the difference in AI versus the difference in obtained score is given in Fig. 1. Each point represents one ear of one subject.

The differences in obtained scores range from slightly positive to clearly negative values. The largest value is 0.07 and the smallest is -0.19. The mean is -0.016 (standard deviation s.d., 0.08). This is consistent with the conclusion of Vickers *et al.* that, for people with high-frequency dead regions, amplification of frequencies above $1.7Fe$ is typically of no benefit. In fact, none of the positive differences in obtained scores is significantly different from zero (based on *t*-tests). In contrast, all but one of the changes in AI are positive. The mean change is 0.084 (s.d. 0.06). The (Pearson) correlation between the score differences and the AI differences is 0.44, which is not significant at the 0.05 level. Figure 1 of the letter by Rankovic (2002) shows that, for AI values below about 0.5, the function relating proportion correct to the AI has a slope close to 1. Thus, an increase in AI of 0.1 would be expected to give an increase in proportion correct VCV identification of 0.1. For five out of nine ears, the change in AI is 0.1 or more, and for two ears it is above 0.15. A person fitting a hearing aid might well consider intelligibility increases of 10%–15% worthwhile to try to achieve. However, the data indicate that intelligibility never increased by more than 7%. Based on a related-samples *t*-test, the differences in AI are significantly greater than the differences in obtained score ($p=0.0034$).

The above analysis is based on only nine cases. Further data are needed to establish clearly whether a test for diagnosing dead regions provides useful information over and

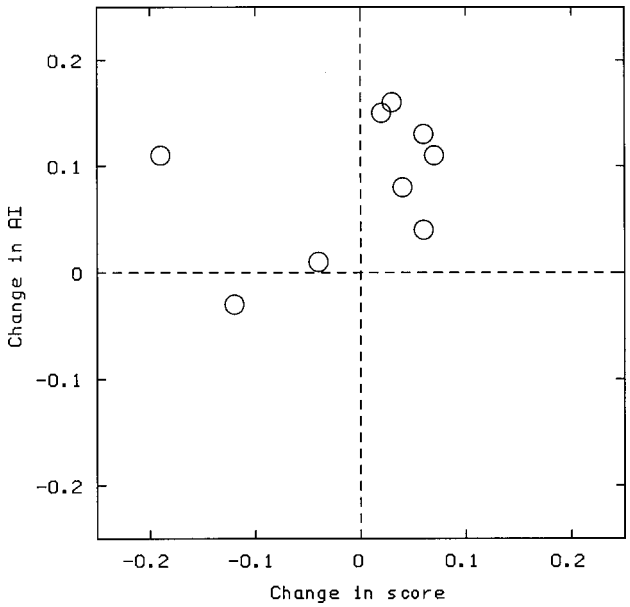

FIG. 1. A scatter plot of the change in AI produced by changing the low-pass cutoff frequency from 1.7*Fe* to the maximum cutoff frequency used (7.5 kHz), taken from Rankovic (2002), and the corresponding change in speech identification score, taken from Vickers *et al.* (2001). Each point represents one ear of a subject with a high-frequency dead region starting at frequency *Fe*.

above that provided by deriving the AI from the audiogram. However, the analysis does suggest that application of the Fletcher AI to people with high-frequency dead regions would sometimes lead to the expectation that amplification of frequencies above 1.7*Fe* would give a worthwhile improvement in speech intelligibility (10%–15%), when in fact the improvement would typically be 7% or less. Other researchers have noted that speech identification scores can differ markedly across individuals with similar audiograms, and some have suggested that those showing poorer-than-expected speech scores (and failing to benefit from amplification) may have dead regions (Halpin *et al.*, 1994; Ching *et al.*, 1998; Hogan and Turner, 1998; Turner and Cummings, 1999).

In conclusion, application of the Al to people with high-frequency dead regions might lead the clinician to spend time and effort trying to achieve the large required gain at high frequencies, only to find that this effort was fruitless. Furthermore, achieving sufficient gain might involve penalties in terms of an increased susceptibility to acoustic feedback (for example, produced by jaw movements), a tightly fitting unvented earmold (necessary to reduce acoustic feedback but perhaps leading to physical discomfort and an increased occlusion effect), and increased distortion in the hearing aid. I maintain, therefore, that a test for dead regions, such as the TEN test (Moore *et al.*, 2000), can be clinically useful, especially for people with hearing losses at high frequencies between about 60 and 90 dB, and when the hearing loss exceeds 60 dB at a frequency below 2 kHz. For larger losses, dead regions may be common, but it may be difficult in practice to apply sufficient gain to restore the audibility of speech. For dead regions starting above about 2.5 kHz, amplification should probably be provided for frequencies at least up to about 4 kHz, so the amplification strategy would not differ markedly from that for a person without a dead region.

ACKNOWLEDGMENTS

I thank Hedwig Gockel and Tom Baer for helpful comments.

Ching, T., Dillon, H., and Byrne, D. (**1998**). ''Speech recognition of hearing-impaired listeners: Predictions from audibility and the limited role of high-frequency amplification,'' J. Acoust. Soc. Am. **103**, 1128–1140.

Fletcher, H. (**1953**). *Speech and Hearing in Communication* (Van Nostrand, New York).

Halpin, C., Thornton, A., and Hasso, M. (**1994**). ''Low-frequency sensorineural loss: Clinical evaluation and implications for hearing aid fitting,'' Ear Hear. **15**, 71–81.

Hogan, C. A., and Turner, C. W. (**1998**). ''High-frequency audibility: Benefits for hearing-impaired listeners,'' J. Acoust. Soc. Am. **104**, 432–441.

Moore, B. C. J., and Glasberg, B. R. (**1998**). ''Use of a loudness model for hearing aid fitting. I. Linear hearing aids,'' Br. J. Audiol. **32**, 317–335.

Moore, B. C. J., Huss, M., Vickers, D. A., Glasberg, B. R., and Alcántara, J. I. (**2000**). ''A test for the diagnosis of dead regions in the cochlea,'' Br. J. Audiol. **34**, 205–224.

Rankovic, C. M. (**2002**). ''Articulation index predictions for hearing-impaired listeners with and without cochlear dead regions,'' J. Acoust. Soc. Am. **111**, 2545–2548.

Turner, C. W., and Cummings, K. J. (**1999**). ''Speech audibility for listeners with high-frequency hearing loss,'' Am. J. Audiol. **8**, 47–56.

Vickers, D. A., Moore, B. C. J., and Baer, T. (**2001**). ''Effects of lowpass filtering on the intelligibility of speech in quiet for people with and without dead regions at high frequencies,'' J. Acoust. Soc. Am. **110**, 1164–1175.

Effect of duration on amplitude-modulation masking (L)

Rebecca E. Millman[a)]
Department of Physiological Sciences, The Medical School, Framlington Place, Newcastle upon Tyne NE2 4HH, United Kingdom

Christian Lorenzi
Laboratoire de Psychologie Experimentale, UMR CNRS 8581, Universite Rene Descartes, 71 Avenue Edouard Vaillant, 92774 Boulogne-Billancourt, France and Institut Universitaire de France

Frédéric Apoux and Christian Füllgrabe
Laboratoire de Psychologie Expérimentale, UMR CNRS 8581, Université René Descartes, 71 Avenue Edouard Vaillant, 92774 Boulogne-Billancourt, France

Gary G. R. Green
Department of Physiological Sciences, The Medical School, Framlington Place, Newcastle upon Tyne NE2 4HH, United Kingdom

Sid P. Bacon
Psychoacoustics Laboratory, Department of Speech and Hearing Science, Arizona State University, P.O. Box 871908, Tempe, Arizona 85287-1908

(Received 21 May 2001; revised 14 January 2002; accepted 7 March 2002)

Detection thresholds for a signal sinusoidal amplitude modulation (SAM) were measured in the presence of an additional, masking SAM. Signal and masker modulations were applied synchronously to a gated white noise carrier. The masker modulation frequency was fixed at 16 Hz and the signal modulation frequency ranged from 2 to 256 Hz. Modulation masking patterns were measured in three listeners for stimulus durations of 500, 1000, and 2000 ms. The results showed that modulation masking was reduced or abolished at signal modulation frequencies of 2, 14, and 18 Hz when stimulus duration was increased from 500 to 2000 ms. The effect at 2 Hz suggests that fringe effects in modulation masking previously reported by Bacon and Grantham [S. P. Bacon and D. W. Grantham, J. Acoust. Soc. Am. **91**, 3451–3455 (1992)] were at least partly due to an increase in masker modulation duration. The reduction in modulation masking observed at signal modulation frequencies of 14 and 18 Hz was similar to that at 2 Hz, suggesting that listeners use a low-frequency temporal envelope beat cue (in this case at 2 Hz) when the distance between the signal and masker modulations is small.
[DOI: 10.1121/1.1475341]

PACS numbers: 43.66.Mk, 43.66.Dc [MRL]

I. INTRODUCTION

Modulation masking has been used to estimate the degree of frequency selectivity of the auditory system in the amplitude modulation domain (for a recent review see Ewert and Dau, 2000). In a pioneering study, Houtgast (1989) showed that detection thresholds for a 2-s signal sinusoidal amplitude modulation (SAM) applied to a broadband noise carrier increase if additional, continuous masker AM is superimposed on that carrier. The masker AM used in this case was a narrow band of noise (half an octave wide) with a center frequency of 4, 8, or 16 Hz. Modulation masking patterns showing the amount of masking as a function of signal frequency were bandpass and peaked at the masker frequency. This indicated that masking is most effective when the signal modulation frequency falls within the masker-modulation band. Houtgast (1989) interpreted these results as evidence for frequency selectivity in the amplitude modulation domain.

In a concurrent study using the same masking paradigm, Bacon and Grantham (1989) presented both the signal and masking SAM only during the 500-ms observation intervals. The results were consistent with Houtgast (1989) in that the greatest amount of modulation masking occurred when the frequency of the signal SAM was near the modulation frequency of the masking SAM. However, although the amount of masking decreased as the signal modulation frequency was decreased below the masker frequency, masking increased again at low (2-8 Hz) signal modulation frequencies. This ''upturn'' in masking was not reported by Houtgast (1989).

Bacon and Grantham (1992) suggested this discrepancy might be due to the fact that the masker was modulated throughout an experimental run in Houtgast (1989), but only during the 500-ms observation intervals in Bacon and Grantham (1989). They addressed this possibility by assessing ''fringe effects'' on modulation masking. In their study, both the signal and masker carriers were presented continuously and the signal SAM was 500-ms long. When the masking SAM was present, it was presented only during the signal

a)Electronic mail: r.e.millman@ncl.ac.uk

SAM or started for a certain amount of time before and/or continued after the signal SAM. The duration of this ''fringe'' ranged from 62.5 ms to continuous (masker modulated throughout the experimental run). Masking patterns obtained without a fringe were consistent with those observed in the authors' previous work (Bacon and Grantham, 1989), including the increase (upturn) in masking at low modulation frequencies (2–8 Hz). The fringe had its greatest effect (a 4–6 dB decrease in masking) at low modulation frequencies (2–8 Hz), and little or no effect at other modulation frequencies.

Bacon and Grantham (1992) explored a number of hypotheses to account for their observations including adaptation, perceptual grouping, and temporal pattern discrimination. An additional experiment in which the respective contributions of the forward and backward fringe were examined led Bacon and Grantham to conclude that their results could not be explained through adaptation alone, since masking release at 2 Hz was also observed with only a backward fringe.

Further consideration of the methodology used by Houtgast (1989) and Bacon and Grantham (1989) reveals an additional source of discrepancy between these two studies, namely differences in overall stimulus duration. In Houtgast (1989), the signal and masker SAM duration was much longer than in Bacon and Grantham (1989). The aim of the present work was to investigate the effect of duration on modulation maskings for synchronous signal and masker modulations, so as to determine whether this methodological difference could have contributed to the different results.

II. METHODS

A. Listeners

Three listeners (aged between 22 and 28 years) took part in this experiment. All listeners had pure-tone audiograms within normal limits for octave frequencies between 0.25 and 8 kHz, and had extensive experience as listeners in psychoacoustic experiments.

B. Stimuli

Stimuli were generated using a 16-bit D/A converter at a sampling frequency of 44.1 kHz and delivered binaurally via Sennheiser HD 565 earphones at a level of 75 dB SPL (rms). Each trial consisted of a standard and a target stimulus presented successively in random order to the listener. The standard consisted of a white noise carrier $n(t)$ sinusoidally amplitude modulated at the masker frequency. The expression describing the standard (i.e., the masker alone) was

$$S(t) = c[1 + m_m \cos(2\pi f_m t)]n(t) \tag{1}$$

where m_m is the modulation depth of the masker, fixed at 0 in the unmasked condition and 0.5 in the masked condition, f_m is the masker modulation frequency, fixed at 16 Hz, and c is a multiplicative compensation term defined below. The target consisted of white noise carrier $n(t)$ amplitude modulated by the sum of two sinusoidal modulators, the signal and the masker modulators. The expression describing the target (i.e., the signal-plus-masker waveform) was

$$T(t) = c[1 + m_m \cos(2\pi f_m t + \phi_m) + m_s \cos(2\pi f_s t + \phi_s)]n(t) \tag{2}$$

where m_s is the modulation depth of the signal, f_s is the signal modulation frequency, ϕ_s is the starting phase of the signal modulator, and ϕ_m is the starting phase of the masker modulator. The starting phases of the masker and signal modulator were 0 and 270 degrees, respectively. This ensured there was always a phase difference of 90 degrees between the onset of the signal and masker modulators (Bacon and Grantham, 1992). The term c is a compensation factor (Bacon and Grantham, 1989) set such that the overall power was the same in all intervals. The expression for c is given as follows:

$$c = [1 + (m_m^2 + m_s^2 + 2m_m m_s)/2]^{-0.5} \tag{3}$$

Statistically independent realizations of the white noise carrier were used in all experiments (i.e., within and between trials). In the main experiment both the signal and the masking SAMs were applied (synchronously) over the full duration of the carrier. The standard and target duration was either 500, 1000, or 2000 ms, including 25-ms rise/fall times shaped using a raised-cosine function. The interstimulus interval was 1 s. For each stimulus duration, thresholds for signal modulation frequency alone were obtained for modulation rates of 2, 4, 8, 14, 16, 18, 32, 64, 128, and 256 Hz. Modulation detection thresholds were then measured as a function of f_s but in the presence of the 16-Hz masker. An additional experiment was run in which the standard and target duration was 2000 ms. When present, the 16-Hz masking SAM was applied over the full duration of the 2000-ms carrier. However, the 2-Hz signal SAM started 750 ms after the onset of the masking SAM and ended 750 ms before the offset of the masking SAM. This supplementary experiment (called the ''fringe condition'') corresponded to the paradigm used by Bacon and Grantham (1992) that investigated forward- and backward-fringe effects on modulation masking. In each experimental condition, the amount of masking was taken as the difference between the unmasked and masked detection thresholds, expressed on a decibel scale ($20 \log m$). Listeners were tested individually in a soundproof booth.

C. Procedure

Modulation detection thresholds were obtained using an adaptive two-interval, two-alternative forced choice procedure with a two-down, one-up stepping rule that estimates the modulation depth required for 70.7% correct detection. The listeners had to choose which interval contained the signal modulation and received visual feedback at the end of each trial. The step size of the signal modulation depth m_s corresponded initially to a factor of 1.585 (4 dB) and was reduced to 1.26 (2 dB) after the first two reversals. The mean of the last 10 reversals in a block of 14 reversals was used as the detection threshold estimate for that block. Thresholds reported here are the mean of three estimates.

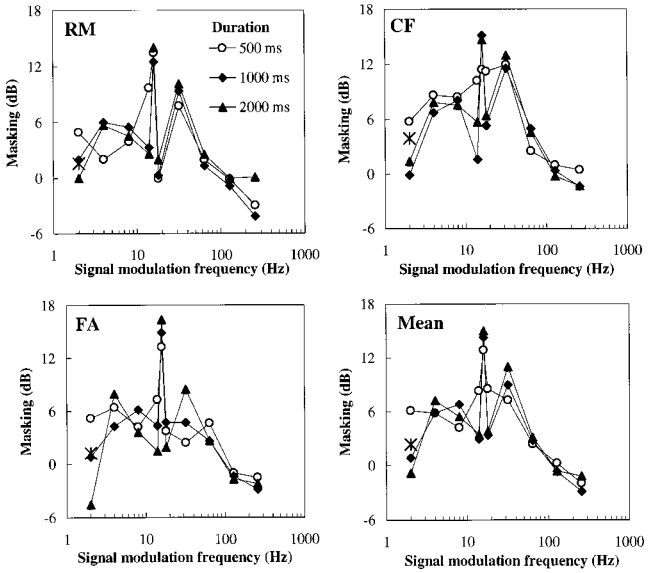

FIG. 1. Amount of modulation masking (masked modulation thresholds minus unmasked modulation thresholds) as a function of signal modulation frequency for a 16-Hz masker modulation frequency. The stimulus duration was 500 ms (open circles), 1000 ms (closed diamonds), and 2000 ms (closed triangles). The star shows the amount of masking produced by a 2000-ms, 16-Hz masking modulation on the detection of a 500-ms, 2-Hz signal modulation temporally centered in the masker.

III. RESULTS

Figure 1 shows individual and mean modulation masking patterns for stimulus durations of 500, 1000, and 2000 ms. The isolated point (star) at a signal modulation frequency of 2 Hz shows the amount of modulation masking produced by a 2000-ms masking SAM on the detection of a 500-ms signal SAM temporally centered in the masking SAM (the ''fringe'' condition). Overall, the results are in agreement with previous studies showing that, for each stimulus duration tested, the greatest mean amount of masking occurs when the signal modulation frequency is near the masker modulation frequency. Modulation masking is reduced or abolished at signal modulation frequencies of 2, 14, and 18 Hz when stimulus duration increases from 500 to 2000 ms. The decrease in masking is about 7 dB at a signal modulation frequency of 2 Hz and 5 dB for signal modulation frequencies of 14 and 18 Hz. The average amount of masking measured in the ''fringe condition'' for a 500-ms signal modulation frequency of 2 Hz is about 2 dB. Surprisingly, modulation masking increases by about 2–4 dB at signal modulation frequencies of 16 and 32 Hz when the stimulus duration increases from 500 to 2000 ms.

IV. DISCUSSION

The increase in stimulus duration eliminated the upturn in modulation masking patterns previously observed at 2 Hz. No effect of duration was observed at 4 and 8 Hz. This result suggests that at the lowest signal modulation frequency (i.e., 2 Hz), differences in signal and masker modulation duration were, at least in part, responsible for the discrepancy between the results of Bacon and Grantham (1989) and Houtgast (1989). The amount of masking measured in the ''fringe condition'' (2 dB) is in between the amount of masking measured in the ''synchronous conditions'' for a 500-ms (6 dB) and a 2000-ms (−1 dB) signal and masker duration. This suggests that at extremely low signal modulation frequencies, it is not the masker duration (and hence the fringe) alone that contributes to the reduced masking, but that the signal duration *per se* is also important. However, another explanation is still required to account for the fringe effects reported at 4 and 8 Hz by Bacon and Grantham (1992) because the increase in stimulus duration does not affect modulation masking at these signal modulation frequencies.

The decrease in masking observed at a 2-Hz signal modulation frequency with increasing duration is incompatible with an interpretation in terms of temporal pattern discrimination or perceptual grouping because the masker and signal are always gated together when they are both present. However, this result remains consistent with the interpretation in terms of adaptation effects proposed by Bacon and Grantham (1992). It may reflect a decline in the modulation of neural activity over time due to adaptation (Smith *et al.*, 1985). If the response modulation to the masker is initially large but later declines to some steady-state, then the relative response modulation to the signal modulation should be larger during the steady-state portion of the neural response. This could occur when both signal and masker modulations are of sufficient duration (e.g., 2000 ms). Such effects would be most apparent at low signal modulation frequencies where relatively few complete signal modulation cycles would exist following the initial large response to the masker.

An increase in stimulus duration produces a similar reduction in modulation masking at signal modulation frequencies of 2, 14, and 18 Hz. Listeners reported hearing a 2-Hz beat cue under these conditions which is consistent with the idea that listeners use a low temporal beat cue when the spectral distance (Δf) between the signal and masker modulations is small (Strickland and Viemeister, 1996), e.g., with a 16-Hz masker, Δf is 2 Hz when the signal modulation frequency is 14 or 18 Hz.

The signal and masker modulation frequencies used in this study encompass the range of modulation frequencies (2–16 Hz) present in continuous speech (e.g., Steeneken and Houtgast, 1980). The results presented here therefore suggest that the deleterious effect of fluctuating background noise on speech perception should be reduced when *both* the speech and noise segments are sufficiently long, or if background noise precedes or follows the speech signal.

ACKNOWLEDGMENTS

The authors would like to thank Wes Grantham and another anonymous reviewer for their helpful comments on an earlier version of this paper. This study was done while R. E. Millman was a visiting Ph.D. student at the Laboratoire de Psychologie Expérimentale (UMR CNRS 8581, France). R. E. Millman was supported by the BBSRC, C. Lorenzi was supported by the Cognitique Program (MENRT), and F. Apoux was supported by a CIFRE grant. NIDCD Grant No. DC01376 awarded to S. P. Bacon supported the manuscript preparation in part.

Bacon, S. P., and Grantham, D. W. (**1989**). ''Modulation masking: Effects of modulation frequency, depth, and phase,'' J. Acoust. Soc. Am. **85**, 2575–2580.
Bacon, S. P., and Granthham, D. W. (1992). ''Fringe effects in modulation masking,'' J. Acoust. Soc. Am. **91**, 345–3455.
Ewert, S. D., and Dau, T. (**2000**). ''Characterising frequency selectivity for envelope fluctuations,'' J. Acoust. Soc. Am. **108**, 1181–1196.
Houtgast, T. (**1989**). ''Frequency selectivity in the amplitude-modulation domain,'' J. Acoust. Soc. Am. **85**, 1676–1680.
Smith, R. L., Brachman, M. L., and Frisina, R. D. (**1985**). ''Sensitivity of auditory-nerve fibers to changes in intensity: A dichotomy between decrements and increments,'' J. Acoust. Soc. Am. **78**, 1310–1316.
Steeneken, H. J. M., and Houtgast, T. (**1980**). ''A physical method for measuring speech-transmission quality,'' J. Acoust. Soc. Am. **67**, 318–326.
Strickland, E. A., and Viemeister, N. F. (**1996**). ''Cues for discrimination of envelopes,'' J. Acoust. Soc. Am. **99**, 3638–3646.

Analysis of one-dimensional wave scattering by the random walk method

B. V. Budaev[a] and D. B. Bogy[b]
Department of Mechanical Engineering, University of California, Berkeley, California 94720-1740

(Received 24 May 2001; accepted for publication 7 February 2002)

The random walk method is applied to a one-dimensional Helmholtz equation with a variable wave number. The solution is represented as a mathematical expectation of a specified functional on paths in a complex space. This solution degenerates to the ray-method approximation in domains where the latter method may be used, but the probabilistic formulas presented describe also backscattered waves whose existence is not explained by the standard asymptotic techniques. The numerical results confirm the efficiency of the random walk approach to the analysis of wave propagation. © *2002 Acoustical Society of America.* [DOI: 10.1121/1.1474441]

PACS numbers: 43.20.Bi, 43.20.Dk, 03.65.Ge [ANN]

I. INTRODUCTION

It was recently shown[1] that problems of wave propagation may be addressed by a random walk method combining the physical clarity of the approximate ray method[2,3] with advantages of both exact analytical methods and direct numerical techniques. As with the ray method, the random walk method is based on the Liouville representation $\psi(x) = \phi(x)e^{iS(x)}$ of solutions of the Helmholtz equation $\nabla^2\psi + k^2\psi = 0$. The phase $S(x)$ is determined by the eikonal equation $(\nabla S)^2 = k^2$, which admits efficient analysis by the Hamilton–Jacobi technique of classical mechanics.[4] When the eikonal $S(x)$ is determined, the amplitude $\phi(x)$ has to be computed from the complete transport equation $i\nabla^2\phi - 2\nabla(S)\cdot\nabla(\phi) - \nabla^2(S)\phi = 0$, whose rigorous treatment distinguishes the random walk method from asymptotic approaches, such as the ray method or the method of parabolic equations,[5,6] that employ different approximations to this equation.

The central idea of the random walk method is to represent the exact solution of the complete transport equation as a mathematical expectation of a specified functional on the space of Brownian motions. The obtained solution may be either numerically simulated or it may be used for deriving various approximate solutions. In particular, in certain circumstances, the exact solution provided by the random walk method straightforwardly degenerates to the well-known asymptotes of the ray method. However, the random walk method, as a rigorous approach, makes it possible to study, at least in principle, any phenomenon described by the considered equations, including, for example backscattering, which is predicted by neither the ray method nor by a more general parabolic equation method.

Probabilistic methods have been increasingly used in recent years for analysis of wave propagation[7,8] in random media. In Ref. 8 the competitiveness of probabilistic methods in wave propagation is discussed, and in Refs. 7 and 8 these methods are used to study the transport of energy by waves propagating in random media. Such transport is described by first-order differential equations and a probabilistic method is developed in these papers for their analysis. Here, instead, we deal with problems in nonrandom media but employ probabilistic methods for the analysis of the second-order auxiliary equations whose first-order components are also known in ray theory as transport equations.

Here, we consider a simple one-dimensional example demonstrating that, within the context of the random walk method, backscattering may be explained as propagation along complex rays that may turn around, while the real rays considered in the classical ray theory go strictly along straight lines. This example shows the potential of random walk methods, both for theoretical analysis of wave propagation and for computational applications.

II. ONE-DIMENSIONAL SCATTERING PROBLEM

Consider the one-dimensional Helmholtz equation

$$\psi'' + \Omega^2 k^2(x)\,\psi = 0, \tag{2.1}$$

with a frequency $\Omega > 0$ and with a variable wave number

$$k(x) = k_\pm + o\left(\frac{1}{|x|^\delta}\right), \quad \delta > 0 \quad \text{as } x \to \pm\infty, \tag{2.2}$$

approaching certain limits $k_\pm$ as $x \to \pm\infty$.

The scattering problem consists of finding a solution of Eq. (2.1) with the following structure at infinity:

$$\psi(x) = \begin{cases} e^{i\Omega k_- x} + T_- e^{-i\Omega k_- x} + o(1), & \text{as } x \to -\infty, \\ T_+ e^{i\Omega k_+ x} + o(1), & \text{as } x \to +\infty, \end{cases} \tag{2.3}$$

where the term $e^{i\Omega k_- x}$ represents the incident wave arriving from $-\infty$. The scalar constants T_- and T_+ are interpreted as reflection and transmission coefficients of the potential $V(x) = \Omega^2 k^2(x)$. Computation of the coefficients $T_\pm$ is often considered the main task of the scattering problem. Here, however, we will focus on the general problem of computing the total wave field $\psi(x)$ satisfying (2.1)–(2.3).

To make the presentation more transparent, we focus here on a particular case with the wave number $k(x)$ defined by an analytic formula

[a]Electronic mail: budaev@cml.me.berkeley.edu
[b]Electronic mail: dbogy@cml.me.berkeley.edu

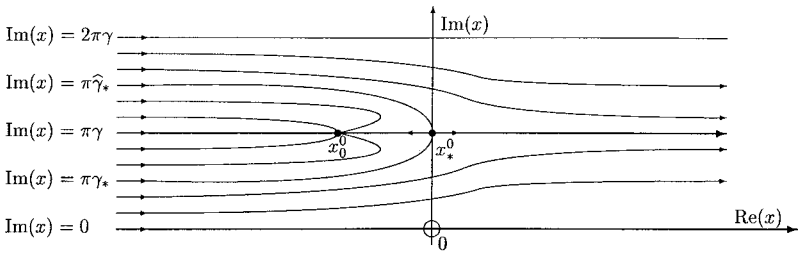

FIG. 1. Complex rays on $\mathbb{C}_+$.

On $\mathbb{C}_+$ most of the rays run from $\mathrm{Re}(x)\to-\infty$ to either $\mathrm{Re}(x)\to\infty$ or to a zero of the wave number $k(x)$. There are also isolated rays that go to the poles of $k(x)$.

$$k(x)\equiv k_\gamma(x)=\frac{k_-+k_+e^{x/\gamma}}{1+e^{x/\gamma}}=\frac{k_-}{1+e^{x/\gamma}}+\frac{k_+}{1+e^{-x/\gamma}},\qquad (k_-<k_+),\tag{2.4}$$

where, for definiteness, we assume that $k_-<k_+$. If $\gamma>0$, this function smoothly increases from k_- to k_+ as x varies from $-\infty$ to $+\infty$. In the limit $\gamma\to0$ function (2.4) degenerates to a step function

$$k_0(x)\equiv\lim_{\gamma\to0}k_\gamma(x)=\begin{cases}k_-, & \text{if } x<0,\\ k_+, & \text{if } x>0,\end{cases}\tag{2.5}$$

which provides a means for estimating the reflection and transmission coefficients T_- and T_+ for smooth but arbitrarily steep wave numbers $k(x)$. Indeed, the scattering problem (2.1)–(2.3) with the step-function wave number $k(x)=k_0(x)$ has the elementary exact solution

$$\psi_0(x)=\begin{cases}e^{i\Omega k_-x}+T_-^0e^{-i\Omega k_-x}, & T_-^0=\dfrac{k_--k_+}{k_-+k_+} \quad \text{if } x<0,\\ T_+^0e^{+i\Omega k_+x}, & T_+^0=\dfrac{2k_-}{k_-+k_+} \quad \text{if } x>0,\end{cases}\tag{2.6}$$

suggesting that the constants T_-^0 and T_+^0 from (2.6) may approximate the reflection and transmission coefficients from (2.3) corresponding to wave numbers $k_\gamma(x)$ for a sufficiently small parameter γ.

III. THE EIKONAL

We seek a solution of the problem (2.1)–(2.3) in the Liouville form

$$\psi(x)=\phi(x)\,e^{i\Omega S(x)}.\tag{3.1}$$

Then, Eq. (2.1) may be split onto the eikonal equation

$$[S'(x)]^2-k^2(x)=0,\tag{3.2}$$

and the "complete" transport equation

$$\frac{i}{2\Omega}\phi''-A\,\phi'-\frac{1}{2}B\,\phi=0,\tag{3.3}$$

whose coefficients are explicitly defined by formulas

$$A(x)=S'(x),\quad B(x)=S''(x).\tag{3.4}$$

The eikonal equation in the one-dimensional case is best analyzed by extension to the complex plane where x is considered as a complex variable and $k(x)$ is an analytic wave number.

Let $\mathbb{C}_+$ and $\mathbb{C}_-$ be two copies of the complex plane, and let the eikonal's gradient $S'(x)$ be defined on these copies by

$$S'(x)=\pm k(x),\quad x\in\mathbb{C}_\pm,\tag{3.5}$$

which conform with (3.2). First, we determine the "rays" defined as integral lines of the one-dimensional complex vector field $S'(x)$, i.e., as curves $x(t)$ on a complex plane satisfying an ordinary differential equation $(d/dt)\,x(t)=S'(x(t))$.

The rays form $2i\pi\gamma$-periodic structures on $\mathbb{C}_\pm$. Figure 1 shows one period of this structure on $\mathbb{C}_+$, where $S'(x)=k(x)$. For $\mathrm{Re}(x)\ll0$ on $\mathbb{C}_+$ all rays point in the positive direction parallel to the real axis. As $\mathrm{Re}(x)$ increases, these rays split into two groups. Rays originating in the strips $|\mathrm{Im}(x)-2n\pi\gamma|<\pi\gamma_*$, where γ_* is a certain point in $0<\gamma_*<\gamma$, continue their paths toward $\mathrm{Re}(x)\to+\infty$, gradually drifting closer to the axis $\mathrm{Im}(x)=(2n+1)\,\pi\gamma$. Rays originating in the strips $|\mathrm{Im}(x)-(2n+1)\,\pi\gamma|<\pi(\gamma-\gamma_*)$ have principally different structures as they are attracted to the nearest zeros

$$x_0^n=\gamma\ln\left(\frac{k_-}{k_+}\right)+i\pi\gamma(2n+1),\quad n=0,\pm1,\pm2,\ldots,\tag{3.6}$$

of the wave number $k(x)$. These two groups of rays are separated by isolated rays that go directly to the nearest one of the poles

$$x_*^n=i\pi\gamma(2n+1),\quad n=0,\pm1,\pm2,\ldots,\tag{3.7}$$

of $k(x)$, which, in the considered case with $k_-<k_+$, are always located to the right of the zeros x_0^n.

It is instructive to emphasize the principal difference between complex and real rays. Rays launched from the real axis never leave this axis, never change their direction, and go straight from $-\infty$ to ∞. On the contrary, a ray launched off of the real axis from a complex point may be captured by zeros x_0^n of the wave number $k(x)$.

On the plane $\mathbb{C}_-$ the rays follow the same lines as on $\mathbb{C}_+$, but run in the opposite direction. Thus, on $\mathbb{C}_-$ all rays end at $\mathrm{Re}(x)\to-\infty$, while they start either from $\mathrm{Re}(x)\to+\infty$, or from the zeros x_0^n of the wave number $k(x)$.

From the above it follows that on $\mathbb{C}_+$ all rays originate from $\mathrm{Re}(x)\to-\infty$, but some of the rays are captured by points from (3.6), whereas the opposite is true on $\mathbb{C}_-$; all rays on $\mathbb{C}_-$ run to infinity $\mathrm{Re}(x)\to-\infty$, but some of the rays originate from x_0^n. These features of $\mathbb{C}_\pm$ make it possible to construct a two-sheet manifold $\mathfrak{S}$ on which all the rays corresponding to $k(x)$ start and end at infinity. Indeed, such $\mathfrak{S}$ may be introduced as a junction $\mathfrak{S}=\mathbb{C}_+\cup\mathbb{C}_-$, where the

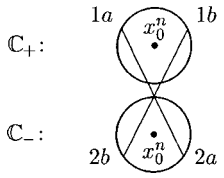

Points '1a' and '1b' of a small circle around x_0^n on $\mathbb{C}_+$ are identified with the the points '2a' and '2b' of a circle of the same radius around x_0^n on $\mathbb{C}_-$.

FIG. 2. Attachment of sheets along circles around zeros x_0^n of $k(x)$.

complex planes $\mathbb{C}_+$ and $\mathbb{C}_-$ are attached to each other along infinitely small circles surrounding zero points x_0^n of $k(x)$, and identified according to the rules

$$[x_0^n+\varepsilon e^{i\theta}]_{\text{on }\mathbb{C}_+}=[x_0^n-\varepsilon e^{i\theta}]_{\text{on }\mathbb{C}_-},\quad \varepsilon\to 0, \tag{3.8}$$

illustrated in Fig. 2.

To determine the eikonal $S(x)$ satisfying (3.2) let us first notice that

$$\int k(x)\mathrm{d}x=K(x)+\text{const}, \tag{3.9}$$

where $K(x)$ is an analytic function

$$\begin{aligned}K(x)&=k_-x+\gamma(k_+-k_-)\ln(1+e^{x/\gamma})\\&=k_+x+\gamma(k_+-k_-)\ln(1+e^{-x/\gamma}),\end{aligned} \tag{3.10}$$

defined on $\mathbb{C}_+$ with slits originating at the logarithmic singularities of $K(x)$ located at the poles x_*^n of $K(x)$. For definiteness, we fix the branch of $K(x)$ by the condition

$$K(x)=k_\pm x+o(e^{-|x|/\gamma}),\ \text{ as }\ \mathrm{Re}(x)\to\pm\infty, \tag{3.11}$$

and we fix this branch on $\mathbb{C}_+$ by slits between the points x_*^{2n-2} and x_*^{2n-1}.

In the above we defined rays on a two-sheet manifold $\mathfrak{S}$ constructed from two copies $\mathbb{C}_+$ and $\mathbb{C}_-$ of the complex plane. Then, we introduced the function $K(x)$ defined on the planes $\mathbb{C}_+$ and $\mathbb{C}_-$ with specified slits. Let us assume that each sheet of $\mathfrak{S}$ has these slits. Then, the eikonal $S(x)$ satisfying (3.5) may be defined on $\mathfrak{S}$ by the formula

$$S(x)=\pm K(x),\quad x\in\mathbb{C}_\pm, \tag{3.12}$$

where $K(x)$ is the function from (3.10).

It is instructive to observe that $S(x)$ from (3.12) is a piecewise analytic function on $\mathfrak{S}$ with a continuous derivative $S'(x)$ satisfying (3.5) and (3.2). It also follows from (3.11) that on $\mathbb{C}_+$ and $\mathbb{C}_-$ of $\mathfrak{S}$ the eikonal $S(x)$ has the asymptotic behavior

$$S(x)=\begin{cases}k_\pm x+o(e^{-|x|/\gamma}),\ \ x\to\pm\infty,\ \ \mathrm{Re}(x)\in\mathbb{C}_+,\\ -k_\pm x+o(e^{-|x|/\gamma}),\ \ x\to\pm\infty,\ \ \mathrm{Re}(x)\in\mathbb{C}_-,\end{cases} \tag{3.13}$$

which suggests that the component $\mathbb{C}_+$ of $\mathfrak{S}$ supports the waves propagating from $\mathrm{Re}(x)\to-\infty$ to $\mathrm{Re}(x)\to+\infty$, while the component $\mathbb{C}_-$ supports waves propagating in the opposite direction.

IV. PROBABILISTIC SOLUTION OF THE TRANSPORT EQUATION

After the eikonal $S(x)$ is defined on the two-sheet manifold $\mathfrak{S}$, the complete transport equation (3.3) may be explicitly solved on this surface by exact probabilistic formulas provided by the random walk methods briefly discussed in the Introduction.

Consider the complete transport equation (3.3) in the domain $\mathfrak{S}$ with the "boundary" conditions

$$\lim_{\mathrm{Re}(x)\to\infty}\phi(x)=\chi(x_\infty),$$

$$\chi(x_\infty)=\begin{cases}1, & \text{if } x_\infty\in\mathbb{C}_+,\ \mathrm{Re}(x_\infty)\to-\infty,\\ 0, & \text{if } x_\infty\in\mathbb{C}_+,\ \mathrm{Re}(x_\infty)\to+\infty.\end{cases} \tag{4.1}$$

The solution ϕ of this problem is represented by the probabilistic formula

$$\phi(x)=\mathbf{E}\{I\chi(\xi_\infty^x)\,e^{-1/2\int_0^\infty S''(\xi_t^x)\,\alpha^2(\xi_t^x)\,\mathrm{d}t}\}, \tag{4.2}$$

where $\mathbf{E}$ denotes the mathematical expectation evaluated over all random walks ξ_t^x on $\mathfrak{S}$ governed by the stochastic differential equation

$$\mathrm{d}\xi_t^x=-S'(\xi_t^x)\,\alpha^2(\xi_t^x)\,\mathrm{d}t+\sqrt{\frac{\mathrm{i}}{\Omega}}\,\alpha(\xi_t^x)\mathrm{d}w_t, \tag{4.3}$$

with the standard one dimensional Brownian motion w_t, and with an auxiliary smooth function $\alpha(x)$ whose particular choice may be made as convenient for a considered particular problem. In many cases the simplest choice $\alpha(x)\equiv 1$ is sufficient, but in every particular case another choice may be advantageous.

Random walk (4.3) on the manifold $\mathfrak{S}$ is a superposition of the standard Brownian motion w_t multiplied by some factor, and of the deterministic drift along the vector field $A=-S'(x)\alpha^2(x)$. Based on the structure of the integral lines of $S'(x)$ discussed above, we can derive here some qualitative conclusions about the amplitude ϕ defined by the mathematical expectation (4.2).

Let x be a point on $\mathbb{C}_+$ located far left of the zeros x_0^n of the wave number $k(x)$, i.e., $-u<\mathrm{Re}(x)\ll\mathrm{Re}(x_0^0)$. The vector field $A=-S'$ in this domain is estimated as $A=-1+o(1)$, and its integral lines are close to straight lines running parallel to the real axis in the negative direction. Therefore, paths (4.3) almost certainly run out to $\mathrm{Re}(x)\to-\infty$ on $\mathbb{C}_+$ where the boundary conditions are set by (4.1) to unity. It is also clear that along the paths ξ_t^x we have $S''=o(1)$, which results in the estimate

$$\phi(x)\approx 1,\quad \text{if } x\in\mathbb{C}_+,\ \mathrm{Re}(x)\ll 0. \tag{4.4}$$

Similarly, if x is located on $\mathbb{C}_-$ and $\mathrm{Re}(x)\gg 0$, then paths ξ_t^x almost certainly run out to $\mathrm{Re}(x)\to\infty$ in a domain where the boundary conditions are set by (4.1) to zero, which leads to the estimates

$$\phi(x)\approx 0,\quad \text{if } x\in\mathbb{C}_-,\ \mathrm{Re}(x)\gg 0. \tag{4.5}$$

Next, let x be a real point of the right side of $\mathbb{C}_+$, i.e., $x\in\mathbb{C}_+$, $\mathrm{Re}(x)\gg 1$, and $\mathrm{Im}(x)=0$. Then the paths (4.3) launched from x have nonzero chances to run out to infinity either on the left side of $\mathbb{C}_+$ or somewhere else. In both of

these cases the derivative $S''(x)$ may also be distinct from zero along the path ξ_t^x. All of these result in the estimate

$$\phi(x) \approx T_+, \quad \text{if } x \in \mathbb{C}_+, \ \text{Re}(x) \gg 0, \tag{4.6}$$

where T_+ is a constant whose exact value may not be provided by this qualitative reasoning. Similarly, we get the estimate

$$\phi(x) \approx T_-, \quad \text{if } x \in \mathbb{C}_-, \ \text{Re}(x) \ll 0, \tag{4.7}$$

valid if x is a real point in the left side of the sheet $\mathbb{C}_-$, i.e., $x \in \mathbb{C}_-$, $\text{Re}(x) \gg 0$, $\text{Im}(x) = 0$.

It is clear that the asymptotics of $\phi(x)$ on $\mathbb{C}_+$ provided by (4.4) and (4.7) agree with the pre-exponential coefficients from the first line of (2.3). Similarly, the asymptotics of $\phi(x)$ on $\mathbb{C}_-$ provided by (4.5) and (4.7) conform with the pre-exponentials from the second line of (2.3). We will see below that this coincidence makes it possible to use the amplitude ϕ defined by the probabilistic formula (4.2) to construct the solution of the scattering problem (2.1)–(2.3).

Finally, having the eikonal $S(x)$ and the amplitude $\phi(x)$ completely defined on the sheets $\mathbb{C}_\pm$ by formulas (3.12) and (4.2), we readily represent the solution of the scattering problem (2.1)–(2.3) as a superposition

$$\psi(x) = \psi_f(x) + \psi_b(x), \tag{4.8}$$

of the "forward" and of the "backscattered" waves $\psi_f(x)$ and $\psi_b(x)$, defined by the expressions

$$\psi_f(x) = \phi(x_+)\, e^{i\Omega K(x)}, \quad \psi_b(x) = \phi(x_-)\, e^{-i\Omega K(x)}, \tag{4.9}$$

where x is a point on the real axis; and x_+, x_- are the points corresponding to x. Comparing (4.8) and (4.9) with the asymptotics (3.11) of $K(x)$ and with the asymptotics (4.4)–(4.7) of the amplitude $\phi(x)$, one may readily see that $\psi(x)$ defined by (4.8) has the required asymptotics (2.3).

V. NUMERICAL RESULTS

To get an indication of the numerical efficiency of the random walk approach to problems of wave propagation, we simulated solutions of the scattering problem (2.1)–(2.4) with

$$\Omega = 1, \ \ k_- = 1, \ \ k_+ = 4, \ \ 0.1 \leqslant \gamma \leqslant 0.6. \tag{5.1}$$

The results of the numerical simulation are shown in Fig. 3.

The top diagram of Fig. 3 shows profiles of the wave numbers $k_\gamma(x)$ defined by (2.4). The steepest line corresponds to $\gamma = 0.1$, the most gradual line corresponds to $\gamma = 0.6$, and four other lines correspond to intermediate values of γ with the increment 0.1. Since all wave numbers $k_\gamma(x)$ in the selected range of the parameter γ become practically constant outside the interval $x \in [-3,3]$, we estimate that further computations of the wave fields may be restricted to the interval $x \in [-5,5]$.

The next diagram of Fig. 3 shows results of the numerical simulation of the amplitude $\phi_f(x) \equiv \phi(x_+)$ of the forward wave $\psi_f(x)$ from (4.9). The values of $\phi_f(x)$ are computed by the probabilistic formula (4.2). The lines on this graph display absolute values of the amplitudes $\phi_f(x)$ of the forward waves corresponding to different profiles of the wave number defined by (2.4) with the parameter γ varying from 0.1 to 0.6 as discussed above. The phases of $\phi_f(x)$ are not plotted because they never differed from zero by more than $\pm 10°$. Similar to the top graph of Fig. 3, the steepest line of the second graph corresponds to $\gamma = 0.1$, and the most gradual line corresponds to $\gamma = 0.6$ with the other lines corresponding to the intermediate values of γ.

In the domain $x < -3$ all lines of the second graph of Fig. 3 approach unity, which perfectly conforms with the estimate (4.4) and with the physical interpretation of the forward wave in this domain, where it is interpreted as the incident wave $\psi_{inc} = 1 \cdot e^{i\Omega k_- x}$.

In the domain $x > 0$ the amplitudes of the forward wave also approach some constant levels, which may be identified, according to (2.2), with the transmission coefficients $T_+ = T_+(\gamma)$ corresponding to the different profiles of the wave number from (2.4) determined by γ. The steepest line on the second graph of Fig. 3 corresponds to $\gamma = 0.1$, and the most gradual line corresponds to $\gamma = 0.6$. From the diagram we see that as γ increases, the transmission coefficient $T_+(\gamma)$ also increases from the level $T_+(0.1) \approx 0.4$ corresponding to $\gamma = 0.1$, up to the level $T_+(0.6) \approx 0.5$ which remains practically unchanged for all $\gamma > 0.6$.

Let us see if the values obtained for the transmission coefficients perfectly match the values of these coefficients suggested by qualitative considerations.

Indeed, from (2.6) it follows that if the wave number $k(x) = k_\gamma(x)$ is defined as a piecewise constant function (2.5) with the parameters assigned by (5.1), then $T_+^0 = 0.4$ is the exact value of the transmission coefficient in this case. Therefore, the approximation $T_+(0.1) \approx 0.4$ obtained from the computations, may be interpreted as an indication that the smooth wave number $k_\gamma(x)$ with $\gamma = 0.1$ approximates sufficiently well the piecewise constant wave number $k_0(x)$ from (2.5), and vice versa.

On the other hand, from the ray method it follows that if the wave number $k_\gamma(x)$ is sufficiently smooth, then the amplitude ϕ_f of the forward wave may be approximated as

$$\phi_f(x) \approx \phi_r(x) = \sqrt{\frac{k_-}{k(x)}}, \tag{5.2}$$

where $\phi_r(x)$ is the exact solution of the reduced transport equation

$$2k\phi_r' - k'\phi_r = 0, \quad \phi_r(-\infty) = k_-, \tag{5.3}$$

which is customarily considered in the ray theory as an approximation to the complete transport equation (3.3), (3.4), produced by the rigorous analysis of the scattering problem (2.1)–(2.3). Then, in the ray theory the transmission coefficient is approximated as $T_+ \approx \phi_r(+\infty) = \sqrt{k_-/k_+}$, which does not depend on the particular profile of the wave number $k(x)$, but depends only on its asymptotes $k_\pm$ at $\text{Re}(x) \to \pm\infty$. In the particular case of (5.1) the approximation (5.2), (5.3) gives exactly the value $T_+ = 0.5$, which was obtained from random walk simulation for the wave numbers $k_\gamma(x)$ with $\gamma > 0.6$. This agreement may be viewed as another confirmation of the effectiveness of the random walk approach to problems of wave propagation. Additionally, these results may be interpreted as an indication that the ray method remains accurate for problems of scattering on a po-

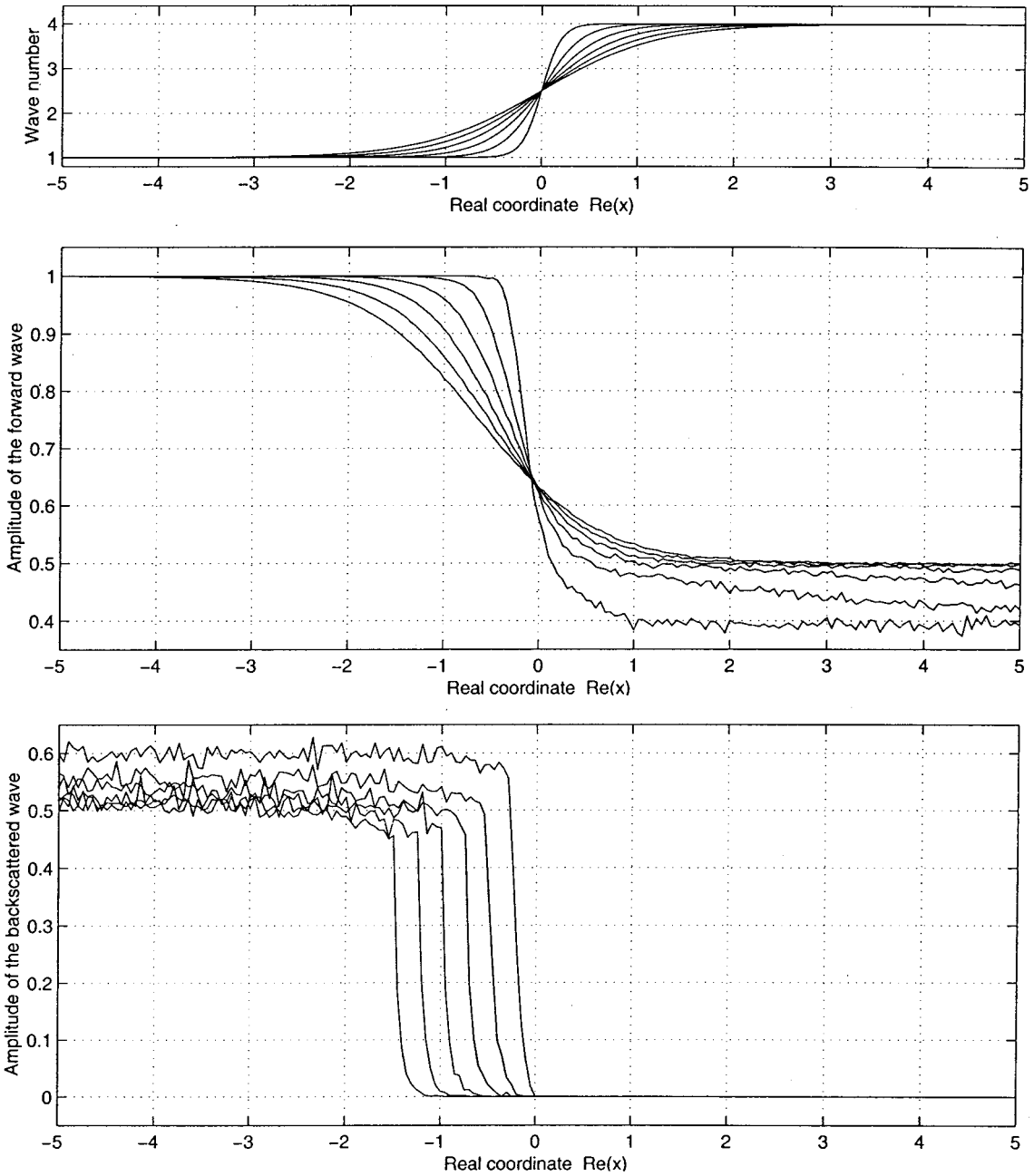

FIG. 3. Simulation of reflection and transmission coefficients.

tential whose profile is smoother than that of the wave number $k_\gamma(x)$ with $\gamma > 0.6$.

The last diagram of Fig. 3 shows results of the numerical simulation of the amplitude $\phi_b(x) \equiv \phi(x_-)$ of the backward wave $\psi_b(x)$ from (4.9). The values of $\phi_b(x)$ are computed by the probabilistic formula (4.2). The lines on this graph display absolute values of the amplitudes $\phi_b(x)$ of the backward waves corresponding to different profiles of the wave number defined by (2.4) with the parameter γ varying from 0.1 to 0.6 as discussed above. In the domain $\mathrm{Re}(x) > 0$ all lines of the second graph of Fig. 3 approach zero, which perfectly conforms with the estimate (4.5) and with the physical interpretation of the backscattered wave, which should not exist on the right of the jump of the wave number.

In the domain $\mathrm{Re}(x) < -2$ the amplitudes of the backscattered waves approach some constant levels, which may be identified, according to (2.2), with the reflection coefficients $T_- = T_-(\gamma)$ corresponding to the different profiles of the wave number from (2.4) determined by γ. The highest line on the second graph of Fig. 3 corresponds to $\gamma = 0.1$, and the lowest line corresponds to $\gamma = 0.6$. From the diagram we see that as γ increases, the reflection coefficient $T_-(\gamma)$ also decreases from the level $T_-(0.1) \approx 0.6$ corresponding to $\gamma = 0.1$, down to the level $T_+(0.6) \approx 0.5$, which remains practically unchanged for all $\gamma > 0.6$.

It is easy to see that the values obtained for the reflection coefficients perfectly match the values of these coefficients suggested by qualitative considerations.

Indeed, from (2.6) it follows that if the wave number $k(x) = k_\gamma(x)$ is defined as a piecewise constant function (2.5)

with the parameters assigned by (5.1), then $T_-^0 = 0.6$ is the exact value of the transmission coefficient in this case. Therefore, the approximation $T_+(0.1) \approx 0.6$ obtained from the computations may be interpreted as another indication that the smooth wave number $k_\gamma(x)$ with $\gamma = 0.1$ approximates sufficiently well the piecewise constant wave number $k_0(x)$ from (2.5), and vice versa.

On the other hand, if the wave number $k_\gamma(x)$ is sufficiently smooth, then the amplitude ϕ_f of the forward wave may be approximated by the ray-method formula (5.3) which predicts that, in the considered cases, the transmission coefficient must be close to $T_+ = 0.5$, independently of the particular profile of the wave number. Therefore, although the ray method does not provide any estimate of the backscattered waves, it is clear that in the absence of energy dissipation backscattered waves must exist, and that the reflection coefficient must be close to $T_- = 0.5$ for any sufficiently smooth profile of the wave number. And the graphs of the last digram of Fig. 3 approach exactly this limit $T_- = 0.5$ as parameter γ increases and makes the wave number smoother.

Comparing the graphs in Fig. 3, one may notice that the forward waves are computed more accurately and stably than the backward waves. This is explained by the different structure of the rays determining forward and backward waves. Numerical errors of random walk methods are primarily caused by the discretization and by the averaging of a finite number of paths instead of considering all possible trajectories. These reasons equally affect computations of both the forward and backward waves. However, computation of the backward waves has an additional difficulty related to the penetration of the random walks from one sheet to another. Theoretically, paths may move from one sheet to the another only through the isolated roots of the wave number, but the presented computations employed algorithms where the paths were allowed to move from one sheet to another through finite ''holes,'' which simplifies the computations but reduces the accuracy of the results. There are different ways to improve the computation of the backscattered wave. For example, it may be achieved by a special choice of the auxiliary function $\alpha(x)$ in (4.2) and (4.3), or the solution of the complete transport equation (3.3) near the roots x_0^n of the wave number may be studied by analytical methods. Our goal in this paper, however, is to focus on the general exposure of possibilities of the random walk method, and we do not go into detail of any specific technique.

VI. DISCUSSION AND CONCLUSION

The random walk methods presented here determine solutions of the Helmholtz equation as an average of values of a specified functional computed over the trajectories of the motion composed from the deterministic drift along the classic rays and random complex-valued fluctuations. As with direct numerical techniques the approach is not limited to specific geometric configurations and may be equally applied to problems with nonhomogeneous parameters as well as to problems with constant coefficients. And as with analytic or asymptotic techniques, the random walk method makes it possible to compute a solution at individual points without computing it on dense meshes. Also, solutions of the Helmholtz equation produced by the random walk method have a physically meaningful interpretation describing wave propagation as transport of some quantities along specified trajectories in the complex space. Such trajectories follow classical rays in general, but they are not forced to stay on these real-valued rays. This last detail is important, because it explains such phenomena as diffraction and backscattering, which consist of the penetration of waves into the domains unreachable by classical real-valued rays.

The probabilistic approach to the analysis of the Helmholtz equation may be extended far beyond the simple example considered here. In future papers we plan to consider the application of this method to two- and three-dimensional problems of wave propagation and to extend this method to problems of elasticity.

ACKNOWLEDGMENTS

This research was supported by NSF Grant No. CMS-0098418 and by the William S. Floyd, Jr. Distinguished Professorship in Engineering held by D. Bogy.

[1] B. V. Budaev and D. B. Bogy, ''Probabilistic solutions of the Helmholtz equation,'' J. Acoust. Soc. Am. **109**, 2260–2262 (2001).
[2] J. B. Keller, ''A geometric theory of diffraction,'' in *Calculus of Variations and its Applications* (McGraw-Hill, New York, 1958), pp. 27–52.
[3] V. P. Maslov and M. V. Fedoriuk. *Semi-classical Approximation in Quantum Mechanics* (Reidel, Dordrecht, 1981).
[4] V. I. Arnold, *Mathematical Methods of Classical Mechanics* (Springer, Berlin, 1978).
[5] V. A. Fock, *Electromagnetic Diffraction and Propagation Problems* (Pergamon, Oxford, 1965).
[6] V. A. Fock and M. A. Leontovich, ''Solution of the problem of propagation of electromagnetic waves along the earth's surface by the method of parabolic equation,'' J. Phys. (Moscow) **10**, 13 (1946).
[7] G. Bal, J. B. Keller, G. Papanicolaou, and L. Ryzhik, ''Transport theory for acoustic waves with reflection and transmission at interfaces,'' Wave Motion **30**, 303–327 (1999).
[8] G. Bal, G. Papanicolaou, and L. Ryzhik, ''Probabilistic theory of transport processes with polarization,'' SIAM (Soc. Ind. Appl. Math.) J. Appl. Math. **60**, 1639–1666 (2000).

Reflection of drill-string extensional waves at the bit-rock contact

Flavio Poletto[a] and Massimo Malusa
Istituto Nazionale di Oceanografia e di Geofisica Sperimentale—OGS, Borgo Grotta Gigante 42/c, 34010 Sgonico, Trieste, Italy

(Received 25 May 2000; accepted for publication 28 March 2002)

Downward propagating extensional waves are partially reflected at the bit-rock contact. The evaluation of the reflection coefficient is important to obtain while drilling information about the acoustic properties of the formations. The scope of this work is to estimate the bit-rock reflection coefficient, assuming a flat drill bit in perfect contact with the formation. Using the low-frequency approximation, which holds when the wavelength is much larger than the lateral dimensions of the borehole, the drill-string is assumed to be a laterally free rod, and the formation an homogeneous and isotropic medium. This work shows that the reflection coefficient of the extensional waves depends, along with the elastic properties of the formation, on the ratio of the cross sections of the drill-string and borehole. The impedance of the drilled rock can be calculated from the measured reflection coefficient, which is related to the amplitude of waves produced in the string and in the formation by a working drill-bit.
[DOI: 10.1121/1.1480423]

PACS numbers: 43.20.El, 43.40.Cw, 43.58.Bh, 43.55.Rg [DEC]

I. INTRODUCTION

The vibrations generated in the drill-string while drilling are partially reflected and transmitted at the bit-rock contact. The drill-bit reflection coefficient of the down-hole extensional waves can be analyzed to determine the elastic properties of the drilled formation and characterize the drill-string behavior.

Several researchers have investigated the drilling process using surface and down-hole measurements of the drill-string vibrations, with the purpose of determining the dynamic and kinematic behavior of the bit (Hutchinson *et al.*, 1995), of reducing undesired vibrations and risks, and optimizing the rate of penetration. In particular, earlier works aimed at understanding the behavior of the drill-string and of the rig-structure system, and obtaining information on the rock properties, were based on the theory of impedances. For instance, Lutz *et al.* (1972), developed a theoretical interpretation of the longitudinal vibrations measured at the top of the drill-string to simulate on the computer the dynamic phenomena of drilling, and give an instantaneous log of the formation while being drilled (SNAP log).

Recently, other researchers have analyzed the model of the drill-string transmission line and vibrations to correct the drill-bit seismograms used for reverse vertical profiling (RVSP). Booer and Meehan (1993) used a model-based approach to interpret the rig measurements and determine the bit-to-rock reflection coefficient by inverting the drill-string reflectivity. Malusa *et al.* (1998) provided an optimum fitting of the drill-string numerical model. These results allow the location of the bit on the seismograms produced by the bit vibrations and the comparison of the contrast of impedances at the bit with the conventional borehole-log data. The interpretation of the estimated drill-bit reflection coefficient becomes more difficult in the presence of the many nonlinear phenomena, like bouncing, stick-slip, whirling and energy losses involved in the drilling process. The coupling between the drill-bit and the rock also depends on the variation of the drilling parameters, such as weight-on-bit (WOB), rate-of-penetration (ROP), torque-on-bit (TOB), velocity of rotation (RPM), and pressure of the drilling mud.

The model proposed in this work is the following: the drill-string is represented by a rod, with a flat bit coupled to the formation. The formation is isotropic and homogeneous and the transmitted wave field is represented as plane compressional waves in the low-frequency approximation (i.e., wavelengths that are much longer than the borehole radius). Lateral-bending effects and conversions of the extensional string-waves to shear and flexural modes are not considered. (Chin, 1994; Drumheller, 1993). The relation between the rock impedance scaled by the ratio of the rod-to-borehole cross-sections and the reflection coefficient is obtained by assuming that the bit is not working (rotating). Then, the bit is assumed to be working as a vertical displacement source to obtain the relations between the calculated drill-bit reflection coefficient and the amplitude of the waves generated in the drill-string and in the formation.

This paper is organized as follows. First, we describe the stress–strain constitutive model of the rod in the borehole. Second, we compute the reflection coefficient at the bit-rock interface. Then, we express this coefficient as a function of the elastic properties of the rod and of the rock, and calculate the relation between the acoustic impedance of the formation and the reflection coefficient. A displacement source is then introduced to calculate the amplitude of the waves in the string and the formation. Finally, we consider some numerical and real examples and discuss the results.

[a]Electronic mail: fpoletto@ogs.trieste.it

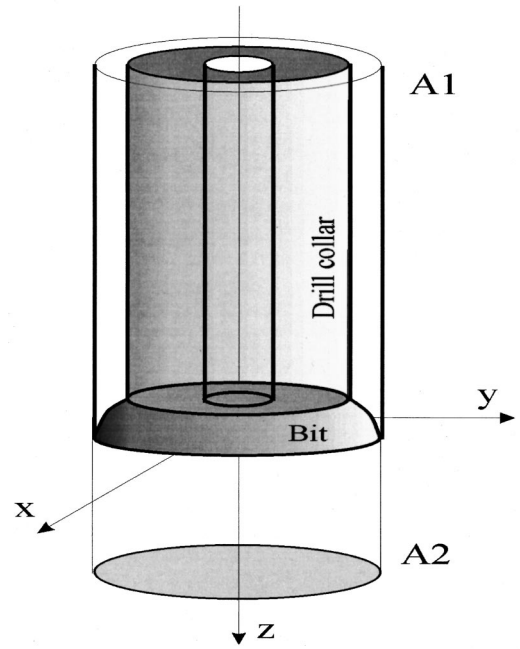

FIG. 1. An idealized semi-infinite drill-string is assumed as a rod in a borehole, which is drilled in an infinite homogeneous and isotropic medium. The vertical axial direction is the z. The rod is laterally free. The bit is flat and coupled to the formation at the interface contact. The cross section of the rod is A_1, while the bit area equals the borehole cross-section A_2. Different stress conditions are present at the opposite sides of the bit interface, internally in the rod and externally in the formation.

II. CONSTITUTIVE EQUATIONS

Let us consider a borehole in a homogeneous, isotropic, and unbounded medium containing a semi-infinite rod (Fig. 1). We assume the low-frequency approximation, which holds when the minimum wavelength is much larger than the borehole lateral dimensions—in this approximation, the choice of rectangular coordinates to calculate the extensional waves in a rod does not entail the generality of the results (Kolsky, 1953). The vertical (axial) dimension is *z*, while *x* and *y* are the horizontal coordinates. We also assume that the borehole has no drilling-mud, and that the rod is laterally free, coupled to the formation only at the bit contact. The bit is in a not working state and its bottom interface is a flat surface. The bit area, A_2, equals the cross section of the borehole, while the rod cross section, A_1, equals the cross section of the drill collars in the bottom hole assembly (BHA).

Let σ_x, σ_y, and σ_z be the normal-stress components, and u, v, and w the displacements in the *x*, *y*, and *z* directions, respectively. The strain–stress constitutive relations (Jaeger, 1969) are

$$E\epsilon_x=\sigma_x-\nu(\sigma_y+\sigma_z), \tag{1}$$

$$E\epsilon_y=\sigma_y-\nu(\sigma_z+\sigma_x), \tag{2}$$

$$E\epsilon_z=\sigma_z-\nu(\sigma_x+\sigma_y), \tag{3}$$

where

$$\epsilon_x=\frac{\partial u}{\partial x}, \quad \epsilon_y=\frac{\partial v}{\partial y}, \quad \epsilon_z=\frac{\partial w}{\partial z}, \tag{4}$$

are the normal strains, E is the Young's modulus, and ν is the Poisson's ratio, which is related to the *P*-wave (V_P) and *S*-wave (V_S) velocities by

$$\frac{2(1-\nu)}{1-2\nu}=\left(\frac{V_P}{V_S}\right)^2. \tag{5}$$

Let us consider an extensional stress-wave traveling in the rod and incident at the bit-rock interface. The stress conditions are different in the rod and the formation.

In the following, we denote with the subindexes 1 and 2 the field variables and material properties in the rod and formation, respectively. Since the rod is assumed laterally free in the borehole, the lateral stresses are $\sigma_{x1}=\sigma_{y1}=0$, and, using Eq. (3) we obtain

$$E_1\epsilon_{z1}=\sigma_{z1}. \tag{6}$$

On the other hand, the stress conditions are different in the formation, where the rock coupled to the bit is surrounded by other rock. Using the hypothesis of isotropy for the horizontal stress in the formation, it is $\sigma_{x2}=\sigma_{y2}\neq 0$. We assume that the induced strain is different from zero only in the vertical direction (the surrounding rock produces a reaction stress, which has the effect of compensating the horizontal relative displacements. However, this approximation does not hold if we model the bit as a point source). Then

$$\epsilon_{x2}=\epsilon_{y2}=0. \tag{7}$$

Using equations from (1)–(3), and (7), gives

$$\sigma_{x2}=\sigma_{y2}=\frac{\nu_2}{1-\nu_2}\sigma_{z2}. \tag{8}$$

Equation (8) corresponds to the well-known result (Jaeger, 1969) that for actual rocks the vertical principal-stress due to the vertical-load of the weight of the column of rock is roughly three times (exactly three times in a Poisson's medium) the horizontal principal-stress components. Using Eqs. (3) and (8), we obtain the relation between the vertical strain and stress in the formation,

$$E_2\epsilon_{z2}=\frac{(1+\nu_2)(1-2\nu_2)}{1-\nu_2}\sigma_{z2}. \tag{9}$$

III. REFLECTION COEFFICIENT

Since the bit is coupled to the formation, the continuity condition of the displacement at the bit-rock interface ($z=0$) implies

$$w_1=w_2. \tag{10}$$

The continuity condition of the vertical force at the interface is

$$A_1\sigma_{z1}=A_2\sigma_{z2}. \tag{11}$$

Substituting Eqs. (6) and (9) in (11) gives

$$A_1E_1\epsilon_{z1}=A_2E_2\epsilon_{z2}\frac{1-\nu_2}{(1+\nu_2)(1-2\nu_2)}. \tag{12}$$

Let the reflection and transmission coefficients be c_0 and $t_0=1+c_0$, and consider the plane wave solutions

$$w_1 = \exp[\iota(\omega t - k_1 z)] + c_0 \exp[\iota(\omega t + k_1 z)], \tag{13}$$

and

$$w_2 = t_0 \exp[\iota(\omega t - k_2 z)], \tag{14}$$

in the rod and formation, respectively. From Eq. (4) it follows that at $z=0$ we have

$$\epsilon_{z1} = -\iota k_1 (1 - c_0) \exp(\iota \omega t), \tag{15}$$

and

$$\epsilon_{z2} = -\iota k_2 (1 + c_0) \exp(\iota \omega t). \tag{16}$$

Substituting these results into Eq. (12), we obtain the reflection coefficient at the bit interface

$$c_0 = \frac{a-1}{a+1}, \tag{17}$$

where a is given by

$$a = \left(\frac{A_1 E_1 k_1}{A_2 E_2 k_2}\right) \frac{(1+\nu_2)(1-2\nu_2)}{1-\nu_2}. \tag{18}$$

On the other hand, for the continuity of the angular frequency ω, the ratio of the wave numbers in the rod and formation is

$$\frac{k_1}{k_2} = \frac{V_{P2}}{V_{E1}}, \tag{19}$$

where V_{E1} is the velocity of the extensional wave in the rod. Let ρ be the mass density. The velocity of the extensional wave in the rod (Kolsky, 1953) is

$$V_{E1} = \sqrt{\frac{E_1}{\rho_1}}. \tag{20}$$

The compressional velocity of the formation can be expressed as

$$V_{P2} = \sqrt{\frac{1-\nu_2}{(1+\nu_2)(1-2\nu_2)}} \sqrt{\frac{E_2}{\rho_2}}. \tag{21}$$

Using Eqs. (18)–(21), we obtain

$$a = \frac{A_1}{A_2} \frac{\sqrt{\rho_1 E_1}}{\rho_2 V_{P2}}, \tag{22}$$

and, using Eq. (17), the reflection coefficient at the bit can be written as

$$c_0 = \frac{A_1 \sqrt{\rho_1 E_1} - A_2 \rho_2 V_{P2}}{A_1 \sqrt{\rho_1 E_1} + A_2 \rho_2 V_{P2}}. \tag{23}$$

Since E_1, and ρ_1 are known, Eq. (23) gives the reflection coefficient in function of the ratio of the cross sections and the elastic parameters of the formation. On the other hand, Eq. (18) gives

$$a = \frac{1+c_0}{1-c_0}, \tag{24}$$

and using Eq. (23) we estimate the impedance of the drilled rock as

$$\rho_2 V_{P2} = \frac{A_1}{A_2} \sqrt{\rho_1 E_1} \frac{1-c_0}{1+c_0}. \tag{25}$$

Using Eq. (25), the impedance of the drilled formation can be computed by measuring c_0 from reflections in drill-bit data (Malusa *et al.*, 1998). With an alternative approach, c_0 can also be estimated by measuring the amplitude of the direct roller-cone drill-bit waves, which is related to the contrast of the impedances at the bit-rock interface (Lutz *et al.*, 1972; Clayer *et al.*, 1990). The numerical algorithm for solving wave propagation in the presence of an imperfect contact was considered, for instance, by Carcione (1996). Here, for simplicity, we assume that the working drill bit is a monochromatic source, and that the vertical relative displacement between drill string and formation is given by

$$\delta \exp(\iota \omega t) = w_2 - w_1, \tag{26}$$

where δ is a constant related to the magnitude of the acting monochromatic force. The balance of the forces at the bit interface gives

$$A_1 \sigma_{z1} = A_2 \sigma_{z2}. \tag{27}$$

We introduce the plane wave solutions

$$w_1 = \alpha_1 \exp[\iota(\omega t + k_1 z)], \tag{28}$$

and

$$w_2 = \alpha_2 \exp[\iota(\omega t - k_2 z)], \tag{29}$$

where α_1 and α_2 are constant amplitudes. With a way of reasoning similar to that already used, at $z=0$ we obtain

$$A_1 \sqrt{\rho_1 E_1} \alpha_1 = -A_2 \rho_2 V_{P2} \alpha_2, \tag{30}$$

and, after some calculations, we obtain

$$\frac{\alpha_2}{\alpha_1} = -\frac{1+c_0}{1-c_0}, \tag{31}$$

where c_0 is given by Eq. (23). From Eq. (26) it is

$$\delta = \alpha_2 - \alpha_1. \tag{32}$$

Using Eqs. (31) and (32) gives the amplitude of the extensional drill-string wave, by

$$\alpha_1 = -\frac{\delta}{2}(1-c_0), \tag{33}$$

and the amplitude of the compressional wave in the formation, by

$$\alpha_2 = \frac{\delta}{2}(1+c_0). \tag{34}$$

These relations also show that the amplitude of the seismograms obtained by correlating the drill-string and geophone measurements is indicatively proportional to $(1-c_0^2)$, with c_0 given by Eq. (23). In any case, we have to consider that the plane-wave approximation may yield an overestimate of radiated energy. Use of the point-force assumption may give better results and leads to the calculation of a complex reflection coefficient.

TABLE I. Drill-collar and drill-bit diameters.

Drill strings	d_1 (m)	D_1 (m)	D_2 (m)
1	0.070	0.203	0.324
2	0.073	0.165	0.216

IV. EXAMPLES

We use the following values for the elastic properties of steel: $E_1 = 206$ GPa, and $\rho_1 = 7840$ kg/m^3. The cross-section A_1 is calculated by considering only the drill-collars in the BHA close to the bit, since the reflection coefficients between pipes and drill-collars are known (Poletto *et al.*, 2001). In the first example, we compare the models of two drill-strings (Table I) in the same formation, in which $V_{P2} = 4100$ m/s and $\rho_2 = 2400$ kg/m^3 is assumed. In the first drill-string, the bit diameter (D_2) is 0.324 m, the internal (d_1) and external (D_1) diameters of the drill collar are 0.070 and 0.203 m, respectively, and the ratio $A_1/A_2 = 0.38$. In the second case, the bit diameter is 0.216 m, the internal and external diameters of the drill-collar are 0.073 and 0.165 m, respectively, and the ratio $A_1/A_2 = 0.47$. Using Eq. (23), we obtain $c = 0.216$, and $c = 0.315$, in the first and second drill-string, respectively.

Figure 2 shows results obtained using real axial-pilot roller-cone-bit data measured for seismic-while-drilling RVSP surveying (Miranda *et al.*, 1996). The data were acquired with depth intervals of about 20 m, from 500 to 2500 m depth. Each acquisition level corresponds to about 45 min of continuous drilling. Figure 2(a) shows the lithostratigraphic profile and the variation of A_1/A_2. Figure 2(b) shows the reflection coefficients calculated by the optimum fit of the drill-bit data to the numerical model of the drill-string multiples. The measured drill-bit reflection coefficient (thin curve) is compared with the theoretical reflection coefficient (thick curve) calculated by using Eq. (23) and conventional sonic-log data. Figure 2(c) shows the acoustic impedance calculated while-drilling using drill-bit data (thin curve) and Eq. (25). It is compared with the acoustic impedance measured by conventional sonic-log data (thick curve). The average trends of drill-bit and sonic-log data are in good agreement. The main differences between the two curves are interpreted as the effects due to the simplified model used for calculating the drill-bit reflection coefficient and to the presence of noise in drill-bit data.

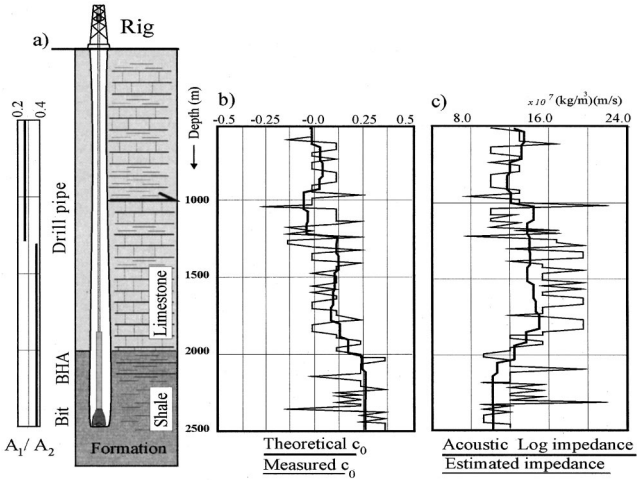

FIG. 2. (a) The well with the lithostratigraphic profile and the variation of A_1/A_2. (b) The measured reflection coefficient (thin curve), compared with the theoretical reflection coefficient (thick curve) calculated by using conventional sonic-log data. (c) The acoustic impedance calculated using drill-bit data (thin curve) and the acoustic impedance measured by conventional sonic-log data (thick curve).

V. CONCLUSIONS

The drill-bit reflection coefficient is obtained assuming ideal conditions and considering extensional waves. Actually, at the bit-rock contact, shear waves in the formation and flexural waves in the string are also produced, and the results given in Eqs. (23) and (25) have to be considered as the plane-wave approximation of c_0. Under this low-frequency approximation, the results obtained from sonic-log data show a good average trend with the coefficient measured in real drill-bit data. The calculated values should be regarded as reference values, obtained with the maximum and perfect coupling of the cross sections at the bit-rock interface, in the absence of drilling noise. In realistic cases, the bit is working, not-flat and the section of contact is probably reduced, thus increasing A_1/A_2 and c_0, which often ranges from negative values to 0.5. In the analysis of actual data obtained using drill-bits with different shapes and performances, it could be considered the influence of the drilling parameters. The effective drill-bit cross section to be used in the calculus of c_0 should depend on the weight-on-bit (WOB) and mud pressure, which influence the coupling, on the rate-of-penetration (ROP), on the velocity of rotation (RPM), as well as on the presence of cuttings under the bit. For these reasons, the model needs an extension, to better approximate the point-source model using a complex reflection coefficient, and to include the actual bit performances and drilling conditions.

ACKNOWLEDGMENT

The authors thank José M. Carcione for useful technical comments.

Booer, A. K., and Meehan, R. J. (**1993**). "Drilling imaging—An interpretation of surface drilling vibrations," SPE Drilling & Completion, June, 93–98.

Carcione, J. M. (**1996**). "Elastodynamics of a non-ideal interface: Application to crack and fracture scattering," J. Geophys. Res., [Space Phys.] **101**, 28177–28188.

Chin, W. C. (**1994**). *Wave Propagation in Petroleum Engineering* (Gulf, Publishing Co.).

Clayer, F., Vandiver, J.K., and Lee, H.Y. (**1990**). "The Effect of Surface and Downhole Boundary Conditions on the Vibration of Drillstrings." SPE Paper No. 20447.

Drumheller, D.S (**1993**). "Coupled extensional and bending motion in elastic vaveguides," Wave Motion **17**, 319–327.

Hutchinson, M., Dubinsky, V., and Henneuse, H. (**1995**). "An MWD downhole assistant driller," Society of Petroleum Engineers, Paper No. 30523.

Jaeger, J. C. (**1969**). *Elasticity, Fracture and Flow with Engineering and Geological Applications* (Science Paperbacks, London), p. 55.

Kolsky, H. (**1953**). *Stress Waves in Solids* (Clarendon, Oxford).

Lutz, J., Raynaud, M., Gastalder, S., Quichaud, C., Raynald, J., and Muckerloy, J.A. (**1972**) ''Instantaneous logging based on a dynamic theory of drilling,'' J. Petr. Tech., June, 750–758.

Malusa, M., Poletto, F., Miranda, F., and Bernasconi, G. (**1998**). ''SWD interpretation by modeling of pilot and seismic signals: Extended Abstracts,'' 60th Meeting and Exposition of EAEG, Paper No. 10-51.

Miranda, F., Aleotti, L., Abramo, F., Poletto, F., Craglietto, A., Persoglia, S., and Rocca, F. (**1996**). ''Impact of Seismic 'While drilling' technique on exploration wells,'' First Break **14**, 55–68.

Poletto, F., Malusa, M., and Miranda, F. (**2001**). ''Numerical modeling and interpretation of drillstring waves,'' Geophysics, Soc. Expl. Geophys, **66**, 1569–1581.

A direct mixed-body boundary element method for packed silencers

T. W. Wu[a)]
Department of Mechanical Engineering, University of Kentucky, Lexington, Kentucky 40506

C. Y. R. Cheng
Nelson Industries, Inc., Stoughton, Wisconsin 53589

P. Zhang
Department of Mechanical Engineering, University of Kentucky, Lexington, Kentucky 40506

(Received 13 August 2000; revised 11 March 2002; accepted 19 March 2002)

Bulk-reacting sound absorbing materials are often used in packed silencers to reduce broadband noise. A bulk-reacting material is characterized by a complex mean density and a complex speed of sound. These two material properties can be measured by the two-cavity method or calculated by empirical formulas. Modeling the entire silencer domain with a bulk-reacting lining will involve two different acoustic media, air and the bulk-reacting material. Traditionally, the interior silencer domain is divided into different zones and a multi-domain boundary element method (BEM) may be applied to solve the problem. However, defining different zones and matching the elements along each interface is tedious, especially when the zones are intricately connected. In this paper, a direct mixed-body boundary element method is used to model a packed silencer without subdividing it into different zones. This is achieved by summing up all the integral equations in different zones and then adding the hypersingular integral equations at interfaces. Several test cases, including a packed expansion chamber with and without an absorbing center bullet, and a parallel baffle silencer, are studied. Numerical results for the prediction of transmission loss (TL) are compared to experimental data. [DOI: 10.1121/1.1476920]

PACS numbers: 43.20.Fn, 43.50.Gf [VWS]

I. INTRODUCTION

Reactive mufflers and packed silencers used in industry usually contain very complex internal components such as extended inlet/outlet tubes, thin baffles, perforated tubes, and bulk-reacting sound absorbing materials. Although the interior fluid domain is bounded, the boundary element method (BEM) is still an ideal analysis tool due to its surface-only meshing scheme. Recently, Wu and his co-workers[1,2] have developed a so-called ''direct mixed-body BEM'' for the analysis of reactive mufflers. In the context of this method, each surface component has its own attribute, such as ''regular,'' ''thin,'' and ''perforated.'' Due to the use of constant elements, a BEM model can be easily created by assembling different surface components together. The mesh is also automatically refined at each frequency step of calculation. This means a very coarse mesh is used at low frequencies, and the mesh is automatically refined as the frequency goes up. With the component assembly capability of the direct mixed-body BEM, there is no need to do the tedious multi-domain zoning and interface matching as required by the conventional multi-domain BEM.[3,4]

For packed silencers, the BEM modeling becomes even more challenging because there are at least two different acoustic media involved, air and the bulk-reacting sound absorbing material. A bulk-reacting sound absorbing material is characterized by a complex speed of sound and a complex mean density.[5] These two material properties are related to the propagation constant and the characteristic impedance which can be either measured by the two-cavity method[5] or calculated by empirical formulas if the flow resistivity of the material is known.[6] The traditional modeling approach is to use the multi-domain BEM[7] in which each subdomain is still homogeneous. However, the internal geometry of a typical packed silencer is usually quite complex and there may be too many subdomains intricately connected together. It is impractical to define so many subdomains and try to match the boundary conditions at all interfaces.

The finite element method (FEM) may be an alternative way to model a packed silencer. However, it should be noted that sound pressure is not continuous everywhere. Bulk-reacting linings are usually covered by a perforated thin surface. At the perforated interface, the pressure jump is related to the normal velocity by an empirical transfer impedance. On the other hand, a rigid thin plate with no perforation could occasionally be placed between air and a certain side of a bulk-reacting material. At the rigid thin plate interface, sound pressure has a jump but the normal velocities on both sides are zero. Since each 3-D brick finite element has six surfaces, it is very tedious to go through every different interface and assign an appropriate interface condition. In addition, 3-D finite element meshes are hard to visualize because they represent the fluid domain, not the muffler/silencer geometry. This is especially true when the internal geometry is very complex.

From the design point of view, the BEM is still a pre-

a)Electronic mail: timwu@engr.uky.edu

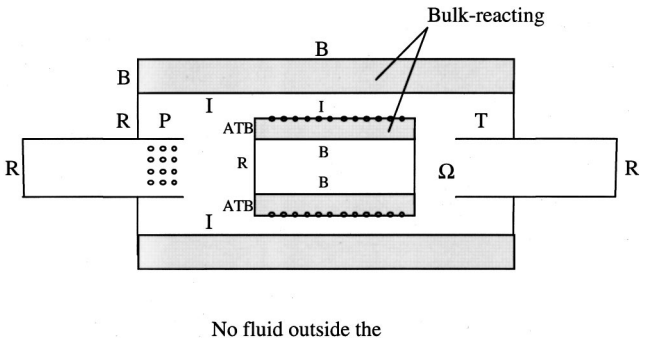

FIG. 1. Types of surfaces modeled in the direct mixed-body BEM.

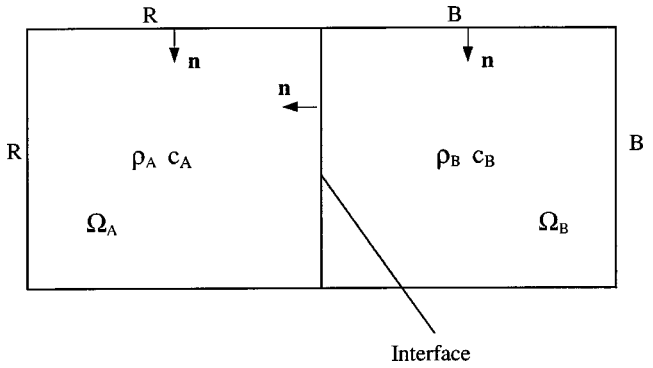

FIG. 2. A simplified two-medium problem. The interface can be I, or IP, or ATB.

ferred method for muffler/silencer analysis because the BEM mesh represents the true muffler/silencer geometry. In this paper, the direct mixed-body BEM for reactive mufflers[1,2] is extended to the analysis of packed silencers. With reference to Fig. 1, each surface in a silencer model has its own surface attribute. In other words, a surface can be either ''regular'' (R), ''thin'' (T), ''perforated'' (P), ''bulk reacting'' (B), ''interface'' (I), ''perforated interface'' (IP), or ''air-thin-bulk reacting'' (ATB). The R surfaces include the exterior silencer surfaces (with no bulk-reacting packing), the inlet/outlet tubes, and the inlet/outlet ends. The T surfaces are the thin components inside the silencer, such as the extended inlet/outlet tubes, thin baffles, flow plugs, and internal connecting tubes. The P surfaces are designated for perforated surfaces with air on both sides. The B surfaces are the exterior surfaces with the bulk-reacting material. The I surfaces are the interfaces between the bulk-reacting material and air. The IP surfaces are the perforated interfaces between the bulk-reacting material and air. The ATB surfaces represent the rigid thin plates between the bulk-reacting material and air. Of all the surfaces shown in Fig. 1, R, T, and P surfaces have been used in reactive mufflers,[1,2] and B, I, IP, and ATB are additional new surfaces defined for packed silencers.

The basic idea of the direct mixed-body BEM actually comes from the conventional multi-domain BEM. The difference is that the integral equations of all subdomains are summed up. The idea of adding integral equations together was discussed by Copley in 1968.[8] The numerical system is then supplemented by adding the hypersingular integral equations[9] at interfaces. Since the integral equations of all subdomains are summed up, the method actually becomes a single-domain BEM. As such, there is no need to define subdomains and match interface conditions anymore.

This paper begins with the derivation of the integral equations for a simplified two-medium configuration. The interface between air and the bulk-reacting material could be either I, IP, or ATB. Then the complete integral equations for a combination of different surfaces are presented. Several test cases, including a packed simple expansion chamber with and without an absorbing center bullet, and a parallel baffle silencer, are used to verify the formulation. The BEM predictions for the transmission loss (TL) are compared to the experiment results.

II. TWO-MEDIUM PROBLEM

A simplified two-medium problem is shown in Fig. 2 for derivation purposes. Let ρ_A and c_A denote the mean density and speed of sound of air, and ρ_B and c_B denote the mean density and speed of sound of the bulk-reacting material, respectively. Note that ρ_B and c_B are both complex numbers and are related to the propagation constant and the characteristic impedance by

$$c_B=\frac{i\omega}{\Gamma_B}, \tag{1}$$

$$\rho_B=\frac{Z_B}{c_B}, \tag{2}$$

where $i=\sqrt{-1}$, ω is the angular frequency, Γ_B is the propagation constant, and Z_B is the characteristic impedance. Both Γ_B and Z_B can be measured by the two-cavity method,[5] or calculated by empirical power law approximations if the flow resistivity of the bulk-reacting material is known.[6] The governing differential equations for this two-medium problem in the frequency domain are

$$\nabla^2 p+k_A^2 p=0 \quad \text{in air,} \tag{3}$$

$$\nabla^2 p+k_B^2 p=0 \quad \text{in the bulk-reacting material,} \tag{4}$$

where p is the sound pressure, and k_A and k_B are the wave numbers in air and the bulk-reacting material, respectively. Three kinds of interfaces between air and the bulk-reacting material will be considered in the latter part of this paper. With reference to Fig. 2, the interior domain of the air side is denoted by Ω_A and the bulk-reacting material by Ω_B. Let $\mathbf{n}$ be the unit normal vector. The unit normal vector on R or B is pointing into the interior acoustic domain, and on the interface the normal is pointing into the air side. Then the Helmholtz integral equation can be written for each domain. If the $e^{+i\omega t}$ convention is adopted, the boundary integral equations are

$$\int_{\mathrm{R}}\left(p\frac{\partial\psi_A}{\partial n}+i\rho_A\omega v_n\psi_A\right)dS$$

$$+\int_{\text{interface}}\left(p\frac{\partial\psi_A}{\partial n}+i\rho_A\omega v_n\psi_A\right)dS$$

$$=\begin{cases}4\pi p(P), & P\in\Omega_A, \quad (5a)\\ 2\pi p(P), & P\in \mathrm{R}+\text{interface}, \quad (5b)\\ 0, & P\in\Omega_B+\mathrm{B}, \quad (5c)\end{cases}$$

$$\int_{\mathrm{B}}\left(p\frac{\partial\psi_B}{\partial n}+i\rho_B\omega v_n\psi_B\right)dS$$

$$-\int_{\text{interface}}\left(p\frac{\partial\psi_B}{\partial n}+i\rho_B\omega v_n\psi_B\right)dS$$

$$=\begin{cases}4\pi p(P), & P\in\Omega_B, \quad (6a)\\ 2\pi p(P), & P\in \mathrm{B}+\text{interface}, \quad (6b)\\ 0, & P\in\Omega_A+\mathrm{R}, \quad (6c)\end{cases}$$

where v_n is the normal velocity, P is the collocation point, and ψ_A and ψ_B are the free-space Green's functions in air and the bulk-reacting material, respectively. A negative sign is used in front of the integral over the interface in Eq. (6) because the normal at the interface is pointing into air. Due to the use of constant elements, the solid angle at P on the surface is always 2π. The explicit expressions for the two Green's functions are

$$\psi_A=\frac{e^{-ik_Ar}}{r}, \quad (7a)$$

$$\psi_B=\frac{e^{-ik_Br}}{r}, \quad (7b)$$

where $r=|P-Q|$, and Q is any integration point on the boundary.

The direct mixed-body BEM begins with summing up Eqs. (5) and (6). There are three kinds of interfaces considered in this paper: I, IP, and ATB. They are discussed individually in the following.

A. Interface I

At the I interface, the bulk-reacting material is in direct contact with air. Both p and v_n are continuous across the interface. Summing up Eqs. (5) and (6) yields

$$\int_{\mathrm{R}}\left(p\frac{\partial\psi_A}{\partial n}+i\rho_A\omega v_n\psi_A\right)dS$$

$$+\int_{\mathrm{B}}\left(p\frac{\partial\psi_B}{\partial n}+i\rho_B\omega v_n\psi_B\right)dS$$

$$+\int_{\mathrm{I}}\left[p\left(\frac{\partial\psi_A}{\partial n}-\frac{\partial\psi_B}{\partial n}\right)+i\omega v_n(\rho_A\psi_A-\rho_B\psi_B)\right]dS$$

$$=\begin{cases}4\pi p(P), & P\in\Omega_A+\Omega_B, \quad (8a)\\ 2\pi p(P), & P\in \mathrm{R}+\mathrm{B}, \quad (8b)\\ 4\pi p(P), & P\in \mathrm{I}. \quad (8c)\end{cases}$$

Note that on R and B surfaces, either p or v_n or a local impedance is specified as the boundary condition, and there is only one unknown variable at each node. Equation (8b) is sufficient for providing the necessary equation to solve the unknown variable at each node. However, at interface I, neither p nor v_n is known *a priori*. Equation (8c) itself would not be sufficient to solve the two unknowns at each node on I. An additional equation is needed to supplement Eq. (8c).

To provide the additional equation, the hypersingular normal-derivative integral equations corresponding to Eqs. (5b) and (6b), respectively, are first written. They are

$$\int_{\mathrm{R}}\left(p\frac{\partial^2\psi_A}{\partial n\partial n^P}+i\rho_A\omega v_n\frac{\partial\psi_A}{\partial n^P}\right)dS$$

$$+\int_{\mathrm{I}}\left(p\frac{\partial^2\psi_A}{\partial n\partial n^P}+i\rho_A\omega v_n\frac{\partial\psi_A}{\partial n^P}\right)dS$$

$$=2\pi\frac{\partial p}{\partial n}(P), \quad P\in \mathrm{I} \ \text{ from the air side}, \quad (9)$$

$$\int_{\mathrm{B}}\left(p\frac{\partial^2\psi_B}{\partial n\partial n^P}+i\rho_B\omega v_n\frac{\partial\psi_B}{\partial n^P}\right)dS$$

$$-\int_{\mathrm{I}}\left(p\frac{\partial^2\psi_B}{\partial n\partial n^P}+i\rho_B\omega v_n\frac{\partial\psi_B}{\partial n^P}\right)dS$$

$$=2\pi\frac{\partial p}{\partial n}(P), \quad P\in \mathrm{I} \ \text{ from the bulk-reacting side}, \quad (10)$$

where n^P is the unit normal vector at P and the normal derivative with respect to n^P is taken with respect to the coordinates of P. It should be noted that although both p and v_n are continuous across interface I, $\partial p/\partial n$ is not. Using the relationship $\partial p/\partial n=-i\rho\omega v_n$ in each of Eqs. (9) and (10) and then summing up the two equations produce

$$\int_{\mathrm{R}}\left(p\frac{\partial^2\psi_A}{\partial n\partial n^P}+i\rho_A\omega v_n\frac{\partial\psi_A}{\partial n^P}\right)dS+\int_{\mathrm{B}}\left(p\frac{\partial^2\psi_B}{\partial n\partial n^P}\right.$$

$$\left.+i\rho_B\omega v_n\frac{\partial\psi_B}{\partial n^P}\right)dS+\int_{\mathrm{I}}\left[p\left(\frac{\partial^2\psi_A}{\partial n\partial n^P}-\frac{\partial^2\psi_B}{\partial n\partial n^P}\right)\right.$$

$$\left.+i\omega v_n\left(\rho_A\frac{\partial\psi_A}{\partial n^P}-\rho_B\frac{\partial\psi_B}{\partial n^P}\right)\right]dS$$

$$=-2\pi i\omega(\rho_A+\rho_B)v_n(P), \quad P\in \mathrm{I}. \quad (11)$$

Equation (11) provides the additional equation to supplement Eq. (8c) for the two unknowns at each node on I. Note that although both Eqs. (9) and (10) are hypersingular, Eq. (11) is only weakly singular because the strong singularities in the two Green's functions cancel out in subtraction.

B. Perforated interface IP

At the IP interface, a perforated metal sheet is used to separate the bulk-reacting material from air. The usual practice is to assume that the normal velocity is continuous and let sound pressure have a jump across the perforated interface. If both sides of the perforated interface are air, Sullivan and Crocker[10] have carried out an experimental study and proposed an empirical transfer impedance formula that re-

lates the pressure jump to the normal velocity. Unfortunately, no experimental study has been done in the case of a perforated interface between air and a bulk-reacting material. At this point, we just assume that a very thin layer of air gap exists between the perforated interface and the bulk-reacting material. With this assumption, we can still apply the Sullivan and Crocker formula. In other words,

$$p_B - p_A = \rho_A c_A \xi v_n, \tag{12}$$

where ξ is the dimensionless transfer impedance, and p_A and p_B are the sound pressure on the air side and the bulk-reacting side, respectively. At room temperature and in the absence of mean flow, a simple empirical formula given by Sullivan and Crocker in the linear regime is[10]

$$\xi = \frac{1}{\rho_A c_A \sigma}(2.4 + i0.02f), \tag{13}$$

where f is frequency in Hz, and σ is the porosity (the open to the total area ratio). Note that the two constants 2.4 and 0.02 are in the MKS units. Alternative empirical formulas that use additional parameters such as wall thickness, hole diameter, and Mach number are also available and have been applied in modeling.[2]

At the IP interface, there are two independent unknowns, p_A and v_n. The third unknown p_B can be expressed in terms of the two independent unknowns via Eq. (12). That is,

$$p_B = p_A + \rho_A c_A \xi v_n. \tag{14}$$

Substitute Eq. (14) into Eq. (6) and then sum up Eqs. (5) and (6). This produces

$$\begin{aligned}
&\int_R \left(p \frac{\partial \psi_A}{\partial n} + i\rho_A \omega v_n \psi_A \right) dS \\
&+ \int_B \left(p \frac{\partial \psi_B}{\partial n} + i\rho_B \omega v_n \psi_B \right) dS + \int_{IP} \left[p_A \left(\frac{\partial \psi_A}{\partial n} - \frac{\partial \psi_B}{\partial n} \right) \right. \\
&\left. - \rho_A c_A \xi v_n \frac{\partial \psi_B}{\partial n} + i\omega v_n (\rho_A \psi_A - \rho_B \psi_B) \right] dS \\
&= \begin{cases} 4\pi p(P), & P \in \Omega_A + \Omega_B, \quad (15a) \\ 2\pi p(P), & P \in R + B, \quad (15b) \\ 4\pi p_A(P) + 2\pi \rho_A c_A \xi v_n(P), & P \in IP. \quad (15c) \end{cases}
\end{aligned}$$

Since there are two unknowns at each node on IP, Eq. (15c) needs a companion normal-derivative integral equation similar to Eq. (11). That is,

$$\begin{aligned}
&\int_R \left(p \frac{\partial^2 \psi_A}{\partial n \partial n^P} + i\rho_A \omega v_n \frac{\partial \psi_A}{\partial n^P} \right) dS + \int_B \left(p \frac{\partial^2 \psi_B}{\partial n \partial n^P} \right. \\
&\left. + i\rho_B \omega v_n \frac{\partial \psi_B}{\partial n^P} \right) dS + \int_{IP} \left[p_A \left(\frac{\partial^2 \psi_A}{\partial n \partial n^P} - \frac{\partial^2 \psi_B}{\partial n \partial n^P} \right) \right. \\
&\left. - \rho_A c_A \xi v_n \frac{\partial^2 \psi_B}{\partial n \partial n^P} + i\omega v_n \left(\rho_A \frac{\partial \psi_A}{\partial n^P} - \rho_B \frac{\partial \psi_B}{\partial n^P} \right) \right] dS \\
&= -2\pi i \omega (\rho_A + \rho_B) v_n(P), \quad P \in IP. \quad (16)
\end{aligned}$$

Unlike Eq. (11), Eq. (16) is indeed hypersingular because of the term due to the transfer impedance ξ.

C. Air-thin-bulk reacting interface ATB

Thin metal plates without perforation are occasionally used to separate the bulk-reacting material from air. One example is the end flanges of the absorbing center bullet shown in Fig. 1. Another example of ATB is the frame of a splitter used in a parallel baffle silencer (to be shown later as a test case). Since a thin metal plate is assumed to be rigid, the normal velocities on both sides of the surface are zero. Sound pressure does have a jump across the ATB interface. When Eqs. (5) and (6) are summed up, we have

$$\begin{aligned}
&\int_R \left(p \frac{\partial \psi_A}{\partial n} + i\rho_A \omega v_n \psi_A \right) dS + \int_B \left(p \frac{\partial \psi_B}{\partial n} + i\rho_B \omega v_n \psi_B \right) dS \\
&+ \int_{ATB} \left(p_A \frac{\partial \psi_A}{\partial n} - p_B \frac{\partial \psi_B}{\partial n} \right) dS \\
&= \begin{cases} 4\pi p(P), & P \in \Omega_A + \Omega_B, \quad (17a) \\ 2\pi p(P), & P \in R + B, \quad (17b) \\ 2\pi [p_A(P) + p_B(P)], & P \in ATB. \quad (17c) \end{cases}
\end{aligned}$$

There are still two unknowns at each node on ATB, p_A and p_B. The companion normal-derivative integral equation to Eq. (17c) is

$$\begin{aligned}
&\int_R \left(p \frac{\partial^2 \psi_A}{\partial n \partial n^P} + i\rho_A \omega v_n \frac{\partial \psi_A}{\partial n^P} \right) dS \\
&+ \int_B \left(p \frac{\partial^2 \psi_B}{\partial n \partial n^P} + i\rho_B \omega v_n \frac{\partial \psi_B}{\partial n^P} \right) dS \\
&+ \int_{ATB} \left(p_A \frac{\partial^2 \psi_A}{\partial n \partial n^P} - p_B \frac{\partial^2 \psi_B}{\partial n \partial n^P} \right) dS = 0, \quad P \in ATB.
\end{aligned} \tag{18}$$

Equation (18) is not only hypersingular, but also it has two hypersingular kernels.

III. COMPLETE INTEGRAL EQUATIONS

The boundary integral equations derived in the previous section for the two-medium problem are now combined with the direct mixed-body boundary integral equations for reactive mufflers reported in Refs. 1 and 2. The result is a set of boundary integral equations for a general silencer/muffler configuration as shown in Fig. 1. With reference to Fig. 1, the interior domain of the whole silencer is denoted by Ω, regardless whether it is air or the bulk-reacting material. The unit normal vector on either R or B is pointing into the interior acoustic domain. Note that in the direct BEM, there is no acoustic medium outside the silencer. Since both sides of P or T are air, the unit normal vector on P or T can be pointing into either side of the perforated/thin surface. The side into which the normal is pointing is called the positive side, while the opposite side is called the negative side. Sound pressure on the positive side is denoted by p^+, and on the negative side p^-. The unit normal vector on I or IP or ATB is pointing into the air side.

The complete boundary integral equations are

$$\int_{\mathrm{R}}\left(p\frac{\partial\psi_A}{\partial n}+i\rho_A\omega v_n\psi_A\right)dS+\int_{\mathrm{T+P}}\frac{\partial\psi_A}{\partial n}(p^+-p^-)dS+\int_{\mathrm{B}}\left(p\frac{\partial\psi_B}{\partial n}+i\rho_B\omega v_n\psi_B\right)dS$$
$$+\int_{\mathrm{I}}\left[p\left(\frac{\partial\psi_A}{\partial n}-\frac{\partial\psi_B}{\partial n}\right)+i\omega v_n(\rho_A\psi_A-\rho_B\psi_B)\right]dS+\int_{\mathrm{IP}}\left[p_A\left(\frac{\partial\psi_A}{\partial n}-\frac{\partial\psi_B}{\partial n}\right)-\rho_A c_A\xi v_n\frac{\partial\psi_B}{\partial n}+i\omega v_n(\rho_A\psi_A-\rho_B\psi_B)\right]dS$$
$$+\int_{\mathrm{ATB}}\left(p_A\frac{\partial\psi_A}{\partial n}-p_B\frac{\partial\psi_B}{\partial n}\right)dS=\begin{cases}4\pi p(P), & P\in\Omega, \quad (19a)\\ 2\pi p(P), & P\in\mathrm{R+B}, \quad (19b)\\ 2\pi[p^+(P)+p^-(P)], & P\in\mathrm{T+P}, \quad (19c)\\ 4\pi p(P), & P\in\mathrm{I}, \quad (19d)\\ 4\pi p_A(P)+2\pi\rho_A c_A\xi v_n(P), & P\in\mathrm{IP}, \quad (19e)\\ 2\pi[p_A(P)+p_B(P)], & P\in\mathrm{ATB}, \quad (19f)\end{cases}$$

and

$$\int_{\mathrm{R}}\left(p\frac{\partial^2\psi_A}{\partial n\partial n^P}+i\rho_A\omega v_n\frac{\partial\psi_A}{\partial n^P}\right)dS+\int_{\mathrm{T+P}}\frac{\partial^2\psi_A}{\partial n\partial n^P}(p^+-p^-)dS+\int_{\mathrm{B}}\left(p\frac{\partial^2\psi_B}{\partial n\partial n^P}+i\rho_B\omega v_n\frac{\partial\psi_B}{\partial n^P}\right)dS$$
$$+\int_{\mathrm{I}}\left[p\left(\frac{\partial^2\psi_A}{\partial n\partial n^P}-\frac{\partial^2\psi_B}{\partial n\partial n^P}\right)+i\omega v_n\left(\rho_A\frac{\partial\psi_A}{\partial n^P}-\rho_B\frac{\partial\psi_B}{\partial n^P}\right)\right]dS+\int_{\mathrm{IP}}\left[p_A\left(\frac{\partial^2\psi_A}{\partial n\partial n^P}-\frac{\partial^2\psi_B}{\partial n\partial n^P}\right)-\rho_A c_A\xi v_n\frac{\partial^2\psi_B}{\partial n\partial n^P}\right.$$
$$\left.+i\omega v_n\left(\rho_A\frac{\partial\psi_A}{\partial n^P}-\rho_B\frac{\partial\psi_B}{\partial n^P}\right)\right]dS+\int_{\mathrm{ATB}}\left(p_A\frac{\partial^2\psi_A}{\partial n\partial n^P}-p_B\frac{\partial^2\psi_B}{\partial n\partial n^P}\right)dS=\begin{cases}-4\pi\, i\rho_A\omega v_n(P), & P\in\mathrm{T}, \quad (20a)\\ 4\pi\dfrac{ik_A}{\xi}[p^+(P)-p^-(P)], & P\in\mathrm{P}, \quad (20b)\\ -2\pi i\omega(\rho_A+\rho_B)v_n(P), & P\in\mathrm{I+IP}, \quad (20c)\\ 0, & P\in\mathrm{ATB}. \quad (20d)\end{cases}$$

Since the thin surfaces (T) are usually assumed rigid, the right-hand side of Eq. (20a) can be set to zero. Equations (19) and (20) together form the complete set of integral equations necessary to solve a general silencer problem depicted in Fig. 1. In summary, the unknown on R and B is either sound pressure p or the normal velocity v_n, depending on what is prescribed as the boundary condition; the unknown on T and P is the pressure jump p^+-p^-; the unknowns on I are sound pressure p and the normal velocity v_n; the unknowns on IP are sound pressure on the air side p_A and the normal velocity v_n; the unknowns on ATB are p_A and p_B.

The transmission loss (TL) of a silencer may be evaluated by several different methods in the BEM computation. These include the conventional four-pole transfer matrix method,[3,4] the three-point method,[1,11] the improved four-pole method,[2] and the impedance matrix method.[12] The method used in this paper is the impedance matrix method.

IV. TEST CASES

Several test cases are given in this section to verify the BEM formulation. The bulk-reacting lining material used in all test cases is polyester, which has a flow resistivity of 16 000 MKS rayls/m. The first test case is a packed cylindrical expansion chamber as shown in Fig. 3. The radius of the inlet and outlet tubes is $r=2.54$ cm (1 in.). The length and the radius of the chamber are $L=45.72$ cm (18 in.) and $R=10.16$ cm (4 in.), respectively. Since the model is rotational symmetric, only a small sector has to be modeled in the BEM. Two different packing configurations are tested. In the first packing configuration, the thickness of the polyester lining is $h=1.27$ cm ($\frac{1}{2}$ in.). The BEM is run with two different approaches: the local-reacting approach and the bulk-reacting approach. In the local-reacting approach, the local impedance of the lining is measured and the chamber radius is set at R-h, where the local impedance is applied. In the bulk-reacting approach, the direct-mixed body BEM as described in this paper is applied. Figure 4 shows the comparison between these two approaches along with the experimental data. From the figure, it is seen that both approaches produce a decent result. Since the thickness of the polyester

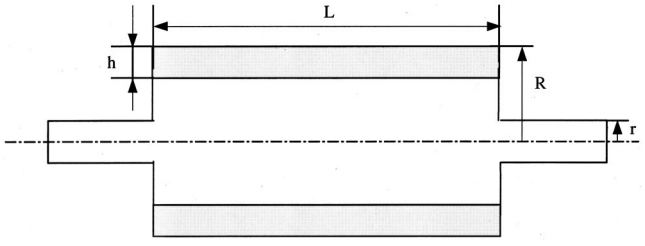

FIG. 3. A packed expansion chamber.

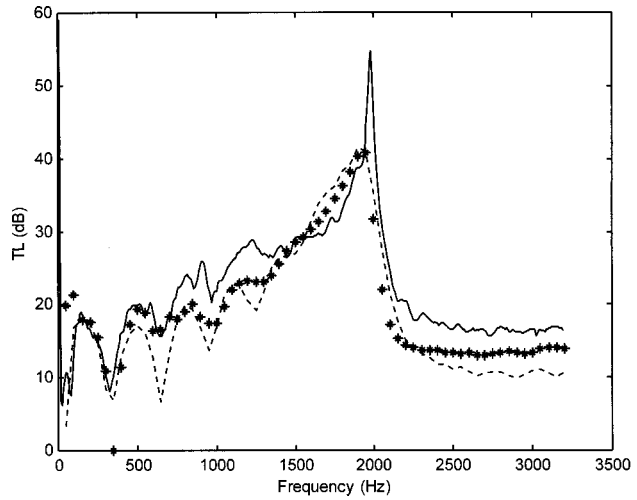

FIG. 4. Transmission loss for the packed expansion chamber with $h=1.27$ cm. Solid line: experiment; dotted line: BEM local-reacting; symbol $*$: BEM bulk-reacting.

is thin enough, the local impedance approach can produce a reasonably good approximation for the lined surface.

In the second packing configuration, the thickness of the polyester lining is increased to $h=2.54$ cm (1 in.). The comparison of the two different approaches and the experimental data is shown in Fig. 5. For this thickness, the interface impedance may not be approximated well by the local impedance. This explains why the local-reacting result is not as good as the bulk-reacting result as demonstrated in Fig. 5.

In the second test case, an absorbing bullet is added to the center of the packed expansion chamber with 2.54-cm (1 in.) lining. The geometry of the silencer is shown in Fig. 6. The absorbing bullet is a 2.54×30.48 cm^2 (1×12 in.^{2}) rigid cylinder wrapped with 2.54 cm (1 in.) thickness polyester material. A perforated metal sheet with 23% porosity is used to cover the polyester lining. This design can yield higher noise attenuation while providing full flow area for low flow resistance. It is noticed ATB elements are used to model the end flanges of the absorbing bullet. Since the model is still

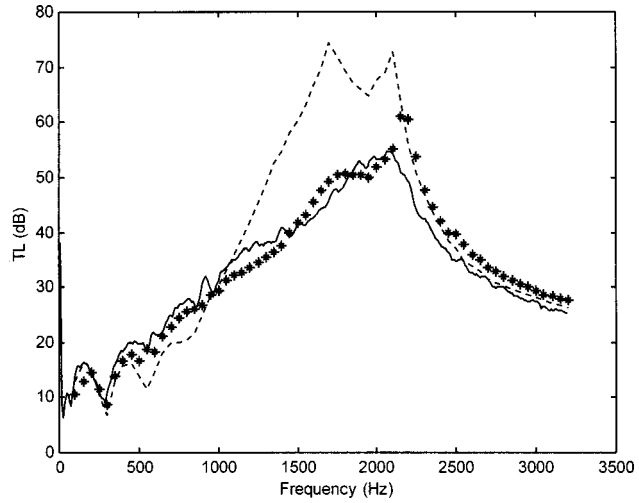

FIG. 5. Transmission loss for the packed expansion chamber with $h=2.54$ cm. Solid line: experiment; dotted line: BEM local-reacting; symbol $*$: BEM bulk-reacting.

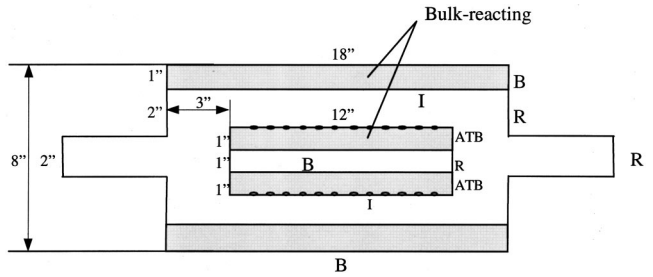

FIG. 6. A packed expansion chamber with an absorbing center bullet (1 in.$=$2.54 cm).

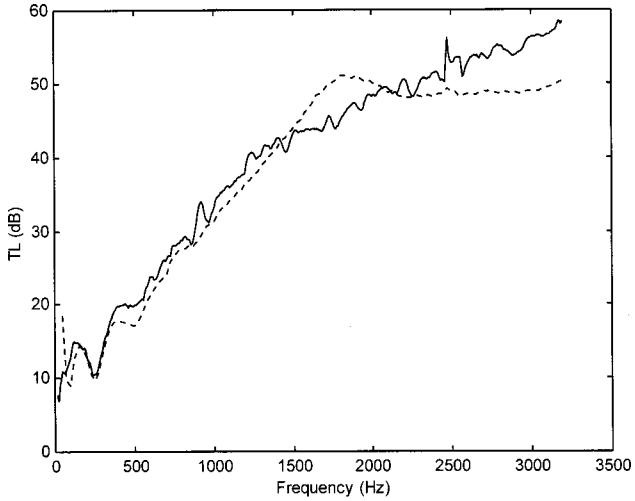

FIG. 7. Transmission loss for the packed expansion chamber with an absorbing center bullet. Solid line: experiment; dotted line: BEM.

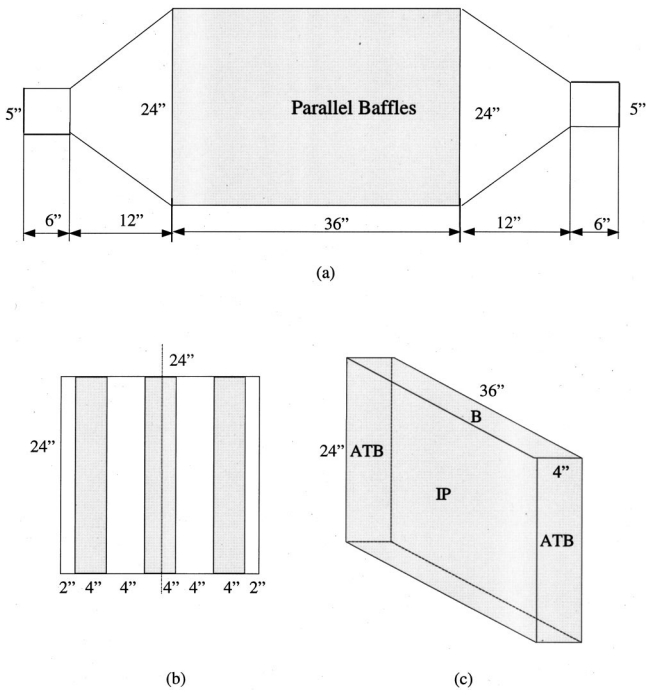

FIG. 8. Parallel baffle silencer (1 in.$=$2.54 cm). (a) Exterior geometry, (b) cross section of the parallel baffles, and (c) splitter geometry.

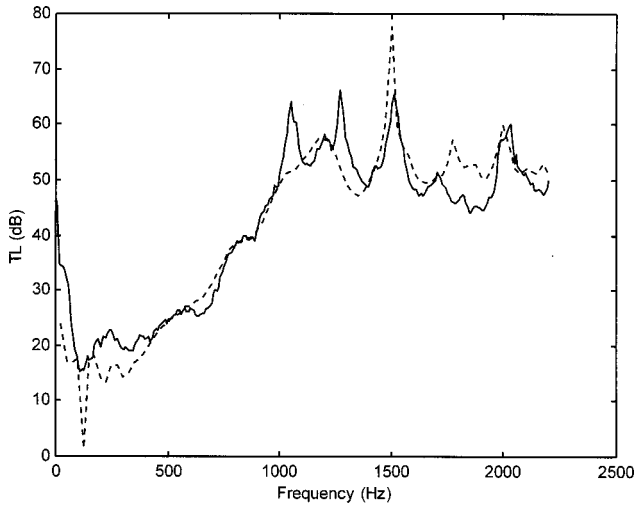

FIG. 9. Transmission loss for the parallel baffle silencer. Solid line: experiment; dotted line: BEM.

rotational symmetric, only a small sector has to be modeled. The BEM result is compared to the experimental data in Fig. 7. It can be seen from Fig. 7 that the comparison between the BEM prediction and measurement is reasonably good. Compare Fig. 7 to Fig. 5 and one can see that the absorbing bullet provides additional noise attenuation beyond 2100 Hz.

The third test case is a parallel baffle silencer. The exterior geometry of the silencer is shown in Fig. 8(a). Both inlet and outlet tubes have a diameter of 12.7 cm (5 in.). The two transition ducts that connect the inlet/outlet tubes to the parallel baffle section have a square cross section of varying dimensions. Figure 8(b) shows the cross section of the parallel baffle section. Three $10.16\times60.96\times91.44$ cm^3 ($4\times24\times36$ in.^{3}) parallel baffles made of polyester are used as center splitters in a $60.96\times60.96\times91.44$ cm^3 ($24\times24\times36$ in.^{3}) rectangular duct. This creates a 5.08 cm (2 in.) air gap at each side of the wall, and two 10.16 cm (4 in.) air gaps in the center. As shown in Fig. 8(c), each polyester splitter is covered by a perforated metal sheet (IP) on its sides and a rigid plate (ATB) at both ends. The porosity of the IP interfaces is 23%. Since the model has two planes of symmetry, only a quarter of the silencer has to be modeled. Figure 9 shows the comparison of the BEM prediction and the experimental data. From the figure, it is seen that the BEM results are in good agreement with the measured results.

V. CONCLUSIONS

The direct mixed-body BEM for reactive mufflers[1,2] is extended to packed silencers with bulk-reacting linings in this paper. Types of surfaces of a packed silencer that can be modeled include ''regular'' (R), ''thin'' (T), ''perforated'' (P), ''bulk-reacting'' (B), ''interface'' (I), ''perforated interface'' (IP), and ''air-thin-bulk reacting'' (ATB). A BEM model can be easily created by just assembling surface components together, with each surface labeled by a surface type. The direct mixed-body BEM is indeed a multi-domain BEM but implemented in a single-domain fashion. This single-domain feature is created by summing up the integral equations for all subdomains and then adding the normal-derivative integral equations at the interfaces. Test cases show that the direct mixed-body BEM produces TL predictions that are in good agreement with measured results.

ACKNOWLEDGMENT

This research was supported by Nelson Industries, Inc.

[1] T. W. Wu and G. C. Wan, ''Muffler performance studies using a direct mixed-body boundary element method and a three-point method for evaluating transmission loss,'' ASME J. Vibr. Acoust. **118**, 479–484 (1996).
[2] T. W. Wu, P. Zhang, and C. Y. R. Cheng, ''Boundary element analysis of mufflers with an improved method for deriving the four-pole parameters,'' J. Sound Vib. **217**, 767–779 (1998).
[3] C. Y. R. Cheng, A. F. Seybert, and T. W. Wu, ''A multidomain boundary element solution for silencer and muffler performance prediction,'' J. Sound Vib. **151**, 119–129 (1991).
[4] C. N. Wang, C. C. Tse, and Y. N. Chen, ''A boundary element analysis of a concentric-tube resonator,'' Eng. Anal. Boundary Elem. **12**, 21–27 (1993).
[5] H. Utsuno, T. Tanaka, T. Fujikawa, and A. F. Seybert, ''Transfer function method for measuring characteristic impedance and propagation constant of porous materials,'' J. Acoust. Soc. Am. **86**, 637–643 (1989).
[6] L. L. Beranek, ed., *Noise and Vibration Control* (Institute of Noise Control Engineering, Cambridge, MA, 1988).
[7] H. Utsuno, T. W. Wu, A. F. Seybert, and T. Tanaka, ''Prediction of sound fields in cavities with sound absorbing materials,'' AIAA J. **28**, 1870–1876 (1990).
[8] L. G. Copley, ''Fundamental results concerning integral representations in acoustic radiation,'' J. Acoust. Soc. Am. **44**, 28–32 (1968).
[9] G. Krishnasamy, L. W. Schmerr, T. J. Rudolphi, and F. J. Rizzo, ''Hypersingular boundary integral equations: some applications in acoustic and elastic wave scattering,'' ASME J. Appl. Mech. **57**, 404–414 (1990).
[10] J. W. Sullivan and M. J. Crocker, ''Analysis of concentric-tube resonators having unpartitioned cavities,'' J. Acoust. Soc. Am. **64**, 207–215 (1978).
[11] G. C. Wan, ''Prediction and measurement of the acoustic performance of mufflers,'' in *Proceedings of the 1995 International Conference on Noise Control Engineering* (1995), pp. 421–424.
[12] G. Lou, T. W. Wu, and C. Y. R. Cheng, ''Impedance matrix synthesis for multiply connected exhaust network systems using the direct mixed-body BEM,'' J. Sound Vib. **238**, 351–362 (2000).

Scattering by a fluid cylinder in a porous medium: Application to trabecular bone

Francine Luppé, Jean-Marc Conoir, and Hervé Franklin
Laboratoire d'Acoustique Ultrasonore et d'Electronique, UMR 6068, Université du Havre, Place R. Schuman, 76610 Le Havre, France

(Received 8 February 2001; revised 8 November 2001; accepted 14 January 2002)

In a trabecular bone, considered as a nondissipative porous medium, the scattering of an incident wave by cylindrical pores larger than the wavelength is studied. The goal is to know if scattering alone may cause such a high attenuation as that observed in calcaneus. The porous medium is modelized via Biot's theory and the scattering by a single pore is characterized from the definition of a scattering matrix. An approximation of weakly disordered medium is then discussed to estimate the effective attenuation and dispersion as a function of frequency. These effective properties are shown to be different of those measured on calcaneus, due to the neglect of wave conversions during the scattering process. © *2002 Acoustical Society of America.* [DOI: 10.1121/1.1460925]

PACS numbers: 43.20.Gp, 43.80.Cs [DEC]

I. INTRODUCTION

Measurements of ultrasonic attenuation through the human calcaneus have proved to be a powerful tool for the diagnosis of osteoporosis,[1–4] as the normalized broadband ultrasonic attenuation (nBUA) is strongly correlated to bone mineral density (BMD).

Calcaneus is a trabecular bone, i.e., a porous medium, so that propagation through it should be modelized via Biot's theory,[5] or the Biot–Stoll's model,[6] as far as the wavelengths involved remain large with respect to the pores sizes.

One main result of the Biot's theory is the prediction of two longitudinal waves, a fast one and a slow one, and, indeed, evidence of a slow wave in cancellous bones has been shown.[7–9] Attenuation and dispersion in Stoll's model are obtained by taking into account the saturating fluid viscosity, as well as the solid and the frame viscoelasticity. However, attempts to account for measured nBUAs via such a modelization are still fruitless.[7,10] Actually, the frequency dependence of the Stoll's parameters that describe frame viscoelasticity is not so easily found in bones.

Another interesting result of experimental studies on ultrasonic propagation through cancellous bones is the possibility for negative dispersion (decreasing phase velocity with increasing frequency) to occur.[11–14]

Negative dispersion, as well as effective attenuation, may be predicted by multiple scattering theories.[15] In human trabecular bones, the pore sizes extend in a wide range, so that the dimensions of the largest ones may approach, or even overcome, the measured wavelengths. These pores, then, may be considered as scatterers. In order to account for the possibility of a slow wave to exist, as well as for the possibility of negative dispersion to occur, we think a rather tempting way is then to modelize cancellous bones as fluid saturated porous media, with the largest pores acting as scatterers. The first step is then to modelize the scattering of one single pore, which is the main object of this paper.

In Sec. II, we recall the simplified Biot's theory for a porous medium where viscosity and viscoelasticity effects are neglected. Section III is devoted to the scattering of a fluid cylinder embedded in such a porous medium; special care is taken to test the consistency of the modelization via energy conservation verifications. The calcaneus case is described in Sec. IV. The effective attenuation and dispersion due to a low scatterer density are calculated in Sec. V by use of a multiple forward scattering approximation that neglects waves conversions.

II. BIOT'S MODELIZATION OF A NONDISSIPATIVE POROUS MEDIUM

In Biot's theory,[5] attenuation is due to viscoelasticity of both the saturating fluid and the solid. Stoll's model[6] extends it to cases where viscoelasticity of the solid frame should also be taken into account in order to describe the actually observed attenuation is a given porous medium. In this paper, we shall consider an ''ideal'' case where attenuation is negligible, as we want to know whether or not the attenuation and dispersion observed on cancellous bones could be mainly due to multiple scattering by the largest pores. All the Stoll's parameters we need, then, are both real and constant; they are

Porosity β, density ρ_s of the solid, density ρ_f of the saturating fluid, structure factor α, bulk moduli K_f of the fluid, K_s of the solid, and K_b of the solid frame (dried porous medium), and shear modulus μ of the frame.

The acoustic waves in the saturated porous medium are described by the acoustic particles displacements $\mathbf{u}$ in the solid and $\mathbf{u}_f$ in the fluid, or by $\mathbf{u}$ and $\mathbf{w}=\beta(\mathbf{u}_f-\mathbf{u})$. Let us call ϕ and ϕ_f the scalar potentials from which $\mathbf{u}$ and $\mathbf{w}$ derive, $\boldsymbol{\psi}$ and $\boldsymbol{\psi}_f$ the potential vectors. In a two-dimension problem, the potential vectors may be chosen such that their nonzero component lies in the direction perpendicular to the acoustic motion plane. Let ψ and ψ_f be these components.

Considering harmonic motions, both ϕ and ϕ_f have to verify the same Helmholtz equation

$$\Delta\phi + k_l^2\phi = 0,$$

while both ψ and ψ_f verify

$$\Delta\psi + k_t^2\psi = 0.$$

The propagation equations set of the longitudinal waves is then

$$\begin{aligned} &\phi(\rho\omega^2 - Hk_l^2) + \phi_f(\rho_f\omega^2 - Ck_l^2) = 0, \\ &\phi(\rho_f\omega^2 - Ck_l^2) + \phi_f(m\omega^2 - Mk_l^2) = 0, \end{aligned} \tag{1}$$

and the propagation equations system of the transverse wave is

$$\psi(\rho\omega^2 - \mu k_t^2) + \psi_f(\rho_f\omega^2) = 0, \quad \rho_f\psi + m\psi_f = 0 \tag{2}$$

with

$$\begin{aligned} &m = \frac{\alpha}{\beta}\rho_f, \quad \rho = (1-\beta)\rho_s + \beta\rho_f, \\ &H = \frac{(K_s - K_b)^2}{D - K_b} + K_b + \frac{4}{3}\mu, \quad C = \frac{K_s(K_s - K_b)}{D - K_b}, \\ &M = \frac{K_s^2}{D - K_b}, \quad D = K_s\left(1 + \beta\left(\frac{K_s}{K_f} - f\right)\right). \end{aligned} \tag{3}$$

System (1) has two independent solutions, corresponding to a fast longitudinal wave and to a slow one, and their respective velocities c_1 and c_2 are obtained by setting the determinant of (1) to zero. System (2) has only one independent solution, corresponding to a shear wave; its velocity c_t is obtained by setting the system (2) determinant to zero.

We define the compatibility coefficients γ_1, γ_2, and γ_t as

$$\begin{aligned} &\gamma_j = \frac{\phi_{fj}}{\phi_j} = \frac{H - \rho c_j^2}{\rho_f c_j^2 - C}, \quad j = 1,2 \\ &\gamma_t = \frac{\psi_f}{\psi} = -\frac{\beta}{\alpha}, \end{aligned} \tag{4}$$

with ϕ_{fj} and ϕ_j the potentials of either the fast longitudinal wave ($j=1$) or the slow longitudinal wave ($j=2$).
Systems (1) and (2) then give

$$\begin{aligned} &H + \gamma_j C = c_j^2\rho_j, \quad \rho_j = \gamma_j\rho_f + \rho, \quad C + \gamma_j M = c_j^2\rho_{fj}, \\ &\rho_{fj} = m\gamma_j + \rho_f, \quad \mu = \rho_t c_t^2, \quad \rho_t = \gamma_t\rho_f + \rho. \end{aligned} \tag{5}$$

III. SCATTERING OF A FLUID CYLINDER IN A NONDISSIPATIVE POROUS MEDIUM

The cylinder, of radius a, is supposed to be infinitely long in the z direction; its density is ρ_0, and sound velocity inside is c_0. Invariance along z is assumed, so that motion takes place only in the (x,y) plane, where polar coordinates (r,θ) indicate the observer position.

We still suppose harmonic waves, with an $e^{-i\omega t}$ time dependence that will be omitted throughout the paper. The theoretical procedure is quite well known when dealing with scattering by cylinders, so we will not detail it, but we will emphasize the special care to be taken in the porous case when dealing with energy.

Consider an incident wave, described by its potential ϕ_{inc} as

$$\phi_{\text{inc}} = H_n^{(2)}(k_{\text{inc}}r)e^{in\theta}, \quad \text{inc} = 1,2,t, \tag{6}$$

with $H_n^{(2)}$ the converging Hankel function of order n.

Whatever the nature of the incident wave, it gives rise to a longitudinal wave in the fluid cylinder

$$\phi_0 = \sum_m s_m^{0\text{inc}} J_m(k_0 r)e^{im\theta}, \tag{7}$$

with J_m the Bessel function of the first kind and order m, two scattered longitudinal waves in the porous medium

$$\phi_1 = \sum_m s_m^{1\text{inc}} H_m^{(1)}(k_1 r)e^{im\theta}, \quad \phi_2 = \sum_m s_m^{2\text{inc}} H_m^{(1)}(k_2 r)e^{im\theta}, \tag{8}$$

and a scattered shear wave in the porous medium

$$\psi = \sum_m s_m^{t\text{inc}} H_m^{(1)}(k_t r)e^{im\theta}, \tag{9}$$

with $H_m^{(1)}$ the diverging Hankel function of order m, so that the scattered waves verify the Sommerfeld radiation condition.

All these waves are linked together from the continuity conditions[16] on the open pores surface cylinder, at $r=a$. These conditions are written in Appendix A.

The continuity conditions must be valid at $r=a$, whatever the value of θ. It follows that $s_m^{0\text{inc}} = s_m^{1\text{inc}} = s_m^{2\text{inc}} = S_m^{t\text{inc}} = 0$, except when $m=n$: there is no conversion of a normal mode n to a different one.
The amplitudes of the scattered waves are then solutions of system (10)

$$\begin{pmatrix} m_{11} & m_{12} & m_{13} & m_{14} \\ m_{21} & m_{22} & m_{23} & m_{24} \\ m_{31} & m_{32} & m_{33} & m_{34} \\ m_{41} & m_{42} & m_{43} & m_{44} \end{pmatrix} \begin{pmatrix} s_n^{1\text{inc}} \\ s_n^{2\text{inc}} \\ s_n^{t\text{inc}} \\ s_n^{0\text{inc}} \end{pmatrix} = \begin{pmatrix} E_1 \\ E_2 \\ E_3 \\ E_4 \end{pmatrix}, \tag{10}$$

with the matrix and vector elements given in Appendix B.

The 4×4 system (10) reduces to the 3×3 system (11) related to the scattering of a fluid cylinder in an elastic solid[17]

$$\begin{pmatrix} m'_{11} & m'_{13} & m'_{14} \\ m'_{31} & m'_{33} & m'_{34} \\ m'_{41} & m'_{43} & m'_{44} \end{pmatrix} \begin{pmatrix} s_n^{1\text{inc}} \\ s_n^{t\text{inc}} \\ s_n^{0\text{inc}} \end{pmatrix} = \begin{pmatrix} E'_1 \\ E'_3 \\ E'_4 \end{pmatrix} \tag{11}$$

as line 2 and column 2 of (10) disappear, and provided that ρ_t, ρ_{jf}, and ρ_j, defined in (5), are to be respectively replaced by ρ_s (elastic solid density), ρ_f, and $-\rho_s$, and all γ_j by 0 so that the elements of system (10) reduce to the corresponding primed elements of system (11). We now define the scattering matrix (S matrix), in order to verify its unity as predicted by energy conservation, and analyze the way the energy of a fast longitudinal incident wave is shared between the different scattered waves.

A. The scattering matrix

The S matrix is a diagonal block matrix, as conversion from mode n to mode $m \neq n$ does not occur. The diagonal block terms, S_n, are 3×3 matrices related to one single mode n

$$S_n = \begin{pmatrix} S_n^{11} & S_n^{12} & S_n^{1t} \\ S_n^{21} & S_n^{22} & S_n^{2t} \\ S_n^{t1} & S_n^{t2} & S_n^{tt} \end{pmatrix}, \tag{12}$$

with S_n^{jk} the amplitude of the scattered wave of type j, $j=1,2,t$, when the incident wave is a converging Hankel function $H_n^{(2)}$ of type $k=1,2,t$.

Each S_n matrix must verify[17]

$$S_n^{\dagger} S_n = \begin{pmatrix} 1 & 0 & 0 \\ 0 & 1 & 0 \\ 0 & 0 & 1 \end{pmatrix} \tag{13}$$

with † indicating transposition and complex conjugation.

In the case of a fluid cylinder in an elastic solid, the S_n^{jk} elements are directly the s_n^{jk} coefficients obtained from system (11) by use of Cramer's rule. As an example

$$S_n^{t1} = s_n^{t1} = \frac{D_n^{[3]}}{D_n} \tag{14}$$

with D_n the system (11) determinant, and $D_n^{[3]}$ the same determinant, except column 3, corresponding to the transverse wave, is replaced by the source column with inc$=1$ in the E_1', E_3', E_4' expressions. However, if one determines the S_n^{jk} elements the same way in the porous case, relation (13) is not verified. Actually, relation (13) indicates that the energy that enters the cylinder is equal to the energy that leaves it: the radial component of the Poynting vector associated with the incident wave is equal to the sum of the Poynting vectors radial components of the scattered waves at $r=a$.

In order to define correctly the scattering matrix elements in the porous case, we then determine the Poynting vectors radial components of all waves.

Let us call **R** and **S** the respectively real and complex Poynting vectors

$$\langle \mathbf{R} \rangle_T = \tfrac{1}{2}\, \Re e(\mathbf{S}), \tag{15}$$

where $\langle\ \rangle_T$ indicates a time average over the $T=2\pi/\omega$ period.

The complex Poynting vector in the porous medium is

$$\mathbf{S} = \bar{\bar{\sigma}} \cdot \frac{\partial \mathbf{u}^*}{\partial t} - P_f \frac{\partial \mathbf{w}^*}{\partial t} = \bar{\bar{\sigma}} \cdot \frac{\partial \mathbf{u}^*}{\partial t} - \gamma P_f \frac{\partial \mathbf{u}^*}{\partial t}, \tag{16}$$

with P_f the pression inside the pores, and $\bar{\bar{\sigma}}$ the rank 2 stress tensor in the solid part of the porous medium. Relatively long but simple calculations, with use of the Wronskien relation on Bessel functions, lead to

For a longitudinal wave $\phi_j = A_j Z_n(k_j r) e^{in\theta} e^{-i\omega t}$, $j=1,2$

$$\left| \left\langle \frac{R_r^j}{\omega} \right\rangle_T \right| = |A_j|^2 \frac{\omega^2}{\pi a} |\rho_j + \gamma_j \rho_{fj}|. \tag{17}$$

For a shear wave $\psi = B Z_n(k_t r) e^{in\theta} e^{-i\omega t}$

$$\left| \left\langle \frac{R_r^t}{\omega} \right\rangle_T \right| = |B|^2 \frac{\omega^2}{\pi a} \rho_t, \tag{18}$$

with $Z_n = H_n^{(2)}$ in the case of an incident wave and $Z_n = H_n^{(1)}$ in the case of a scattered wave.

If, for example, the incident wave is a fast longitudinal wave, the energy conservation law at the surface cylinder reads

$$|\rho_1 + \gamma_1 \rho_{f1}| = |s_n^{11}|^2 |\rho_1 + \gamma_1 \rho_{f1}| + |s_n^{21}|^2 |\rho_2 + \gamma_2 \rho_{f2}| + |s_n^{t1}|^2 \rho_t. \tag{19}$$

We can now define the S_n^{jk} elements as

$$S_n^{11} = s_n^{11}$$
$$S_n^{21} = \sqrt{\frac{|\rho_2 + \gamma_2 \rho_{f2}|}{|\rho_1 + \gamma_1 \rho_{f1}|}}\, s_n^{21}, \quad S_n^{t1} = \sqrt{\frac{\rho_t}{|\rho_1 + \gamma_1 \rho_{f1}|}}\, s_n^{t1}, \tag{20}$$

so that relation (19) gives

$$1 = |S_n^{11}|^2 + |S_n^{21}|^2 + |S_n^{t1}|^2 \tag{21}$$

which is, indeed, the first relation derived from (13).

For the S_n matrix components other than those defined in (20), the normalization factors are the square roots of the ratios of the scattered wave density factor to the incident wave density factor.

In the case of the elastic solid, all density factors reduce to the solid density, so that they all simplify in the S_n matrix components expressions, as shown in (14).

Anticipating the results of Sec. IV, we show in Fig. 1 an example of the evolution of the S_n^{j1} ($j=1,2,t$, and $n=1$) moduli as a function of frequency, for a marrow cylinder of radius $a=1$ mm in a marrow-saturated cancellous bone. When squared, these moduli add up to 1. We verified numerically relation (13) for different values of n. In Fig. 1, the incident wave is fast and longitudinal; one can see that the scattered fast longitudinal wave energy is the largest one, but that the other waves energy is not negligible. The longitudinal slow wave energy reaches a local maximum when the fast longitudinal wave energy passes through a minimum, and vice versa. As n is increased, the curve corresponding to the fast longitudinal wave ($j=1$) stretches towards higher frequencies, so that it gets closer to 1, whatever the frequency. As soon as $n=10$, there is no more energy scattered as a slow or a shear wave.

Relation (13) is a global energy conservation law: the scattered energy that leaves the cylinder is exactly equal to the incident one that enters it. A finer energy balance is also required, between energy in and outside the cylinder. In or-

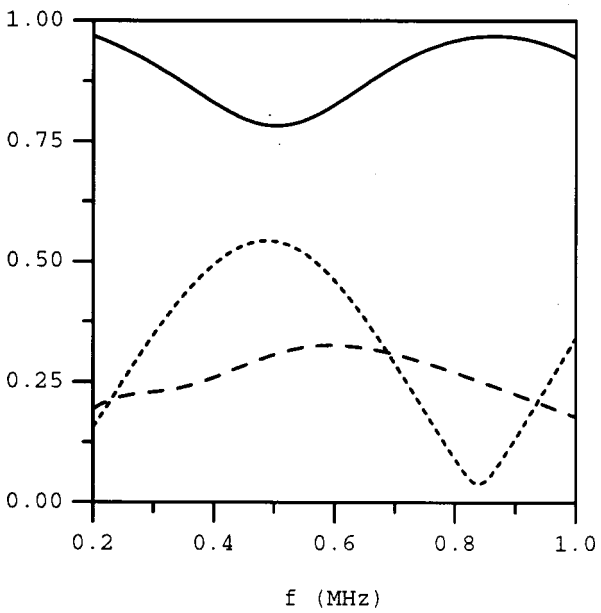

FIG. 1. Marrow cylindrical pore, radius $a=1$ mm in a marrow saturated calcaneus, as defined in Sec. IV. Moduli of the S_1^{j1} (mode $n=1$) scattering matrix elements versus frequency. Solid line: $j=1$; dotted line: $j=2$; dashed line: $j=t$.

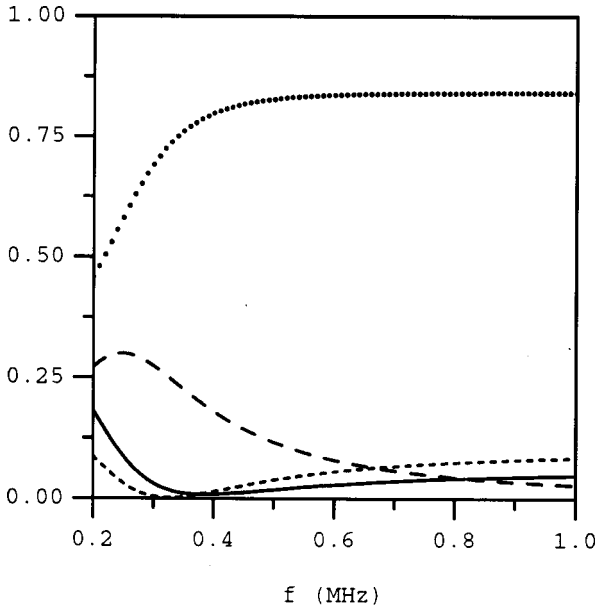

FIG. 2. Marrow cylindrical pore, radius $a=1$ mm in a marrow saturated calcaneus, as defined in Sec. IV. Mode $n=1$, fast incident wave (converging cylindrical wave): energy of the reflected wave (solid line), the scattered slow longitudinal wave (dotted line), the scattered shear wave (dashed line), and the transmitted wave (dots) inside the cylinder, versus frequency.

der to verify it, we have to define the local Debye coefficients of the cylinder/porous medium interface. This is achieved in the next paragraph.

B. The local Debye coefficients

These coefficients appear in the Debye series,[18] which allows the description of the interaction of waves with an obstacle as a sequence of interactions with its surface (partial reflections and transmissions), alternating with propagation inside it. A detailed description of the physical meaning of all coefficients as well as the way to calculate them may be found, in the ultrasonic case, in Refs. 19–21. As an example, if one considers a $H_n^{(2)}(k_1 r)$ wave incident, from the porous medium, at the fluid interface, it gives rise locally to a reflected wave $H_n^{(1)}(k_1 r)$ of amplitude r_{11}, a transmitted wave $H_n^{(2)}(k_0 r)$ of amplitude t_{01}, a reflected slow wave $H_n^{(1)}(k_2 r)$ of amplitude r_{21}, and a reflected shear wave $H_n^{(1)}(k_t r)$ of amplitude r_{t1}. Energy conservation requires that

$$|r_{11}|^2+\frac{\rho_0}{|\rho_1+\gamma_1\rho_{f1}|}|t_{01}|^2+\frac{|\rho_2+\gamma_2\rho_{f2}|}{|\rho_1+\gamma_1\rho_{f1}|}|r_{21}|^2 + \frac{\rho_t}{|\rho_1+\gamma_1\rho_{f1}|}|r_{t1}|^2=1, \tag{22}$$

while the Debye coefficients r_{j1}, t_{01}, $j=1,2,t$ are found from system (10) with $J_n(x_0)$ replaced by $H_n^{(2)}(x_0)$ and $J_n'(x_0)$ by $H_n^{(2)\prime}(x_0)$.

Each term of the summation in (22) is plotted versus frequency in Fig. 2, for $n=1$ and the marrow cylinder in the porous bone, and one may verify that relation (22) actually holds. It is also interesting to notice, from Fig. 2, that the transmitted energy in the pore is larger than all reflected waves energies, and that the reflected shear wave carries more energy than the reflected fast longitudinal wave in the low-frequency band of the figure. There are three other energy relations similar to (22), corresponding to the incidence of each possible wave (slow longitudinal, shear, or incident from the fluid) at the cylinder interface. All these relations have been checked for different values of *n*, in the cancellous bone/marrow cylinder case.

In Secs. III A and III B, we have checked the consistency of our description of the scattering process. Up to now, the incident wave was a cylindrical converging one. In published litterature on calcaneus measurements, the incident wave is supposed to be plane. This is the case we consider now.

C. The case of an incident plane wave in the porous medium

The incident plane wave propagating along the the *x* axis is classically[17] described as

$$\phi_{\text{inc}}=e^{ik_{\text{inc}}x}=\sum_{n=-\infty}^{+\infty} i^n J_n(k_{\text{inc}}r)e^{in\theta},$$

that is

$$\phi_{\text{inc}}=\frac{1}{2}\sum_{n=-\infty}^{+\infty} i^n(H_n^{(1)}(k_{\text{inc}}r)+H_n^{(2)}(k_{\text{inc}}r))e^{in\theta}. \tag{23}$$

1. Case L: The incident wave is a longitudinal one: inc=1,2

The scattered longitudinal waves of type j ($j=1,2$) are then expressed as

$$\phi_j=\frac{1}{2}\sum_{n=-\infty}^{+\infty} i^n(s_n^{jj}-1)H_n^{(1)}(k_j r)e^{in\theta} \quad \text{if } j=\text{inc},$$
$$\phi_j=\frac{1}{2}\sum_{n=-\infty}^{+\infty} i^n s_n^{j\text{inc}}H_n^{(1)}(k_j r)e^{in\theta} \quad \text{if } j\neq\text{inc}. \tag{24}$$

The scattered shear wave is given by

$$\psi=\frac{1}{2}\sum_{n=-\infty}^{+\infty} i^n s_n^{\mathrm{tinc}} H_n^{(1)}(k_t r)e^{in\theta}. \tag{25}$$

2. Case T: The incident wave is a shear one: inc=t

The scattered longitudinal waves of type j ($j=1,2$) are given by

$$\phi_j=\frac{1}{2}\sum_{n=-\infty}^{+\infty} i^n s_n^{jt} H_n^{(1)}(k_j r)e^{in\theta}, \tag{26}$$

and the scattered shear wave by

$$\psi=\frac{1}{2}\sum_{n=-\infty}^{+\infty} i^n (s_n^{tt}-1) H_n^{(1)}(k_t r)e^{in\theta}. \tag{27}$$

Noticing that

$$\begin{aligned} &s_{-n}^{1j}=s_n^{1j}, \quad s_{-n}^{2j}=s_n^{2j}, \quad s_{-n}^{tj}=-s_n^{tj}, \quad j=1,2,\\ &s_{-n}^{1j}=-s_n^{1j}, \quad s_{-n}^{2j}=-s_n^{2j}, \quad s_{-n}^{tj}=s_n^{tj}, \quad j=t, \end{aligned} \tag{28}$$

the scattered waves expressions depend on whether the incident wave is a fast longitudinal one (case 1), a slow longitudinal one (case 2), or a shear one (case T)

Case 1:

$$\begin{aligned} \phi_1&=\frac{1}{2}\sum_{n=0}^{+\infty} \varepsilon_n i^n (s_n^{11}-1) H_n^{(1)}(k_1 r)\cos n\theta,\\ \phi_2&=\frac{1}{2}\sum_{n=0}^{+\infty} \varepsilon_n i^n s_n^{21} H_n^{(1)}(k_2 r)\cos n\theta,\\ \psi&=\frac{1}{2}\sum_{n=0}^{+\infty} \varepsilon_n i^{n+1} s_n^{t1} H_n^{(1)}(k_t r)\sin n\theta. \end{aligned}$$

Case 2:

$$\begin{aligned} \phi_1&=\frac{1}{2}\sum_{n=0}^{+\infty} \varepsilon_n i^n s_n^{12} H_n^{(1)}(k_1 r)\cos n\theta,\\ \phi_2&=\frac{1}{2}\sum_{n=0}^{+\infty} \varepsilon_n i^n (s_n^{22}-1) H_n^{(1)}(k_2 r)\cos n\theta,\\ \psi&=\frac{1}{2}\sum_{n=0}^{+\infty} \varepsilon_n i^{n+1} s_n^{t2} H_n^{(1)}(k_t r)\sin n\theta. \end{aligned} \tag{29}$$

Case T:

$$\begin{aligned} \phi_1&=\frac{1}{2}\sum_{n=0}^{+\infty} \varepsilon_n i^{n+1} s_n^{1t} H_n^{(1)}(k_1 r)\sin n\theta,\\ \psi&=\frac{1}{2}\sum_{n=0}^{+\infty} \varepsilon_n i^{n+1} s_n^{2t} H_n^{(1)}(k_2 r)\sin n\theta,\\ \psi&=\frac{1}{2}\sum_{n=0}^{+\infty} \varepsilon_n i^{n} (s_n^{tt}-1) H_n^{(1)}(k_t r)\cos n\theta, \end{aligned}$$

with ε_n the Neumann factor, equal to 1 for $n=0$ and to 2 for strictly positive values of n.

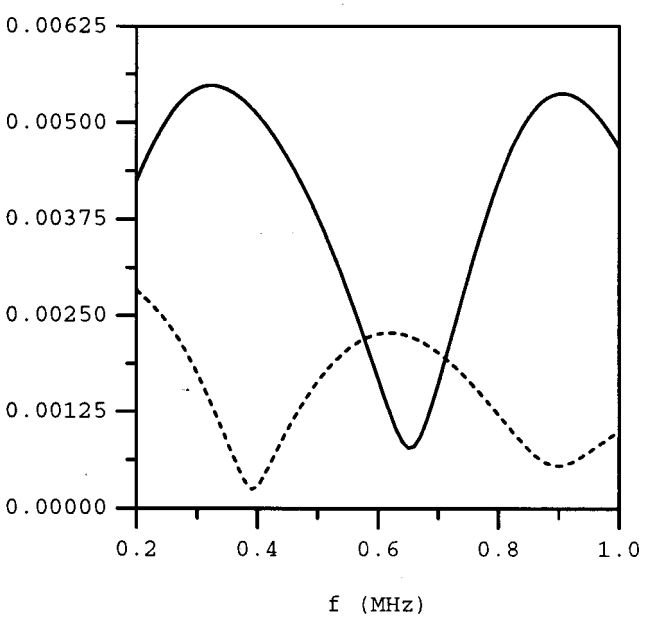

FIG. 3. Marrow cylindrical pore, radius $a=1$ mm in a marrow saturated calcaneus, as defined in Sec. IV. Fast longitudinal incident plane wave propagating in the x direction. Far field amplitudes of the fast longitudinal wave (solid line) and of the slow longitudinal wave (dotted line), observation angle $\theta=0°$.

Far enough from the cylinder, so that the Hankel function's asymptotic expressions may be used, the amplitudes of the scattered waves are, in case (1)

$$\begin{aligned} |\phi_1|&=\frac{1}{\sqrt{2\pi k_1}}\left|\sum_{n=0}^{+\infty} \varepsilon_n (s_n^{11}-1)\cos n\theta\right|,\\ |\phi_2|&=\frac{1}{\sqrt{2\pi k_2}}\left|\sum_{n=0}^{+\infty} \varepsilon_n s_n^{21}\cos n\theta\right|,\\ |\psi|&=\frac{1}{\sqrt{2\pi k_t}}\left|\sum_{n=0}^{+\infty} \varepsilon_n s_n^{t1}\sin n\theta\right|, \end{aligned} \tag{30}$$

with the $r^{-1/2}$ dependence omitted and similar relations holding for the other cases.

Figure 3 shows a plot of these amplitudes, in the direct transmission direction $\theta=0°$ ($\psi=0$), for the case of a fast incident wave on a marrow pore in a trabecular bone. Large dips are seen to occur, exhibiting a smooth resonance behavior. Although it may be interesting to study the cylinder resonances, we focus here on the scattered waves amplitudes. Figure 3 shows that waves conversions are not negligible, as the scattered slow longitudinal wave amplitude may be greater (around 0.6 MHz) than the scattered fast longitudinal wave (remember the incident wave is a fast longitudinal one). Moreover, it seems as if the two longitudinal scattered waves, which are independent solutions of system (1), are coupled, i.e., when the amplitude of one decreases, the other one's increases. This was already the case at a fixed mode number (cf. Fig. 1).

TABLE I. Calcaneus parameters.

In Ref. 10	This paper
$\rho_s = 1800$ kg/m^3	$\rho_s = 1800$ kg/m^3
$\rho_f = 950$ kg/m^3	$\rho_f = 950$ kg/m^3
Marrow	$K_f = \rho_f c_f^{\,2}$
$c_f = 1470$ m/s	
Cortical bone	$\mu_s = \rho_s c_s^2$
$c_1 = 3300$ m/s	$K_s = \rho_s c_l^2 - \frac{4}{3}\mu_s$
$c_s = 1800$ m/s	
Porosity $\beta = 0.72$	$\beta = 0.72$
Structure factor α	Structure factor α
derived from Berryman's law	derived from Berryman's law

IV. THE CALCANEUS AS A POROUS MEDIUM

This section is devoted to the modelization we used for the calcaneus via Biot's theory. The solid part of the calcaneus is supposed to be cortical bone; its fluid part is marrow. The numerical values we chose to describe these two parts are those of McKelvie and Palmer.[10] They are given in Table I, along with the Biot parameters we need, and the correspondance between them.

The Berryman's law for the structure factor is

$$\alpha = 1 - r\left(1 - \frac{1}{\beta}\right). \tag{31}$$

In Ref. 10, the value of r is not specified. We chose $r = 0.25$, following Williams,[22] as well as Hosokawa and Otani.[7,8]

McKelvie and Palmer[10] derived the frame bulk modulus K_b and shear modulus μ from Berryman's self-consistent theory.[23] In this paper, we derive them the same way as Hosokawa and Otani,[7,8] i.e., from Gibson's study of the mechanical behavior of different types of bones.[24] In the case of a cancellous bone with a columnar structure, he predicts a dependence of the frame Young modulus with the bone volume fraction $V_f = 1 - \beta$ as a power of V_f which depends on the traculae orientation with respect to the applied strain. Hosokawa and Otani used

$$K_b = \frac{E_s}{3(1-2\nu_s)} V_f^g, \quad \mu = \frac{E_s}{2(1+\nu_s)} V_f^g, \tag{32}$$

with E_s and ν_s the Young modulus and Poisson modulus of cortical bone, respectively. These are found from

$$E_s = \mu_s \frac{3\lambda_s + 2\mu_s}{\lambda_s + \mu_s}, \quad \lambda_s = \rho_s c_l^2 - 2\mu_s,$$
$$\nu_s = \frac{\lambda_s}{2(\lambda_s + \mu_s)}. \tag{33}$$

The power g, which we will hereafter call the Gibson's coefficient, is still to be found. Figure 4 shows a plot of the calculated fast longitudinal wave speed, obtained by setting system (1) determinant to zero, versus the Gibson's coefficient. In this simple modelization, as no attenuation at all is taken into account, the velocities do not depend on frequency. In Ref. 10, the reported measured velocity c_1 at 500 kHz is 1680 m/s. It corresponds, in our model, to a Gibson's coefficient equal to 2.43, which, in turn, gives $c_2 \simeq 1019$ m/s and $c_t \simeq 684$ m/s.

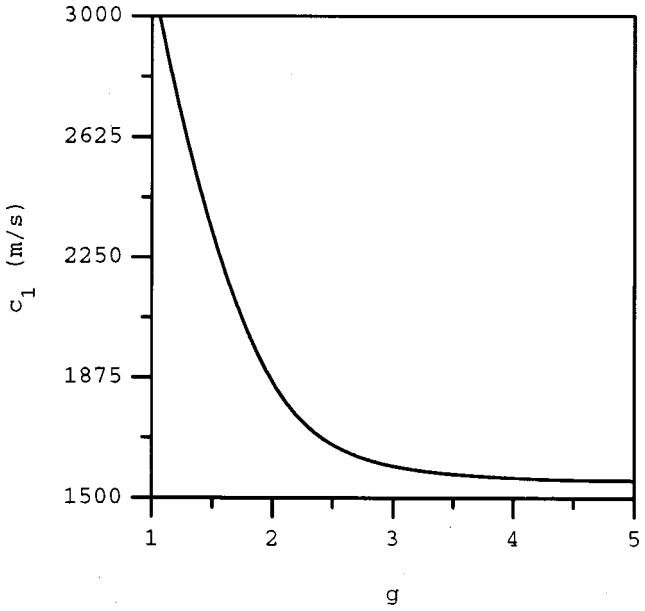

FIG. 4. Nondissipative marrow saturated calcaneus. Calculated fast longitudinal wave speed versus Gibson's coefficient.

In diagnosis applications, the frequency used for ultrasonic propagation through the calcaneus ranges from about 0.2 to 1 MHz. Figure 5 is a plot of the calculated wavelengths of the three waves with $g = 2.43$. The pores sizes (diameters) in a calcaneus range from about 0.5 to 2 mm; these values correspond to the two horizontal lines of Fig. 5. One can see that the fast longitudinal wavelength is only twice the largest pore's size at $f = 0.42$ MHz, so that the Biot hypothesis (large wavelengths compared to pores sizes) is not quite valid. This is the reason why all the preceding

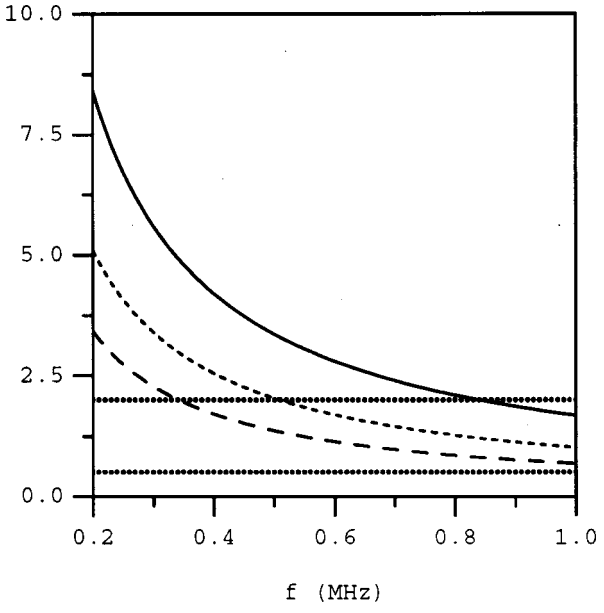

FIG. 5. Nondissipative marrow saturated calcaneus. Calculated wavelength, for a Gibson's coefficient $g = 2.43$, of the fast longitudinal wave (solid line), the slow longitudinal wave (dotted line), and the shear wave (dashed line), versus frequency. Dots: minimum and maximum pores sizes.

figures have been plotted for a pore radius equal to 1 mm.

In Sec. V, we calculate an effective celerity and an effective attenuation due to scattering by the largest pores, but first we discuss below the validity of our very simplified Biot modelization of the human calcaneus.

A. The effect of marrow viscosity

If one takes into account the marrow viscosity $\eta = 1.495\ \mathrm{Nsm}^{-2}$, along with a mean pore size $b = 471\ \mu\mathrm{m}$,[10] the critical frequency defined by Johnson *et al.*[25] is given by

$$f_c = \frac{1}{\pi}\frac{\eta}{\rho_f b^2} \approx 2 \quad \mathrm{kHz}.$$

At frequencies large compared to f_c, the acoustic waves dispersion is negligible.[25] The usual frequency band in osteoporosis diagnosis—0.2 to 1 MHz—is far beyond this critical frequency, so that the Gibson's coefficient value we chose, after having neglected the marrow viscosity, should be correct.

The marrow viscosity, of course, does induce acoustic attenuation. In this paper, however, we are interested only in characterizing the scattering effects, both on the dispersion and on the attenuation of acoustic waves. This is the reason why we neglect the marrow viscosity.

B. Slow wave observation in *in vivo* experiments

The main characteristic of a Biot medium is the slow wave. As we already mentioned in the Introduction, experimental evidence of this wave has been shown in calcaneus, but, as far as we know, this was never the case in *in vivo* experiments. *In vivo* experiments[1,2,4] are usually conducted with the patient's foot immersed in a water bath, in which immersion transducers are placed. The incident wave is propagating through water, transmitted through the skin, and then incident on the skin–calcaneus interface. This interface corresponds to a closed-pores continuity condition. With such a continuity condition, the transmission coefficient of the slow wave approaches zero.[26] Slow waves then can be excited only by scattering mechanisms inside the calcaneus, as scattering by the largest pores, as shown in Fig. 4.

V. EFFECTIVE ATTENUATION AND DISPERSION IN CALCANEUS DUE TO SCATTERING

Effective attenuation (dispersion) in a heterogeneous medium is the attenuation (dispersion) that would be measured in an equivalent homogeneous medium, called the effective medium. In the homogeneous porous bone described in Sec. IV, a plane-incident fast wave propagates unperturbed. Whenever that wave encounters scatterers, it gives rise to scattered waves in all directions, which, in turn, may also be scattered by other pores. The transmitted fast wave is then no longer a plane wave. In effective medium theories, one considers the acoustic transmission in the incidence direction as if it were due to a plane wave propagating in the effective medium, with a complex wave number k_{eff} related to the scattering process.[27–29]

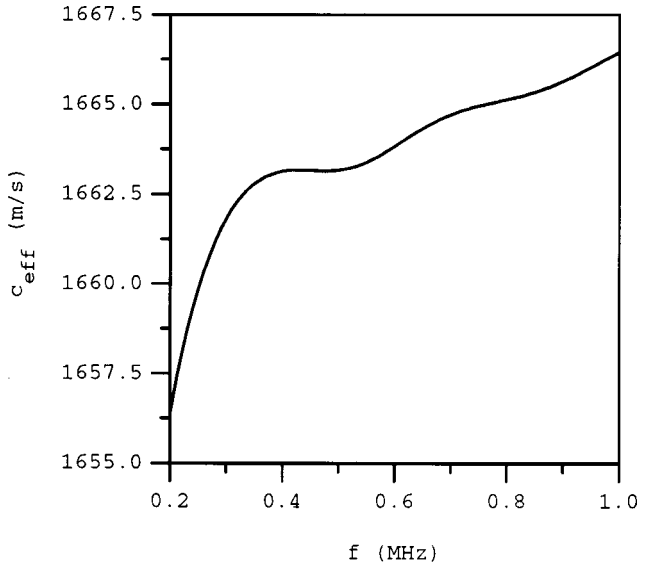

FIG. 6. Effective fast wave velocity in the multiple forward scattering approximation. All scatterers are cylindrical pores, radius 1 mm. The homogeneous scatterer density d is equal to $3d_{\min}$.

Assuming a low homogeneous scatterer density, and all scatterers to be identical, the effective complex wave number is given in the multiple forward scattering approximation by[28]

$$k_{\mathrm{eff}} = k_1\left(1 - \frac{dA}{2k_1^2}\right), \tag{34}$$

with d the number of scatterers per unit area that actually participate in the emergence of a coherent wave, and A the forward scattering amplitude of one scatterer in the far field, defined by[28]

$$\phi_s(r, \theta = 0) = -\frac{i}{4}\sqrt{\frac{2}{\pi}}e^{-i(\pi/4)}\frac{A}{\sqrt{k_1 r}}e^{ik_1 r}. \tag{35}$$

In relation (34), the scatterers are assumed to be in a homogeneous medium that is insonified by a plane wave of wave number k_1, and they all scatter waves of the same type, i.e., with that same wave number k_1. This is obviously not the case in the porous bone we consider here, as a fast plane wave gives rise to fast, slow, and shear waves. In a first approximation, however, we shall compute an effective wave number from (34), with A obtained from the comparison of (35) with (29) as

$$A = 2i\sum_{n=0}^{+\infty}\varepsilon_n(s_n^{11} - 1), \tag{36}$$

so that

$$k_{\mathrm{eff}} = k_1 - \frac{d}{k_1}i\sum_{n=0}^{+\infty}\varepsilon_n(s_n^{11} - 1). \tag{37}$$

In Ref. 13, the velocity dispersion in calcaneus is obtained from the inspection of circular regions of interest, 7 mm in diameter. The sample thickness is about 12.5 mm. The d scatterers density (scatterer diameter=2 mm) may then ex-

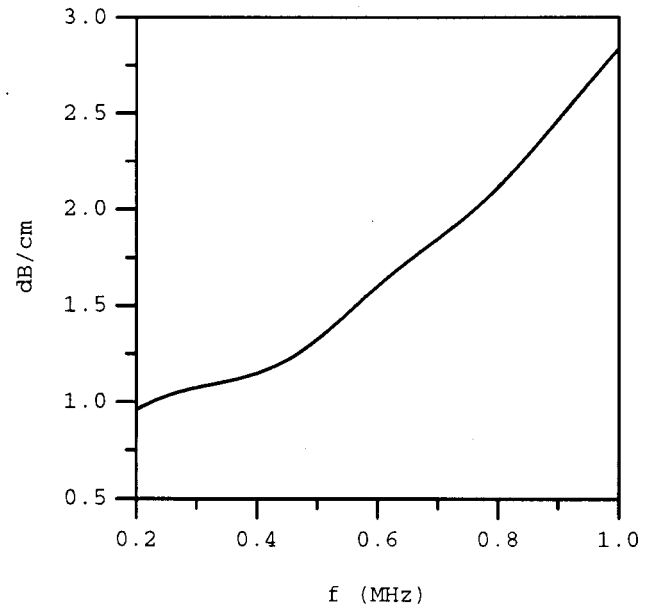

FIG. 7. Effective fast wave attenuation in the multiple forward scattering approximation. All scatterers are cylindrical pores, radius 1 mm. The homogeneous scatterer density d is equal to $3d_{\min}$.

tend at most from $d_{\min}=10^6/(7\times 12.5)\ \mathrm{m}^{-2}$ to $d_{\max}=3\times 6\times d_{\min}$.

The effective velocity deduced from (37) is plotted in Fig. 6 as a function of frequency, for $d=3\times d_{\min}$, while the effective attenuation, defined from the imaginary part of k_{eff} as $20\Im m(k_{\mathrm{eff}})/(100\ln 10)$ in dB/cm, is plotted in Fig. 7. Whatever the value of d, in the $d_{\min}$–$d_{\max}$ range, the dispersion curve shape is the same, but the effective velocity at a given frequency decreases as d increases. The effective attenuation increases as d increases.

The comparison of Figs. 6 and 7, respectively, to Figs. 5(c) and (d) of Ref. 13 shows that the effective attenuation deduced from (37) is about one-fifth of the actual one, and that the negative velocity dispersion experimentally observed is not predicted from (37). Figures 6 and 7, however, actually show that multiple scattering by the largest pores, even for very low scatterer density, induces an effective velocity dispersion and a non-negligible effective attenuation in an originally nondissipative medium.

The discrepancy observed between experiment and effective properties deduced from (37) may be explained by the neglect in relation (37) of the waves conversions shown in Fig. 4. More realistic properties should be obtained from a modelization that includes waves conversions due to scattering, as, for example in Refs. 15 and 30. This work is in progress.

VI. CONCLUSION

The attenuation and dispersion measured in calcaneus may be due to various phenomena, such as viscoporoelasticity and/or scattering. In most papers, only one of these phenomena is studied: the calcaneus is either modelized as a viscous porous medium, or as a liquid medium with scatterers (trabeculae) inside.

In this paper, we have considered the calcaneus as a nondissipative porous medium, with the largest pores acting as scatterers. The measured attenuation and dispersion are then supposed to be the effective properties of the coherent fast wave in the direct transmission direction. These effective properties should be calculated with a modelization including wave conversion as well as pore sizes distribution. Such modelizations have been done, in the case of an elastic medium, in Refs. 15 and 30. Having calculated the exact (as shown by energy conservation) scattered amplitudes by one single pore, we shall now try to extend the modelizations in Refs. 15 and 30 to the case of a porous medium.

ACKNOWLEDGMENTS

We wish to thank Jean-Louis Izbicki of our laboratory for fruitful discussions, and Pascal Laugier of the Laboratoire d'Imagerie Paramétrique for helpful informations on calcaneus and osteoporosis diagnosis.

APPENDIX A: THE CONTINUITY CONDITIONS AT $r=a$

Depending on whether the incident wave is a longitudinal one (case L) or a shear one (case T), these continuity conditions are

Continuity of the radial particles flow:

$$\begin{aligned}
&\Gamma_{\mathrm{inc}}\frac{\partial\phi_{\mathrm{inc}}}{\partial r}+\Gamma_1\frac{\partial\phi_1}{\partial r}+\Gamma_2\frac{\partial\phi_2}{\partial r}-\frac{\Gamma_t}{r}\frac{\partial\psi}{\partial\theta}\\
&\quad=\frac{\partial\phi_0}{\partial r}\ \text{ with }\ \Gamma_j=1+\gamma_j\quad j=1,2,t,\mathrm{inc}\quad(\text{case L}),\\
&-\frac{\Gamma_{\mathrm{inc}}}{r}\frac{\partial\phi_{\mathrm{inc}}}{\partial\theta}+\Gamma_1\frac{\partial\phi_1}{\partial r}+\Gamma_2\frac{\partial\phi_2}{\partial r}-\frac{\Gamma_t}{r}\frac{\partial\psi}{\partial\theta}\\
&\quad=\frac{\partial\phi_0}{\partial r}\quad(\text{case T});
\end{aligned}\tag{A1}$$

Equilibrium of fluid pressure:

$$\begin{aligned}
&\rho_{f\mathrm{inc}}\phi_{\mathrm{inc}}+\rho_{f1}\phi_1+\rho_{f2}\phi_2=\rho_0\phi_0\quad(\text{case L}),\\
&\rho_{f1}\phi_1+\rho_{f2}\phi_2=\rho_0\phi_0\quad(\text{case T});
\end{aligned}\tag{A2}$$

Equilibrium of normal traction:

$$\begin{aligned}
&-2\mu\frac{\partial^2(\phi_{\mathrm{inc}}+\phi_1+\phi_2)}{\partial r^2}+k_{\mathrm{inc}}^2(H-2\mu+\gamma_{\mathrm{inc}}C)\phi_{\mathrm{inc}}\\
&\quad+k_1^2(H-2\mu+\gamma_1C)\phi_1+k_2^2(H-2\mu+\gamma_2C)\phi_2\\
&\quad+2\mu\left[-\frac{1}{r^2}\frac{\partial\psi}{\partial\theta}+\frac{1}{r}\frac{\partial^2\psi}{\partial r\,\partial\theta}\right]=\rho_0\omega^2\phi_0\quad(\text{case L}),\\
&-2\mu\left(\frac{\partial^2\phi_1}{\partial r^2}+\frac{\partial^2\phi_2}{\partial r^2}\right)+k_1^2(H-2\mu+\gamma_1C)\phi_1\\
&\quad+k_2^2(H-2\mu+\gamma_2C)\phi_2+2\mu\left[-\frac{1}{r^2}\frac{\partial(\psi+\phi_{\mathrm{inc}})}{\partial\theta}\right.\\
&\quad\left.+\frac{1}{r}\frac{\partial^2(\psi+\phi_{\mathrm{inc}})}{\partial r\,\partial\theta}\right]=\rho_0\omega^2\phi_0\quad(\text{case T});
\end{aligned}\tag{A3}$$

Equilibrium of normal traction:

$$
\begin{aligned}
&-2\mu\frac{\partial^2(\phi_{\rm inc}+\phi_1+\phi_2)}{\partial r^2}+k_{\rm inc}^2(H-2\mu+\gamma_{\rm inc}C)\phi_{\rm inc}\\
&\quad+k_1^2(H-2\mu+\gamma_1 C)\phi_1+k_2^2(H-2\mu+\gamma_2 C)\phi_2\\
&\quad+2\mu\left[-\frac{1}{r^2}\frac{\partial\psi}{\partial\theta}+\frac{1}{r}\frac{\partial^2\psi}{\partial r\partial\theta}\right]=\rho_0\omega^2\phi_0\quad\text{(case L)},\\
&-2\mu\left(\frac{\partial^2\phi_1}{\partial r^2}+\frac{\partial^2\phi_2}{\partial r^2}\right)+k_1^2(H-2\mu+\gamma_1 C)\phi_1\\
&\quad+k_2^2(H-2\mu+\gamma_2 C)\phi_2+2\mu\left[-\frac{1}{r^2}\frac{\partial(\psi+\phi_{\rm inc})}{\partial\theta}\right.\\
&\quad\left.+\frac{1}{r}\frac{\partial^2(\psi+\phi_{\rm inc})}{\partial r\partial\theta}\right]=\rho_0\omega^2\phi_0\quad\text{(case T)};
\end{aligned}
\tag{A4}
$$

Equilibrium of tangential traction:

$$
\begin{aligned}
&-2\left[\frac{1}{r}\frac{\partial^2(\phi_{\rm inc}+\phi_1+\phi_2)}{\partial r\partial\theta}-\frac{1}{r^2}\frac{\partial(\phi_{\rm inc}+\phi_1+\phi_2)}{\partial\theta}\right]+\frac{1}{r^2}\frac{\partial^2\psi}{\partial\theta^2}\\
&\quad-\frac{\partial^2\psi}{\partial r^2}+\frac{1}{r}\frac{\partial\psi}{\partial r}=0\quad\text{(case L)},\\
&-2\left[\frac{1}{r}\frac{\partial^2(\phi_1+\phi_2)}{\partial r\partial\theta}-\frac{1}{r^2}\frac{\partial(\phi_1+\phi_2)}{\partial\theta}\right]+\frac{1}{r^2}\frac{\partial^2(\psi+\phi_{\rm inc})}{\partial\theta^2}\\
&\quad-\frac{\partial^2(\psi+\phi_{\rm inc})}{\partial r^2}+\frac{1}{r}\frac{\partial(\psi+\phi_{\rm inc})}{\partial r}=0\quad\text{(case T)}.
\end{aligned}
\tag{A5}
$$

APPENDIX B: THE MATRIX ELEMENTS OF SYSTEM (10)

Letting

$$x_j=k_j a,\quad j=1,2,t,0,\text{inc},$$

the matrix elements in (10) are

$$
\begin{aligned}
&m_{1j}=\Gamma_j x_j H_n^{(1)\prime}(x_j),\quad j=1,2\\
&m_{13}=-in\Gamma_t H_n^{(1)}(x_t),\quad m_{14}=-x_0 J_n'(x_0).\\
&m_{2j}=\rho_{fj}H_n^{(1)}(x_j),\quad j=1,2\\
&m_{23}=0,\quad m_{24}=-\rho_0 J_n(x_0).\\
&m_{3j}=2x_j H_n^{(1)\prime}(x_j)+\left(\frac{\rho_j}{\rho_t}x_t^2-2n^2\right)H_n^{(1)}(x_j),\quad j=1,2\\
&m_{33}=2in(x_t H_n^{(1)\prime}(x_t)-H_n^{(1)}(x_t)),\\
&m_{34}=-\frac{\rho_0}{\rho_t}x_t^2 J_n(x_0).\\
&m_{4j}=2in(-x_j H_n^{(1)\prime}(x_j)+H_n^{(1)}(x_j)),\quad j=1,2\\
&m_{43}=2x_t H_n^{(1)\prime}(x_t)+(x_t^2-2n^2)H_n^{(1)}(x_t),\\
&m_{44}=0,
\end{aligned}
$$

and

$$
\begin{aligned}
&E_1=-x_{\rm inc}\Gamma_{\rm inc}H_n^{(2)\prime}(x_{\rm inc}),\quad E_2=-\rho_{f\rm inc}H_n^{(2)}(x_{\rm inc}),\\
&E_3=-2x_{\rm inc}H_n^{(2)\prime}(x_{\rm inc})-\left(\frac{\rho_{\rm inc}}{\rho_t}x_t^2-2n^2\right)H_n^{(2)}(x_{\rm inc})\\
&E_4=-2in(-x_{\rm inc}H_n^{(2)\prime}(x_{\rm inc})+H_n^{(2)}(x_{\rm inc})),\\
&\quad\text{in case (L)},
\end{aligned}
$$

and

$$
\begin{aligned}
&E_1=in\Gamma_{\rm inc}H_n^{(2)}(x_{\rm inc}),\quad E_2=0,\\
&E_3=-2in(x_{\rm inc}H_n^{(2)\prime}(x_{\rm inc})-H_n^{(2)}(x_{\rm inc})),\\
&E_4=-2x_{\rm inc}H_n^{(2)\prime}(x_{\rm inc})+(x_t^2-2n^2)H_n^{(2)}(x_{\rm inc}),\\
&\quad\text{in case (T)}.
\end{aligned}
$$

[1] P. Laugier, B. Fournier, and G. Berger, "Ultrasound parametric imaging of the calcaneus: *In vivo* results with a new device," Calcif. Tissue Int. **58**, 326–331 (1996).

[2] C. Roux, B. Fournier, P. Laugier, C. Chappard, S. Kolta, M. Dougados, and G. Berger, "Broadband ultrasound attenuation imaging: A new imaging method in osteoporosis," J. Bone Miner. Res. **11**(8), 1112–1118 (1996).

[3] P. Laugier, P. Drouin, A. M. Laval-Jeantet, and G. Berger, "*In vitro* assessment of the relationship between acoustic properties and bone mass density of the calcaneus by comparison of ultrasound parametric imaging and quantitative computed tomography," Bone **20**(2), 157–165 (1997).

[4] F. Lefebvre, G. Berger, and P. Laugier, "Automatic detection of the boundary of the calcaneus from ultrasound parametric images using an active contour model; clinical assessement," IEEE Trans. Med. Imaging **17**(1), 45–52 (1998).

[5] M. A. Biot, "Theory of propagation of elastic waves in a fluid-saturated porous solid," J. Acoust. Soc. Am. **28**, 168–191 (1956).

[6] R. D. Stoll, "Wave attenuation in saturated sediments," J. Acoust. Soc. Am. **47**, 1440–1447 (1970).

[7] A. Hosokawa and T. Otani, "Ultrasonic wave propagation in bovine cancellous bone," J. Acoust. Soc. Am. **101**, 558–562 (1997).

[8] A. Hosokawa and T. Otani, "Acoustic anisotropy in bovine cancellous bone," J. Acoust. Soc. Am. **103**, 2718–2722 (1998).

[9] P. H. F. Nicholson and R. Strelitzki, "Ultrasonic slow waves in air-saturated cancellous bone," Ultrasonics **37**, 445–449 (1999).

[10] M. L. McKelvie and S. B. Palmer, "The interaction of ultrasound with cancellous bone," Phys. Med. Biol. **36**(10), 1331–1340 (1991).

[11] R. Strelitzki and J. A. Evans, "On the measurement of the velocity of ultrasound in the *os calcis* using short pulses," Eur. J. Ultrasound **4**, 205–213 (1996).

[12] P. H. F. Nicholson, G. Lowett, C. M. Langton, J. Dequeker, and G. Van der Perre, "A comparison of time-domain and frequency-domain approaches to ultrasonic velocity measurement in trabecular bone," Phys. Med. Biol. **41**, 2421–2435 (1996).

[13] P. Droin, G. Berger, and P. Laugier, "Velocity dispersion of acoustic waves in cancellous bone," IEEE Trans. Ultrason. Ferroelectr. Freq. Control **45**(3), 581–592 (1998).

[14] K. A. Wear, "Measurements of phase velocity and group velocity in human calcaneus," Ultrasound Med. Biol. **26**(4), 641–646 (2000).

[15] V. K. Varadan, Y. Ma, and V. V. Varadan, "Multiple scattering of compressional and shear waves by fiber-reinforced composite materials," J. Acoust. Soc. Am. **80**, 333–339 (1986).

[16] H. Deresiewicz and R. Skalak, "On uniqueness in dynamic poroelasticity," Bull. Seismol. Soc. Am. **53**(4), 783–788 (1960).

[17] S. G. Solomon, H. Uberall, and K. B. Yoo, "Mode conversion and resonance scattering of elastic waves from a cylindrical fluid-filled cavity," Acustica **55**, 147–159 (1984).

[18] H. M. Nussenzweig, "High frequency scattering by a transparent sphere. I Direct reflection and transmission," J. Math. Phys. **10**(1), 82–124 (1969).

[19] J. M. Conoir, "Diffusion acoustique en géométrie séparable: Une méthode d'acquisition des séries de Debye généralisées," C.R. Acad. Sci. Paris, tome 301, série 2, **7**, 471–473 (1985).

[20] E. B. Danila, J. M. Conoir, and J. L. Izbicki, "The generalized Debye series expansion: Treatment of the concentric and nonconcentric cylindrical fluid–fluid interfaces," J. Acoust. Soc. Am. **98**, 3326–3342 (1995).

[21] E. B. Danila, J. M. Conoir, and J. L. Izbicki, "Generalized Debye series: Part 1, treatment of the concentric cylindrical fluid-solid interfaces," Acust. Acta Acust. **84**, 21–37 (1998).

[22] J. L. Williams, ''Ultrasonic wave propagation in cancellous and cortical bone: Prediction of some experimental results by Biot's theory,'' J. Acoust. Soc. Am. **91**, 1106–1112 (1992).
[23] J. G. Berryman, ''Long wavelength propagation in composite elastic media,'' J. Acoust. Soc. Am. **68**, 1809–1831 (1980).
[24] L. J. Gibson, ''The mechanical behavior of cancellous bone,'' J. Biomech. **18**(5), 317–328 (1985).
[25] D. L. Johnson and T. J. Plona, ''Acoustic slow waves and the consolidation transition,'' J. Acoust. Soc. Am. **72**, 556–565 (1982).
[26] P. N. J. Rasolofosaon, ''Importance of the interface hydraulic condition on the generation of second bulk compressional wave in porous media,'' Appl. Phys. Lett. **52**, 780–782 (1988).
[27] A. Ishimaru, *Wave Propagation and Scattering in Random Media* (Academic, New York, 1978).
[28] J. Groenenboom and R. Snieder, ''Attenuation, dispersion, and anisotropy by multiple scattering of transmitted waves through distributions of scatterers,'' J. Acoust. Soc. Am. **72**, 556–565 (1982).
[29] D. Sornette, ''Acoustic waves in random media. I. Weak disorder regime,'' Acustica **67**, 199–215 (1989).
[30] G. C. Gaunaurd and H. Uberall, ''Resonance theory of the effective properties of perforated solids,'' J. Acoust. Soc. Am. **71**, 282–294 (1982).

Characterizing holes in duct walls using resonance frequencies

M. H. F. de Salis
Acoustics Research Unit, School of Architecture and Building Engineering, University of Liverpool, P.O. Box 147, Liverpool L69 3BX, United Kingdom

N. V. Movchan
Department of Mathematical Sciences, M&O Building, University of Liverpool, P.O. Box 147, Liverpool L69 3BX, United Kingdom

D. J. Oldham
Acoustics Research Unit, School of Architecture and Building Engineering, University of Liverpool, P.O. Box 147, Liverpool L69 3BX, United Kingdom

(Received 15 February 2001; revised 24 January 2002; accepted 15 February 2002)

The current paper demonstrates that the technique recently used by de Salis and Oldham for the sizing and location of blockages in ducts using resonance and antiresonance value shifts [J. Sound Vib. **221**(1), 180–186 (1999)] may be successfully applied to the detection, location, and sizing of small holes in duct walls. It is shown that when the blockage area function reconstruction process is applied using resonance and antiresonance frequencies determined from a single measurement of sound pressure within a duct, the position of a hole in the duct wall is revealed as the beginning of an apparent gradual expansion. This expansion is termed the effective expansion function and emanates from an initial positive dc shift. Once the hole has been located, a simple impedance model of the duct incorporating the hole location and the measured wave number at the first-order duct resonance may be derived which allows the determination of the radius of the side hole from a simple quadratic equation. This hole-sizing technique is also successfully applied to thin slits in duct walls using an equivalent radius approach, and is shown to be highly accurate for slit-shaped holes with cross-sectional length to width aspect ratios of up to 28:1. © *2002 Acoustical Society of America.* [DOI: 10.1121/1.1470506]

PACS numbers: 43.20.Mv, 43.20.Ks [DEC]

I. INTRODUCTION

The ability to detect, locate, and size holes in duct or pipe walls can be of great importance in concealed piped fluid systems, and as such any nonintrusive or simplified technique to achieve this may have significant practical applications. For example, acoustic techniques currently used in the water industry achieve leak detection via the monitoring of acoustic propagation within the pipe walls using correlation techniques. This has proved to be highly successful in metal-walled pipes; further research is underway which seeks to address the difficulties associated with applying the technique in plastic pipes, where the effect of losses are more significant.[1]

Sharp and Campbell have applied a different acoustic technique, that of fluid-borne pulse reflectometry, first to the sizing of bores in pipes[2] and then to leak detection in pipe walls,[3] where the hole position has been shown to coincide with the beginning of an apparent accentuated flare occurring in a pipe of uniform or known cross section. This method was also successful in sizing circular side holes of varying dimension using the known hole location and the duct impedance determined from the pulse reflectometry technique. The pipe tested in Sharp and Campbell's work[3] was 5 mm in radius and approximately 0.733 m in length, while the holes sized were limited to circular geometry and were relatively large in comparison to the pipe diameter, being from 1 to 3 mm in radius. The algorithm used in their method is mathematically elegant and exact in its location and sizing of the hole but is limited, as the experimental technique requires an additional measurement lead-up tube of at least twice the length of the test pipe. This lead-up tube is required to measure incident and reflected pulses and must be of extended length to prevent secondary reflections from its termination point from interfering with the reflected impulse which characterizes the test pipe to be modeled. This problem has been largely overcome by employing the primary pulse generator in an additional role as a time-delayed active absorber which cancels the reflected pulse upstream of the capture microphone, thus reducing interference from subsequent reflections.[4]

Recent work by de Salis and Oldham[5,6] has shown that the internal profile of a finite length section of duct or pipe can also be established using resonance and antiresonance frequencies determined from a single measurement of the duct-transfer function using pseudorandom noise. This technique was made possible by the excellent signal to noise ratio obtained using maximum length sequence (MLS) analysis, thus allowing accurate location of the antiresonance frequencies in addition to the resonance frequencies of a test duct.

The current paper shows that the technique developed by de Salis and Oldham for blockage detection can also be applied successfully to the location and sizing of holes in the

walls of circular ducts. The technique requires that the duct termination conditions be of a closed–open nature with a driver located at the closed rigid end. All reflections from the terminations of the duct are required for the analysis[5–7] and the technique is therefore suited to the detection of holes and blockages in ducts of extended length. The method is rapid and robust due to the comparative simplicity of processing and the high signal to noise levels provided by the MLS analysis, and can be applied simply using a driver mounted in one termination and a microphone located in the wall of the duct.

The hole-sizing approach is greatly simplified by making the assumption that the characteristic dimension of the hole is small relative to the duct cross-sectional radius and may therefore be accurately modeled as a simple orifice in a plane wall. This will often be the case for minor leaks and especially in the case of thin slits and cracks, where it is shown that this characteristic dimension will tend to the value of the smaller cross dimension, i.e., the slit width. Theoretical analysis shows that viscous losses modeled in Sharp and Campbell's work can be discounted, which simplifies the analysis. The technique is shown to be capable of accurately detecting, locating, and sizing circular holes in the duct wall down to very small (relative to the duct cross-sectional diameter) dimensions using a completely automated computational analysis. The technique is also successfully applied to rectangular and slit-shaped orifices where accurate sizing is achieved based upon an equivalent radius approach. This approach is shown to be valid for circumferential slits of large length to width aspect ratios.

II. THEORY

A. Location of a hole in a duct wall by reconstruction of the bore effective expansion function

The work of Sharp and Campbell,[2–4] involving the reconstruction of the internal area function of small-bore pipes, has shown that a hole in the pipe wall gives rise to an apparent gradual expansion of the bore emanating from the position of that hole. The work of de Salis and Oldham[5–7] has demonstrated that the internal profile or blockage area function of a duct can be determined by utilizing the high noise immunity of a maximum length sequence (MLS) measurement system to reveal the resonance and antiresonance frequencies of the duct by means of a single measurement of the loudspeaker voltage to sound-pressure transfer function within the duct. The expression for the blockage area function $A_b(x)/A_0(x)$ of a duct with closed–open end conditions in de Salis and Oldham's work[5,6] is given by

$$\frac{A_b(x)}{A_0(x)}=\left[1-\exp\left(\sum_{n=1}\left[\frac{L_e}{n\pi}\right]^2\mu_{(a)n}\cos\left(\frac{2n\pi x}{L_e}\right)-\sum_{n=1}\left[\frac{2L_e}{(2n-1)\pi}\right]^2\chi_n\cos\left(\frac{(2n-1)\pi x}{L_e}\right)-a_0\right)\right], \tag{1}$$

where $A_b(x)$ is the blockage cross-sectional area, $A_0(x)$ is the cross-sectional area of the unblocked duct, L_e is the end-corrected duct length for the closed–open duct and a_0 is an added dc component which is equal to the ratio of blockage to duct volume.[8] As detailed in Ref. 5, the value χ_n is the nth blockage-induced duct resonance value shift and is calculated from the measured resonance frequencies $f_n^{(b)}$ of a partially blocked duct and the calculated resonance frequencies $f_k^{(cu)}$ of a theoretical unblocked duct of uniform cross section, identical length, and approximately identical volume, where

$$\chi_n=\frac{4\pi^2}{c^2}([f_n^{(b)}]^2-[f_k^{(cu)}]^2),\quad n=k. \tag{2}$$

The frequencies $f_k^{(cu)}$ are determined from the measured values of $f_n^{(b)}$ as follows:[5]

$$N\to\infty,\quad f_k^{(cu)}=\frac{(2k-1)}{N^2}\sum_{n=1}^{N}f_n^{(b)},\quad k=1,2,3,..., \tag{3}$$

where N is the number of longitudinal resonance frequencies inclusive from $N=1$ used in the calculation. Similarly, $\mu_{(a)n}$ is the nth blockage-induced antiresonance value shift of the duct and is calculated from the measured antiresonance frequencies in the partially blocked duct $f_{(a)n}^{(b)}$ and the calculated antiresonance frequencies $f_{(a)k}^{(cu)}$ of a theoretical unblocked duct of identical length and approximately identical volume but of uniform cross section

$$\mu_{(a)n}=\frac{4\pi^2}{c^2}([f_{(a)n}^{(b)}]^2-[f_{(a)k}^{(cu)}]^2),\quad n=k. \tag{4}$$

The frequencies $f_{(a)k}^{(cu)}$ are determined from the measured values of $f_{(a)n}^{(b)}$ as follows:

$$N\to\infty,\quad f_{(a)k}^{(cu)}=\frac{k}{N!}\sum_{n=1}^{N}f_{(a)n}^{(b)},\quad k=1,2,3,..., \tag{5}$$

where N is the number of longitudinal antiresonance frequencies inclusive from $N=1$ used in the calculations. Using the single measurement technique[5,6] to determine the resonance and antiresonance frequencies of the partially blocked duct, it was found that taking $N=15$ in Eqs. (3) and (5) gave a sufficiently accurate approximation to make the reconstruction process valid. This also tied in with the limitations of the experimental procedure.[5–7] However, it should be noted that while the first 15 longitudinal modes of the test duct were below the cross modal cut-on frequency, shorter and/or wider ducts would have fewer longitudinal modes below the cut-on frequency. With the advent of cross-modal activity, the longitudinal modes become difficult to differentiate from cross modes in the frequency domain, leaving less useful modes for analysis and subsequently reducing the accuracy of the method.

The blockage area or duct internal area profile function $A_b(x)/A_0(x)$ in Eq. (1) is thus described in terms of the resonance value shifts χ_n and antiresonance value shifts $\mu_{(a)n}$ obtained under a single set of boundary conditions. As noted in the earlier work of Wu and Fricke, using two sets of measurements for each of two sets of boundary conditions,[8] this type of perturbation analysis is valid only for relatively small changes in internal profile, that is, when $A_b(x)/A_0(x)<0.5$ and length of blockage $L_b<L_e/4$. However, while re-

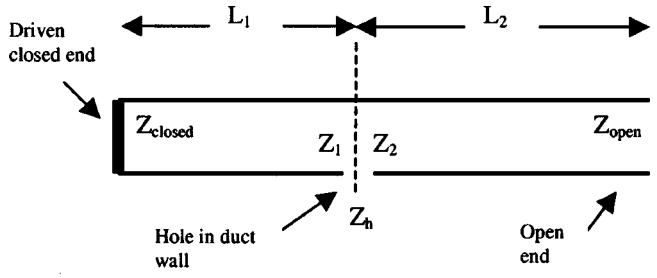

FIG. 1. Impedance model of a closed–open-ended duct driven at the closed end and incorporating a hole in the duct side wall.

constructions of blockage area functions $A_b(x)/A_0(x)$ which transcend these limits tend to lose accuracy, the method is still valid as a means of blockage detection.

The following sections will show that the single measurement approach described above can also detect, locate, and size a small hole cut into a duct wall. As noted by Sharp and Campbell,[3] the effect of the hole is seen as an apparent expansion, termed the effective expansion function, which is displayed in the form of a negative gradient beginning from the position of the hole and continuing towards the end of the duct. The technique described in this paper may be argued as being somewhat simpler than that of Sharp and Campbell[3] both in terms of processing the required algorithm and also in terms of the experimental method, which does not require the exclusion of unwanted reflections from the analysis. As previously noted, in this case the reflections from terminations are integral to the method.

B. Sizing of a hole in a duct wall

The technique set out in Sec. I A will reveal the resonance and antiresonance characteristics of the duct system and will also locate the position of a hole in a duct wall. If the hole in the wall of a duct with closed–open ends as illustrated in Fig. 1 is known to be of circular cross section, then the resonance and antiresonance characteristics may be used to size the hole using the acoustic impedance model of the duct described below. This model will be a function of the radius of the hole and a number of other parameters including the impedance at the driver end. However, the impedance of the fluid in the duct at the driver end for this type of system is generally difficult to determine using direct methods. Therefore, this impedance is approximated at resonance and antiresonance by making qualified assumptions about the condition of the duct–driver system at these frequencies.

1. Impedance model of a duct with an orifice in the side wall

An impedance model of a duct with a small hole in the wall is shown in Fig. 1. For the purpose of the model, the duct is effectively split into two sections. The left-hand section is bounded by the plane of the driver and the plane of the hole, while the right-hand section is bounded by the plane of the hole and the plane of the open end. The complex impedance at the end of the left-hand section is denoted by Z_1 and the input impedance of the right-hand section by Z_2. The impedance of the wall orifice Z_h may then be expressed as

$$\frac{1}{Z_h}=\frac{1}{Z_1}-\frac{1}{Z_2}. \tag{6}$$

This can be rearranged to give

$$Z_h=\frac{Z_1Z_2}{Z_2-Z_1}. \tag{7}$$

The impedance Z_1 of the initial section of duct may be determined from the impedance Z_{closed} of the fluid at the driver end using the impedance model for a section of duct with impedance terminations. Adapting the expression for mechanical impedance of a section of duct in Ref. 9, then the acoustic impedance Z_1 can be written as

$$Z_1=\frac{\rho c}{S_{\text{duct}}}\left[\frac{Z_{\text{closed}}-j\left(\frac{\rho c}{S_{\text{duct}}}\right)\tan(kL_1)}{\left(\frac{\rho c}{S_{\text{duct}}}\right)-jZ_{\text{closed}}\tan(kL_1)}\right], \tag{8}$$

where k is the acoustic wave number, L_1 is the longitudinal distance from the closed driver end of the duct to the orifice, ρ is the density of air, c is the speed of sound in air, and S_{duct} is the cross-sectional area of the duct.

The value of the fluid impedance Z_{closed} at the driver is now required to evaluate Z_1, and there are two conditions which lend themselves to simple approximations, i.e., resonance and antiresonance. First, at resonance the impedance of the fluid in the duct adjacent to the driver closely matches the impedance of the driver which maximizes power transmission into the duct. Making the assumption that the impedance of the closed driver end is very large when compared to the characteristic impedance of free air leads to the assumption that the impedance Z_{closed} of the fluid next to the driver also becomes very large as the system becomes resonant. Equation (8) now becomes

$$Z_1=\frac{\rho c}{S_{\text{duct}}}\left[\frac{j}{\tan(k_nL_1)}\right], \tag{9}$$

where k_n is the wave number of the duct system at resonance. It should be noted that the assumption of a high ratio of driver to fluid impedance may be invalid where drivers of low impedance are utilized or where narrow pipes with a high characteristic impedance are analyzed.

Second, at antiresonance the pressure close to the driver goes to a minimum. The assumption this time is that the impedance Z_{closed} of the fluid next to the driver end is poorly matched to the large impedance of the closed end and becomes very small as the system approaches antiresonance. Equation (8) then becomes

$$Z_1=-\frac{\rho c}{S_{\text{duct}}}[j\tan(k_{(a)n}L_1)], \tag{10}$$

where $k_{(a)n}$ is the wave number of the duct system at antiresonance.

Similarly, the impedance Z_2 in Fig. 1 may be expressed in terms of Z_{open}. Utilizing the standard equation for an unflanged open ended duct,[9] Z_2 may be expressed as follows:

$$Z_2 = \frac{\rho c}{S_{\text{duct}}} \times \left[\frac{\frac{1}{4}(kr_{\text{duct}})^2 + j[0.6(kr_{\text{duct}}) + \tan(kL_2)]}{[1 - 0.6(kr_{\text{duct}})\tan(kL_2)] + j(\frac{1}{4}(kr_{\text{duct}})^2)\tan(kL_2)} \right], \tag{11}$$

where r_d is the cross-sectional radius of the duct.

Substituting (9) or (10) and (11) into (7) yields the impedance of the orifice Z_h.

2. Impedance Z_h of the orifice

The representation for the impedance of an orifice as a side branch in a duct wall, where the dimensions of the slit are small compared to acoustic wavelength, may be found in standard texts[9] and is given by

$$Z_h = \frac{\rho c \mathbf{k}_h^2}{4\pi} + j\frac{\rho c L' \mathbf{k}_h}{\pi r_h^2}, \tag{12}$$

where r_h is the radius of the orifice, $\mathbf{k}_h$ is the complex wave number of propagation in the side orifice

$$\mathbf{k}_h = k - j\frac{\alpha}{r_h}, \tag{13}$$

the term α/r_h accounts for viscous losses in the hole and has the form

$$\alpha = \frac{1}{c}\left[\sqrt{\frac{\mu\omega}{2\rho}} + (\gamma - 1)\sqrt{\frac{\kappa\omega}{2\rho c_p}} \right], \tag{14}$$

where μ is the gas viscosity ($1.8*10^{-5}$ kg m^{-1} s^{-1} for air at 293 K), γ is the ratio of specific heats (1.4 for air), κ is the thermal conductivity ($3*10^{-6}$ Wm^{-1} k^{-1} for air), and c_p is the specific heat at constant pressure (1004.15 J Kg^{-1} K^{-1} for air).

The loss term α in Eq. (14) is similar to the term used in Sharp and Campbell's work,[3] with the difference being that in this case it is independent of the hole radius which may be noted in Eq. (13) where r_h appears independently of α.

The length L' in Eq. (12) is equal to the thickness of the duct wall L_h plus additional end corrections terms,[3,10] and may be expressed as

$$L' = L_h + r_h\left[1.5 - 0.58\left(\frac{r_h}{r_d}\right)^2 \right], \tag{15}$$

where r_d is the radius of the main duct section.

The bracketed term in r_h on the right-hand side of Eq. (15) evaluates the end correction of the side hole. It is apparent that the second term inside the brackets in Eq. (15) will tend to zero as r_h becomes small in comparison to r_d. Therefore, for small values of r_h, e.g., $r_h/r_d < 0.2$, the simplified expression for the length L' of an orifice in a plane pipe wall may be used, where

$$L' = L_h + 1.5r_h. \tag{16}$$

3. Calculation of the orifice radius r_h

Evaluating and equating the imaginary parts of Eq. (7) gives

$$\text{Im}(Z_h) = \frac{\text{Im}(Z_2)[(\text{Re}(Z_1))^2 + (\text{Im}(Z_1))^2] - \text{Im}(Z_1)[(\text{Re}(Z_2))^2 + (\text{Im}(Z_2))^2]}{[\text{Re}(Z_1) - \text{Re}(Z_2)]^2 + [\text{Im}(Z_1) - \text{Im}(Z_2)]^2}. \tag{17}$$

As noted at the beginning of this section, the proposed hole location technique described in Sec. I A will yield all the required parameters to evaluate the real and imaginary parts of Z_1 using Eq. (9) or (10) and the real and imaginary parts of Z_2 using Eq. (11). Substituting these results into Eq. (17) evaluates Im(Z_h). To evaluate the hole radius r_h using this result, we substitute Eqs. (13) and (16) into Eq. (12), which yields

$$\text{Im}(Z_h) = \rho c k\left(-\frac{\alpha}{2\pi r_h} + \frac{1.5r_h + L_h}{\pi r_h^2} \right), \tag{18}$$

which may be rearranged thus

$$\frac{\pi}{\rho c k}\text{Im}(Z_h) r_h^2 - \left(1.5 - \frac{\alpha}{2}\right) r_h - L_h = 0. \tag{19}$$

As previously noted, the viscous loss term α is constant and independent of r_h, and as such the effect of losses in Eq. (18) may be rapidly assessed.

It may be noted that even at limiting ultrasonic frequencies $\alpha/2$ evaluated from (14) makes up less than 0.5% of the total term in r_h. Therefore, it may be deduced that viscous losses are insignificant in any evaluation of Im(Zh) or r_h, and Eq. (18) now simplifies to

$$\frac{\pi}{\rho c k}\text{Im}(Z_h) r_h^2 - 1.5r_h - L_h = 0. \tag{20}$$

Equation (20) is a quadratic equation and may be solved in the standard way to yield r_h. It may be noted that the use of the simplified expression for L' in Eq. (15) has reduced Eq. (18) from the more complex cubic equation utilized by Sharp and Campbell.[3]

4. Calculation of the geometrical equivalent radius r_h of a square or rectangular orifice

It can be shown that within certain limits the above approach may also be applied to orifices of other geometries where the ''radius'' of the hole will now correspond to a geometrical equivalent radius for the hole area. In the current work this technique will be applied to circumferentially orientated rectangular-shaped orifices in the duct wall. The geometrical equivalent radius, denoted here by r_{he}, is the radius of a circular hole whose area is equivalent to the area of the square or rectangular orifice in question. For a rectangular slit of cross-sectional dimensions a and b, the equivalent radius r_{he} is given by

$$r_{he} = \sqrt{\frac{ab}{\pi}}. \tag{21}$$

In the current approach the radius r_{he} will be evaluated from $\mathrm{Im}(Z_h)$ by substituting r_{he} for r_h in Eq. (20).

When substituting r_{he} into Eq. (20), it should perhaps be noted that viscous losses for a rectangular or other arbitrary-shaped side orifice will be larger than for a circular orifice of equal area. The increase in viscous losses will be directly proportional to the increase in perimeter to cross-sectional area ratio of the orifice. This is important in the transmission loss of slits, where accurate evaluation of the real part of the impedance is required and in such cases a geometrical equivalent radius approach has been found[11] to be limited to slits of cross-dimensional aspect ratio smaller than 8:1. This becomes crucial where the wavelength of sound approaches the depth of the hole and the system displays resonant tendencies. The current sizing approach uses the fundamental resonant and antiresonant frequencies of the duct, and the wavelength of sound is very large compared to the hole dimensions and as such hole acts as a lumped element. Also, the approach employs only the imaginary part of the impedance of the slit, and it may be shown that even if α in Eq. (19) was increased by 1000 times to compensate for an associated increase in perimeter, this would do little to influence the value of the imaginary part of the impedance in the frequency range of interest. Therefore, Eq. (20) will be used to evaluate r_{he} from values of $\mathrm{Im}(Zh)$ for the time being. However, there are other limitations when using Eq. (20) to size slits of large cross-dimensional aspect ratio. These limitations will be referred to in a later section.

III. EXPERIMENTAL ANALYSIS

A series of experiments was carried out to validate the theoretical approach described above. The duct used in the experiments was a 2-m-long plastic duct of 0.1 m diameter and wall thickness of 5.5 mm. The experimental setup is illustrated in Fig. 2. The duct characteristics were determined using the maximum length sequence (MLS) analysis, a technique which has been widely used for diagnosis of enclosed spaces in such areas as architectural acoustics.[12] The substantial noise immunity and versatility of the MLS system has also been utilized to good effect in previous work by the authors.[5–7] The duct had a cut-on frequency for transverse modes of approximately 1900 Hz. The duct was excited by a piezoelectric driver attached to one end while the other end of the duct was left open. The excitation signal applied consisted of a 16 384-point maximum length sequence (MLS) of 2-kHz bandwidth and 8-kHz sampling rate. A microphone situated in the wall of the duct close to the driver was used to record the distorted MLS signal emanating from the driver allowing generation of the frequency transfer function of loudspeaker voltage to sound pressure in the duct. In each case four averages of the MLS signal were taken, making a total measurement time of approximately 8 s. A typical transfer function from measurements in the test duct with a small side hole is shown in Fig. 3. The MLS analysis has sufficient noise immunity to reveal the antiresonance residuals in the transfer function in addition to the resonance characteristics of the system. Strongly defined longitudinal resonance and antiresonance frequencies may be noted below the duct cut-on frequency. Less obvious is the irregular spacing of the duct harmonics due to the presence of a small hole in the duct wall. This characteristic facilitates the location of the hole using Eqs. (1)–(5). The frequency resolution of the transfer function was kept at 1 Hz at all times, as earlier work in the reconstruction of blockage functions using a similar technique[5–7] has shown that little benefit in terms of increased accuracy is gained from increasing the frequency

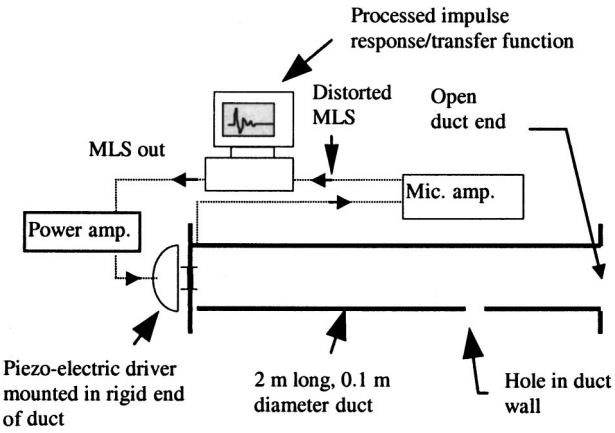

FIG. 2. Test rig for a closed–open-end duct of circular cross section with a hole in the duct side wall.

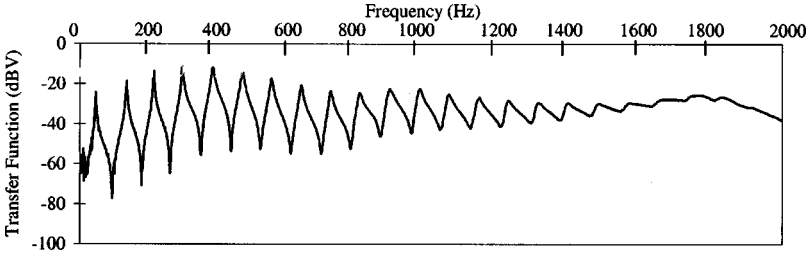

FIG. 3. Typical measured transfer function of loudspeaker voltage to sound pressure at the microphone measured in the duct setup of Fig. 2.

resolution to a finer degree. This was also noted in the current work in terms of the accuracy of positioning and sizing of a hole in the duct wall.

The measured duct transfer function was imported into the MATLAB numerical processing package and a simple routine was utilized to select the resonance and antiresonance frequencies of the duct. The resonance and antiresonance frequencies of the duct with unperforated walls were subsequently calculated from Eqs. (3) and (5), and the resonance and antiresonance value shifts were processed using Eqs. (2) and (4). The apparent internal area function of the duct, which will be termed the effective expansion function, was then calculated using Eq. (1) to reveal the position of the hole in the duct wall. The end-corrected length of the duct L_e in Eq. (1) was determined from the fundamental resonance frequency of the unperforated closed–open duct f_1^0 from Eq. (3) as follows:

$$L_e = \frac{1}{4}\frac{c}{f_1^0}, \tag{22}$$

where the speed of sound c was estimated using the standard expression

$$c = 331.45\sqrt{(1 + T/373.6)}, \tag{23}$$

with T being the measured ambient temperature in Kelvin. Use of Eqs. (22) and (23) eliminates the need for prior knowledge of the length of the duct system, which simplifies the process and may be beneficial in conditions where this is difficult to ascertain.

The first 15 resonance and antiresonance values determined using Eqs. (2) and (4), respectively, were found to be adequate for the reconstruction of the effective expansion function to enable successful location of a side hole. The resonance and antiresonance frequencies required to obtain these values were located well below the cut-on frequency for transverse modes and were generally strongly defined as shown in Fig. 3. This strong definition made them well suited to the computational selection process for resonance and antiresonance frequencies in the MATLAB routine used in the hole location and sizing routines. Once determined from the reconstruction achieved using Eq. (1), the longitudinal position of the hole relative to the driver, denoted by L_1 in Fig. 1, was used in conjunction with one measured wave number, i.e., k_n at resonance or $k_{(a)n}$ at antiresonance to size the hole in the duct wall as set out in Sec. II B.

A. Filtration

As in previous work,[5–7] filtration was applied to the transfer functions in MATLAB to exclude areas of the frequency range superfluous to the analysis and to smooth out spurious peaks and troughs in the transfer function, thus preventing contamination of the computational resonance and antiresonance frequency selection process. Low-frequency distortion is thought to arise due to poor response of the microphone and loudspeaker at low frequencies and subsequent low signal to noise ratios.[6] Figure 4(a) shows the low-frequency section of the transfer function in Fig. 3 without filtration and Fig. 4(b) shows the same transfer function after filtration has been employed to smooth out localized distortions. The effect of a hole in the duct wall at the lower end of the spectrum is illustrated to some degree in Fig. 4, which shows the positions of the first few resonances and antiresonances of the same duct with unperforated walls. The wall orifice as a side branch in a duct is well known as having high-pass characteristics[9] and Fig. 4 illustrates the effect of a small hole in the duct wall on the low-frequency response, an effect which diminishes towards the upper end of the frequency range.

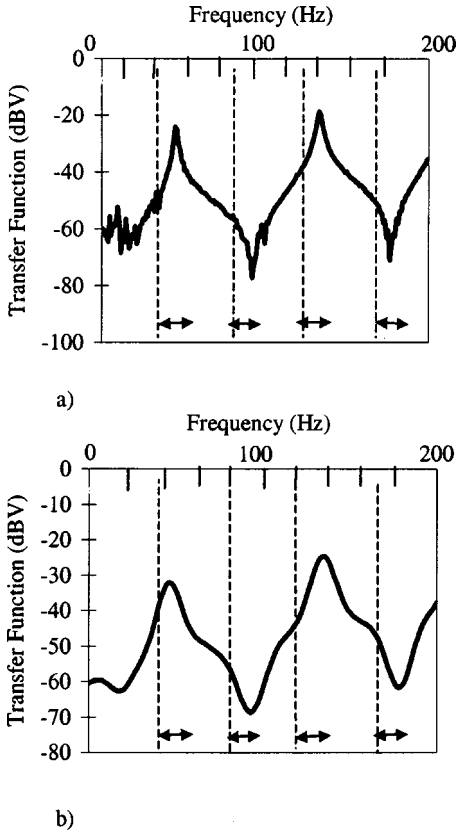

FIG. 4. Measured transfer function 0–200 Hz of partially blocked duct shown in Fig. 2: (a) Unfiltered; (b) filtered. Positions of resonance and antiresonance frequencies of duct with unperforated wall shown by dotted lines.

IV. DETECTION AND LOCATION OF HOLES IN A DUCT WALL

A. Reconstruction of the effective expansion function to reveal hole location

Once the measurement of the transfer function in the duct had been completed, the expression in Eq. (1) was used to reconstruct the effective expansion function of the duct. After this reconstruction, the effect of the hole in the duct wall was immediately noticeable and its position could be determined. The effective expansion function of the duct of 50-mm radius with a hole of 5-mm radius in the wall at a position of 1.42 m from the driver end of the duct is shown in Fig. 5(a). A substantial positive dc shift above the zero plane is apparent leading up to the position of the hole. Experience has shown that a positive dc shift of this type is associated with an expansion in the duct. This correlates with earlier work[5–8] where negative dc shifts were found to occur

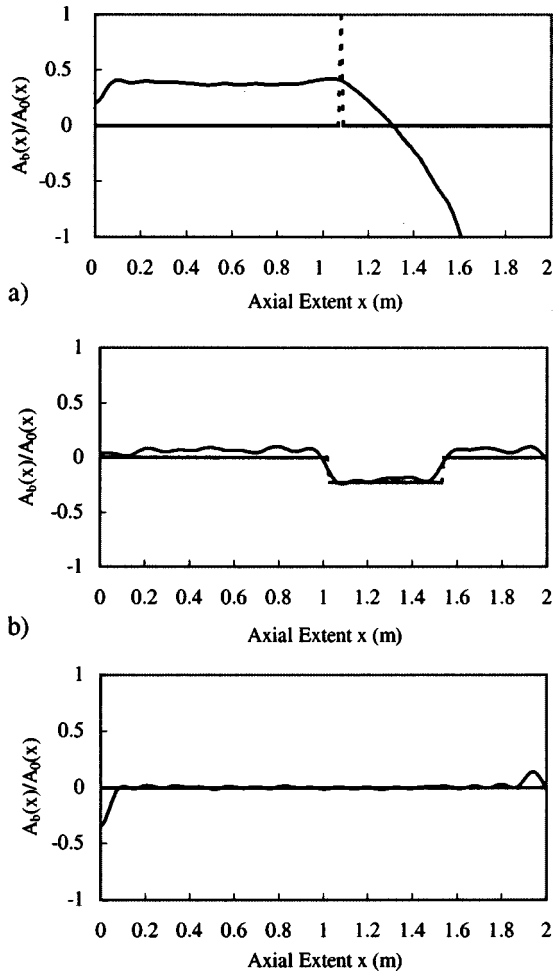

FIG. 5. Effective expansion function reconstruction from Eq. (1) of 2-m long, 0.1-m duct of circular cross section: (a) With small hole in the wall at 1.09 m from driver end. Position of hole denoted by - - -; (b) with expansion chamber. Reconstructed ———, actual - - -; (c) uniform duct with unholed wall.

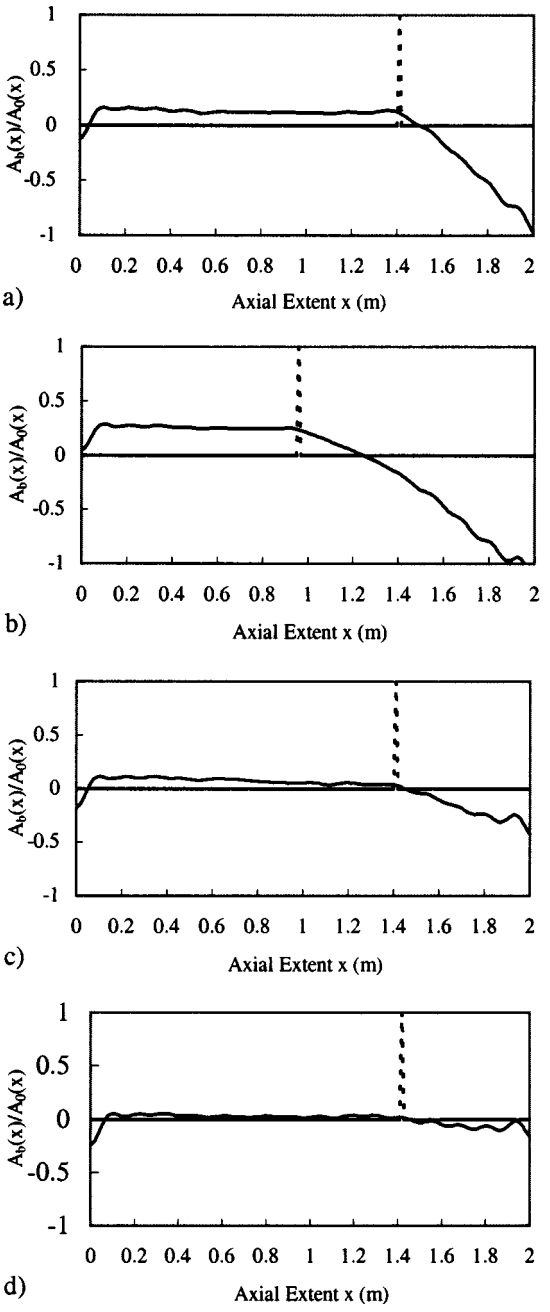

FIG. 6. Effective expansion function reconstruction from Eq. (1) of 2-m long; 0.1-m duct of circular cross section shown in Fig. 2 with various hole configurations: (a) 5-mm radius side hole at 1.42 m from driver end; (b) 4.5-mm radius side hole at 0.965 m from driver end; (c) 2.75-mm radius side hole at 1.42 m from driver end; (d) 0.75-mm radius side hole at 1.42 m from driver end. Position of hole denoted by - - -.

when reconstructing constricting blockage area functions in ducts. The large positive dc shift shown is thus typical of a large expansion in the duct, which is effectively how the hole is represented in the effective expansion function reconstruction. The dc correction term a_0 in Eq. (1), which was used in earlier work to correct the dc shift in blockage area function reconstructions, has not been used in the effective expansion function reconstructions in the current work, as the notion of accurately reconstructing a blockage in the duct is now defunct. At the position of the hole a sharp point of inflexion occurs and from this point the curve drops steadily, crossing the zero line and continuing into what appears to be a flaring expansion towards the end of the duct. This negative gradient is distinguished from other negative gradients in the reconstruction by its axial extent and also by its continuation below the zero expansion line of the reconstruction. Figure 5(b) shows a typical effective expansion function for an actual expansion in the duct. The position of the expansion is clearly marked in Fig. 5(b) in addition to a much smaller positive dc shift than for the example of the hole in the duct wall in Fig. 5(a). Figure 5(c) shows the reconstruction for the case of the unperforated duct. A small deviation is noted at the ends, but this can be easily differentiated from the hole in Fig. 5(a), or the expansion in Fig. 5(b).

Further reconstructions of effective expansion function of the duct with wall holes of circular and other geometry of varying size and location are shown in Fig. 6. The effect of the hole becomes less noticeable as it becomes smaller, although using the computational routine described in the following section it was still possible to accurately detect and locate the smallest hole used in the tests, which was of 0.75-mm radius at 1.415 m from the driver. The reconstruc-

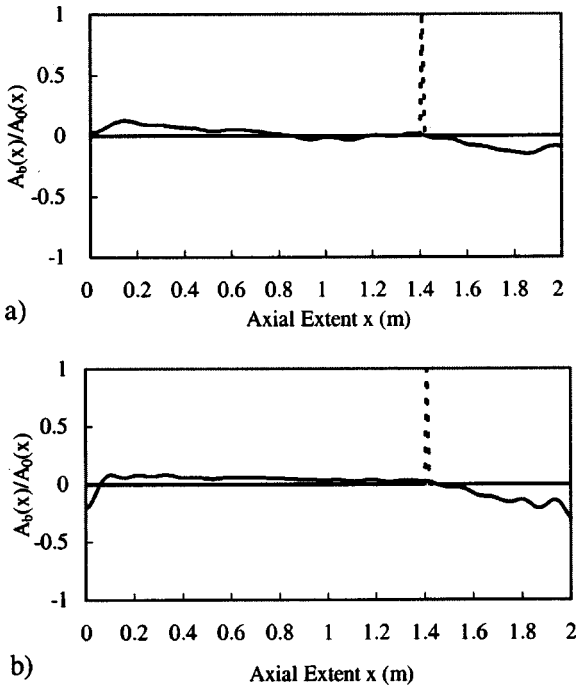

FIG. 7. Effective expansion function reconstruction from Eq. (1) of 2-m long; 0.1-m diameter duct of circular cross section with 1.75-mm radius hole at 1.42 m from driver end: (a) Determined from unfiltered transfer function; (b) determined from filtered transfer function. Position of hole denoted by - - -.

tion of the effective expansion function of the holed duct in this case is shown in Fig. 6(d). The effect of the hole is still noticeable but more difficult to determine by eye.

1. Filtration effects

As previously mentioned, the transfer functions used were generally filtered to smooth out localized distortions before use in the hole location process. The effect of filtration on a transfer function is shown by comparison of Figs. 4(a) and (b). While smoothing filtration was not always required for accurate positioning of the hole, the effects of distortion were sometimes quite substantial. A good example of the effect of smoothing filtration where it was of vital importance to the reconstruction and hole location process is shown in Fig. 7. Figure 7(a) shows the reconstruction of a fairly small hole without application of smoothing filtration, and Fig. 7(b) shows reconstruction from the filtered transfer function. The improvement appears to be relatively minor, but is sufficient to enable computational determination of the hole position as described in the following section. The effect on the accuracy of hole location and sizing due to the rounding of the transfer functions after filtration has not been quantified in this work. However, previous experience involving the reconstruction of blockages has shown negligible loss in accuracy when comparing blockage reconstructions from filtered transfer functions with those reconstructed from transfer functions not requiring filtration.[5–7]

B. Computational determination of hole location

With the exception of very small holes, in the majority of the previous effective expansion function figures the approximate location of the hole is readily apparent to the eye. However, using a computational routine to automate the process of location may often be of benefit in terms of time and accuracy. Where a computational routine is used, the typical characteristics of the effective expansion function can be used as a recognition tool. The routine picks out the negative gradient occurring over a relatively large spatial window and recognizes that the gradient encroaches into the negative area function zone. From this, the point of inflexion defining the hole location may be traced back to the beginning of the descent using differential gradient detection routines based on regression analysis of a number of different reconstructions of holes of known position.

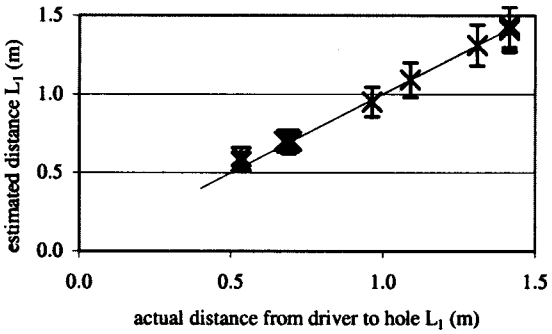

FIG. 8. Distance L_1 from driver to hole computationally determined from effective expansion function reconstructions plotted against actual distance L_1 for holes of various size and location (with 10% tolerance vertical error bars). Line of correlation ———.

A MATLAB computational routine was thus written using the above descriptors to locate the side hole from the reconstruction figures. Figure 8 shows excellent correlation between the true value of longitudinal distance of the side hole from the driver and the computationally determined value derived from the reconstruction of the effective expansion function.

V. SIZING OF CIRCULAR HOLES IN A DUCT WALL

The sizing of cylindrical holes in the duct wall was undertaken using the technique set out in Sec. II B employing the measured wave number values both at resonance k_n and at antiresonance $k_{(a)n}$ determined from the duct transfer function and the values L_1 and L_2 relating to the hole position in Fig. 1. L_1 and L_2 were computationally determined from reconstructions of effective expansion functions similar to those shown in Figs. 6 and 7. The hole-sizing technique proved to be insensitive to the minor errors associated with the indirect computational determination of L_1 and L_2, which are highlighted in Fig. 8. Estimations of hole radii employing the computationally determined values of L_1 and L_2 were as accurate in all cases as the estimations employing the actual geometrically measured values of L_1 and L_2. The entire process including measurement and computation took under 10 s to determine the location and radius of the hole in the duct wall using a typical midrange PC.

Figure 9 shows the estimation of radius r_h for holes at 1.42 m from the driver end using the above approach. These estimated values are plotted against the actual values of the hole radius. Figure 9(a) shows estimations using Eq. (9) in

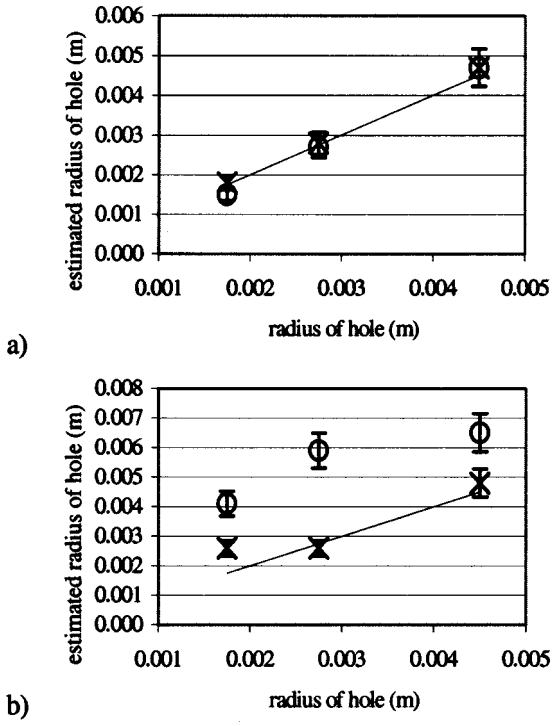

FIG. 9. Acoustically determined values of r_h for circular holes of various sizes and locations plotted against actual r_h values (with 10% vertical error bars): (a) r_h determined using effective expansion function reconstruction and measured resonance wave numbers; k_1 (×), k_2 (○). (b) r_h determined using effective expansion function reconstruction and antiresonance wave numbers; $k_{(a)1}$ (×), $k_{(a)2}$ (○).

the approach in Sec. II B for each of the first two orders of resonance wave number k_n determined from measurements in the holed duct. Figure 9(b) shows estimations using Eq. (10) with the first two orders of wave number at antiresonance $k_{(a)n}$. Estimations in Fig. 9(a) are highly accurate, all within 10% of the actual hole size. Estimations in Fig. 9(b) show wide variation, although the first-order evaluations are generally more stable. Estimations using higher orders of resonance and antiresonance frequencies became highly aberrant in all cases.

The wave numbers at first-order resonance were generally found to be the most accurate for use in the hole-sizing process, and this is supported by Fig. 9(a). This correlates with the discussion in Sharp and Campbell[3] which notes problems with hole sizing when the hole is located close to a pressure node. The first mode is the only mode which guarantees that a small hole cannot be located close to a pressure node, and thus use of the first mode may perhaps be expected to give the greatest accuracy. All subsequent hole-sizing estimations presented in the current paper are calculated using measured values of k_1. Figure 10 shows good correlation between values of r_h estimated in this manner and the corresponding geometrical measurements for a number of different-sized circular holes positioned at 1.42 m from the driver end of the duct.

As noted previously, an orifice in a duct wall is well known as a high-pass filter for waves propagating in a duct,[9] and therefore its introduction may be expected to have more effect on the lower-frequency resonances and antiresonances

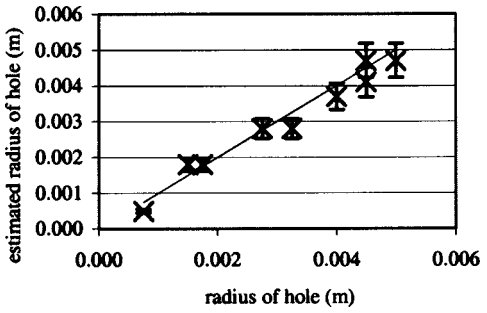

FIG. 10. Acoustically determined values of r_h for circular holes of various sizes and locations plotted against actual r_h values (with 10% vertical error bars). Values of r_h determined using bore profile reconstruction and first resonance wave number k_1.

of the duct. This theory is supported by Fig. 4, which shows the large shifts from the resonance and antiresonance frequencies of the duct with unperforated walls occurring for the first few orders. The margin for error in calculating the hole sizes resulting from limits of frequency resolution would thus be expected to be at their least for these lower orders of resonance, and this is supported by the experimental results.

VI. DETECTION, LOCATION, AND SIZING OF RECTANGULAR AND SLIT-SHAPED HOLES IN A DUCT WALL

Holes in duct walls resulting from mechanical damage or material stress are unlikely to be circular in nature and may often occur as thin cracks. As such, it is pertinent to see how well the hole-sizing technique may be applied to rectangular slits of varying aspect ratio, i.e., the ratio of cross-sectional length to width. An equivalent area method was therefore used as set out in Sec. II B 4 to compute the geometrical equivalent radius of a rectangular slit cut into the wall of the duct after the slit has been located as described previously. The current technique was applied to circumferential slits only. Slits in the axial direction were not considered in the analysis.

Figure 11 shows the reconstruction of the effective expansion function for a typical thin slit in the duct located by the process. Figures 12–14 show the equivalent radial estimations r_{he} for various slits using the acoustic analysis of Sec. II B and the distance from driver to hole L_1 computa-

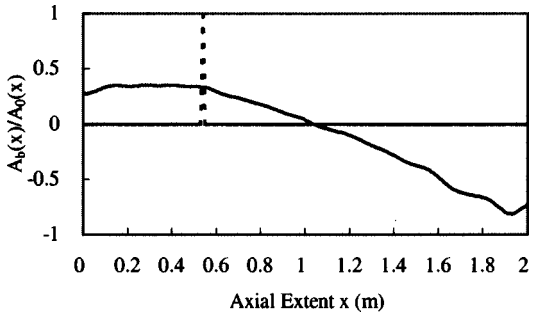

FIG. 11. Effective expansion function reconstruction of 2-m long, 0.1-m diameter duct of circular cross section with rectangular slit of 12 mm length and 2.5 mm width in the wall at 0.54 m from driver. Position of hole denoted by - - -.

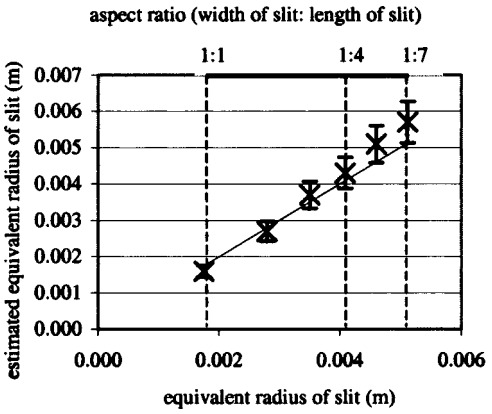

FIG. 12. Acoustically determined values of geometric equivalent radius r_{he} for slit-shaped holes of 3.5-mm width and varying aspect ratio as a function of actual r_{he} value (with 10% vertical error bars). Slits positioned at 0.675 m from driver. Values of r_{he} determined using bore profile reconstruction and first resonance wave number k_1.

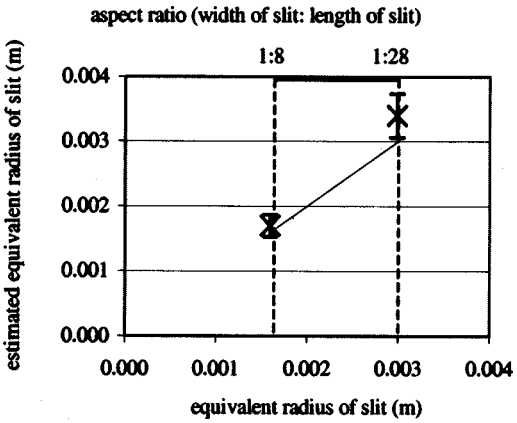

FIG. 14. Acoustically determined values of geometric equivalent radius r_{he} for slit-shaped holes of 1-mm width and varying aspect ratio as a function of actual r_{he} value (with 10% vertical error bars). Slits positioned at 0.454 m from driver. Values of r_{he} determined using effective expansion function reconstruction and first resonance wave number k_1.

tionally determined from the associated effective expansion function reconstructions similar to those of Fig. 11. These are plotted against the actual geometrical equivalent radii of the slits calculated from the cross-sectional areas.

The agreement between the actual and estimated values of r_{he} was shown to be generally within 10% for the slits, with larger errors generally occurring when sizing slits of larger aspect ratio. Figure 14 shows that for the thinnest slits of 1 mm breadth, estimations of geometrical equivalent radius are within 15% of the actual value for slits of up to 28 mm length corresponding to an aspect ratio of 28:1. Thus, for this degree of accuracy and in this limited case it may be argued that the equivalent radius approach has proven to be valid for slits of much larger aspect ratio than the limiting figure of 8:1 noted previously in the transmission loss work of Sauter and Soroka[11] and as predicted in the theoretical discussion of Sec. II B 4.

While the results in Figs. 12–14 show good engineering accuracy, it is noted that overestimation of r_{he} occurs where slits of large aspect ratio are sized. This overestimation may be attributed to the second term in Eq. (20), which will accurately estimate the end correction for a circular aperture but overestimates end correction for a slit. As the slit gets thinner and longer the end correction becomes dominated by the shorter dimension and thus the end correction is shorter than the geometric equivalent radius would suggest. An equivalent loss expression used for equivalent mean radius of a rectangular flow duct[10] may be applied to the second term of Eq. (20) instead of r_{he} to account for this. The equivalent mean radius term is simply the area of the slit divided by its perimeter. With manipulation, this equivalent mean radius may alternatively be expressed as a function of the aspect ratio of the longer to shorter cross dimension of the slit R and the geometric equivalent radius from Eq. (21). The resulting expression can now be used to replace the second term on the left-hand side of Eq. (20). Combining this approach with a regression analysis from the experimental results generates a more accurate expression to evaluate the geometric equivalent radius r_{he} from the hole impedance Z_h, where

$$\frac{\pi}{\rho c k}\mathrm{Im}(Z_h)r_{he}^2-\left(\frac{2\sqrt{\pi R}}{1+R}\right)r_{he}-L_h=0, \tag{24}$$

where R is the aspect ratio of the longer to shorter cross-sectional dimension of the slit.

Figure 15 shows the estimated results for r_{he} for the same test-hole configurations as in Fig. 14, this time using Eq. (24) and known values of R. The correlation with the geometrical equivalent radii evaluated using Eq. (24) is much stronger than that of Fig. 14 and is accurate for larger aspect ratios. Generally, of course, the aspect ratio of the slit R will be an unknown quantity and therefore it is difficult to see how Eq. (24) could be used in the reciprocal sizing approach. However, Fig. 14 shows that Eq. (20) can still give a good degree of accuracy for slits of fairly large aspect ratio. The accuracy of the simplified approach using Eq. (20) will increase as the hole area and duct wall thickness decrease, i.e., as the significance of the end correction term decreases.

The extended length of the slit may raise concerns as the ratio of slit length to duct curvature becomes larger.[3] However, this does not appear to be a problem in any of the test cases as the dimension governing end reflection of the slit

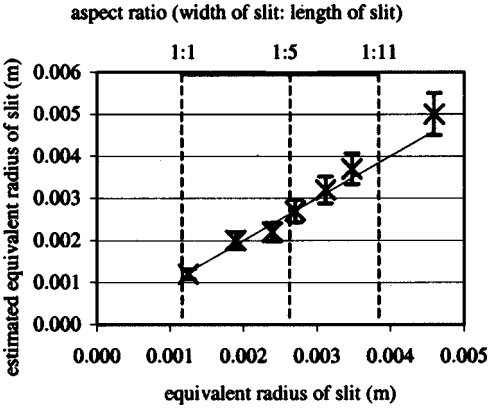

FIG. 13. Acoustically determined values of geometric equivalent radius r_{he} for slit-shaped holes of 2.5-mm width and varying aspect ratio as a function of actual r_{he} value. Slits positioned at 0.535 m from driver (with 10% vertical error bars). Values of r_{he} determined using effective expansion function reconstruction and first resonance wave number k_1.

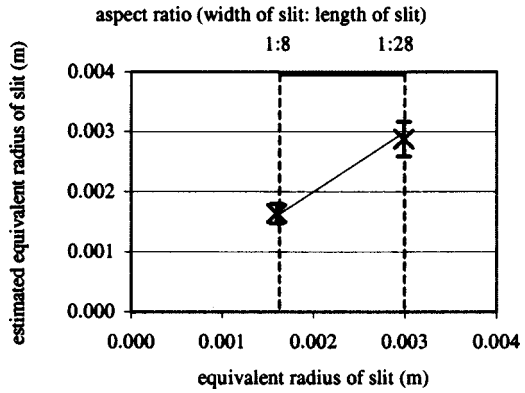

FIG. 15. Acoustically determined values of geometric equivalent radius r_{he} from Eq. (24) for slit-shaped holes of 1 mm width and varying aspect ratio as a function of actual r_{he} value. Slits positioned at 0.454 m from driver (with 10% vertical error bars). Values of r_{he} determined using first resonance wave number k_1.

tends to default to the width of the slit as the slit gets longer and thinner. Thus, where the width of the slit remains small in comparison to the radius of the main duct, the effect of duct curvature remains negligible.

Equation (24) may be rearranged to give a simple expression for the imaginary impedance $\mathrm{Im}(Z_s)$ of a slit in a duct wall

$$\mathrm{Im}(Z_s)=\frac{\rho ck}{\pi r_{he}^2}\left[\left(\frac{2\sqrt{\pi R}}{1+R}\right)r_{he}+L_h\right]=\frac{\rho ck}{ab}\left[\frac{2ab}{(a+b)}+L_h\right], \tag{25}$$

where a and b are the cross-sectional dimensions of the slit.

Equation (25) adequately describes the imaginary impedance of slits used in the current investigation where the dimensions of the slit are small in relation to acoustic wavelength. However, a more rigorous investigation of the limiting conditions under which this expression is valid is beyond the scope of the current work.

VII. CONCLUSIONS

A technique has been developed for the detection, location, and sizing of small apertures in a duct wall using the resonance and antiresonance frequencies of the duct determined from a single transfer function measurement. The process is made possible by the high noise immunity of the maximum length sequence used to excite the duct which allows the accurate determination of the duct antiresonance frequencies in addition to the determination of the duct resonance frequencies. The technique reconstructs a spatial function termed the effective expansion function of the duct from which the position of the hole may be ascertained by eye or detected automatically using a simple computational routine. Following the location of a hole, it may be sized using an impedance model of the duct. The impedance model incorporates the computed length of the duct, the location of hole in the wall, and the measured resonance and antiresonance wave numbers utilizing assumptions about the radius-dependent impedance characteristics of the side hole and the impedance condition at the duct driver at these frequencies. The location of the hole using this method is shown to be highly accurate and subsequent sizing of the hole is found to be most accurate using the measured first-order resonance wave number of the duct, which returns radial estimations to within 10% of the actual radius of circular holes. The technique is shown to be rapid to apply and robust mainly due to the noise immunity of the excitation system but also to the smoothing filtration routines which are applied to the transfer functions to avoid resonance and antiresonance selection errors occurring as a result of localized distortion. The detection, location, and sizing technique has also been successfully applied to slit-shaped holes where the sizing process approximates the slit as a circular hole of equal area and therefore yields an equivalent radius. Equivalent radius estimations using the technique described above and the impedance model for a circular side hole are found to be highly accurate for slits with aspect ratios of up to 28:1. The equivalent area method is therefore shown to be applicable to slits of larger aspect ratio than may be expected from earlier work using equivalent areas for modeling of transmission loss characteristics of slit-shaped holes in plane walls.[11]

ACKNOWLEDGMENTS

The authors would like to thank the Engineering and Physical Sciences Research Council of the United Kingdom for their support of this work.

[1] J. M. Muggleton, M. J. Brennan, and R. J. Pinnington, "Wavenumber prediction of waves in buried plastic pipes for water leak detection," Seventh International Congress on Sound and Vibration, Garmisch-Partenkirchen, Germany, pp. 985–992 (2000).
[2] D. B. Sharp, A. Myers, R. Parks, and D. M. Campbell, "Bore reconstruction by pulse reflectometry and its potential for the taxonomy of brass instruments," Proceedings of the 15th International Congress on Acoustics, Trondheim, Norway, pp. 481–484 (1995).
[3] D. B. Sharp and D. M. Campbell, "Leak detection in pipes using acoustic pulse reflectometry," Acustica **83**(3), 560–566 (1997).
[4] D. B. Sharp, "Increasing the length of tubular objects that can be measured using acoustic pulse reflectometry," Meas. Sci. Technol. **9**(9), 1469–1479 (1998).
[5] M. H. F. de Salis and D. J. Oldham, "The development of a rapid single spectrum method for determining the blockage characteristics of a finite length duct," J. Sound Vib. **243**(4), 625–640 (2001).
[6] M. H. F. de Salis and D. J. Oldham, "Determination of the blockage area function of a finite duct from a single pressure response measurement," J. Sound Vib. **221**(1), 180–186 (1999).
[7] M. H. F. de Salis and D. J. Oldham, "A rapid technique to determine the internal area function of finite-length ducts using maximum length sequence analysis," J. Acoust. Soc. Am. **108**, 44–52 (2000).
[8] Q. Wu and F. Fricke, "Determination of blocking locations and cross-sectional area in a duct by eigenfrequency shifts," J. Acoust. Soc. Am. **87**, 67–75 (1990).
[9] L. E. Kinsler, A. R. Frey, A. B. Coppens, and J. V. Sanders, *Fundamentals of Acoustics*, 3rd ed. (Wiley, New York, 1982).
[10] *CIBS Guide, C4: Flow of Fluids in Ducts and Pipes* (Chartered Institute of Building Services Engineers, London, 1977).
[11] A. Sauter and W. W. Soroka, "Sound transmission of rectangular slots of finite depth between reverberant rooms," J. Acoust. Soc. Am. **47**, 5–11 (1970).
[12] I. Campbell and G. Ese, "Use of maximum length sequences (MLS) as a measurement tool for architectural acoustics," J. Build. Acoust. **4**(4), 295–301 (1997).

Implosion of an underwater spark-generated bubble and acoustic energy evaluation using the Rayleigh model

Silvano Buogo and Giovanni B. Cannelli
Consiglio Nazionale delle Ricerche, Istituto di Acustica "O. M. Corbino," Via Fosso del Cavaliere 100, 00133 Roma, Italy

(Received 20 May 2001; accepted for publication 5 March 2002)

The growth, collapse, and rebound of a vapor bubble generated by an underwater spark is studied by means of high-speed cinematography, simultaneously acquiring the emitted acoustic signature. Video recordings show that the growth and collapse phases are nearly symmetrical during the first two or three cycles, the bubble shape being approximately spherical. After 2–3 cycles the bubble behavior changes from a collapsing/rebounding regime with sound-emitting implosions to a pulsating regime with no implosions. The motion of the bubble wall during the first collapses was found to be consistent with the Rayleigh model of a cavity in an incompressible liquid, with the inclusion of a vapor pressure term at constant temperature within each bubble cycle. An estimate of the pressure inside the bubble is obtained measuring the collapse time and maximum radius, and the amount of energy converted into acoustical energy upon each implosion is deduced. The resulting value of acoustic efficiency was found to be in agreement with measurements based on the emitted acoustic pulse. [DOI: 10.1121/1.1476919]

PACS numbers: 43.25.Yw, 43.30.Lz, 47.55.Dz [MAB]

I. INTRODUCTION

The generation of intense sound waves in water is almost invariably associated with the generation of bubbles. Cavitation can be induced by tensile forces due to the negative peak of an applied ultrasound wave, or by thermal and chemical processes that cause a violent expansion of the liquid, as it is in the case of explosions and electric sparks.[1] A considerable amount of acoustic and optical data on underwater explosions in marine environment is available back from the years 1940–1950, when explosives were widely used as pulsed sound sources for military purposes.[2] On the other hand, fewer studies were dedicated to sound generated by high-power sparkers, being mainly devoted to the analysis and prediction of pressure-time curves,[3] and more recently to the understanding of breakdown phenomena in water.[4] The interest in these sources has reduced since the 70's, when other devices, such as the airgun, were preferred due to their higher repeatability, despite a longer pulse duration.[5] The direct observation of cavitation bubbles in high-power sparkers has generally been avoided, since it would require optical measurements of great accuracy which are difficult to obtain in sea experiments even at moderate depths, while the operation of traditional marine sparkers in a laboratory tank is often impractical.

Pulsed sound emitted by underwater sparks is similar in principle to that emitted by explosions, although some differences exist. Underwater explosions cause the formation of gas globes, which may evolve in a series of up to ten contractions and expansions in form of damped spherical oscillations. Pressure peaks appearing at the end of each contraction are both weaker in amplitude and longer in duration compared with the first pulse.[6] On the other hand, sea experiments showed that spark-generated bubbles are relatively short-lived, and that pressure pulses due to cavitation are often comparable with the primary pulse that occurs when the bubble is created by spark breakdown in the liquid.[7] This suggests that the bubble wall velocity at the end of the collapse phase may reach very high values due to a large pressure difference between the surrounding liquid and the bubble interior. The sudden reversal of liquid motion taking place at the end of the bubble collapse was found to be responsible for efficient sound generation when the spark is generated near a rigid surface. Numerical methods showed that a rigid boundary severely distorts the bubble shape during its collapse.[8] These studies led to the conclusion that the understanding of cavitation mechanisms is essential for the characterization of a family of sound sources, named paraboloidal sparkers, in which the spark is generated at the focal point of a rigid paraboloidal reflector with focal distance in the range 1–10 cm. These sound sources convert electrostatic energy of up to 1 kJ into acoustic energy focused along a main axis, yielding pressure pulses with energy density near 10 J/m^2, equivalent to a source level near 230 dB *re*: 1 μPa, with signal bandwidth over 300 kHz.[9] In such conditions the cavitation pulse is very similar to the primary pulse due to spark breakdown,[10] or even more powerful than the primary pulse.[11]

In the present work, an experiment is described that allowed a direct visualization of bubbles generated by underwater sparks in the kJ energy range. Video recordings, integrated with acoustic data, provided a way to confirm the validity of the Rayleigh model, that has been proposed for the bubble growth and collapse.[12] The acoustic efficiency of the sparker was evaluated by direct observation of maximum bubble radius and estimating the internal pressure by analyzing experimental radius/time plots, to give more accurate results than if purely acoustic data were considered.

 0001-4966/2002/111(6)/2594/7/$19.00

II. EXPERIMENT

The aim of the experiment was to visualize the evolution of the vapor bubble generated by the sparker, simultaneously acquiring the emitted acoustic wave. This was done in a laboratory tank 6 m long, 4 m wide, and 5.5 m deep, filled with fresh water. The water temperature was 20 °C, and its electrical conductivity was $0.06\,\Omega^{-1}\,\mathrm{m}^{-1}$. The sparker source used in the experiments is a suitably modified prototype that was first designed and patented for high-resolution acoustic imaging in marine environment.[13] It consists of two opposed tungsten electrodes with hemispherical tips, with a diameter of 10 mm and gap distance of 2 mm. The electrodes are located at the focal point of a paraboloidal reflector with 20-cm diameter and 10-cm focal length. The purpose of the reflector is to focus along its main axis a portion of the acoustic energy of the spark. In this configuration, the paraboloid was seen to be capable of doubling the acoustic intensity along its main axis, compared with an omnidirectional sparker source.[9] The sparker is connected to a capacitor bank with total capacitance 360 μF that can be charged up to a voltage of 2.35 kV, giving a maximum electrostatic energy of 1 kJ. Although the electrode size and shape was optimized for operation in seawater, whose electrical conductivity is higher by two orders of magnitude than that of fresh water, the acoustic signature of the sparker proved to be repeatable also in fresh water, provided that the electrode gap did not exceed 3 mm. For a 2-mm gap, the electrostatic energy threshold for a repeatable spark was found to be approximately 400 J.

The acoustic wave generated by the sparker is measured at a distance of 1.5 m along the main paraboloidal axis by a Reson TC4034 hydrophone with nominal bandwidth 350 kHz and receive sensitivity -216.5 dB *re*: 1 V/μPa. The hydrophone signal is filtered between 500 Hz and 500 kHz and acquired using a 12-bit PC-hosted A/D board with sampling rate of 1 Msample/s, with a typical record length of 24 ms.

A glass window on one of the tank walls, at a depth of 2.5 m, allowed a fast camera to be placed approximately 1 m away from the underwater source. Continuous backlighting was used by placing the light source directly above the water surface and using a 45-deg mirror positioned along the camera optical axis (see Fig. 1). The high-speed camera, a Photec 16-mm full-frame rotating prism unit, used 100-ft. acetate-based films that allowed the selection of a maximum film speed of 7000 frames/s. The actual film speed was somewhat lower due to film acceleration at startup, and was measured to be (6500 ± 100) frames/s using timing marks provided by the camera. The resulting frame period was 154 μs, with an exposure time of 60 μs. The camera sends a trigger pulse to both the firing circuit of the sparker and the hydrophone signal acquisition, thus synchronizing optical and acoustical measurements. After film processing, up to 140 frames were digitized for a total time of about 20 ms, including a few ms before the spark and the complete evolution of the vapor bubble. Each frame was processed to enhance brightness and contrast, and finally converted to a gray-scale image with a 0.3-mm resolution.

The bubble proved to be slightly compressed along the x direction coaxial with the electrodes, due to the interference of the electrodes with the liquid motion. To evaluate the effective radius, the bubble shape was assumed to be that of an ellipsoid having axial symmetry along x, with diameters H and W, respectively, as shown in Fig. 2. The work done in displacing the liquid to create a bubble is proportional to the bubble volume; thus, the reported value of an equivalent spherical bubble radius was obtained by measuring H and W and calculating the radius of a sphere of equal volume, given by $R = \frac{1}{2}(W \cdot H^2)^{1/3}$.

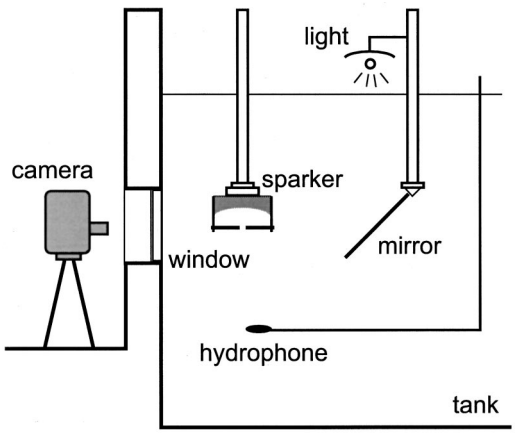

FIG. 1. Tank experiment setup. The sparker source is mounted with the paraboloidal axis pointing downwards. The hydrophone is located on-axis, 1.5 m below the source. The fast camera is operated through a viewport in the tank wall, and backlighting is provided using floodlights near the surface and a 45° mirror placed along the optical axis. The source–camera distance is 1 m, and the source depth is 2.5 m.

III. RESULTS

A. Optical data

Figure 3 shows a sample of a film taken during a 720-J spark, with one of every 5 frames presented. The complete sequence of frames is available online at http://www.idac.rm.cnr.it/ual/. Each frame is labeled with the elapsed time after spark breakdown, the first of the series

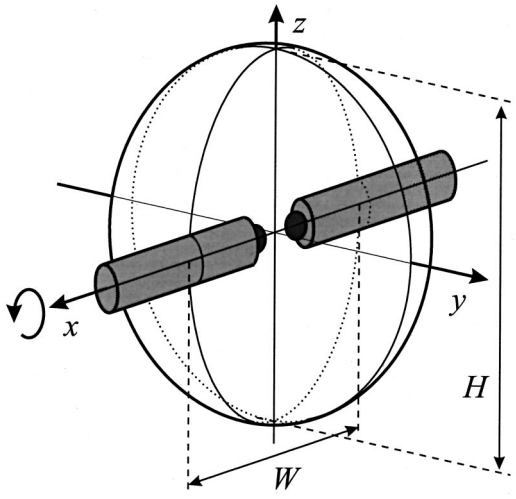

FIG. 2. Bubble geometry used to determine the effective bubble radius for a nonspherical shape. W is the dimension along x, and H is the dimension along both Y and Z.

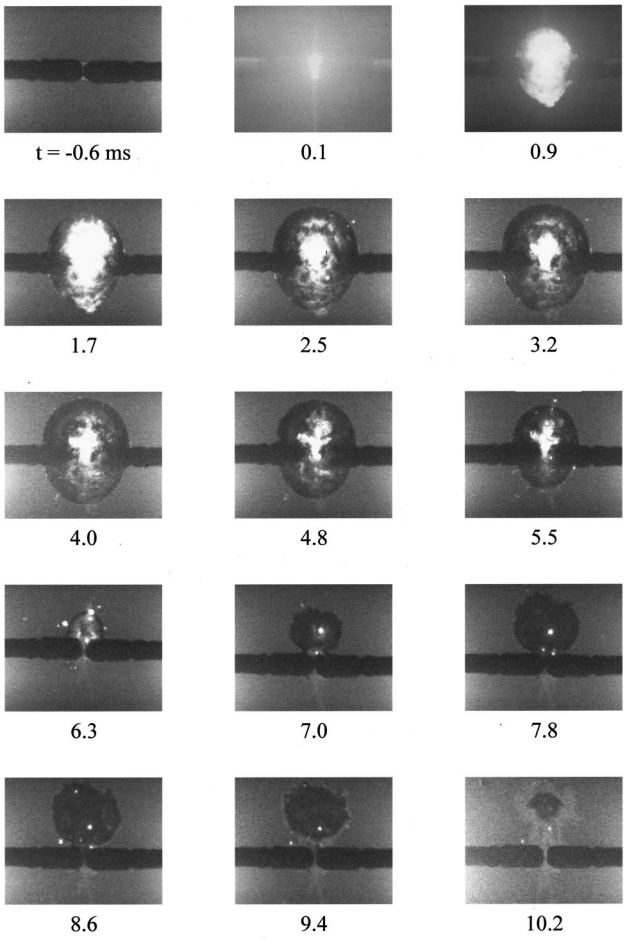

FIG. 3. Selected frames showing bubble growth and collapse for a 720-J spark. Each frame is labeled with the time elapsed since (or before, if negative) spark breakdown. The frame period is 154 μs.

being taken before breakdown. In the pre-breakdown phase, after the electric field is applied, the liquid in the electrode gap starts to appear brighter near the electrode surface. About 3–4 ms before breakdown, a darker region develops near one of the electrodes moving towards the other electrode. When this dark region bridges the gap, breakdown occurs and a bright flash is emitted. The breakdown process is much faster than the frame period, so that the very next frame

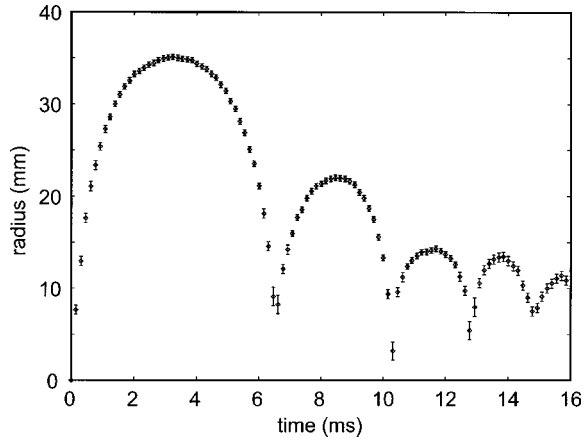

FIG. 4. Plot of bubble radius versus time, measured from the complete sequence of frames sampled in Fig. 3.

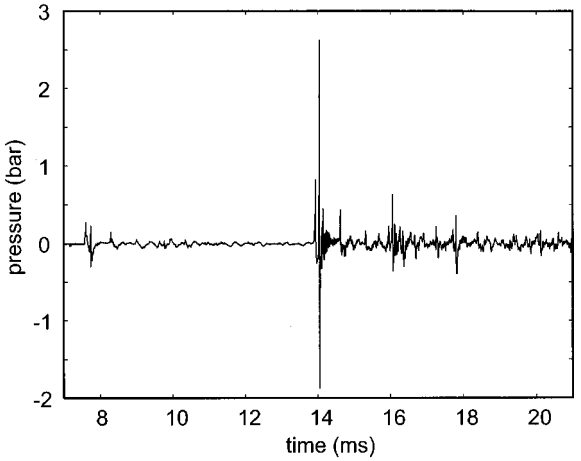

FIG. 5. Acoustic signature of the paraboloidal sparker, recorded during the bubble evolution shown in Fig. 3. The voltage is applied at zero time, the primary pulse appears at 7.7 ms, and the first bubble pulse at 14 ms.

shows a plasma bubble already several mm in radius. The average bubble wall velocity up to this point, obtained by dividing this bubble radius by the frame period, is around 60 m/s, the initial value probably being much higher. The bubble contents show some luminescence that keeps fading away for approximately 1–2 ms, starting from the outer shell towards the center.

Figure 4 shows the time plot of the effective bubble radius, measured as explained in Sec. II. The bubble period is 6.3 ms in the first cycle, 3.8 ms in the second, and decreases to about 2 ms in the third and following rebounds. An implosion takes place at the end of the first three cycles, as the lower half of the bubble wall starts to bend inwards, forming a tip that reduces the bubble to a negligible size, and eventually impacts on the upper gas/liquid interface. The final tip velocity for the first implosion, measured between two successive frames, is of the order of 150 m/s. As the bubble rebounds, its center is displaced in the same direction of the tip by about 2 cm, and grows mostly in that direction. After the third cycle, the bubble collapses down to a size which is no longer negligible, entering into a pulsating regime with an oscillating mean radius. The tip is less pronounced in this phase and does not reach the opposite interface, so that an acoustic pulse is not generated even if the bubble still deviates from spherical symmetry.

Bubble jetting, buoyancy, and the rigid paraboloidal surface tend to displace the bubble upwards. Each time the bubble rebounds after an implosion with jetting, its growth is more pronounced towards the direction of the tip. Buoyancy and the rigid surface do not seem to affect perceptibly the dynamics of the bubble in its early stages, when the bubble shape remains approximately spherical except for the interference due to the electrodes. When the transition to the pulsating regime takes place, the bubble has reduced its distance from the paraboloidal surface from 10 cm to 6–7 cm, and the bubble is increasedly attracted towards the surface.

B. Acoustic data

Figure 5 shows the acoustic signature of the spark detected by the hydrophone in the same experiment represented

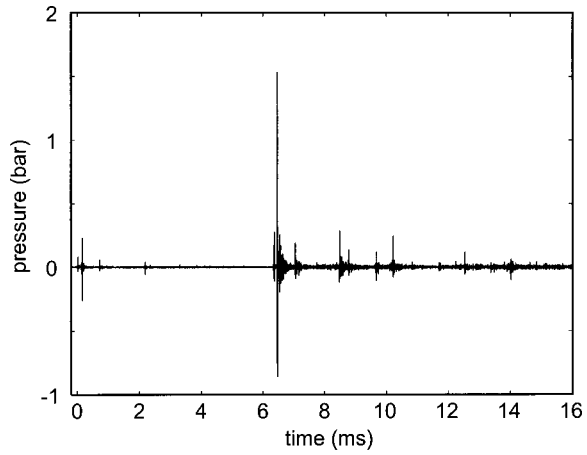

FIG. 6. Acoustic signature of the paraboloidal sparker, same as Fig. 5 after bandpass filtering from 50 to 450 kHz. Zero time is set to breakdown time, to allow a direct comparison with Fig. 4.

in Figs. 3 and 4. Water breakdown takes place 7.6 ms after the voltage is applied to the electrodes. A relatively weak primary pulse due to breakdown is followed by the first bubble pulse after 6.4 ms, both being followed by several reflection pulses due to tank walls and bottom. In the first bubble pulse two peaks are visible, 130 μs apart, due to the direct wave and the wave reflected by the paraboloidal surface. The direct peak shows the typical shape of a spark-generated wave, with a sharp positive peak followed by a broader negative peak. The negative peak partly overlaps with the reflected peak, which exhibits a more complex structure caused by diffraction due to the limited aperture of the reflector.

After the first bubble pulse, the hydrophone signal is dominated by reverberation noise and the analysis of pulse shape can be only approximate. A comparison among acoustic records of sparks with different discharge energies allowed the discrimination between bubble pulses and tank reflections, the former ones being energy dependent, while the latter ones remain at a fixed position relative to the direct pulse. A total of three bubble pulses, occurring at 14, 16.8, and 20 ms, shows strongly decreasing amplitudes but equal duration.

The same signal is presented in Fig. 6 after bandpass filtering between 50 and 450 kHz, to reduce reverberation noise and to view more clearly the succession of bubble pulses. The time origin is shifted to breakdown time, and the range is the same as in Fig. 4, to allow a direct comparison. Pulses at 6.3, 10.2, and 12.6 ms are due to bubble implosion, while further pulses are due to reflections. A careful analysis reveals, for each pulse, the presence of the tank bottom echo after a delay of 2 ms.

Acoustic data also confirm that no appreciable sound is emitted during bubble growth and collapse. However, some of the low-intensity sound in the kHz range measured between the primary and the bubble pulse could be emitted by microbubbles, of the order of 1 mm or less, that are seen to be continuously produced and reabsorbed during the evolution of the main bubble.

IV. RAYLEIGH MODEL

The description of the dynamics of a vapor bubble is greatly simplified if one assumes that the bubble wall motion is slow enough so that evaporation and condensation can maintain a constant pressure inside the bubble. If this condition is satisfied, the liquid motion can be treated formally in the same manner as for an empty cavity, only subtracting the pressure inside the bubble where the saturated vapor pressure p_v inside the bubble is opposed to the hydrostatic pressure p_∞ as acting on the outside of the bubble wall. The simplest model for a vapor bubble collapsing from a maximum radius $R_{\max}$ to a negligible size is the Rayleigh model, which applies in general to the isobaric collapse of an empty spherical cavity.[14] By imposing the conservation of mass, valid for an incompressible liquid, an expression for the bubble wall velocity $\dot{R}$ during the collapse is obtained,[15] which is properly modified here also to take into account the internal vapor pressure

$$\dot{R}=-\left[\frac{2(p_\infty-p_v(T))}{3\rho}\left(\frac{R_{\max}^3}{R^3}-1\right)\right]^{1/2}, \tag{1}$$

where ρ is the liquid density and R the instantaneous bubble radius. Since the vapor pressure p_v is a function of the liquid temperature T, an explicit solution can be obtained only for an isothermal collapse. During bubble expansion, evaporation takes place in a liquid shell, in contact with higher temperature vapor inside the bubble, whose width is equal to the thermal diffusion length. Similarly, condensation takes place during bubble collapse. The latent heat of evaporation exchanged between vapor and the liquid shell causes a temperature variation in the liquid that affects the vapor temperature, and, ultimately, the vapor pressure. Such an effect is more important at higher water temperature; while near 20 °C, the temperature variation in the liquid shell due to this effect is a fraction of a °C only, causing a negligible variation in the vapor pressure.[16] Therefore, the bubble evolution can be assumed isothermal for most of its lifetime, except during the first growth, when the initial plasma may cool down adiabatically until the bubble reaches its maximum radius, after which the vapor starts to condense due to bubble contraction. To account for a decrease in vapor temperature between multiple bubble cycles it is simply assumed that the cooling of the bubble contents takes place in a stepwise manner at the end of each bubble cycle, when the vapor is almost completely condensed.

Considering the bubble collapse, the pressure difference between the undisturbed liquid and the bubble interior is readily obtained from the expression for the collapse time according to the Rayleigh model, which gives

$$p_\infty-p_v(T)=0.837\rho\frac{R_{\max}^2}{t_c^2}, \tag{2}$$

where t_c is the collapse time. For a hydrostatic pressure of 1.25 bar at a depth of 2.5 m, measured values of $R_{\max}$ and t_c yield a pressure difference of 0.94 and 1.19 bar for the first and second collapse, respectively. The resulting vapor pressure inside the bubble is 0.3 and 0.06 bar, respectively, corresponding to a vapor temperature of 69 °C and 36 °C. These

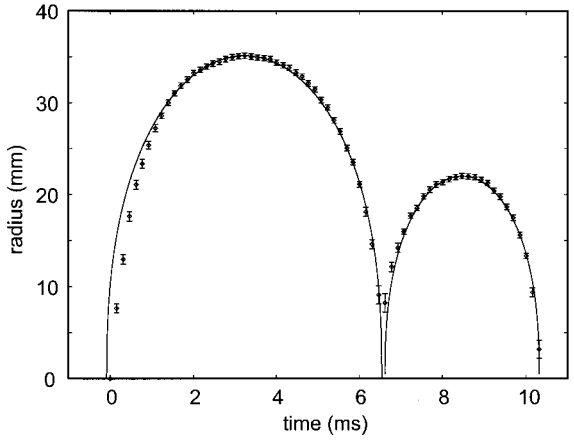

FIG. 7. Plot of bubble radius vs time during the first two cycles, experiment (dots) and Rayleigh model (line). The curve derived from the model for the collapse phase is plotted symmetrically also in the growth phase, to show the initial deviation of experimental data from the model.

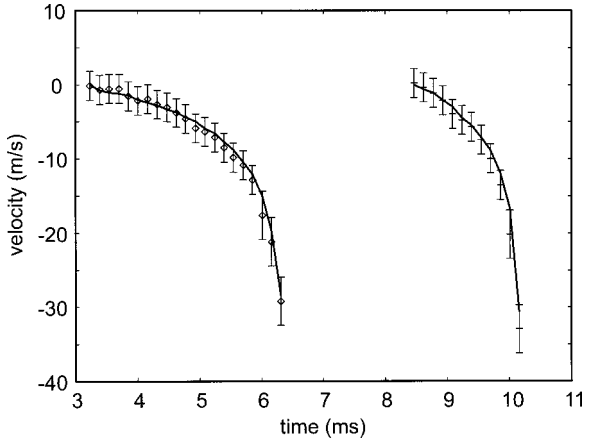

FIG. 8. Time plot of bubble wall velocity during collapse, derived from experimental data (dots) and from the Rayleigh model (line) using Eq. (1).

values are not unreasonable, and suggest that the bubble may have already cooled down almost to ambient temperature in only two cycles. After that, the vapor pressure reaches a negligible value, and the bubble oscillates like a gas-filled cavity. When this happens, the equilibrium radius is around 10 mm, less than one-third of the maximum radius. These oscillations can be considered, in principle, to be neither isobaric nor isothermal, and indeed the Rayleigh model fails to predict the correct pressure inside the bubble which turns out to be negative, clearly a meaningless result.

The Rayleigh model for the collapse has been validated calculating the radius-time plot by integrating numerically Eq. (1) with the forward scheme

$$R(t_{n+1}) = R(t_n) - \Delta t \left[\frac{2(p_\infty - p_v(T))}{3\rho} \left(\frac{R_{\max}^3}{R^3(t_n)} - 1 \right) \right]^{1/2}, \tag{3}$$

where $R(t_n) = R(n\Delta t)$ with a fixed time step $\Delta t = 5 \cdot 10^{-7}$ s and the initial condition $R(t_0) = (1 - 10^{-8}) R_{\max}$. A constant vapor pressure $p_v(T)$ is assumed, which is obtained from Eq. (2). The result is shown in Fig. 7, together with the experimental points of the first two bubble cycles. During the collapse phase, the model lies within the measurement uncertainty. The theoretical curves for the collapse are also plotted for the growth phase, symmetrically around the point of maximum radius. A deviation of real data from the Rayleigh model occurs during the growth phase at higher vapor temperature, as has been discussed above. Immediately after breakdown, the bubble grows faster than predicted by the model, indicating that the internal pressure is certainly not constant. An estimate of bubble wall velocity during the first two collapses was also obtained using, for the nth frame, finite differences between frames $n-1$ and $n+1$. Figure 8 shows that there is substantial agreement between the obtained experimental values and those predicted by Eq. (1).

V. ACOUSTIC EFFICIENCY

The acoustic efficiency η of the sparker can be defined as the ratio of the acoustic energy E_{ac} of the bubble pulse to the electrostatic energy E_{es}, which is delivered to the electrodes, assuming that the contribution of pulses due to breakdown and bubble rebounds is negligible. Typical values of η found in the literature are between 25%–30% for 75-m deep, 10- to 60-kJ sparks[7] and 5%–10% for near-surface, 1-kJ sparks.[12]

The actual value of E_{es} at the electrodes is generally lower than the energy stored in the capacitor bank. In the present case, some energy loss might come from the air sparker. The air sparker can act as a switch, in which part of the energy is used to ionize the gas in the electrode gap. Energy losses from the capacitors down to the electrodes may account for a significant part of the total energy, and values near 50% have been reported for shots in the range 100–200 J with 1.2–2.0-kV charge voltage.[17]

The emitted acoustic energy can be evaluated by integrating, both in time and space, the acoustic intensity of the wave associated with the pressure peak in the signature. As an alternative, the amount of energy converted into acoustic energy can be estimated by measuring the bubble potential energy from its maximum size. Assuming an isobaric collapse, the bubble energy E_b available for each implosion is equal to the work W done by the liquid on the bubble during its collapse, which is obtained by multiplying the pressure by the initial maximum bubble volume

$$E_b = W = \tfrac{4}{3}\pi R_{\max}^3 (p_\infty - p_v). \tag{4}$$

The difference in bubble energy between the first two cycles can be considered to be entirely converted into acoustical energy, since at that time electric phenomena have already ceased. On the other hand, the amount of gas/vapor mixture contained in the bubble is minimal, so that its thermal energy dissipated in the surrounding liquid may be neglected. The acoustic energy radiated by the first bubble implosion is therefore given by the difference in bubble energy

$$E_{\text{ac}} = E_b' - E_b'', \tag{5}$$

where the single and double primes denote values of the first and second bubble cycle, respectively. Using Eq. (4) and substituting the pressure difference from Eq. (2), one obtains

$$E_{\text{ac}} = \frac{4}{3}\pi \cdot 0.837 \rho \left(\frac{R_{\max}'^5}{t_c'^2} - \frac{R_{\max}''^5}{t_c''^2} \right). \tag{6}$$

TABLE I. Energy values characterizing the first bubble pulse obtained using Eq. (6) and measuring the pressure pulse energy density, and corresponding acoustic efficiency.

E_{es}, Electrostatic energy (J)	720
E_b', Bubble energy at first cycle (J)	16.9
E_b'', Bubble energy at second cycle (J)	5.3
$E_{ac}=E_b'-E_b''$ (J)	11.6
E, pulse energy density @1 m (J/m^2)	0.9
$4\pi\mathbf{E}$, total energy (J)	11.4
Acoustic efficiency	1.6%

Experimental data show that the result of Eq. (6) is appreciable only between the first and second cycle, for which there is a substantial agreement with values obtained by acoustic measurements. Table I lists energy values characterizing the first bubble pulse obtained using Eq. (6) and the energy density **E** calculated from hydrophone data, reduced to a distance of 1 m assuming spherical spreading. The value of **E** is obtained by integrating the spherical wave of the direct peak, which must be isolated from the rest of the signature. The total energy is finally obtained as $4\pi\mathbf{E}$.

VI. DISCUSSION

A number of approximations have been made to be able to apply a simple Rayleigh model to the bubble. Two main reasons may limit the accuracy of this model. The first concerns the rate of evaporation and condensation of vapor molecules, which might not be fast enough to keep up with the bubble volume change, so that the internal pressure does not remain constant throughout the collapse, as the model requires. The second deals with the bubble interior, which could also contain a significant portion of incondensable gas, coming from the dissociation of water due to the spark. Both these effects tend to slow down the bubble wall motion during the collapse phase. The present observations suggest that these effects are not important until the bubble has reduced to a size for which shape asymmetry appears. The bubble shape tends to be more spherical during the growth phase rather than during the collapse phase. As the bubble grows, the internal pressure is equally distributed over the surface. On the other hand, the collapse is mainly governed by the liquid inertia, and is influenced by the difference in hydrostatic pressure and the presence of rigid boundaries. Therefore, a small amount of incondensable gas might have a stabilizing effect on the bubble evolution, preventing an excessive fragmentation upon each implosion, but at the same time ensuring that the reversal of liquid motion be sufficiently sudden to produce a sharp pressure pulse.

The fact that the bubble is displaced by a jet tip upon each implosion bears some consequences in the acoustic signature of the paraboloidal sparker. If the implosion takes place away from the focal point, the emitted pressure wave cannot be efficiently focused by the paraboloidal reflector, and the far-field pressure along the axis is reduced. For this reason, in the second and following bubble pulses the peak of the reflected wave appears weaker than that of the direct wave.

The value of acoustical efficiency obtained in the present work turns out to be substantially lower than that (around 5%), obtained in previous studies with the same range of electrostatic energy.[12] This is most likely due to the fact that the present experiments were made in fresh water, while the previous ones were made using salt water with salinity equal to that of seawater. The most evident difference between the two cases is the different breakdown time, which is the time required to fully vaporize the liquid in the electrode gap. Seawater breaks down much faster, and less energy is required to initiate a spark. This can be explained considering that, due to the temperature dependency of its electrical conductivity, the liquid is thermally instable during pre-breakdown heating.[18] Since more energy is required to heat up to the vaporization of weakly conducting fresh water, compared with highly conducting seawater, this energy is subtracted from that which is made available for bubble generation after breakdown.

VII. CONCLUSIONS

The present work shows that the vapor bubble generated by an underwater spark has some unique characteristics which make it substantially different from bubbles generated by other means, such as explosives. Compared with other pulsed sound sources, sparkers have the advantage of producing bubbles which are largely made up of vapor. After a first powerful implosion, this vapor bubble evolves with few rebounds and oscillations that may introduce spurious pulses in the acoustic signature. The limited number of observed pulses seems to be associated with a fast transition of the bubble between two regimes, only one being acoustically active. Direct observations of bubble collapse time and maximum radius suggest a possible explanation of this transition in terms of the Rayleigh model for the collapse of a cavity under constant pressure. As long as the vapor remains sufficiently hot, it provides a constant pressure under which the bubble wall can accelerate during its collapse, coming to a sudden stop with a powerful implosion. The model suggests that 2–3 cycles are enough to cool the bubble contents down to ambient temperature. After the vapor pressure has become negligible, the compressibility of the residual gas inside the bubble acts as the restoring force, and this was seen to prevent the bubble from imploding.

Further work is in progress to repeat the present experiment in the laboratory tank using salt water as the liquid medium, with the same salinity as seawater. Salt water makes the spark more repetitive, and lowers the minimum required electrostatic energy, thus allowing to perform experiments with a wider range of energies.

[1] R. J. Urick, *Principles of Underwater Sound*, 3rd ed. (McGraw-Hill, New York, 1983), Chap. 4.
[2] R. H. Cole, *Underwater Explosions* (Princeton U.P., Princeton, 1948).
[3] D. D. Caulfield, "Predicting sonic pulse shapes of underwater spark discharges," Deep-Sea Res. Oceanogr. Abstr. **9**, 339–348 (1962).
[4] A. H. Olson and S. P. Sutton, "The physical mechanisms leading to electrical breakdown in underwater arc sound sources," J. Acoust. Soc. Am. **94**, 2226–2231 (1993).
[5] R. McQuillin, M. Bacon, and M. Barclay, *An Introduction to Seismic Interpretation* (Graham & Trotman, London, 1979).
[6] D. E. Weston, "Underwater explosions as acoustic sources," Proc. Phys. Soc. **76**, 233 (1960).
[7] J. A. Cook, A. M. Gleeson, R. M. Roberts, and R. L. Rogers, "A spark-

generated bubble model with semi-empirical mass transport,'' J. Acoust. Soc. Am. **101**, 1908–1920 (1997).
[8] J. R. Blake, B. B. Taib, and G. Doherty, ''Transient cavities near boundaries. I. Rigid boundary,'' J. Fluid Mech. **170**, 479–497 (1986).
[9] S. Buogo and G. B. Cannelli, ''Source level and directivity pattern of an underwater pulsed sound generator based on electrical discharge,'' Acoust. Lett. **23(3)**, 54–59 (1999).
[10] G. B. Cannelli and E. D'Ottavi, ''Tuned array of paraboloidal transducers for high resolution marine prospecting,'' in *Acoustical Imaging*, edited by H. Lee and G. Wade (Plenum, New York, 1991), Vol. 18, pp. 501–510.
[11] G. B. Cannelli, E. D'Ottavi, L. Pitolli, and G. Pontuale, ''Acoustic cavitation-based transducer for sub-sea bottom structure imaging,'' in *Acoustical Imaging*, edited by P. Tortoli and L. Masotti (Plenum, New York, 1996), Vol. 22, pp. 613–618.
[12] G. B. Cannelli, E. D'Ottavi, and A. Prosperetti, ''Bubble activity induced by high-power marine sources,'' Oceans '90, Washington, D.C., pp. 533–537 (1990).
[13] G. B. Cannelli and E. D'Ottavi, ''Echographic technique-based method and apparatus to detect structures and anomalies of the subsoil and/or sea bottom and the like,'' U.S. Patent No. 4,899,845 (1990) and European Patent No. EP 0320466 (1992).
[14] Lord Rayleigh, ''On the pressure developed in a liquid during the collapse of a spherical cavity,'' Philos. Mag. **34**, 94–98 (1917).
[15] T. G. Leighton, *The Acoustic Bubble* (Academic, London, 1994).
[16] A. Prosperetti and M. S. Plesset, ''Bubble dynamics and cavitation,'' Annu. Rev. Fluid Mech. **9**, 145–185 (1977).
[17] J. A. Cook, Report PHY 380N, University of Texas at Austin, Applied Research Laboratories, Austin, TX (1990).
[18] V. Z. Zhekul and G. B. Rakovskii, ''Theory of electrical discharge formation in a conducting liquid,'' Sov. Phys. Tech. Phys. **28**, 4–8 (1983).

Numerical analysis of dipole sound source around high speed trains

Takehisa Takaishi,[a] Akio Sagawa, Kiyoshi Nagakura, and Tatsuo Maeda
Railway Technical Research Institute, Shiga 521-0013, Japan

(Received 23 January 2002; revised 23 March 2002; accepted 23 March 2002)

As the maximum speed of high speed trains increases, the effect of aeroacoustic noise on the sound level on the ground becomes increasingly important. In this paper, the distribution of dipole sound sources at the bogie section of high speed trains is predicted numerically. The three-dimensional unsteady flow around a train is solved by the large eddy simulation technique. The time history of vortices shows that unstable shear layer separation at the leading edge of the bogie section sheds vortices periodically. These vortices travel downstream while growing to finally impinge upon the trailing edge of the section. The wavelength of sound produced by these vortices is large compared to the representative length of the bogie section, so that the source region can be regarded as acoustically compact. Thus a compact Green's function adapted to the shape can be used to determine the sound. By coupling the instantaneous flow properties with the compact Green's function, the distribution of dipole sources is obtained. The results reveal a strong dipole source at the trailing edge of the bogie section where the shape changes greatly and the variation of flow with time is also great. On the other hand, the bottom of the bogie section where the shape does not change, or the leading edge and boundary layer where the variation of flow with time is small, cannot generate a strong dipole source. © *2002 Acoustical Society of America.*
[DOI: 10.1121/1.1480833]

PACS numbers: 43.28.Ra, 43.50.Nm, 43.50.Lj [MSH]

I. INTRODUCTION

In 1964 high speed trains called ''Shinkansen'' started commercial service in Japan with a maximum speed of 210 km/h (131 miles/h). Since then Japan Railway companies (formerly Japanese National Railways) have progressively raised the speed of Shinkansen trains. The environmental quality standards established by the Japanese government require that the peak noise level must not exceed 75 dB(A). Because rolling noise was dominant in the early days, wheels and rails have been profiled periodically. Then spark noise, generated by the contact breaks between overhead line equipment and pantograph, became dominant. This noise was reduced when all pantographs were connected electrically to avoid contact loss. The introduction of these measures permitted the maximum speed of Shinkansen to be increased to 270 km/h. Then, however, aeroacoustic noise from upper parts of the train became dominant. The largest sound source was the aeroacoustic noise from pantographs. This was reduced by installing large pantograph covers and specially designed low-noise pantographs.[1] Now that the noise from all there sources has been reduced, aeroacoustic noise from lower parts of the train have become an important problem. Since the dominant frequency of aeroacoustic noise is far lower than that of other sources, such as rolling noise, it cannot totally be reduced by noise barriers. Therefore, the reduction of aeroacoustic noise is one of the key requirements for further increases in train speed.

In order to reduce aeroacoustic noise several kinds of wind tunnel tests have been performed at the Maibara Wind Tunnel, which has an excellent low background noise level. Experimental results with a 1/5 scale model Shinkansen[2] show that the aeroacoustic sound from lower parts of train is generated mainly at bogie sections as shown in Fig. 1. Another conclusion from tests with 1/25 scale mirror image models[3] shows that the frequency of large scale vortices shed from the upstream edge of the bogie section is not greater than 500 Hz (20 Hz at full scale). Because the wavelength of sound caused by these vortices is about 17 m at full scale, the sound propagates over noise barriers whose standard height is 2 m, and affects the sound level at measurement points by the track.

In the past, most numerical simulations of the aeroacoustic noise of trains[4,5] calculated the pressure fluctuations at the body surface and then estimated the acoustic pressure fluctuations in the far field by Curle's equation.[6] However, they could not identify the structure of sound sources in the flow directly. Lighthill's stress tensor[7] merely shows the distribution of quadrupole sound sources. On the other hand, Hardin *et al.*[8] calculated the sound radiation from a cylinder with the compact Green's function.

In this paper, the distribution of dipole sound sources at the bogie section of high speed trains is predicted numerically by coupling the instantaneous flow properties with the compact Green's function. The large eddy simulation (LES) scheme and its predictions are described in Sec. II. In Sec. III, the dipole generated sound predicted by Howe's equation[9] is compared numerically with that given by Curle's formula.

[a]Electronic mail: takaishi@rtri.or.jp

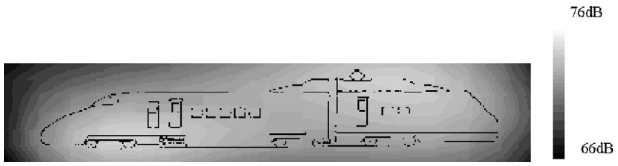

FIG. 1. Contour of the sound pressure level of 1/5 scale model Shinkansen that is tested in the wind tunnel (Ref. 2). The sound pressure level is measured by using a sound concentrating microphone with a paraboloidal reflector whose diameter is 1 m.

II. UNSTEADY FLOW SIMULATION BY LES

A. Formation

The large eddy simulation (LES) technique directly computes energy-containing eddies that are larger than the grid scale, and the effect of the smallest scales of turbulence is modeled through a subgrid scale stress term. To separate the large from the small scales, a physical variable ϕ is filtered and defined as a space-averaged variable. Since the governing equations are discretized by the finite volume method, a top-hat filter is provided implicitly,

$$\overline{\phi}(\mathbf{y}) = \int \phi(\mathbf{y}')H(\mathbf{y},\mathbf{y}')d\mathbf{y}', \tag{1}$$

where H is the top-hat filter function satisfying

$$H(\mathbf{y},\mathbf{y}') = 1/V \quad \text{for } \mathbf{y}' \in \text{computational cell}$$
$$= 0 \quad \text{otherwise} \tag{2}$$

and V is the volume of the computational cell.

Because the train speed considered in this study is 300 km/h (83.3 m/s) and its Mach number is sufficiently small relative to unity, the flow around trains can be regarded as incompressible. If the filtering operation (1) is applied to the equations of continuity and momentum for incompressible flow, the filtered governing equations for the grid scale take the form

$$\frac{\partial \overline{u_i}}{\partial y_i} = 0, \tag{3}$$

$$\frac{\partial \overline{u_i}}{\partial t} + \overline{u_j}\frac{\partial \overline{u_i}}{\partial y_j} = -\frac{1}{\rho}\frac{\partial \overline{p}}{\partial y_i} + \frac{\partial}{\partial y_i}(-\tau_{ij} + 2\nu\overline{S_{ij}}), \tag{4}$$

where $\overline{S_{ij}}$ is the grid scale rate of strain tensor

$$\overline{S_{ij}} = \frac{1}{2}\left(\frac{\partial \overline{u_i}}{\partial y_j} + \frac{\partial \overline{u_j}}{\partial y_i}\right), \tag{5}$$

and τ_{ij} is the subgrid scale stress tensor

$$\tau_{ij} = \overline{u_i u_j} - \overline{u_i}\,\overline{u_j}. \tag{6}$$

The governing equations for the grid scale are converted to a system of algebraic equations by the finite volume method with unstructured cells. The convection terms are discretized by second-order upwind methods, and the diffusion terms by second-order central-differenced methods, respectively.

The time derivative is discretized using the second-order accurate backward differences:

Thus $\partial\phi/\partial t = F(\phi)$ becomes

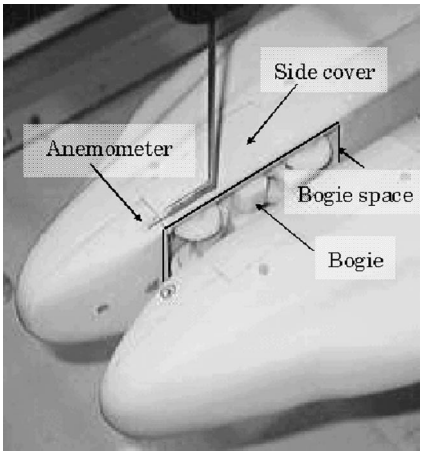

FIG. 2. In order to simulate the effect of the ground that moves relative to the vehicle in the real condition, a pair of mirror image 1/25 scale models are placed symmetrically, and their plane of symmetry is assumed to be the moving ground (Ref. 3).

$$\phi^i = \tfrac{4}{3}\phi^n - \tfrac{1}{3}\phi^{n-1} + \tfrac{2}{3}\Delta t F(\phi^i). \tag{7}$$

The pressure-implicit with splitting of operators methods[10] are used for pressure–velocity coupling.

The subgrid scale stress tensor τ_{ij} is simplified by the eddy viscosity model

$$\tau_{ij} = -2\nu_e\overline{S_{ij}}, \tag{8}$$

where the eddy viscosity is modeled by the Smagorinsky–Lilly hypothesis

$$\nu_e = L_s^2\sqrt{\overline{S_{ij}}\,\overline{S_{ij}}}. \tag{9}$$

L_s is the mixing length for subgrid scales and is computed by using

$$L_s = \min(0.42d,\ C_s V^{1/3}), \tag{10}$$

where d is the distance to the closest wall. In this study Smagorinsky constant C_s is fixed as 0.1.

From experimental results of wind tunnel tests[2] the aeroacoustic sound from lower parts of the train was confirmed to be generated mainly at bogie sections as shown in Fig. 1. Figure 2 shows a schematic diagram of the measurements with 1/25 scale mirror image models.[3] Although high-frequency noise is generated by wheels, low-frequency sound, which cannot be totally reduced by noise barriers, seems to be generated by the cavity of the bogie section. Hence, the calculated domain is limited to the zone around the car that includes the bogie section. Figure 3 shows a schematic of the computational domain. As we mainly focus on the low-frequency components, the bogie (wheels) is removed and the effect of the three-dimensional flow around the front shape is also neglected.

In order to make a comparison with the experimental results from 1/25 scale models, the size of the computational domain is also 1/25 of the real trains.

The cavity length (153 mm) of the bogie space is chosen as the representative length L. Then, the distance from the flow inlet to the leading edge of the cavity and that from the trailing edge of the cavity to the flow outlet are set at $2L$,

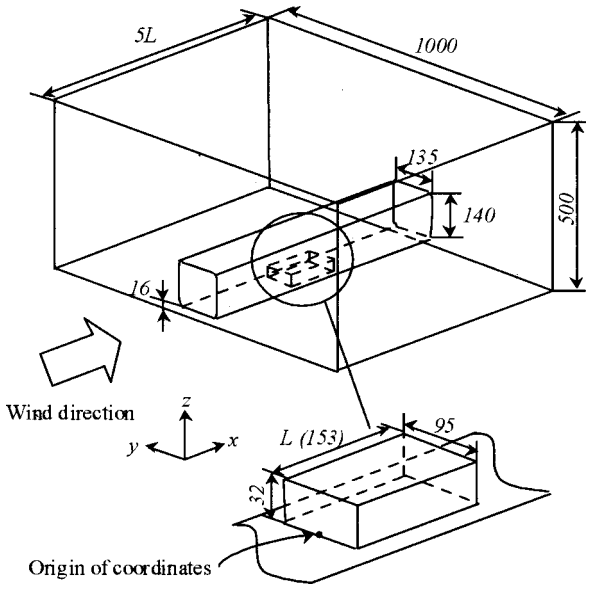

FIG. 3. Computational domain of unsteady flow around the train. As we mainly focus on the low-frequency components, the bogie (wheels) is removed.

respectively. The space between the ground and the bottom of the vehicle is set as 16 mm. The center of the leading edge of the cavity is set as the origin of the coordinates, train running (main flow) direction as the x axis, side direction as the y axis, and vertical direction as the z axis. The number of grid points inside the bogie section is $51\times31\times21$. The number of cells included in the whole computational domain is 661 350.

The stochastic components of the flow at the inlet boundaries are accounted for by superposing random perturbations on individual velocity components. In order to make the conditions of simulation coincide with the experimental test conditions, the mean flow velocity is set to 300 km/h (83.3 m/s), and the turbulence intensity is set to 0.3%. The zero diffusion flux condition is applied at the outlet; the velocity gradient in the flow direction is assumed to be zero and the conditions of the outflow plane are extrapolated from within the domain. The no-slip condition for velocity is applied at the ground and the train surface.

As the initial condition ($t=0$ s) for LES calculation, the time-steady solution obtained by the $k-\varepsilon$ model is used. The physical time step Δt is set to 2.5×10^{-4} s.

Unsteady flow simulation by LES is performed using FLUENT version 5. The estimation of the dipole sound in Sec. III is performed by programming a shell module.

B. Results

The following discussion uses data acquired after the time history of the drag exerted on the train becomes fully periodic ($t=0.225$–0.250 s).

Figure 4 shows three-dimensional distributions of vortices around a train. They are the views from the bottom of a train, and indication of the ground boundary is omitted. Each figure shows iso-surfaces of vorticity vector in each direction. The unstable shear layer separation at the leading edge of the bogie section sheds vortices periodically. These vortices travel downstream while growing to finally impinge upon the trailing edge of the section. Longitudinal vortices are formed along the side covers of the bogie section and roll up at the trailing edge.

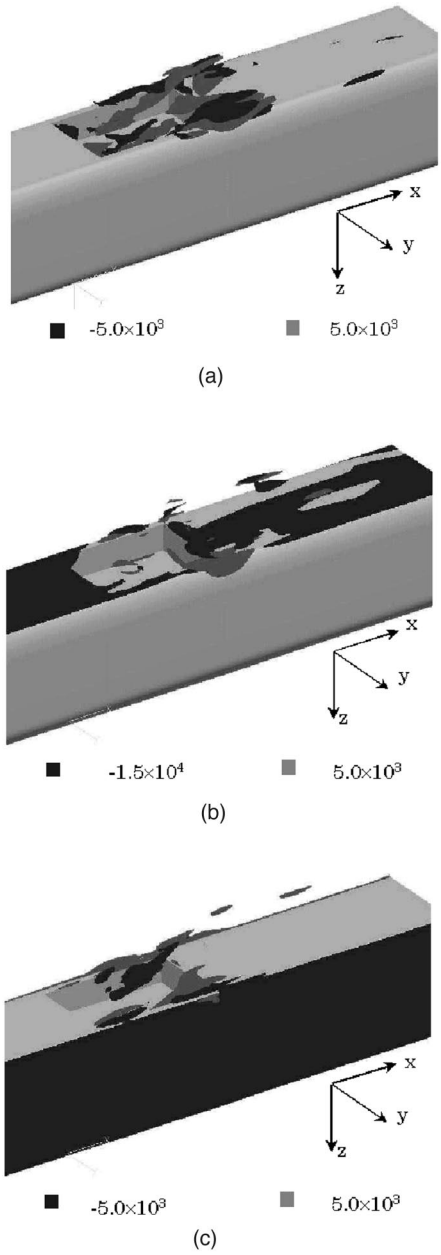

FIG. 4. Iso-surface of vorticity vector: (a) x component, (b) y component, and (c) z component. They are the views from the bottom of a train, and indication of the ground boundary is omitted.

The incompressible pressure fluctuation is expressed in the logarithmic scale in the same way as for the sound pressure,

$$\text{pressure fluctuation level (dB)} = 20\log\frac{\sqrt{\langle p^2\rangle}}{p_0},\qquad p_0=2\times10^{-5}\ \text{Pa},\tag{11}$$

where $\langle\ \rangle$ denotes time-averaged value.

Figure 5 shows the distribution of pressure fluctuation at the bogie section. Point marks in each graph show the ex-

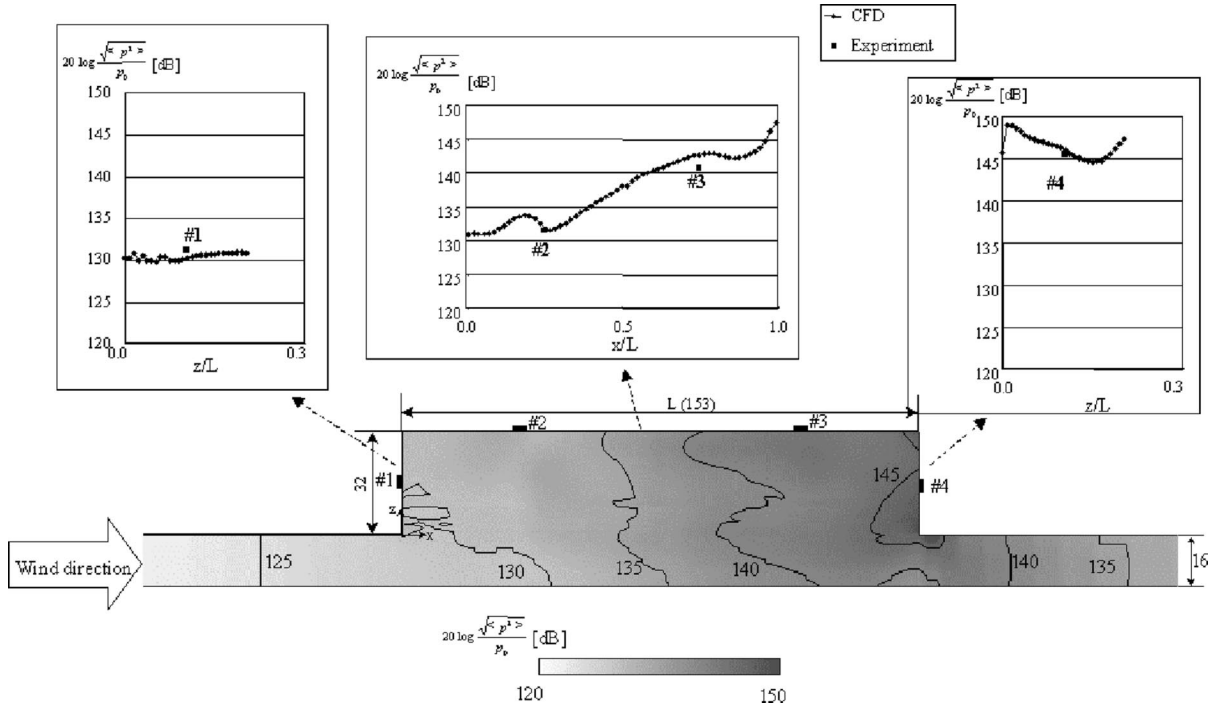

FIG. 5. Distribution of pressure fluctuation level [Eq. (11)] at $y=0$. Each graph shows the profile along the inner wall of the bogie section.

perimental data acquired by the wind tunnel tests with 1/25 mirror image models. LES results prove to agree well with the experimental results. The pressure fluctuation level is high around the trailing edge of the bogie section where the turbulence level and change of vorticity over time is also large. The pressure fluctuation at the bottom of the bogie section is also large because of the motion of vortices.

III. ESTIMATION OF DIPOLE SOUND SOURCE

In Sec. II, the instantaneous flow properties around a train are solved by the LES technique. Hence, in this section, the distribution of dipole sound sources around trains is predicted numerically by coupling the instantaneous flow properties with the compact Green's function.

A. Compact Green's function

The theory of aerodynamic sound was first developed by Lighthill,[7] who reformulated the Navier–Stokes equation into an exact, inhomogeneous wave equation. Howe[9,11] simplified Lighthill's equation for high Reynolds number flow at low Mach number,

$$\frac{1}{c_0^2}\frac{\partial^2 B}{\partial t^2}-\nabla^2 B=\mathrm{div}(\omega\times\mathbf{u}), \tag{12}$$

where

$$B\equiv\frac{p}{\rho_0}+\frac{1}{2}u^2. \tag{13}$$

The right-hand side of Eq. (12) implies that vortices in the flow can be sound sources.

If fixed surfaces are present in the flow, Green's theorem yields the following relation from Eq. (12):

$$B(\mathbf{x},t)=\int G(\mathbf{x},\mathbf{y},t-\tau)\frac{\partial}{\partial y_j}(\omega\times\mathbf{u})_j(\mathbf{y},\tau)d\mathbf{y}\,d\tau - \int_S G(\mathbf{x},\mathbf{y},t-\tau)\frac{\partial B}{\partial y_j}(\mathbf{y},\tau)n_j dS\,d\tau, \tag{14}$$

where the unit normal vector $\mathbf{n}$ on S is directed into the fluid. The Green's function $G(\mathbf{x},\mathbf{y},t-\tau)$ satisfies

$$\frac{1}{c_0^2}\frac{\partial^2 G}{\partial t^2}-\nabla^2 G=\delta(\mathbf{x}-\mathbf{y})\,\delta(t-\tau) \tag{15}$$

in the fluid and its normal derivative is 0 on S, namely,

$$\frac{\partial G}{\partial n}=0 \quad \text{on } S. \tag{16}$$

The divergence theorem provides

$$\int G\,\mathrm{div}(\omega\times\mathbf{u})d\mathbf{y}=-\int_S G(\omega\times\mathbf{u})_j n_j dS-\int(\omega\times\mathbf{u})\cdot\nabla G\,d\mathbf{y}. \tag{17}$$

On the other hand, the momentum equation for fluid can be expressed in Crocco's form for high Reynolds number flow.

$$\frac{\partial u_i}{\partial t}+\frac{\partial B}{\partial y_i}=-(\omega\times\mathbf{u})_i. \tag{18}$$

Substituting Eqs. (17) and (18) into (14), we obtain

$$B(\mathbf{x},t)=-\int(\omega(\mathbf{y},\tau)\times\mathbf{u}(\mathbf{y},\tau))\cdot\frac{\partial G}{\partial\mathbf{y}}(\mathbf{x},\mathbf{y},t-\tau)d\mathbf{y}\,d\tau + \int_S G(\mathbf{x},\mathbf{y},t-\tau)\frac{\partial u_j}{\partial\tau}(\mathbf{y},\tau)n_j dS\,d\tau. \tag{19}$$

The second term should be 0 if surfaces are rigid.

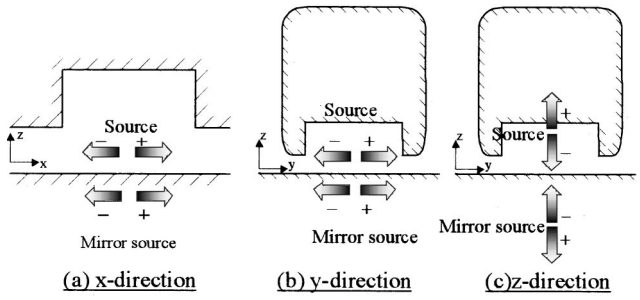

FIG. 6. Model of dipole sound sources close to the ground. By mirror sources, dipole sound sources in the x direction (a) and y direction (b) will be doubled. In contrast, the sources in the z direction (c) will be canceled by equal and opposite image dipoles.

If the observation point **x** is far from the source region, Eq. (13) can be approximated as

$$B \cong \frac{p_a}{\rho_0}, \tag{20}$$

and the acoustic pressure fluctuation in the far field is

$$p_a(\mathbf{x},t) = -\rho_0 \int \{\omega(\mathbf{y},\tau) \times \mathbf{u}(\mathbf{y},\tau)\} \cdot \frac{\partial G}{\partial \mathbf{y}}(\mathbf{x},\mathbf{y},t-\tau)\, d\mathbf{y}\, d\tau. \tag{21}$$

If the source region is compact, the three-dimensional Green's function may be expanded around the source region in the form[9]

$$G_c \cong \frac{1}{4\pi|\mathbf{x}|}\,\delta\left(t-\tau-\frac{|\mathbf{x}|}{c_0}\right) + \frac{\mathbf{x}\cdot\mathbf{Y}}{4\pi c_0|\mathbf{x}|^2}\,\frac{\partial}{\partial t}\,\delta\left(t-\tau-\frac{|\mathbf{x}|}{c_0}\right) + \frac{1}{|\mathbf{x}|}O\left[\left(\frac{2\pi l}{\lambda}\right)^2\right]. \tag{22}$$

In this equation, Y_j denotes the velocity potential of an imaginary flow around the body that has unit speed in the j direction at large distances from the body. This velocity potential must satisfy Laplace's equation

$$\nabla^2 Y_j = 0 \tag{23}$$

in the fluid and also

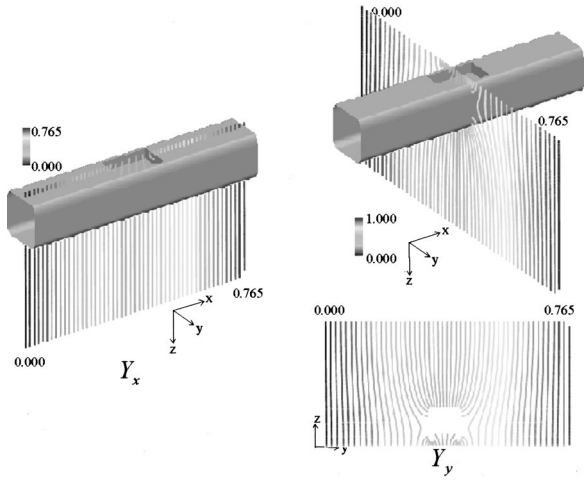

FIG. 7. Contours of the velocity potential **Y** around the train.

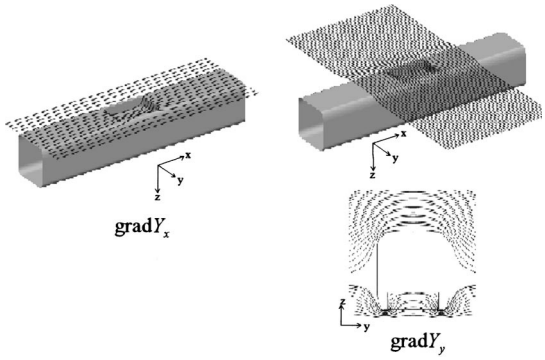

FIG. 8. Streamlines of the $\mathbf{Y}'$ flows. The velocity potential **Y** depends on the body shape, but does not represent a real flow.

$$\frac{\partial Y_j(\mathbf{y})}{\partial n} = 0 \tag{24}$$

on surfaces. The Green's function governs the acoustical properties of the system: the velocity potential **Y** depends on the body shape, but does not represent a real flow. The second term of Eq. (22),

$$G_c \cong \frac{\mathbf{x}\cdot\mathbf{Y}}{4\pi c_0|\mathbf{x}|^2}\,\frac{\partial}{\partial t}\,\delta\left(t-\tau-\frac{|\mathbf{x}|}{c_0}\right), \tag{25}$$

represents the production of dipole sound, and is called "the compact Green's function."[9]

In the present problem, the frequency of the unsteady drag force exerted on the train by the periodic shedding of vortices is about 200 Hz. Also, the experiments confirm that

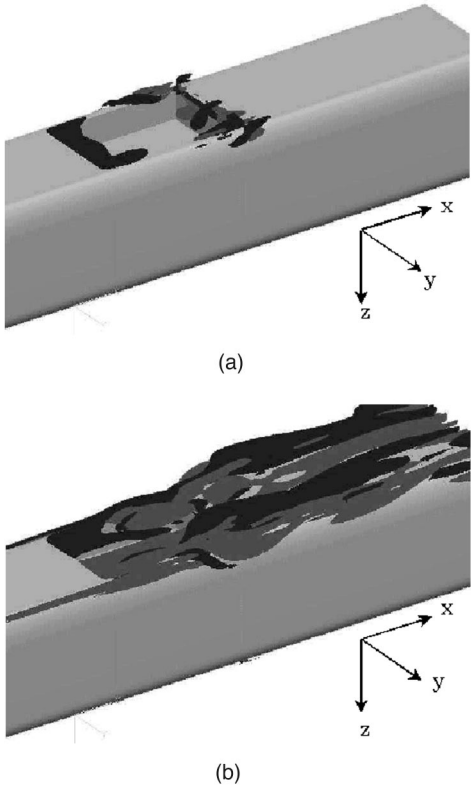

FIG. 9. Distribution of instantaneous force exerted on each fluid element [expressed as the integrand of Eq. (28)]: (a) x component and (b) y component.

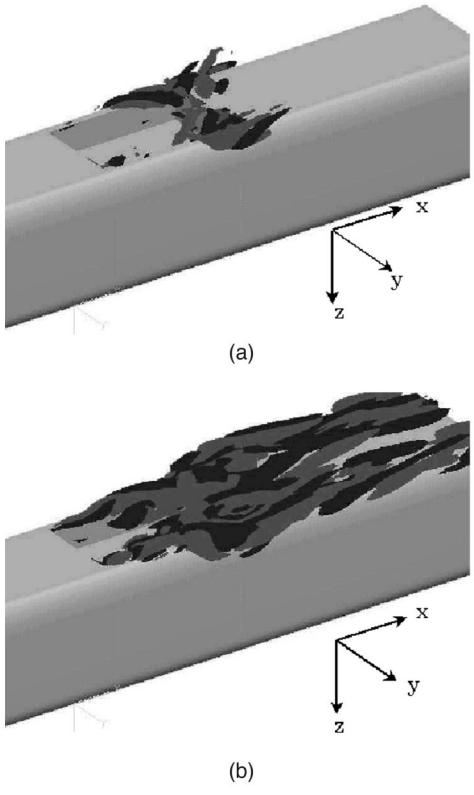

FIG. 10. Distribution of dipole sound source [expressed as the integrand of Eq. (27)]: (a) x component and (b) y component.

the frequency of large scale vortices generated by flow separation at the upstream edge of the bogie section is not greater than 500 Hz. The wavelength of sound produced by these vortices is about 0.5–2 m, which is large compared with the representative length of the bogie section (0.153 m). Therefore, when the low frequency sound that propagates over noise barriers is taken into consideration, sound sources satisfy the condition of compactness.

Dipole sound sources close to the ground can be modeled as shown in Fig. 6. The effect of the ground is replaced by mirror sources.[12,13] By mirror sources, dipole sound sources in the x and y directions will be doubled. In contrast, the sources in the z direction will be canceled by equal and opposite image dipoles. As a result, the effective three-dimensional compact Green's function becomes

$$G_c(\mathbf{x},\mathbf{y},t-\tau)\approx\frac{x_j Y_j(\mathbf{y})}{2\pi c_0|\mathbf{x}|^2}\frac{\partial\delta}{\partial t}\left(t-\tau-\frac{|\mathbf{x}|}{c_0}\right),\quad j=1,2. \tag{26}$$

Here $j=1$ and 2 denotes the x and y component, respectively.

Substituting Eq. (26) into Eq. (21), we obtain

$$P_a=-\frac{\rho_0 x_j}{2\pi c_0|\mathbf{x}|^2}\frac{\partial}{\partial t}\int(\omega\times\mathbf{u})(\mathbf{y},t-|\mathbf{x}|/c_0)\cdot\text{grad}\ Y_j d\mathbf{y},\quad j=1,2. \tag{27}$$

This is the final form of the acoustic pressure fluctuation in the far field that is produced by dipole sound sources close to the ground.

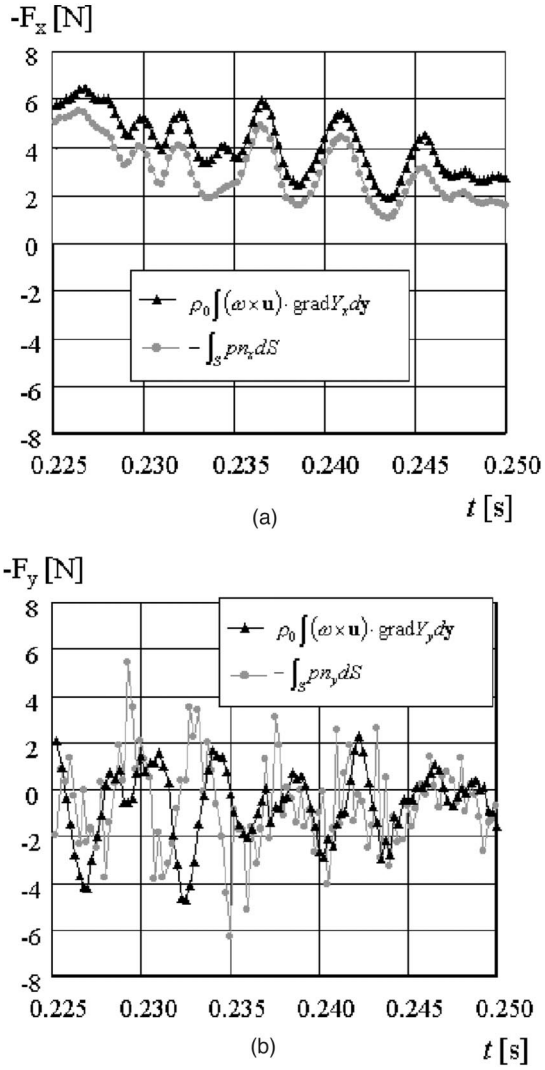

FIG. 11. Time histories of force exerted on the train: (a) x component and (b) y component. A numerical comparison of Eqs. (28) and (29).

The force **F** exerted on an incompressible inviscid fluid by a body is generally given as[9]

$$F_i=-\rho_0\int(\omega\times\mathbf{u})\cdot\text{grad}\ Y_i d\mathbf{y}. \tag{28}$$

The force is also given by the surface integral of the pressure

$$F_i=\int_S pn_i dS. \tag{29}$$

By using the relation between Eqs. (28) and (29), Eq. (27) is rewritten in the form

$$P_a=\frac{x_j}{2\pi c_0|\mathbf{x}|^2}\frac{\partial}{\partial t}\int_S p(\mathbf{y},t-|\mathbf{x}|/c_0)n_j dS,\quad j=1,2. \tag{30}$$

This coincides with the surface integral of Curle's equation.[6] If the pressure distribution on the boundary surface is measured in detail to estimate the force exerted on the body, the far field pressure will be calculated by Eq. (30). On the other hand, the relation between flow and radiated sound is not determined directly from this equation.

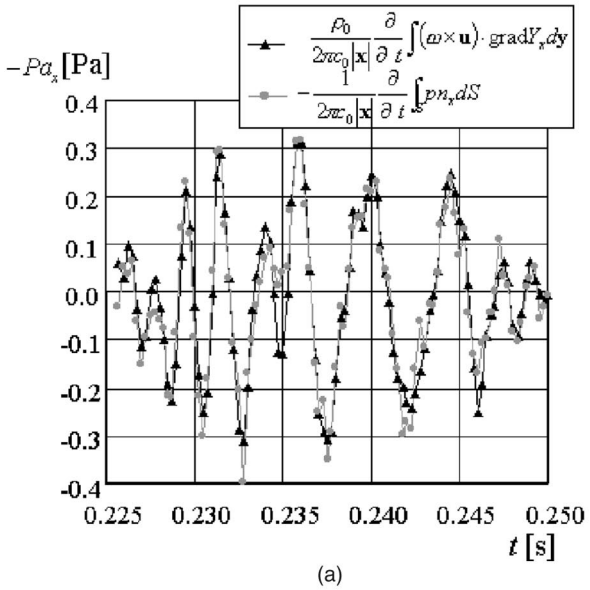

(a)

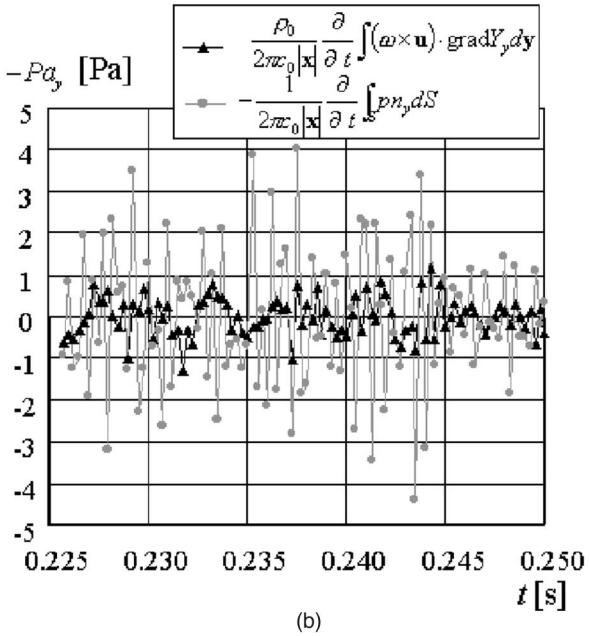

(b)

FIG. 12. Time histories of the sound pressure at $|\mathbf{x}|=4.42$ m: (a) x component and (b) y component. A numerical comparison between Curle's equation (30) and Howe's equation (27).

Howe's method selects a Green's function whose normal derivative at the boundary surface is zero as in Eq. (16). Then the effect of the boundary surface is included in the Green's function and the acoustic pressure fluctuation in the far field is expressed in a volume integral as Eq. (27). Since Eq. (27) is expressed in terms of the motion of vortices, the relation between the flow and radiated sound is explicit.

B. Results

First, Laplace's equation (23) is solved numerically with boundary condition (24). Figure 7 shows contours of the velocity potential $\mathbf{Y}$ around the train.

Figure 8 shows the streamlines of the $\mathbf{Y}'$ flows. In each figure, the velocity has unit speed in the x and y directions at large distance from the train. The streamlines curve along the shape of the bogie section.

Next, both the instantaneous properties of flows and compact Green's function are obtained numerically, the distribution of dipole sources around a train is obtained by Eq. (28). Figure 9 shows the distribution of the instantaneous force exerted on the each fluid element, i.e., the integrand of Eq. (28).

Figure 10 shows the distribution of the time derivative of the instantaneous force. Since the volume integral of these parts, namely Eq. (27), yields the acoustic pressure fluctuation of the dipole sound in the far field, each component of the integrand in (27) can be regarded as a dipole sound source. The results show that a strong dipole source is generated at the trailing edge and the side covers of the bogie section where the shape changes greatly and the variation of flow over time is also great. On the other hand, the bottom of the bogie section where the shape does not change, or the leading edge and boundary layer where the variation of flow in time is small, do not appear to be strong dipole sources.

In order to make a numerical comparison of Curle's equation (30) and Howe's equation (27), time histories of the force exerted on the train are evaluated by both volume and surface integrals. Figure 11 shows the time histories of force exerted on the train. The two integrals in the x direction are confirmed to agree well. On the other hand, the integrals in the y direction do not agree well. Figure 12 shows the time histories of the sound pressure. Integrals in Fig. 11 are differentiated with respect to time. Since each dipole has the angular directivity as shown in Eqs. (27) and (30), the sound pressure fluctuation at an arbitrary point $\mathbf{x}$ is written as the sum of each component multiplied by its directivity,

$$P_a=\frac{x_j}{|\mathbf{x}|}Pa_j, \quad j=1,2. \tag{31}$$

For the x component, Howe's equation (27) agrees numerically with Curle's equation (30). On the other hand, y components do not agree with each other. This is not unexpected, but is a consequence of errors in the numerical scheme. Indeed, for ideal flow conditions there would be no net side force on a symmetric body shape of the train. In our case the force is produced by random differences in the pressure on opposite sides of the train—any errors are magnified in Curle's formula because of the relatively large integration region.

Although the sideways sound is not well-estimated numerically, separation at the bogie section which affects the sound into streamwise direction must have influence on it. Suppression of this separation or impingement of flow at the trailing edge will reduce the low frequency noise from high speed trains.

IV. CONCLUSION

By coupling the instantaneous flow properties with the compact Green's function, the distribution of dipole sources is obtained. As a result, the following major conclusions are obtained.

(1) The unstable shear layer separation at the leading edge of the bogie section sheds vortices periodically. These vortices travel downstream while growing to finally impinge upon the trailing edge of the section. Longitudinal vortices are formed along the side covers of the bogie section and roll up at the trailing edge.

(2) A strong dipole source is generated at the trailing edge and the side covers of the bogie section where the shape changes greatly and the variation of flow over time is also great. On the other hand, the bottom of the bogie section where the shape does not change, or the leading edge and boundary layer where the variation of flow in time is small, do not appear to be strong dipole sources.

(3) The sound radiated into the streamwise direction is predicted by Howe's equation. It agrees numerically with that given by Curle's formula.

(4) The random sound radiated to the side is not well-estimated numerically. However, it must be strongly influenced by separation at the bogie section.

Suppression of this separation or impingement of flow at the trailing edge will reduce the low frequency noise from high speed trains.

[1] A. Sagawa, S. Ono, H. Hotta, and T. Aso, ''Aeroacoustic noise generated from high-speed trains in Japan,'' AIAA J. **99**, 1894 (1999).

[2] T. Takaishi, Y. Zenda, and Y. Shimizu, ''Wind tunnel tests for reducing aeroacoustic noise from high-speed trains,'' Proceedings of the World Congress on Railway Research (on CD-ROM), 1999.

[3] T. Takaishi, Y. Zenda, and Y. Shimizu, ''Study on the aeroacoustic noise from shinkansen with mirror image models,'' Quarterly Report of RTRI **42**, 110–114 (2001).

[4] B. S. Holmes, J. B. Dias, B. A. Jaroux, T. Sassa, and Y. Ban, ''Predicting the wind noise from the pantograph cover of a train,'' Int. J. Numer. Methods Fluids **24**, 1307–1319 (1997).

[5] C. Kato, A. Iida, M. Hattori, and S. Inadama, ''Numerical simulation of aerodynamic sound source inthe wake of a complex objects,'' AIAA-2000-1942 (2000).

[6] N. Curle, ''The influence of solid boundaries on aerodynamic sound,'' Proc. R. Soc. London, Ser. A **231**, 1187 (1955).

[7] M. J. Lighthill, ''On sound generated aerodynamically,'' Proc. R. Soc. London Ser. A **211**, 564–587 (1952).

[8] J. C. Hardin and S. L. Lamkin, ''Aeroacoustic computation of cylinder wake flow,'' AIAA J. **22**, 51–57 (1984).

[9] M. S. Howe, *Acoustics of Fluid-Structure Interactions* (Cambridge University Press, Cambridge, 1998).

[10] R. I. Issa, ''Solution of implicitly discretized fluid flow equations by operator splitting,'' J. Comput. Phys. **62**, 40–65 (1983).

[11] M. S. Howe, ''Contributions to the theory of aerodynamic sound, with application to excess jet noise and the theory of the flute,'' J. Fluid Mech. **71**, 625–673 (1975).

[12] A. Powell, ''Aerodynamic noise and the plane boundary,'' J. Acoust. Soc. Am. **32**, 982–990 (1960).

[13] M. E. Goldstein, *Aeroacoustics* (McGraw–Hill, New York, 1976).

Time reversed reverberation focusing in a waveguide

J. F. Lingevitch[a)]
Naval Research Laboratory, Washington, DC 20375

H. C. Song and W. A. Kuperman
Marine Physical Laboratory, Scripps Institute of Oceanography, University of California–San Diego, La Jolla, California 92093-0701

(Received 14 February 2001; revised 16 January 2002; accepted 4 March 2002)

Time reversal mirrors have been applied to focus energy at probe source locations and point scatterers in inhomogeneous media. In this paper, we investigate the application of a time reversal mirror to rough interface reverberation processing in a waveguide. The method is based on the decomposition of the time reversal operator which is computed from the transfer matrix measured on a source-receiver array [Prada *et al.*, J. Acoust. Soc. Am. **99**, 2067–2076 (1996)]. In a similar manner, reverberation data collected on a source-receiver array can be filtered through an appropriate temporal window to form a time reversal operator. The most energetic eigenvector of the time reversal operator focuses along the interface at the range corresponding to the filter delay. It is also shown that improved signal-to-noise ratio measurement of the time reversal operator can be obtained by ensonifying the water column with a set of orthogonal array beams. Since these methods do not depend upon *a priori* environmental information, they are applicable to complex shallow water environments. Numerical simulations with a Pekeris waveguide demonstrate this method. © *2002 Acoustical Society of America.* [DOI: 10.1121/1.1479148]

PACS numbers: 43.30.Gv, 43.30.Hw, 43.30.Vh [SAC]

I. INTRODUCTION

Recent experiments have demonstrated time reversal mirrors (TRMs) in the ultrasonic laboratory[1,2] and in ocean acoustics.[3–5] Time reversal mirrors often involve a probe source or scattering from compact objects. In this paper we examine the application of a TRM to scattering from a rough boundary in a waveguide. The method employed is based upon the DORT method for the decomposition of the time reversal operator (TRO).[6–8] In this case, probe pulses are projected from the source-receiver array (SRA) and the backscattered signal due to the interface roughness is recorded. A temporal window corresponding to a desired focusing range from the SRA is applied to the reverberation data and the resulting time series data are used to form the TRO. The highest energy eigenvector of the TRO corresponds to the SRA weighting function for focusing along the interface at the desired range. This extends the previous work on time reversed focusing in two ways. First, reverberation from the rough interface which is often regarded as a source of clutter in sonar performance is utilized to probe the waveguide. Second, an extended interface as opposed to a compact scatterer is used to form the time reversal operator. In Sec. II we describe the scattering model implemented to simulate reverberation from a rough interface in a Pekeris waveguide. Section III describes the processing of the reverberation data using time reversal techniques. A generalized method utilizing orthogonal array beams for measuring the time reversal operator is also described. In Sec. IV simulations in a Pekeris waveguide illustrate these methods.

[a)]Work done while at the Marine Physical Laboratory; electronic mail: jfl@aslan.nrl.navy.mil

II. REVERBERATION MODEL

We consider a geometry where a source-receiver array is oriented vertically in the water column as shown in Fig. 1. Roughness at the sediment interface scatters an outgoing wave generated at the SRA and the reverberation is recorded at each element of the array. For the simulations in this paper, the backscattered pressure field is computed from perturbation theory. A Pekeris waveguide with a flat pressure release surface at $z=0$ and perturbed interface at $z=D+\gamma(\mathbf{r})$ is considered where γ is the deformation from a flat surface and $\mathbf{r}$ is the horizontal position vector; position vectors in three dimensions are denoted by $\mathbf{x}=(\mathbf{r},z)$. Factoring out a harmonic time dependence $\exp(-i\omega t)$ from the wave equation for pressure yields

$$\nabla^2 p + k_j^2 p = \delta(\mathbf{x}-\mathbf{x}_s), \tag{1}$$

where the subscripts $j=1,2$ will denote material parameters above and below the sediment interface, respectively, and the source location is $\mathbf{x}_s$. The total pressure is expanded in a perturbation series

$$p = p_0 + s, \tag{2}$$

where p_0 is the outgoing pressure field of the unperturbed problem (flat bottom) and s is the leading order scattered pressure due to interface roughness. The scattered pressure s satisfies Eq. (1) without the explicit source term; it is forced through the interface conditions. An integral equation for s follows from applying Green's theorem,

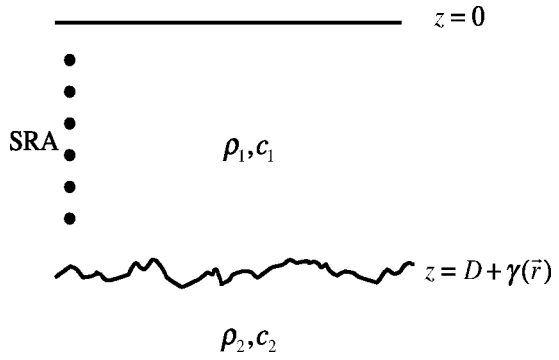

FIG. 1. Pekeris waveguide with a rough interface. For simulations in Sec. IV, $c_1=1500$ m/s, $c_2=1600$ m/s, $\rho_1=1000$ kg/m^3, $\rho_2=1900$ kg/m^3, and $D=100$ m. The rough interface is modeled with one-dimensional Goff–Jordan power-law spectrum (Ref. 18) with a correlation length of $L=15$ m and mean square roughness $\langle \gamma^2 \rangle = 0.01$ m^2.

$$s(\mathbf{r},z)=\rho_1 \int d\mathbf{r}' \left(\left[s(\mathbf{r}',D)\, \frac{1}{\rho}\, \frac{\partial G(\mathbf{r}-\mathbf{r}',z,D)}{\partial z'} \right] - \left[\frac{1}{\rho}\, \frac{\partial s(\mathbf{r}',D)}{\partial z'} \right] G(\mathbf{r}-\mathbf{r}',z,D) \right), \tag{3}$$

where G is the Green's function of the unperturbed problem, the contour of integration is along $z=D$, and the square brackets denote the jump of the enclosed quantity across the interface.[9] The jump conditions are obtained by expanding the interface conditions for pressure to leading order about $z=D$ yielding

$$[s(\mathbf{r},D)] = -\gamma(\mathbf{r}) \left[\frac{\partial p_0(\mathbf{r},D)}{\partial z} \right], \tag{4}$$

$$\left[\frac{1}{\rho}\, \frac{\partial s(\mathbf{r},D)}{\partial z} \right] = -\gamma(\mathbf{r}) \left[\frac{1}{\rho}\, \frac{\partial^2 p_0(\mathbf{r},D)}{\partial z^2} \right] + \nabla_\perp \gamma \cdot \left[\frac{1}{\rho} \nabla_\perp p_0(\mathbf{r},D) \right], \tag{5}$$

where $\nabla_\perp$ is the horizontal gradient. The perturbation theory assumes a small ratio of roughness height to acoustic wavelength $k\gamma \ll 1$, small interface slope $|\nabla\gamma| \ll 1$, and that multiple scattering can be neglected.[10–12] The modal representation of the scattered field is derived by expanding the Green's function and p_0 in terms of modes. For computational efficiency we consider two-dimensional propagation with a line source geometry where the far-field Green's function is

$$G(\mathbf{x},\mathbf{x}') = \frac{-i}{2\rho(z')} \sum_m \phi_m(z)\, \phi_m(z')\, \frac{e^{ih_m|x-x'|}}{h_m}, \tag{6}$$

and $\{\phi_m, h_m\}$ are the set of propagating modes and horizontal wave numbers of the unperturbed problem.[13] Substituting Eqs. (4)–(6) into Eq. (3) and evaluating the expression for the backscattered field at $x=0$ yields

$$s(z;z_s) = \frac{1}{4} \sum_{m,n} (h_m h_n)^{-1} \left(\left[\frac{h_m h_n + k^2}{\rho} \right] + \frac{[\rho]}{\rho_2^2} \sqrt{(h_m^2-k_2^2)(h_n^2-k_2^2)} \right) \phi_m(D)\, \phi_m(z_s) \times \phi_n(D)\, \phi_n(z) \int_{-\infty}^{\infty} \gamma(x) e^{i(h_m+h_n)|x|} dx. \tag{7}$$

Equation (7) has been simplified using the boundary condition relating the modes functions of the Pekeris waveguide and their derivatives at the interface

$$\frac{1}{\rho_1}\, \frac{d\phi_m(D)}{dz} = \frac{1}{\rho_2} \sqrt{h_m^2 - k_2^2}\, \phi_m(D). \tag{8}$$

The backscattered field due to multiple sources is obtained by superposition and broadband pulses are modeled with Fourier synthesis.

III. TIME REVERSAL PROCESSING OF REVERBERATION DATA

This section describes our method for processing reverberation data collected on the source-receiver array. The data are recorded on an N channel SRA which is configured to transmit an incident pulse of length τ starting at $t=t_0$ (transmit mode). The resulting reverberation time series is then recorded on each element (receive mode). The switching time between transmit and receive modes is assumed to be small so that only the short range reverberation signal is lost. Assuming that only single scattering is important, a specific range R will contribute to the received reverberation over a time window

$$w(t;R,\Delta) = \begin{cases} 1, & |t-t_c-t_0| \leqslant \Delta/2 \\ 0, & |t-t_c-t_0| > \Delta/2\,, \end{cases} \tag{9}$$

where $t_c = 2Rc_0^{-1}$ is the approximate round-trip travel time and Δ is the width of the temporal window which depends on the source pulse length and the dispersive properties of the waveguide; for the examples in this paper we choose $\Delta=\tau$. The reference speed c_0 is an average modal group speed. Due to dispersion in the waveguide, a span of ranges of width Δr (which depends on the time window Δ) will contribute to the reverberation in the windowed time series. We apply the DORT method to the central frequency component of the reverberation data to obtain a SRA weighting vector which focuses back to the interface at the range R. The weighting vector used is the highest energy eigenvector of the time reversal operator. In the following the DORT method for point scatterers is summarized and a generalization of the method to obtain higher signal-to-noise measurements of the eigenvectors is described.

Time reversal operator

The time reversal invariance of the wave equation implies that in principle energy can be focused back to its source.[6,7] Direct experimental verification of time reversal focusing in the oceanic waveguide has been recently demonstrated using a source-receiver array and a probe source.[3,4,14] Time reversal mirrors have also been applied to focusing on

scatterers in inhomogeneous media.[1,2,6,7,15] In the case of several point targets whose scattered waves overlap in the time domain, decomposition of the time reversal operator by the DORT method yields SRA weighting functions for focusing at each scatterer separately. Importantly, this method assumes no *a priori* knowledge of the waveguide properties. Previous implementations of the DORT method were based on measurements of the element-to-element impulse responses of the source-receiver array. Here, an equivalent method based on orthogonal array beams is described for measuring the time reversal operator. Array beams enhance the backscattered signal strength by ensonifying the water column with the full source array rather than single elements as described in the original DORT formulation.

We consider a source-receiver array with N elements. The original DORT algorithm is based on the measurement of the response matrix $k_{ij}(t)$, the backscattered field on channel i of the SRA due to an impulsive signal broadcast from channel j. The Fourier transform of this quantity is the transfer matrix $K_{ij}(\omega)$. We assume that the fluid density is uniform over the SRA so that K is a symmetric matrix by reciprocity. The time reversal operator is defined by K^*K where the asterisk denotes complex conjugation; it is a Hermitian matrix with N orthogonal eigenvectors and nonnegative eigenvalues.[6] The eigenvectors correspond to the SRA weighting functions that focus on individual scatterers in the waveguide. In the ocean environment, measurement of the response matrix k_{ij} can be difficult due to significant background noise levels particularly for the weaker returns associated with long ranges. Greater signal-to-noise ratios are possible by probing the waveguide with N orthogonal beams rather than the individual source array elements. Given a complete set of orthogonal array weighting vectors $S=\{\mathbf{e}_j|1\leqslant j\leqslant N\}$, the beam response $\tilde{k}_{ij}(t)$ is the backscattered field projected onto the $\mathbf{e}_i$ direction due to an array impulse weighted by the source function $\mathbf{e}_j$. The Fourier transform of $\tilde{k}_{ij}$ is $\tilde{K}$ and related to K by a similarity transformation,

$$\tilde{K}=E^TKE, \tag{10}$$

where the superscript T denotes transpose and E is an orthogonal matrix of the column vectors S satisfying $E^TE=EE^T=I$. The original DORT method is recovered when $E=I$. We note that $\tilde{K}$ is also a symmetric matrix so that reciprocity also applies in array beam space. The time reversal operator in this representation satisfies $\tilde{K}^*\tilde{K}=E^TK^*KE$ which can be decomposed in terms of the eigenvalues λ_i and eigenvectors $\mathbf{u}_i$ of K^*K as

$$\tilde{K}^*\tilde{K}=\sum_{i=1}^{N}\lambda_i(E^T\mathbf{u}_i)(E^T\mathbf{u}_i)^H,$$

where the superscript H denotes the conjugate transpose. Thus the time reversal operator in array beam space decomposes into the same eigenvalues λ_i with eigenvectors $E^T\mathbf{u}_i$. If the number of array elements is a power-of-two, a convenient set of array beams which maximize the transmitted power are the Hadamard–Walsh functions defined by the recursion relationship,[16]

$$H_N=\begin{bmatrix}H_{N/2} & H_{N/2}\\ H_{N/2} & -H_{N/2}\end{bmatrix},\quad H_2=\begin{bmatrix}1 & 1\\ 1 & -1\end{bmatrix}.$$

The matrix E of normalized weighting functions is then $E=(1/\sqrt{N})H_N$.

It is appropriate to mention here that we should be able to achieve TRM focusing from a single reverberation return (or single snapshot) instead of the N reverberations required to construct a TRO since a segment of reverberation data is considered as a transfer function from the distribution of sources along the interface. A single snapshot, however, requires a high signal to noise ratio (SNR) whereas the TRO

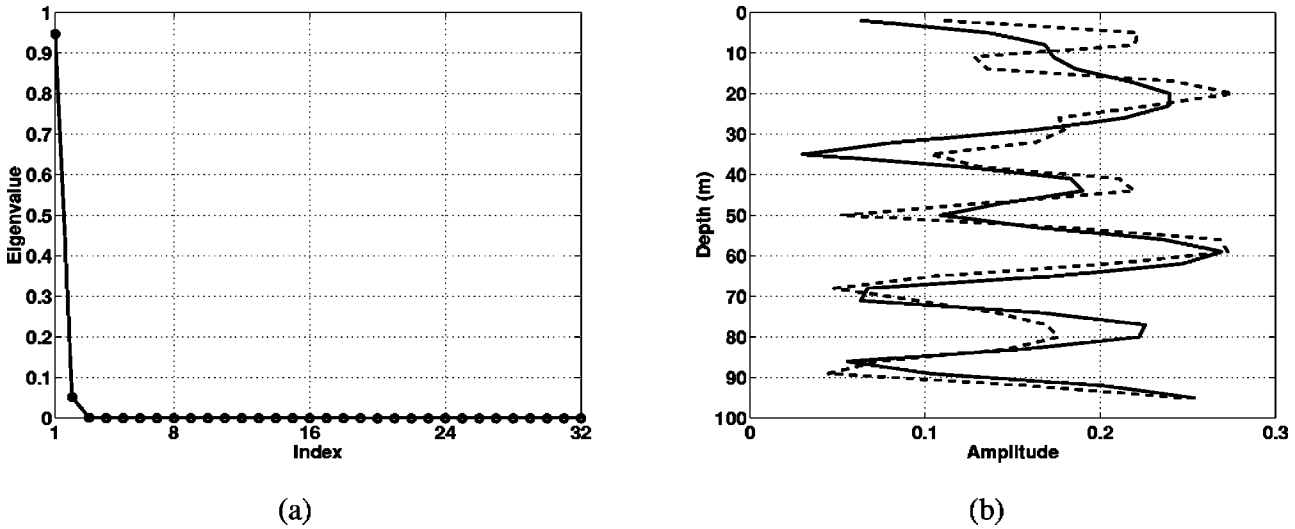

FIG. 2. (a) Eigenvalues and (b) amplitude of the first eigenvector of the time reversal operator. The time reversal operator is constructed from the reverberation returns at the center frequency of 200 Hz after applying a time window of $\Delta=50$ ms at $t_c+t_0\approx 1.58$ s which corresponds approximately to a round-trip travel time from the array to 1 km range. The vertical source/receive array (SRA) consists of 32 elements with the top element at 2 m depth. The source function is a Gaussian impulse with a width of $\tau=50$ ms resulting in a patch size of $c_0\tau/2=37.5$ m. In comparison, the magnitude of the transfer function at the center frequency due to a point scatterer located at $(x,z)=(1000,100)$ m is superposed (dashed). The overlap of the two vectors is 0.9.

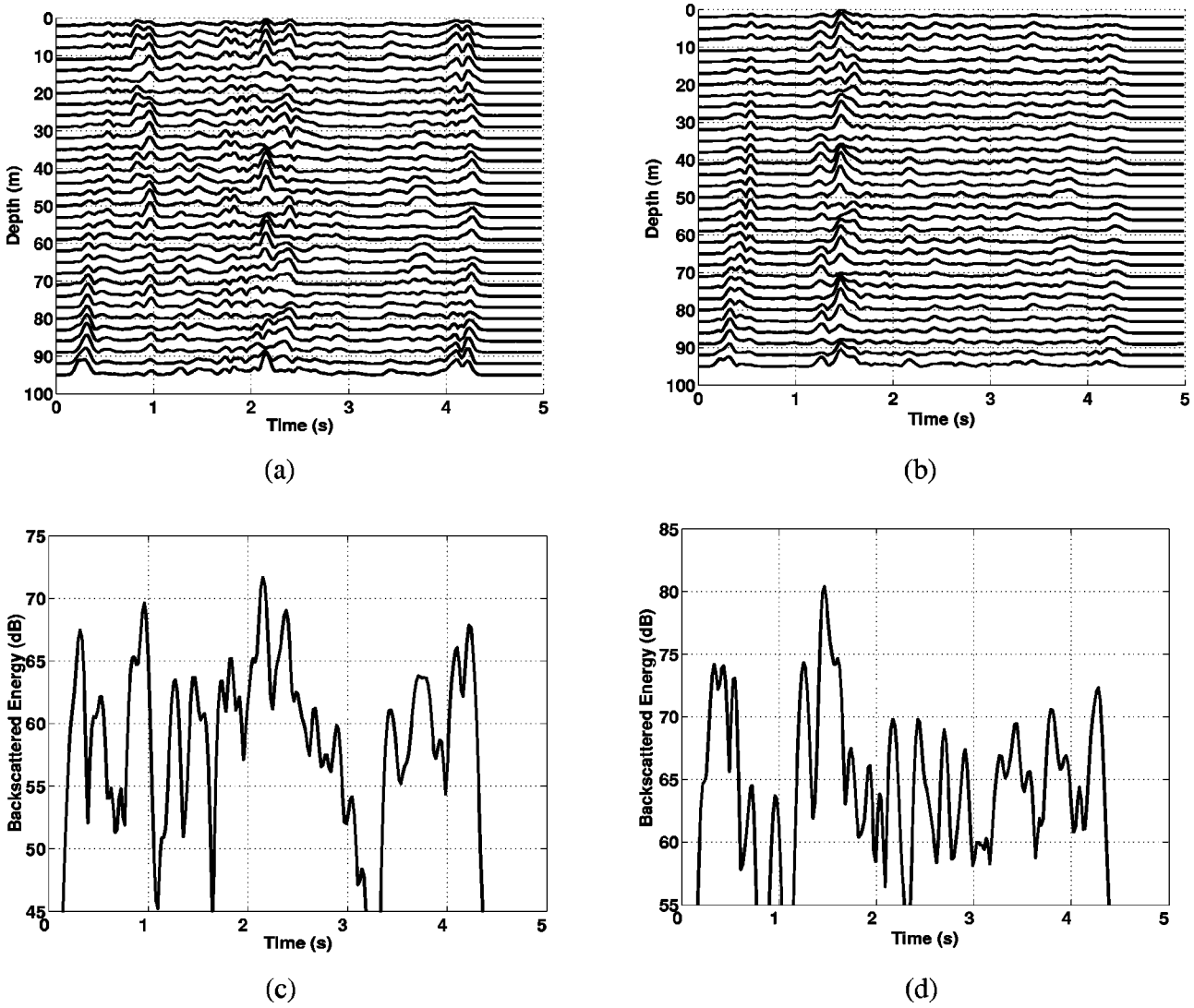

FIG. 3. (a) Reverberation from broadside transmission of a 50 ms Gaussian pulse with 32 channels. (b) Reverberation from 50 ms Gaussian pulse with array elements weighted by the first eigenvector of the time reversal operator as shown in Fig. 2(b). (c) and (d) The signal energy summed over all elements corresponding to (a) and (b), respectively. Note that the reverberation signal is maximized at $t=1.5$ s corresponding to a distance of 1 km from the SRA, approximately 10 dB above the background.

exploits a redundancy in the N measurements such that it effectively increases the SNR by $20\log N$ dB above the single snapshot measurement. The other issue is that a single snapshot, either in a phone or beam space, can hardly ensonify the field uniformly along the interface as compared to the N measurements in TRO approach. Finally, the preceding approach assumes that the rough interface and the environment are frozen during the N snapshot measurement. In practice, reverberation from all azimuthal directions will contribute to the field measured on the array and the environment will fluctuate. The azimuthal contributions to the reverberation can be modeled with random realizations of the rough surface. We observe that a single snapshot sample shows similar focusing as the N measurements in TRO approach in Sec. IV, but more detailed analysis is in preparation to include the effect of random realizations of the roughness.

IV. SIMULATIONS

Simulations in a Pekeris waveguide are used to demonstrate time reversed reverberation focusing in this section. The waveguide parameters are $\rho_1=1000\,\mathrm{kg/m^3}$, $c_1=1500\,\mathrm{m/s}$, $\rho_2=1900\,\mathrm{kg/m^3}$, $c_2=1600\,\mathrm{m/s}$, bottom attenuation $\alpha_2=0.8\,\mathrm{dB/\lambda}$, and depth $D=100\,\mathrm{m}$ for the waveguide shown in Fig. 1. The surface is pressure release and the rough interface realizations are modeled with the one-dimensional Goff–Jordan power-law spectrum[17,18]

$$P(q)=\pi L(1+(qL)^2)^{-3/2}, \tag{11}$$

where q is the horizontal wave number and $L=15\,\mathrm{m}$ is the correlation length of the roughness. In the simulations, the rough surface realizations extend from $0\leqslant x\leqslant 3$ km with a root mean square roughness height of 10 cm. The source-receiver array is vertical and consists of 32 transducer elements located in range at $x=0$ m and in depth at $\{z_i|z_i=2+3(i-1),1\leqslant i\leqslant 32\}$ meters. The source function used to probe the reverberation is a Gaussian impulse with amplitude A, center frequency ω_0, width τ, and delay t_0 given by $s(t)=A\exp(-\tau^{-2}(t-t_0)^2-i\omega_0 t)$. The mode functions and eigenvalues used to evaluate the backscattered field in Eq. (7) are computed with KRAKEN.[19]

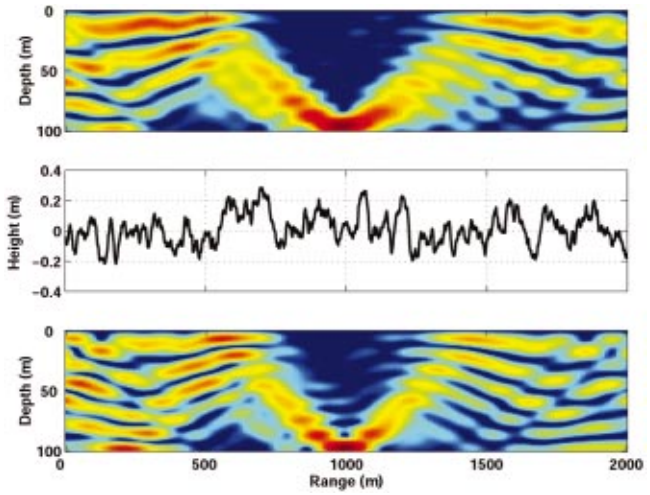

FIG. 4. Top panel: the intensity plot versus range and depth at center frequency of 200 Hz due to transmission of the first eigenvector of time reversal operator with the roughness shown in the middle panel. In comparison, the bottom panel shows the time reversal focusing for a point scatterer located at $(x,z)=(1000,100)$ m. Note that the spatial focusing in the top panel is broader due to distribution of sources along the interface as compared to a point scatterer in the bottom. The average modal group speed was assumed 1450 m/s for computation of time window corresponding to 1 km range. The dynamic range of the color plot is 20 dB.

The pulse parameters in our simulations are $\tau=50$ ms, $f_0=(2\pi)^{-1}\omega_0=200$ Hz and $t_0=0.2$ s. The time reversal operator is computed at the center frequency f_0 after applying a time window $w_1=w(t, 1\text{ km}, 50\text{ ms})$ to the reverberation which is modeled by the modal sum of Eq. (7). The eigenvalues and the first eigenvector $\mathbf{e}_1$ of the time reversal operator are shown in Fig. 2. For comparison, the transfer function $\mathbf{e}_{ps}$ at the center frequency due to a point scatter located at $\mathbf{x}=(1000,100)$ m is superimposed in a dashed line. The overlap between the two vectors is $|\mathbf{e}_1\cdot\mathbf{e}_{ps}|\approx 0.9$, a degradation of 1 dB. Figure 3 is a comparison of the reverberation time series due to (a) a broadside transmission from the SRA and (b) a transmission with elements weighted by the first eigenvector of the time reversal operator as shown in Fig. 2(b). The reverberation energy summed over all elements $E(t)=\Sigma|p_i(t)|^2$ of the SRA is shown in (c) and (d), respectively. In Fig. 3(d) the reverberation energy is maximized at $t=1.5$ s corresponding to a distance of 1 km from the SRA and the amplitude is approximately 10 dB above the background. Figure 4 shows the intensity plot in range and depth at the center frequency of 200 Hz confirming the spatial focusing property. The top panel is due to transmission of the first eigenvector of time reversal operator with the roughness shown in the middle. In comparison, the bottom panel shows the time reversal focusing for a point scatterer at $(x,z)=(1000,100)$ m. The average modal group speed was chosen 1450 m/s for computation of time window corresponding to 1 km range. Although it is not shown here, time reversal of a single snapshot of the reverberation due to a broadside transmission shows a similar result to Fig. 4 as noted in Sec. III. Figure 5 shows the time-depth distribution of energy at various ranges $x=0.6$, 0.8, 1.0, 1.2 km from the SRA. As expected, a strong focus of the energy is observed near the bottom at a range of 1 km from the SRA.

V. CONCLUSIONS

Focusing with a time reversal operator is extended to the case of stochastic reverberation returns from a rough sediment interface in an ocean waveguide. The weighting function for the source array is computed from the first eigenvec-

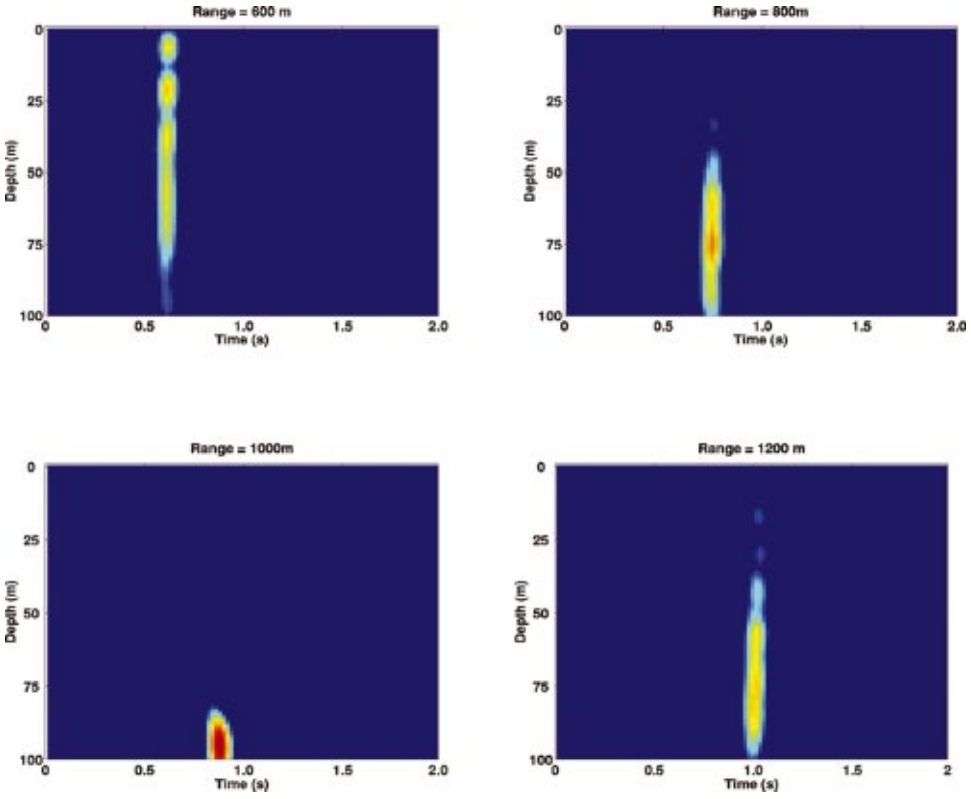

FIG. 5. Intensity snapshots versus time and depth due to the transmission of 50 ms Gaussian pulse with array elements weighted by the first eigenvector of the time reversal operator as shown in Fig. 2(b). The four plots show the intensity at four different ranges of $x=0.6$, 0.8, 1.0, 1.2 km from the SRA. Note the strong energy focus near at the bottom at a range of 1 km. The dynamic range of the color plot is 20 dB.

tor of the time reversal operator after selecting a time window corresponding to the intended focal range along the interface. In addition, the time reversal operator, originally formulated in the phone space, is generalized to the array beam space. Array beams will be useful in practical applications because they provide a greater power input than single source elements for measurement of backscatter from the rough interface which are usually very weak. Numerical simulations with a Pekeris waveguide demonstrate the proposed method.

ACKNOWLEDGMENTS

This work was supported by the Office of Naval Research. The authors would like to thank Seongil Kim and Brian Tracey for their helpful discussions.

[1] M. Fink, ''Time-reversed acoustics,'' Sci. Am. **281**, 91–97 (1999).
[2] M. Fink, ''Time reversal acoustics,'' Phys. Today **50**, 34–40 (1997).
[3] W. S. Hodgkiss, H. C. Song, W. A. Kuperman, T. Akal, C. Ferla, and D. R. Jackson, ''A long-range and variable focus phase-conjugation experiment in shallow water,'' J. Acoust. Soc. Am. **105**, 1597–1604 (1999).
[4] W. A. Kuperman, W. S. Hodgkiss, H. C. Song, T. Akal, C. Ferla, and D. R. Jackson, ''Phase conjugation in the ocean: Experimental demonstration of an acoustic time-reversal mirror,'' J. Acoust. Soc. Am. **103**, 25–40 (1998).
[5] H. C. Song, W. A. Kuperman, and W. S. Hodgkiss, ''A time-reversal mirror with variable range focusing,'' J. Acoust. Soc. Am. **103**, 3234–3240 (1998).
[6] C. Prada, J. L. Thomas, and M. Fink, ''The iterative time reversal process: Analysis of the convergence,'' J. Acoust. Soc. Am. **97**, 62–71 (1995).
[7] C. Prada, S. Manneville, D. Spoliansky, and M. Fink, ''Decomposition of the time reversal operator: Detection and selective focusing on two scatters,'' J. Acoust. Soc. Am. **99**, 2067–2076 (1996).
[8] N. Mordant, C. Prada, and M. Fink, ''Highly resolved detection and selective focusing in a waveguide using D.O.R.T. method,'' J. Acoust. Soc. Am. **105**, 2634–2642 (1999).
[9] B. H. Tracey and H. Schmidt, ''Seismo-acoustic field statistics in shallow water,'' IEEE J. Ocean. Eng. **22**, 317–331 (1997).
[10] W. A. Kuperman, ''Coherent component of specular reflection and transmission at a randomly rough two-fluid interface,'' J. Acoust. Soc. Am. **58**, 365–370 (1975).
[11] W. A. Kuperman and F. Ingenito, ''Attenuation of the coherent component of sound propagating in shallow water with rough boundaries,'' J. Acoust. Soc. Am. **61**, 1178–1187 (1977).
[12] W. A. Kuperman and H. Schmidt, ''Self-consistent perturbation approach to rough surface scattering in stratified elastic media,'' J. Acoust. Soc. Am. **86**, 1511–1522 (1989).
[13] F. B. Jensen, W. A. Kuperman, M. B. Porter, and H. Schmidt, *Computational Ocean Acoustics* (American Institute of Physics, New York, 1994).
[14] H. C. Song, W. A. Kuperman, W. S. Hodgkiss, T. Akal, and C. Ferla, ''Iterative time reversal in the ocean,'' J. Acoust. Soc. Am. **105**, 3176–3184 (1999).
[15] T. D. Mast, A. I. Nachman, and R. C. Waag, ''Focusing and imaging using eigenfunctions of the scattering operator,'' J. Acoust. Soc. Am. **102**, 715–725 (1997).
[16] A. M. Earnshaw and S. D. Blostein, ''A combined soft-decision deinterleaver/decoder for the IS95 reverse link,'' IEEE Trans. Veh. Technol. **49**, 448–456 (2000).
[17] H. Schmidt and W. A. Kuperman, ''Spectral representations of rough interface reverberation in stratified ocean waveguides,'' J. Acoust. Soc. Am. **97**, 2199–2209 (1995).
[18] J. Goff and T. Jordan, ''Stochastic modeling of seafloor morphology: Inversion of sea beam data for second order statistics,'' J. Geophys. Res., [Solid Earth Planets] **93**, 13589–13608 (1988).
[19] M. B. Porter, ''The KRAKEN Normal Mode Program,'' SACLANT Undersea Research Center SM-245, La Spezia, Italy, 1991.

Matched-field processing gain degradation caused by tidal flow over continental shelf bathymetry

Marshall H. Orr and Peter C. Mignerey[a)]
Acoustics Division 7120, Naval Research Laboratory, Washington, DC 20375-5320

(Received 19 March 2001; revised 1 October 2001; accepted 18 February 2002)

Temporally variable, range dependent sound-speed profiles measured during ebb flow and estimated for slack flow are used to quantify the variability of matched-field signal-processing gain degradation in shallow water propagation channels controlled by tidally driven stratified flow over variable bathymetry. Calculations along a 9.3 km range establish phase changes in the acoustic signal as the primary cause of a 3–9 dB degradation in the coherent matched-field processing output of a full water column vertical array. The work indicates that over a tidal cycle acoustic signal properties and matched-field processing gain can be expected to change continuously in a shallow water stratified channel that has bathymetry variability. Acoustic signals propagating in such tidal flow-controlled environments may be expected to display repeatable (over successive tidal cycles) and predictable changes in their phase coherent properties. These results suggest that matched-field processor replica fields used in the shelf/slope propagation environment will have to be updated regularly during a tidal cycle to maintain maximum processor gain. [DOI: 10.1121/1.1472496]

PACS numbers: 43.30.Re [DLB]

I. INTRODUCTION

The flow of stratified water over sloping bathymetry is known to result in temporal and spatial variability in the density and associated sound speed fields.[1–15] Shallow water currents are largely driven by the tide. Consequently, acoustic signals propagating over fixed paths in the continental shelf and slope environment are expected to be temporally variable and exhibit some degree of repeatability in their properties over a tidal cycle. The quantitative impact of flow-induced sound-speed variability on phase-coherent acoustic signal processors has not been previously addressed.

This work quantifies the temporal and spatial variability of an acoustic signal's phase and amplitude and the resultant gain of a matched field processor along a propagation path whose sound-speed field is perturbed by tidally driven stratified fluid flow over bathymetry.

This work suggests that stratified tidal flow over bathymetry will control the temporal and spatial properties of acoustic signals and that these properties may be estimated or predicted by using nonhydrostatic hydrodynamic models to calculate the temporal and spatial variability of the density and associated sound-speed field profile.

II. BACKGROUND

The flow characteristics of a stratified fluid depend on the buoyancy frequency, the velocity gradient as a function of depth, and the slope of the ocean bottom. The gradient Richardson number, a measure of fluid stability, largely governs the type of fluid phenomena, e.g., lee wave, internal tide, hydraulic jump, etc., that will occur for a specific combination of bottom slope gradient, water column stratification, and vertical current shear. An extensive literature describing the variety of fluid processes associated with stratified flow over bathymetry exists.[1–15]

To the authors' knowledge, the only theoretical or numerical study of acoustic propagation through flow controlled sound-speed fields was done by Sherwin.[16] He presented numerical simulations that related variations in the sound-speed field to tidal flow across a continental shelf break and slope. He used a two-dimensional *f*-plane hydrodynamic model to simulate linear internal tides generated by a barotropic tide impinging on the continental slope and shelf. An acoustic ray-tracing model was used to demonstrate that acoustic signal intensity fluctuations caused by the flow induced time varying sound speed were as large as 5 dB. Sherwin did not address the phase coherent properties of the acoustic signals.

We have used physical oceanographic data[17] taken during ebb tide flow over depth variable bathymetry to construct a range-dependent sound speed profile. The data were also used to simulate a slack-flow sound-speed profile. Complex acoustic signals were propagated through a 9.3 km propagation path for the ebb and slack tidal flow conditions. Changes in the performance of a matched field processor for the two propagation conditions were calculated.[18]

III. EXPERIMENT

The data set used to develop the range-dependent sound-speed field was taken aboard the R/V Endeavor on the New Jersey Shelf, during the Shallow Water Acoustics Random Media Propagation Experiment[17] (SWARM-95). A shipboard acoustic Doppler current profiler (ADCP), a tow-yo CTD, and a 200 kHz high frequency acoustic flow visualization system were used to characterize the propagation channel during ebb tide flow as the ship steamed along a 9.3 km track over variable bathymetry ($z=33-56$ m). The data were taken from 13:52 to 16:52 EDT on 25 July 1995. The tow-yo

[a)]Electronic mail: mignerey@wave.nrl.navy.mil

TABLE I. Range colors for the CTD casts plotted in Figs. 1–4.

Cast	Range (km)	Color
1	0.2	Blue
5	1.2	Green
9	2.5	Red
13	4.1	Cyan
17	6.1	Magenta
21	9.2	Yellow

CTD system was cycled from $z=7$ m to ~7 m above the bottom. Ten and one half full CTD cycles were obtained providing 21 profiles for the temperature and salinity as a function of depth. The range and plot colors for six of those profiles are listed in Table I. The temperature profiles, Fig. 1, exhibit two distinct layers of water separated by a thermocline extending from 15–24 m and below which is 9 C deep water. The salinity profiles, Fig. 2, show a halocline residing at 18 m and the sound-speed field, Fig. 3, has a downward refracting profile above the thermocline. Bottom bathymetry was extracted from the high frequency acoustic flow visualization data set.

The shipboard RD Instruments 150 kz Doppler current profiler (ADCP) measured the depth/range-dependent fluid velocity field. Velocity components were obtained at 4 m depth intervals between $z=11$ m and ~10 m above bottom. The ADCP measurements were averaged over 1 min time intervals. They were further averaged over the duration of each CTD half-cycle to obtain 21 velocity profiles that were in coincidence with the CTD profiles. The accuracy of the resulting velocity estimates is ± 0.013 m/s. Velocity was calculated in true East and North projections. To determine the down-slope current shown in Fig. 4, the velocity components were projected onto a unit vector pointing down the slope gradient that was obtained from a navigation chart. The current versus depth profiles for casts 1, 5, 9 in the shallow region show velocity maxima at 15 and 23 m separated by a local minimum at 19 m. Profiles 13, 17, and 21 in the deep

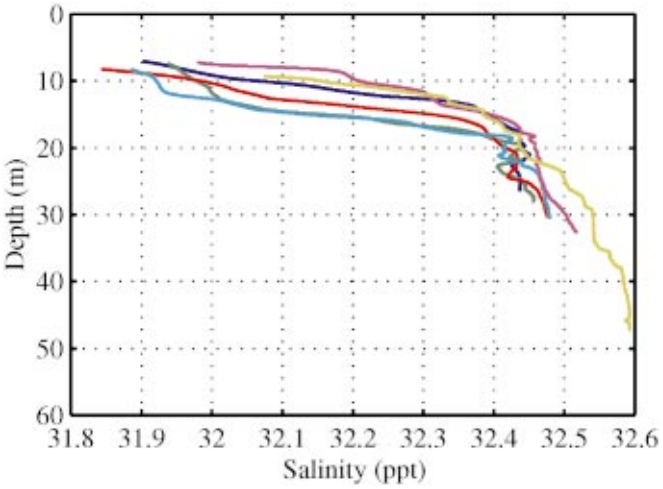

FIG. 2. Salinity versus depth profiles from the tow-yo CTD showing the halocline location. See Table I for the range color key.

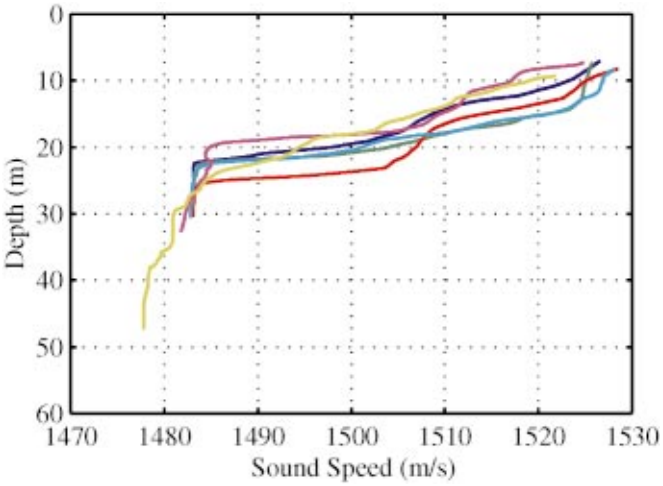

FIG. 3. Sound speed versus depth showing a downward refracting profile above the thermocline. See Table I for the range color key.

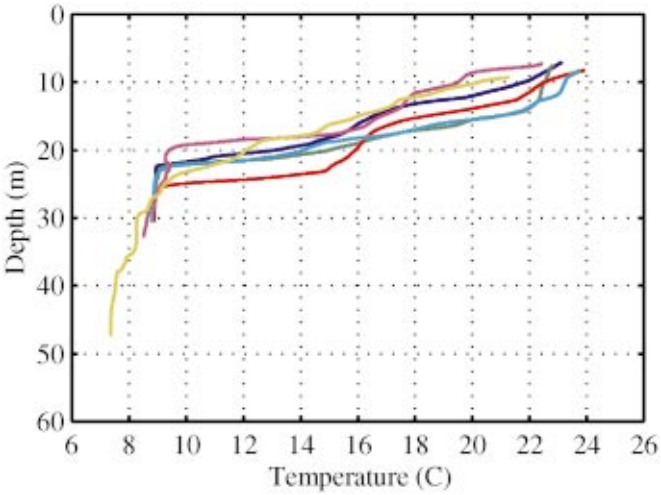

FIG. 1. Temperature versus depth profiles from the tow-yo CTD showing two distinct layers of water separated by a thermocline. See Table I for the range color key.

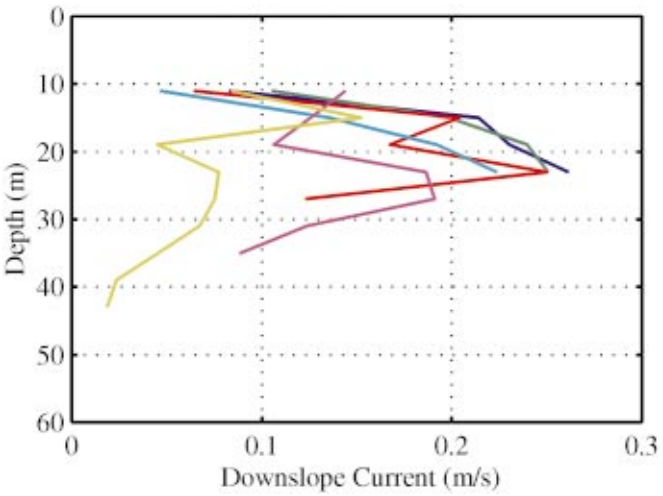

FIG. 4. Current versus depth profiles for casts 1, 5, and 9 in the shallow region and casts 13, 17, and 21 in the deep region. See Table I for the range color key.

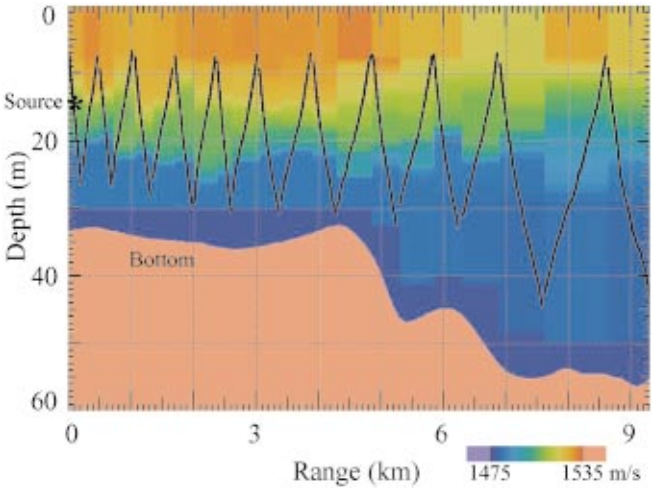

FIG. 5. Interpolated speed of sound for the measured ebb-flow state as a function of range and depth. The position of the CTD tow-fish that acquired the data is shown in black.

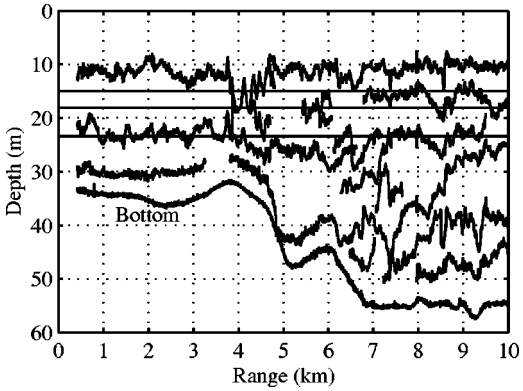

FIG. 6. Digitized high-frequency acoustic backscatter layers detected during ebb flow down the slope showing an internal jump with flow separation on the slope. The bottom curve traces the ocean floor. The three horizontal lines mark the location of: (upper) the top edge of the thermocline coincident with an ADCP velocity maximum, (middle) halocline coincident with an ADCP velocity minimum, (lower) the bottom edge of the thermocline coincident with an ADCP velocity maximum.

region show velocity maxima at 15 and 25 m separated by a local minimum at 19 m.

IV. ENVIRONMENT

A. Sound speed

The sound speeds calculated from the tow-yo CTDs are shown as a function of depth in Fig. 3. In the shallow section (~30 m) of the transect, a strong negative gradient in the upper water column is followed by a nearly isovelocity layer just above the ocean bottom. The gradient exhibits a number of step-like structures. In the deeper section of water (0–48 m) another negative gradient followed by near isovelocity water is observed. The sound-speed profiles, shown in Fig. 3, are downward refracting above the thermocline. The positions where these data were acquired are shown in Fig. 5 (black lines) superimposed on a two-dimensional interpolation of the sound-speed field. A horizontal interpolation was done in a piecewise constant manner over the time and range interval spanned by each tow. The most shallow data points were extended up to the surface and the deepest points were extended down to a scattering layer that resides 5 m above the bottom. A 5-m-thick cold boundary layer with a 1477.8 m/s speed of sound is assumed to lie upon the bottom. The reasons for this assumption are presented in the following. Geoacoustic parameters consistent with those obtained in the SWARM-95 experiment[17] were used to characterize the bottom. A 5-m-thick layer of sediment with a sound speed of 1600 m/s and density of 1800 kg/m^3 is assumed to lie above a semi-infinite half-space with a 1750 m/s sound speed.

The sound-speed field in Fig. 5 is referred to herein as the ''ebb flow'' case. Acoustic fields were propagated through both this environment and that of a ''slack-flow'' case. The two environments are the same except the slack-flow speed of sound within the water is held constant at 1477.8 m/s below a depth of 30 m for all ranges. The slack-flow sound-speed profile representation is supported by Long's laboratory experiments[19] and computer simulations of shelf hydrodynamics by Lamb.[20] Both show significant downward depression of relatively warm water for off-shelf flow, in agreement with our high-frequency backscatter data shown in Figs. 6 and 7, and followed by recovery to stratified equilibrium during the slack-flow phase of the flow. In this backscatter data, the lowest scattering layer that resides approximately 5 m above the bottom follows the slope down into cold water and then rises back up to a depth of 30 m downstream in the deepest water. CTD data obtained from below this layer are cold with a sound speed of 1477.8 m/s. From this we conclude the scattering layer marks the top edge of a cold, dense layer of water that rests on the bottom. Thus we feel it is appropriate to model the slack-flow environment with a uniform layer of cold water below 30 m.

B. Flow visualization

Scattering layers detected with a 200 kHz nadir incident backscattering system imaged the locations of the density steps in the density structure of the water column. These density steps are seen in the sound speed versus depth plots, Fig. 3. Digitized records of the scattering layers versus range are shown in Figs. 6 and 7. The data for both figures were obtained approximately 20 min to 3 h apart during the same

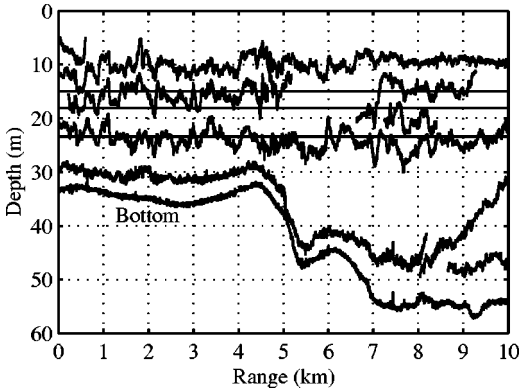

FIG. 7. High-frequency backscatter layers during the same ebb-flow phase as in Fig. 6 shows the persistence of the internal jump over time spans 20 min–3 h later. The data curves are the same as in Fig. 6.

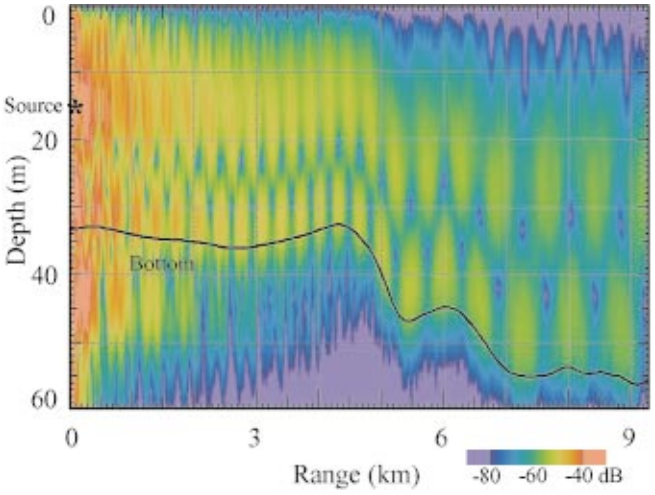

FIG. 8. Acoustic-field amplitude for a 200 Hz source located in the shallow region at a depth of 15 m. The environment is ebb flow. The dynamic range is −40 dB (red) to −80 dB (blue) relative to the source level. Light red and light blue mark out-of-range data.

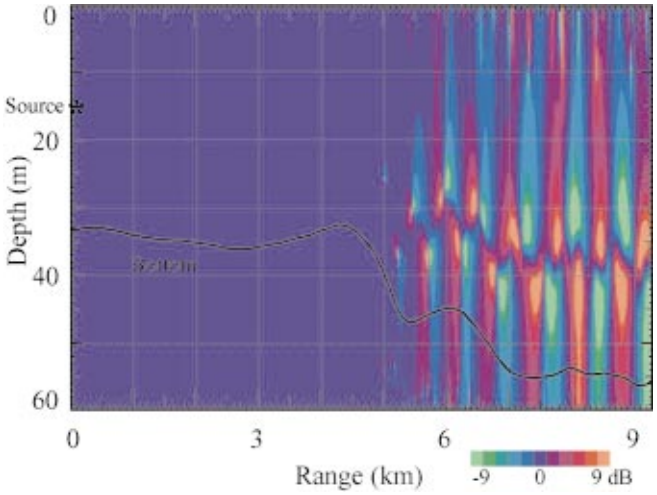

FIG. 10. Acoustic-field amplitude difference: ebb flow minus slack flow. The dynamic range is −9 dB (green) to 9 dB (red). Blue marks 0 dB difference while light red and light green mark out-of-range data.

ebb current phase that was flowing off of the shelf. As the flow proceeded from shallow to deep water, the deeper scattering layers separated (moving downward) showing the presence of a hydraulic jump. Analogous fluid phenomena have been inferred from acoustic and radar backscattering records by other investigators (e.g., Farmer and Smith,[21] Orr and Hess[22]).

The separation of the scattering layers and associated changes in the sound-speed structure are flow controlled, i.e., tidally controlled. When the flow speed slows to zero the vertically displaced scattering layers in the deeper water will return to nearly horizontal layers (Long[19]). One of the main features in the record is the hydraulic jump seen in the region between 0.6 km and approximately 3 km down-range of the slope-break. The upper and lower horizontal lines mark the positions of maxima in the velocity profile that are coincident with sharp steps in the thermocline or sound-speed structure. The high spatial-frequency variability seen in the digitized records is caused by internal waves. Their perturbation of the sound-speed structure is not included in the transmission loss calculations to be presented.

Note there is a strong similarity between the shape of the jump in our Figs. 6 and 7 and those presented in Figs. 2–5 by Long.[19] Supporting evidence for our interpretation comes by evaluating the internal Froude number, F_i, as defined by Long.[19] For flows of this type $F_i = u/\sqrt{gH\Delta\rho/\overline{\rho}}$, where u is the barotropic current, g is the acceleration of gravity, H is water depth, $\Delta\rho$ is the difference between maximum and minimum density, and $\overline{\rho}$ is the mean density. The internal Froude numbers we measure are $F_i = 0.17$ in the shallow region and $F_i = 0.10$ in the deep region while Long[19] observes jumps for $F_i \geqslant 0.14$. Thus, we believe we are seeing a transition from supercritical flow to subcritical flow.

C. Currents

As indicated, the current profiles shown in Fig. 4 were measured using a ship-borne ADCP. The shallow water (~30 m) current profiles (casts 1, 5, and 9) show a pair of local

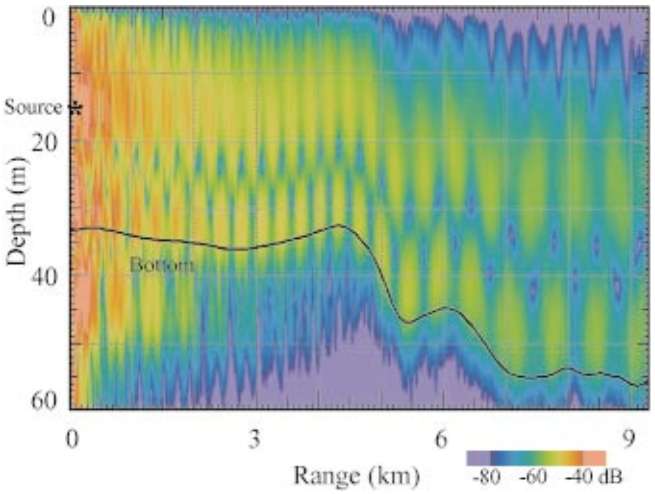

FIG. 9. Acoustic-field amplitude for a 200 Hz source located in the shallow region at a depth of 15 m. The environment is slack flow. The dynamic range is −40 dB (red) to −80 dB (blue) relative to the source level. Light red and light blue mark out-of-range data.

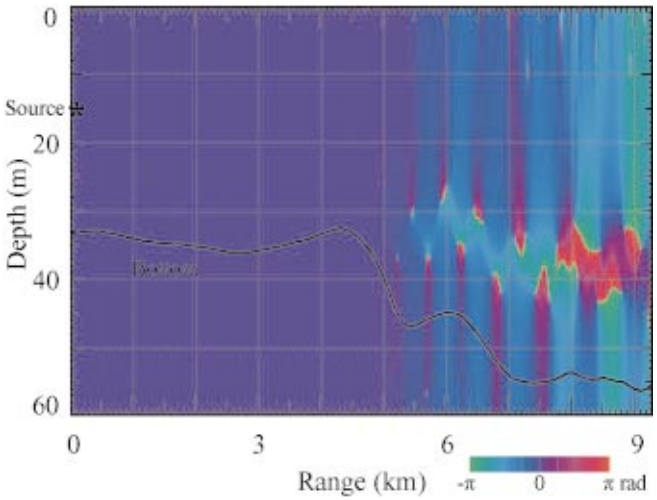

FIG. 11. Acoustic-field phase difference: ebb flow minus slack flow. The range is $-\pi$ (green) to $+\pi$ (red). Blue marks no phase difference.

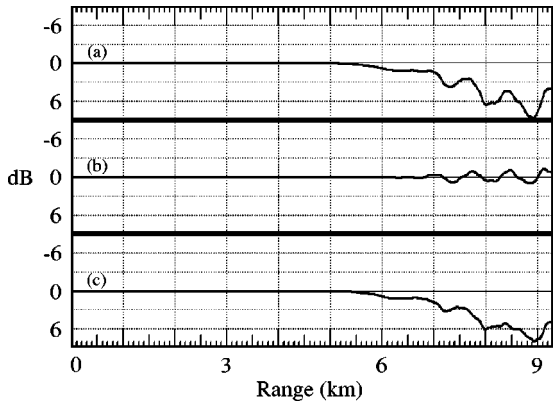

FIG. 12. Environmentally induced matched-field processor degradation: (a) total coherent array-processor loss, (b) loss due to amplitude errors, (c) loss due to phase errors.

velocity maxima. One maximum occurs at 15 m coincident with the upper edge of the thermocline and the other at 23 m coincident with the lower edge. The currents (casts 13, 17, and 21) measured in deeper water (~60 m) exhibit significant depth-dependent variability consistent with that produced by flow separation and hydraulic jumps. The maximum velocity gradients over the entire region are $0.025 \pm 0.005\ \mathrm{s}^{-1}$. These current gradients are quite large in relation to the mean current, 0.140 ± 0.068 m/s, over water depths of 30–55 m.

V. ACOUSTIC PROPAGATION

The range-dependent complex acoustic field has been calculated using the sound-speed profiles for both the ebb-tide flow and slack tide. The difference between the two propagation conditions has been quantified by comparing the two acoustic field's power and phase variability as a function of range from a source that was located upstream from the bathymetric variability, see Fig. 5.

Simulated acoustic fields propagating through both ebb-flow and slack-flow environments were generated using a parabolic equation model. The source was placed at a depth of 15 m in 33 m of water. The signals propagated down slope into deep water. Figure 8 shows the calculated acoustic field for a 200 Hz source under ebb-flow conditions. At this frequency, the field appears to be dominated by the second mode with significant energy levels in the deep region where the two environments differ. This propagation configuration should be a good probe of the relative difference between the two acoustic fields caused by the flow-induced sound-speed variability.

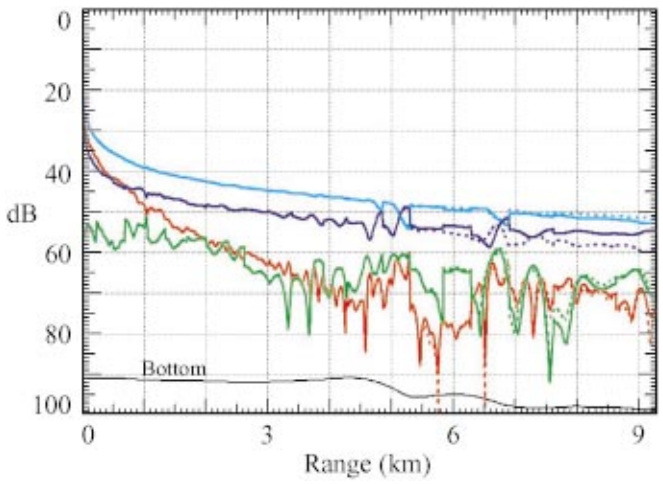

FIG. 13. Acoustic mode energy as a function of range for four modes under two flow conditions: ebb flow (solid line), slack flow (dotted line); mode 1 (blue), mode 2 (cyan), mode 3 (green), mode 4 (red). The bottom bathymetry is shown below in black.

Figure 9 shows the same calculation for slack-flow conditions. The main difference between the ebb-flow and slack-flow acoustic fields is a realignment of nulls that cause as much as ± 9 dB difference in local field levels at various points within the deep region. Figure 10 shows the resulting difference in field levels as a function of range and depth. The realignment of nulls also causes very large relative phase differences, up to π radians, between the phase of the two fields as shown in Fig. 11. Although the field intensity is weak near nulls, Fig. 11 also exhibits significant phase errors in regions where the fields shown in Figs. 8 and 9 are strong. In the following we demonstrate that such phase errors cause degradation in the output of a matched-field array processor.

To determine the impact of tidally driven environmental changes on coherent array processing, the slack-flow acoustic field was first matched against itself and then against the ebb-flow acoustic field using a linear matched-field processor defined over a vertical line array spanning the water column. Matched-field array gain degradation is then defined as follows. Letting $\mathbf{e}=[e(r,z_i)]^t$ represent the expected slack-flow acoustic field on a vertical array, where r is range, z depth, i hydrophone index, and letting $\mathbf{f}=[f(r,z_i)]^t$ represent the measured ebb-flow field at the array elements, the matched-field array gain degradation is given by the ratio of the matched-field processor power to the expected power, $D(r) = |\mathbf{e}^t\mathbf{f}|^2/|\mathbf{e}^t\mathbf{e}|^2$. The numerator, $|\mathbf{e}^t\mathbf{f}|^2$, is the output of a linear matched-field processor which may be interpreted as a cross correlation between the expected and measured acoustic fields as measured at the hydrophone locations. The cross correlation is sensitive to errors in the measured field, $f(r,z_i)$. The product, $D(r)$, may be split into an amplitude component, $A(r)=|\mathbf{f}|^2/|\mathbf{e}|^2$, and a phase component given by the inner product of unit vectors, $P(r)=|\hat{\mathbf{e}}^t\hat{\mathbf{f}}|^2$, where $\hat{\mathbf{e}} = \mathbf{e}/|\mathbf{e}|$ and $\hat{\mathbf{f}}=\mathbf{f}/|\mathbf{f}|$. The array gain degradation is then expressed as the product, $D(r)=A(r)P(r)$. The amplitude component represents degradation due to a change in power flux through the array aperture and the phase component represents degradation due to a relative misalignment between the steering and data vectors that is caused by phase mismatch at the complex valued array elements. Note that as inner products over the array aperture, these quantities are insensitive to those hydrophones situated near nulls where the phase errors are largest but where the field is weakest. Rather, array gain degradation is caused by an accumulation of errors across the entire aperture with the heaviest contribution coming from those hydrophones receiving a large field amplitude of uncertain phase.

The degradation (difference between the slack-flow and ebb-flow matched-field processor outputs) due to flow-

induced acoustic field mismatch is shown in Fig. 12. The upper curve, Fig. 12(a), shows $10\log_{10} D(r)$, the total coherent array-processor loss with a dynamic range of ± 9 dB. Mismatch between the ebb-flow and slack-flow environments causes as much as 9 dB loss in the output. Loss due to amplitude variability alone, $10\log_{10} A(r)$, shown in Fig. 12(b), is about ± 1 dB, which is relatively small. Thus the total power flux through the water column is not greatly affected by tidal flow changes in the sound-speed structure. Flow-induced phase changes are the primary cause of coherent degradation. A plot of the loss due to flow-induced phase changes, $10\log_{10} P(r)$, shown in Fig. 12(c), accounts for most of the 9 dB degradation. These calculations show that small, flow-induced changes in the sound-speed field can cause sufficient variability in the phase of an acoustic field to significantly degrade the output of a matched-field processor. The resulting phase mismatch between the replica and received acoustic fields is the fundamental cause of coherent processor degradation.

The influence of the hydrodynamic flow state on the first four modes of a 200 kHz acoustic field is shown in Fig. 13. These data were obtained by projecting the simulated acoustic fields from the parabolic equation model onto a set of eigenfunctions obtained by running a normal mode model for the same environments. The solid lines trace mode energy for the ebb-flow case and the dotted lines for the slack-flow case. Although the second mode dominates the acoustic field, the first mode is more sensitive to environmental changes. The difference in mode 1 energy ranges from 3 to 5 dB between slack and ebb flow in the deep region. The difference in mode 2 energy is less than 2 dB. Note that where mode 1 loses energy, modes 2 and 3 gain. The energy difference is caused by a flow-controlled shift of acoustic energy into the higher modes.

VI. CONCLUSIONS

Matched-field signal processing gain degradation of 3–9 dB was calculated for a shallow water propagation channel with a temporally variable sound-speed profile controlled by tidally driven stratified flow over bathymetric relief. This work suggests that matched field processor replica fields used in the shelf/slope propagation environment will have to be regularly updated during a tidal cycle to maintain maximum processor gain. The calculations, for a 9.3 km range, show that signal phase changes were significant and the primary cause of degradation in the coherent matched-field processor output of a full-water-column vertical array. The work indicates that acoustic signal properties in a stratified shallow water channel can be expected to change continuously over a tidal cycle. Because the tidal flow is cyclic it is expected that shallow water acoustic signals may display repeatable and predictable changes in their phase coherent properties (e.g., with a $\sim$12 h period if the M2 tide is dominate). The above-presented analysis demonstrates the control of an acoustic field and matched field processor gain by tidally induced stratified flow over bathymetry. Such control suggests that coupling of nonhydrostatic fluid dynamic models with acoustic propagation models may be necessary to achieve environmentally adaptive matched field processing.

ACKNOWLEDGMENT

This work was supported by the Office of Naval Research.

[1] J. S. Turner, *Buoyancy Effects in Fluids* (Cambridge University Press, Cambridge, 1973).
[2] D. Halpern, "Observations on short-period internal waves in Massachusetts Bay," J. Mar. Res. **29**, 116–132 (1971).
[3] L. R. Haury, M. G. Briscoe, and M. H. Orr, "Tidally generated internal wave packets in Massachusetts Bay," Nature (London) **278**, 312–317 (1979).
[4] H. Sandstrom and J. A. Elliott, "Internal tide and solitons on the Scotian Shelf: A nutrient pump at work," J. Geophys. Res. **89**, 6415–6426 (1984).
[5] R. D. Pingree, G. T. Mardell, and A. L. New, "Propagation of internal tides from the upper slopes of the Bay of Biscay," Nature (London) **321**, 154–158 (1986).
[6] D. Brickman and J. W. Loder, "Energetics of the internal tide on northern Georges Bank," J. Phys. Oceanogr. **23**, 409–424 (1993).
[7] Y. Kuroda and H. Mitsudera, "Observation of internal tides in the East China Sea with an underwater sliding vehicle," J. Geophys. Res. **100**, 10801–10816 (1995).
[8] P. Brandt, A. Rubino, D. Quadfasel, W. Alpers, J. Sellschopp, and H. V. Fiekas, "Evidence for the influence of Atlantic-Ionian stream fluctuations on the tidally induced internal dynamics in the Strait of Messina," J. Phys. Oceanogr. **29**, 1071–1080 (1999).
[9] C. Y. Lee and R. C. Beardsley, "The generation of long nonlinear internal waves in a weakly stratified shear flow," J. Geophys. Res. **79**, 453–462 (1974).
[10] T. Maxworthy, "A note on the internal solitary waves produced by tidal flow over a three-dimensional ridge," J. Geophys. Res. **84**, 338–346 (1979).
[11] P. G. Baines, "On internal tide generation models," Deep-Sea Res. **29**, 307–338 (1982).
[12] P. G. Baines and F. Xin-Hua, "Internal tide generation at a continental shelf slope/junction: A comparison between theory and a laboratory experiment," Dyn. Atmos. Oceans **9**, 297–314 (1985).
[13] P. E. la Violette, D. R. Johnson, and D. A. Brooks, "Sun-glitter photographs of Georges Bank and the Gulf of Maine from the space shuttle," Oceanography (The Oceanography Society, MD) **3**, 43–49 (1990).
[14] J. C. Preisig and T. F. Duda, "Coupled acoustic mode propagation through continental-shelf internal solitary waves," IEEE J. Ocean. Eng. **22**, 256–269 (1997).
[15] T. F. Duda and J. C. Preisig, "A modeling study of acoustic propagation through moving shallow-water solitary wave packets," IEEE J. Ocean. Eng. **24**, 16–32 (1999).
[16] T. J. Sherwin, "A numerical investigation of semi-diurnal fluctuations in acoustic intensity at a shelf edge," in *Ocean Variability and Acoustic Propagation* (Kluwer Academic, Dordrecht, 1991), pp. 579–592.
[17] J. R. Apel *et al.*, "An overview of the 1995 SWARM shallow-water internal wave acoustic scattering experiment," IEEE J. Ocean. Eng. **22**, 465–500 (1997).
[18] M. H. Orr and P. C. Mignerey, "Flow-controlled acoustic propagation channels on continental shelves," J. Acoust. Soc. Am. **106**, 2302(A) (1999).
[19] R. R. Long, "A laboratory model resembling the "Bishop-Wave" phenomenon," Bull. Am. Meteorol. Soc. **34**, 205–211 (1953).
[20] K. G. Lamb, "Numerical experiments of internal wave generation by strong tidal flow across a finite amplitude bank edge," J. Geophys. Res. **99**, 843–864 (1994).
[21] D. M. Farmer and J. D. Smith, "Tidal interaction of stratified flow with a sill in Knight Inlet," Deep-Sea Res., Part A **27**, 239–254 (1980).
[22] M. H. Orr and F. R. Hess, "Remote sensing of internal waves, isopycnal surfaces and interleaving water masses in the vicinity of Hudson Canyon," EOS Trans. Am. Geophys. Union **59**, 1107 (1978).

The high-frequency backscattering angular response of gassy sediments: Model/data comparison from the Eel River Margin, California

Luciano Fonseca[a)]
Center for Coastal and Ocean Mapping, University of New Hampshire, Durham, New Hampshire 03824 and PETROBRAS/Research Center, Cidade Universitaria, Ilha do Fundao, Rio de Janeiro, RJ, 21949-900, Brazil

Larry Mayer[b)]
Center for Coastal and Ocean Mapping, University of New Hampshire, Durham, New Hampshire 03824

Dan Orange[c)]
AOA Geophysics, Marine Geoscience Division, 123 Walker Valley Road, Castroville, California 95012-9733

Neal Driscoll[d)]
Woods Hole Oceanographic Institution, Woods Hole, Massachusetts 02543

(Received 25 January 2001; revised 4 December 2001; accepted 18 February 2002)

A model for the high-frequency backscatter angular response of gassy sediments is proposed. For the interface backscatter contribution we adopted the model developed by Jackson *et al.* [J. Acoust. Soc. Am. **79**, 1410–1422 (1986)], but added modifications to accommodate gas bubbles. The model parameters that are affected by gas content are the density ratio, the sound speed ratio, and the loss parameter. For the volume backscatter contribution we developed a model based on the presence and distribution of gas in the sediment. We treat the bubbles as individual discrete scatterers that sum to the total bubble contribution. This total bubble contribution is then added to the volume contribution of other scatters. The presence of gas affects both the interface and the volume contribution of the backscatter angular response in a complex way that is dependent on both grain size and water depth. The backscatter response of fine-grained gassy sediments is dominated by the volume contribution while that of coarser-grained gassy sediments is affected by both volume and interface contributions. In deep water the interface backscatter is only slightly affected by the presence of gas while the volume scattering is strongly affected. In shallow water the interface backscatter is severely reduced in the presence of gas while the volume backscatter is only slightly increased. Multibeam data acquired offshore northern California at 95 kHz provides raw measurements for the backscatter as a function of grazing angle. These raw backscatter measurements are then reduced to scattering strength for comparison with the results of the proposed model. The analysis of core samples at various locations provides local measurements of physical properties and gas content in the sediments that, when compared to the model, show general agreement.
[DOI: 10.1121/1.1471911]

PACS numbers: 43.30.Gv, 43.30.Ft, 43.30.Hw [DLB]

I. INTRODUCTION

Fine-grained sediments from continental margins are frequently rich in bubbles of free gas (Richardson and Davis, 1998). These gas bubbles, even in very small quantities, can dominate and change the geoacoustic characteristics of seafloor sediment and have a significant effect on the propagation of acoustic waves (Lyons *et al.*, 1996; Anderson *et al.*, 1998; Wilkens and Richardson, 1998). Anderson *et al.* (1998) describe three types of bubbles in sediments, in order of increasing size and disturbance: (1) interstitial bubbles, which are very small bubbles within the undistorted interstitial pore spaces of the sediment; (2) reservoir bubbles, which are a reservoir of gas occupying a region of undistorted sediment solid framework larger than the normal pore space; and (3) sediment displacing bubbles, which are bubble cavities that are larger than the normal interstitial space and that are surrounded by either undisturbed or slightly distorted sediments. While the nature of the effect on acoustic propagation will differ with the type of bubbles, in general, if gas bubbles are trapped in the sediment structure, their scattering contribution will be stronger than the contribution of other scatterers and will control the total backscattering response. In this paper, we propose a high-frequency (to 100 kHz) acoustic backscatter model for the seafloor that takes into account the contribution of gas bubbles and then we test the model against both multibeam sonar backscatter data and core data collected in regions known to have gassy sediments.

Traditionally, high-frequency backscatter cross-section models consider two different processes: interface scattering

[a)]Electronic mail: luciano@ccom.unh.edu
[b)]Electronic mail: lmayer@unh.edu
[c)]Electronic mail: dan_orange@aoageophysics.com
[d)]Electronic mail: ndriscoll@whoi.edu

and volume scattering (Ivakin, 1998). The interface scattering occurs at the water–sediment interface, where the sea floor acts as a reflector and scatterer of the incident acoustic energy. A portion of the incident acoustic energy will be transmitted into the seafloor. This transmitted energy will be scattered by heterogeneities in the sediment structure, which are the source of the volume scatter (Novarini and Caruthers, 1998). In the approach developed in this paper we explore how that these two contributions are affected by the presence of gas.

For the interface backscatter contribution we have adopted the model developed by Jackson *et al.* (1986), but added modifications to accommodate gas bubbles. Interface backscatter is normally dependent on the acoustic impedance as well as the acoustic attenuation in sediments, both of which are affected by the presence of gas. The results of Anderson and Hampton (1980a, b), who modeled the influence of gas bubbles on sediment properties, will be used to estimate the changes in interface backscatter.

Models for volume scattering include refraction at the water–sediment interface and attenuation in the sediment, both of which are altered when gas is present. For the volume backscatter contribution we have developed a model based on the presence and distribution of gas in the sediment. We treat bubbles as individual discrete scatterers that integrate to create the total bubble contribution. The integration is based on the statistical distribution of bubble sizes, derived from measured histograms in muddy sediments (Anderson *et al.*, 1998). This total bubble contribution is then added to the volume contribution of other discrete scatterers.

To test the ideas outlined above we use data collected on the highly sedimented Eel River Margin offshore northern California. The Eel River basin was extensively investigated as part of the *STRATAFORM* (STRATA FORmation on the Margins) project, a multiyear, multiinvestigator program funded by the U.S. Office of Naval Research (Nittrouer, 1998). During this project, an immense database of marine information was collected (Mayer *et al.*, 1999), including multibeam sonar backscatter data collected at 95 kHz and numerous core sampling sites with measurements of sediment physical properties and free gas content. Multibeam sonar systems map the seabed through a wide range of grazing angles, revealing subtle differences in the backscatter response for different materials on the seafloor (de Moustier and Alexandrou, 1991). In this study, multibeam-sonar raw backscatter measurements will be reduced to scattering strength for comparison with the results of the proposed model. The analysis of core data provides local measurements of physical properties and gas content that are used as input parameters for the model. The model results at the core locations are then compared to the multibeam-sonar measurement.

II. INTERFACE BACKSCATTER

The composite roughness model developed by Jackson *et al.* (1986) estimates the interface backscattering cross section (σ_r) for a particular seafloor type as a function of frequency and grazing angle. It is based on a hybrid method that takes into account the Rayleigh–Rice small perturbation solution, with the local grazing angle dependent on the slope of the large-scale surface. This model defines the seafloor type based on five parameters that reflect sediment physical properties and seafloor roughness [Eq. (1)]: (a) two parameters for impedance: sound velocity ratio (ν) and density ratio (ρ), (b) one parameter for attenuation: loss parameter (δ), and (c) two parameters for roughness: the spectral strength (ω_2) and the spectral exponent of bottom relief (λ). The acoustic frequency (f) and the grazing angle (θ) of the wave front with the seafloor are treated as given parameters. The modeling function for σ_r is calculated as a combination of the Kirchhoff solution for grazing angles near vertical incidence and the composite roughness solution for other angles. The actual expression and solution for Eq. (1) can be found in Mourad and Jackson (1989):

$$\sigma_r(\theta,f)=F(\theta,f;\rho,\nu,\delta,\omega_2,\lambda), \tag{1}$$

where σ_r is the interface backscattering cross-section per unit solid angle per unit area, θ is the grazing angle, f is frequency, ρ is the ratio of sediment mass density to water mass density, ν is the ratio of sediment sound speed to water sound speed, δ is the loss parameter: ratio of imaginary to real wave number for the sediment, ω_2 is the spectral strength of bottom relief spectrum (cm^4) at wave number 1 cm^{-1}, and λ is the spectral exponent of bottom relief spectrum.

In our approach we assume that this interface backscattering will be affected by the presence of gas bubbles in the sediment through their impact on seafloor geoacoustic properties. An extra parameter ξ, which is the volume fraction of free gas in the sediment, is added to the model. The model parameters most affected by the gas content are the density ratio, the sound speed ratio, and the loss parameter. While there may be large-scale features such as pockmarks or mud volcanoes (with length scales of tens to hundreds of meters) associated with gas expulsion (Hovland and Judd, 1989), these features will have little influence on the small footprints of the 95-kHz multi-beam echo sounder. Thus, to a first approximation, we assume that the model roughness parameters will not be influenced by the presence of gas.

The interface backscattering cross section per unit solid angle per unit area σ_r, modified to take into account the gas content of sediments, is now dependent on six parameters:

$$\sigma_r(\theta,f)=F(\theta,f;\xi,\rho(\xi),\nu(\xi),\delta(\xi),\psi_2,\lambda), \tag{2}$$

where ξ is free gas = gas volume/total sediment volume.

The influence of gas bubbles on sediments was modeled by Anderson and Hampton (1980a, b). We apply this approach to derive expressions for $\rho(\xi)$, $\nu(\xi)$, and $\delta(\xi)$. One simplification used in this work is to consider marine sediments as water-saturated aggregates of particles with no rigid skeletal frame. In doing this, we follow the approach of Jackson and Ivakin (1998), who assume that the shear modulus of elasticity for the marine sediments is zero. This is a reasonable assumption for the upper few decimeters of unconsolidated sediments (the probable limit of penetration of a 95-kHz sonar), especially for silt and clays (Mourad and

Jackson, 1989). Another assumption is that the sediment volume does not change when gas is added, i.e., gas just replaces the water in the sediment body. With these assumptions, the density ratio of gassy sediment, with a volume fraction ξ of free gas, will be

$$\rho(\xi)=\frac{\rho_s-\xi(\rho_w-\rho_g)}{\rho_w}, \tag{3}$$

where ρ_g is the density of the gas, ρ_w is the density of interstitial water, and ρ_s is the density of the gas-free water/sediment aggregate.

The sound speed in gassy sediments is highly dependent on the resonance frequency of gas bubbles. The resonance frequency for a gas bubble of radius a, inside a water/sediment aggregate is inversely proportional to the bubble size [Eq. (4)]:

$$f_0=\frac{1}{2\pi a}\left(\frac{3\gamma P_0}{A\rho_s}\right)^{1/2}, \tag{4}$$

where f_0 is the resonance frequency for a gas bubble of radius a, a is the bubble radius, γ is the ratio of specific heat of the gas, P_0 is the ambient hydrostatic pressure, and A is the polytropic coefficient.

The polytropic coefficient characterizes the thermodynamic process involved during bubble pulsation and the relationship between bubble volume and pressure (Anderson and Hampton, 1980a). In the range of frequencies of multibeam sonar, the full expression for the polytropic coefficient A should be used [Eq. 5(a)]. The auxiliary variable B of Eq. 5(b) is the thermal damping constant:

$$A=(1+B^2)\left(1+\frac{3(\gamma-1)}{x}\left(\frac{\sinh x-\sin x}{\cosh x-\cos x}\right)\right), \tag{5a}$$

$$B=3(\gamma-1)\times\left(\frac{x(\sinh x+\sin x)-2(\cosh x-\cos x)}{x^2(\cosh x-\cos x)+3(\gamma-1)(\sinh x-\sin x)}\right), \tag{5b}$$

where $x=a\sqrt{2\pi f\rho_g s_p/C_g}$, s_p is the specific heat at constant pressure of the gas, and C_g is the thermal conductivity of the gas.

One of the most difficult quantities to model is the distribution of gas bubble sizes. Gas bubbles in fine-grained sediments exist in a range of sizes, but have rarely been directly measured. Anderson *et al.* (1998) used an x-ray CT scanner to produce both a qualitative and quantitative characterization of bubble size population from cores collected in muddy sediments from Eckernfoerde Bay, on the Baltic coast. Their technique has a resolution limit of 0.42 mm and thus their size distribution histograms appear to be the larger bubble segment of a peaked size distribution similar to that seen for populations of bubbles in seawater near the ocean surface (Farmer and Vagle, 1989). The number of bubbles Anderson *et al.* (1998) observed in their sediment samples

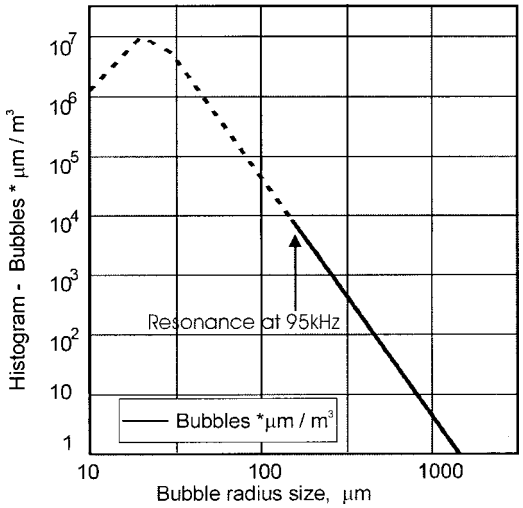

FIG. 1. Bubble size histogram. Number of bubbles per unit volume (m^3) over a bubble radius bin of 1 μm.

increased monotonically as bubble size decreased. Although they were unable to measure bubbles smaller than 0.42 mm, Anderson *et al.* (1998) speculate that the peak in their size distribution may be near this resolution limit, but they also present circumstantial evidence (the increase in normally incident energy between 15 and 30 kHz, returned from the sediment–water interface) for the existence of very small bubble in the upper few cm of the sea floor. The histograms of bubble size in muddy sediments depict slightly smaller bubble sizes than those found in water due to the higher viscosity of the mud. Boyle and Chotiros (1995) used a similar histogram for bubble sizes in soft sediments. The histogram used in our examples is based on these three previous works and is normalized for a water depth of 20 m. It follows the distribution measured by Anderson *et al.* for the larger bubble fraction and allows the probability of small size bubbles as discussed by Boyle and Chotiros. The minimum bubble radius used in the modeling is 180 μm, which is the resonance radius at 95 kHz for the deepest part of the survey area. For bubbles larger than the minimum size, the histogram decreases monotonically with a constant slope on a log–log graph (Fig. 1). The dashed part of the histogram was not actually used in the calculations, and shows only a probable theoretical shape for the bubble size distribution. Based on this histogram, we can define a probability density function $z(a)$ of bubble sizes:

$$z(a)=\frac{\partial Z_a(a)}{\partial a}, \tag{6}$$

where z is the probability density function of bubble sizes and Z_a is the bubble distribution: bubbles per unit volume with radius less than a.

For the sound-speed ratio, we used the expression for gassy water formulated by Silberman (1957), but adapted for the case of fine-grained sediments. The bulk modulus of elasticity of the water, present in the original expression, is substituted with the bulk modulus of the gas-free water/sediment aggregate:

$$\nu(\xi)=\frac{c_s}{c_w\sqrt{(1/2)(1+\rho_s c_x^2 X_1/\gamma P_0)[1\pm\sqrt{1+(\rho_s c_s^2 Y_1/(\gamma P_0+\rho_s c_s^2 X_1))^2}]}}, \tag{7}$$

where c_s is the sound speed for the gas-free water/sediment aggregate and c_w is the sound speed in water.

The expressions for X_1 and Y_1 are the same used by Anderson and Hampton (1980a), modified to take into account the proposed bubble distribution:

$$X_1=\int_{a_{\min}}^{a_{\max}}\frac{\xi(1-f^2/f_0^2(a))}{(1-f^2/f_0^2(a))+d_c^2(a)f^4/f_0^4(a)}z(a)\,da, \tag{8a}$$

$$Y_1=\int_{a_{\min}}^{a_{\max}}\frac{d^c(a)f^2/f_0^2(a)}{(1-f^2/f_0^2(a))+d_c^2(a)f^4/f_0^4(a)}z(a)\,da, \tag{8b}$$

where

$$d_c(a)=B+\frac{\rho_s a^3 w^3 A}{3\gamma P_0 c_s}+\frac{8\pi f\mu A}{3\gamma P_0}$$

is the bubble damping constant and μ is the viscosity of the gas-free water/sediment aggregate.

The attenuation of sound in the aggregate is also a function of the bubble distribution (Anderson and Hampton, 1980a), and can be expressed as

$$\alpha(\xi)=\frac{\pi f\nu(\xi)c_w\rho_s}{\gamma P_0}Y_1, \tag{9}$$

where $\alpha(\xi)$ is the attenuation coefficient in dB/m for a gassy sediment.

Finally, the loss parameter is defined as the ratio of the imaginary part to the real part of the complex sediment acoustic wave number. It is related to the attenuation coefficient, the frequency, and the sound speed in the gassy sediment (Mourad and Jackson, 1989):

$$\delta(\xi)=\frac{\alpha(\xi)\nu(\xi)c_w\ln(10)}{40\pi f}. \tag{10}$$

III. VOLUME BACKSCATTER

In areas predominantly covered with sediments, the volume scattering from subbottom sediment layers or from discrete scatters within the upper sediment layers can contribute extensively to the total backscattering cross section intensity. The model for volume scattering should include refraction at the sediment interface and attenuation in the sediment itself. On a rough seafloor, the penetration of the acoustic field in the sediment is very small for grazing angles smaller than the critical angle. This is an important issue because this reduces drastically the volume backscattering contribution for shallow grazing angles. The refracted energy will be attenuated as it travels through the sediment structure, making the attenuation coefficient a key parameter for the estimation of volume scattering.

In their approach for determining volume scatter, Jackson and Briggs (1992) consider the sediment a statistically homogeneous semi-infinite propagation medium delimited by a rough surface. With this simplification they define a volume backscattering cross section equivalent to the interface, using a similar solution to the one proposed by Stockhausen (1963). The total volume contribution is dependent on a free parameter σ_2, which is calculated based on the ratio of the sediment volume scattering cross section to sediment attenuation coefficient. In our proposed model, we regard the parameter σ_2 as a measurement of the volume contribution of general heterogeneities. Its equivalent volume scattering cross section will be added to the calculated volume scattering cross section from gas bubbles.

The scattering mechanism of bubbles in a lossy fluid was studied by Anderson and Hampton (1980b). In their formulation, the total scattering cross section of sound though a bubble screen is highly dependent on the resonance frequency of the bubbles. The actual acoustic cross section at resonance can be hundreds of times the bubble physical cross section. If we have a distribution of bubble sizes in the sediment body, we can calculate the sediment volume backscattering cross section per unit of volume, as the sum of the contribution of all individual bubbles within that volume (Boyle and Chotiros, 1995). The following expression extends the formulation of Anderson and Hampton (1980b) for the probability density function of bubble sizes of Eq. (6):

$$\Sigma_b=\int_{a_{\min}}^{a_{\max}}\frac{a^2}{[(f_0(a)/f)^2-1]^2+(f_0(a)/f)^4 d_c(a)^2}z(a)\,da, \tag{11}$$

where Σ_b is the backscattering cross section for a bubble distribution.

The volume backscattering cross section of bubbles Σ_b is calculated per unit of volume, as the bubble distribution accounts for number of bubbles per unit of volume. Consequently, Σ_b should be scaled to reflect the volume fraction of free gas ξ. This scaled contribution is then added to the volume scattering cross section of other heterogeneities (other than gas bubbles), as described by the parameter σ_2. The total volume scattering cross section will be

$$\sigma_v(\theta)=\frac{5(\xi\Sigma_b+\sigma_2\alpha(\xi))c_w|1-R^2(\theta)|^2\sin^2(\theta)}{40\pi f|P(\theta)|^2\,\mathrm{Im}|P(\theta)|}, \tag{12}$$

where σ_v is the volume backscattering cross-section equivalent to the interface, σ_2 is the volume scattering parameter, $R(\theta)$ is the complex reflection coefficient, and $P(\theta)$ is the complex function for the forward loss model, as defined in Mourad and Jackson (1989).

The small-scale backscattering cross section of Eq. (2), as well as the equivalent volume cross section of Eq. (12), should be averaged over the bottom slope to account for the

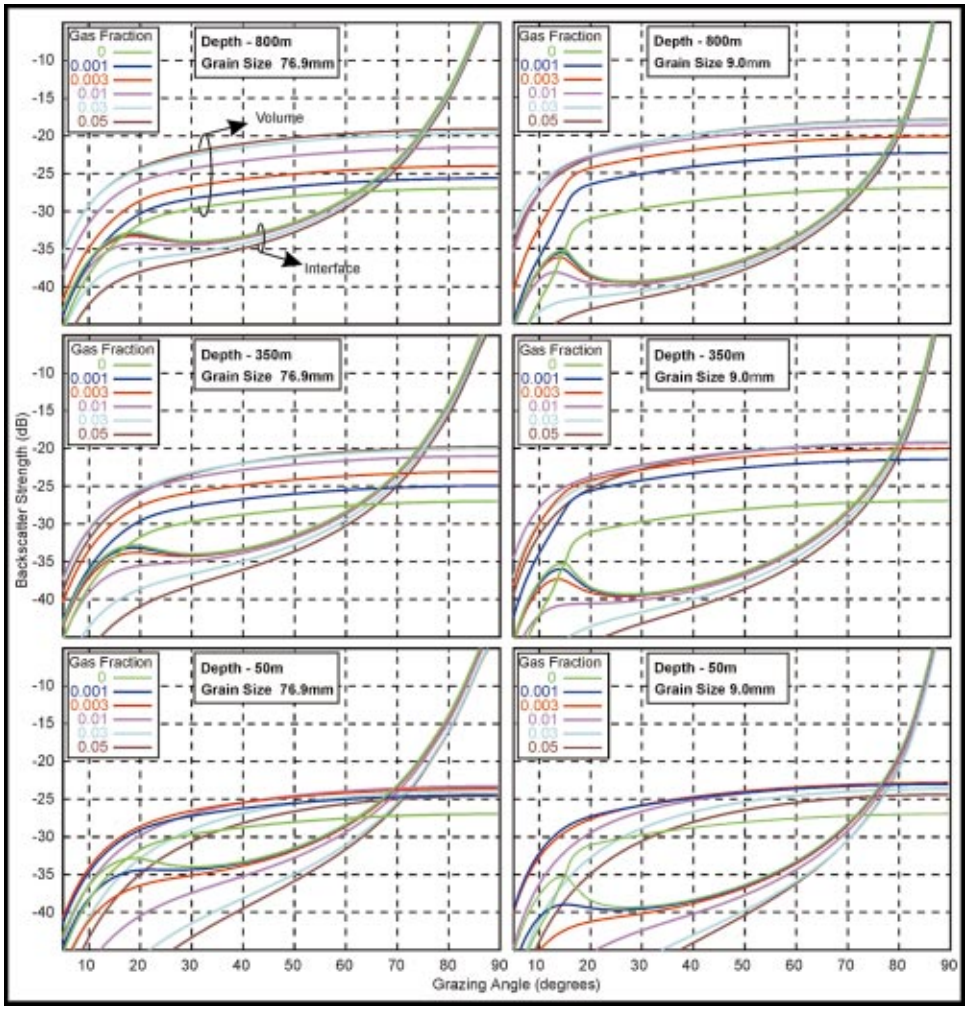

FIG. 2. Simulation of model results for two different grain sizes (columns) and three different depths (rows). The model response is calculated for various gas fractions ranging from 0 to 0.05 (5%). Model parameters for grain size 76.9 μm are $\nu=1.061$, $\rho=1.757$, $\delta=0.0193$, $w_2=0.00136\ \mathrm{cm}^4$, $\gamma=3.25$, and $\sigma_2=0.001$, and for grain size 9.0 μm are $\nu=1.039$, $\rho=1.664$, $\delta=0.00272$, $w_2=0.00052\ \mathrm{cm}^4$, $\gamma=3.25$, and $\sigma_2=0.001$.

effects of local slope and shadowing (Jackson *et al.*, 1986). The numerical solution for Eqs. (2) and (12) reveals a complex relationship involving grain size, depth, and gas fraction. In Fig. 2, the model response is calculated for various gas fractions using two different grain sizes (left and right columns of Fig. 2, respectively). The same computation is repeated for three different depths: 50, 350, and 800 m (rows of Fig. 2). The result of this modeling shows that the backscatter response of fine-grained, gassy sediments is basically controlled by the volume contribution, while coarser grain size sediments present both volume and interface backscatter contributions due to existence of gas.

In deeper waters, the interface backscatter is only slightly reduced by the presence of gas, as a consequence of the higher bubble stiffness at higher ambient pressure [Eq. (7)]. Bubble stiffness is defined as the product of the specific heat of the gas and the ambient pressure (γP_0). On the other hand, even small amounts of gas can cause a large increase in the volume contribution in deep water, i.e., increased scattering cross section [Eq. (12)]. In shallow waters, there is a severe reduction in interface backscatter with an increase in gas content. This is due to the decrease of sediment sound speed in the presence of gas below resonance (Anderson *et al.*, 1998; Wilkens and Richardson, 1998). The volume backscatter contribution in shallow water increases with increased gas content but much less than the increases found in deep water, a result of the higher attenuation from the bubbles at lower ambient pressure (Fig. 2, bottom row). Thus, in shallow water, the gain in volume contribution is sometimes not enough to compensate for the loss in interface backscatter, yielding a net decrease in the total backscatter response.

Another interesting exercise is to calculate the model response for the range of seafloor roughness expected to be found in sediments of the Eel River Margin, that is ω_2 from $0.000\,50\ \mathrm{cm}^4$ to $0.002\,00\ \mathrm{cm}^4$, and λ equal to 3.25 (Applied Physics Laboratory, 1994). The result of this modeling shows that the backscatter response for grazing angles from 30 to 60 degrees of gassy sediments has a maximum increase of 1.2 dB when the seafloor roughness is changed from the minimum to the maximum value. On the other hand, the roughness parameters show a strong influence in the backscatter response in the angular sector near normal incidence i.e., grazing angles from 60 to 90 degrees. Thus, the backscatter angular response of gassy sediments in the angular sector from 30 to 60 degrees is less affected by seafloor roughness, and appears to be controlled by volume contribution.

IV. A TEST ON THE EEL RIVER MARGIN

As a general test of the ideas outlined above we used multibeam sonar and core data collected from the Eel River

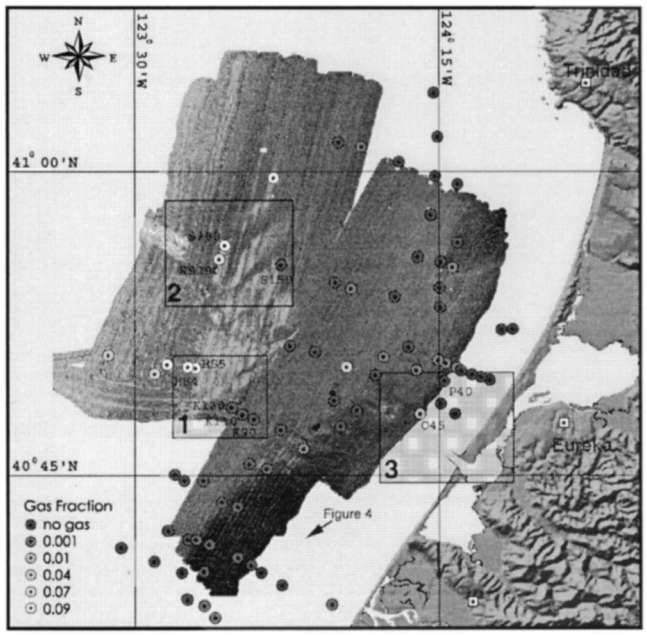

FIG. 3. Location map showing acoustic backscatter mosaics on the Eel River Margin from the EM1000 multibeam survey at 95 kHz. High backscatter is displayed in lighter shades of gray; low backscatter in darker tones. The brightness of the symbols is related to the amount of free gas in the sediment, as measured in core samples. The reference boxes demarcate the zoom areas for examples 1–3.

Margin offshore northern California, a region known to be rich in gassy sediments. The offshore Eel River Basin is located on the eastern border of the North American Plate, from Cape Mendocino extending 200 km northwards to Cape Sebastian, Oregon (Field *et al.*, 1980). The eastern boundary of the basin is the coastline and the western boundary is the continental slope, which coincides with the crustal plate boundary of the Juan de Fuca Plate.

This margin was the focus of a multidisciplinary, 5-year ONR-sponsored study of the processes responsible for generating the preserved stratigraphic record (STRATAFORM; Nittrouer, 1998). In the course of this study, an immense database of marine information has been collected (Mayer *et al.*, 1999), including multibeam sonar bottom backscatter collected at 95 kHz, and numerous core sampling sites with measurements of sediment physical properties and free gas content (Fig. 3).

The multibeam sonar data was collected with a Simrad EM1000, 95 kHz system installed aboard the Humboldt State University research vessel PACIFIC HUNTER. The EM1000 forms 60 roll stabilized 3.3×2.5-degree beams over a swath width of 150 degrees in water depths up to 200 m. In deeper water, 48 beams are produced over a swath width of 120 degrees to about 600-m depth and 60 degrees beyond 600 m. In addition to the bathymetric data, the EM1000 also provides raw measurements of the bottom backscatter as a function of grazing angle for each of the beams. All acquisition parameters are recorded and thus the raw data can be corrected for the removal of the time-varying gains, such as source level, receiver sensitivity, and angle-varying gains. Given that the detailed bathymetry is known from the multibeam time-of-flight measurements, true grazing angles with respect to a bathymetric model can be calculated as well as corrections for footprint size and residual beam pattern (Fonseca, 2001). Applying these corrections, the EM1000 backscatter data from the Eel River Margin was converted to true scattering strength for comparison with the results of the proposed model.

Interpreted much like sidescan sonar imagery (except with angular resolution), the backscatter mosaic of the Eel River Margin reveals several interesting spatial patterns (Fig. 3). A zone of extremely high backscatter (bright areas in Fig. 3) is found in the middle of the western (deep) edge of the survey area. The high backscatter in this region has been correlated with the outcrop of a large structural feature (a breached anticline) and blocky crusts of authigenic carbonate related to methane expulsion (Orange *et al.*, 1999; Yun *et al.*, 1999). The high-backscatter streaks in the middle of the survey area are thought to be associated with grain size changes and the outcrop of indurated sediment (Goff *et al.*, 1999). More intriguing is the general trend of high backscatter in the deep water and low backscatter in shallow water, a relationship which is counter-intuitive when the general trend of grain size (decreasing from shallow water to deep water) is considered. This enigma was noted by Goff *et al.* (1999) and Borgeld *et al.* (1999), who suggest several possible mechanisms (increased surface roughness in finer grained sediments, increased penetration, and contribution of subsurface layering in finer-grained sediments) for this anomalous relationship. The complex relationship among gas content, water depth, and grain size described in the model presented here may offer another possible mechanism.

A. Evidence for gas in the shallow sediments of the Eel River Margin

The Eel River Basin is a tertiary forearc basin with conditions ideal for the generation and movement of both thermogenic and biogenic gas. Deep-seated source beds combined with differential sediment loading and a large amount of tectonic activity have resulted in overpressured zones and the migration of gas from deep layers to the surface and near-surface (Yun *et al.*, 1999). In addition to the deep sources of gas, extremely high modern sedimentation rates and large quantities of organic material supplied by numerous floods provide an excellent source of biogenic gas (Summerfield and Nittrouer, 1999). Numerous lines of evidence support the ubiquitous presence of both thermogenic and biogenic gas in the sediments of the Eel River Margin. These include (1) observation of gas plumes in the water column (Yun *et al.*, 1999); (2) direct measurements on cores (Kvenvolden and Field (1981) and this study (Orange, personal communication); (3) seismic evidence (wipeout zones and other acoustic anomalies), at a range of frequencies from low frequency multichannel seismic to high-frequency boomers, chirp sonars, and 3.5-kHz profilers (Field and Kvenvolden, 1987; Yun *et al.*, 1999); (4) the presence of authigenic carbonates (Orange *et al.*, 1999) and near-surface hydrates (Field and Kvenvolden, 1985); (5) towed electromagnetic surveys (Evans *et al.*, 1999), (6) surface structures associated with

gas (pockmarks and sediment failure features); and (7) commercial gas fields onshore with expected recovery of over 3.34 km^3 of natural gas (Parker, 1987).

While there is overwhelming evidence for the presence of gas in the sediments of the Eel River Margin, the more pertinent question, with respect to testing the model proposed here, is whether there is evidence for gas in the upper few decimeters of the sediment column. Given the 95 kHz frequency of the multibeam sonar used to survey the area, we would expect that penetration into, and interaction with, the subsurface would be limited to the upper few decimeters (to perhaps 1 m depending on sediment type and grazing angle). The near-surface distribution of gas is more difficult to quantify. Anderson *et al.* (1998) in their study of Eckernfoerde Bay noted that the gas bubbles they were able to measure (those greater than 0.42 mm equivalent spherical radius) were not present in the upper few decimeters of the sediment column due to sulfate reduction. They do, however, report that cores recovered from another bay (Macklenberg Bay) did show small gas bubbles in the upper 2 cm of the sediment column and that frequency-dependent reflectivity data from Eckernforde Bay implied the presence of very small bubbles in the upper few centimeters of the seafloor.

Several lines of evidence (both indirect and direct) imply that gas may be present in the upper few decimeters of the sediments of the Eel River Margin. Unlike Eckernfoerde Bay, which is a semi-inclosed fjord-like bay with bottom waters that often experience hypoxia and occasionally anoxia and whose gas source is strictly biogenic (Richardson and Davis, 1998), the Eel River Basin is an open ocean continental margin environment with well-mixed water masses and both thermogenic and biogenic sources of gas. High-resolution 3.5 kHz, boomer, and chirp sonar data all show regions of ''wipeout zones'' (acoustic turbidity), some of which extend to the surface and even into the water column (Field and Kvenvolden, 1987; Yun *et al.*, 1999; and Fig. 4). In addition reduced halos and mats of the sulfate oxidizing bacterium *Beggiatoa sp* have been seen on the seafloor in areas of the Eel River Margin (Orange, 1999) indicating the slow seepage of methane to the seafloor. Further evidence for near-surface gas is provided by Evans *et al.* (1999) who made resistivity measurements using a towed electromagnetic sensor and interpreted low apparent porosities to indicate the presence of gas in the upper few meters of the sediment column, particularly in the shallow water regions of the Eel River Margin, which showed anomalously low backscatter.

Direct evidence of the presence of shallow gas in the Eel River Margin comes from the analysis of gas content in shallow cores. Kvenvolden and Field (1981) analyzed 1- to 2-m-long gravity cores from a diapiric structure in the deeper waters of the Eel River basin (400–500 m) and found high concentrations of methane (both biogenic and thermogenic) throughout the cores including samples from depths as shallow as 6–14 cm below the seafloor. As part of the STRATAFORM project, hundreds of cores were collected in the Eel River Basin, with some showing visual evidence of gas (Borgeld *et al.*, 1999); a small number of these cores were analyzed for gas content. A subset of those analyzed,

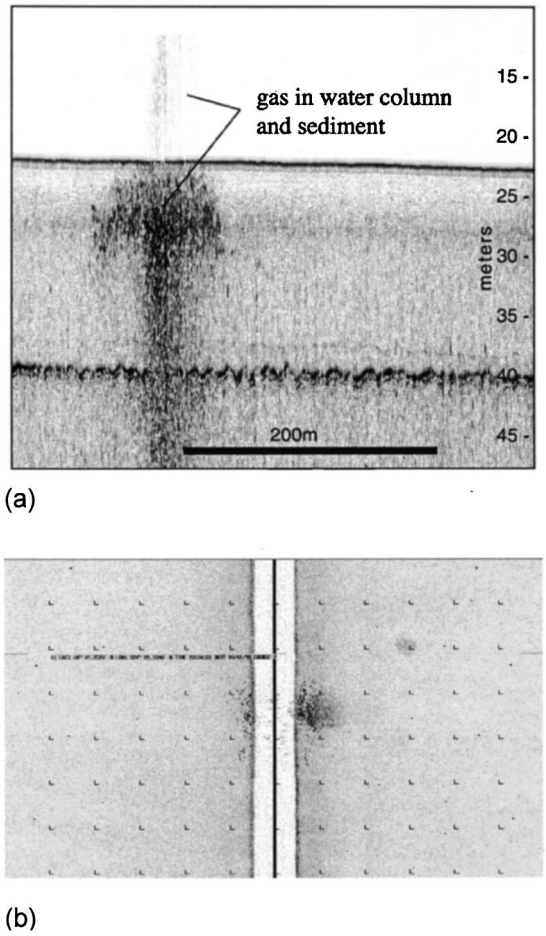

FIG. 4. Evidence that gas may be present in shallow sediments of the Eel River Margin: (a) High-resolution 3.5-kHz chirp profile, showing a region of acoustic turbidity, which extends to the surface and into the water column. (b) Same area surveyed by a 100-kHz sidescan sonar. See Fig. 3 for location. Source: Neal Driscoll.

representing multiple samples from areas of differing backscatter, depth, and gas content are used here to test the proposed model. The areas and core sites selected are shown in Fig. 3.

The core data presented here were collected by Dan Orange on the University of Washington research vessel THOMAS THOMPSON (Cruise TN096) in 1999. During this leg, several types of cores were collected including Vibracores, piston cores, and box cores; core lengths ranged from more than 5 m to less than 25 cm. Analysis of gas content followed the procedure of Kvenvolden and Redden (1980), whereby sediment is taken immediately after core recovery from an approximately 10 cm interval of the core (typically about 10 cm above its base). The sediment is extruded from the core liner into a 0.95 l can with two septa-covered holes on the top. Sodium azide is added to the sample and the water level adjusted until a 100 ml headspace remains. The samples are then sealed and frozen for later analysis in the lab. In the laboratory, the samples are thawed and shaken for 10 min and the headspace sampled by syringe for hydrocarbon gases. Analyses were performed on an HP gas chromatograph with both flame ionization and thermal conductivity detectors.

It must be noted that while these analyses are indicative

TABLE I. Physical properties measured at selected core sites.

Core	Grain size (μm)	Sound speed (m/s)	Density (kg/m^3)	Water depth (m)	Gas fraction	Gas content	Site
HS4	9.0	1552	1786	318	0.0954	V. High	1
HS5	9.0	1553	1809	320	0.0951	V. High	1
K130	9.0	1543	1701	125	0.0	None	1
K110	16.7	1544	1696	114	0.0	None	1
K90	16.7	1545	1690	104	0.0	None	1
S280	9.6	1583	1800	258	0.075	High	2
RS290	9.6	1583	1800	267	0.067	High	2
S150	13.6	1567	1794	151	0.0	None	2
O45	76.9	1575	1796	39	0.01	Low	3
P40	125.0	1560	1784	40	0.0	None	3

of the presence, absence, and perhaps relative abundance of gas at a sample location, they do not provide an accurate measure of the *in situ* abundance of free gas in the sample, and in particular, in the upper decimeters of the seafloor. Thus, while we report the measured value in Table I, we will use these values only as indicators of the relative gas content of the seafloor sediments. In addition to the gas content, the mean grain size, sound speed, and saturated bulk density of the sediment were also measured on the core samples. These data are presented in Table I and are used as inputs into the model presented above. There are no available measurements for the sediment roughness and compressional wave attenuation for the studied sites. For these values, a parametrization in terms of the bulk grain size was used following the method described in the *APL-UW High-Frequency Ocean Environment Acoustic Models Handbook* (Applied Physics Laboratory, 1994).

Although it would be better to have the full grain size distribution in order to explain backscattering differences due to physical properties, only the mean grain size was available for the core sites. The parameter σ_2 cannot be directly measured, and one average value (0.01) was used (Applied Physics Laboratory, 1994). This assumption can lead to an overestimate of the effect of gas bubbles, because σ_2 is a measurement of sediment heterogeneities other than gas. Fortunately, the effect scattering contribution of gas bubbles is normally many times higher than the contribution of other scatterers, making the use of a constant σ_2 an acceptable assumption. Another factor that would increase the volume contribution is the presence of multiple scattering (Jackson and Ivakin, 1998). Table II shows values of physical parameters that are common for all four examples. The model was

TABLE II. Values of common parameters used to evaluate the model at selected sites A, B, C, and D.

Seawater density	ρ_w	1022 kg/m^3
Seawater sound speed	c_w	1485 m/s
Gas density	ρ_g	1.24 kg/m^3
Gas ratio of specific heats	γ	1.403
Gas specific heat at constant pressure	s_p	240 cal/kg
Gas thermal conductivity	C_g	5.6×10^{-3} cal/(m s °C)
Muddy sediment viscosity	μ	1.0×10^{-3} kg/(m s)
Ambient hydrostatic pressure	P_0	$(1.0135\times10^5$ $+9.806\,65{*}\rho_w{*}$depth) N/m^2

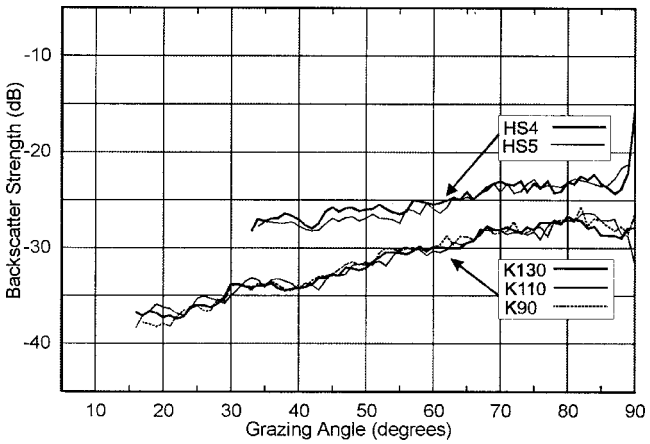

FIG. 5. Backscattering strength measured by a Simrad EM1000 multibeam sonar (95 kHz) around core sites HS4, HS5, K90, K110, and K130.

run for each core site using the parameters presented in Tables I and II; these results as well as comparisons to the measured multibeam sonar backscatter in the area will be discussed in the next section.

B. Area 1 (Humboldt Slide) mid-depth range

Area 1 (Fig. 3) encompasses five core locations, which have variable gas fractions and associated backscatter. Cores HS-4 and HS-5 have high gas fractions: 0.0951 and 0.0980, respectively. The average depth for these two cores is 330 m. Cores K90, K110, and K130, on the other hand, have no measured gas; their average depth is 114 m. Backscatter images from a SIS-1000 deep-towed sidescan sonar reveal a dense distribution of pockmarks through this area (the Humboldt Slide zone), providing evidence for widespread, but focused, gas and fluid venting (Gardner *et al.*, 1999). Figure 5 shows the backscattering strength measured at these core sites by the EM1000 multibeam sonar. The displayed curves are an average of 50 sonar pings around the core sites, which represents on average a linear distance of 100 m. There is a 5 dB difference in the backscatter response (average backscatter for grazing angles from 30 to 60 degrees) between sites with and without measured gas. This difference cannot be explained by the differences in physical properties measured at these five core sites (Tables I and II).

The backscatter angular response can be calculated using sediment properties measured at the core sites (Table I). The parameters used as input for the model are $\nu=1.039$, $\rho=1.664$, $\delta=0.002\,72$, $w_2=0.000\,52$ cm^4, $\gamma=3.25$, and $\sigma_2=0.0010$, with no gas. The result is shown in Fig. 6 for the interface backscatter and the total (volume+interface) backscatter. The model was then run a second time, including the very high gas fraction of 0.098, which changed the following model parameters: $\nu=0.939$, $\rho=1.571$, and $\delta=0.0695$, and generated an equivalent volume contribution of $\sigma_2=0.0068$ (including contributions from gas and other heterogeneities). Note that the model shows about 6 dB difference (average backscatter for grazing angles from 30 to 60 degrees) between sites with high gas content and those with no measured gas, which is similar to what is shown in Fig. 5. The difference in absolute values between data and model

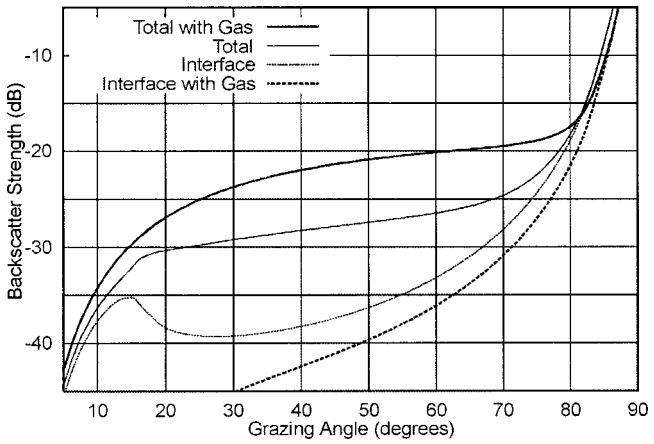

FIG. 6. Model response using the sediment properties measured at the core sites HS4, HS5, K90, K110, and K130.

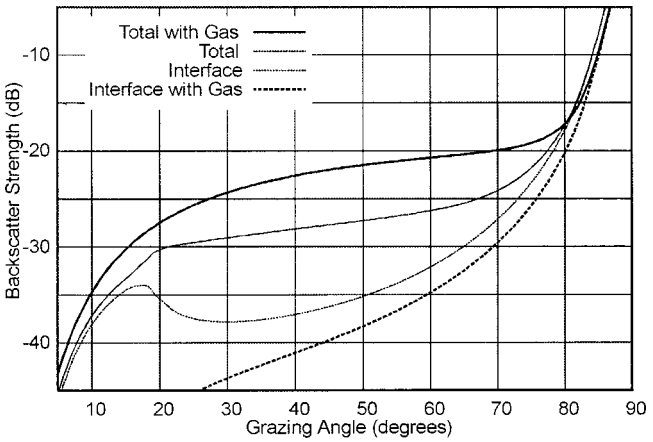

FIG. 8. Model response using the sediment properties measured at the core sites RS280, S280, and S150.

(Figs. 5 and 6) is small, which may be explained by calibration problems in multibeam sonar systems. There was a small reduction of interface backscatter due to the low sound speed ratio of the gassy sediment. The volume backscatter of the gassy sediment is considerably higher, which results in a net increase in the backscatter response.

C. Area 2 (mid-depth range)

Area 2 (Fig. 3) contains cores S280 and RS290 which have moderately high gas fractions: 0.075 and 0.067, respectively. These two cores are located at an average depth of 253 m. Core S150 at 151 m of depth has no measured gas. The existence of near-surface gas in this area is demonstrated by acoustic anomalies on Huntec seismic profiles (Yun *et al.*, 1999). Figure 7 shows the backscattering strength measured at these core sites by the EM1000 multibeam sonar. The final response is an average of 50 sonar pings around the core sites. There is an average of 4 dB difference in the backscatter response between sites with and without measured gas, although the sites have basically the same sediment properties.

Figure 8 shows the model response using the sediment properties measured at the core sites (Table I) and the common values in Table II. The parameters used as input for the model are $\nu=1.0552$, $\rho=1.755$, $\delta=0.00290$, $w_2=0.00052\ \mathrm{cm}^4$, $\gamma=3.25$, and $\sigma_2=0.001$, with no gas. The model was run a second time including the moderately high gas fraction of 0.075, which changed the following model parameters: $\nu=0.972$, $\rho=1.683$, and $\delta=0.0532$, and generated an equivalent volume contribution of $\sigma_2=0.0055$ (including contributions from gas and other heterogeneities). Note that the model predicts a 4 dB increase in backscatter strength when gas is included and that this is consistent with the difference seen in the measured backscatter between gassy (RS280 and S280) and non-gassy (S150) sites (Fig. 7). At these depths (336 m for Area 1 and 252 m for Area 2) the presence of gas has the effect of slightly lowering the interface backscattering component and significantly increasing the volume backscattering component.

D. Area 3 (shallow water)

Area 3 (Fig. 3) contains two core locations in relatively shallow water (39 m). Core O45 had a measured gas fraction of 0.010, while core P40 had no measured gas. These two cores are also inside the zone of acoustic turbidity, interpreted from high-frequency seismic profiles, to be caused by the presence of gas (Yun *et al.*, 1999). Figure 9 shows the backscattering strength measured at these two core sites by

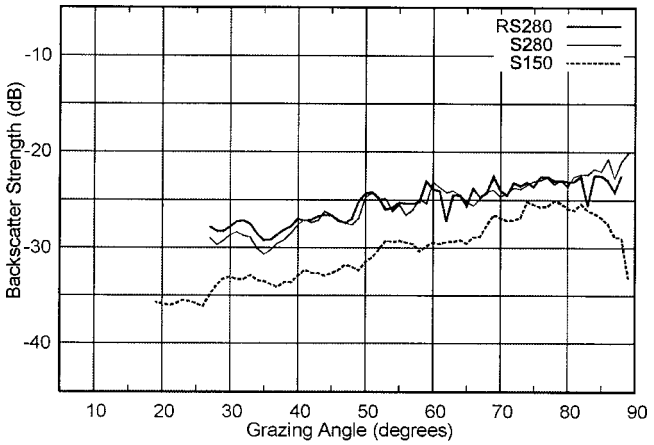

FIG. 7. Backscattering strength measured by a Simrad EM1000 multibeam sonar (95 kHz) around core sites RS280, S280, and S150.

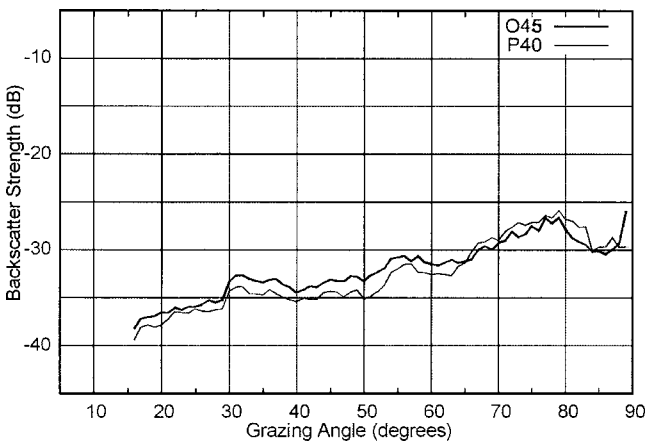

FIG. 9. Backscattering strength measured by a Simrad EM1000 multibeam sonar (95 kHz) around core sites O45 and P40.

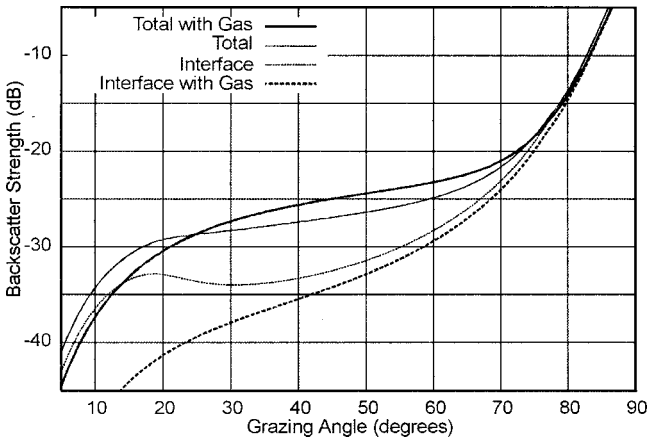

FIG. 10. Model response using the sediment properties measured at the core sites O45 and P40.

the Simrad EM1000 multibeam sonar. There is almost no difference at the backscatter strength between the sites.

The model response is calculated using the sediment properties measured at the core sites and common values of Table II. The parameters used as input for the model are $\nu = 1.061$, $\rho = 1.757$, $\delta = 0.019\,72$, $w_2 = 0.001\,20\ \mathrm{cm}^4$, $\gamma = 3.25$, and $\sigma_2 = 0.0010$, with no gas. The model was run a second time including the low gas fraction of 0.01, which changed the following model parameters: $\nu = 0.891$, $\rho = 1.747$, and $\delta = 0.0768$, and generated an equivalent volume contribution of $\sigma_2 = 0.0011$ (including contributions from gas and other heterogeneities). When gas is added, the model predicts a very small difference between the two sites (Fig. 10). In shallow water (39 m) there is a severe reduction of interface backscatter due to the very low sound speed ratio of the gassy sediment. The increase in volume backscatter of the gassy sediment is not high enough to compensate for the interface backscatter reduction. This relatively small volume scatter is a consequence of the higher attenuation of gassy sediment in shallow water. In shallow water, the ambient pressure is lower, which increases the attenuation in the gassy sediment, according to Eq. (9).

V. CONCLUSIONS

Gas is an important and common sediment heterogeneity on continental margins which may explain some of the backscatter-response anomalies seen in the sediments on the Eel River Margin. A model has been proposed that shows that gas affects both the interface and volume contribution of the backscatter angular response. Gas normally increases the volume contribution and weakens the interface contribution, but the relationship is complicated by changes in depth and sediment properties. The backscatter response of fine-grained gassy sediments (grain size $<10\ \mu$m) is basically controlled by the volume contribution to backscattering. Coarser sediments (grain size $>60\ \mu$m) present both significant changes in volume and interface backscatter in the presence of gas.

The model was tested by inputting physical properties measured on cores collected in a region also surveyed with a 95 kHz multibeam sonar. The cores selected for input into the model were cores that had also been analyzed for gas content and these values were used to estimate the relative abundance of gas at the core sites. While the head-space analyses used for determining gas content are not necessarily an accurate representation of the *in situ* concentration of free gas in the cores, they are indicative of the presence, absence and perhaps relative abundance of gas in the upper few meters of the seafloor. Both the gas measurements and the multibeam backscatter showed a high degree of lateral variability.

Raw time series of the 95 kHz multibeam sonar backscatter as a function of angle of incidence were corrected for source and receiver gain changes, area of insonification, true grazing angle, and residual beam patterns resulting in a georeferenced record of true scattering strength. The measured backscatter (averaged over about 100 m around each core site) was then compared to the model output for each core site and for a range of gas contents. The measured results were generally in agreement with the model and with the results predicted for the measured gas contents.

Depth plays an important role in the backscatter response of gassy sediments. In deep water (deeper than 400 m), the predicted interface backscatter is only slightly affected by the presence of gas, a consequence of the higher bubble stiffness at higher ambient pressure. On the other hand, a small amount of gas yields a very-high predicted volume contribution in deep water. In shallow water (less than 100 m), the predicted interface backscatter is severely reduced when the sediment is charged with free gas, due to the decrease of sediment sound speed. The predicted volume contribution in shallow water is lower, due to higher attenuation from the bubbles at lower ambient pressure. In shallow water, the gain in volume contribution is sometimes not enough to compensate for the loss in interface backscatter, resulting in a net decrease in the total backscatter response.

While the results presented here are encouraging in terms of the potential for using multibeam sonar as a qualitative and quantitative indicator of the gas content of near-surface sediments, much more work needs to be done. In particular, the model needs to be tested under controlled conditions where near-surface sediment samples can be collected and maintained under *in situ* conditions (as described in Anderson *et al.*, 1998). New developments in pressure-maintaining core barrels (e.g., Pettigrew, 1992) should greatly aid in this effort. In addition, the models need to be extended to include the effect of multiple scattering, which should provide a more accurate prediction of the total scattering due to gas bubbles.

ACKNOWLEDGMENTS

This study was made possible by funding from the Office of Naval Research Contract No. N00014-00-1-0092. Special thanks for Janet Yun for the Eel Shelf data that she provided. The authors express their appreciation to Brian Calder for all the valuable suggestions and the support with the model programming.

Anderson, A., Abegg, F., Hawkins, J. A., Duncan, M. E., and Lyons, A. P. (**1998**). ''Bubble populations and acoustic interaction with the gassy floor of Echernförde Bay,'' Continental Shelf Res. **18**, 1807–1838.

Anderson, A., and Hampton, L. D. (**1980a**). ''Acoustics of gas-bearing sediments I. Background,'' J. Acoust. Soc. Am. **67**, 1865–1889.
Anderson, A., and Hampton, L. D. (**1980b**). ''Acoustics of gas-bearing sediments II. Measurements and models,'' J. Acoust. Soc. Am. **67**, 1890–1903.
Applied Physics Laboratory. (**1994**). *High-Frequency Ocean Environmental Acoustic Models Handbook*, Applied Physics Laboratory Technical Report APL-UW TR 9407, University of Washington, Seattle, WA, Chap. 4.
Borgeld, J. C., Clarke, J. E. Hughes, Goff, J. A., Mayer, L. A., and Curtis, J. A. (**1999**). ''Acoustic backscatter of the 1995 flood deposit on the Eel shelf,'' Mar. Geol. **194**, 183–196.
Boyle, F. A., and Chotiros, N. P. (**1995**). ''A model for high-frequency acoustic backscatter from gas bubbles in sandy sediments at shallow grazing angles,'' J. Acoust. Soc. Am. **98**, 531–541.
de Moustier, C., and Alexandrou, D. (**1991**). ''Angular dependence of 12 kHz Seafloor Acoustic Backscatter,'' J. Acoust. Soc. Am. **90**, 522–531.
Evans, R. L., Law, L. K., St. Louis, B., Cheesman, S., and Sananikone, K. (**1999**). ''The shallow porosity structure of the Eel shelf, northern California: results of a towed electromagnetic survey,'' Mar. Geol. **154**, 211–226.
Farmer, D. M., and Vagle, S. (**1989**). ''Waveguide propagation of ambient sound in the ocean-surface bubble layer,'' J. Acoust. Soc. Am. **86**, 1897–1908.
Field, M. S., and Kvenvolden, K. A. (**1985**). ''Gas hydrates on the northern California continental margin,'' Geology **13**, 517–520.
Field, M. S., and Kvenvolden, K. A. (**1987**). ''Preliminary report on gaseous hydrocarbons in sediments and seeps offshore Eel River basin, California,'' in *Tectonics, Sedimentation and Evolution of the Eel River Basin and Other Coastal Basins of Northern California*, edited by H. Schymiczek and R. Suchsland, San Joaquin Geological Society Miscellaneous Publication, Vol. 37, pp. 55–60.
Field, M. S., Clarke, H., and White, M. E. (**1980**). ''Geology and geologic hazards of offshore Eel River Basin, Northern California Continental Margin,'' USGS Open-file report 80-1080.
Fonseca, L. (**2001**). ''A model for backscattering angular response of gassy sediments: Applications to petroleum exploration and development programs,'' Ph.D. Thesis, Ocean Engineering, University of New Hampshire.
Gardner, J. V., Prior, D. B., and Field, M. E. (**1999**). ''Humboldt Slide—a large shear-dominated retrogressive slope failure,'' Mar. Geol. **154**, 323–338.
Goff, J. A., Orange, D. L., Mayer, L. A., and Hughes Clarke, J. E. (**1999**). ''Detailed investigation of continental shelf morphology using a high-resolution swath sonar survey: the Eel margin, northern California,'' Mar. Geol. **154**, 255–270.
Hovland, M., and Judd, A. G. (**1989**). *Seabed Pockmarks and Seepages: Impact on Geology, Biology and the Marine Environment* (Graham & Trotman, Norwell, MA).
Ivakin, A. N. (**1998**). ''A unified approach to volume and roughness scattering,'' J. Acoust. Soc. Am. **103**, 827–837.
Jackson, D. R., and Briggs, K. B. (**1992**). ''High-frequency bottom backscattering: Roughness versus sediment volume scattering,'' J. Acoust. Soc. Am. **92**, 962–977.
Jackson, D. R., Winebrenner, D. P., and Ishimaru, A. (**1986**). ''Application of the composite roughness model to high-frequency bottom backscattering,'' J. Acoust. Soc. Am. **79**, 1410–1422.
Jackson, D. R., and Ivakin, A. N. (**1998**), ''Scattering from elastic sea beds: First-order theory,'' J. Acoust. Soc. Am. **103**, 336–345.
Kvenvolden, K., and Field, M. (**1981**). ''Thermogenic hydrocarbons in unconsolidated sediment of Eel River Basin, Offshore Northern California,'' AAPG Bull. **65**, 1642–1646.
Kvenvolden, K. A., and Redden, G. D. (**1980**). ''Hydrocarbon gas in sediment from the shelf, slope and basin of the Bering Sea,'' Geochim. Cosmochim. Acta **44**, 1145–1150.
Lyons, A. P., Duncan, M. E., Anderson, A. L., and Hawkins, J. A. (**1996**). ''Predictions of the acoustic scattering response of free-methane bubbles in muddy sediments.'' J. Acoust. Soc. Am. **99**, 163–172.
Mayer, L., Fonseca, L., Pacheco, M., Galway, S., Martinez, J. V., and Hou, T. (**1999**). ''The STRATAFORM GIS CD,'' U.S. Office of Naval Research distribution.
Mourad, P. D., and Jackson, D. R. (**1989**), ''High frequency sonar equation models for bottom backscatter and forward loss,'' in *Proceedings of OCEANS'89* (IEEE, New York), pp. 1168–1175.
Nittrouer, C. A. (**1998**). ''STRATAFORM: Overview of its design and synthesis of its results,'' Mar. Geol. **154**, 3–12.
Novarini, J. C., and Caruthers, J. W. (**1998**). ''A simplified approach to backscattering from a rough seafloor with sediment inhomogeneities,'' J. Ocean. Eng. **23**(3), 157–166.
Orange, D. L. (**1999**). ''Tectonics, sedimentation, and erosion in northern California: submarine geomorphology and sediment preservation potential as a result of three competing process,'' Mar. Geol. **154**, 368–382.
Orange, D. L., Angell, M., and Lapp, D. (**1999**). ''Applications of multibeam mapping to exploration and production: Detecting seeps, mapping geohazards, and managing data overload with GIS,'' The Leading Edge, **18**, 495–501.
Parker, J. D. (**1987**). ''Geology of the Tompkins Hill gas field, Humboldt County, California,'' in *Tectonics, Sedimentation and Evolution of the Eel River Basin and Other Coastal Basins of Northern California*, edited by H. Schymiczek and R. Suchsland, San Joaquin Geological Society Miscellaneous Publication, Vol. 37, pp. 83–88.
Pettigrew, T. L. (**1992**). ''The design and operation of a wireline pressure core sampler (PCS),'' ODP Tech. Note 17.
Richardson, M. D., and Davis, A. M. (**1998**). ''Modeling methane-rich sediments of Eckernförde Bay,'' Continental Shelf Res. **18**(14–15), 1671–1688.
Silberman, E. (**1957**). ''Sound velocity and attenuation in bubbly mixtures measured in standing wave tubes,'' J. Acoust. Soc. Am. **29**, 925–953.
Stockhausen, J. H. (**1963**). ''Scattering from the Volume of an Inhomogeneous Half-Space,'' Naval Research Establishment, Canada, Report 63/9.
Summerfield, C. K., and Nittrouer, C. A. (**1999**). ''Modern accumulation rates and a sediment budget for the Eel shelf: a flood dominated depositional environment,'' Mar. Geol. **154**, 227–242.
Wilkens, R. H., and Richardson, M. D. (**1998**). ''The influence of gas bubbles on sediment acoustic properties: *in situ*, laboratory, and theoretical results from Eckernfoerde Bay, Baltic Sea,'' Continental Shelf Res. **18**, 1859–1892.
Yun, W. J., Orange, D. L., and Field, M. E. (**1999**). ''Subsurface Gas Offshore Northern California and its Link to Submarine Geomorphology,'' Mar. Geol. **154**, 357–368.

Single bubble sonoluminescence driven by non-simple-harmonic ultrasounds

Weizhong Chen,[a] Xi Chen, Meijun Lu, Guoqing Miao, and Rongjue Wei
Institute of Acoustics and State Key Laboratory of Modern Acoustics, Nanjing University, Nanjing 210093, China

(Received 11 January 2002; revised 22 March 2002; accepted 26 March 2002)

The dependence of the single bubble sonoluminescence (SBSL) on the waveforms of the driving ultrasound has been investigated by both experiment and numerical calculation. Three types of non-simple-harmonic waves, the rectangular, triangular and as well as the sinusoidal wave with a pulse, are used to drive the SBSL in our research. The triangular wave is the most effective, while the rectangular wave is the worst and the sinusoidal wave in the middle. However, the rectangular wave drives the brightest SBSL among those waves if the sound pressure amplitude keeps constant. When we use a simple-harmonic wave with a pulse as the driving sound, stable and periodic SBSL flashes have been observed. An increase in the flash intensity can be observed as the pulse is put at a suitable phase related to the sinusoidal wave. All of the observations are investigated numerically. Well qualitative agreements between the numerical simulations and the experimental measurements have been achieved. © *2002 Acoustical Society of America.*
[DOI: 10.1121/1.1480417]

PACS numbers: 43.35.Hl, 78.60.Mq, 43.25.+y, 42.65.Re [RR]

I. INTRODUCTION

Sonoluminescence is a phenomenon of the light emission from the cavities (air bubbles) in liquid driven by the ultrasound. A wonderful experiment conducted by Gaitan and Crum[1] has allowed the observation of the sonoluminescence in a single cavity, known as the single bubble sonoluminescence (SBSL). A series of experiments[2–10] revealed a number of surprising and intriguing properties of the SBSL. The light of the SBSL is broadband in wavelength from shorter than 200 to over 800 nm,[2] and lasts in a very short duration about 40 to 400 ps during each sound cycle.[3,4] The line emission has also been observed in the spectrum of an extremely dim SBSL.[5] Furthermore, some interesting experiments have shown that the SBSL has a very sensitive dependence on the parameters, such as the ambient pressure,[3,6] the temperature,[3,7] the dissolved gas concentration,[11] and so on. The theoretical explanation of the source of the SBSL ranges from the bremsstrahlung,[12] the Casimir effect,[13] to the proton-tunneling radiation.[14] However, the final answer concerning the formation mechanism of the SBSL still remains open.

In the most experimental[1–9] and theoretical[12–14] works the forcing ultrasounds are simple harmonic waves at the frequencies $\omega/2\pi$ of several tens of kilohertz,

$$P(t)=P_a \cos \omega t, \tag{1}$$

where P_a is the forcing pressure amplitude of the ultrasound. One can enhance the intensity of the SBSL in various ways. Recently many efforts have been taken to upscale the SBSL intensity by changing the driving waveforms from the simple harmonic wave. Theoretically it has been suggested that the SBSL can be enhanced with the addition of an acoustic spike drive.[15] Holzfuss *et al.* have boosted the SBSL emission by using an optimized bimodal ultrasound,[10] such that

$$P(t)=P_1 \cos \omega t+P_2 \cos(2\omega t+\phi_2), \tag{2}$$

where P_1 and P_2 are the driving pressure amplitudes of the fundamental and its second harmonic, respectively, and ϕ_2 the relative phase between them. A raise of the maximum photocurrent up to as much as three times that driven by a pure simple harmonic wave has been achieved in the experiment. As usually done, they did not keep the driving sound power constant when the driving ultrasound changed from the single mode to the dimode. Their experiment only shows that the maximum SBSL emission can be upscaled by a suitable bimodal ultrasound. The bimodal driving ultrasound consisted of the fundamental and its third harmonic,

$$P(t)=P_1 \cos \omega t+P_3 \cos(3\omega t+\phi_3), \tag{3}$$

with P_3 and ϕ_3 being the driving pressure amplitudes and phase of the third harmonic, has also been used to drive the SBSL.[16] Furthermore, Hargreaves and Matula[16] conducted another experiment by using two transducers driven by a simple harmonic wave and a spike, respectively. Although a strongly acoustic radiation from the spike makes the stable bubble levitation impossible, a transient increase of 200% in the SBSL intensity has been first observed experimentally, which supports the prediction of the Moss *et al.* spiking SBSL.[15] The loss of the stability of the bubble levitation means that spiking bubble every acoustic cycle steadily may not be feasible.[16]

In this paper we report the effects of the forcing waveforms on the intensity of the SBSL. Two kinds of the well-known non-simple-harmonic waves, the rectangular and triangular waves, together with the single harmonic wave, are used to drive the SBSL experiment. Contrast to the works mentioned above,[10,16] we are interested in the efficiencies of

[a]Electronic mail: wzchen@nju.edu.cn

 0001-4966/2002/111(6)/2632/6/$19.00

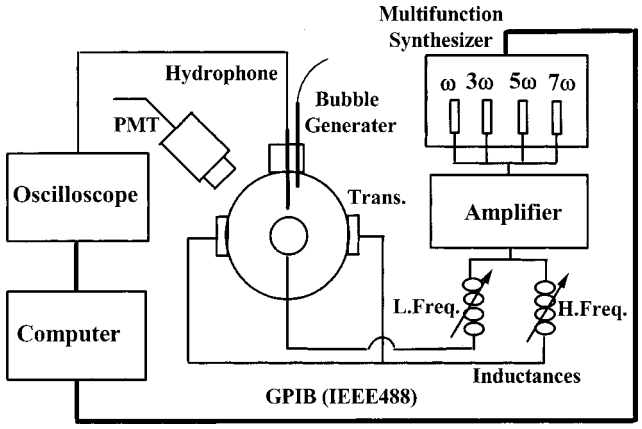

FIG. 1. A sketch of the experimental setup of the SBSL driven by non-simple-harmonic waves.

the well-known waveforms to drive the SBSL emission. A sinusoidal drive with a pulse formed by two pairs of parallel transducers is also used in the experiment and such that a strong stability has been achieved. As a supplement of the work of a Hargreaves and Matula,[16] a raise of the light emission from the periodic, steady, spiking SBSL further proves the prediction of Moss *et al.*[15] After the experimental investigation, we also give a numerical calculation for explaining our observations, and a well qualitative agreement has been achieved between the numerical and the experimental results. In the first section we will introduce our experimental setup and the main procedure. The experimental results are shown in Sec. II, and in Sec. III we give the numerical results that are in a well qualitative agreement with those observed in experiment. Finally, there is a simple summary.

II. EXPERIMENTAL SETUP AND TECHNIQUE

The experimental setup (see Fig. 1) consists of a spherical acoustic resonator, an ultrasound power amplifier, and a set of the SBSL emission measurers. The acoustic resonator is a 100 ml flask cemented symmetrically with two pairs of parallel transducers. The degassed filtered water is filled to the flask. The water in the flask resonates at the frequency of about 24.5 kHz. A pair of electrodes are inserted into the water at the depth of about 1 cm as a bubble generator. We also insert a needle hydrophone (TNU001A, NTR Systems, Inc.) into the water about 2 cm over the sonoluminescing bubble to monitor the ultrasound waveform in the water directly. The SBSL radiation is measured by a photomultiplier tube (PMT). As mentioned in Ref. 10, comparing with the single frequency driving, the multifrequency driving is difficult in experiments because of two factors: the transducers' response and the standing wave formation.

The rectangular and triangular waves can be described by

$$P(t)=P_a\sum_{n=1}^{N} a_n \sin((2n-1)\omega t), \tag{4}$$

where

$$a_n=\frac{4}{(2n-1)\pi}, \quad \text{for the rectangular wave,} \tag{5}$$

$$a_n=\frac{8(-1)^{n+1}}{(2n-1)^2\pi^2}, \quad \text{for the triangular wave,} \tag{6}$$

with integer N being ∞, or large enough. Considering the feasibility in the experiment, we truncate the integer N at 4, which means the waves are superposed by the fundamental and its suitable triple, quintic, and septuple harmonics. The reason of the truncation is not only due to the limitation of the frequency responses of the transducers and the power amplifier (Brüel and Kjaer 2713), but also due to the lack of the significance for larger N. The fourth-order truncated polynomials of Eq. (4) with Eqs. (5) and (6) have already been good approximations of ideal rectangular and triangular waves, respectively [see Figs. 2(a) and (b)]. We use a four-channel multifunction synthesizer (HP8904A) as a signal source. The synthesized signal is amplified by the power amplifier, then connected to two impedance matching inductances resonated at lower (2ω) and higher (4ω) frequencies, respectively. Finally, the electrical driving voltages are added to the two pairs of parallel transducers in response at lower and higher frequencies, respectively. Of course, we will not be able to obtain the same sound pressure in water as that of the electrical signal, because of the different responses of both transducers and the current to the different frequencies. In order to approach the object waveform as soon as possible, it is convenient to define an error function χ^2 in frequency space instead of in the time region, such as

$$\chi^2=\sum_{n=2}^{4}((a_n-A_n)^2+(\phi_n-\Phi_n)^2), \tag{7}$$

where A_n and Φ_n for $n=2,3,4$ are the measured sound pressures and the relative phases of the components at frequencies $3\omega/2\pi$, $5\omega/2\pi$, $7\omega/2\pi$, and a_n and ϕ_n for $n=2,3,4$ are their object values, respectively. The waveform of the driving sound in time region is acquired by the needle hydrophone, then fed to a digital real-time oscilloscope, finally connected to a computer through the GPIB(IEEE488). A_n and Φ_n come from the FFT of the waveform data. An optimizing arithmetic is employed to search the best parameters of the input electrical signal. If the error function is not in its minimum, the computer will adjust parameters of the signal source through the GPIB. The electrical signal is finally fixed by minimizing the error function χ^2, and the output sound pressures arrive at their object waveforms. This optimizing arithmetic has to be run repeatedly when we change the driving amplitude P_a because the frequency response functions of the transducers and amplifier change with the amplitude variation. Figures 2(a) and (b) show, respectively, the experimental driving pressure waveforms of the rectangular and triangular waves. They are different from their original electrical signals [see the insets in Figs. 2(a) and (b)].

Also, we use a sinusoidal wave with a pulse as a driving ultrasound, which is first suggested by Moss and his colleagues.[15] A recent experiment[16] shows that the spiking SBSL may not be feasible because the spike (pulse) wave destroyed the levitation of the luminescencing bubble. In our experiment, we superpose a pulse to the simple harmonic wave in an electrical signal (the electrical spike) instead of

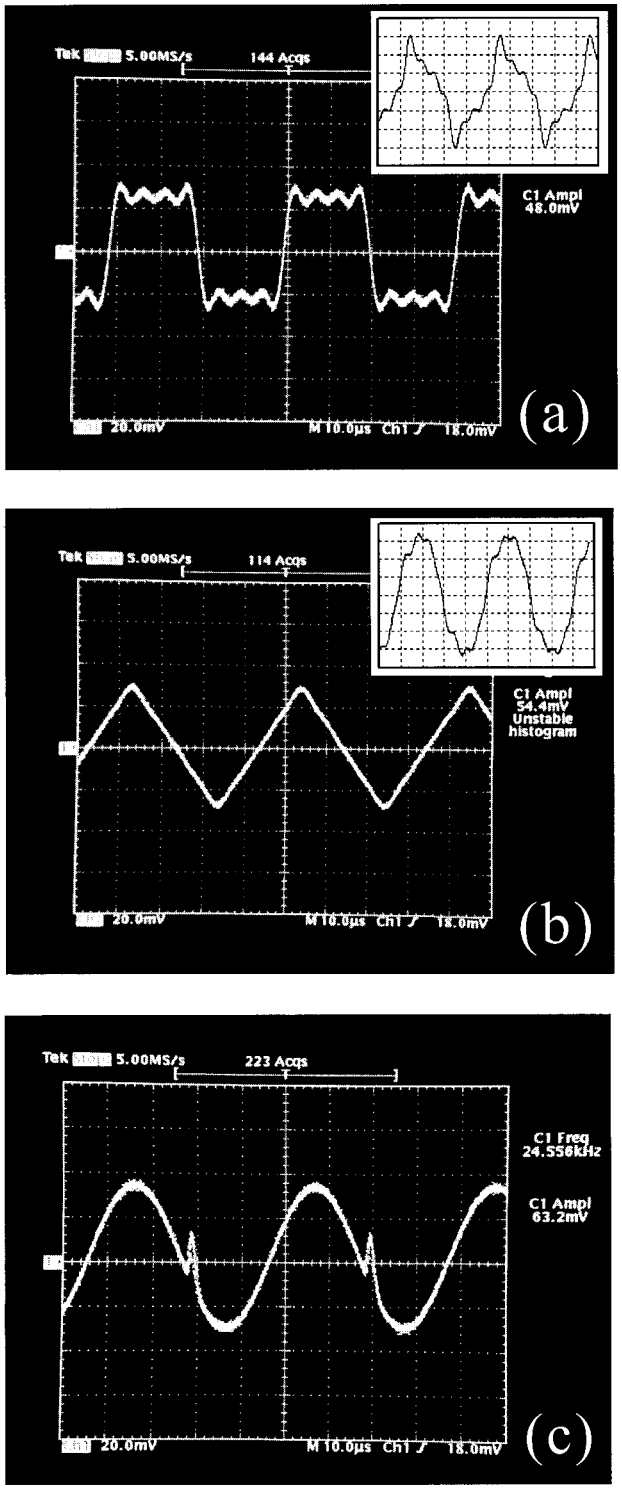

FIG. 2. Measured waveforms of the driving sound pressures. (a) Rectangular wave. (b) Triangular wave. (c) Sinusoidal wave with a pulse. The insets in (a) and (b) are their originally electrical signals.

the acoustic signal (the acoustic spike), so that we can keep the bubble levitation well. We can easily generate the spike driving signal in an electrical form. Two channels of the multifunction synthesizer are enough to generate the original electrical signal: one of them is for a sinusoidal wave and another for a pulse. It is not necessary to use the optimizing arithmetic because of no special requirement for the pulse shape. The experimental pressure waveform of the spiking

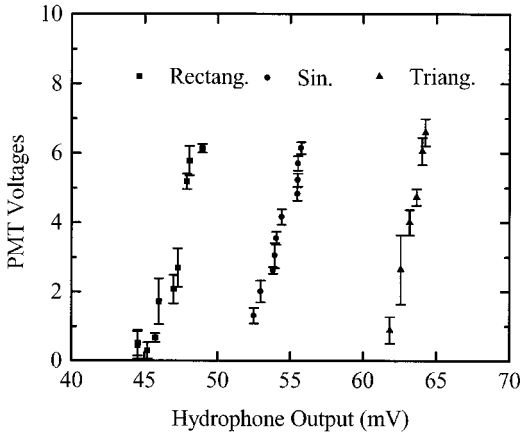

FIG. 3. The measured intensity of the SBSL flashes as a function of the sound pressure amplitude. The solid circles are the results driven by the sinusoidal waves, and squares and triangles are those driven by rectangular and triangular waves, respectively.

driving is shown in Fig. 2(c). Comparing with the acoustic spike,[16] the advantage of the electrical spike has weak acoustic radiation, which makes the bubble levitation possible.

All experiments are conducted at ambient temperature $10°\pm1$ °C.

III. EXPERIMENTAL RESULTS

We have measured the relation between the SBSL intensity and the sound pressure amplitude under the driving of three types of the sound waveforms, the rectangular, triangular, and the sinusoidal as well. In Fig. 3 it can be seen that the different waveform possesses a different driving effect; although the SBSL intensity increases for all three cases with increasing of sound pressure amplitude. For getting a same strength of the SBSL flashes, the rectangular wave needs the lowest sound pressure amplitude, and the triangular wave, the largest. However, if we keep the sound power unchanged, the result is the opposite, i.e., the triangular wave is more effective to make the SBSL than the simple harmonic and rectangular waves (see Fig. 4). The sound power in Fig. 4 comes from the waveform measurement and sphere wave

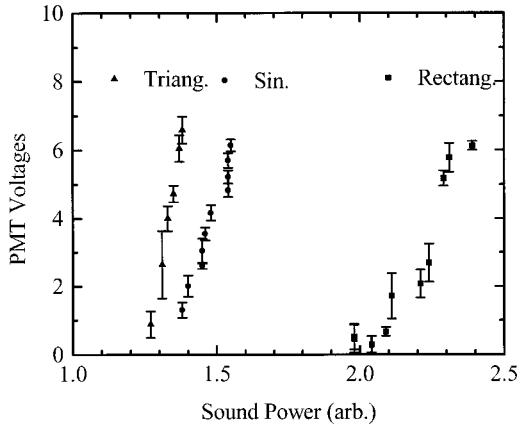

FIG. 4. The measured intensity of the SBSL flashes as a function of the sound power. The solid circles are the results driven by the sinusoidal wave, and squares and triangles are those driven by rectangular and triangular waves, respectively.

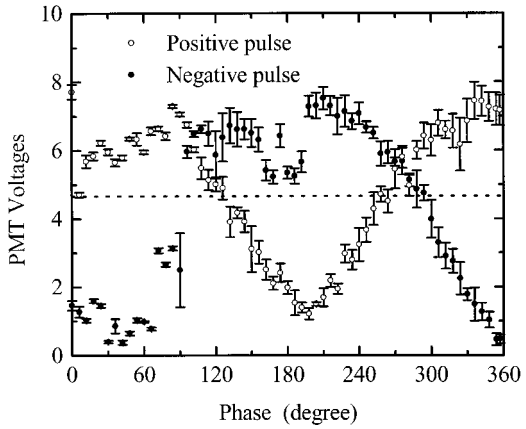

FIG. 5. The measured intensity of the SBSL flashes driven by a sinusoidal wave ($\cos \omega t$) with a pulse as a function of the phase position of the pulse. The open circles are the experimental data driven by a $\cos \omega t$ superposing a positive pulse [see Fig. 2(c)]; and the solid ones are those by a $\cos \omega t$ with a negative pulse. The dotted line shows the SBSL intensity driven by a pure sinusoidal wave.

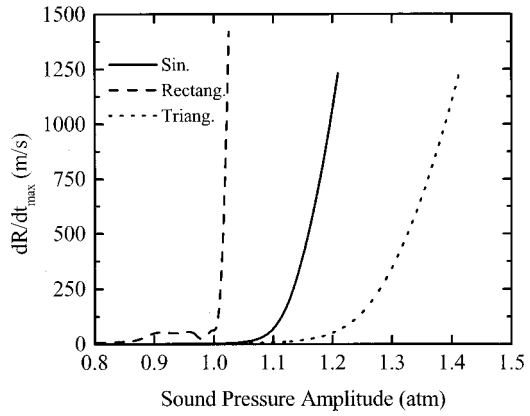

FIG. 6. The numerical results of the maximum velocity of the bubble wall as a function of the sound pressure amplitude. The solid curve is the result driven by a sinusoidal wave, and the dashed and dotted curves are those driven by rectangular and triangular waves, respectively.

assumption. The data are somewhat scattered due to the complexity of the experiment. We believe that the main error comes from the regeneration of the bubble and the change of its position under the different driving condition.

We also drive the water by a superposition of a sinusoidal wave and a pulse wave at the same frequency. Although the spiking drive decreases the stability of the levitation of the bubble,[16] a simple harmonic pressure with a small pulse is still a good drive to make the SBSL. In our experiment, a stable and periodic SBSL driven by the sinusoidal wave with a pulse has been observed, and the results show both the positive pulse and the negative pulse can change the strength of the SBSL flashes, whether increasing or decreasing flashes relates to the phase position as the pulse is added in. A suitable spike can boost the SBSL flashes, as Moss *et al.* predicted.[15] Figure 5 shows the dependence of the SBSL intensity on the phase position of the pulse. Although there are also jumps in the data, we are still easy to conclude that in order to enhance the flashes, the positive pulse should be added in the positive phase of the sinusoidal wave, that is, for a $\cos \omega t$ the positive pulse should be added in the phase region from $-\pi/2$ to $\pi/2$. If it is added in the negative phase of the $\cos \omega t$, say, $(\pi/2, 3\pi/2)$, the pulse will weaken the SBSL flashes (see the open circles in Fig. 5). Of course, the negative pulse added in the negative phase will upscale the SBSL flashes, an otherwise negative pulse added in the positive phase will weaken the SBSL flashes (see the solid circles in Fig. 5). As a comparison, we also give the SBSL flash intensity without the spike, see the dotted line in Fig. 5.

The data in Figs. 3–5 have been arranged over the five time measurements. The error bars in these figures show the standard deviation of the measurements.

IV. NUMERICAL SIMULATION

Numerical simulations have been carried out using the uniform adiabatic model. The Rayleigh–Plesset equation (RP) describes the dynamics of the bubble radius,

$$R\ddot{R}+\frac{3}{2}\dot{R}^2=\frac{1}{\rho_l}(P_g(R,t)-P_a(t)-P_0) + \frac{R}{\rho_l c_l}\frac{d}{dt}(P_g(R,t)-P_a(t))-4\nu\frac{\dot{R}}{R}-\frac{2\sigma}{\rho_l R}, \quad (8)$$

where the overdot stands for the derivative with respect for the time t, R is the bubble radius, $P_g(R,t)$ and P_0 are the gas pressure inside the bubble and the ambient pressure; ρ_l, c_l, ν, and σ, are the density, the sound velocity, the kinetic viscosity, and the surface tension of the liquid, respectively. In a simplified model, we regard the bubble motion as an adiabatic process,

$$P_g(R,t)=P_0\left(\frac{R_0^3-a^3}{R^3-a^3}\right)^{\gamma}, \quad (9)$$

where $a=R_0/8.54$ is the hard core van der Waals radius for gas bubble,[18] the exponent γ is the adiabatic exponent of the gas, 1.4 for the biatomic gas, $P_0=1.0336\times10^5$ Pa is the ambient pressure, and R_0 is the ambient radius of the bubble (4.5 μm here), respectively. For our experiment the parameters of the water are $\rho_l=1000$ kg/m^3, $c_l=1500$ m/s, $\nu=1.433\times10^{-6}$ m^2/s, $\sigma=7.46\times10^{-2}$ N/s. The frequency of the fundamental of the drive is 24.5 kHz, and the temperature of the system is controlled at $T_0=283$ K. The computation shows that the evolution of the bubble radius is different under different driving wave, similar to those shown in Ref. 16. It can be seen from the calculation that the triangular wave makes a larger expansion of the bubble radius than that of the sinusoidal wave under the same driving power, while the rectangular wave does the lowest expansion. So, we can conclude that the triangular wave is the most efficient among all these types of driving waveforms.

Furthermore, according to the shock wave mechanism[12] the temperature inside the bubble or the SBSL intensity relates to the velocity of the bubble wall, dR/dt. Figures 6 and 7 plot the maximum velocity of the bubble wall as functions of the sound pressure amplitude and sound power, respectively. A well qualitative agreement with the experimental measurements in Figs. 3 and 4 has been achieved. The nu-

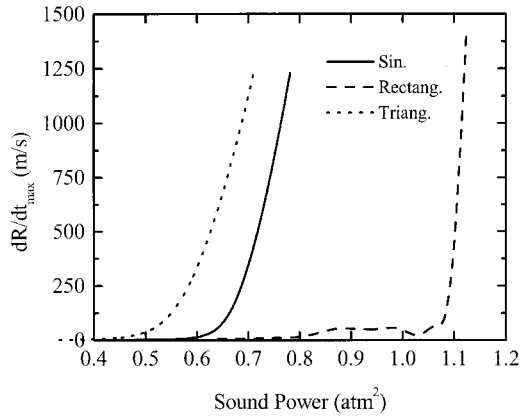

FIG. 7. The numerical results of the maximum velocity of the bubble wall as a function of the sound power. The solid curve is the result driven by a sinusoidal wave, and the dashed and dotted curves are those driven by rectangular and triangular waves, respectively.

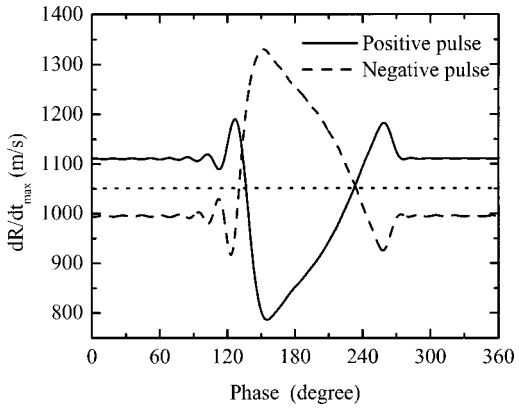

FIG. 9. The numerical result of the SBSL intensity driven by a sinusoidal wave with a pulse as a function of the position of the pulse. The solid curve is for a positive pulse and the dashed curve for a negative one. The dotted line is the value of $dR/dt_{\max}$ driven by a pure sinusoidal wave. The amplitude of the single harmonic wave is set at 1.2 atm.

merical calculation can also show why the rectangular wave can drive the bubble at very low amplitude of the sound pressure. In Fig. 8 we print out three radius–time curves. Although the rectangular wave is at lowest amplitude (1.08 atm), it drives the largest bubble motion over the sinusoidal wave at 1.25 atm and triangular wave at 1.35 atm. The reason is quite simple. The rectangular wave possesses the largest power at the same amplitude. At the same time, under the drive of the rectangular wave, the bubble cannot expand completely, so the constriction and the rebound of the bubbles take place during the expansion phase of the drive (see Fig. 8). Therefore the rectangular wave is not the most efficient to drive SBSL.

In the same way, we drive the water by a sinusoidal wave with a pulse function as the following:

$$P(t)=P_a\left(\beta+\frac{1}{\pi}\sum_{n=1}^{N}\left(c_n\cos(n\omega t)+d_n\sin(n\omega t)\right)\right), \tag{10}$$

$$c_n=\frac{1}{n}(\sin(2n\pi(\alpha+\beta))-\sin(2n\pi\alpha)), \tag{11}$$

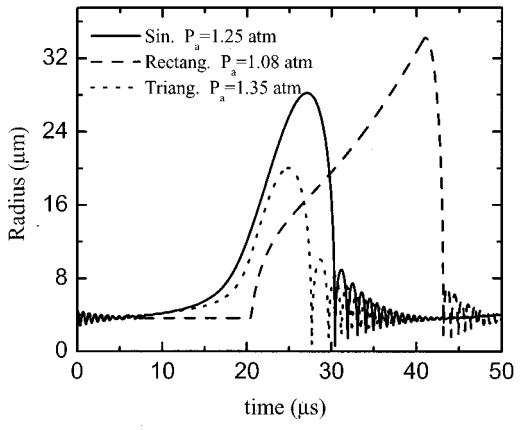

FIG. 8. The radius evolution curves. The rectangular wave (dashed) drives the largest bubble radius at the lowest pressure amplitude.

$$d_n=\frac{1}{n}(\cos(2n\pi\alpha)-\cos(2n\pi(\alpha+\beta))), \tag{12}$$

where α is the relative phase of the pulse, and β the ratio of the pulse width to the cycle period. We can obtain a relation between the maximum velocity of the bubble wall, $(dR/dt)_{\max}$, and the phase position of the pulse with respect to the sinusoidal wave (see Fig. 9). In Fig. 9, the amplitude of the sinusoidal wave is set at 1.2 atm. The maximum velocity driven by this pure sinusoidal wave is about 1050 m/s, as shown by a dotted line in Fig. 9. We can see that the numerical results in Fig. 9 is also in good agreement with that observed in the experiment (Fig. 5).

V. CONCLUSIONS

In summary, our experiments show again that the intensity of the SBSL flashes is sensitive to the driving waveform of the ultrasound.[10,16] Both a well-known rectangular wave and a triangular wave can also drive the SBSL with quite a strong stability. Like the sinusoidal wave we usually use, under these non-simple-harmonic waves the SBSL flashes will also become bright as the sound amplitude or power increases within a quite wide region of the parameters. Their effects on the SBSL flash, however, are different. For a given amplitude, the rectangular wave yields the strongest flashes, the triangular wave the weakest, and the sinusoidal wave in the middle. On the other hand, if we keep the constant sound power the result will be reversed, that is, the triangular wave can make the bubble emit the brightest flashes. Therefore, the triangular wave is a more effectively driving source than the sinusoidal wave we usually used in the SBSL experiment. These experimental observations have been compared with the numerical calculations based on the Rayleigh–Plesset equation. Well qualitative agreements have been achieved. In the numerical calculation, we can understand the dependence of the SBSL on the driving waveform clearly. For a given amplitude of the driving sound, the rectangular wave possesses much larger sound power than that of other waveforms, so it drives the SBSL flash to the brightest. But under the drive of the rectangular wave, the bubble

cannot expand completely. Therefore the rectangular wave is not the best waveform at a given sound power. On the opposite, the bubble can grow completely and effectively under the drive of the triangular wave, so the triangular wave is the most effective waveform. In conclusion, we can say that the bubble seems to prefer the triangular wave as a driving sound. Furthermore, the experiment shows that a suitable pulse added into a sinusoidal wave can enhance the strength of the SBSL flashes with a strong stability. Our experiment proves that the spiking SBSL[15] is feasible not only in a transient proceeding,[16] but also periodically. The positive pulse, of course, must be added in the compression phase and the negative one in the expansion phase in order to raise the SBSL flashes. As mentioned in Refs. 10 and 16–18, all of the non-simple-harmonic sounds, of course, will more or less decrease the stability of the bubble levitation, and the sinusoidal wave can produce a moderate SBSL with the strongest stability.

ACKNOWLEDGMENTS

This work was partly supported by the National Natural Science Foundation of China (Grant No. 10174036), the TransCentury Training Programme Foundation for the Talents by the State Education Commission of China, and the Special Funds for major State Based Research Projects of China.

[1] D. F. Gaitan, L. A. Crum, C. C. Church, and R. A. Roy, ''Sonoluminescence and bubble dynamics for a single, stable, cavitation bubble,'' J. Acoust. Soc. Am. **91**, 3166–3188 (1992).
[2] R. Hiller, S. J. Putterman, and B. P. Barber, ''Spectrum of synchronous picosecond sonoluminescence,'' Phys. Rev. Lett. **69**, 1182–1185 (1992).
[3] R. Killer, K. Weninger, S. J. Putterman, and B. P. Barber, ''Effect of noble-gas doping in single-bubble sonoluminescence,'' Science **266**, 248–250 (1994).
[4] R. Pecha *et al.*, ''Resolving the sonoluminescence pulse shape with a streak camera,'' Phys. Rev. Lett. **81**, 717–720 (1998).
[5] J. B. Young, J. A. Nelson, and W. Kang, ''Line emission in single-bubble sonoluminescence,'' Phys. Rev. Lett. **86**, 4934–4937 (2001).
[6] M. Dan and J. D. N. Cheeke, ''Ambient pressure effect on single-bubble sonoluminescence,'' Phys. Rev. Lett. **83**, 1870–1873 (1999).
[7] S. Hilgenfeldt, D. Lohse, and W. C. Moss, ''Water temperature dependence of single bubble sonoluminescence,'' Phys. Rev. Lett. **80**, 1332–1335 (1998).
[8] R. Hiller, S. J. Putterman, and K. R. Weninger, ''Time-resolved spectra of sonoluminescence,'' Phys. Rev. Lett. **80**, 1090–1093 (1998).
[9] T. J. Matula and L. A. Crum, ''Evidence for gas exchange in single-bubble sonoluminescence,'' Phys. Rev. Lett. **80**, 865–868 (1998).
[10] J. Holzfuss, M. Rüggeberg, and R. Mettin, ''Boosting sonoluminescence,'' Phys. Rev. Lett. **81**, 1961–1963 (1998).
[11] R. G. Holt and D. F. Gaitan, ''Observation of stability boundaries in the parameter space of single bubble sonoluminescence,'' Phys. Rev. Lett. **77**, 3791–3794 (1996).
[12] C. C. Wu and P. H. Roberts, ''A model of sonoluminescence,'' Proc. R. Soc. London, Ser. A **445**, 323–349 (1993).
[13] C. Eberlein, ''Sonoluminescence as quantum vacuum radiation,'' Phys. Rev. Lett. **76**, 3842–3845 (1996).
[14] J. R. Willison, ''Sonoluminescence: proton-tunneling radiation,'' Phys. Rev. Lett. **81**, 5430–5433 (1998).
[15] W. C. Moss, D. B. Clarke, J. W. White, and D. A. Young, ''Sonoluminescence and the prospects for table-top microthermonuclear fusion,'' Phys. Lett. A **211**, 69–74 (1996).
[16] K. Hargreaves and T. Matula, ''The radial motion of a sonoluminescence bubble driven with multiple harmonics,'' J. Acoust. Soc. Am. **107**, 1774–1776 (2000).
[17] S. Hilgenfeldt and D. Lohse, ''Predictions for upscaling sonoluminescence,'' Phys. Rev. Lett. **82**, 1036–1039 (1999).
[18] R. Löfstedt, B. P. Barber, and S. J. Putterman, ''Toward a hydrodynamic theory of sonoluminescence,'' Phys. Fluids A **5**, 2911–2928 (1993).

Application of narrow band laser ultrasonics to the nondestructive evaluation of thin bonding layers

Y.-H. Liu, T.-T. Wu,[a] and C.-K. Lee
Institute of Applied Mechanics, National Taiwan University, Taipei, Taiwan

(Received 9 June 2000; revised 2 April 2001; revised 20 January 2002; accepted 28 January 2002)

In this paper, a modified laser induced grating technique (LIG) has been utilized to generate narrow band surface waves in an epoxy-bonded copper-aluminum layered structure. A high performance optical interferometer system was utilized to detect the laser-generated surface waves. The dispersion of surface wave in an epoxy-bonded copper-aluminum specimen was measured and compared with the theoretical solution. An inverse algorithm based on the simplex method was then introduced to determine the bonding thickness as well as the elastic properties of the bonding layer. The inversion results demonstrated that the thickness in the μm range or the elastic properties of the bonding layer could be successfully determined. [DOI: 10.1121/1.1463449]

PACS numbers: 43.35.Ns, 43.35.Yb [SGX]

I. INTRODUCTION

Due to the noncontact feature, laser-generated ultrasounds have shown its potential in nondestructive evaluation of materials.[1] The pulsed laser-generated Lamb waves in thin composite plates[2–7] have been employed to investigate the possible applications in the NDE of such structures. Laser-generated ultrasonic bulk wave[8] and surface waves[9–14] have also been applied to the determination of elastic constants or defects of composite structures. The point-source/point-receiver technique has been adopted by most of the existing studies to ensure the broadband generation of ultrasonic waves. With the point generation, a relative large laser power has to be focused on a point with small area to improve the measuring sensitivity and this usually results to partial damage of the testing specimen. As the dimensions of the specimen is getting smaller and smaller, the power of the pulsed laser has to be minimized and limited in the thermoelastic range. On the other hand, increase of laser power also results to a decrease in the central frequency of the laser-generated ultrasonic waves.

Different from the focused point source method, the laser induced grating (LIG) technique can be utilized to generate coherent surface acoustic waves (SAWs) of a few MHz to the GHz range.[15,16] In this technique, two short pulsed laser beams with identical frequency are used to form interference fringes on the surface of solid specimens. Although the laser beam is not focused to give high intensity on the surface, the ordered fringes do increase the generated SAW amplitudes for propagation direction normal to the fringes. To further enhance the SAW amplitude, the scanning single beam (SSB) approach[17–19] and the scanning interference fringes (SIF) approach[20] can be adopted.

In this paper, a modified laser induced grating method (LIG) was proposed to generate narrow band surface waves in a thin epoxy-bonded layered structure. A high performance Doppler interferometer system[21,22] was utilized to detect the laser-generated waves. The dispersion of SAW in an epoxy-bonded copper-aluminum specimen was measured and compared with the theoretical solution. An inverse algorithm based on the simplex method was then introduced to determine the bonding thickness as well as the elastic properties of the bonding layer.

II. THE LASER INDUCED GRATING TECHNIQUE

The basic principle of the LIG technique is illustrated in Fig. 1(a). In the figure, a pulsed laser beam is split into two pulsed laser beams of the same frequency ω and then incident on the surface of a solid. On denoting the amplitudes and wave number of the incident light beams as I_1, I_2, and k, the intensity of the interfered laser beams can be expressed as

$$I^2 = I_1^2 + I_2^2 + 2I_1 I_2 \cos(2k \sin\theta)x, \tag{1}$$

where x-axis lies on the specimen surface and is normal to the interference fringes. θ is the incident angle of the laser beam to the normal of the surface. From the last term of Eq. (1), the spacing of the static interference fringes Λ can be obtained, by setting $(2k \sin\theta)\Lambda = 2\pi$, as $2\Lambda = \lambda/\sin\theta$, where λ is the wavelength of the incident light beam. On the other hand, as θ is small, $\sin\theta$ can be approximated as $\sin\theta \approx d/2S$, where d is the distance between the beam splitter and the beam reflector, while S is the distance between the splitter (and reflector) and the specimen surface [Fig. 1(a)]. To generate ultrasonic surface waves in the MHz range, we note that the incident angle must be very small. For example, for the use of the second harmonics of an Nd-YAG pulsed laser ($\lambda = 532$ nm) to generate a 5 MHz surface wave on a steel sample (3000 m/s is assumed for the Rayleigh wave velocity), the incident angle is approximately 0.025 deg. To ensure this small angle, the distance S from the beam splitter to the sample surface is very long and is not practical for nondestructive applications.

[a]Author to whom correspondence should be addressed.

 0001-4966/2002/111(6)/2638/6/$19.00

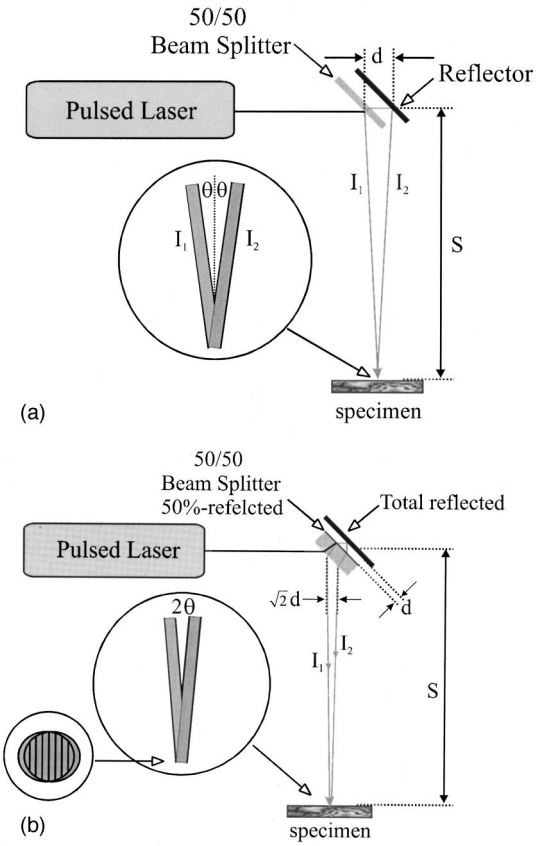

FIG. 1. (a) Basic principle of the LIG technique. (b) Modified laser beam path of the LIG technique.

In this study, a modified laser beam path of the LIG technique is proposed. Figure 1(b) shows that a reflector is placed parallel and just next to the beam splitter (50% reflection) with a small distance d. As shown in the figure, the beam I_2, which is transmitted through the beam splitter and then reflected back into the beam splitter, forms a small horizontal gap $\sqrt{2}d$. As the incident angle is small, $\sin\theta$ can be approximated as $d/\sqrt{2}S$. With this modified arrangement, for a fixed S, the distance d can be adjusted precisely to a very small value to achieve a small incident angle θ.

It is worth noting that on using the modified LIG technique, the amplitudes of the two incident beams are not equal in general. For example, for the case of a beam splitter with 50% reflection, the amplitude of I_1 is 50% and that of I_2 is 25% of the incident beam. For $I_1 \neq I_2$, from Eq. (1), we note that it is impossible to obtain totally destructive interference. Therefore, in addition to the grating induced signals, the finite aperture laser source with intensity $I_1^2+I_2^2$ may generate a low frequency signal as well. However, this unwanted signal could be overcome by using digital filtering technique or using a special designed beam splitter to make $I_1=I_2$.

III. DISPERSION OF SURFACE WAVES IN A THIN LAYERED STRUCTURE

For point source acting on a layered half space, it is known that the wave signals received at two different receivers are different in both the amplitudes and phases due to the wave dispersion in the layered structure. Since the pulsed laser utilized in this study generates stable source, instead of using one LIG source and two optical receivers, one optical receiver and two LIG sources were utilized. The advantage of this alternative is that only one optical receiver is needed in the experiment, further, the precision of the change of the source to receiver distance can be controlled by a precise translation stage.

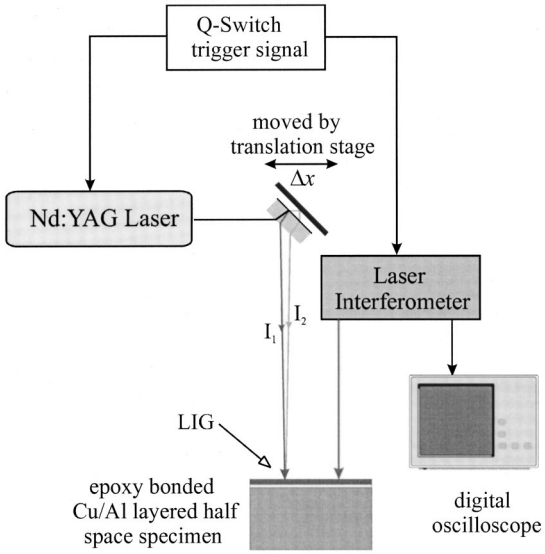

FIG. 2. Experimental set-up of the laser ultrasonic experiment.

A. Experimental setup

Shown in Fig. 2 is the experimental setup utilized in this study. An Nd:YAG pulsed laser (Quanta-Ray, GCR-130) (wavelength 532 nm) was utilized to generate narrow band elastic waves in the layered specimen based on the LIG technique. The duration of the laser pulse utilized was 10 ns. The layered specimen was fixed on a precision translation stage to accurately control the distance between the source and the receiver. To achieve a truly noncontact measurement, in addition to the noncontact pulsed laser source, an optical interferometer[21,22] was utilized to measure the generated elastic wave signals. The received voltage signals from the interferometer were recorded by a 250 MHz digital oscilloscope (LeCroy 9354CM) and then sent into a personal computer to do further signal processing. A trigger signal synchronized with the laser source was utilized to trigger the digital oscilloscope.

In this study, an epoxy bonded copper-aluminum layered half space specimen was made. The thickness of the copper thin plate is 0.1 mm. A small epoxy specimen was made from the same mixture as that used for bonding the copper thin plate on the aluminum block. The elastic wave velocities of the epoxy were measured by the ultrasonic pulse-echo method with a 5 MHz ultrasonic transducer. The measured results of the epoxy sample were

$$C_L = 2558.9 \text{ m/s}, \quad C_T = 1116.0 \text{ m/s}, \quad \rho = 1137.8 \text{ kg/m}^3.$$

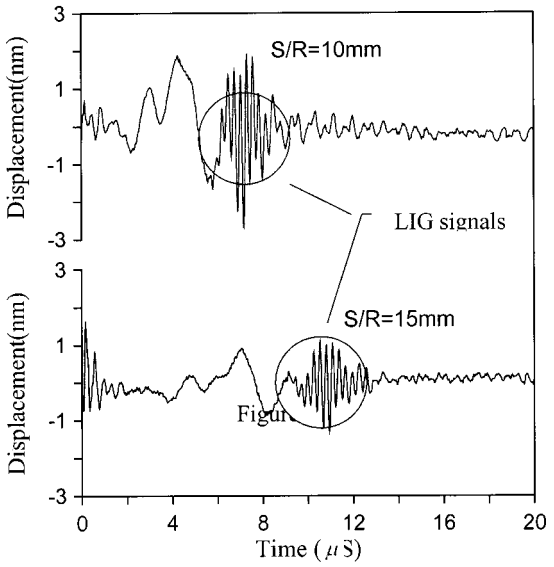

FIG. 3. Wave signals received at two different positions on the surface of the specimen. The source-receiver distance of the upper trace is 10mm, while the lower trace is 15mm.

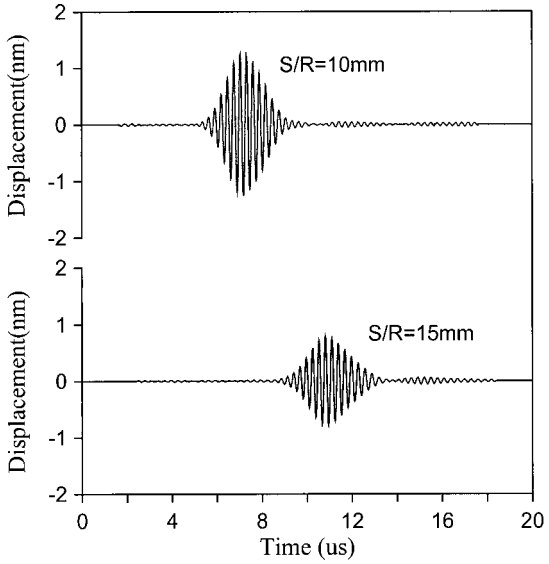

FIG. 4. The wave signals after filtering.

B. The experimental dispersion curve

In the LIG experiment, the distance S between the splitter (and reflector) and the specimen surface was set equal to 50 cm. The diameter of the LIG source is approximately equal to 5 mm.

Figure 3 shows the wave signals (wave displacement perpendicular to the sample surface) received at two different positions on the surface of the specimen. The upper trace is the wave signal received with the source–receiver distance equal to 10 mm, while the source–receiver distance is equal to 15 mm for the lower trace. Results show that, in addition to the LIG induced signal (the circled region), the finite aperture laser source also generates a background signal with lower frequency. As explained in Sec. II, the background signal is generated due to the squared terms $I_1^2+I_2^2$ in Eq. (1), which behave like an area source with aperture approximately equal to the diameter of the LIG source.

The central frequency of the LIG induced surface wave signals can be obtained by using the spectrum analysis. To eliminate the unwanted signals due to the unequal intensity of the two incident beams, a band-pass filter was used. The wave signals after filtering are shown in Fig. 4. The results show that the unwanted background signals could be filtered out almost completely. The cross-correlation function was then used to estimate the time delay of the two wave signals. The central frequency of the filtered signals shown in Fig. 4 is 3.5 MHz. The time delay between these two signals with 5 mm distance difference is 2.988 μs, therefore, the velocity can easily be calculated as 1673.4 m/s. It is worth noting that the signals shown in Fig. 4 are wave bursts with very narrow bandwidth, therefore, the wave velocity calculated by the cross-correlation method could be assumed equal to the phase velocity approximately.

On changing the gap distance d between the beam splitter and reflector lens, various interference fringes Λ can be obtained. And then, the corresponding surface wave velocity with different frequencies can be determined accordingly. The square symbols shown in Fig. 5 denote the measured velocity dispersion of the LIG induced surface wave. The highest frequency of the surface waves generated by the LIG technique was 10 MHz.

The theoretical dispersion curves of this study were calculated using a general-purpose computer program[12] for the calculation of the dispersion curves of isotropic as well as anisotropic layered media. The lines shown in Fig. 5 are the dispersion curves of an epoxy-bonded copper-aluminum specimen with different bonding thickness ranging from 0 H to 0.2 H. Results show that the phase velocity of the fundamental surface wave mode decreases from the Rayleigh surface wave velocity of aluminum to a local minimum and then increases to that of copper. The shapes of the dispersion curves are strongly dependent on the thickness of the epoxy-bonding layer in such a way that the thicker the epoxy-bonding layer, the deeper the dip in the dispersion curves.

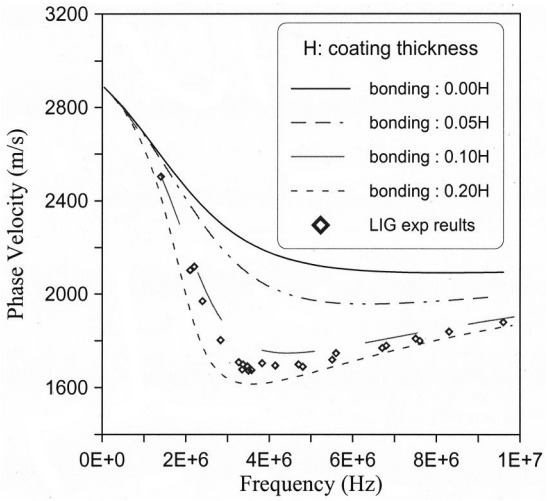

FIG. 5. The measured phase velocity dispersion (squares) and the calculated phase velocity dispersion (lines) of the fundamental mode of surface waves in the layered specimen with different bonding thickness.

TABLE I. Lists of the initial guesses and the inverse results of the bonding thickness. Initial guesses of the thickness are ranging from 0.0 H to 1.0 H.

$H1$ (H)	$H2$ (H)	Number of iterations	Thickness (H)	Error ($\times 10^{-4}$)
0.2	0.3	20	0.1362	1.0405
0.3	0.5	23	0.1362	1.0404
0.5	0.7	24	0.1361	1.0404
0.5	1.0	25	0.1361	1.0403
0.1	0.2	19	0.1362	1.0404
0.0	0.1	23	0.1362	1.0403

IV. INVERSION OF BONDING THICKNESS AND BONDING PROPERTIES

The forward calculations of the phase velocity dispersions showed that the shapes of the dispersion curves are strongly dependent on the thickness of the epoxy-bonding layer. From Fig. 5, it can be found approximately that the thickness of the bonding layer thickness lies between 0.1 H and 0.2 H.

To further determine the thickness (or elastic properties) of the bonding layer quantitatively, an inverse algorithm, which adopts the simplex method,[23] is used. In the following, an error function which defines the difference between the measured (ν_m) and the guessed (ν_g) phase velocities was defined as

$$e=\frac{\Sigma_{i=1}^{N}[\nu_m(i)-\nu_g(i)]^2}{\Sigma_{i=1}^{N}[\nu_m(i)]^2}, \tag{2}$$

where i represents the discrete frequency and N is the number of data points utilized in the inversion process. In the inversion process, say for recovering the bonding thickness, initial guesses of the bonding thickness were made first, then the forward computer program for calculating the phase velocity dispersion of surface wave in a layered medium was utilized to calculate the guessed phase velocities (ν_g). The value of the error function can thus be obtained from Eq. (2). The true thickness of the bonding layer was determined by finding the minimum of the error function using the simplex method.

A. Inversion of bonding thickness

If the elastic properties of the epoxy are assumed known, the thickness of the epoxy layer can be obtained inversely. The measured phase velocities shown in Fig. 5 were adopted to determine the bonding thickness of the epoxy layer. Since only one parameter is to be inversely determined (the bonding thickness), two initial guesses of the thickness are required in the simplex algorithm. To test the influence of the initial guesses on the inverse result, a variety of initial guesses of the thickness ranging from 0.0 H to 1.0 H were utilized (Table I). From Table I, one finds that the true thickness can be obtained even for very poor initial guesses. For example, in the fourth try of Table I, the initial guesses were 0.5 H and 1.0 H, the iterations needed to converge to the true value is only 25. The inversion results showed that the bonding layer thickness of the specimen was 0.136 H. Shown in Fig. 6 is the comparison of the measured and the calculated (with the bonding thickness equal to 0.136 H) phase velocity dispersion. The results show very good agreements between these two dispersion curves. Since the thickness of the copper layer is 100 μm, the epoxy-bonding layer is determined to be 13.6 μm.

B. Inversion of ρ, C_L, and C_T of epoxy-bonding layer

The longitudinal and transverse wave velocities are related to the density and the elastic moduli of a solid, and therefore, measurements of the elastic wave velocities of a bonding layer are useful in accessing the bonding quality. As shown in a previous paper by the authors,[13] to accelerate and improve the inversion accuracy, reasonable constraints on the inversion parameters are found very useful. In this study, the constraints on the density, longitudinal wave velocity and transverse wave velocity were set as $550<\rho<1800$ kg/m^3, $1600<C_L<3900$ m/s, and $500<C_T<1700$ m/s. We note that the constraints are very reasonable for they cover most of the elastic wave velocities and density of the commercially available epoxy.

The measured phase velocities shown in Fig. 5 were again adopted to determine ρ, C_L, and C_T of the thin epoxy layer inversely. Since the number of unknowns is three, four sets of initial guesses are required in the simplex inversion algorithm. The initial guesses and the inverse results of density, longitudinal, and transverse wave velocities of the epoxy-bonding layer are shown in Table II. In this study, five

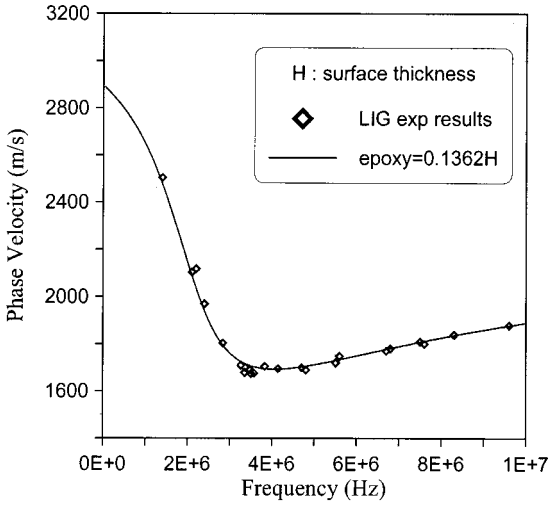

FIG. 6. The comparison of the measured and the calculated (with the bonding thickness equal to 0.136 H) phase velocity dispersions.

TABLE II. Lists of the initial guesses and the inverse results of the density, the longitudinal, and transverse wave velocities of the bonding layer.

Group	Guess d (kg/m^3)	Guess C_L (m/s)	Guess C_T (m/s)	Error ($\times 10^{-4}$)	Density (kg/m^3)	C_L (m/s)	C_T (m/s)
1	1150	2500	1100				
	950	2200	900				
	750	1900	700				
	550	1600	500	1.0365	1158.15	2512.26	1108.15
2	1400	2750	1350				
	1200	2550	1150				
	1000	2350	950				
	800	2150	750	1.0430	1154.45	2504.45	1104.45
3	1800	3850	1700				
	1600	3450	1500				
	1400	3050	1300				
	1200	2650	1200	1.0290	1146.097	2542.19	1098.67
4	1250	2700	1200				
	1200	2600	1150				
	1150	2500	1000				
	1050	2400	1000	1.0339	1154.44	2527.17	1104.44
5	1200	2650	1150				
	1150	2550	1000				
	1100	2450	1050				
	1050	2350	900	1.0271	1150.99	2551.97	1091.32

different groups of initial guesses were tested. The four sets of initial guesses in each group are shown in the second to the fourth column of the table. The last three columns are the inversion results of ρ, C_L, and C_T, respectively. Results show that in spite of the big difference of the initial guess, the inversion results do converge nicely to a similar value. The average inverse values of the five inversion groups are $\rho = 1152.8$ kg/m^3, $C_L = 2527.6$ m/s, and $C_T = 1101.4$ m/s. The averaged inversion results of the density, the longitudinal wave velocity, and the transverse wave velocity of the epoxy are within 2% difference with those of the measured ones shown in Sec. III A, i.e., $\rho = 1137.8$ kg/m^3, $C_L = 2558.9$ m/s, and $C_T = 1116.0$ m/s.

V. CONCLUDING REMARKS

In this paper, a modified laser induced grating technique (LIG) has been utilized to generate narrow band surface waves in an epoxy-bonded copper-aluminum layered structure. A high performance optical interferometer system was utilized to detect the laser-generated waves. The dispersion of SAW in an epoxy-bonded copper-aluminum specimen was measured and compared with the theoretical solution. An inverse algorithm based on the simplex method was introduced to determine the bonding thickness as well as the elastic properties of the bonding layer. The inversion results demonstrated that the thickness or the elastic properties of the thin bonding layer could be successfully determined. We note that in the current experimental setup, the interference fringes Λ cannot be controlled accurately, so the velocity dispersion was measured using the cross correlation of responses at two different locations. However, if the interference fringes Λ can be controlled or determined accurately, the phase velocity dispersion can be measured in a more straightforward way.[16–18] In addition, on adopting the scanning interference fringe approach (SIF) of the phase velocity scanning method,[20] much higher frequency surface waves can be generated, and therefore, much thinner layered specimen can be evaluated inversely.

ACKNOWLEDGMENT

The authors thank the financial support of this research from the National Science Council of ROC through Grant No. NSC 89-2212-E-002-009.

[1] C. B. Scruby and L. E. Drain, *Laser Ultrasonics: Techniques and Applications* (IOP Publishing Ltd., Bristol, England, 1990).
[2] D. A. Hutchins, K. Lundgren, and S. B. Palmer, "A laser study of the transient Lamb waves in thin materials," J. Acoust. Soc. Am. **85**, 1441–1448 (1989).
[3] R. J. Dewhurst, C. Edwards, A. D. W. Mckie, and S. B. Palmer, "Estimation of the thickness of thin metal sheet using laser generated ultrasound," Appl. Phys. Lett. **51**, 1066–1068 (1987).
[4] H. Nakano and S. Nagai, "Laser generation of anti-symmetric Lamb waves in thin plates," Ultrasonics **29**, 230–234 (1991).
[5] M. Veidt and W. Sachse, "Ultrasonic point-source/point-receiver measurements in thin specimens," J. Acoust. Soc. Am. **96**, 2318–2326 (1994).
[6] P. A. Doyle and C. M. Scala, "Ultrasonic measurement of elastic constants for composite overlays," Rev. Prog. Quant. Nondestr. Eval. **10B**, 1453–1459 (1991).
[7] L. P. Scudder, D. A. Hutchin, and N. Guo, "Laser-generated ultrasonic guided waves in fiber-reinforced plates—Theory and experiment," IEEE Trans. Ultrason. Ferroelectr. Freq. Control **43**, 870–880 (1996).
[8] T.-T. Wu and Y.-H. Liu, "On the measurement of anisotropic elastic constants of fiber reinforced composite plate using ultrasonic bulk wave and laser generated Lamb wave," Ultrasonics **37**, 405–412 (1999).
[9] K. Castagnede, K. Y. Kim, W. Sachse, and M. O. Thompson, "Determination of the elastic constants of anisotropic materials using laser-generated ultrasonic signals," J. Appl. Phys. **70**, 150–157 (1991).
[10] T.-T. Wu and J.-F. Chai, "Propagation of surface waves in anisotropic solids: Theoretical calculation and experiment," Ultrasonics **32**, 21–29 (1994).
[11] J.-F. Chai and T.-T. Wu, "Determinations of anisotropic elastic constants using laser generated surface waves," J. Acoust. Soc. Am. **95**, 3232–3241 (1994).

[12] T.-T. Wu and Y.-C. Chen, ''Dispersion of laser generated surface waves in an epoxy-bonded layered medium,'' Ultrasonics **34**, 793–799 (1996).
[13] T.-T. Wu and Y.-H. Liu, ''Inverse analyses of thickness and elastic properties of a bonding layer using laser generated surface waves,'' Ultrasonics **37**, 23–30 (1999).
[14] T.-T. Wu and Y.-Y. Chen, ''Analyses of laser generated surface waves in delaminated layered structures using wavelet transform,'' J. Appl. Mech. **66**, 507–513 (1999).
[15] G. Cachier, ''Optical excitation of high-amplitude surface waves,'' Appl. Phys. Lett. **17**, 419–420 (1970).
[16] A. Harata, H. Nishimura, and T. Sawada, ''Laser-induced surface acoustic waves and photothermal surface gratings generated by crossing two pulsed laser beams,'' Appl. Phys. Lett. **57**, 132–134 (1990).
[17] K. Yamanaka, Y. Nagata, and T. Koda, ''Selective excitation of single-mode acoustic waves by phase velocity scanning of a laser beam,'' Appl. Phys. Lett. **58**, 1591–1593 (1991).
[18] Y. Tsukahara, ''Analysis of the elastic wave excitation in solid plates by phase velocity scanning of a laser beam,'' Appl. Phys. Lett. **59**, 2384–2385 (1991).
[19] K. Yamanaka, Y. Nagata, and T. Koda, ''Generation of dispersive acoustic waves by the phase velocity scanning of a laser beam,'' Review of Progress in QNDE, 11, edited by D. O. Thompson and D. E. Chimenti (Plenum Press, New York, 1992), p. 633.
[20] H. Nishino, Y. Tsukahara, Y. Nagata, T. Koda, and K. Yamanaka, ''Excitation of frequency surface acoustic waves by phase velocity scanning of a laser interference fringe,'' Appl. Phys. Lett. **62**, 2036–2038 (1993).
[21] C. K. Lee and T. W. Wu, ''Differential laser interferometer for nanometer displacement measurements,'' AIAA J. **33**, 1675–1680 (1995).
[22] C. K. Lee, G. Y. Wu, C. T. Teng, W. J. Wu, C. T. Lin, etc., ''A high performance Doppler interferometer for advanced optical storage systems,'' Jpn. J. Appl. Phys. **38**(1), 3B, 1730–1741 (1999).
[23] J. A. Nelder and R. Mead, ''A simplex method for function minimization,'' Comput. J. (UK) **7**, 308–313 (1965).

Determination of embedded layer properties using adaptive time-frequency domain analysis

L. Wang, B. Xie, and S. I. Rokhlin[a)]
Edison Joining Technology Center, The Ohio State University, Nondestructive Evaluation Program, 1248 Arthur E. Adams Drive, Columbus, Ohio 43221

(Received 13 November 2001; accepted for publication 7 March 2002)

A general model for determination of the complete set of acoustical and geometrical properties of an isotropic layer embedded between isotropic or anisotropic multilayered solids is developed. These properties include density, longitudinal and shear elastic moduli, layer thickness, and loss factors, simultaneously determined from two measurements, one at normal and one at oblique incidence. The inversion model is an extension of the method proposed by Lavrentyev and Rokhlin [J. Acoust. Soc. Am. **102**, 3467 (1997)] which is applicable to thick substrates. In this new method, the inversion model mimics an experiment by using the same time-domain gating of the signal reflected from the embedded layer. This allows application of this method to layered solids when reflections from different layers overlap in the time domain. The sensitivity of the method, its stability against data scatter, and the effect of the oblique incident angle are evaluated. The effect of plane-wave approximation versus beam approximation in the inverse algorithm is discussed. Experimental results are given to demonstrate examples of adhesive layer property reconstruction.
 [DOI: 10.1121/1.1473634]

PACS numbers: 43.35.Ns, 43.35.Zc, 43.60.Pt, 43.20.Gp [YHB]

I. INTRODUCTION

Layered structures such as thin films, coatings, and adhesive bonds are widely used in different manufactured goods and in the microelectronic and aerospace industries. Various ultrasonic technologies have been developed to evaluate the integrity and measure the properties of these structures.[1–25] The material signatures obtained by acoustic microscopy[1] and Lamb waves techniques[2–4] are very useful nondestructive characteristic tools for these layered structures.

Ultrasonic spectroscopy has long been used for layer characterization.[5–19] For example, in adhesive joints the resonance spectrum of the adhesive layer at normal incidence has been applied to determine ultrasonic velocity and attenuation, and correlate these with the joint cohesive strength.[6,7] Through-thickness resonance measurements at normal incidence were used in Refs. 8 and 9 to calculate both the thickness and the modulus of an adhesive layer. The oblique reflected spectrum from imperfect interfaces has been demonstrated to be very sensitive to the interfacial properties.[10–14] A low-frequency through-transmission ultrasonic technique was proposed in Ref. 5 to determine the thickness or density of a thin layer.

Kinra *et al.*[16–19] developed a method to determine the properties of a thin layer from the normal reflection/transmission spectrum. Because the reflection/transmission spectrum at normal incidence depends on two nondimensional parameters (nondimensional impedance and thickness), the three independent layer properties (density, thickness, and longitudinal modulus) cannot be decoupled with sufficient accuracy. Additional relations necessary to obtain layer properties can be obtained from oblique measurement. This was done by Lavrentyev and Rokhlin,[20] who developed an ultrasonic method for simultaneous determination of all properties of the layer: density, thickness, and longitudinal and shear moduli and attenuations, using ultrasonic measurements at two angles, normal and one oblique. In this method, the ultrasonic wave interaction with a layer is described by six nondimensional parameters. A two-step inversion algorithm to determine the layer properties is based on two consecutive inversion searches in two three-dimensional spaces of the layer parameters: one for normal and one for oblique incidence measurements. This allows one to reduce the number of parameters to be measured. In Ref. 20, the bond between the layer and the substrates has been assumed perfect, the substrate properties are known, and the layer is isotropic. The inclusion of imperfect interfaces in this model has been described in Ref. 21.

The model developed in Ref. 20 neglects the effect of time-domain signal gating; i.e., it assumes that the signal reverberation inside the adhesive layer is not affected by the interference with the multiple reflections in the substrates. For thick substrates, as shown at normal incidence in Fig. 1, there is no interference between the multiple reflections inside the imbedded layer and the reflection from the substrate surface. In Fig. 1, the first signal (marked ''s1'') corresponds to the reflection from the top surface of the sample, the third signal (marked ''s2'') is the second reflection inside the substrate, and the second signal (marked ''a'') is the reflected signal from the imbedded layer (interface thin adhesive layers). Since signals corresponding to multiple reflections inside the adhesive layer and the reflection from the substrate surface are separated in the time domain, one can consider in the model the substrates as semispaces;[20] this significantly simplifies the inversion of the embedded layer properties from the experimental data. Such a method imposes some limitations on embedded layer and substrate thickness. These were partially overcome by Lavrentyev and Rokhlin[20] by

a)Author to whom correspondence should be addressed. Electronic mail: rokhlin.2@osu.edu

 0001-4966/2002/111(6)/2644/10/$19.00

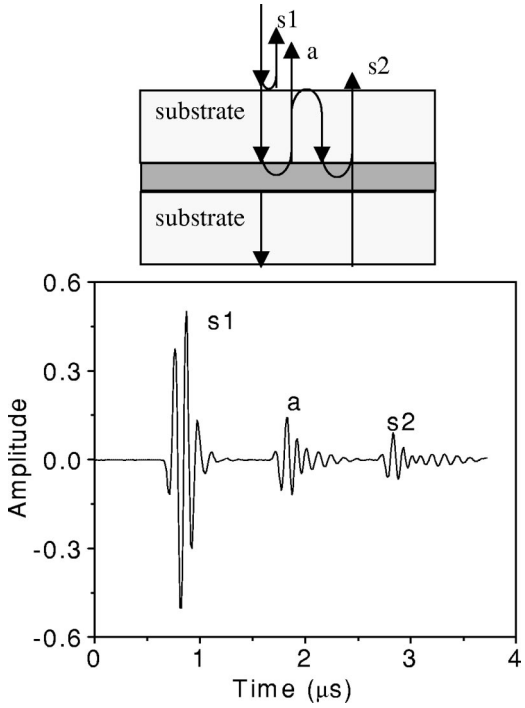

FIG. 1. A time-domain reflected signal for a thin layer between thick substrates. The reflections from the adhesive layer are separated from those reflected from the substrate top and bottom. Substrates are 3.27-mm-thick aluminum plates; adhesive layer thickness is 0.17 mm. Longitudinal velocity for aluminum is 6.4 mm/μs, for adhesive 2.4 mm/μs.

gating only a limited number of reverberations in the embedded (adhesive) layer at normal incidence; however, the number of reflections in the embedded layer was assumed to be *a priori* known.

For thin substrates, the multiple reflections inside the adhesive layer and the reflection from the substrate surface completely overlap and interface with each other, as shown in Fig. 2. In this case, one can consider the system as a thin, multilayered laminate and the reflection spectrum of this laminate is determined from the total time-domain signal, and the ultrasonic spectrum for the whole structure is used to determine the layer properties.[21–23] However, as shown by Nagy and Adler,[4] the sensitivity of the ultrasonic signature to the embedded layer properties is much smaller when the total laminate signature is analyzed compared to when only the

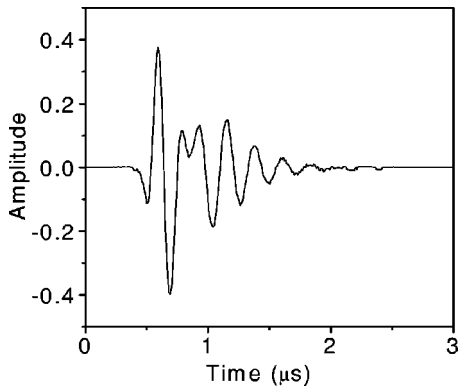

FIG. 2. A time-domain reflection for a three layer laminate. The thickness of the top aluminum substrate is 0.11 mm and bottom substrate 0.07 mm. Adhesive layer thickness is 0.05 mm.

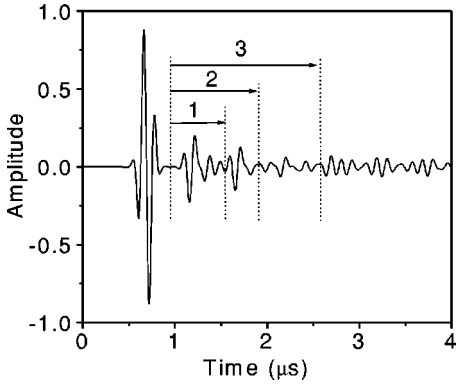

FIG. 3. A ''partial'' interference time-domain reflection at normal incidence. The multiple reflections inside the adhesive layer are inseparable from the multireflection inside the substrate. Substrate thickness is 1.63 mm and adhesive layer thickness is 0.17 mm.

signature from the interface layer is considered. It was also shown by Xie *et al.*[23] that the same holds for layer property reconstruction from the reflection/transmission spectrum of the three-layer laminate system.

Therefore, when possible, it is advantageous to gate the interface layer reflection, even when such reflections cannot be easily separated in the time domain. Such a situation arises in the intermediate substrate/adhesive layer thickness when the multiple reflections inside the adhesive layer and the reflections from the substrate surface are ''partially'' overlapped and interfere with each other, as shown in Fig. 3. In this paper, we will discuss a general algorithm applicable in these intermediate cases, which accounts for the time-domain gating effect. We call this algorithm the adaptive time-frequency domain analysis. This general algorithm can potentially be used for a wide variety of layered structures.

II. INVERSION ALGORITHM

A. Definition of the unique set of material parameters

The acoustic response from the embedded layer depends on six parameters: elastic moduli λ, μ, thickness h, density ρ, and longitudinal and shear attenuations α_l, α_t ($\alpha_{l,t}$ defined in Ref. 20 as the ratio of the imaginary to the real part of the wave number)

$$\lambda, \mu, h, \rho, \alpha_l, \alpha_t. \tag{1}$$

To simplify the layer properties determination, one has to formulate a minimal set of independent parameters of the layer. Lavrentyev and Rokhlin[20] have proposed six nondimensional parameters which can be separated into two groups of nondimensional parameters and are uniquely determined by normal and oblique spectra.

The normal reflection spectrum depends on three nondimensional parameters

$$Z_n = \frac{Z_1}{Z_0}, \quad H_n = \frac{h\omega_0}{V_l}, \quad \alpha_l, \tag{2}$$

where $\omega_0 = 1$ MHz for convenience as a normalization factor and V_l is the longitudinal velocity in the layer. $Z_l = \rho V_l$ and $Z_0 = \rho_0 V_{l0}$ correspond to the acoustic impedance of the layer and the substrate, respectively, V_{l0} and ρ_0 are the substrate

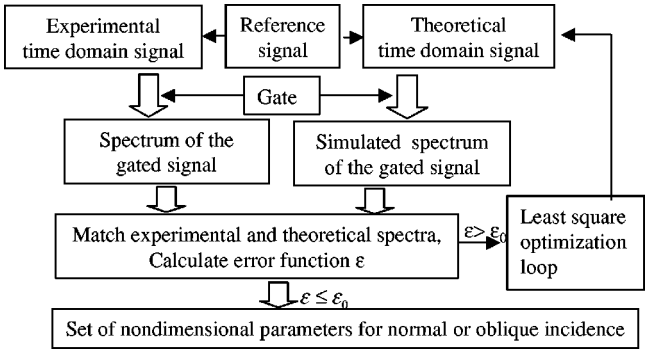

FIG. 4. Flow chart for inversion algorithm.

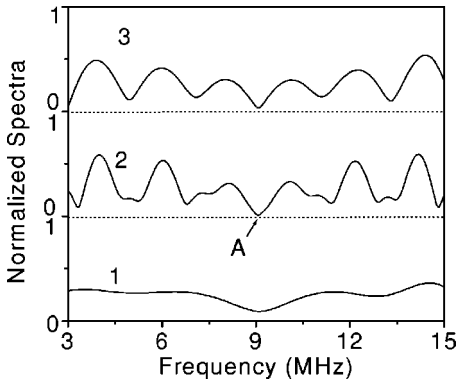

FIG. 5. Spectra corresponding to different time-domain gates shown in Fig. 3.

velocity and density. The oblique incident reflection coefficients, in addition to the three parameters defined by Eq. (2), depend on three more nondimensional parameters, defined in Ref. 20 as

$$H_{t\theta}=\frac{h\omega_0}{V_t}\cos(\theta_t), \quad H_{l\theta}=\frac{h\omega_0}{V_l}\cos(\theta_l), \quad \alpha_t, \tag{3}$$

where V_t is the shear velocity in the embedded layer; θ_l and θ_t are the longitudinal and shear wave refraction angles. However, when the incident angle is larger than the critical angle, $H_{t\theta}$ and $H_{l\theta}$ become complex, which complicates the inversion algorithm. In order to avoid this problem, we replace these two parameters by

$$C_l=\frac{V_l}{V_{l0}}, \quad C_t=\frac{V_t}{V_{t0}}, \tag{4}$$

where V_{l0} and V_{t0} are substrate longitudinal and shear velocities. Refraction angles θ_l and θ_t are obtained from Eq. (4) and Snell's law. Using these two new parameters, the relations between dimensional and nondimensional parameters given by Eq. (1) are determined as

$$\rho=\frac{Z_n\rho_0}{C_l}; \quad h=\frac{H_nC_lV_{l0}}{\omega_0};$$
$$\lambda+2\mu=\rho C_l^2V_{l0}^2; \quad \mu=\rho C_t^2V_{t0}^2, \tag{5}$$

which are simpler than those determined using the original parameters [Eq. (3)].

B. Time-frequency domain analysis

The nondimensional parameters are determined from the normal and oblique reflection spectra of the bonding layer. Since, in some cases, the bonding layer reflection cannot be separated from the substrate reflections (Fig. 3), the reflected spectrum from the layer depends on the gate size and position. In order to correctly account for the gate effect in the inversion model, one has to calculate the time-domain signal in the same time-domain gate as one used for the data collection in the experiment.

The flow chart shown in Fig. 4 outlines the inversion algorithm for determination of the six nondimensional parameters from normal and oblique time-domain reflected signals. It includes two steps: first Z_n, H_n, α_l are determined from a reflection signal at normal incidence; then, considering Z_n, H_n, α_l as known, three more nondimensional parameters C_l, C_t, α_t are determined from an oblique incident signal. The corresponding dimensional parameters are obtained using Eq. (5).

Both experimental and theoretical signals are bounded in time using the same time gate. The start and end positions of the gate are selected as discussed below. To deconvolve the transducer frequency response and ultrasonic beam parameters (see below), a reflected reference signal is used to calculate the transducer frequency response for the simulated reflection signal in the model. The reference signal is measured from the bottom of the plate identical to the top substrate. From the gated experimental and simulated signals, the spectrum is calculated and matched by least-squares minimization of the sum of squared deviations between the spectra, considering the nondimensional parameters as independent variables in a multidimensional space

$$\varepsilon=\min\sum_{f=f_1}^{f_2}(|R_t(\mathbf{X})|-|R_e(\mathbf{X}_0)|)^2. \tag{6}$$

Here, $R_t(\mathbf{X})$ and $R_e(\mathbf{X}_0)$ are the spectra of the gated experimental and theoretical signals. $\mathbf{X}$ is an iterated set of nondimensional parameters; $\mathbf{X}_0$ is the actual set of material properties. f_1 and f_2 are the bonds of the frequency range in which minimization is performed. The frequency bounds are selected based on the transducer bandwidth and the resonance frequency of the adhesive layer. The algorithm is adaptive: in each iteration the time-domain signal is calculated and adapts to the gate in the same position as the measured signal. After the parameters Z_n, H_n, α_l are obtained from the normal incident experiment measurement, a similar procedure is used to calculate the additional three parameters at oblique incidence.

C. Signal gating

Due to the interference of the reflections from the embedded layer and the substrate as shown in Fig. 3, the reflection spectrum will depend on the gate position and length. As an example, Fig. 5 shows the corresponding spectra for the three gated "partially" interfering signals shown in Fig. 3 for the normal incidence. Gate #1 just includes part of the multiple reflections within the adhesive layer; the corresponding spectrum (1) in Fig. 5 shows the adhesive resonance pattern

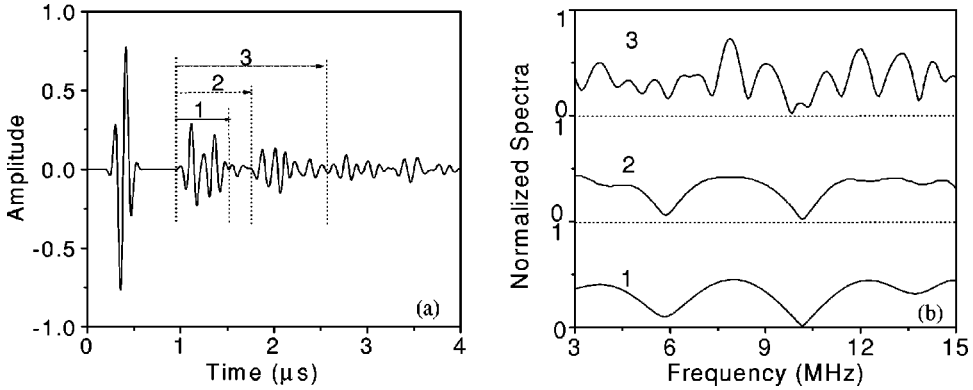

FIG. 6. Effect of time gating for oblique incidence. Experimental conditions and the sample are the same as those in Fig. 3. (a) Time-domain signal at 17° incident angle in water. (b) Spectra corresponding to different time-domain gates shown in (a).

with shallow oscillations. These oscillations do not represent the actual adhesive layer response, since reverberations in the layer are only partially accounted for. In gate #2, part of the substrate reflection is included; however, the corresponding spectra show the resonance of the bonding layer indicated by arrow "A." As the size of the time-domain gate increases (gate #3) and includes additional substrate reflections, the dip corresponding to the resonance of the bonding layer becomes obscure (top spectrum 3).

Figure 6(a) shows the time-domain signal for the oblique measurement for the same sample. The spectra for the three time-domain gates are given in Fig. 6(b). Gates #1 and #2 include several first reflections within the adhesive layer; the corresponding spectra in Fig. 6(b) have two resonance dips. In gate #3, in addition to the multiple reflection within the adhesive layer, some reflections from the substrates are included; the corresponding spectra show very complicated behavior where the layer resonance is difficult to identify. In Sec. III of this paper, we will demonstrate that in this algorithm the different time-domain gatings have negligible effect on layer property reconstruction.

D. Time-domain signal calculation

To calculate the time-domain signals, we need to consider the configuration of the experiment shown in Fig. 7. The probe consists of one normal and two oblique incident transducers. The coupling fluid between the transducers and the specimen is usually water. The output voltage for the two-dimensional beam approximation for this experiment can be written in the far field as

$$V_{\text{out}}(t)=\int_{-\infty}^{+\infty} F_T(\omega)F_R(\omega)e^{i\omega t}\,d\omega \times \int_0^{\pi/2} P_T(\theta)P_R(\theta)R(\theta,\omega) \times e^{2i(\omega/V_f)(z_0\cos\theta+x_0\sin\theta)}d\theta, \tag{7}$$

where $F_T(\omega)$ and $F_R(\omega)$ are the frequency responses of the transmitter and receiver, respectively. $P_T(\theta)$ and $P_R(\theta)$ are the angular responses of the transducers; x_0 and z_0 are the coordinates of the center position of the receiver as shown in Fig. 7. $R(\theta,\omega)$ is the plane-wave reflection coefficient from the layered sample which is formed by substrates and Al_2O_3 oxide, priming and adhesive layers. V_f is velocity in fluid.

Alternatively, we consider the plane-wave approximation when $P_T(\theta)P_R(\theta)=\delta(\theta-\theta_0)$, approximating the output voltage $V_{\text{out}}(t)$ as

$$V_{\text{out}}(t)=\int_{-\infty}^{+\infty} F_T(\omega)F_R(\omega)e^{i\omega t}R(\theta_0,\omega) \times e^{2i(\omega/V_f)(z_0\cos\theta_0+x_0\sin\theta_0)}d\omega. \tag{8}$$

The reflection coefficient for normal incidence is calculated recursively using the acoustic impedance algorithm.[24] For oblique incidence, in Ref. 20 the transfer matrix method was used for computations of the reflection coefficient from the interphase and adhesive layers (the substrates have been considered as semispaces). In the method described here, the substrates with arbitrary thicknesses must be included in the computation leading to instability of the transfer matrix algorithm for thicker substrates. For this reason, we utilize the computationally efficient and unconditionally stable recursive stiffness matrix method, in which the plane-wave reflection R from and transmission T coefficients through a multilayered elastic medium are calculated[25] as

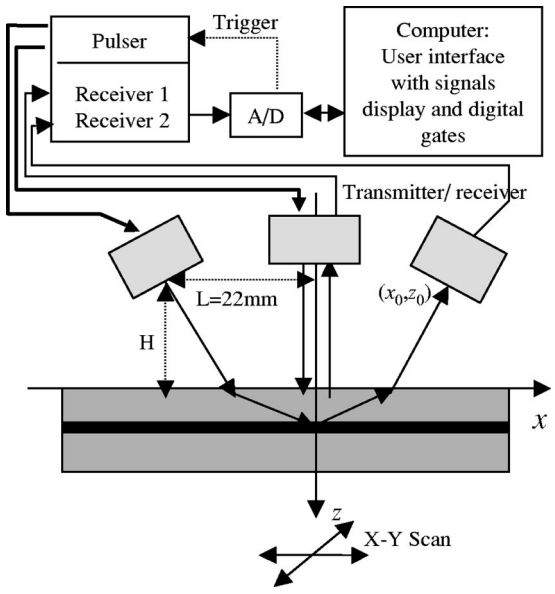

FIG. 7. Schematic of the experimental system for angle beam measurements of properties of an embedded layer.

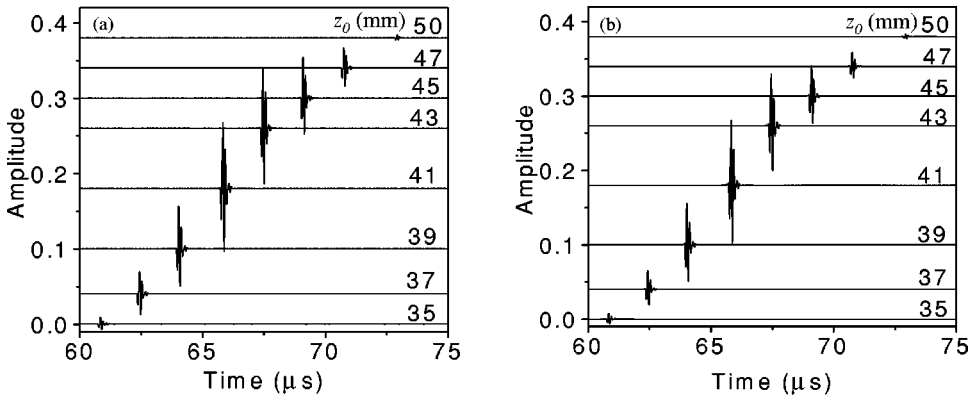

FIG. 8. Comparison of beam model with experiment: reflected time-domain signals at different defocus positions from an aluminum half space. (a) Experiment; (b) theory.

$$R=\frac{(\mathbf{S}_{11}(2,2)-\Lambda)(\mathbf{S}_{22}(2,2)-\Lambda)-\mathbf{S}_{12}(2,2)\mathbf{S}_{21}(2,2)}{(\mathbf{S}_{11}(2,2)+\Lambda)(\mathbf{S}_{22}(2,2)-\Lambda)-\mathbf{S}_{12}(2,2)\mathbf{S}_{21}(2,2)}, \tag{9}$$

$$T=\frac{2\Lambda\mathbf{S}_{21}(2,2)}{(\mathbf{S}_{11}(2,2)+\Lambda)(\mathbf{S}_{22}(2,2)-\Lambda)-\mathbf{S}_{12}(2,2)\mathbf{S}_{21}(2,2)}, \tag{10}$$

where $\mathbf{S}_{ij}(2,2)$ are the elements of the submatrices $\mathbf{S}_{ij}$ of the global compliance matrix $\mathbf{S}$ and $\Lambda=\cos\theta/(i\omega\rho_f V_f)$, ρ_f is the fluid density, and V_f is the acoustic velocity in the fluid, θ is the incident angle. The method of calculating the global compliance matrix $\mathbf{S}$ for multilayered isotropic solids is given in the Appendix and for an anisotropic case in Ref. 25.

For angle beam measurements, the received signal will depend on transducer position (x_0,z_0). Comparison of computations using model [Eq. (7)] with the measured reflected signals from the top surface of a thick aluminum block at different focus positions is shown in Fig. 8. As expected, the reflection amplitude increases as the focus point approaches the sample surface and reaches maximum at the focus position, and then decreases as the focus position goes below the sample surface. Comparing the experimental and theoretical results given in Figs. 8(a) and (b), we can see that the model [Eq. (7)] describes the beam focus effect and the dependence on the transducer position sufficiently accurately. In the next section we propose an experimental method to deconvolve the beam effect, allowing one to use the plane-wave approximation (8) instead of Eq. (7) in the inversion algorithm to speed computation.

E. Reference spectrum and deconvolution of beam effects and transducer response

The success of the inverse solution discussed above depends on the accuracy of the model's approximation of the measurement at both normal and angular reflections. As discussed in Sec. D, the beam focus position has significant effect on the amplitude of the reflected signals. One may use the exact beam model [Eq. (7)] to calculate the theoretical time-domain signal; however, since it should be calculated at each iteration step of the inversion process, the computations become too time-consuming especially when reconstruction is performed over the total scanned area of the sample. The beam model also requires knowledge of the precise mechanical position of the transducer head and its geometry. All this introduces unnecessary complexity into the inversion process.

Here, we propose to deconvolve the beam effect using reference measurements and after the deconvolution to use a plane-wave approximation for the time-domain signal calculations. As a reference, we measure the transducer frequency response at normal and oblique incidence from the bottom of a reference sample with the same physical and geometrical properties as the top substrate of the layered sample. A schematic of the immersion measurement shows in Fig. 9 the ultrasonic beam focused on the bond layer of the test sample [Fig. 9(a)] and on the bottom surface of the unbounded top substrate for the reference measurement [Fig. 9(b)]. In the reference measurement, we assume that the reflections from the top and bottom surface of the substrate can be separated in the time domain, since signals reflected from the layer bottom [Fig. 9(b)] are much shorter than those from the adhesive layer [Fig. 9(a)] which are affected by reverberations in the adhesive layer. For very thin or multilayered substrates, the reflection from the bottom surface of the top substrate [Fig. 9(b)] cannot be separated from the reflection from the sample top. In this situation, one can use a thick reference sample and measure the reference signal by focusing the beam on the top surface of the sample; however, in this case the deconvolution of the beam effect is less precise.

For the case of Fig. 9(b), the plane-wave transmission and reflection coefficients at each interface along the path in the reference sample are calculated using the known properties of the substrate and the fluid, where the total reflection coefficient along this path is $R_{fsf}=T_{fs}R_{sf}T_{sf}$; T_{fs} and T_{sf} are the transmission coefficients from fluid to solid or solid to fluid, respectively; R_{sf} is the reflection at the solid–fluid

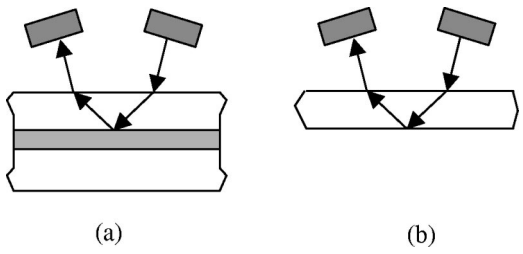

FIG. 9. Schematics of reference measurements for oblique incidence. The reference sample (b) has the same properties as the top substrate of the tested sample (a). Both measurement conditions are the same.

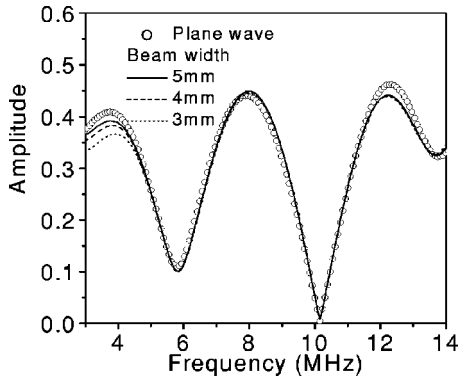

FIG. 10. Comparison for oblique incidence of the beam model and the plane-wave model with beam deconvolution. The spectrum is almost independent of beamwidth, which indicates that the beam effect is deconvolved with the use of reference measurement. The parameters are the same as for Fig. 3 and Fig. 6 using gate one.

interface. If we denote the measured spectrum of the reflection signal from the bottom surface of the reference sample as $f(\omega)$, then the transducer response included in Eqs. (7) and (8) may be written as

$$f_T(\omega) f_R(\omega) = f(\omega)/R_{fsf}. \tag{11}$$

Since the reference measurements were performed using the actual transducer assembly, the transducer response calculated from Eq. (11) includes the amplitude variation introduced by the beam effect. Next, we substitute this transducer response into the plane-wave model [Eq. (8)] and because we use the same measurement setup for the test and the reference samples, we obtain the theoretical time-domain response for layered structures accounting approximately for the beam effect. The simulated time-domain signal is gated and used to calculate the spectrum. Finally, we normalize the gated spectrum by the transducer response [Eq. (11)] to obtain a deconvolved reflection spectrum, which depends only on the properties of the layered structure. The same deconvolution is performed with the gated experimental signal and the error function [Eq. (6)] is determined.

To illustrate numerically the applicability of the beam deconvolution method, in Fig. 10 we compare the ultrasonic spectra of gated time-domain signals obtained by the beam model and by the plane-wave model with the reference deconvolution. One can see that the spectrum of the gated signal is almost independent of beamwidth and very close to the plane-wave solutions deconvolved on the reference signal. In our method we opted to use the plane-wave model [Eq. (8)] to calculate the theoretical spectra and to avoid the integration over incident angle; also, the geometry of the transducer assembly need not be accounted for in this case (except the incident angle).

III. ANALYSIS OF THE INVERSION ALGORITHM

A. Stability and sensitivity

We use the least-squares algorithm for the minimization of the sum of squared deviations between the gated experimental and calculated spectra, Eq. (6). This involves searching for one of the minimums of the error function in the three-dimensional parameter space. The initial guesses and accuracy of the measurement will affect the convergence of the algorithm and in some cases may result in convergence to a minimum other than that corresponding to the real parameters.

To study the susceptibility of the inversion algorithm to the measured data scatter, the procedure used in Ref. 20 has been applied. A set of embedded layer properties is used to generate numerically the time-domain signals with different levels of random scatter added. Then, these signals are used to determine the properties of the layer using our inversion algorithm. Due to data scatter, the reconstructed set of the layer properties is not exactly equal to the original set. The difference serves as a measure of the effects of the data scatter level and the quality of initial guesses on the inversion algorithm. For each random scatter level and initial guess, the procedure is repeated 100 times. As an example, the relative error between the reconstructed parameter values and the exact original values are plotted as histograms in Fig. 11. The random data scatter of the signal peak amplitudes is 2%. In these figures, the initial guesses are 20% off the exact values. Figure 11(a) shows the scatter effect on H_n and Z_n. The error for H_n is within 0.5% and for Z_n is 2%. Figure 11(b) shows the scatter effect on C_l and C_t. The distribution of errors for these two parameters is almost the same and is below 1%. The results demonstrate that improving the reconstruction quality of Z_n is most important, because when one converts from nondimensional parameters to dimensional parameters [Eq. (5)], error in Z_n propagates to all dimensional parameters.

To investigate the influence of initial guesses and the sensitivity of measurements to the different layer parameters,

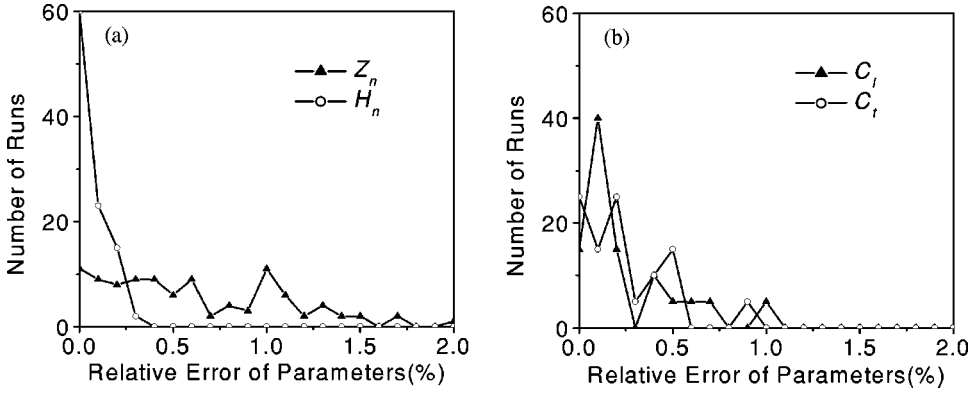

FIG. 11. The results of reconstruction of four nondimensional parameters from synthetic "noisy" time-domain signals with 2% scatter. Initial guesses are 20% off the exact values.

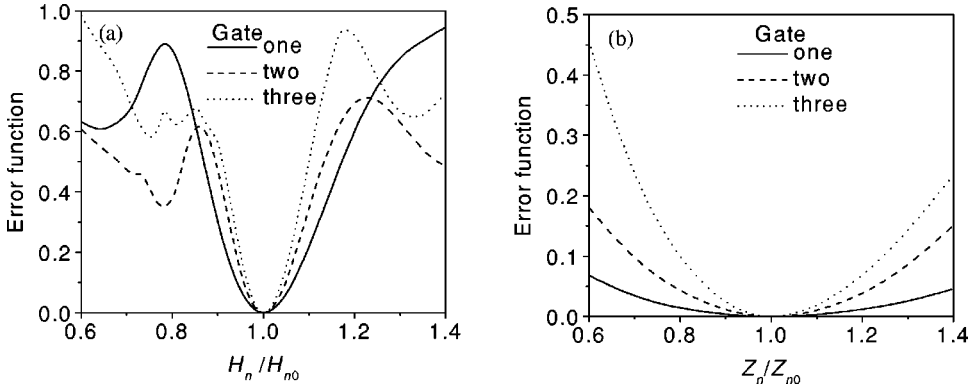

FIG. 12. Error function distribution at normal measurement for different gating size shown in Fig. 3.

we plot the error function in Figs. 12 and 13 for the different gate positions indicated in Fig. 3. Figure 12(a) shows the error function versus nondimensional thickness H_n for the normal incidence. As expected, the results are very sensitive to the variation of H_n due to significant change of the spectrum with the parameter and shift in the minimum position. The error function has a very sharp slope, which indicates high sensitivity. However, a local minimum appears just beyond 20% of H_{n0}; thus, the algorithm may converge to this minimum if the initial guesses are too far from the actual values. Increasing gate width can slightly improve the sensitivity, but it also shrinks the convergence range. Figure 12(b) shows the error function for the nondimensional impedance Z_n. It has no local minimum within 40% of the expected value Z_{n0}; however, the small slope of the error function indicates low speed of convergence and potentially larger error in the reconstruction. This is consistent with results of Fig. 11(a) with relatively larger reconstruction error resulting from the measured data scatter. The dotted curve in Fig. 12(b), which corresponds to gate #3 in Fig. 3, shows higher sensitivity. It indicates that accounting for more reflection in the adhesive layer increases the sensitivity to the acoustic impedance. As discussed above and in Ref. 20, the stability and accuracy of the algorithm are mainly determined by the sensitivity to the acoustic impedance. Therefore, the longer gate at normal incidence measurements improve the accuracy of the reconstruction. Figure 13 shows the error function for the oblique incident measurement. It shows that the error function has relatively higher sensitivity to both normalized longitudinal C_l and shear velocities C_t. As shown in Figs. 12 and 13, increasing the gate size leads to slightly higher sensitivity (larger slope of the error functions) and small shrinkage of the convergence range. Therefore, after inclusion in the gate of several reflections within the embedded layer, the reconstruction results in our adaptive time-frequency method are not very sensitive to the gate size. This is important for the robustness of the method when using actual scanning data of bond with variable layer parameters.

B. Incident angle selection

The incident angle from the fluid is selected to be a few degrees above the first critical angle in the substrate so as to have a shear wave incident on the adhesive layer. Avoiding being close to the critical angle minimizes the beam distortion and longitudinal wave excitation and additionally assumes the well-pronounced minima of the reflection spectra attributed to the adhesive layer. Figure 14 shows the gated spectrum at four different incident angles from fluid: 15°, 17°, 20°, 25°. These angles correspond to 32.8, 37.8, 45.8, and 62.3 deg of incidence of the SV transverse wave on the adhesive layer. At 17° incidence the resonance dips are the sharpest and thus this incident angle is selected for our measurement with aluminum bonded substrates.

IV. EXPERIMENTAL RESULTS AND DISCUSSION

The angle beam reflection measurements were performed using a specially designed contact scanning ultrasonic measurement system which includes a transducer array, mechanical scanning system, and processing software.[26] A computer-controlled two-channel ultrasonic scanning apparatus has been developed to collect ultrasonic data over the bonded area. The acoustic array, which is shown in Fig. 7, includes three transducers: one normal and two oblique

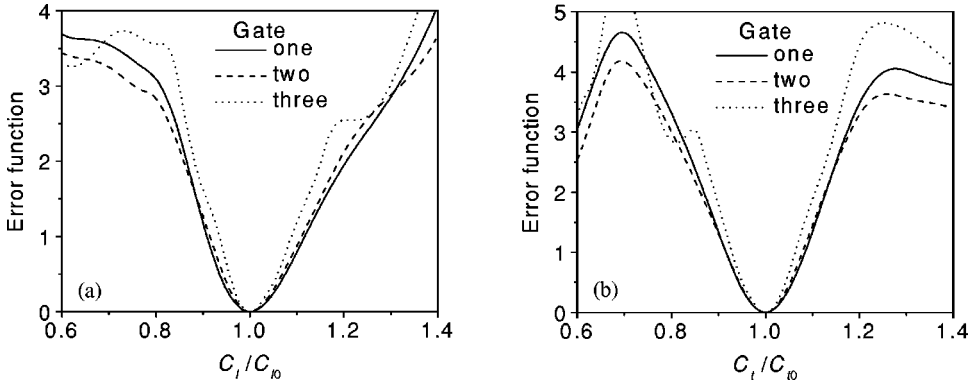

FIG. 13. Error function distribution at oblique measurement for different gating size shown in Fig. 6(a).

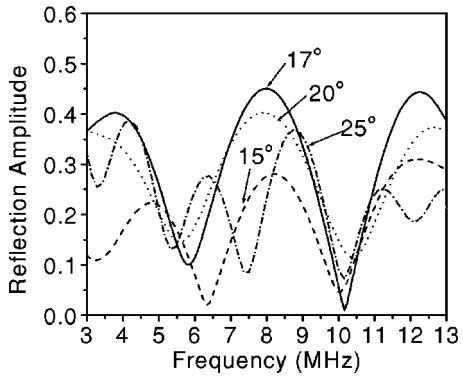

FIG. 14. Angle selection criterion for oblique incidence. Deconvolved reflection spectra at different incident angles.

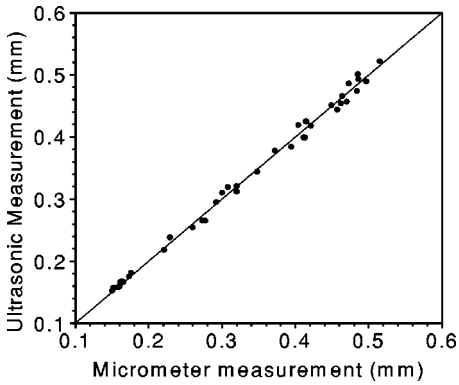

FIG. 15. Comparison of thickness measurement using micrometer and ultrasound methods.

transducers symmetrically positioned about the normal axis *z*. The half distance L between the oblique transducers is 22 mm ($x_0 = 22$ mm), as shown in Fig. 7. The center frequency is 10 MHz and transducer diameter is 12 mm. The distance H (z_0) between the transducer array and the sample is adjusted to focus the oblique beam on the embedded layer with unknown properties. The pulse receivers are triggered by a computer-controlled 12-bit, 125-MHz A/D board (the trigger and data acquisition are controlled by the software). The received time-domain analog signals for normal and oblique incidences are digitized and displayed, and the software-controlled digital rectangular gates are applied to truncate the digitized signals. The size and position of the gates are adjusted to include the interface reflected signals and if needed adjoin substrate reflections as shown in Fig. 3. As was discussed in Sec. III A, the reconstruction results are not sensitive to reasonable gate length and position variations, since the reconstruction algorithm uses exactly the same digital gate for experimental and simulated signals.

A 12- by 12-in. Al-to-Al bonded sample manufactured at Boeing was used for measurement. The aluminum substrate thickness is 1.63 mm and the thickness of the adhesive layer varies from 0.15 to 0.5 mm. Due to variation of bond line thickness, different degrees of interference between the reflections from substrate and adhesive layer are observed at different locations in the joint. The sample was scanned and data from normal and oblique incidence were collected.

The original algorithm proposed in Ref. 20 cannot be used for adhesive layer properties reconstruction for this sample due to significant interference between the reflection from the bond layer and the substrates; therefore, this sample is well suited for the adaptive time-frequency inversion algorithm to be applied. The adhesive layer properties were reconstructed in the postprocessing mode from the collected data after the beam deconvolution with the reference signal. The reconstruction results show that longitudinal and shear moduli and density of the adhesive do not change significantly with location in the sample and have values around 7.0 GPa, 1.3 GPa, and 1.2 g/cm^3, respectively; however, the adhesive layer has variable thickness. To determine the accuracy of the reconstruction, we compare point by point ultrasonically measured thickness with micrometer measurements. The results are shown in Fig. 15; the relative standard deviation between these two measurements is less than 2%. With thickness increase the interference between the substrate and bond line reflections increases causing increase in the absolute error of ultrasonic reconstruction. However, the adaptive time-frequency algorithm is applicable to all thickness ranges. One should note that reconstruction of elastic moduli has the same accuracy as that of the thickness; thus, independent measurement of thickness provides indirect information on the reconstruction quality for the other parameters.

Two examples showing the quality of the spectrum matches are given in Fig. 16. Figure 16(a) shows the deconvolved spectrum for normal incidence and Fig. 16(b) for oblique incidence. The spectra correspond to a point with bonding layer thickness 0.3 mm. The open circles are experimental results and the lines represent theoretical results calculated using the reconstructed properties. The re-

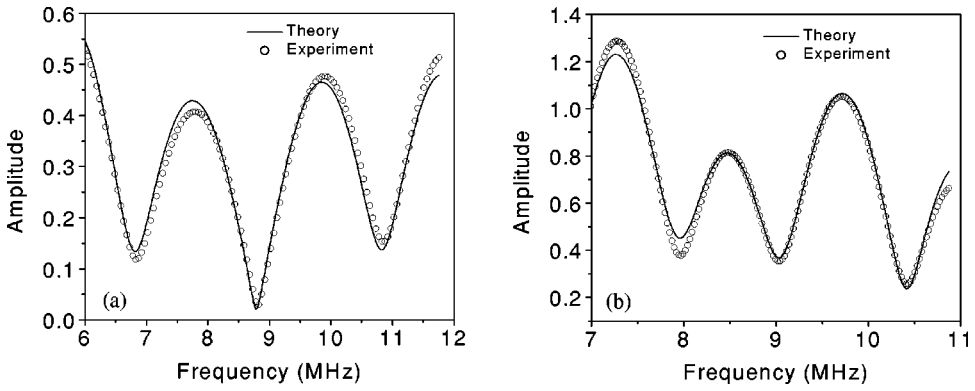

FIG. 16. Comparison of experimental (circles) and calculated (line) reflection spectra at the position with layer thickness 0.3 mm. (a) Normal; (b) oblique. The calculation performed using reconstructed values of the layer.

sults indicate good spectra match for the reconstructed layer parameters.

V. CONCLUSION

A time-frequency adaptive algorithm for determination of the properties of a layer inside an isotropic multilayered solid is discussed. These properties, including density, elastic moduli, layer thickness, and loss factors are simultaneously determined from measurement at two incident angles: normal and one oblique. This method uses the localized resonance, which corresponds to the spectrum in the time-domain gate and therefore is applicable for arbitrary laminates without limitation of substrate thickness. It is shown that the time gate length has significant effect on the spectrum of the localized resonance; however, it has little effect on the sensitivity and convergence of the reconstruction method, which is important for application. The results also show that this method is sensitive to layer properties and is robust against data scatter. Reference measurements have been applied to deconvolve the beam effect. Experimental results are given to demonstrate the reconstruction of properties of adhesive layers with variable thicknesses. Finally, one should note that the inversion algorithm is exact and is applicable to substrates and the embedded layer of arbitrary thicknesses; however, for better computation efficiency, when substrates are thin or have thickness comparable with that of the embedded layer one should gate[22,23] a total reflection signal and perform inversion in the frequency domain.

ACKNOWLEDGMENTS

This work was sponsored by the Federal Aviation Administration under Contract No. DTFA03-98-D-00008 and performed at The Nondestructive Evaluation Program at The Ohio State University as part of the Center for Aviation Systems Reliability program through the Airworthiness Assurance Center of Excellence. Partial support and experimental sample provided by Boeing are greatly appreciated. The authors thank Dr. Bill Shepperd and Dr. Richard Bossi from Boeing for encouragement and helpful discussions.

APPENDIX: LAYER AND GLOBAL COMPLIANCE MATRIX CALCULATION

The compliance matrix $\mathbf{S}_m$ for the mth layer is defined as

$$\begin{bmatrix} \mathbf{u}_{m-1} \\ \mathbf{u}_m \end{bmatrix} = \mathbf{S}^m \begin{bmatrix} \boldsymbol{\sigma}_{m-1} \\ \boldsymbol{\sigma}_m \end{bmatrix} = \begin{bmatrix} \mathbf{S}_{11}^m & \mathbf{S}_{12}^m \\ \mathbf{S}_{21}^m & \mathbf{S}_{22}^m \end{bmatrix} \begin{bmatrix} \boldsymbol{\sigma}_{m-1} \\ \boldsymbol{\sigma}_m \end{bmatrix}, \tag{A1}$$

where $\boldsymbol{\sigma}_{m-1}$ and $\boldsymbol{\sigma}_m$ are the stresses on the top and bottom surfaces of the layer m; $\mathbf{u}_{m-1}$ and $\mathbf{u}_m$ are displacements. Below, we provide the compliance matrix $\mathbf{S}^m$ elements for an isotropic medium, for an anisotropic case given in Ref. 25

$$\begin{aligned}
\mathbf{S}_{11}^m(1,1) &= \sin\,\theta_l \mathrm{ctg}\theta_t(\Delta_1(e_t^2-e_l^2)+\Delta_2(1-e_l^2e_t^2))/\Delta;\\
\mathbf{S}_{11}^m(1,2) &= (\sin(2\theta_t+\theta_l)\Delta_1(e_l^2+e_t^2)+\sin(2\theta_t-\theta_l)\\
&\quad\times\Delta_2(1+e_l^2e_t^2)+4e_le_t(1-4\sin^2\,\theta_t)\\
&\quad\times\sin 2\theta_l\,\cos 2\theta_t\,\cos\,\theta_t)/\Delta;\\
\mathbf{S}_{12}^m(1,1) &= \frac{2\sin\,\theta_l}{\sin\,\theta_t}((e_l-e_t^2e_l)\sin^2 2\theta_t\,\cos\,\theta_l\\
&\quad+(e_t-e_l^2e_t)\cos^2 2\theta_t\mathrm{ctg}\theta_t\,\sin\,\theta_l)/\Delta;\\
\mathbf{S}_{12}^m(1,2) &= 2(e_l-e_t-e_l^2e_t+e_t^2e_t)\\
&\quad\times\cos\,\theta_t\,\sin 2\theta_l\,\cos 2\theta_t/\Delta;\\
\mathbf{S}_{11}^m(2,2) &= -\cos\,\theta_l(\Delta_1(e_t^2-e_l^2)+\Delta_2(e_l^2e_t^2-1))/\Delta;
\end{aligned} \tag{A2}$$

$$\mathbf{S}_{11}^m(2,1) = -\mathbf{S}_{11}^m(1,2); \quad \mathbf{S}_{12}^m(2,1) = \mathbf{S}_{12}^m(1,2);$$

$$\begin{aligned}
\mathbf{S}_{12}^m(2,2) &= 2\cos\,\theta_l/\sin\,\theta_t((e_l-e_l^2e_l)\cos^2 2\theta_t\,\sin\,\theta_l\\
&\quad+2(e_t-e_l^2e_t)\sin 2\theta_t\,\sin^2\,\theta_t\,\cos\,\theta_l)/\Delta;
\end{aligned}$$

$$\mathbf{S}_{21}^m(1,1) = -\mathbf{S}_{12}^m(1,1); \quad \mathbf{S}_{21}^m(1,2) = \mathbf{S}_{12}^m(1,2);$$

$$\mathbf{S}_{22}^m(1,1) = -\mathbf{S}_{11}^m(1,1); \quad \mathbf{S}_{22}^m(1,2) = \mathbf{S}_{11}^m(1,2);$$

$$\mathbf{S}_{21}^m(2,1) = \mathbf{S}_{12}^m(1,1); \quad \mathbf{S}_{21}^m(2,2) = -\mathbf{S}_{12}^m(2,2);$$

$$\mathbf{S}_{22}^m(2,1) = -\mathbf{S}_{22}^m(1,2); \quad \mathbf{S}_{22}^m(2,2) = -\mathbf{S}_{11}^m(2,2);$$

where $\Delta = i\omega\rho V_t((1+e_l^2e_t^2)\Delta_2^2-(e_l^2+e_t^2)\Delta_l^2-8e_le_t\,\sin 2\theta_l \times\sin 2\theta_t\,\cos^2 2\theta_t)$,

$$\Delta_l = 2\sin\,\theta_t\,\sin(\theta_l+2\theta_t)-\frac{\sin\,\theta_l}{\sin\,\theta_t}\cos 2\theta_t$$

$$\Delta_2 = 2\sin\,\theta_t\,\sin(\theta_l-2\theta_t)-\frac{\sin\,\theta_l}{\sin\,\theta_t}\cos 2\theta_t$$

θ_l, θ_t are refraction angles for longitudinal and shear wave, respectively. These angles are related to the wave number by $\sin\,\theta_{l,t}=k/k_{l,t}$, $\cos\,\theta_{l,t}=k_z^{l,t}/k_{l,t}$ and $k_z^{l,t}=\sqrt{k_{l,t}^2-k^2}$. $e_l = e^{ik_z^l h_m}$, $e_t = e^{ik_z^t h_m}$. h_m is the thickness of layer m.

The total compliance matrix $\mathbf{S}$ for the N layered solid immersed in fluid, which relates the stresses and displacements at the top and bottom surfaces of the layered solid, obtained from the layer compliance matrixes $\mathbf{S}^m$ by the recursive algorithm

$$\mathbf{S}^M = \begin{bmatrix} \mathbf{S}_{11}^{M-1}+\mathbf{S}_{12}^{M-1}(\mathbf{S}_{11}^m-\mathbf{S}_{22}^{M-1})^{-1}\mathbf{S}_{21}^{M-1} & -\mathbf{S}_{12}^{M-1}(\mathbf{S}_{11}^m-\mathbf{S}_{22}^{M-1})^{-1}\mathbf{S}_{12}^m \\ \mathbf{S}_{21}^m(\mathbf{S}_{11}^m-\mathbf{S}_{22}^{M-1})^{-1}\mathbf{S}_{21}^{M-1} & \mathbf{S}_{22}^m-\mathbf{S}_{21}^m(\mathbf{S}_{11}^m-\mathbf{S}_{22}^{M-1})^{-1}\mathbf{S}_{12}^m \end{bmatrix}, \tag{A3}$$

where $\mathbf{S}^M$ is the total compliance matrix for the top m layers, $\mathbf{S}_{ij}^{M-1}$ is the total compliance matrix for the top $m-1$ layers, $\mathbf{S}_{ij}^m$ are 2*2 submatrices for the mth layer compliance matrix $\mathbf{S}^m$.

[1] Y. C. Lee, J. D. Achenbach, M. J. Nystrom, S. R. Gilbert, B. A. Block, and B. W. Wessels, ''Line-focus acoustic microscopy measurements of Nb2O/MgO and BaTiO/LaAlO thin film/substrate configurations, '' IEEE Trans. Ultrason. Ferroelectr. Freq. Control **42**, 376–380 (1995).
[2] P. C. Xu, A. K. Mal, and Y. Bar-Cohen, ''Inversion of leaky Lamb wave data to determine cohesive properties of bonds,'' Int. J. Eng. Sci. **28**, 331–346 (1998).
[3] C. C. H. Guyott and P. Cawley, ''The ultrasonic vibration characteristics of adhesive joints,'' J. Acoust. Soc. Am. **83**, 632–640 (1988).
[4] P. B. Nagy and L. Adler, ''Nondestructive evaluation of adhesive joints by guided waves,'' J. Appl. Phys. **66**, 4658–4663 (1989).
[5] F. H. Chang, P. L. Flynn, D. E. Gordon, and J. R. Bell, ''Principles and application of ultrasonic spectroscopy in NDE of adhesive bonds,'' IEEE Trans. Sonics Ultrason. **SU-23**, 344–338 (1976).
[6] P. L. Flynn, ''Cohesive bond strength prediction for adhesive joints,'' J. Test. Eval. **7**, 168–171 (1979).
[7] L. Adler, K. V. Cook, and W. A. Simpson, ''Ultrasonic frequency analysis,'' in *Research Techniques in Nondestructive Testing*, edited by R. S. Sharpe (Academic, New York, 1977), Vol. 3, pp. 1–49.
[8] C. C. H. Guyott and P. Cawley, ''Evaluation of the cohesive properties of adhesive joints using ultrasonic spectroscopy,'' NDT Int. **21**, 233–240 (1988).
[9] C. C. H. Guyott and P. Cawley, ''The ultrasonic vibration characteristics of adhesive joints,'' J. Acoust. Soc. Am. **83**, 632–640 (1988).
[10] S. I. Rokhlin and D. Maron, ''Study of adhesive bonds using low frequency obliquely incident ultrasonic waves,'' J. Acoust. Soc. Am. **80**, 585–590 (1986).
[11] A. Pilarski and J. L. Rose, ''Ultrasonic oblique incidence for improved sensitivity in interface weakness determination,'' NDT Int. **21**, 241–246 (1988).
[12] A. Pilarski, J. L. Rose, and K. Balasubramaniam, ''The angular and frequency characteristics of reflectivity from a solid layer embedded between two solids with imperfect boundary conditions,'' J. Acoust. Soc. Am. **87**, 532–542 (1990).
[13] S. I. Rokhlin, W. Wang, Y. J. Wang, and J. L. Hammill, ''Evaluation of weak interfaces in adhesive joints,'' Proceedings of the 1989 ASNT Fall Conference, pp. 41–50.
[14] W. Wang and S. I. Rokhlin, ''Evaluation of interfacial properties in adhesive joints of aluminum alloys using angle-beam ultrasonic spectroscopy,'' J. Adhes. Sci. Technol. **5**, 647–666 (1991).
[15] W. Huang and S. I. Rokhlin, ''Application of low frequency ultrasonic through-transmission method for thin film characterization,'' in *Review of Progress in QNDE*, edited by D. O. Thompson and D. E. Chimenti (Plenum, New York, 1994), Vol. 13B, pp. 1485–1493.
[16] V. K. Kinra and V. Dayal, ''A new technique for ultrasonic nondestructive evaluation of thin specimens,'' Exp. Mech. **28**, 288–297 (1988).
[17] V. K. Kinra and V. R. Iyer, ''Ultrasonic measurement of the thickness, phase velocity, density or attenuation of a thin viscoelastic film. I. The forward problem,'' Ultrasonics **33**, 95–109 (1995).
[18] V. K. Kinra and V. R. Iyer, ''Ultrasonic measurement of the thickness, phase velocity, density or attenuation of a thin viscoelastic film. II. The inverse problem,'' Ultrasonics **33**, 111–122 (1995).
[19] S. E. Hanneman and V. K. Kinra, ''A new technique for ultrasonic nondestructive evaluation of adhesive joints. I. Theory. II. Experiment,'' Exp. Mech. **32**, 323–339 (1992).
[20] A. Lavrentyev and S. I. Rokhlin, ''Determination of elastic moduli, density, attenuation, and thickness of a layer using ultrasonic spectroscopy at two angles,'' J. Acoust. Soc. Am. **102**, 3467 (1997).
[21] L. Wang, A. Baltazar, and S. I. Rokhlin, ''Determination of bulk and interfacial properties of a bonding layer from normal and oblique reflection spectra,'' in *Review of Progress in QNDE*, edited by D. O. Thompson and D. E. Chimenti (Plenum, New York, 1999).
[22] A. Lavrentyev and S. I. Rokhlin, ''An ultrasonic method for determination of elastic moduli, density, attenuation and thickness of a polymer coating on a stiff plate,'' Ultrasonics **39**, 211–221 (2001).
[23] Q. Xie, A. Lavrentyev, and S. I. Rokhlin, ''Ultrasonic characterization of thin plate bonding,'' in *Review of Progress in QNDE*, edited by D. O. Thompson and D. E. Chimenti (Plenum, New York, 1998), Vol. 17B, pp. 1355–1362.
[24] L. M. Brekhovskikh, *Waves in Layered Media* (Academic, New York, 1960).
[25] L. Wang and S. I. Rokhlin, ''Stable reformulation of transfer matrix method for wave propagation in layered anisotropic media,'' Ultrasonics **39**, 407–418 (2001).
[26] S. I. Rokhlin, A. Baltazar, B. Xie, and J. Chen, ''Ultrasonic characterization of environmental degradation of adhesive bonds,'' in *Review of Progress in QNDE*, edited by D. O. Thompson and D. E. Chimenti (Plenum, New York, 2000), Vol. 20B, pp. 1082–1089.

Thermoacoustics with idealized heat exchangers and no stack

Ray Scott Wakeland[a] and Robert M. Keolian
The Pennsylvania State University, Graduate Program in Acoustics, P.O. Box 30, State College, Pennsylvania 16804-0030

(Received 27 August 2001; revised 7 March 2002; accepted 22 March 2002)

A model is developed for thermoacoustic devices that have neither stack nor regenerator. These ''no-stack'' devices have heat exchangers placed close together in an acoustic standing wave of sufficient amplitude to allow individual parcels of gas to enter *both* exchangers. The assumption of perfect heat transfer in the exchangers facilitates the construction of a simple model similar to the ''moving parcel picture'' that is used as a first approach to stack-based engines and refrigerators. The model no-stack cycle is shown to have potentially greater inviscid efficiency than a comparable stack model. However, losses from flow through the heat exchangers and on the walls of the enclosure are greater than those in a stack-based device due to the increased acoustic pressure amplitude. Estimates of these losses in refrigerators are used to compare the possible efficiencies of real refrigerators made with or without a stack. The model predicts that no-stack refrigerators can exceed stack-based refrigerators in efficiency, but only for particular enclosure geometries. [DOI: 10.1121/1.1479145]

PACS numbers: 43.35.Ud, 07.20.Pe, 44.27.+g [SGK]

I. INTRODUCTION

Two types of device are widely discussed in the published literature of thermoacoustics. One is based on a ''stack'' operating in an acoustic standing wave. The other uses a regenerator in a traveling wave. Originally, both varieties suffered from poor efficiency but offered operational simplicity. Orifice pulse tube refrigerators,[1] for example, exchanged the dissipation of acoustic power (inefficiency) for the elimination of moving parts from the cryogenically cold part of the device (simplicity). Researchers at Los Alamos have found ways to recover acoustic power in pulse tube refrigerators[2] and even to make regenerator-based prime movers of exceedingly high efficiency[3] by using sophisticated acoustical feedback networks to combine the advantages of resonance with the traveling wave phasing required in the locale of the regenerator.

This paper explores a different type of device that we hope will improve upon the efficiency of stack-based devices while retaining the simple enclosures that produce standing wave acoustic fields. We call it a ''no-stack'' device, because it operates in a manner thermodynamically similar to a stack-based device, but has only heat exchangers, and no stack. Our analysis suggests that under some circumstances a no-stack refrigerator will surpass the efficiency of a stack-based device, provided that the appropriate type of enclosure is used.

A. The no-stack idea

In stack-based thermoacoustics, a stack, flanked by heat exchangers, is located near the pressure antinode of a one-dimensional standing wave. The length of the stack is many times the displacement amplitude of the gas at the stack location, as illustrated in Fig. 1(a). The stack uses imperfect thermal contact between gas and solid to allow many parcels of gas to act in a way that is often likened to a ''bucket brigade,'' shuttling energy between the heat exchangers even though no single parcel of gas comes into thermal contact with both exchangers.[4] Imperfect heat exchange is an inefficiency intrinsic to the operation of a stack. Figure 1(b) shows the configuration of a no-stack device. The stack is removed and the heat exchangers are moved closer together, leaving a small ''no-stack gap.'' The pressure amplitude must be great enough that a single parcel of gas can traverse the gap between the heat exchangers.

B. Historical background

The authors know of only three references to thermoacoustic devices with no stack. The first is Warren Marrison's 1958 patent[5] on no-stack thermoacoustic prime movers for electricity generation. Marrison specifies that the no-stack gap be located halfway between pressure node and antinode; that the heat exchangers be spaced ''as close [together] as possible without...physical contact''; and that the heat-exchanger spacing be $y_0/\delta_\kappa = \sqrt{\pi/2} \simeq 1.25$. (This is Swift's notation,[6] where $2y_0$ is the plate spacing and δ_κ is the thermal penetration depth.) That is, Marrison uses imperfect heat exchange to ''optimize the phase lag'' necessary for work production in a standing-wave engine. The devices discussed in the present paper are different in that we assume excellent thermal contact at the exchanger and require a significant no-stack gap size for phasing.

The second reference appears as Figs. 9 and 10 of the 1984 patent[7] by Wheatley, Swift, and Migliori. Many of Wheatley's writings emphasize the importance of a ''second thermodynamic medium'' (a stack) that is generally taken to be ''continuously distributed.'' The 1984 patent, however, also describes ''an embodiment of the invention wherein the second thermodynamic medium consists of a set of circular wire mesh screens.'' The figures make it clear that the

[a]Electronic mail: wakeland@psu.edu

 0001-4966/2002/111(6)/2654/11/$19.00

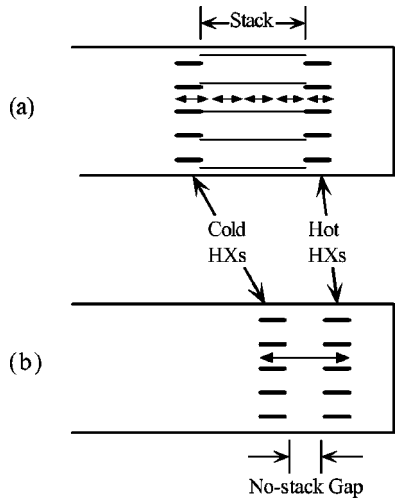

FIG. 1. (a) In a conventional stack-based thermoacoustic device the peak-to-peak excursion of each gas parcel (shown by the small horizontal arrows) is much less than the length of the stack. (b) In a no-stack device the spacing between the heat exchangers (HXs) is decreased and the amplitude is increased so that a single parcel enters both exchangers.

screens are not touching (i.e., not *continuous*), but ''the spacing between adjacent elements...must be less than the double amplitude...of the gas at that point.'' Wheatley *et al.* present this idea as a segmented stack, but it is in some ways similar to several no-stack devices in series. Unlike Marrison's invention, this arrangement could work both as an engine and as a refrigerator.

In the final reference,[8] which appears in 1986, Wheatley dismisses Marrison's device as a ''zero efficiency engine.'' This characterization is based on the fact that in a no-stack device both power and efficiency depend on amplitude, whereas ''when a continuously distributed second medium is used, the efficiency does not depend on the oscillation amplitude'' (Wheatley is discussing an inviscid model). He argues that in Marrison's engine ''the efficiency approaches zero as $2x_1$ approaches zero.'' At this point Wheatley makes no mention of his segmented stack, which also requires nonvanishing amplitude.

C. Idealizations and outline

The present paper is an exploration of the possibilities of no-stack thermoacoustics. We consider the simplest idealized model of the no-stack thermoacoustic cycle, assuming perfect heat exchangers; either one of these ideal heat exchangers can bring any gas that comes into it immediately to the exchanger's temperature. The acoustic field is assumed to be a standing wave; that is, the pressure is taken to be in phase with the displacement, even though some mechanical power must flow in or out via the acoustics. The temperature difference between the heat exchangers is assumed to be small compared to the absolute mean temperature. Sections III and IV show that no-stack refrigerators require high pressure amplitudes; nevertheless, this investigation uses a few expressions from linear acoustics, so the model is expected to become less accurate at extremely high amplitudes (above, say, 30% of mean pressure).

In Sec. II, all losses except thermal losses at the heat exchangers are ignored. Section II shows that the *inviscid* efficiency of a no-stack device can greatly exceed that of a comparable stack, i.e., a stack operating with an inviscid gas at the same power and temperatures. To investigate whether a *real* no-stack device might have these same advantages, in Sec. III we estimate the remaining losses in a no-stack refrigerator in order to compare the resulting overall efficiency to that of a particular stack-based refrigerator. The introduction to Sec. III describes our method of combining these other losses with the inviscid model of Sec. II to calculate the overall efficiency of the no-stack refrigerator, and describes the stack-based refrigerator that we use as a basis of comparison. Sections III A–III C detail the assumptions made in estimating these losses, some of which are based on the quasi-steady-flow approximation. The conclusion of Sec. III is that the high amplitude sound required for a no-stack refrigerator causes the conventional long, narrow, resonant enclosure to be unsuitable for a no-stack device. In Sec. IV the loss models are modified to consider a no-stack refrigerator in a short, nonresonant enclosure, with the conclusion that this configuration could achieve the desired efficiency improvement, making this a promising path for further research into no-stack refrigeration.

II. IDEALIZED THERMODYNAMIC CYCLE

A. Critical gradient and critical exchanger spacing

One of the most important concepts in standing-wave thermoacoustics is the idea of the critical temperature gradient. Each longitudinal position in a standing wave is associated with a displacement amplitude x_1 and a temperature amplitude T_1. We specify each position along the resonator by the distance x_0 to the nearest pressure antinode. The critical gradient[9,10] is $\nabla T_{\mathrm{crit}} \equiv T_1/x_1$, as shown in Fig. 2(a) for several locations in a resonator. The shaded curves indicate a half-wavelength standing wave with pressure antinodes at the closed ends. The arrows represent gas parcels oscillating back and forth in the horizontal direction. The horizontal component of each arrow shows the parcel's displacement, while the vertical component shows that parcel's temperature fluctuations about the mean temperature; the slope of the arrow then represents the critical gradient at that location. The arrow with the dashed box around it is shown enlarged in Fig. 2(b). As in stack-based devices, the critical gradient separates refrigerators from prime movers, as discussed in the following.

A useful idea in no-stack thermoacoustics is the critical heat exchanger spacing, x_{crit}, which we define to be

$$x_{\mathrm{crit}} \equiv \frac{T_{\mathrm{hx}}}{\nabla T_{\mathrm{crit}}}, \tag{1}$$

as illustrated in Fig. 2(c). Here $2T_{\mathrm{hx}}$ and $2x_{\mathrm{hx}}$ are the temperature difference and the distance between the two heat exchangers. Figures 2(d)–(f) show why this spacing is ''critical.'' In Fig. 2(d), ideal heat exchangers with temperatures $T_m \pm T_{\mathrm{hx}}$ have been introduced with their inside edges at $\pm x_{\mathrm{crit}}$. The heat exchangers are indicated by the thick, shaded lines. The exchangers modify the process line in xT

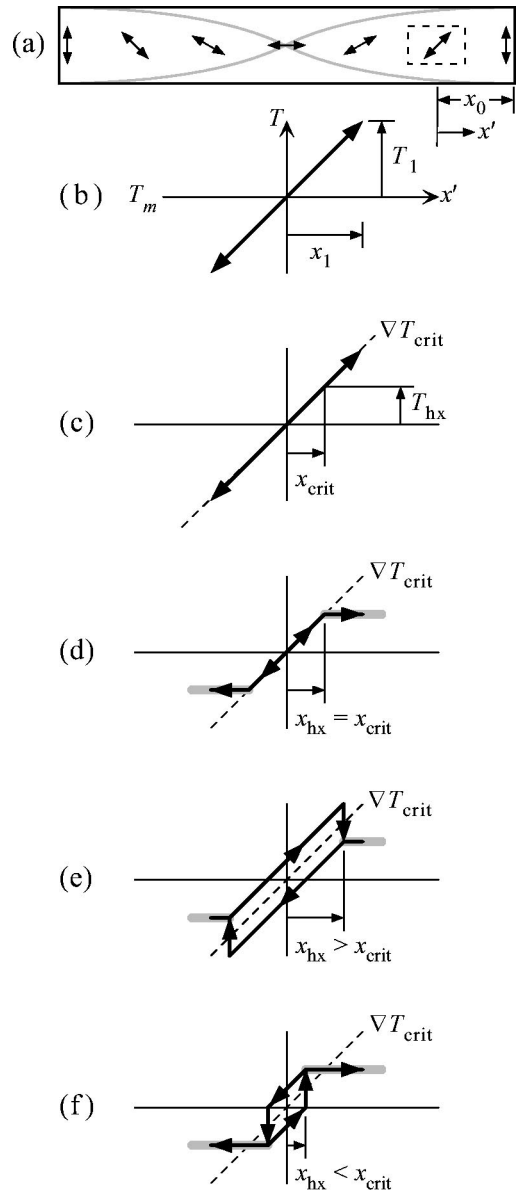

FIG. 2. (a) Arrows indicate the displacement (horizontal component) and temperature (vertical component) fluctuations at several locations in a half-wavelength resonator. The slope of each arrow is the critical temperature gradient at that location. (b) The parcel in the dashed box is shown enlarged and labeled. (c) The critical heat exchanger spacing $2x_{\rm crit}$ is determined by $\nabla T_{\rm crit}$ and the exchanger temperature difference $2T_{\rm hx}$. (d) Heat exchangers located at $\pm x_{\rm crit}$ influence the gas temperature within the exchangers but not between them, and cause no net heat exchange. (e) Exchanger spacing greater than $x_{\rm crit}$ results in a refrigerator. (f) $x_{\rm hx}<x_{\rm crit}$ results in a prime mover.

space, holding the gas at $\pm T_{\rm hx}$ while the parcel is in an exchanger. The particular exchanger spacing of $x_{\rm hx}=x_{\rm crit}$ is the only one for which the part of the process line *between* the exchangers is unchanged, and for which the parcel absorbs no net heat at either exchanger. In contrast, if $x_{\rm hx}>x_{\rm crit}$, as shown in Fig. 2(e), then the process line between the exchangers is split, with different paths as the parcel moves to the left or to the right. The parcel absorbs heat at the cold exchanger and rejects heat at the hot exchanger. This is a no-stack refrigerator. Here the heat exchanger gradient

$$\nabla T_{\rm hx} \equiv \frac{T_{\rm hx}}{x_{\rm hx}} \tag{2}$$

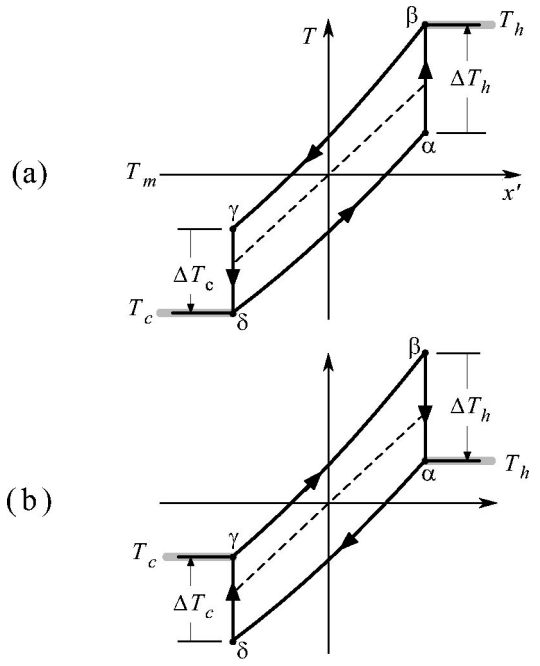

FIG. 3. Representations in xT space of the Brayton cycles for no-stack devices in the idealized heat exchanger model. This figure also serves to define ΔT_h, ΔT_c, T_h, T_c, and the points α, β, γ, and δ. (a) In an engine, $T_c=T_\delta$ and $T_h=T_\beta$. (b) In a refrigerator, $T_c=T_\gamma$ and $T_h=T_\alpha$. The dashed lines have slope $\nabla T_{\rm crit}$.

is less than $\nabla T_{\rm crit}$. In Fig. 2(f), $x_{\rm hx}<x_{\rm crit}$ and $\nabla T_{\rm hx}>\nabla T_{\rm crit}$. The parcel absorbs heat on the hot side and rejects heat on the cold side. As it turns out, net work is also done on the gas, so this is a no-stack prime mover. If we define the heat exchanger gradient $\nabla T_{\rm hx}$ by Eq. (2), then it plays the same role in no-stack thermoacoustics that the stack temperature gradient (denoted ∇T_m in Ref. 6) does in stack-based thermoacoustics, with $\nabla T_{\rm hx}<\nabla T_{\rm crit}$ for refrigerators and $\nabla T_{\rm hx}>\nabla T_{\rm crit}$ for prime movers.

B. Work and efficiency

In an idealized no-stack device with perfect heat exchangers, the gas undergoes an instantaneous temperature change when it arrives at a heat exchanger. These temperature changes are therefore isobaric, so this model of no-stack thermoacoustics is represented by the Brayton cycle: adiabatic compression, isobaric heating (or cooling), adiabatic expansion, and isobaric cooling (or heating). This cycle has been used since Wheatley[11] as a heuristic rough approximation to the cycle of the working gas in a stack. The Brayton cycle is much closer to the physical reality of a no-stack device since most of the compression/expansion takes place in the no-stack gap, where the gas is far from any surface and is nearly adiabatic. The cycle is shown in xT-space for an engine in Fig. 3(a) and a refrigerator in Fig. 3(b). These drawings assume that x_0, the equilibrium distance from the pressure antinode to the center of the no-stack gap, is much smaller than half a wavelength, so that the absolute pressure p is related to the displacement x' from the equilibrium position toward the pressure antinode by

$$p(x_0-x')^\gamma = p_m x_0^\gamma, \tag{3}$$

where p_m is the equilibrium pressure and γ is the ratio of the isobaric to isochoric specific heats, c_p/c_v. Figure 3 defines four points in xT-space labeled α, β, γ, and δ, and two temperature changes, ΔT_h and ΔT_c. Since segments $\delta\alpha$ and $\gamma\beta$ are both adiabats,

$$\frac{T_\beta}{T_\gamma}=\frac{T_\alpha}{T_\delta}, \tag{4}$$

or, equivalently,

$$\frac{\Delta T_h}{\Delta T_c}=\frac{T_\alpha}{T_\delta}. \tag{5}$$

The first-law efficiency η_{I} of the Brayton cycle engine depicted in Fig. 3(a) is

$$\eta_{\mathrm{I}}\equiv\frac{W}{Q_h}=\frac{\Delta T_h-\Delta T_c}{\Delta T_h}=\frac{T_\alpha-T_\delta}{T_\alpha}, \tag{6}$$

where W is the work output and Q_h is the heat input in each cycle. The ideal "Carnot" efficiency η_c is given by $(T_h-T_c)/T_h=(T_\beta-T_\delta)/T_\beta$, so the second-law efficiency[12] η_{II} is

$$\eta_{\mathrm{II}}\equiv\frac{\eta_{\mathrm{I}}}{\eta_c}=\frac{T_\alpha-T_\delta}{T_\beta-T_\delta}\left(\frac{T_\beta}{T_\alpha}\right). \tag{7}$$

The temperature gradient between exchangers is $\nabla T_{\mathrm{hx}}=(T_\beta-T_\delta)/2x_{\mathrm{hx}}$. In Fig. 3, the dashed lines have slope ∇T_{crit}, the derivative of the adiabat that passes through the mean temperature T_m at x_0. We see in Fig. 3 that $\nabla T_{\mathrm{crit}}\simeq(T_\alpha-T_\delta)/2x_{\mathrm{hx}}$ for amplitudes that are not too large. Furthermore, $T_\beta/T_\alpha\simeq 1$ when $T_{\mathrm{hx}}\ll T_m$. If we define the normalized standing-wave temperature gradient Γ for no-stack devices as

$$\Gamma_n\equiv\frac{\nabla T_{\mathrm{hx}}}{\nabla T_{\mathrm{crit}}}, \tag{8}$$

then

$$\eta_{\mathrm{II}}\simeq\frac{1}{\Gamma_n}. \tag{9}$$

The subscript n here and elsewhere signifies "no-stack," whereas s denotes an equivalent quantity for a stack.

For the refrigerator [Fig. 3(b)], the coefficient of performance is given by

$$\mathrm{COP}\equiv\frac{Q_c}{W}=\frac{\Delta T_c}{\Delta T_h-\Delta T_c}=\frac{T_\delta}{T_\alpha-T_\delta}, \tag{10}$$

the Carnot coefficient of performance is

$$\mathrm{COP}_c=\frac{T_\gamma}{T_\alpha-T_\gamma}, \tag{11}$$

and

$$\eta_{\mathrm{II}}\equiv\frac{\mathrm{COP}}{\mathrm{COP}_c}=\frac{T_\alpha-T_\gamma}{T_\alpha-T_\delta}\left(\frac{T_\delta}{T_\gamma}\right)\simeq\Gamma_n\frac{T_\delta}{T_\gamma}\simeq\Gamma_n. \tag{12}$$

These results (that $\eta_{\mathrm{II}}\simeq 1/\Gamma$ for an engine and $\eta_{\mathrm{II}}\simeq\Gamma$ for a refrigerator) are the same as for a short stack with temperature gradient $\nabla T_{\mathrm{stack}}$ and $\Gamma_s\equiv\nabla T_{\mathrm{stack}}/\nabla T_{\mathrm{crit}}$, using either a Brayton cycle model[13] or the first-order inviscid Navier–Stokes equations in the boundary-layer limit.[14] For models of both stack- and no-stack-based devices, the normalized temperature gradient is a direct measure of the inviscid efficiency. The highest inviscid efficiency occurs when ∇T_{hx} approaches ∇T_{crit}, with the heat flow simultaneously tending toward zero.

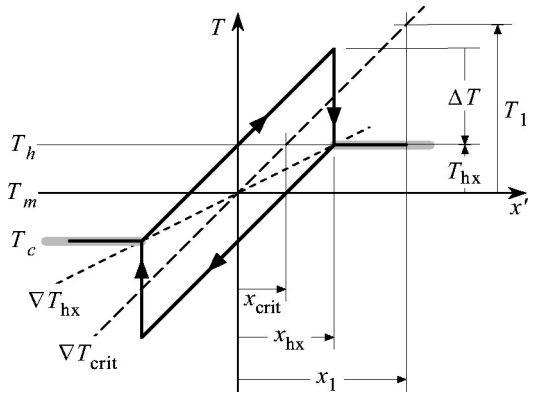

FIG. 4. The relationships between important no-stack variables are illustrated graphically. The situation shown here of $\nabla T_{\mathrm{hx}}<\nabla T_{\mathrm{crit}}$ represents a refrigerator with the approximation $\Delta T_h\cong\Delta T_c$.

It should be noted that for many prime movers the approximation that $T_{\mathrm{hx}}\ll T_m$ is poor. Accurate modeling of prime movers with large T_{hx} would require a more complete model, including the temperature dependence of gas properties and the effects of thermal radiation. This is part of our motivation for concentrating on refrigerators later in this paper.

C. Heat

In a refrigerator, work is required to cyclically absorb heat at one temperature and reject it at a higher temperature, and this work is rejected as additional heat at the hot heat exchanger. As a result, $\Delta T_h>\Delta T_c$ in Eq. (5). In position-temperature diagrams of the Brayton cycle (Fig. 3), the difference in magnitude between ΔT_h and ΔT_c arises from the difference in the curvatures of the adiabatic process lines at higher and lower temperatures. However, even at pressure amplitudes that are large by "acoustics" standards, the differences between these two curves are small enough that $\Delta T_h\simeq\Delta T_c$. For the purposes of calculating heats, ignoring the small difference between ΔT_h and ΔT_c results in expressions that are simple and amenable to interpretation. This approach is similar to that used by Swift in Sec. I of his 1988 review article[6] and is consistent with the idealization that the thermoacoustic components operate in a pure standing wave. In this section we use the approximation $\Delta T_h\simeq\Delta T_c=\Delta T$, and approximate the adiabats $\gamma\beta$ and $\delta\alpha$ as straight lines, both with slope ∇T_{crit}. The variables used in this section are summarized in Fig. 4.

The rate at which heat is absorbed from the cold heat exchanger and deposited on the hot heat exchanger is

$$\dot{Q}_n=\rho_m c_p V\,\Delta T\,f. \tag{13}$$

Here ρ_m is the mean density of the gas, V is the volume of gas that comes into thermal contact with *both* exchangers

(the ''working'' gas), ΔT is the temperature change of the gas when it enters an exchanger, and f is the operating frequency. For succinctness, we often use the terms ''heat'' or ''heat flow'' as abbreviations for ''rate of heat transfer.''

The working volume is $V=2A_{\rm fr}(x_1-x_{\rm hx})$, where $A_{\rm fr}$ is the frontal cross-sectional area of the enclosure; this is true regardless of the porosity of the exchangers. The temperature drop (see Fig. 4) is $\Delta T=2\nabla T_{\rm crit}(x_{\rm hx}-x_{\rm crit})$, so the heat absorbed by the gas at the cold exchanger is

$$\dot{Q}_n=\begin{cases} A_{\rm fr}\dfrac{2\omega}{\pi}\rho_m c_p \nabla T_{\rm crit}(x_1-x_{\rm hx})(x_{\rm hx}-x_{\rm crit}) \\ \quad \text{if} \quad |x_1|\geqslant|x_{\rm hx}| \\ 0 \quad \text{if} \quad |x_1|<|x_{\rm hx}| \end{cases}. \tag{14}$$

This expression also holds for a prime mover if the minus sign on $\dot{Q}_n$ resulting from the factor $(x_{\rm hx}-x_{\rm crit})$ is interpreted to mean that heat is rejected to the cold exchanger.

D. Heat exchanger position for maximum heat flow in a no-stack refrigerator

For any no-stack device (either refrigerator or prime mover) to operate in this idealized heat exchanger model, the acoustic pressure amplitude $p_{1n}=p-p_m$ must be great enough[15] that $|x_1|>|x_{\rm hx}|$. To operate as a *refrigerator*, there is the additional condition that $|x_{\rm hx}|$ must be greater than $|x_{\rm crit}|$. That is, for a refrigerator, $x_{\rm hx}$ must be *between* $x_{\rm crit}$ and x_1: $\dot{Q}_n\to 0$ as $x_{\rm hx}\to x_1$ because the working volume shrinks to zero; $\dot{Q}_n\to 0$ as $x_{\rm hx}\to x_{\rm crit}$ because the temperature drop vanishes. With the no-stack gap centered at a x_{0n}, and with fixed temperatures and fixed pressure amplitude (i.e., fixed $x_{\rm crit}$ and x_1), then $\dot{Q}_n$ is greatest when the inner edges of the heat exchangers are located halfway between $x_{\rm crit}$ and x_1, i.e., when

$$x_{\rm hx}=\tfrac{1}{2}(x_1+x_{\rm crit}). \tag{15}$$

Equation (15) maximizes heat flow, not inviscid efficiency, for a given pressure amplitude. No-stack devices require large acoustic amplitudes. Since flow and enclosure losses at large amplitude are costly to support, it is reasonable to expect that the greatest *overall* efficiency will be achieved by a design with large $\dot{Q}_n$, i.e., with $x_{\rm hx}\simeq\frac{1}{2}(x_1+x_{\rm crit})$. For perfect heat exchangers, it would never make sense to make $x_{\rm hx}$ greater than this, since doing so would reduce both cooling power and efficiency. Reducing $x_{\rm hx}$ slightly from $\frac{1}{2}(x_1+x_{\rm crit})$ may increase efficiency somewhat, but at the cost of reduced power density. This topic is examined further in Sec. IV.

E. Heat exchanger position for maximum work from a no-stack engine

For an engine, the considerations for heat exchanger placement are similar, although not identical. To operate as a prime mover, $x_{\rm hx}$ must be between zero and $x_{\rm crit}$, with $|x_1|>|x_{\rm hx}|$. As in the refrigerator case, the inviscid efficiency is maximized as $x_{\rm hx}$ approaches $x_{\rm crit}$, but in this same limit the heat flow, and thus the useful work generated, go to zero. For perfect heat exchangers, the heat and the work also go to zero as $x_{\rm hx}$ approaches zero. The work generated is maximized between these two extremes. Since $\dot{W}_n=\eta_1\dot{Q}_n$, and $\eta_{\rm I}=\eta_c\eta_{\rm II}\simeq\eta_c/\Gamma_n=\eta_c x_{\rm hx}/x_{\rm crit}$,

$$\dot{W}_n\simeq\eta_c\frac{x_{\rm hx}}{x_{\rm crit}}\dot{Q}_n. \tag{16}$$

The heat $\dot{Q}_n$ is given by Eq. (14), so

$$\dot{W}_n\propto x_{\rm hx}(x_1-x_{\rm hx})(x_{\rm hx}-x_{\rm crit}), \tag{17}$$

the magnitude of which is maximized when

$$\frac{x_{\rm hx}}{x_{\rm crit}}=\frac{1}{3}\left(1+\frac{x_1}{x_{\rm crit}}-\sqrt{\left(\frac{x_1}{x_{\rm crit}}\right)^2-\frac{x_1}{x_{\rm crit}}+1}\right). \tag{18}$$

This expression for $x_{\rm hx}/x_{\rm crit}$ is relatively insensitive to $x_1/x_{\rm crit}$, and evaluates to 0.5 for $x_1/x_{\rm crit}\gg 1$ and 0.33 for $x_1/x_{\rm crit}=1$. For perfect heat exchangers, this formula gives the lower bound to the preferred $x_{\rm hx}$. There is no advantage to decreasing $x_{\rm hx}$ below this value since both the work developed by the engine and the efficiency would suffer. As for the refrigerator case, since it is costly to support the large acoustic amplitudes associated with a no-stack device, the best *overall* prime mover efficiency is expected to occur with $x_{\rm hx}$ close to this value, but pushed somewhat toward $x_{\rm crit}$ for better inviscid efficiency, at the cost of some power production.

F. Comparison of stack and no-stack inviscid efficiencies for refrigerators

Our objective is to determine whether there are circumstances in which a no-stack device might outperform a stack-based device. Because a prime mover is likely to have a large $T_{\rm hx}$, a prime-mover model accurate enough for this sort of comparison would need to account for the effects of thermal radiation and of temperature variations in the gas properties. To keep the analysis reasonably short, the remainder of this paper focuses on refrigerators.

All refrigerator designs contain trade-offs between such factors as efficiency, power, mean pressure, sound speed, and size. We endeavor to make the comparison between stack-based and no-stack devices ''fair'' by constraining the hot and cold exchanger temperatures to be the same in the two devices, and by assuming that the two devices use the same gas at the same mean pressure. In the present section we also require that they operate at the same useful refrigerating power; that is, that there is the same rate of heat transfer from metal to gas at the cold heat exchanger.

To proceed with the analysis, it is useful to find an expression for $\dot{Q}_n$ as a function of p_{1n} in which $x_{\rm hx}$ is allowed to vary with x_1 so that $x_{\rm hx}$ is always equal to $\frac{1}{2}(x_1+x_{\rm crit})$. In an ideal gas with sound speed a and wave number $k\equiv\omega/a$, the critical gradient as a function of position is given by[16]

$$\nabla T_{\rm crit}=(\gamma-1)T_m k\cot(kx_0), \tag{19}$$

and, also,

$$\rho_m c_p=\frac{\gamma}{\gamma-1}\frac{p_m}{T_{\rm m}}. \tag{20}$$

Applying these relations and Eq. (15) to Eq. (14) gives $\dot{Q}_n$ as a function of p_{1n} with x_{hx} adjusted for maximum heat flow,

$$\dot{Q}_{n_{\max}} = \frac{A_{\mathrm{fr}}}{2\pi}\frac{a}{\gamma p_m}\tan(kx_{0n})(p_{1n}-p_{1\mathrm{crit}})^2. \tag{21}$$

Here $p_{1\mathrm{crit}} \equiv \rho_m c_p \nabla T_{\mathrm{crit}} x_{\mathrm{crit}}$ is the critical pressure amplitude below which the working volume is zero. In Eq. (21) and all subsequent equations, $\dot{Q}_{n_{\max}}=0$ for $|p_{1n}|<|p_{1\mathrm{crit}}|$ is implied.

The expression analogous to Eq. (21) for a stack centered at x_{0s} and with normalized temperature gradient Γ_s is[17]

$$\dot{Q}_s = \frac{A_{\mathrm{fr}}}{4}\frac{a}{\gamma p_m}\tan(kx_{0s})(1-\Gamma_s)p_{1s}^2. \tag{22}$$

We want to compare stack and no-stack refrigerators operating with the same rate of heat transfer from the cold exchanger, so we set $\dot{Q}_s = \dot{Q}_{n_{\max}}$, giving

$$p_{1n}-p_{1\mathrm{crit}} = p_{1s}\sqrt{\frac{\pi}{2}\frac{\tan(kx_{0s})}{\tan(kx_{0n})}(1-\Gamma_s)}. \tag{23}$$

Stacks are typically operated at about $\Gamma_s=0.5$ as a compromise between power ($\Gamma_s\to 0$) and efficiency ($\Gamma_s\to 1$). If the devices are at the same location in the standing wave ($x_{0s}=x_{0n}$), and with $\Gamma_s=0.5$, then $\sqrt{(\pi/2)(1-\Gamma_s)}=0.89\simeq 1$. It is interesting to note that to run the inviscid no-stack device at the same power as the inviscid stack device under these conditions requires that the amount that the no-stack pressure exceeds the critical pressure, $p_{1n}-p_{1\mathrm{crit}}$, is nearly the *same* as the pressure amplitude p_{1s} in the stack-based device.

The second-law efficiency of the inviscid stack is approximately Γ_s. The inviscid no-stack second-law efficiency[18] is approximately Γ_n, which, from Eqs. (1), (2), (8), and (15), is

$$\Gamma_n = \left[1+\frac{1}{2}\frac{p_{1n}-p_{1\mathrm{crit}}}{p_{1\mathrm{crit}}}\right]^{-1}. \tag{24}$$

Once again setting $\dot{Q}_{n_{\max}}=\dot{Q}_s$, we have the final result,

$$\Gamma_n = \left[1+\frac{\gamma-1}{\gamma}\sqrt{\frac{\pi}{8}\frac{\tan(kx_{0s})}{\tan(kx_{0n})}(1-\Gamma_s)}\,\frac{p_{1s}/p_m}{T_{\mathrm{hx}}/T_m}\right]^{-1}. \tag{25}$$

Consider, for example, the following typical conditions for a stack-based thermoacoustic refrigerator (these particular conditions are selected to facilitate later comparison to a particular stack-based device): $p_{1s}/p_m=3.60\%$, $\Gamma_s=0.500$, $T_{\mathrm{hx}}=13.1\,\mathrm{K}$, $T_m=290\,\mathrm{K}$, and $\gamma=5/3$. If $x_{0n}=x_{0s}$, then $p_{1\mathrm{crit}}/p_m=11.3\%$, $(p_{1n}-p_{1\mathrm{crit}})/p_m=3.2\%$, and $p_{1n}/p_m=14.5\%$, giving $\eta_{\mathrm{II}}\simeq\Gamma_n\simeq 0.88$, which is quite large. That is, the no-stack device has a considerably higher inviscid efficiency (88%) than the comparable stack device (50%).

What accounts for this high inviscid efficiency? Thermal inefficiency comes from heat transport through a temperature difference. A stack is often described in terms of a series of gas parcels; in a refrigerator, each parcel absorbs heat from the stack at one location and rejects heat to the stack at a location with a higher temperature. The next gas parcel in the series removes heat from this higher temperature location and rejects heat at a yet higher temperature further along the stack. The advantage of using a stack is that a large temperature difference can be spanned with low-amplitude sound even though the temperature spanned by each gas parcel is small. The cost is that the overall process involves a large number of heat transfers across temperature drops. In a no-stack refrigerator, a large pressure amplitude allows absorption of heat at one exchanger and rejection of heat at the other, so only *two* temperature drops are involved in the process, reducing thermal entropy generation. Furthermore, it is not a case of many small temperature drops versus two large temperature drops. To make a fair comparison we must consider two devices with *similar rates of heat removal from the cold exchanger*. This refrigeration power is proportional to the size of the temperature drop of the gas at the cold exchanger, which is about the same in both cases for similar heat exchangers. Thus, the difference in inviscid efficiencies of stack-based and no-stack refrigerators results from the difference between many small temperature drops versus only two temperature drops that are similarly small.

III. ESTIMATION OF LOSSES: CONVENTIONAL GEOMETRY

We have shown that a no-stack device can have a greater inviscid efficiency than a comparable stack-based device. Unfortunately, the no-stack design is subject to greater losses of other types. In the remaining sections we model these losses to estimate whether the *overall* efficiency of a no-stack refrigerator can meet or exceed that of a stack-based design. We will conclude that it can, but because of losses on the walls of the resonator, a no-stack design *cannot* use the long, narrow resonator geometry that has been a common stack-based configuration. Other enclosure geometries must be used to make a no-stack device viable.

Our method is to calculate the overall first-law efficiency $\mathrm{COP}_{\mathrm{net}}$ for a no-stack refrigerator using

$$\mathrm{COP}_{\mathrm{net}} = \frac{\dot{Q}_{\mathrm{net}}}{\dot{W}_{\mathrm{net}}} = \frac{\dot{Q}_{\mathrm{inviscid}}-\dot{Q}_{\mathrm{conduction}}-\dot{Q}_{\mathrm{nuisance}}}{\dot{W}_{\mathrm{inviscid}}+\dot{W}_{\mathrm{shear}}+\dot{W}_{\mathrm{minor}}+\dot{W}_{\mathrm{enclosure}}}, \tag{26}$$

which we then compare to the known efficiency of a stack-based device with the same $\dot{Q}_{\mathrm{net}}$ under the same conditions of temperature, gas mixture, and pressure. The terms $\dot{Q}_{\mathrm{inviscid}}$ and $\dot{W}_{\mathrm{inviscid}}$ are heat and work rates derived from the inviscid theory of Sec. II. The useful heat $\dot{Q}_{\mathrm{net}}$ is the inviscid heat $\dot{Q}_{\mathrm{inviscid}}$ minus two parasitic terms: $\dot{Q}_{\mathrm{conduction}}$, the thermal conduction back down the temperature gradient through the gas; and $\dot{Q}_{\mathrm{nuisance}}$, which is made up of those parts of the dissipation that must be removed from the cold heat exchanger by the refrigerator as a nuisance heat load. The total required power $\dot{W}_{\mathrm{net}}$ includes $\dot{W}_{\mathrm{inviscid}}$ plus three other terms: $\dot{W}_{\mathrm{shear}}$ and $\dot{W}_{\mathrm{minor}}$, which are two types of flow loss in the heat exchangers; and $\dot{W}_{\mathrm{enclosure}}$, which includes all of the thermal and viscous losses on the walls of the enclosure. Each of these terms is described in detail in the following.

As a standard of comparison, consider the stack-based device known as SETAC.[19] Ballister and McKelvey used a

TABLE I. Summary of gas properties and measured operating conditions (''performance'') for a particular operating condition of SETAC, a conventional stack-based thermoacoustic refrigerator.

Gas properties	SETAC performance
$T_m = 290$ K	$f = 320$ Hz
$p_m = 2.07$ MPa	$T_{\rm hx} = 13.1$ K
$\rho_m = 5.17$ kg/m^3	$P_A/p_m = 3.60\%$
$a = 817$ m/s	$\dot{W}_{\rm net} = 166$ W
$\gamma = 1.67$	$\dot{Q}_{\rm net} = 274$ W
$k_0 = 0.133$ W m^{-1} K^{-1}	$\dot{Q}_{\rm net}/A_{\rm fr} = 1.55$ W/cm^2
$\mu = 2.01\times10^{-5}$ kg s^{-1} m^{-1}	$\eta_{\rm II_{net}} = 16.7\%$

pressurized gas mixture of 94.4% helium and 5.6% argon in SETAC to achieve the gas properties[20] listed in Table I. Table I also contains the experimental conditions[21] for which they obtained their maximum $\eta_{\rm II}$ of 16.7%, absorbing 294 W of heat at 241.0 K and rejecting heat at 303.2 K, using two stacks that were each 11 cm in diameter, for an areal power density of $\dot{Q}_{\rm net}/A_{\rm fr} = 1.55$ W/cm^2.

The basic geometry of SETAC is depicted in Fig. 5, though the resonator has been simplified in shape to a uniform cylinder. The heat exchangers in SETAC are basically parallel plates, with a porosity Ω of 0.7 and a plate thickness of 152 μm. For parallel plates, Ω is simply the fraction of the frontal area that is clear for the passage of gas. To achieve good thermal contact in the exchangers, the plate spacing y_0/δ_κ in the heat exchangers for the no-stack model has been reduced to 0.63, half of the $\sqrt{\pi/2}$ suggested by Marrison. In order to keep plate thickness above 100 μm, Ω has been reduced to 0.5 in the exchangers for the no-stack model, resulting in $y_0 = 108$ μm. This small porosity reduces the performance of the model refrigerator, but ensures that the exchangers in the model represent a realistic design.

The terms $\dot{Q}_{\rm inviscid}$ and $\dot{W}_{\rm inviscid}$ in Eq. (26) come directly from the inviscid theory of Sec. II. Assuming that the heat exchangers are positioned as described in Sec. II D, the heat from *two* sets of heat exchangers of area $A_{\rm fr}$ is

$$\dot{Q}_{\rm inviscid} = 2\dot{Q}_{n_{\max}}, \tag{27}$$

as given by Eq. (21). From Eqs. (10) to (12), the acoustic power required to drive the thermodynamic cycle is

$$\dot{W}_{\rm inviscid} = \frac{\dot{Q}_{\rm inviscid}}{\Gamma_n {\rm COP}_c}. \tag{28}$$

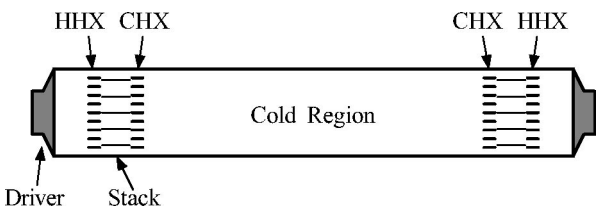

FIG. 5. The geometry used for comparison of a stack to a no-stack refrigerator. The half-wavelength resonator has a driver at each end. The hot heat exchangers (HHXs) face the ends. The cold heat exchangers (CHXs) face the central section of the resonator; wall losses in this central region become a nuisance load on the cold heat exchanger.

The remainder of this section is devoted to modeling the loss terms of a device with the same geometry as SETAC, but with the stacks replaced by no-stack gaps.

A. Heat exchanger flow losses

Flow losses in the heat exchangers have the potential to be relatively large in a no-stack device, for two reasons. First, in a no-stack device there is a relatively large volume of gas that suffers flow losses while passing through one or the other exchanger, but which does not enter *both* exchangers, and therefore is not part of the working gas. Second, because of the high amplitudes required in no-stack devices, the gas moves at relatively high speeds, exacerbating flow-loss problems. In particular, so-called ''minor losses'' arising from the sudden changes in gas cross-sectional area at heat exchangers can become large in high-speed flows. The power dissipated by minor losses grows as velocity cubed, so at high speeds it becomes increasingly important relative to dissipation from ordinary viscous shear, which grows only as velocity squared.

In the present model, losses in the heat exchangers are estimated using the quasi-steady approximation.[22,23] That is, we assume that the results from steady flow hold at each instant of time, and average the loss over the cycle period.

The quasi-steady loss due to ordinary laminar viscous shear in the exchangers is[24]

$$\dot{W}_{\rm shear} = 4A_{\rm fr}\frac{1}{2}\left(\frac{1}{2}\rho_m|u_{\rm hx}|^3\right)\left(f_F\frac{4L_{\rm hx}}{D_h}\right)\Omega, \tag{29}$$

where f_F is the Fanning friction factor, $L_{\rm hx}$ is the exchanger length, D_h is the hydraulic diameter of the exchanger pores, Ω is the porosity of the exchanger, and $|u_{\rm hx}| = \omega|x_1|/\Omega$ is the increased peak speed within the exchanger due to the flow constriction. The leading factor of 4 accounts for a total of four heat exchangers, and the free-standing factor of $\frac{1}{2}$ is the result of the time average.[25] For heat exchangers constructed of parallel plates of spacing $2y_0$, the hydraulic diameter is $4y_0$, and the friction factor is $f_F = 24/{\rm Re} = 24\mu/\rho_m D_h u_{\rm hx}$, where μ is the shear viscosity and Re is the Reynolds number. The exchanger length $L_{\rm hx}$ is set to $2(x_1 - x_{\rm hx})/\Omega$, which is the length of the working gas within the reduced cross-sectional area of the exchanger. The hot and cold exchangers are identical; the fact that the gas has slightly different volumes at the hot and cold exchangers due to pressure variations is neglected in this model. The flow is laminar in all the heat exchanger geometries that we have considered for no-stack applications. Equation (29) is an excellent approximation to the real part of the more exact thermoacoustic expression[26] provided that $y_0 \lesssim \delta_\kappa = \sqrt{k_0/\rho_m c_p \pi f}$.

The quasi-steady minor loss is

$$\dot{W}_{\rm minor} = 4A_{\rm fr}\frac{4}{3\pi}\left(\frac{1}{2}\rho_m|u_{\rm hx}|^3\right)K\Omega, \tag{30}$$

where K is a minor loss coefficient that includes both entry and exit effects. The factor $4/3\pi \simeq 0.424$ is the result of the time average.[25] For K we use[27]

$$K = 0.5(1-\Omega)^{0.75} + (1-\Omega)^2, \tag{31}$$

TABLE II. Design parameters and model results for a no-stack device matching the gas properties and temperatures of the stack-base device listed in Table I, the conventional geometry shown in Fig. 5, and having the same diameter as SETAC.

No-stack parameters	Model results
$P_A/p_m = 37.4\%$	$\dot{Q}_{\text{inviscid}} = 14\,900$ W
$kx_{0n} = 0.0718$	$\dot{Q}_{\text{conduction}} = 8$ W
$y_0 = 54.2\ \mu$m	$\dot{Q}_{\text{nuisance}} = 30\,200$ W
$y_0/\delta_\kappa = 0.630$	$\dot{W}_{\text{inviscid}} = 3030$ W
$\Omega = 0.500$	$\dot{W}_{\text{shear}} = 1230$ W
$R = 0.055$ m	$\dot{W}_{\text{minor}} = 207$ W
$\Gamma_n = 0.465$	$\dot{W}_{\text{enclosure}} = 2400$ W
	$\dot{W}_{\text{net}} = 6870$ W
	$\dot{Q}_{\text{net}} = 11\,900$ W
	$\dot{Q}_{\text{net}}/A_{\text{fr}} = 62.5$ W/cm^2
	$\eta_{\text{II}_{\text{net}}} = 16.4\%$

where the first term is for the entrance and the second is for the exit.

B. Enclosure losses

Enclosure losses are estimated assuming a cylindrical half-wavelength resonator, following the treatment in Sec. III B of Ref. 6. The power dissipated is

$$\dot{W}_{\text{enclosure}} = \dot{W}_{\text{sides}} + \dot{W}_{\text{ends}} = A_{\text{fr}} \frac{\pi}{4} \frac{p_m a}{\gamma} \delta_k \left(\frac{P_A}{p_m}\right)^2 \left(\frac{\sqrt{\sigma}}{R} + \frac{\gamma - 1}{R}\right) + A_{\text{fr}} \frac{\pi}{4} \frac{p_m a}{\gamma} \delta_k \left(\frac{P_A}{p_m}\right)^2 \frac{2(\gamma - 1)}{L_{\text{res}}}, \tag{32}$$

where $L_{\text{res}} = a/2f$ is the length of the resonator, R is the radius ($A_{\text{fr}} = \pi R^2$), $\sigma = \mu c_p / k_0$ is the Prandtl number of the gas, and P_A is the pressure amplitude at the end caps, which is related to p_{1n} by $p_{1n} = P_A \cos kx_{0n}$.

C. Net heat

The useful heat of Eq. (27) is diminished by thermal conduction from the hot exchangers to the nearby cold exchangers through the gas in the no-stack gaps. In the quiescent gas,

$$\dot{Q}_{\text{conduction}} = 2A_{\text{fr}} k_0 \nabla T_{\text{hx}}, \tag{33}$$

where k_0 is the thermal conductivity of the gas. The acoustical operation of the device changes the mean temperature profile of the gas between the exchangers in ways that are not well understood.[28] This loss might be as great as $\dot{Q}_{\text{conduction}} = 2A_{\text{fr}} k_0 \nabla T_{\text{crit}}$, but $\nabla T_{\text{crit}} \simeq \nabla T_{\text{hx}}$ for the case we are considering, and $\dot{Q}_{\text{conduction}}$ ends up being small compared to the other losses anyway (see Table II), so we use Eq. (33).

For a half-wavelength resonator with refrigeration components at both ends, the dissipation of acoustic power on the enclosure walls occurs mostly in the cold parts of the device (see Fig. 5). This energy, and the acoustic energy dissipated in the cold exchangers, must be removed from the otherwise insulated device through the heat exchangers. Since the cold parts of the refrigerator are in much better thermal contact with the cold exchangers than the hot exchangers, we make the conservative estimate that all of this energy ends up on the cold exchanger as a "nuisance load" that subtracts from the refrigeration power available to extract heat from the cold exchangers. Thus, for this geometry we set

$$\dot{Q}_{\text{nuisance}} = \dot{W}_{\text{sides}} + \tfrac{1}{2}(\dot{W}_{\text{shear}} + \dot{W}_{\text{minor}}) \tag{34}$$

as defined by Eqs. (29), (30), and (32). Equation (34) also slightly overestimates $\dot{Q}_{\text{nuisance}}$ since not all of the sidewall area is actually in the cold region.

D. Comparison of stack and no-stack overall efficiencies for the conventional geometry

By incorporating the loss terms of Secs. III A–III D into Eq. (26) we can estimate the efficiency of complete, working, no-stack refrigerators of various designs. We wish to compare the use of stacks to the use of no-stack gaps in the design of thermoacoustic refrigerators. The designers of the reference stack-based device (SETAC) adjusted parameters such as stack length and location in order to improve its performance as much as they could. To make a fair comparison between stack-based and no-stack designs, the no-stack design should also be optimized. In order to search for high-efficiency design configurations, the authors created a computer spreadsheet model and adjusted various design parameters.

If losses on the resonator walls are neglected, the model reveals design trade-offs similar to those for stack-based devices. For given pressure amplitude and exchanger temperatures, larger kx_{0n} results in higher $\dot{Q}_n$ but lower efficiency. As kx_{0n} is reduced, $\eta_{\text{II}_{net}} \equiv \text{COP}_{\text{net}}/\text{COP}_c$ increases to some maximum, beyond which the increase in $\dot{Q}_{\text{conduction}}$ outweighs the decrease in the flow loss terms.

When resonator losses are included, however, the situation is very different, and it becomes difficult to find any efficient design. Both kx_{0n} and P_A/p_m must be adjusted in a compromise between heat power and *enclosure* losses. Because enclosure losses are already large at $p_1 = p_{1\text{crit}}$, where the device has only begun to refrigerate, the pressure amplitude is driven to a very high value. The spreadsheet's "solver" add-in (Microsoft Excel 2000) was used to speed the search for the most efficient combination of kx_{0n} and P_A/p_m for this geometry. The results are summarized in Table II.

The design in Table II has almost the same efficiency as SETAC, but is not really comparable because this efficiency is attainable only at a very high pressure amplitude (37.4%), resulting in a device with 40 times the heat pumping capacity of SETAC. Among the obvious problems with this design is the tremendous amount of heat (63 W/cm^2) that must pass through the small heat exchangers. An ironic result of the geometry studied here is that $\Gamma_n = 0.465$, so the hoped-for inviscid efficiency advantage of the no-stack arrangement has not been realized. Furthermore, this "solution" has such a high amplitude that the gas in the resonator would probably

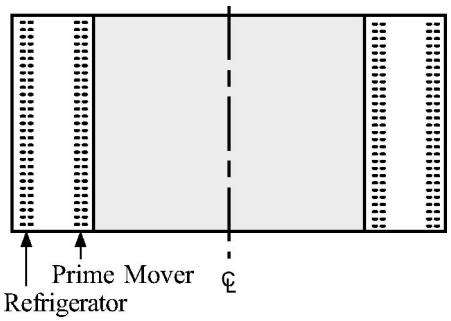

FIG. 6. This annular resonator (shown in cross section), in which the gas motion is radial, is favorable for no-stack devices because it has a large ratio of heat-exchanger area to enclosure surface area.

be driven into turbulent flow, making resonator losses even higher than we have estimated. Our conclusion is that the potential advantages of the no-stack method are not realized in a conventional half-wavelength resonator. Despite the fact that the model presented in Table II is not a realistic design, we have included it because this sort of table shows where the weaknesses of the design are, and points the way to the improvements in Sec. IV.

E. Efficiency and aspect ratio

Examining Table II, we see that the ordinary linear thermal and viscous losses on the walls of the resonant enclosure turn out to be a large fraction of the total loss in this model no-stack refrigerator. This is because enclosure losses grow as p_{1n}^2, whereas the heat flows grow as $(p_{1n}-p_{1\,\mathrm{crit}})^2$. This makes the tube-like aspect ratio of Fig. 5 unfavorable for operation with no stack, particularly because of the contribution of the sidewalls to the nuisance load. Increasing the ratio of resonator end area to resonator length corrects this problem. The contribution of $\dot{W}_{\mathrm{sides}}$ to the total loss becomes less than $\dot{W}_{\mathrm{ends}}$ when

$$\frac{R}{L_{\mathrm{res}}} \geqslant \frac{\sqrt{\sigma}+(\gamma-1)}{2(\gamma-1)}. \tag{35}$$

For the SETAC gas mixture, this occurs when $R/L_{\mathrm{res}} \simeq 1$. Increasing the radius of the cylinder to 1.26 m (approximately its length) and reoptimizing kx_{0n} and P_A results in a second-law efficiency of 42% at $P_A/p_m = 24\%$ and with the cold exchangers passing 9.2 W/cm^2. This would be excellent performance, rivaling the best regenerator-based device to date. With a frontal area of 5 m^2, however, this would be an industrial-sized chiller.

One way to make a resonator with a large ratio of heat exchanger area to sidewall area is to use an annular, radial geometry. Some researchers in our group are pursuing the geometry shown in Fig. 6. With this configuration, one set of exchangers is a prime mover and one set is a refrigerator. If we modify the model under the assumption that all (not half) of the sidewall losses are nuisance heat, then the no-stack refrigerator portion of this device has a second-law efficiency of 35%. Even assuming the use of air at atmospheric pressure, a frequency of 550 Hz for reduced size, and a suboptimum pressure amplitude of 25%, this model predicts a respectable $\eta_{\mathrm{II}} = 17\%$.

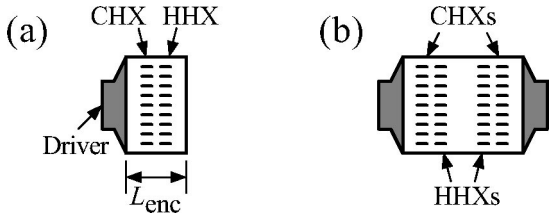

FIG. 7. Alternative geometries for no-stack refrigerators with improved performance.

The overall conclusion of Sec. III is that an enclosure is only appropriate for a no-stack device if it has a large ratio of end area to sidewall area. To keep a *resonant* device of this shape from being quite large would require a high operating frequency, with concomitantly small thermal penetration depth and gas displacement. These small acoustic length scales would require small heat exchanger dimensions, possibly limiting heat transfer rates. In Sec. IV we examine the use of a nonresonant enclosure that would allow a small no-stack refrigerator to operate efficiently using heat exchangers with roughly the same dimensions as in those used in SETAC, the reference stack-based device.

IV. ESTIMATION OF LOSSES: ALTERNATIVE GEOMETRY

One way to produce a short, wide aspect ratio in a small device is to use the configuration shown in Fig. 7(a)—a small, nonresonant enclosure of length L_{enc}, with the driver used more like the piston in a compressor than like a loudspeaker at the end of a resonator. The large reduction in enclosure surface area results in the high efficiency that we have been seeking, but requires a driver that can produce both high pressure and large volume velocity.

This alternative geometry can be modeled in the same way as the conventional geometry, with some modifications. The terms $\dot{W}_{\mathrm{inviscid}}$, $\dot{W}_{\mathrm{shear}}$, $\dot{W}_{\mathrm{minor}}$, $\dot{Q}_{\mathrm{inviscid}}$, and $\dot{Q}_{\mathrm{conduction}}$ are the same as in Eqs. (28), (29), (30), (27), and (33), except that each is reduced by a factor of 2 because now there is only one set of heat exchangers. The enclosure loss of Eq. (32) is replaced by

$$\dot{W}_{\mathrm{enclosure}} \simeq A_{\mathrm{fr}} \frac{\pi}{4} \frac{p_m a}{\gamma} \delta_k \left(\frac{P_A}{p_m}\right)^2 \frac{2(\gamma-1)}{(a/2f)} \left[1+\frac{L_{\mathrm{enc}}}{R}\right], \tag{36}$$

where L_{enc} is the length of the short, nonresonant enclosure. Equation (36) is the loss on the end caps (the ''1'' in square brackets) plus the thermal loss on the sidewalls (the L_{enc}/R term), with the assumption that $L_{\mathrm{enc}} \ll a/2f$. A small viscous term has been dropped from Eq. (36). If we pick the enclosure length so that $L_{\mathrm{enc}} = 2x_0$, then half the total enclosure area is on the cold side, so Eq. (34) is replaced by

$$\dot{Q}_{\mathrm{nuisance}} = \frac{\dot{W}_{\mathrm{enclosure}}}{2} + \frac{\dot{W}_{\mathrm{shear}} + \dot{W}_{\mathrm{minor}}}{4}. \tag{37}$$

Division by 4 is necessary for the exchanger term since there were four exchangers in the original model, but only one contributes to $\dot{Q}_{\mathrm{nuisance}}$ in this device.

TABLE III. Design parameters and model results for a no-stack device matching the gas properties and temperatures of the stack-base device listed in Table I but in a small, nonresonant enclosure of length $L_{\text{res}}=2x_0$.

No-stack parameters	Model results
$P_A/p_m=26.0\%$	$\dot{Q}_{\text{inviscid}}=1190$ W
$kx_{0n}=0.0358$	$\dot{Q}_{\text{conduction}}=10$ W
$y_0=54.2\ \mu$m	$\dot{Q}_{\text{nuisance}}=48$ W
$y_0/\delta_\kappa=0.630$	$\dot{W}_{\text{inviscid}}=186$ W
$\Omega=0.500$	$\dot{W}_{\text{shear}}=21$ W
$R=0.055$ m	$\dot{W}_{\text{minor}}=4$ W
$\Gamma_n=0.606$	$\dot{W}_{\text{enclosure}}=71$ W
	$\dot{W}_{\text{net}}=282$ W
	$\dot{Q}_{\text{net}}=1130$ W
	$\dot{Q}_{\text{net}}/A_{\text{fr}}=11.9$ W/cm^2
	$\eta_{\text{II}_{\text{net}}}=38.0\%$

With these modifications, optimization of $\eta_{\text{II}_{\text{net}}}$ results in the greatly improved characteristics shown in Table III. The driver needs to produce 282 W of acoustic power at 26% of mean pressure. The model predicts that this refrigerator has 3.85 times the chilling capacity of SETAC with only 1.7 times the input power. Since there is only one set of exchangers, this means that each exchanger would have to transport about eight times as much heat as a SETAC exchanger. The demands on the driver and heat exchangers are high, but not outrageous, as they were with the design that used a small-sized device of the conventional geometry.

The exchanger flow losses have been reduced in this model by pushing the exchangers close to the pressure antinode, as in Fig. 1. The midpoint between the exchangers is at $kx_{0n}=0.036$, about a fifth of the $kx_{0s}=0.2$ typical of the most efficient positioning of a stack. As might be expected, efficiency optimization has reduced kx_{0n} to the point that $\dot{Q}_{\text{conduction}}$ is roughly the same size as the exchanger flow losses. The largest loss is $\dot{W}_{\text{inviscid}}$, which causes doubt about the validity of the assumptions leading to the use of $x_{\text{hx}}=\frac{1}{2}(x_1+x_{\text{crit}})$ as the best exchanger spacing. However, freeing the spreadsheet solver to adjust x_{hx} as well as kx_{0n} and P_A/p_m when optimizing η_{II} boosts the efficiency from 38.0% to only 39.0%, with the best value of $(x_{\text{hx}}-x_{\text{crit}})/(x_1-x_{\text{crit}})$ being about 0.36 rather than 0.5. The required pressure amplitude, however, increases from 26% to almost 29%. If p_{1n}/p_m is held fixed at the lower value of 26%, the best $(x_{\text{hx}}-x_{\text{crit}})/(x_1-x_{\text{crit}})$ is 0.40 and $\eta_{\text{II}}=38.7\%$. Adjusting x_{hx} in this way reduces the power density by 9%.

By placing two of the systems in Fig. 7(a) back-to-back, it becomes possible to eliminate the shared wall, as in Fig. 7(b), further reducing enclosure surface area, and with the added benefit of built-in vibration cancellation. With this arrangement, the model predicts a second law efficiency of 42.6% at $p_{1n}/p_m=26\%$. This configuration, therefore, appears feasible.

V. TWO-STAGE NO-STACK

Before concluding this study, we wish to mention a design strategy that we had hoped would provide even higher efficiencies, but which proved disappointing. The 1984 patent of Wheatley *et al.* includes the idea of a segmented stack. This suggests a similar arrangement of several stages of no-stack devices in series. Indeed, the 1984 segmented stack superficially appears to be equivalent to serial no-stack segments. The 1984 patent makes it clear, however, that the discreet stack segments are still acting as *stack*, in that they are in imperfect thermal contact with the gas, and that the spacing between the stacks is noncritical. For serial no-stack operation, on the other hand, the intersegment spacing is critical but the degree of thermal contact within the segments is not.

It turns out that implementation of a series of no-stack segments always reduces the efficiency of our models. It may, nevertheless, be useful when the optimum pressure amplitude for a single stage is too high. For example, the model annular refrigerator described in Sec. III E is most efficient ($\eta_{\text{II}}=27.5\%$) when $p_{1n}/p_m=42.7\%$, which might be unrealistic. If the pressure amplitude is restricted arbitrarily to 25%, the efficiency drops to 17.2%. An alternative is to use two stages of no-stack refrigeration, each accomplishing half the total temperature lift. With T_{hx} cut in half, $p_{1\text{crit}}$ is also halved, allowing efficient operation near 20% pressure amplitude. The heat and the enclosure losses are both reduced by a factor of 4 (compared to a single stage at $p_{1n}/p_m=42.7\%$), so these parts of the model do not change the overall efficiency. The exchanger flow losses drop by a factor of 8, but these are small. The important cycle work $\dot{W}_{\text{inviscid}}$, however is reduced by only a factor of 2, since there are now two refrigeration stages. The combined result is a drop in overall efficiency, *compared to the operating point of* $p_{1n}/p_m=42.7\%$. In a situation where this amplitude was unattainable, however, it would make more sense to compare the two-stage arrangement to a single-stage operating at $p_{1n}/p_m=25\%$ with $\eta_{\text{II}}=17.2\%$. The two-stage system model is optimized at $p_{1n}/p_m=19.9\%$ with $\eta_{\text{II}}=17.6\%$, so the two-stage system is preferable in this circumstance, particularly since the power density is actually 65% *greater* in the two-stage model than in the single-stage device with suboptimal amplitude.

For the small, nonresonant design of Fig. 7, the two-stage option would be useful only if driver requirements of the single-stage design could not be met. In this case, the two-stage proach would operate at about $p_{1n}/p_m=12.2\%$ (as opposed to 26%), η_{II} would drop from 38% to 23%, and the power density would drop by a factor of 3.85, to that of SETAC. This is a substantial reduction in performance, but the efficiency remains higher than that of the reference stack-based device.

We conclude that using two no-stack stages may be worth considering when an initial design appears to require an excessively high amplitude, but is not, in general, a desirable approach. We have not identified any situations for which the use of more than two no-stack stages seems to be advantageous.

VI. CONCLUSIONS

This investigation shows that a standing-wave-based thermoacoustic device with no stack can have a very high

intrinsic inviscid efficiency, but has other problematic inefficiencies. Particularly severe are the losses that occur on the walls of the enclosure, which are not a major consideration in stack-based devices. Increasing the acoustic pressure amplitude from 3.6% to 26%, for example, increases these losses by a factor of 52. For traditional geometries, most of this loss is converted into a nuisance heat load. As a result, few geometries are viable. Our model predicts that a conventional arrangement, with small diameter heat-exchangers at the ends of a long resonator, is no more efficient than a stack-based design, even at very high amplitudes, and makes unrealistic demands on the heat exchangers, and, for that matter, on the theoretical model.

To produce an efficient no-stack device, the enclosure must have a large ratio of exchanger area to sidewall area. Resonant devices with this aspect ratio must either be large or must operate at high frequency. Short, nonresonant enclosures are a possible alternative. Our models of pressurized no-stack refrigerators in these configurations have second-law efficiencies of around 40%, rivaling regenerator-based thermoacoustic devices. Efficient no-stack refrigeration, therefore, appears to be workable.

Some of the practical lessons of this study are: that setting the heat exchanger spacing to $x_{hx}=\frac{1}{2}(x_1+x_{crit})$ is a useful initial design strategy for no-stack refrigerators; that efficiency optimization of the useful geometries results in the thermoacoustic components being placed considerably closer to the pressure antinode than in stack-based devices; and that using two no-stack stages may be useful in situations where the amplitude required for efficient operation of a single stage is unattainable, but should not be an initial design strategy.

ACKNOWLEDGMENTS

We wish to thank Stefan Turneaure for important discussions concerning no-stack prime movers, and Anthony Atchley for early discussions of thermoacoustics without a stack. This work is supported by the Office of Naval Research, with supplementary support from the Pennsylvania Space Grant Consortium.

[1] P. Kittel, "Ideal orifice pulse tube refrigerator performance," Cryogenics **32**, 843–844 (1992).
[2] G. W. Swift, D. L. Gardner, and S. Backhaus, "Acoustic recovery of lost power in pulse tube refrigerators," J. Acoust. Soc. Am. **105**, 711–724 (1999).
[3] S. Backhaus and G. W. Swift, "A thermoacoustic-Stirling heat engine: Detailed study," J. Acoust. Soc. Am. **107**, 3148–3166 (2000).
[4] J. Wheatley, T. Hofler, G. W. Swift, and A. Migliori, "An intrinsically irreversible thermoacoustic heat engine," J. Acoust. Soc. Am. **74**, 153–170 (1983). See Sec. V.
[5] W. A. Marrison, "Heat-controlled acoustic wave system," U.S. Patent No. 2,836,033 (27 May 1958).
[6] G. W. Swift, "Thermoacoustic engines," J. Acoust. Soc. Am. **84**, 1145–1180 (1988).
[7] J. C. Wheatley, G. W. Swift, and A. Migliori. "Intrinsically irreversible heat engine," U.S. Patent No. 4,489,553 (25 December 1984).
[8] J. C. Wheatley, "Intrinsically irreversible or natural heat engines," in *Frontiers in Physical Acoustics* (Soc. Italiana de Fisica, Bologna, Italy, 1986), pp. 395–475. Enrico Fermi Summer School: XCIII Corso.
[9] J. C. Wheatley, G. W. Swift, and A. Migliori, "The natural heat engine," Los Alamos Sci. **14**, 2–33 (1986); LAUR 86-2699.
[10] J. Wheatley, T. Hofler, G. W. Swift, and A. Migliori, "Understanding some simple phenomena in thermoacoustics with applications to acoustical heat engines," Am. J. Phys. **53**, 147–162 (1985); Eqs. (16) and (18).
[11] See Ref. 9. This explanation seems to have originated with Gifford and Longsworth. See W. E. Gifford and R. C. Longsworth, "Surface heat pumping," in *Advances in Cryogenic Engineering* (Plenum, New York, 1966), Vol. 11, Chap. C-7, pp. 171–179.
[12] See, for example, J. S. Hsieh, *Engineering Thermodynamics* (Prentice–Hall, Englewood Cliffs, NJ, 1993), pp. 291–292, or K. Wark, Jr., *Advanced Thermodynamics for Engineers* (McGraw–Hill, New York, 1995), Sec. 3-2-4. Hsieh uses the term "effectiveness" and the symbol ϵ for the second-law figure of merit.
[13] See Ref. 10, Eqs. (24) and (25).
[14] See Ref. 6, Eqs. (40) and (41).
[15] One member of our group, S. T., has found experimentally that no-stack prime-mover onset can occur for $|x_1|<|x_{hx}|$. We believe that this phenomenon involves a slightly nonuniform temperature gradient in the no-stack gap near the edges of the heat exchangers. The analysis requires accounting for differences in the instantaneous heat conducted between parcels, so that working parcels must be treated individually and simultaneously. The much simpler model considered in the present paper assumes a uniform temperature gradient in the gap and cannot account for this more subtle mechanism of onset in no-stack engines, on which we hope to report in the future.
[16] See Ref. 6, Eq. (24). Notice that Swift places $x=0$ at a pressure node rather than at an antinode.
[17] See Ref. 6, Eq. (29).
[18] The "inviscid efficiencies" for both stack and no-stack devices include only those thermal losses required to operate the thermodynamic cycles. They do not include thermal conduction down the temperature gradient or losses on the enclosure walls due to thermal relaxation.
[19] S. L. Garrett, "High-power thermoacoustic refrigerator," U.S. Patent No. 5,647,216 (15 July 1997). See Fig. 1.
[20] S. C. Ballister and D. J. McKelvey, "Shipboard electronics thermoacoustic cooler," Master's thesis, The Naval Postgraduate School, 1995, DTIC No. ADA 300 514.
[21] See Ref. 20, p. 62. The value 16.7% is an overall η_{II}, using the measured fluid temperatures, and therefore including temperature drops in the heat exchangers. Using a heat exchanger model, they inferred gas temperatures at the ends of the stack, from which they calculated an η_{II} of 25.7% for the stack alone.
[22] D. Gedeon, "Mean-parameter modeling of oscillating flow," J. Heat Transfer **108**, 513–518 (1986).
[23] J. R. Seume and T. W. Simon, "Flow oscillation effects in tubes and porous material: Unresolved issues," in *Fluid Flow and Heat Transfer in Reciprocating Machinery*, Proceedings, ASME Winter Annual Meeting, December 1987, edited by T. Morel, J. E. Dudenhoefer, T. Uzkan, and P. J. Singh (American Society of Mechanical Engineers, New York, 1987), FED-Vol. 62, HTD-Vol. 93, pp. 55–62.
[24] W. M. Kays and A. L. London, *Compact Heat Exchangers*, 3rd ed. (Krieger, Malibar, FL, 1998). Third edition copyright 1984. Originally published in 1955. See Eqs. (1)–(5).
[25] G. W. Swift and W. C. Ward, "Simple harmonic analysis of regenerators," J. Thermophys. Heat Transfer **10**, 652–662 (1996). See Sec. II A.
[26] G. W. Swift, "Thermoacoustic engines and refrigerators," in *Encyclopedia of Applied Physics* (Wiley-VCH, New York, 1997), Vol. 21, pp. 245–264. See Eq. (16). Our Eq. (29) neglects the second term of Swift's equation (16), which represents thermoacoustic losses within the heat exchanger, because our heat exchangers are assumed to be isothermal.
[27] I. E. Idelchik, *Handbook of Hydraulic Resistance*, 3rd ed. (Begell House, New York, 1996), pp. 222 and 518. Note the missing power of 0.75 in the version on p. 222. These expressions are very similar to the curves on p. 112 of Ref. 24.
[28] G. Swift, "Thermoacoustics: A unifying perspective for some engines and refrigerators," to be published by the Acoustical Society of America, 2002; until then, a draft is available online at http://www.lanl.gov/projects/thermoacoustics/Book/index.html.

The acoustic emission of a distributed mode loudspeaker near a porous layer

E. Yu. Prokofieva and Kirill V. Horoshenkov[a)]
Department of Civil and Environmental Engineering, University of Bradford, Bradford BD7 1DP, United Kingdom

N. Harris
New Transducers Limited, Cygnet House, Hinchingbrooke Business Park, Huntingdon PE29 6FW, United Kingdom

(Received 25 July 2001; accepted for publication 12 March 2002)

Experimental and theoretical modeling of the vibro-acoustic performance of a distributed mode loudspeaker (DML) suggest that their acoustic emission can be significantly affected by the presence of a porous layer. The amplitude of the surface velocity of the panel and the acoustic pressure on the porous surface are reduced largely in the vicinity of structural resonances due to the additional radiation damping and visco-thermal absorption phenomenon in the porous layer. The experimental results suggest that a porous layer between a rigid base and a DML panel can considerably alter its acoustic emission in the near field and in the far field. This is illustrated by a reduction in the level of fluctuations in the emitted acoustic pressure spectra. These fluctuations are normally associated with the interference between the sound emitted by the front surface of the speaker and that emitted from the back. Another contribution comes from the pronounced structural resonances in the surface velocity spectrum. The results of this work suggest that the acoustic boundary conditions near a DML can be modified by the porous layer so that a desired acoustic output can be attained. © *2002 Acoustical Society of America.* [DOI: 10.1121/1.1476687]

PACS numbers: 43.38.Ar, 43.40.Le [SLE]

I. INTRODUCTION

A distributed mode loudspeaker (DML) is an emerging alternative to more conventional cone speaker designs. Original DML panels have been developed by the New Transducers Limited (NXT Limited) in the form of a thin rectangular elastic plate.[1,2] The acoustic energy is emitted by the panel in a broad frequency range due to transverse vibration, which is excited at specific positions and diffracts complexly on the edges of the plate. The locations at which the periodical force is applied are carefully selected to ensure the maximum radiation conditions within the desired frequency range.

One of the most interesting aspects of the DML is its pseudo-diffuse acoustic emission which is a result of the relatively large area of the plate, which contributes to the emitted acoustic field. Diffuse radiation does not support the generation of standing waves in enclosed spaces and may have a positive psychological effect upon the listener.

Although general theoretical models to predict the radiation from vibrating DML panels into air have been available for many years (see, e.g., Ref. 3), there have been only recent studies on the radiation damping of a simply supported vibrating panel induced by porous media.[4–6] These works suggest that when a panel radiates into a porous layer, then the radiation damping is typically higher than that for radiation into air, which can have a significant effect on its acoustic emission. The theoretical and numerical results from two independent analyses are presented in Ref. 6. The first was a modal analysis of the problem where a finite-thickness porous layer is separated from plate by a finite air-gap. The second is a plate radiation model with an infinite baffle and with a semi-infinite absorbent layer. In both the theoretical models and in the experimental work the absorbent layer was assumed to behave as an equivalent fluid with a rigid frame for which the dynamic density, ρ_a, and the propagation constant, Γ_a, are routinely calculated. The results show that the damping in the plate is strongly dependent on the flow resistivity of the porous medium and on the width of the air space. This effect can be exploited to improve the design of DML speaker systems.

Some of the original results have already been discussed in Ref. 7. This work presents a more extended numerical and experimental investigation into the problem. The paper is organized in the following manner. In Sec. II we discuss the theoretical model by Cummings *et al.*,[6] which can be used to predict the surface velocity of the panel and the acoustic pressure on the porous layer. Section III presents some numerical results to illustrate the significance of the presence of the porous layer near the vibrating DML panel. In Sec. IV we discuss the experimental results which were obtained for the acoustic pressure emitted by the panel and its directivity pattern.

II. THEORY

An elegant formulation has been proposed by Cummings *et al.*[6] to predict the vibration velocity of a baffled DML panel which is loaded with an acoustical layer of finite dimensions. It is assumed that a typical DML panel is a thin,

[a)]Author to whom correspondence should be addressed.

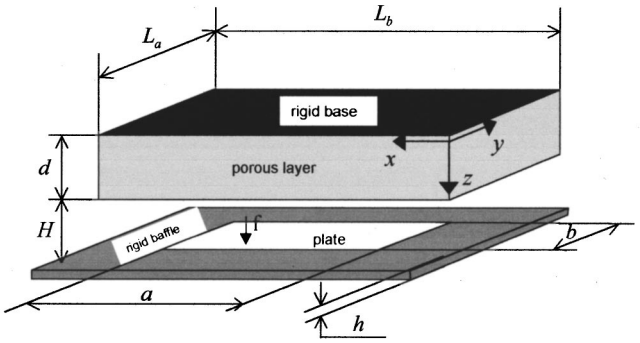

FIG. 1. Sound radiation by a vibrating plate into porous layer.

rectangular plate of relatively small mass, simply supported and driven by an oscillating point force f (see Fig. 1). The transverse vibration pattern which is generated in the panel is affected if the panel is radiating close to an acoustical layer.

To solve this problem three coupled acoustical elements are considered:[6] the plate, the air gap, and the absorbent layer. We shall look for a solution in the form of normalized mode decompositions of displacement and acoustic pressure.

The transverse displacement of a thin plate w can be determined from the equation of plate motion (e.g., Ref. 8, Chap. 8)

$$D\nabla^4 w+\rho\frac{\partial^2 w}{\partial t^2}=0, \tag{1}$$

where ρ is the mass density of the plate material, $D=Eh^3/12(1-\nu^2)$ is the plate stiffness, E is the Young modulus, h is the thickness of the plate, and ν is the Poisson ratio. The time dependence $e^{-i\omega t}$ is assumed and suppressed throughout.

A common method for the solution of (1) is to use the normal modal decomposition in which the transverse response of the plate may be expressed in terms of its mode shapes as

$$w=\sum_{i=1}^{n_s}\phi_{si}(x,y)q_{si}(\omega), \tag{2}$$

where q_{si} is the response of the ith structural mode. For a simply supported plate of the mass M_p in a rigid baffle the mass normalized mode shapes are given as

$$\phi_{si}=(2/\sqrt{M_p})\sin[(x+a/2-L_a/2)m_i\pi/a]\times\sin[(y+b/2-L_b/2)n_i\pi/b], \tag{3}$$

where m_i and n_i are the modal numbers for the ith structural mode.

The acoustic pressure on the surface of the porous layer can also be presented in terms of the mode shapes as

$$p_f(x,y,\omega)=\sum_{i=1}^{n_f}\phi_{fi}(x,y)q_{fi}(\omega), \tag{4}$$

where the normalized mode shapes are given by

$$\phi_{fi}=(2c/\sqrt{L_aL_bH})\sin(m_i\pi x/L_a)\sin(n_i\pi y/L_b) \tag{5}$$

and q_{fi} is the response of the layer to the ith mode, L_a and L_b are the lateral dimensions of the porous layer, H is the thickness of the air gap, and c is the sound speed in air.

TABLE I. Mechanical parameters of the DML panel and its dimensions.

Parameter	Value
Dimensions (m)	0.367×0.415
Thickness (m)	0.0065
Density (kg/m^3)	100.62
Young's modulus (N/m^2)	3.69×10^8
Poisson ratio	0.3

Utilizing the boundary conditions on the surface of the plate, using Eq. (1) and modal decomposition representations (2) and (4) the velocity of the plate and the pressure in the air gap can be determined from the system of two coupled matrix equations[6]

$$(-\omega^2\mathbf{I}+i\omega\mathbf{D}+\mathbf{U}_s^2)\mathbf{q}_s+\mathbf{S}^T\mathbf{q}_f=\mathbf{f},$$
$$\rho\omega^2\mathbf{S}\mathbf{q}_s+(-\omega^2\mathbf{I}+i\omega\mathbf{R}+\mathbf{U}_f^2)\mathbf{q}_f=0, \tag{6}$$

where $\mathbf{S}=\int_{(L_a-a)/2}^{(L_a+a)/2}\int_{(L_b-b)/2}^{(L_b+b)/2}\Phi_f^T\Phi_s\,dydx$ is the coupling matrix, $D_{ii}=2\zeta_i\omega_{si}$ is the diagonal structural damping matrix, $\mathbf{U}_{s_{ii}}^2=\omega_{si}^2$ is the diagonal stiffness matrix, and $\mathbf{f}=f\Phi_s^T(x_l,y_l)$ is the forcing vector. The fluid damping caused by the absorbing layer is given by

$$R_{ii}=\mathrm{Re}\left\{\frac{c^2\rho\lambda_{a_i}}{Hi\omega\rho_a}\left[\frac{\cos\lambda_{a_i}d+i(\rho\lambda_{a_i}/\rho_a\lambda_i)\sin\lambda_{a_i}d}{\sin\lambda_{a_i}d-i(\rho\lambda_{a_i}/\rho_a\lambda_i)\cos\lambda_{a_i}d}\right]\right\}, \tag{7}$$

where $\lambda_{ai}^2=(\omega/c_a)^2-(m_i\pi/L_a)^2-(n_i\pi/L_b)^2$, $\lambda_i^2=(\omega/c)^2-(m_i\pi/L_a)^2-(n_i\pi/L_b)^2$, c_a is the complex sound speed in the porous layer, and ρ_a is the dynamic density of the effective fluid.

Finally, the fluid stiffness is given by

$$\Omega_{fii}^2=\omega_{fi}^2-\frac{1}{\omega}\mathrm{Im}\left\{\frac{c^2\rho\lambda_{a_i}}{Hi\omega\rho_a}\left[\frac{\cos\lambda_{a_i}d+i(\rho\lambda_{a_i}/\rho_a\lambda_i)\sin\lambda_{a_i}d}{\sin\lambda_{a_i}d-i(\rho\lambda_{a_i}/\rho_a\lambda_i)\cos\lambda_{a_i}d}\right]\right\}. \tag{8}$$

Equations (6) can be solved directly for q_s and q_f. The displacement of the plate and the acoustic pressure in the air gap can then be calculated from Eqs. (2) and (4), respectively.

The choice of the simply supported boundary conditions is convenient, but not restrictive, because it is possible to obtain straightforward solution. Similar results can be obtained for other types of boundary conditions by adopting the appropriate mode shapes ϕ_{si} in normal model decomposition representations (2) and (4).

III. NUMERICAL RESULTS

Equations (6) were solved to calculate the surface velocity of a DML panel and the acoustic pressure spectra in the air gap between the panel and the porous layer. For this investigation a 6.5-mm-thick DML panel was adopted. The mechanical parameters and dimension of the panel provided in Table I. The dimensions of the panel were 415

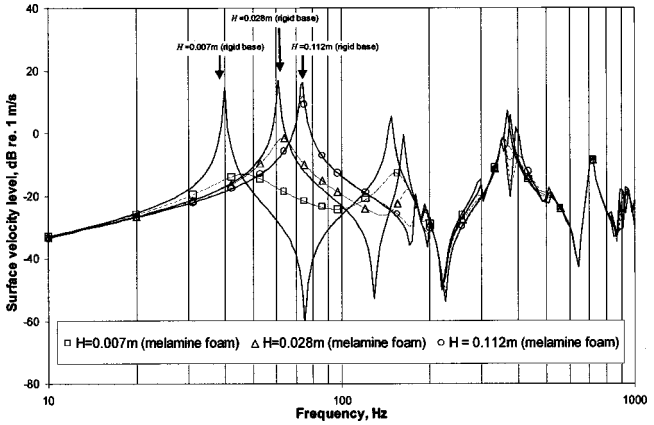

FIG. 2. Numerical modeling of the effect of a porous layer on the surface velocity of a vibrating DML panel.

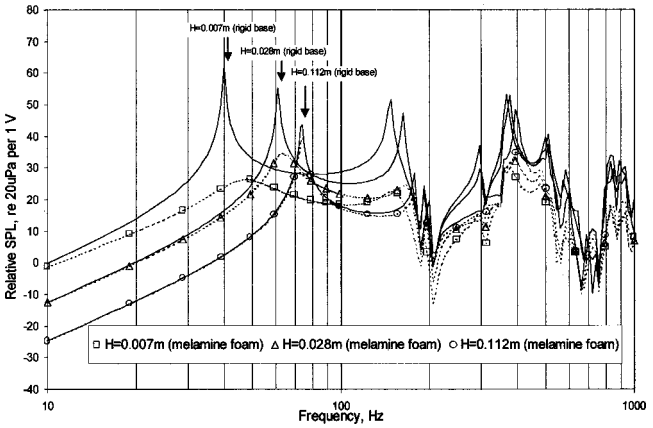

FIG. 3. Numerical modeling of the effect of a porous layer on the sound pressure level between the porous layer and a vibrating DML panel.

$\times 367\ \mathrm{mm}^2$ and it was assumed that the panel was simply supported and driven by a unit point force, which was applied simultaneously at two particular locations (0.155 mm, 0.185 m) and (0.205 m, 0.240 m). The porous layer was a 25-mm-thick melamine foam attached to a rigid base. The lateral dimensions of the porous layer were $500\times 500\ \mathrm{mm}^2$ and its flow resistivity was $R=9800\ \mathrm{Pa\cdot s\cdot m^{-2}}$. The lateral dimensions of the rigid base were $500\times 500\ \mathrm{mm}^2$ and it was assumed in the calculations that the flow resistivity of the rigid base is considerably high ($R=10^7\ \mathrm{Pa\cdot s\cdot m^{-2}}$). The air gap between the panel and the layer was set to $H=7$ mm.

The receiver position was at the center of panel. The acoustical properties of the porous layer were modeled using the Delany and Bazley empirical model[9] so that $c_a=\omega/k_a$ and

$$\rho_a=Z_a k_a/\omega.$$

This model provided the values for the complex dynamic density, sound speed, and acoustic attenuation in porous layer. In this way the effect of the reactive component of the surface acoustic impedance of the porous layer has been taken into account.

The predicted surface velocity spectra in the center of the panel are shown in Fig. 2 for three different widths of the air gap $H=0.007$, 0.028, and 0.112 m. When the panel radiates near a rigid base, in the absence of the porous layer, clear structural resonances are identified in the velocity spectrum. These resonances are associated with the structural modes of the simply supported, acoustically loaded plate. The position of first and second structural resonances appears to be affected strongly by the width of the air gap. As the width of the air gap reduces, the resonance frequency decreases as a result of the increased acoustical loading of the plate. For this particular configuration it can be shown that any further increase of the width of the air beyond the value $H=0.112$ m results in a very little change of the velocity spectrum. When the same panel is loaded with an acoustically porous layer the amplitude of the surface velocity near the first two structural resonance frequencies is suppressed and the level of the first antiresonance is significantly affected for $H=0.007$ m and $H=0.028$ m, resulting in more uniform velocity spectra (see Fig. 2). The damping in the panel around the resonance peaks increases as a result of the enhanced fluid–structure interaction between the vibrating panel and the porous layer. In the case of larger air gaps the effect of the porous layer is marginal. The results suggest that in the presence of the porous layer the resonance frequency shifts still occur, but when the width of the air gap is small the relative change is smaller than in the case of the rigid base (see Fig. 2). For example, the relative shift in the first resonance frequency between $H=0.112$ m and $H=0.028$ m is 46% when no porous layer is present. This value is 38% when a 25-mm layer of melamine foam is attached to the rigid base.

The sound pressure level spectra between the panel and the porous layer is shown in Fig. 3 for the adopted configurations and the parameters of the plate. In the case of $H=0.007$ m air gap there appears to be a considerable reduction of the sound pressure spectrum caused by the proximity of the porous layer, which acts effectively as an acoustic absorber and provides the medium to support the interfacial acoustic flow between parts of the planar radiator. The extra damping provided by the porous layer results in a more uniform sound pressure spectra, which is often a desirable effect in audio engineering applications. The acoustic absorption in the porous medium results in the 15–20-dB reduction of the sound pressure levels through the considered frequency range. As the width of the air gap increases, the effect of the porous layer becomes marginal and, in the case of the air gap $H=0.112$ m, the sound pressure spectrum follows closely that predicted in the case of the rigid base (see Fig. 3).

IV. EXPERIMENTAL DATA

A set of measurements was carried out to determine the radiation from DML panels with and without porous material. The spectral and directivity characteristics of the acoustic field emitted by a DML panel in the presence of a porous layer were investigated in the semi-anechoic chamber at the University of Bradford. The basic experimental setup is shown in Fig. 4. The DML panel used in the experiments was unbaffled. The mechanical parameters and dimensions of the panel were as listed in Table I. Measurements were conducted with and without a 25-mm layer of melamine foam, which was applied to the rigid base. The rigid base

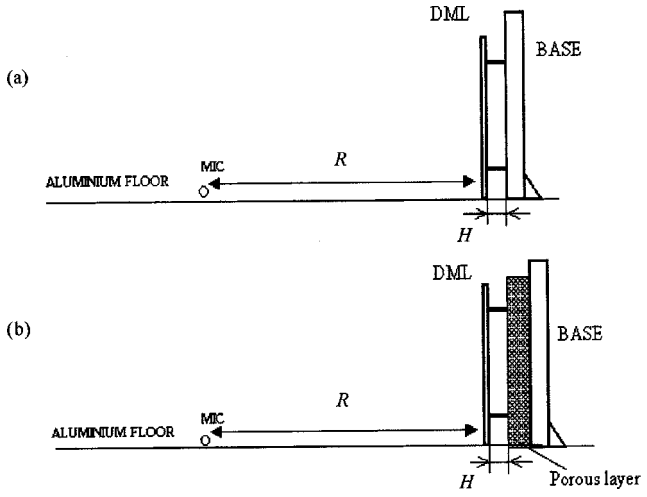

FIG. 4. Experimental setup.

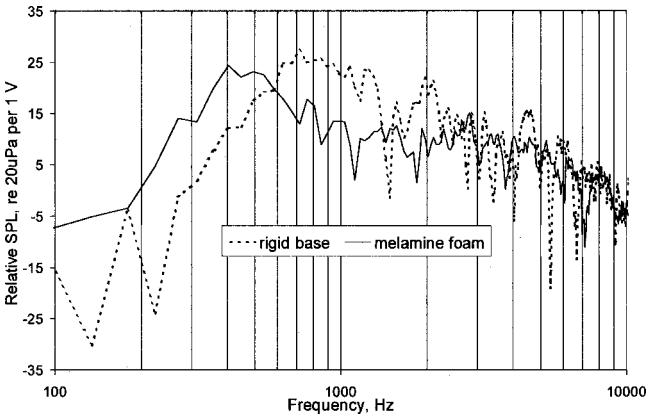

FIG. 6. The sound pressure level spectra measured at 2.0 from the DML panel and $H=0.025$ m.

was manufactured from 25-mm-thick, laminated MDF (medium density fiberboard) to ensure good acoustic reflection and low transmission characteristics. The lateral dimensions and the dimensions of the rigid base and porous material used in the experiments were $500\times500\ \mathrm{mm}^2$. It was assumed that a larger rigid barrier and a rigid barrier of the adopted dimensions would have very similar influence on the radiation from a DML panel provided that the air gap is small in comparison with the dimensions of the panel. In this case most of the acoustic interaction between the vibrating panel and the porous layer is taking place within the immediate area between the panel and the layer.

The flow resistivity of this foam was as given in Sec. III. The air gap H was kept constant in the experiments with and without the porous layer. The value of the air gap was set to 0.007 and 0.025 m during the experiments. Measurements were carried out at the distance $L=1.0$ and 2.0 m between the microphone and the DML as shown in Fig. 4. A maximum length sequences (MLS) data acquisition and signal processing system was used in the experiments. The detailed information about the adopted MLS system is presented in Ref. 10.

The dimensions of the chamber and the signal-to-noise ratio were sufficient to carry out the analysis of the acoustic output from the panel in the frequency range between 100 and 10 000 Hz. Because of certain limitations of the microphone position system it is difficult to conduct the measurements of the acoustic output from the panel placed on the floor. But the experiments showed that the $500\times500\ \mathrm{mm}^2$ base was working well and gave the suitable results. The comparison between sound pressure spectra from panel is shown in Fig. 4(a) and from the same panel placed on the floor of chamber together with the base is presented in Fig. 5.

The effect of the porous layer on the sound pressure level spectrum is shown in Figs. 6 and 7. The air gap in this case is 25 mm. The results suggest that, as expected, the introduction of a porous layer between the base and the panel considerably affects its acoustic emission. In the case of a 25-mm layer of melamine foam the major effects are the reduction of the level of the fluctuations in the acoustic pressure spectra and the considerable improvement of the low-frequency output between 100 and 600 Hz. It is anticipated that the fluctuations result from the interference between the sound emitted by the opposite faces of the vibrating panel. The porous layer affects the amplitude and phase of the sound wave, which is emitted from the back face of the panel, so that interference maxima and minima in the far-field acoustic spectra are not allowed to develop fully. The layer also controls the interference pattern in the air gap, so

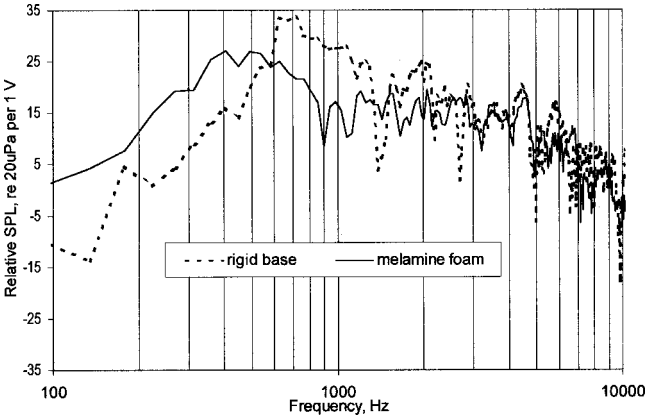

FIG. 5. The sound pressure level spectra measured at 1.0 m from the DML panel $H=0.025$ m.

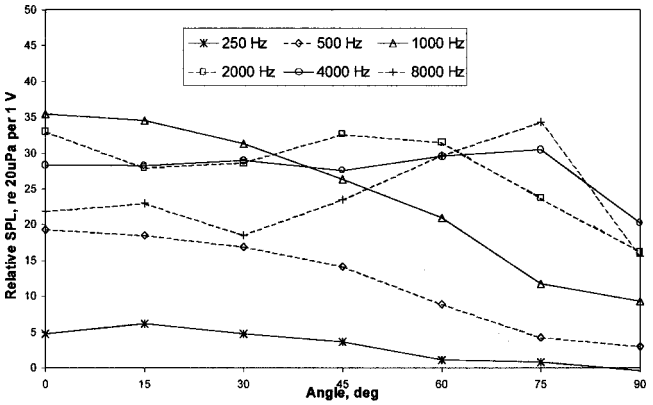

FIG. 7. The directivity pattern for the acoustic emission from a DML plate near a rigid base. $R=1.0$ m and $H=0.025$ m.

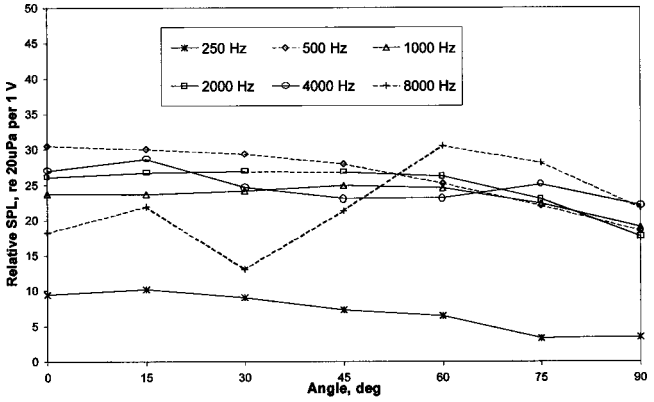

FIG. 8. The directivity pattern for the acoustic emission from a DML panel near a porous layer. $R=1.0$ m and $H=0.025$ m.

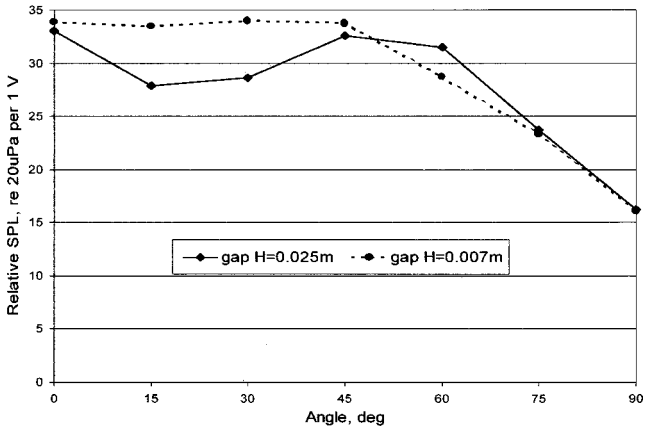

FIG. 10. The effect of the width air-gap on directivity pattern of the DML near the rigid base. $R=1.0$ m, frequency: 2000 Hz.

that some individual resonances which inevitably occur between the rigid base and the vibrating plate appear consistently suppressed (see Figs. 6 and 7). The introduction of a porous layer generally reduces the acoustic output in the medium- and high-frequency range, although at lower frequencies, below 500 Hz, the level of sound increases by up to 10 dB. This is a highly desirable effect which can be exploited in sound reproduction systems.

An experimental investigation was carried out to determine the effect of the absorbing layer on the horizontal directivity of the radiating DML panel. The sound pressure level spectra were measured at several horizontal angles between 0 and 90 degrees, which were measured from the normal to the panel at the distance of 1.0 m. A comparison was made between the results for the conditions described before, with and without the porous layer. The results of the comparison are shown in Figs. 8 and 9 where the octave band sound pressure levels are plotted against the horizontal angle. Figure 8 shows the sound pressure levels for the panel near the rigid base case and Fig. 9 shows the levels of pressure for the panel near a 25-mm layer of foam and 25 mm of the air gap. The data shown in these graphs suggest that the presence of a porous layer generally results in a more uniform directivity pattern of the acoustic emission from a vibrating DML panel. In this process the level of fluctuations in the directivity pattern is reduced by approximately 10–15 dB.

In the low-frequency range (250 Hz) the levels of sound seem to increase by 5–6 dB if the panel is loaded with an acoustically porous layer (Fig. 9). The increase is observed for all angles considered. This may be attributed to the elimination of the ''acoustic shortcut'' effect between the sound emitted by the opposite faces in the case of the porous layer. Figure 9 suggests that the proximity of the porous layer had a little effect on the acoustic emission in the higher frequency range (8000 Hz). This can be explained by the relatively low coherence between the acoustic emission from different areas of the panel and the reduced acoustic coupling between the layer and the panel. There also appears to be a considerable roll-off in the levels of sound at 500 and 1000 Hz (see Fig. 8) as the angle of incidence increases in the case of the panel being near the rigid base. This phenomenon is not observed if the panel is loaded with an acoustically porous layer, and it can be associated with the destructive interference effects between acoustic waves emitted by the opposite faces of the vibrating panel. This phenomenon needs further investigation.

The effect of the width of the air gap on the sound pressure levels at different angles of incidence is shown in Figs. 10 and 11. There is a pronounced directivity pattern in the case when no porous material is attached to the rigid base. This is likely to result from the interference between

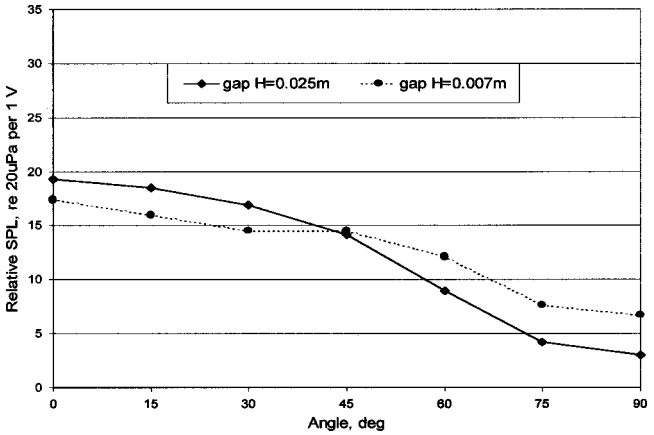

FIG. 9. The effect of the width air-gap on directivity pattern of the DML near the rigid base. $R=1.0$ m, frequency: 500 Hz.

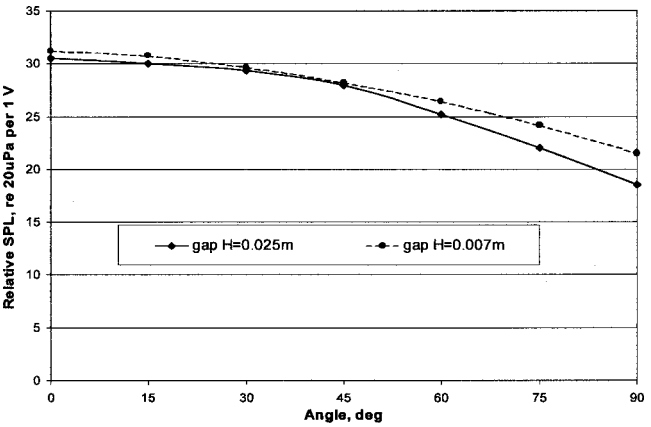

FIG. 11. The effect of the width air-gap on directivity pattern of the DML near a porous layer. $R=1.0$ m, frequency: 500 Hz.

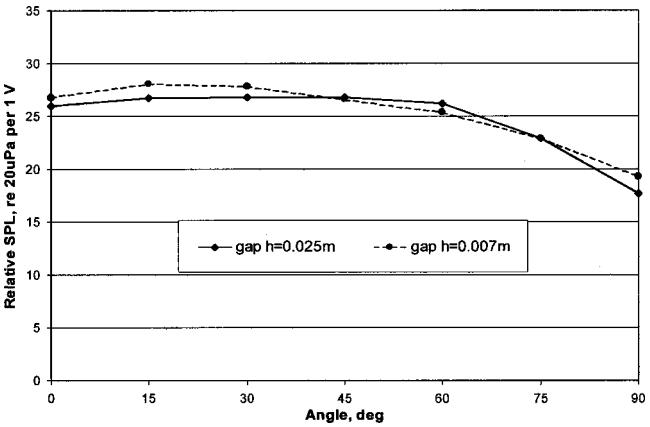

FIG. 12. The effect of the width air-gap on directivity pattern of the DML near a porous layer. $R=1.0$ m, frequency: 2000 Hz.

the sound emitted from the front and from the back surfaces of the plate. At 500 Hz the smaller air gap results in smaller fluctuation of the levels as a function of the angle (see Fig. 10).

At 2000 Hz the directivity pattern is relatively flat in the range of angles from 0 to 45 degrees when the width of the air gap is 0.007 m. When the width of the air gap is 0.025 m the sound pressure level fluctuates within 5-dB range for angles between 0 and 45 degrees. The sound pressure level is reduced considerably by 15–17 dB for greater angles (see Fig. 11).

The application of porous material on a rigid base results in a more stable output throughout the frequency range and in different directions of sound propagation (see Fig. 12). There is some reduction of the sound pressure level as the angle of incidence increases, although it is limited in comparison with the rigid base case (from 500 to 4000 Hz). The effect of the width of the air gap on SPL is small in the case when the porous layer is present.

V. CONCLUSIONS

The purpose of this work was to carry out a theoretical and experimental investigation to determine the effect of an acoustically porous layer on the surface velocity and the acoustic emission of a DML panel. It has been shown that when the panel radiates near an acoustically porous layer the amplitude of the resonance peaks in the surface velocity spectrum is reduced and the spectrum appears to be more uniform. This effect is associated with additional damping induced by the porous layer and the acoustic flow through the porous medium.[6] It has been shown that the level of the sound pressure spectrum between the panel and the porous layer is reduced and appears more uniform near the frequencies of the structural resonance. In this way the interference between the acoustic output from the opposite faces of the panel is reduced and the emitted acoustic pressure spectrum measured in near and far fields can prove to be more uniform.

The experimental work shows that the porous layer has a pronounced effect on the levels of sound emitted by the DML panel. The major effect is the increased acoustic output in the frequency range of 100–600 Hz and the general reduction of the level of the fluctuations in the acoustic pressure spectra. There is some reduction of the acoustic output in the medium and higher frequency ranges, which is compensated by an almost 10-dB increase in the sound pressure level in the low-frequency range and by a more homogeneous sound pressure level spectrum across the considered frequency range. The experimental data also suggest that the presence of a porous layer generally results in a more uniform directivity pattern of the acoustic emission from a vibrating DML panel. There also appears to be a considerable roll-off in the level of sound at the medium and higher frequencies, which requires further investigation.

The influence of air gap width was investigated. In the case of rigid base at the low frequencies the acoustic output is increased if the width of the air gap between rigid base and vibrating panel is increased. In the medium range of frequencies the sound pressure level is reduced when the air gap is increased. If the porous layer is attached, the decreasing of the width of the air gap has a small effect on the acoustic output of the panel.

ACKNOWLEDGMENTS

This work has been supported jointly by NXT Limited and by the University of Bradford. The authors would like to express their thanks to Henry Azima of NXT Limited for his support of this work. The authors are also grateful to Professor David Hothersall for his constructive comments on this manuscript.

[1] V. P. Gontcharov, N. P. R. Hill, and V. J. Taylor, ''Measurement aspects of distributed mode loudspeakers,'' in Proceedings of the 106th Convention of the Audio Engineering Society (1999).
[2] H. Azima and J. Panzer, ''Distributed mode loudspeakers (DML) in small enclosures,'' in Proceedings of the 106th Convention of the Audio Engineering Society (1999).
[3] F. G. Leppington, E. G. Broadbent, and K. H. Heron, ''The acoustic radiation efficiency of rectangular panels,'' Proc. R. Soc. London, Ser. A **382**, 245–271 (1982).
[4] R. J. M. Craik, D. Tomlinson, and R. Wilson, ''Radiation into porous medium,'' Proc. Inst. Acoust. **22**, Part 2, 383–388 (2000).
[5] C. K. Amedin, A. Berry, Y. Champoux, and J-F. Allard, ''Sound field of a baffled piston source covered by porous medium layer,'' J. Acoust. Soc. Am. **98**, 1757–1766 (1995).
[6] A. Cummings, H. J. Rice, and R. Wilson, ''Radiation damping in plates, induced by porous media,'' J. Sound Vib. **221**, 143–167 (1999).
[7] E. Prokofieva, K. V. Horoshenkov, and N. Harris, ''The effect of porous materials on the acoustic response of DML panel,'' in CD-ROM Proceedings of the 110th Convention of the Audio Engineering Society, Amsterdam, May 2001.
[8] M. C. Junger and D. Feit, *Sound, Structures and their Interaction* (Acoustical Society of America and American Institute of Physics, Woodbury, NY, 1993).
[9] M. E. Delany and E. N. Bazley, ''Acoustical properties of fibrous absorbent materials,'' Appl. Acoust. **3**, 105–116 (1970).
[10] http://www.winmls.com

Generalization of a model of hysteresis for dynamical systems[a)]

Jean C. Piquette[b)] and Elizabeth A. McLaughlin
Naval Undersea Warfare Center, Division Newport, 1176 Howell Street, Newport, Rhode Island 02841

Wei Ren and Binu K. Mukherjee
Department of Physics, Royal Military College of Canada, Kingston, Ontario K7K 7B4, Canada

(Received 24 September 2001; revised 15 March 2002; accepted 4 April 2002)

A previously described model of hysteresis [J. C. Piquette and S. E. Forsythe, J. Acoust. Soc. Am. **106**, 3317–3327 (1999); **106**, 3328–3334 (1999)] is generalized to apply to a dynamical system. The original model produces theoretical hysteresis loops that agree well with laboratory measurements acquired under quasi-static conditions. The loops are produced using three-dimensional rotation matrices. An iterative procedure, which allows the model to be applied to a dynamical system, is introduced here. It is shown that, unlike the quasi-static case, self-crossing of the loops is a realistic possibility when inertia and viscous friction are taken into account. [DOI: 10.1121/1.1481061]

PACS numbers: 43.38.Ar, 43.20.Px, 43.30.Yj [SLE]

I. INTRODUCTION

A model of hysteresis is described in Refs. 1 and 2. That model accommodates hysteresis by first introducing a data transformation that collapses the hysteresis loops into one-dimensional curves. Since this transformation effectively eliminates hysteresis, an anhysteretic model[3] can be least squares fitted to the result. While this model of hysteresis has been well verified by application to laboratory data, the use of three-dimensional rotation matrices, which the model incorporates, makes it unclear how it might be applied to a dynamical system, such as a transducer. A generalization of the model that makes such application straightforward is described here. [Readers unfamiliar with other work done in hysteresis modeling may wish to consult Refs. 4–7, and references within. Those who would like to see a study of the transducer properties of lead magnesium niobate (PMN), the material of primary applications interest here, may wish to consult Ref. 8.]

In Sec. II an iterative procedure is described for effecting the model generalization. By replacing the stress term of the original model[3] with suitable dynamic (and static) terms, an ordinary differential equation, solvable by the usual methods, is produced. The iterative process renders the solutions of the differential equation consistent with the rotations of the original model of hysteresis.[1,2] A specific numerical example of the process is given in Sec. III. It is shown here that, unlike the quasi-static case, self-crossing of the loops is a realistic possibility when inertia and viscous friction are taken into account. A summary and the conclusion are given in Sec. IV.

II. THEORY MODIFICATIONS FOR DYNAMIC EFFECTS

We first consider what must be done to render the model of Refs. 1 and 2 applicable to a dynamic system. It is emphasized at the outset that, while the drive frequency is introduced here as a specific parameter that must be taken into account, any explicit frequency dependence of the model parameters is ignored. That is, the effects of frequency are accounted for only through their influences upon the inertia and viscous loss mechanisms contained in the system. If other parameters, such as the permittivity, are frequency dependent, it is assumed that the values of these parameters are evaluated at the frequency of interest. That is, no specific model of the variation of these parameters with frequency is advanced here.

The dynamic system of interest is shown in Fig. 1. Here, a PMN rod of length L_0, operating in the length-expander mode, drives a mass M. It is assumed that the mass of the driver is insignificant compared with that of the driven mass. The driven mass is also subject to a viscous frictional force, associated with which is the viscous coefficient b. It is also assumed that the driver is subjected to a constant stress T_0, such as might be supplied by a prestress bolt in a transducer.

It is first necessary to apply the model of Refs. 1 and 2 (in its original form) to quasi-static laboratory polarization and strain data acquired from the active material (herein assumed to be PMN). A data transformation that collapses the hysteresis loops from the measured data into one-dimensional curves, through the use of three-dimensional rotation matrices, was introduced in Refs. 1 and 2. Quasi-static laboratory data are thus still required for implementation of the present dynamical version of the theory, in order that the required rotation angles can be ascertained. An *anhysteretic* theory[3] is then applied to the resulting one-dimensional curves to determine the required model parameters via least squares fitting. The *inverse* rotations are applied to the anhysteretic theory to yield a *theoretical* hysteretic (but still quasi-static) polarization loop. The interested reader is directed to Refs. 1 and 2 for more details of the original theory of hysteresis.

The *strain* equation of the original anhysteretic model,[3] viz.,

[a)]A preliminary version of this work was reported at the 2001 ONR Workshop on Transducers and Transduction Materials, Baltimore, MD, May 2001.

[b)]Electronic mail: piquettejc@npt.nuwc.navy.mil

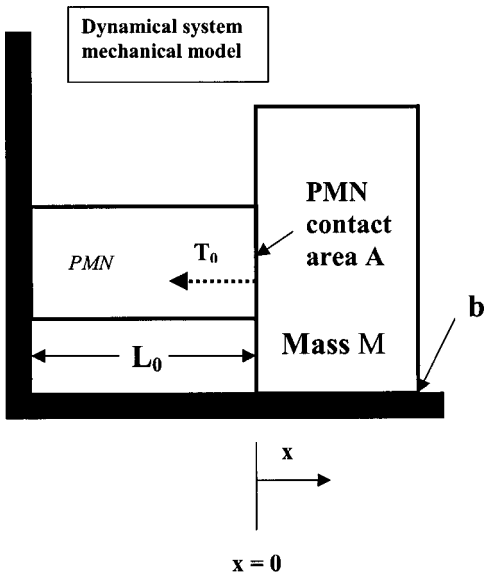

FIG. 1. Dynamical system to which the theory of Refs. 1 and 2 is herein generalized to apply. PMN—lead magnesium niobate driver. L_0—unstressed length of driver. T_0—constant prestress. A—face area of driver. M—driven mass (assumed much larger than driver mass). b—coefficient of viscous friction. x—position coordinate.

$$S_3 = s_{33}^D T_3 + Q_{33} D_3^2, \tag{1}$$

first is transformed into a differential equation by replacing the external stress T_3 with suitable dynamic and static terms (cf. Fig. 1). This gives

$$\frac{x}{L_0} = -\frac{s_{33}^D M \ddot{x}}{A} - \frac{s_{33}^D b \dot{x}}{A} + s_{33}^D T_0 + Q_{33} D_3^2. \tag{2}$$

[Equation (2) is derived by separately isolating the PMN rod and the mass M driven by it, and applying standard methods of dynamics, using Eq. (1) to describe the dynamics of PMN. In this way the stress term T_3 of Eq. (1) is evaluated as the reaction supplied by the external mass, including the assumed constant stress T_0. In Eqs. (1) and (2) we have replaced the notations β_1 and β_2 originally used in Ref. 3 with the more commonly used notations s_{33}^D and Q_{33}, respectively.] In Eqs. (1) and (2), Q_{33} is the electrostriction constant, b is the coefficient of viscous friction (which acts on the driven mass), L_0 is the original length of the active material, A is the end-face area of the active material, s_{33}^D is the elastic compliance at constant D, S_3 is the strain, and T_3 is the stress. (T_0 in Fig. 1 is a constant stress, such as a prestress. It is only a portion of the total external stress T_3 ''seen'' by the active material, owing to the dynamic effects of the reaction force arising from the contact between the active material and the driven mass M.) Over-dots denote time derivatives. Each time Eq. (2) is solved for $x(t)$, the (current) hysteretic version of D_3 is substituted, and thus acts as a source (or driving) term in this differential equation. The *initial* version of the hysteretic D_3 source function required in Eq. (2) to start the iterative procedure is obtained by carrying out the theoretical solution for D_3 as detailed in Refs. 1 and 2, applied to the quasi-static laboratory data, replacing the external stress T_3 with the constant value T_0 (i.e., inertial effects are initially ignored). That is, the initial form of the D_3 source function simply results from applying the original theory of Refs. 1 and 2 to the quasi-static laboratory polarization and strain data acquired from the active material.

TABLE I. Parameter values used in an example calculation for the system of Fig. 1.

$M = 2$ kg $\quad L_0 = 0.0625$ m $\quad A = 5\times10^{-3}$ m^2 $\quad b = 1.0\times10^4$ N·s/m
$T_0 = -4.13\times10^7$ N/m^2 $\quad s_{33}^D = 8.7\times10^{-12}$ m^2/N
$E_{\text{drive}} = E_{\text{bias}} = 6.7\times10^5$ V/m
$\nu_{\text{res}} = \frac{1}{2\pi}\sqrt{\frac{A}{s_{33}^D L_0 M}} \Rightarrow \nu_{\text{res}} = 10\,800$ Hz

The *dynamic* solution for the system of Fig. 1 is then computed by the following procedure:

(1) Substitute the current *hysteretic* D_3 (initially quasi-static) into Eq. (2), and solve for $x(t)$.

(2) Use Eq. (1) to determine the new ''current'' stress T_3, evaluating the required strain S_3 using the solution of Eq. (2), together with the ''current'' (hysteretic) D_3.

(3) A new (approximately) anhysteretic strain versus electric field hysteresis loop is now computed by applying the *original* rotation matrices (as originally derived from the quasi-static laboratory data) to the *new* strain versus E-field loop obtained from combining the solution of Eq. (2) with the given E. A corresponding approximately anhysteretic D vs E hysteresis loop is computed by applying the rotation matrices to the current hysteretic D_3.

(4) Solve the E-field equation from the original anhysteretic model,[3] viz.,

$$E_3 = \frac{D_3 - P_0}{\sqrt{(\varepsilon_0 \varepsilon_{33}^T)^2 - a(D_3 - P_0)^2}} - 2Q_{33} T_3 D_3, \tag{3}$$

for a *new* (approximately) anhysteretic D_3. Here the approximately anhysteretic value of dynamic stress T_3, as determined by substituting the approximately anhysteretic S_3 and D_3 from step 3 into Eq. (1), is used.

(5) Apply the *inverse* rotations of Refs. 1 and 2 to the current (approximately anhysteretic) D_3 to produce a *new* hysteretic D_3.

Steps 1–5 are then iterated until the solution does not change. This typically requires three iterations.

III. EXAMPLE

As a specific example, consider the parameter values shown in Table I. The results of applying the iterative process using these numerical values are shown in Figs. 2–4. (In these figures, the term ''polarization'' is used to denote the D-field within the sample. Owing to the very large permittivity of PMN, the polarization and D-field are essentially equivalent. The term ''strain'' refers to the relative change in length of the PMN rod, compared with its initial length.) The original quasi-static data required for initializing the iterative procedure are also shown for reference in each of these figures, so that the changes caused by the system dynamics may be more easily seen. (It is worthwhile noting that the theory described here closely matches the shown quasi-static data if

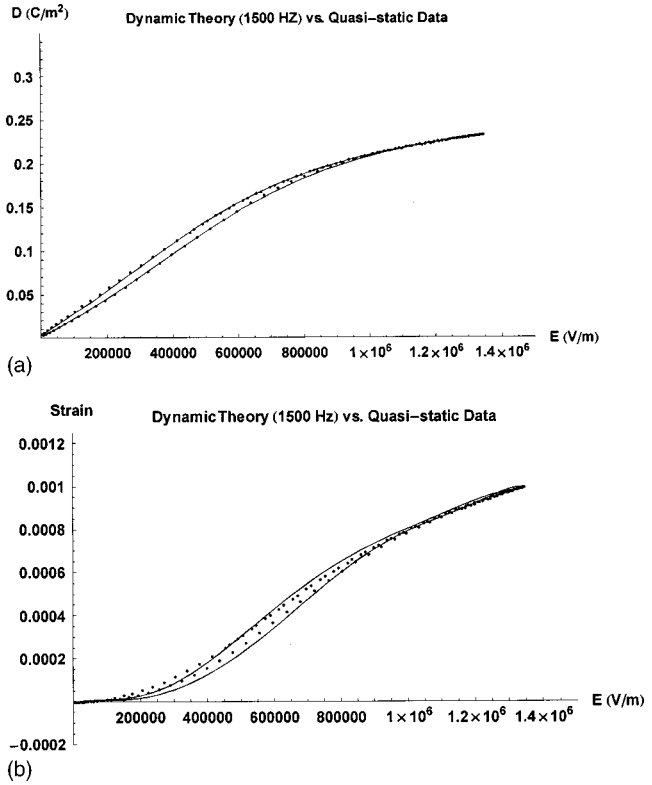

FIG. 2. Computed response of the system of Fig. 1 when driven at a frequency of 1500 Hz (solid lines). Quasi-static data (dots) are shown for reference. (a) Polarization. (b) Strain.

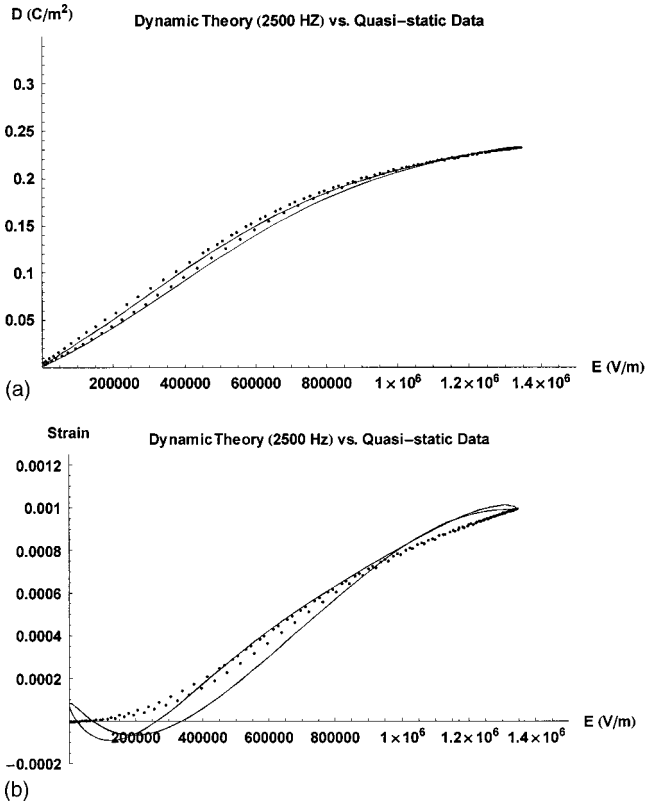

FIG. 3. Computed response of the system of Fig. 1 when driven at a frequency of 2500 Hz (solid lines). Quasi-static data (dots) are shown for reference. (a) Polarization. (b) Strain.

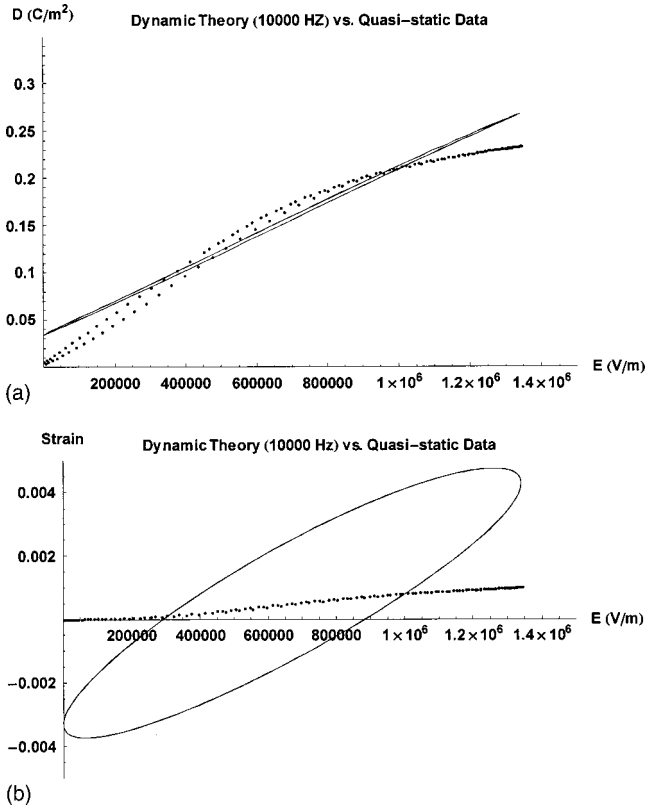

FIG. 4. Computed response of the system of Fig. 1 when driven at a frequency of 10 000 Hz (solid lines). Quasi-static data (dots) are shown for reference. (a) Polarization. (b) Strain.

the drive frequency is sufficiently low that inertia and viscous friction become negligible.)

At the 1500-Hz frequency considered in Figs. 2(a) and (b), the effects of inertia are just starting to become visible, as can be seen from the slight departure of the solid-line curves from the dots. As can be seen in Fig. 3(b), where the drive frequency is now 2500 Hz, self-crossing of the hysteresis loop is a realistic possibility in a dynamic system, whereas this should never occur in a quasi-static system.[9] The self-crossing seen here arises from the interaction of hysteresis with the effects of both viscous friction and inertia.

Finally, in Figs. 4(a) and (b) is shown the system response as resonance (10 800 Hz) is approached. The drive considered here is 10 000 Hz, or just slightly below resonance. At this point, the effects of viscous friction overwhelm the effects of hysteresis, and the elliptical shape of the loop seen in Fig. 4(b) is almost entirely due to viscous friction. The influence of the inertial effects are also significant, as is reflected by the modified polarization response seen in Fig. 4(a).

IV. SUMMARY, DISCUSSION, AND CONCLUSION

A theory of hysteresis[1,2] has been generalized to apply to a dynamical system by introducing an iterative procedure. A standard kind of ordinary differential equation is also introduced. (The driving source term in this equation incorporates

the effects of hysteresis into the solution.) It was shown that self-crossing of a hysteresis loop is a realistic possibility in a dynamic system.

It should be understood that the presence of hysteresis in a transducer drive material is very undesirable, especially from the point of view of ''wasted'' energy that must be supplied to the material by the power amplifier. Significant also is the undesirable generation of output harmonics owing to hysteresis. However, by suitable preforming the driving voltage waveform,[10] it is possible to linearize the output response.

ACKNOWLEDGMENTS

This work was supported by the In-House Laboratory Independent Research Program (ILIR) of the Naval Undersea Warfare Center, Division Newport, and by the Office of Naval Research, Code 321.

[1] J. C. Piquette and S. E. Forsythe, ''One-dimensional phenomenological model of hysteresis I. Development of theory,'' J. Acoust. Soc. Am. **106**, 3317–3327 (1999).
[2] J. C. Piquette and S. E. Forsythe, ''One-dimensional phenomenological model of hysteresis II. Applications,'' J. Acoust. Soc. Am. **106**, 3328–3334 (1999).
[3] J. C. Piquette and S. E. Forsythe, ''A nonlinear material model for lead magnesium niobate (PMN),'' J. Acoust. Soc. Am. **101**, 289–296 (1997).
[4] R. C. Smith and C. L. Hom, ''Domain wall theory for ferroelectric hysteresis,'' J. Intell. Mater. Syst. Struct. **10**, 195–213 (1999).
[5] A. N. Soukhojak and Y-M. Chiang, ''Generalized rheology of active materials,'' J. Appl. Phys. **88**, 6902–6909 (2000).
[6] K. Mayergoyz, *Mathematical Models of Hysteresis* (Springer-Verlag, New York, 1991).
[7] D. C. Jiles and D. L. Atherton, ''Theory of ferromagnetic hysteresis,'' J. Magn. Magn. Mater. **61**, 48–60 (1986).
[8] K. M. Rittenmeyer, ''Electrostrictive ceramics for underwater transducer applications,'' J. Acoust. Soc. Am. **95**, 849–856 (1994).
[9] B. Jaffe, W. R. Cook, and H. Jaffe, *Piezoelectric Ceramics* (Academic, New York, 1971), p. 40.
[10] J. C. Piquette, E. A. Mclaughlin, G. Yang, and B. K. Mukherjee, ''Nonlinear output control in hysteretic, saturating materials,'' J. Acoust. Soc. Am. **110**, 865–876 (2001).

An approximated 3-D model of the Langevin transducer and its experimental validation

Antonio Iula,[a] Riccardo Carotenuto, and Massimo Pappalardo
Dipartimento di Ingegneria Elettronica, Università Roma Tre, Via della Vasca Navale, 84, 00146 Roma, Italy

Nicola Lamberti
Dipartimento d'Ingegneria dell'Informazione ed Ingegneria Elettrica, Università di Salerno, Via Ponte Don Melillo, 84084 Fisciano (SA), Italy

(Received 4 September 2001; accepted for publication 16 March 2002)

In this work, an approximated 3-D analytical model of the Langevin transducer is proposed. The model, improving the classical 1-D approach describing the thickness extensional mode, allows us to predict also the radial modes of both the piezoelectric ceramic disk and the loading masses; furthermore, it is able to describe the coupling between radial and thickness extensional modes. In order to validate the model, the computed frequency spectrum is compared with that obtained by measurements carried out on 13 manufactured samples of different thicknesses to diameter ratios. The comparison shows that the model predicts with quite good accuracy the resonance frequencies of the two lowest frequency modes, i.e., those of practical interest, all over the explored range. Finally, the coupling effect between thickness and radial modes on the frontal displacement is measured and discussed. © *2002 Acoustical Society of America.* [DOI: 10.1121/1.1476684]

PACS numbers: 43.38.Fx [SLE]

I. INTRODUCTION

The Langevin transducer basically consists of a piezoelectric ceramic disk sandwiched between two cylinder-shaped loading masses. This structure is usually prestressed by inserting a bolt along its principal axis in order to increase the mechanical strength of the piezoelectric ceramic.

This kind of composite transducer is widely used in underwater sonar and communication systems[1–5] as well as in a large variety of industrial applications[6,7] due to its ability to vibrate in thickness-extensional mode at low frequency, avoiding the need for high driving voltages.

The Langevin structure can be analyzed with the classical one-dimensional theory;[8–10] however, this approach is able to describe only the thickness-extensional modes and therefore does not take into account the unavoidable lateral vibrations of both the piezoelectric ceramic and the loading masses.

The predictions of the lateral vibrations of the Langevin transducer is indeed very useful both in power and in broadband applications; in fact, in the first case any possible lateral coupling, which polarizes the motion in some direction other than axial, must be avoided, while in the second a bandwidth enlargement can be achieved by exploiting the coupling between thickness-extensional and lateral modes.[11–13]

The 3-D analysis of the Langvein transducer can be performed by using finite element methods (FEM). This approach is very powerful and is widely used in transducers' analysis of any geometry.[11–15] However, with respect to analytical modeling, it gives less physical insight and it is more time consuming.

Analytical multi-dimensional modeling of piezoelectric ceramic structures is rather complex, due to the unsolvable differential coupled equations' system which describes the element vibration. Nevertheless, some attempts in this direction have been made.[16–19] In particular, some of the authors proposed an approximated 3-D matrix model of cylinder-shaped piezoelectric ceramics which takes into account the coupling between thickness and radial modes and which is also able to describe the interactions with the external media.[20]

In the present work, this 3-D approximated approach is extended to the classical Langevin configuration, and the improvements with respect to the 1-D model are shown. The proposed model is experimentally validated by comparing the computed frequency spectrum with that obtained by measurements carried out on 13 manufactured prototypes of different aspect ratios. Finally, measurements of the frontal displacement, carried out by means of an interferometric technique at the main resonance frequencies, are shown in order to highlight the effect of the coupling between radial and thickness modes.

II. THE MATRIX MODEL

Figure 1 shows the classical Langevin transducer configuration; it is composed of a piezoelectric ceramic disk with radius a and thickness $2 \cdot b$, poled along the thickness direction and electroded on its flat surface. The ceramic disk is sandwiched between two cylinder-shaped loading masses having the same radius and thicknesses of $2 \cdot b_1$ and $2 \cdot b_2$, respectively. When an alternating voltage V is applied to the electrodes of the piezoelectric ceramic element, all the modes of the structure can be excited, depending on the frequency of the driving signal.

A 3-D analytical model of cylinder-shaped piezoelectric

[a]Electronic mail: iula@uniroma3.it

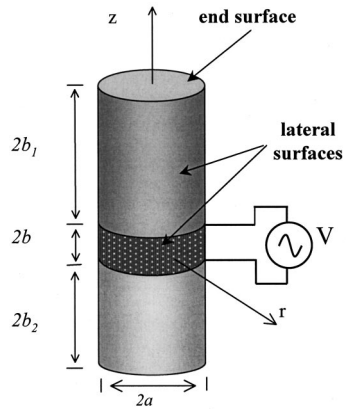

FIG. 1. Schematic view of the classical Langevin transducer.

ceramics[20] was recently proposed by some of the authors. It was derived by assuming that the coordinate axes are pure mode propagation directions (i.e., the mechanical displacements u_r and u_z depend only on r and z, respectively) and by imposing both electrical and mechanical boundary conditions in an integral way. By means of this model, the piezoelectric ceramic element has been described as a four-port system with three mechanical ports (one for each surface) and one electric port. The linear equations which relate the electrical variables (current I and voltage V) to the mechanical variables (forces F_i and velocities v_i, $i=1,...,3$) in the frequency domain are

$$F_1=\frac{Z_1}{j}\left[\left(\frac{k_1aJ_0(k_1a)-J_1(k_1a)}{k_1aJ_1(k_1a)}\right)+\frac{c_{12}^D}{k_1ac_{11}^D}\right]v_1 + \frac{2\pi ac_{13}^D}{j\omega}(v_2+v_3)+\frac{4bh_{31}}{j\omega a}I, \tag{1}$$

$$F_2=\frac{2\pi ac_{13}^D}{j\omega}v_1+\frac{Z_3}{j}\left(\frac{v_2}{\tan(2k_3b)}+\frac{v_3}{\sin(2k_3b)}\right)+\frac{h_{33}}{j\omega}I, \tag{2}$$

$$F_3=\frac{2\pi ac_{13}^D}{j\omega}v_1+\frac{Z_3}{j}\left(\frac{v_2}{\sin(2k_3b)}+\frac{v_3}{\tan(2k_3b)}\right)+\frac{h_{33}}{j\omega}I, \tag{3}$$

$$V=\frac{4bh_{31}}{j\omega a}v_1+\frac{h_{33}}{j\omega}v_2+\frac{h_{33}}{j\omega}v_3+\frac{I}{j\omega C_0}, \tag{4}$$

where c_{ij} and h_{ij} $(i,j=1,...,3)$ are the elastic and piezoelectric constants, respectively, $\varepsilon_{33}^S=1/\beta_{33}^S$ is the dielectric permittivity, ρ is the mass density, $\overline{v_1}=\sqrt{c_{11}^D/\rho}$ and $\overline{v_3}=\sqrt{c_{33}^D/\rho}$ are the wave propagation velocities and $k_1=\omega/\overline{v_1}$ and $k_3=\omega/\overline{v_3}$ are the wave numbers in the r and z directions, respectively, $Z_1=\rho\overline{v_1}4\pi ab$ and $Z_3=\rho\overline{v_3}\pi a^2$ are the piezoelectric ceramic mechanical impedances along the r and z directions, and $C_0=\pi a^2/\beta_{33}^S 2b$ is the so-called "clamped capacity" of the piezoelectric ceramic.

Following the same approach the two loading masses are modeled as three-port systems. Each system can be simply obtained from Eqs. (1)–(3) by setting to zero the piezoelectric constants h_{31} and h_{33}, and, due to the isotropy of the material, by imposing $c_{33}=c_{11}$ and $c_{13}=c_{12}$, and by suppressing the subscripts for Z and k. With these assumptions we obtain

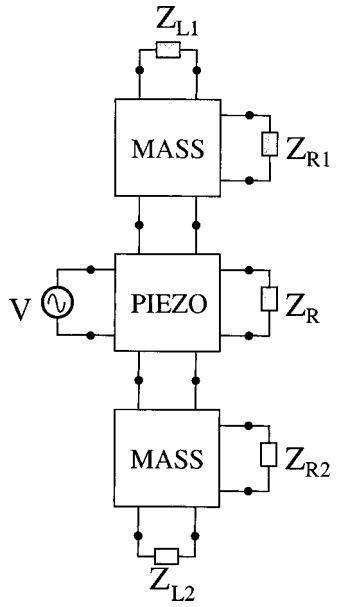

FIG. 2. The six-port system representation.

$$F_1=\frac{Z}{j}\left[\left(\frac{kaJ_0(ka)-J_1(ka)}{kaJ_1(ka)}\right)+\frac{c_{12}}{kac_{11}}\right]v_1 + \frac{2\pi ac_{12}}{j\omega}(v_2+v_3), \tag{5}$$

$$F_2=\frac{2\pi ac_{12}}{j\omega}v_1+\frac{Z}{j}\left(\frac{v_2}{\tan(2kb)}+\frac{v_3}{\sin(2kb)}\right), \tag{6}$$

$$F_3=\frac{2\pi ac_{12}}{j\omega}v_1+\frac{Z}{j}\left(\frac{v_2}{\sin(2kb)}+\frac{v_3}{\tan(2kb)}\right). \tag{7}$$

The full model of the Langevin transducer is easily obtained by connecting the mechanical ports which correspond to the contacting surfaces (see Fig. 2); in this way, the transducer is modeled as a six-port system. It should be noted that the continuity of the velocities at the interfaces between the piezoelectric ceramic and the masses is imposed only in the z direction.

All the transfer functions of the system can be computed by loading the five mechanical ports with the mechanical impedances of the surrounding media, and applying an alternating voltage to the electric port. In the design of the Langevin transducer the most useful relations are the electrical input impedance (Z_i) and the transmission transfer functions (TTF_n), defined, respectively, as

$$Z_i=\frac{V}{I}, \tag{8}$$

$$TTF_n=\frac{F_n}{V}, \tag{9}$$

where the subscript n indicates the mechanical port considered. The output displacement u_n at each port is then given by the relation

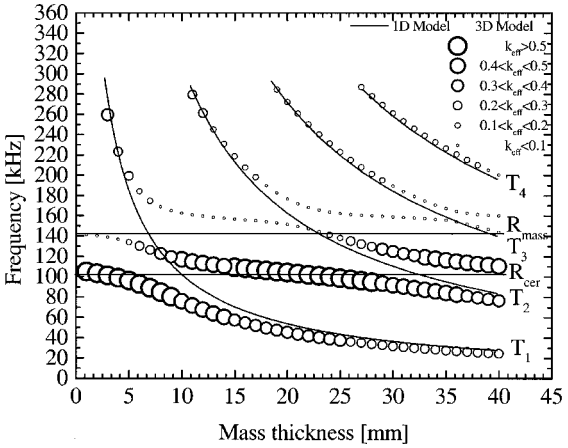

FIG. 3. The frequency spectrum versus the thickness of the loading masses.

$$u_n = \frac{1}{j\omega}\,\frac{F_n}{Z_n}. \tag{10}$$

III. NUMERICAL RESULTS

Figure 3 shows the frequency spectrum, i.e., the map of the resonance frequencies of the transducer, computed with the proposed 3-D model. It is obtained by varying the thickness of the loading masses from 1 to 40 mm. The results were obtained by assuming PZT-5A by Morgan-Matroc[21] ($2a=20$ mm, $2b=2$ mm) as the piezoelectric ceramic material, and steel (mass density $\rho=8$ kg/m^3, Young modulus $E=17.7\times10^{10}$ N/m^2, Poisson ratio $\sigma=0.3$) as the mass material.

The diameter of the circles is proportional to the effective electromechanical coupling factor (k_{eff}), which, as it is well known, is defined as

$$k_{\text{eff}} = \sqrt{\frac{f_p^2 - f_s^2}{f_p^2}}, \tag{11}$$

where f_s and f_p can be assumed to be the frequencies of maximum and minimum admittance.

For comparison, Fig. 3 also shows the frequency spectrum of the Langevin transducer computed with the classical 1-D thickness extensional model[10] (solid curves T_1, T_2, T_3, and T_4), and two straight lines representing the resonance frequencies of the pure radial modes of the piezoelectric ceramic R_{cer} and of the masses R_{mass}, which are computed under the hypothesis of thin disks.[22] By increasing the mass thickness, the resonance frequency of the pure thickness mode T_1 decreases, as well as the harmonics corresponding to T_2, T_3, and T_4, while the R_{cer} and R_{mass} are constant because they only depend on the diameter of the structure.

The plot of Fig. 3 shows that the 3-D model is able to predict both thickness and radial resonance frequencies of the structure. The plot also shows that there is agreement between 3-D and 1-D results only in the regions of the spectra where the resonance frequencies of pure modes are sufficiently distant. On the contrary, in regions where pure modes come closer, the 3-D model is able to predict their deviation from 1-D trends caused by the coupling existing between them. It should be noted that the radial resonance frequency of the masses computed with the 3-D model approaches R_{mass} only when the masses are very thin; elsewhere it is higher than R_{mass}.

As far as the values of k_{eff} are concerned, Fig. 3 shows that in the regions where two modes are strongly coupled, these modes present very similar values of k_{eff}, even if in ''undisturbed'' regions these values are quite different. This behavior indicates that, in coupling regions, the two modes cannot be considered pure modes, because their vibrational characteristics are somehow mixed. On the other hand, when the transducer has an aspect ratio for which coupling between modes does not occur, the k_{eff} value permits us to establish for each resonance frequency the nature of the corresponding mode (radial or thickness), without resorting to comparisons with 1-D models.

We also computed, for each sample, the electrical input impedance, the transmission transfer function, and the frontal displacement at one end surface as a function of frequency. The transducer was assumed to work in air; however, in order to take into account the internal losses, the mechanical ports were loaded with specific acoustic impedances of 0.1 MPa·s/m. As an example, Fig. 4 shows the results obtained for a transducer with mass thicknesses of 14 mm. Figure 4(a) shows the magnitude of the input impedance versus frequency. Comparing this plot with Fig. 3, we can recognize that the resonance frequencies correspond to the first thickness mode ($T_1^{3\text{D}}$), and the radial modes of the piezoelectric ceramic ($R_{\text{cer}}^{3\text{D}}$) and of the masses ($R_{\text{mass}}^{3\text{D}}$), respectively. From the plot of the transmission transfer function [Fig. 4(b)], it can be seen that the maximum value, as expected, is obtained at the resonance frequency of the thickness mode; however, a quite good response is also observed at the resonance frequency of the radial mode R_{cer}^{3D}. The response at the resonance frequency of the radial mode $R_{\text{mass}}^{3\text{D}}$ is negligible. Similar considerations can be made for the frontal displacements [see Fig. 4(c)]. Finally, it should be noted that, as the model was derived assuming a pistonlike motion, the force and the displacement of Figs. 4(b) and 4(c) are the mean values on the terminal surfaces.

IV. EXPERIMENTAL VALIDATION

In order to experimentally validate the proposed model, we manufactured 13 Langevin transducers of different lengths ranging from 2.5 to 32.5 mm. Piezoelectric ceramic and mass materials and dimensions are those described in the previous section.

Each prototype was prestressed with the jig shown in Fig. 5. The Langevin structure, whose masses are provided with flanges, is placed into the jig, composed of two threaded elements. By means of a jig adapter, a torque wrench is used to tighten the ceramic disk between the two masses, obtaining a good control of the prestress, which is applied only to the piezoelectric ceramic element. In order to avoid shear stresses during wrenching operations, a thin layer of grease was laid at the interfaces between the piezoelectric ceramic and the masses. Measurements were conducted with the transducer mounted in the jig; this experimental solution avoids the need for a hole in the structure to insert a pre-

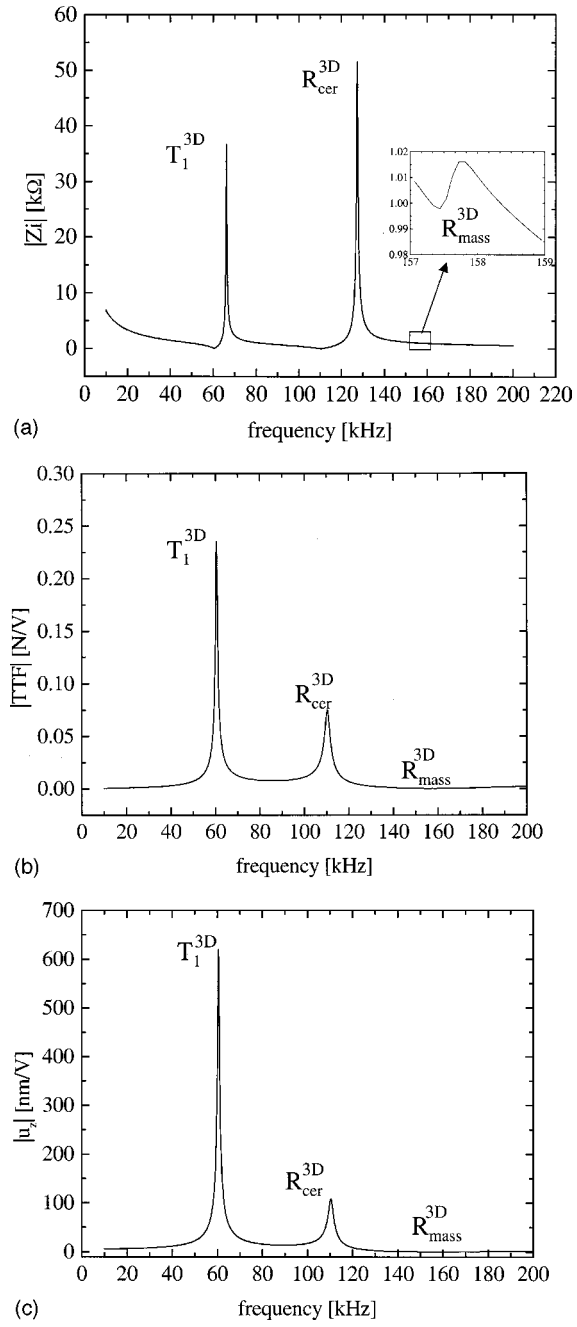

FIG. 4. Modulus of the input impedance (a), modulus of the transmission transfer function (b), and modulus of the frontal displacement (c) for a transducer with masses of 14-mm length.

stress bolt and, therefore, allows a more realistic comparison with the results of the model, which is derived for a cylinder and not for ring-shaped elements. In fact, as shown in recent works,[23,24] the frequency behavior of the radial modes of disks and rings is substantially different.

Figure 6 shows the experimental frequency spectrum; also in this case, the diameter of the circles is proportional to the k_{eff}. In this plot, the frequency spectrum computed with the proposed model is reported in solid curves.

The experimental results reported in Fig. 6 were obtained by applying to the Langevin transducer a light prestress (corresponding to an applied torque of about 2 N·m), just sufficient to ensure the mechanical contact between the

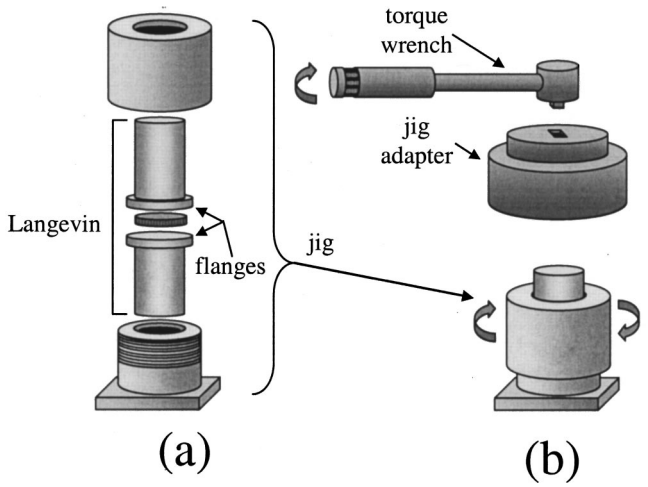

FIG. 5. (a) Exploded view of the transducer and of the jig. (b) The asembled structure, the accessory torque wrench, and its jig adapter.

piezoelectric ceramic and the masses. This is the best experimental approximation of the hypotheses imposed deriving the model, which does not take into consideration any prestress, and describes the contact between the piezoelectric ceramic and the masses by imposing the continuity of displacements only in the thickness direction. In fact, both the light prestress and the use of grease should allow radial sliding.

The comparison between computed and experimental results shows that the model predicts with quite good accuracy the two lowest resonance frequencies all over the explored range. In particular, it is noteworthy the agreement observed in the region where these two modes are strongly coupled, i.e., where the diameter and the whole length of the structure are comparable. A further agreement can be observed by comparing the behavior of the experimental k_{eff} in Fig. 6 with that computed with the 3-D model in Fig. 3.

As far as the higher frequencies modes are concerned, measurements only partly confirm the results of the model; this is probably due to the presence of other modes of different nature which are not predicted by the model.

In order to better investigate the effect of the coupling

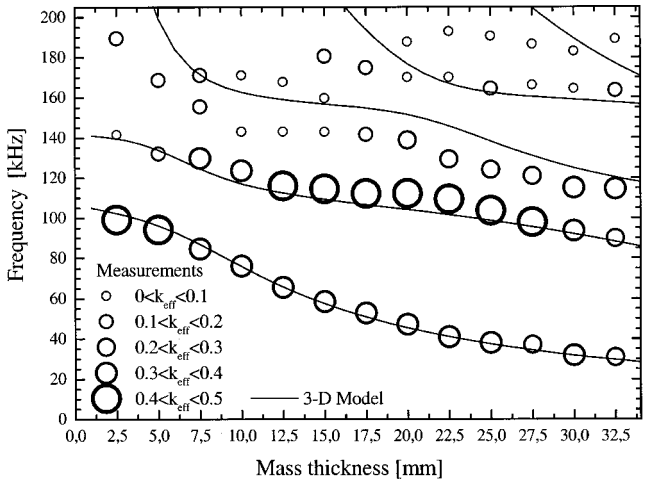

FIG. 6. Comparison between measured and computed frequency spectra.

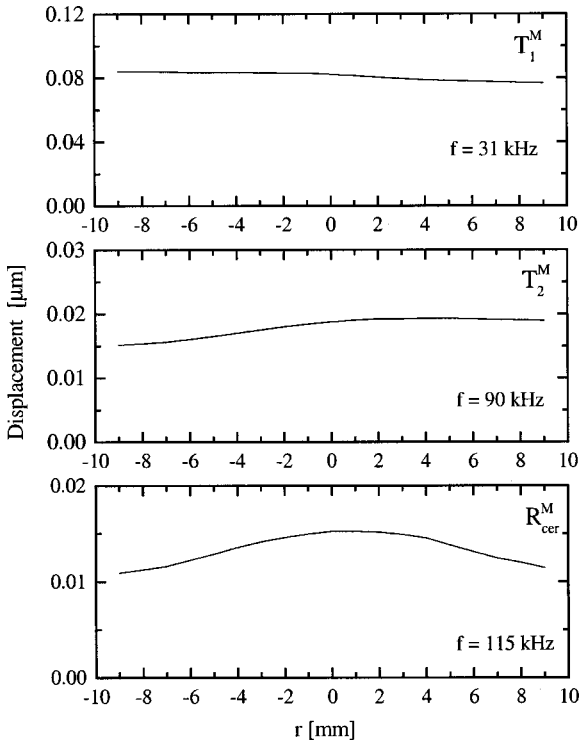

FIG. 7. Frontal displacement of the transducer with massses of 32.5-mm length.

between the thickness and the radial modes, we measured the frontal displacement of the terminal surface by means of an interferometric technique, for three different transducers at the main resonance frequencies.

Figure 7 shows the shapes of the frontal displacement measured on the sample with masses of 32.5-mm length at

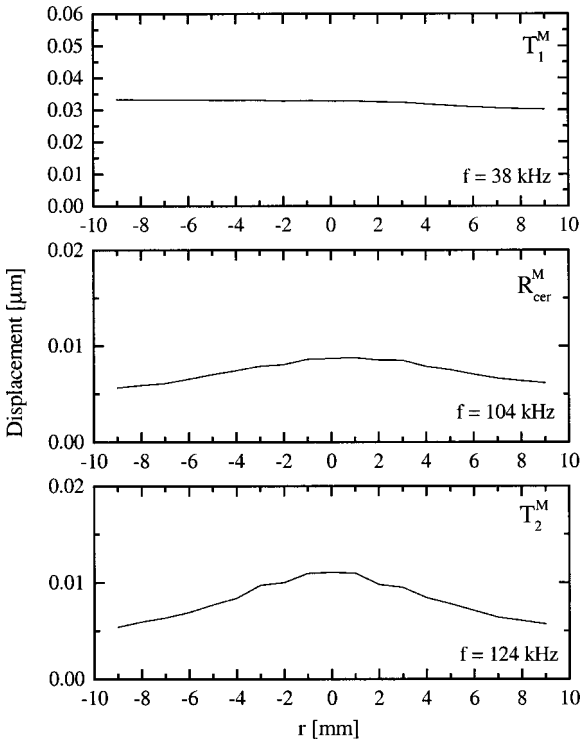

FIG. 8. Frontal displacement of the transducer with masses of 25-mm length.

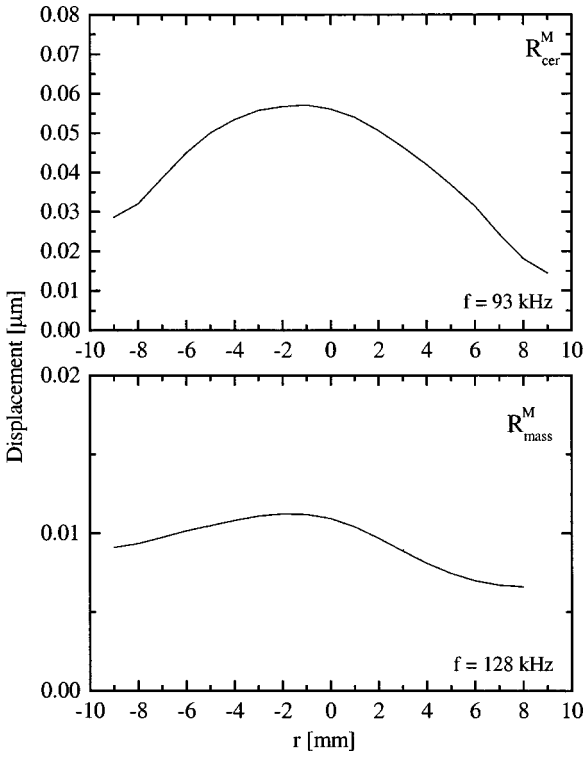

FIG. 9. Frontal displacement of the transducer with masses of 5-mm length.

the three lowest resonance frequencies. As can be seen from the plot of Fig. 6, for this aspect ratio, the resonance frequencies are quite distant; therefore the modes can be considered uncoupled. The lowest frequency mode presents a clear pistonlike motion, and can be considered as a pure thickness extensional mode. Also, the second mode has an almost flat axial displacement and can be recognized as the first harmonic of the fundamental thickness mode. The third mode has the typical displacement shape of radial modes.[25]

The displacements of the transducer with masses of 25-mm length are shown in Fig. 8. For this aspect ratio, the low-frequency mode can still be recognized as a pure thickness extensional mode, due to the flatness of its displacement. However, it is not possible to distinguish which of the two other modes is the thickness extensional and which is the radial, because the shapes of the displacement are very similar and the amplitudes comparable. By the observation of Fig. 6, it is evident that these two modes are strongly coupled; in the figure, we indicated the lower frequency mode as R_{cer}^M only because its k_{eff} has a greater value than the other.

The displacements at the first two resonance frequencies for the transducer with masses of 5-mm length are shown in Fig. 9. The low-frequency mode can be recognized as a radial mode both for its displacement shape and for the high k_{eff} value shown in Fig. 6. It should be noted that, at this frequency, the mean displacement of the transducer is comparable with those observed for the fundamental thickness mode of transducers of Figs. 7 and 8. The second mode, for this sample, is R_{mass}^M.

V. CONCLUSION

In this work, an approximated 3-D model of the Langevin transducer has been proposed. The model represents an

improvement with respect to the 1-D approach because it is able to describe the radial modes of the structure and their coupling with thickness extensional modes. The comparison with experimental results shows that, for any aspect ratio of the transducer, the model is able to predict with quite good accuracy the two lowest resonance frequencies, which are those mainly used in practical applications.

The proposed model therefore seems to be a useful analyical tool which permits us to extend the design of Langevin transducers also to structure with the diameter comparable or greater than the total length. It can be used in broadband applications, where the coupling between radial and thickness modes can be exploited to enlarge the bandwidth, and in power applications due to its capability to predict the fundamental resonance frequency of the transducer for any aspect ratio.

[1] T. Inoue, T. Nada, T. Tsuchiya, T. Nakanishi, T. Miyama, and M. Konno, ''Tonpilz piezoelectric transducers with acoustic matching plates for underwater color image transmission,'' IEEE Trans. Ultrason. Ferroelectr. Freq. Control **40**, 121–129 (1993).

[2] R. F. W. Coates, ''The design of transducers and arrays for underwater data transmission,'' IEEE J. Ocean. Eng. **16**, 123–135 (1991).

[3] M. P. Hayes and P. T. Gough, ''Broad-band syntetic aperture sonar,'' IEEE J. Ocean. Eng. **17**, 80–94 (1992).

[4] S. G. Schock, L. R. Leblanc, and S. Panda, ''Spatial and temporal pulse design considerations for a marine sediment classification sonar,'' IEEE J. Ocean. Eng. **19**, 406–415 (1994).

[5] R. F. W. Coates, ''Underwater acoustic communication,'' Sea Technol. **35**(7), 41–47 (1994).

[6] S. W. Or, H. L. W. Chan, V. C. Lo, and C. W. Yuen, ''Dynamics of ultrasonics transducers used for wire bondings,'' IEEE Trans. Ultrason. Ferroelectr. Freq. Control **45**, 1453–1460 (1998).

[7] L. Shuyu, ''Study on the Multifrequency Langevin Ultrasonic Transducer,'' Ultrasonics **33**, 445–448 (1995).

[8] W. P. Mason, *Electromechanical Transducers and Wave Filters*, 2nd ed. (Van Nostrand, New York, 1948), pp. 195–209, 399–404.

[9] D. A. Berlincourt, D. R. Curran, and H. Jaffe, ''Piezoelectric and Piezomagnetic Materials and their Function in Transducers,'' in *Physical Acoustics*, edited by W. P. Mason (Academic, New York, 1964), Vol. 1.

[10] E. A. Neppiras, ''The pre-stressed piezoelectric sandwich transducer,'' *1973 Ultrasonic International Conference Proceedings*, pp. 295–302.

[11] J. N. Decarpigny, J. C. Debus, B. Tocquet, and D. Boucher, ''In air analysis of piezoelectric Tonpilz transducers in a wide frequency band using a mixed finite element—plane wave method,'' J. Acoust. Soc. Am. **78**, 1499–1507 (1985).

[12] D. W. Hawkins and P. T. Gough, ''Multiresonance design of a Tonpilz transducer using the finite element method,'' IEEE Trans. Ultrason. Ferroelectr. Freq. Control **43**, 782–790 (1998).

[13] Q. Yao and L. Bjorno, ''Broadband Tonpilz Underwater acoustic transducers based on multimode optimization,'' IEEE Trans. Ultrason. Ferroelectr. Freq. Control **44**, 1060–1065 (1997).

[14] H. Allik, K. M. Webman, and J. T. Hunt, ''Vibrational response of sonar transducers using piezoelectric finite elements,'' J. Acoust. Soc. Am. **56**, 1782–1791 (1974).

[15] R. Lerch, ''Simulation of piezoelectric devices by two- and three-dimensional finite elements,'' IEEE Trans. Ultrason. Ferroelectr. Freq. Control **37**, 233–247 (1990).

[16] C. G. Hutchens and S. A. Morris: ''A two-dimensional equivalent circuit for the tall thin piezoelectric bar,'' in *1985 IEEE Ultrasonic Symposium Proceedings* (IEEE, New York, 1985), pp. 671–676.

[17] G. Hayward and D. Gilles, ''Block diagram modeling of tall, thin parallelepiped piezoelectric structures,'' J. Acoust. Soc. Am. **86**, 1643–1653 (1989).

[18] N. Lamberti and M. Pappalardo, ''A General Approximated Two-Dimensional Model for Piezoelectric Array Elements,'' IEEE Trans. Ultrason. Ferroelectr. Freq. Control **42**, 243–252 (1995).

[19] M. Brissaud, ''Characterization of Piezoceramic,'' IEEE Trans. Ultrason. Ferroelectr. Freq. Control **38**, 603–617 (1991).

[20] A. Iula, N. Lamberti, and M. Pappalardo, ''An approximated 3-D model of cylinder-shaped piezoceramic elements for transducer design,'' IEEE Trans. Ultrason. Ferroelectr. Freq. Control **45**, 1056–1064 (1998).

[21] Vernitron Bulletin, *Five Modern Piezoelectric Ceramics*, January 1972, No. 66011/E.

[22] A. H. Meitzler, H. M. O'Bryan, and H. F. Tiersten, ''Definition and Measurement of Radial Mode Coupling Factors in Piezoelectric Ceramic Materials with Large Variation in Poisson's Ratio,'' IEEE Trans. Sonics Ultrason. **20**, 233–239 (1973).

[23] A. Iula, N. Lamberti, and M. Pappalardo, ''A Model for the Theoretical Characterization of Thin Piezoceramic Rings,'' IEEE Trans. Ultrason. Ferroelectr. Freq. Control **43**, 370–375 (1996).

[24] A. Iula, N. Lamberti, R. Carotenuto, and M. Pappalardo, ''Analysis of the Radial Symmetrical Modes of Thin Piezoceramic Rings,'' IEEE Trans. Ultrason. Ferroelectr. Freq. Control **46**, 1047–1049 (1999).

[25] E. A. G. Shaw, ''On the resonant variations of thick barium titanate disks,'' J. Acoust. Soc. Am. **28**, 38–50 (1956).

Electrical characterization of plate piezoelectric transducers bonded to a finite substrate

Yves Deblock, Pierre Campistron, Marc Lippert, and Christian Bruneel
IEMN-UMR CNRS 8520, Boîte Postale 69, Avenue Poincaré, 59652 Villeneuve d'Ascq, France

(Received 14 December 2000; accepted for publication 14 September 2001)

This article presents a new technique for characterizing piezoelectric transducers attached to a finite substrate. It consists of determining the impedance of the transducer cleared of the effects caused by finite dimensions of the substrate. This technique is validated by comparison with measurements on a transducer mounted on an effectively half-infinite substrate. It is applied for the electrical matching of a lithium niobate plate transducer bonded to a fused quartz rod. © *2002 Acoustical Society of America.* [DOI: 10.1121/1.1416904]

PACS numbers: 43.38.Fx, 43.60.Qv [SLE]

I. INTRODUCTION

The measurement of the electrical impedance is of great important step in designing piezoelectric transducers. It provides complete electrical characteristics of the transducer and comparison with predictions.

At megahertz frequencies transducers are often attached to a substrate. This is the case, for example, with plate transducers which become too thin and fragile to be used as standing alone. The presence of the substrate may cause large variations of the electrical impedance of the transducer. This occurs with bounded substrate having end faces flat and parallel to the transducer and when the attenuation of waves in the substrate is low. These variations are due to the reflections of the acoustics waves between ends of the substrate and are not relevant to the characteristics of the transducer.

More meaningful is the impedance of the transducer bonded to a half-infinite substrate. it is the purpose of this article to derive a process for determining this impedance, denoted as Z_0, from the measured one, and suitable for plate transducers bonded to a finite length rod. The process consists of smoothing the impedance over an aperture which depends on the length of the rod and the velocity of waves propagating inside.

In order to validate the process, the impedance of the transducer is measured, then processed, and compared with that measured when the rod is modified to behave as a half-infinite substrate. As an illustration the process is applied for designing an electrical matching network of a lithium niobate plate transducer bonded to a fused quartz rod.

II. THEORY

A. Electrical impedance of a piezoelectric thin plate transducer rigidly bonded to a substrate of finite thickness and end faces parallel to the transducer

An analytical expression of the electrical impedance of a piezoelectric thin plate transducer rigidly bonded to a half-infinite substrate has been established by Auld.[1] This expression is derived from the assumption that the thickness of the transducer is small compared with its transverse dimensions, allowing the use of a one-dimensional model for the description of waves propagating inside the transducer and the substrate. This electrical impedance is written as

$$Z_0=\frac{1}{j2\pi fC_0}+\frac{K^2}{2\pi fC_0}\frac{1}{\theta}\frac{2Z_p(\cos\ \theta-1)+jZ_l\ \sin\ \theta}{Z_l\ \cos\ \theta+jZ_p\ \sin\ \theta} \tag{1}$$

with $\theta=\pi f/f_0$.

f is the frequency. f_0 is the half-wavelength resonant frequency of the transducer, and C_0 is the static capacitance. K is the electromechanical coupling constant for the piezoelectrical material. Z_l represents the mechanical impedance of the substrate and Z_p is the mechanical impedance of the plate.

If the transducer is bonded to a finite length substrate having faces parallel to the transducer, the characteristic impedance Z_l of Eq. (1) is replaced by an impedance Z_a. This impedance describes the multiple reflections of waves inside the substrate. This impedance is written as

$$Z_a=Z_l\frac{1-e^{-j\beta}}{1+e^{-j\beta}} \tag{2}$$

with $\beta=2k_ll$.

Here k_l represents the wave number describing the wave propagation in the substrate and l is the thickness of the substrate.

Thus the expression of the electrical impedance of the transducer bonded to a finite thickness substrate is obtained by the substitution of (2) into (1) as follows:

$$Z=\frac{1}{j2\pi fC_0}+\frac{K^2}{2\pi fC_0}\frac{1}{\theta}\times\frac{2Z_p(1+e^{-j\beta})(\cos\ \theta-1)+jZ_1(1-e^{-j\beta})\ \sin\ \theta}{Z_l(1-e^{-j\beta})\cos\ \theta+jZ_p(1+e^{-j\beta})\sin\ \theta}. \tag{3}$$

The denominator $D=Z_l(1-e^{-j\beta})\cos\ \theta+jZ_p(1+e^{-j\beta})\sin\ \theta$ of Eq. (3) can be factorized as

$$D=(Z_l\cos\ \theta+jZ_p\sin\ \theta)\times\left[1-\frac{Z_l\cos\ \theta-jZ_p\sin\ \theta}{Z_l\cos\ \theta+jZ_p\sin\ \theta}e^{-j\beta}\right]. \tag{4}$$

Taking into account losses in the bonded material, β is complex and

$$\left|\frac{Z_l\cos\,\theta - jZ_p\sin\,\theta}{Z_l\cos\,\theta + jZ_p\sin\,\theta}e^{-j\beta}\right| < 1.$$

As a consequence, $1/D$ can be written as

$$\frac{1}{D} = \frac{1}{Z_l\cos\,\theta + jZ_p\sin\,\theta} \times\left[1+\sum_{n=1}^{\infty}\left(\frac{Z_l\cos\,\theta - jZ_p\sin\,\theta}{Z_l\cos\,\theta + jZ_p\sin\,\theta}\right)^n e^{-jn\beta}\right]. \quad (5)$$

On the other hand, the numerator $N=2Z_p(1+e^{-j\beta})(\cos\,\theta - 1)+jZ_1(1-e^{-j\beta})\sin\,\theta$ of Eq. (3) can be factorized as

$$N=[2Z_p(\cos\,\theta-1)+jZ_1\sin\,\theta] \times\left[1+\frac{2Z_p(\cos\,\theta-1)-jZ_l\sin\,\theta}{2Z_p(\cos\,\theta-1)+jZ_l\sin\,\theta}e^{-j\beta}\right]. \quad (6)$$

Finally, the substitution of Eqs. (5) and (6) into Eq. (3) gives

$$Z=\frac{1}{j2\pi fC_0}+\frac{K^2}{2\pi fC_0}\frac{1}{\theta}\frac{2Z_p(\cos\,\theta-1)+jZ_l\sin\,\theta}{Z_l\cos\,\theta+jZ_p\sin\,\theta} \times\left[1+\frac{2Z_p(\cos\,\theta-1)-jZ_l\sin\,\theta}{2Z_p(\cos\,\theta-1)+jZ_l\sin\,\theta}e^{-j\beta}\right] \times\left[1+\sum_{n=1}^{\infty}\left(\frac{Z_l\cos\,\theta-jZ_p\sin\,\theta}{Z_l\cos\,\theta+jZ_p\sin\,\theta}\right)^n e^{-jn\beta}\right] \quad (7)$$

or

$$Z=Z_0+\sum_{n=1}^{\infty}Z_n e^{-jn\beta}. \quad (8)$$

The electrical impedance of the transducer is written as the sum of Z_0, the impedance of interest, and an infinite series whose coefficients Z_n (with $n>0$) may be obtained by comparing Eq. (7) with Eq. (8).

Within narrow frequency windows, it may be assumed that the frequency variations of the impedance are due to the complex exponential $\exp -j\beta$. This assumption holds when the thickness of the transducer is much smaller than the thickness of the bonded substrate, that is when $v_l/2l \ll f_0$, where v_l is the acoustical wave velocity in the bonded substrate. As a consequence, Eq. (8) can be thought of as a trigonometric Fourier series. Z_n represents the coefficients of the series and are different whatever the frequency window. We denote Δf and f_{cent} the width and the center of a window, respectively.

B. Determination of Z_0

Here Z_0 is obtained by averaging the electrical impedance over the frequency window Δf. Δf is chosen by looking at the impedance in the time domain. In the frequency domain Δf acts as a unity rectangle window. As a consequence, the inverse Fourier transform of the electrical impedance gives a series of discrete impulses having a $\sin(\pi\Delta ft)/(\pi\Delta ft)$ shape and located at $t_n=(2nl/v_l)$, where n is integer and t is the time. The electrical impedance can be weighted by a window of the same width giving reduced sidelobes, such as the Hann window.[2] Δf is chosen to avoid overlapping of consecutive main lobes of the inverse Fourier transform of the Hann window and must be narrow enough to keep Eq. (8) valid.

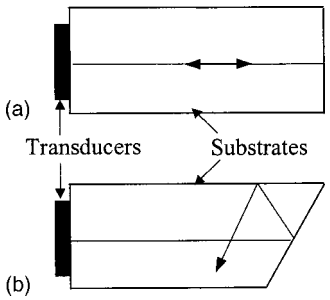

FIG. 1. Plate transducers attached to bounded substrates. (a) Both end faces of the substrate are parallel. (b) The free face of the substrate is obliquely cut.

Finally, Z_0 is deduced from the measured impedance by the integration

$$Z_0(f_{\text{cent}})\approx\frac{2}{\Delta f}\int_{\Delta f}W(f-f_{\text{cent}})Z(f)\,df, \quad (9)$$

where $W(f-f_{\text{cent}})$ is the Hann window centered at f_{cent} and $\Delta f \geqslant 2v_l/l$.

The frequency characteristics of Z_0 are obtained by sweeping the frequency f_{cent} around the transducer resonance.

III. EXPERIMENTS

A. Validation of the method

The validation procedure operates in two steps. In the first step the electrical impedance of the transducer bonded to a substrate of finite thickness and end faces parallel to the transducer [cf. Fig. 1(a)] is measured and Z_0 is calculated from Eq. (9). In the second step the electrical impedance is measured as one face of the substrate is obliquely cut [cf. Fig. 1(b)]. In this case the waves reflected by the oblique face do not interfere with the wave generated by the transducer and the substrate behaves as half-infinite. As a consequence this impedance must be the same as Z_0.

The validation procedure deals with a transducer made of a lithium niobate plate bonded to a fused quartz rod. The resonance frequency of the transducer is 55 MHz and the length of the rod is 10 mm. The longitudinal acoustic waves propagate in fused quartz at 6000 m/s.

The procedure uses a network analyzer combined with an impedance test set. The analyzer is driven by a computer through GPIB (general protocol interface bus). Series of uniformly spaced impedance samples are measured over Δf and sent to the computer for averaging according to Eq. (9). The center frequency f_{cent} is swept over the required frequency range.

Figure 2 shows the real and imaginary parts of the electrical impedance of this transducer. Figure 3 zooms the real part of this impedance around the center frequency. As it can be seen the fluctuations on the impedance are quasi-

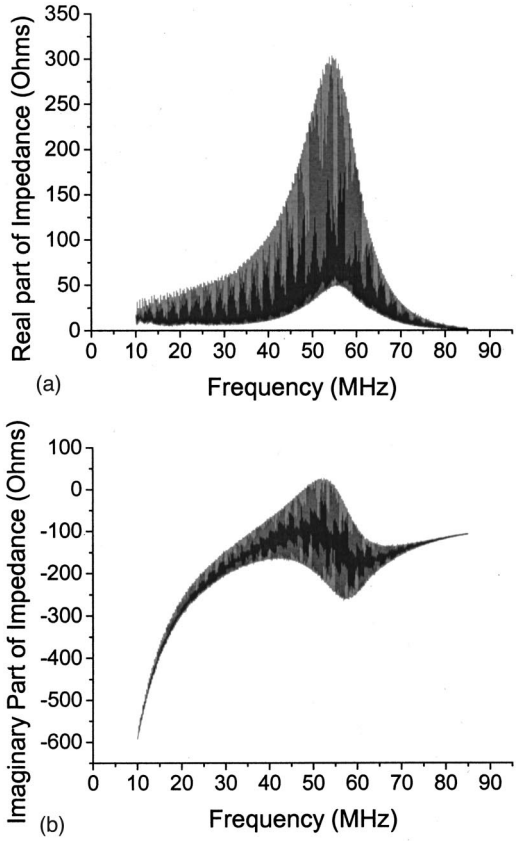

FIG. 2. Electrical impedance of a 55-MHz plate transducer bonded to a fused quartz rod of 10-mm length: (a) real part and (b) imaginary part.

periodically spaced by 300 kHz, which corresponds to $1/t_l = v_l/2l$. The plots of Fig. 4 show the result of the averaging process applied to the impedance of Fig. 2. On the same figure is plotted the impedance of the transducer when the end of the bonded substrate is obliquely cut. The correlation between the half-infinite data and the derivation from finite data in both real and imaginary parts demonstrates validation of the procedure.

B. Illustration of the method: Electrical matching of a plate transducer bonded to a fused quartz rod

The transducer to match is a lithium niobate plate whose resonance frequency is 21 MHz. This transducer is rigidly bonded to a fused quartz rod of 10-mm length, using a thin layer of indium.

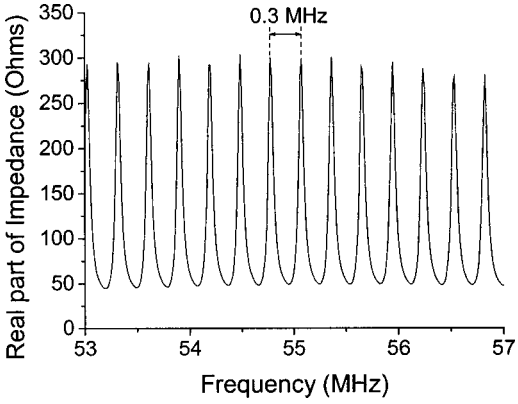

FIG. 3. Zoom of Fig. 2(a) around the resonance of the transducer.

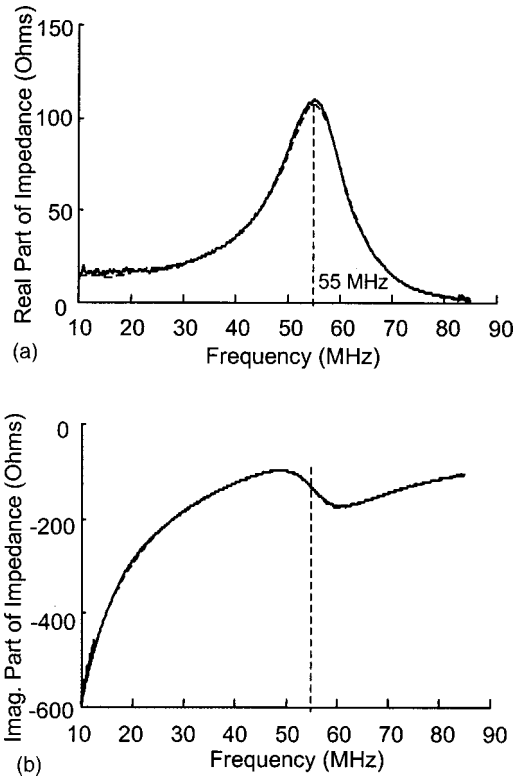

FIG. 4. Computed impedance Z_0 of the 55-MHz transducer (---). Electrical impedance of the transducer as the free end of the rod is obliquely cut (—): (a) real parts and (b) imaginary parts.

The average process performed on the impedance gives the plots of Fig. 5. The structure of the chosen circuit to match the transducer around the resonance is the low-pass filter of Fig. 6. The role of the capacitance C is to decrease the resistance of the transducer down to the characteristic impedance of the electrical source R_0, typically 50 Ω. The self-inductance L annihilates the reactive effect of the parallel association of the transducer and C. The expressions of C and L derived from Ref. 3 are

$$C = \frac{\sqrt{2}}{R_p \omega_c sh(a)} + \frac{1}{X_p \omega_m}, \tag{10}$$

$$L = \frac{R_0 \sqrt{2}}{\omega_c sh(a)}, \tag{11}$$

with

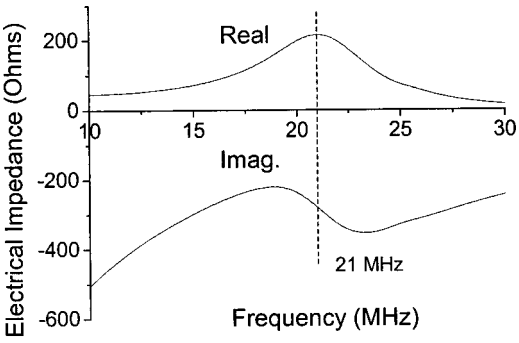

FIG. 5. Computed impedance Z_0 of a 21-MHz transducer bonded to a fused quartz delay line of 10-mm length.

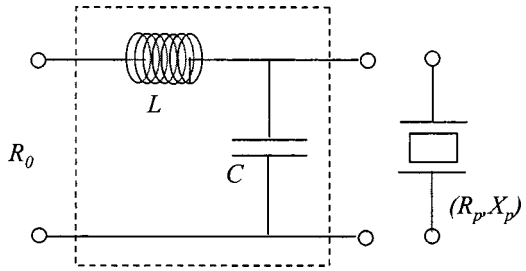

FIG. 6. (LC) matching network.

$$a=\frac{1}{2}sh^{-1}\left(\frac{1}{\epsilon}\right), \quad \epsilon=\sqrt{\frac{1}{G_m}-1},$$

$$G_m=1-\left(\frac{R_p-R_0}{R_p+R_0}\right)^2, \quad \omega_c=\omega_m\sqrt{2}.$$

Here ω_m represents the angular frequency for which the transducer is exactly matched, ω_c is the cutoff angular frequency of the filter, and (R_p, C_p) are the components of the parallel representation of the transducer at ω_m.

The matching network is designed from the characteristics of Fig. 5 and the calculation of C and L from Eqs. (10) and (11), respectively. For a matching frequency of 21 MHz, $L=1.3$ μH and $C=23$ pF. The actual matching network exhibits the values $L=1.2$ μH and $C=31$ pF and a parasitic series resistance of 2.5 Ω is also measured. Figure 7 shows the electrical impedance of the matched transducer. As it can be seen in this figure, the real part of the impedance reaches roughly 50 Ω and the imaginary part cancels near 19 and 21 MHz. The efficiency of the matching is checked by the rf pulse equipment of Fig. 8. The pulse generator outputs a rf pulse whose carrier frequency is the matching frequency of the transducer. The width of the pulse is chosen large enough so that a CW mode can be assumed. The directional bridge allows the separation of the electrical signal incident on the transducer from the signal issued from it. All the rf pulses are displayed on the oscilloscope.

Figure 9 shows the train of rf pulses issued from the transducer using the experimental setup of Fig. 8 before the insertion of the matching network. The first pulse represents the reflection of the pulse incident on the transducer. This pulse results from the electrical mismatching between the

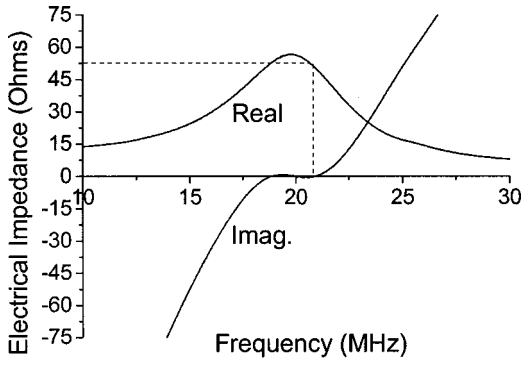

FIG. 7. Computed electrical impedance of the matched 21-MHz transducer.

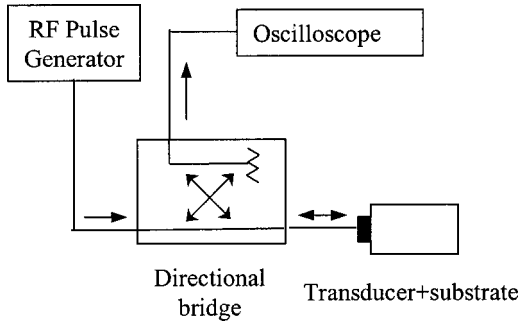

FIG. 8. Experimental arrangement of generation and detection of rf pulses.

transducer and R_0. It is followed by a series of pulses, the origin being the partial conversion of acoustical energy into electrical energy.

Figure 10 shows the train of rf pulses as the matching network is added. The comparison of Fig. 9 with Fig. 10 shows the effect of the matching network. The electrical reflected pulse is largely attenuated due to the almost complete conversion of electrical energy into acoustical energy. The simultaneous amplitude increase of the second pulse and decrease of the following pulses show that the conversion from acoustical into electrical energy is also improved. However, this conversion is not 100% efficient because a series of small pulses still exists. The imperfect conversion reciprocity is explained by losses in the transducer, the substrate, and the matching network. One also notes that the matching does not influence the pulse transitions where the CW mode cannot be assumed.

The efficiency of the electrical matching is also characterized by the conversion ratio η between electrical and acoustical energies. Assuming the reciprocity property of a transducer, η may be determined by

$$\eta=\frac{P}{P_0}, \tag{12}$$

where P represents the power of the first pulse reflected at the end of the quartz rod for which only two electrical energy to acoustical energy and vice versa conversions occur. Here P_0 represents the reflected power as the transducer is disconnected from the directional bridge.

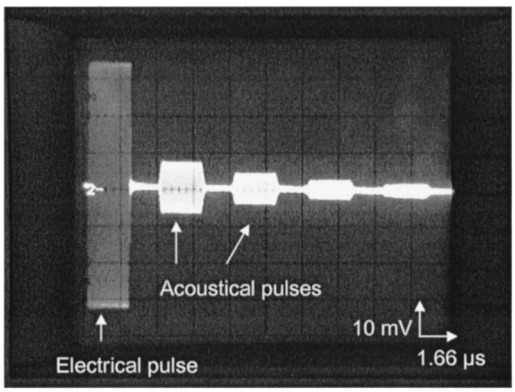

FIG. 9. Detected train of rf pulses issued from the 21-MHz transducer before matching. The carrier frequency is 21 MHz.

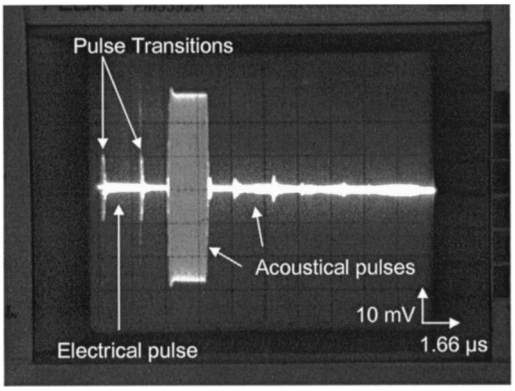

FIG. 10. Detected train of rf pulses issued from the 21-MHz transducer after matching. The carrier frequency is 21 MHz.

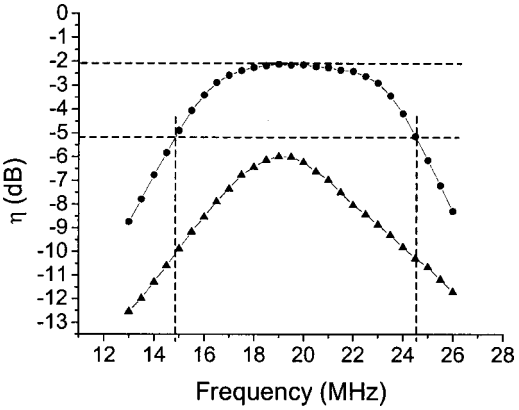

FIG. 11. The conversion ratio of the 21-MHz transducer, before matching (▲) and after matching (●).

Figure 11 shows the conversion ratio of the transducer before and after matching. A large bandwidth close to 10 MHz and small insertion losses lying in the interval (-5 dB, -2 dB) are obtained for the matched transducer.

IV. CONCLUSION

A method has been presented for determining the intrinsic impedance Z_0 of a transducer bonded to a substrate of finite thickness. It has been validated by comparison with measurements on a transducer mounted on an effectively infinite substrate. This method has been applied for designing electrical matching elements of a 21-MHz lithium niobate transducer bonded to a fused quartz rod. It has also been efficiently applied for matching transducers whose resonance frequencies range from 10 to 100 MHz.

This method is based on the averaging of the transducer impedance over a sweeping aperture. Due to its principle this method is simple to implement and efficient as far as the conditions of applications are satisfied.

The characteristics of Z_0 depend on the properties of both the substrate and the transducer properties. f_0, C_0, and K, as defined in Z_0, are intrinsic characteristics of the stand-alone transducer. Although bonding the transducer to the substrate causes translation of the peak resonance, a good approximation of f_0 is the frequency at which the real part of Z_0 is maximum. C_0 is obtained from the evaluation of the imaginary part of Z_0 at f_0, and K by the ratio between real and imaginary parts of Z_0 at f_0.

[1] B. A. Auld, *Acoustic Fields and Waves in Solids* (Wiley, New York, 1973), Vol. 1, Chap. 9.
[2] F. J. Harris, "On the use of windows for harmonic analysis with the discrete Fourier transform," Proc. IEEE **66**, 51–83 (1979).
[3] W. K. Chen, *The Circuits and Filters Handbook* (IEEE, New York, 1995), Sec. 73, pp. 2300–2302.

The analysis and interpretation of some special properties of higher order symmetric Lamb waves: The case for plates

M. F. Werby
NRL Code 7180, Stennis Space Center, Mississippi 39529 and Department of Physics, Catholic University of America, Washington, D.C. 20064

H. Überall
Department of Physics, Catholic University of America, Washington, D.C. 20064

(Received 5 January 2001; accepted for publication 8 February 2002)

Results derived from exact linear homogeneous elastodynamic theory are used for two-dimensional unloaded plates in order to understand certain features generated by proper symmetric Lamb modes. It is shown that S_1 modes for all elastic materials have a phase velocity defined below the usual critical frequency and which initially exhibits anomalous dispersion (has a negative slope with respect to frequency). Over a certain range, it has a phase velocity that is double valued. In addition, there are an infinite number of proper symmetric Lamb modes that have this characteristic for materials with a Poisson ratio equal to 1/3. It also appears that all A_{3n} modes are anomalous when $V_L \leqslant 2V_T$. The cause and implication of these effects are examined, including an associated negative group velocity over a small frequency zone for these modes. Further, it is noted that all proper symmetric Lamb modes have a plateau region in phase velocity with respect to wave number. It is shown that this always occurs for a phase velocity corresponding to the longitudinal bulk velocity of the elastic material. These issues are examined along with how one may obtain material parameters and possibly plate thickness from their dispersion curves. © *2002 Acoustical Society of America.* [DOI: 10.1121/1.1473637]

PACS numbers: 43.40.Dx, 43.35.Cg [ADP]

I. INTRODUCTION

A multitude of elastic vibrations or modes is predicted and observed for both unloaded and fluid-loaded elastic plates of uniform thickness.[1–3] In the following discussions, symmetry is defined relative to a plane at the midpoint of and parallel to the defining surfaces of the plate. The two lowest modes are pure, inhomogeneous interface waves that arise from mode conversion. One of these modes, labeled S_0, is symmetric and exists for all real frequencies. The other interface mode labeled A_0 is antisymmetric and exists at all frequencies for unloaded plates. For loaded plates, it begins to manifest itself when its phase velocity equals that of the ambient fluid. The remaining class of modes originates in the body of the material. Here, symmetric and antisymmetric modes emerge as governed by the mathematics of exact elasticity theory. These modes, labeled S_j and A_j, are the proper symmetric and antisymmetric Lamb modes, respectively, where j is a positive integer and designates the order of the mode.[3] It is possible to excite either of the elastic bulk waves in much the same way that modes in a fluid waveguide are excited. Proper Lamb modes usually begin as standing waves related to one of the elastic bulk waves and the plate thickness, which determines the critical frequency. When they begin to travel, they couple with the remaining bulk wave and form inhomogeneous waves.[3] In this work, the focus is on proper symmetric Lamb modes excited on isotropic unloaded elastic plates. In all cases the critical frequency is easy to determine, and subsequent to its inception, the wave propagates in a dispersive manner with a characteristic phase velocity that varies with frequency. There are, however, some striking anomalies observed for symmetric waves. In particular, the S_1 mode occurs below the usual critical frequency, and has anomalous dispersion over a small frequency zone in that region with a turning point in frequency at which point the phase velocity appears to be double valued. Indeed, at some point $dK_T/dV_x = 0$, where K_T is the wave number of the transverse wave and V_x is the phase velocity identified with a specific Lamb wave. The consequence of this is that the group velocity[4–8] takes on a negative value[6–10] at the onset of this wave. There are other exceptions similar to S_1 waves, namely for materials with a Poisson ratio ν equal to 1/3. In that case, analysis presented in this work shows that there are an infinite number of such waves and they bifurcate from a common critical frequency in which one of the bifurcations behaves like the S_1 wave while the remaining wave behaves in the usual fashion of a symmetric mode. Moreover, depending on the material, the S_1 Lamb mode may be generated by either initially exciting the longitudinal bulk mode or the transverse bulk mode—depending on the relative value of the bulk velocities—and the effect is still the same. Another interesting feature is that symmetric waves have a relatively broad plateau region (referred to here as the symmetric plateau) that is explained in terms of the transition region when the phase velocity comes close to the value of the longitudinal bulk wave. The A_{3n} antisymmetric Lamb modes for all positive integers n also exhibit the same properties when $V_L \leqslant 2V_T$, and this has been reported in the literature.[8] In the following sections, these waves are analyzed and it is shown why they must behave as they do. Group velocity[6–11] and its meaning are discussed in the context of the S_1 anomaly. Since these modes are the main sub-

 0001-4966/2002/111(6)/2686/6/$19.00

ject of discussion, they will subsequently be referred to as anomalous Lamb modes. Several simplified expressions useful for analysis are derived and results for three elastic materials in which the Poisson ratio $\nu=1/3$, $\nu>1/3$, and $\nu<1/3$ are examined.

II. TWO-DIMENSIONAL PLATE EQUATIONS FROM EXACT LINEAR PLATE THEORY

The derivation of the dispersion equations described here is based on using the point of reference (the x–y plane for $z=0$) as a plane midway between the outer and inner surface of the defining surfaces of the plate.[1–3] It allows one to uncouple the dispersion equations into expressions that predict symmetric and antisymmetric vibrations relative to the reference plane. Proper Lamb modes are initiated in a manner similar to a fluid waveguide; that is, they are independent of coupling of the longitudinal and transverse waves at inception and are determined by plate thickness and only one of the bulk waves. Critical frequency is defined as that value when the Lamb waves are strictly standing waves along z. They subsequently become coupled as the waves travel. In the following, the waves are monochromatic with wave number k_x and angular frequency ω. This leads to expressions for the potential functions

$$\varphi(x,z)=\Phi(z)e^{i(k_x x-\omega t)}, \tag{1}$$

$$\psi(x,z)=\Psi(z)e^{i(k_x x-\omega t)}, \tag{2}$$

where separability of the coordinates is used. These expressions are subject to the boundary conditions at the plate boundaries. The wave numbers for the transverse and compressional modes along the z axis are $S_z^2=k_x^2-K_T^2$ and $Q_z^2=k_x^2-K_L^2$, respectively. Here, L designates the longitudinal and T the transverse wave. The most general solutions are

$$\varphi(x,z)=\{A_s ch(zQ_z)+B_a sh(zQ_z)\}e^{i(k_x x-\omega t)}, \tag{3a}$$

$$\psi(x,z)=\{C_s ch(zS_z)+D_a sh(zS_z)\}e^{i(k_x x-\omega t)}, \tag{3b}$$

where *ch* and *sh* may be cos, or cosh and sin, or sinh, respectively, depending on their arguments. The plate has thickness $h=2d$. The conditions for the normal stress and for the transverse traction—each of which is zero for an exterior vacuum—yield two independent expressions, one symmetric and the other antisymmetric relative to the zero planes. This procedure conveniently leads to independent dispersion equations for the phase velocities for each of the symmetries. Only the symmetric equation is required in this analysis, and it is

$$(k_x^2+S_z^2)^2 sh(S_z d)ch(Q_z d)-4k_x^2 S_z Q_z cs(S_z d)ch(Q_z d)=0. \tag{4}$$

The expression for the eigenvalue or dispersion equation for the symmetric mode may be obtained from Eq. (4). There are two considerations in this analysis, which are referred to as case I and case II, and are related to the allowed range of V_x. We use the following notation:

$$B_L=\sqrt{1-(V_L/V_x)^2} \quad \text{and} \quad B_T=\sqrt{1-(V_T/V_x)^2}.$$

The expressions are then

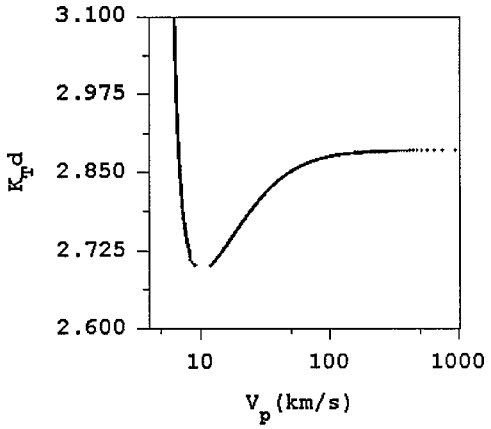

FIG. 1. Turning point of $K_T d$ with respect to V_p for anomalous S_1 Lamb wave for free steel plate.

Case I $V_x>V_L$:

$$(V_x/V_T)^2(2(V_T/V_x)^2-1)^2\tan(hf\pi B_T/V_T)/B_T = -4(V_T/V_L)B_L \tan(hf\pi B_L/V_L). \tag{5}$$

Case II $V_L>V_x>V_T$:

$$(V_x/V_T)^2(2(V_T/V_x)^2-1)^2\tan(hf\pi B_T/V_T)/B_T = 4(V_T/V_L)B_L \tanh(hf\pi B_L/V_L). \tag{6}$$

III. ANALYSIS OF PROPER S_1 LAMB MODES

The critical frequency of a proper symmetric Lamb mode corresponds to the situation where it forms a standing wave in the z direction. This occurs when k_x is zero so that $V_x=\omega/k_x$ is infinite. This can happen for the symmetric wave when either[3]

$$hf/V_L=(2n-1)/2, \tag{7a}$$

or

$$hf/V_T=m, \tag{7b}$$

where n and m are positive integers. The phase velocities of the proper symmetric Lamb modes become smaller as frequency increases with a limit approaching the value of the transverse wave velocity. The critical frequency has the same conditions as other Lamb modes. However, the S_1 wave exists at values of $K_T d$ below critical frequency—refer to Fig. 1. The phase velocity V_p approaches infinity at critical frequency, but then assumes a negative slope and the value of $K_T d$ is actually required to go below critical frequency. Its value then begins to increase at the point that the slope reverses direction. The value of $K_T d$ again passes through critical frequency and V_x is a double-valued function of $K_T d$ for part of the domain of existence. This is illustrated in Fig. 1. It will be demonstrated that this happens for all elastic materials for the S_1 mode. It is easy to see that the critical frequency for S_1 modes occurs when $hf/V_L=1/2$, for $V_L<2V_T$. Otherwise, it occurs when $hf/V_T=1$. In either case, one of the conditions defines the S_1 Lamb mode and the other the S_2 Lamb mode. The fact that they may be generated by either bulk wave at critical frequency has no bearing on the nature of that mode. The effect is still a characteristic

of the S_1 Lamb mode. As one approaches critical frequency for the symmetric Lamb mode one has to a good approximation

$$(V_x/V_T)^2\tan(hf\pi/V_T)\cong -4(V_T/V_L)\tan(hf\pi/V_L), \quad (8)$$

for large values of V_x. Note that B_L and B_T both approach unity here. For the case when $V_L<2V_T$, S_1 is initiated when $hf/V_L=1/2$ to ensure that it approaches infinity as V_x approaches infinity. The right-hand side (rhs) then goes from a negative number to a positive number. However, the left-hand side (lhs) remains negative since tan is in a negative quadrant and it remains so (while V_x is still very large) for small increases of hf while $hf/V_T=V_L/2V_T<1$. This means that if hf is slightly increased just after critical frequency, then the rhs of Eq. (8) becomes positive while the lhs remains negative. That would require an unacceptable imaginary value for V_x. Thus, hf/V_L may only decrease while V_x is still large, since then the lhs and the rhs both have the same signs. With decreasing phase velocities B_L and B_T decrease sufficiently so that finally hf may increase again, since hfB_L/V_L remains suitably small for the tan to remain in the required quadrant. Below, we will demonstrate that the arguments of all symmetric Lamb modes remain in the same quadrants until $V_x=V_L$ and there is a transition to case II. On the other hand, if $V_L>2V_T$ the arguments to establish the anomalous nature of the S_1 are quite similar. Then, $hf/V_T=1$ in order to account for the infinite value of V_x. However, since $V_T/V_L<1/2$ and the rhs is still in the positive quadrant, while the lhs enters quadrant 3 which is also positive, once again there will be an imbalance in signs. Again, this can be rectified if hf/V_T is forced to be smaller after critical frequency so that the argument of the tan on the rhs remains in a negative quadrant, and the balance in signs is maintained. As the phase velocity decreases, B_L and B_T become sufficiently small and hf/V_T may increase while hfB_T/V_T remains in the required quadrant for tan to have the value to maintain sign balance. In the following, we explain why this happens for the S_1 Lamb mode for all elastic materials. Moreover, for symmetric Lamb modes it is easy to show that this may happen again for materials for which

$$\frac{V_L}{V_T}=\frac{2m}{2n-1}, \quad (9)$$

where n and m are positive integers and $n\leqslant m$. It is interesting that this is a rational number that is a ratio of even integers to odd integers, and when this is not satisfied, the effect will never occur again for symmetric Lamb modes. The next section deals with the simplest condition, $V_L=2V_T$.

IV. THE BIFURCATION OF SYMMETRIC WAVES WHEN $2V_T=V_L$

When a material has the property $2V_T=V_L$, all of the Lamb modes generated by the longitudinal bulk waves have the same critical frequencies as alternate symmetric Lamb modes generated by the transverse bulk wave [when m is odd in Eq. (7b)]. The condition required for both waves to occur is that a sign balance is maintained. This happens when one of the waves has a value of hf that constrains each of the tan to remain in quadrants of opposite sign. Thus, hf is required to increase for one of the waves and to decrease for the other. Symmetric modes interfere and are members of the same space; they must exist in separate quadrants after inception in order not to violate orthogonality. This requirement to enter adjacent quadrants is the origin of the bifurcation. The modes S_{3n}, where n is a positive integer, do not form bifurcated pairs with other symmetric modes for this case. However, an examination of the antisymmetric modes indicates that these modes have the same critical frequency as all A_{3n} antisymmetric modes. Thus, for this example S_3 and A_3 have the same critical frequencies. Since these modes are independent, it is not expected that either will influence the other. However, when $V_L\leqslant 2V_T$, then the same analysis used here indicated that the A_{3n} antisymmetric modes are anomalous. Thus, we find the remarkable fact that for materials with $\nu=1/3$ all symmetric Lamb modes are bifurcated and one of the pairs is anomalous.

V. THE ATYPICAL BEHAVIOR OF THE GROUP VELOCITY OF ANOMALOUS LAMB MODES

A plot of K_Td vs V_x exhibits a minimum for K_T for the S_1 modes with respect to V_x. This is a stationary point of K_T with respect to V_x, since then $dK_T/dV_x=0$. Others have reported a calculated negative group velocity for the S_1 mode around critical frequency for plates[3,9,10] and for shells.[12–16] To avoid the apparent absurdity that energy flows towards its source, some authors suggest that it merely means that phase and group velocity are out of phase,[3,9] and one suggests that it really means that it is the phase velocity that is negative.[9] Others object to the notion of a negative group velocity.[6–8] Recall that the standard expression of group velocity

$$V_{gx}=d\omega/dk_x, \quad (10)$$

is inferred from the first term of the asymptotic expansion of the time-domain solution[17]

$$\psi(t)=\psi(t_0)\frac{e^{\pm i\pi/4}e^{i(r-td\omega/dk_x)}}{\sqrt{tdV_{gx}/dk_x}}. \quad (11)$$

It is to be remembered that K_T is directly proportional to ω, while k_x is a function of its respective mode. Clearly, because $k_x=0$ at critical frequency and V_x is a maximum, Eq. (10) then leads to a positive number for increasing ω and a negative number for decreasing ω on either side of the critical frequency. Equation (11) is an approximate solution in the time domain under suitable conditions. One consequence of it is that as long as $r-d\omega/dk_xt=0$ one can identify $d\omega/dk_x$ with the rate of energy flow in time, commonly referred to as group velocity, V_{gx}. To determine the validity of Eq. (11) in the region of interest, one can show that $dK_T/dV_x=(V_{gx}/V_T)dk_x/dV_x$ in this region, since $dk_x/dV_x>0$ and $dK_T/dV_x<0$ until the minimum, after which $dK_T/dV_x>0$. Thus, V_{gx} ranges from zero through a negative value and again through zero to a positive value and thus goes through a minimum over part of the region where it is negative. One may deduce from this that when there is anomalous dispersion, $dV_{gx}/dk_x=0$ at some point over the

range between $k_x=0$ and $dk_x/dV_x=0$. This indicates that Eq. (11) is not valid in this range. (Note that the statement is that group velocity is stationary with respect to k_x and not K_T.) Clearly identifying $d\omega/dk_x$ with the rate of energy flow is simply not a useful statement when Eq. (11) is not valid. The next order of approximation is[17]

$$\Psi(t)=\frac{1}{\sqrt{2\pi}}e^{i(k_0r-\omega_0t)}\int_{-\infty}^{\infty}\psi(\bar{k})e^{i(x\bar{k}-y\bar{k}^3)}d\bar{k}. \tag{12}$$

This expression is not useful to infer a rate of energy flow. Indeed, since the amplitude is under the integral, it then is referred to as amplitude modulated.

VI. INITIAL RAPID FALLOFF OF THE PHASE VELOCITY FOR THE S_1 MODE

The S_1 phase velocity falls off more rapidly than the usual Lamb modes. One may ascertain that the argument of the tangent function on the rhs of Eq. (8) is constrained to be less than $\frac{1}{2}$ for case I

$$\frac{hf}{V_L}\sqrt{1-(V_L/V_x)^2}<1/2. \tag{13}$$

To derive an approximate expression for the S_1 phase velocity after critical frequency, the two sides may be approximately equated after critical frequency $hf/V_L\approx 1/2$ and one obtains an approximate expression for $V_x>V_L$ when $V_L<2V_T$

$$\frac{V_x}{V_T}=\frac{2V_Lhf}{V_T\sqrt{4(hf)^2-V_L^2}}, \tag{14}$$

or

$$\frac{V_x}{V_T}=\frac{hf}{\sqrt{(hf)^2-V_T^2}}, \tag{15}$$

when $V_L>2V_T$. These expressions are not valid when $V_x<V_L$, but they are useful to account for the rapid falloff of the phase velocity of the S_1 mode.

VII. THE BROAD PLATEAU REGION FOR SYMMETRIC MODES

It has been noted that the dispersion curves of the symmetric Lamb modes reach a plateau or flat region in phase velocity for thin plates and shells[18] over a finite range of frequency before undergoing a sharp decrease in value, after which they approach their asymptotic limit. It is obvious that this occurs when $V_x=V_L$, so that $hfB_T/V_T=m$ where m is a positive integer. This leads to the condition

$$k_Td=hf\pi/V_T=m\pi\sqrt{2(1-\nu)}, \tag{16}$$

where the integer $m\geqslant 1$. All symmetric Lamb modes (assuming thin plates) exhibit the plateau region and this offers one a method for determining the compressional velocity. It is easy to see that prior to this transition region the arguments of the tan functions (case I) must remain in the same quadrants since once the quadrants are set any transition on the rhs will cause a sign change. The only transition allowed is when $V_x=V_L$. After this transition the rhs is always positive and case II applies. This means that the lhs remains positive too, or that the argument of the tangent function stays in the same positive quadrant

$$hf\pi\sqrt{1-(V_T/V_x)^2}/V_T\leqslant m\pi/2. \tag{17}$$

This leads to the approximate expression for V_x for suitably high hf

$$V_x\approx\frac{2hfV_T}{\sqrt{(2hf)^2-m^2V_T^2}}. \tag{18}$$

Expression (18) may be used to show that the phase velocity of proper symmetric Lamb modes approaches the transverse velocity as hf approaches a large number.

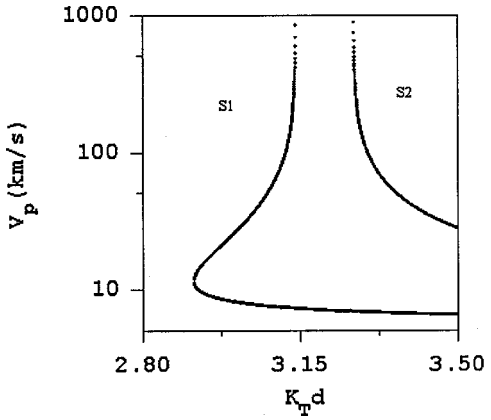

FIG. 3. Comparison of the S_1 and S_2 Lamb modes on a steel plate.

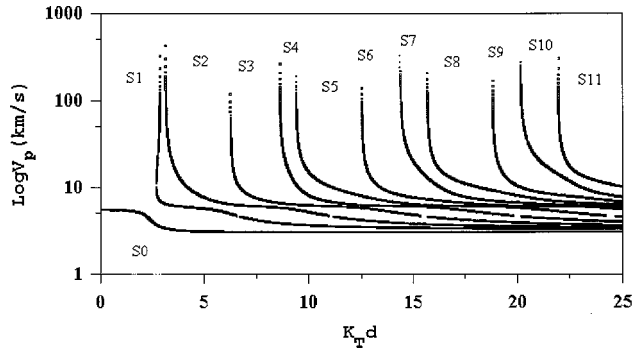

FIG. 2. First 12 symmetric Lamb modes on a steel plate ($V_L=5.95$ km/s, $V_T=3.24$ km/s).

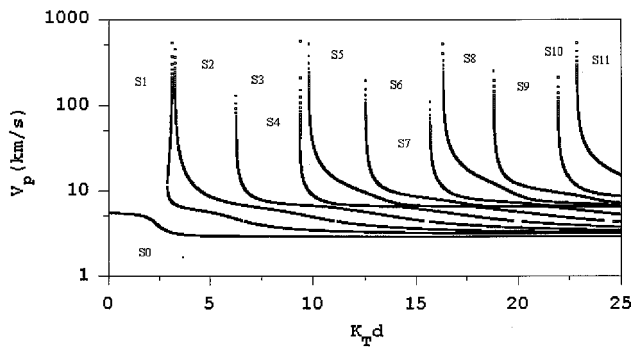

FIG. 4. First 12 symmetric Lamb modes on an aluminum plate ($V_L=6.35$ km/s, $V_T=3.05$ km/s).

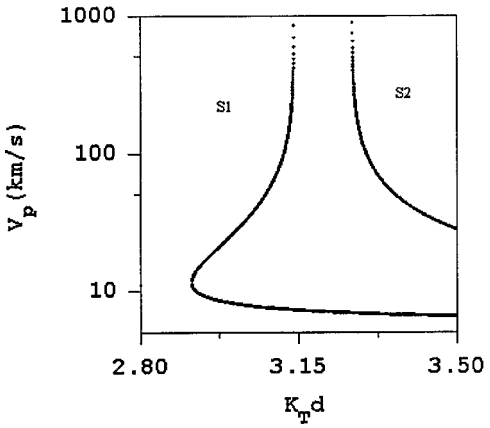

FIG. 5. Comparison of the S_1 and S_2 Lamb modes on an aluminum plate.

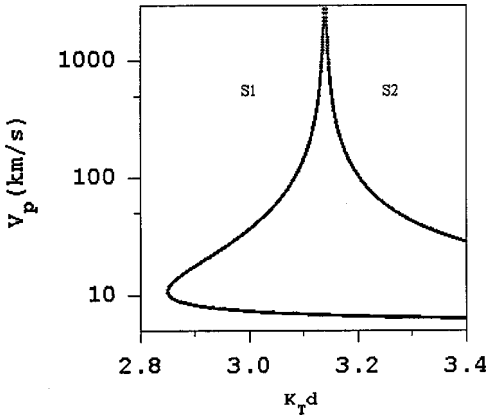

FIG. 7. Comparison of the S_1 and S_2 Lamb modes on a nickel plate.

VIII. EXAMPLES OF CALCULATION AND PREDICTION

The symmetric Lamb modes for steel ($V_L<2V_T$), aluminum ($V_L>2V_T$), and nickel ($V_L=2V_T$) are analyzed here. Figure 2 illustrates the first 12 symmetric Lamb modes for a thin steel plate. Here, the critical frequency for S_1 is defined by Eq. (7a), which is related to the compressional bulk wave, and S_2 by Eq. (7b) related to the transverse bulk wave. One sees that out to mode 12 no other symmetric Lamb modes have the peculiar property of the S_1 mode. Figure 3 compares the S_1 and S_2 Lamb modes and demonstrates the anomalous behavior of the S_1 mode for steel. Figure 4 illustrates the first 12 symmetric Lamb modes for aluminum. Here, the transverse bulk wave generates S_1 while S_2 is generated by the longitudinal bulk wave. These two modes are illustrated in Fig. 5. The dispersion curves for steel and aluminum are quite similar. Figure 6 illustrates the first 12 symmetric Lamb modes for nickel, where $V_L=6$ km/s$=2$ V_T. It is clear that when $2n-1=m$ [see Eqs. (7a) and (7b)], pairs of Lamb modes have the same critical frequency and initially appear as one wave. After inception, the wave then bifurcates leading to two modes as predicted in the main text. One is the initial frequency-modulated mode, while the other is a normal Lamb mode. These waves separate since no two symmetric Lamb modes can occupy the same quadrants at the same frequency, because orthogonality would be violated otherwise. Indeed $S_1,S_4,S_7,S_{10},\ldots,$ are all frequency-modulated waves while their counterparts $S_2,S_5,S_8,S_{11},\ldots,$ are normal waves. For that case the modes S_{3n} are not members of the bifurcated symmetric waves, but interestingly, they have the same critical frequency as the A_{3n} modes, which for this case appear to be anomalous. Figures 7 and 8 illustrate examples of these waves for S_1 and S_2 and for S_4 and S_5. One may observe the symmetric plateau in all of the calculations, which confirms Eq. (16) and their occurrence[18] when $V_x=V_L$. For completeness, we illustrate in Fig. 9 the first 12 symmetric wave group velocities for steel. Note that the values of the group velocities of the proper Lamb modes peak in the region where the symmetric plateaus occur (as should be expected). At critical frequency the group velocities are zero, since a standing wave transfers no energy. One observes a minimum corresponding to a point of rapid falloff of the phase velocity. The group velocities are seen to have asymptotic values corresponding to the transverse bulk velocity as expected.

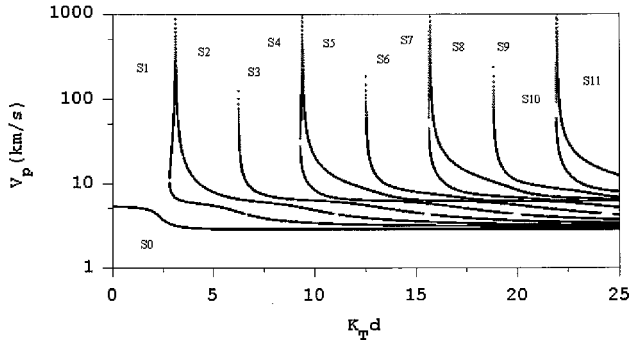

FIG. 6. First 12 symmetric Lamb modes on a nickel plate ($V_L=6$ km/s, $V_T=3$ km/s).

XI. SUMMARY

In this study, it is shown that the S_1 mode is always an anomalous Lamb mode. The reason for this is explained in terms of the arguments of the tan of the plate equations that are constrained to specific quadrants. It is further shown that there are an infinite number of such waves when $V_L/V_T=2m/(2n-1)$ for symmetric modes. The particular case of $V_L/V_T=2$ ($\nu=1/3$) was calculated for nickel in which all symmetric Lamb modes are bifurcated, with the class S_{3n}

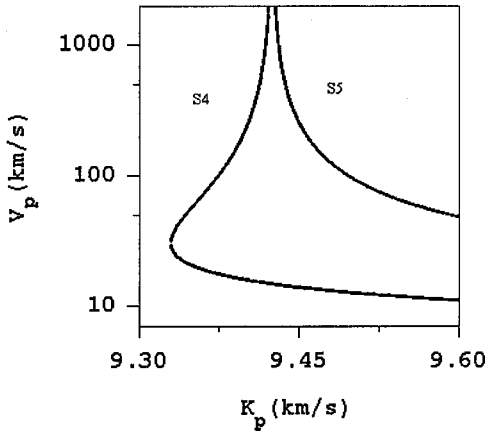

FIG. 8. Comparison of the S_4 and S_5 Lamb modes on a nickel plate.

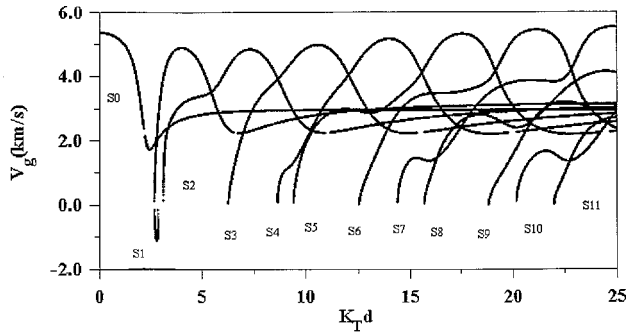

FIG. 9. Group velocities for the first 12 symmetric Lamb modes on a steel plate ($V_L = 5.95$ km/s, $V_T = 3.24$ km/s).

associated with the A_{3n} modes in which the paired mode A_{3n} is an anomalous Lamb mode. If one accepts the arguments here, the expression for group velocity that predicts a negative value is simply not applicable in the small range in wave numbers where the Lamb modes are anomalous, and that the mode is amplitude modulated in time for that range. Further, there is a departure in analogy between a fluid waveguide and the anomalous Lamb mode, since the cutoff value for a fluid waveguide is the same as that for critical frequency, but the cutoff value for the anomalous Lamb mode falls below critical frequency and is to restate the case double valued in that range. Simple expressions are derived that illustrate certain features of the symmetric Lamb modes. The symmetric plateau and its origin were examined. An expression for the location of the symmetric plateau [Eq. (16)] is easily seen to apply to the dispersion curves. These ultrasonic modes have value in nondestructive testing since they are sensitive to the makeup of a material and can signal aberrations. Some of the results may also be used in target identification when applied to fluid-loaded shells.

ACKNOWLEDGMENTS

We are greatly indebted to the Acoustics Division under the leadership of Dr. E. Franchi of NRL Code 7100, as well as the director of NRL, Dr. T. Coffey, and the Office of Naval Research for the continued funding of this research.

[1] Lord Rayleigh, Proc. London Math. Soc. **20**, 225 (1889).
[2] H. Lamb, Proc. R. Soc. London, Ser. A **93**, 114 (1917).
[3] I. A. Viktorov, *Rayleigh and Lamb Waves* (Plenum, New York, 1967).
[4] W. R. Hamilton, Proc. R. Irish Acad. **1**, 267 (1830); **1**, 341 (1830).
[5] Lord Rayleigh, *Theory of Sound*, 2nd ed. (1894).
[6] M. Laue, Ann. Phys. (Leipzig) **18**, 523 (1905).
[7] A. Sommerfeld, ''Festschrift zum 70. *Geburtstage von Heinrich Weber*'' (Teubner, Leipzig, 1912); A. Sommerfeld, ''About the propagation of light in dispersive media,'' Ann. Phys. (Leipzig) **44**, 177 (1914).
[8] L. Brillouin, *Wave Propagation and Group Velocity* (Academic, New York, 1960).
[9] I. Tolstoy and E. Usdin, ''Wave propagation in elastic plates: Low and high mode dispersion,'' J. Acoust. Soc. Am. **29**, 37 (1957).
[10] J. Wolf, T. D. K. Nook, R. Kille, and W. G. Mayer, ''Investigation of Lamb waves having a negative group velocity,'' J. Acoust. Soc. Am. **83**, 122 (1988).
[11] A. Bernard, M. J. S. Lowe, and M. Deschamps, ''Guided waves energy velocity in absorbing and nonabsorbing plates,'' J. Acoust. Soc. Am. **110**, 186–196 (2001).
[12] M. F. Werby, ''Recent developments in scattering from submerged elastic and rigid objects,'' in *Acoustic Resonance Scattering*, edited by H. Überall (Gordon and Breach Science, New York, 1992), pp. 277–304.
[13] M. F. Werby and M. K. Broadhead, ''Study of higher order Lamb resonances on elastic shells: Their prediction and interpretation,'' in *SPIE Proc. Automatic Object Recognition II*, Vol. 1700, April 1992, pp. 341–349.
[14] H. B. Ali and M. F. Werby, ''The importance of the symmetric Lamb wave and high-frequency scattering from spherical shells,'' in *SPIE Proc. Automatic Object Recognition II*, Vol. 1700, April 1992, pp. 350–359.
[15] G. Kaduchak, D. H. Hughes, and P. Marston, ''Enhancement of the backscattering of high-frequency tone bursts by thin spherical shells associated with backward wave: Observation and ray approximation,'' J. Acoust. Soc. Am. **96**, 3704 (1994).
[16] G. Kaduchak and P. Marston, ''Traveling wave decomposition of surface displacements associated with scattering by a cylindrical shell: Numerical evaluation displaying guided forward and backward wave properties,'' J. Acoust. Soc. Am. **98**, 3501 (1995).
[17] I. Tolstoy and C. S. Clay, *Ocean Acoustics* (McGraw-Hill, New York, 1966), pp. 40–48.
[18] H. Überall, B. Hosten, M. Deschamps, and A. Gérard, ''Repulsion of phase-velocity dispersion curves and the nature of plate vibrations,'' J. Acoust. Soc. Am. **96**, 908 (1994).

Free interfacial vibrations in cylindrical shells

Julius D. Kaplunov[a)]
Department of Mathematics, University of Manchester, Oxford Road, Manchester M13 9PL, United Kingdom

Maria V. Wilde
Department of Mathematical Theory of Elasticity and Biomechanics, Saratov State University, Astrakhanskaya str. 83, Saratov 410601, Russia

(Received 12 July 2001; revised 28 February 2002; accepted 12 March 2002)

The 2D equations in the Kirchhoff–Love theory are subjected to asymptotic analysis in the case of free interfacial vibrations of a longitudinally inhomogeneous infinite cylindrical shell. Three types of interfacial vibrations, associated with bending, super low-frequency semi-membrane, and extensional motions, are investigated. It is remarkable that for extensional modes natural frequencies have asymptotically small imaginary parts caused by a weak coupling with propagating bending waves. Bending and extensional vibrations correspond to Stonely-type plate waves, while semi-membrane ones are strongly dependent on shell curvature and do not allow flat plate interpretation. The paper represents generalization of the recent authors' publication [Kaplunov *et al.*, J. Acoust. Soc. Am. **107**, 1383–1393 (2000)] dealing with edge vibrations of a semi-infinite cylindrical shell. [DOI: 10.1121/1.1474442]

PACS numbers: 43.40.Ey [JGM]

I. INTRODUCTION

For many years localized vibrations of elastic bodies have been studied for massive solids of rectangular or cylindrical shape (e.g., see Refs. 1–4). The associated phenomenon is often referred to as an edge resonance.

Recently the theory of edge vibrations has been proposed for semi-infinite shells.[5] The consideration in Ref. 5 starts from asymptotic analysis of free localized vibrations in the framework of the Kirchhoff–Love theory of shells. Apparently for the first time the link between edge vibrations and Rayleigh-type extensional and bending surface waves has been established. Three types of localized vibrations (bending vibrations, extensional vibrations, and super-low-frequency semi-membrane vibrations) have been revealed. Short-wavelength limits for bending and extensional vibrations correspond to bending and extension of a semi-infinite plate with certain mixed boundary condition on faces. It is interesting that for extensional vibrations natural frequencies possess asymptotically negligible imaginary parts caused by radiation into infinity with small-amplitude bending waves coupled with the sought for extensional ones. For semi-membrane vibrations the effect of the shell curvature is essential and they cannot be treated in terms of flat plate vibrations.

In this paper we extend the approach of Ref. 5 to infinite longitudinally inhomogeneous cylindrical shells (Fig. 1). The dynamic equations in the Kirchhoff–Love theory of shells are subjected to asymptotic study as the relative thickness tends to zero. The boundary conditions at the interface simulate perfect contact. The results obtained for interfacial vibrations are similar in a sense to those for edge vibrations. The main difference is that interfacial dynamic phenomena are very sensitive to material parameters. In particular, semi-membrane interfacial vibrations only occur provided that the lowest critical frequencies for both materials coincide. In the case of bending and extensional vibrations the effect of material parameters is similar to that for relevant Stonely-type plate waves.

To our best knowledge only two papers deal with interfacial vibrations. Reference 6 is concerned with reflection of Lamb waves at the interface of longitudinally inhomogeneous plate with traction free faces. Other authors' recent publication (see Ref. 7) includes elements of a theoretical consideration for short-wavelength extensional and bending vibrations of shells of revolution. Analysis in Ref. 7 is completed below by deriving asymptotic formulas for semi-membrane vibrations specific only for cylindrical shells as well as estimates for imaginary parts of natural frequencies in the case of extensional vibrations. In addition, the present paper contains numerical results justifying proposed asymptotic formulas.

II. STATEMENT OF THE PROBLEM

Consider free harmonic vibrations of an infinite inhomogeneous circular cylindrical shell composed of two semi-infinite homogeneous shells welded at the material interface (Fig. 1). Let the mid-surface of the shell be referred to the coordinates (s,θ), where s $(-\infty<s<\infty)$ is the meridian arc length and θ $(0\leqslant\theta<2\pi)$ is the angular coordinate. The parallel $s=0$ corresponds to the interface. We also introduce the dimensionless variable $\xi=s/R$ $(-\infty<\xi<\infty)$, where R is the radius of the mid-surface. Below we mark all the quantities

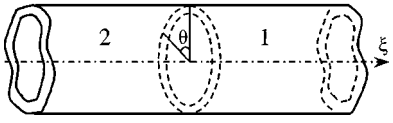

FIG. 1. Longitudinally inhomogeneous infinite cylindrical shell.

[a)]Electronic mail: kaplunov@ma.man.ac.uk

related to the right shell ($0\leqslant\xi<\infty$) by the superscript "1," and those related to the left shell ($-\infty<\xi\leqslant 0$) by the superscript "2." In particular, $E^{(k)}$ ($k=1,2$) is the Young modulus, $\rho^{(k)}$ ($k=1,2$) is the mass density, and $\nu^{(k)}$ ($k=1,2$) is the Poisson ratio.

Let us assume that vibrations of the shell are described by the Kirchhoff–Love theory of shells[8] and write out the equations of motion in terms of displacements. They are

$$\begin{aligned}
&\frac{d^2u^{(k)}}{d\xi^2}-\frac{1}{4}\,\nu_4^{(k)}n^2u^{(k)}-\frac{1}{4}\,\nu_1^{(k)}n\,\frac{dv^{(k)}}{d\xi}-\nu^{(k)}\frac{dw^{(k)}}{d\xi}\\
&\quad+\nu_2^{(k)}q^{(k)}\lambda u^{(k)}=0,\\
&\frac{1}{4}\,\nu_1^{(k)}n\,\frac{du^{(k)}}{d\xi}+\frac{1}{4}\,\nu_4^{(k)}\frac{d^2v^{(k)}}{d\xi^2}-n^2v^{(k)}\\
&\quad+\frac{1}{3}\,\eta^2\left[\nu_4^{(k)}\frac{d^2v^{(k)}}{d\xi^2}-n^2v^{(k)}\right]-nw^{(k)}\\
&\quad+\frac{1}{3}\,\eta^2n\left(\nu_3^{(k)}\frac{d^2w^{(k)}}{d\xi^2}-n^2w^{(k)}\right)+\nu_2^{(k)}q^{(k)}\lambda v^{(k)}=0, \qquad (1)\\
&-\nu^{(k)}\frac{du^{(k)}}{d\xi}+nv^{(k)}-\frac{1}{3}\,\eta^2n\left(\nu_3^{(k)}\frac{d^2v^{(k)}}{d\xi^2}-n^2v^{(k)}\right)\\
&\quad+w^{(k)}+\frac{1}{3}\,\eta^2\left[\frac{d^4w^{(k)}}{d\xi^4}-2n^2\frac{d^2w^{(k)}}{d\xi^2}+n^4w^{(k)}\right]\\
&\quad-\nu_2^{(k)}q^{(k)}\lambda w^{(k)}=0
\end{aligned}$$

with

$$\begin{aligned}
&\lambda=\frac{\rho^{(1)}\omega^2R^2}{E^{(1)}}, \quad \eta=\frac{h}{R}, \quad q^{(k)}=\frac{E^{(1)}\rho^{(k)}}{E^{(k)}\rho^{(1)}},\\
&\nu_1^{(k)}=2(1+\nu^{(k)}), \quad \nu_2^{(k)}=1-\nu^{(k)^2},\\
&\nu_3^{(k)}=2-\nu^{(k)}, \quad \nu_4^{(k)}=2(1-\nu^{(k)}),
\end{aligned}$$

where $u^{(k)}$ and $v^{(k)}$ are the tangential displacements of the mid-surface along the axes ξ and θ, respectively, $w^{(k)}$ is the transverse displacement of the mid-surface, λ is the dimensionless frequency parameter, ω is the circular frequency, $2h$ is the thickness, η is the small geometrical parameter, and $n=0,1,2,...$ is the circumferential wave number.

In Eqs. (1) the angular coordinate is separated by the formulas

$$\begin{aligned}
&u^{(k)}(\xi,\theta)=u^{(k)}(\xi)\sin n\theta, \quad v^{(k)}(\xi,\theta)=v^{(k)}(\xi)\cos n\theta,\\
&w^{(k)}(\xi,\theta)=w^{(k)}(\xi)\sin n\theta,
\end{aligned}$$

and the term $\exp(i\omega t)$, expressing time dependence, is suppressed.

We impose at $\xi=0$ contact conditions corresponding to perfect contact. They are

$$\begin{aligned}
&u^{(1)}-u^{(2)}=0, \quad v^{(1)}-v^{(2)}=0, \quad w^{(1)}-w^{(2)}=0,\\
&\frac{dw^{(1)}}{d\xi}-\frac{dw^{(2)}}{d\xi}=0, \qquad (2)\\
&T_1^{(1)}-T_1^{(2)}=0, \quad S_{12}^{(1)}+H_{12}^{(1)}-(S_{12}^{(2)}+H_{12}^{(2)})=0,\\
&M_1^{(1)}-M_1^{(2)}=0, \quad N_1^{(1)}+nH_{12}^{(1)}-(N_1^{(2)}+nH_{12}^{(2)})=0
\end{aligned}$$

with

$$\begin{aligned}
&T_1^{(k)}=\frac{1}{\nu_2^{(k)}\gamma^{(k)}}\left(\frac{du^{(k)}}{d\xi}-\nu^{(k)}nv^{(k)}-\nu^{(k)}w^{(k)}\right),\\
&S_{12}^{(k)}+H_{12}^{(k)}=\frac{1}{\nu_1^{(k)}\gamma^{(k)}}\left(nu^{(k)}+\frac{dv^{(k)}}{d\xi}\right.\\
&\qquad\left.+\frac{2}{3}\,\eta^2\left(\frac{dv^{(k)}}{d\xi}+n\,\frac{dw^{(k)}}{d\xi}\right)\right),\\
&M_1^{(k)}=\frac{\eta^2}{3\nu_2^{(k)}\gamma^{(k)}}\left(-\nu^{(k)}nv^{(k)}+\frac{d^2w^{(k)}}{d\xi^2}-\nu^{(k)}n^2w^{(k)}\right), \qquad (3)\\
&N_1^{(k)}+nH_{12}^{(k)}=-\frac{\eta^2}{3\nu_2^{(k)}\gamma^{(k)}}\\
&\qquad\times\left(-\nu_3^{(k)}n\,\frac{dv^{(k)}}{d\xi}+\frac{d^3w^{(k)}}{d\xi^3}-\nu_3^{(k)}n^2\frac{dw^{(k)}}{d\xi}\right),\\
&\gamma^{(k)}=\frac{E^{(1)}}{E^{(k)}}, \quad \nu_3^{(k)}=2-\nu^{(k)},
\end{aligned}$$

where $T_1^{(k)}$ is the longitudinal stress resultant, $S_{12}^{(k)}$ is the membrane shear force, $M_1^{(k)}$ is the bending stress couple, $H_{12}^{(k)}$ is the twisting stress couples, and $N_1^{(k)}$ is the transverse shear force. The dimensionless quantities above are expressed in terms of their dimension analogs as

$$\begin{aligned}
&\{T_1^{(k)},S_{12}^{(k)},N_1^{(k)}\}=\frac{R}{2E^{(1)}h}\cdot\{\tilde{T}_1^{(k)},\tilde{S}_{12}^{(k)},\tilde{N}_1^{(k)}\},\\
&\{M_1^{(k)},H_{12}^{(k)}\}=\frac{1}{2E^{(1)}h}\{\tilde{M}_1^{(k)},\tilde{H}_{12}^{(k)}\},
\end{aligned}$$

where the dimension quantities are marked by "$\sim$."

In this paper we require only the leading order decay as $|\xi|\to\infty$. In doing so, we allow also small-amplitude waves propagating from $\xi=0$ to infinity.

The exact solution of the problems (1) and (2) is presented in Appendix. It is utilized below only for testing of efficiency of asymptotic expansions.

III. AN ASYMPTOTIC ANALYSIS

Let us analyze the problem (1) and (2) as $\eta\to 0$. We present the parameters n and λ as

$$n\sim\eta^{-q}, \quad \lambda\sim\eta^{-2a} \qquad (4)$$

and assume that the quantities q and a satisfy the inequalities

$$0\leqslant q<1, \quad a<1.$$

These inequalities define the range of applicability of the Kirchhoff-Love theory of shells expressed in terms of a wavelength (the first inequality) and a frequency (the second inequality).[9] They state that a wavelength is much greater than the thickness of the shell and the period of vibration exceeds considerably the time elastic waves take to propagate the distance between the faces of the shell.

TABLE I. Types of vibrations and corresponding asymptotic behaviors.

Type of vibrations	Asymptotic behaviors
Bending vibrations	$a=2q-1,\ \frac{1}{2}\leqslant q<1$ Asymptotic behavior 1.1: $\partial/\partial\xi\sim\eta^{-q},\ u\sim\eta^{q},\ v\sim\eta^{q},\ w\sim\eta^{0},$ $T_1\sim\eta^{0},\ S_{12}\sim\eta^{0},\ M_1\sim\eta^{2-2q},$ $H_{12}\sim\eta^{2-2q},\ N_1\sim\eta^{2-3q}$ Asymptotic behavior 1.2: $\partial/\partial\xi\sim\eta^{-q},\ u\sim\eta^{2-3q},\ v\sim\eta^{2-3q},\ w\sim\eta^{0},$ $T_1\sqcap\eta^{2-2q},\ S_{12}\sim\eta^{2-4q},\ M_1\sim\eta^{2-2q},$ $H_{12}\sim\eta^{2-2q},\ N_1\sim\eta^{2-3q}$
Super-low-frequency semi-membrane vibrations	$a=2q-1,\ 0\leqslant q<\frac{1}{2}$ Asymptotic behavior 2.1: $\partial/\partial\xi\sim\eta^{1/2-2q},\ u\sim\eta^{1/2},\ v\sim\eta^{q},\ w\sim\eta^{0},$ $T_1\sim\eta^{1-2q},\ S_{12}\sim\eta^{3/2-3q},\ M_1\sim\eta^{2-2q},$ $H_{12}\sim\eta^{5/2-3q},\ N_1\sim\eta^{5/2-4q}$ Asymptotic behavior 2.2: $\partial/\partial\xi\sim\eta^{-1/2},\ u\sim\eta^{1/2},\ v\sim\eta^{1-q},\ w\sim\eta^{0},$ $T_1\sim\eta^{1-2q},\ S_{12}\sim\eta^{1/2-q},\ M_1\sim\eta,$ $H_{12}\sim\eta^{3/2-q},\ N_1\sim\eta^{1/2}$
Extensional vibrations	$a=q,\ q\geqslant 0$ Asymptotic behavior 3.1: $\partial/\partial\xi\sim\eta^{-q},\ u\sim\eta^{-q},\ v\sim\eta^{-q},\ w\sim\eta^{0},$ $T_1\sim\eta^{-2q},\ S_{12}\sim\eta^{-2q},\ M_1\sim\eta^{2-2q},$ $H_{12}\sim\eta^{2-2q},\ N_1\sim\eta^{2-3q}$ Asymptotic behavior 3.2: $\partial/\partial\xi\sqcap\eta^{-1/2-1/2q},\ u\sim\eta^{1/2+1/2q},\ v\sim\eta^{1},\ w\sim\eta^{0},$ $T_1\sim\eta^{1-q},\ S_{12}\sim\eta^{1/2-1/2q},\ M_1\sim\eta^{1-q},$ $H_{12}\sim\eta^{3/2-3/2q},\ N_1\sim\eta^{1/2-3/2q}$

As for edge vibrations,[5] we start from the traditional asymptotic approach in the shell theories (Refs. 9, 10 and many others). The asymptotic behaviors, corresponding to bending, extensional, and semi-membrane interfacial vibrations, are presented in Table I. Below we exploit the so-called separation method[8] by setting

$$x(\xi)=x_b(\xi)+\eta^{\kappa}x_a(\xi) \tag{5}$$

in Eqs. (1) and (2), where x denotes the unknown quantities $u^{(k)}$, $v^{(k)}$, $w^{(k)}$, $T_1^{(k)}$, $S_{12}^{(k)}$, $H_{12}^{(k)}$, $M_1^{(k)}$, and $N_1^{(k)}$. The quantities with the subscript "b" correspond to solutions possessing the asymptotic behavior 1.1, 2.1, and 3.1 [the basic SSS (strain and stress states) reflecting a general physical idea about each of the three vibration types] while the quantities with the subscript "a" correspond to solutions possessing the asymptotic behavior 1.2, 2.2, and 3.2 (the additional SSS corresponding to shell motions which may occur along with the relevant basic SSS). To determine the quantity κ we should require the consistency of interactive processes when satisfying contact conditions (2).

In common to all the formal asymptotic procedures including consideration of the recent paper in Ref. 5, the relations of this section are justified *a posteriori* by constructing associated expansions. In doing so, we also clarify physical meaning of initial settings.

IV. BENDING VIBRATIONS

The bending vibrations are characterized by $\frac{1}{2}\leqslant q<1$ (see Table I), i.e., they correspond to large values of parameter n. Below we concentrate on the case $q>\frac{1}{2}$ in which the original problem allows the most efficient asymptotic treatment. Taking into account the asymptotic behaviors 1.1 and 1.2 we set

$$\begin{aligned}
&\xi=\eta^{q}\xi_*,\quad n=\eta^{-q}n_*,\quad \lambda=\eta^{2-4q}\lambda_*,\\
&u_{\mathrm{b}}^{(k)}=\eta^{q}u_{\mathrm{b}}^{*(k)},\quad v_{\mathrm{b}}^{(k)}=\eta^{q}v_{\mathrm{b}}^{*(k)},\quad w_{\mathrm{b}}^{(k)}=\eta^{0}w_{\mathrm{b}}^{*(k)},\\
&T_{\mathrm{b1}}^{(k)}=\eta^{0}T_{\mathrm{b1}}^{*(k)},\quad S_{\mathrm{b12}}^{(k)}=\eta^{0}S_{\mathrm{b12}}^{*(k)},\\
&M_{\mathrm{b1}}^{(k)}=\eta^{2-2q}M_{\mathrm{b1}}^{*(k)},\\
&H_{\mathrm{b12}}^{(k)}=\eta^{2-2q}H_{\mathrm{b12}}^{*(k)},\quad N_{\mathrm{b1}}^{(k)}=\eta^{2-3q}N_{\mathrm{b1}}^{*(k)}
\end{aligned} \tag{6}$$

and

$$\begin{aligned}
&u_{\mathrm{a}}^{(k)}=\eta^{2-3q}u_{\mathrm{a}}^{*(k)},\quad v_{\mathrm{a}}^{(k)}=\eta^{2-3q}v_{\mathrm{a}}^{*(k)},\\
&w_{\mathrm{a}}^{(k)}=\eta^{0}w_{\mathrm{a}}^{*(k)},\quad T_{\mathrm{a1}}^{(k)}=\eta^{2-4q}T_{\mathrm{a1}}^{*(k)},\\
&S_{\mathrm{a12}}^{(k)}=\eta^{2-4q}S_{\mathrm{a12}}^{*(k)},\quad M_{\mathrm{a1}}^{(k)}=\eta^{2-2q}M_{\mathrm{a1}}^{*(k)},\\
&H_{\mathrm{a12}}^{(k)}=\eta^{2-2q}H_{\mathrm{a12}}^{*(k)},\quad N_{\mathrm{a1}}^{(k)}=\eta^{2-3q}N_{\mathrm{a1}}^{*(k)},
\end{aligned} \tag{7}$$

assuming that the quantities with the asterisk are of the same asymptotic order and differentiation with respect to the variable ξ_* does not change the asymptotic order of unknowns. By substituting Eqs. (5)–(7) into Eqs. (2) we obtain

$$\begin{aligned}
&\eta^{q}(u_{\mathrm{b}}^{*(1)}-u_{\mathrm{b}}^{*(2)})+\eta^{\kappa+2-3q}(u_{\mathrm{a}}^{*(1)}-u_{\mathrm{a}}^{*(2)})=0,\\
&\eta^{q}(v_{\mathrm{b}}^{*(1)}-v_{\mathrm{b}}^{*(2)})+\eta^{\kappa+2-3q}(v_{\mathrm{a}}^{*(1)}-v_{\mathrm{a}}^{*(2)})=0,\\
&\eta^{0}(w_{\mathrm{b}}^{*(1)}-w_{\mathrm{b}}^{*(2)})+\eta^{\kappa}(w_{\mathrm{a}}^{*(1)}-w_{\mathrm{a}}^{*(2)})=0,\\
&\eta^{-q}\left(\frac{dw_{\mathrm{b}}^{*(1)}}{d\xi_*}-\frac{dw_{\mathrm{b}}^{*(2)}}{d\xi_*}\right)+\eta^{\kappa-q}\left(\frac{dw_{\mathrm{a}}^{*(1)}}{d\xi_*}-\frac{dw_{\mathrm{a}}^{*(2)}}{d\xi_*}\right)=0,\\
&\eta^{0}(T_{\mathrm{b1}}^{*(1)}-T_{\mathrm{b1}}^{*(2)})+\eta^{\kappa+2-4q}(T_{\mathrm{a1}}^{*(1)}-T_{\mathrm{a1}}^{*(2)})=0,\\
&\eta^{0}(S_{\mathrm{b12}}^{*(1)}-S_{\mathrm{b12}}^{*(2)}+O(\eta^{2-2q}))\\
&\quad+\eta^{\kappa+2-4q}(S_{\mathrm{a12}}^{*(1)}-S_{\mathrm{a12}}^{*(2)}+O(\eta^{2q}))=0,\\
&\eta^{2-2q}(M_{\mathrm{b1}}^{*(1)}-M_{\mathrm{b1}}^{*(2)})+\eta^{\kappa+2-2q}(M_{\mathrm{a1}}^{*(1)}-M_{\mathrm{a1}}^{*(2)})=0,\\
&\eta^{2-3q}(N_{\mathrm{b1}}^{*(1)}+n_*H_{\mathrm{b12}}^{*(1)}-(N_{\mathrm{b1}}^{*(2)}+n_*H_{\mathrm{b12}}^{*(2)}))\\
&\quad+\eta^{\kappa+2-3q}(N_{\mathrm{a1}}^{*(1)}+n_*H_{\mathrm{a12}}^{*(1)}-(N_{\mathrm{a1}}^{*(2)}+n_*H_{\mathrm{a12}}^{*(2)}))=0.
\end{aligned} \tag{8}$$

To provide a consistent iterative process we separate Eqs. (8) into two groups: homogeneous contact conditions for the quantities with the subscript "b" and nonhomogeneous contact conditions for the quantities with the subscript "a." It can be easily verified that such a separation occurs provided that $\kappa=4q-2$. As a result, the contact conditions for the basic SSS become

$$\begin{aligned}
&w_{\mathrm{b}}^{*(1)}-w_{\mathrm{b}}^{*(2)}+O(\eta^{4q-2})=0,\\
&\frac{dw_{\mathrm{b}}^{*(1)}}{d\xi_*}-\frac{dw_{\mathrm{b}}^{*(2)}}{d\xi_*}+O(\eta^{4q-2})=0,\\
&M_{\mathrm{b1}}^{*(1)}-M_{\mathrm{b1}}^{*(2)}+O(\eta^{4q-2})=0,\\
&N_{\mathrm{b1}}^{*(1)}+n_*H_{\mathrm{b12}}^{*(1)}-(N_{\mathrm{b1}}^{*(2)}+n_*H_{\mathrm{b12}}^{*(2)})+O(\eta^{4q-2})=0.
\end{aligned} \tag{9}$$

Thus, the initial problem is reduced to a simpler one for the basic SSS. Approximate equations for determining solutions possessing the asymptotic behaviors 1.1 and 1.2 are obtained in Ref. 5. In particular, the equation for the function $w_b^{*(k)}$ is

$$\frac{1}{3}\left(\frac{d^4 w_b^{*(k)}}{d\xi_*^4} - 2n_*^2 \frac{d^2 w_b^{*(k)}}{d\xi_*^2} + n_*^4 w_b^{*(k)}\right) - \nu_2^{(k)} q^{(k)} \lambda_* w_b^{*(k)} + O(\eta^{4q-2}) = 0. \tag{10}$$

Contact problem (10) and (9) coincides with that for bending of an infinite inhomogeneous plate in the classical Kirchhoff theory for certain mixed boundary conditions on its sides (see Refs. 5 and 7).

The solution of Eq. (10) is

$$w_b^{*(k)} = C_1^{(k)} \exp((-1)^k r_{*1}^{(k)} \xi_*) + C_2^{(k)} \exp((-1)^k r_{*2}^{(k)} \xi_*) \tag{11}$$

with

$$r_{*1,2}^{(k)} = \sqrt{n_*^2 \mp (3\nu_2^{(k)} q^{(k)} \lambda_*)^{1/2}}.$$

By substituting Eq. (11) into Eqs. (9) we arrive at a frequency equation. It is

TABLE II. Natural frequencies of bending vibrations.

n	Λ^{ex}	Λ^{as}	ε
25	15.373 733	15.449 667	0.494
26	17.991 575	18.073 925	0.458
27	20.930 051	21.019 101	0.425
28	24.214 313	24.310 350	0.397
29	27.870 460	27.973 775	0.371
30	31.925 541	32.036 429	0.347
31	36.407 554	36.526 315	0.326
32	41.345 446	41.472 384	0.307
33	46.769 113	46.904 536	0.290
34	52.709 399	52.853 622	0.274
35	59.198 099	59.351 441	0.259

$$\begin{vmatrix} 1 & 1 & -1 & -1 \\ r_{*1}^{(1)} & r_{*2}^{(1)} & r_{*1}^{(2)} & r_{*2}^{(2)} \\ f_1^{(1)} & f_2^{(1)} & -f_1^{(2)} & -f_2^{(2)} \\ g_1^{(1)} & g_2^{(1)} & g_1^{(2)} & g_2^{(2)} \end{vmatrix} = 0, \tag{12}$$

where

$$f_i^{(k)} = \frac{r_{*i}^{(k)2} - \nu^{(k)} n_*^2}{\nu_2^{(k)} \gamma^{(k)}}, \quad g_i^{(k)} = \frac{r_{*i}^{(k)} (r_{*i}^{(k)2} - (2-\nu^{(k)}) n_*^2)}{\nu_2^{(k)} \gamma^{(k)}}.$$

Equation (12) corresponds to the dispersion relation for the Stoneley-type bending wave investigated for the first time in Ref. 11. Therefore, free bending interfacial vibrations

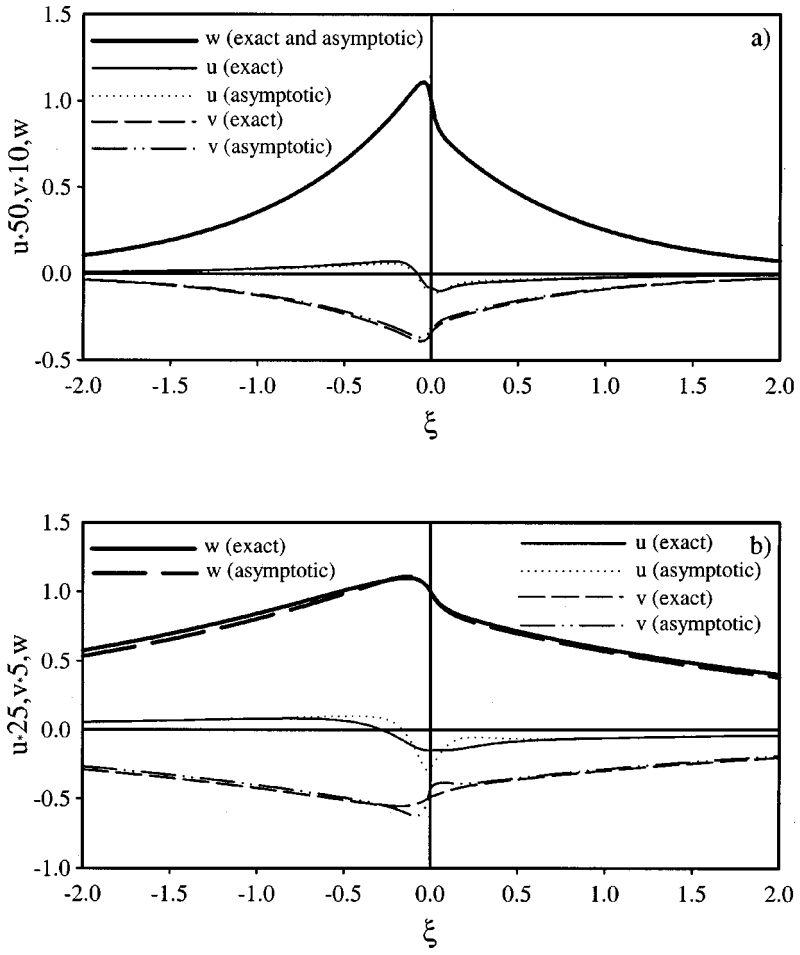

FIG. 2. Natural forms of bending vibrations.

can be treated in terms of standing Stoneley-type bending waves.

If the Stoneley-type bending wave exists for the chosen problem parameters, then Eq. (12) has a root $\lambda_* = \Lambda_*^{as}$ representing the leading-order asymptotic behavior for natural frequencies of the shell. By determining the constants in Eq. (11) we obtain the leading-order asymptotic behavior for the displacement w. By using Eq. (5) and the approximate equations for $u_b(\xi)$, $v_b(\xi)$, and $u_a(\xi)$, $v_a(\xi)$ (see Ref. 5) we can determine the leading-order asymptotic behaviors for the displacements u and v.

Numerical data are presented in Table II. Here Λ^{ex} are the exact values of natural frequencies, while Λ^{as} are their asymptotic estimates. The relative error is given by $\varepsilon = |\Lambda^{as} - \Lambda^{ex}|/\Lambda^{ex} \times 100\%$. The problem parameters are $\nu^{(1)} = 0.4$, $\nu^{(2)} = 0.3$, $E^{(1)}/E^{(2)} = 6$, $\rho^{(1)}/\rho^{(2)} = 6.5$, $h = 0.01$, and $R = 1$. The associated natural forms are plotted in Fig. 2(a) for $n = 30$. The graphs in Fig. 2(a) together with Table I demonstrate high efficiency of the asymptotic formulas. The approximation error increases as the parameter n decreases. The aforementioned tendency is illustrated by comparing the natural forms in Fig. 2(a) with those for $n = 10$ presented in Fig. 2(b) ($\Lambda^{ex} = 0.384$, $\Lambda^{as} = 0.396$, $\varepsilon = 3.021$). For small n flat platelike bending vibrations transform to super-low-frequency semi-membrane ones. The latter are strongly dependent of shell curvature.

V. SUPER-LOW-FREQUENCY SEMI-MEMBRANE VIBRATIONS

For the super-low-frequency vibrations all the quantities of the basic SSS and the additional SSS can be expressed in terms of the functions $v_b^{(k)}$ and $w_a^{(k)}$, respectively. The asymptotic behavior 2.1 yields (see Table I)

$$\begin{aligned}
&\xi = \eta^{-1/2+2q}\xi_*, \quad n = \eta^{-q} n_*, \quad \lambda = \eta^{2-4q}\lambda_*, \\
&u_b^{(k)} = \eta^{1/2} u_b^{*(k)}, \quad v_b^{(k)} = \eta^{q} v_b^{*(k)}, \quad w_b^{(k)} = \eta^{0} w_b^{*(k)}, \\
&T_{b1}^{(k)} = \eta^{1-2q} T_{b1}^{*(k)}, \quad S_{b12}^{(k)} = \eta^{3/2-3q} S_{b12}^{*(k)}, \\
&M_{b1}^{(k)} = \eta^{2-2q} M_{b1}^{*(k)}, \\
&H_{b12}^{(k)} = \eta^{5/2-3q} H_{b12}^{*(k)}, \quad N_{b1}^{(k)} = \eta^{5/2-4q} N_{b1}^{*(k)}.
\end{aligned} \tag{13}$$

By substituting Eqs. (13) into Eqs. (1) and after an asymptotic simplification we obtain the equation in the function $v_b^{*(k)}$

$$\frac{d^4 v_b^{*(k)}}{d\xi_*^4} + \left(\frac{1}{3\nu_2^{(k)}} n_*^4 (n_*^2 - 1)^2 - q^{(k)} \lambda_* n_*^2 (n_*^2 + 1) \right) v_b^{*(k)} + O(\eta^{1-2q}) = 0, \tag{14}$$

which coincides with the governing equation in the semi-membrane theory of shells.[8,10]

The formulas for all the other quantities of the basic SSS expressed in terms of $v_b^{*(k)}$ can be written as

$$\begin{aligned}
n_* u_b^{*(k)} &= -n_*^2 \frac{dv_b^{*(k)}}{d\xi_*} - \eta^{1-2q} \frac{2\nu_2^{(k)}}{1-\nu^{(k)}} \frac{d^3 v_b^{*(k)}}{d\xi_*^3} + O(\eta^{2-4q}), \\
n_* w_b^{*(k)} &= -n_*^2 v_b^{*(k)} - \eta^{1-2q} \nu^{(k)} \frac{d^2 v_b^{*(k)}}{d\xi_*^2} + O(\eta^{2-4q}), \\
n_* T_{b1}^{*(k)} &= -\frac{1}{\gamma^{(k)}} \frac{d^2 v_b^{*(k)}}{d\xi_*^2} + O(\eta^{1-2q}), \\
n_*^2 S_{b12}^{*(k)} &= -\frac{1}{\gamma^{(k)}} \frac{d^3 v_b^{*(k)}}{d\xi_*^3} + O(\eta^{1-2q}), \\
M_{b1}^{*(k)} &= n_* (n_*^2 - 1) \frac{\nu^{(k)}}{3\nu_2^{(k)}\gamma^{(k)}} v_b^{*(1)} + O(\eta^{1-2q}), \\
N_{b1}^{*(k)} + n_* H_{b12}^{*(k)} &= n_* (n_*^2 - 1) \frac{\nu_3^{(k)}}{3\nu_2^{(k)}\gamma^{(k)}} \frac{dv_b^{*(k)}}{d\xi_*} + O(\eta^{1-2q}).
\end{aligned} \tag{15}$$

Starting from the asymptotic behavior 2.2 we set

$$\begin{aligned}
&\xi = \eta^{1/2}\xi_*, \quad n = \eta^{-q} n_*, \quad \lambda = \eta^{2-4q}\lambda_*, \\
&u_a^{(k)} = \eta^{1/2} u_a^{*(k)}, \quad v_a^{(k)} = \eta^{1-q} v_a^{*(k)}, \\
&w_a^{(k)} = \eta^{0} w_a^{*(k)}, \quad T_{a1}^{(k)} = \eta^{1-2q} T_{a1}^{*(k)}, \\
&S_{a12}^{(k)} = \eta^{1/2-q} S_{a12}^{*(k)}, \quad M_{a1}^{(k)} = \eta M_{a1}^{*(k)}, \\
&H_{a12}^{(k)} = \eta^{3/2-q} H_{a12}^{*(k)}, \quad N_{a1}^{(k)} = \eta^{1/2} N_{a1}^{*(k)}
\end{aligned} \tag{16}$$

and obtain the equation in the function $w_a^{*(k)}$

$$\frac{1}{3\nu_2^{(k)}} \frac{d^4 w_a^{*(k)}}{d\xi_*^4} + w_a^{*(k)} + O(\eta^{1-2q}) = 0 \tag{17}$$

that corresponds to a static boundary layer. The other functions are related to the function $w_a^{*(k)}$ as

$$\begin{aligned}
u_a^{*(k)} &= -\frac{\nu^{(k)}}{3\nu_2^{(k)}} \frac{d^3 w_a^{*(k)}}{d\xi_*^3} + O(\eta^{1-2q}), \\
v_a^{*(k)} &= -\frac{2+\nu^{(k)}}{3\nu_2^{(k)}} n_* \frac{d^2 w_a^{*(k)}}{d\xi_*^2} + O(\eta^{1-2q}), \\
S_{a12}^{*(k)} &= -\frac{1}{3\nu_2^{(k)}\gamma^{(k)}} n_* \frac{d^3 w_a^{*(k)}}{d\xi_*^3} + O(\eta^{1-2q}), \\
M_{a1}^{*(k)} &= \frac{1}{3\nu_2^{(k)}\gamma^{(k)}} \frac{d^2 w_a^{*(k)}}{d\xi_*^2} + O(\eta^{1-2q}), \\
N_{a1}^{*(k)} &= \frac{1}{3\nu_2^{(k)}\gamma^{(k)}} \frac{d^3 w_a^{*(k)}}{d\xi_*^3} + O(\eta^{1-2q}).
\end{aligned} \tag{18}$$

Then we substitute Eq. (5) into Eqs. (2) utilizing relations (13) and (16). We have

$$\begin{aligned}
&\eta^{1/2}(u_b^{*(1)} - u_b^{*(2)}) + \eta^{\kappa+1/2}(u_a^{*(1)} - u_a^{*(2)}) = 0, \\
&\eta^{q}(v_b^{*(1)} - v_b^{*(2)}) + \eta^{\kappa+1-q}(v_a^{*(1)} - v_a^{*(2)}) = 0, \\
&\eta^{0}(w_b^{*(1)} - w_b^{*(2)}) + \eta^{\kappa}(w_a^{*(1)} - w_a^{*(2)}) = 0,
\end{aligned}$$

$$\eta^{1/2-2q}\left(\frac{dw_{\rm b}^{*(1)}}{d\xi_*}-\frac{dw_{\rm b}^{*(2)}}{d\xi_*}\right)+\eta^{\kappa-1/2}\left(\frac{dw_{\rm a}^{*(1)}}{d\xi_*}-\frac{dw_{\rm a}^{*(2)}}{d\xi_*}\right)=0,$$

$$\eta^{1-2q}(T_{\rm b1}^{*(1)}-T_{\rm b1}^{*(2)})+\eta^{\kappa}O(\eta^{1-2q})=0,$$

$$\eta^{3/2-3q}(S_{\rm b12}^{*(1)}-S_{\rm b12}^{*(2)}+O(\eta))$$
$$+\eta^{\kappa+1/2-q}(S_{\rm a12}^{*(1)}-S_{\rm a12}^{*(2)}+O(\eta))=0, \tag{19}$$

$$\eta^{2-2q}(M_{\rm b1}^{*(1)}-M_{\rm b1}^{*(2)})+\eta^{\kappa+1}(M_{\rm a1}^{*(1)}-M_{\rm a1}^{*(2)})=0,$$

$$\eta^{5/2-4q}(N_{\rm b1}^{*(1)}+n_*H_{\rm b12}^{*(1)}-(N_{\rm b1}^{*(2)}+n_*H_{\rm b12}^{*(2)}))$$
$$+\eta^{\kappa+1/2}(N_{\rm a1}^{*(1)}+n_*H_{\rm a12}^{*(1)}-(N_{\rm a1}^{*(2)}+n_*H_{\rm a12}^{*(2)}))=0.$$

By exploiting linear dependence between $S_{\rm a12}^{*(k)}$ and $N_{\rm a1}^{*(k)}$ we have $\kappa=1-2q$ and separate Eqs. (19) into two groups: the homogeneous contact conditions for the function $v_{\rm b}^{*(k)}$,

$$v_{\rm b}^{*(1)}-v_{\rm b}^{*(2)}+O(\eta^{2-4q})=0,$$

$$\frac{dv_{\rm b}^{*(1)}}{d\xi_*}-\frac{dv_{\rm b}^{*(2)}}{d\xi_*}+O(\eta^{1-2q})=0,$$

$$\frac{1}{\gamma^{(1)}}\frac{d^2v_{\rm b}^{*(1)}}{d\xi_*^2}-\frac{1}{\gamma^{(2)}}\frac{d^2v_{\rm b}^{*(2)}}{d\xi_*^2}+O(\eta^{1-2q})=0, \tag{20}$$

$$\frac{1}{\gamma^{(1)}}\frac{d^3v_{\rm b}^{*(1)}}{d\xi_*^3}-\frac{1}{\gamma^{(2)}}\frac{d^3v_{\rm b}^{*(2)}}{d\xi_*^3}+O(\eta^{1-2q})=0,$$

and the nonhomogeneous contact conditions for the function $w_{\rm a}^{*(k)}$,

$$w_{\rm a}^{*(1)}-w_{\rm a}^{*(2)}+O(\eta^{1-2q})=0,$$

$$\frac{dw_{\rm a}^{*(1)}}{d\xi_*}-\frac{dw_{\rm a}^{*(2)}}{d\xi_*}+O(\eta^{1-2q})=0,$$

$$\frac{1}{3\nu_2^{(1)}\gamma^{(1)}}\frac{d^2w_{\rm a}^{*(1)}}{d\xi_*^2}-\frac{1}{3\nu_2^{(2)}\gamma^{(2)}}\frac{d^2w_{\rm a}^{*(2)}}{d\xi_*^2}+n_*(n_*^2-1)$$
$$\times\left(\frac{\nu^{(1)}}{3\nu_2^{(1)}\gamma^{(1)}}v_{\rm b}^{*(1)}-\frac{\nu^{(2)}}{3\nu_2^{(2)}\gamma^{(2)}}v_{\rm b}^{*(2)}\right)+O(\eta^{1-2q})=0, \tag{21}$$

$$\frac{1}{3\nu_2^{(1)}\gamma^{(1)}}\frac{d^3w_{\rm a}^{*(1)}}{d\xi_*^3}-\frac{1}{3\nu_2^{(2)}\gamma^{(2)}}\frac{d^3w_{\rm a}^{*(2)}}{d\xi_*^3}+O(\eta^{1-2q})=0.$$

Asymptotic behaviors for natural frequencies follow from basic contact problem (14) and (20). The frequency equation is

$$\left(\frac{1}{\gamma^{(1)}}\beta^{(1)^2}+\frac{1}{\gamma^{(2)}}\beta^{(2)^2}\right)^2+2\frac{1}{\gamma^{(1)}\gamma^{(2)}}\beta^{(1)}\beta^{(2)}(\beta^{(1)^2}+\beta^{(2)^2})$$
$$=0 \tag{22}$$

with

$$\beta^{(k)}=\left(n_*^2\left(\frac{1}{3\nu_2^{(k)}}n_*^2(n_*^2-1)^2-q^{(k)}\lambda_*(n_*^2+1)\right)\right)^{1/4},$$
$$\beta^{(k)}>0.$$

It is obvious that the equalities $\beta^{(1)}=\beta^{(2)}=0$ follow from Eq. (22) and are equivalent to

$$q^{(1)}\nu_2^{(1)}=q^{(2)}\nu_2^{(2)}. \tag{23}$$

Therefore, the interfacial super-low-frequency vibrations occur only under the condition (23). Notice that interfacial bending vibrations exist in this case as well since as it is shown in Ref. 11 that the bending Stonely-type wave may be excited provided that the above-mentioned condition holds.

Let us assume that problem parameters satisfy Eq. (23). Then the leading-order asymptotic behavior of the sought for natural frequency is given by

$$\Lambda\approx\lambda_1 \tag{24}$$

with

$$\lambda_1=\frac{\eta^2}{3\nu_2^{(1)}q^{(1)}}\frac{n^2(n^2-1)^2}{n^2+1}.$$

However, for such frequencies the roots of the characteristic equation corresponding to Eq. (14) are equal to zero, i.e., λ_1 represents the lowest critical frequency. To describe localization of vibrations we have to refine the solution obtained. To this end we set

$$\Lambda=\lambda_1(1-\delta), \tag{25}$$

where $\delta\sim\eta^{4d}$ with unknown $d>0$. In this case the asymptotic behavior 2.1 must be changed by

Asymptotic behavior 2.1a: $\partial/\partial\xi\sim\eta^{1/2-2q+d}$, $u\sim\eta^{1/2+d}$, $v\sim\eta^q$, $w\sim\eta^0$,

$$T_1\sim\eta^{1-2q+2d},\quad S_{12}\sim\eta^{3/2-3q+3d},\quad M_1\sim\eta^{2-2q},$$

$$H_{12}\sim\eta^{5/2-3q+d},\quad N_1\sim\eta^{5/2-4q+d}.$$

The latter yields

$$\xi\sqcap\eta^{-1/2+2q-d}\xi_*,\quad n=\eta^{-q}n_*,$$

$$\lambda=\eta^{2-4q}\lambda_*,\quad \lambda_*=\lambda_{1*}(1-\eta^{4d}\delta_*),$$

$$u_{\rm b}^{(k)}=\eta^{1/2+d}u_{\rm b}^{*(k)},\quad v_{\rm b}^{(k)}=\eta^q v_{\rm b}^{*(k)},$$

$$w_{\rm b}^{(k)}=\eta^0\psi_{\rm b}^{*(k)},\quad T_{\rm b1}^{(k)}=\eta^{1-2q+2d}T_{\rm b1}^{*(k)}, \tag{26}$$

$$S_{\rm b12}^{(k)}=\eta^{3/2-3q+3d}S_{\rm b12}^{*(k)},\quad M_{\rm b1}^{(k)}=\eta^{2-2q}M_{\rm b1}^{*(k)},$$

$$H_{\rm b12}^{(k)}=\eta^{5/2-3q+d}H_{\rm b12}^{*(k)},\quad N_{\rm b1}^{(k)}=\eta^{5/2-4q+d}N_{\rm b1}^{*(k)},$$

where

$$\lambda_{1*}=\frac{1}{3\nu_2^{(1)}}\frac{1}{q^{(1)}}\frac{n_*^2(n_*^2-1)^2}{n_*^2+1}.$$

The equation in the function $v_{\rm b}^{*(k)}$ becomes

$$\frac{d^4v_{\rm b}^{*(k)}}{d\xi_*^4}-\eta^{1-2q-2d}q^{(k)}\lambda_{1*}(2n_*^2+(1-2\nu^{(k)}))\frac{d^2v_{\rm b}^{*(k)}}{d\xi_*^2}$$
$$+q^{(k)}\lambda_{1*}n_*^2(n_*^2+1)\delta_*v_{\rm b}^{*(k)}+O(\eta^{1-2q+2d})=0. \tag{27}$$

Expressions for other functions are

$$
\begin{aligned}
&n_*^3 u_{\mathrm{b}}^{*(k)} \\
&\quad = -n_*^2 \frac{dv_{\mathrm{b}}^{*(k)}}{d\xi_*} - \nu_1^{(k)} \Bigg[\eta^{1-2q+2d} \frac{d^3 v_{\mathrm{b}}^{*(k)}}{d\xi_*^3} + \eta^{2-4q} \\
&\qquad \times \left(\frac{\nu^{(k)}}{3\nu_2^{(k)}} n_*^4 (n_*^2 - 1) - q^{(k)} \lambda_{1*} (\nu^{(k)} n_*^2 - 1) \right) \frac{dv_{\mathrm{b}}^{*(k)}}{d\xi_*} \Bigg] \\
&\qquad + O(\eta^{2-4q+4d}),
\end{aligned}
$$

$$
n_* w_{\mathrm{b}}^{*(k)} = -n_*^2 v_{\mathrm{b}}^{*(k)} - \eta^{1-2q+2d} \nu^{(k)} \frac{d^2 v_{\mathrm{b}}^{*(k)}}{d\xi_*^2} + O(\eta^{2-4q}),
$$

$$
\begin{aligned}
n_* T_{\mathrm{b1}}^{*(k)} &= -\frac{1}{\gamma^{(k)}} \left(\frac{d^2 v_{\mathrm{b}}^{*(k)}}{d\xi_*^2} + \eta^{1-2q-2d} n_*^2 \nu^{(k)} \right. \\
&\quad \left. \times \left(\frac{n_*^2 (n_*^2 - 1)}{3\nu_2^{(k)}} - q^{(k)} \lambda_{1*} \right) v_{\mathrm{b}}^{*(k)} \right) + O(\eta^{1-2q+2d}),
\end{aligned}
$$

$$
\begin{aligned}
&n_*^2 (S_{\mathrm{b12}}^{*(k)} + H_{\mathrm{b12}}^{*(k)}) \\
&\quad = -\frac{1}{\gamma^{(k)}} \left(\frac{d^3 v_{\mathrm{b}}^{*(k)}}{d\xi_*^3} + \eta^{1-2q-2d} \right. \\
&\qquad \left. \times \left(\frac{n_*^2 S^{(k)}}{3\nu_2^{(k)}} - q^{(k)} \lambda_{1*} (\nu^{(k)} n_*^2 - 1) \right) \frac{dv_{\mathrm{b}}^{*(k)}}{d\xi_*} \right) \\
&\qquad + O(\eta^{1-2q+2d}),
\end{aligned}
$$

with $s^{(k)} = \nu^{(k)} n_*^4 + (2 - 3\nu^{(k)}) n_*^2 - 2(1 - \nu^{(k)})$; the functions $M_{\mathrm{b1}}^{*(k)}$ and $N_{\mathrm{b1}}^{*(k)} + n_* H_{\mathrm{b12}}^{*(k)}$ are the same as in Eqs. (15).

A refined equation for the static boundary layer can be written as

$$
\begin{aligned}
&\frac{1}{3\nu_2^{(k)}} \frac{d^4 w_{\mathrm{a}}^{*(k)}}{d\xi_*^4} + w_{\mathrm{a}}^{*(k)} - \eta^{1-2q} \frac{4}{3\nu_2^{(k)}} n_*^2 \frac{d^2 w_{\mathrm{a}}^{*(k)}}{d\xi_*^2} \\
&\quad + O(\eta^{2-4q}) = 0.
\end{aligned} \tag{29}
$$

Other sought for quantities of the additional SSS take the form

$$
\begin{aligned}
u_{\mathrm{a}}^{*(k)} &= -\frac{\nu^{(k)}}{3\nu_2^{(k)}} \frac{d^3 w_{\mathrm{a}}^{*(k)}}{d\xi_*^3} - \eta^{1-2q} \frac{1 - 2\nu^{(k)}}{3\nu_2^{(k)}} n_*^2 \frac{dw_{\mathrm{a}}^{*(k)}}{d\xi_*} \\
&\quad + O(\eta^{2-4q}), \\
v_{\mathrm{a}}^{*(k)} &= -\frac{2 + \nu^{(k)}}{3\nu_2^{(k)}} n_* \frac{d^2 w_{\mathrm{a}}^{*(k)}}{d\xi_*^2} + \eta^{1-2q} \frac{1}{3\nu_2^{(k)}} n_* \\
&\quad \times ((5 + 2\nu^{(k)}) n_*^2 - \nu_1^{(k)} \nu_3^{(k)}) w_{\mathrm{a}}^{*(k)} + O(\eta^{2-4q}), \\
T_{\mathrm{a1}}^{*(k)} &= -\frac{1}{3\nu_2^{(k)} \gamma^{(k)}} n_*^2 \frac{d^2 w_{\mathrm{a}}^{*(k)}}{d\xi_*^2} + O(\eta^{1-2q}), \\
S_{\mathrm{a12}}^{*(k)} + H_{\mathrm{a12}}^{*(k)} &= -\frac{1}{3\nu_2^{(k)} \gamma^{(k)}} n_* \frac{d^3 w_{\mathrm{a}}^{*(k)}}{d\xi_*^3} - \eta^{1-2q} n_* \\
&\quad \times \frac{2n_*^2 - \nu^{(1)}}{3\nu_2^{(1)} \gamma^{(1)}} \frac{dw_{\mathrm{a}}^{*(1)}}{d\xi_*} + O(\eta^{2-4q}),
\end{aligned} \tag{30}
$$

$$
M_{\mathrm{a1}}^{*(k)} = \frac{1}{3\nu_2^{(k)} \gamma^{(k)}} \frac{d^2 w_{\mathrm{a}}^{*(k)}}{d\xi_*^2} + O(\eta^{1-2q}),
$$

$$
\begin{aligned}
N_{\mathrm{a1}}^{*(k)} + n_* H_{\mathrm{a12}}^{*(k)} &= \frac{1}{3\nu_2^{(k)} \gamma^{(k)}} \frac{d^3 w_{\mathrm{a}}^{*(k)}}{d\xi_*^3} - \eta^{1-2q} \\
&\quad \times \frac{\nu_3^{(1)}}{3\nu_2^{(1)} \gamma^{(1)}} n_*^2 \frac{dw_{\mathrm{a}}^{*(1)}}{d\xi_*} + O(\eta^{2-2q}).
\end{aligned}
$$

Instead of Eqs. (19) we obtain

$$
\begin{aligned}
&\eta^{1/2+d} (u_{\mathrm{b}}^{*(1)} - u_{\mathrm{b}}^{*(2)}) + \eta^{\kappa+1/2} (u_{\mathrm{a}}^{*(1)} - u_{\mathrm{a}}^{*(2)}) = 0, \\
&\eta^{q} (v_{\mathrm{b}}^{*(1)} - v_{\mathrm{b}}^{*(2)}) + \eta^{\kappa+1-q} (v_{\mathrm{a}}^{*(1)} - v_{\mathrm{a}}^{*(2)}) = 0, \\
&\eta^{0} (w_{\mathrm{b}}^{*(1)} - w_{\mathrm{b}}^{*(2)}) + \eta^{\kappa} (w_{\mathrm{a}}^{*(1)} - w_{\mathrm{a}}^{*(2)}) = 0, \\
&\eta^{1/2-2q+d} \left(\frac{dw_{\mathrm{b}}^{*(1)}}{d\xi_*} - \frac{dw_{\mathrm{b}}^{*(2)}}{d\xi_*} \right) \\
&\quad + \eta^{\kappa-1/2} \left(\frac{dw_{\mathrm{a}}^{*(1)}}{d\xi_*} - \frac{dw_{\mathrm{a}}^{*(2)}}{d\xi_*} \right) = 0, \\
&\eta^{1-2q+2d} (T_{\mathrm{b1}}^{*(1)} - T_{\mathrm{b1}}^{*(2)}) + \eta^{\kappa+1-2q} (T_{\mathrm{a1}}^{*(1)} - T_{\mathrm{a1}}^{*(2)}) = 0, \\
&\eta^{3/2-3q+3d} (S_{\mathrm{b12}}^{*(1)} + H_{\mathrm{b12}}^{*(1)} - (S_{\mathrm{b12}}^{*(2)} + H_{\mathrm{b12}}^{*(2)})) \\
&\quad + \eta^{\kappa+1/2-q} (S_{\mathrm{a12}}^{*(1)} + S_{\mathrm{a12}}^{*(1)} - (S_{\mathrm{a12}}^{*(2)} + H_{\mathrm{a12}}^{*(2)})) = 0, \\
&\eta^{2-2q} (M_{\mathrm{b1}}^{*(1)} - M_{\mathrm{b1}}^{*(2)}) + \eta^{\kappa+1} (M_{\mathrm{a1}}^{*(1)} - M_{\mathrm{a1}}^{*(2)}) = 0, \\
&\eta^{5/2-4q+d} (N_{\mathrm{b1}}^{*(1)} + n_* H_{\mathrm{b12}}^{*(1)} - (N_{\mathrm{b1}}^{*(2)} + n_* H_{\mathrm{b12}}^{*(2)})) \\
&\quad + \eta^{\kappa+1/2} (N_{\mathrm{a1}}^{*(1)} + n_* H_{\mathrm{a12}}^{*(1)} - (N_{\mathrm{a1}}^{*(2)} + n_* H_{\mathrm{a12}}^{*(2)})) = 0
\end{aligned} \tag{31}
$$

with Eqs. (28) and (30). In Eqs. (31) we put $\kappa = 1 - 2q$ as above.

After elementary transformations the fifth and sixths formulas in Eqs. (31) become

$$
\begin{aligned}
&\eta^{1-2q+2d} \left(\frac{1}{\gamma^{(1)}} \frac{d^2 v_{\mathrm{b}}^{*(1)}}{d\xi_*^2} - \frac{1}{\gamma^{(2)}} \frac{d^2 v_{\mathrm{b}}^{*(2)}}{d\xi_*^2} \right) \\
&\quad - \eta^{2-4q} n_*^2 \lambda_{1*} \left(\frac{\nu^{(1)} q^{(1)}}{\gamma^{(1)}} v_{\mathrm{b}}^{*(1)} - \frac{\nu^{(2)} q^{(2)}}{\gamma^{(2)}} v_{\mathrm{b}}^{*(2)} \right) \\
&\quad + O(\eta^{2-4q+4d} + \eta^{3-6q}) = 0, \\
&\eta^{3/2-3q+3d} \left(\frac{1}{\gamma^{(1)}} \frac{d^3 v_{\mathrm{b}}^{*(1)}}{d\xi_*^3} - \frac{1}{\gamma^{(2)}} \frac{d^3 v_{\mathrm{b}}^{*(2)}}{d\xi_*^3} \right) \\
&\quad - \eta^{5/2-5q+d} \lambda_{1*} \left[\frac{q^{(1)}}{\gamma^{(1)}} (\nu_3^{(1)} n_*^2 + 1 - 2\nu^{(1)}) \frac{dv_{\mathrm{b}}^{*(1)}}{d\xi_*} \right. \\
&\quad \left. - \frac{q^{(2)}}{\gamma^{(2)}} (\nu_3^{(2)} n_*^2 + 1 - 2\nu^{(2)}) \frac{dv_{\mathrm{b}}^{*(2)}}{d\xi_*} \right] + \eta^{5/2-5q} n_*^3 (n_*^2 - 1) \\
&\quad \times \left(\frac{\nu^{(1)}}{3\nu_2^{(1)} \gamma^{(1)}} \frac{dw_{\mathrm{a}}^{*(1)}}{d\xi_*} - \frac{\nu^{(2)}}{3\nu_2^{(2)} \gamma^{(2)}} \frac{dw_{\mathrm{a}}^{*(2)}}{d\xi_*} \right) \\
&\quad + O(\eta^{5/2-5q+4d} + \eta^{7/2-7q}) = 0.
\end{aligned} \tag{32}
$$

It follows from Eqs. (32) that

TABLE III. Natural frequencies of super low-frequency vibrations and their deviations from critical frequency.

n	$\Lambda^{ex}\cdot 10^3$	$\Lambda^{as}\cdot 10^3$	ε	$\Delta_{ex}\cdot 10^6$	$\Delta_{as}\cdot 10^6$	ε_1
2	0.002 857 117 9	0.002 857 112 2	0.000 20	0.000 022 56	0.000 030 64	35.81
3	0.022 856 600 5	0.022 856 333 4	0.001 17	0.000 517 67	0.000 809 42	56.36
4	0.084 029 634 2	0.084 026 973 1	0.003 17	0.003 879 97	0.006 640 33	71.14
5	0.219 762 431 9	0.219 748 229 5	0.006 46	0.017 516 97	0.031 990 30	82.62
6	0.472 913 568 6	0.472 860 076 9	0.011 31	0.058 807 33	0.112 896 07	91.98
7	0.895 836 643 6	0.895 675 763 6	0.017 96	0.162 209 00	0.324 236 35	99.89
8	1.550 378 615 5	1.549 965 415 3	0.026 65	0.388 610 70	0.803 815 43	106.84
9	2.507 870 804 4	2.506 926 659 4	0.037 65	0.836 733 04	1.784 142 00	113.23
10	3.849 116 931 9	3.847 145 196 9	0.051 23	1.655 969 68	3.632 738 07	119.37

$d=\frac{1}{3}-\frac{2}{3}q<\frac{1}{2}-q.$

Let us express the first derivative of $w_a^{*(k)}$ in terms of $v_b^{*(k)}$ by solving the contact problem (17) and (21). As a result we obtain the homogeneous contact conditions for the function $v_b^{*(k)}$:

$$
\begin{aligned}
&v_b^{*(1)}-v_b^{*(2)}+O(\eta^{6d})=0,\\
&\frac{dv_b^{*(1)}}{d\xi_*}-\frac{dv_b^{*(2)}}{d\xi_*}+O(\eta^{2d})=0,\\
&\frac{1}{\gamma^{(1)}}\frac{d^2v_b^{*(1)}}{d\xi_*^2}-\frac{1}{\gamma^{(2)}}\frac{d^2v_b^{*(2)}}{d\xi_*^2}-\eta^d n_*^2\lambda_{1*}\\
&\quad\times\left(\frac{\nu^{(1)}q^{(1)}}{\gamma^{(1)}}v_b^{*(1)}-\frac{\nu^{(2)}q^{(2)}}{\gamma^{(2)}}v_b^{*(2)}\right)+O(\eta^{4d})=0,
\end{aligned}
\tag{33}
$$

$$
\begin{aligned}
&\frac{1}{\gamma^{(1)}}\frac{d^3v_b^{*(1)}}{d\xi_*^3}-\frac{1}{\gamma^{(2)}}\frac{d^3v_b^{*(2)}}{d\xi_*^3}\\
&\quad-\eta^d\lambda_{1*}\left[\frac{q^{(1)}}{\gamma^{(1)}}(\nu_3^{(1)}n_*^2+1-2\nu^{(1)})\frac{dv_b^{*(1)}}{d\xi_*}\right.\\
&\quad\left.-\frac{q^{(2)}}{\gamma^{(2)}}(\nu_3^{(2)}n_*^2+1-2\nu^{(2)})\frac{dv_b^{*(2)}}{d\xi_*}\right]\\
&\quad+\frac{\sqrt{2}}{(3\nu_2^{(1)}q^{(1)})^{1/4}}D\lambda_{1*}n_*^2(n_*^2+1)\\
&\quad\times\left(\frac{\nu^{(1)}q^{(1)}}{\gamma^{(1)}}v_b^{*(1)}-\frac{\nu^{(2)}q^{(2)}}{\gamma^{(2)}}v_b^{*(2)}\right)+O(\eta^{3d})=0
\end{aligned}
$$

with

$$
D=\frac{(\gamma^{(1)}q^{(2)}\nu^{(2)}-\gamma^{(2)}q^{(1)}\nu^{(1)})((q^{(1)})^{1/4}\gamma^{(2)}+(q^{(2)})^{1/4}\gamma^{(1)})}{((q^{(1)})^{1/2}\gamma^{(2)}+(q^{(2)})^{1/2}\gamma^{(1)})^2+2(q^{(1)}q^{(2)})^{1/4}\gamma^{(1)}\gamma^{(2)}((q^{(1)})^{1/2}+(q^{(2)})^{1/2})}.
$$

To within the error $O(\eta^d)$ we obtain from the problems (27) and (33)

$$
\begin{aligned}
\Lambda\approx&\frac{\eta_1^{(1)^2}}{q^{(1)}}\frac{n^2(n^2-1)^2}{n^2+1}\\
&\times\left(1-(2D^2)^{4/3}\left(\frac{\eta_1^{(1)^2}}{q^{(1)}}\lambda_1 n^2(n^2+1)\right)^{1/3}\right).
\end{aligned}
\tag{34}
$$

It is clear that the associated natural form describes exponentially decaying vibrations.

Comparison of numerical and asymptotical results is presented in Table III. Here the notations for Λ^{ex}, Λ^{as}, and ε are the same as in Table II. We also calculate the deviations $\Delta_{ex}=\lambda_1^{ex}-\Lambda^{ex}$, $\Delta_{as}=\lambda_1-\Lambda^{as}$, and the relative error $\varepsilon_1=|\Delta_{as}-\Delta_{ex}|/\Delta_{ex}\times 100\%$, where λ_1^{ex} is the exact value of the lowest critical frequency. The problem parameters are the same as before except $h=0.001$.

By solving the problems (27) and (33) we can also determine the quantity δ to within the error $O(\eta^{3d})$. The refined asymptotic values Λ^{as} and Δ_{as} are compared with their exact analogs Λ^{ex} and Δ_{ex} in Table IV.

The natural forms are plotted in Fig. 3 for $n=5$. It is clear that the super-low-frequency vibrations also possess, in a sense, a bending type behavior, i.e., the transverse displacement prevails. However, the consideration above demonstrates that they cannot be reduced to bending vibrations of a flat plate. Considerable deviation of the transverse displacement of a flat plate from that of a shell in the case of super-low-frequency vibrations is illustrated by numerical data in Fig. 3 as well.

VI. EXTENSIONAL VIBRATIONS

For the sake of simplicity we assume $q>0$, i.e., consider short-wavelength vibrations. The asymptotic behaviors 3.1 and 3.2 yield

$$
\begin{aligned}
&n=\eta^{-q}n_*,\quad \lambda=\eta^{-2q}\lambda_*,\quad u_b^{(k)}=\eta^{-q}u_b^{*(k)},\\
&v_b^{(k)}=\eta^{-q}v_b^{*(k)},\quad w_b^{(k)}=\eta^0 w_b^{*(k)},\\
&T_{b1}^{(k)}=\eta^{-2q}T_{b1}^{*(k)},\quad S_{b12}^{(k)}=\eta^{-2q}S_{b12}^{*(k)},\\
&M_{b1}^{(k)}=\eta^{2-2q}M_{b1}^{*(k)},\\
&H_{b12}^{(k)}=\eta^{2-2q}H_{b12}^{*(k)},\quad N_{b1}^{(k)}=\eta^{2-3q}N_{b1}^{*(k)}
\end{aligned}
\tag{35}
$$

TABLE IV. The same as Table III for refined asymptotic values.

n	$\Lambda^{ex}\times 10^3$	$\Lambda^{as}\times 10^3$	ε	$\Delta_{ex}\times 10^6$	$\Delta_{as}\times 10^6$	ε_1
2	0.002 857 117 9	0.002 857 120 3	0.000 09	0.000 022 56	0.000 022 56	0.005
3	0.022 856 600 5	0.022 856 625 5	0.000 11	0.000 517 67	0.000 517 35	0.062
4	0.084 029 634 2	0.084 029 739 5	0.000 13	0.003 879 97	0.003 873 94	0.155
5	0.219 762 431 9	0.219 762 746 9	0.000 14	0.017 516 97	0.017 472 83	0.252
6	0.472 913 568 6	0.472 914 347 5	0.000 16	0.058 807 33	0.058 625 52	0.309
7	0.895 836 643 6	0.895 838 242 5	0.000 18	0.162 209 00	0.161 757 50	0.278
8	1.550 378 615 5	1.550 381 028 0	0.000 16	0.388 610 70	0.388 202 74	0.105
9	2.507 870 804 4	2.507 871 804 1	0.000 04	0.836 733 04	0.838 997 31	0.271
10	3.849 116 931 9	3.849 106 854 8	0.000 26	1.655 969 68	1.671 080 11	0.912

and

$$
\begin{aligned}
&u_a^{(k)}=\eta^{1/2+(1/2)q}u_a^{*(k)},\quad v_a^{(k)}=\eta v_a^{*(k)},\\
&w_a^{(k)}=\eta^0 w_a^{*(k)},\quad T_{a1}^{(k)}=\eta^{1-q}T_{a1}^{*(k)},\\
&S_{a12}^{(k)}=\eta^{1/2-(1/2)q}S_{a12}^{*(k)},\quad M_{a1}^{(k)}=\eta^{1-q}M_{a1}^{*(k)},\\
&H_{a12}^{(k)}=\eta^{3/2-(3/2)q}H_{a12}^{*(k)},\quad N_{a1}^{(k)}=\eta^{1/2-(3/2)q}N_{a1}^{*(k)}.
\end{aligned}
\tag{36}
$$

For the quantities with the subscripts "b" and "a" we, respectively, set

$$\xi=\eta^q\xi_*$$

and

$$\xi=\eta^{1/2+(1/2)q}\xi_*.$$

By substituting Eqs. (5), (35), and (36) into Eqs. (2) we obtain

$$
\begin{aligned}
&\eta^{-q}(u_b^{*(1)}-u_b^{*(2)})+\eta^{\kappa+1/2+(1/2)q}(u_a^{*(1)}-u_a^{*(2)})=0,\\
&\eta^{-q}(v_b^{*(1)}-v_b^{*(2)})+\eta^{\kappa+1}(v_a^{*(1)}-v_a^{*(2)})=0,\\
&\eta^{0}(w_b^{*(1)}-w_b^{*(2)})+\eta^{\kappa}(w_a^{*(1)}-w_a^{*(2)})=0,\\
&\eta^{-q}\left(\frac{dw_b^{*(1)}}{d\xi_*}-\frac{dw_b^{*(2)}}{d\xi_*}\right)+\eta^{\kappa-1/2-(1/2)q}\\
&\quad\times\left(\frac{dw_a^{*(1)}}{d\xi_*}-\frac{dw_a^{*(2)}}{d\xi_*}\right)=0,\\
&\eta^{-2q}(T_{b1}^{*(1)}-T_{b1}^{*(2)})+\eta^{\kappa+1-q}(T_{a1}^{*(1)}-T_{a1}^{*(2)})=0,\\
&\eta^{-2q}(S_{b12}^{*(1)}-S_{b12}^{*(2)}+O(\eta^2))+\eta^{\kappa+1/2-(1/2)q}\\
&\quad\times(S_{a12}^{*(1)}-S_{a12}^{*(2)}+O(\eta^{1-q}))=0,\\
&\eta^{2-2q}(M_{b1}^{*(1)}-M_{b1}^{*(2)})+\eta^{\kappa+1-q}(M_{a1}^{*(1)}-M_{a1}^{*(2)})=0,\\
&\eta^{2-3q}(N_{b1}^{*(1)}+n_*H_{b12}^{*(1)}-(N_{b1}^{*(2)}+n_*H_{b12}^{*(2)}))\\
&\quad+\eta^{\kappa+1/2-(3/2)q}(N_{a1}^{*(1)}-N_{a1}^{*(2)}+O(\eta^{1-q}))=0.
\end{aligned}
\tag{37}
$$

Analysis of these equations yields $\kappa=0$. The homogeneous contact conditions for the basic SSS are

$$
\begin{aligned}
&u_b^{*(1)}-u_b^{*(2)}+O(\eta^{1/2+(3/2)q})=0,\\
&v_b^{*(1)}-v_b^{*(2)}+O(\eta^{1+q})=0,\\
&T_{b1}^{*(1)}-T_{b1}^{*(2)}+O(\eta^{1+q})=0,\\
&S_{b12}^{*(1)}-S_{b12}^{*(2)}+O(\eta^{1/2+(3/2)q})=0
\end{aligned}
\tag{38}
$$

while the nonhomogeneous ones for the additional SSS become

$$
\begin{aligned}
&w_a^{*(1)}-w_a^{*(2)}+w_b^{*(1)}-w_b^{*(2)}=0,\\
&\frac{dw_a^{*(1)}}{d\xi_*}-\frac{dw_a^{*(2)}}{d\xi_*}+O(\eta^{1/2-(1/2)q})=0,\\
&M_{b1}^{*(1)}-M_{b1}^{*(2)}+O(\eta^{1-q})=0,\\
&N_{a1}^{*(1)}-N_{a1}^{*(2)}+O(\eta^{3/2-(3/2)q})=0
\end{aligned}
\tag{39}
$$

with

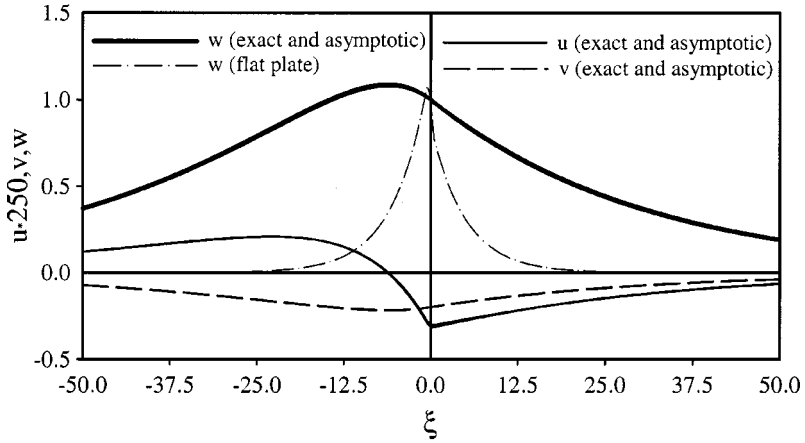

FIG. 3. Natural forms of super-low-frequency vibrations.

$$w_{\mathrm{b}}^{*(k)}=-\frac{1}{\nu_2^{(k)}q^{(k)}}\lambda_*^{-1}\left[\left(\frac{1}{R_1^{(k)}}+\frac{\nu^{(k)}}{R_2^{(k)}}\right)\frac{du_{\mathrm{b}}^{*(k)}}{d\xi_*}-\left(\frac{\nu^{(k)}}{R_1^{(k)}}+\frac{1}{R_2^{(k)}}\right)\frac{n_*}{B^{(k)}}v_{\mathrm{b}}^{*(k)}\right]+O(\eta^q).$$

It is shown in Ref. 5 that governing approximate equations in the case of the asymptotic behaviors 3.1 and 3.2 coincide with the 2D equations of plate extension and the 1D equation of beam bending, respectively. Let us write them out for the problem considered:

$$\begin{aligned}&\frac{d^2u_{\mathrm{b}}^{*(k)}}{d\xi_*^2}-\frac{1-\nu^{(k)}}{2}\frac{n_*^2}{B^{(k)^2}}u_{\mathrm{b}}^{*(k)}-\frac{1+\nu^{(k)}}{2}\frac{n_*}{B^{(k)}}\frac{dv_{\mathrm{b}}^{*(k)}}{d\xi_*}\\&\quad+\nu_2^{(k)}q^{(k)}\lambda_*u_{\mathrm{b}}^{*(k)}+O(\eta^q)=0,\\&\frac{1+\nu^{(k)}}{2}\frac{n_*}{B^{(k)}}\frac{du_{\mathrm{b}}^{*(k)}}{d\xi_*}+\frac{1-\nu^{(k)}}{2}\frac{d^2v_{\mathrm{b}}^{*(k)}}{d\xi_*^2}-\frac{n_*^2}{B^{(k)^2}}v_{\mathrm{b}}^{*(k)}\\&\quad+\nu_2^{(k)}q^{(k)}\lambda_*v_{\mathrm{b}}^{*(k)}+O(\eta^q)=0,\end{aligned}\tag{40}$$

and

$$\frac{1}{3}\frac{d^4w_{\mathrm{a}}^{*(k)}}{d\xi_*^4}-\nu_2^{(k)}q^{(k)}\lambda_*w_{\mathrm{a}}^{*(k)}+O(\eta^{1-q})=0.\tag{41}$$

Problems (40) and (38) coincide with that for extension of a longitudinally inhomogeneous plate with mixed boundary conditions on its sides. The latter allows separating independent variables. By solving this problem we arrive at the frequency equation

$$\Delta=\begin{vmatrix}n & r_2^{(1)} & -n & r_2^{(2)}\\ r_1^{(1)} & n & r_1^{(2)} & -n\\ f_1^{(1)} & f_2^{(1)} & f_1^{(2)} & -f_2^{(2)}\\ g_1^{(1)} & g_2^{(1)} & -g_1^{(2)} & g_2^{(2)}\end{vmatrix}=0,\tag{42}$$

where

$$f_1^{(k)}=\frac{(1-\nu^{(k)})r_1^{(k)}n}{\nu_2^{(k)}\gamma^{(k)}},\quad f_2^{(k)}=\frac{r_2^{(k)^2}-\nu^{(k)}n^2}{\nu_2^{(k)}\gamma^{(k)}},$$

$$g_1^{(k)}=\frac{r_1^{(k)^2}+n^2}{\nu_1^{(k)}\gamma^{(k)}},\quad g_2^{(k)}=\frac{2r_2^{(k)}n}{\nu_1^{(k)}\gamma^{(k)}},$$

with

$$r_1^{(k)}=\sqrt{n^2-\nu_1^{(k)}q^{(k)}\lambda},\quad r_2^{(k)}=\sqrt{n^2-\nu_2^{(k)}q^{(k)}\lambda}.$$

Equation (42) corresponds to a Stoneley-type extensional wave. This is the classical Stoneley wave in the theory of plane strain[12] presented in terms of generalized plane stress. The leading order asymptotic behavior $\Lambda\approx\Lambda_{\mathrm{S}}$ follows from this equation.

Let us now estimate small imaginary parts of natural frequencies studied for edge vibrations in Ref. 5. To this end we have to satisfy contact conditions in the second-order iteration. Let us first restore terms of the order $O(\eta^{1/2+3q/2})$ in Eqs. (38). We get

$$\begin{aligned}&n_{\mathrm{b}}^{*(1)}-u_{\mathrm{b}}^{*(2)}+\eta^{1/2+(3/2)q}(u_{\mathrm{a}}^{*(1)}-u_{\mathrm{a}}^{*(2)})=0,\\&v_{\mathrm{b}}^{*(1)}-v_{\mathrm{b}}^{*(2)}+O(\eta^{1+q})=0,\\&T_{\mathrm{b}1}^{*(1)}-T_{\mathrm{b}1}^{*(2)}+O(\eta^{1+q})=0,\\&S_{\mathrm{b}12}^{*(1)}-S_{\mathrm{b}12}^{*(2)}+\eta^{1/2+(3/2)q}(S_{\mathrm{a}12}^{*(1)}-S_{\mathrm{a}12}^{*(2)})=0.\end{aligned}\tag{43}$$

By solving the problem (41) and (39) we express the function $w_{\mathrm{a}}^{*(k)}$ in terms of $u_{\mathrm{b}}^{*(k)}$ and $v_{\mathrm{b}}^{*(k)}$. Then we calculate the quantities $u_{\mathrm{a}}^{*(k)}$ and $S_{\mathrm{a}12}^{*(k)}$ by the formulas

$$\begin{aligned}&u_{\mathrm{a}}^{*(k)}=\frac{\nu^{(k)}}{3\nu_2^{(k)}q^{(k)}}\lambda_*^{-1}\frac{d^3w_{\mathrm{a}}^{*(k)}}{d\xi_*^3}+O(\eta^{1-q}),\\&S_{\mathrm{a}12}^{*(k)}=\frac{1}{3\nu_2^{(k)}q^{(k)}\gamma^{(k)}}n_*\lambda_*^{-1}\frac{d^3w_{\mathrm{a}}^{*(k)}}{d\xi_*^3}+O(\eta^{1-q})\end{aligned}\tag{44}$$

and substitute the imaginary parts of them into Eqs. (43). Finally, we arrive at homogeneous contact conditions for the functions $u_{\mathrm{b}}^{*(k)}$ and $v_{\mathrm{b}}^{*(k)}$. They are

$$\begin{aligned}&u_{\mathrm{b}}^{*(1)}-u_{\mathrm{b}}^{*(2)}-i\eta^{1/2+(3/2)q}\lambda_*^{-5/4}DAK_u=0,\\&v_{\mathrm{b}}^{*(1)}-v_{\mathrm{b}}^{*(2)}+O(\eta^{1+q})=0,\\&\frac{1}{\nu_2^{(1)}\gamma^{(1)}}\left(\frac{du_{\mathrm{b}}^{*(1)}}{d\xi_*}-\nu^{(1)}n_*v_{\mathrm{b}}^{*(1)}\right)-\frac{1}{\nu_2^{(2)}\gamma^{(2)}}\left(\frac{du_{\mathrm{b}}^{*(2)}}{d\xi_*}-\nu^{(2)}n_*v_{\mathrm{b}}^{*(2)}\right)=0,\\&\frac{1}{\nu_1^{(1)}\gamma^{(1)}}\left(n_*u_{\mathrm{b}}^{*(1)}+\frac{dv_{\mathrm{b}}^{*(1)}}{d\xi_*}\right)-\frac{1}{\nu_1^{(2)}\gamma^{(2)}}\left(n_*u_{\mathrm{b}}^{*(2)}+\frac{dv_{\mathrm{b}}^{*(2)}}{d\xi_*}\right)\\&\quad-i\eta^{1/2+(3/2)q}n_*\lambda_*^{-5/4}DAK_s=0,\end{aligned}\tag{45}$$

where

$$A=\frac{1}{\nu_2^{(1)}q^{(1)}}\left(\nu^{(1)}\frac{du_{\mathrm{b}}^{*(1)}}{d\xi_*}-n_*v_{\mathrm{b}}^{*(1)}\right)-\frac{1}{\nu_2^{(2)}q^{(2)}}\left(\nu^{(2)}\frac{du_{\mathrm{b}}^{*(2)}}{d\xi_*}-n_*v_{\mathrm{b}}^{*(2)}\right),$$

$$K_u=q^{(1)}\gamma^{(2)}\nu^{(2)}-q^{(2)}\gamma^{(1)}\nu^{(1)},\quad K_s=q^{(1)}-q^{(2)},$$

$$D=\frac{\frac{1}{(q^{(1)}q^{(2)})^{1/4}}\left(\left(\frac{q^{(1)}}{3\nu_2^{(2)}}\right)^{1/4}\frac{\gamma^{(2)}}{3\nu_2^{(1)}}+\left(\frac{q^{(2)}}{3\nu_2^{(1)}}\right)^{1/4}\frac{\gamma^{(1)}}{3\nu_2^{(1)}}\right)}{\left(\left(\frac{q^{(1)}}{3\nu_2^{(1)}}\right)^{1/2}\gamma^{(2)}+\left(\frac{q^{(2)}}{3\nu_2^{(2)}}\right)^{1/2}\gamma^{(1)}\right)^2+2\left(\frac{q^{(1)}}{3\nu_2^{(1)}}\frac{q^{(2)}}{3\nu_2^{(2)}}\right)^{1/4}\gamma^{(1)}\gamma^{(2)}\left(\left(\frac{q^{(1)}}{3\nu_2^{(2)}}\right)^{1/2}+\left(\frac{q^{(2)}}{3\nu_2^{(1)}}\right)^{1/2}\right)}.$$

TABLE V. Natural frequencies of extensional vibrations.

n	Re Λ^{ex}	Re Λ^{as}	ε_1	Im $\Lambda^{ex}\times 10^4$	Im $\Lambda^{as}\times 10^4$	ε_2
5	8.494 846	8.394 244	1.184	0.005 569	0.003 060	45.056
6	12.190 038	12.087 711	0.839	0.006 515	0.003 352	48.548
7	16.556 099	16.452 718	0.624	0.007 429	0.003 621	51.263
8	21.593 336	21.489 265	0.482	0.008 327	0.003 871	53.518
9	27.301 898	27.197 351	0.383	0.009 217	0.004 105	55.459
10	33.681 866	33.576 976	0.311	0.010 104	0.004 327	57.170
11	40.733 285	40.628 141	0.258	0.010 990	0.004 539	58.701
12	48.456 183	48.350 845	0.217	0.011 877	0.004 740	60.086
13	56.850 578	56.745 089	0.186	0.012 766	0.004 934	61.350
14	65.916 482	65.810 873	0.160	0.013 658	0.005 120	62.512
15	75.653 902	75.548 196	0.140	0.014 555	0.005 300	63.586

The sought for estimate follows from the problems (40) and (45). It is

$$\operatorname{Im}\Lambda_2 \approx \eta^{1/2}(\Lambda_S)^{-5/4} D \frac{\Delta_1\varphi_1^{(1)}+\Delta_2\varphi_2^{(1)}+\Delta_3\varphi_1^{(2)}+\Delta_4\varphi_2^{(2)}}{(d\Delta/d\lambda)|_{\lambda=\Lambda_S}} \tag{46}$$

with

$$\varphi_1^{(k)}=\frac{(1-\nu^{(k)})r_1^{(k)}n}{\nu_2^{(k)}q^{(k)}}, \quad \varphi_2^{(k)}=(-1)^k\frac{\nu^{(k)}r_2^{(k)^2}-n^2}{\nu_2^{(k)}q^{(k)}},$$

where Δ is defined by Eq. (42), Λ_S is the root of Eq. (42), Δ_j ($j=\overline{1,4}$) represents the determinant Δ calculated at $\lambda=\Lambda_S$ in which jth column is replaced by

$$\begin{bmatrix} K_u \\ 0 \\ 0 \\ nK_s \end{bmatrix}.$$

Comparison of asymptotic and numerical results is demonstrated in Table V. Here $\Lambda^{ex}=\operatorname{Re}\Lambda^{ex}+i\operatorname{Im}\Lambda^{ex}$ are the exact values of natural frequencies, $\operatorname{Re}\Lambda^{as}=\Lambda_S$, $\operatorname{Im}\Lambda^{as}$ are calculated by the Eq. (46), and the relative errors are defined as

$$\varepsilon_1=|\operatorname{Re}\Lambda^{as}-\operatorname{Re}\Lambda^{ex}|/\operatorname{Re}\Lambda^{ex}\times 100\%,$$

$$\varepsilon_2=|\operatorname{Im}\Lambda^{as}-\operatorname{Im}\Lambda^{ex}|/\operatorname{Im}\Lambda^{ex}\times 100\%.$$

The problem parameters are the same as in Table II except $h=0.0001$. The associated natural forms are presented in Fig. 4 for $n=10$, $h=0.001$. The figure illustrates that the magnitudes of localized tangential vibrations exceed considerably the magnitudes of propagating bending vibrations.

VII. CONCLUDING REMARKS

The interfacial vibrations considered in the paper do not occur for arbitrary combination of problem parameters. As it follows from the consideration above for bending and extensional shell vibrations, analysis of the relevant Stonely-type plate waves provides appropriate conditions for their existence. In the case of semi-membrane vibrations formula (23) represents the condition for coincidence of the lowest critical frequencies corresponding to both semi-infinite shells. Since Eq. (22) is only the leading-order approximation for the frequency equation, the lowest critical frequencies may differ in secondary terms.

Our analysis is restricted to boundary conditions simulating perfect contact at the interface. In analogy to edge vibrations investigated in Ref. 1 we could expect localized interfacial vibrations for other contact conditions as well.

The results of the paper can be applied to a finite cylindrical shell, if the shell length is much greater than a typical size of the vibrating zone localized near the interface. In doing so, an ''infinite'' limit for a finite shell depends on the type of interface vibrations.

It should also be emphasized that a weak interaction with bending modes resulting in the shift of the extensional frequencies from the real axis as well as a weak decay in the case of semi-membrane vibrations may be considerably af-

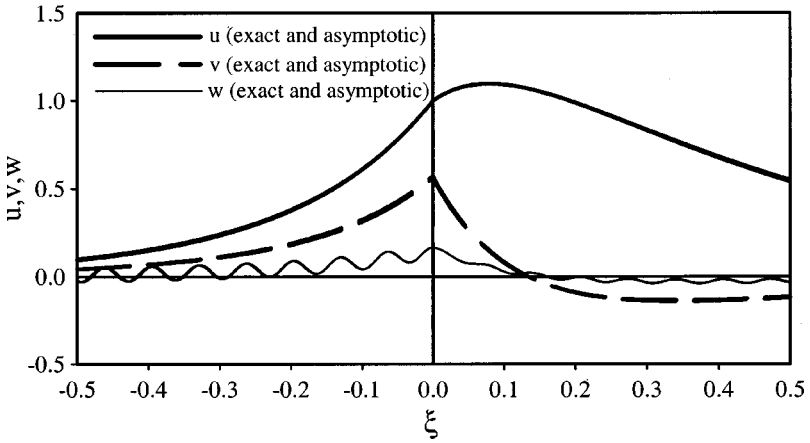

FIG. 4. Natural forms of extensional vibrations.

fected by structural damping. Further considerations should be based on multi-parameter analysis involving asymptotic estimation of structural damping.

ACKNOWLEDGMENTS

The work was partly supported by INTAS (Grant No. YSF 2001/1-7) and in the case of the first author also by Russian Foundation of Basic Research (Grant Nos. 98-15-96017 and 99-01-01123).

APPENDIX: EXACT SOLUTION

Let us derive the exact solution of the problem (1) and (2). Particular solutions of Eqs. (1) can be written as

$$u^{(k)}(\xi)=u_0^{(k)}\exp((-1)^k r^{(k)}\xi),$$
$$v^{(k)}(\xi)=v_0^{(k)}\exp((-1)^k r^{(k)}\xi), \tag{A1}$$
$$w^{(k)}(\xi)=w_0^{(k)}\exp((-1)^k r^{(k)}\xi),$$

where $r^{(k)}$, $u_0^{(k)}$, $v_0^{(k)}$, and $w_0^{(k)}$ are the sought for constants. By substituting Eqs. (A1) into Eqs. (1) we arrive at a linear algebraic system in the coefficients $u_0^{(k)}$, $v_0^{(k)}$, and $w_0^{(k)}$. It is

$$\begin{aligned}
&(r^{(k)2}-\tfrac{1}{4}\nu_4^{(k)}n^2+\nu_2^{(k)}q^{(k)}\lambda)u_0^{(k)}-(-1)^k\tfrac{1}{4}\nu_1^{(k)}nr^{(k)}v_0^{(k)}\\
&\quad-(-1)^k\nu^{(k)}r^{(k)}w_0^{(k)}=0,\\
&(-1)^k\tfrac{1}{4}\nu_1^{(k)}nr^{(k)}u_0^{(k)}+[-\tfrac{1}{4}\nu_4^{(k)}r^{(k)2}+n^2-\nu_2^{(k)}q^{(k)}\lambda\\
&\quad-\tfrac{1}{3}\eta^2(\nu_4^{(k)}r^{(k)2}-n^2)]v_0^{(k)}\\
&\quad+n[1+\tfrac{1}{3}\eta^2(n^2-\nu_3^{(k)}r^{(k)2})]w_0^{(k)}=0,\\
&-(-1)^k\nu^{(k)}r^{(k)}u_0^{(k)}+n[1+\tfrac{1}{3}\eta^2(n^2-\nu_3^{(k)}r^{(k)2})]v_o^{(k)}\\
&\quad+[1+\tfrac{1}{3}\eta^2(r^{(k)2}-n^2)^2-\nu_2^{(k)}q^{(k)}\lambda]w_0^{(k)}=0.
\end{aligned} \tag{A2}$$

The constant $r^{(k)}$ denotes a root of the characteristic equation associated with the system (A2):

$$a_0^{(k)}r^{(k)8}+a_1^{(k)}r^{(k)6}+a_2^{(k)}r^{(k)4}+a_3^{(k)}r^{(k)2}+a_4^{(k)}=0. \tag{A3}$$

The coefficients of Eq. (A3) can be found in Ref. 5. To provide either the decay of the solution at infinity or to satisfy the radiation condition, we choose roots with $\mathrm{Re}\, r^{(k)}>0$ or $\mathrm{Re}\, r^{(k)}=0$ and $\mathrm{Im}\, r^{(k)}>0$. For each of these roots $r_i^{(k)}$ ($i=\overline{1,4}$) we find from Eqs. (A2) the constants $u_i^{(k)}$, $v_i^{(k)}$, and $w_i^{(k)}$. The general solution becomes

$$\begin{aligned}
u^{(k)}(\xi)&=\sum_{i=1}^{4}B_i^{(k)}u_i^{(k)}\exp((-1)^k r_i^{(k)}\xi),\\
v^{(k)}(\xi)&=\sum_{i=1}^{4}B_i^{(k)}v_i^{(k)}\exp((-1)^k r_i^{(k)}\xi),\\
w^{(k)}(\xi)&=\sum_{i=1}^{4}B_i^{(k)}w_i^{(k)}\exp((-1)^k r_i^{(k)}\xi),
\end{aligned} \tag{A4}$$

where $B_i^{(k)}$ are arbitrary constants.

Then we satisfy the boundary conditions (2). By inserting Eqs. (A4) into Eqs. (2) we obtain a linear algebraic system in the constants $B_i^{(k)}$. The result is

$$\begin{aligned}
&\beta_{ij}B_j^{(1)}+\beta_{i,j+4}B_j^{(2)}=0,\\
&\beta_{i+4,j}B_j^{(1)}+\beta_{i+4,j+4}B_j^{(2)}=0,\quad i,j=\overline{1,4},
\end{aligned} \tag{A5}$$

where

$$\begin{aligned}
&\beta_{1j}=u_j^{(1)},\quad \beta_{1,j+4}=-u_j^{(2)},\quad \beta_{2j}=v_j^{(1)},\\
&\beta_{2,j+4}=-v_j^{(2)},\quad \beta_{3j}=w_j^{(1)},\quad \beta_{3,j+4}=-w_j^{(2)},\\
&\beta_{4j}=-r_j^{(1)}w_j^{(1)},\quad \beta_{4,j+4}=-r_j^{(2)}w_j^{(2)},\\
&\beta_{5j}=\frac{1}{\nu_2^{(1)}\gamma^{(1)}}(r_j^{(1)}u_j^{(1)}+\nu^{(1)}nv_j^{(1)}+w_j^{(1)}),\\
&\beta_{5,j+4}=-\frac{1}{\nu_2^{(2)}\gamma^{(2)}}(-r_j^{(2)}u_j^{(2)}+\nu^{(2)}nv_j^{(2)}+w_j^{(2)}),\\
&\beta_{6j}=\frac{1}{\nu_1^{(1)}\gamma^{(1)}}\Big(nu_j^{(1)}-r_j^{(1)}v_j^{(1)}\\
&\qquad-\frac{4}{3}\eta^2(r_j^{(1)}v_j^{(1)}+r_j^{(1)}nw_j^{(1)})\Big),\\
&\beta_{6,j+4}=-\frac{1}{\nu_1^{(2)}\gamma^{(2)}}\Big(nu_j^{(2)}+r_j^{(2)}v_j^{(2)}\\
&\qquad+\frac{4}{3}\eta^2(r_j^{(2)}v_j^{(2)}+r_j^{(2)}nw_j^{(2)})\Big),\\
&\beta_{7j}=\frac{\eta_1^{(1)2}}{\gamma^{(1)}}(-\nu^{(1)}nv_j^{(1)}+(r_j^{(1)2}-\nu^{(1)}n^2)w_j^{(1)}),\\
&\beta_{7,j+4}=-\frac{\eta_1^{(2)2}}{\gamma^{(2)}}(-\nu^{(2)}nv_j^{(2)}+(r_j^{(2)2}-\nu^{(2)}n^2)w_j^{(2)}),\\
&\beta_{8j}=-\frac{\eta_1^{(1)2}}{\gamma^{(1)}}r_j^{(1)}(-\nu_3^{(1)}nv_j^{(1)}+(r_j^{(1)2}-\nu_3^{(1)}n^2)w_j^{(1)}),\\
&\beta_{8,j+4}=-\frac{\eta_1^{(2)2}}{\gamma^{(2)}}r_j^{(2)}(-\nu_3^{(2)}nv_j^{(2)}+(r_j^{(2)2}-\nu_3^{(2)}n^2)w_j^{(2)}),\\
&\qquad j=\overline{1,4}.
\end{aligned} \tag{A6}$$

The natural frequencies λ can be determined from the equation

$$\det(\beta_{ij})=0,\quad i,j=\overline{1,8}. \tag{A7}$$

For each of them we calculate the constants $B_i^{(k)}$ from Eqs. (A5) and get the natural form defined by Eqs. (A4).

[1] E. A. G. Shaw, "On the resonant vibrations of thick barium titanate disks," J. Acoust. Soc. Am. **20**, 38–50 (1956).

[2] D. C. Gazis and R. D. Mindlin, "Extensional vibrations and waves in a circular disk and a semi-infinite plate," J. Appl. Mech. **27**, 541–547 (1960).

[3] P. J. Torvik, "Reflection of wave trains in semi-infinite plates," J. Acoust. Soc. Am. **41**, 346–353 (1967).

[4] R. D. Gregory and I. Gladwell, "The reflection of a symmetric Rayleigh-Lamb wave at the fixed or free edge of a plate," J. Elast. **13**, 185–206 (1983).

[5] J. D. Kaplunov, L. Yu. Kossovich, and M. V. Wilde, "Free localized vi-

brations of a semi-infinite cylindrical shell,'' J. Acoust. Soc. Am. **107**, 1383–1393 (2000).
[6] I. P. Getman and O. N. Lisickii, ''Reflection and transmission of acoustic waves at the interface of separation of two elastic semi-strips,'' Prikl. Mat. Mekh. **52**, 1044–1048 (1998) [English transl.: Appl. Math. Mech.].
[7] J. D. Kaplunov and M. V. Wilde, ''Edge and interfacial vibrations in elastic shells of revolution,'' ZAMP **51**, 530–549 (2000).
[8] A. L. Goldenveizer, *Theory of Elastic Thin Shells* (Pergamon, Oxford, 1961).
[9] J. D. Kaplunov, L. Yu. Kossovich, and E. V. Nolde, *Dynamics of Thin Walled Elastic Bodies* (Academic, San Diego, 1998).
[10] A. L. Goldenveizer, V. B. Lidskii, and P. E. Tovstik, *Free Vibrations of Thin Elastic Shells* (Nauka, Moscow, 1979).
[11] A. S. Silbergleit and I. B. Suslova, ''Contact bending waves in thin plates,'' Akust. Zh. **29**, 186–191 (1983) [English transl.: Sov. Acoust.].
[12] R. Stoneley, ''The elastic waves at the interface of separation of two solids,'' Proc. R. Soc. London, Ser. A **106**, 416–429 (1924).

Nonlinear seismo-acoustic land mine detection and discrimination

Dimitri Donskoy,[a] Alexander Ekimov, Nikolay Sedunov, and Mikhail Tsionskiy
Davidson Laboratory, Stevens Institute of Technology, 711 Hudson Street, Hoboken, New Jersey 07030

(Received 4 September 2001; revised 16 February 2002; accepted 21 March 2002)

A novel technique for detection and discrimination of artificial objects, such as land mines, pipes, containers, etc., buried in the ground, has been developed and tested. The developed approach utilizes vibration (using seismic or airborne acoustic waves) of buried objects, remote measurements of soil surface vibration (using laser or microwave vibrometers), and processing of the measured vibration to extract mine's ''vibration signatures.'' The technique does not depend upon the material from which the mine is fabricated whether it be metal, plastic, wood, or any other material. It depends upon the fact that a mine is a ''container'' whose purpose is to contain explosive materials and associated detonation apparatus. The mine container is in contact with the soil in which it is buried. The container is an acoustically compliant article, whose compliance is notably different from the compliance of the surrounding soil. Dynamic interaction of the compliant container and soil on top of it leads to specific linear and nonlinear effects used for mine detection and discrimination. The mass of the soil on top of a compliant container creates a classical mass–spring system with a well-defined resonance response. Besides, the connection between mass (soil) and spring (mine) is not elastic (linear) but rather nonlinear, due to the separation of the soil/mine interface in the tensile phase of applied dynamic stress. These two effects, constituting the mine's vibration signature have been measured in numerous laboratory and field tests, which proved that the resonance and nonlinear responses of a mine/soil system can be used for detection and discrimination of buried mines. Thus, the fact that the mine is buried is turned into a detection advantage. Because the seismo-acoustic technique intrinsically detects buried containers, it can discriminate mines from noncompliant false targets such as rocks, tree roots, chunks of metal, bricks, etc. This was also confirmed experimentally in laboratory and field tests. [DOI: 10.1121/1.1477930]

PACS numbers: 43.40.Ga, 43.25.Ts, 43.28.En [ANN]

I. INTRODUCTION

The most commonly used devices for land mine detection are metal detectors that work by measuring the disturbance of an emitted electromagnetic field caused by the presence of metallic objects in the ground. For ferromagnetic objects, magnetometers are employed. These sensors measure the disturbance of the earth's natural electromagnetic field. Neither of these types of detectors can differentiate a mine from metallic debris; this leads to up to 1000 false alarms for each real mine (Gros and Bruschini[1]). In addition, most modern antipersonnel mines are made out of plastic or wood with very few metal parts in them, so the metal detectors cannot detect them. Newer methods of mine detection involve ground-penetrating radar, infrared imaging, x-ray backscattering, thermal neutron activation, and some others, *detection and remediation technologies*.[2] Most of these methods rely on imaging and very often cannot differentiate a mine from rocks and other debris.

Acoustic methods of detecting mines were always a primary approach for underwater mine detection. However, earlier attempts to use acoustic energy for land mine detection were not successful due to a number of deficiencies. One method, by House and Pape,[3] identifies a buried object by viewing the images of the acoustic energy reflected from the soil and, therefore is unable to differentiate a mine from debris with similar acoustic reflectivity. Other methods, including Rogers and Don[4] and Caulfield,[5] are based on the comparison of a reflected acoustic signal with a reference signal in order to provide detection of the object. The difference between these two signals indicates the presence of an object. The drawback of these methods is that any variations in the physical properties of the ground (density, porosity, moisture content, etc.) as well as the presence of nontarget objects (rocks, tree and grass roots, debris, etc.) will create a difference from the reference signal and, consequently, lead to the high false-alarm rates. Recent advances in sound and vibration measurement techniques and signal processing have opened new possibilities for land mine detection using seismic/acoustic energy; see Donskoy,[6–9] Sabatier and Xiang,[10–12] Scott *et al.*[13,14]

The essence of the seismic/acoustic approach is to excite low-frequency (typically below 1000 Hz) vibration of a buried mine and measure surface vibration signature above the mine using remote sensors. Excitation of a mine and surrounding soil is achieved by using airborne (acoustic) or solid-borne (seismic) waves. Remote sensing is achieved with laser-doppler vibrometers (Sabatier, Donskoy) or microwave vibrometers (Scott, Donskoy). Understanding and correct processing of a mine's vibrating signatures is a key ele-

[a]Electronic mail: ddonskoy@stevens-tech.edu

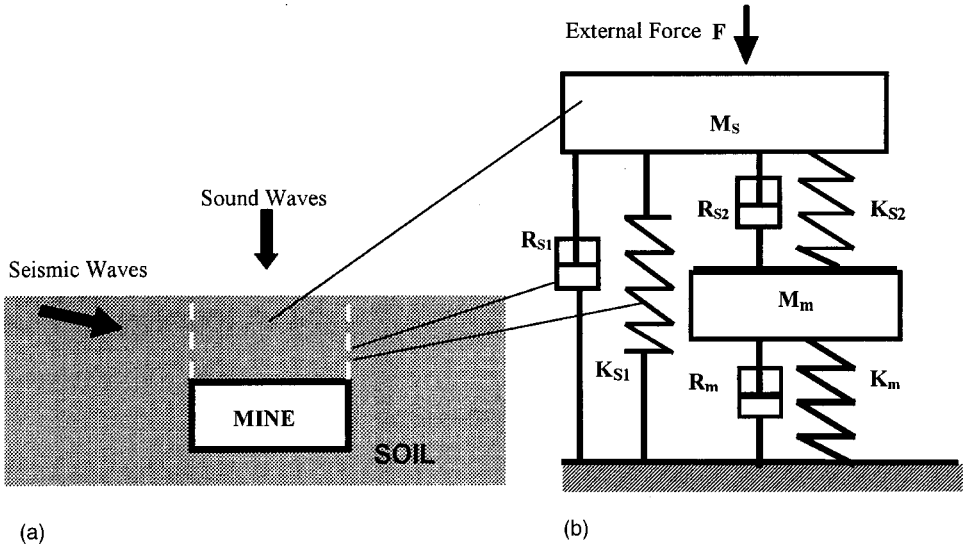

FIG. 1. Mine buried in soil and excited with sound or seismic waves (a), and an equivalent mechanical (dynamical) diagram of this mine/soil system (b).

ment of seismo-acoustic detection. This article concentrates on a physical model, which explains and predicts vibration signatures of different mines under different soil conditions and lays a foundation for the detection techniques. The article also describes laboratory and field experimental results with real mines, which support and validate the developed detection approach.

II. PHYSICAL MECHANISM OF SEISMO-ACOUSTIC DETECTION

One of the critical elements in successful implementation of a new technical concept is the development of an adequate physical model of the system under test: in our case it is a mine/soil system. The appropriate model leads to optimum detection algorithms and helps to estimate the mine detection capabilities of the technique applied to various mine types, burial depths, and soil conditions.

Any physical model of a dynamic system starts with a comparison of the wavelength and characteristic geometric size of the system. If the wavelength is shorter than the size of the target, the wave approach should be used. If the wavelength is longer than the target, the lump-element approach is more appropriate. In the case of a mechanical system such as a soil/mine system, the use of the lump-element (mass–spring–dashpot) approach is justified as long as low-frequency waves are used. These low-frequency waves have wavelengths which are greater than the size of a mine and its burial depth. Thus, typical sizes of antipersonnel (AP) mines are in the range of 5–10 cm and their burial depths are up to 5 cm. Typical sizes of antitank (AT) mines are in the range of 20–30 cm and their burial depths are up to 20 cm. Wavelengths in soil can be varied depending on the soil characteristics. Typically, the wavelengths are greater than 30 cm in the frequency range of hundreds of Hz, the range where the most successful practical results were obtained.[6–14]

The first such lump-element model was introduced in 1999; see Donskoy.[7] According to this earlier version of the model, the soil on top of the mine has mass (inertia) and stiffness, determined by the compressibility of the soil, and is supported by a compliant mine's top. For simplicity, the dynamic mass of the mine's top diaphragm was neglected, so the resulting dynamic mechanical model of the mine/soil system consists of soil mass and its stiffness (due to soil bulk compressibility), mine stiffness, and damping coefficients for the soil and the mine, respectively. The resulting spring–mass system suggested the presence of the resonance response of the mine/soil system which was observed in numerous laboratory and field tests.[6–14]

In order to quantify this model, we conducted measurements of the dynamic mechanical impedances of the live mines and determined each mine's characteristic parameters, such as their dynamic masses, stiffnesses, and damping coefficients. The results of these measurements are presented in the next section. One important finding was that most of the tested mines exhibited a clearly defined mechanical resonance of their casing. This indicates that the dynamic mass of the mine's casing may have significant impact on the overall dynamic response of the mine/soil system and must be included in the model.

Another significant factor to be accounted for is the effect of the shear stiffness of the soil. Since the soil column above the mine may move differently (with greater displacement) from the surrounding soil, the shear stiffness of the soil (along with the corresponding damping) must be introduced into the model as well.

Buried in soil, mine and soil (on top of the mine) create a unified soil/mine system [Fig. 1(a)], whose dynamic behavior could be described using the equivalent mechanical (dynamical) diagram shown in Fig. 1(b). In this diagram, M_S is the mass of the soil on top of the vibrating mine diaphragm; K_{S1} and K_{S2} are the shear and the compression stiffnesses of soil; R_{S1} and R_{S2} are the soil damping coefficients due to shear and compression motion of the soil, respectively. Parameters K_m, M_m, and R_m are the dynamic mechanical parameters of the mine top diaphragm: dynamic stiffness, mass, and damping coefficient, respectively.

The introduced soil parameters are depth dependent. The following formulas can be used to evaluate these parameters:

$$M_S \cong \rho A H, \tag{1}$$

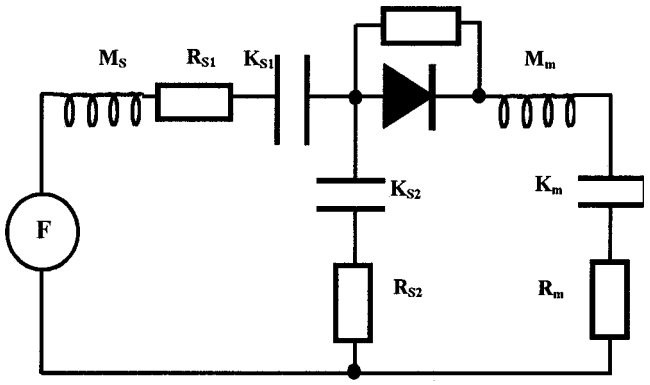

FIG. 2. Equivalent electrical diagram of the mine–soil mechanical system.

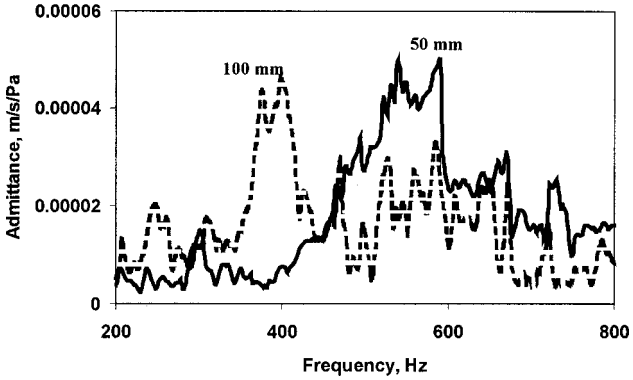

FIG. 3. Admittance of sand above solid-steel disk buried at 2 and 4 in.

where H is the burial depth, A is the effective area of the upper compliant diaphragm of the mine, and ρ is the density of the soil. The shear and compression stiffnesses, K_{S1} and K_{S2}, of the soil can be evaluated from the soil effective shear modulus, G, and compressibility, C, (Mitchell[15]) by evaluating total shear and compressive forces acting on the vibrating soil column above the compliant mine diaphragm. For evaluation purposes we use a uniform cylindrical soil column on top of a circular mine diaphragm with radius R. The column is under a normal stress, σ, and its side surface is under a shear stress, τ. Spring stiffness is defined as a ratio of an applied external force to the resulting deformation, so

$$K_{S2}=(\sigma A)/\Delta_n, \quad K_{S1}=(\tau S)/\Delta_s, \tag{2}$$

where $S=2\pi RH$ is the side area of the column, $A=\pi R^2$ is the area of the column foundation, $\Delta_n=\varepsilon H$ and $\Delta_s=\gamma(\lambda/4)$ are normal and shear deformations, respectively, and λ is the shear wavelength. Here, the deformations are defined using respective normal and shear strains, ε and γ, multiplied by characteristic lengths. In dynamic (acoustic) problems, the characteristic length could be estimated as a quarter of the respective wavelength: compression wave (P wave) for the normal deformation and shear wave (S wave) for the shear deformation. In the outlined problem, however, the height of the column, H, is much less than the wavelength of the P wave, so H is used as a characteristic length for the normal deformation. Substituting the defined deformations into Eq. (2) and taking into account the stress–strain relationships for the normal and shear deformations, the effective soil column stiffnesses can be evaluated as

$$K_{S1}\cong\frac{8\pi}{\lambda}GRH, \quad K_{S2}\cong\frac{1}{C}\frac{A}{H}. \tag{3}$$

The soil damping coefficients, R_{S1} and R_{S2}, are both proportional to the depth, H. The actual values of the damping coefficients could vary in a wide range depending on soil type and conditions.

Analysis of this system is easy to perform using an equivalent electrical diagram in which external force, F, is equivalent to a voltage generator; masses, stiffnesses, and damping parameters are represented by inductances, capacitors, and resistances, respectively, as shown in Fig. 2. In this diagram, an additional nonlinear element (a diode with a shunt resistor) is introduced to account for the nonlinear behavior of the system due to separation effect at the soil–mine interface.[6] This separation is due to a weak bonding between soil particles and mine surface. As a result, polarized elastic wave then passes across this interface, mine surface and soil will stay together and move as one during the compression phase of the wave, and then separate under the tensile phase. This nonlinear action, the closing and opening of the interface, will distort the wave and, therefore, generate signals with frequencies different from the frequencies of the imposed vibration which be used for the detection and identification of buried mines.

Figure 2 completes the linear and nonlinear model of the mine/soil dynamic system. There is no doubt that the behavior of the real soil and its interaction with the mine can be more complicated than the model suggests. Thus, the soil could exhibit a certain degree of nonlinearity, especially loose or unconsolidated soil. The proposed model by no means claims to be a comprehensive description of the complicated system under consideration. However, as any engineering model, it helps to understand the physical mechanisms involved, and provides qualitative as well as quantitative evaluation of the dynamic behavior of a soil/mine system. This is essential for the development and optimization of the detection technique. Since the model operates with a limited number of measurable or easily estimated parameters, it could also be incorporated into detection-enhancing signal-processing algorithms.

III. EXPERIMENTAL VALIDATION OF THE MODEL

A. Resonance behavior of the soil/mine system

The physical model of the soil/mine system, presented by the diagrams in Fig. 1(b) and Fig. 2, suggests that this system should have resonances. The system should have a resonance even if a buried object (mine, rock, or any object which has compressibility significantly different from the compressibility of soil) does not have any resonances on its own. This is because of the mass–spring nature of the soil column on top of the object. This hypothesis can be easily tested by measuring the frequency dependence of impedance (or admittance, which is inverse impedance) of the soil on top of a buried solid nonresonating object such as a steel disk. As Fig. 3 shows, indeed, there is clear resonance response of the sand above solid foundation, as steel disk. As

the depth, H, increases, the resonance frequency shifts down due to increased mass of the sand column, since $M_S \sim H$. In the absence of the buried foundation, there were no such resonance responses observed.

These and other similar laboratory experiments, conducted in the Davidson Laboratory's 5000-kg sand- and dirt-filled tank, clearly demonstrated the mass–spring-like behavior of the soil column of the soil/mine system introduced in the previous section.

The next step in validating the model would be replacement of a solid object with a compliant one, such as a mine, and measuring both linear and nonlinear responses of the system. The numerous laboratory experiments with mine casings (both antitank and antipersonnel mines) yielded results consistent with the developed model.[6–9] The ultimate test, however, is the field test with real mines buried in real (outdoor) soil. In the following sections we describe the field tests, which provided additional validation of the model.

B. Nonlinear response

The nonlinear interface between soil and mine, represented by a diode on the diagram in Fig. 2, creates significant nonlinear distortion of the probing vibration, causing generation of harmonics and combination frequencies. These effects, however, take place only on the interface with compliant objects, such as mines, whose stiffness, K_m, is comparable or smaller than the soil stiffnesses. Solid (rigid) objects, such as rocks, metals debris, or tree roots, do not produce appreciable nonlinear distortion, as can be seen from the Fig. 2 diagram. Thus, for rigid object $K_m \gg K_{S2}$, the high impedance of the capacitor K_m effectively blocks current through the respective part of the circuit which also contains the nonlinear element (diode). Going back from the electrical to the mechanical diagram, there is no motion (no current) at the noncompliant (rigid) surface of a solid object and, therefore, there is no nonlinear interaction.

As for any nonlinear mechanical system, the nonlinearity can be introduced using nonlinear stress/strain relationships. Under the small strains, the nonlinear contribution can be approximated with the second (quadratic) term in the Taylor's expansion of the stress/strain relationship at the interface

$$\sigma = \alpha_m \varepsilon + \varepsilon \beta^2, \tag{4}$$

where σ is the normal stress applied to the interface, ε is the normal strain, and α_m and β_m are the linear and nonlinear parameters of the soil/mine interface, respectively. A similar relationship can also be introduced for soil with its linear, α_s, and nonlinear, β_s, parameters. For soil $\alpha_s = 1/C$, where C is the soil compressibility.[15] Physical mechanisms for soil and soil/mine interface nonlinearities are quite different. In porous soil, the nonlinear behavior is associated with the microstructure of the pores,[16,17] while the soil/mine nonlinearity is due to separation effect at the interface. For the nonlinear mine detection, β_s must be much smaller than β_m

$$\beta_s \ll \beta_m . \tag{5}$$

There are no data on β_s for soil at low frequencies (below 1000 Hz); however, for known practical applications of soil acoustics (strains are much less than 0.01%), β_s is considered negligibly small. Nevertheless, the validity of the relationship (5) can only be determined experimentally.

These nonlinear effects can be confirmed with a simple test by measuring nonlinear response from soil with no buried objects, and above buried compliant and noncompliant objects as shown in Fig. 4. In this test, the biharmonic signal with frequencies $f_1 = 400$ Hz and $f_2 = 650$ Hz was broadcast (with a loudspeaker) toward sand with a buried compliant mine casing (antipersonnel mine VS50), Fig. 4(a) sand without any object, Fig. 4(b); and sand with a buried solid steel disk, Fig. 4(c). The respective spectra of the sand surface vibration, measured with an accelerometer, are shown on the right-hand side of these figures. The signal with the difference frequency $f_2 - f_1$ on the spectrum in Fig. 4(a) clearly demonstrate the result of nonlinear interaction at the compliant mine interface. There is no nonlinear interaction (no difference frequency signal) at the noncompliant interface with the solid object, or in the absence of any object.

Similar tests were conducted in the field with real ''live'' mines buried in gravel or dirt. Strong nonlinear responses from buried mines and no responses from buried ''false targets'' such as solid steel pieces, rocks, and wood pieces were observed. These results are discussed below in Sec. V.

IV. IDENTIFICATION PARAMETERS OF MINES

Dynamic mechanical parameters of the mines (stiffness, K_m, dynamic mass, M_m, and damping coefficient, R_m) which we call the identification parameters, can be determined using measurements of the mine's dynamic impedances. The impedance, Z_m, of the mechanical system is defined as the ratio of the applied force to the resulting vibration velocity. For a one-degree mechanical system, it is determined by the following formula:

$$Z_m = -jK_m/\omega + R_m + j\omega M_m , \tag{6}$$

where ω is the angular frequency.

The impedance measurements were performed in August, 2000 at the U.S. Army's testing facilities. Live mines (with explosive charge but without fuses) were placed on $2 \times 2 \times 2$-cubic feet concrete foundation flush with the ground level. External force (airborne acoustic pressure) was applied in the range 30–800 Hz and measured with a microphone. Vibration velocity, V, of the mine's top diaphragm was measured with a noncontact laser-doppler vibrometer. The resulting magnitudes of the dynamic impedances (per unit area) of mines, $z_m = P/V$, were calculated and recorded as a function of frequency.

The measurements were taken for two representative mines of the same kind and demonstrated good data repeatability. Figures 5–7 show the typical impedances of antitank (AT) mines. Remarkably, most of the AT mines exhibited clearly defined mechanical resonances of their casing (shown as minimum on these graphs). Most of the resonances were found between 100 and 400 Hz. Some antipersonnel (AP) mines have resonances as well. Regardless of the resonances, most of the measured live mines (we measured nearly 50 AP and AT mines) had a higher compliance (lower stiffness) than the surrounding soil.

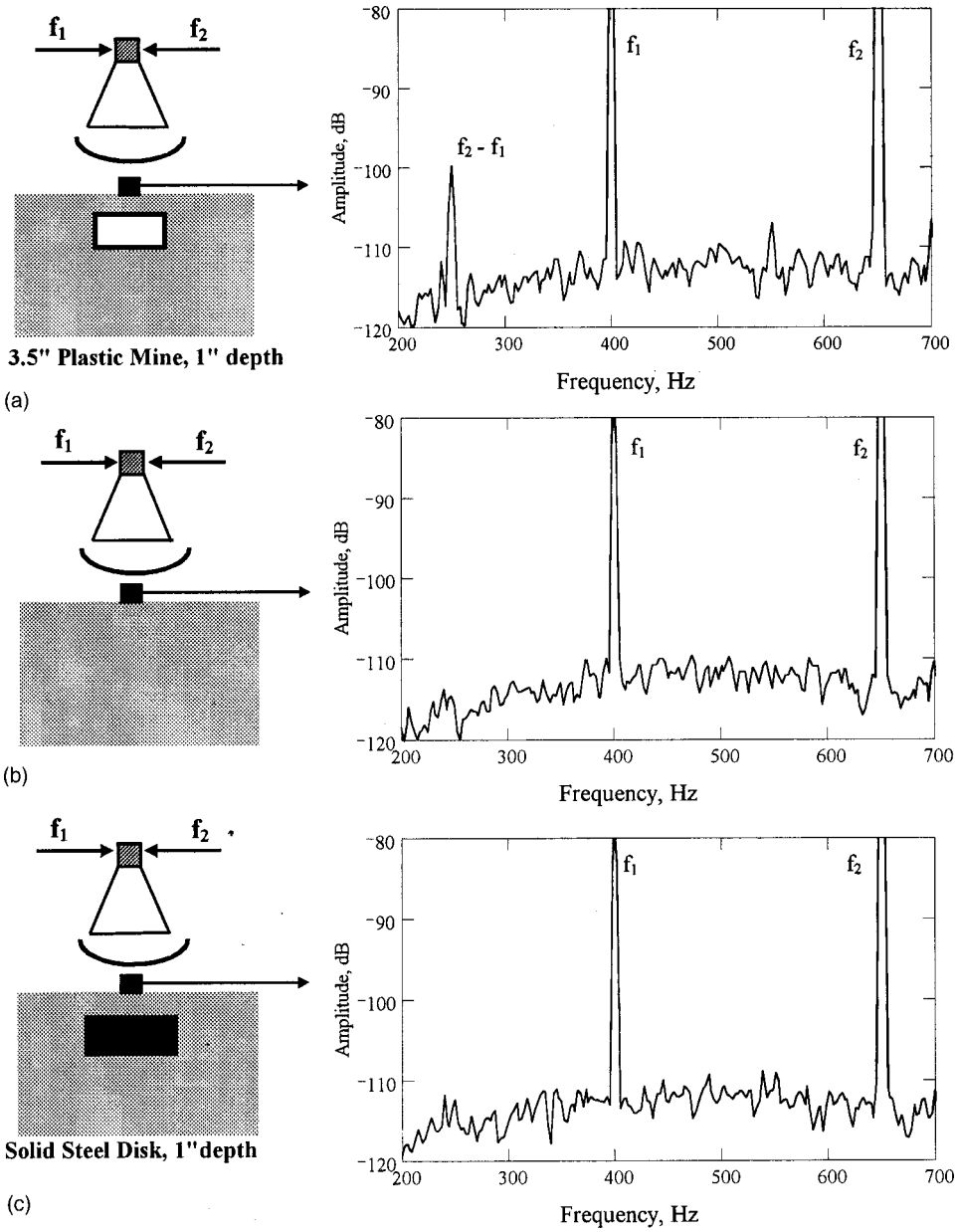

FIG. 4. Spectra of surface vibration under biharmonic excitation with frequencies f_1 and f_2; (a) the nonlinear response with the difference frequency, f_2-f_1, above buried compliant mine; (b) no mine—no nonlinear response; (c) buried noncompliant solid-steel disk shows no nonlinear response.

Table I shows dynamic parameters of some mines determined from their measured impedances and the formula (6) by curve fitting of the calculated impedance into the measured impedance curve. All parameters are normalized to area and denoted by lower-case letters. Most of the mines have stiffness below 10^8 Pa/m.

The soil compression stiffness K_{S2} can also be estimated using impedance measurements of soil. Under normal sound

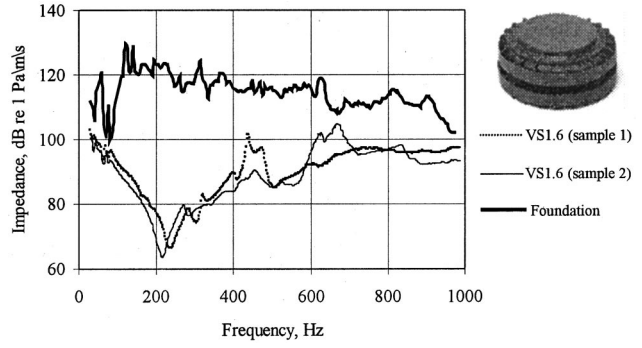

FIG. 5. Impedance of two samples of AT plastic mine VS1.6 and a foundation.

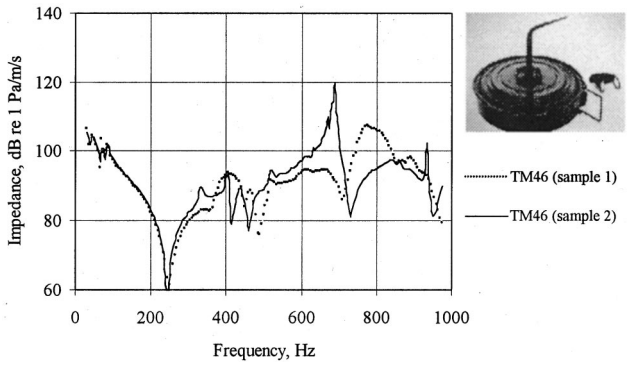

FIG. 6. Impedance of two samples of AT metal mine TM-46.

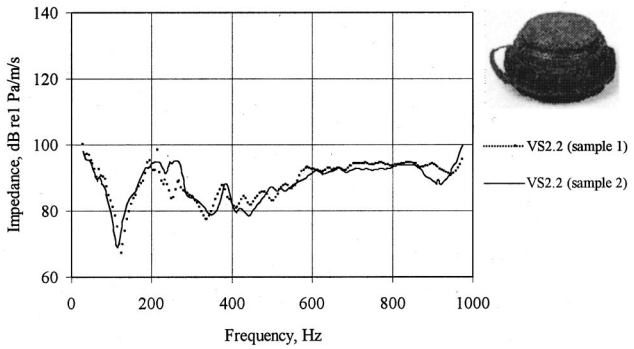

FIG. 7. Impedance of two samples of AT plastic mine VS2.2.

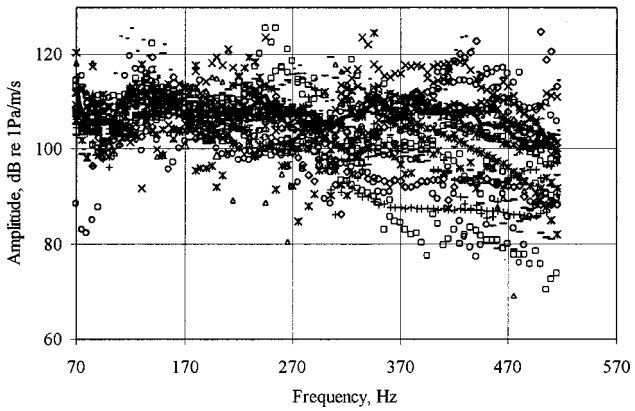

FIG. 8. Impedance of gravel surface measured at 23 off-mine locations.

incidence, the soil impedance, z_s, is approximately equal to $\sqrt{\rho/C}$, where ρ is the soil density and C is the soil compressibility. In our field measurements, z_s was about 3×10^5 Pa/m/s (see Fig. 8), so for the typical burial depth $H=10$ cm (soil column height), the soil stiffness (per unit area) $k_{S2}=1/\mathrm{CH}\approx z_s^2/\rho H$ and is well over 10^8 Pa/m and the stiffness of the concrete foundation and rigid targets such as rock or a piece of metal are above 10^9 Pa/m.

This comparison confirms that in the specified frequency range, the stiffness of most of the mines is less than the compression stiffness of the soil and much less than the stiffness of the rigid targets, which explains the detection and discrimination capabilities of the linear and nonlinear seismo-acoustic technique, as was outlined in the earlier papers.[6–9]

In order to conclude the discussion of mine dynamic parameters, the nature of the mine resonances should be explained. We believe that with a few exceptions, these resonances are due to the bending resonance of the mine casing's upper diaphragm. If we simplify the diaphragm as a circular plate, hinge-supported along its perimeter; the bending resonance of such a plate can be evaluated using the following formula:[18]

$$f_0\cong 0.92\frac{h}{R^2}\sqrt{\frac{E}{12(1-\nu^2)\rho}}, \tag{7}$$

where h and R are the thickness and radius of the plate, respectively, and E, ν, ρ are the material parameters of the plate (Young's modulus, Poisson's ratio, and density, respectively). This formula gives quite an accurate estimate of the resonance frequency. Thus, for the steel plate 1 mm thick with 0.1 m radius, the resonance frequency is 290 Hz, which is in the range of the measured resonance frequencies (see Table I).

V. FIELD TESTS

Field tests were conducted at the U.S. Army's outdoor test facilities in June, 2001. The facilities offer an opportunity to perform measurements under a broad variety of conditions: several soil types and various live mines buried at different depths. The major objective of the tests was experimental validation of the developed nonlinear seismo-acoustic detection technique and the supporting physical model. We concentrated on two types of measurements: impedance measurements and nonlinear interaction of acoustic/seismic waves. These measurements were taken in gravel and sandy soil off and above buried mines. Three types of plastic antitank (AT) mines (M19, VS1.6, and VS2.2) and three types of plastic antipersonnel (AP) mines (M14, VS50, and TS50) buried at different depths (up to 130 mm for AT mines and up to 50 mm for AP mines) were used in the test.

A. Impedance measurements

The impedance measurements of soil off and above buried mines provide important information about validity of the developed model. They also help us better understand the

TABLE I. Dynamic parameters of live mines.

Mine type	Resonance frequency f_0 (Hz)	Dynamic stiffness $k_m\times10^7$ (Pa/m)	Dynamic mass m_m (kg/m^2)	Damping coefficient r_m (kg/sm^2)	Description
TS-50	520	10	9	4 000	AP Plastic
VS-50	330	6	13	3 300	AP Plastic
PONZ-2	380	50	85	26 000	AP Plastic
VS-1.6	220	2.5	12	1 700	AT Plastic
TMA-5	190	0.2	1.4	300	AT Plastic
SH-55	280	2.5	8	3 000	AT Plastic
VS-HCT-2	465	2.8	3.3	500	AT Plastic
TM-46	250	4	16	1 200	AT Metal
TMA-4	250	17	65	20 000	AT Metal
PMN	none	13			AP Metal
AT-72	200	2	14	1 800	AT Wood

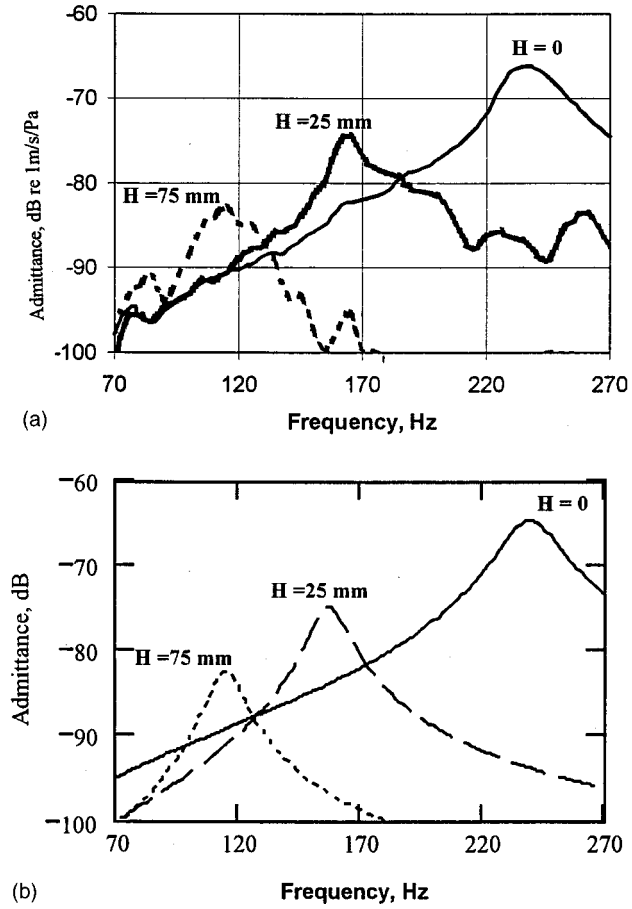

FIG. 9. Impedance dependence on mine burial depth: (a) field data for AT mine VS1.6; (b) calculated data for the same mine.

performance of the linear acoustic detection approach developed by the University of Mississippi (Sabatier and Xiang[10–12]).

The impedance of soil surface was determined by applying an external pressure (frequency-swept sound waves from a speaker) and measuring the acoustic pressure, P, with a microphone suspended about 10 mm above the surface. The resulting vibration velocity, V, was measured with a laser-doppler vibrometer and the impedance (per unit area) was calculated as $z=P/V$. The measurements were conducted in the frequency range 70–520 Hz. At the highest frequency, the sound wavelength in air is 0.63 m, which is much greater than the distance between the microphone and the surface. Therefore, the phase shift between incident and reflected from the surface sound waves is negligibly small and the measured pressure is the total pressure applied to the surface.

1. Variability of soil impedance

Figure 8 shows impedances measured at 23 off-mine locations on gravel surfaces. These data demonstrate that the impedance variation is relatively small (within 20-dB range) at the low frequencies (below 300 Hz) and much greater (as much as within 50-dB range) at the higher frequencies. Fortunately, most AT mines have resonances with much lower impedances than soil in the very same range below 300 Hz (see Figs. 5–7 and Table I). This impedance contrast, coupled with the low variability of the soil impedance at these frequencies, explains successful detection of AT mines achieved by the University of Mississippi.[10–12]

The situation with AP mines is not that fortunate. AP mines exhibit low impedances in the frequency range above 300 Hz. At these frequencies, wide variation of soil impedance may create significant problems in achieving low false-alarm detection using the linear acoustic approach.

2. Effect of mine's burial depth

Analysis of the developed model shows that the mine's depth is an important parameter affecting the resonance frequency of the mine/soil system and, most importantly, the magnitude of the system impedance. The lower the impedance of the mine/soil system, the greater the contrast with surrounding soil, and, as a result, the easier to find the mine. As the depth increases, the resultant impedance tends to increase as well, thus reducing the contrast. Figure 9(a) demonstrates this effect for AT mine VS1.6, buried in gravel at 0 m, 25 mm, and 75 m. Figure 9(b) shows similar results calculated using the spring–mass model and the mine parameters from the Table I. In the calculations we used depth-dependent soil parameters defined by formulas (1) and (3): $M_S \sim H$, $K_{S2} \sim H^{-1}$, $R_{S1} \sim H$, and $R_{S2} \sim H$. For shear stiffness K_{S1}, however, the dependence $K_{S1} \sim H^{0.5}$ is better fitted with the experimental data. The dependence $K_{S1} \sim H$, introduced by the formula (2), is based on the assumption that the shear stress is developed between the side surface of the soil column above the mine and the surrounding soil. In fact, the stress is distributed within the soil, so the resultant effective shear force may have more complicated dependence with the depth.

B. Nonlinear detection

The demonstration of the nonlinear detection was conducted using two signals: a shaker transmitted one, with the frequency f_1, and a speaker broadcast another one, with the frequency f_2. Both frequencies were swept with the same step 5 Hz toward each other, i.e., $f_{n1}=f_{01}+5n$ and $f_{n2}=f_{02}-5n$, where f_{01} and f_{02} are the initial frequencies, $n=1,2,...,N$, and N is the total number of steps. The result of the nonlinear interaction of these signals was observed at the sum frequency $f_+=f_{n1}+f_{n2}=f_{01}+f_{02}$. Such a sweeping algorithm allows us to observe the result of the nonlinear interaction at the fixed frequency $f_{01}+f_{02}$, while sweeping signals in the whole range from f_{01} to f_{02}.

In this test we chose the combination of acoustic (airborne) and seismic (soil-borne) excitation in order to avoid any possibility of direct nonlinear interaction of the signals except in soil. In most of the tests the acoustic signal started with $f_{01}=70$ Hz and seismic waves were swept down from $f_{02}=300$ Hz. The total number of steps was $N=23$ and $f_+=370$ Hz.

In this test we used 20-W seismic source positioned approximately 1 m from a mine and 300-W speaker positioned about 0.5 m from the mine. Soil vibration was measured with a laser-doppler vibrometer.

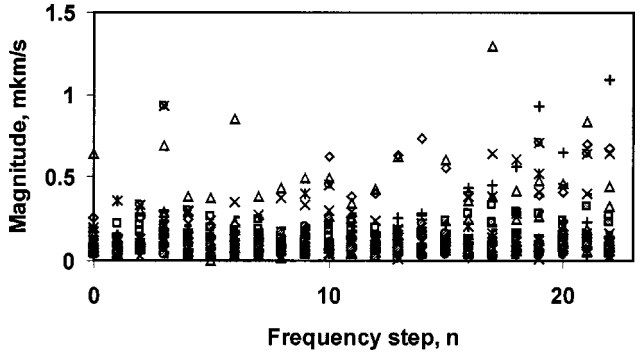

FIG. 10. Nonlinearity on gravel surface measured at 28 off-mine locations.

1. Off-mine soil nonlinearity

As with the impedance measurements, off-mine variability and level of nonlinearity is key in understanding the possibilities and limitations of the respective detection scheme. Figure 10 shows nonlinearity (f_+ magnitude as a function of the frequency step, n) measured at 28 off-mine locations on a gravel lane. These measurements show very small (near or equal to the noise floor of the setup) nonlinear vibration, as well as small variability between various locations. Similar measurements in sandy soil demonstrated the same low level and very small variability of the nonlinear vibration.

2. Nonlinear response above buried mines

The nonlinear response above buried mines was much higher than that off-mine for all measured mines at almost all depths, thus validating the condition (5). Figures 11 and 12 show magnitude of the sum frequency f_+ as the frequencies of the probing waves are swept as described above. All data is averaged over a number of locations above mines. These numbers are indicated in the respective figure captions for each curve. Figure 11 shows nonlinear responses above AT plastic mine M19 buried at 25 mm, 75 mm, and 125-mm depths in gravel. As expected, the magnitude decreases with depth. Still, even at 125 mm the nonlinear response above mine is about 10–15 dB higher than that of averaged off-mine nonlinearity, also shown in the figure. Figure 12 shows the same results for the AP plastic mine VS50. Similar results were also obtained for the rest of the tested AT and AP mines in gravel and sandy soils.

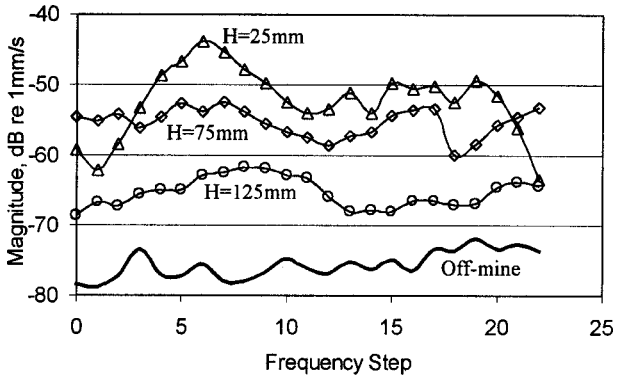

FIG. 11. Averaged nonlinear response of AT plastic mine M19 buried in gravel at the depths 25 mm (averaged over six locations above the mine); 75 mm (nine locations), and 125 mm (four locations). Solid line is the off-mine nonlinearity averaged over 28 locations.

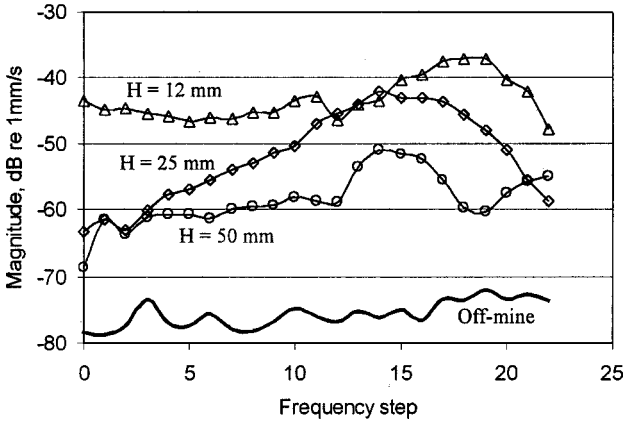

FIG. 12. Averaged nonlinear response of AP plastic mine VS50 buried in gravel at the depths 12 mm (averaged over three locations above the mine), 25 mm (two locations), and 50 mm (two locations). Solid line is the off-mine nonlinearity averaged over 28 locations.

3. False target response

One of the most important features of nonlinear detection is its insensitivity to false targets such as rocks, chunks of metal, or wood. Figure 13 demonstrates this, showing the nonlinear response above buried rocks, a heavy metal plate, and a piece of wood. For comparison, the off-mine response and the response above mine M19 (buried at 75-mm depth in the same gravel lane as the false targets) are shown in this figure as well. Again, as in many laboratory tests,[6–8] the nonlinear response from the false targets is as small as off-mine response and is much smaller than that of on-mine.

VI. CONCLUDING REMARKS

The experimental data presented above support and validate the developed physical model of the soil/mine dynamic system. The model, in turn, explains and predicts the field experimental results, such as shown in Fig. 10, and helps to optimize the detection algorithms.

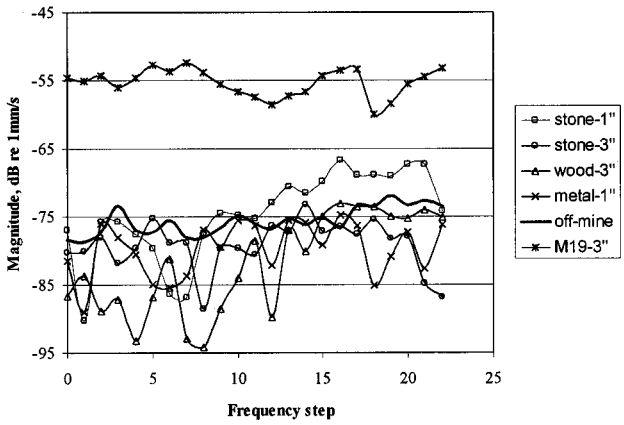

FIG. 13. Nonlinear responses from false targets (wood, steel, rocks) compared with off-mine and on-mine (M19 at 75-mm depth) responses.

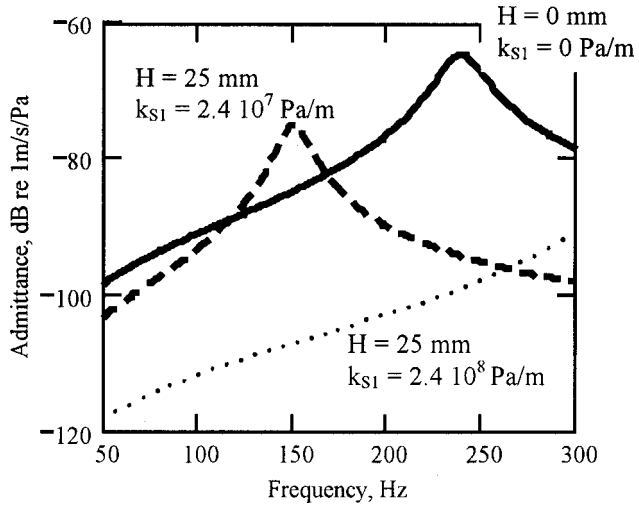

FIG. 14. The effect of increased shear stiffness k_{S1} on the admittance of AT plastic mine VS1.6. Solid curve—admittance of the mine at 0 depth; dashed curve—admittance at 25-mm (1 in.) depth; dotted curve—admittance, then k_{S1} is 10 times higher.

There are two detection algorithms: the linear detection based on the impedance contrast on- and off-mine (this approach has been pursued by the University of Mississippi[10–12] and the Georgia Institute of Technology[13,14]) and the nonlinear detection developed at the Stevens Institute of Technology[6–9]).

The model presented in this paper explains the optimum linear detection (maximum contrast of soil surface vibration on and off the buried mine—on/off contrast) that takes place in the vicinity of the soil/mine resonance. In addition to resonance, the maximum contrast is also directly proportional to the stiffness contrast between the soil and the mine; that is, the more compliant the mine relative to soil compliance, the greater the on/off contrast.

Analysis of the developed model also indicates that the soil damping coefficient, R_{S1}, and stiffness, K_{S1}, associated with shear deformations, have a very strong impact on linear detection, in fact, much stronger than the parameters R_{S2}, and K_{S2}, associated with compression tension in soil. Figures 14 and 15 illustrate the effect of parameters K_{S1} and R_{S1}

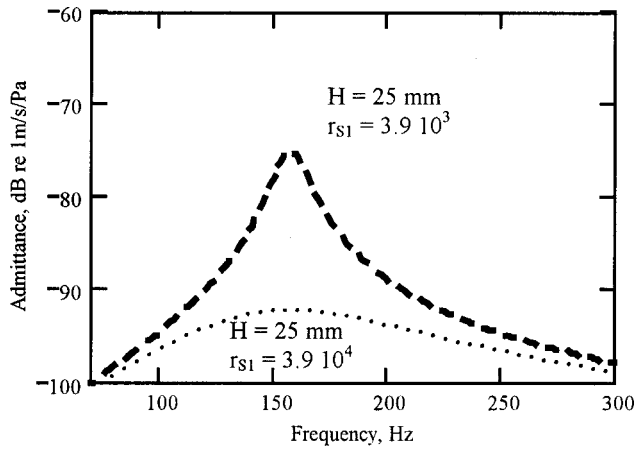

FIG. 15. The effect of increased shear friction, r_{S1}, on the admittance of AT plastic mine VS1.6. Dashed curve—admittance above the mine at 25-mm (1 in.) depth; dotted curve—admittance, then r_{S1} is 10 times higher.

on the surface vibration velocity above the buried mine. Solid and dashed curves in Fig. 14 show admittance of VS1.6 AT mine at 0 mm and 25-mm depths, respectively. These are the same responses as shown in Fig. 9(b) for the respective depths. The dotted curve in the Fig. 14 shows the calculated admittance above the same mine at the same depth ($H=25$ mm) with all soil parameters unchanged except the shear stiffness k_{S1}, which is 10 times higher as the dashed curve. Such a k_{S1} increase could be due to various factors: soil compaction, different soil type (clay instead of sand), freezing temperatures, etc. As Fig. 14 shows, higher shear stiffness can lead to significant decrease in the admittance (higher impedance) above a mine, reducing on/off mine impedance contrast, and diminishing the detection performance. This shear stiffness effect on on/off contrast is quite understandable: stronger shear forces between the surrounding soil (off-mine) and the soil column above the mine (on-mine) equalize soil vertical deformations on- and off-mine.

The increase of the damping coefficient r_{S1} (associated with shear deformation/friction and radiation losses in soil) leads to a similar deteriorating effect on linear mine detection, as shown in Fig. 15. Here, the dashed curve is the same as the dashed curve in Fig. 14. The dotted curved demonstrates the effect of tenfold increase in r_{S1}, while all other parameters are unchanged.

Nonlinear detection is based on the interaction of the probing seismic/acoustic waves (with frequencies f_2 and f_1) at the soil/mine interface. The product of such an interaction is vibration with the combination frequencies $f_2 \pm f_1$. This effect depends on the nonlinear parameter, β_m, of the nonlinear interface. At the interface, there is no shear stress (no bonding between soil and mine surface); therefore, the nonlinear parameter β_m does not depend on shear stiffness of the soil. The high nonlinear on/off contrast, determined by the condition (5), might take place even for soil with high shear stiffness. This statement is yet to be validated in the field. The dependence of β_m on other soil and mine parameters and burial depth is also a subject of future investigations.

ACKNOWLEDGMENTS

This material is based upon work supported by the U.S. Army Research Office and Night Vision and Electronic Sensors Directorate (part of the U.S. Army Communications-Electronics Command). The authors thank Dr. Charles Cannon and Dr. Tomas Witten for their valuable comments and support of this work. The authors also thank Mr. John Fasulo and his colleagues for their assistance in conducting field tests.

[1] B. Gros and C. Bruschini, "Sensor technologies for detection of antipersonnel mines. A survey of current research and system developments," *Proceedings of the International Symposium on Measurement and Control in Robotics* (ISMCR, Brussels, 1996), pp. 211–217.
[2] Detection and Remediation Technologies for Mines and Minelike Targets III, in SPIE Proceedings, edited by A. C. Dubey, J. F. Harvey, and J. T. Broach, Vol. 3392, Part 1. (1998).
[3] L. J. House and D. B. Pape, "Method and apparatus for acoustic energy identification of objects buried in soil," US Patent No. 5357063 (1993).
[4] C. G. Don and A. J. Rogers, "Using acoustic impulses to identify a buried nonmetallic object," J. Acoust. Soc. Am. **95**, 2837–2838 (1994).

[5] D. D. Caulfield, ''Acoustic detection apparatus,'' US Patent No. 4922467 (1989).
[6] D. M. Donskoy, ''Nonlinear vibro-acoustic technique for land mine detection,'' in Detection and Remediation Technologies for Mines and Minelike Targets III, SPIE Proceedings, edited by A. C. Dubey, J. F. Harvey, and J. T. Broach, Vol. 3392, pp. 211–217 (1998).
[7] D. M. Donskoy, ''Nonlinear siesmo-acoustic technique for land mine detection and discrimination,'' in Detection of Abandoned Land Mines, IEE Conference Publication No. 458, Edinburgh, UK, 1998, pp. 244–248.
[8] D. M. Donskoy, ''Detection and discrimination of nonmetallic mines,'' in Detection and Remediation Technologies for Mines and Minelike Targets IV, SPIE Proceedings, edited by A. C. Dubey, J. F. Harvey, and J. T. Broach, Vol. 3710, pp. 239–246 (1999).
[9] D. M. Donskoy, N. Sedunov, A. Ekimov, and M. Tsionskiy, ''Optimization of seismo-acoustic land mine detection using dynamic impedances of mines and soil,'' in Detection and Remediation Technologies for Mines and Minelike Targets VI, SPIE Proceedings, edited by A. C. Dubey, J. F. Harvey, J. T. Broach, and V. George, Vol. 4394, pp. 575–582 (2001).
[10] J. M. Sabatier and N. Xiang, ''Laser-doppler based acoustic-to-seismic detection of buried mines,'' in Detection and Remediation Technologies for Mines and Minelike Targets IV, SPIE Proceedings, edited by A. C. Dubey, J. F. Harvey, and J. T. Broach, Vol. 3710, pp. 215–222 (1999).
[11] N. Xiang and J. M. Sabatier, ''Land mine detection measurements using acoustic-to-seismic coupling,'' in Detection and Remediation Technologies for Mines and Minelike Targets V, SPIE Proceedings, edited by A. C. Dubey, J. F. Harvey, J. T. Broach, and V. George, Vol. 3710, pp. 645–655 (2000).
[12] N. Xiang and J. M. Sabatier, ''Anti-personnel mine detection using acoustic-to-seismic coupling,'' in Detection and Remediation Technologies for Mines and Minelike Targets VI, SPIE Proceedings, edited by A. C. Dubey, J. F. Harvey, J. T. Broach, and V. George, Vol. 4394, pp. 535–541 (2000).
[13] W. R. Scott, Jr., C. Schroeder, and J. S. Martin, ''Acousto-electromagnetic sensor for locating land mines,'' in Detection and Remediation Technologies for Mines and Minelike Targets IV, SPIE Proceedings, edited by A. C. Dubey, J. F. Harvey, and J. T. Broach, Vol. 3710, pp. 176–186 (1999).
[14] W. R. Scott, S. Lee, G. D. Larson, J. S. Martin, and G. S. McCall, ''Use of high-frequency seismic waves for the detection of buried land mines,'' in Detection and Remediation Technologies for Mines and Minelike Targets VI, SPIE Proceedings, edited by A. C. Dubey, J. F. Harvey, J. T. Broach, and V. George, Vol. 4394, pp. 543–553 (2001).
[15] J. K. Mitchell, *Fundamentals of Soil Behavior* (Wiley, New York, 1993), p. 170.
[16] M. A. Biot, ''Nonlinear and semilinear reology of porous solids,'' J. Geophys. Res. **78**, 4924–4937 (1973).
[17] D. M. Donskoy, K. Khashanah, and T. G. McKee, ''Nonlinear acoustic waves in porous media in the context of Biot's theory,'' J. Acoust. Soc. Am. **102, Pt. 1**, 2521–2528 (1997).
[18] E. Skudrzyk, *Simple and Complex Vibratory Systems* (University Press, University Park and London, 1968), pp. 280–290.

Coupling analysis of a matched piezoelectric sensor and actuator pair for vibration control of a smart beam

Young-Sup Lee,[a] Paolo Gardonio, and Stephen J. Elliott
Institute of Sound and Vibration Research, University of Southampton, Southampton SO17 1BJ, England

(Received 30 July 2001; revised 14 March 2002; accepted 19 March 2002)

This paper presents a theoretical and experimental study of the *in-plane* and *out-of-plane* coupling of a *matched* piezoelectric sensor/actuator pair bonded on a beam. Both the sensor and actuator are triangularly shaped polyvinylidene fluoride (PVDF) transducers and are intended to provide a compact sensor/actuator system for beam vibration control. The measured sensor–actuator frequency response function has shown an unpredicted increase in magnitude with frequency, which was found, to be due to in-plane vibration coupling. An analytical model has been developed to decompose the sensor–actuator response function into an in-plane contribution and an out-of-plane contribution. This in-plane coupling can limit the feedback control gains when a direct velocity feedback control is applied. A method called the *jωs compensation method* is proposed to identify the effect of the in-plane vibration coupling at low frequencies. Even after this compensation, however, there was unexpected strong out-of-plane coupling at even modes, which may have been caused by a lack of accuracy in the shaping of the PVDF sensor and actuator. Numerical simulations have confirmed the sensitivity of the matched sensor/actuator pair with shaping errors. © *2002 Acoustical Society of America.* [DOI: 10.1121/1.1476921]

PACS numbers: 43.40.Vn, 43.38.Fx [JGM]

I. INTRODUCTION

Conventional discrete collocated point sensor and actuator pairs offer an extremely robust active feedback control system, particularly when direct velocity feedback (DVFB) is implemented.[1] This strategy is unconditionally stable for any type of primary disturbance acting on a structure, in spite of having a very simple controller. It would be attractive to use the DVFB technique with distributed sensor/actuator pairs for developing smart structures. An arrangement having a sensor and actuator with the same shape on either side of a structure was suggested by Lee,[2] and a number of structural control systems adopting the arrangement have been implemented.[3–8] When a distributed sensor and actuator of the same but arbitrary shape are positioned on either side of a structure, the transducers are said to be *matched*.[6]

A triangularly shaped piezoelectric sensor has been shown to measure the tip velocity of a cantilever beam.[9] A smart cantilever beam is considered here with a matched piezoelectric sensor/actuator pair, having the same triangular shape, bonded on the beam. The triangularly shaped piezoelectric actuator can produce a transverse force at the tip.[10] Thus, the transfer function between the two distributed transducers bonded on either side of the beam should have the property of a *driving point mobility*[11] at the tip of the beam. The transfer function of the sensor/actuator configuration would then have a strictly positive real part (SPR) property,[12] with alternating pole/zero pairs along the imaginary axis in the Laplace domain and the real part of the frequency response function (FRF) always being positive. This discussion assumes that the matched sensor/actuator pair is coupled only by the *out-of-plane* motion of a beam onto which they are bonded.[6] A velocity feedback control system connected to such a matched sensor/actuator pair would then be guaranteed to be unconditionally stable, and so could greatly attenuate tip vibration, generated by slewing of the beam for example. However, the forces generated by a distributed actuator include not only *out-of-plane* forces but also *in-plane* forces.[8,9,13] Also, a matched sensor detects both the out-of-plane flexural and in-plane longitudinal and shear vibrations. The behavior of a matched sensor/actuator pair could thus be very different from that of a traditional point collocated pair because of the inclusion of the in-plane coupling. The transfer function of a practical matched sensor/actuator pair is shown not to be SPR in this paper. This is a critical problem that limits both the control effectiveness of a matched sensor/actuator pair and the stability of a velocity feedback control system.

Therefore, in the design of active vibration control (AVC) systems, it is very important to take into account both the in-plane and out-of-plane coupling effects of a matched sensor and actuator pair. In order to cancel in-plane coupling in a matched pair, Yang and Huang[14] suggested the use of a double sensor/actuator pairs arrangement, and Cole *et al.*[15] proposed a pair of sensoriactuators, which could provide ways of detecting and actuating only out-of-plane motion. In this paper, after a theoretical modeling and analyses of the out-of-plane and in-plane coupling in Secs. II–V, a different way of avoiding these problems is proposed by compensating for the in-plane coupling in Sec. VI. Finally, shaping error effects of piezoelectric transducers are discussed in Sec. VII.

[a]Electronic mail: y.lee@soton.ac.uk

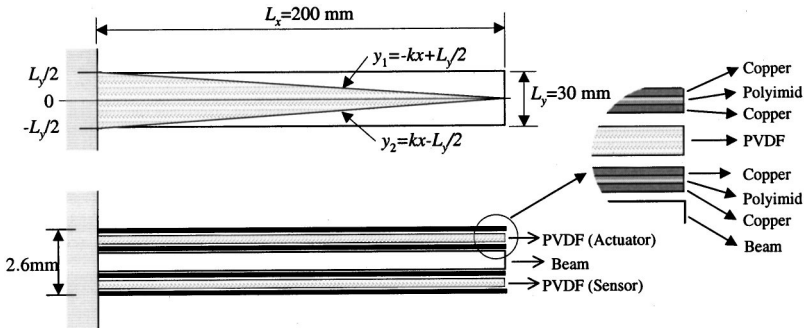

FIG. 1. Arrangement of a matched piezoelectric sensor/actuator pair bonded on a cantilever beam. A triangularly shaped actuator bonded on the cantilever beam and its spatial sensitivity function $S(x)$ is defined by two lines y_1 and y_2.

II. A TRIANGULARLY SHAPED PIEZO-SENSOR/ACTUATOR PAIR

A. Experimental beam with PVDF transducers

The aluminum cantilever beam (length×width ×thickness: $L_x \times L_y \times 2h_s$, $L_x \gg L_y$) used in the experiment was fabricated by Thomson Marconi and has two similarly shaped triangular PVDF films, which are bonded to either side of the beam, as illustrated in Fig. 1. In fact, the beam was developed for a wider investigation and has two PVDF layers on each side, as described in Lee,[9] but the outer layers were not used in the experiments reported here, and apart from increasing the overall damping, their effect on the dynamics is expected to be relatively small.

The top and bottom films are used as an actuator and a sensor, respectively. The geometry and physical properties of the beam and the PVDF film are given in Table I. The triangular-shaped sensor and actuator can excite and detect the out-of-plane vibration at the tip of the cantilever beam, as described below. Four electrode and electrical insulation layers are bonded to the PVDF films, as illustrated in Fig. 1. Each layer consists of two copper films and one polyimid film. The electrical insulation layers are very important when piezoelectric transducers are used to shield the signal electrodes of the transducers from electro-magnetic interference, including possible unwanted electrical coupling. The total thickness of the beam structure is about 2.6 mm, which has been greatly exaggerated in Fig. 1 for clarity.

B. Out-of-plane excitation due to a piezoelectric triangularity shaped actuator

For the analysis of out-of-plane actuation by a triangularly shaped actuator, both the beam and the PVDF actuator are regarded as two-dimensional elements. The spatial sensitivity function of a triangular actuator as shown in Fig. 1 is expressed as

$$S(x,y) = -k(x - L_x), \tag{1}$$

where $k = L_y/(2L_x)$ which is about 0.075 in this case. Thus, the two lines in Fig. 1 can be written as $y_1 = -kx + L_y/2$ and $y_2 = kx - L_y/2$. The forced out-of-plane motion $w(x,y)$ for the beam–actuator assembly, with a spatial sensitivity $S(x,y)$ of the piezoactuator, is given by the following fourth-order partial differential equation:[9]

$$[D_s + D_{\text{pe}}(x,y)]\nabla^4 w(x,y) + (m_s + m_{\text{pe}})\frac{\partial^2 w(x,y)}{\partial t^2} = -h_{\text{act}} V_3(t) L_{\text{pe}}[S(x,y)], \tag{2}$$

where the subscripts s and pe represent the beam structure and the piezoactuator, D_s and D_{pe} are their flexural rigidity.[8] $\nabla^4 = \nabla^2\nabla^2$, and the Laplacian operator $\nabla^2 = \partial^2/\partial x^2 + \partial^2/\partial y^2$ for a rectangular two-dimensional beam. $m_s = \rho_s 2h_s$ and $m_{\text{pe}} = \rho_{\text{pe}} 2h_{\text{pe}}$ are the two masses per unit area, where ρ_s and ρ_{pe} are the densities of the materials, $h_{act} = h_s + h_{\text{pe}}/2$ (h_s is the half-thickness of the beam and h_{pe} is the thickness of the piezoactuator). $V_3(t)$ is the applied voltage to the piezoelectric actuator in the out-of-plane direction, e_{31}, e_{32}, e_{36} are the piezoelectric stress constants,[2] and $L_{\text{pe}}[S(x,y)]$ is a differential operator that is defined as

$$L_{\text{pe}}[S(x,y)] = e_{31}\frac{\partial^2 S(x,y)}{\partial x^2} + 2e_{36}\frac{\partial^2 S(x,y)}{\partial x \partial y} + e_{32}\frac{\partial^2 S(x,y)}{\partial y^2}. \tag{3}$$

After some manipulation with the spatial sensitivity function of the triangular actuator, Eq. (3) can be expressed using the Macauley notation as[10]

$$\begin{aligned} &e_{31}\frac{\partial^2 S(x,y)}{\partial x^2} + 2e_{36}\frac{\partial^2 S(x,y)}{\partial x \partial y} + e_{32}\frac{\partial^2 S(x,y)}{\partial y^2} \\ &= e_{31}(\langle x\rangle^{-2} - \langle x - L_x\rangle^{-2})(\langle y - kx + L_y/2\rangle^0 \\ &\quad - \langle y + kx - L_y/2\rangle^0) - 2ke_{31}(\langle x\rangle^{-1} - \langle x - L_x\rangle^{-1}) \\ &\quad \times (\langle y - kx + L_y/2\rangle^{-1} + \langle y + kx - L_y/2\rangle^{-1}) \\ &\quad + (k^2 e_{31} + e_{32})(\langle x\rangle^0 - \langle x - L_x\rangle^0)(\langle y - kx + L_y/2\rangle^{-2} \\ &\quad - \langle y + kx - L_y/2\rangle^{-2}). \end{aligned} \tag{4}$$

TABLE I. Geometry and physical properties of the beam and PVDF film.

Parameters	Beam	PVDF film
Dimension	$L_x \times L_y = 200 \times 300$ mm	$L_x \times L_y = 200 \times 300$ mm
Thickness	$2h_s = 1$ mm	$h_{\text{pe}} = 0.5$ mm
Mass density	$\rho_s = 2700$ kgm^{-3}	$\rho_s = 1780$ kgm^{-3}
Young's modulus	$Y_s = 7.1 \times 10^{10}$ Nm^{-2}	$Y_{\text{pe}} = 2.0 \times 10^9$ Nm^{-2}
Poisson ratio	$\nu_s = 0.33$	$\nu_{\text{pe}} = 0.29$
Hysteresis loss factor	$\eta_s = 0.05$	⋯
Piezoelectric stress constants	⋯	$e_{31} = 0.052$ NV^{-1}m^{-1} $e_{32} = 0.021$ NV^{-1}m^{-1} $e_{36} = 0$ NV^{-1}m^{-1}

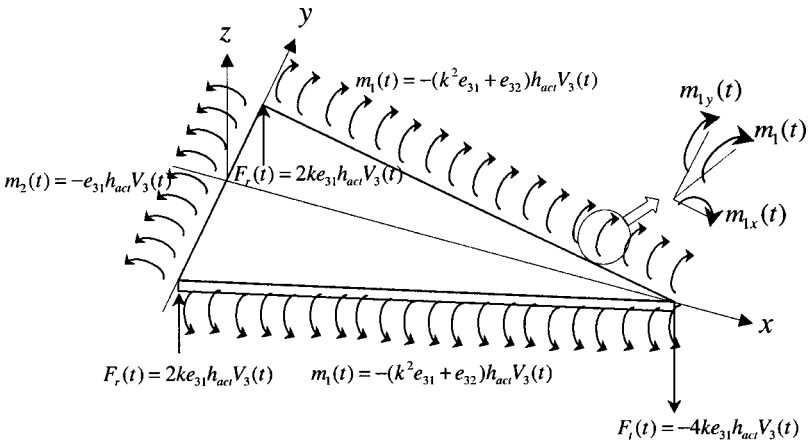

FIG. 2. Distribution of out-of-plane forces due to a triangularly shaped piezoactuator bonded on a cantilever beam. The line-bending moment $m_1(t)$ due to a triangularly shaped piezoactuator can be decomposed into $m_{1x}(t)$ and $m_{1y}(t)$.

The first term in Eq. (4) indicates the existence of a line-bending moment with a magnitude proportional to e_{31} at $x=0$ along the y axis and a line-bending moment at $x=L_x$ along the y axis. The second term indicates that concentrated transverse point forces act at $(0,L_y/2)$ and $(0,-L_y/2)$, both with a magnitude proportional to $-2ke_{31}$, and at $(L_x,0)$, with a magnitude proportional to $4ke_{31}$. The third term implies that two line moments with a magnitude proportional to $k^2e_{31}+e_{32}$ act along the two sides of the triangular actuator.

Thus, the out-of-plane concentrated forces and line-bending moments are given, by using the forcing term in Eq. (2), as

$$F_t(t) = -4ke_{31}h_{\text{act}}V_3(t), \quad F_r(t) = 2ke_{31}h_{\text{act}}V_3(t),$$
$$m_1(t) = -(k^2e_{31}+e_{32})h_{\text{act}}V_3(t), \quad m_2(t) = -e_{31}h_{\text{act}}V_3(t). \tag{5}$$

If only the out-of-plane vibration of the beam is considered, then Eq. (5) indicates that the actuator excites the beam with a concentrated downward point force $F_t(t)$ at the tip ($x=L_x$), and two concentrated upward point forces, $F_r(t)$ at the two corners where the beam is clamped as illustrated in Fig. 2. Also, line-bending moments $m_1(t)$ and $m_2(t)$ act along the two slopes of the triangular actuator. The effect of the out-of-plane excitations $F_r(t)$ and $m_2(t)$ along the two lateral edges of the triangular piezoactuator are balanced by the clamping forces at the end of the beam. In addition, the line-bending moment $m_1(t)$ can be decomposed into two components of $m_{1x}(t)$ (x-direction component) and $m_{1y}(t)$ (y-direction component) as shown in Fig. 2.

Therefore, the out-of-plane excitations of the beam can be approxiamted by a concentrated point force $F_r(t)$ at the tip and the x-directional line moment component $m_{1x}(t)$ as illustrated in Fig. 2.

C. Out-of-plane response of a triangularly shaped PVDF sensor

The charge output from a two-dimensional piezosensor, which is subject to out-of-plane motion, is expressed by[2]

$$q_{\text{oop}}(t) = -h_{\text{sen}}\int_0^{L_x}\int_0^{L_y} S(x,y)\left[e_{31}\frac{\partial^2 w}{\partial x^2} + e_{32}\frac{\partial^2 w}{\partial y^2} + 2e_{36}\frac{\partial^2 w}{\partial x\,\partial y}\right]dx\,dy. \tag{6}$$

Since $e_{36}=0$ for PVDF and considering the vibration of the beam to be one-dimensional in the z direction, $w(x,t)$, Eq. (6) can be rewritten as

$$q_{\text{oop}}(t) = -e_{31}h_{\text{sen}}L_y\int_0^{L_x} S(x,y)\frac{\partial^2 w}{\partial x^2}dx. \tag{7}$$

The properties of the triangularly shaped piezosensor, as shown in Fig. 1, are that

$$S(0,y) = kL_x,\ S(L_x,y) = 0, \text{ and } \frac{\partial S(x,y)}{\partial x} = -k \quad \text{for } 0 \leqslant x \leqslant L_x. \tag{8}$$

So, when the beam is subject to the out-of-plane motion, the triangular PVDF sensor can generate charge output proportional to the tip displacement of the beam as[9]

$$q(t) = -e_{31}h_{\text{sen}}L_y k w(L_x,t), \tag{9}$$

where $h_{\text{sen}} = h_s + h_{\text{pe}}/2$ and $w(L_x,t)$ is the flexural tip position of the cantilever beam.

If the out-of-plane displacement $w(x,t)$ of the beam is now expressed in terms of modal expansion, as $w(x,t) = \Sigma_{n=1}^{\infty} B_n(t)\phi_n(x)$, where $B_n(t)$ is the out-of-plane modal amplitude at the nth mode and $\phi_n(x) = \cosh k_n x - \cos k_n x - \alpha_n(\sinh k_n x - \sin k_n x)$ is the out-of-plane mode shape,[16] in which k_n is the nth mode wave number and α_n is a constant. Then, the charge output $q_{\text{oop}}(t)$ by the triangular sensor can be written, from Eq. (9), as

$$q_{\text{oop}}(t) = -e_{31}h_{\text{sen}}L_y k\sum_{n=1}^{\infty} B_n(t)\phi_n(L_x). \tag{10}$$

The out-of-plane transverse beam vibration, when the concentrated force $F_t(t)$ and the x-directional line-bending moment $m_{1x}(t)$ derived in Sec. II B are applied, is given by the following harmonic relation as:

$$w(x,\omega) = \sum_{n=1}^{\infty}\phi_n(x)B_n(\omega) = \sum_{n=1}^{\infty}\frac{\phi_n(x)[2\int_0^{L_x} m_{1x}(\omega)\phi_n'(x)dx + F_t(\omega)\phi_n(L_x)]}{M_n[\omega_n^2(1+j\eta_s)-\omega^2]}, \tag{11}$$

where $M_n = \int_0^{L_x} \rho_s A_s \phi_n^2(x) dx$ is the out-of-plane mode mass, $\phi_n'(x) = \partial \phi_n(x)/\partial x$, ω_n is the natural frequency, and η_s is the hysteretic loss factor of the beam for the out-of-plane motion. After some manipulation, the harmonic out-of-plane modal amplitude $B_n(\omega)$ is expressed, considering the magnitude of the bending moment $m_{1x}(\omega)$ is independent of x, as

$$B_n(\omega) = -\frac{\phi_n(L_s)[2m_{1x}(\omega) + F_t(\omega)]}{M_n[\omega_n^2(1+j\eta_s) - \omega^2]}, \tag{12}$$

where the negative sign can be obtained by reversal of poling on the piezoactuator element. Therefore, the harmonic out-of-plane charge output $q_{\text{oop}}(\omega)$ of the triangularly shaped piezoelectric sensor bonded on one side of the cantilever beam can be expressed as

$$q_{\text{oop}}(\omega) = C_o(\omega) \sum_{n=1}^{\infty} \frac{\phi_n^2(L_x)}{[\omega_n^2(1+j\eta_s) - \omega^2]}, \tag{13}$$

where $C_o(\omega) = e_{31} h_{\text{sen}} L_y k[2m_{1x}(\omega) + F_t(\omega)]/M_n$. Using the expression for the out-of-plane forces $F_t(\omega)$ and $m_{1x}(\omega)$, the transfer function $T_{\text{oop}}(\omega)$ between the input voltage $V_3(\omega)$ to the piezoactuator and the *time derivative* of the out-of-plane charge output $q_{\text{oop}}(\omega)$, i.e., the current, of the piezosensor can be written by

$$T_{\text{oop}}(\omega) = j\omega \frac{q_{\text{oop}}(\omega)}{V_3(\omega)} = j\omega \frac{C_o(\omega)}{V_3(\omega)} \sum_{n=1}^{\infty} \frac{\phi_n^2(L_x)}{[\omega_n^2(1+j\eta_s) - \omega^2]}. \tag{14}$$

It should be noted that the term $\phi_n^2(L_x)$ in the numerator of Eq. (14) indicates that the sensor and actuator are collocated at $x = L_x$. Thus, all out-of-plane modes are actuated and sensed in the same phase because the two modal components have the same sign and the out-of-plane transfer function $T_{\text{oop}}(\omega)$ is strictly positive real (SPR).[12] An SPR system can be defined as "a system for which all the complex conjugate pairs of poles and zeros are alternating with each other as well as located in the left-hand side in the s-plane." Thus, the phase response of $T_{\text{oop}}(\omega)$ lies between $\pm 90°$. The real part of the FRF of such a system is always greater than zero for all frequencies.

III. MEASURED SENSOR–ACTUATOR FREQUENCY RESPONSE FUNCTIONS

Two sensor–actuator FRFs were measured on the smart beam in the frequency range of 0–1000 Hz using two configurations: with an *accelerometer/shaker* (using integration) and with a matched triangular PVDF sensor/actuator pair, as shown in Fig. 3. The measured FRF of the accelerometer/shaker configuration as illustrated in Fig. 4(a) shows the typical features of a driving point mobility, where the resonances alternate with antiresonances, which occurs at the frequencies quite close to the following resonance. Also, the phase response lies between $\pm 90°$; this has the SPR property, and the amplitude tends to decrease with frequency.[17] However, the response plotted in Fig. 4(b), measured with the triangular PVDF sensor/actuator pair configuration, shows an unexpected rising trend of amplitude with frequency, whose behavior is quite different from that of Fig. 4(a). The thin line in the phase response of Fig. 4(b) shows the measured phase lag in this experiment. It was found that part of the phase lag was caused by the low-pass filter in a signal conditioner (B&K type 2635), which was used to pick up the charge output signal from the piezosensor. After compensating for this phase lag, the phase response of the PVDF actuator–sensor pair alone is plotted as the thick line in the phase response of Fig. 4(b).

The theory developed in Sec. II predicted that the two measured responses in Fig. 4 should have been of similar form. In order to investigate the differences between these two measured sensor–actuator FRFs, the in-plane coupling of the matched PVDF sensor/actuator pair has been included in the analysis.

IV. IN-PLANE COUPLING BETWEEN THE SENSOR AND ACTUATOR PAIR

The in-plane forces can induce in-plane strains in the beam, which would not normally be detected when an accelerometer is used for the detection of out-of-plane motion, for example. However, the charge output of the piezoelectric sensor will be affected by both the in-plane and out-of-plane strains as pointed out by Yang and Huang.[14] The *in-plane coupling* is analyzed below.

The charge output from a two-dimensional piezosensor, which is subject to in-plane motion, is expressed by[2]

$$q_{\text{ip}}(t) = \int_0^{L_x} \int_0^{L_y} S(x,y) \times \left[e_{31} \frac{\partial u}{\partial x} + e_{32} \frac{\partial v}{\partial y} + e_{36} \left(\frac{\partial u}{\partial y} + \frac{\partial v}{\partial x} \right) \right] dx\, dy, \tag{15}$$

where u and v represent the in-plane displacement to the x and y dirctions, respectively. If the beam is subject to the in-plane longitudinal vibration to the x direction only, the in-plane charge output $q_{\text{ip}}(t)$ of a shaped piezosensor bonded on one side of the beam can be written as

$$q_{\text{ip}}(t) = e_{31} L_y \int_0^{L_x} S(x,y) \frac{\partial u(x,t)}{\partial x} dx = e_{31} L_y \sum_{m=1}^{\infty} A_m(t) \int_0^{L_x} S(x,y) \frac{\partial \psi_m(x)}{\partial x} dx, \tag{16}$$

where the in-plane displacement can be expressed in terms of an expansion of in-plane modes as $u(x,t) = \Sigma_{m=1}^{\infty} A_m(t) \psi_m(x)$, where $m = 1,2,3,...$, is the in-plane longitudinal mode number, $A_m(t)$ is the modal amplitude, and the in-plane mode shape is given by $\psi_m(x) = \sin[(2m-1)\pi/2L_x]x$ for a uniform cantilever beam.[16] The integration in Eq. (16) can be simplified by a partial integration, and assuming

$$\int_0^{L_x} S(x,y) \frac{\partial \psi_m(x)}{\partial x} dx = k \int_0^{L_x} \psi_m(x) dx,$$

the in-plane charge output $q_{ip}(t)$ of the piezosensor can be expressed as

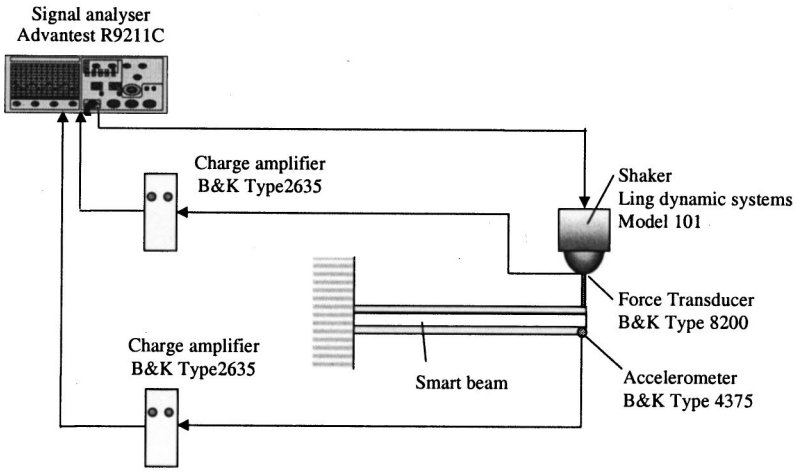

(a)

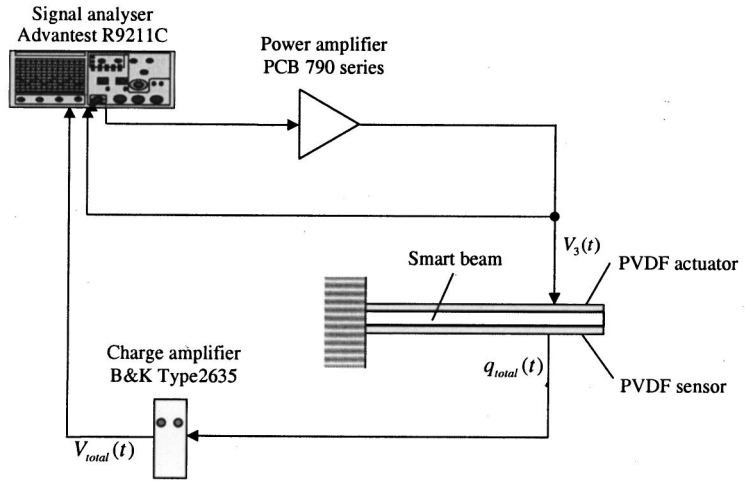

(b)

FIG. 3. Two measurement setups with different sensor/actuator configurations for the experimental cantlilever beam. (a) A point-collocated accelerometer and shaker configuration. (b) A matched PVDF sensor/actuator configuration.

$$q_{\mathrm{ip}}(t)=e_{31}L_y k\sum_{m=1}^{\infty}A_m(t)\int_0^{L_x}\psi_m(x)dx. \tag{17}$$

In order to obtain the in-plane modal amplitude $A_m(t)$ of the cantilever beam, the x-directional in-plane force $f_{1x}(\omega)$ acting along the beam is applied. The harmonic in-plane longitudinal displacement can be expressed as

$$u(x,\omega)=\sum_{m=1}^{\infty}\frac{\psi_m(x)\int_0^{L_x}\psi_m(x)f_{1x}(\omega)dx}{M_m[\omega_m^2(1+j\eta_s)-\omega^2]}, \tag{18}$$

where $M_m=\int_0^{L_x}\rho_s A_s\psi_m^2(x)dx$ is the in-plane modal mass of the smart beam, the in-plane natural circular frequency is given[16] by $\omega_m=[(2m-1)\pi]/2L_x\sqrt{Y_s/\rho_s}$. Thus, the harmonic in-plane modal amplitude $A_m(\omega)$ can be expressed as

$$A_m(\omega)=\frac{\int_0^{L_x}\psi_m(x)f_{1x}(\omega)dx}{M_m[\omega_m^2(1+j\eta_s)-\omega^2]}. \tag{19}$$

The x-directional in-plane force by the piezoactuator can be calculated as below. The longitudinal motion of a beam under in-plane force can be expressed as[16]

$$\frac{\partial F_x}{\partial x}-\rho_s A_s\frac{\partial^2 u}{\partial x^2}=0, \tag{20}$$

where u is the in-plane displacement. The stress fields both on the beam and piezoactuator can be expressed respectively as

$$\sigma_x^s=Y_s\varepsilon_x^s,\ \sigma_x^{\mathrm{pe}}=Y_{\mathrm{pe}}[\varepsilon_x^s-\varepsilon_x^{\mathrm{pe}}]=Y_{\mathrm{pe}}\left[\frac{\partial u}{\partial x}-S(x,y)\frac{d_{31}V_3}{h_{\mathrm{pe}}}\right], \tag{21}$$

where $\varepsilon_x^s=\partial u/\partial x$ is the in-plane strain of the beam and $\varepsilon_x^{\mathrm{pe}}$ is the free strain of the piezoelectric material. The in-plane force F_x in the beam can thus be given by

$$F_x=\int_{-h_s}^{h_s}\sigma_x^s dz+\int_{h_s}^{h_s+h_{\mathrm{pe}}}\sigma_x^{\mathrm{pe}}dz. \tag{22}$$

After some manipulation, Eq. (20) can be rewritten as

$$Y_x A_c\frac{\partial^2 u}{\partial x^2}-\rho_c A_c\frac{\partial^2 u}{\partial t^2}=f_x(t), \tag{23}$$

where the combined in-plane stiffness of the smart beam is given as $Y_cA_c=2Y_sh_s+2Y_{\mathrm{pe}}h_s+Y_{\mathrm{pe}}h_{\mathrm{pe}}$, and ρ_c and A_c are

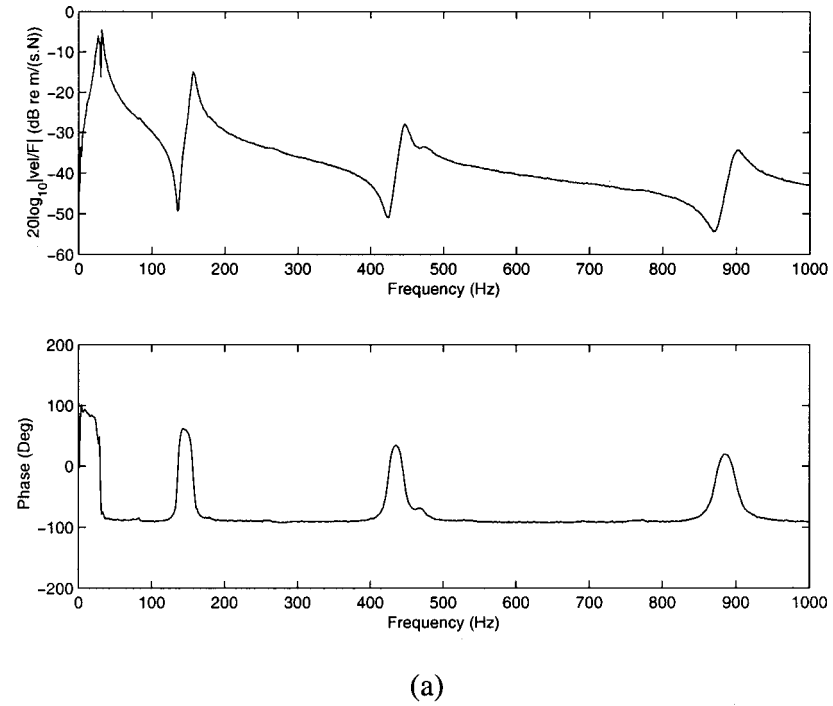

(a)

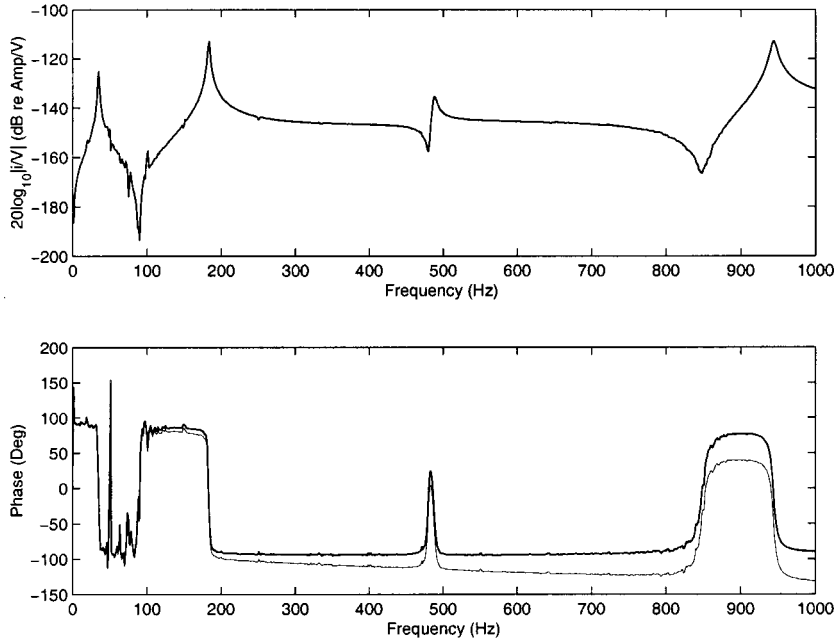

(b)

FIG. 4. Two measured sensor–actuator FRFs. (a) Point-collocated FRF: Shaker input and integrated accelerometer (velocity) output. (b) Matched FRF: PVDF actuator input and sensor output. In the phase response, thick line and thin line indicates after compensation on phase lag and before compensation, respectively.

the combined density and sectional area of the smart beam, respectively. The forcing function $f_x(t)$ is given by

$$f_x(t)=2h_{\text{act}}e_{31}\frac{\partial S(x,y)}{\partial x}\,\frac{V_3(t)}{h_{\text{pe}}}, \tag{24}$$

where $e_{31}\approx Y_{\text{pe}}d_{31}$ for a beam. Considering the boundary condition of the experimental beam, the x-directional in-plane force by the piezoactuator $f_1(t)$ only is meaningful, which can be expressed by

$$f_{1x}(t)=-2h_{\text{act}}e_{31}V_3(t)/h_{\text{pe}}. \tag{25}$$

Because the magnitude of the in-plane force $f_{1x}(\omega)$ is independent of x, after some manipulation, the harmonic charge output of the shaped piezosensor in Eq. (17) becomes

$$q_{\text{ip}}(\omega)=C_i(\omega)\sum_{m=1}^{\infty}\frac{[\int_0^{L_x}\psi_m(x)dx]^2}{[\omega_m^2(1+j\,\eta_s)-\omega^2]}, \tag{26}$$

where $C_i(\omega)=e_{31}L_y k f_{1x}(\omega)/M_m$. The transfer function $T_{\text{ip}}(\omega)$ between the input voltage $V_3(\omega)$ to the piezoactuator to the *time derivative* of the in-plane charge output $q_{\text{ip}}(\omega)$, i.e., the current, of the piezosensor can finally be written as

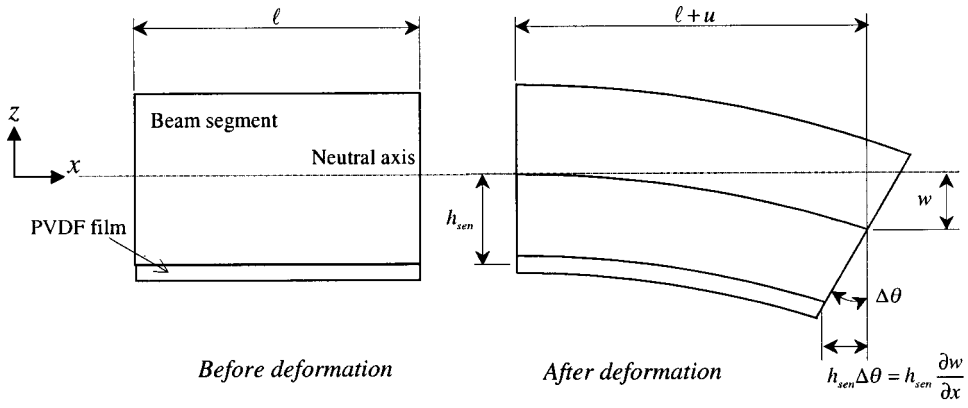

FIG. 5. The geometry of coupled in-plane and out-of-plane deformation of a small segment of a flexible beam with a PVDF sensor when the beam is subject to both the in-plane longitudinal force and the out-of-plane transverse force.

$$T_{\mathrm{ip}}(\omega) = -j\omega\frac{q_{\mathrm{ip}}(\omega)}{V_3(\omega)} = -j\omega\frac{C_i(\omega)}{V_3(\omega)}\sum_{m=1}^{\infty}\frac{[\int_0^{L_x}\psi_m(x)dx]^2}{[\omega_m^2(1+j\eta_s)-\omega^2]}, \tag{27}$$

where the negative sign is introduced to be consistent with Eq. (12). The coupling term $[\int_0^{L_x}\psi_m(x)dx]^2$ in the numerator of Eq. (27) for the in-plane transfer function can be compared with the term $\phi_n^2(L_x)$ in Eq. (14) for the out-of-plane transfer function. All in-plane modes are thus coupled with the same phase, since the excitation and sensing have the same sign. Thus, the phase response of $T_{\mathrm{ip}}(\omega)$ in Eq. (27) lies between $-90°$ and $-270°$.

V. COUPLED FREQUENCY RESPONSE FUNCTION

The total charge output of a piezosensor is the *addition* of the in-plane charge output and the out-of-plane charge output, that is $q_{\mathrm{total}}(t)=q_{\mathrm{ip}}+q_{\mathrm{oop}}(t)$. Considering the Euler–Bernoulli beam theory,[16] the strain ε_x in the x direction of the piezosensor bonded on the beam as shown in Fig. 5, when it is subject to both the in-plane longitudinal and the out-of-plane transverse motion within linear elasticity, is given by[2]

$$\varepsilon_x = \frac{\partial}{\partial x}\left(u - h_{\mathrm{sen}}\frac{\partial w}{\partial x}\right) = \frac{\partial u}{\partial x} + \left(-h_{\mathrm{sen}}\frac{\partial^2 w}{\partial x^2}\right). \tag{28}$$

Due to the dynamics of a beam, the out-of-plane transverse strain and the in-plane longitudinal strain of the piezosensor generated by the piezoactuator have different signs from each other. Thus, the total transfer function for the matched PVDF sensor and actuator pair can be written, using Eqs. (14), (27), and (28), as

$$T_{\mathrm{total}} = T_{\mathrm{ip}} + T_{\mathrm{oop}}. \tag{29}$$

The two individual predicted FRFs are plotted in Fig. 6 below 1000 Hz. The out-of-plane response (thick line) and the in-plane response (dashed line) are plotted together with their addition in Eq. (29) for the coupled response (thin line). This coupled response now shows a similar trend to the measured one in Fig. 4(b). This indicates that the in-plane behavior of the beam with a matched piezoelectric sensor/actuator pair is crucial for the understanding of its overall behavior. The phase responses of the out-of-plane and coupled motions

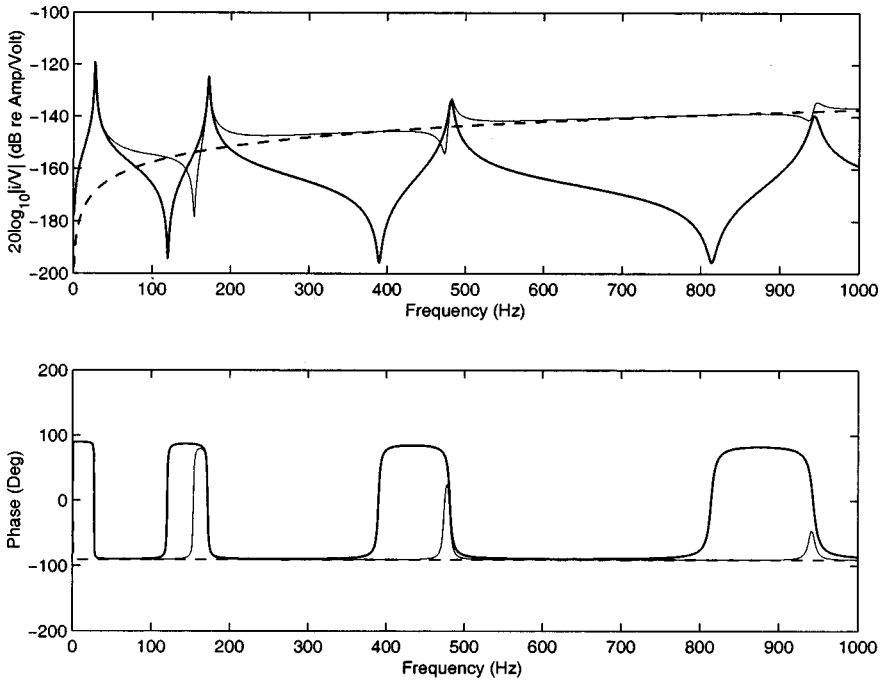

FIG. 6. Calculated FRFs below 1000 Hz of the matched piezoelectric sensor and actuator: pure out-of-plane response (thick line), pure in-plane response (dashed line), and the combined response (thin line).

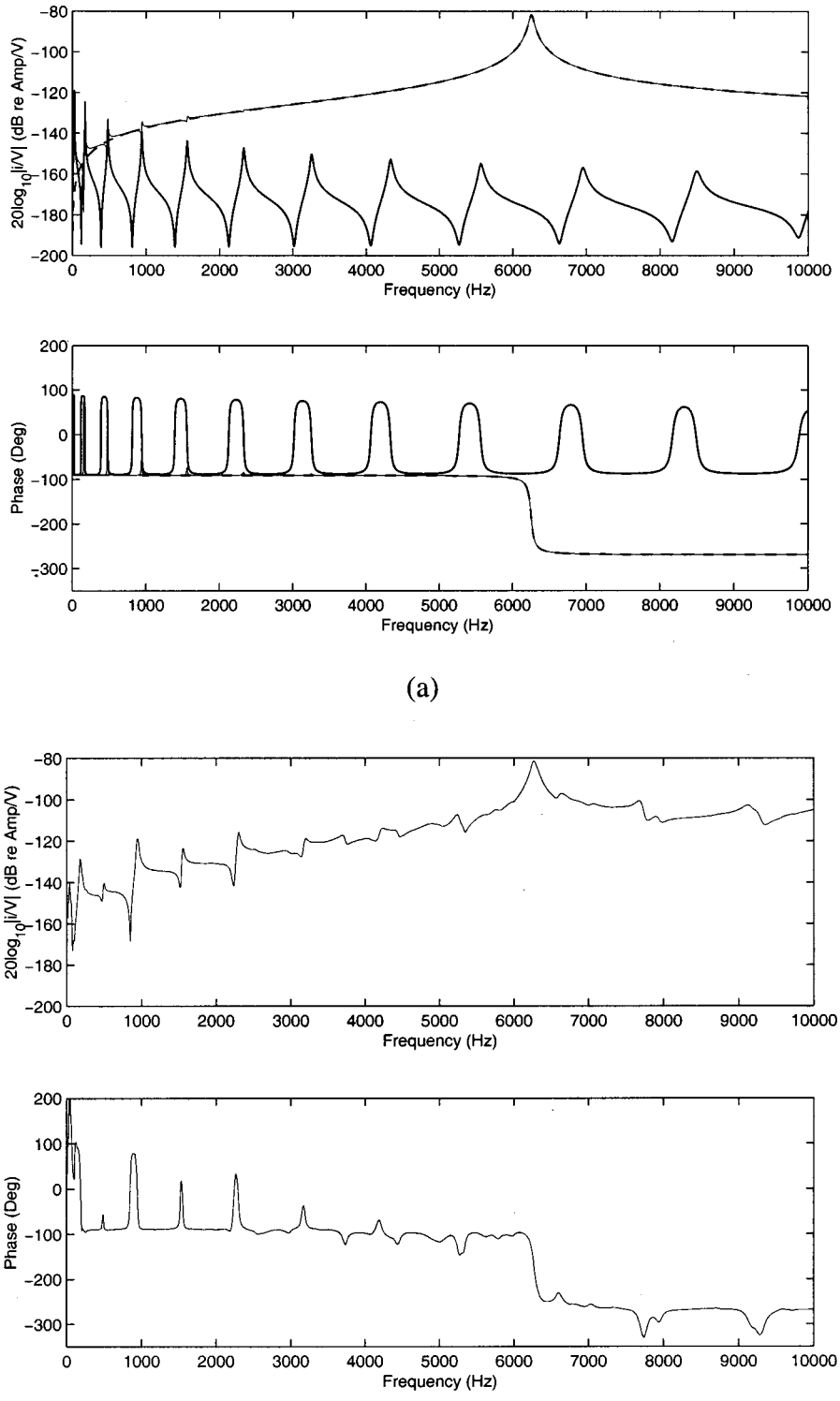

FIG. 7. Comparison of the calculated and measured FRFs between the matched PVDF sensor/actuator pair in the frequency range of 0–10 000 Hz. (a) Calculated responses: total response T_{total} (thin line), out-of-plane response T_{oop} (thick line), and in-plane response T_{ip} (dashed line). Because T_{ip} (dashed line) falls exactly on top of T_{total} (thin line), the dashed line is not visible, except at low frequencies. (b) Measured (total) response.

in Fig. 7 lies between $\pm 90°$ in the frequency range below 1000 Hz. However, the phase response of the in-plane motion is $-90° \leqslant \angle T_{\text{ip}} \leqslant -270°$.

Figure 7(a) shows the calculated total (thin line), out-of-plane (thick line), and in-plane (dashed line) responses of the smart beam over the extended frequency range of 0–10 000 Hz. Because the in-plane response (dashed line) falls exactly on top of the coupled response (thin line), the dashed line is not visible, except at low frequencies, in Fig. 7(a). The first predicted natural frequency of the in-plane mode is around 6250 Hz. The out-of-plane response is dominant only in the very low frequency range below about 100 Hz, and the in-plane response completely dominates the out-of-plane response after about the fourth out-of-plane resonance (around 1000 Hz). The phase response also indicates that the out-of-plane motion is overwhelmed by the in-plane motion at higher frequencies.

Figure 7(b) shows the measured FRF over this extended

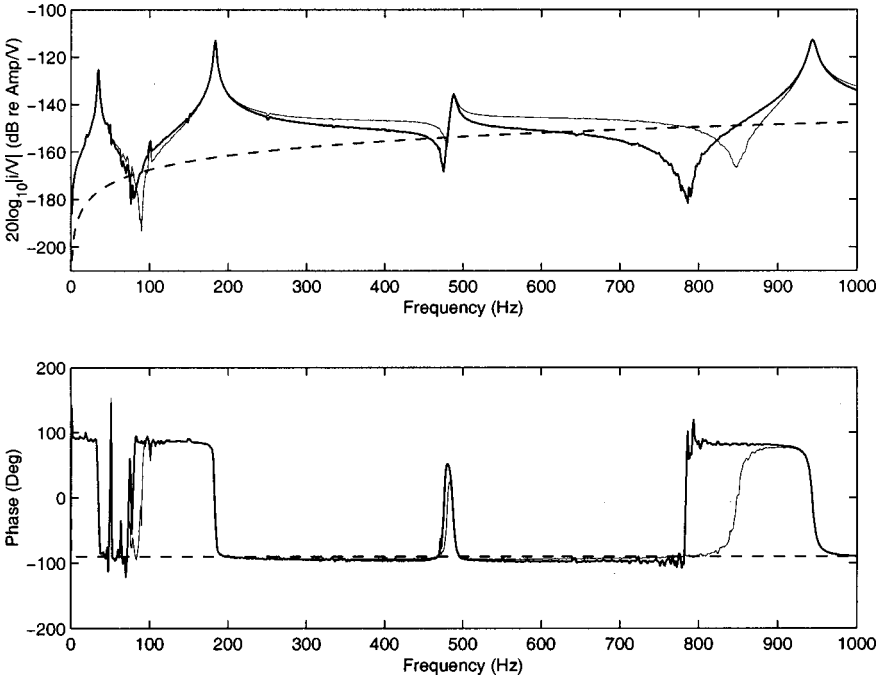

FIG. 8. Extraction of pure out-of-plane FRF (thick lines) from the measured total FRF (thin lines) by subtracting the in-plane FRF (dashed lines) component.

frequency range and shows a very similar trend to the calculated FRF in Fig. 7(a), although there is some discrepancy after about 9000 Hz. The smaller peaks in the measured total FRF represent stronger out-of-plane contribution than predicted in the calculated FRFs. This might be caused by shaping and matching errors in piezoelectric transducers; this will be discussed in detail below. However, both the measured and the calculated phase response indicate that the coupled FRF loses its SPR property at the first in-plane resonance frequency when the phase undergoes a sudden 180° shift. Both the increasing amplitude of the in-plane coupling and the 180° phase shift at the in-plane resonance suggest that the configuration with a matched piezoelectric sensor and actuator pair as shown in Fig. 1 is not feasible for direct velocity feedback control.

VI. COMPENSATION FOR IN-PLANE COUPLING AT LOW FREQUENCIES

As suggested by Cole *et al.*[15] and Yang and Huang,[14] it may be possible to extract the out-of-plane response from the coupled response by eliminating the in-plane response using multiple actuators and sensors. A new approach for the elimination of the in-plane coupling at low frequencies suggested in this paper, which is based on the physics of the in-plane vibration behavior of a structure.

Figure 7(a) shows that the amplitude of the out-of-plane response (thick line) becomes smaller with the increase of frequency, whereas the amplitude of the in-plane response (dashed line) tends to increase with frequency and it becomes larger than that of the out-of-plane response above about 50 Hz.

One very important physical aspect, as shown in Fig. 7(a), is that in the frequency range of interest (below 1000 Hz) the in-plane response is within its *stiffness controlled* range[18] of the first in-plane mode. The in-plane FRF of the cantilever beam within the stiffness controlled range could be expressed as $T_{ip} \approx j\omega/k_{in}$, where k_{in} is the in-plane stiffness of the beam. And, the in-plane FRF could be plotted as a curve against frequency in a log scale as shown in Fig. 8. The in-plane FRF could thus be approximated *at low frequencies* as

$$T_{ip}(\omega) \approx j\omega s, \tag{30}$$

where the in-plane compliance $s = 1/k_{in}$ is a constant. This suggests that the purely out-of-plane FRF can be estimated by subtracting the estimated in-plane FRF from the total measured sensor–actuator FRF. This method will be called the *jωs compensation method* from now on. This can be expressed from Eq. (29) as

$$T_{oop} = T_{total} - T_{ip} \approx T_{total} - j\omega s. \tag{31}$$

The compliance s is determined here simply to match the experimental data; however, in practice it could be estimated by an adaptive method.

As can be seen from Fig. 8, the measured response after the compensation of the in-plane coupling shows a more similar response to the measured response using the accelerometer/shaker configuration in Fig. 4(a) than that before the $j\omega s$ compensation. The extracted T_{oop} also maintains the SPR property, in the frequency range of 0–1000 Hz, although over a wider frequency range compensating for the only in-plane stiffness cannot remove the effects of the in-plane response. $j\omega s$ compensation could thus provide a new approach to the acquisition of the purely out-of-plane response of a structure with a matched sensor/actuator pair.

However, from Fig. 8, there are still unexpectedly strong peaks at even modes, such as the second and fourth out-of-plane modes, after the $j\omega s$ in-plane compensation. This problem is discussed in the next section.

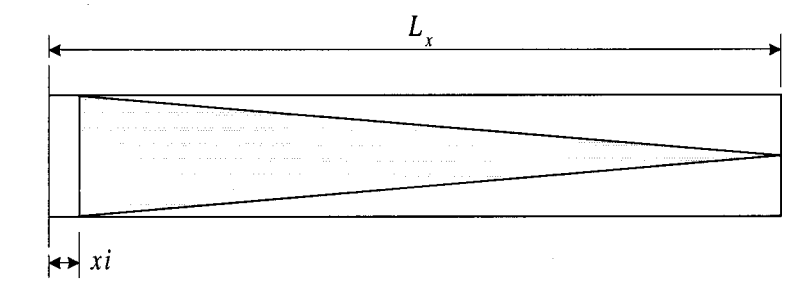

(a)

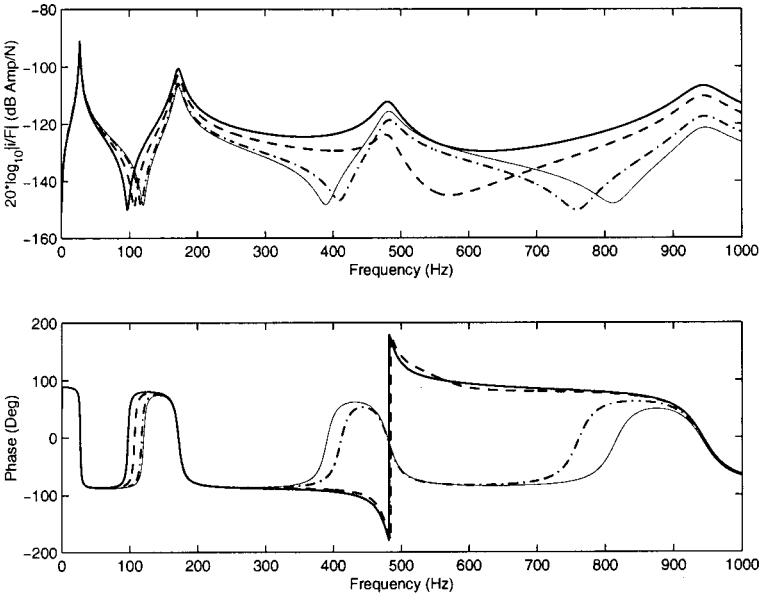

(b)

FIG. 9. (a) A computer simulation model of a triangularly shaped PVDF sensor with shaping errors bonded on a cantilever beam. Thick line is the erroneous shape and dashed line is the designed exact shape. (b) Effects of shaping errors by xi in the PVDF sensor. Shaping error by xi when $xf=L_x$: $xi=0$ for exact shape (thin line), $xi=1$ mm (dashed and dotted line), $xi=5$ mm (dashed line), and $xi=10$ mm (thick line).

VII. EFFECTS OF SHAPING ERRORS OF PIEZOELECTRIC TRANSDUCERS

Lee and Moon[19] showed that the response of modal actuators and sensors could be sensitive to small errors in the shapes of the transducers, particularly affecting the response at higher frequencies. After some investigation of the shaping errors of the PVDF sensor and actuator used in constructing the experimental smart beam, it was found that the two PVDF transducers were not identical or perfectly matched with each other. The PVDF sensor and actuator are bonded about 2 and 5 mm away, respectively, from the clamped end of the beam with some minor cutting errors, especially in the sharp edges of the signal electrodes of the PVDF film at the tip position. In this section the effect of these shaping errors is analyzed theoretically.

An analysis for predicting a precise effect due to transducer shaping errors requires modeling of the experimental beam not as a beam but as a *plate*, because the misalignment in the matched triangular sensor/actuator pair could cause two-dimensional responses such as tip twisting. However, since it has been found that the shaping error at the clamped end was relatively much bigger than the tip mismatching error, which can excited/detect a tip twisting, a cantilever beam model was used for this shaping error analysis.

For a simpler analysis, only a piezosensor with shaping errors of $\hat{S}(x,y)$ is considered when a tip out-of-plane force is applied, which excites the smart beam at the tip. Then, the harmonic transfer function $\hat{T}_{\text{oop}}(\omega)$ can be given after some manipulation, when the tip transverse force input $F_t(L_x)$ is applied, as

$$\hat{T}_{\text{oop}}(\omega)=j\omega\frac{\hat{q}_{\text{oop}}(\omega)}{F_t(\omega)}$$

$$=\frac{j\omega e_{31}h_{\text{sen}}L_y}{M_n}\sum_{n=1}^{\infty}\frac{\phi_n(L_x)\int_0^{L_x}\hat{S}(x,y)\dfrac{\partial^2\phi_n(x)}{\partial x^2}dx}{[\omega_n^2(1+j\eta_s)-\omega^2]}, \tag{32}$$

where $\hat{q}_{\text{oop}}(\omega)$ is the harmonic charge output of the sensor with error.

Thus, the integration in Eq. (32) is the esssential source of the shaping error problem because it cannot satisfy the properties of the triangularly shaped sensor as given in Eq. (8). So, the actual properties can be written as $\hat{S}(0,y)\neq kL_x$ and $\partial\hat{S}(x,y)/\partial x\neq -k$ for $0\leqslant x\leqslant L_x$. Thus, the integration result of Eq. (32) with the sensor with error becomes, using a partial integration, as

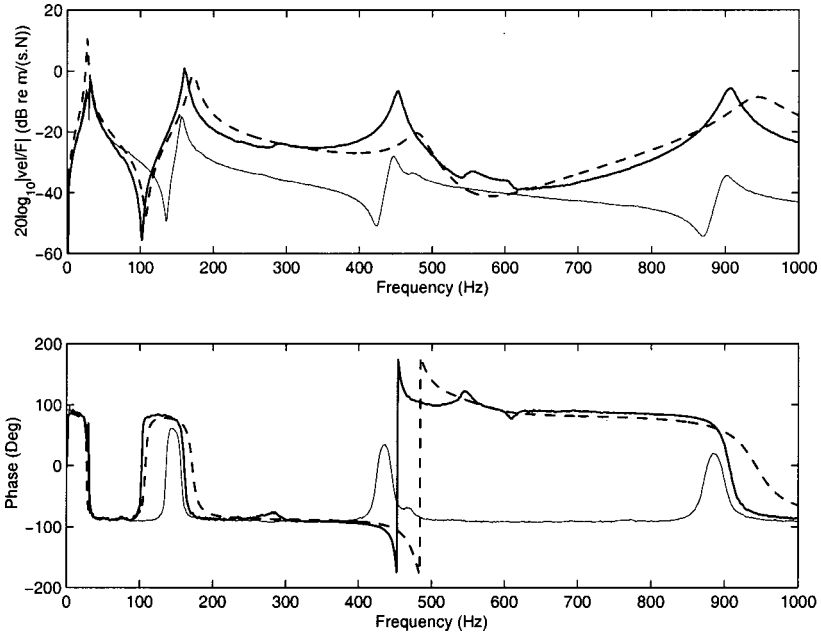

FIG. 10. Shaping error effects: Comparison of the measured responses (shaker and accelerometer—thin lines; shaker and erroneously shaped PVDF sensor—dashed lines) and the calculated (thick lines) FRFs with the erroneously shaped PVDF sensor when a tip transverse force is applied.

$$\hat{q}_{\text{oop}}(t) = -e_{31}h_{\text{sen}}L_y\left\{\left[\hat{S}(x,y)\frac{\partial w(x,t)}{\partial x}\right]_0^{L_x} - \int_0^{L_x}\frac{\partial \hat{S}(x,y)}{\partial x}\,\frac{\partial w(x,t)}{\partial x}\,dx\right\}$$
$$\neq -e_{31}h_{\text{sen}}L_y k w(L_x). \tag{33}$$

On this basis, the PVDF sensor can generate an additional charge output due to the shaping error. A computer simulation for an analytical cantilever beam model with an erroneously shaped PVDF sensor based on Eq. (32) is considered as illustrated in Fig. 9(a), where *xi* is the distance from the clamped end of the beam to the end of the sensor.

Figure 9(b) shows the responses with shaping errors when *xi* varies, in which the thin line represents the exact shape, the dashed and dotted line is for $xi=1$ mm, the dashed line is for $xi=5$ mm, and the thick line is for $xi=10$ mm. The response with the bigger *xi* showed the larger magnitude difference comapred with the exact shape. Resonance frequencies are almost the same as each other but the antiresonance frequencies are different or even gone. This is because excessive *xi* can generate an additional charge output which has the opposite sign compared to the charge output with the exact shape as shown in Eq. (33). Since the sign changes at the third and the fourth modes in Fig. 9(b) have been caused by excessive *xi*, so a small *xi* such as 1 mm could not change the sign, as shown in Fig. 9(b), because the additional charge output is smaller compared to the true out-of-plane charge output.

Apart from computer simulation, a measurement was made with the erroneously shaped PVDF sensor bonded on the beam when a shaker (Ling Dynamics model V201) excites the beam transversely at the tip. The input force signal was measured from a force transducer (B&K type 8200) via a signal conditioner (B&K type 2635 charge amplifier), and both the charge outputs from the PVDF sensor and an accelerator (B&K type 4375) were measured at the same time in the frequency range below 1000 Hz. In the case of the erroneous PVDF sensor, the harmonic current output $i(\omega)$ [the time derivative of the charge output $q(\omega)$] was measured to obtain a velocity signal.

The experimental FRFs and the simulation results with the erroneously shaped sensor are compared in Fig. 10. The thin line in Fig. 10 represents a typical feature of driving point mobility response of a cantilever beam with the point-collocated accelerometer/shaker configuratioan as described in Sec. III. However, the thic line measured with the shaker and the erroneous PVDF sensor configuration shows that the second, third, and fourth resonances are excessively large compared to the response with the accelerometer/shaker configuration. It also can be seen that the first and the second modes are detected as SPR responses, but the third and the fourth are not. The computer simulation results with the shaker and the erroneous PVDF sensor (thick dashed line) when $xi=5$ mm show a very similar trend with the measured ones.

The origin of this mismatching between the two measured FRFs was the shaping error of the PVDF sensor. Thus, the fact that the higher modes such as the third and fourth modes could be detected with a non-SPR property by the erroneously shaped sensor as shown in Fig. 10 is demonstrated both experimentally and theoretically. Similarly, the effect of shaping errors in the PVDF actuator also can be calculated with the above process. This is one of the possible shortcomings of all piezoelectric sensors as well as actuators, and this problem could become more serious with the more complex shaping of the sensor/actuator, as pointed out by Preumont *et al.*[20] Therefore, the unexpected peaky second and fourth out-of-plane resonances were caused by the erroneously shape PVDF sensor as well as actuator.

VIII. CONCLUSIONS

This paper has presented a study of a matched triangularly shaped PVDF sensor and actuator pairbonded on either

side of a smart cantilever beam for vibration control. The piezoelectric transducer pair was expected to allow both the excitation and the detection of transverse vibration at the tip position of the beam, since a traditional point-collocated sensor/actuator pair can provide a strictly positive real (SPR) property to a control system, which guarantees unconditional stability of its controller using direct velocity feedback strategy. However, the measurement results with the PVDF sensor/actuator pair showed a different response compared with the response obtained with a conventional accelerometer (with integration)/shaker configuration, which measures the driving point mobility having the SPR property.

The phase response measured with the matched sensor/actuator pair showed a phase lag due to a low-pass filter installed inside a signal conditioner, which was used to pick up the charge output from the piezosensor. The magnitude response measured with the piezo pair also showed an unexpected increasing trend with frequency, which has been proven to be caused by the in-plane vibration coupling.

An analytical model was developed to decompose the coupled FRF into an in-plane contribution and an out-of-plane contribution. The in-plane force by the piezoactuator and the charge output of the piezosensor bonded on the smart beam were analyzed in detail. The analytical coupled FRF was then very similar to the measured one. It was thus demonstrated that the increasing magnitude trend with frequency was indeed caused by the in-plane motion coupling.

The real part of the FRF between this matched piezosensor/actuator pair became negative, which indicates the pair cannot satisfy the SPR property, above the first in-plane resonance frequency. Thus, the matched piezo pair cannot be used for DVFB control with unconditional stability. A compensation method called the *jωs compensation method* was proposed to identify the in-plane vibration coupling at low frequencies. Because the in-plane response in the low-frequency range can be defined as being *stiffness controlled* response, the in-plane motion at low frequencies could be modeled as a simple spring with a compliance *s*. Unwanted strong out-of-plane resonances were measured with the smart beam at even modes even after the in-plane compensation. These were caused by the errors in the shaping of the PVDF sensor and actuator. A computer simulation with erroneously shaped transducers showed a similar FRF with the measured one and showed that abnormal peaky responses at certain modes could be possible due to shaping error of a piezoelectric sensor or/and actuator. These shaping errors should be removed with a very careful construction process for a shaped piezoelectric sensor/actuator.

ACKNOWLEDGMENTS

The smart beam used in this work is supported by EU DAFNOR (*Distributed Active Foils for NOise Reduction*) project. The authors would like to than Thomson Marconi, who built the smart beam.

[1] M. J. Balas, ''Direct velocity feedback control of large space structures,'' J. Guid. Control **2**, 252–253 (1979).
[2] C. K. Lee, ''Theory of laminated piezoelectric plates for the design of distributed sensors/actuators. I. Governing equations and reciprocal relationships,'' J. Acoust. Soc. Am. **87**, 1144–1158 (1990).
[3] C. K. Lee, W. W. Chiang, and T. C. O'Sullivan, ''Piezoelectric modal sensor/actuator pairs for critical active damping vibration control,'' J. Acoust. Soc. Am. **90**, 374–384 (1991).
[4] H. S. Tzou, ''A new distributed sensor and actuator theory for intelligent shells,'' J. Sound Vib. **153**, 335–349 (1992).
[5] S. E. Burke, J. E. Hubbard, Jr., and J. E. Meyer, ''Distributed transducers and collocation,'' Mech. Syst. Signal Process. **7**, 349–361 (1993).
[6] M. E. Johnson and S. J. Elliott, ''Active control of sound radiation using volume velocity cancellation,'' J. Acoust. Soc. Am. **98**, 2174–2186 (1995).
[7] J. S. Vipperman and R. L. Clark, ''Implications of using collocated strain-based transducers for output active structural acoustic control,'' J. Acoust. Soc. Am. **106**, 1392–1399 (1999).
[8] P. Gardonio, Y.-S. Lee, S. J. Elliott, and S. Debost, ''Analysis and measurement of a matched volume velocity sensor and uniform force actuator for active structural acoustic control,'' J. Acoust. Soc. Am. **110**, 3025–3031 (2001).
[9] Y.-S. Lee, ''Active control of smart structures using distributed piezoelectric transducers,'' Ph.D. dissertation, University of Southampton (2000).
[10] J. M. Sullivan, J. E. Hubbard, Jr., and S. E. Burke, ''Modeling approach for two-dimensional distributed transducers of arbitrary spatial distribution,'' J. Acoust. Soc. Am. **99**, 2965–2974 (1996).
[11] L. Cremer and M. Heckl, *Structure-Borne Sound*, 2nd ed. (Springer, Berlin, 1988).
[12] S. J. Elliott, *Signal Processing for Active Control* (Academic, New York, 2001).
[13] G. P. Gibbs and C. R. Fuller, ''Excitation of thin beams using asymmetric piezoelectric actuators,'' J. Acoust. Soc. Am. **92**, 3221–3227 (1992).
[14] S. Y. Yang and W. H. Huang, ''Is a collocated piezoelectric sensor/actuator pair feasible for an intelligent beam,'' J. Sound Vib. **216**, 529–538 (1998).
[15] D. G. Cole, W. R. Saunders, and H. H. Robertshaw, ''Modal parameter estimation for piezostructures,'' ASME J. Vibr. Acoust. **117**, 431–438 (1995).
[16] R. E. D. Bishop and D. C. Johnson, *The Mechanics of Vibration* (Cambridge University Press, Cambridge, 1960).
[17] D. J. Ewins, *Modal Testing: Theory and Practice* (Wiley, New York, 1984).
[18] D. J. Mead, *Passive Vibration Control* (Wiley, New York, 1999).
[19] C. K. Lee and F. C. Moon, ''Modal sensor/actuators,'' ASME J. Appl. Mech. **57**, 434–441 (1990).
[20] A. Preumont, A. Francois, and S. Debru, ''Piezoelectric array sensing for real-time, broadband sound radiation measurement,'' ASME J. Vibr. Acoust. **121**, 446–452 (1999).

Robust active control of broadband noise in finite ducts

S. Liu, J. Yuan,[a] and K.-Y. Fung
Department of Mechanical Engineering, The Hong Kong Polytechnic University, Hung Hom, Kowloon, Hong Kong, People's Republic of China

(Received 24 May 2001; accepted for publication 12 March 2002)

This study focuses on robust active control of broadband noise in finite ducts. Our analytical and experimental studies suggest the existence of several technical flaws in the path models of conventional active noise control (ANC) systems. These are sensitivity of the path model with respect to boundary conditions, and nonminimum phase (NMP) secondary and reference paths. For finite ducts with small cross sections, the traveling wave model (TWM) may be adopted to find an effective solution to these problems and lead to a robust ANC system. Since many practical ''noisy'' ducts are finite with small cross sections, the proposed ANC has many practical applications. Its robustness and ability to suppress broadband noise will be explained theoretically and verified experimentally. © *2002 Acoustical Society of America.* [DOI: 10.1121/1.1476683]

PACS numbers: 43.50.Ki [MRS]

I. INTRODUCTION

Active control of broadband noise is an active research topic with many publications in the literature. Its commercial application, for instance in ventilation ducts, lags behind research by a relatively large margin. Reliability is one of the problems to be solved before the technology can become commercially viable. The mathematical model of an ANC system is reasonably simple compared to other linear control systems. Available control techniques would be amply capable of maintaining reliable ANC performance, if only acoustical path transfer functions were linear time invariant (LTI). The reliability problem in an ANC system must be a result of not having accounted for some important uncertainties in the control system. In order to improve reliability, one should identify and eliminate as many, if not all, such uncertainties as possible.

The key to reliable ANC is a reliable reference signal. In practice an ANC system takes its reference signal inside the sound field. An internal model, by offline identification, is used to shield the reference signal from all other effects except the primary source. This study will analyze the potential threat of external variances, such as a variance of the environment, to the stable control of a semi-open field like a finite duct. Such variances, via the reflection path, may exceed the tolerable level to destabilize an otherwise stable ANC system. Another problem with conventional ANCs is the NMP secondary path when the sensor does not collocate with the speaker. It makes an ideal ANC transfer function unstable and compromises the cancellation performance for broadband ANC applications.

We will explain and demonstrate here how the use of traveling wave model (TWM) would lead to a robust broadband ANC. For finite ducts of small cross sections, path transfer functions of an ANC system are sensitive to external variances and the condition of the open end. TWM provides a way to reduce such sensitivity and improve the robustness of an ANC system. It allows the replacement of acoustic feedback cancellation by echo cancellation, which has proven very reliable in telecommunication[1] as a very successful application of the LMS algorithm. With TWM, the secondary path becomes a delay operator if actuator dynamics are ignored. Even when combined with actuator dynamics, the new secondary path model is independent of external influences in the duct outlet. An algorithm is developed for online noninvasive identification of the secondary path plus actuator dynamics. The new ANC system has a reduced computational burden, improved accuracy, and better cancellation of broadband noise than otherwise.

II. CONVENTIONAL ANC MODEL AND TWM

Figure 1 plots a typical feedforward adaptive ANC scheme for ducts, showing a primary noise source, a secondary source, an upstream reference sensor, and a downstream error sensor. Respectively, $P(z)$ and $R(z)$ represent the transfer functions from the noise source $n(z)$ to the error and reference microphones, and $S(z)$ and $F(z)$ represent the transfer functions from control signal $u(z)$ to the error and reference microphones. The error signal $e(z)$, measured by the downstream microphone, is related to the primary noise $n(z)$ by

$$e(z)=\left[P(z)+\frac{S(z)H(z)R(z)}{1-H(z)\Delta F(z)}\right]n(z), \tag{1}$$

where $\Delta F(z)=F(z)-\hat{F}(z)$. The system is stable if and only if all roots of $1-H(z)\Delta F(z)$ are inside the unit circle. If $F(z)$ were LTI, a reasonably accurate offline estimate of $\hat{F}(z)$ would be able to maintain stability for Eq. (1).

A. Problems with conventional ANCs

Unfortunately, $F(z)$ is sensitive to the boundary conditions of the duct outlet, which could be affected by humidity, temperature, or the presence of an object. The variation of $F(z)$ may deteriorate ANC performance or even cause an excessive ΔF to destabilize an otherwise stable ANC system. (In our experiment, a well-converged ANC scheme was ob-

[a]Author to whom correspondence should be addressed. Electronic mail: mmjyuan@polyu.edu.hk

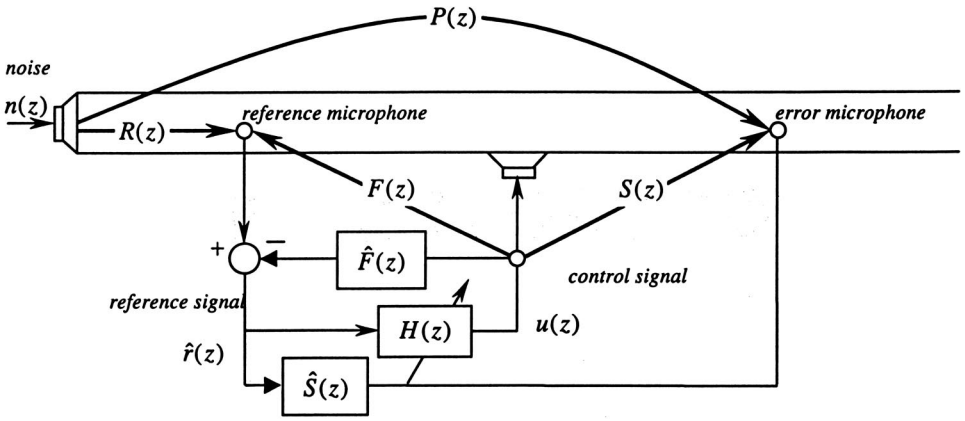

FIG. 1. Conventional feedforward ANC system.

served to diverge suddenly when a person moved near the duct outlet.) This is the first problem to be solved in this study.

In an ideal case where $\Delta F=0$, ''perfect'' cancellation in Eq. (1) requires $H(z)=-P(z)/S(z)R(z)$ as a digital filter. This filter is unstable if $S(z)$ or $R(z)$ is NMP, which is unfortunately true in almost all practical cases when the error and reference sensors do not collocate with the speaker. The NMP effects may not be too much of a problem if the primary source consists of a finite number of sinusoidal waves. It is always possible to find an imperfect but stable filter that matches the perfect but unstable filter at a finite number of frequencies. For a broadband primary source, however, the NMP effects prohibit the implementation of $H(z)=-P(z)/S(z)R(z)$. This is the second problem to be addressed here.

Most finite ducts contain reverberant sound fields where path transfer functions have infinite impulse responses (IIR). An ANC usually uses finite impulse response (FIR) filters with large numbers of coefficients to approximate $S(z)$ and $F(z)$. It means slow convergence, heavy computational burden, and large estimation errors when identifying $\hat{S}(z)$ and $\hat{F}(z)$. Besides, both $S(z)$ and $F(z)$ are sensitive to environment variations. A small variance in the reflection at either end of a finite duct could cause significant variances in $S(z)$ and $F(z)$. It is desirable to use a new model that has shorter impulse response, and is less sensitive to boundary conditions. This is the third objective of this study.

B. Canceling acoustic feedback as "echos"

Although TWM is limited to finite ducts of small cross section, many practical ''noisy'' ducts fall into this category. The model has been used for measurement of acoustic properties[2–4] and, in at least two cases, for ANC in ducts.[5,6] It enables noninvasive online identification of the acoustic paths in an ANC system.[5] This study demonstrates additional advantages of TWM not seen previously in the literature.

Figure 2 plots a block diagram of TWM, where transfer functions in the Z domain are used to describe the wave paths. A nomenclature of all symbols is provided in Table I. An important advantage of TWM is related to a potentially detrimental problem in conventional ANCs, for which all roots of $1-H(z)\Delta F(z)$ must be inside a unit circle to maintain stability. This condition is not guaranteed if an ANC uses an offline estimate $\hat{F}(z)$ to cancel $F(z)$. Applying block diagram algebra to Fig. 2, one can get

$$F(z)=\left.\frac{w_u^+(z)+w_u^-(z)}{u(z)}\right|_{n(z)=0}=\frac{(A+C\cdot B\cdot R_d)\cdot(1+R_u)}{1-C^2\cdot R_u\cdot R_d}. \tag{2}$$

The resonance of $F(z)$ is determined by denominator $D(z)=1-C^2(z)R_u(z)R_d(z)$, where $R_u(z)$ and $R_d(z)$ model the up- and downstream reflections, respectively. The variance of $R_u(z)$ and $R_d(z)$ will inevitably affect $D(z)$ and the resonant frequencies of the duct. While $R_u(z)$ may be a LTI transfer function due to the fixed condition deep inside the duct, $R_d(z)$ is subject to outside conditions. The motion of an object near the duct outlet, for example, could cause a sudden change δR_d. Differentiating Eq. (2) with respect to R_d, one can see that $\delta F(z)\propto \delta R_d/D^2$. Since $D=0$ near the resonance peaks, $F(z)$ is very sensitive to δR_d and δR_u.

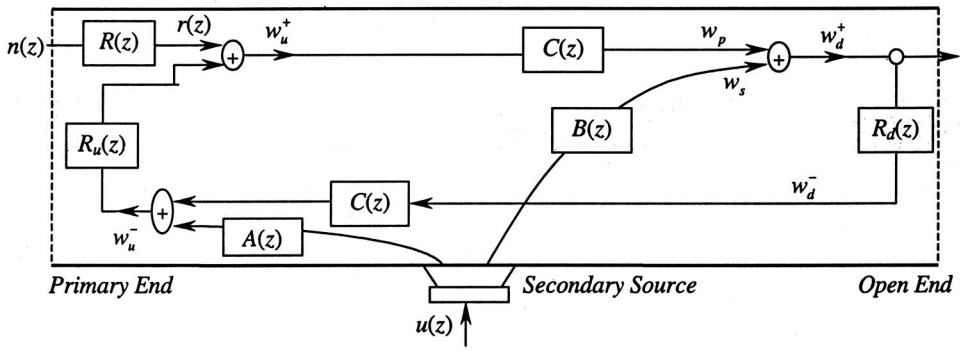

FIG. 2. Traveling wave model of duct acoustics.

TABLE I. Nomenclature of the traveling wave model.

Symbol	Explanation
$R_u(z)$ and $R_d(z)$	Up- and downstream reflection coefficients
w_u^+ and w_u^-	Traveling waves obtained by an upstream sensor pair
w_d^+ and w_d^-	Traveling waves obtained by a downstream sensor pair
$A(z)$ and $B(z)$	Up- and downstream paths of the secondary source
$C(z)$	Forward and backward path model from upstream sensor pair to downstream sensor pair
$n(z)$	Primary noise source signal
$r(z)$	Reference signal
$u(z)$	Secondary noise source signal

Physically, resonant frequencies of a musical instrument will change due to the variance of its boundary conditions.[7] A small δR_d or δR_u could cause a small drift of resonant frequencies in a duct. Such a drift may not be audible by human ears, but its contribution to $\Delta F(z)$ is not negligible. Consider, for example, a simple continuous $F(s)=1/(s^2+0.01s+100)$ and assume initially $F(s)=\hat{F}(s)$. Obviously, $\Delta F(s)$ is not zero if $F(s)$ drifts while $\hat{F}(s)$ remains fixed. A 1% drift of $F(s)$ from its initial form to $F(s)=1/(s^2+0.01s+101)$ causes a significant $\Delta F(s)$ shown in Fig. 3, where the magnitude is $|\Delta F(j\omega)|$ and the phase is degree. Reducing the drift in resonance frequency can only narrow the spike without reducing $\sup|\Delta F(j\omega)|$ Instead, $\sup|\Delta F(j\omega)|$ is inversely proportional to the damping ratio of the resonance. It increases to infinity if the damping ratio of the resonance reduces to zero.

In a finite duct, $F(z)$ may consist of many lightly damped resonant terms. Most ANC schemes use a FIR $\hat{F}(z)$ to approximate an IIR $F(z)$. It is impossible to have an initial $\Delta F(z)=0$ in the first place. The variance of the boundary conditions may cause the resonant frequencies to shift significantly.[8] Therefore $\Delta F(z)$ could have many spikes like, if not worse than, the one shown in Fig. 3. Roots of $1-H(z)\Delta F(z)$ may drift outside the unit circle, causing instability to an otherwise stable ANC. The best strategy for a robust controller is to remove uncertainties whenever possible from its model. Other strategies can only tolerate small bounded effects of those uncertainties that cannot be removed. For ANC applications $|\Delta F(j\omega)|$ could not be characterized by a small bound as illustrated in the previous example. It is possible that $|\Delta F(j\omega)|$ exceeds the tolerance of any robust controllers. Therefore, the best strategy is to eliminate the cause of such a potential threat from the controller model.

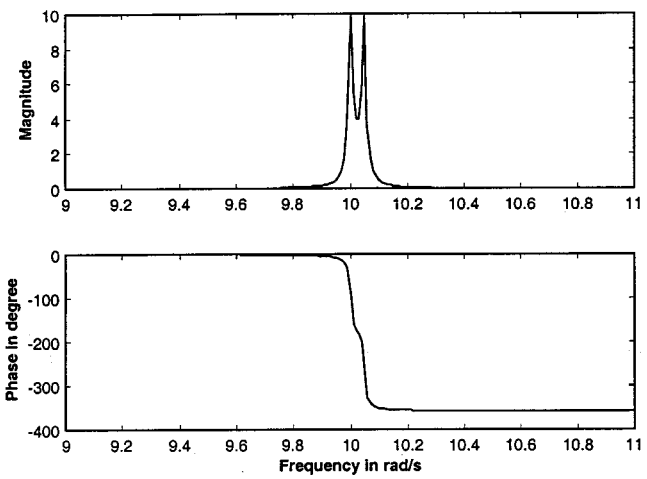

FIG. 3. $\Delta F(s)=1/(s^2+0.01s+101)-1(s^2+0.001s+100)$.

This is possible for finite ducts with small cross sections. The TWM enables one to design a new ANC without the internal model $\hat{F}(z)$. Figure 2 suggests

$$\hat{r}(z)=w_u^+(z)-\hat{R}_u(z)\cdot w_u^-(z), \tag{3}$$

where $\hat{r}(k)$ is an estimate of $r(k)$ and $\hat{R}_u(z)$ an estimate of $R_u(z)$ that includes the delay of w_u^- traveling backward and then bouncing to the upstream sensor pair. If the external environment variation causes a variance of $R_d(z)$, the magnitude and phase of w_u^- will be affected since

$$w_u^-(z)=A(z)u(z)+C^2(z)R_d(z)w_u^+(z)+C(z)B(z)R_d(z)u(z),$$

where the first term is the upstream control wave, the second term is a bounced version of w_u^+ while the third term is a bounced version of downstream control wave. There is, however, no need for explicit online identification of $R_d(z)$, $A(z)$, or $C(z)$. As long as w_u^- can be separated by the two-microphone method, the signal can be used directly in Eq. (3) to "bundle" the entire upstream wave. Online implementation of Eq. (3) is equivalent to echo cancellation in telecommunications,[1] which is a very successful application of the LMS algorithm. Our experiment also verifies the reliability of this approach.

C. Secondary path

In Fig. 2, $B(z)$ is the counterpart of the secondary path $S(z)$ of Fig. 1. It is theoretically a delay operator if actuator dynamics are ignored. In reality, actuator dynamics are inevitable. A recent study[9] found the combined dynamics of the speaker-amplifier to be

$$M(s)=\frac{U(s)}{V(s)}=\frac{k_0 s}{s^2+k_1 s+k_2}, \tag{4}$$

where $U(s)$ is the particle velocity and $V(s)$ is the voltage to the amplifier. If one considers $M^{\#}(s)=(s^2+k_1s+k_2)/k_0(s+\sigma)$, where $\sigma>0$ is a very small constant, then $M^{\#}(s)M(s)=s/(s+\sigma)\approx 1$ almost everywhere except zero frequency. $M^{\#}(s)$ is called the pseudo-inverse of $M(s)$ in this study. It is used to compensate for the actuator dynamics.

In our experiment, the impulse response of $\hat{B}(z)$ is identified by an online LMS and its frequency response plotted by the "freqz( )" command of MatLab using the impulse response as FIR filter coefficients. The magnitude plot, shown in the upper part of Fig. 4, matches the magnitude response of Eq. (4) very well, with an almost linear phase response. It agrees with the theoretical prediction that $B(z)$ is a delay operator if speaker dynamics are ignored. The corresponding $\hat{S}(z)$ is identified for the same duct, as shown in the lower part of Fig. 4. The phase shift of $\hat{S}(z)$ is nonlinear and approximately four times that of $\hat{B}(z)$ when locations of the speaker and downstream sensor are the same. Both plots are

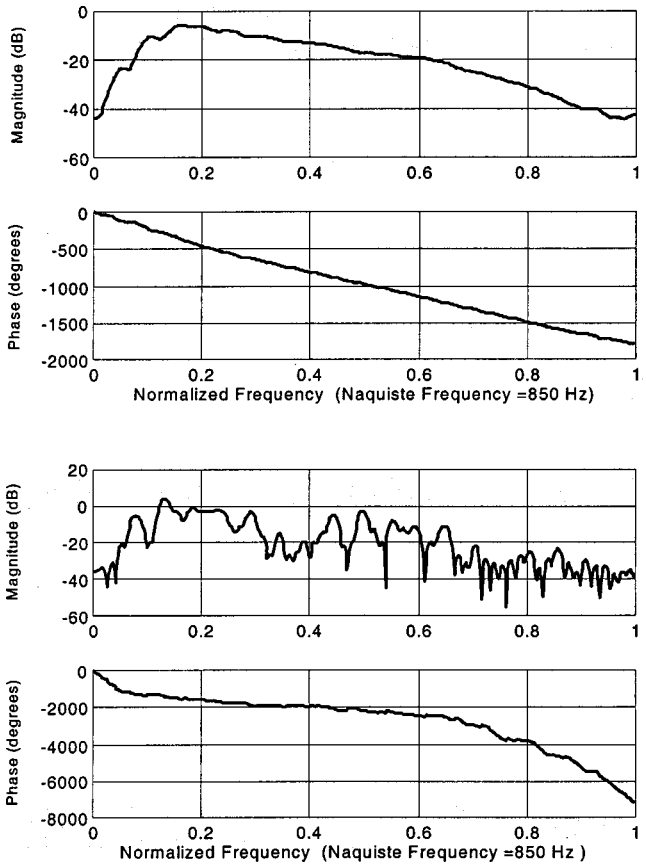

FIG. 4. Frequency responses of $\hat{B}(z)$ (upper) and $\hat{S}(z)$ (lower).

generated by the "freqz( )" command of MatLab using the respective impulse response as FIR filter coefficients; the large phase shift of $\hat{S}(z)$ agrees with a well-known observation that $S(z)$ is NMP if the actuator dynamics are ignored.

Considering actuator dynamics, we may approximately match the upper part of Fig. 4 to $\hat{B}(z)=\hat{M}(z)z^{-k_b}$, where k_b is an integer by a proper selection of the sampling frequency and $\hat{M}(z)$ represents the estimated speaker dynamics. The delay part can be compensated for by an upstream reference signal like a conventional ANC. The speaker dynamics $\hat{M}(z)$ can be compensated for by a pseudo inverse $M^{\#}(z)$ such that

$$M^{\#}(z)M(z)\approx 1 \tag{5}$$

almost everywhere except zero frequency. This is a very useful feature not possessed by $S(z)$, which is NMP even if the actuator dynamics are ignored. If the primary source consists of a finite number of sinusoidal noises, a NMP $S(z)$ may not be too much of a problem as explained previously. If the primary source is a broadband noise, however, a NMP $S(z)$ will degrade cancellation performance, as to be demonstrated experimentally.

D. Less variant path models with shorter impulse responses

Referring to Fig. 3, a small drift in resonant frequency can cause significant phase error in $\Delta F(s)$ in a simple numerical example. The phase error can be as large as 180 degrees. The same problem may happen to $\Delta S(z)$ if $\hat{S}(z)$ is available by offline identification. Since $S(z)$ and $F(z)$ are in the same sound field, both share the same denominator $D(z)$ that is sensitive to δR_d. The variance of $S(z)$ will degrade the performance of an ANC, since the filtered-x LMS will not converge properly if the phase error of $\hat{S}(z)$ exceeds 90 degrees.

On the contrary, $B(z)$ is independent of the boundary conditions because it is a delayed version of speaker dynamics. The speaker transfer function is certainly independent of the reflections of both ends of the duct. The delay part is due to a forward propagation path that is also independent of reflections of the duct outlet.

The impulse responses of $\hat{B}(z)$ and $\hat{S}(z)$ are identified and shown respectively in Fig. 5. One can see that $\hat{B}(z)$ can be modeled with half the number of coefficients as that of $\hat{S}(z)$, (64 versus 128). Since the accuracy of LMS degrades as the number of coefficients to be identified increases, fewer coefficients means better estimation accuracy if other conditions remain the same.

III. ACTIVE NOISE CONTROL AND IMPLEMENTATION

A. ANC transfer function

Figure 6 presents a partial diagram of the new ANC system. The objective is to minimize the forward traveling wave seen by the downstream sensor pair, i.e., $w_d^+=w_p+w_s\rightarrow 0$. The system is similar to a conventional ANC system, except that its primary path is $C(z)$ and its secondary path is $B(z)$. The primary wave and the secondary wave merge at the downstream sensor pair to produce

$$C(z)w_u^+(z)+B(z)H(z)\hat{r}(z)=w_d^+(z).$$

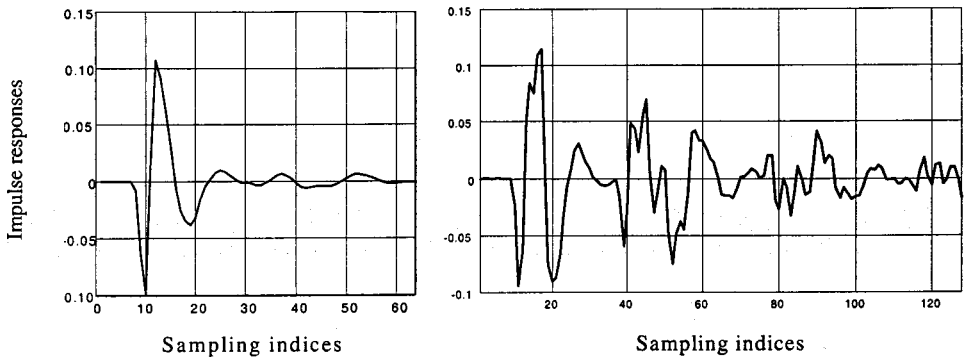

FIG. 5. Impulse responses of $\hat{B}(z)$ (left) and $\hat{S}(z)$ (right).

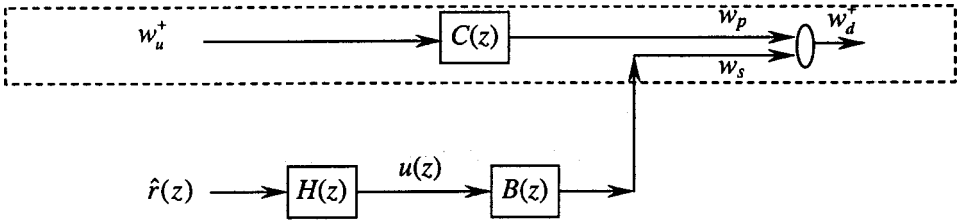

FIG. 6. Block diagram of the new ANC system.

Equation (3) indicates $w_u^+ = \hat{r}(z) + \hat{R}_u(z) w_u^-$. Substituting into the above equation, one obtains

$$[C(z) + B(z)H(z)]\hat{r}(z) + C(z)\hat{R}_u(z) w_u^-(z) = w_d^+(z). \tag{6}$$

Referring to Fig. 2, one can see that w_u^- consists of a reflected version of w_d^+ plus the backward contribution of $u(z) = H(z)\hat{r}(z)$, namely,

$$w_u^- = C(z)R_d(z)w_d^+ + A(z)H(z)\hat{r}(z).$$

Substituting this into (6), one obtains

$$w_d^+(z) = \frac{C(z) + H(z)[\hat{R}_u(z)C(z)A(z) + B(z)]}{1 - \hat{R}_u(z)C^2(z)R_d(z)}\hat{r}(z). \tag{7}$$

The system is stable if $|\hat{R}_u(z)C^2(z)R_d(z)| < 1$ for all $z = \exp(j\omega)$. This is not difficult since both $|C(z)| < 1$ and $|R_d(z)| < 1$ for all $z = \exp(j\omega)$, due to their passive nature. The objective of $w_d^+ \to 0$ is achievable even if $\hat{R}_u(z)$ does not match $R_u(z)$ perfectly. This means a relaxed requirement on the reference signal. The corresponding ANC transfer function is

$$H(z) = -\frac{C(z)}{B(z) + \hat{R}_u(z)C(z)A(z)}. \tag{8}$$

Let k_a, k_b, and k_c represent the delays of $A(z)$, $B(z)$, and $C(z)$, respectively. These waves transfer functions are very close to the ideal expressions $A(z) = M(z)z^{-k_a}$, $B(z) = M(z)z^{-k_b}$, and $C(z) = z^{-k_c}$ in practice. The sampling frequency of the ANC system and the location of the sensors may be adjusted properly such that k_a, k_b, and k_c are integers. Figure 2 indicates $k_c = k_a + k_b$ because the actuator locates between the up- and downstream sensor pairs. As a result, Eq. (8) becomes a casual filter:

$$H(z) = \frac{-M^{-1}(z)z^{-(k_c - k_b)}}{[1 + R_u(z)z^{-(k_c + k_a - k_b)}]} = \frac{-M^{-1}(z)z^{-k_a}}{1 + R_u(z)z^{-2k_a}}. \tag{9}$$

The roots of $1 + R_u(z)z^{-2k_a}$ are inside a unit circle since $R_u(z)$ represents passive reflection. It follows that $H(z)$ would be casual and realizable if $M(z)$ can be compensated for by $M^{\#}(z)$. The ideal expression of Eq. (7), upon substitution of Eq. (9) and pseudo-inverse $M^{\#}(z)$, can be written as

$$w_d^+(z) = \frac{[1 - M^{\#}(z)M(z)]z^{-k_c}}{1 - R_u(z)R_d(z)z^{-2k_c}} r(z),$$

which is close to zero almost everywhere except zero frequency because of Eq. (5). "Perfect" cancellation of noise is possible in a wide frequency range by the new ANC. On the contrary, the ideal transfer function of a conventional ANC is not stable since $S(z)$ and $R(z)$ are NMP even if speaker dynamics are ignored.

Practically, the new ANC transfer function $H(z)$ is adjusted by an online filtered-x LMS algorithm, like a conventional ANC. The similarity between Fig. 6 and a conventional ANC block diagram allows one to apply the noninvasive method[10,11] for online adaptation of $\hat{B}(z)$, $\hat{C}(z)$, and $\hat{H}(z)$. Both $B(z)$ and $C(z)$ are independent of boundary conditions and almost invariant unless the in-duct humidity or temperature changes drastically. The new ANC is able to converge to a reasonably good cancellation state using an offline $\hat{C}(z)$ in our experiment. An estimate of $B(z)$, however, is obtained by an online noninvasive algorithm to be explained in Sec. III D.

B. Wave separation in time domain

For a finite duct of small cross section, the sound field is a linear wave propagating system with plane waves. One may use w^+ and w^- to denote the forward and backward waves measured at x_1. The forward and backward waves at x_2 can be expressed as w^+e^{-jkL} and w^-e^{+jkL} as shown in Fig. 7. Here L is the distance between x_1 and x_2; e^{-jkL} is a delay factor with possible attenuation depending on whether the wave number k is real or complex. Let p_1 and p_2 represent the sound pressure signals at x_1 and x_2. Then

$$p_1 = w^+ + w^-, \quad p_2 = w^+e^{-jkL} + w^-e^{+jkL}.$$

The above equation implies

$$w^+(k) = \frac{p_1(k) - p_2(k)z^{-N}}{1 - z^{-2N}},$$

$$w^-(k) = \frac{p_2(k)z^{-N} - p_1(k)z^{-2N}}{1 - z^{-2N}},$$

where z^{-N} represents the discrete-time delay between the two microphones. This equation enables the new ANC scheme to obtain w_u^+ and w_u^- in time domain by an upstream

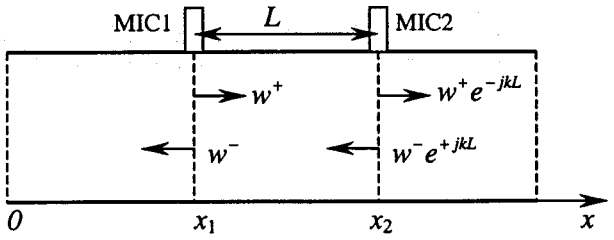

FIG. 7. Separation of traveling waves in a duct.

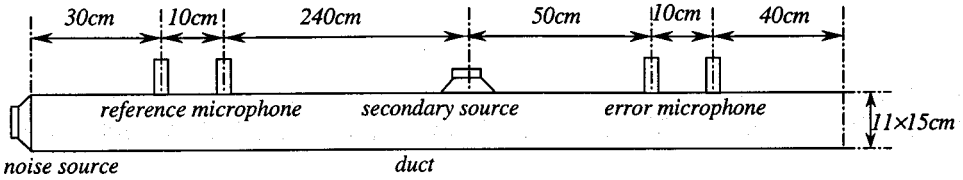

FIG. 8. Experimental setup of the proposed ANC system.

sensor pair. Similarly, a downstream sensor pair leads to w_d^+ and w_d^-.

The principle of wave separation has been applied to measure the absorption coefficients with a reasonable accuracy.[2–4] The error of wave separation is primarily due to the phase or magnitude mismatch of a sensor pair. Accurate wave separation only requires near identical response of a sensor pair. This is similar to the requirement for intensity probes[12] and three-dimensional intensity sensors,[13] but much less stringent than the identical sensor array in sonar systems. In our experiment, sensor mismatch can be easily controlled within 5% and expected to be less in the future as more sophisticated microphones with lower distortion become available. Further reduction of mismatch effect is possible by the use of microphone arrays.[4]

C. Offline identification of $C(z)$

The transfer function $C(z)$, of the "primary" path, describes the propagation of w_u^+ to w_d^+ in the absence of $u(z)$. Since $C(z)$ is independent of the boundary conditions this study uses an offline-estimated $\hat{C}(z)$. A LMS algorithm uses w_u^+ as the input and w_d^+ as the output signal to minimize

$$\min_{D(z)} \|e(z)\| = \min_{D(z)} \|w_d^+(z) - \hat{w}_d^+(z)\| = \min_{D(z)} \|w_d^+(z) - \hat{C}(z)\cdot w_u^+(z)\|.$$

The experimental data indicates that $\hat{C}(z) \rightarrow C(z) = z^{-k_c}$.

D. Online identification of $B(z)$

$B(z)$ is the transfer function of the "secondary" path, which describes the relation of the antisound w_s and the control signal $u(z)$. Figure 6 suggests that one can obtain $w_s(z)$ by

$$w_s(z) = w_d^+(z) - C(z)\cdot w_u^+(z),$$

where w_d^+ and w_u^+ are available by the wave separation algorithm described in Sec. III B; $C(z)$ can be substituted by its offline estimate $\hat{C}(z)$. Using w_s as the output and u as the input signal, an online LMS algorithm can be expressed as

$$\min_{B(z)} \|w_s(z) - \hat{B}(z)\cdot u(z)\|. \tag{10}$$

At convergence, the process obtains $\hat{B}(z) \rightarrow B(z)$, as shown in Figs. 4 and 5.

IV. EXPERIMENTAL RESULTS

The proposed ANC was tested in a 3.8-m duct with cross section 11×15 cm^2, as shown in Fig. 8. Two pairs of microphones were installed to separate the traveling waves in up- and downstream locations. The controller is a digital signal processing (DSP) board installed in a PC. The signals are sampled at 3.4 kHz, separated into traveling waves, and down-sampled to 1.7 kHz. Online echo cancellation of Eq. (3) enables the ANC to obtain the reference signal $\hat{r}(z)$ without the internal model. The filtered-x LMS is applied for online adaptation of $\hat{H}(z)$. Equation (10) is implemented for online identification of $\hat{B}(z)$ that is used to get the filtered-x signal.

The experimental results are plotted in Figs. 9 and 10, respectively. Theoretically, the resonant frequencies of a 3.8-m duct are $f_n = (2n-1)c/4L$ if one end is open.[14] The measured resonance frequencies match the theoretical values very well as shown in Figs. 9 and 10 by the spectra of uncontrolled noises. If both ends of the duct are closed, however, the resonant frequencies would be $f_n = nc/2L$.[14] This means the variance of resonant frequencies could be $\delta f_n = c/4L = 22.4$ Hz if the duct outlet varies between two extreme cases of completely open and completely closed. It is 100% for the first mode and 33% for the second mode.

The significant difference between two sets of resonant frequencies indicate a strong possibility that both $\Delta F(z)$ and $\Delta S(z)$ could have infinitely many peaks as significant as what is shown in Fig. 3. This also explains why a conventional ANC could diverge (at least once in our experiment) when a person moves near the outlet of the duct. Motions of objects near the outlet cause a δR_d that, in turn, causes the variation of $F(z)$ or $S(z)$ to threaten an otherwise stable adaptation process. Such a threat may or may not destabilize an ANC, depending on the estimated $\hat{F}(z)$ and the degree of δR_d. The new ANC is designed to reduce such a threat. It suppresses the broadband noise with a satisfactory performance shown in Fig. 9. A conventional ANC, tested under the same conditions, cannot achieve the same attenuation due to the NMP effects of $S(z)$ and $R(z)$. The performance of a conventional ANC scheme is deteriorated, even destabilized

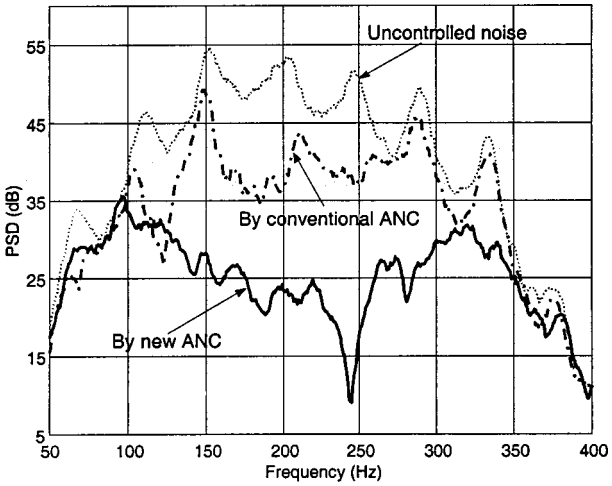

FIG. 9. Cancellation result for white noise.

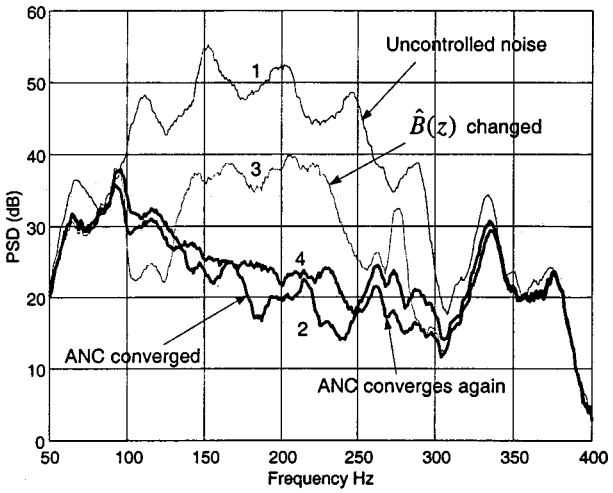

FIG. 10. Robust adaptation of the ANC system: (1) Uncontrolled noise, (2) ANC converged, (3) $\hat{B}(z)$ changed, and (4) ANC converges again.

occasionally, by the motions of objects near the outlet due to the sensitivity of both $S(z)$ and $F(z)$ with respect to the variation of duct outlet.

Robustness of the new ANC is tested with respect to the environmental changes near the outlet of the testing data. One can even block the duct outlet with an object without affecting the performance of the new ANC. If the outlet is blocked, every resonance frequency of $F(z)$ and $S(z)$ will change by $\delta f_n = 22.4$ Hz as explained above. The new ANC is independent of such effect and maintains stable adaptation since $B(z)$ is independent of the reflection effects. While $\hat{B}(z)$ contains inevitable errors as shown in Figs. 4 and 5, it approximates a delayed version of speaker transfer function very well. Both the delay part and the speaker dynamics are independent of the variation of the duct outlet. That is why the new ANC is much more robust than a conventional ANC with respect to the variation of the duct outlet. The wave decomposition method shields the new ANC scheme from the open-end effects.

In another test, $\hat{B}(z)$ was changed arbitrarily after the ANC had converged to a stable cancellation state. Such a change, equivalent to an unpredicted jump of $\Delta B(z)$, triggered a sudden deterioration of ANC performance as shown in Fig. 10, but the new ANC was able to stay stable and then converge again. With these tests, the new ANC has demonstrated its robustness with respect to variations of the external environment, the estimation error, or sudden change of $\Delta B(z)$. The new design has significantly reduced two important potential causes of instability. There may exist other threats to the reliable operation of ANC. These remain to be identified and solved by a further extensive study.

One may think the proposed method as equivalent to the directional source method by Swinbanks,[15] because both methods are related to direction of wave propagation. There is, however, a very significant difference between the two methods. If a directional secondary source is used here, $A(z)$ in Fig. 2 will be removed since the control wave only travels to the outlet. But this does not prevent the downstream wave from bouncing back in a *finite* duct. The reflection in a finite duct causes acoustical feedback even when a directional speaker is used. Both $F(z)$ and $S(z)$ are needed to synthesize an ANC by the conventional method. If we apply block diagram algebra to Fig. 2 with $A(z)$ removed, then we can get $F(z) = C \cdot B \cdot R_d(1+R_u)/(1-C^2 \cdot R_u \cdot R_d)$ and a similar expression for $S(z)$. These transfer functions may still be NMP and are surely sensitive to the variation of the external environment because the denominator remains unchanged. The proposed method is still needed to separate the traveling waves in order to eliminate problems associated with the NMP $F(z)$ and $S(z)$ and their sensitivity to the variation of reflections. The directional speaker method is effective in *long* ducts or free fields as suggested by the title of Ref. 15. In that case, the reflection wave is assumed negligible and need not be separated from the sensed signals.

V. CONCLUSION

This study identifies some existing problems in conventional ANC systems. These are potential threats to system stability due to the variation $\Delta F(z)$; NMP secondary path $S(z)$ and reference path $R(z)$; sensitivity of both $F(z)$ and $S(z)$ with respect to boundary conditions; and the IIR $F(z)$ and $S(z)$ in finite ducts. The TWM provides a very effective solution to these problems.

The solution is limited to finite ducts of small cross sections so that the two-microphone method can separate the traveling waves without being affected by the cross modes. This is the same limitation to the two-microphone method. Since many practical ''noisy'' ducts are finite with small cross-sectional areas, the proposed ANC has many applications. Its robustness and ability to suppress noise in a wide frequency range have been explained theoretically and verified experimentally.

This study used low-pass filters to cut off the cross-mode frequencies and did not test the two-microphone method under the influence of the cross modes. If the two-microphone method fails in the presence of cross modes, a possible solution might be the use of the 3D energy intensity sensor.[13] That, however, requires a more extensive study.

ACKNOWLEDGMENTS

The work described in this paper was substantially supported by a grant from the Research Grants Council of the Hong Kong Special Administration Region (Project No. PolyU 5175/01E). S.L. was supported by a Central Research Grant GT006.

[1] F. A. Westall and S. F. A. Ip, *Digital Signal Processing in Telecommunications* (Chapman and Hall, London, 1993).
[2] J. P. Smith, B. D. Johnson, and R. A. Burdisso, ''A broadband passive-active sound absorption system,'' J. Acoust. Soc. Am. **106**, 2646–2652 (1999).
[3] ''Standard test method for impedance and absorption of acoustical materials by the impedance tube method,'' ASTM C384 (ASTM, Philadelphia, 1990).
[4] S.-H. Jang and J.-G. Ih, ''On the multiple microphone method for measuring in-duct acoustic properties in the presence of mean flow,'' J. Acoust. Soc. Am. **103**, 1520–1526 (1998).
[5] J. Yuan and K.-Y. Fung, ''A traveling wave approach to active noise control in ducts,'' J. Sound Vib. **219**(2), 307–321 (1999).

[6] J. K. Kim and J. G. Ih, ''Active noise control in a duct by using the wave decomposition technique,'' ACTIVE 97, pp. 287–294.
[7] J. W. S. Rayleigh, *The Theory of Sound* (Dover, New York, 1945).
[8] E. Esmailzadeh, A. Alasty, and A. R. Ohadi, ''Hybrid active noise control of a done-dimensional acoustic duct,'' ASME Trans. J. Vib. Acoust. **124**(1), 10–18 (20002).
[9] H. R. Pota and A. G. Kelkar, ''Modeling and control of acoustic ducts,'' ASME Trans. J. Vib. Acoust. **123**(1), 2–10 (2001).
[10] W. C. Nowlin, G. S. Guthart, and G. K. Toth, ''Noninvasive system identification for multichannel broadband active noise control,'' J. Acoust. Soc. Am. **107**, 2049–2060 (2000).
[11] W. C. Nowlin, G. S. Guthart, and G. K. Toth, ''Experimental results for multichannel feedforward ANC with noninvasive system identification,'' J. Acoust. Soc. Am. **107**, 2039–2048 (2000).
[12] F. J. Fahy, *Sound Intensity*, 2nd ed. (E & FN Spon, London, 1995).
[13] J. W. Parkins, S. D. Sommerfeldt, and J. Tichy, ''Error analysis of a practical energy density sensor,'' J. Acoust. Soc. Am. **108**, 211–222 (2000).
[14] D. E. Hall, *Basic Acoustics* (Wiley, New York, 1987).
[15] M. A. Swinbanks, ''The active control of sound propagating in long ducts,'' J. Sound Vib. **49**, 411–436 (1973).

Measured anisotropic air flow resistivity and sound attenuation of glass wool

Viggo Tarnow
Department of Mechanical Engineering, Technical University of Denmark, Bygning 358, DK 2800 Lyngby, Denmark

(Received 31 August 2001; accepted for publication 12 March 2002)

The air flow resistivity of glass wool has been measured in different directions. The glass wool was delivered from the manufacturer as slabs measuring $100\times600\times900$ mm^3, where the surface 600×900 mm^2 was parallel with the conveyor belt used in the manufacturing. Directions in the glass wool are described by a coordinate system with the *X* axis perpendicular to the conveyor belt, the *Z* axis in the direction the conveyor belt moves, and the *Y* axis perpendicular to the two other axes. It was found that the resistivities in the *Y* and *Z* directions were equal in all cases. For density 14 kg/m^3 the mean resistivity in the *X* direction was 5.88 kPa s m^{-2} and in the *Y* direction 2.94 kPa s m^{-2}. For density 30 kg/m^3 the mean resistivity in the *X* direction was 15.5 kPa s m^{-2} and in the *Y* direction 7.75 kPa s m^{-2}. A formula for prediction of resistivity for other densities is given. By comparing measured values of sound attenuation with results calculated from resistivity data, it is demonstrated that the measured attenuation can be predicted in a simple manner. [DOI: 10.1121/1.1476686]

PACS numbers: 43.58.Vb, 43.20.Jr, 43.55.Ev [SLE]

I. INTRODUCTION

Many materials used for acoustic isolation and attenuation are open so air can flow through them. It has been known for many years that air flow resistivity can be used to predict the acoustical properties of acoustical materials. The resistivity is measured by sending an air flow with constant velocity through a sample of the material, and measuring the air velocity and pressure drop over the sample.

Delany and Bazley[1] have given very popular formulas for the acoustical properties of fiber materials where the only parameters are air flow resistivity, air density, and sound velocity in air. The researchers of the school of porous materials in Le Mans, France, have studied the acoustical properties by using resistivity as one of several parameters. A review has been presented by Allard.[2] In parallel with this work, Keith Attenborough in England worked on theories for predicting acoustical properties of fiber materials.[3]

Bies and Hansen[4] measured the resistivity of many sorts of fiber materials, and they plotted the resistivity versus the density of the material. In the following, data for air flow resistivity of glass wool as a function of bulk density will be presented.

Many different measuring devices have been used. Stinson and Daigle[5] reviewed many earlier setups and presented a new one. Iannace *et al.*[6] described a method that uses water to displace air in a tube with the same diameter as the sample. The measurement reported in the following uses an existing device that produces a constant air flow that can be measured with error less than 1%. The pressure drop over a sample is measured by an electronic nanometer with a resolution of 0.01 Pa.

Measurements by the author[7] showed that the sound attenuation of glass wool is anisotropic, and it is interesting to measure the resistivity of the glass wool used for the measurements of attenuation (and phase velocity) to see whether the usual methods used to predict the attenuation of acoustic sinusoidal waves works for the attenuation in different directions. This paper presents measurements of resistivity in three main directions in glass wool, and investigates whether these resistivities can be used to predict the attenuation of sound waves at audio frequencies.

II. MODEL FOR COMPUTING THE RESISTIVITY FROM FIBER DIAMETERS AND MASS DENSITY

The arrangement of glass fibers in glass wool is very complicated and one knows only a little about it. Great simplifications of the actual geometry are necessary to get a model that yields acoustic attenuation. In the classical theory of porous materials, one assumes that the material is solid with circular holes. This model is very far from the actual geometry of glass wool. Alternatively, one could assume that the fibers all have the same diameter and are parallel but placed randomly. In this case it is shown in a paper by the author[8] that the resistivity $R_\perp$ for flow perpendicular to fibers is

$$R_\perp = \frac{4\pi\eta}{b^2[-0.640\cdot\ln d - 0.737 + d]}, \tag{1}$$

where η is the viscosity of air, b^2 is the mean area per fiber, and d is the volume density of fibers, which equals fiber volume divided by total volume. The resistivity for flow parallel with the fiber $R_\parallel$ was shown in Ref. 8 to be half the value for flow perpendicular to fibers, $R_\parallel = R_\perp/2$. This model has one direction with low resistivity, and perpendicular directions have high resistivity. This is not found in glass wool, where there is one direction with high resistivity and perpendicular directions have low resistivity.

We need a model with high resistivity in one direction and low resistivity in all directions perpendicular to this di-

rection. In glass wool the fibers are mainly placed in dense layers separated by less dense layers. One could imagine that in a volume of perhaps 1 cm^3 there are 20 parallel layers, and in each layer the fibers are parallel and perpendicular to the X axis of a rectangular XYZ coordinate system, but the directions of the fibers vary from layer to layer. The fiber directions are evenly distributed in the YZ plane, and to get the macroscopic resistivity, an average is done over the directions. In this model the resistivity in the X direction is high, and the resistivity is low for directions in the YZ plane. The resistivity R_x in the X direction is equal to the resistivity of flow perpendicular to parallel fibers, because all fibers in the model are perpendicular to the X direction and interaction between layers is neglected, $R_x = R_\perp$. In this model the resistivities in the Y and Z directions are equal, which is also observed experimentally. Other arrangements of fibers could be imagined. One could assume that in a layer the fibers are locally parallel but the direction of fibers change from place to place. This model would also require an average over the directions of fibers in the YZ plane to get the macroscopic resistivity.

To compute the resistivity in the Y direction it is convenient to use the conductivity tensor G_{ij}, where i and j can take the values x, y, z. The conductivity tensor is defined by the following equation:

$$u_i = \sum_{j=x,y,z} G_{ij} \frac{\partial p}{\partial x_j}, \tag{2}$$

where u_i is the macroscopic velocity and p is the macroscopic pressure. We compute the components of the tensor in case all the fibers are parallel to each other. If they are perpendicular to the X direction, and the angle from the Z axis to the fibers is ν, then the conductivity tensor has the components

$$G = \begin{bmatrix} G_\perp & 0 & 0 \\ 0 & G_\perp \cos^2 \nu + G_\parallel \sin^2 \nu & (G_\parallel - G_\perp) \sin \nu \cdot \cos \nu \\ 0 & (G_\parallel - G_\perp) \sin \nu \cdot \cos \nu & G_\perp \sin^2 \nu + G_\parallel \cos^2 \nu \end{bmatrix}, \tag{3}$$

where $G_\perp = 1/R_\perp$ and $G_\parallel = 1/R_\parallel$. It is physically reasonable to assume that a pressure gradient is given in the glass wool, in this case, from Eq. (2) it is seen that one must make an average over the conductivity tensor. We average over the angle and take all angles for equally probable. This gives the average tensor $\langle G \rangle$, which equals

$$\langle G \rangle = \begin{bmatrix} G_\perp & 0 & 0 \\ 0 & G_\perp/2 + G_\parallel/2 & 0 \\ 0 & 0 & G_\perp/2 + G_\parallel/2 \end{bmatrix}. \tag{4}$$

Because $G_\parallel / G_\perp = R_\perp / R_\parallel = 2$, the resistivity tensor becomes

$$R = R_\perp \begin{bmatrix} 1 & 0 & 0 \\ 0 & \frac{2}{3} & 0 \\ 0 & 0 & \frac{2}{3} \end{bmatrix}. \tag{5}$$

III. MEASUREMENT SETUP

The setup is shown in Fig. 1. The samples are cut from glass wool slabs with a tube, which has a sharp edge. The diameters of the samples are 76 mm and the length 100 mm. After the samples have been cut, the tube, with the sample inside, is mounted in the setup shown in Fig. 1. The air stream through the sample comes from the cylinder-shaped bell, which is a little heavier than the contra weight to the right. The fall velocity of the bell was measured with a stop watch. To find the air velocity through the sample, the fall velocity of the bell was multiplied by the ratio 6.27 between the area of the bell and cross section area of the sample. The air velocity through the samples ranged from 11 to 6 mm/s. The pressure drop over the sample was measured by a digital manometer with a resolution of 0.01 Pa.

The resistivity R is found from the present reading p, the length of the sample l, and the measured air velocity u:

$$R = \frac{p}{lu}. \tag{6}$$

After the pressure and fall velocity of the bell were measured, the sample was removed from the sample holder and weighed. From the weight and the volume of the sample, the mass density of the sample was calculated.

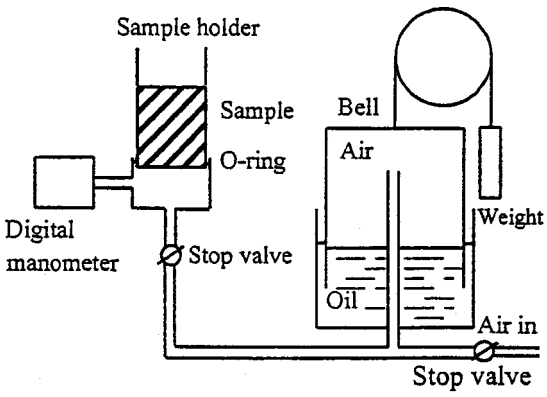

FIG. 1. The setup for measuring air flow resistivity of glass wool. Air is let into the movable bell, which is sealed by an oil reservoir below. When the bell is full, the inlet valve is closed and the stop valve before the sample holder is opened. The bell falls as air flows through the sample. The fall velocity of the bell is measured, and the pressure drop over the sample is measured. From these measurements and the dimensions of the sample and the area of the bell, the resistivity is found.

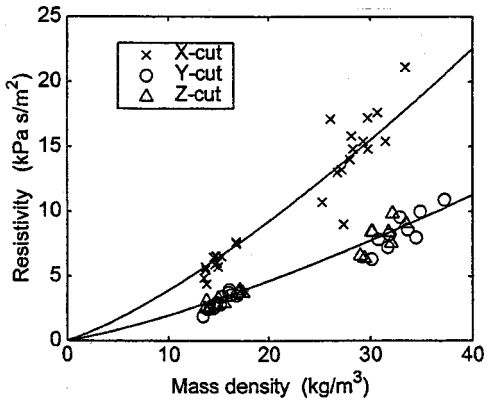

FIG. 2. Resistivity versus mass density for two types of glass wool with mean density 14 and 30 kg/m^3. The resistivity was measured in three perpendicular directions *X*, *Y*, and *Z*. The *X* direction is perpendicular to fibers. The upper curve is the resistivity in the *X* direction, calculated from Eq. (1), and the lower curve is the resistivity for the *Y* and *Z* directions found by dividing the resistivities in the *X* direction by 2.

The accuracy of the pressure measurement was limited by fluctuations of the pressure reading about 0.05 Pa. The velocity was measured with an accuracy of 0.5%. The overall accuracy of the measurement of resistivity was better than 2%.

IV. RESULTS OF MEASUREMENTS

The glass wool came from a major producer. It was delivered in slabs measuring $100\times600\times900$ mm^3. A rectangular coordinate system is used to describe the directions in the glass wool. The *X* axis is perpendicular to the large surface, 600×900 mm^2. This surface is parallel to the conveyor belt used in the manufacture. The *Z* axis is in the direction of the movement of the conveyor belt, and the *Y* axis is perpendicular to the two other axes. Samples were cut from different places and directions in the glass wool slabs, covering the whole slab evenly. No dependence on location was seen in the resistivity and density, but the variation of the data showed that the glass wool is inhomogeneous in both resistivity and density. The results are shown in Fig. 2. One can see that the resistivity for a given density is highest in the *X* direction and the resistivities in the *Y* and *Z* directions are equal within the scatter of the data. In the paper by Castagnede *et al.*,[9] it was assumed that the resistivity is proportional to the mass density, but the direct measurement in Fig. 2 shows this is not the case.

In Fig. 2 the curve for the *X* direction was computed from Eq. (1). The density d was found from $d=\rho_w/\rho_f$, where ρ_w is the density of glass wool and $\rho_f=2550$ kg/m^3 is the density of glass in the fibers. The area per fiber b^2 was computed from $b^2=\pi a^2/d$, where a is the radius of the fibers. To fit the curve to the data, a was adjusted to 5.15 μm. Measurement with a microscope gave a fiber radius of 3.4 μm with a standard deviation of 1.3 μm. The fitted radius is somewhat higher than the directly measured radius. Therefore, the glass wool is more open on a microscopic scale than one would expect with a completely random distribution of parallel fibers. A possible explanation could be that the fibers have a tendency to cling together in pairs. This is supported by microscopic inspection of glass wool samples.

The resistivity curve for the *Y* and *Z* direction is 0.50 times the one for the *X* direction. From acoustical measurements Allard *et al.*[10] deduced the ratio $R_y/R_x=0.6$ for glass wool with $R_x=25\,000$ Pa s m^{-2}. The ratio 0.50 found here is not in accordance with the calculation above, which gave the ratio 0.667. The reason for the discrepancy could be the layered structure of the glass wool. A cut perpendicular to the *Y* or *Z* axis of glass wool of density 15 kg/m^3 shows an irregular layered structure with dense layers about 0.3 mm thick and approximately parallel with the *YZ* plane. The distances between the dense layers are about 0.6 mm. This structure is consistent with the large difference in the elastic moduli for the different directions. The elastic modulus for compression in the *X* direction is approximately 50 times smaller than the one for compression in the *Y* and *Z* directions.[7] Obviously the less dense layers have a very low stiffness. The resistivity in the *Y* direction is smaller than for a homogeneous model because when the air flows through the glass wool in the *Y* direction, most air will flow between the dense layer, where the local resistivity is smallest. This means that the overall resistivity measured will be smaller than the resistivity for a homogeneous distribution of fibers. Therefore, we measure the ratio 0.50 instead of 0.667.

V. CONSTANT AIR FLOW RESISTIVITY AND SOUND ATTENUATION

For many years it has been assumed that the sound velocity and attenuation of sinusoidal sound waves in fiber materials could be calculated from the resistivity measured with steady air flow and the frequency. The formulas by Delany and Bazley[1] are very popular. However, they are empirical and not accurate at low frequencies. An alternative is to compute the wave number and characteristic impedance by formulas for complex mass density ρ_d and compressibility given by Wilson.[11] I prefer here the complex resistivity R, instead of the complex mass density, because the resistivity is real and constant at low frequencies. By definition, $R=-i\omega\rho_d$, where ω is the angular frequency, and we use the complex time factor $e^{-i\omega t}$. The complex resistivity R is

$$R=\frac{-i\omega\rho}{1-(1-i\omega\tau_R)^{-1/2}}, \tag{7}$$

where $\rho=1.20$ kg/m^3 is the mass density of air at 20 °C and 1 atm pressure, and τ_R is a time constant. The time constant is related to the constant air flow resistivity R_i, where i stands for *x*, *y*, or *z*. The low-frequency limit of Eq. (7) gives

$$\tau_{Ri}=\frac{2\rho}{R_i}. \tag{8}$$

The compressibility of air between fibers depends on frequency, being isothermal at low frequencies and adiabatic at high frequencies. Wilson's formula for the complex compressibility C is

$$C=\frac{1}{\gamma P}\left[1+\frac{\gamma-1}{(1-i\omega\tau_C)^{1/2}}\right], \tag{9}$$

where $\gamma=1.40$ for atmospheric air, P is the atmospheric air pressure, and τ_C is a time constant. To find a relation between constant flow resistivity and the compressibility time constant we assume the fibers are parallel. Stinson and Champoux[12] derived a relation between resistivity and compressibility. Their derivation assumed flow in tubes, but the differential equations and boundary conditions for local velocity and temperature are the same for flow in tubes and flow parallel to parallel fibers. Therefore their derivation is also valid for parallel fibers. Equation (8) in their paper reads $C=(1/\gamma P)\{\gamma-(\gamma-1)[\rho/\rho_d(N\omega)]\}$, where N is Prandtl number, which for atmospheric air is $N=0.71$. ($N=c_p\eta/\kappa$, where c_p is the air heat capacity at constant pressure, η is the air viscosity, and κ is the heat conductivity of air.) If $\rho_d(N\omega)$ is calculated from our Eq. (7) and set into Stinson and Champoux's equation for compressibility, one gets Eq. (9) with $\tau_C=N\tau_\parallel$, where $\tau_\parallel$ is the resistivity time constant for flow parallel with parallel fibers. In Ref. 8 it is shown that for parallel fibers the resistivity perpendicular to the fibers is two times the resistivity parallel with the fibers. We now apply Eqs. (7) and (8) to parallel fibers. It then follows from Eq. (8) that the time constant for flow parallel to fibers is two times the one for perpendicular flow. We know the perpendicular resistivity R_x from measurements on real glass wool, and from Eq. (8) one gets the time constant for perpendicular flow with $R_i=R_x$. This time constant is multiplied by 2 to get the time constant for parallel flow, and this is multiplied by N to give Eq. (10):

$$\tau_C=\frac{4N\rho}{R_x}. \tag{10}$$

We assume that the glass wool is restrained mechanically from moving under influence of the sound wave. The sound wave number k is then

$$k=\sqrt{i\omega RC}, \tag{11}$$

and the characteristic impedance is

$$Z=\sqrt{\frac{iR}{\omega C}}. \tag{12}$$

For plane harmonic waves in glass wool, the real part of the wave number k gives the phase shift per meter of the sound pressure amplitude, and the imaginary part of the wave number gives the relative attenuation of sound pressure per meter. The phase shift of the wave is mainly determined by the inertia of the air itself, and it is not very sensitive to parameters of a model, but the sound attenuation is sensitive to these parameters. Therefore, we compare a calculation of the attenuation from Eqs. (9)–(11) with measurements of attenuation. The measurements were done on a pile of glass wool in which an approximately plane wave could propagate without reflections from boundaries. The sound pressures on each side of the layer of glass wool 0.200 m thick were measured with microphones. The attenuation in decibels was divided by this thickness to give the attenuation per meter.

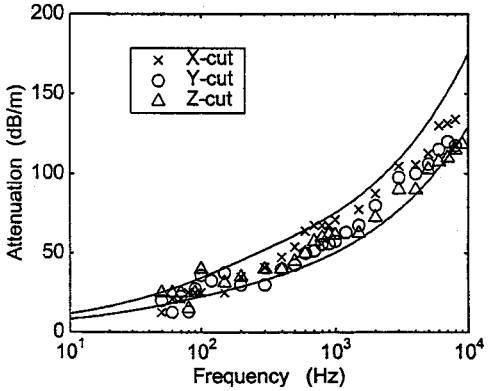

FIG. 3. Measured attenuation per meter for plane sound waves in glass wool of mean density 14 kg/m^3, in three perpendicular directions *X*, *Y*, and *Z*. The *X* direction is perpendicular to the fibers. The upper curve is the attenuation in the *X* direction, calculated from the measured resistivities by Eqs. (8)–(11). The lower curve is the attenuation in the *Y* and *Z* directions calculated in the same way.

The glass wool layer was perpendicular to the propagation direction of the sound wave. Further details of the measurements were given in Ref. 7. For the light glass wool of mean density 14 kg/m^3, the results are shown in Fig. 3. The lines were calculated from a mean resistivity, which was calculated by Eq. (1) from the mean density in the same way as the curves in Fig. 2 were found. For mass density 14 kg/m^3, the mean resistivity was $R_x=5880$ Pa s m^{-2} and $R_y=2940$ Pa s m^{-2}. For the *X* direction the calculated curves are a little higher than the measured points in the 700–8000 Hz frequency range. In the 50–600 Hz frequency range, the measured points are below the curve, due to movements of the glass wool caused by the sound wave. The glass wool is dragged by the friction between fibers and moving air in the sound waves.[7,13] Calculation of the wave number by Eq. (11) assumes the fibers do not move. This may be the case in some applications of glass wool, if the movement of the glass wool is mechanically constrained. The measured attenuations per meter in the *Y* and *Z* directions are almost equal and a little higher than the curve calculated from the resistivity. The elastic moduli in the *Y* and *Z* direction are about 50 times the one for the *X* direction,[7] thus the glass wool has much higher mechanical stiffness in these directions. Therefore, there is little movement of fibers with sound waves in these directions, and most of the measured points are above the curve calculated for fixed fibers.

The attenuation of sound waves in glass wool of density 30 kg/m^3 is shown in Fig. 4. The mean resistivity for this density was computed in the same way as above, and the resistivities were $R_x=15500$ Pa s m^{-2} and $R_y=7750$ Pa s m^{-2}. Most points were obtained from attenuation measurements with a glass wool layer 0.200 m thick, but the data for *X* directions in the 1500–8000 Hz frequency range was measured with a layer 0.100 m thick. The data for the *X* direction are close to the curve in the 700–8000 Hz frequency range. They are below the curve in the 50–600 Hz frequency range, because the glass wool moves with the sound wave, which was shown in Refs. 7 and 13. The data for *Y* and *Z* directions follow the curve because the glass

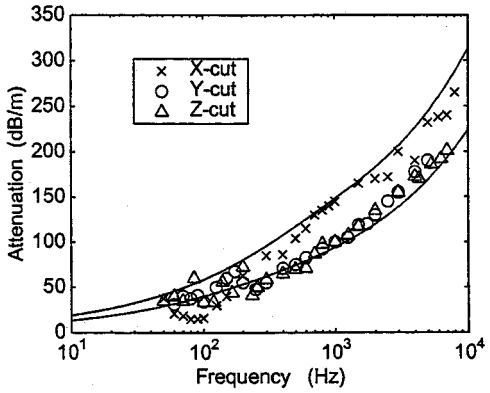

FIG. 4. Measured attenuation per meter for plane sound waves in glass wool of mean density 30 kg/m^3, in three perpendicular directions *X*, *Y*, and *Z*. The *X* direction is perpendicular to the fibers. The upper curve is the attenuation in the *X* direction, calculated from the measured resistivities by Eqs. (8)–(11). The lower curve is the attenuation in the *Y* and *Z* directions calculated in the same way.

wool does not move, due to the high mechanical stiffness of the glass wool in these directions.[7]

VI. CONCLUSION

The measured constant air flow resistivities of glass wool with density 14 and 30 kg/m^3 were used to compute the attenuation per meter of plane sound waves. The calculated attenuation was reasonably close to direct measured attenuation per meter. Given the constant air flow resistivity, one can compute the wave number from Eqs. (7)–(11), provided the fibers do not move. This procedure can be expected to be valid in the 0–10 000 Hz frequency range. It has the proper low-frequency limit and better theoretical foundation then the empirical equations of Delany and Bazley.[1] Even without direct experimental data for the characteristic impedance, it is reasonable to assume that the characteristic impedance could be predicted from constant air flow resistivity by Eq. (12) and Eqs. (7)–(10).

[1] M. E. Delany and E. N. Bazley, "Acoustical properties of fibrous absorbent materials," Appl. Acoust. **3**, 105–116 (1970).
[2] J. F. Allard, *Propagation of Sound in Porous Media: Modeling Sound Absorbing Materials* (Chapman and Hall, London, 1993).
[3] K. Attenborough, "Acoustical characteristics of rigid fibrous absorbents and granular-materials," J. Acoust. Soc. Am. **73**, 785–799 (1983).
[4] D. A. Bies and C. H. Hansen, "Flow resistance information for acoustical design," Appl. Acoust. **13**, 357–391 (1980).
[5] M. R. Stinson and G. A. Daigle, "Electronic system for the measurement of flow resistance," J. Acoust. Soc. Am. **83**, 2422–2428 (1988).
[6] G. Iannace, C. Ianniello, L. Maffei, and R. Romano, "Steady-state airflow and acoustic measurement of the resistivity of loose granular materials," J. Acoust. Soc. Am. **106**, 1416–1419 (1999).
[7] V. Tarnow, "Measurements of anisotropic sound propagation in glass wool," J. Acoust. Soc. Am. **108**, 2243–2247 (2000).
[8] V. Tarnow, "Airflow resistivity of models of fibrous acoustic materials," J. Acoust. Soc. Am. **100**, 3706–3713 (1996).
[9] B. Castagnede, A. Akine, B. Brouard, and V. Tarnow, "Effects of comparison on the sound absorption of fibrous materials," Appl. Acoust. **61**, 173–182 (2000).
[10] J. F. Allard, R. Bourdier, and A. L'Esperance, "Anisotropic effect in glass wool on normal impedance in oblique incidence," J. Sound Vib. **114**, 233–238 (1987).
[11] D. K. Wilson, "Relaxation-matched modeling of propagation through porous media including fractal pore structure," J. Acoust. Soc. Am. **94**, 1136–1145 (1993).
[12] M. R. Stinson and Y. Champoux, "Propagation of sound and the assignment of shape factors in model porous materials having simple pore geometries," J. Acoust. Soc. Am. **91**, 685–695 (1992).
[13] V. Tarnow, "Fiber movements and sound attenuation in glass wool," J. Acoust. Soc. Am. **105**, 234–240 (1999).

One source for distortion product otoacoustic emissions generated by low- and high-level primaries

Andrei N. Lukashkin,[a] Victoria A. Lukashkina, and Ian J. Russell
School of Biological Sciences, University of Sussex, Falmer, Brighton BN1 9QG, United Kingdom

(Received 18 October 2001; revised 21 March 2002; accepted 24 March 2002)

Distortion product otoacoustic emissions (DPOAE) elicited by tones below 60–70 dB sound pressure level (SPL) are significantly more sensitive to cochlear insults. The vulnerable, low-level DPOAE have been associated with the postulated active cochlear process, whereas the relatively robust high-level DPOAE component has been attributed to the passive, nonlinear macromechanical properties of the cochlea. However, it is proposed that the differences in the vulnerability of DPOAEs to high and low SPLs is a natural consequence of the way the cochlea responds to high and low SPLs. An active process boosts the basilar membrane (BM) vibrations, which are attenuated when the active process is impaired. However, at high SPLs the contribution of the active process to BM vibration is small compared with the dominating passive mechanical properties of the BM. Consequently, reduction of active cochlear amplification will have greatest effect on BM vibrations and DPOAEs at low SPLs. To distinguish between the ''two sources'' and the ''single source'' hypotheses we analyzed the level dependence of the notch and corresponding phase discontinuity in plots of DPOAE magnitude and phase as functions of the level of the primaries. In experiments where furosemide was used to reduce cochlear amplification, an upward shift of the notch supports the conclusion that both the low- and high-level DPOAEs are generated by a single source, namely *a nonlinear amplifier with saturating I/O characteristic.* © *2002 Acoustical Society of America.* [DOI: 10.1121/1.1479151]

PACS numbers: 43.64.Jb, 43.64.Bt, 43.64.Kc [BLM]

I. INTRODUCTION

The vulnerability of distortion product otoacoustic emissions (DPOAEs) to various cochlear traumas is level dependent. In rodents, DPOAEs elicited by low-level tones (the levels of primaries, L_1 and L_2, are below 60–70 dB SPL) are significantly more sensitive to hypoxia and post-mortem conditions (Schmiedt and Adams, 1981; Kemp and Brown, 1984; Lonsbury-Martin *et al.*, 1987; Whitehead *et al.*, 1992; Rebillard *et al.*, 1993; Frolenkov *et al.*, 1998). Reduction of the endocochlear potential severely decreases low-level, and has only a small effect on the high-level, DPOAEs (Kemp and Brown, 1984; Whitehead *et al.*, 1992; Mills *et al.*, 1993; Mills and Rubel, 1994; Frolenkov *et al.*, 1998). The same dependence of the DPOAE amplitude on the level of primaries was found for gentamicin-treated (Brown *et al.*, 1989) and noise-damaged ears (Zurek *et al.*, 1982; Schmiedt, 1986). The level dependence of the DPOAE vulnerability led to speculation that the sources of DPOAEs generated by primaries below 60–70 dB SPL were different from those generated for levels above 60–70 dB (Brown, 1987; Norton and Rubel, 1990; Whitehead *et al.*, 1990). It was proposed that the vulnerable, low-level DPOAEs were associated with the active cochlear process, whereas the relatively robust high-level DPOAE component was attributable to passive, nonlinear macromechanical properties of the cochlear partition. However, despite its relative stability, the high-level DPOAE itself can be affected by auditory fatigue (Mom *et al.*, 2001) and acoustical trauma (Wiederhold *et al.*, 1986; Whitehead *et al.*, 1992; Hamernik *et al.*, 1996) or by combined treatment with aminoglycosides and ethacrinic acid (Whitehead *et al.*, 1992). It also can be suppressed by mercurial sulfhydryl reagents (Frolenkov *et al.*, 1998), which effectively block the OHC motility in vitro (Kalinec and Kachar, 1993).

Differences in the vulnerability of the low- and high-level DPOAEs may be a natural consequence of the way the cochlear operates at low and high sound pressure levels. Basilar membrane (BM) vibrations are boosted by an active process (Gold, 1948) whose contribution to the BM mechanical response, in absolute terms, increases with increasing sound pressure level (SPL) until saturation of the hair cell transducer conductance (Patuzzi *et al.*, 1989). However its relative contribution is greatest at low SPLs. At high SPLs, responses of the BM are dominated by the passive mechanical properties of the cochlea. Consequently, any reduction in the magnitude of the active cochlear feedback will have greatest effect on BM vibrations and DPOAE characteristics at low SPLs.

In this paper we provide evidence that the low- and high-level DPOAEs are generated by the same source, *being a nonlinear amplifier with saturating I/O characteristic.* Differences in susceptibility to cochlear insults between the low- and high-level DPOAEs are observed when only the efficiency of the amplification, but not the asymptotic values of the nonlinearity, is affected. This conclusion is supported by experiments where furosemide weakens the efficiency of the cochlear amplifier.

[a]Electronic mail: a.lukashkin@sussex.ac.uk

 0001-4966/2002/111(6)/2740/9/$19.00

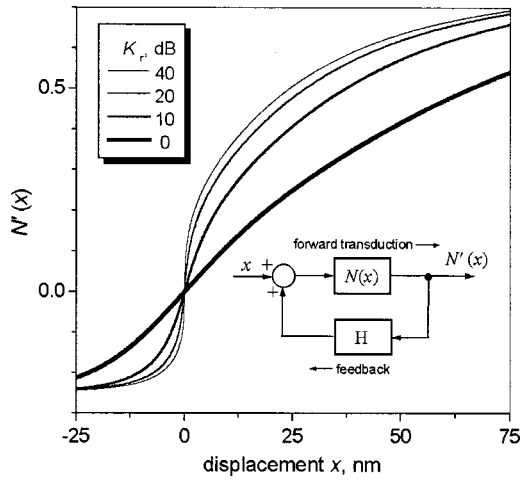

FIG. 1. Nonlinearity, $N'(x)$, of the hair cell mechano-electrical transducer with positive feedback given by Eq. (3). The nonlinearity was normalized for maximum transducer conductance $G_{\mathrm{tr\,max}}=5.5$ nS (Géléoc *et al.*, 1997) and modified by moving its operating point into the point of inflection of the function (i.e., when $x_{\mathrm{set}}=0$ nm). $N(x)$ is the nonlinearity given by Eq. (2) with $a_1=0.092\ \mathrm{nm}^{-1}$, $a_2=0.025\ \mathrm{nm}^{-1}$, $x_1=19$ nm, $x_2=45$ nm, which are the parameters used by Géléoc *et al.* (1997) to fit their experimental data. H is the feedback gain constant. Relative gain, K_r, for each curve is indicated in decibels re gain without feedback ($K_r=0$ dB). Note that each curve has the same asymptote for large displacements x.

II. THEORETICAL BACKGROUND

In a model that has been published previously (Lukashkin and Russell, 1999) we took as a first approximation, the basolateral membrane potential, which drives the OHC motility (Ashmore, 1987; Santos-Sacchi and Dilger, 1988) to be considered proportional to the total charge flow through the mechanoelectrical transducer channels. Hence, the nonlinearity of the mechanoelectrical transducer can be assumed to be the main contributor to the cell's nonlinear voltage responses (Patuzzi *et al.*, 1989; Santos-Sacchi, 1993) and is the dominant DPOAE producing nonlinearity, $N(x)$. The nonlinearity $N(x)$ is considered to be in the form,

$$N(x)=G_{\mathrm{tr}}-G_{\mathrm{tr}}(0), \tag{1}$$

where x is the displacement of the hair bundle from its resting position, $G_{\mathrm{tr}}(x)$ is the conductance of the hair cell mechanoelectrical transducer, and $G_{\mathrm{tr}}(0)$ is the transducer conductance with zero displacement of the hair bundle. The conductance of the transducer $G_{\mathrm{tr}}(x(t))$ is given by (Crawford *et al.*, 1989)

$$G_{\mathrm{tr}}(x)=G_{\mathrm{tr\,max}}\{1+\exp(a_2[x_2-x0-x_{\mathrm{set}}-x]) \times[1+\exp(a_1[x_1-x0-x_{\mathrm{set}}-x])]\}^{-1}, \tag{2}$$

where $G_{\mathrm{tr\,max}}$ is the maximal transducer conductance and x_{set} is the steady state displacement of the hair bundle determining operating point of the nonlinearity. A constant $x0 \approx 22.4$ nm is used to move the operating point into the point of inflection of the function (2) for a given set of constants $a_1=0.092\ \mathrm{nm}^{-1}$, $a_2=0.025\ \mathrm{nm}^{-1}$, $x_1=19$ nm, $x_2=45$ nm (Géléoc *et al.*, 1997).

The simplest way to mimic the presence of the cochlear active process is to introduce a positive feedback as shown in Fig. 1. At this stage we consider feedback as a formal description of the cochlear amplification without specifying particular mechanisms. When the feedback is introduced, the nonlinear input–output function, $N'(x)$, is defined by

$$N'(x)=G_{\mathrm{tr}}(x,N(x))-G_{\mathrm{tr}}(0) =G_{\mathrm{tr\,max}}\{1+\exp(a_2[x_2-x0-x_{\mathrm{set}}-x-HN'(x)]) \times[1+\exp(a_1[x_1-x0-x_{\mathrm{set}}-x-HN'(x)])]\}^{-1} -G(0), \tag{3}$$

where H is the feedback gain constant. When feedback is absent, i.e., $H=0$, Eq. (3) is reduced to Eq. (2). The gains of the nonlinear functions $N(x)$ and $N'(x)$ near their operating point are

$$K=\left.\frac{dN(x)}{dx}\right|_{x=0}, \quad K'=\left.\frac{dN'(x)}{dx}\right|_{x=0}, \tag{4}$$

where the derivatives are calculated at the operating point x_{set}. Then the relative gain K_r achieved by the system due to the existence of the feedback is

$$K_r=K'/K=\left.\frac{dN'(x)}{dN(x)}\right|_{x=0}. \tag{5}$$

Figure 1 gives examples of $N'(x)$ for a few values of K_r. The algorithm for calculation of the constant H can be found elsewhere (Lukashkin and Russell, 1999).

We consider the output of the nonlinearity $N'(x)$ in the presence of a two-sinusoidal input signal $x=L_1\cos(2\pi f_1 t)+L_2\cos(2\pi f_2 t)$, where $f_2>f_1$. Without loss of generality we limit our theoretical analysis of the distortion product (DP) behavior at the output to the two frequency components most commonly measured in the DPOAE spectrum, f_2-f_1 and $2f_1-f_1$. The amplitude and phase behavior of the even DPs (e.g., f_2-f_1, f_2+f_1) is trivial at the output of a nonlinear function, which is symmetrical to its point of inflection, e.g., the one-exponential Boltzmann function. The amplitude of all even DPs is zero only when the operating point of the nonlinearity is situated at the point of inflection of the function, i.e., when nonlinearity is purely odd, $N(-x)=-N(x)$. In terms of our model it corresponds to $x_{\mathrm{set}}=0$. The two-exponential Boltzmann function [Eq. (3) and Fig. 1] that is used in this paper to model the OHC mechanoelectrical transducer is asymmetrical to its point of inflection. This function shows the same behavior of the DPs at its output as is observed for the one-exponential Boltzmann but for relatively small input signals. However, when the output strongly saturates the DP amplitude becomes zero and the phase angle transforms for nonzero x_{set} (Lukashkin and Russell, 1998, 1999; Fahey *et al.*, 2000). This phenomenon manifests itself as a deviation of the amplitude notch in the f_2-f_1 DP from the line $x_{\mathrm{set}}=0$ in the two-dimensional space of the amplitude of the primaries and the operating point of the nonlinearity (Fig. 2, top left). The direction of the deviation of this amplitude minimum depends on the specific type of the nonlinear function. The minimum is deflected in a positive direction away from the point of inflection for the two-exponential Boltzmann function shown in Fig. 1. For the same nonlinearity, the odd DP at frequency $2f_1-f_2$ has two local minima and corresponding phase changes in the vicin-

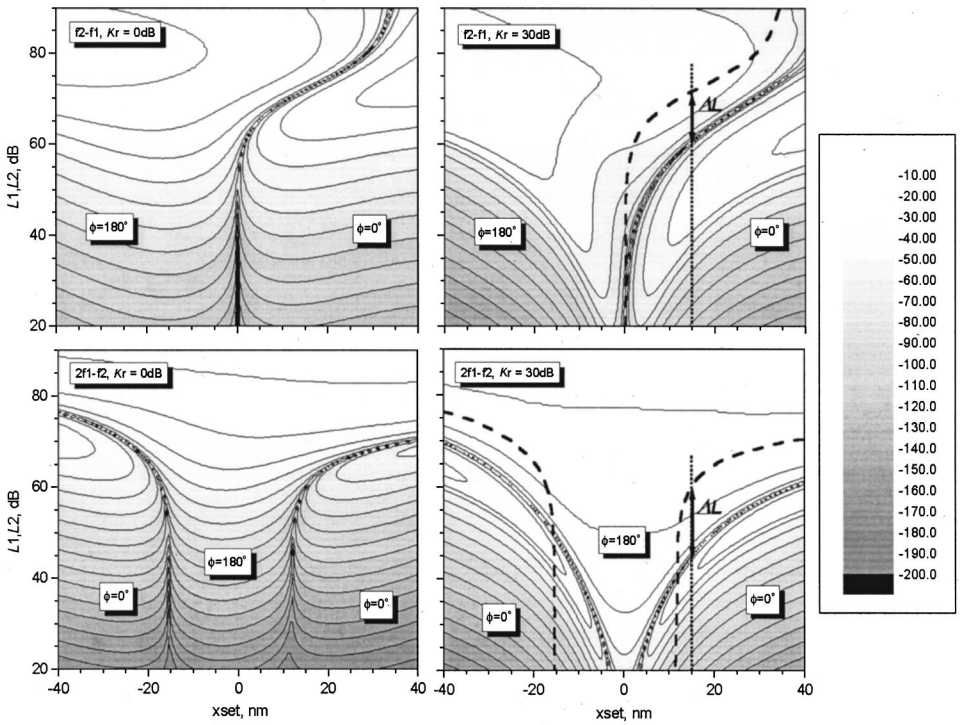

FIG. 2. Calculated amplitude contour plots of the DPs at frequences f_2-f_1 (top row) and 2 f_1-f_2 (bottom row) calculated for nonlinearity $N'(x)$ without feedback (left column, $K_r=0$ dB) and with feedback gain K_r of 30 dB (right columns). DP amplitudes are calculated by direct numerical solution of Eq. (3) for equally growing amplitudes of the primaries $L_1=L_2$ and different operating point x_{set} of the nonlinearity. H is calculated according to Lukashkin and Russell (1999) for $x_{\text{set}}=0$. The labels indicate the phase angle for each part of the curve limited by the notch. Dashed curves over the right column plots denote projections of the amplitude notches observed for nonlinearity without feedback (left columns). Double arrows indicate displacement, ΔL, of the notch along the axis of the primary amplitudes after introducing of the feedback. The displacement is shown for a specific position of the operating point $x_{\text{set}}=15$ nm used to calculate responses in Figs. 3 and 4. L_1 and L_2 are given in decibels *re* 0.01 nm. The amplitude of the DPs are expressed in decibels *re* $G_{\text{tr max}}$. The gray scale on the right shows the corresponding amplitude of the DPs. The step between each contour is 10 dB.

ity of the point of inflection (Fig. 2, bottom left). Again, both notches deflect from a straight line when the output becomes intensely saturated. In the presence of positive feedback, i.e., for the system with amplification, the output of the nonlinearity $N'(x)$ saturates more strongly for the same input signal x (Fig. 1). As a consequence, the DP minima become displaced away from straight lines at smaller amplitudes, L_1, L_2, of the input sinusoids (Fig. 2, right column). Arrows in Fig. 2, right column, indicate this downward shift, ΔL, of the notches for a particular position of the operating point $x_{\text{set}}=15$ nm. The shift gradually increases with increasing feedback efficiency (Fig. 3).

Figure 3 also shows that the amplitude of the DPs depends strongly on K_r, i.e., on the efficiency of the feedback, when the amplitudes of the primaries at the input of the nonlinearity $N'(x)$ are small. However, there is no sizable alteration of the DP amplitudes calculated for different K_r for the highest amplitudes of the primaries, when the output of the nonlinearity saturates strongly. The value of $x_{\text{set}}=15$ nm (dotted line in Fig. 2, right column) was chosen for calculation of the responses in Fig. 3 to obtain the amplitude notches and corresponding phase changes of the DPs. The type of minima in the DP amplitude/level functions shown in Fig. 3 is regularly observed in the DPOAE amplitude growth functions recorded from rodents. The amplitude notch and corresponding phase transition in the $2f_1-f_2$ growth functions are not observed at any amplitude of the primaries when the operating point is situated near the point of inflection [Fig. 2, bottom row, see also Fig. 4(b) in Lukashkin and Russell (1999)]. This may be the situation in the human ear (Lukashkin and Russell, 1999, 2001). However, in this case the low- and high-level DP amplitudes show the same dependence on the efficiency of the feedback as is illustrated in Fig. 3. Similarly, the notch is absent in the f_2-f_1 growth functions when the operating point is placed below the point of inflection [Fig. 2, top row, see also Fig. 4(a) in Lukashkin and Russell, 1999].

If the input amplitudes of the primaries are kept constant, nonmonotonic changes in the DP amplitudes might also occur when the feedback gain alone is varied (Fig. 4). This is because the position of the notch on the DP growth functions depends on the efficiency of the feedback (Fig. 3). It has been shown (Lukashkin and Russell, 1999) that the exact values of the feedback gains and amplitude of the primaries, when the notch appears, depend on the position of the operating point of the nonlinearity $N'(x)$. Generally, it could be observed that DP amplitude depended on the gain in three different ways (Fig. 4). This dependence is monotonic for both very low-level and high-level, saturating inputs but the responses at the extreme ranges of the inputs are of opposite phase. However, a notch and a corresponding phase transition are observed for intermediate amplitudes of the primaries. The DPs can demonstrate apparently paradoxical behavior when their amplitudes increase with decreasing of

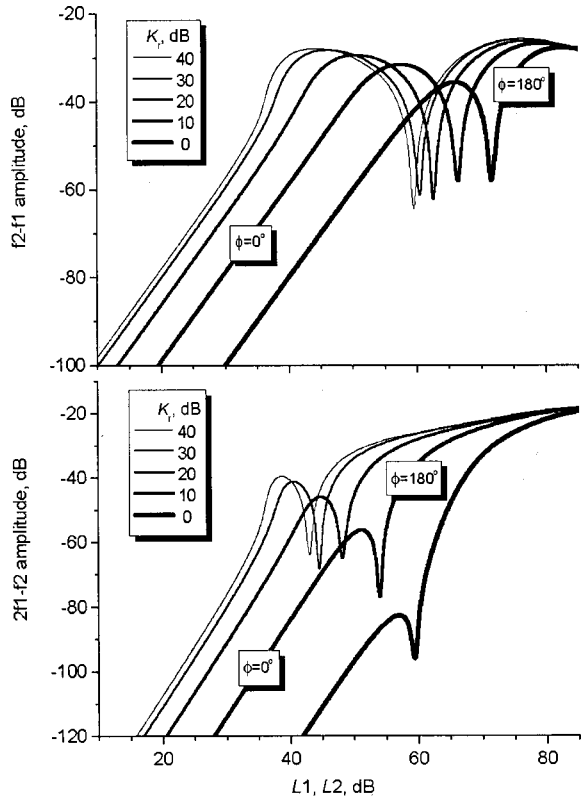

FIG. 3. Calculated amplitude growth functions for f_2-f_1 (top) and $2f_1$-f_2 (bottom) frequency components at the output of the nonlinearity $N'(x)$ for different efficiency of the feedback. The curves are calculated by direct numerical solution of Eq. (3). H is calculated according to Lukashkin and Russell (1999) for $x_{set}=0$. Relative gain, K_r, for each curve is indicated in decibels re gain without feedback ($K_r=0$ dB). DP amplitudes are calculated for equally growing amplitudes of the primaries $L_1=L_2$. The labels indicate the phase angle for each part of the curve limited by the notch. Amplitudes, L_1 and L_2, of both primaries are given in decibels *re* 0.01 nm. The amplitude of the DP is expressed in decibels *re* $G_{tr\,max}$.

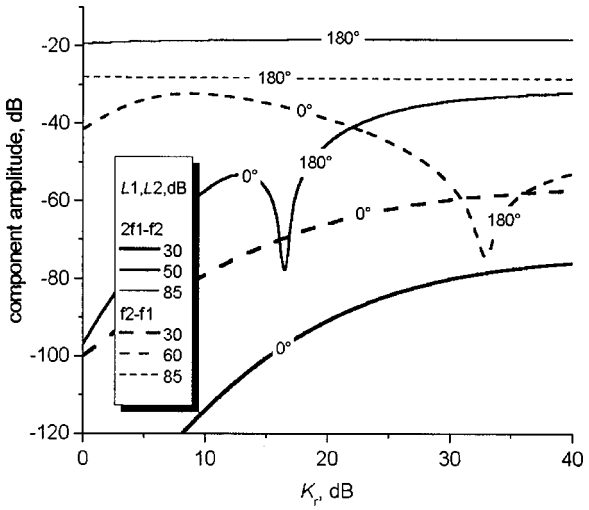

FIG. 4. Calculated dependence of the $2f_1$-f_2 (solid lines) and f_2-f_1 (dashed lines) components at the output of the nonlinearity $N'(x)$ on relative gain K_r. The curves are calculated by direct numerical solution of Eq. (3). H is calculated according to Lukashkin and Russell (1999) for $x_{set}=0$. L_1 and L_2 are equal and shown for each curve inside the panel in decibels re 0.01 nm. The amplitude of the DPs is expressed in decibels *re* $G_{tr\,max}$. The amplitude of the DPs is expressed in decibels *re* $G_{tr\,max}$. The phase angle is indicated for each part of the curve limited by the notch.

the feedback gain (Fig. 4, curve for f_2-f_1 with $L_1=L_2=60$ dB). It happens when the DP amplitude for the chosen model parameters and the highest gain (40 dB in Fig. 4) is decreased while being situated on one of the slopes of the DP amplitude notch. Again, the dependence of the DP amplitudes on the gain is always monotonic for f_2-f_1 if the operating point is situated below the point of inflection of the nonlinearity (Fig. 2, top row). The dependence is always monotonic for $2f_1-f_2$ if the operating point is located in the vicinity of the point of inflection (Fig. 2, bottom row).

Our theoretical analysis reveals a distinguishing feature of the DP growth functions generated by a single, saturating, nonlinearity with built-in amplification. That is an upward shift of the notch with corresponding phase change when the system amplification becomes less efficient (Figs. 2, 3). A shift in the opposite direction would be expected if the notch were due to phase cancellation between the vulnerable ''active'' emission prevailing at low levels of the primaries, and the robust ''passive'' emission dominating at the high primary levels (Brown, 1987; Norton and Rubel, 1990; Whitehead *et al.*, 1990; Mills, 1997). Indeed, if a cochlea insult affects the active cochlear process and decreases the amplitude of the ''active'' emission, then the ''passive'' emission would dominate at even lower levels of the primaries. The other two observations: vulnerability of the low-level and stability of the high-level emission (Fig. 3), and also nonmonotonic dependence of the emission amplitude on amplification (Fig. 4), are insufficient criteria for distinguishing between the ''two sources'' and ''one source'' hypotheses.

There is a third frequently forgotten possibility. Input to the mechanoelectrical transducer channels can change its phase angle abruptly because of multiple vibration modes of the organ of Corti—tectorial membrane complex (Zwislocki, 1986; Kiang, 1990; Ruggero *et al.*, 1996; Lin and Guinan, 2000). If the complex switches from one mode of vibration to another then the corresponding amplitude notches and phase discontinuities would appear in the DPOAE growth functions. However, this scenario can be easily identified because the amplitude notches should occur at the same level of the input signal for all DPOAE frequency components.

III. METHODS

Pigmented guinea pigs (250–350 g) were anaesthetized with the neurolept anaesthetic technique (0.06 mg/kg body weight atropine sulphate s.c., 30 mg/kg pentobarbitone i.p., 250 μl/kg Hypnorm i.m.). Additional injections of Hypnorm were given every 40 min. Additional doses of pentobarbitone were used as needed to maintain a nonreflexive state. The heart rate was monitored with a pair of skin electrodes placed on both sides of the thorax. The animals were tracheotomized and artificially respired, and their core temperature was maintained at 38 °C with a heating blanket and head holder. The middle ear cavity of the ear used for the DPOAE measurements was open to equilibrate air pressure on the both sides of the tympanic membrane. Furosemide (100 mg/kg b.w.) was injected intraperitoneally.

Sound was delivered to the tympanic membrane by a closed acoustic system comprising two Bruel and Kjaer 4134

$\frac{1}{2}$ in. microphones for delivering tones and a single Bruel and Kjaer 4133 $\frac{1}{2}$ in. microphone for monitoring sound pressure at the tympanum. The microphones were coupled to the ear canal via 1-cm-long, 4-mm-diam tubes to a conical speculum, the 1-mm-diam opening of which was placed 1 mm from the tympanum. The closed sound system was calibrated *in situ* for frequencies between 1 and 50 kHz. Known sound pressure levels were expressed in dB SPL *re* 2×10^{-5} Pa. White noise for acoustical calibration and tone sequences for auditory stimulation were synthesised by a Data Translation 3010 board at 200 kHz and delivered to the microphones through low-pass filters (100 kHz cutoff frequency). Signal from the measuring amplifier was digitized at 200 kHz using the same board and averaged in the time domain. Amplitudes and phase angles of the spectral peaks were obtained by performing a Fast Fourier Transform on a time-domain averaged signal 4096 points in length. The maximum level of the system distortion measured with an artificial ear cavity for the highest levels of primaries used in this study ($L_1=L_2+10$ dB$=80$ dB SPL) was 70 dB below the primary level. Experimental control, data acquisition, and data analysis were performed using a PC with programs written in Testpoint (CEC, MA, USA).

The following experimental procedures were used.

(i) DPOAE-grams (f_2 swept, f_2/f_1 ratio was constant, levels L_1 and L_2 of the primaries were constant, L_2 was 10 dB below L_1) were recorded for different levels of primaries to study frequency dependence of the furosemide effects.

(ii) DPOAE growth functions were recorded during simultaneous increase of L_1 and L_2 (L_2 was 10 dB below L_1).

All procedures involving animals were performed in accordance with UK Home Office regulations.

IV. RESULTS

A. Nonmonotonic growth functions for different DPOAE frequency components

Experimental data for different DPOAEs (i.e., f_2-f_1, $2f_1-f_2$, $2f_2-f_1$) show amplitude notches and corresponding phase change that occur at different levels of the primaries (Fig. 5). This observation immediately excludes the possibility that the appearance of the notch is due to a change in the mode of vibration of the organ of Corti-tectorial membrane complex (Zwislocki, 1986; Kiang, 1990; Ruggero *et al.*, 1996; Lin and Guinan, 2000).

B. Effect of furosemide on the local minima of DPOAE growth functions

The main ototoxic action of furosemide is based on its ability to suppress the endocochlear potential (Sewell, 1984) and hence the driving voltage for the OHC motility/stiffness change. Data concerning the action of furosemide on the OHC motor are controversial. Kalinec and Kachar (1993) report that furosemide has no effect on the OHC motility.

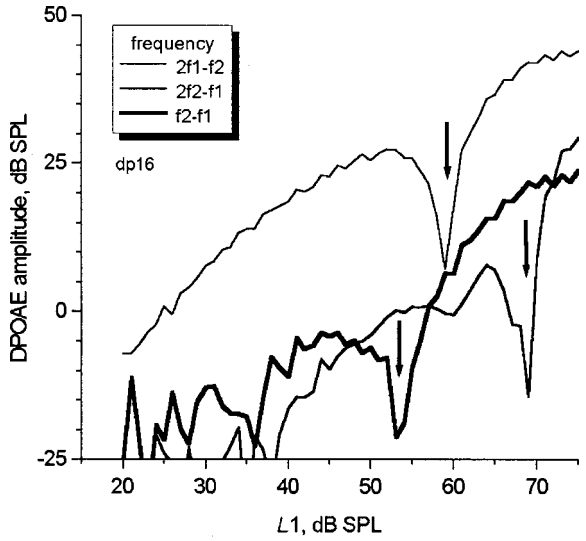

FIG. 5. Growth functions of a few DPOAE frequency components recorded from a guinea pig. Frequencies of the components are indicated inside the panel. Arrows help to identify position of the amplitude notches. f_2 is fixed at 12 kHz and f_2/f_1 ratio is 1.23. L_2 is 10 dB SPL below L_1. Average noise levels ($\pm$SD) for f_2-f_1, $2f_1$-f_2 and $2f_2$-f_1 frequency components are -21 ± 4, -25 ± 3 and -28 ± 4 dB SPL, respectively.

Very recently Santos-Sacchi *et al.* (2001) find that furosemide has a strong effect on the OHC nonlinear capacitance. However, in terms of our model it is not critical if furosemide suppresses both the endocochlear potential and the OHC motor because both effects result in a decrease in the efficiency of cochlear amplification. It is critical for the interpretation of our experiments on the effects of furosemide on DPOAE generation that furosemide has never been demonstrated to interfere with the mechanoelectrical transducer, which is likely to be the strongest inner ear nonlinearity (Patuzzi *et al.*, 1989; Santos-Sacchi, 1993) responsible for the DPOAE generation.

Similar results were obtained from eight guinea pigs for f_2 of 8, 12, 20 kHz and f_2/f_1 ratio of 1.21–1.25. Injection of furosemide leads to a shift to higher levels of the DPOAE amplitude notch and a corresponding phase transition in the growth functions of the $2f_1-f_2$ and f_2-f_1 components (Fig. 6) as predicted by the "single source" hypothesis. The shift of the notch position shown in Fig. 6 is greater for the f_2-f_1 component ($\Delta L\approx20$ dB, top right) than for $2f_1-f_2$ ($\Delta L\approx7$ dB, top left). The sharpness of the amplitude notch correlates with the rate and size of the phase change. Sharp notches (before injection in the top left-hand panel of Fig. 6 and 23 min after injection in the top right-hand panel) are always accompanied by an abrupt phase jump of 180°. However, the phase changes are more gradual and smaller in size for shallower amplitude minima.

C. Dependence of the furosemide response on the level of primaries

Changes in the DPOAE amplitude and phase angle depend on the level of the primaries and are different for $2f_1-f_2$ and f_2-f_1 components (Fig. 7). The amplitude and phase angle of $2f_1-f_2$ was stable during the whole experi-

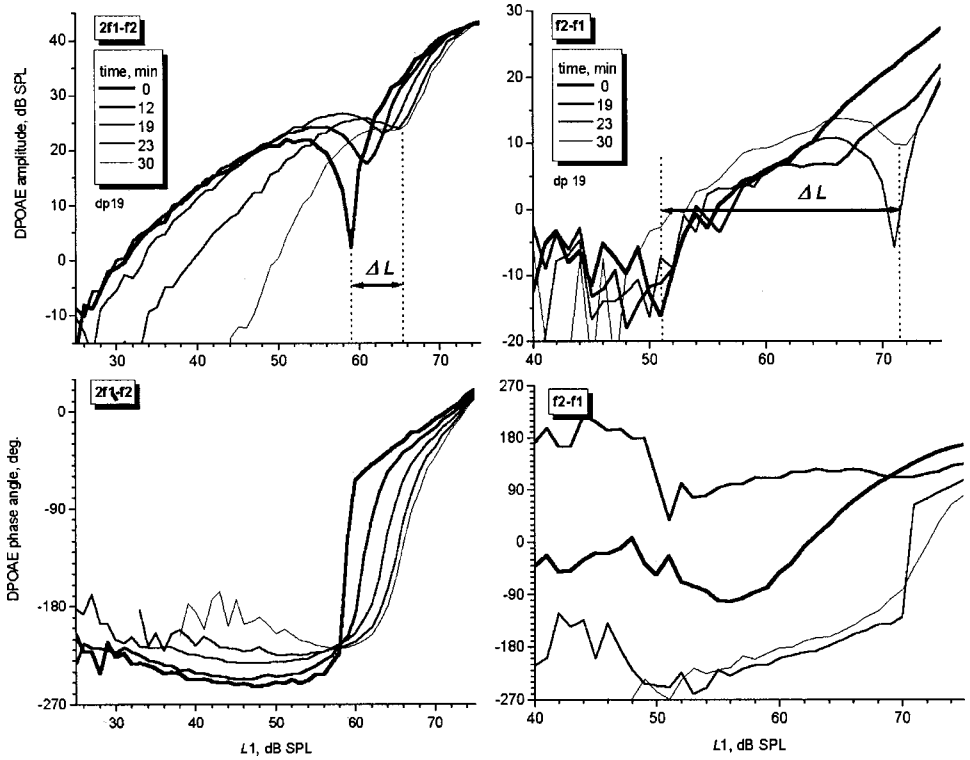

FIG. 6. Dependence of the DPOAE amplitude (top row) and phase angle (bottom row) on the levels L_1 and L_2 of the primaries recorded from a guinea pig before and after injection of furosemide (100 mg/kg b. w.). The thickest curves show response before the injection (0 min of the furosemide action). Time after the injection is indicated inside the panels for each column. f_2 is fixed at 8 kHz. f_2/f_1 ratio is 1.24. L_2 is 10 dB SPL below L_1. Double arrows between two dotted vertical lines show maximal upward shift ΔL of the notch position. Average noise levels ($\pm$SD) for f_2-f_1 and 2 f_1-f_2 frequency components are -17 ± 4, -22 ± 3 dB SPL, respectively.

ment (up to 2 h after furosemide injection) for the highest levels of primaries used ($L_1=75$ dB SPL, Fig. 7, top left). For low-level primaries ($L_1=35$ dB SPL, Fig. 7, top left) the $2f_1-f_2$ amplitude dropped below the noise floor of about -20 dB SPL and eventually partially recovered. The time course of the amplitude changes for the moderate-level primaries depended on the position of the response relative to the notch in the $2f_1-f_2$ growth functions before furosemide injection (Fig. 6, top left). When the level of the primaries corresponded to the low-level slope of the notch in the nonmodified growth function, then the initial increase is followed by a subsequent reduction in the amplitude of $2f_1-f_2$ ($L_1=57$ dB SPL, Fig. 7, top left). A notch with a corresponding phase change of about 180° can be observed in the time dependence of $2f_1-f_2$ ($L_1=62$dB SPL, Fig. 7, left column) when the level of the primaries generate emission

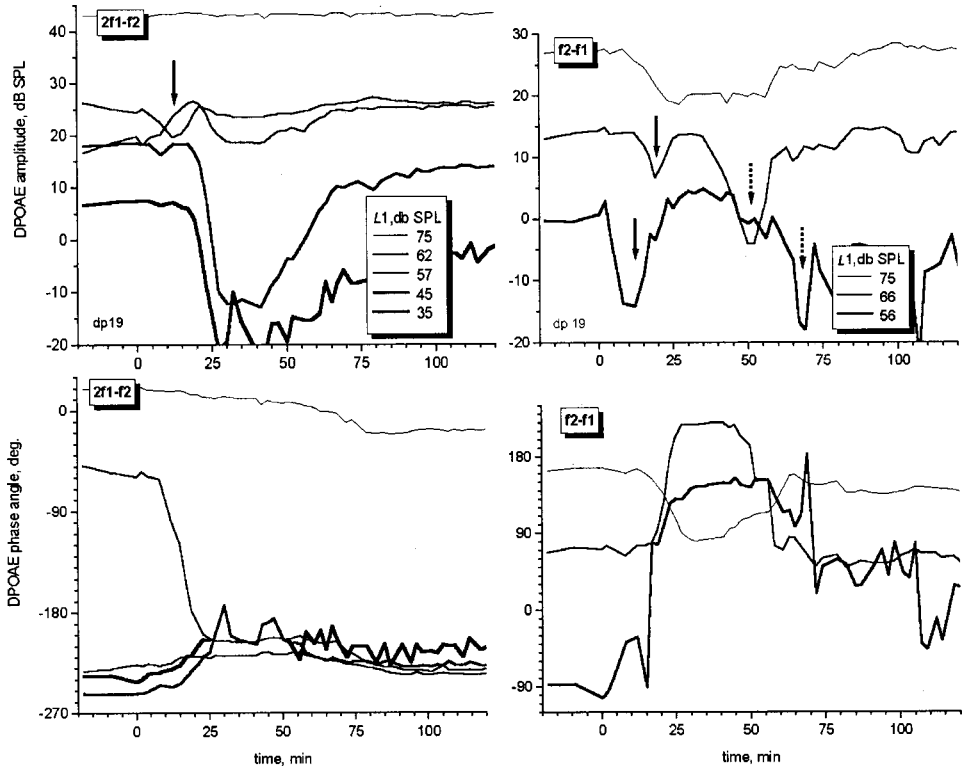

FIG. 7. Response of DPOAE recorded from a guinea pig to injection of furosemide (100 mg/kg b. w.) as a function of time after the injection. Zero time corresponds to the moment of injection. The same preparation as in Fig. 6 is shown. L_1 is indicated inside the panels for each column. Solid arrows help to identify position of the amplitude notches accompanied by phase discontinuities (bottom row). Dotted arrows (top right) indicate reverse transition observed for f_2-f_1 during recovery stage. Phase dependence of the 2 f_1-f_2 component for L_1 of 35 dB SPL (bottom left) has a break between 25 and 50 min. of furosemide action because the amplitude is below or at the noise floor during this period.

on the high-level slope of the notch in the nonmodified level function (Fig. 6, top left). It is apparent that the time pattern of the $2f_1-f_2$ component, described previously for moderate-level primaries, is specific for the shift of the amplitude notch to higher levels.

Changes in the f_2-f_1 amplitude and phase angle with time after furosemide injection (Fig. 7, right column) also can be explained in terms of the shift of the growth function notch to higher levels. However, the large alteration of the notch position and the appearance of the notch in the growth function before furosemide injections at slightly suprathreshold f_2-f_1 amplitudes make the time course of the effect quite distinctive. In contrast to $2f_1-f_2$ behavior, the amplitude of f_2-f_1 decreases and the phase angle changes even for the highest levels of primaries used ($L_1=75$ dB SPL, Fig. 7, right columns). These changes occur in the phase and magnitude of f_2-f_1 because of the appearance of the notch just below this level of L_1 (Fig. 6, top right). Because the f_2-f_1 amplitude is still steeply recovering from the notch when L_1 is 75 dB SPL, it is reasonable to suggest that, for higher levels of the primaries, the amplitude reaches its prefurosemide value. The notch appears at $L_1 \approx 51-53$ dB SPL before furosemide injection (Figs. 5 and 6, top right) and at $L_1 \approx 71-72$ dB SPL during the maximal effect of furosemide (Fig. 6, top right). Therefore, for all L_1 situated between these two extremes, the time course of the furosemide effect is similar to the one described for $2f_1-f_2$ when the level of the primaries corresponds to the high-level slope of the notch in the nonmodified level function. Namely, amplitude notches and corresponding phase changes appear (solid arrows in Fig. 7, right columns, $L_1=56$ and 66 dB SPL) in the time dependence of the DPOAE. In the same figure, the dotted arrows indicate the reversal in DPOAE amplitude and phase that occurs during the recovery process to restore the magnitude and phase of the DPOAEs to the prefurosemide conditions. Augmentation of the f_2-f_1 amplitude is observed for $L_1=56$ dB SPL after the first transition. The growth functions recorded during this period of time (Fig. 6, top right, 30 min) reveal that augmentation of the amplitude is observed for all L_1 below about 65 dB SPL. The ''single source'' hypothesis also predicts (Fig. 4) this relative increase in the amplitude of the DPOAE.

D. Frequency dependence of the furosemide response

The time course of the furosemide effect was frequency dependent (Fig. 8). For low-level primaries (f_1 and f_2 are 30 and 20dB SPL, respectively, in Fig. 8) the first signs of the furosemide effect appeared in the high frequency region when f_2 is set to frequencies above 20 kHz. This observation is in agreement with the findings of Sewell (1984), who documented the greater effect of furosemide on afferent fibers with higher characteristic frequency. It has also been reported (Cooper and Rhode, 1995) that the low-frequency region of the cochlea is much less sensitive to cochlear insults. The most robust range of f_2 where the $2f_1$-f_2 component still can be seen above the noise floor coincides with the region of the maximum emission between 10 and 15 kHz.

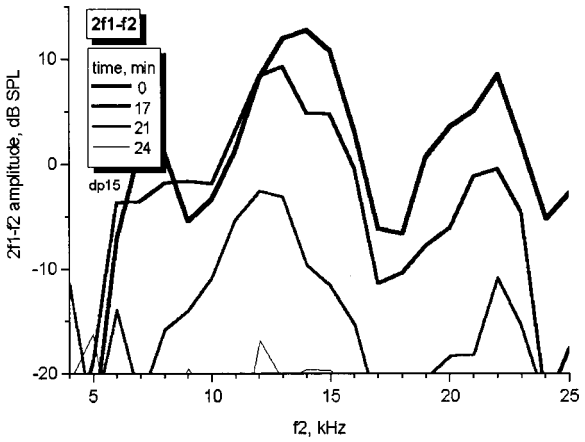

FIG. 8. Frequency dependence of the furosemide effect (100 mg/kg b. w.) recorded in a guinea pig. f_2 changes with 1 kHz step while f_2/f_1 ratio is kept constant at 1.23. Time after the furosemide injection is indicated inside the panel. Zero time corresponds to the moment of injection. L_2 is 10 dB SPL below L_1.

V. DISCUSSION

DPOAEs generated by low-level tones are far more vulnerable to cochlear insult than are those generated by high-level primary tones (Schmiedt and Adams, 1981; Kemp and Brown, 1984; Lonsbury-Martin *et al.*, 1987; Whitehead *et al.*, 1992; Mills *et al.*, 1993; Rebillard *et al.*, 1993; Mills and Rubel, 1994; Frolenkov *et al.*, 1998; Mom *et al.*, 2001). Low-level DPOAEs drop dramatically in amplitude in compromised cochleae while the amplitudes of high-level emissions remain relatively stable under the same conditions. To account for this phenomenon, it has been proposed that one DPOAE source predominates at low levels of the primaries and other dominates at high levels (Brown, 1987; Norton and Rubel, 1990; Whitehead *et al.*, 1990; Mills, 1997). According to this ''two sources'' hypothesis, at low levels of the primaries, an ''active,'' metabolically dependent, emission prevails over a ''passive'' emission that is associated with robust nonlinear mechanical properties of the cochlear partition. At high levels of the primaries, the ''passive'' emission dominates the DPOAE making it less susceptible to ototoxic effects. However, similar level dependence of DPOAE sensitivity is expected if the emission is generated by a single nonlinearity with saturating I/O characteristic, which is associated with the energy delivering active cochlear process (Gold, 1948). According to the ''one source'' hypothesis, the relative invulnerability of the high-level DPOAE is to be expected, and indeed observed. This is because the contribution of the active cochlear process is minimal at high SPLs even in healthy cochleae when the output of the DPOAE generating nonlinearity saturates at high input levels. The ''one source'' and ''two sources'' hypotheses predict opposite shifts in the amplitude notch in the DPOAE growth functions after a reduction in the active cochlear feedback. The notch should appear at lower levels of the primaries if the notch is due to phase cancellation between the vulnerable ''active'' emission prevailing at low levels of the primaries, and the robust ''passive'' emission dominating at the high primary levels (Brown, 1987; Norton and Rubel, 1990; Whitehead *et al.*, 1990; Mills, 1997). Indeed, if a cochlea insult effects

the active cochlear process and decreases the amplitude of the ''active'' emission, then the ''passive'' emission would dominate at even lower level of the primaries. However, after injection of furosemide the notch occurs at higher levels of the primaries. Therefore, we are in favor of the ''one source'' mechanism of the DPOAE generation at low- and high-level primaries up to at least 75 dB SPL. The single saturating nonlinearity with associated amplification also can account for the complex dependence of the DPOAE amplitude and phase angle on time after furosemide application.

In the work we are reporting here, we do not specifically question the existence of multiple sites of DPOAE generation. In fact, there is strong evidence in support of the DPOAE re-emission from the DPOAE characteristic place (Brown *et al.*, 1996; Moulin and Kemp, 1996; Wable *et al.*, 1996; Whitehead *et al.*, 1996; Fahey and Allen, 1997; He and Schmiedt, 1997; Heitmann *et al.*, 1998; Talmadge *et al.*, 1999; Faulstich and Kössl, 2000; Knight and Kemp, 2000) and in support of multiple reflection of the DPs within the cochlea (Stover *et al.*, 1996; Talmadge *et al.*, 1998).

Our conclusion is more limited: *we have shown that the different vulnerabilities of low and high-level DPOAEs does not support the hypothesis that they have different sources*. It is also worth noting that differences, similar to those reported here, in the vulnerability between low- and high-level emission have been recorded from the ears of a moth with only two receptor cells and without the cochlear's tonotopic organization (Coro and Kössl, 2001).

The unambiguous concept of a saturating nonlinearity with associated amplification, together with data that supports the importance of OHC motility for generating high-level DPOAEs (Frolenkov *et al.*, 1998), has significant basic and diagnostic implications. We can deduce that the nonlinear cochlear amplifier, which depends on OHC activity, is the main source of DPOAEs recorded for levels of primaries below about 75 dB SPL. We can also conclude that any pathology leading to the generation of ''passive-like'' DPOAEs is not due to dysfunction of the OHC mechanoelectrical transducer. Emissions of this kind appear because cochlear amplification is impaired due to for example, a reduction in the endocochlear potential (Ruggero and Rich, 1991; Mills *et al.*, 1994) or to feedback desynchronization (Legan *et al.*, 2000).

Obviously Eq. (3) alone cannot explain all the characteristics of the DPOAE. In particular, the notches of the calculated frequency components at the output of the nonlinearity $N'(x)$ are sharper and narrower (Fig. 3), and the corresponding phase changes are more abrupt than the notches and phase changes of the measured DPOAEs (Fig. 6). The model includes a ''perfect'' point-like nonlinearity and the depth of the notches in this case is limited only by the resolution of the model, i.e., by the number of calculations. The broadening and decrease in the depth of the notch in the experimental curves might be anticipated because the DPOAEs are generated by a distributed nonlinearity from an extended region of the cochlear partition with some phase gradients along the region (Russell and Nilsen, 1997). The vector summation of the DPOAEs from different parts of this prolonged region might lead to a partial cancellation of the notch and corresponding phase change. This partial elimination of the notch may also occur because of broadening of the f_2 peak, i.e., the place of DPOAE generation, at high levels of the primaries (Russell and Nilsen, 1997) and subsequent phase cancellation between DPOAEs originating from different parts of the broad peak. In this case the notches are smeared and phase changes are less abrupt. Also, the phase angles of the input signals are constant in our calculations but there is a level dependence of the BM response in the cochlea (Russell and Nilsen, 1997). Slopes of the DPOAE growth functions (Figs. 6 and 7) are also different from the slopes of the calculated responses (Fig. 3). The shallow slopes of the DPOAEs simply reflect compression of the input of the DPOAE producing nonlinearity due to the compression of the organ of Corti mechanical responses (Withnell and Yates, 1998). The increase of the $2f_1$-f_2 slope to 2.8 during the peak action of furosemide (Fig. 6, top left, 30 min) is close to the theoretically predicted slope of 3 and also supports this point of view. However, our main conclusion in favor of one source of the low- and high-level DPOAEs is based on the analysis of the role of the active cochlear process and the distinctive shift of the amplitude notches. Neither partial cancellation of the amplitude notches, nor compression of the nonlinearity input, can effect this conclusion.

ACKNOWLEDGMENT

This work was supported by the Wellcome Trust.

Ashmore, J. F. (**1987**). ''A fast motile response in guinea-pig outer hair cells: The cellular basis of the cochlear amplifier,'' J. Physiol. (London) **338**, 323–347.

Brown, A. M. (**1987**). ''Acoustic distortion from rodent ears: A comparison of responses from rats, guinea pigs and gerbils,'' Hear. Res. **31**, 25–38.

Brown, A. M., Harris, F. P., and Beveridge, H. A. (**1996**). ''Two sources of acoustic distortion products from the human cochlea,'' J. Acoust. Soc. Am. **100**, 3260–3267.

Brown, A. M., McDowell, B., and Forge, A. (**1989**). ''Acoustic distortion products can be used to monitor the effects of chronic gentamicin treatment,'' Hear. Res. **42**, 143–156.

Cooper, N. P., and Rhode, W. S. (**1995**). ''Nonlinear mechanics at the apex of the guinea-pig cochlea,'' Hear. Res. **82**, 225–243.

Coro, F., and Kössl, M. (**2001**). ''Components of the $2f_1$-f_2 distortion-product otoacoustic emission in a moth,'' Hear. Res. **162**, 126–133.

Crawford, A. C., Evans, M. G., and Fettiplace, R. (**1989**). ''Activation and adaptation of transducer currents in turtle hair cells,'' J. Physiol. (London) **419**, 405–434.

Fahey, P. F., and Allen, J. B. (**1997**). ''Measurement of distortion product phase in the ear canal of the cat,'' J. Acoust. Soc. Am. **102**, 2880–2891.

Fahey, P. F., Stagner, B. B., Lonsbury-Martin, B. L., and Martin, G. K. (**2000**). ''Nonlinear interactions that could explain distortion product interference response areas,'' J. Acoust. Soc. Am. **108**, 1786–1802.

Faulstich, M., and Kössl, M. (**2000**). ''Evidence for multiple DPOAE components based upon group delay of the $2f_1$-f_2 distortion in the gerbil,'' Hear. Res. **140**, 99–110.

Frolenkov, G. I., Belyantseva, I. A., Kurc, M., Mastroianni, M. A., and Kachar, B. (**1998**). ''Cochlear outer hair cell electromotility can provide force for both low and high intensity distortion product otoacoustic emissions,'' Hear. Res. **126**, 67–74.

Géléoc, G. S. G., Lennan, G. W. T., Richardson, G. P., and Kros, C. J. (**1997**). ''A quantitative comparison of mechanoelectrical transduction in vestibular and auditory hair cells of neonatal mice,'' Proc. R. Soc. London, Ser. B **264**, 611–621.

Gold, T. (**1948**). ''Hearing. II. The physical basis of the action of the cochlea,'' Proc. R. Soc. London **135**, 492–498.

Hamernik, R. P., Ahroon, W. A., and Lei, S. F. (**1996**). ''The cubic distortion product otoacoustic emissions from the normal and noise-damaged chinchilla cochlea,'' J. Acoust. Soc. Am. **100**, 1003–1012.
He, N., and Schmiedt, R. A. (**1997**). ''Fine structure of the 2 f_1-f_2 acoustic distortion product: Effects of primary level and frequency ratios,'' J. Acoust. Soc. Am. **101**, 3554–3565.
Heitmann, J., Waldmann, B., Schnitzler, H. U., Plinkert, P. K., and Zenner, H. P. (**1998**). ''Suppression of distortion product otoacoustic emissions (DPOAE) near 2 f_1-f_2 removes DP-gram fine structure-Evidence for a secondary generator,'' J. Acoust. Soc. Am. **103**, 1527–1531.
Kalinec, F., and Kachar, B. (**1993**). ''Inhibition of outer hair cell electromotility by sulfhydryl specific reagents,'' Neurosci. Lett. **157**, 231–234.
Kemp, D. T., and Brown, A. M. (**1984**). ''Ear canal acoustic and round window correlates of 2 f_1-f_2 distortion generated in the cochlea,'' Hear. Res. **13**, 39–46.
Kiang, N. Y. S. (**1990**). ''Curious oddments of auditory-nerve studies,'' Hear. Res. **49**, 1–16.
Knight, R. D., and Kemp, D. T. (**2000**). ''Indications of different distortion product otoacoustic emission mechanisms from a detailed f_1, f_2 area study,'' J. Acoust. Soc. Am. **107**, 457–473.
Legan, P. K., Lukashkina, V. A., Goodyear, R. J., Kössl, M., Russell, I. J., and Richardson, G. P. (**2000**). ''A targeted deletion in α-tectorin reveals that the tectorial membrane is required for the gain and timing of cochlear feedback,'' Neuron **28**, 273–285.
Lin, T., and Guinan, Jr., J. J. (**2000**). ''Auditory-nerve-fiber responses to high-level clicks: Interference patterns indicate that excitation is due to the combination of multiple drives,'' J. Acoust. Soc. Am. **107**, 2615–2630.
Lonsbury-Martin, B. L., Martin, G. K., Probst, R., and Coats, A. C. (**1987**). ''Acoustic distortion products in rabbit ear canal. I. Basic features and physiological vulnerability,'' Hear. Res. **28**, 173–189.
Lukashkin, A. N., and Russell, I. J. (**1998**). ''A descriptive model of the receptor potential nonlinearities generated by the hair cell mechanoelectrical transducer,'' J. Acoust. Soc. Am. **103**, 973–980.
Lukashkin, A. N., and Russell, I. J. (**1999**). ''Analysis of the f_2-f_1 and 2 f_1-f_2 distortion components generated by the hair cell mechanoelectrical transducer: Dependence on the amplitudes of the primaries and feedback gain,'' J. Acoust. Soc. Am. **106**, 2661–2668.
Lukashkin, A. N., and Russell, I. J. (**2001**). ''Origin of the bell-like dependence of the DPOAE amplitude on primary frequency ratio,'' J. Acoust. Soc. Am. **110**, 3097–3106.
Mills, D. M. (**1997**). ''Interpretation of distortion product otoacoustic emission measurements. I. Two stimulus tones,'' J. Acoust. Soc. Am. **102**, 413–429.
Mills, D. M., Norton, S. J., and Rubel, E. W. (**1993**). ''Vulnerability and adaptation of distortion product otoacoustic emissions to endocochlear potential variation,'' J. Acoust. Soc. Am. **94**, 2108–2122.
Mills, D. M., Norton, S. J., and Rubel, E. W. (**1994**). ''Development of active and passive mechanics in the mammalian cochlea,'' Aud. Neurosci. **1**, 77–99.
Mills, D. M., and Rubel, E. W. (**1994**). ''Variation of distortion product otoacoustic emission with furosemide injection,'' Hear. Res. **77**, 183–199.
Mom, T., Bonfils, P., Gilain, L., and Avan, P. (**2001**). ''Origin of cubic difference tones generated by high-intensity stimuli: Effect of ischemia and auditory fatigue on the gerbil cochlea,'' J. Acoust. Soc. Am. **110**, 1477–1488.
Moulin, A., and Kemp, D. T. (**1996**). ''Multicomponent acoustic distortion product otoacoustic phase in humans. II. Implications for distortion product otoacoustic emissions generation,'' J. Acoust. Soc. Am. **100**, 1640–1662.
Norton, S. J., and Rubel, E. W. (**1990**). ''Active and passive ADP components in mammalian and avian ears,'' in *Mechanics and Biophysics of Hearing*, edited by P. Dallos, C. D. Geisler, J. W. Matthews, M. A. Ruggero, and C. R. Steele (Springer, New York), pp. 219–226.
Patuzzi, R. B., Yates, G. K., and Johnstone, B. M. (**1989**). ''Outer hair cell receptor current and sensorineural hearing loss,'' Hear. Res. **42**, 47–72.
Rebillard, G., Klis, J. F. L., Lavigne-Rebillard, M., Devaux, P., Puel, J. L., and Pujol, R. (**1993**). ''Changes in 2 f_1-f_2 distortion product otoacoustic emission following alterations of cochlear metabolism,'' Br. J. Audiol. **27**, 117–121.
Ruggero, M. A., and Rich, N. C. (**1991**). ''Furosemide alters organ of Corti mechanics: Evidence for feedback of outer hair cells upon the basilar membrane,'' J. Neurosci. **11**, 1057–1067.
Ruggero, M. A., Rich, N. C., Shivapuja, B. G., and Temchin, A. N. (**1996**). ''Auditory-nerve responses to low-frequency tones: Intensity dependence,'' Aud. Neurosci. **2**, 159–185.
Russell, I. J., and Nilsen, K. E. (**1997**). ''The location of the cochlear amplifier: Spatial representation of a single tone on the guinea pig basilar membrane,'' Proc. Natl. Acad. Sci. U.S.A. **94**, 2660–2664.
Santos-Sacchi, J. (**1993**). ''Harmonics of outer hair cell motility,'' Biophys. J. **65**, 2217–2227.
Santos-Sacchi, J., and Dilger, J. P. (**1988**). ''Whole cell currents and mechanical responses of isolated outer hair cells,'' Hear. Res. **35**, 143–150.
Santos-Sacchi, J., Wu, M., and Kakehata, S. (**2001**). ''Furosemide alters nonlinear capacitance in isolated outer hair cells,'' Hear. Res. **159**, 69–73.
Schmiedt, R. A. (**1986**). ''Acoustic distortion in the ear canal. I. Cubic difference tones: Effect of acute noise injury,'' J. Acoust. Soc. Am. **79**, 1481–1490.
Schmiedt, R. A., and Adams, J. C. (**1981**). ''Stimulated acoustic emissions in the ear canal of the gerbil,'' Hear. Res. **5**, 295–305.
Sewell, W. F. (**1984**). ''The effect of furosemide on the endocochlear potential and auditory-nerve fiber tuning curves in cats,'' Hear. Res. **14**, 305–314.
Stover, L. J., Neely, S. T., and Gorga, M. P. (**1996**). ''Latency and multiple sources of distortion product otoacoustic emissions,'' J. Acoust. Soc. Am. **99**, 1016–1024.
Talmadge, C. L., Long, G. R., Tubis, A., and Dhar, S. (**1999**). ''Experimental confirmation of the two-source interference model for the fine structure of distortion product otoacoustic emissions,'' J. Acoust. Soc. Am. **105**, 275–292.
Talmadge, C. L., Long, G. R., Tubis, A., and Piskorski, P. (**1998**). ''Modeling otoacoustic emission and hearing threshold fine structures,'' J. Acoust. Soc. Am. **104**, 1517–1543.
Wable, J., Collet, L., and Chèry-Croze, S. (**1996**). ''Phase delay measurements of distortion product otoacoustic emissions at 2 f_1-f_2 and 2 f_2-f_1 in human ears,'' J. Acoust. Soc. Am. **100**, 2228–2235.
Whitehead, M. L., Lonsbury-Martin, B. L., and Martin, G. K. (**1990**). ''Actively and passively generated acoustic distortion at 2 f_1-f_2 in rabbits,'' in *Mechanics and Biophysics of Hearing*, edited by P. Dallos, C. D. Geisler, J. W. Matthews, M. A. Ruggero, and C. R. Steele (Springer, New York), pp. 243–250.
Whitehead, M. L., Lonsbury-Martin, B. L., and Martin, G. K. (**1992**). ''Evidence for two discrete sources of 2 f_1-f_2 distortion-product otoacoustic emission in rabbit. II. Differential physiological vulnerability,'' J. Acoust. Soc. Am. **92**, 2662–2682.
Whitehead, M. L., Stagner, B. B., Martin, G. K., and Lonsbury-Martin, B. L. (**1996**). ''Visualization of the onset of distortion-product otoacoustic emissions, and measurement of their latency,'' J. Acoust. Soc. Am. **100**, 1663–1679.
Wiederhold, M. L., Mahoney, J. W., and Kellogg, D. L. (**1986**). ''Acoustic overstimulation reduces 2 f_1-f_2 cochlear emissions at all levels in the cat,'' in *Peripheral Auditory Mechanisms*, edited by J. B. Allen, J. L. Hall, A. E. Hubbard, S. T. Neely, and A. Tubis (Springer, New York), pp. 322–329.
Withnell, R. H., and Yates, G. K. (**1998**). ''Onset of basilar membrane nonlinearity reflected in cubic distortion tone input-output function,'' Hear. Res. **123**, 87–96.
Zurek, P. M., Clark, W. W., and Kim, D. O. (**1982**). ''The behaviour of acoustic distortion products in the ear canal of chinchillas with normal or damaged ears,'' J. Acoust. Soc. Am. **72**, 774–780.
Zwislocki, J. J. (**1986**). ''Analysis of cochlear mechanics,'' Hear. Res. **22**, 155–169.

Interaction between adenosine triphosphate and mechanically induced modulation of electrically evoked otoacoustic emissions

Desmond L. Kirk
The Auditory Laboratory, Department of Physiology, The University of Western Australia, 35 Stirling Highway, Crawley 6009, WA, Australia

(Received 24 May 2001; revised 5 December 2001; accepted 6 December 2001)

It was shown previously that electrically evoked otoacoustic emissions (EEOAEs) can be amplitude modulated by low-frequency bias tones and enhanced by application of adenosine triphosphate (ATP) to scala media. These effects were attributed, respectively, to the mechano-electrical transduction (MET) channels and ATP-gated ion channels on outer hair cell (OHC) stereocilia, two conductance pathways that appear to be functionally independent and additive in their effects on ionic current through the OHC. In the experiments described here, the separate influences of ATP and MET channel bias on EEOAEs did not combine linearly. Modulated EEOAEs increased in amplitude, but lost modulation at the phase and frequency of the bias tone (except at very high sound levels) after application of ATP to scala media, even though spectral components at the modulation sideband frequencies were still present. Some sidebands underwent phase shifts after ATP. In EEOAEs modulated by tones at lower sound levels, substitution of the original phase values restored modulation to the waveform, which then resembled a linear summation of the separate effects of ATP and low-frequency bias. While the physiological meaning of this procedure is not clear, the result raises the possibility that a secondary effect of ATP on one or more nonlinear stages in the transduction process, which may have caused the phase shifts, obscured linear summation at lower sound levels. In addition, ''acoustic enhancement'' of the EEOAE may have introduced nonlinear interaction at higher levels of the bias tones. [DOI: 10.1121/1.1448315]

PACS numbers: 43.64.Jb, 43.64.Gz, 43.64.Me, 43.64.Ld, 43.64.Kc [BLM]

I. INTRODUCTION

Electrically evoked otoacoustic emissions (EEOAE) can be amplitude modulated by low-frequency tones, such that the EEOAE's modulation envelope follows the waveform of the cochlear microphonic (CM) evoked by the tone. It has been proposed (Yates and Kirk, 1998) that the underlying source of motility or its mechanical output is in some way sensitive to the status of the mechano-electrical transduction (MET) channels of outer hair cells (OHC). A closed-channel bias, produced when the acoustic stimulus displaces the basilar membrane to scala tympani, is associated with a reduction in peak-to-peak amplitude of the EEOAE waveform and an open bias (scala vestibuli displacement) with an increase. A marked ''acoustic enhancement'' (Mountain and Hubbard, 1989) of the emission occurs during the scala vestibuli phase at higher levels (>90–100 dB SPL) of the bias tone (Kirk and Yates, 1998a).

EEOAEs are also enhanced when ATP is applied by iontophoresis into endolymph (Kirk and Yates, 1998b). This is accompanied by reductions in both the dc endocochlear potential (EP) and the CM (see also Munoz *et al.*, 1995, 1999), consistent with an increase in the shunt conductance out of scala media. While there are several potential targets for ATP in scala media, on both sensory and nonsensory structures, an action on P2X receptors on the stereocilia of OHCs (Housley *et al.*, 1999) seems a likely explanation for the increase in the EEOAE (Kirk and Yates, 1998b).

Both an open bias of MET channels (Ohmori, 1987) and ATP (Housley *et al.*, 1998) increase the apical conductance of OHCs. A direct influence of the OHC's apical conductance on the strength of the electrical drive or an indirect effect on the gain of OHC motility, via the intracellular potential (Santos-Sacchi, 1989), have been put forward as two possible explanations of the apparent sensitivity of the EEOAEs to changes in the apical conductance of OHCs (Kirk and Yates, 1998a). However, the high-level enhancement of the emission, during mechanical bias to scala vestibuli at sound levels well above saturation of the CM and presumably changes in the MET conductance, is not easily consistent with either of these propositions. Both the acoustic enhancement induced during open channel bias and ATP can increase the EEOAE by 10–15 dB or more.

ATP-sensitive and mechano-sensitive ion channels share several common features (Surprenant *et al.*, 1995). However, while the mechanically gated and ATP-gated ion channels on OHC stereocilia are in close spatial proximity (Housley *et al.*, 1999; Jaramillo and Hudspeth, 1991), their respective conductances appear to be functionally independent, and additive in their combined influence on the ionic current through the cell (Glowatzki *et al.*, 1997). This report investigates the extent to which independence and additivity are

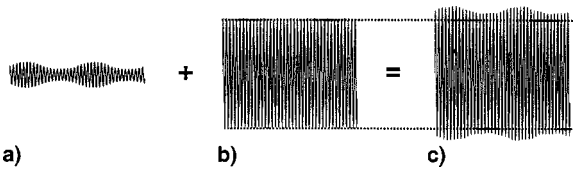

FIG. 1. (a) Simulation of the modulation of a sinusoidal EEOAE by a lower frequency. The low-frequency modulator was generated through a simple Boltzmann function and then combined multiplicatively with the higher frequency waveform. (b) An unmodulated sinusoid representing additional energy, generated when ATP activates a parallel conductance, independent of the MET conductance. (c) The sum of the waveforms in (a) and (b).

evident in the combined effects of ATP and the status of the MET channels on EEOAEs.

If mechanically gated and ATP-gated conductances in OHCs were to influence the EEOAE output independently and additively, then the separate effects of the two in combination should sum linearly. This is simulated in Fig. 1. In the ''EEOAE'' on the left (a) a high-frequency sine wave has been amplitude modulated at a lower frequency. The low-frequency component was generated by a first-order Boltzmann function, known to provide a good fit to the extracellular CM and thus presumably the modulation of the MET conductance (Patuzzi and Rajan, 1990). The waveform in (b) represents a parallel, ATP-gated conductance and is 15 dB larger than the waveform in (a). Fifteen dB is the amount by which EEOAEs were increased on average by ATP in the present data (see also Kirk and Yates, 1998b). The waveform in (c) is the sum of (a) and (b), essentially the modulated EEOAE (MET conductance) riding on an unmodulated ''pedestal'' (ATP-gated conductance).

II. METHODS

Experiments were performed on pigmented guinea pigs (250–400 grams). The animals were anesthetized with Nembutal (35 mg/kg i.p. initially; 15 mg/kg after 2.5 h), and Hypnorm (Fentanyl citrate/Fluanisone; 1.5 ml/kg i.m. repeated at 45-min intervals). In some instances, muscular paralysis was induced (Alloferin 0.3 ml/kg i.m.) during data collection to reduce noise levels in the ear canal and potential middle-ear effects. In unparalyzed animals the anesthetic regime induced continuous deep anesthesia, evidenced by lack of withdrawal response and absence of spontaneous respiration. During paralysis potentially noxious stimulation produced no change in heart rate. Cochleas contributing to the results were in good condition (as assessed from the compound action potential at the round window) throughout the experiment. EEOAEs were generated by sinusoidal currents, applied through micropipette electrodes (2–4-μm tip diameter, dc resistance 5–10 megohms) in scala media of the second cochlear turn.

Generally, two micropipettes were placed in scala media. One was filled with 200 mM KCl and was used for electrical stimulation and recording of the CM. ATP was applied by iontophoresis (-5 μA dc, 2 min) through the second pipette, which was filled with 10 mM ATP (disodium salt Sigma) in 200 mM KCl. It is estimated (see Kirk and Yates, 1998b) that the final endolymphatic [ATP] would have reached 320 μM.

A desktop computer equipped with a multimedia sound card (Crystal CDB4231) and custom software generated the electrical and acoustical stimuli and recorded the responses (EEOAE from the ear canal and CM from scala media). The ear canal sound field was monitored through a condenser microphone (Bruel & Kjaer 4943) and filtered electronically before online display and storage to disk.

Electrical stimulation of scala media was paired with acoustical stimulation with low-frequency bias tones (86 Hz) well below the electrical frequencies used (1421–3057 Hz). Bias-tone levels were between 60–108 dB SPL. While the upper end of this intensity range may seem unphysiological in terms of the absolute sensitivity of the cochlea, the tone durations were at most 3 s and the frequency was, in any case, so low as to be incapable of causing damage, even with more prolonged exposure. The electrical and acoustical stimuli were phase locked and their frequencies were constrained in the ratio $n+1/2$ (n is an integer), so that precisely $2n+1$ cycles of the electrical stimulus accompanied every 2 cycles of the acoustical frequency. This frequency ratio ensured that harmonics of the low-frequency acoustical stimulus interleaved with the harmonics of the electrical frequency and with the potential intermodulation frequencies ($f_e \pm m f_a$: m is an integer).

The electronically filtered emission waveforms were subsequently processed mathematically, taking advantage of the frequency interleaving of the sound harmonics and the intermodulation components. The Fourier spectrum of the raw waveform was calculated and a waveform free of acoustical stimulus contamination was obtained by setting to zero all components other than the fundamental of the electrical stimulus and all intermodulation frequencies with magnitudes more than 3 dB above the noise level. A waveform free of residual acoustical stimulus contamination and harmonic distortion was then reconstructed by inverse transforming back to the time domain. This procedure effectively extracts from the recording only those components that are related to the electrical stimulus (see Yates and Kirk, 1998).

In order to examine the influence of the modulation sidebands (Hubbard and Mountain, 1983) on the shapes of the waveforms, phase and magnitude values at the sideband frequencies were extracted from Fourier transforms of EEOAEs recorded before ATP and substituted into those obtained after ATP. Up to five pairs of sidebands (upper and lower) were substituted. New waveforms were reconstructed by inverse Fourier transform. All numerical procedures were carried out in MICROSOFT EXCEL 2000.

The care and use of the animals used in this study conformed to the requirements of the National Health and Medical Research Council of Australia and all institutional protocols.

III. RESULTS

The real EEOAE behaved quite differently from the simulated emission in Fig. 1. The two left-hand columns of Fig. 2 show EEOAEs (2110 Hz) modulated by 86-Hz tones over a range of sound levels from 66 to 108 dB SPL, before

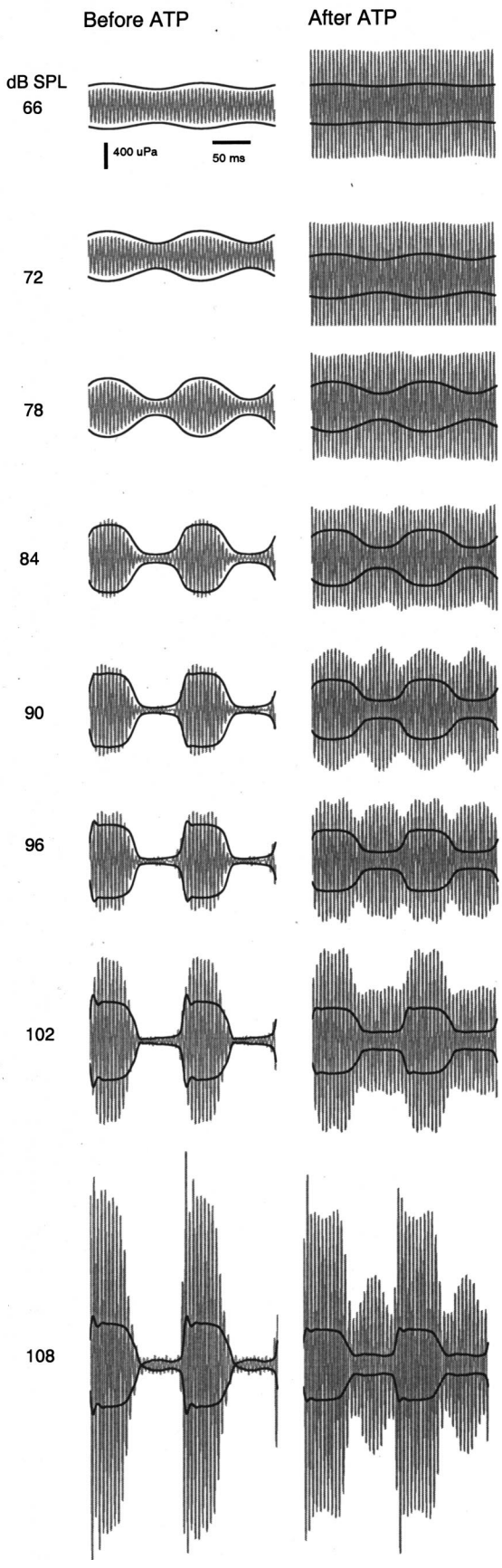

FIG. 2. EEOAE waveforms (2110 Hz, 10 μA ac) recorded with 86-Hz bias tones at sound levels 66–108 dB SPL (as indicated); before (left) and after (right) application of ATP to scala media. The CM ''envelope'' (darker lines) formed by the scala media CM (lower trace) and its mirror image (upper trace) represents changes in the MET conductance evoked by the bias tone.

and after application of ATP to scala media. The CMs generated by the 86-Hz tones presented separately are drawn (darker lines) over the EEOAE waveforms. EEOAE and CM amplitudes from this set of data are plotted as functions of the intensity of the 86-Hz bias tone in Fig. 3(a).

In Fig. 2, the CM traces describe a ''MET conductance envelope,'' whose lower and upper boundaries are, respectively, the CM, as recorded from scala media, and its mirror image. This envelope, which expands during the phase of scala vestibuli displacement (open MET channels) and contracts during the scala tympani phase (closed channels), was fitted to the EEOAE waveforms as described previously (Yates and Kirk, 1998). Briefly, the CM was scaled in amplitude and a vertical offset was applied so the envelopes at the lower sounds levels matched as closely as possible the modulation of the corresponding EEOAEs. The scaling and offset factors, and thus the assumed MET conductance envelope, were held constant over the entire range of sound levels. The CM phase has been shifted (-320 μs) to compensate for the propagation of the EEOAE to the ear canal.

Before application of ATP, the EEOAEs exhibited the pattern of amplitude modulation reported previously (Kirk and Yates, 1998a). Modulation of the waveforms matched the CM envelope reasonably closely at lower levels of the 86-Hz bias tone. At 84 dB SPL and above, where the CM intensity function saturated [see Fig. 3(a)], the EEOAE was progressively enhanced. This ''acoustic enhancement'' (Mountain and Hubbard, 1989) increased along with the sound level of the bias tone, and is evident as an increase in peak-to-peak amplitude, exclusively during the scala vestibuli phase (increased MET conductance) of the low-frequency bias.

After ATP the amplitude of the EEOAE increased and the CM decreased as expected (Kirk and Yates, 1998b; Munoz *et al.*, 1995). Amplitude modulation at the frequency of the bias tone was absent except at the two highest sound levels. Modulation at double the bias frequency was present at 90, 96, and, to a lesser extent at 108 dB SPL. The CM evoked by the 86-Hz bias tone was reduced by 35%–55% (3–7 dB) and the magnitude of the EEOAE (measured as the level of the spectral peak at the carrier frequency) was increased by 11.3 dB at 66 dB SPL but by only 2.8 dB at 108 dB SPL. The marked level dependence of ATP-induced increases in the EEOAE is associated with a net reduction in the effectiveness of acoustic enhancement after ATP, particularly at the lower sound levels [Fig. 3(a)].

In Fig. 2, the shapes of the EEOAE waveforms after ATP are obviously not as predicted by the simple additive model presented earlier in Fig. 1. At the lower sound levels (66–84 dB SPL) the modulation envelope flattens out after ATP. At 90–96 dB SPL a double modulation pattern appears. At the highest sound levels (102 and 108 dB SPL) the waveforms are modulated at the frequency of the bias tone, but the peak-to-peak amplitudes during the scala vestibuli phase are approximately the same as before ATP. The acoustic enhancement during this phase of the low-frequency bias did not sum linearly with the ATP-induced increase in amplitude.

This series of measurements was performed in four cochleas and the effects of ATP on the magnitude and the am-

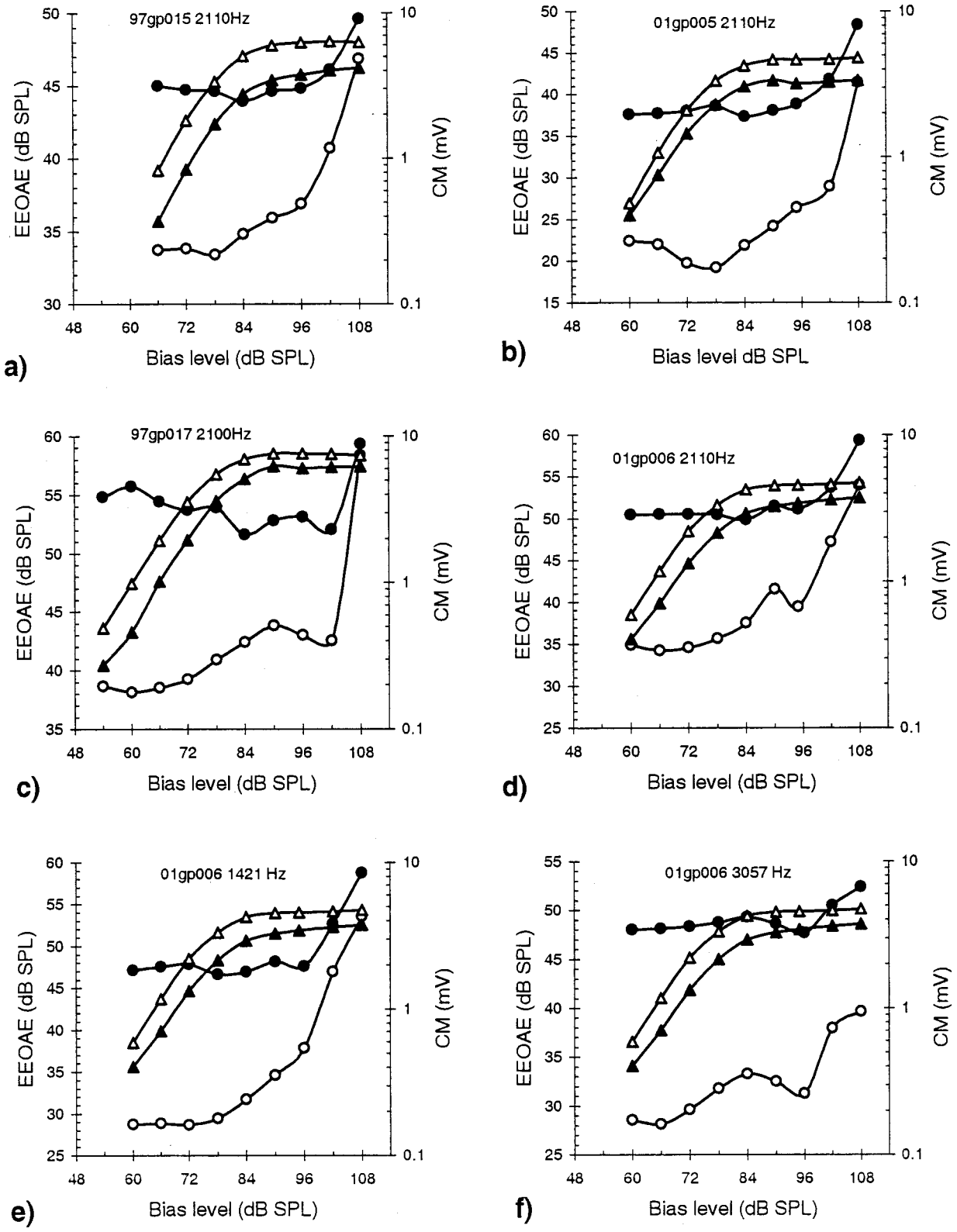

FIG. 3. EEOAE magnitudes enhanced by 86-Hz bias tones (circles) and amplitudes of the CM (triangles) in response to the bias tone presented alone; before (open symbols) and after (filled symbols) ATP. Data in (a), (b), and (c) are from three cochleas in which the ac stimulus was 2110 Hz, 10 μA. Data in (d), (e), and (f) are from the same cochlea but with ac stimulation at the indicated frequencies.

plitude modulation of the EEOAEs were essentially the same, with only minor variations. In Fig. 3, panels (b)–(f) are intensity functions from the three additional cochleas. Data in panels (d)–(f) are from the same cochlea but were obtained at different electrical stimulation frequencies. The same trends are evident in all examples. After ATP there was no acoustic enhancement of the EEOAE at the lower sound levels. At levels well above saturation of the CM intensity function, the EEOAE amplitude increased sharply, as it did before ATP, but by a relatively smaller amount.

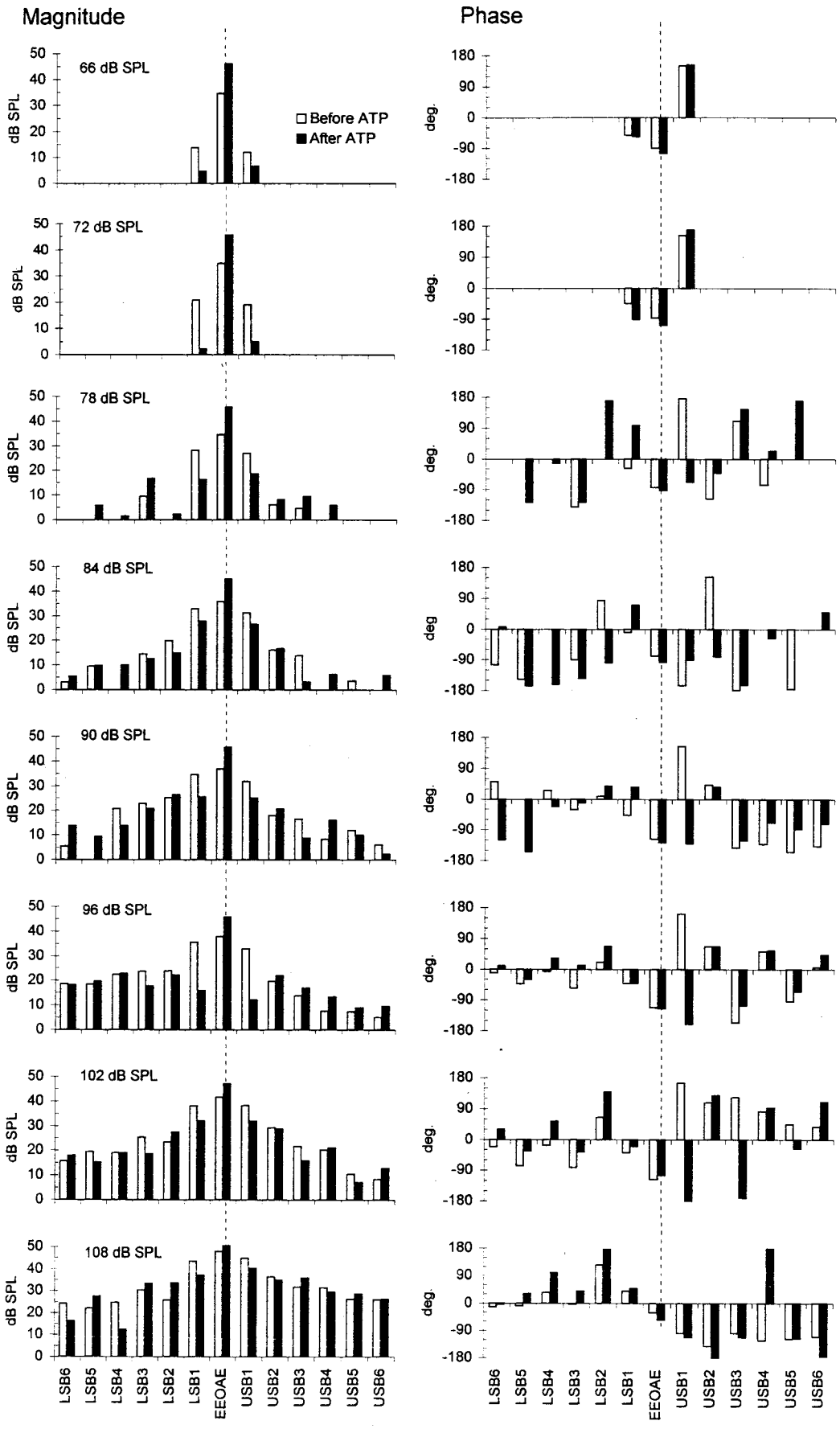

FIG. 4. Magnitudes (left) and phase angles (right) of the spectral components of the modulated waveforms (recorded before and after ATP) of Fig. 2. The ''EEOAE'' component (marked by the broken vertical line) is energy at the electrical stimulation frequency (2110 Hz). LSB 1,...,6 and USB 1,...,6 are the modulation sidebands present at the EEOAE frequency plus or minus integer multiples of the 86-Hz bias frequency.

A. Modulation sidebands

The magnitudes and phase values of the spectral components of the EEOAE waveforms from Fig. 2 are plotted in Fig. 4. The upper and lower modulation sidebands (Hubbard and Mountain, 1983), denoted USB and LSB, respectively, occur at frequencies 2110 Hz$\pm m$.86 Hz (m is an integer). The first point to note is the presence of sidebands well above the noise floor (-5 to 0 dB SPL) in the magnitude spectra of EEOAEs that appeared unmodulated after ATP. For example, at 78 and 84 dB SPL there are some sidebands with magnitudes after ATP slightly higher than before.

Second, while the phase of the carrier frequency component (2110 Hz) of the EEOAE was relatively unaltered by ATP and relatively constant over the range of sound levels, there are shifts in the phases of some sidebands. Before ATP, the sideband phase varied, in some cases, with changes in sound level. In some sidebands there were phase shifts, relative to baseline values, after the application of ATP. Sideband phase at a given sound level was otherwise stable, over repeated measurements without applications of ATP (data not shown).

The changes demonstrated in Figs. 2, 3, and 4 were not produced when the dc iontophoresis current was applied through pipettes containing only 200 mM KCl (see also Kirk and Yates, 1998b).

The shape of a complex waveform depends on the phase as well as the magnitude of each of its spectral components. In order to examine how the changes in the sidebands had influenced the waveforms, phase and magnitude values measured before ATP were substituted into the Fourier spectra of the EEOAEs recorded after ATP. New waveforms were reconstructed by inverse Fourier transform.

Figure 5 presents representative data from three cochleas: 97gp015 [see Figs. 2 and 3(a)], and 97gp017 and 01gp006 [see Figs. 3(c) and (d)]. In each set of data the left-most column shows the phase spectra of those EEOAEs in the same row, before (column 2) and after (column 3) ATP. In the fourth column the sideband phase angles measured after ATP have been restored to their original values. In the fifth column, the sideband magnitudes have been restored. Only the sidebands were altered, the carrier component at the electrical stimulation frequency was not changed. While it is possible that the restoration of sideband phase might have some physiological legitimacy (see Sec. IV), restoring the sideband magnitudes actually adds nonexistent energy to the waveform.

There were EEOAEs in which the substitution of sideband phase alone restored the simple amplitude modulation that had been lost after ATP. Examples in Fig. 5 are those EEOAEs modulated by tones at 84 dB SPL in 97gp015 (row 2), at 66 and 72 dB SPL in 97gp017 (rows 4, 5), and at 72 dB SPL 01gp006 (row 7).

Restoration of modulation by magnitude substitution alone was evident at 70 dB SPL and 96 dB SPL in 97gp015 (rows 1 and 3) and 90 dB SPL in 97gp017 (row 6). In some instances (rows 5, 8) substitution of sideband magnitude produced modulation opposite in phase to the original.

The relative lack of acoustic enhancement after ATP, the loss of clean amplitude modulation at the bias frequency, and the complex shifts in sideband phase, are not consistent with independence and additivity of ATP and MET-induced effects on EEOAEs.

However, a limited form of additivity, contingent upon restoration of the sideband phase, is apparent in Fig. 6.

The data presented here are from three cochleas and are EEOAEs whose modulation was restored by substitution of sideband phase alone. These EEOAEs were modulated by tones at the lower end of the intensity range, in most instances at levels below saturation of the CM intensity function and the onset (before ATP) of pronounced acoustic enhancement of the EEOAE.

Figure 6 is essentially a comparison of these waveforms with the simulation in Fig. 1. The original ''before'' and ''after'' emissions are in columns 1 and 2. The waveforms in column 3 (''ATP effect'') were derived from EEOAEs recorded in the same experimental sequence as those in their respective rows, but without the low-frequency bias tone. They were obtained by direct subtraction of the EEOAE recorded before ATP from the EEOAE recorded after ATP (both without the bias tone). They are assumed to be the net contribution of ATP-induced effects to the generation of the EEOAE, equivalent to panel (b) in Fig. 1. The waveforms in column 4 are those recorded after ATP, with the bias tone, in which the original sideband phase values (up to five pairs) have been restored. Most are reasonably close to a linear summation of the corresponding two waveforms on the left, although generally the depth of the amplitude modulation is less. This is consistent with the reduction in sideband magnitude that followed ATP (Fig. 4), which may in turn be associated with the loss of CM amplitude. Column 5 shows reconstructed waveforms in which the phase substitution involved only the first pair of sidebands, USB1 and LSB1 (column 6). In most examples there is little difference between the waveforms in columns 4 and 5, indicating that shifts in the phases of USB1 and USB2 were predominantly responsible for the change in modulation induced by ATP, as would be expected. These two sidebands are produced by the fundamental frequency of the modulator and thus determine the fundamental modulation frequency.

IV. DISCUSSION

When two known influences on EEOAEs, namely ATP in scala media and low-frequency bias of the MET-channel conductance were combined, the outcome was not as predicted by a model (Fig. 1) that assumed independence and additivity of the ATP-gated and MET conductance pathways in OHCs (Glowatzki *et al.*, 1997). Amplitude modulation in phase with the low-frequency bias was absent in EEOAEs that had been enhanced by ATP, except at very high levels of the bias tone. However, the frequency spectra even of those EEOAEs showing little visible amplitude modulation after ATP still contained prominent components at modulation sideband frequencies. The phases of some sidebands had changed after ATP, but the carrier phase remained constant.

In some waveforms, predominantly those modulated at lower levels of the bias tone, the original modulation patterns could be restored by substitution of the original sideband phase into the spectra of EEOAEs recorded after ATP. These

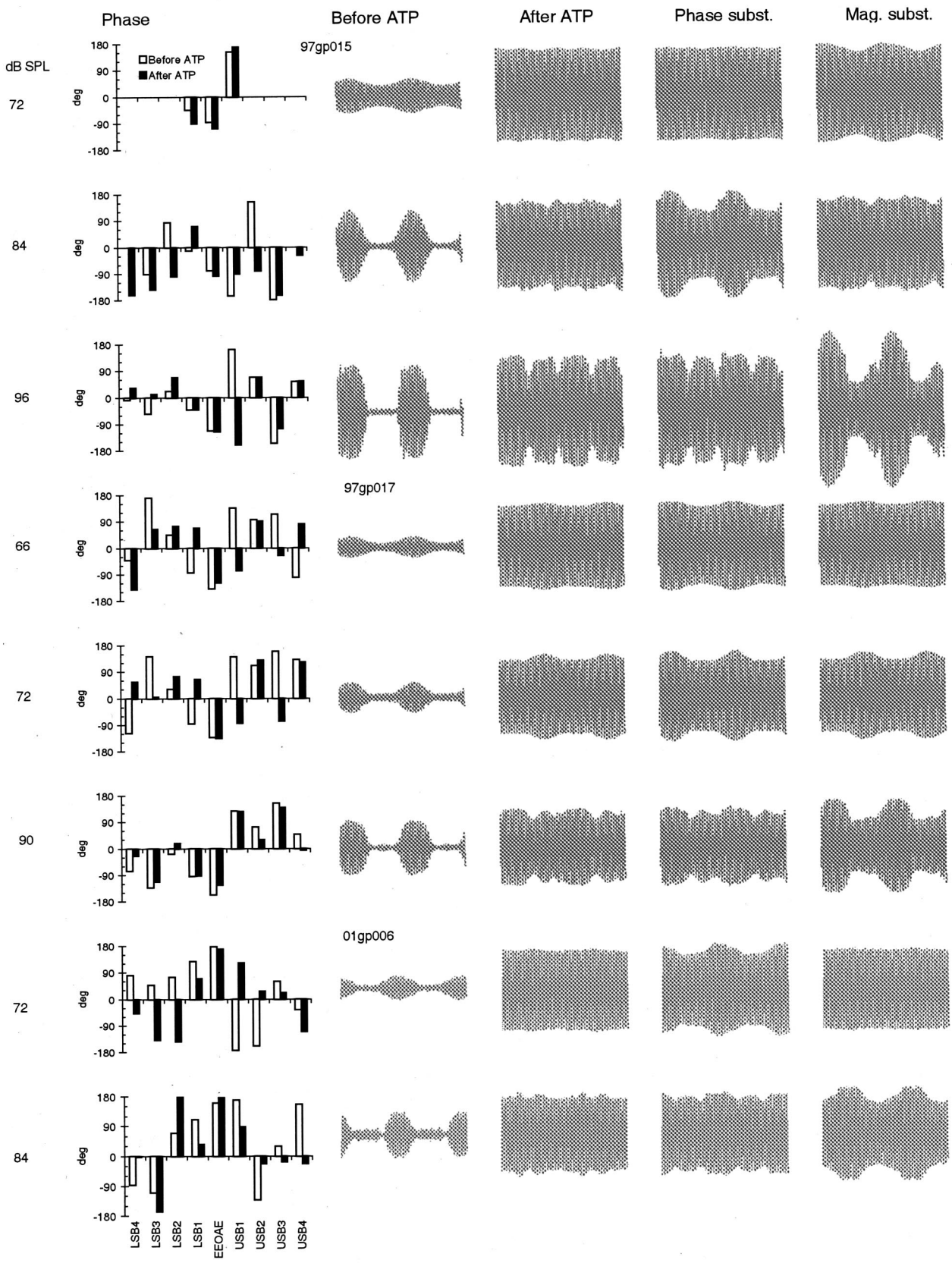

FIG. 5. Substitution of sideband phase and magnitude. Column 1 shows the phase spectra of the EEOAEs in each respective row, recorded before (column 2) and after (column 3) ATP. Waveforms in column 4 have been reconstructed from those in column 3 by replacing the sideband phase values measured after ATP with those measured before ATP. In column 5 the original sideband magnitudes have been substituted. Only the sidebands were altered. The spectral component at the carrier frequency (2110 Hz) was not changed. The data are from three cochleas. Sound levels of the 86-Hz bias tones were as indicated on the left.

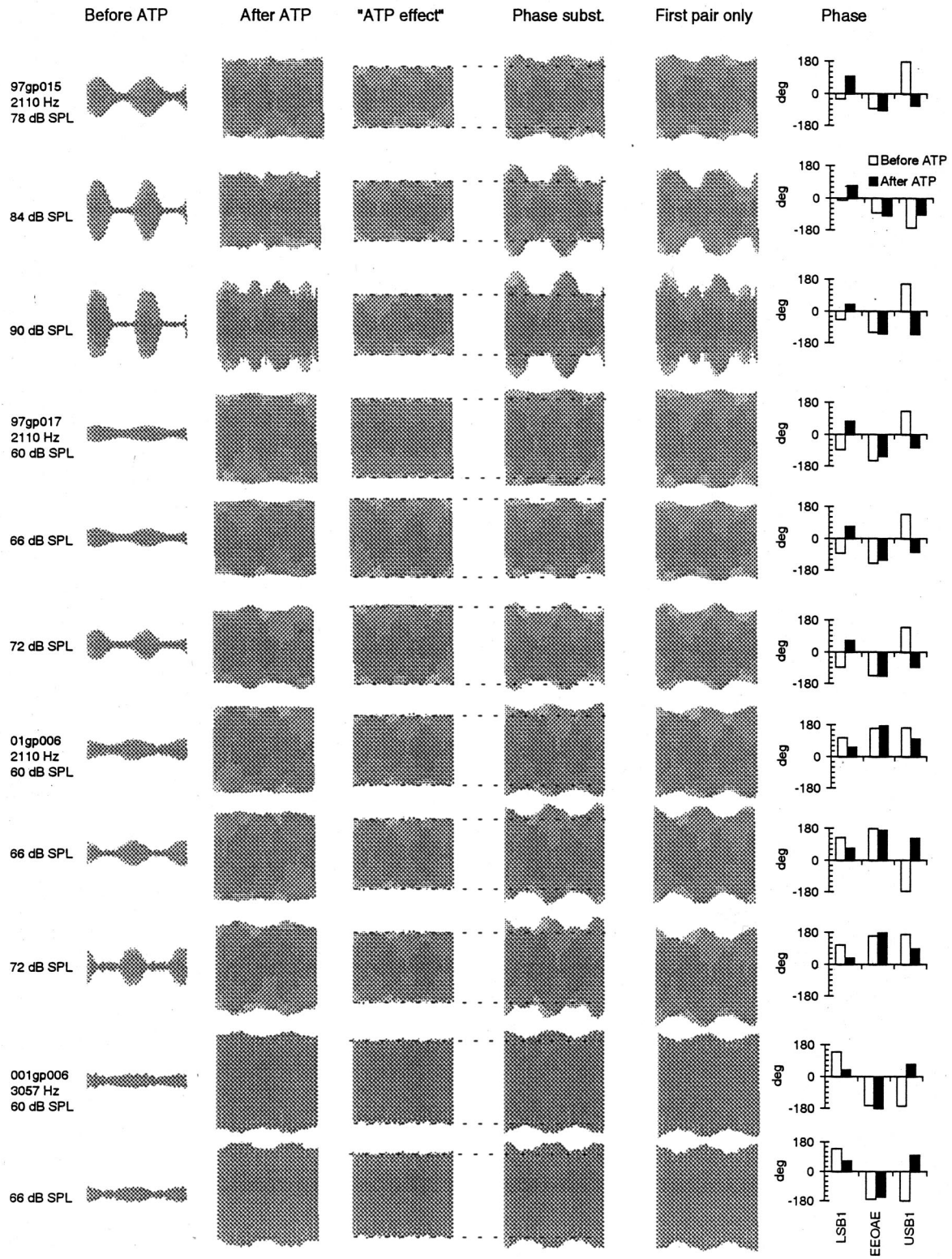

FIG. 6. EEOAEs in which substitution of the original phase values restored the modulation envelope. The waveforms in columns 1 and 2 were recorded before and after ATP, respectively. Column 3 (''ATP effect'') contains waveforms that were derived from the difference between EEOAEs recorded without the low-frequency bias tone before and after ATP. The original waveform was simply subtracted from the waveform that was enhanced by ATP. The result is assumed to be the net contribution of ATP-gated conductance to the generation of the EEOAE. Columns 4 and 5 show waveforms reconstructed from those in column 2 by substitution of the original sideband phase. In column 4 the phases of all sidebands with magnitudes above the noise floor have been changed. In column 5 only the first pair LSB1 and USB1 has been modified. Phase spectra before and after ATP, showing only the carrier and the first sideband pair, are in column 4. Animal designation and stimulation parameters (ac frequency and bias-tone level) are shown to the left of each row.

''reconstructed'' EEOAEs were then similar in both amplitude and waveform shape to a linear summation of the original modulated emission and an amplitude-enhancement due to ATP.

Since the ATP-induced phase shifts occurred independently of the carrier phase, which remained relatively constant, it is reasonable to attribute them to an effect of ATP on the modulation of the EEOAE rather than on its generation.

Two processes, each of them nonlinear, that might contribute to the modulation of EEOAEs are changes in the open probability of the MET channels during the low-frequency bias and the asymmetrical voltage-length relationship of the OHC membrane motor (Santos-Sacchi, 1989). It has been proposed (Yates and Kirk, 1998) that the former could directly modulate an electrical drive to OHC motility and the latter influence the gain of somatic motility in phase with the intracellular receptor potential elicited by the low-frequency bias tone.

Modulation sidebands are related to the fundamental and higher harmonic components in the modulator's frequency spectrum, and some would be sensitive to changes in the distortion producing nonlinearity. Shifts in the operating point on the MET transfer function have been shown, in both theory and experiment to influence both the phase and magnitude of some distortion components generated in the cochlea (Frank and Kossl, 1996, 1997; Kirk *et al.*, 1997; Kirk and Patuzzi, 1997; van Emst *et al.*, 1997).

Small shifts in MET operating point, estimated by fitting a first-order Boltzmann function to the extracellular CM (Kirk *et al.*, 1997; Patuzzi and Rajan, 1990), and possibly due to length change (Brownell *et al.*, 1985) induced by depolarization of OHCs by ATP, were apparent in the present data (not shown) but it is unlikely that these were responsible for the loss of modulation after ATP.

In EEOAEs whose modulation could be restored after ATP by phase substitution, the first pair of sidebands was the predominant influence. It is the fundamental frequency of the modulator that gives rise to the first pair of sidebands, and these in turn determine the fundamental phase and frequency of the modulation envelope. Operating point shifts on the MET transfer function influence predominantly, if not exclusively, the even-order distortion components in the cochlea. These include the summating potential and the second harmonic in the CM and the f_2-f_1 distortion tone (Frank and Kossl, 1996; Kirk and Patuzzi, 1997; van Emst *et al.*, 1997) but not the fundamental. Even a highly asymmetrical nonlinearity modeled on a second-order Boltzmann function, which showed level-dependent changes in both odd and even order distortion (Lukashkin and Russell, 1998), did not predict changes in the fundamental.

In any event, a shift in the phase of the low-frequency fundamental would change the phase of the amplitude modulation but would not eliminate it. The amplitude modulation underwent phase reversal in some instances, but the more usual outcome at lower levels of the bias tone was a flattening out of the modulation envelope. Significantly also, there was never any change in the phase of the CM, indicating that where the amplitude modulation did undergo phase reversal, the MET channel conductance *per se* was probably not responsible.

The sideband phase shifts are puzzling. It is not obvious how a change in any single nonlinear stage in the generation of a modulated EEOAE waveform could be responsible, by itself, for the loss of modulation. Rather, it would seem necessary that multiple stages were involved, with at least one of them introducing phase opposition after ATP.

There is potential for interaction between various electrical nonlinearities in the OHC that would be capable of influencing the active mechanics (Patuzzi, 1996; Santos-Sacchi, 1993). In addition, potential targets for ATP include the supporting cells of the organ of Corti (Chen and Bobbin, 1998; Jarlebark *et al.*, 2000; Sugasawa *et al.*, 1996) that may influence the passive mechanics of the system.

As to the original question of the independence and additivity of the ATP and MET-induced effects on EEOAEs, the waveform plots in Fig. 6 suggest that at certain sound levels the two influences are additive when a ''secondary ATP effect'' which shifts the sideband phase is compensated for. The mere existence of the phase shifts, however, indicates the two influences are not strictly independent.

The acoustic enhancement at higher sound levels adds another complication. Acoustic enhancement of EEOAEs has been discussed extensively and attributed to reduction in the gain of a negative feedback loop, although there have been arguments for (Hubbard and Mountain, 1990; Nakajima *et al.*, 2000; Roddy *et al.*, 1994) and against (Kirk and Yates, 1996) this explanation of the phenomenon. It has been suggested (Kirk and Yates, 1998a) that the enhancement that appears during the scala vestibuli phase of a low-frequency bias may be distinct from the enhancement induced by high-frequency sound. Whatever the case, it is clear (Fig. 3) that acoustic enhancement here did not add to the ATP-induced enhancement of the EEOAE, except at sound levels above ~100 dB SPL, where the CM intensity function was well past saturation. This nonadditivity may indicate that the two phenomena, enhancement by ATP and enhancement by sound, share a common origin. It again argues against essential independence of ATP-induced and mechanical influences on EEOAEs.

ACKNOWLEDGMENTS

This work was supported by the National Health and Medical Research Council of Australia (Project Grant No. 139003) and by the University of Western Australia. Data acquisition software was developed by the late Graeme Yates.

Brownell, W. E., Bader, C. R., Bertrand, D., and de Ribaupierre, Y. (**1985**). ''Evoked mechanical responses of isolated cochlear outer hair cells,'' Science **227**(4683), 194–196.

Chen, C., and Bobbin, R. P. (**1998**). ''P2X receptors in cochlear Deiters' cells,'' Br. J. Pharmacol. **124**, 337–344.

Frank, G., and Kossl, M. (**1996**). ''The acoustic two-tone distortions $2f1-f2$ and $f2-f1$ and their possible relation to changes in the operating point of the cochlear amplifier,'' Hear. Res. **98**, 104–115.

Frank, G., and Kossl, M. (**1997**). ''Acoustical and electrical biasing of the cochlea partition. Effects on the acoustic two tone distortions $f2-f1$ and $2f1-f2$,'' Hear. Res. **113**, 57–68.

Glowatzki, E., Ruppersberg, J. P., Zenner, H. P., and Rusch, A. (**1997**). ''Mechanically and ATP-induced currents of mouse outer hair cells are independent and differentially blocked by d-tubocurarine,'' Neuropharmacology **36**, 1269–1275.
Housley, G. D., Raybould, N. P., and Thorne, P. R. (**1998**). ''Fluorescence imaging of Na+ influx via P2X receptors in cochlear hair cells,'' Hear. Res. **119**, 1–13.
Housley, G. D., Kanjhan, R., Raybould, N. P., Greenwood, D., Salih, S. G., Jarlebark, L., Burton, L. D., Setz, V. C., Cannell, M. B., Soeller, C., Christie, D. L., Usami, S., Matsubara, A., Yoshie, H., Ryan, A. F., and Thorne, P. R. (**1999**). ''Expression of the P2X(2) receptor subunit of the ATP-gated ion channel in the cochlea: Implications for sound transduction and auditory neurotransmission,'' J. Neurosci. **19**, 8377–8388.
Hubbard, A. E., and Mountain, D. C. (**1983**). ''Alternating current delivered into the scala media alters sound pressure at the eardrum,'' Science **222**, 510–512.
Hubbard, A. E., and Mountain, D. C. (**1990**). ''Haircell forward and reverse transduction: Differential suppression and enhancement,'' Hear. Res. **43**, 269–272.
Jaramillo, F., and Hudspeth, A. J. (**1991**). ''Localization of the hair cell's transduction channels at the hair bundle's top by iontophoretic application of a channel blocker,'' Neuron **7**, 409–420.
Jarlebark, L. E., Housley, G. D., and Thorne, P. R. (**2000**). ''Immunohistochemical localization of adenosine 5′-triphosphate-gated ion channel P2X(2) receptor subunits in adult and developing rat cochlea,'' J. Comp. Neurol. **421**, 289–301.
Kirk, D. L., and Patuzzi, R. B. (**1997**). ''Transient changes in cochlear potentials and DPOAEs after low-frequency tones: The 'two-minute bounce' revisited,'' Hear. Res. **112**, 49–68.
Kirk, D. L., and Yates, G. K. (**1996**). ''Frequency tuning and acoustic enhancement of electrically evoked otoacoustic emissions in the guinea pig cochlea,'' J. Acoust. Soc. Am. **100**, 3714–3725.
Kirk, D. L., and Yates, G. K. (**1998a**). ''Enhancement of electrically evoked oto-acoustic emissions associated with low-frequency stimulus bias of the basilar membrane towards scala vestibuli,'' J. Acoust. Soc. Am. **104**, 1544–1554.
Kirk, D. L., and Yates, G. K. (**1998b**). ''ATP in endolymph enhances electrically evoked oto-acoustic emissions from the guinea pig cochlea,'' Neurosci. Lett. **250**, 149–152.
Kirk, D. L., Moleirinho, A., and Patuzzi, R. B. (**1997**). ''Microphonic and DPOAE measurements suggest a micromechanical mechanism for the 'bounce' phenomenon following low-frequency tones,'' Hear. Res. **112**, 69–86.
Lukashkin, A. N., and Russell, I. J. (**1998**). ''A descriptive model of the receptor potential nonlinearities generated by the hair cell mechanoelectrical transducer,'' J. Acoust. Soc. Am. **103**, 973–980.
Mountain, D. C., and Hubbard, A. E. (**1989**). ''Rapid force production in the cochlea,'' Hear. Res. **42**, 195–202.
Munoz, D. J., Thorne, P. R., Housley, G. D., Billett, T. E., and Battersby, J. M. (**1995**). ''Extracellular adenosine 5′-triphosphate (ATP) in the endolymphatic compartment influences cochlear function,'' Hear. Res. **90**, 106–118.
Munoz, D. J., Thorne, P. R., and Housley, G. D. (**1999**). ''P2X receptor-mediated changes in cochlear potentials arising from exogenous adenosine 5′-triphosphate in endolymph,'' Hear. Res. **138**, 56–64.
Nakajima, H. H., Hubbard, A. E., and Mountain, D. C. (**2000**). ''Effects of acoustic trauma on acoustic enhancement of electrically evoked otoacoustic emissions,'' J. Acoust. Soc. Am. **107**, 2603–2614.
Ohmori, H. (**1987**). ''Gating properties of the mechano-electrical transducer channel in the dissociated vestibular hair cell of the chick,'' J. Physiol. (London) **387**, 589–609.
Patuzzi, R. (**1996**). ''Cochlear micromechanics and macromechanics,'' in *The Cochlea*, edited by A. N. Popper, R. R. Fay, and P. Dallos (Springer, New York), pp. 186–257.
Patuzzi, R., and Rajan, R. (**1990**). ''Does electrical stimulation of the crossed olivo-cochlear bundle produce movement of the organ of Corti?,'' Hear. Res. **45**, 15–32.
Roddy, J., Hubbard, A. E., Mountain, D. C., and Xue, S. (**1994**). ''Effects of electrical biasing on electrically evoked otoacoustic emissions,'' Hear. Res. **73**, 148–154.
Santos-Sacchi, J. (**1989**). ''Asymmetry in voltage-dependent movements of isolated outer hair cells from the organ of Corti,'' J. Neurosci. **9**, 2954–2962.
Santos-Sacchi, J. (**1993**). ''Harmonics of outer hair cell motility,'' Biophys. J. **65**, 2217–2227.
Sugasawa, M., Erostegui, C., Blanchet, C., and Dulon, D. (**1996**). ''ATP activates a cation conductance and Ca(2+)-dependent Cl- conductance in Hensen cells of guinea pig cochlea,'' Am. J. Physiol. **271**, C1817–1827.
Surprenant, A., Buell, G., and North, R. A. (**1995**). ''P2X receptors bring new structure to ligand-gated ion channels,'' Trends Neurosci. **18**, 224–229.
van Emst, M. G., Klis, S. F., and Smoorenburg, G. F. (**1997**). ''Identification of the nonlinearity governing even-order distortion products in cochlear potentials,'' Hear. Res. **114**, 93–101.
Yates, G. K., and Kirk, D. L. (**1998**). ''Cochlear electrically evoked emissions modulated by mechanical transduction channels,'' J. Neurosci. **18**, 1996–2003.

Asymmetry of masking between complex tones and noise: The role of temporal structure and peripheral compression

Hedwig Gockel[a)]
CNBH, Department of Physiology, University of Cambridge, Downing Street, Cambridge CB2 3EG, England

Brian C. J. Moore[b)]
Department of Experimental Psychology, University of Cambridge, Downing Street, Cambridge CB2 3EB, England

Roy D. Patterson[c)]
CNBH, Department of Physiology, University of Cambridge, Downing Street, Cambridge CB2 3EG, England

(Received 30 July 2001; revised 16 January 2002; accepted 28 March 2002)

Thresholds for the detection of harmonic complex tones in noise were measured as a function of masker level. The rms level of the masker ranged from 40 to 70 dB SPL in 10-dB steps. The tones had a fundamental frequency (F0) of 62.5 or 250 Hz, and components were added in either cosine or random phase. The complex tones and the noise were bandpass filtered into the same frequency region, from the tenth harmonic up to 5 kHz. In a different condition, the roles of masker and signal were reversed, keeping all other parameters the same; subjects had to detect the noise in the presence of a harmonic tone masker. In both conditions, the masker was either gated synchronously with the 700-ms signal, or it started 400 ms before and stopped 200 ms after the signal. The results showed a large asymmetry in the effectiveness of masking between the tones and noise. Even though signal and masker had the same bandwidth, the noise was a more effective masker than the complex tone. The degree of asymmetry depended on F0, component phase, and the level of the masker. The maximum difference between masked thresholds for tone and noise was about 28 dB; this occurred when the F0 was 62.5 Hz, the components were in cosine phase, and the masker level was 70 dB SPL. In most conditions, the growth-of-masking functions had slopes close to 1 (on a dB versus dB scale). However, for the cosine-phase tone masker with an F0 of 62.5 Hz, a 10-dB increase in masker level led to an increase in masked threshold of the noise of only 3.7 dB, on average. We suggest that the results for this condition are strongly affected by the active mechanism in the cochlea. © *2002 Acoustical Society of America.* [DOI: 10.1121/1.1480422]

PACS numbers: 43.66.Dc, 43.66.Mk, 43.66.Nm [MRL]

I. INTRODUCTION

Noises mask tones more effectively than tones mask noises. Reports of this asymmetry have come from studies investigating masked thresholds and also, to some extent, from studies investigating partial loudness (Hellman, 1972; Schroeder *et al.*, 1979). The present paper considers masked thresholds only. Masking asymmetry is of practical importance, since it has to be taken into account in the design of ''perceptual coders'' used to reduce the bit rate in digital recording and transmission systems (Brandenburg and Stoll, 1994; Gilchrist and Grewin, 1996). However, there have been very few studies of masking asymmetry using complex tone maskers, as opposed to pure tones, even though the former are more common than the latter in speech and music.

In many studies of masking, thresholds were measured for the detection of a sinusoidal signal in the presence of a narrow-band noise masker with the same center frequency. When the roles of signal and masker were reversed and the noise was masked by the tone, much lower thresholds were obtained (Hellman, 1972; Schroeder *et al.*, 1979; Moore *et al.*, 1998). The asymmetry has been explained in two ways. One possibility is that the task is performed by comparing overall level across the intervals in a forced-choice trial. When the masker is a tone, the masker level does not fluctuate from one interval to the next. This makes it easy to detect a small increment in level produced by adding a noise signal to the tone masker. However, when the masker is a narrow-band noise, the level fluctuates markedly from one interval to the next, and this makes it more difficult to detect the change in level produced by adding a tone to the noise (Bos and de Boer, 1966; Hellman, 1972). A second possibility is that, when a tone masker is used, the detection cue is the *within-interval* level fluctuation introduced by the noise signal (Moore *et al.*, 1998); the masker alone has no within-interval fluctuation, so this cue is highly salient. A noise masker fluctuates randomly in level within each interval, so the level-fluctuation cue is not available in this case, except to the extent that the tone signal *reduces* the amount of fluctuation (Moore, 1975; Richards, 1992; Richards and Nekrich, 1993).

[a)]Electronic mail: hedwig.gockel@mrc-cbu.cam.ac.uk
[b)]Electronic mail: bcjm@cus.cam.ac.uk
[c)]Electronic mail: roy.patterson@mrc-cbu.cam.ac.uk

Hall (1997) showed that the asymmetry of masking was not restricted to the combination of pure tones with noise. He varied the bandwidth of both the signal and the masker, from 0 to 256 Hz; the 0-bandwidth stimulus was a pure tone, while other stimuli were noiselike. Masked thresholds were highest, and essentially constant, for signal bandwidths smaller than or equal to that of the masker. For signal bandwidths exceeding that of the masker, thresholds decreased with increasing signal bandwidth and with decreasing masker bandwidth. Hall concluded that, for signal bandwidths smaller than or equal to the masker bandwidth, the results could be explained by a model based on long-term average energy, and that, for greater signal bandwidths, the temporal structure of the signal must be used as an additional cue. Verhey (2002) replicated Hall's empirical findings and showed that the results could be explained using a model incorporating a modulation filter bank (Dau *et al.*, 1997; Derleth and Dau, 2000), i.e., a sufficient cue was present in the envelope spectra of the stimuli.

Recently, Treurniet and Boucher (2001) investigated the role of harmonicity in masking. They compared thresholds for detection of an 800-Hz-wide noise in three maskers: a harmonic tone complex (fundamental frequency 88 Hz; components with random starting phases), an inharmonic tone complex, and a Gaussian noise. In all three cases, the masker spectrum covered the same frequency range (88 Hz to about 3960 Hz). Thresholds were lowest with the harmonic masker, highest with the noise masker, and intermediate with the inharmonic tone complex. They explained these results in terms of a model based on the modulation patterns present at the output of an array of auditory filters. For a harmonic masker, the frequency differences between adjacent partials are identical, and the dominant modulation rate is the same at the outputs of all auditory filters, being equal to the fundamental frequency. For an inharmonic masker, the frequency differences are not constant and the envelope modulation rate varies across filters. The model is based on the idea that lower variability in modulation rate facilitates detection of a signal-induced change in the variability.

In a second experiment, Treurniet and Boucher (2001) compared the effectiveness of a sine-phase harmonic complex masker with that of a random-phase harmonic complex. Detection thresholds for the 800-Hz-wide noise signal did not differ between the two phase conditions. This result is surprising and contrasts with the results of earlier studies which showed that threshold for detecting a sinusoidal signal in the presence of a harmonic complex masker is lower for masker component phases giving a highly modulated waveform than for phases giving a less modulated waveform (Mehrgardt and Schroeder, 1983; Smith *et al.*, 1986; Kohlrausch and Sander, 1995; Carlyon and Datta, 1997b; Summers and Leek, 1998). This effect has often been explained by the ability to ''listen in the dips'' of a modulated masker. The important factor seems to be the degree of modulation of the masker after basilar-membrane (BM) filtering, as some of the studies used Schroeder-phase complexes, which have an almost flat physical envelope (Smith *et al.*, 1986; Kohlrausch and Sander, 1995; Carlyon and Datta, 1997b; Summers and Leek, 1998). Stimuli with components added in sine phase (Mehrgardt and Schroeder, 1983; Smith *et al.*, 1986), cosine phase (Alcántara and Moore, 1995; Alcántara *et al.*, 1996) or Schroeder-positive phase (Smith *et al.*, 1986; Kohlrausch and Sander, 1995; Carlyon and Datta, 1997b; Summers and Leek, 1998) all appear to lead to highly modulated internal waveforms.

The effect of masker-component phase is level dependent (Carlyon and Datta, 1997b; Summers and Leek, 1998) and explanations of the effect and its level dependence involve fast-acting compression in the cochlea (Carlyon and Datta, 1997a; Summers and Leek, 1998). The level dependent gain leads to more amplification of low-level portions of the BM-filtered waveform than of higher-level portions, and this selective amplification of low-level portions increases the effectiveness of ''dip listening'' or decreases the overall effectiveness of maskers with highly modulated waveforms (Summers and Leek, 1998). Because of the absence of a phase effect in their data, Treurniet and Boucher (2001) concluded that the effect of harmonicity could not be explained by a strategy of listening in the dips. Note, however, that in their experiment ''frozen'' maskers were employed, i.e., a fixed ''random'' phase relationship was used throughout the experiment. By chance, the specific random phase used might have led to a highly modulated waveform on the BM and this might explain why no effect of masker component phase (sine versus random) was observed.

The aim of the present study was to investigate the asymmetry of masking between harmonic complex tones and noises with the same bandwidth when the bandwidth is broad. As mentioned above, Hall (1997) reported high thresholds for signals with bandwidths smaller than or equal to that of the masker, although, except for the case of zero bandwidth, all of his stimuli were noiselike. If the relative bandwidth of the signal and masker is the key variable governing asymmetry of masking, no difference would be expected when reversing the role of a signal and masker with equal bandwidth. There is, however, evidence that the relative bandwidth of the signal and noise is not the only relevant factor. Patterson and Datta (1996) reported that threshold for detecting an iterated rippled noise (IRN) masked by noise with the same bandwidth is about 10 dB greater than threshold for the noise masked by IRN. IRN is produced by making a copy of a random noise, delaying it by d ms relative to the original, and adding it back to the original noise. When this process is repeated more than about four times, the resulting sound has a strong pitch, corresponding to $1/d$, even though it maintains many of its stochastic properties. Patterson and Datta (1997) reported that the masking asymmetry between noise and IRN persists even when the pitch is low (corresponding to 62.5 Hz) and the frequency region of the stimuli is relatively high (above 1.6 kHz). This means that it is unlikely that models based on the excitation patterns of the stimuli would be successful in explaining the asymmetry (Patterson and Datta, 1997). Krumbholz *et al.* (2001) also investigated the masking asymmetry between noise and IRN as a function of delay of the IRN and the frequency region of the stimuli. When the reciprocal of the delay was above about 30 Hz, threshold generally decreased as d decreased, and threshold increased with increasing frequency

region; however, the effects were the same for ''noise masked by IRN'' and ''IRN masked by noise'' and thus the asymmetry of masking was constant at about 10 dB. They reviewed a range of time-domain models of auditory processing that focus on the time intervals in the neural activity patterns in the auditory nerve (Meddis and Hewitt, 1991; Patterson *et al.*, 2000; Pressnitzer *et al.*, 2001), and most of them were successful in accounting for the basic masking asymmetry.

In the current study, we explore further the role of temporal parameters in the asymmetry of masking and in particular the role of the envelope at the output of individual auditory filters. The asymmetry of masking was measured as a function of the fundamental frequency (F0), and the starting phases of the components of the harmonic complex. In addition, the level of the masker was varied. Masker level is of interest since the effect of masker component phase is stronger at moderately high masker levels (Carlyon and Datta, 1997a, b; Summers and Leek, 1998), and since the slope of the growth-of-masking function can give some insight into the possible role of compression in the cochlea in producing the asymmetry of masking.

Another parameter of interest was the synchrony of the onsets and offsets of the signal and masker. In a variety of paradigms, onset and offset asynchrony have been shown to be powerful cues for perceptual segregation of two concurrent sounds (Darwin and Carlyon, 1995). Simultaneous masking can also be affected by onset asynchrony, although the effects are small except when the signal is brief (Zwicker, 1965a, b; Elliott, 1969) or when the signal and masker do not overlap spectrally (Bacon and Viemeister, 1985; McFadden and Wright, 1990, 1992). In a related study, we are investigating the effect of onset asynchrony on the partial loudness of stimuli identical to the ones used here, and find that the effect is substantial in some conditions. Accordingly, we included this parameter in the present study, even though previous research suggests there will be little effect for the conditions of the current experiment (long duration signals with the masker and signal filtered into the same frequency region).

In addition, absolute thresholds were measured for each signal. This was done for two reasons. First, we wished to determine whether absolute threshold was affected by temporal structure. Second, we wished to test the hypothesis that both absolute thresholds and masked thresholds for signals presented in cosine-phase harmonic complexes depend on the ''active'' mechanism in the cochlea, which determines the gain applied to low-level signals (Ruggero, 1992) or to the low-amplitude portions of complex waveforms (Recio and Rhode, 2000). If this is the case, there should be a correlation (across subjects) between absolute thresholds and masked thresholds in the cosine-phase masker. Previous research has revealed a correlation between measures of cochlear compression and absolute threshold in subjects with cochlear hearing loss (Moore *et al.*, 1999c), but it is not known whether such a correlation might occur for normal-hearing subjects.

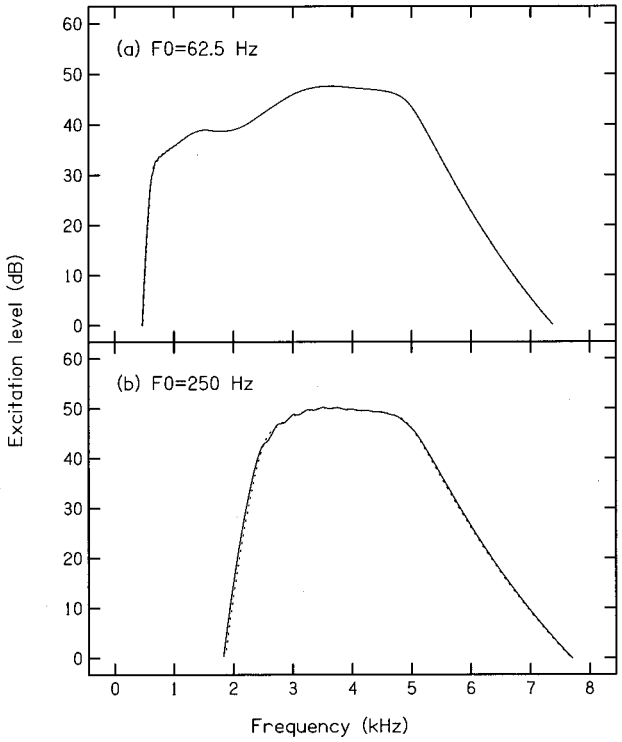

FIG. 1. Calculated long-term excitation patterns (Glasberg and Moore, 1990) for the tone (solid lines) and noise (dashed lines) stimuli for the 62.5-Hz F0 (a, top) and the 250-Hz F0 (b, bottom). The overall level was 50 dB SPL for each stimulus.

II. METHOD

A. Stimuli

The sound to be detected is hereafter called the probe. We used either a harmonic complex-tone probe masked by a noise, or a noise probe masked by a harmonic complex tone. The complex tones had an F0 of 62.5 or 250 Hz. The components were added in either random phase (RPH) or cosine phase (CPH). All tones were bandpass filtered into a frequency region from the 10th harmonic to 5000 Hz at the 3-dB down points. The slope of the filter outside the passband was 100 dB/oct. Thus, the passband was from 625 to 5000 Hz for the 62.5-Hz F0, and from 2500 to 5000 Hz for the 250-Hz F0. As a result, the components of the harmonic complexes were unresolved by the peripheral auditory system (Plomp, 1964; Moore and Ohgushi, 1993). The CPH complex would be expected to produce a waveform whose envelope, at the output of each auditory filter, had a higher degree of modulation than that of the RPH complex. The noise presented with a given complex tone (either as probe or masker) was a Gaussian noise filtered in the same way as the given complex.

Figures 1(a) and (b) show excitation patterns (Glasberg and Moore, 1990) for the tone (solid line) and noise (dashed line) stimuli for the 62.5-Hz F0 and the 250-Hz F0 conditions, respectively. These excitation patterns include the effects of the diffuse field response of the headphones (see below), which boosts the level around 3000 Hz by 12–15 dB (Shaw, 1974). Note that these excitation patterns are based on the power spectra of the stimuli and do not depend on the starting phases of the components. For the 62.5-Hz F0, the

excitation patterns of the noise and complex tone are essentially identical. For the higher F0, they differ very slightly on the low-frequency side. If differences in the long-term excitation patterns of the probe and masker are the key factor leading to masking asymmetry (Hall, 1997), then no asymmetry of masking should occur for these stimuli, regardless of masker component phase. If, on the other hand, the temporal structure of the stimuli is important, then both phase effects and masking asymmetry may be expected.

The maskers had an overall rms level of 40, 50, 60, or 70 dB SPL. The duration of the probe was always 700 ms (including ramps). The masker was gated either synchronously with the probe (the ''synchronous'' condition), or its duration was 1300 ms, in which case it was gated on 400 ms before and off 200 ms after the probe (the ''asynchronous'' condition). In the synchronous condition, all signals were gated with 40-ms, raised-cosine onset and offset ramps. In the asynchronous condition, the probe was gated with 40-ms and the masker was gated with 80-ms raised-cosine onset and offset ramps, respectively.

The stimuli were generated digitally in advance using a sampling rate of 25 kHz. The tones were generated by adding up sinusoids with frequencies ranging from F0 up to 10 kHz, while the noise was generated in the temporal domain by sampling from a Gaussian distribution. Bandpass filtering was then performed with a 900-tap digital FIR filter with a linear phase response. Ten different realizations were produced for each RPH complex tone and for the Gaussian noise; one of the ten was picked at random for each presentation. The signal and the masker were played out through separate channels of a Tucker-Davis Technologies (TDT) DD1 16-bit digital-to-analog converter and low-pass filtered at 10 kHz (TDT FT6-2). They were separately attenuated using two programmable attenuators (TDT PA4) and then added (TDT SM3). Stimuli were fed to a headphone buffer (TDT HB6) and presented monaurally via headphones with a diffuse-field response (AKG K 240 DF). Subjects were seated individually in an IAC double-walled sound-attenuating booth.

B. Procedure

A two-interval two-alternative forced-choice task was used. The masker was presented in both intervals, which were marked by a light and separated by 200 ms of silence. The subjects were required to indicate the interval containing the probe. Feedback was provided following each response. The level of the probe was adjusted using a three-down one-up adaptive rule (Levitt, 1971) tracking 79% correct responses. At the beginning of each threshold measurement, the probe level was 15 dB above that of the masker, which made the task easy in all conditions. Initially, the probe level was increased or decreased in 5-dB steps. Following four reversals, the step size was reduced to 2 dB and eight further reversals were obtained. The threshold estimate was defined as the mean of the probe levels at the last eight reversals.

At least four threshold estimates were obtained for each condition from each subject. If thresholds for a given subject and condition varied by more than 3 dB, two additional threshold estimates were obtained. The reported thresholds correspond to the mean of these four to six estimates, for each condition and subject. The total duration of a single session was about 2 h, including rest times. The conditions were presented in a counterbalanced order. Half of the subjects started with the synchronous condition, and half with the asynchronous condition. In each of these conditions, for half of the subjects the complex tone was used as probe first, and for half the noise was used as a probe first. The level of the masker and the starting phase of the complex tone varied randomly (one threshold was obtained for each condition in turn, before additional measurements were obtained in any other condition). To familiarize subjects with the procedure and equipment, they participated in one threshold measurement in each condition, before data collection proper commenced.

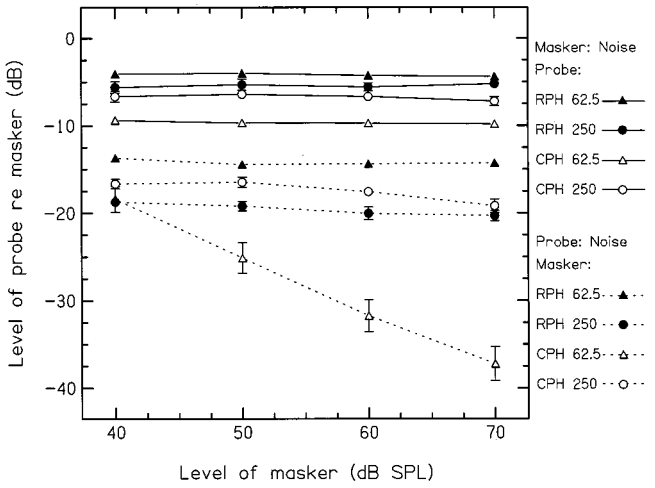

FIG. 2. Masked thresholds averaged across subjects and onset conditions. Error bars indicate ± one standard error across subjects. Thresholds are expressed in dB relative to the masker level and plotted as a function of masker level. Points connected by a continuous line show thresholds when the probe was a RPH or CPH tone. Points connected by a dashed line show thresholds when the probe was a noise. Triangles show results when a tone stimulus with F0 = 62.5 Hz was present, either as a probe or a masker. Circles show results when a tone stimulus with F0 = 250 Hz was present. Filled symbols indicate that a RPH stimulus was present, either as a probe or as a masker. Open symbols indicate that a CPH stimulus was present.

Absolute thresholds for each signal were measured after the main experiment was completed, using the same three-down one-up adaptive procedure as before. Four threshold estimates were obtained for each signal and each subject; the mean of the four is reported.

C. Subjects

Six subjects participated. Four of them were tested using both F0s in all conditions. Two additional subjects participated only using the 62.5-Hz F0. Their ages ranged from 19 to 39 years, and they all had normal hearing at audiometric frequencies between 500 and 5000 Hz.

III. RESULTS

A. Masked thresholds

The results were similar across subjects and for the two onset conditions and so mean results across subjects and onset conditions are plotted in Fig. 2, together with the associ-

ated standard errors across subjects. Mean threshold for detection of the probe is expressed in dB relative to the level of the masker and is plotted as a function of masker level. Points connected by a continuous line show thresholds when the probe was a complex tone (hereafter we refer to the harmonic complex tones simply as tones); points connected by a dashed line show thresholds when the probe was a noise. Comparison of results with the same symbol but different line types allows assessment of the asymmetry of masking.

1. Tone probes

Thresholds for the detection of the tone probes (continuous lines) were lower for CPH (open symbols) than for RPH tones (filled symbols). This was true for both F0s, but the effect of phase was more pronounced for the 62.5-Hz F0 (triangles) than for the 250-Hz F0 (circles). For the CPH probes, thresholds were markedly lower for F0 = 62.5 Hz than for F0 = 250 Hz. However, for the RPH probes, there was a small effect in the opposite direction. The signal-to-masker ratio at threshold was largely independent of masker level.

2. Noise probes

For the noise probes (dashed lines), thresholds were highest, and independent of level, in the RPH masker with an F0 of 62.5 Hz (filled triangles). The CPH masker with the same F0 produced the lowest thresholds overall (open triangles); successive 10-dB increases in masker level from 40 dB led to increases in probe threshold of only 3.2, 3.4 and 4.5 dB. Thus, relative threshold decreased markedly with increasing masker level. For the 62.5-Hz F0, thresholds for the noise probes were slightly lower (by 0.7 dB on average) in the synchronous onset conditions than in the asynchronous onset conditions. This was the only difference observed between the two onset conditions. For the 250-Hz F0, threshold was slightly higher in the CPH masker (open circles) than in the RPH masker (filled circles), the opposite pattern to that found for the lower F0. There was also a slight decrease in relative threshold with increasing masker level, for both RPH and CPH maskers. For the RPH masker, threshold was higher for the 62.5-Hz F0 than for the 250-Hz F0. In contrast, for the CPH masker, threshold was markedly lower for the lower F0.

3. Asymmetry of masking

In all conditions, thresholds for the tone probes (continuous lines) were higher than thresholds for the noise probe (dashed lines). Thus, clear asymmetry of masking was observed, even though the probe and masker always had equal bandwidths. The asymmetry of masking can be quantified as threshold for a given complex tone masked by a noise minus threshold for the noise masked by the same complex at the same masker level (difference between results with the same symbols connected by different line types). The asymmetry defined in this way was about 10 dB for the RPH complex tone with an F0 of 62.5 Hz. For a CPH complex tone with the same F0, the asymmetry ranged from 10 dB at a masker level of 40 dB SPL to 28 dB at a masker level of 70 dB SPL. For the 250-Hz F0, the asymmetry for the RPH complex was about 14 dB on average, with a tendency to increase with increasing masker level. For the same F0, the asymmetry for the CPH complex was about 11 dB on average, again with a tendency to increase with increasing masker level.

It should be noted that, based solely on the data presented here, one cannot decide whether the asymmetry of masking is caused by a change in the masker (noise versus tone), or by a change in the probe (noise versus tone), or an interaction of the two. However, thresholds for a wideband noise probe presented in a noise masker of identical bandwidth are similar to the thresholds for complex tone probes in a noise masker of identical bandwidth obtained in the present experiment. For example, Bos and de Boer (1966) and also Schacknow and Raab (1976) found noise intensity discrimination thresholds, specified as signal-to-masker ratio in dB, in the range -5 to -9 dB for bandwidths between approximately 2.5 and 5 kHz. Thus, for noise probes, which is the most relevant case with regard to perceptual audio coding, masked thresholds depend strongly on whether the masker is a noise or a tone complex. For a noise probe, the threshold difference between a tone masker and noise masker would be similar to the difference found here when switching the roles of signal and masker.

B. Statistical analyses

Within-subjects analyses of variance (ANOVAs) were conducted on relative threshold expressed as signal-to-masker ratio in dB. The Huynh–Feldt correction was used when the condition of sphericity was not satisfied. To simplify the interpretation of the results, and because the number of subjects was different for the two F0s, separate ANOVAs were conducted on various subsets of the data. Except where stated, the ANOVAs were based on six subjects for F0 = 62.5 Hz and four subjects for F0 = 250 Hz. In what follows, only significant effects will be mentioned.

1. Tone as probe

(a) F0 = 250 Hz (circles): A three-way ANOVA (onset × phase × level) showed a significant main effect of phase [$F(1,3) = 17.4$, $p = 0.025$]; the mean threshold was 1.3 dB lower for the CPH tone than for the RPH tone. (b) F0 = 62.5 Hz (triangles): A three-way ANOVA (onset × phase × level) showed a significant main effect of phase [$F(1,5) = 277.5$, $p < 0.001$]; the mean threshold was 5.4 dB lower for the CPH tone than for the RPH tone. (c) Both F0s: A four-way ANOVA (F0 × onset × phase × level), restricted to the data for the four subjects who were tested using both F0s, showed a highly significant main effect of phase [$F(1,3) = 436.1$, $p < 0.001$], and a significant interaction between F0 and phase [$F(1,3) = 61.8$, $p = 0.004$], indicating that the size of the phase effect depended on F0, being larger for the lower F0.

2. Noise as probe

(a) F0 = 250 Hz: A three-way ANOVA (onset × phase × level) showed that thresholds in the CPH masker were significantly higher (by about 2.1 dB) than in the RPH masker [$F(1,3) = 40.2$, $p = 0.008$]. The main effect of level

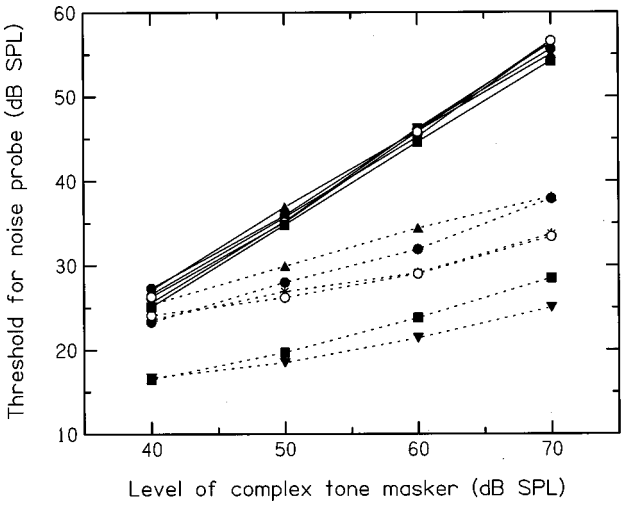

FIG. 3. Individual masked thresholds (in dB SPL) for the noise probe plotted as a function of the level of the tone masker with an F0 of 62.5 Hz. Solid and dashed lines connect the thresholds obtained using the RPH and the CPH maskers, respectively. The six different symbols indicate results for six different subjects.

was also significant [$F(3,9)=6.4$, $p=0.022$]; relative threshold decreased slightly with increasing masker level. (b) F0 = 62.5 Hz: A three-way ANOVA (onset × phase × level) gave highly significant main effects of phase [$F(1,5)=65.2, p<0.001$] and of level [$F(3,15)=532.6$, $p<0.001$]. There was a marginally significant main effect of onset [$F(1,5)=7.4$, $p=0.042$], thresholds being slightly (0.7 dB) lower in the synchronous than in the asynchronous condition. More importantly, there was a highly significant interaction between phase and level [$F(3,15)=158.5$, $p<0.001$], indicating that masker level affected threshold differently for the CPH and the RPH maskers; there was no effect of level for the RPH masker, but a large decrease in relative threshold with increasing masker level for the CPH masker.

C. Individual differences in the detection of noise in a tone masker

Differences in performance among subjects were generally small, except in one condition. Rather large variations were observed for an F0 of 62.5 Hz, with the noise as probe and the CPH tone masker (open triangles connected by dashed lines in Fig. 2). Figure 3 shows individual thresholds (in dB SPL) for this condition (dashed lines), and for the RPH masker with the same F0 (solid lines), plotted as a function of the masker level. For the RPH masker, individual differences in overall performance were small (maximally about 3 dB). For the CPH masker, thresholds differed considerably between subjects, by as much as 13 dB for the highest masker level.

D. Absolute thresholds

Table I presents individual thresholds in quiet for all probes used in the experiment. Threshold in quiet showed a trend to be lower for the CPH tone complex than for the RPH tone complex or the corresponding noise. Separate repeated measures ANOVAs were run on the data for each F0, since six and four subjects participated in the low and high F0 conditions, respectively. Thresholds differed significantly across probes for F0 = 62.5 Hz [$F(2,10)=7.1$, $p=0.012$], but not for F0 = 250 Hz. An ANOVA using the data from both F0s (and four subjects only) showed no significant effect of probe type.

E. Relation between masked and absolute thresholds

In the introduction, we advanced the hypothesis that both absolute threshold and masked threshold for a noise probe in a CPH masker would depend on the operation of the active mechanism in the cochlea. In the case of masked threshold, the active mechanism might play a role because threshold depends on ''dip listening,'' at least for low F0s. The detection of a signal in a dip might depend partly on forward masking from the preceding masker peak, and extra gain applied to the low-level signal might reduce this forward masking. If this hypothesis is correct, there should be a correlation across subjects between absolute and masked thresholds, provided that the active mechanism varies in ''strength'' across subjects. The results showed only small individual differences in masked threshold for the noise probe in the CPH masker with F0 = 250 Hz, probably because the waveform dips are too brief to allow dip listening at this F0. However, for F0 = 62.5 Hz, marked individual differences were found, as shown in Fig. 3.

To test the active-mechanism hypothesis, for each subject, we calculated the mean absolute threshold across the three probe types for F0 = 62.5 Hz. We also calculated the mean relative threshold across masker level for the noise

TABLE I. Thresholds in quiet (in dB SPL) for each subject and probe. The subjects are ordered according to their thresholds (from high to low) for the noise probe in the presence of a CPH tone masker with an F0 of 62.5 Hz. The symbols representing the subjects are the same as in Fig. 3.

		F0 = 62.5 Hz				F0 = 250 Hz			
Subject	(Age)	CPH	RPH	Noise	Mean	CPH	RPH	Noise	Mean
▲	(39)	5.5	6.8	7.7	**6.7**	7.3	8.7	6.4	**7.5**
●	(33)	11.2	12.0	11.6	**11.6**	9.9	10.6	9.0	**9.8**
*	(20)	10.0	10.5	11.5	**10.7**	7.7	7.0	9.2	**8.0**
○	(20)	7.3	9.7	8.1	**8.4**				
■	(19)	2.9	3.5	2.9	**3.1**	2.8	4.1	3.9	**3.6**
▼	(22)	0.8	2.1	2.4	**1.8**				
Mean		**6.3**	**7.4**	**7.4**		**6.9**	**7.6**	**7.1**	

probe in the 62.5-Hz CPH masker for each subject. We then calculated the Pearson product-moment correlation coefficient between the individual absolute and masked thresholds. The obtained value of 0.8 was statistically significant at the 0.05 level (one-tailed), which is consistent with the hypothesis. Note that a perfect correlation would not be expected, as absolute threshold is influenced by factors other than the ''strength'' of the active mechanism. For example, the gain provided by the middle ear can vary markedly across individuals (Aibara *et al.*, 2001). In addition, there might be other mechanisms which would lead to a correlation between masked and absolute thresholds. Thus, the correlation cannot be regarded as proving the active-mechanism hypothesis. However, the correlation is consistent with this hypothesis.

IV. DISCUSSION

The results from the synchronous and asynchronous onset conditions were very similar. As mentioned in the Introduction, this was expected, and is consistent with earlier findings. We have no explanation for the slightly lower thresholds for the noise probes in the synchronous compared to the asynchronous onset conditions. The following discussion applies to both onset conditions. The results showed a clear asymmetry of masking between the tone and noise maskers in all conditions, but with larger effects in some cases than in others. We begin with a general discussion of why asymmetry of masking occurs for these stimuli, and then consider specific mechanisms that might account for the detailed features of the results.

A. Asymmetry of masking

Thresholds for detection of the noise in the harmonic complex tones were always lower than for detection of the tones in the noise. This asymmetry was as large as 28 dB for the CPH tone with F0 of 62.5 Hz, and it was around 14 dB for the RPH tone with F0 of 250 Hz. This general effect confirms that the relative bandwidth of probe and masker is not the key variable determining whether asymmetry of masking will occur between two stimuli (see also Patterson and Datta, 1996; Krumbholz *et al.*, 2001). The crucial factor seems to be the temporal structure of the probe and the masker, not their long-term spectra.

The asymmetry may result from the same type of mechanism as proposed by Moore *et al.* (1998) to account for asymmetry of masking between a pure tone and a narrow-band noise of the same center frequency. When the masker is a periodic sound (either a pure tone or a complex tone), the masker alone is perfectly regular and it sounds steady; in models such as the auditory image model (AIM) proposed by Patterson *et al.* (1992, 1995), the masker produces a stable auditory image. When the noise probe is added to the masker, it introduces an irregularity, which is heard as a fluctuation or slight roughness in the sound; in the AIM model, the auditory image would show some instability. This instability provides a within-interval cue indicating the presence of the noise probe.

When the masker is a noise, it has inherent fluctuations, which lead to an unstable auditory image. When a tone probe is added to a noise, detection might be based on the increase in energy produced by the probe. However, this cue would be limited in effectiveness by the random fluctuations in level of the noise masker (Bos and de Boer, 1966). An alternative detection cue is the increased regularity in the sound introduced by the tone probe, which might be heard as a weak pitch or a ''rattle.'' The auditory image would show an increase in regularity at some time intervals when the tone probe was present. This cue would be less effective than the change in auditory image produced by adding a noise probe to a tone masker, because it is easier to detect a slight decrease in regularity from perfect regularity than it is to detect a slight increase in regularity from a high degree of irregularity (Pollack, 1968).

It may also be possible to account for the basic features of the asymmetry of masking using a model incorporating an array of modulation filters (Dau *et al.*, 1997; Derleth and Dau, 2000). As mentioned in the Introduction, Verhey (2002) was able to use such a model to account for the asymmetry of masking for noises with different bandwidths, as measured by Hall (1997) and replicated by Verhey (2002). This model might be able to predict some aspects of the asymmetry of masking found with the stimuli used here. For example, in response to a complex tone masker, activity at the output of the modulation filter bank would be restricted mainly to modulation filters tuned to the F0 and (to a lesser extent) higher harmonics of F0. The introduction of the noise probe would introduce activity at the outputs of other, previously relatively inactive, modulation filters, which might provide a salient detection cue. In contrast, in response to a noise masker, modulation filters covering a wide range of center frequencies would be activated (depending on the bandwidth of the noise), which might make extra modulation produced by the presence of a tone probe difficult to detect.

While either the AIM model or the modulation filter bank model may be able to account for some basic aspects of the asymmetry of masking found in our data, there are other aspects of the data that probably require the inclusion of additional processes, such as BM compression. These aspects are considered in more detail in the following sections.

B. Tones as probes

For all complex tones as probes, thresholds were roughly constant when expressed relative to the masker level. Thresholds for the detection of tone probes in noise were generally lower for CPH than for RPH probes. This may be related to the fact that the envelopes of the CPH probes had larger and sharper peaks than those of the RPH probes. The larger peaks in the CPH probes would lead to momentary increases in probe-to-masker ratio, which might facilitate detection in two ways. First, subjects may be able to select the most appropriate times for detecting the signal, via a ''multiple looks'' mechanism (Viemeister and Wakefield, 1991). It is, however, questionable whether the period of the higher F0 probe would be long enough for such a mechanism to apply. Second, the regular temporal sequence of the CPH peaks might enhance detection by evoking a pitch or ''rattle'' percept or by exciting a modulation filter tuned to the F0 of the probe.

The effect of probe phase was much stronger for the 62.5-Hz F0 than for the 250-Hz F0. There are at least two possible, not mutually exclusive factors, which might account for this. The first factor is the limited temporal resolution of the auditory system (see, e.g., Moore, 1997). Listeners are less sensitive to amplitude modulation at high rates than at low rates (Viemeister, 1979; Kohlrausch *et al.*, 1995). For the lower F0, detection of the envelope modulation introduced by the CPH probe would have been easier than for the higher F0. The second factor is the difference in number of components interacting at the output of a given auditory filter. For the lower F0, four times as many components would fall within the passband of a given auditory filter than for the higher F0. Thus, the envelope of the CPH tone with the lower F0 would exhibit greater modulation after auditory filtering than that of the CPH tone with the higher F0. The more pronounced modulation would produce greater momentary probe-to-masker ratios, resulting in lower thresholds for the CPH tone at the lower F0 than at the higher F0.

The larger phase effect at the lower F0 was partly caused by the fact that threshold for the RPH probe was higher for the 62.5-Hz F0 than for the 250-Hz F0. This may be related to the degree of perceptual similarity of the probe and the noise masker for the two F0s. A RPH tone containing only high harmonics sounds rather noiselike when its F0 is low; it sounds more tonelike when the F0 is high (Warren and Bashford, 1981; Roberts *et al.*, 2002). So, the RPH tone with the higher F0 may be easier to detect in a noise masker than the RPH tone with the lower F0 because it sounds more different from the masker.

Note that earlier experiments showed no effect of the phase of complex tone probes on detection thresholds in noise (Horst and Ritsma, 1981; Langhans and Kohlrausch, 1992). Possible reasons for this might be that the F0 (10 Hz) was below the pitch range in the study of Langhans and Kohlrausch (1992) and that the difference between crest factors of CPH and RPH stimuli was not very large [a factor of 4 in our study compared to a factor of 2 in the study of Horst and Ritsma (1981)]. Also, in the latter study, the use of a single ''frozen'' RPH stimulus might have improved performance for the RPH tone thereby reducing the ''potential'' difference between thresholds for the RPH and the CPH tones.

C. Noise as probe, F0 = 62.5 Hz

Thresholds for detecting the noise probe in the 62.5-Hz F0 tone masker were lower for the CPH masker than for the RPH masker, especially for the higher masker levels. This contrasts with the finding of Treurniet and Boucher (2001) that detection thresholds for an 800-Hz-wide noise signal did not differ for a sine-phase harmonic complex masker and a random-phase harmonic complex masker, with F0 = 88 Hz and level = 55 dB SPL. As noted earlier, their failure to find a phase effect may be associated with the use of a ''frozen'' random-phase masker; a fixed set of random starting phases was used. Although this resulted in a relatively flat envelope for the stimulus (see their Fig. 3), the waveform on the BM might, by chance, have contained distinct dips at some places, providing predictable opportunities for dip listening.

The large phase effect in our data was probably caused by the greater envelope modulation of the CPH than the RPH masker. The dips in the envelope would provide momentary improvements in probe-to-masker ratio. For the RPH masker, threshold was constant relative to the masker level. However, for the CPH masker, relative threshold decreased markedly with increasing masker level. This indicates that one or more level-dependent factors influenced detection of the noise probe in the CPH masker.

One possible factor is the broadening of auditory filters with increasing level (Weber, 1977; Glasberg and Moore, 1990; Rosen and Baker, 1994). As a result, the number of components interacting at the output of a given auditory filter would increase with increasing level. This would lead to longer and deeper valleys in the (output) waveform envelope. This could partly explain the decrease in relative threshold of the noise probe with increasing masker level. A similar argument has been put forward by Carlyon and Datta (1997b) to explain their finding that the amount of signal threshold variation in the masking period pattern (MPP) obtained with a positive Schroeder-phase masker increased as the masker level increased.

The second factor which probably contributed to the decrease in relative threshold of the noise probe with increasing level of the CPH masker at 62.5 Hz is the level-dependent gain observed in the healthy cochlea. The gain is greatest for low input levels, and reduces with increasing level. Compressive input/output (I/O) functions have been measured for the BM (Sellick *et al.*, 1982; Ruggero *et al.*, 1992) and inner hair cells (Russell and Sellick, 1978). The I/O function of the BM is almost linear for input levels below 20–40 dB SPL, but it is compressive for sound levels from 20 to 40 up to at least 90 dB SPL (Johnstone *et al.*, 1986; Yates, 1990). At high levels the response may become more linear, although this is controversial (Ruggero *et al.*, 1997; Russell and Murugasu, 1997). For a masker level of 40 dB SPL (overall rms equivalent diffuse-field level), both the high-and low-level portions of the waveform on the BM would fall in the low-level, relatively linear region of the BM I/O function. Low- and high-level portions of the waveform would therefore receive approximately the same amount of gain. With increasing masker level above 40 dB SPL, the high-level portions of the waveform would fall more and more into the compressive region of the I/O function. The low-level portions of the waveform would still be in the more linear region of the I/O function, and so be subject to more gain than the higher-level portions (see Javel and Mott, 1988, for a similar argument). There are two ways in which this might lead to a reduction of relative threshold with increasing masker level for the CPH masker:

(a) Detection thresholds may correspond to a constant ratio of the average long-term excitation (*after* compression) of the masker-plus-signal and the masker alone. Based on the arguments given above, the input signal-to-maker ratio required to achieve a constant output ratio would decrease with increasing masker level. This ap-

pears to be the sort of mechanism assumed by Summers and Leek (1998) to explain their results obtained with Schroeder-phase maskers and sinusoidal or speech signals. Using fixed signal levels of 60, 70, or 80 dB SPL, they found that the masker level at threshold was higher for positive Schroeder-phase maskers than for negative Schroeder-phase maskers. The Schroeder-positive masker is assumed to produce a highly peaky waveform on the BM, while the Schroeder-negative phase produces a waveform with a much flatter envelope (Kohlrausch and Sander, 1995). However, in the data of Summers and Leek, the difference between the two maskers *decreased* with increasing level of the sinusoidal signal, which is opposite to the pattern found here for CPH and RPH maskers. Summers and Leek explained the decreasing difference by the relatively high level of the maskers; for the higher signal levels, the masker levels fell in the range where the BM response becomes more linear, in which case BM compression provides less benefit for signal detection in the Schroeder-positive masker.

(b) Detection thresholds may depend on listening in the dips. When the masker waveform on the BM is highly peaky, as it would be for the CPH masker, the ability to listen in the dips may be partly limited by forward masking from the masker peaks (Bacon and Lee, 1997; Bacon *et al.*, 1997). The amount of forward masking depends on the height of the peaks. If the peaks are high enough in level to fall into the compressive region of the I/O function of the BM, but the dips remain in the more linear low-level region, then a 10-dB increase in masker level can be offset by a less than 10-dB increase in signal level. A mechanism like this has been proposed to explain the shallow growth-of-masking functions that are typically observed in forward masking (Bacon and Lee, 1997; Bacon *et al.*, 1997; Moore, 1997; Plack and Oxenham, 1998).

The idea that BM compression is at least partly responsible for the decrease in relative threshold with increasing level for the noise probe in the 62.5-Hz CPH masker is consistent with our finding of a significant correlation between threshold in this condition and absolute threshold.

D. Noise as probe, F0=250 Hz

Thresholds for the noise in the 250-Hz F0 tone masker were about 2 dB *higher* when the masker was in CPH than when it was in RPH. This effect of phase was opposite to that found for the lower F0. Since the compression on the BM is assumed to be very fast acting (Recio *et al.*, 1998), this is not consistent with the first explanation given in the previous section, namely, that detection threshold corresponds to a constant ratio of the average long-term excitation (*after* compression) of the masker-plus-signal and the masker alone. If this were the case, the CPH masker should always be less effective than the RPH masker (Carlyon and Datta, 1997a).

A possible explanation comes from consideration of auditory processes following BM filtering and compression. It has been proposed that temporal resolution is partly limited by a process that ''smoothes'' the output of the cochlea. This has been modeled by a low-pass filter (Viemeister, 1979) or by a sliding temporal integrator, sometimes called a temporal window (Moore *et al.*, 1988; Plack and Moore, 1990; Oxenham and Moore, 1994). We applied such a model to the present stimuli. The model was similar to that described by Oxenham and Moore (1994), Moore *et al.* (1999a) and Glasberg *et al.* (2001). Briefly, it consists of an array of gammatone filters (Patterson *et al.*, 1995), each followed by a rectifier, an instantaneous compressive nonlinearity and a sliding temporal integrator modeled as a pair of back-to-back exponential functions. For simplicity, we consider here only the output of a single ''channel'' centered at 4000 Hz. The nonlinearity in the model is implemented by raising the instantaneous rectified amplitude to a power less than 1 (0.7), and hence it is not level dependent. It is meant to represent BM compression for mid-range levels. Note that raising the amplitude to the power 0.7 corresponds to raising the intensity to the power 0.35 (Oxenham and Moore, 1994).

Figure 4(a) shows the output of the sliding temporal integrator in response to a 250-Hz CPH tone. The temporal integrator removes most of the fluctuation that would be present at the output of the auditory filter. Thus, for this F0, there is little opportunity for dip listening. However, a distinct fluctuation at a 250-Hz rate (4-ms period) remains. Figure 4(b) shows the effect of adding a noise to the CPH tone with a relative level of −18 dB, roughly the same as threshold for the noise probe in the CPH masker. The noise introduces an increase in the amount of fluctuation in the output, which may serve as a detection cue. Figure 4(c) shows the output of the sliding temporal integrator in response to a 250-Hz RPH tone with the same rms level as for Fig. 4(a). The overall magnitude is higher than for Fig. 4(a), as BM compression results in a higher overall output magnitude for the RPH tone. However, the fluctuation in the output is smaller than in Fig. 4(a), because the waveform of the RPH tone is less peaky. Figure 4(d) shows the effect of adding a noise to the tone with a relative level of −18 dB, the same level as for Fig. 4(b). The noise increases the fluctuation in the output. Although the magnitude of the increase is similar to that in Fig. 4(b), the increase in Fig. 4(d) may be more salient, as the ''background'' fluctuation is smaller. Note that the decrease in ''background'' fluctuation in Fig. 4(c) relative to Fig. 4(a) is large (about a factor of 4) compared to the increase in ''DC'' value (about a factor of 1.3). Thus, even if the DC value has some influence, the effect of the change in background fluctuation is likely to be dominant.

To summarize this argument: the noise signal may be detected by virtue of the increase in the amount of fluctuation that it produces at the output of the sliding temporal integrator. A similar assumption has been made in the past to account for modulation detection thresholds, using measures such as the variance of the output (Viemeister, 1979; Strickland and Viemeister, 1996), the ratio of the highest sample value to the lowest sample value (Green and Forrest, 1988; Strickland and Viemeister, 1996) and the standard deviation (Moore *et al.*, 1999b). When the task is to detect an increase in amount of fluctuation against background fluctuation, then thresholds increase as the amount of background fluctuation

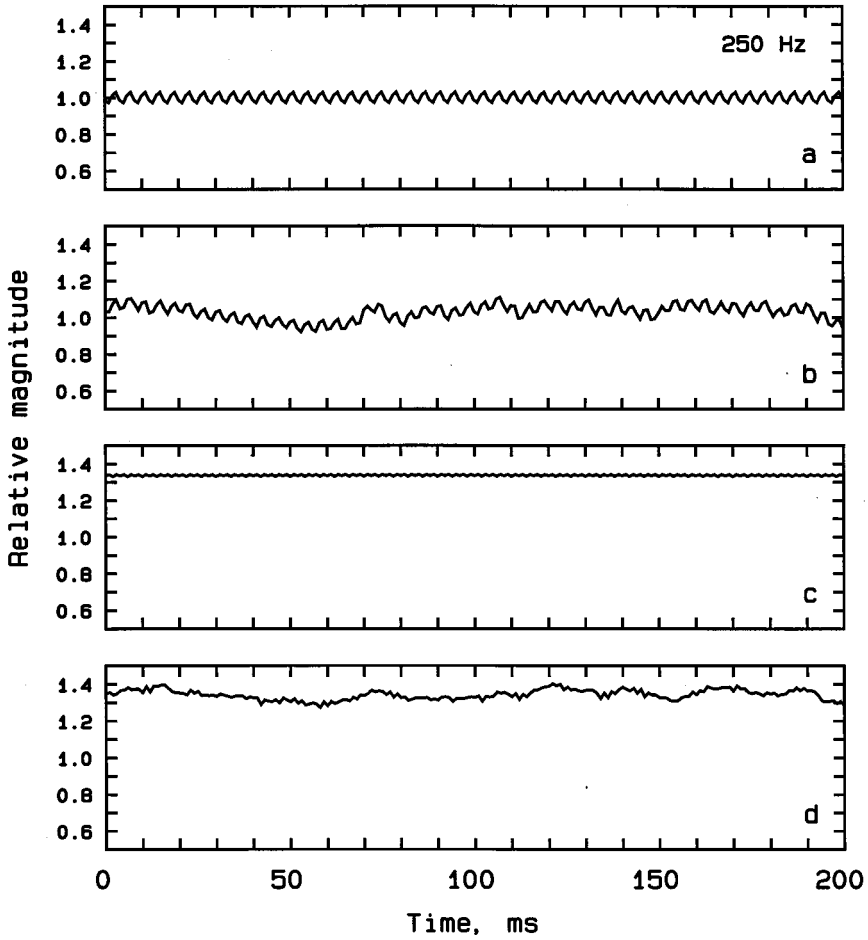

FIG. 4. Panel (a) shows the output of the sliding temporal integrator (see text for details) in response to a CPH complex tone with F0 = 250 Hz. Panel (b) shows the output when a noise was added to the CPH tone with a relative level of −18 dB. Panel (c) shows the output in response to a RPH complex tone with F0 = 250 Hz and with the same rms level as for panel (a). Panel (d) shows the output when a noise was added to the RPH tone with a relative level of −18 dB. The magnitude values on the ordinate are all on the same (arbitrary) scale.

increases (Ozimek and Sek, 1988; Wakefield and Viemeister, 1990). Since the background fluctuation is greater for our CPH than for our RPH masker, this could explain the higher detection thresholds for the noise probe in the former. Note that these arguments apply only to the 250-Hz F0. For the 62.5-Hz F0, the output of the temporal integrator shows large dips for the CPH masker, and these would provide ample opportunity for dip listening, as discussed earlier.

For the RPH-tone masker, threshold for detecting the noise was approximately 5 dB lower with the 250-Hz F0 than with the 62.5-Hz F0 masker. This effect may depend on the degree of perceptual similarity of the probe and masker. As noted earlier, a RPH tone containing only high harmonics sounds rather noiselike when its F0 is low, whereas it sounds more tonelike when the F0 is high (Warren and Bashford, 1981; Roberts *et al.*, 2002). A noise probe may be difficult to detect in a RPH masker with a low F0 because it sounds similar to the masker, whereas a noise probe in a RPH masker with a higher F0 may be easier to detect because it sounds very different from the masker.

E. Implications for perceptual coders

Perceptual coders are used to reduce the bit rate in digital audio recording and transmission systems (Brandenburg and Stoll, 1994; Gilchrist and Grewin, 1996). These coders depend on the masking properties of the human ear (Moore, 1996); the number of bits allocated to a specific frequency band in a specific time frame (and hence the level of quantization noise in that band) is determined by a calculated masked threshold for that band in that frame, where the masking is produced by the audio signal which is to be coded. The goal is to reduce the quantization noise to below masked threshold. The coders usually take into account the fact that a noise is more easily masked by a noise than by a tone. Hence, they have algorithms for assessing the ''tonality'' of the sound to be coded in a given frame. When the sound is assessed to be tonal, the estimated masked threshold is reduced relative to the case where the sound is judged to be noiselike. To our knowledge, this reduction is a fixed amount, independent of the overall level of the sound. Our data suggest that, for sounds with low to medium fluctuation rates and highly peaked waveforms, the reduction should be level dependent, and at high levels it may need to be as large as 30 dB. This amount of reduction is larger than typically used in current perceptual coders.

V. SUMMARY AND CONCLUSIONS

Harmonic complex tones and noise differed in their efficiency as mutual maskers even when they had identical long-term excitation patterns. For both synchronous and asynchronous onsets, noise was the more effective masker. The degree of asymmetry depended strongly on the starting phases of the components of the complex tones. For the CPH-tone masker with F0 = 62.5 Hz, the asymmetry also

depended on the level of the masker. The level effect was explained by BM compression, which enhances the ability to extract information from waveform dips. There was a positive correlation between absolute threshold of individual listeners and their threshold for noise in the CPH 62.5-Hz masker; this is consistent with the hypothesis that BM compression plays a role in these conditions. The results suggest that changes may be needed in algorithms for the reduction of bit rate in systems for the digital recording and transmission of speech and music signals.

ACKNOWLEDGMENTS

This work was supported by the MRC (Grant No. G9900362). We thank Brian Glasberg for carrying out the modeling described in Sec. IV D. We also thank Marjorie Leek, Armin Kohlrausch, and an anonymous reviewer for helpful comments.

Aibara, R., Welsh, J. T., Puria, S., and Goode, R. L. (**2001**). ''Human middle-ear sound transfer function and cochlear input impedance,'' Hear. Res. **152**, 100–109.

Alcántara, J. I., and Moore, B. C. J. (**1995**). ''The identification of vowel-like harmonic complexes: Effects of component phase, level, and fundamental frequency,'' J. Acoust. Soc. Am. **97**, 3813–3824.

Alcántara, J. I., Holube, I., and Moore, B. C. J. (**1996**). ''Effects of phase and level on vowel identification: Data and predictions based on a nonlinear basilar-membrane model,'' J. Acoust. Soc. Am. **100**, 2382–2392.

Bacon, S. P., and Lee, J. (**1997**). ''The modulated-unmodulated difference: Effects of signal frequency and masker modulation depth,'' J. Acoust. Soc. Am. **101**, 3617–3624.

Bacon, S. P., and Viemeister, N. F. (**1985**). ''The temporal course of simultaneous tone-on-tone masking,'' J. Acoust. Soc. Am. **78**, 1231–1235.

Bacon, S. P., Lee, J., Peterson, D. N., and Rainey, D. (**1997**). ''Masking by modulated and unmodulated noise: Effects of bandwidth, modulation rate, signal frequency and masker level,'' J. Acoust. Soc. Am. **101**, 1600–1610.

Bos, C. E., and de Boer, E. (**1966**). ''Masking and discrimination,'' J. Acoust. Soc. Am. **39**, 708–715.

Brandenburg, K., and Stoll, G. (**1994**). ''ISO-MPEG-1 Audio: A generic standard for coding of high-quality digital audio,'' J. Audio Eng. Soc. **42**, 780–792.

Carlyon, R. P., and Datta, A. J. (**1997a**). ''Excitation produced by Schroeder-phase complexes: Evidence for fast-acting compression in the auditory system,'' J. Acoust. Soc. Am. **101**, 3636–3647.

Carlyon, R. P., and Datta, A. J. (**1997b**). ''Masking period patterns of Schroeder-phase complexes: Effects of level, number of components, and phase of flanking components,'' J. Acoust. Soc. Am. **101**, 3648–3657.

Darwin, C. J., and Carlyon, R. P. (**1995**). ''Auditory grouping,'' in *Hearing*, edited by B. C. J. Moore (Academic, San Diego).

Dau, T., Kollmeier, B., and Kohlrausch, A. (**1997**). ''Modeling auditory processing of amplitude modulation. II. Spectral and temporal integration,'' J. Acoust. Soc. Am. **102**, 2906–2919.

Derleth, R. P., and Dau, T. (**2000**). ''On the role of envelope fluctuation processing in spectral masking,'' J. Acoust. Soc. Am. **108**, 285–296.

Elliott, L. L. (**1969**). ''Masking of tones before, during, and after brief silent periods in noise,'' J. Acoust. Soc. Am. **45**, 1277–1279.

Gilchrist, N., and Grewin, C. (**1996**). *Collected Papers on Digital Audio Bit Rate Reduction* (Audio Engineering Society, New York).

Glasberg, B. R., and Moore, B. C. J. (**1990**). ''Derivation of auditory filter shapes from notched-noise data,'' Hear. Res. **47**, 103–138.

Glasberg, B. R., Moore, B. C. J., and Peters, R. W. (**2001**). ''The influence of external and internal noise on the detection of increments and decrements in the level of sinusoids,'' Hear. Res. **155**, 41–53.

Green, D. M., and Forrest, T. G. (**1988**). ''Detection of amplitude modulation and gaps in noise,'' in *Basic Issues in Hearing*, edited by H. Duifhuis, J. W. Horst, and H. P. Wit (Academic, New York).

Hall, J. L. (**1997**). ''Asymmetry of masking revisited: Generalization of masker and probe bandwidth,'' J. Acoust. Soc. Am. **101**, 1023–1033.

Hellman, R. P. (**1972**). ''Asymmetry of masking between noise and tone,'' Percept. Psychophys. **11**, 241–246.

Horst, J. W., and Ritsma, R. J. (**1981**). ''Anomalous auditory filter bandwidth derived from direct masking of complex signals,'' J. Acoust. Soc. Am. **69**, 1770–1777.

Javel, E., and Mott, J. B. (**1988**). ''Physiological and psychophysical correlates of temporal processes in hearing,'' Hear. Res. **34**, 275–294.

Johnstone, B. M., Patuzzi, R. P., and Yates, G. K. (**1986**). ''Basilar membrane measurements and the travelling wave,'' Hear. Res. **22**, 147–153.

Kohlrausch, A., and Sander, A. (**1995**). ''Phase effects in masking related to dispersion in the inner ear. II. Masking period patterns of short targets,'' J. Acoust. Soc. Am. **97**, 1817–1829.

Kohlrausch, A., Fassel, R., and Dau, T. (**2000**). ''The influence of carrier level and frequency on modulation and beat-detection thresholds for sinusoidal carriers,'' J. Acoust. Soc. Am. **108**, 723–734.

Krumbholz, K., Patterson, R. D., and Nobbe, A. (**2001**). ''Asymmetry of masking between noise and iterated rippled noise: Evidence for time-interval processing in the auditory system,'' J. Acoust. Soc. Am. **110**, 2096–2107.

Langhans, A., and Kohlrausch, A. (**1992**). ''Spectral integration of broadband signals in diotic and dichotic masking experiments,'' J. Acoust. Soc. Am. **91**, 317–326.

Levitt, H. (**1971**). ''Transformed up-down methods in psychoacoustics,'' J. Acoust. Soc. Am. **49**, 467–477.

McFadden, D., and Wright, B. A. (**1990**). ''Temporal decline of masking and comodulation detection differences,'' J. Acoust. Soc. Am. **88**, 711–724.

McFadden, D., and Wright, B. A. (**1992**). ''Temporal decline of masking and comodulation masking release,'' J. Acoust. Soc. Am. **92**, 144–156.

Meddis, R., and Hewitt, M. (**1991**). ''Virtual pitch and phase sensitivity studied using a computer model of the auditory periphery. I: Pitch identification,'' J. Acoust. Soc. Am. **89**, 2866–2882.

Mehrgardt, S., and Schroeder, M. R. (**1983**). ''Monaural phase effects in masking with multicomponent signals,'' in *Hearing-Physiological Bases and Psychophysics*, edited by R. Klinke and R. Hartmann (Springer, Berlin).

Moore, B. C. J. (**1975**). ''Mechanisms of masking,'' J. Acoust. Soc. Am. **57**, 391–399.

Moore, B. C. J. (**1996**). ''Masking in the human auditory system,'' in *Collected Papers on Digital Audio Bit-Rate Reduction*, edited by N. Gilchrist and C. Grewin (Audio Engineering Society, New York).

Moore, B. C. J. (**1997**). *An Introduction to the Psychology of Hearing*, 4th ed. (Academic, San Diego).

Moore, B. C. J., and Ohgushi, K. (**1993**). ''Audibility of partials in inharmonic complex tones,'' J. Acoust. Soc. Am. **93**, 452–461.

Moore, B. C. J., Alcántara, J. I., and Dau, T. (**1998**). ''Masking patterns for sinusoidal and narrowband noise maskers,'' J. Acoust. Soc. Am. **104**, 1023–1038.

Moore, B. C. J., Peters, R. W., and Glasberg, B. R. (**1999a**). ''Effects of frequency and duration on psychometric functions for detection of increments and decrements in sinusoids in noise,'' J. Acoust. Soc. Am. **106**, 3539–3552.

Moore, B. C. J., Sek, A., and Glasberg, B. R. (**1999b**). ''Modulation masking produced by beating modulators,'' J. Acoust. Soc. Am. **106**, 908–918.

Moore, B. C. J., Glasberg, B. R., Plack, C. J., and Biswas, A. K. (**1988**). ''The shape of the ear's temporal window,'' J. Acoust. Soc. Am. **83**, 1102–1116.

Moore, B. C. J., Vickers, D. A., Plack, C. J., and Oxenham, A. J. (**1999c**). ''Inter-relationship between different psychoacoustic measures assumed to be related to the cochlear active mechanism,'' J. Acoust. Soc. Am. **106**, 2761–2778.

Oxenham, A. J., and Moore, B. C. J. (**1994**). ''Modeling the additivity of nonsimultaneous masking,'' Hear. Res. **80**, 105–118.

Ozimek, E., and Sek, A. (**1988**). ''AM difference limens for noise bands,'' Acustica **66**, 153–160.

Patterson, R. D., and Datta, J. (**1996**). ''The detection of iterated rippled noise (IRN) masked by IRN,'' Br. J. Audiol. **30**, 148.

Patterson, R. D., and Datta, J. (**1997**). ''Detecting Iterated Ripple Noise (IRN) in IRN: the spectral position of the listening band,'' Br. J. Audiol. **31**, 131.

Patterson, R. D., Allerhand, M. H., and Giguère, C. (**1995**). ''Time-domain modeling of peripheral auditory processing: A modular architecture and a software platform,'' J. Acoust. Soc. Am. **98**, 1890–1894.

Patterson, R. D., Yost, W. A., Handel, S., and Datta, A. J. (**2000**). ''The perceptual tone/noise ratio of merged iterated rippled noises,'' J. Acoust. Soc. Am. **107**, 1578–1588.

Patterson, R. D., Robinson, K., Holdsworth, J., McKeown, D., Zhang, C.,

and Allerhand, M. (**1992**). ''Complex sounds and auditory images,'' in *Auditory Physiology and Perception, Proceedings of the 9th International Symposium on Hearing*, edited by Y. Cazals, L. Demany, and K. Horner (Pergamon, Oxford).
Plack, C. J., and Moore, B. C. J. (**1990**). ''Temporal window shape as a function of frequency and level,'' J. Acoust. Soc. Am. **87**, 2178–2187.
Plack, C. J., and Oxenham, A. J. (**1998**). ''Basilar-membrane nonlinearity and the growth of forward masking,'' J. Acoust. Soc. Am. **103**, 1598–1608.
Plomp, R. (**1964**). ''The ear as a frequency analyzer,'' J. Acoust. Soc. Am. **36**, 1628–1636.
Pollack, I. (**1968**). ''Detection and relative discrimination of auditory 'jitter','' J. Acoust. Soc. Am. **43**, 308–315.
Pressnitzer, D., Patterson, R. D., and Krumbholz, K. (**2001**). ''The lower limit of melodic pitch,'' J. Acoust. Soc. Am. **109**, 2074–2084.
Recio, A., and Rhode, W. S. (**2000**). ''Basilar membrane responses to broadband stimuli,'' J. Acoust. Soc. Am. **108**, 2281–2298.
Recio, A., Rich, N. C., Narayan, S. S., and Ruggero, M. A. (**1998**). ''Basilar-membrane responses to clicks at the base of the chinchilla cochlea,'' J. Acoust. Soc. Am. **103**, 1972–1989.
Richards, V. M. (**1992**). ''The detectability of a tone added to narrow bands of equal-energy noise,'' J. Acoust. Soc. Am. **91**, 3424–3435.
Richards, V. M., and Nekrich, R. D. (**1993**). ''The incorporation of level and level-invariant cues for the detection of a tone added to noise,'' J. Acoust. Soc. Am. **94**, 2560–2574.
Roberts, B., Glasberg, B. R., and Moore, B. C. J. (**2002**). ''Primitive stream segregation of tone sequences without differences in F0 or passband,'' J. Acoust. Soc. Am. (submitted).
Rosen, S., and Baker, R. J. (**1994**). ''Characterising auditory filter nonlinearity,'' Hear. Res. **73**, 231–243.
Ruggero, M. A. (**1992**). ''Responses to sound of the basilar membrane of the mammalian cochlea,'' Curr. Opin. Neurobiol. **2**, 449–456.
Ruggero, M. A., Robles, L., Rich, N. C., and Recio, A. (**1992**). ''Basilar membrane responses to two-tone and broadband stimuli,'' Philos. Trans. R. Soc. London B **336**, 307–315.
Ruggero, M. A., Rich, N. C., Recio, A., Narayan, S. S., and Robles, L. (**1997**). ''Basilar-membrane responses to tones at the base of the chinchilla cochlea,'' J. Acoust. Soc. Am. **101**, 2151–2163.
Russell, I. J., and Murugasu, E. (**1997**). ''Medial efferent inhibition suppresses basilar membrane responses to near characteristic frequency tones of moderate to high intensities,'' J. Acoust. Soc. Am. **102**, 1734–1738.
Russell, I. J., and Sellick, P. M. (**1978**). ''Intracellular studies of hair cells in the mammalian cochlea,'' J. Physiol. **284**, 261–280.
Schacknow, P. N., and Raab, D. H. (**1976**). ''Noise-intensity discrimination: Effects of bandwidth conditions and mode of masker presentation,'' J. Acoust. Soc. Am. **60**, 893–905.
Schroeder, M. R., Atal, B. S., and Hall, J. L. (**1979**). ''Optimizing digital speech coders by exploiting masking properties of the human ear,'' J. Acoust. Soc. Am. **66**, 1647–1652.
Sellick, P. M., Patuzzi, R., and Johnstone, B. M. (**1982**). ''Measurement of basilar membrane motion in the guinea pig using the Mössbauer technique,'' J. Acoust. Soc. Am. **72**, 131–141.
Shaw, E. A. G. (**1974**). ''Transformation of sound pressure level from the free field to the eardrum in the horizontal plane,'' J. Acoust. Soc. Am. **56**, 1848–1861.
Smith, B. K., Sieben, U. K., Kohlrausch, A., and Schroeder, M. R. (**1986**). ''Phase effects in masking related to dispersion in the inner ear,'' J. Acoust. Soc. Am. **80**, 1631–1637.
Strickland, E. A., and Viemeister, N. F. (**1996**). ''Cues for discrimination of envelopes,'' J. Acoust. Soc. Am. **99**, 3638–3646.
Summers, V., and Leek, M. R. (**1998**). ''Masking of tones and speech by Schroeder-phase harmonic complexes in normally hearing and hearing-impaired listeners,'' Hear. Res. **118**, 139–150.
Treurniet, W. C., and Boucher, D. R. (**2001**). ''A masking level difference due to harmonicity,'' J. Acoust. Soc. Am. **109**, 306–320.
Verhey, J. L. (**2002**). ''Modeling the influence of inherent envelope fluctuations in simultaneous masking experiments,'' J. Acoust. Soc. Am. **111**, 1018–1025.
Viemeister, N. F. (**1979**). ''Temporal modulation transfer functions based on modulation thresholds,'' J. Acoust. Soc. Am. **66**, 1364–1380.
Viemeister, N. F., and Wakefield, G. H. (**1991**). ''Temporal integration and multiple looks,'' J. Acoust. Soc. Am. **90**, 858–865.
Wakefield, G. H., and Viemeister, N. F. (**1990**). ''Discrimination of modulation depth of SAM noise,'' J. Acoust. Soc. Am. **88**, 1367–1373.
Warren, R. M., and Bashford, Jr., J. A. (**1981**). ''Perception of acoustic iterance: pitch and infrapitch,'' Percept. Psychophys. **29**, 395–402.
Weber, D. L. (**1977**). ''Growth of masking and the auditory filter,'' J. Acoust. Soc. Am. **62**, 424–429.
Yates, G. K. (**1990**). ''Basilar membrane nonlinearity and its influence on auditory nerve rate-intensity functions,'' Hear. Res. **50**, 145–162.
Zwicker, E. (**1965a**). ''Temporal effects in simultaneous masking and loudness,'' J. Acoust. Soc. Am. **38**, 132–141.
Zwicker, E. (**1965b**). ''Temporal effects in simultaneous masking by white-noise bursts,'' J. Acoust. Soc. Am. **37**, 653–663.

Transformation of external-ear spectral cues into perceived delays by the big brown bat, *Eptesicus fuscus*

James A. Simmons[a)]
Department of Neuroscience, Brown University, Providence, Rhode Island 02912

Janine M. Wotton and Michael J. Ferragamo
Biology Department, Gustavus Adolphus College, St. Peter, Minnesota 56082

Cynthia F. Moss
Department of Psychology, University of Maryland, College Park, Maryland 20742

(Received 16 February 2000; revised 28 January 2002; accepted 1 February 2002)

The external-ear transfer function for big brown bats (*Eptesicus fuscus*) contains two prominent notches that vary from 30 to 55 kHz and from 70 to 100 kHz, respectively, as sound-source elevation moves from −40 to +10 degrees. These notches resemble a higher-frequency version of external-ear cues for vertical localization in humans and other mammals. However, they also resemble interference notches created in echoes when reflected sounds overlap at short time separations of 30–50 μs. Psychophysical experiments have shown that bats actually perceive small time separations from interference notches, and here we used the same technique to test whether external-ear notches are recognized as a corresponding time separation, too. The bats' performance reveals the elevation dependence of a time-separation estimate at 25–45 μs in perceived delay. Convergence of target-shape and external-ear cues onto echo spectra creates ambiguity about whether a particular notch relates to the object or to its location, which the bat could resolve by ignoring the presence of notches at external-ear frequencies. Instead, the bat registers the frequencies of notches caused by the external ear along with notches caused by the target's structure and employs spectrogram correlation and transformation (SCAT) to convert them all into a family of delay estimates that includes elevation. © *2002 Acoustical Society of America.*
[DOI: 10.1121/1.1466869]

PACS numbers: 43.66.Gf, 43.66.Mk, 43.80.Lb [WA]

I. INTRODUCTION

Echolocating big brown bats (*Eptesicus fuscus*) transmit wideband, frequency-modulated (FM) biosonar sounds covering frequencies roughly from 20 to 100 kHz and perceive objects from echoes of these sounds returning to the ears (Griffin, 1958; Popper and Fay, 1995). These bats employ sonar for orientation in a surprisingly wide variety of situations (Simmons *et al.*, 2001). The bat's primary perceptual dimension for registering objects is target range from the delay of FM echoes (Simmons, 1973, 1980, 1989). Behavioral experiments have established that these bats remember an ''image'' (for sense of term, see Simmons, 1989) consisting of an estimate for the delay of each replica of the broadcast included in a cluster of reflections (Simmons *et al.*, 1995). Here, we examine how the acoustic properties of the bat's external ears contribute one component to this delay image.

Big brown bats receive FM echoes with an integration-time of about 300–400 μs, probably originating in the bandpass and lowpass filter stages involved in auditory transduction (Simmons *et al.*, 1989) and carried over in recovery times of neural responses in the auditory brainstem (reviewed by Casseday and Covey, 1995; Pollak and Casseday, 1989). Two reflected replicas of the broadcast arriving closer together than this integration-time merge into a single sound for purposes of detection. However, the bat's FM sounds are several milliseconds long, whereas the integration-time is less than half a millisecond, so the echo waveforms can overlap and still be detected as separate FM sweeps. Consequently, the bat's internal representation of FM echoes must be shorter than the sounds themselves. This representation takes the form of an auditory spectrogram made up of segments of the FM sweeps segregated by the bandpass filters in the cochlea and the excitatory tuning curves of auditory neurons (Simmons *et al.*, 1996). To the bat, overlap of two echoes only occurs when their respective spectrograms merge at a time separation of 300–400 μs (Saillant *et al.*, 1993; Simmons *et al.*, 1989).

Reflections from multiple glints interfere with each other if they are closer together than the integration-time, and the resulting modulation of the echo spectrum affects the performance of bats in psychophysical discrimination experiments (Mogdans and Schnitzler, 1990; Schmidt, 1992; Simmons *et al.*, 1989). The spectrogram created by interference contains peaks and notches in amplitude at specific frequencies according to the time-separation of the reflections (see Beuter, 1980; Dear *et al.*, 1993; Mogdans and Schnitzler, 1990; Schmidt, 1992; Saillant *et al.*, 1993). These notches are the most prominent features of the interference spectrum (Altes, 1984). For echoes arriving in the same phase, notches are

[a)]Electronic mail: james_simmons@brown.edu

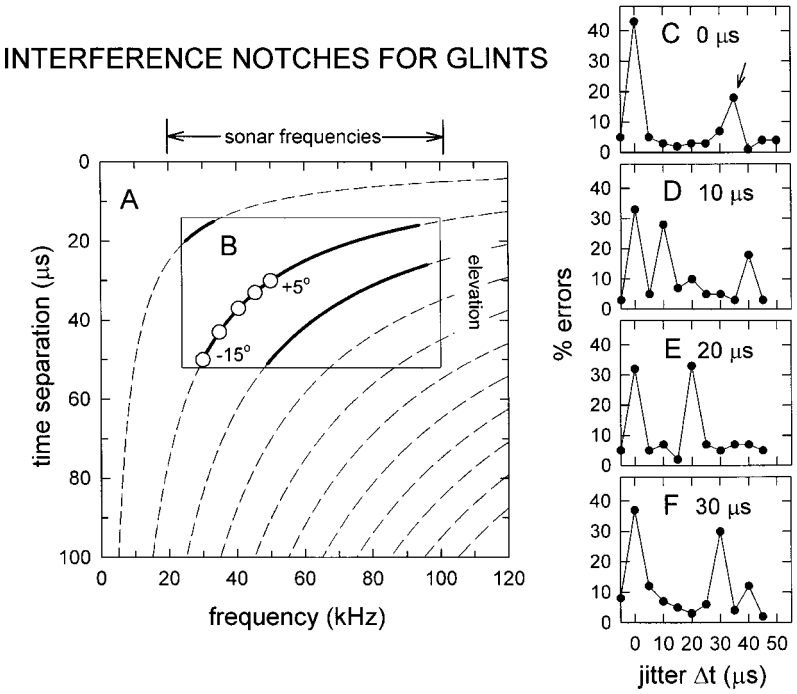

FIG. 1. (a) Family of curves tracing the relation between the time separation of two overlapping echoes in μs and the frequencies of interference notches (dashed curves). Counting the lines from left to right, they correspond to $n=0,1,2,...,10,11$ in Eq. (1). (b) Inset showing relation between sound-source elevation and frequencies of interference notches (solid curves superimposed on dashed curves) in the bat's external-ear transfer function (data-points from $+5$ to -15 degrees from Fig. 2). (c) Percentage errors obtained from a big brown bat in the jittered echo experiment with single-glint replicas of the broadcast for simulated echoes *a* and *b* [Simmons *et al.*, 1990b; see also Figs. 4(b), (e), and (h)]. The secondary error peak in the curve (arrow) at 35 μs is the focus of the present experiments. (d)–(f) Percentage errors obtained from the same bat in the jittered echo experiment with overlapping two-glint replicas of the broadcast for simulated echo *a* at time separations of 10, 20, or 30 μs (Simmons, 1993). Error peak at 0 μs corresponds to the arrival-time of simulated echoes from the first glint, while peaks at 10 μs (d), 20 μs (e), or 30 μs (f) correspond to the arrival-time of simulated echoes from the second glint.

located at odd-harmonic frequencies (f_n, in ratios of 1,3,5...) given by Eq. (1):

$$f_n=(2n+1)/2t_s, \quad \text{where} \quad n=0,1,2,3,\ldots. \tag{1}$$

Figure 1(a) plots the frequencies of interference notches for echo time separations from 0 to 100 μs. As delay separation increases (downward on vertical axis), the frequencies of particular notches become lower (leftward on horizontal axis), and the frequency spacing of neighboring notches becomes smaller (frequency spacing is the reciprocal of the time separation). For example, at a time separation of 10 μs there is just one notch at 50 kHz, but at a time separation of 20 μs there are two notches at 25 and 75 kHz, and at a time separation of 40 μs there are numerous notches at 12.5, 37.5, 62.5, 87.5, and 112.5 kHz. The big brown bat can directly detect only those notches that are included in its sonar frequencies [top of Fig. 1(a)].

One interpretation of Fig. 1(a) is that interference notches provide useful timbrelike ''spectral coloration'' to echoes from complex objects (Neuweiler, 2000; Schmidt, 1992). FM bats are capable of discriminating between targets of different shape or texture whose echoes differ in their interference spectra (Bradbury, 1970; Griffin, 1967; Habersetzer and Vogler, 1983; Schmidt, 1988; Simmons *et al.*, 1974). However, consideration of the acoustic origin for this spectral coloration (see Simmons and Chen, 1989) has raised the possibility that FM bats might perceive not merely the coloration but instead the time-separation between overlapping reflections—that is, the glints themselves (Simmons, 1980). Several different psychophysical experiments have demonstrated unequivocally that the big brown bat indeed does perceive and, crucially, *remember* the arrival-times of each of the broadcast replicas embedded in the compound reflection from multiple glints. In an ordinary echo-delay discrimination procedure, big brown bats remember the delay for both the first and the second of two echoes only 100 μs apart (Simmons *et al.*, 1990a). In a more sensitive procedure employing jittered echoes, bats remember the delays of both the first and the second echoes at separations of 10, 20, and 30 μs (Saillant *et al.*, 1993; Simmons, 1993). These separations are all well inside the 300–400 μs integration-time. Tests to determine the threshold for two-point resolution of echoes reveal that the limit is about 2 μs (Simmons *et al.*, 1998).

Figures 1(c)–(f) illustrate the performance of a representative big brown bat in a jittered-echo task where the bat is rewarded for detecting the presence of changes in the arrival-time of alternating echoes (Simmons, 1993; Simmons *et al.*, 1990b). The curves show the percentage errors made by the bat as a function of the size of the time jitter between alternating echoes. In Fig. 1(c), the stimuli consist of a single electronically delivered echo for each of the bat's broadcasts, and this single echo shifts in delay back and forth from one broadcast to the next. If these jittering echoes really do differ in delay, the bat detects the jitter, performing at only a few percent errors. However, if the jitter is zero, the bat's performance is at chance ($\sim$50% errors). In Fig. 1(d), one of the two jittering stimuli consists of *two* echoes at delays separated by 10 μs, while the other consists of only one echo. This double echo simulates two target glints and alternates with the single echo in the jitter task. The bat's performance curve in Fig. 1(d) has two peaks, one at zero and one at 10 μs, indicating that the bat remembered both of these delay values when comparing the double and single jittering stimuli. In Fig. 1(e), the double echoes are separated by 20 μs, and there are two error peaks separated by 20 μs. In Fig. 1(f), the double echoes are separated by 30 μs, and there are two error peaks separated by 30 μs.

Because the 10–30 μs delay separations in Figs. 1(d)–(f) are considerably shorter than the integration-time of 300–400 μs, any information about them would have been trans-

posed from the dimension of delay itself into the peak-and-notch pattern along the frequency axis [Fig. 1(a)] during *convolution* of the FM sounds with the integration-time of the auditory filters. The bat's ability to recover numerical delay estimates for both echoes requires *deconvolution* to take place subsequent to formation of auditory spectrograms by the inner ear. [Figure 1(a) illustrates deconvolution by determining the correct time position for some specific horizontal slice of the plot given only the locations of the notches in frequency.] This cascade of convolution and deconvolution has been modeled as spectrogram correlation and transformation (SCAT; Saillant *et al.*, 1993). The SCAT process is the first large-scale computational model of biosonar to use a time-frequency representation extending all the way from the acoustic signals to perception, while incorporating critical aspects of auditory coding (Simmons *et al.*, 1992, 1996). It goes beyond processing of single echoes to consider the formation of delay-axis images for multiple-echo ''scenes,'' an aspect of echolocation that has begun to receive attention (Moss and Surlykke, 2001; Simmons *et al.*, 1995). Both coherent and noncoherent versions of SCAT have been developed for evaluation against the performance of bats in experiments such as those illustrated in Figs. 1(c)–(f) (Saillant, 1995), and several important advances towards understanding echolocation have been made independently by several groups using the model (e.g., Matsuo *et al.*, 2001; Peremans and Hallam, 1998). One of these advances directly affects the experiments described here.

In the jitter performance curves there usually is a third error peak in the region of 35 μs [arrow in Fig. 1(c)] that does not correspond to one of the nominal electronic delays. This additional peak is the focus of the work we report here. It was discovered in the first jitter experiment using analog delay lines (Simmons, 1979) and confirmed in new experiments using digital delay lines (Simmons *et al.*, 1990b). Because the time separation of the peak at zero and the additional peak at 35 μs corresponds approximately to the spacing of the central peak and the first side-peak in the cross-correlation function of *Eptesicus* biosonar sounds with echoes (Saillant *et al.*, 1993; Simmons, 1979), it was initially taken to represent the bat's perception of this side-peak and, thus, of the crosscorrelation function itself. In effect, the additional peak at 35 μs circumstantially appeared to represent the bat's perception of the phase of echoes relative to broadcasts. This conclusion stirred much controversy because ''the mammalian'' auditory system is widely assumed to be insensitive to stimulus phase for single-frequency stimuli above a few kiloHertz (Beedholm and Mohl, 1998; Menne and Hackbarth, 1986; Pollak, 1993; Schnitzler *et al.*, 1985). The controversy persisted even though the phase of wideband FM signals is analytically very different from the phase of single-frequency stimuli (Simmons, 1980). Coding of FM phase requires merely that the latency jitter of neurons registering the timing of ultrasonic frequencies in FM sweeps be smaller than the period at some frequencies, a condition satisfied in existing neurophysiological data from the auditory brainstem (Haplea *et al.*, 1994; see Casseday and Covey, 1995). To address issues raised in this controversy, less circumstantial tests for phase sensitivity were designed and incorporated into new jitter experiments (Moss and Simmons, 1993; Simmons and Grinnell, 1988; Simmons *et al.*, 1990b), and the results demonstrated that big brown bats perceive delay with information conveyed by the phase of echoes. Once the secondary error peak at 35 μs no longer served as the evidence for the bat's perception of echo phase, the experiments reported here were designed to identify whether there might be another source of this peak.

Interference between overlapping reflections from multiple glints is not the only way that spectral notches are introduced into echoes—the bat's external ear creates notches as echoes pass down through its structures to the eardrum. The acoustic effects of the big brown bat's external ear on sound reception (Jen and Chen, 1988; Wotton *et al.*, 1995, 1997) are much like the effects observed in humans (Asano *et al.*, 1990; Batteau, 1967; Blauert, 1983; Butler and Belendiuk, 1977; Djupesland and Zwislocki, 1973; Fisher and Freedman, 1968; Flynn and Elliott, 1965; Hebrank and Wright, 1974; Hiranaka and Yamasaki, 1983; Middlebrooks, 1992; Middlebrooks and Green, 1991; Shaw, 1982; Shaw and Teranishi, 1968; Wightman and Kistler, 1989; Wright *et al.*, 1974), in cats (Calford and Pettigrew, 1984; Musicant *et al.*, 1990; Phillips *et al.*, 1982; Rice *et al.*, 1992), in guinea pigs (Carlile and Pettigrew, 1987), and in ferrets (Carlile, 1990). In each case, the location and strength of a well-defined peak-and-notch pattern in the spectrum of sounds reaching the eardrum depends on the elevation of the sound source. The primary difference between bats and other mammals is in the *scale* of these effects—the frequencies at which the major directional effects occur are considerably higher in the big brown bat (at 25–90 kHz) than in humans (at 6–12 kHz) or cats (at 8–18 kHz), which is roughly in keeping with the size differences of the ears in these species (bats$<$cats$<$humans; see Guppy and Coles, 1988; Simmons, 1982). Figure 1(b) [inset to Fig. 1(a)] shows the approximate frequencies of notches in the directional transfer function of the big brown bat's external ear as thicker solid lines superimposed on the thinner dashed lines of Fig. 1(a) (Wotton *et al.*, 1995, 1997). Two prominent external-ear notches appear over the bat's sonar frequencies [arrow at top of Fig. 1(a)]. They shift together in frequency according to the elevation of the sound source. On average, they correspond to the placement of second- and third-order [$n=1$ and 2 in Eq. (1)] interference notches from time separations of about 15 to 50 μs [superimposition of solid and dashed lines in Figs. 1(a) and (b)].

The measurements of external-ear notches plotted in Fig. 1(b) were made acoustically by placing a microphone at the location of the eardrum in a detached external-ear preparation (Wotton *et al.*, 1995). Behavioral measurements have also been made of the frequency of external-ear notches in echoes delivered to the bat from different elevations. Big brown bats were trained to discriminate between electronically generated echoes with a notch placed in their spectrum at a frequency of 30, 35, 40, 45, or 50 kHz and echoes without such a notch (Wotton *et al.*, 1996). These echoes were delivered to the bat from loudspeakers placed at elevations from -20 to $+20$ degrees (in 5-degree steps). When the frequency of the external-ear notch at one particular el-

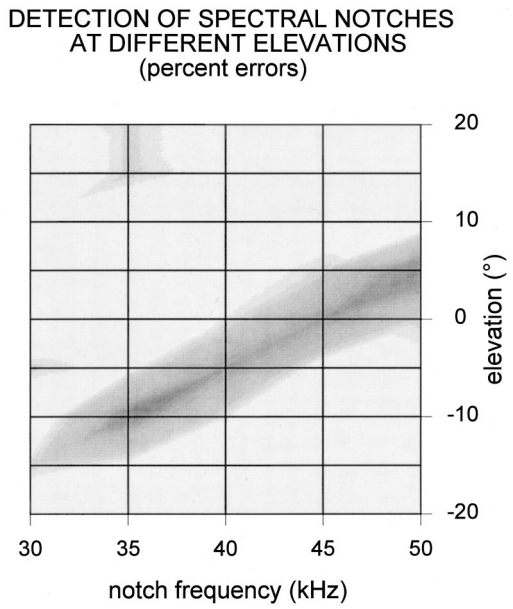

FIG. 2. Surface plot of mean percentage errors made by two big brown bats in experiments on detection of a spectral notch at 30, 35, 40, 45, or 50 kHz in artificial echoes delivered from elevations of −20 to +20 degrees (Wotton *et al.*, 1996). Darkest shade shows highest errors; lightest shade shows lowest errors. The sloping shaded region traces the frequencies at which masking shows that the bats perceive the external-ear notch for different elevations.

evation corresponded to the frequency of the stimulus notch introduced electronically, the bats failed to detect the echoes that had the electronic notch because the external-ear notch masked its presence. Figure 2 shows the mean performance of two bats as the percentage of errors achieved for different electronic notch frequencies and elevations (shaded from white at low errors to dark gray at high errors). The diagonal sloping band of poor performance in Fig. 2 (darkest shading) traces the perceived frequency of the external-ear notch at different elevations from its masking effect on the electronic notches. These frequencies have been transposed onto Fig. 1(b) as the five data points (open circles labeled +5 to −15 degrees) showing external-ear notches in the coordinates of the glint-interference plot of Fig. 1(a).

The question we address here is whether the spectral notches introduced by the bat's external ear are caught up in the deconvolution process, along with the interference notches created by the glint structure of the target, and transformed into an estimate of an extraneous time separation that ought to be dependent on the elevation of the target. The curves and data-points in Figs. 1(a) and (b) predict that this delay estimate should be somewhere in the region of 30 to 50 μs. Does the secondary error peak at 35 μs in Fig. 1(c) (arrow) come from notches in the frequency response of the bat's external ears? To test this hypothesis, in experiment 1 the jitter procedure was modified to allow for vertical movement of the loudspeakers that delivered the artificial echoes. If the location of the behavioral error peak at 35 μs actually does originate in the external ear's response, this peak should move to shorter times of 25–30 μs for loudspeaker elevations that are 15 degrees higher because the external-ear notches move to higher frequencies (Fig. 2). Conversely, this error peak should move to longer times of 40–45 μs for loudspeaker elevations that are 15 degrees lower because the notches move to lower frequencies. Two more experiments were done to assess the relation between external-ear notches and notches introduced into echoes by the target, prior to reception by the external ear. In experiment 1, the echoes returned electronically to the bat contained frequencies from 20 to 85 kHz, nearly the full bandwidth of the bat's FM broadcasts. In experiment 2, the echoes were filtered to a narrow region around 55 kHz, which excludes frequencies of 20–50 kHz and 60–100 kHz where external-ear notches are present. In experiment 3, the echoes were filtered to a different narrow frequency band around 45 kHz, which preserves frequencies of 40–50 kHz where the external-ear notches *do* occur.

II. METHOD

The experiments described here were carried out using three bats of the species *Eptesicus fuscus* (see Kurta and Baker, 1990), collected in houses in the State of Rhode Island and Providence Plantations (identified as bats 3, 5, and 6 in Simmons *et al.*, 1990b). The bats were trained in a two-choice discrimination task (2AFC; see Moss and Schnitzler, 1995) to distinguish between sonar echoes that *jittered* or *alternated* in delay and echoes that were *stationary* in delay. Stimulus echoes were produced by an electronic target simulator incorporated into the two-choice behavioral procedure. Figure 3 shows the psychophysical paradigm for jittering-echo experiments (Simmons *et al.*, 1990b). Each bat was trained to sit on an elevated, Y-shaped platform and broadcast echolocation sounds towards the left and right to find an electronically simulated target that appeared to alternate in target range from one sonar emission to the next. This jittering target (represented by echoes *a* and *b* in Fig. 3) was presented either on the bat's left or the bat's right in the two-choice task, with the stationary target (*c*) presented on the other side. The bat was rewarded with a piece of a mealworm offered in forceps for every correct response, which was to move forward towards to the jittering target (arrow). Responses to the stationary (nonjittering) stimulus were not rewarded, and a brief time-out period was introduced before proceeding to the next trial.

The target simulator is described in detail elsewhere, together with various procedures developed to calibrate it and eliminate stimulus artifacts that might interfere with the bat's use of echo delay as the chief cue for the discrimination (Simmons, 1993; Simmons *et al.*, 1990b). These sources also describe the use of amplitude-latency trading to demonstrate that the curve in Fig. 1(c) represents perceived values of delay that depend on the latencies of neural responses rather than spurious performance not involving perception of delay itself (Beedholm and Mohl, 1998; Menne *et al.*, 1989; Pollak, 1993; Schnitzler *et al.*, 1985). The experiments reported here involve only the use of digital electronic delays.

The jittering echoes (*a* alternating with *b* in Fig. 3) and stationary echoes (*c* alternating with *c*) were simulated electronically by picking up the bat's sonar transmissions with two Brüel & Kjaer Model 4138 condenser microphones (*m* in Fig. 3), amplifying and filtering the signals with Rockland

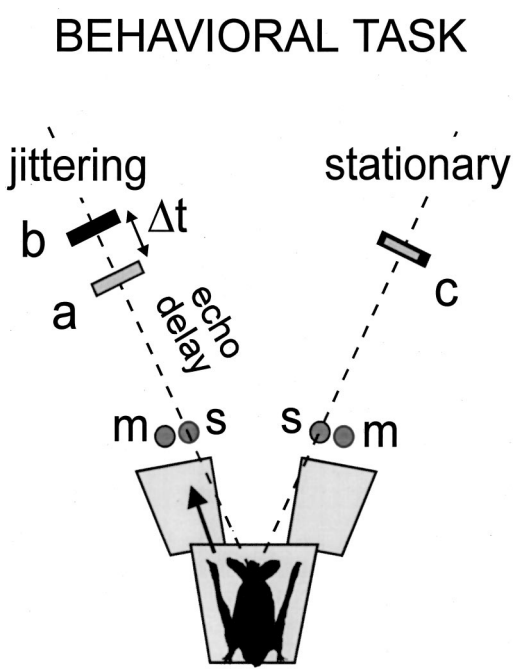

FIG. 3. Diagram of the jittered-echo procedure and the two-choice psychophysical method for determining the shape of the bat's echo-delay images in terms of the delays the images are perceived to contain (Simmons *et al.*, 1990b). The bat sits on the Y-shaped platform, broadcasts sonar sounds into microphones (m), whose output signals are delayed and then returned to the bat as simulated echoes from one of the two loudspeakers (s) according to which microphone the bat aims its sounds towards. If delivered from the jittering channel, the delays of successive echoes alternate between two values (a, b); if from the stationary channel, the delays are fixed (c).

Model 442 variable bandpass filters normally set to a passband from 15 to 100 kHz, and then returning these recorded sounds back to the bat from two RCA Type 112343 electrostatic loudspeakers (s). The echoes produced by this means were timed to arrive at appropriate delays following the bat's transmissions to mimic echoes from a target at a specific distance. The microphones (m) and loudspeakers (s) were about 20 cm from the bat's observing position on the Y-shaped platform, so the acoustic travel time from the bat to the microphones and then back from the loudspeakers was about 1.16 ms. The total delay of echoes was regulated by adding an electronic delay to this propagation delay, assuming that each centimeter of simulated target range would require 58 μs more delay. In the experiments, the overall delay of echoes from the simulated stationary target (c) was fixed 3.275 ms, which corresponds to a distance of about 56 cm. The jittering echoes (a and b) were presented at delays that were centered on 3.275 ms but were shifted by $\pm$ half the jitter interval ($\pm\Delta t/2$) around that value (Simmons *et al.*, 1990b). The stimuli are described later in terms of the size of the jitter interval because this is the principal independent variable being manipulated, but the absolute echo delays used to achieve different amounts of jitter always were arranged around 3.275 ms.

The delay of stimulus echoes was adjusted electronically using digital delay devices (*delay* in Fig. 3) that sampled the bat's signals at 730 kHz (12-bit accuracy) and then stored them for a preset time in a buffer memory before playing them back through a digital-to-analog converter. Because the numerical value of delay depends only on digital control of the address of the word being read out from the memory through the D-to-A converter, no delay-dependent changes in the spectrum of echoes were introduced by the digital delay lines, so no apparatus-related artifacts are suspected (see Beedholm and Mohl, 1998). The left and right channels of the simulator each contained two digital programmable delay lines for presenting echoes at any desired times from 0 to about 41 ms following emissions, and associated electronic components were used to switch one or another of these delay-lines on for each of the bat's broadcasts (Simmons *et al.*, 1990b). The critical feature of these jittered-echo experiments is that this switching system delivered only *one electronic echo to the bat for each sonar broadcast*. Depending on whether the left or right microphone received the stronger signal for any of the bat's broadcasts, only the corresponding left or right delay system and loudspeaker was activated to deliver an echo. Succcessive broadcasts yielded echoes only from the channel the bat aimed its sounds towards. This contingency requires the bat to remember the delay of one echo for comparison with the delay of the next to detect whether jitter is present. The jittering stimulus was created by setting the delays of the echoes for successive broadcasts (a, b) so that they alternated back and forth over the jitter interval (Δt). The stationary stimulus (c) was created by setting the delays so that successive echoes always had the same delay. Both the stationary and the jittering stimuli were generated by alternately switching the bat's broadcasts between delay values created by two different delay-lines; whether the stimuli jittered depended only the values of delay actually selected digitally, not on whether the signal passed through any one piece of hardware.

The frequency response for the left and right channels of the target simulator was limited by the loudspeakers to a range from 20 kHz to about 85 kHz (Simmons *et al.*, 1990b), but it could be further restricted to a narrower range by resetting the bandpass filters to any desired high- and lowpass cut-off frequencies. The highest frequency present in the sounds reaching the bat's ears was about 85 kHz, for a Nyquist sampling frequency of 170 kHz. The actual digital sampling frequency of the apparatus was about 730 kHz, which is much higher than the Nyquist frequency to be sure that the time-series sound-pressure waveform of simulated sonar echoes would be faithfully reproduced in the analog signals delivered to the loudspeakers. (Whereas sampling at the Nyquist frequency is the minimum adequate to determine the bat signal's spectrum, sampling at rates several times the Nyquist frequency is necessary to reproduce its cycle-by-cycle waveform.)

At the beginning of the jitter experiment, the jitter interval (Δt) was set to a value in the range of 50 to 70 μs, which is easy for bats to detect—they normally achieve about 90%–95% correct responses (Simmons, 1979; Simmons *et al.*, 1990b). The size of this interval then was reduced gradually from 50–70 μs to 0 μs in steps of approximately 5 μs. On two occasions, a smaller delay step-size of 2.5 μs was used to interpose a data-point between two 5-μs points because the performance of the bat suggested that a smaller interval would better capture an intervening peak in perfor-

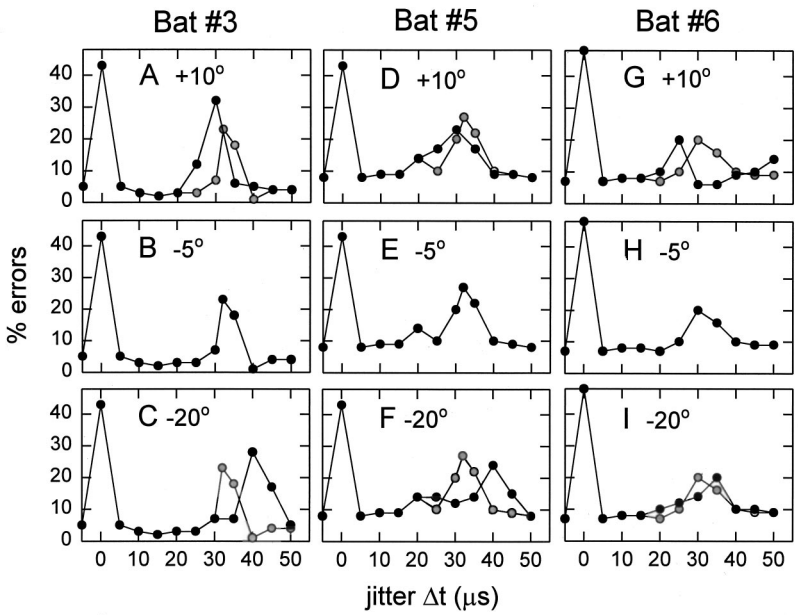

FIG. 4. *Results of experiment 1*: Graphs showing the jittering-echo discrimination performance (percentage errors; black lines, black circles) of three big brown bats (bats 3, 5, and 6) with loudspeakers at elevations of $+10$, -5, and -20 degrees. The curves from the middle plots (b, e, h) showing performance at -5 degrees are repeated (gray lines, gray circles) in the upper (a, d, g) and lower (c, f, i) plots to facilitate comparisons. The bats all perform near chance (50%) when the jittering echoes have the same delay, $\Delta t = 0$ μs, and they also all have a secondary region of poor performance at $\Delta t = 25$ to 45 μs. For all three bats the location of this secondary peak depends on the elevation of the loudspeakers.

mance that was straddled by the 5-μs interval. The 5-μs step size was the largest interval used because it is shorter than the Nyquist sampling interval for the stimuli. The data from the jitter discrimination experiments consist of the mean performance of each bat on 40 to 60 trials conducted at each jitter interval before moving to the next smaller interval in the series. To display the results, the percentage of correct responses or errors for each bat was graphed as a function of the size of the jitter interval (Δt) from 50–70 μs down to 0 μs in steps of 5 μs. During the course of this decreasing series of jitter intervals, the bat's performance eventually reaches chance, about 50% correct responses, when the jitter interval is zero. However, the level of performance does not decline monotonically to chance; instead it passes through a region of poor performance around 35 μs [arrow in Fig. 1(c)] and then recovers again for jitter intervals from 25 μs down to very near 0 μs.

To assess the possible role of the external ear in causing the bat to make errors at certain jitter intervals, the positions of the loudspeakers on the bat's left and right (s in Fig. 3) were changed by ± 15 degrees in elevation relative to the bat. The Y-shaped platform used for two-choice tests was tilted downward at an angle of 15–20 degrees to accommodate the bat's inclined stance on its thumbs and feet with the wings folded. While the bat stood on the platform for its response on each trial, its head and body were not parallel to the plane of the platform but were held at an angle about 10 degrees higher, as estimated from photographs, which left the eye–nostril plane of the bat's head still tilted about 5 degrees below the horizontal. The loudspeakers used in the basic jitter experiments (Simmons *et al.*, 1990b) protruded 10 degrees above the plane of the platform, and the bat's posture and movements kept the eye–nostril plane about 5 degrees above the loudspeakers, which placed the microphones roughly in line with the bat's open mouth. The normal position of the loudspeakers thus was at an elevation of about -5 degrees relative to the bat's head.

III. EXPERIMENT 1

A. Hypothesis

Experiment 1 explicitly tested the possibility that the region of poor performance around 35 μs in Fig. 1(c) (arrow) is elevation dependent by repeated the basic jitter experiment for jitter values in this region (20–50 μs depending on the bat) using different elevations of the loudspeakers (s). The essential experimental manipulation was to change the position of these loudspeakers by moving them either 15 degrees higher or 15 degrees lower than normal. The three loudspeaker positions were designated by their elevations as $+10$, -5, and -20 degrees relative to the bat's eye–nostril plane. It is unlikely that serial order effects are present because the three bats were run at different times interspersed among different jitter experiments that measured acuity in the submicrosecond range, performance for echo phase shifts, or acuity as a function of changes in echo bandwidth controlled by the bandpass filters in the microphone circuit (Simmons *et al.*, 1990b).

B. Results

Three *Eptesicus* (3, 5, and 6) completed experiment 1 with the loudspeakers moved upward or downward by 15 degrees from their normal position at -5 degrees relative to the bat's head in its posture on the platform. Figure 4 shows the results for each bat at each elevation of the loudspeakers. The *middle* row of graphs [Figs. 5(b), (e), and (h); black lines, black circles] shows the basic jitter discrimination performance for each of these bats at loudspeaker positions of -5 degrees elevation (see Simmons *et al.*, 1990b). The curve for each bat shows errors in the range of only 5%–10% for jitter intervals (Δt) from 50 μs down to 40 μs (performance was also this good for jitter intervals >50 μs), with a region of poorer performance of 20%–30% errors at 30 to 35 μs, and good performance again at jitter intervals from 25 μs down to only 5 μs. At 0 μs, performance was

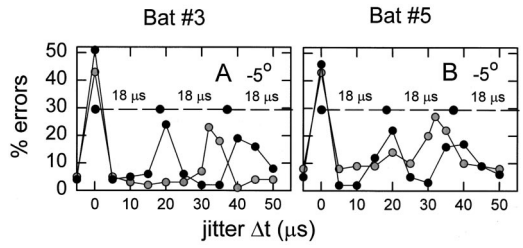

FIG. 5. *Results of experiment 2*: Graphs (a, b) showing the jittering-echo discrimination performance (percentage errors; black lines, black circles) of two big brown bats (bats 3 and 5) with loudspeakers at an elevation of −5 degrees and echoes restricted to around 55 kHz. The bat's performance at −5-degree elevation with the full bandwidth of echoes [gray lines, gray circles, from Figs. 4(b) and (e)] is shown to facilitate comparisons. Both bats shift the pattern of error peaks from 0 and 30–35 μs (gray) to 0, 20, and 35–40 μs (black).

always near chance, or 50%, thus forming the primary peak in the error curve. Each bat also exhibited a second, lower peak in the error curve at 30–35 μs when the loudspeaker was at an elevation of −5 degrees relative to its head.

The *top* row of graphs [Figs. 4(a), (d), and (g); black lines, black circles] shows the change in performance of these same three bats in the region of the secondary error peak when the loudspeakers were moved up to an elevation of +10 degrees. (For each bat, the gray lines with gray circles repeat the data from −5 degrees elevation to facilitate comparison of results by eye.) There is a shift in the location of the secondary region of poor performance to shorter time values, from 30–35 μs to 25–30 μs. The *bottom* row of graphs [Figs. 4(c), (f), and (i); black lines, black circles] shows the performance of the bats when the loudspeakers were moved down to an elevation of −20 degrees. (Again, the gray lines with gray circles repeat the data from −5 degrees elevation.) Here there is a shift in the location of the secondary region of poor performance to longer time values, from 30–35 μs to 35–45 μs. For all three bats, the secondary error peak in the performance curve marked by the arrow in Fig. 1(c) shifted to shorter time values for the higher loudspeaker elevation and longer time values for the lower elevation. Pooling data from all three bats, the exchange of the peak in the error curves between locations over a span of 5 μs from −5 to +10 degrees and again from −5 to −20 degrees is statistically significant using the binominal distribution for 2AFC data.

C. Discussion

For each bat, the location of the secondary error peak in Fig. 4 depends systematically on the vertical position of the loudspeakers. In each case, the peak was shifted by about 5 μs in the direction predicted from the external-ear transfer function (Fig. 2). The higher external-ear notch frequency associated with higher elevations (Fig. 1) leads to a shorter time value, while the lower notch frequency at lower elevations leads to a longer time value. Moreover, the locations of the error peaks along the time axis in Fig. 4 are approximately where they would be expected from reading the time values associated with the five data-points on the interference-notch graph in Figs. 1(a) and (b). Depending on elevation, the expected range of time values is roughly 30–50 μs from the vertical axis of Fig. 1(a), while the error peaks actually are located at values of 25–45 μs. To a first approximation, big brown bats appear to treat the notch in the external-ear transfer function at frequencies of 30–50 kHz as though it were a second-order interference notch in the echoes [$n=1$ in Eq. (1)], and they engage this notch in their deconvolution process (Saillant *et al.*, 1993; Simmons *et al.*, 1996) when they transform the time-frequency structure of echoes into remembered delays.

IV. EXPERIMENT 2

A. Hypothesis

The echoes used as stimuli in experiment 1 had almost the full bandwidth of the bat's FM biosonar sounds, limited only by the frequency response of the loudspeakers in the highest-frequency region (see Simmons *et al.*, 1990b). Echo frequencies extended from 20 kHz to about 85 kHz, which includes the frequencies of spectral notches produced by the external ear [Fig. 1(b)]. What happens to the bat's performance when the frequency range of the external-ear notches is deliberately removed from echoes prior to reception? In experiment 2, electronic echoes were restricted to the region of 55 kHz using the Rockland Model 442 variable bandpass filters already part of the microphone circuit. All echoes (*a*, *b*, and *c* in Fig. 3) were filtered identically and then increased in overall amplitude by 2 dB to compensate for the measured loss in signal strength at the 55-kHz center frequency of the passband due to the filters' characteristics. The narrow passband thus affected the jittering and stationary echoes alike. The filters gave 24-dB/oct rolloffs to yield 3-dB lowpass and highpass cutoffs at frequencies of about 50 and 60 kHz, respectively. Using these filter settings, the jitter experiment was carried out with the loudspeakers at the normal elevation of −5 degrees. This 55-kHz band is special because it excludes the frequency region around 40–45 kHz where the bat's most prominent external-ear notch occurs at a loudspeaker elevation of −5 degrees (see Fig. 2). In the absence of a recognizable external-ear notch at 40–45 kHz and also at frequencies above 60 kHz (because this notch region is obliterated from 55-kHz echoes, too), we hypothesized that the bat should perceive only those delay separations that satisfy the impulse response for band-limited echoes at 55 kHz. The jitter performance curve should contain multiple error peaks at a nominal spacing of approximately $1/55$ kHz$=18$ μs. In other respects, experiment 2 was conducted exactly as was experiment 1.

B. Results

Two of the bats (bats 3 and 5) went through experiment 2 with the loudspeakers at the normal elevation of −5 degrees. Figures 5(a) and (b) show both bats' performance in the 55-kHz band-limited condition (black lines, black circles) compared to performance with practically the full bandwidth of the bat's sounds [gray lines, gray circles; taken from Figs. 4(b) and (e), respectively]. [Data for bat 3 were given in Fig. 11 of Simmons *et al.* (1990b).] Consistently for both bats, the shape of the performance curve for

narrow-band 55-kHz echoes is different from that obtained in the same task with broadband echoes. In Fig. 5, instead of a main error peak at 0 μs and a single secondary error peak at 30–35 (gray), there is a main peak at 0 μs and secondary peaks located at 20 μs and 35–45 μs (black). Each peak is well defined, being surrounded by a low error rate on its flanks. These error peaks represent statistically significant departures from the low error rates prevailing at intermediate delays using the binomial distribution.

C. Discussion

When the bandwidth of echoes is restricted to 50–60 kHz, they simulate a periodic impulse response with a series of peaks at times of 0,18,36,54,... μs. The locations of these theoretical peaks are indicated in Figs. 5(a) and (b) by the horizontal dashed lines (with black circles at 18-μs separations). In these same plots, the jitter performance curves for the two bats in experiment 2 have multiple error peaks at 0, 20, and 35–40 μs. The bats' performance thus corresponds approximately to the simulated target impulse response. The elevation-dependent error peak, formerly located at about 35 μs for an elevation of -5 degrees, is no longer present, presumably because the external-ear notches that signify interference at a delay separation of 35 μs are no longer recognizable in the echoes due to the wholesale absence of frequencies below 50 kHz and above 60 kHz.

V. EXPERIMENT 3

A. Hypothesis

The echoes in experiment 2 were restricted to the region of 55 kHz to exclude frequencies from 20 to 50 kHz and from 60 to 100 kHz, thereby preventing echoes from containing the frequency regions most important for conveying external-ear notches. The echoes used in Experiment 3 were band-limited, too, but this time to a frequency of 40 kHz. In this case the Rockland filters gave 24-dB/octave rolloffs with 3-dB lowpass and highpass cutoff points at about 35 and 45 kHz, respectively. This passband gave continuous coverage of frequencies where the bat's most prominent external-ear notch occurs at loudspeaker elevations of 0° to $-10°$ (Fig. 2), and appreciable coverage was present over a somewhat wider band of frequencies occupied by the notch at elevations from at least $+5°$ to $-15°$. Again, in experiment 3, all echoes (*a*, *b*, and *c* in Fig. 3) were filtered identically and then increased in overall amplitude by 2 dB to compensate for the measured loss in signal strength at the 40-kHz center frequency. The target impulse response simulated by these echoes has an average period of 1/40 kHz$=25$ μs, with a main peak at 0 μs followed by a series of side peaks at 0,25,50,75... μs.

Figure 6 illustrates our hypothesis of what would be expected in experiment 3 from using the 40-kHz narrow-band echoes in the jitter experiment. If the bat's performance curve is determined by the target impulse response, we would expect to see a series of error peaks at 0, 25, and 50 μs on the horizontal axis of Fig. 7 (horizontal dashed line with three black circles separated by 25-μs intervals at the top of the graph). The black curve in Fig. 6 shows the approximate percentage errors that a bat should achieve in experiment 3. Besides the three error peaks at 0, 25, and 50 μs, this solid curve has three additional error peaks representing the delays derived from spectral notches introduced by the external ear. At the normal loudspeaker elevation of -5 degrees, the expected external-ear delay should be 30–35 μs, based on the single secondary error peak at 30 to 35 μs in Figs. 4(b), (e), and (h). In experiment 3, this single secondary peak should be replaced by a series of secondary peaks separated by 25-μs intervals and offset to the right of zero by 30–35 μs (horizontal dashed line with three black circles at the middle of Fig. 6). These additional peaks should shadow the main peaks and appear to follow them 10 μs later, at 10, 25, and 60 μs on the time axis of Fig. 6. (The real offset of the external-ear peaks is 35 μs, but each external-ear peak winds up only 10 μs later than the nearest peak from the simulated target's impulse response.) Knowing that 55-kHz echoes leads to error peaks at 0, 20, and 35–40 μs in experiment 2, the prediction of three error peaks at 0, 25, and 50 μs in experiment 3 should come as no surprise. However, the bat's external ear contributes three additional predicted error peaks at 10, 35, and 60 μs, which is a more complicated result. If these additional peaks do occur in experiment 3 for a loudspeaker elevation of -5 degrees (black curve in Fig. 6), then a test of whether they originate in external-ear notches would be to repeat the 40-kHz experiment at a different loudspeaker elevation, just as was done in experiment 1 for broadband echoes. The gray curve in Fig. 6 shows expected results for the 40-kHz echoes with the loudspeaker at an elevation of -20 degrees instead of -5 degrees. The target-related error peaks in the -5 degrees hypothetical performance curve at 0, 25, and 50 μs (black curve) should remain in the same locations for an elevation of -20 degrees (gray curve), but the external-ear peaks at

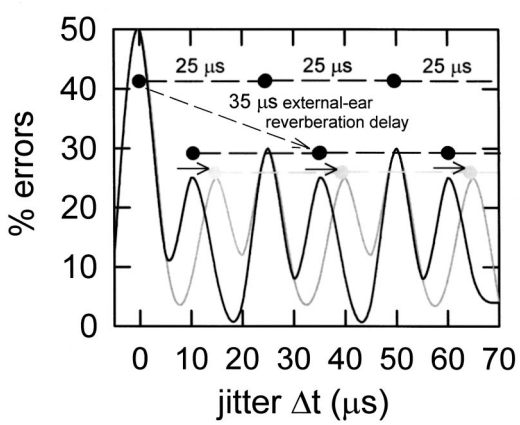

FIG. 6. Graph showing the jitter discrimination performance (percentage errors) expected to occur if the simulated echoes are filtered to a narrow band around 40 kHz (3-dB points at 35 and 45 kHz) for loudspeaker elevations of -5 degrees (black curve) and -20 degrees (gray curve). The basis for this prediction is that the simulated target impulse response contains a series of peaks separated by 25 μs (horizontal dashed line with black circles at top of plot) plus an added series of peaks shifted to the right by the external-ear reverberation delay of 35 μs, and still separated by 25 μs (horizontal dashed line with black circles at middle of plot). Experiment 3 tests whether the bat's performance contains this configuration of peaks, and whether the peaks corresponding to the external-ear reverberation change with loudspeaker elevation (black curve *versus* gray curve).

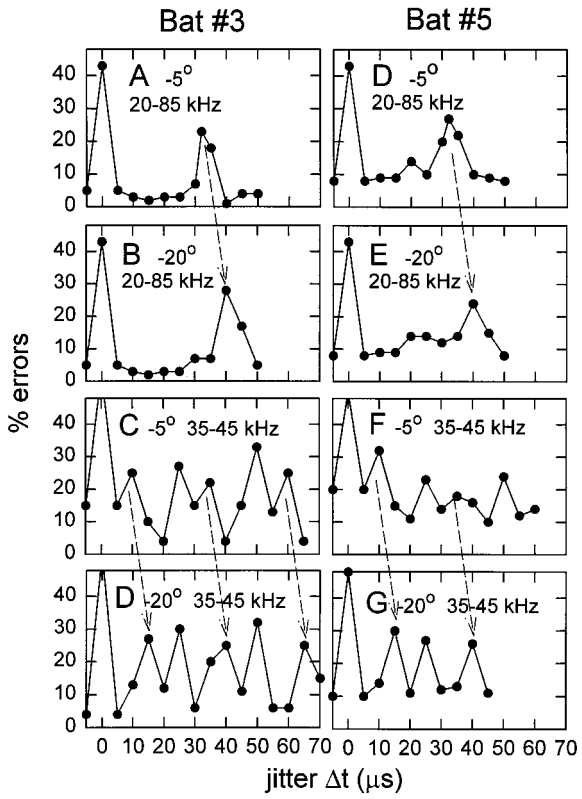

FIG. 7. *Results of experiment 3*: Graphs showing the jittering-echo discrimination performance (percentage errors; black lines, black circles) of two big brown bats (bats 3 and 5) with loudspeakers at elevations of −5 and −20 degrees and echoes restricted to around 40 kHz. The top two rows of plots (a, b and d, e) show performance for the full bandwidth of echoes (20–85 kHz) from experiment 1 [Figs. 4(b), (c), (e), and (f)] for comparison. The bottom two rows of plots (c, d, f, g) show performance for the narrow-band echoes (35–45 kHz) in experiment 3. The bats perform near chance (50%) when the jittering echoes (a, b) have the same delay, $\Delta t = 0$ μs, and, when the loudspeakers are at −5 degrees (c, f), they also have multiple secondary peaks of poor performance at $\Delta t = 10$, 25, 35, 50, and 60 μs. When the loudspeakers are at −20 degrees (d, g), the bats also have multiple secondary peaks of poor performance at $\Delta t = 15$, 25, 40, 50, and 65 μs. The series of peaks at 0, 25, and 50 μs do not shift with loudspeaker elevation, while the series of peaks at 10, 35, and 60 μs shift to the right by 5 μs (sloping arrows in c, d and f, g) when the loudspeakers are moved 15° down. The single secondary error peak in experiment 1 also shifts by 5 μs (sloping arrow in a, b and d, e) when the loudspeakers are moved 15 degrees down.

10, 35, and 60 μs should move to the right by about 5 μs to locations of 15, 40, and 65 μs (gray curve; see short horizontal arrows in Fig. 6). This outcome is what would be expected if the external-ear delay increased from 35 to 40 μs, as it did in experiment 1. Experiment 3 was carried out with loudspeaker elevations of −5 and −20 degrees using echoes filtered to the 35–45-kHz frequency band and jitter intervals from 0 to 45–70 μs. In other respects, experiment 3 was conducted exactly as was experiment 1.

B. Results

Two of the bats (bats 3 and 5) completed experiment 3. One bat (bat 3) finished all trials at −5- and −20-degree loudspeaker elevations, while the other bat (bat 5) finished all trials at the −5-degree elevation and trials from 0 to 45 μs at the elevation of −20 degrees. Figure 7 shows the performance of bats 3 and 5 in experiment 3 at loudspeaker elevations of −5 degrees [Figs. 7(c) and (f)] and −20 degrees [Figs. 7(d) and (g)], for comparison with data from experiment 1 [Figs. 7(a, d) and (b, e)]. Consistently for both bats, the shape of the performance curve for 40-kHz narrow-band echoes at −5 degrees is different from the curve obtained in the same task with broadband echoes, and different, too, than the curve obtained for echoes band-limited to 55 kHz. Instead of a main error peak at 0 μs and a single secondary error peak at 30–35 μs (for the broadband echoes at an elevation of −5 degrees), there are multiple peaks located at 0, 10, 25, 35, 50, and 60 μs [Figs. 7(c) and (f)]. These peaks represent statistically significant departures from the low level of errors expected at locations away from 0 μs using the binomial distribution.

C. Discussion

When the bandwidth of echoes is restricted to 35–45 kHz, they simulate a periodic target impulse response with a series of peaks at times of 0,25,50,... μs. The locations of these theoretical peaks are indicated in Fig. 6 by the upper horizontal dashed line with black circles at 25-μs separations. Preserving the frequencies of the most prominent external-ear notch in these narrow-band echoes should lead to a complex impulse response for the stimuli at the bat's eardrum with additional peaks offset from the target's peaks by 35 μs. Their locations are indicated in Fig. 6 by the lower horizontal dashed line with black circles for external-ear reverberation delay. Comparing Figs. 7(a) and (d) with Figs. 7(c) and (f), the bats' performance curves for a loudspeaker elevation of −5 degrees change from one primary error peak at 0 μs plus a secondary peak at 30–35 μs for broadband echoes to a complex pattern of multiple error peaks at 0, 10, 25, 35, 50, and 60 μs for 40-kHz narrow-band echoes. This arrangement of peaks is consistent with the prediction (black curve in Fig. 6) that both the simulated target impulse response and the external-ear reverberation time should contribute to the shape of the jitter performance curve. Moreover, when the loudspeakers were moved from −5 degrees to an elevation of −20 degrees, the error peaks at 0, 25, and 50 μs remained in place [Figs. 7(d) and (g)] while the error peaks at 10, 40, and 60 μs each shifted to the right by about 5 μs to 15, 40, and 65 μs [following the sloping dashed arrows in Figs. 7(d) and (g)]. This new arrangement of peaks also is consistent with the prediction (black and gray curves in Fig. 6) that both the simulated target impulse response and the elevation-dependent external-ear reverberation time contribute to the shape of the jitter performance curve. Note that the movement of the three putative secondary external-ear error peaks in experiment 3 is the same as the movement of the single putative secondary external-ear error peak in experiment 1 (compare sloping arrows connecting the different plots in Fig. 7).

VI. CONCLUSIONS

The primary outcome of experiments 1–3 concerns the nature of the biosonar images perceived by big brown bats. Taken together, the results demonstrate that the notches in

the directional transfer function for the big brown bat's external ear are treated the same way as interference notches introduced into echoes by multiple reflections from the target. They are caught up in the SCAT deconvolution process that underlies wideband biosonar imaging and converted into numerical estimates for time separations. The bat's perception of delay estimates derived from the external ear's acoustic properties as well as from the target's glints confirms that the big brown bat's images correspond approximately to the impulse response of the target-range scene constructed from echoes reaching the eardrum (Simmons *et al.*, 1992; Simmons, 1989, 1996). Given the limitation on purely time-domain representation from the long integration-time of echo reception, we conclude that this impulse response arises from time-frequency SCAT computations carried out by the auditory nervous system (Saillant *et al.*, 1993; Sanderson and Simmons, 2000, 2002; Simmons *et al.*, 1996). Inasmuch as the perceived delays are manifested as error peaks in the performance curves from jittered-echo experiments, these curves are themselves plots of the impulse response of the stimuli, obtained by using the bat as a time-frequency processor.

The appearance of error peaks at approximately the predicted, elevation-dependent delay values of 25–50 μs in experiment 1 shows that perceived values of delay derived from the external-ear response can be expected to occur for bats echolocating in natural conditions, where they receive essentially the full bandwidth of echoes from targets at distances up to several meters. The failure of additional error peaks (besides those related to the target) to occur in experiment 2 with narrow-band echoes shows that their manifestation is tied to reception of frequencies containing external-ear notches. The reappearance of the elevation-dependent error peaks in experiment 3 shows that the narrow-band condition itself is not the reason for the disappearance of the peaks in experiment 2. Instead, their disappearance is due to removal of frequencies containing external-ear notches. The complicated result obtained in experiment 3 shows that each of the target-related delay estimates, derived from the timing and interference of replicas of the broadcast impinging on the external ears, comes to be associated with corresponding delay estimates that depend on the elevation of the target.

Because spectral notches in echoes have more than one source, they are ambiguous indicators of the acoustic environment to the bat. Echolocating big brown bats certainly are exposed to masking between elevation and perceived spectral features—they cannot detect a notch at a particular frequency in the spectrum of echoes if the sounds arrive from an elevation where the external-ear transfer function places its own notch at the same frequency (Wotton *et al.*, 1996; see Fig. 2). Convergence of both the target's glints and the external ears on the echo spectrum creates uncertainty about whether any particular spectral notch signifies information about the target's shape or about its elevation. However, during aerial pursuits FM bats do not exhibit any obvious deficits in the accuracy of vertical localization of airborne targets related to their shape (although careful observations might disclose them). Moreover, FM bats maneuver successfully through complex obstacle arrays (Schnitzler and Henson, 1980; Simmons *et al.*, 1995) or perform unexpectedly difficult tasks in nature (Simmons *et al.*, 2001) where there is great scope for multiple reflections to interfere with each other while simultaneously the external ears introduce notches into echoes according to elevation, so they might have developed methods for resolving ambiguous spectral cues, presumably by exploiting characteristics of their auditory representation of FM broadcasts and echoes.

The SCAT model of auditory processing in FM biosonar is a hybrid computational system that creates parallel/convergent time-domain and frequency-domain representations (Saillant, 1995; Saillant *et al.*, 1993). SCAT's parallel time and frequency representations offer computational advantages if information can be passed back and forth between the two domains during processing (Simmons *et al.*, 1992). The logic is that the time-domain (impulse response) and frequency-domain (spectral) representations are both multi-valued functions, but in certain instances each can be transformed into a single value of the other. For example, a series of spectral notches, which requires a whole sequence of frequency-amplitude coefficients for its description, often can be represented by a single time separation, assuming that the notches are created by interference [Fig. 1(a)]. In the course of a recent investigation aimed at improving the SCAT model, the potential ambiguity between interference notches and external-ear notches was directly addressed by exploiting back-and-forth convergences in the dual SCAT architecture to mitigate crosstalk between the target's glints and its elevation, at least for targets having a simple glint structure (Matsuo *et al.*, 2001). One way to resolve this ambiguity would be to block out a specific region of frequencies in echoes to be reserved for registering the elevation of targets from external-ear notch cues by ignoring notches at these frequencies as far as target reconstruction is concerned. Target impulse responses derived from SCAT would be incomplete due to the deliberate exclusion of notches at these ''forbidden'' frequencies, but there would be reduced confusion between target shape and elevation. This recent study achieved an ingenious solution by exchanging information between the time- and frequency-domains in several stages (see especially Fig. 5 in Matsuo *et al.*, 2001)—(1) blocking out echo frequencies associated with the most prominent external-ear notch (see Fig. 2), (2) estimating the target impulse response from the pattern of notches in the remainder of the echo spectrum, (3) sharpening the peak of this incomplete impulse response and transforming it back into the frequency domain to estimate only the target's contribution to the spectrum, including the forbidden frequencies, (4) transforming this purified target-related spectrum back into the time domain, and (5) subtracting the purified target impulse response from the more complex impulse response obtained from the original echo spectrum before blocking, which includes both the target and the external ear's effects, to leave a residue that isolates the external ear's effects. Otherwise, the most conservative conclusion is that the results obtained in experiments 1–3 just shift the locus of target versus external-ear ambiguity from the frequency domain, where common practice finds it convenient to describe the stimuli, to the time domain, where the results show that *Eptesicus*

may actually perceive the ambiguity to exist. The broader conclusion is that the characteristics of the external-ear response may be *incorporated into perception of target range itself* by becoming attached to the object as a sort of ghost glint at an elevation-dependent time separation. To the bat, sonar targets thus may be perceived as having glints at specific delays for the purpose of determining their elevation, which is a different proposition than just that elevation is determined from the frequencies of notches in the external-ear transfer function.

ACKNOWLEDGMENTS

This research was was supported by NIDCD Grant No. DC-00511, by ONR Grant No. N00014-89-J-3055, by NIMH Research Scientist Development Award MH-00521, and by a grant from the Deafness Research Foundation. We thank numerous colleagues who have provided advice or assistance in the conduct of this research.

Altes, R. A. (**1984**). ''Texture analysis with spectrograms,'' IEEE Trans. Sonics Ultrason. **SU-31**, 407–417.

Asano, F., Suzuki, Y., and Sone, T. (**1990**). ''Role of spectral cues in median plane localization,'' J. Acoust. Soc. Am. **88**, 159–168.

Batteau, D. W. (**1967**). ''The role of the pinna in human localization,'' Proc. R. Soc. London, Ser. B **168**, 158–180.

Beedholm, K., and Mohl, B. (**1998**). ''Bat sonar: An alternative interpretation of the 10-ns jitter result,'' J. Comp. Physiol., A **182**, 259–266.

Beuter, K. J. (**1980**). ''A new concept of echo evaluation in the auditory system of bats,'' in *Animal Sonar Systems*, edited by R.-G. Busnel and J. F. Fish (Plenum, New York), pp. 747–761.

Blauert, J. (**1983**). *Spatial Hearing: The Psychophysics of Human Sound Localization* (MIT, Cambridge, MA).

Bradbury, J. W. (**1970**). ''Target discrimination by the echolocating bat, *Vampyrum spectrum*,'' J. Exp. Zool. **173**, 23–46.

Butler, R. A., and Belendiuk, K. (**1977**). ''Spectral cues utilized in the localization of sound in the median sagittal plane,'' J. Acoust. Soc. Am. **61**, 1264–1269.

Calford, M. B., and Pettigrew, J. D. (**1984**). ''Frequency dependence of directional amplification at the cat's pinna,'' Hear. Res. **14**, 13–19.

Carlile, S. (**1990**). ''The auditory periphery of the ferret. I: Directional response properties and the pattern of interaural level differences,'' J. Acoust. Soc. Am. **88**, 2180–2195.

Carlile, S., and Pettigrew, A. G. (**1987**). ''Directional properties of the auditory periphery in the guinea pig,'' Hear. Res. **31**, 111–122.

Casseday, J. H., and Covey, E. (**1995**). ''Mechanisms for analysis of auditory temporal patterns in the brainstem of echolocating bats,'' in *Neural Representation of Temporal Patterns*, edited by E. Covey, H. L. Hawkins, and R. F. Port (Plenum, New York), pp. 25–51.

Dear, S. P., Fritz, J., Haresign, T., Ferragamo, M. J., and Simmons, J. A. (**1993**). ''Tonotopic and functional organization in the auditory cortex of the big brown bat, *Eptesicus fuscus*,'' J. Neurophysiol. **70**, 1988–2009.

Djupesland, G., and Zwislocki, J. J. (**1973**). ''Sound pressure distribution in the outer ear,'' Acta Oto-Laryngol. **75**, 350–352.

Fisher, H., and Freedman, S. (**1968**). ''The role of the pinna in auditory localization,'' J. Aud Res. **8**, 15–26.

Flynn, W. E., and Elliott, D. M. (**1965**). ''Role of the pinna in hearing,'' J. Acoust. Soc. Am. **38**, 104–105.

Griffin, D. R. (**1958**). *Listening in the Dark* (Yale U. P., New Haven CT; reprinted by Cornell U. P., Ithaca, NY, 1986).

Griffin, D. R. (**1967**). ''Discriminative echolocation by bats,'' in *Animal Sonar Systems: Biology and Bionics*, edited by R.-G. Busnel (Laboratoire de Physiologie Acoustique, Jouy-en-Josas-78, France), pp. 273–300.

Guppy, A., and Coles, R. B. (**1988**). ''Acoustical and neural aspects of hearing in the Australian gleaning bats, *Macroderma gigas* and *Nyctophylus gouldi*,'' J. Comp. Physiol., A **162**, 653–668.

Habersetzer, J., and Vogler, B. (**1983**). ''Discrimination of surface-structured targets by the echolocating bat *Myotis myotis* during flight,'' J. Comp. Physiol., A **152**, 275–282.

Haplea, S., Covey, E., and Casseday, J. H. (**1994**). ''Frequency tuning and response latencies at three levels in the brainstem of the echolocating bat, *Eptesicus fuscus*,'' J. Comp. Physiol., A **174**, 671–683.

Hebrank, J., and Wright, D. (**1974**). ''Spectral cues used in the localization of sound sources in the median plane,'' J. Acoust. Soc. Am. **56**, 1829–1834.

Hiranaka, Y., and Yamasaki, H. (**1983**). ''Envelope representations of pinna impulse responses relating to three-dimensional localization of sound sources,'' J. Acoust. Soc. Am. **73**, 291–296.

Jen, P. H.-S., and Chen, D. (**1988**). ''Directionality of sound pressure transformation at the pinna of echolocating bats,'' Hear. Res. **34**, 101–118.

Kurta, A., and Baker, R. H. (**1990**). ''*Eptesicus fuscus*,'' Mammalian Species **356**, 1–10.

Matsuo, I., Tani, J., and Yano, M. (**2001**). ''A model of echolocation of multiple targets in 3D space from a single emission,'' J. Acoust. Soc. Am. **110**, 607–624.

Menne, D., and Hackbarth, H. (**1986**). ''Accuracy of distance measurement in the bat *Eptesicus fuscus*: Theoretical aspects and computer simulations,'' J. Acoust. Soc. Am. **79**, 386–397.

Menne, D., Kaipf, I., Wagner, I., Ostwald, J., and Schnitzler, H.-U. (**1989**). ''Range estimation by echolocation in the bat *Eptesicus fuscus*: trading of phase versus time cues,'' J. Acoust. Soc. Am. **85**, 2642–2650.

Middlebrooks, J. C. (**1992**). ''Narrow-band sound localization related to external ear acoustics,'' J. Acoust. Soc. Am. **92**, 2607–2624.

Middlebrooks, J. C., and Green, D. M. (**1991**). ''Sound localization by human listeners,'' Annu. Rev. Psychol. **42**, 135–159.

Mogdans, J., and Schnitzler, H. U. (**1990**). ''Range resolution and the possible use of spectral information in the echolocating bat, *Eptesicus fuscus*,'' J. Acoust. Soc. Am. **88**, 754–757.

Moss, C. F., and Schnitzler, H.-U. (**1995**). ''Behavioral studies of auditory information processing,'' in *Hearing by Bats*, edited by A. N. Popper and R. R. Fay (Springer-Verlag, New York), pp. 87–145.

Moss, C. F., and Simmons, J. A. (**1993**). ''Acoustic image representation of a point target in the bat, *Eptesicus fuscus*: evidence for sensitivity to echo phase in bat sonar,'' J. Acoust. Soc. Am. **93**, 1553–1562.

Moss, C. F., and Surlykke, A. (**2001**). ''Auditory scene analysis by echolocation in bats,'' J. Acoust. Soc. Am. **110**, 2207–2226.

Musicant, A. D., Chan, J. C. K., and Hind, J. E. (**1990**). ''Direction-dependent spectral properties of cat external ear: New data and cross-species comparisons,'' J. Acoust. Soc. Am. **87**, 757–781.

Neuweiler, G. (**2000**). *The Biology of Bats* (Oxford U. P., New York).

Peremans, H., and Hallam, J. (**1998**). ''The spectrogram correlation and transformation receiver, revisited,'' J. Acoust. Soc. Am. **104**, 1101–1110.

Phillips, D. P., Calford, M. B., Pettigrew, J. D., Aitkin, L. M., and Semple, M. N. (**1982**). ''Directionality of sound pressure transformation at the cat's pinna,'' Hear. Res. **8**, 13–28.

Pollak, G. D. (**1993**). ''Some comments on the proposed perception of phase and nanosecond time disparities by echolocating bats,'' J. Comp. Physiol., A **172**, 523–531.

Pollak, G. D., and Casseday, J. H. (**1989**). *The Neural Basis of Echolocation in Bats* (Springer, New York).

Popper, A. N., and Fay, R. R. (**1995**). *Hearing by Bats* (Springer, New York).

Rice, J. J., May, B. J., Spirou, G. A., and Young, E. D. (**1992**). ''Pinna-based spectral cues for sound localization in cat,'' Hear. Res. **58**, 132–152.

Saillant, P. A. (**1995**). ''Neural Computations for Biosonar Imaging in the Big Brown Bat,'' Ph.D. dissertation, Brown Univ. Graduate School, Providence, RI.

Saillant, P. A., Simmons, J. A., Dear, S. P., and McMullen, T. A. (**1993**). ''A computational model of echo processing and acoustic imaging in frequency-modulated echolocating bats: The spectrogram correlation and transformation receiver,'' J. Acoust. Soc. Am. **94**, 2691–2712.

Sanderson, M. I., and Simmons, J. A. (**2000**). ''Neural responses to overlapping FM sounds in the inferior colliculus of echolocating bats,'' J. Neurophysiol. **83**, 1840–1885.

Sanderson, M. I., and Simmons, J. A. (2002). ''Selectivity for echo spectral shape and delay in the auditory cortex of the big brown bat, *Eptesicus fuscus*,'' J. Neurophysiol. (in press).

Schmidt, S. (**1988**). ''Evidence for a spectral basis of texture perception in bat sonar,'' Nature (London) **331**, 617–619.

Schmidt, S. (**1992**). ''Perception of structured phantom targets in the echolocating bat, *Megaderma lyra*,'' J. Acoust. Soc. Am. **91**, 2203–2223.

Schnitzler, H.-U., and Henson, O. W., Jr. (**1980**). ''Performance of airborne

animal sonar systems: I. Microchiroptera,'' in *Animal Sonar Systems*, edited by R.-G. Busnel and J. F. Fish (Plenum, New York), pp. 109–181.
Schnitzler, H.-U., Menne, D., and Hackbarth, H. (**1985**). ''Range determination by measuring time delays in echolocating bats,'' in *Time Resolution in Auditory Systems*, edited by A. Michelsen (Springer, Berlin), pp. 180–204.
Shaw, E. A. G. (**1982**). ''External ear response and sound localization,'' in *Localization of Sound: Theory and Applications*, edited by R. Gatehouse (Amphora, Groton, CT), pp. 30–41.
Shaw, E. A. G., and Teranishi, R. (**1968**). ''Sound pressure generated in an external-ear replica and real human ears by a nearby sound source,'' J. Acoust. Soc. Am. **44**, 240–249.
Simmons, J. A. (**1973**). ''The resolution of target range by echolocating bats,'' J. Acoust. Soc. Am. **54**, 157–172.
Simmons, J. A. (**1979**). ''Perception of echo phase information in bat sonar,'' Science **204**, 1336–1338.
Simmons, J. A. (**1980**). ''The processing of sonar echoes by bats,'' in *Animal Sonar Systems*, edited by R.-G. Busnel and J. F. Fish (Plenum, New York), pp. 695–714.
Simmons, J. A. (**1982**). ''The external ears as receiving antennae in echolocating bats,'' J. Acoust. Soc. Am. Suppl. 1 **72**, S41–S42.
Simmons, J. A. (**1989**). ''A view of the world through the bat's ear: The formation of acoustic images in echolocation,'' Cognition **33**, 155–199.
Simmons, J. A. (**1993**). ''Evidence for perception of fine echo delay and phase by the FM bat, *Eptesicus fuscus*,'' J. Comp. Physiol., A **172**, 533–547.
Simmons, J. A. (**1996**). ''Formation of perceptual objects from the timing of neural responses: Target-range images in bat sonar,'' in *The Mind-Brain Continuum: Sensory Processes*, edited by R. Llinás and P. S. Churchland (MIT, Cambridge, MA), pp. 219–250.
Simmons, J. A., and Chen, L. (**1989**). ''The acoustic basis for target discrimination by FM echolocating bats,'' J. Acoust. Soc. Am. **86**, 1333–1350.
Simmons, J. A., and Grinnell, A. D. (**1988**). ''The performance of echolocation: Acoustic images perceived by echolocating bats,'' in *Animal Sonar: Processes and Performance*, edited by P. Nachtigall and P. W. B. Moore (Plenum, New York), pp. 353–385.
Simmons, J. A., Eastman, K. M., and Horowitz, S. S. (**2001**). ''Versatility of biosonar in the big brown bat, *Eptesicus fuscus*,'' Acoustics Research Letters Online **2**, 43–48.
Simmons, J. A., Ferragamo, M. J., and Moss, C. F. (**1998**). ''Echo-delay resolution in sonar images of the big brown bat, *Eptesicus fuscus*,'' Physica A **95**, 12647–12652.
Simmons, J. A., Moss, C. F., and Ferragamo, M. (**1990a**). ''Convergence of temporal and spectral information into acoustic images of complex sonar targets perceived by the echolocating bat, *Eptesicus fuscus*,'' J. Comp. Physiol., A **166**, 449–470.
Simmons, J. A., Saillant, P. A., and Dear, S. P. (**1992**). ''Through a bat's ear,'' IEEE Spectrum March, 46–48.
Simmons, J. A., Ferragamo, M. J., Moss, C. F., Stevenson, S. B., and Altes, R. A. (**1990b**). ''Discrimination of jittered sonar echoes by the echolocating bat, *Eptesicus fuscus*: The shape of target images in echolocation,'' J. Comp. Physiol., A **167**, 589–616.
Simmons, J. A., Freedman, E. G., Stevenson, S. B., Chen, L., and Wohlgenant, T. J. (**1989**). ''Clutter interference and the integration time of echoes in the echolocating bat, *Eptesicus fuscus*,'' J. Acoust. Soc. Am. **86**, 1318–1332.
Simmons, J. A., Ferragamo, M. J., Saillant, P. A., Haresign, T., Wotton, J. M., Dear, S. P., and Lee, D. N. (**1995**). ''Auditory dimensions of acoustic images in echolocation,'' in *Hearing by Bats*, edited by A. N. Popper and R. R. Fay (Springer-Verlag, New York), pp. 146–190.
Simmons, J. A., Saillant, P. A., Ferragamo, M. J., Haresign, T., Dear, S. P., Fritz, J., and McMullen, T. A. (**1996**). ''Auditory computations for biosonar target imaging in bats,'' in *Auditory Computation*, edited by H. L. Hawkins, T. A. McMullen, A. N. Popper, and R. R. Fay (Springer-Verlag, New York), pp. 401–468.
Simmons, J. A., Lavender, W. A., Lavender, B. A., Doroshow, D. A., Kiefer, S. W., Livingston, R., Scallet, A. C., and Crowley, D. E. (**1974**). ''Target structure and echo spectral discrimination by echolocating bats,'' Science **186**, 1130–1132.
Wightman, F. L., and Kistler, D. J. (**1989**). ''Headphone simulation of free-field listening. I: Stimulus synthesis,'' J. Acoust. Soc. Am. **85**, 858–867.
Wotton, J. M., Haresign, T., and Simmons, J. A. (**1995**). ''Spatially dependent acoustic cues generated by the external ear of the big brown bat, *Eptesicus fuscus*,'' J. Acoust. Soc. Am. **98**, 1423–1445.
Wotton, J. M., Jenison, R. L., and Hartley, D. J. (**1997**). ''The combination of echolocation emission and ear reception enhances directional spectral cues of the big brown bat, *Eptesicus fuscus*,'' J. Acoust. Soc. Am. **101**, 1723–1733.
Wotton, J. M., Haresign, T., Ferragamo, M. J., and Simmons, J. A. (**1996**). ''The influence of sound source elevation and external ear notch cues on the discrimination of spectral notches by the big brown bat, *Eptesicus fuscus*,'' J. Acoust. Soc. Am. **100**, 1764–1776.
Wright, D., Hebrank, J. H., and Wilson, B. (**1974**). ''Pinna reflections as cues for localization,'' J. Acoust. Soc. Am. **56**, 957–962.

Mechanisms of modulation gap detection[a)]

Aleksander Sek
Institute of Acoustics, Adam Mickiewicz University, 85 Umultowska Street, 61-614 Poznan, Poland

Brian C. J. Moore[b)]
Department of Experimental Psychology, University of Cambridge, Downing Street, Cambridge CB2 3EB, England

(Received 13 August 2001; revised 4 January 2002; accepted 7 March 2002)

It has been postulated that the central auditory system contains an array of modulation filters, each responsive to a different range of modulation frequencies present at the outputs of the (peripheral) auditory filters. In the present experiments, we tested what we call the ''dip hypothesis,'' that a gap in modulation is detected using the ''dip'' in the output of the modulation filter tuned to the modulator frequency. In experiment 1, the task was to detect a gap in the sinusoidal amplitude modulation imposed on a 4-kHz carrier. The modulator preceding the gap ended with a positive-going zero-crossing. There were three conditions, differing in the phase at which the modulator started at the end of the gap; zero-phase, at a positive-going zero-crossing; π-phase, at a negative-going zero-crossing; and ''preserved'' phase, at the phase the modulator would have had if it had continued without interruption. Modulation frequencies were 5, 10, 20, and 40 Hz. Psychometric functions for detection of the gap were measured using a two-alternative forced-choice task. For the zero-phase and preserved-phase conditions, the detectability index, d', increased monotonically with increasing gap duration. For the π-phase condition, performance was good ($d'>1$) for small gap durations, and initially worsened with increasing gap duration, before improving again for longer gap durations. This is the pattern of results expected from the dip hypothesis, provided that the modulation filters have Q values of 2 or more. However, it is also possible that a rhythm cue was used to improve performance in the π-phase condition for short gap durations; the introduction of the gap markedly disrupted the regular rhythm produced by the modulator peaks. In experiment 2, the rhythm cue was disrupted by varying the modulator period randomly around its nominal value, except for the modulator periods immediately before and after the gap. This markedly impaired performance, and resulted in psychometric functions that were very similar for the zero-phase and π-phase conditions. This pattern of results is inconsistent with the dip hypothesis. For both experiments, modulation gap ''thresholds'' ($d'\approx 1$) were roughly constant when expressed as a proportion of the modulator period. Possible mechanisms of modulation gap detection are discussed and evaluated.
[DOI: 10.1121/1.1474445]

PACS numbers: 43.66.Mk, 43.66.Nm, 43.66.Ba [MRL]

I. INTRODUCTION

The perception of amplitude changes has often been modeled by a sequence of stages, including a bank of bandpass filters (the auditory filters), each followed by a nonlinear device and a ''smoothing'' device. Usually, the smoothing device is thought of as occurring after the auditory nerve; it is assumed to reflect a relatively central process. The output of the smoothing device is fed to a decision device. The smoothing device has been modeled by a low-pass filter (Viemeister, 1979) or by a sliding temporal integrator (temporal window) (Festen and Plomp, 1981; Moore *et al.*, 1988; Plack and Moore, 1990; Oxenham and Moore, 1994). However, more recently it has been proposed that modulation perception depends on a second stage of filtering in the auditory system (Dau *et al.*, 1997a, b). It is assumed that the envelopes of the outputs of the auditory filters are fed to a second array of overlapping bandpass filters tuned to different envelope modulation rates. This set of filters is usually called a ''modulation filter bank'' (MFB). The concept of the MFB implies that the auditory system performs a limited resolution spectral analysis of the envelope at the output of each auditory filter.

The MFB is assumed to exist in a specialized part of the brain that contains an array of neurons each tuned to a different modulation rate (Martens, 1982; Kay, 1982; Dau *et al.*, 1997a, b). Each neuron can be considered as a filter in the modulation domain. Neurons with appropriate properties have been found in the cochlear nucleus (Møller, 1976), the inferior colliculus (Rees and Møller, 1983; Schreiner and Langner, 1988; Lorenzi *et al.*, 1995) and auditory cortex (Schulze and Langner, 1997, 1999). For a review see Palmer (1995). However, the tuning in the modulation domain found in physiological studies is typically sharper than required to fit the psychoacoustic data (see below).

Although the concept of the MFB has received considerable attention in recent years (Bacon and Grantham, 1989; Houtgast, 1989; Strickland and Viemeister, 1996; Dau *et al.*,

[a)]A preliminary version of the first experiment of this paper was presented in Sek and Moore, J. Acoust. Soc. Am. **101**, 3082 (1997).
[b)]Author to whom correspondence should be addressed. Electronic mail: bcjm@cus.cam.ac.uk

1999; Moore *et al.*, 1999; Derleth and Dau, 2000; Ewert and Dau, 2000; Moore and Sek, 2000), it is still controversial. The present experiments were intended to explore further the concept of a MFB, and particularly to examine whether the ability to detect a gap in a modulator can be explained in terms of the properties of the output of a single modulation filter tuned to the modulator frequency. The experiments were inspired by an experiment of Shailer and Moore (1987), which was argued to provide evidence for ''ringing'' in the (peripheral) auditory filters.

Shailer and Moore (1987) studied the detection of temporal gaps in sinusoids. Each sinusoid was presented in a continuous noise with a spectral notch at the frequency of the sinusoid, in order to mask spectral splatter associated with the abrupt offset and onset of the sinusoid on either side of the gap. The results were strongly affected by the phase at which the sinusoid was turned off and on to produce the gap. Three phase conditions were used. For all conditions, the portion of the sinusoid preceding the gap ended with a positive-going zero-crossing. The three conditions differed in the phase at which the sinusoid was turned on at the end of the gap; for the ''standard'' phase condition, the sinusoid started at a positive-going zero-crossing; for the ''reversed'' phase condition, the sinusoid started at a negative-going zero-crossing; and for the ''preserved'' phase condition the sinusoid started at the phase it would have had if it had continued without interruption. Psychometric functions for detection of the gap were measured using a two-alternative forced-choice task.

For the preserved-phase condition, performance improved monotonically with increasing gap duration. However, for the other two conditions the psychometric functions were distinctly nonmonotonic, when the frequency of the sinusoidal ''carrier'' was 1 kHz or below. For the standard-phase condition, the gap was difficult to detect when its value was an integer multiple of the period (P) of the signal. Conversely, the gap was easy to detect when its value was $(n+0.5)P$, where $n=0$ or 1. The psychometric function for the reversed-phase condition showed poor performance when the gap duration was $(n+0.5)P$, where $n=0$ or 1, and good performance when the gap duration was nP.

Shailer and Moore (1987) explained these results in terms of ringing at the output of the auditory filter centered at the frequency of the sinusoid. Consider as an example a ''carrier'' frequency of 400 Hz. When the sinusoid is turned off at the start of the gap, the filter continues to respond or ring for a certain time. If the gap duration is 2.5 ms, corresponding to one whole period of the sinusoid, then in the standard-phase condition the sinusoid following the gap is in phase with the ringing response. In this case, the output of the filter shows only a small dip and gap detection is difficult. For a gap duration of 1.25 or 3.75 ms, the sinusoid following the gap is out of phase with the ringing response. Now the output of the filter passes through zero before returning to its steady-state value. The resulting dip in the filter output is larger, and is much easier to detect.

We applied this paradigm in the modulation domain. We are aware of only one previous study on modulation gap detection (Grose *et al.*, 1999); that study focused on the effects of modulating different carriers before and after the gap, and did not examine the effect of modulator phase. One problem in applying the paradigm of Shailer and Moore (1987) is that the hypothetical modulation filters are assumed to have greater relative bandwidths than the auditory filters; Q values for the modulation filters are typically assumed to be 1–2 (Dau *et al.*, 1997a, b; Ewert and Dau, 2000; Lorenzi *et al.*, 2001). For such broad filters, ringing is expected to last only 0.5 to 1 cycle. Hence, in our experiment we focused on modulation gaps with durations below one modulator period.

Because of the expected short duration of ringing in the hypothetical modulation filters, we did not expect to see multiple peaks and dips in the psychometric functions of the type observed in the audio-frequency domain by Shailer and Moore (1987). However, the simulations described below led us to expect that we might still see effects of the starting phase of the modulator at the end of the gap, provided that gap detection in the modulation domain is based on the magnitude of the dip that occurs at the output of the modulation filter tuned to the modulator frequency. Hence, our experiments can be regarded as a specific test of the hypothesis that the detectability of a modulation gap is monotonically related to the magnitude of the dip that occurs at the output of the modulation filter tuned to the modulator frequency. We call this the ''dip hypothesis.''

An additional problem in applying the paradigm of Shailer and Moore (1987) in the modulation domain arises from their finding that phase effects attributable to ringing in the auditory filter disappeared when the sinusoid used to mark the gap had a high frequency (2 kHz and above). They argued that at high audio frequencies, performance was limited by a relatively central process, such as a sliding temporal integrator (Festen and Plomp, 1981; Moore *et al.*, 1988; Plack and Moore, 1990), rather than by ringing in the auditory filters; the gap threshold imposed by the sliding integrator is about 5–7 ms, while the ringing lasts less than 2–3 ms. In principle, something similar might occur for the detection of gaps in modulation; performance might be limited by some process following the hypothetical modulation filter bank, rather than by the magnitude of the dip in the output of the modulation filter tuned to the modulator frequency. If modulation gap thresholds imposed by this more central mechanism were much longer than one modulator period, this would prevent us from seeing the expected effects of dips in the outputs of the modulation filters. However, pilot experiments indicated that thresholds for detecting gaps in the modulation imposed on sinusoidal carriers typically corresponded to much less than one modulator period.

Figure 1 illustrates the rationale of our experiments. The top row shows the three conditions described above transformed to the modulation domain. The gap duration in this example was 0.125 of the modulator period, P_m (100 ms in this example), and the frequency of the sinusoidal ''carrier'' was 4 kHz. The top-left panel shows the stimulus waveform for the standard-phase condition, hereafter referred to as zero phase. The fine structure of the carrier is not visible. The top-middle panel shows the waveform for the reversed-phase condition, hereafter referred to as π phase. The top-right

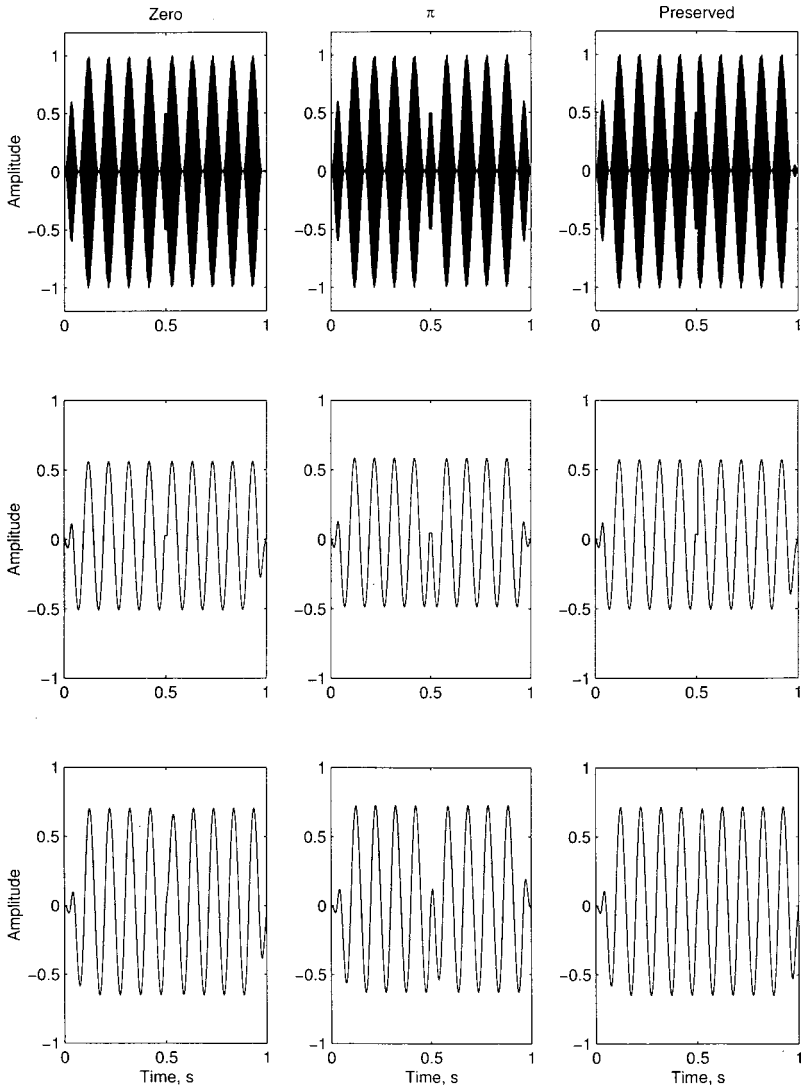

FIG. 1. The top row shows examples of stimuli used in experiment 1, for the three phase conditions (zero, π, and preserved). The modulation rate was 10 Hz and the gap duration was 12.5 ms. The second row shows the Hilbert envelopes at the output of a simulated auditory filter centered on the carrier frequency (4 kHz) in response to the waveforms in the top row. The bottom row shows the output of a simulated modulation filter (center frequency 10 Hz, Q=1) in response to the Hilbert envelopes in the second row.

panel shows the waveform for the preserved-phase condition. Note that, in this case, there is an abrupt jump in amplitude at the end of the gap.

To clarify the exact nature of the stimuli, Fig. 2 shows segments of waveforms immediately adjacent to the gap in the modulator, with the carrier frequency reduced to 200 Hz. This carrier frequency was not used in the experiments, but it is used here for illustrative purposes, to make the fine structure visible. The downwards-pointing arrows indicate the locations of the gaps in the modulator. The abrupt jump in amplitude for the preserved-phase condition can be seen more clearly in this figure.

To illustrate the expected effect of the hypothetical modulation filter tuned to the modulator frequency, the stimuli were initially passed through a simulated auditory filter centered at 4 kHz; this was a gammatone filter (Patterson *et al.*, 1995) with an equivalent rectangular bandwidth of 456 Hz (Glasberg and Moore, 1990). The filter had very little effect on the waveforms. The Hilbert envelope of the filter output was then determined and is plotted in the second row of panels in Fig. 1 (for this plot, the dc component of the envelope has been removed). Finally, the Hilbert envelope determined in this way was passed through a simulated modulation filter centered at the frequency of the modulator. The simulated modulation filter was also based on a gammatone filter, and it had a Q value of 1 (bandwidth equal to center frequency), which is the value assumed by Ewert and Dau (2000). The outcome for this case was not greatly different when the Q value was set to 2, as proposed by Dau and co-workers for modulation filter center frequencies of 10 Hz and above (Dau, 1996; Dau *et al.*, 1997a, b). The output of the simulated modulation filter is plotted in the third row. For the zero-phase condition (left) the output shows a small dip corresponding to the gap. For the π-phase condition (middle), the dip is much larger, while for the preserved-phase condition (right) the dip is very small.

In this paper we test the dip hypothesis that performance in the modulation gap detection task is monotonically related to the magnitude of the dip in the output of the modulation filter tuned to the modulation frequency. For most of the conditions discussed (gap durations up to $0.5P_m$), the depth of the dip, the width of the dip, and its ''area'' were highly correlated, so it is not critical what measure of the dip magnitude is used; henceforth, we use the depth. Based on the dip hypothesis, for very short gap durations good performance is predicted for the π-phase condition, with much poorer performance for the zero-phase condition and performance close to chance for the preserved-phase condition.

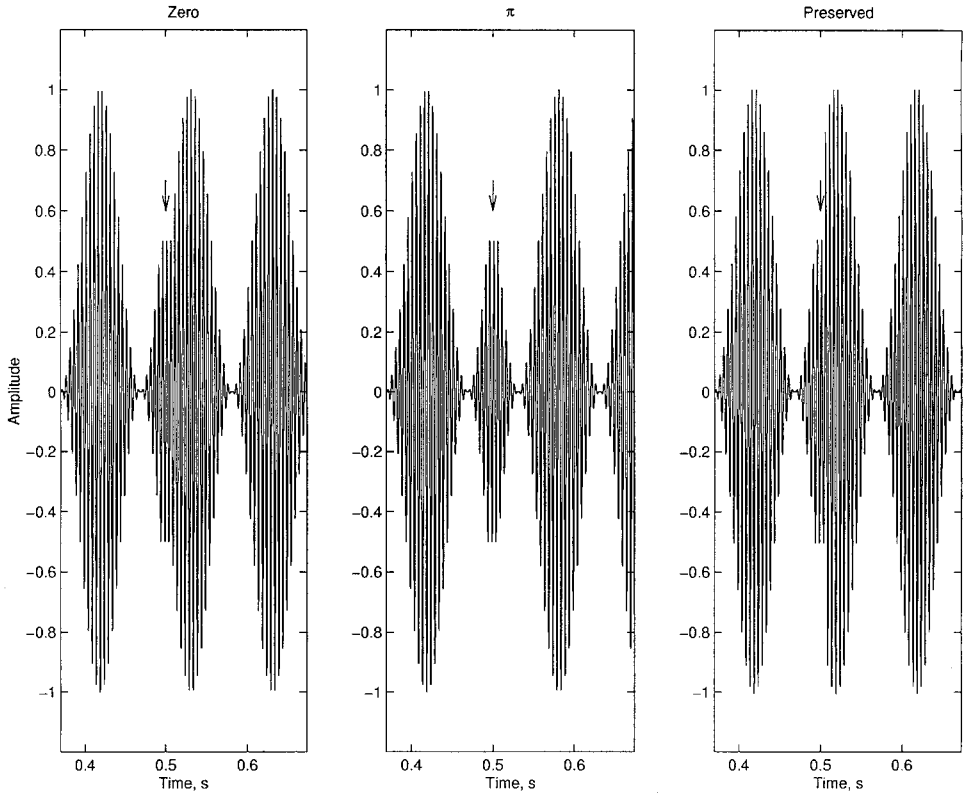

FIG. 2. Portions of stimulus waveforms around the modulator gaps for the three conditions. The gaps are indicated by the arrows. The 200-Hz carrier frequency is used here for illustrative purposes.

Simulations using this simple model indicated that no differences between phase conditions would be expected when the modulator gap duration was equal to or greater than P_m. Because of the low Q of the simulated modulation filter, the ringing response died away quickly, and even for the preserved-phase condition a large dip in the output of the modulation filter occurred for gap durations equal to or greater than P_m. However, differences across phase conditions would be expected for gap durations equal to $0.5P_m$ or less. Hence, in our experiment we mostly used gap durations less than or equal to P_m.

It should be noted that predictions based on the dip hypothesis do not depend *critically* on the assumed form of the modulation filter. Indeed, similar predictions were obtained using a low-pass modulation filter with a cutoff frequency of 100 Hz and a bandpass filter with Q=1. Essentially, any broadly tuned filter would show a large dip at its output for a short modulator gap in the π-phase condition. This depends mainly on the stimulus itself. The main point of the experiments was to test the dip hypothesis; assuming that the modulation filters do exist, can gap detection performance be predicted in terms of the size of the dips at the output of the modulation filter tuned to the modulator frequency? However, it turns out that the results of experiment 1 could only be accounted for in terms of the dip hypothesis if we assumed a modulation filter with Q greater than 1; thus the predictions do depend somewhat on the assumed sharpness of the modulation filter.

II. EXPERIMENT 1: SINUSOIDAL MODULATORS

A. Procedure

Psychometric functions for the detection of a gap in a sinusoidal modulator were measured using a two-interval forced-choice procedure. The modulation was continuous in one interval of a trial, and contained a gap in the other interval, selected at random. The task of the subject was to indicate, by pressing one of two buttons, the interval containing the gap. Feedback was provided by lights following each response. The phase condition and modulation rate were fixed within a block of trials. The method for determining psychometric functions was the same as described by Moore and Sek (1992); the reader is referred to that paper for details. Briefly, each block of 55 trials started with five trials where the signal contained a highly detectable gap (gap duration=P_m), so that subjects ''knew what to listen for.'' Scores for these five trials were discarded. In subsequent trials, five different gap durations were used, in a repeating sequence going from larger values to smaller ones; gap durations were 1, 0.5, 0.25, 0.125, and 0.0625 times P_m. Thus subjects received a ''reminder'' (easy) stimulus once every five trials. Each point on each psychometric function was based on 200 judgments. Pilot experiments suggested that, for the highest modulation rate used (40 Hz), performance was somewhat poorer than for the lower modulation frequencies. Hence, for the 40-Hz modulation rate only, the gap durations used were increased by a factor of 2; gap durations were 2, 1, 0.5, 0.25, and 0.125 times P_m.

B. Stimuli

The carrier was a 4-kHz sinusoid. This relatively high carrier frequency was chosen so that the spectral sidebands produced by the modulation would not be resolved even for the highest modulation frequency used (40 Hz). The carrier level was 70 dB SPL. The modulation frequency was 5, 10, 20, or 40 Hz and the modulation depth was 100% ($m=1$). On each trial, the carrier was presented in two bursts sepa-

rated by a silent interval of 300 ms. Each burst had a 20-ms raised-cosine rise and fall, and an overall duration (including rise/fall times) of 1000 ms. The modulation was applied during the whole of one burst, but contained a gap in the other burst. The three phase conditions described earlier, as illustrated in Fig. 1, were used. The gap was temporally centered in the 1000-ms carrier burst, and always started as the modulator was passing through a positive-going zero-crossing. At the end of the gap, the modulator started either with zero phase, π phase or preserved phase. Because the overall duration of the stimuli was fixed, the modulation patterns at the start and end of the stimuli varied with gap duration and with phase condition. To prevent differences in modulation pattern at the start and end of the signal stimulus from providing useful cues, the starting phase of the modulation in the nonsignal interval (the one without the gap) was selected randomly from trial to trial. This, combined with the fact that the five different gap durations were interleaved within a block of trials, meant that no specific modulation pattern at the start or end of a stimulus was consistently associated with the signal or nonsignal intervals. In the preserved-phase condition with gap duration $=0.25P_m$, there was an abrupt amplitude change at the end of the gap. Pilot experiments indicated that this produced an audible click. To avoid this, for this condition only, we applied a brief raised-cosine ramp to the modulator at the end of the gap, with duration $=0.05P_m$. With this ramp, no click was audible.

Stimuli were generated using a Tucker-Davis array processor (TDT-AP2) in a host PC, and a 16-bit digital to analog converter (TDT-DD1) operating at a 50-kHz sampling rate. The stimuli were attenuated (TDT-PA4) and sent through an output amplifier (TDT-HB6) to a Sennheiser HD580 earphone. Only one ear was tested for each subject. Subjects were seated in a double-walled sound-attenuating chamber.

C. Subjects

Four subjects were tested. One was author AS. The other three subjects were paid for their services. All subjects had absolute thresholds less than 20 dB HL at all audiometric frequencies and had no history of hearing disorders. All had extensive previous experience in psychoacoustic tasks. They were given practice in a selection of conditions until their performance appeared to be stable; this took about 4 h. The thresholds gathered during the practice sessions were discarded.

D. Results

The pattern of results was similar across subjects, so we focus on the mean results. The percent correct for each subject for each condition was converted to the detectability index d' (Hacker and Ratcliff, 1979). The mean d' values, with associated standard errors, are shown as open symbols in Figs. 3–6 (the filled symbols show results from experiment 2, which is described later).

Consider first the results for the 5-Hz modulation rate (Fig. 3). For the zero-phase and preserved-phase conditions (squares and triangles, respectively), d' was close to zero for the shortest gap duration, and increased monotonically with

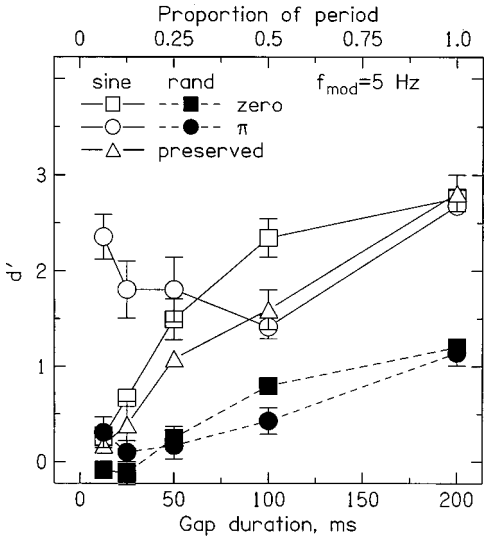

FIG. 3. The open symbols show the mean results of experiment 1 for a modulation rate of 5 Hz. The conditions are identified in the key. The detectability index d' is plotted as a function of modulator gap duration. The filled symbols show results of experiment 2, which used modulator periods randomized in the range 0.5 to 1.5 times the nominal period, except for the periods immediately before and after the gap.

increasing gap duration. Performance was somewhat better for the zero-phase than for the preserved-phase condition for intermediate gap durations. This suggests that spectral splatter associated with the abrupt jumps in amplitude in the preserved-phase condition did not provide a usable cue for detecting the modulator gap. The results for the π-phase condition showed a very different pattern; performance was very good ($d'>2$) for the shortest gap duration, worsened somewhat as the gap duration was increased to $0.5P_m$, and then improved again when the gap duration was increased to P_m.

The results for the other modulation frequencies (Figs. 4–6) were similar in form to those for the 5-Hz modulator. In all cases, d' increased monotonically with increasing gap duration for the zero-phase and preserved-phase conditions. In contrast, d' for the π-phase condition followed a U-shaped function. In all cases, performance was high and

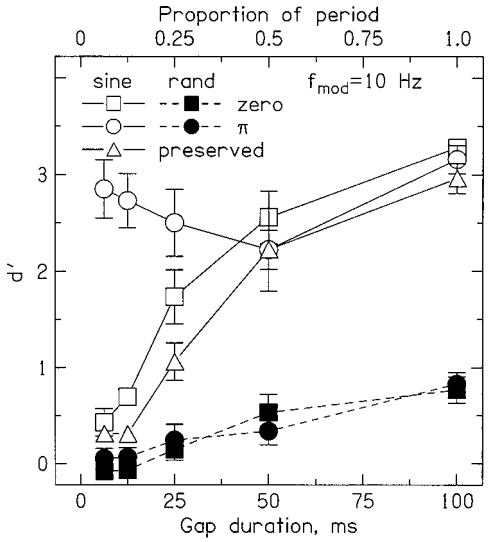

FIG. 4. As Fig. 3, but for a modulation frequency of 10 Hz.

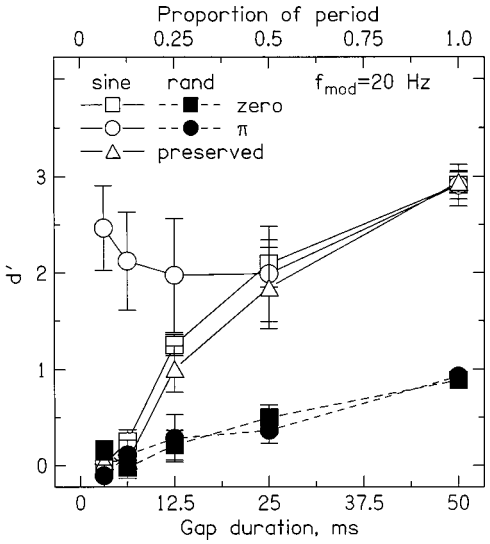

FIG. 5. As Fig. 3, but for a modulation frequency of 20 Hz.

roughly the same for all phase conditions when the gap duration was equal to P_m.

The d' values were subjected to a within-subjects analysis of variance (ANOVA) with factors phase condition, modulation rate, and gap duration expressed as a proportion of P_m. Since a gap duration of $0.0625P_m$ was not used for the modulation rate of 40 Hz, d' values for this case were treated as missing values. All of the main effects and interactions were significant ($p<0.05$), but most of the variance in the data was accounted for by the main effect of gap duration [$F(4,12)=119.2$, $p<0.001$], the main effect of phase condition [$F(2,6)=12.96$, $p=0.007$] and the interaction of gap duration and phase condition [$F(8,24)=32.28$, $p<0.001$]. *Post hoc* tests, based on the least-significant differences test, showed that the mean d' values for the two shortest gap durations were significantly larger for the π-phase condition than for the other two phase conditions (both $p<0.001$). Also, for the π-phase condition, performance was significantly poorer for the gap duration of $0.5P_m$ than for the two shortest gap durations (both $p<0.01$).

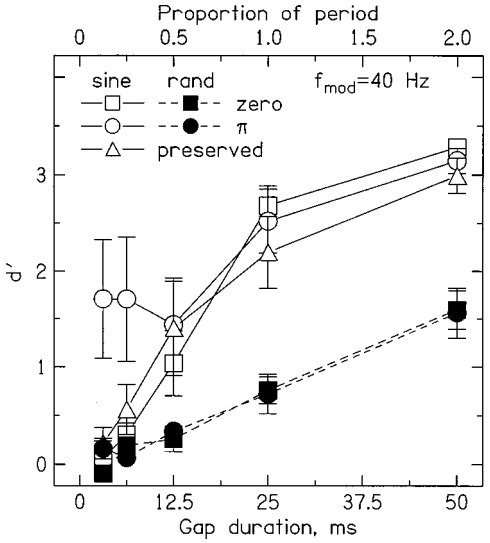

FIG. 6. As Fig. 3, but for a modulation frequency of 40 Hz. Note that the gap durations ranged up to $2P_m$ for this modulation frequency.

The dip hypothesis correctly predicts that, for very short gap durations, performance should be better for the π-phase condition than for the other two conditions. However, assuming a Q value of 1 for the modulation filter (or assuming a low-pass filter), the dip hypothesis does not predict our finding that, for the π-phase condition, performance was significantly poorer for the gap duration of $0.5P_m$ than for the two shortest gap durations. With a Q of 1, the dip in the output of the modulation filter was similar in depth for gap durations of 0.0625, 0.125, and $0.5P_m$ (and was slightly wider for the gap duration of $0.5P_m$ than for the shorter gaps). The pattern of the results is similar to that observed by Shailer and Moore (1987) in the audio frequency domain and explained by them in terms of ringing in the auditory filter. To account for the initial worsening in performance with increasing duration in the π-phase condition in terms of the dip hypothesis, it would be necessary to assume that the Q value of the modulation filter was 2 or more, so that the modulation filter rang for a longer time. A Q value of 2 was assumed by Dau *et al.* (1997a, b), but in the context of a more complex model involving preprocessing stages such as adaptation loops. Ewert and Dau (2000), using a simpler model based on the power spectrum of the envelope, found that a Q value of 1 gave a better fit to their data, and Lorenzi *et al.* (2001) argued that their data could only be fitted by assuming a Q value of 1 or less. Evidently, it is difficult to find a Q value that is consistent with all of the data.

E. Discussion

The pattern of our results is broadly consistent with the dip hypothesis, although it has to be assumed that the Q value of the modulation filter is 2 or more to account for the initial decrease in performance with increasing gap duration found in the π-phase condition. However, there is another way to interpret the results for short gap durations, based on the use of rhythm cues. The regular peaks in the stimulus envelope in the nonsignal interval create a strong sense of a regular rhythm. When the gap is present, it disrupts that rhythm to some extent. For the zero-phase and preserved-phase conditions the disruption is small or zero when the gap duration is small. For example, when the gap duration is $0.0625P_m$, the interpeak interval in the zero-phase condition changes from P_m to $1.0625P_m$ around the point where the gap is present. Subsequent peaks are roughly at their ''expected'' times. In contrast, for the π-phase condition, the interval between envelope peaks changes from P_m to $1.5625P_m$, and subsequent peaks are substantially displaced from their ''expected'' positions. This change in rhythm might provide a salient detection cue for short gap durations in the π-phase condition. When the gap duration is increased to $0.5P_m$, the interpeak interval around the gap for the π-phase condition becomes $2P_m$, and subsequent peaks are exactly at their ''expected'' positions. Thus, the disruption to the rhythm is smaller; this could account for the fact that (for the lower modulation frequencies), performance in the π-phase condition worsened as the gap duration was increased from a very small value up to $0.5P_m$.

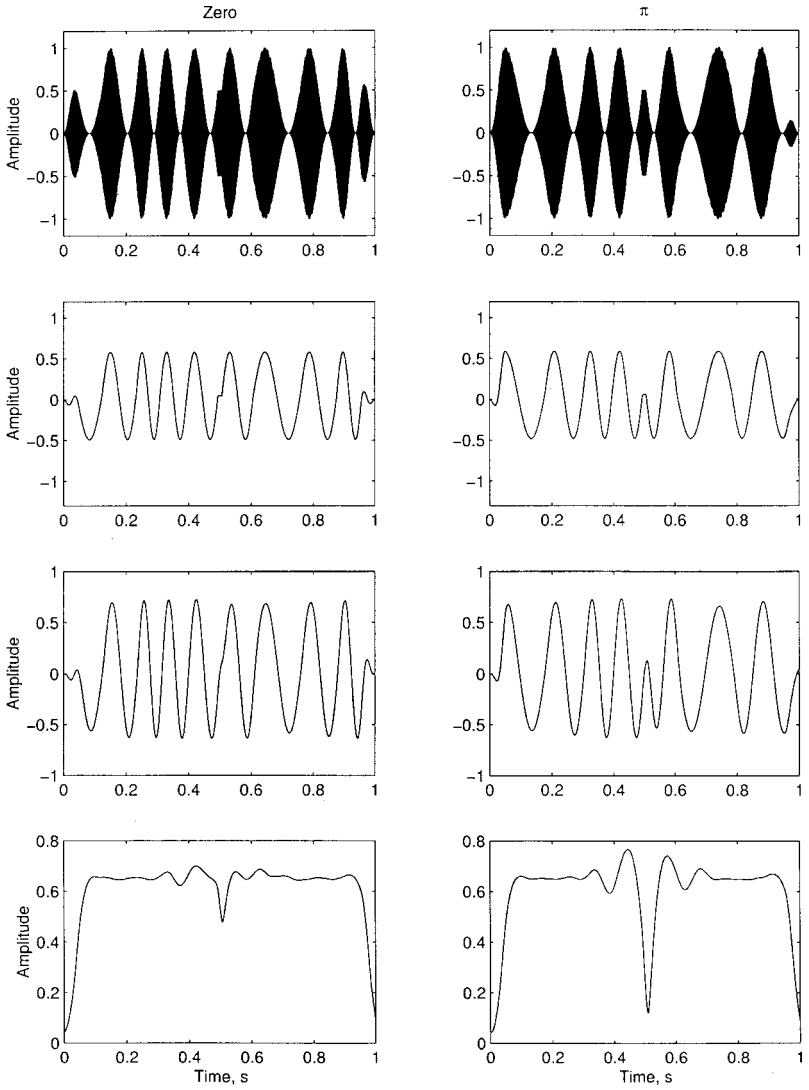

FIG. 7. The top row shows examples of stimuli used in experiment 2, for the two phase conditions (zero and π). The nominal modulation period was 100 ms and the gap duration was 12.5 ms. The second row shows the Hilbert envelopes at the output of a simulated auditory filter centered on the carrier frequency (4 kHz) in response to the waveforms in the top row. The third row shows the output of a simulated modulation filter (center frequency 10 Hz, Q=1) in response to the Hilbert envelopes in the second row. The fourth row shows the Hilbert envelope of the output of the modulation filter, averaged over 150 independent samples of each stimulus.

In summary, the pattern of performance observed in experiment 1 might be explained in terms of the use of rhythm cues for the shorter gap durations. For the longest gap duration, the gap itself was probably used for detection, and it was sufficiently large to allow very good performance for all phase conditions. In the second experiment, we attempted to disrupt the use of rhythm cues by using a modulator whose period varied randomly from one period to the next, except for the periods immediately before and after the gap.

Another potential problem in interpreting the results of experiment 1 is that the introduction of the gap would have produced spectral ''splatter'' in the modulation domain. Calculations of the power spectrum of the modulator showed that this splatter did vary somewhat with gap duration and with phase condition. It is possible that the results were affected to some extent by detection of splatter in the modulation domain, although this seems unlikely, since the modulation filters are assumed to be broadly tuned and since the ''side lobes'' associated with the splatter were at least 20 dB lower in level than the main spectral lobe centered at the modulator frequency; the side lobes one octave above and below the center frequency were more than 30 dB lower in level than the main lobe. The randomization of modulator period used in experiment 2 had the effect of broadening the central lobe of the modulator spectrum, centered at the nominal modulator frequency, to a value at the −3 dB points of about half the modulator frequency. The overall long-term modulation spectrum was smoother (not showing distinct side lobes) and hardly changed with gap duration or phase condition. Thus, the randomization of modulator period used in experiment 2 had the beneficial side effect of making it much less likely that the gap in the modulator was detected via spectral splatter in the modulation domain.

III. EXPERIMENT 2: RANDOM-PERIOD MODULATOR

A. Rationale

Examples of the stimuli used in experiment 2 are shown in the top panels of Fig. 7. The experiment was similar to experiment 1, except that only the zero-phase and π-phase conditions were used and the modulator period was varied randomly around the nominal value P_m (100 ms in this example) within the range $0.5P_m$ to $1.5P_m$ (rectangular distribution). Only the modulator periods immediately before and after the modulator gap were fixed at the value P_m. The gap duration in this example was $0.125P_m$. It is clear that the randomization of the modulator period would severely disrupt rhythm cues of the type described above, so if these cues

were used in experiment 1 for the π-phase condition, performance in that condition would be expected to worsen considerably for short gap durations.

It is important to consider what pattern of performance would be predicted from the dip hypothesis. To assess this, the stimuli were processed through the same model as described in the Introduction, using a Q value of 1 for the simulated modulation filter. Row 2 of Fig. 7 shows the Hilbert envelope of the output of the simulated auditory filter (with the dc component removed), and row 3 shows the output of the simulated modulation filter centered at 10 Hz. The output of the filter shows a very small dip for the zero-phase condition, but shows a distinct dip for the π-phase condition. The first three rows of Fig. 7 show representations of specific samples of the stimuli. To assess what would happen on average, we determined the Hilbert envelope of the output of the modulation filter, and averaged that envelope across 150 samples of the stimuli for each condition. The result is shown in the fourth row of Fig. 7. The mean envelope at the output of the modulation filter shows a slight rise on either side of the gap, which happens because the modulator period was exactly P_m for the periods immediately before and after the gap, but differed from P_m for other periods. More importantly, the dip in the envelope corresponding to the gap is much larger for the π-phase condition than for the zero-phase condition. Thus, the model leads to the prediction that, for short gap durations, performance should be better for the π-phase condition than for the zero-phase condition. Also, the magnitude of the dip for the π-phase condition was similar for the gap durations of $0.0625P_m$ and $0.5P_m$. When a Q value of 2 was assumed, the dip was slightly larger for the gap duration of $0.0625P_m$ than for the gap duration of $0.5P_m$. Thus, the dip hypothesis leads to the prediction that, for the π-phase condition, performance should be at least as good for the shortest gap duration as for the $0.5P_m$ gap duration.

B. Method, stimuli, and subjects

The method, stimuli, and subjects were the same as for experiment 1, except for the randomization of the modulator period and the exclusion of the preserved-phase condition.

C. Results

The results are shown by the filled symbols in Figs. 3–6. The randomization of modulator period clearly disrupted performance. For the two shortest gap durations, d' values were close to zero for both phase conditions for all modulation rates. None of the d' values for the two shortest gap durations differed significantly from zero at the 0.05 level of significance (based on 95% confidence intervals defined by ± 2 standard errors). For the two shortest gap durations, d' values did not differ clearly for the two phase conditions for any modulation rate. These results are not consistent with the prediction based on the dip hypothesis that performance would be better for the π-phase condition than for the zero-phase condition, for short gap durations.

Another prediction based on the dip hypothesis was that, for the π-phase condition, performance should be at least as good for the $0.0625P_m$ gap duration as for the $0.5P_m$ gap duration. In fact, performance was generally better for the $0.5P_m$ gap duration than for the $0.0625P_m$ gap duration. Again the results do not conform to the predictions derived from the dip hypothesis.

The d' values were subjected to a within-subjects ANOVA with factors phase condition, modulation rate, and gap duration expressed as a proportion of P_m. Since a gap duration of $0.0625P_m$ was not used for the modulation rate of 40 Hz, d' values for this case were treated as missing values. The only significant effect was the main effect of gap duration; $F(4,12)=76.76$, $p<0.001$. *Post hoc* tests showed that the mean value of d' for the $0.5P_m$ gap duration was significantly greater than the value of d' for the smallest gap duration at $p<0.001$. This was true both for the data collapsed across phase conditions, and for the phase conditions analyzed separately.

IV. DISCUSSION

The results of experiment 1 showed clear effects of the starting phase of the modulator following the gap; performance for short gap durations was markedly better for the π-phase condition than for the other two phase conditions. Furthermore, performance for the π-phase condition initially worsened with increasing gap duration, before increasing again for longer gap durations. This pattern of results is consistent with what would be predicted from the dip hypothesis, provided the modulation filter is assumed to have a Q value of at least 2. However, we also pointed out that the pattern of the results could be explained by the use of rhythm cues for short gap durations in the π-phase condition.

The stimuli of experiment 2 were chosen to disrupt rhythm cues, while preserving the main features of the predictions based on dips at the output of a modulation filter. The randomization of modulator period resulted in a considerable worsening in performance. In particular, performance in the π-phase condition using short gap durations was much worse in experiment 2 than in experiment 1. This supports the idea that rhythm cues were used in that condition in experiment 1. The results of experiment 2 are not consistent with the predictions of the dip hypothesis.

It might be argued that the substantial worsening of performance in experiment 2 was due to the fluctuations in magnitude at the output of the modulation filter introduced by the random variation in modulator period. Such fluctuations can be seen in row 3 of Fig. 7, although they are relatively small (the fluctuations were slightly larger when we assumed a Q value of 2). In experiment 2, the dip in output of the modulation filter (associated with the gap) had to be detected against a background of random fluctuation, and this would naturally be expected to lead to worse performance. The situation is similar to ''conventional'' gap detection in the audio-frequency domain, where performance is generally worse when the ''carrier'' is a narrow-band noise than when it is a sinusoid of the same center frequency (Moore and Glasberg, 1988).

While this argument is reasonable, it does not account for all aspects of the results for the π-phase condition. For a given mean value of P_m, the amount and type of ''back-

ground'' fluctuation would have been the same for all gap durations. For a gap duration of $0.5P_m$, the value of d' was significantly ($p<0.05$) greater than zero for the π-phase condition for all values of P_m, based on confidence intervals for d' calculated as described by Miller (1996), or based on the standard errors. Thus, on the assumptions of the dip hypothesis, the dip produced by the $0.5P_m$ gap must have been detectable against the background fluctuation. The simulations showed that the size of the dip in the π-phase condition was about as large (or larger with $Q=2$) for the gap duration of $0.0625P_m$ as for the gap duration of $0.5P_m$. Yet, for the π-phase condition, performance was worse for the gap duration of $0.0625P_m$ than for the $0.5P_m$ gap duration. Indeed, d' for the shortest duration did not differ significantly from zero for any modulation rate. We conclude that the results of experiment 2 are not consistent with the dip hypothesis.

It is not entirely clear what cue was used to detect the modulation gap in experiment 2. One possibility is that subjects used a cue based on the time between successive envelope peaks; the gap might have been detected as an elongated interval between successive peaks. We can test this idea by considering the results when the gap duration was $0.5P_m$. For this case, the time between envelope peaks on either side of the gap was smaller for the zero-phase condition ($1.50P_m$) than for the π-phase condition ($2P_m$). However, for this gap duration, d' was at least as high for the zero-phase condition as for the π-phase condition, and was sometimes a little higher. We can also test this idea by comparing results for the zero-phase condition when the gap duration was equal to P_m and the π-phase condition when the gap duration was $0.5P_m$. Performance was consistently better for the former than for the latter, in spite of the fact that, in both cases, the time between envelope peaks on either side of the gap was $2P_m$. We conclude that the results are not consistent with the hypothesis that the gap was detected as an elongated interval between envelope peaks on either side of the gap.

Another possibility is that subjects detected the gap *per se*, i.e., they detected that the stimulus was unmodulated (steady) for a brief period. This would be consistent with the finding that the psychometric functions were similar for the zero-phase and π-phase conditions (except perhaps when the modulator frequency was 5 Hz). Such a cue may also have been used for the longest gap duration in experiment 1; when the gap duration was equal to P_m, performance was essentially the same for all phase conditions, and this was true for all modulation rates used.

In the audio-frequency domain, thresholds for the detection of gaps in a sinusoid have been estimated from data for the preserved-phase condition, for which the psychometric function is monotonic (Shailer and Moore, 1987; Moore *et al.*, 1992, 1993). Thresholds estimated in this way are roughly constant at 5–7 ms for medium to high frequencies, but increase for very low frequencies (200 Hz and below). For our own results, the threshold can be defined as the gap duration required to reach a d' value of approximately 1. In experiment 1, the gap thresholds estimated from the data for the preserved-phase condition were approximately 50, 25, 12.5, and 10 ms, for modulation rates of 5, 10, 20, and 40 Hz, respectively. In other words, gap thresholds were not constant in ms, but were roughly a constant proportion (0.25) of the period of the modulator used to mark the gap, at least for rates up to 20 Hz. In experiment 2, the psychometric functions were monotonic for both phase conditions and d' approached (but usually did not quite reach) 1 when the gap duration was roughly equal to one period of the modulator.

While the results of experiment 2, and of experiment 1 for the longest gap duration, are consistent with the idea that subjects detected the gap *per se*, the nature of the modulation on either side of the gap clearly influences the modulation gap threshold. Perhaps, when the carrier is modulated at a low rate, the carrier needs to be sampled for a relatively long time before the subject can determine that the modulation has ceased. When the modulation has a high rate, the subject can determine more quickly that the modulation has ceased. It is noteworthy that, when expressed as a proportion of P_m, the gap threshold did increase slightly when the modulation frequency was 40 Hz; the gap threshold was about $0.4P_m$, while for lower modulation frequencies it was about $0.25P_m$. Possibly, this indicates a limitation on modulation gap detection imposed by some factor other than the rate of the modulator; for still higher modulation frequencies the gap threshold might approach an asymptotic value in ms, in the same way that gap detection thresholds in the audio-frequency domain approach an asymptotic value for frequencies above about 200 Hz (Shailer and Moore, 1987; Moore *et al.*, 1992, 1993). This remains to be tested.

V. CONCLUSIONS

The following conclusions can be drawn from this study:

(1) For sinusoidal modulation imposed on a high-frequency sinusoidal carrier, the detectability of a brief gap in the modulation depended upon the phase at which the modulator was turned on at the end of the gap. Detectability was higher in the π-phase condition than in the zero-phase or preserved-phase conditions. In the π-phase condition, performance worsened significantly as the gap duration was increased up to $0.5P_m$.

(2) The results for the sinusoidal modulator are broadly consistent with what would be predicted from the dip hypothesis—that the detectability of the modulation gap is related to the magnitude of the dip at the output of a modulation filter tuned to the modulator frequency. To explain the decrease in performance with increasing gap duration in the π-phase condition, it would be necessary to assume that the modulation filter had a Q value of 2 or more. However, the results might also be explained by the use of a rhythm cue for short gap durations in the π-phase condition.

(3) When the modulator period was randomized around the nominal value, except for the modulator periods immediately before and after the gap, performance was markedly disrupted. Detectability was similar for the zero-phase and π-phase conditions, in both cases improving monotonically with increasing gap duration. This pattern of results is not consistent with predictions derived from the dip hypothesis. The results support the idea that, for

the sinusoidal modulator, a rhythm cue was used for short gap durations in the π-phase condition.

(4) The results for the modulator with randomized period are not consistent with the idea that subjects detected the gap as an elongated interval between envelope peaks on either side of the gap.

(5) The results for the modulator with randomized period are consistent with the idea that subjects detected the gap *per se*, i.e., they detected that the stimulus was unmodulated for a certain time. This may also have been the case for the sinusoidal modulator when the gap duration was equal to one modulator period.

(6) Modulation gap ''thresholds,'' estimated from data for the preserved phase condition for the sinusoidal modulator and from both phase conditions for the modulator with randomized period, were roughly a constant proportion of the modulator period on either side of the gap.

ACKNOWLEDGMENTS

This work was supported by the Wellcome Trust and the Medical Research Council (UK). We thank Brian Glasberg and Thomas Stainsby for helpful comments on an earlier version of this paper. We also thank Torsten Dau, Christian Lorenzi, and Marjorie Leek for their incisive and helpful comments.

Bacon, S. P., and Grantham, D. W. (**1989**). ''Modulation masking: effects of modulation frequency, depth and phase,'' J. Acoust. Soc. Am. **85**, 2575–2580.

Dau, T. (**1996**). ''Modeling auditory processing of amplitude modulation,'' Ph.D. Thesis, University of Oldenburg.

Dau, T., Kollmeier, B., and Kohlrausch, A. (**1997a**). ''Modeling auditory processing of amplitude modulation: I. Detection and masking with narrowband carriers,'' J. Acoust. Soc. Am. **102**, 2892–2905.

Dau, T., Kollmeier, B., and Kohlrausch, A. (**1997b**). ''Modeling auditory processing of amplitude modulation: II. Spectral and temporal integration,'' J. Acoust. Soc. Am. **102**, 2906–2919.

Dau, T., Verhey, J. L., and Kohlrausch, A. (**1999**). ''Intrinsic envelope fluctuations and modulation-detection thresholds for narrow-band noise carriers,'' J. Acoust. Soc. Am. **106**, 2752–2760.

Derleth, R. P., and Dau, T. (**2000**). ''On the role of envelope fluctuation processing in spectral masking,'' J. Acoust. Soc. Am. **108**, 285–296.

Ewert, S. D., and Dau, T. (**2000**). ''Characterizing frequency selectivity for envelope fluctuations,'' J. Acoust. Soc. Am. **108**, 1181–1196.

Festen, J. M., and Plomp, R. (**1981**). ''Relations between auditory functions in normal hearing,'' J. Acoust. Soc. Am. **70**, 356–369.

Glasberg, B. R., and Moore, B. C. J. (**1990**). ''Derivation of auditory filter shapes from notched-noise data,'' Hear. Res. **47**, 103–138.

Grose, J. H., Hall, J. W., and Buss, E. (**1999**). ''Modulation gap detection: Effects of modulation rate, carrier separation, and mode of presentation,'' J. Acoust. Soc. Am. **106**, 946–953.

Hacker, M. J., and Ratcliff, R. (**1979**). ''A revised table of d' for M-alternative forced choice,'' Percept. Psychophys. **26**, 168–170.

Houtgast, T. (**1989**). ''Frequency selectivity in amplitude-modulation detection,'' J. Acoust. Soc. Am. **85**, 1676–1680.

Kay, R. H. (**1982**). ''Hearing of modulation in sounds,'' Physiol. Rev. **62**, 894–975.

Lorenzi, C., Micheyl, C., and Berthommier, F. (**1995**). ''Neuronal correlates of perceptual amplitude-modulation detection,'' Hear. Res. **90**, 219–227.

Lorenzi, C., Soares, C., and Vonner, T. (**2001**). ''Second-order temporal modulation transfer functions,'' J. Acoust. Soc. Am. **110**, 1030–1038.

Martens, J.-P. (**1982**). ''A new theory for multi-tone masking,'' J. Acoust. Soc. Am. **72**, 397–405.

Miller, J. (**1996**). ''The sampling distribution of d','' Percept. Psychophys. **58**, 65–72.

Møller, A. R. (**1976**). ''Dynamic properties of primary auditory fibers compared with cells in the cochlear nucleus,'' Acta Physiol. Scand. **98**, 157–167.

Moore, B. C. J., and Glasberg, B. R. (**1988**). ''Gap detection with sinusoids and noise in normal, impaired and electrically stimulated ears,'' J. Acoust. Soc. Am. **83**, 1093–1101.

Moore, B. C. J., and Sek, A. (**1992**). ''Detection of combined frequency and amplitude modulation,'' J. Acoust. Soc. Am. **92**, 3119–3131.

Moore, B. C. J., and Sek, A. (**2000**). ''Effects of relative phase and frequency spacing on the detection of three-component amplitude modulation,'' J. Acoust. Soc. Am. **108**, 2337–2344.

Moore, B. C. J., Peters, R. W., and Glasberg, B. R. (**1992**). ''Detection of temporal gaps in sinusoids by elderly subjects with and without hearing loss,'' J. Acoust. Soc. Am. **92**, 1923–1932.

Moore, B. C. J., Peters, R. W., and Glasberg, B. R. (**1993**). ''Detection of temporal gaps in sinusoids: Effects of frequency and level,'' J. Acoust. Soc. Am. **93**, 1563–1570.

Moore, B. C. J., Sek, A., and Glasberg, B. R. (**1999**). ''Modulation masking produced by beating modulators,'' J. Acoust. Soc. Am. **106**, 908–918.

Moore, B. C. J., Glasberg, B. R., Plack, C. J., and Biswas, A. K. (**1988**). ''The shape of the ear's temporal window,'' J. Acoust. Soc. Am. **83**, 1102–1116.

Oxenham, A. J., and Moore, B. C. J. (**1994**). ''Modeling the additivity of nonsimultaneous masking,'' Hear. Res. **80**, 105–118.

Palmer, A. R. (**1995**). ''Neural signal processing,'' in *Hearing*, edited by B. C. J. Moore (Academic, San Diego).

Patterson, R. D., Allerhand, M. H., and Giguère, C. (**1995**). ''Time-domain modeling of peripheral auditory processing: A modular architecture and a software platform,'' J. Acoust. Soc. Am. **98**, 1890–1894.

Plack, C. J., and Moore, B. C. J. (**1990**). ''Temporal window shape as a function of frequency and level,'' J. Acoust. Soc. Am. **87**, 2178–2187.

Rees, A., and Møller, A. R. (**1983**). ''Responses of neurons in the inferior colliculus of the rat to AM and FM tones,'' Hear. Res. **10**, 301–310.

Schreiner, C. E., and Langner, G. (**1988**). ''Coding of temporal patterns in the central auditory system,'' in *Auditory Function: Neurobiological Bases of Hearing*, edited by G. Edelman, W. Gall, and W. Cowan (Wiley, New York).

Schulze, H., and Langner, G. (**1997**). ''Periodicity coding in the primary auditory cortex of the Mongolian gerbil (Meriones unguiculatus): two different coding strategies for pitch and rhythm?'' J. Comp. Physiol. [A] **181**, 651–663.

Schulze, H., and Langner, G. (**1999**). ''Auditory cortical responses to amplitude modulations with spectra above frequency receptive fields: evidence for wide spectral integration,'' J. Comp. Physiol. [A] **185**, 493–508.

Sek, A., and Moore, B. C. J. (**1997**). ''Detectability of gaps in the modulation of a 4-kHz carrier,'' J. Acoust. Soc. Am. **101**, 3082.

Shailer, M. J., and Moore, B. C. J. (**1987**). ''Gap detection and the auditory filter: phase effects using sinusoidal stimuli,'' J. Acoust. Soc. Am. **81**, 1110–1117.

Strickland, E. A., and Viemeister, N. F. (**1996**). ''Cues for discrimination of envelopes,'' J. Acoust. Soc. Am. **99**, 3638–3646.

Viemeister, N. F. (**1979**). ''Temporal modulation transfer functions based on modulation thresholds,'' J. Acoust. Soc. Am. **66**, 1364–1380.

Effects of age and frequency disparity on gap discrimination[a)]

Jennifer Lister[b)]
Department of Communication Sciences and Disorders, University of South Florida, 4202 East Fowler Avenue PCD 1017, Tampa, Florida 33620

Joan Besing and Janet Koehnke
School of Graduate Medical Education, Seton Hall University, 400 South Orange Avenue, South Orange, New Jersey 07079

(Received 23 April 2001; revised 10 October 2001; accepted 7 March 2002)

Temporal discrimination was measured using a gap discrimination paradigm for three groups of listeners with normal hearing: (1) ages 18–30, (2) ages 40–52, and (3) ages 62–74 years. Normal hearing was defined as pure-tone thresholds $\leqslant$25 dB HL from 250 to 6000 Hz and $\leqslant$30 dB HL at 8000 Hz. Silent gaps were placed between $\frac{1}{4}$-octave bands of noise centered at one of six frequencies. The noise band markers were paired so that the center frequency of the leading marker was fixed at 2000 Hz, and the center frequency of the trailing marker varied randomly across experimental runs. Gap duration discrimination was significantly poorer for older listeners than for young and middle-aged listeners, and the performance of the young and middle-aged listeners did not differ significantly. Age group differences were more apparent for the more frequency-disparate stimuli (2000-Hz leading marker followed by a 500-Hz trailing marker) than for the fixed-frequency stimuli (2000-Hz lead and 2000-Hz trail). The gap duration difference limens of the older listeners increased more rapidly with frequency disparity than those of the other listeners. Because age effects were more apparent for the more frequency-disparate conditions, and gap discrimination was not affected by differences in hearing sensitivity among listeners, it is suggested that gap discrimination depends upon temporal mechanisms that deteriorate with age and stimulus complexity but are unaffected by hearing loss. © *2002 Acoustical Society of America.* [DOI: 10.1121/1.1476685]

PACS numbers: 43.66.Mk, 43.66.Sr, 43.71.Lz [SPB]

I. INTRODUCTION

Older listeners with and without hearing loss often experience difficulty understanding speech (WGSUA, 1988), and a number of investigators have hypothesized that a decline in temporal processing may account for at least some of the problems with speech understanding (e.g., Gordon-Salant and Fitzgibbons, 1993; Strouse *et al.*, 1998; Schneider and Hamstra, 1999; Snell and Frisina, 2000). However, the independent effects of age and hearing loss on temporal cues important for speech understanding have not been clearly defined (e.g., Fitzgibbons and Wightman, 1982; Tyler *et al.*, 1982; Moore *et al.*, 1992).

Because speech is characterized by rapid changes in intensity and frequency over time, the accurate processing of these temporal fluctuations is likely critical for optimal perception of speech. In fact, several researchers have found a significant relationship between temporal processing and speech perception (e.g., Tyler *et al.*, 1982; Dreschler and Plomp, 1985) while others have not (e.g., van Rooij and Plomp, 1990; Divenyi and Haupt, 1997). Studies of temporal processing indicate that, as listeners age and experience hearing loss, they lose the ability to resolve simple temporal cues similar to those important in speech such as silent gaps between spectrally similar and spectrally dissimilar stimuli (e.g., Fitzgibbons and Gordon-Salant, 1994; Lister *et al.*, 2000).

Recent literature describes two primary measures of temporal processing using silent gaps: (1) gap detection, a measure of temporal acuity typically described as a gap detection threshold (GDT) and (2) gap discrimination, a measure of temporal discrimination described here as a gap duration difference limen (GDDL). A GDT is a traditional measure representing the smallest silent interval in a stimulus that a listener can detect, and GDDL represents the smallest change in the duration of a silent interval that a listener can discriminate. In the traditional GDT task, the standard interval consists of a continuous signal or two contiguous signals, and the target interval consists of a signal interrupted by a silent temporal gap of varying duration. Divenyi and Danner (1977) hypothesized that this type of temporal task may rely on detection of gating transients that are present in the target interval and absent in the standard interval.

A number of researchers (e.g., DeFilippo and Snell, 1986; Snell *et al.*, 1994; Grose and Hall, 1996; Phillips *et al.*, 1997; Lister *et al.*, 2000) have employed discrimination tasks to insure the presence of similar gating transients in both the standard and target intervals. In our previous study (Lister *et al.*, 2000), the standard interval contained a 1-ms gap, and the target interval contained a similarly placed gap of varying duration. Such a 1-ms standard gap is below the 3–5-ms gap detection thresholds often reported in the literature for broadband, fixed-frequency markers (e.g., Florentine and Buus, 1984). This type of paradigm has been termed both

[a)]Portions of this work were presented as "Effects of age and reverberation on binaural gap duration discrimination" at the 1999 MidWinter Meeting of the Association for Research in Otolaryngology, St. Petersberg, FL.
[b)]Electronic mail: jlister@chuma1.cas.usf.edu

gap detection (e.g., Grose *et al.*, 2001) and gap discrimination (Lister *et al.*, 2000). The present study employs the procedure used by Lister *et al.* (2000), and the acronym GDDL is used here to describe the task and subsequent results.

Both GDTs and GDDLs have been measured using fixed-frequency markers in which the stimuli before (leading) and after (trailing) the silent gap fall into similar frequency ranges, and frequency-disparate markers in which the leading and trailing markers fall into different frequency ranges. Although both GDTs and GDDLs have been used to investigate age-related changes in temporal processing (e.g., He *et al.*, 1999; Gordon-Salant and Fitzgibbons, 1999) and both fixed-frequency and frequency-disparate markers have been used to investigate the temporal processing abilities of young listeners with normal hearing (e.g., Phillips *et al.*, 1997; Formby *et al.*, 1998), few have studied the effects of age or hearing loss on temporal processing using frequency-disparate markers (Fitzgibbons and Gordon-Salant, 1994, 1995; Lister *et al.*, 2000).

Gap discrimination for young and older listeners with and without hearing loss has been measured for a wide variety of stimuli (e.g., Tyler *et al.*, 1982; Fitzgibbons and Gordon-Salant, 1994, 1995; Lister *et al.*, 2000) but has not always shown clear age-related effects. Fitzgibbons and Gordon-Salant (1994, 1995) examined the effects of age and hearing loss on duration difference limens for tone bursts and silent gaps between fixed-frequency tone bursts. Larger difference limens for both tone bursts and gaps were measured for older listeners, regardless of hearing status. While Tyler *et al.* (1982) measured gap discrimination in fixed-frequency noise band markers for listeners with normal and impaired hearing and found a significant effect of hearing loss, the wide age range (33–76 years) of their hearing-impaired listeners precludes a separation of the effects of age and hearing loss. Studies of gap detection using fixed-frequency stimuli have also shown significant age-related increases in GDTs (e.g., Schneider *et al.*, 1994; Snell, 1997; Strouse *et al.*, 1998; He *et al.*, 1999).

The results of these studies suggest that reduced temporal processing in older listeners may occur independently of peripheral hearing loss for fixed-frequency stimuli. Normal pure-tone thresholds are not indicative of normal temporal processing; rather, age may be the stronger predictor of silent gap resolution.

Use of frequency-disparate markers in the study of temporal processing has been motivated by the fact that temporal cues in speech are surrounded by sounds of different spectral characteristics. Early studies using these types of markers demonstrated that the detection (Williams and Perrott, 1972; Collyer, 1974; Fitzgibbons *et al.*, 1974; Williams and Elfner, 1976; Neff *et al.*, 1982) and discrimination (Kinney, 1961; Divenyi and Danner, 1977) of silent gaps are greatly affected by the frequency composition of the markers bounding the gap.

Recently, Oxenham (2000) and Grose *et al.* (2001) attempted to define this effect of frequency disparity by manipulating the spectral and temporal characteristics of their stimuli for young listeners with normal hearing. Using harmonic tone complexes, Oxenham (2000) measured significantly larger GDTs when the spectral region of the leading and trailing markers differed than when the pitch (f_o) differed between markers filtered for the same spectral region. Grose *et al.* (2001) found that when pure-tone markers were preceded or followed by amplitude- or frequency-modulated markers, listeners perceived a difference that did not significantly impact their ability to discriminate the silent gap. Gap discrimination deteriorated only when the leading and trailing markers were of different frequencies. These results suggest that spectral differences between markers are more disruptive to gap detection or discrimination than other perceptual differences between markers.

Fitzgibbons and Gordon-Salant (1994, 1995) specifically demonstrated age-related changes in gap discrimination between fixed-frequency and frequency-disparate markers. They measured GDDLs between tone-burst markers that differed by as much as $\frac{1}{3}$ oct and found a significant effect of age that was more pronounced for the frequency-disparate stimuli than for the fixed-frequency stimuli. Significant effects of hearing loss on gap discrimination were not apparent.

In an examination of gap discrimination between frequency-disparate noise bands for listeners with normal and impaired hearing, Lister *et al.* (2000) measured larger overall gap thresholds for older listeners with sensorineural hearing loss (four subjects aged 62–71 years) and without hearing loss (three subjects aged 42–51 years) than for young listeners with sensorineural hearing loss (two subjects aged 21–26 years) and without hearing loss (three subjects aged 22–26 years). The gap thresholds of the older listeners increased more dramatically with marker frequency disparity than those of the young listeners whose gap thresholds remained relatively stable for small frequency disparities, regardless of hearing loss. This suggested that the effect of marker frequency composition on temporal discrimination was greater for older listeners with and without hearing loss than for younger listeners with or without hearing loss. Because the oldest listener with normal hearing in that study was 51 and only two subjects under age 30 had hearing loss, the results were interpreted as motivation for the present, more definitive study.

The purpose of the present study was to investigate the effects of stimulus frequency separation on gap discrimination as a function of age. Based on the results of the studies cited above, it was hypothesized that (1) GDDLs would increase with increasing frequency disparity between marker stimuli for all listeners, (2) GDDLs would increase with increasing age for all frequency disparities, and (3) the increase in GDDLs with frequency disparity would be greater for older listeners than for young listeners.

II. METHOD

The experiment was conducted in two stages. First, detection thresholds for the individual noise band markers were measured using an adaptive procedure. Then, GDDLs were measured adaptively for six marker frequency pairs. For measurement of GDDLs, the experimental method used was comparable to that of Phillips *et al.* (1997) and Lister *et al.* (2000).

TABLE I. Average pure tone thresholds (dB HL) for each age group. Average thresholds for each ear are listed separately.

Age group	Mean age	Pure tone thresholds						
		Ear	250 Hz	500 Hz	1 kHz	2 kHz	4 kHz	6 kHz	8 kHz
Young	25.7	Right	4	7	3	0	2	1	5
		Left	5	4	3	1	3	4	3
Middle	46.3	Right	13	12	3	3	3	10	9
		Left	11	10	4	3	5	13	12
Older	66.3	Right	15	10	10	8	15	20	23
		Left	15	8	11	13	14	15	23

A. Subjects

Eighteen listeners participated in the study. All listeners had normal hearing sensitivity, defined as pure-tone thresholds of 25 dB HL or better at frequencies from 250 to 6000 Hz and pure-tone thresholds of 30 dB HL or better at 8000 Hz in both ears. The subjects fell into three age groups of six listeners each: (1) 18–30 years (mean age 25.7), (2) 40–52 years (mean age 46.3), and (3) 62–74 years (mean age 66.3). Average pure-tone air-conduction thresholds for each age group are presented in Table I. Ten of the 18 listeners (five young, two middle-aged, and three older) had participated in previous psychoacoustic experiments and the remaining eight were naive listeners. All listeners participated in one hour of training prior to data collection and were paid for their participation in the study.

B. Stimuli and procedure

To create the marker stimuli, 400-ms samples of Gaussian noise were generated using APPS software (Tucker-Davis Technologies). The noise samples were filtered to create six bands of $\frac{1}{4}$-oct-wide noise geometrically centered at 500, 1000, 1500, 2000, 2500, and 3000 Hz using a Krohn-Hite Corporation Model 390B multi-channel filter (24 dB/oct filter slopes). The filtered noise bands were digitized (20-kHz sampling rate), cropped to 250-ms samples, and shaped with a $\cos^2$ window to create a 0.5-ms rise–fall time. Sixteen samples of each of the six bands of noise were created.

Prior to measurement of GDDLs, individual ear detection thresholds for the six noise bands were measured using an adaptive, two-interval, two-alternative, forced-choice (2I/2AFC) procedure and a two-down, one-up rule targeting 70.7% correct (Levitt, 1971). The target interval contained the 250-ms marker to be detected and the standard interval contained silence. The adaptive procedure continued until eight reversals occurred. A step-size of 4 dB was used for the first four reversals, after which a 2-dB step- size was implemented. Detection thresholds were calculated as the average intensity level of the final four reversals, and each threshold was measured a minimum of two times. If thresholds for a particular marker differed by more than 4 dB, then additional thresholds were measured until two were obtained that differed by 4 dB or less. For all listeners, two appropriate thresholds were obtained in two to three experimental runs.

For the second stage of the experiment, the markers were paired so that the center frequency of the leading marker was always fixed at 2000 Hz, and the center frequency of the trailing marker was randomly assigned to one of the six frequencies listed above for each experimental run. As a result, both the size and the direction of the frequency difference between markers were varied between runs. The center frequency of each marker remained constant within an experimental run, and, on every trial, individual tokens of leading and trailing markers were randomly selected from a library of 16 samples of each of the filtered noise bands. The $\cos^2$ window was used again on the composite signals to create a 10-ms rise–fall time on the onset of the leading marker and offset of the trailing marker while preserving the 0.5-ms rise–fall on the offset of the leading marker and the onset of the trailing marker. The markers were passed through attenuators (TDT PA4) to set the overall level of the paired markers and a low-pass filter with an 8-kHz cutoff (TDT FT6). The signals were presented diotically via Sennheiser HD 265 linear headphones. In many studies of temporal processing, stimuli are presented monotically; however, Oxenham (2000) found no difference between gap thresholds measured monotically and diotically. Therefore, it is not expected that these results would differ from those collected in a monotic condition given similar age and marker conditions.

Each marker pair was separated by a silent temporal gap, and gap discrimination was measured in random order for the six marker center-frequency combinations using a 2I/2AFC paradigm. In the target interval, the gap size was varied adaptively by a factor of 1.2 using a two-down/one-up rule targeting 70.7% correct discrimination (Levitt, 1971). In the standard interval, the markers were separated by a 1-ms gap to insure that similar gating transients were present in both intervals and preclude the use of short-term spectral cues for interval selection.[1] Presentation order of the standard and target intervals was randomized across trials.

The listener's task was to indicate which one of two stimulus intervals contained the marker pair separated by a larger temporal gap. Visual feedback of the correct interval was provided after each response. The adaptive procedure continued until ten reversals occurred; GDDLs were calculated as the average gap size of the final eight reversals minus the standard 1-ms gap. The individual markers were of equal duration within each interval. To maintain a constant overall duration of 500 ms, each marker was shortened by one-half of the gap size for each interval. The interval between marker pairs within a trial was fixed at 500 ms, and an intertrial interval of 500 ms occurred following the listener's response. All stimuli were presented at 35 dB SL relative to

TABLE II. Average noise band detection thresholds (dB SPL) for each age group. Average thresholds for each ear are listed separately.

Age group	Mean age	Noise band detection thresholds						
		Ear	500 Hz	1 kHz	1.5 kHz	2 kHz	2.5 kHz	3 kHz
Young	25.7	Right	16.5	5.2	−2.2	−2.3	−1.8	−7.3
		Left	14.2	4.8	−2.2	−1.7	−4.7	−10.8
Middle	46.3	Right	18.8	4.7	1.3	0.2	−5.0	−6.7
		Left	18.7	4.5	1.8	3.2	0.2	−6.0
Older	66.3	Right	18.2	6.2	1.3	3.8	0.3	−4.3
		Left	18.0	9.5	8.8	11.2	7.3	0.8

each subject's average threshold for the 2000-Hz marker, based on Fitzgibbons and Gordon-Salant's (1987) study indicating that a sensation level of 25–35 dB is sufficient for optimal gap discrimination. Overall dB SPL level was equal for both markers and both ears for each subject but varied slightly between subjects.

All listeners participated in a 1-h training session prior to data collection during which all conditions were presented in a fixed order (i.e., from smallest to largest frequency separation). After training, the listeners completed three runs per condition in random order for a total of 18 runs and a total time of approximately 2 h. Gap sizes were initiated approximately 10 to 20 ms above the GDDL obtained during the training run for that condition. The starting gap sizes varied from 10 to 200 ms with larger starting gaps necessary for older listeners and for larger frequency disparities between leading and trailing markers. If GDDLs for a particular condition differed by a factor of 2 or more, experimental runs for that condition were repeated until three DLs were obtained that differed by less than a factor of 2. Those three DLs were then used to calculate average GDDLs for each condition for each subject. For all young listeners and most middle-aged and older listeners, three acceptable DLs were measured within four experimental runs; however, for two middle-aged and three older listeners, five or six experimental runs were required for one or two conditions. Four of these listeners had not participated in previous psychoacoustic experiments. One naive listener, OS02, participated in seven experimental runs for three conditions before acceptable thresholds were measured. It is possible that the limited experience of these listeners explains the variability in their GDDLs.

III. RESULTS

Average detection thresholds (dB SPL) measured prior to GDDLs for each age group for each of the six noise bands are shown in Table II. Detection thresholds were highest for markers centered at 500 Hz, were lowest for markers centered at 3000 Hz, and were quite similar for noise bands centered at 1500, 2000, and 2500 Hz. Considerable overlap exists among the detection thresholds for the young and middle-age groups; however, slightly elevated noise band thresholds are evident for the older listeners. A two-way analysis of variance (ANOVA) revealed a significant difference among the detection thresholds of the three age groups $[F(2,15)=5.64,\ p=0.02]$ and a significant difference among the detection thresholds for the six noise band frequencies $[F(5,75)=82.789,\ p<0.001]$. The detection thresholds did not differ significantly between ears ($p>0.05$). A Tukey HSD *post-hoc* analysis revealed that the detection thresholds of the young listeners were significantly better than those of the older listeners ($p=0.01$) but the detection thresholds of the young and middle-aged or middle-aged and older listeners did not differ significantly ($p>0.05$).

The GDDL results were examined to determine the effects of age and stimulus frequency disparity on gap discrimination. Figure 1 shows individual GDDLs as a function of the frequency difference between leading and trailing noise band markers in separate panels for each age group. Although large individual differences are present, greater variability was observed for the older listeners (panel c). The young listeners (panel a) show relatively flat gap discrimination functions, indicating relatively little change in perfor-

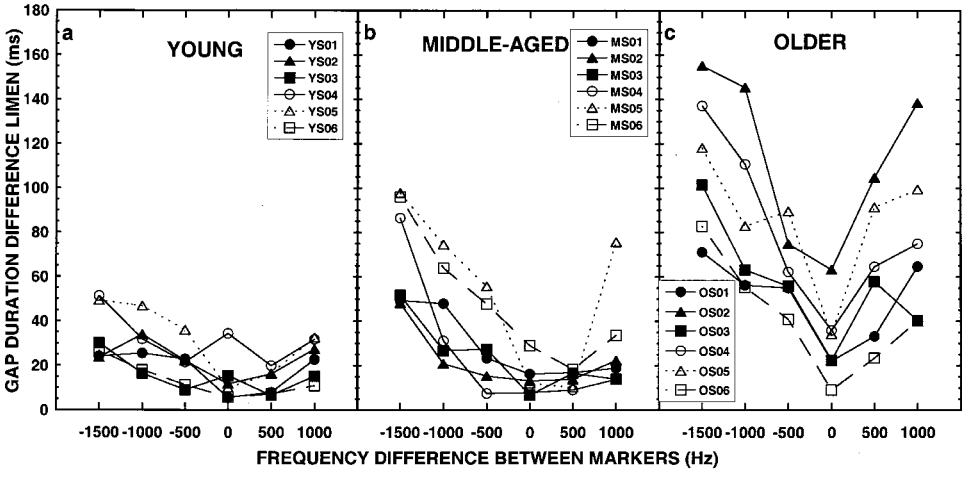

FIG. 1. Gap duration difference limens (GDDLs) in ms as a function of the frequency difference (disparity) between leading and trailing noise markers for listeners with normal hearing aged (a) 18–30 years, (b) 40–52 years, and (c) 62–74 years. The center frequency of the leading marker was always 2000 Hz. Negative frequency disparities indicate conditions in which the center frequency of the trailing marker was less than 2000 Hz and positive frequency disparities indicate conditions in which the center frequency of the trailing marker was greater than 2000 Hz. Each symbol represents the average GDDL for a single listener in a single condition.

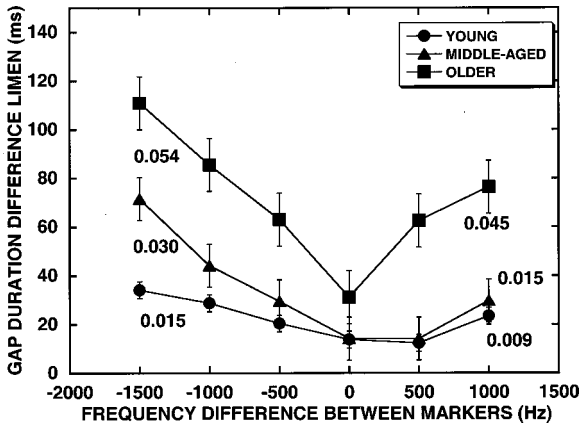

FIG. 2. Gap duration difference limens (GDDLs) in ms as a function of the frequency difference (disparity) between leading and trailing noise markers. The circles represent the performance of the listeners aged 18–30 years. The triangles represent the performance of the listeners aged 40–52 years. The squares represent the performance of the listeners aged 62–74 years. Slope values in ms/Hz are indicated for each age group for the low- and high-frequency sides of the gap discrimination function. Standard error bars are shown for each group and frequency condition.

mance with changes in frequency disparity. For the middle-aged group (panel b), performance was poorest for conditions in which the trailing marker was lower in frequency than the leading marker (negative frequency difference). The older listeners (panel c) show the most dramatic change in performance with frequency disparity. In general, best GDDLs were measured when leading and trailing markers were of the same center frequency (frequency difference of 0), and GDDLs increased as the difference between the center frequency of the leading and trailing markers increased in either direction.

A two-way repeated measures multivariate analysis of variance (MANOVA) revealed that the effect of age group $[R(6,26)=3.98,\ p<0.01]$ was significant. Although the main effect of frequency disparity and the interaction between age and frequency disparity were not significant ($p>0.05$), a Tukey HSD *post-hoc* analysis revealed that the GDDLs for all of the neighboring trailing marker frequencies were significantly different from each other at the $p<0.01$ level with the exception of 2000–2000 Hz vs 2000–2500 Hz. To illustrate the differences among the groups more clearly, average GDDLs and standard errors are plotted as a function of the frequency difference between leading and trailing markers for each age group in Fig. 2. The figure shows greater separation between the young and middle-aged groups for negative frequency disparities (trailing marker frequencies below 2000 Hz) than for positive frequency disparities (trailing marker frequencies above 2000 Hz). The function for the older age group shows distinct differences from the other age groups at all marker frequency disparities. A Tukey HSD *post-hoc* analysis revealed that the performance of the older listeners was significantly poorer than that of the young and middle-aged listeners ($p<0.01$); however, the performance of the young and middle-aged listeners did not differ significantly ($p>0.05$).

Although GDDLs provide an overall estimate of discrimination ability for each condition, these thresholds do not indicate the rate at which GDDLs change with frequency disparity. The data shown in Fig. 2 indicate that GDDLs increase more sharply with increasing frequency disparity for the older listeners than for the young and middle-aged listeners. In order to quantify this difference, the slopes of the lines of best fit (ms/Hz) for equal, 1000-Hz ranges on each side of the GDD function for each subject were determined. Slopes for the low-frequency side of the function (marker differences from 0 to −1000 Hz) were steeper than those for the high-frequency side (marker differences from 0 to 1000 Hz) for the young (0.015 vs 0.009 ms/Hz), middle-aged (0.030 vs 0.015 ms/Hz), and older (0.054 vs 0.045 ms/Hz) listeners. Average slopes for each age group are shown in Fig. 2.

A two-way repeated measures MANOVA revealed a significant effect of age on gap discrimination function slopes $[R(6,26)=3.04,\ p<0.05]$, and the slopes were significantly steeper for the low-frequency side of the gap discrimination function $[R(3,13)=3.85,\ p<0.05]$ than for the high-frequency side. A Tukey HSD *post-hoc* analysis revealed that the function slopes of the older listeners were significantly steeper than those of the young and middle-aged listeners ($p<0.05$) but the slopes of the young and middle-aged listeners did not differ significantly ($p>0.05$).

To quantify the apparent relationship between age and gap discrimination and to determine the relationship between hearing sensitivity and gap discrimination, a multiple regression analysis was performed with the predictors of chronological age and average noise band detection threshold. This analysis revealed that a significant ($p<0.01$) amount of the variance in GDDL for the frequency-disparate markers was accounted for by age (65% for 2000–500 Hz markers, 48% for 2000–1000 Hz markers, 53% for 2000–1500 Hz markers, 49% for 2000–2500 Hz markers, and 44% for 2000–3000 Hz markers). Only 22% of the variance in GDDL for the fixed-frequency (2000–2000 Hz) markers was accounted for by age ($p=0.05$). Age was also a significant ($p<0.01$) predictor of the slope values for both the high- ($R^2=0.53$) and low- ($R^2=0.40$) frequency sides of the gap discrimination function. In contrast, average noise band detection threshold did not account for a significant amount of variance in GDDL or function slopes for any of the marker conditions ($p>0.05$).

IV. DISCUSSION

The purpose of this study was to investigate the effects of age and frequency disparity on gap discrimination in listeners with normal hearing. Previous research has established that increasing frequency disparity between signals that define a silent gap impairs the detection of that gap (e.g., Formby *et al.*, 1993; Phillips *et al.*, 1997; Lister *et al.*, 2000). The discrimination of silent gaps is minimally affected by hearing loss (Gordon-Salant and Fitzgibbons, 1993; Fitzgibbons and Gordon-Salant, 1995; Lister *et al.*, 2000) but clearly deteriorates with age.

The results of Lister *et al.* (2000) established a trend for age-related deterioration of gap discrimination, regardless of hearing status; therefore, hearing loss was controlled in the present study by selecting subjects with normal hearing

across all of the audiometric frequencies. Without the confounding factor of hearing loss that may have obscured the results of previous studies, it was predicted that a clear effect of age would be observed.

The fixed-frequency marker (0-Hz frequency difference) GDDLs measured for the young listeners in this study (14 ms) are larger than those measured previously for similar stimuli in young, normal-hearing listeners: (1) 7 ms by Phillips *et al.* (1997) and (2) 6 ms by Lister *et al.* (2000). The young listeners' GDDLs for the frequency disparate stimuli were also larger than those measured by others. For a marker disparity of 1000 Hz (2000-Hz leading marker followed by a 1000-Hz trailing marker), we measured an average GDDL of 29 ms which is larger than the 12 ms measured by Phillips *et al.* (1997) and the 18 ms measured by Lister *et al.* (2000) for the same marker center frequencies. The GDDLs measured for the middle-aged listeners with normal hearing in this study (14 and 44 ms for the 0- and 1000-Hz disparities) are close to those measured by Lister *et al.* (2000) for three listeners aged 42, 50, and 51 years with normal hearing (5 and 42 ms for the same disparities).

We have no explanation for the differences in gap discrimination ability measured across studies, and it is unclear if these differences are important. It should be noted that the GDDLs of the young listeners in the present study were significantly smaller than those of the older listeners, despite the fact that the young listeners' GDDLs were larger than those measured in other studies.

Gap discrimination function slopes have not been examined extensively in the literature, especially in relation to age; however, gap discrimination function slopes in ms/Hz calculated from Lister *et al.* (2000) for the same ranges used here show significantly steeper low- and high-frequency slopes for their older listeners (0.03 and 0.02 ms/Hz) than for their young listeners (0.008 and 0.007 ms/Hz). In the present study, we measured comparable slope values; low- and high-frequency slopes were 0.054 ms/Hz and 0.045 ms/Hz for the older listeners and were 0.015 ms/Hz and 0.009 ms/Hz for the young listeners (see Fig. 2).

Figure 2 shows a clear effect of age on GDDLs and a similar effect of age for the gap discrimination function slopes. Multiple regression analyses confirm that age is a significant predictor of GDDLs and function slope values. The GDDLs of the older listeners differed significantly from those of the other groups. Observation of the data reveals that the GDDLs for the older listeners are larger for all marker conditions, but the error bars of the three groups overlap for the least frequency-disparate (2000–2000 Hz) marker condition. The differences between the young and middle-aged listeners are most apparent for the most frequency-disparate (2000–500 Hz) marker condition. This suggests a relationship between age and marker complexity in which the effects of age are more apparent for more frequency-disparate stimuli. Further support for this relationship may be found in the function slope data. Significant effects of age on gap discrimination function slopes are apparent; the young and middle-aged listeners had significantly flatter function slopes than the older listeners. The increase in GDDL with frequency disparity that occurred for all listeners was significantly steeper for the older listeners than for the young or middle-aged listeners. Lister *et al.* (2000) found steeper slope values for their older listeners regardless of hearing loss; however, their oldest listener with normal hearing was only 51.

The dependency of gap detection and discrimination on the frequency relationship of the markers bounding the silent gap may be explained using the perceptual ''channel'' theory of temporal processing (Phillips *et al.*, 1997; Formby *et al.*, 1998; Oxenham, 2000; Grose *et al.*, 2001). Phillips *et al.* (1997) and Formby *et al.* (1998) suggested that detection of gaps between markers differing by more than half an octave presented to the same ear (or markers presented to opposite ears) requires between-channel processing across two or more perceptual channels. This theory also suggests that detection of gaps between monaurally presented markers that are close in frequency (less than half an octave apart) utilizes within-channel processing, within a single perceptual channel. In the between-channel case, the listener must detect a gap that exists between the offset of a marker in one channel and the onset of a marker in another channel. For within-channel gap detection, the listener must only monitor the activity in a single channel. Experimental results obtained for listeners with normal and impaired hearing support this hypothesis; measures requiring within-channel processing result in smaller gap thresholds than those that require between-channel processing.

In the work of Phillips *et al.* (1997) and Formby *et al.* (1998), perceptual channels refer to different frequency regions of the ipsilateral auditory system in the monaural case and refer to contralateral auditory pathways in the dichotic case. Because performance is similar for dichotically presented markers and monaurally presented markers that differ by more than half an octave, it is unlikely that the channels are analogous to the auditory filters of the peripheral system. The findings of Phillips *et al.* (1997) and Formby *et al.* (1998) support the existence of centrally located perceptual channels, an idea substantiated by the finding that damage to the peripheral auditory system (i.e., hearing loss) does not consistently affect the processing of silent temporal gaps.

The work of Oxenham (2000) and Grose *et al.* (2001) has explored the strength of this hypothesis by using markers that are perceptually dissimilar but not necessarily frequency disparate. Their results confirm that marker spectral differences are most disruptive to gap detection; gaps between markers that differ in pitch, modulation, and interaural time are as easily resolved as in any within-channel task. Apparently, for markers to represent different perceptual channels, they must differ in spectral characteristics. Resolution of a gap between perceptually different but spectrally fixed-frequency markers does not constitute a between-channel task (Grose *et al.*, 2001). Oxenham (2000) proposes that the perceptual channels important for gap detection depend primarily on peripheral encoding of the marker spectra and higher level neural coding is much less important. This does not explain the findings of normal gap resolution when peripheral encoding of frequency is impaired (i.e., listeners with sensorineural hearing loss have normal gap detection and discrimination), impaired gap resolution when peripheral

encoding of frequency is intact (i.e., older listeners with normal hearing have impaired gap detection and discrimination), or normal gap resolution by those whose peripheral auditory system is bypassed by an auditory brainstem implant (Shannon and Otto, 1990). Further exploration of this topic using groups of listeners across the age range with and without impaired hearing is warranted.

In general terms, the present results suggest that as leading and trailing signals become separated by more than one perceptual channel the discrimination of the gap becomes a between-channel task and gap difference limens increase. This increase occurs with smaller frequency disparities for older listeners than young listeners. It is not surprising that the GDDLs of the older listeners in the present study increase more dramatically with marker frequency disparity than those of young listeners if the older listeners are using between-channel processing for the majority of the gap discrimination signals. For older listeners, gap discrimination may be more difficult than originally thought due to sharply tuned perceptual channels that compel listeners to use between-channel processing for silent gaps between stimuli that differ by as little as $\frac{1}{3}$ oct (see Fig. 2).

Age-related deterioration in the ability to process temporal information between stimuli of different frequencies may ultimately contribute to the speech understanding difficulties reported by older listeners. In fact, a number of investigators have hypothesized that a decline in temporal processing may account for at least some problems with speech understanding associated with aging (e.g., Gordon-Salant and Fitzgibbons, 1993; Strouse *et al.*, 1998; Schneider and Hamstra, 1999; Snell and Frisina, 2000). This is corroborated by the results of Price and Simon (1984) that older listeners with minimal hearing loss require longer silent gaps to perceive differences in stop consonants than young listeners with normal hearing.

Because the leading and trailing markers in the present study were shortened by one-half of the gap size in order to maintain an overall 500-ms interval duration, an extraneous within-channel marker duration cue was created. As a result, listeners may have responded to changes in marker duration in the signal interval instead of changes in gap duration. For the largest overall GDDL (approximately 150 ms), leading and trailing markers were approximately 175 ms in duration. For the smallest GDDLs (5–6 ms), leading and trailing markers were approximately 247 ms in duration. This cue would have been more apparent for the older listeners for whom extreme GDDLs were measured (OS02, OS04, OS05). Marker duration has been shown to affect gap thresholds (Formby and Muir, 1989; Schneider and Hamstra, 1999) when marker durations are relatively brief. Formby and Muir (1989) determined that extraneous marker duration cues may result in underestimates of gap thresholds in cases where the gap threshold is large relative to the marker duration. Therefore, it is possible that the GDDLs of the older listeners were slightly underestimated and larger age-related differences may exist than have been indicated by the present results.

Gap discrimination appears to be minimally affected by differences in peripheral auditory acuity (e.g., Gordon-Salant and Fitzgibbons, 1993; Fitzgibbons and Gordon-Salant, 1994; Lister *et al.*, 2000) but is affected by the frequency composition of the marker stimuli in such a way as to suggest a narrowing of perceptual channels with age. There is a lack of evidence in the literature of narrowing auditory filters with age. In fact, some studies show that critical bandwidths as measured by upward spread of masking and auditory filter shapes actually broaden (Patterson *et al.*, 1982) or remain stable with age (Klein *et al.*, 1990; Sommers and Humes, 1993). This adds support to our hypothesis that the perceptual channels that appear to narrow with age are not limited by peripheral auditory filter widths but are influenced by both peripheral and central encoding mechanisms that become less acute with age.

V. SUMMARY

The results of this study indicate that the factors of age and frequency disparity negatively affect diotic gap discrimination. Significantly larger GDDLs were measured for the older listeners than the young and middle-aged listeners. The GDDLs for all three age groups were quite similar for the least frequency-disparate condition (2000–2000 Hz marker pair) and the young and middle-aged listeners differed noticeably only for the most frequency-disparate condition, the 2000–500 Hz marker pair. Small but significant differences in hearing sensitivity among the listeners were not predictive of GDDLs. These results suggest that gap discrimination relies on a temporal discrimination mechanism that becomes less acute with age; this effect becomes more apparent as the complexity of the stimuli increases. Changes in gap discrimination function slopes also occurred with age. The older listeners had steeper function slopes than the young and middle-aged listeners. Apparently, older listeners have more difficulty processing temporal information between signals of different frequency characteristics than young and middle-aged listeners. Other investigators (Phillips *et al.*, 1997; Formby *et al.*, 1998) have attributed the increase in gap threshold with frequency disparity to within- and between-channel processing. Results of this study indicate that older listeners have sharper perceptual channels and use between-channel processing of gaps for smaller marker frequency disparities than young and middle-aged listeners. Consequently, older listeners have larger GDDLs and steeper gap discrimination function slopes. Because critical bandwidths have been shown to increase (Patterson *et al.*, 1982) or remain stable (Klein *et al.*, 1990; Sommers and Humes, 1993) with age and because age-related changes in temporal discrimination are apparent for listeners without cochlear hearing loss, it is unlikely that the decrease in perceptual channel widths with age is related to peripheral critical bandwidths. Possibly, coding of temporal parameters is accomplished by a central temporal mechanism that compensates very well for deficiencies in the peripheral system (i.e., cochlear hearing loss). Further investigation of the shape and nature of the temporal perceptual channels of older listeners is warranted as they may relate to the speech perception difficulties experienced by these listeners in the presence and absence of hearing loss.

ACKNOWLEDGMENTS

This study represents a portion of the doctoral dissertation written by the first author under the guidance of the co-authors and was supported in part by a grant from Sigma Xi.

[1]Spectral cues (described as ''blips'' or ''hiccoughs'' by the listeners) were perceived in both intervals by all listeners. In the frequency-disparate conditions, this abrupt spectral discontinuity would have occurred regardless of whether there was a gap in the standard interval; however, in the fixed-frequency condition, a spectral discontinuity was created in the standard interval that would not have been present if contiguous markers had been used.

Collyer, C. (**1974**). ''The detection of a temporal gap between two disparate stimuli,'' Percept. Psychophys. **16**, 96–100.

DeFilippo, C., and Snell, K. (**1986**). ''Detection of a temporal gap in low-frequency narrow-band signals by normal-hearing and hearing-impaired listeners,'' J. Acoust. Soc. Am. **80**, 1354–1358.

Divenyi, P., and Danner, W. (**1977**). ''Discrimination of time intervals marked by brief acoustic pulses of various intensities and spectra,'' Percept. Psychophys. **21**, 125–142.

Divenyi, P., and Haupt, K. (**1997**). ''Audiological correlates of speech understanding deficits in elderly listeners with mild-to-moderate hearing loss III: Factor representation,'' Ear Hear. **18**, 189–201.

Dreschler, W., and Plomp, R. (**1985**). ''Relations between psychophysical data and speech perception for hearing impaired subjects II,'' J. Acoust. Soc. Am. **78**, 1261–1270.

Fitzgibbons, P., and Gordon-Salant, S. (**1987**). ''Minimum stimulus levels for temporal gap resolution in listeners with sensorineural hearing loss,'' J. Acoust. Soc. Am. **81**, 1542–1545.

Fitzgibbons, P., and Gordon-Salant, S. (**1994**). ''Age effects on measures of auditory duration discrimination,'' J. Speech Hear. Res. **37**, 662–670.

Fitzgibbons, P., and Gordon-Salant, S. (**1995**). ''Age effects on duration discrimination with simple and complex stimuli,'' J. Acoust. Soc. Am. **98**, 3140–3145.

Fitzgibbons, P., and Wightman, F. (**1982**). ''Gap detection in normal and hearing-impaired listeners,'' J. Acoust. Soc. Am. **72**, 761–765.

Fitzgibbons, P., Pollatsek, A., and Thomas, I. (**1974**). ''Detection of temporal gaps within and between perceptual tonal groups,'' Percept. Psychophys. **16**, 522–528.

Florentine, M., and Buus, S. (**1984**). ''Temporal gap detection in sensorineural and simulated hearing impairments,'' J. Speech Hear. Res. **27**, 449–455.

Formby, C., and Muir, K. (**1989**). ''Effects of randomizing signal level and duration on temporal gap detection,'' Audiology **28**, 250–257.

Formby, C., Barker, C., Abbey, H., and Raney, J. J. (**1993**). ''Detection of silent temporal gaps between narrow-band noise markers having second-formantlike properties of voiceless stop/vowel combinations,'' J. Acoust. Soc. Am. **93**, 1023–1027.

Formby, C., Gerber, M., Sherlock, L., and Magder, L. (**1998**). ''Evidence for an across-frequency, between-channel process in asymptotic monaural temporal gap detection,'' J. Acoust. Soc. Am. **103**, 3554–3560.

Gordon-Salant, S., and Fitzgibbons, P. (**1993**). ''Temporal factors and speech recognition performance in young and elderly listeners,'' J. Speech Hear. Res. **36**, 1276–1285.

Gordon-Salant, S., and Fitzgibbons, P. (**1999**). ''Profile of auditory temporal processing in older listeners,'' J. Speech Hear. Res. **42**, 300–311.

Grose, J., and Hall, J. (**1996**). ''Perceptual organization of sequential stimuli in listeners with cochlear hearing loss,'' J. Speech Hear. Res. **39**, 1149–1158.

Grose, J., Hall, J., Buss, E., and Hatch, D. (**2001**). ''Gap detection for similar and dissimilar gap markers,'' J. Acoust. Soc. Am. **109**, 1587–1595.

He, N., Horwitz, A., Dubno, J., and Mills, J. (**1999**). ''Psychometric functions for gap detection in noise measured from young and aged subjects,'' J. Acoust. Soc. Am. **106**, 966–978.

Kinney, J. (**1961**). ''Discrimination in auditory and visual patterns,'' Am. J. Psychol. **74**, 529–541.

Klein, A., Mills, J., and Adkins, W. (**1990**). ''Upward spread of masking, hearing loss, and speech recognition in young and elderly listeners,'' J. Acoust. Soc. Am. **87**, 1266–1271.

Levitt, H. (**1971**). ''Transformed up-down methods in psychoacoustics,'' J. Acoust. Soc. Am. **49**, 467–477.

Lister, J., Koehnke, J., and Besing, J. (**2000**). ''Binaural gap duration discrimination in listeners with impaired hearing and normal hearing,'' Ear Hear. **21**, 141–150.

Moore, B., Peters, R., and Glasberg, B. (**1992**). ''Detection of temporal gaps in sinusoids by elderly subjects with and without hearing loss,'' J. Acoust. Soc. Am. **92**, 1923–1932.

Neff, D., Jesteadt, W., and Brown, E. (**1982**). ''The relation between gap discrimination and auditory stream segregation,'' Percept. Psychophys. **31**, 493–501.

Oxenham, A. (**2000**). ''Influence of spatial and temporal coding on auditory gap detection,'' J. Acoust. Soc. Am. **107**, 2215–2223.

Patterson, R., Nimmo-Smith, I., Weber, D., and Milroy, R. (**1982**). ''The deterioration of hearing with age: frequency selectivity, the critical ratio, the audiogram, and speech threshold,'' J. Acoust. Soc. Am. **72**, 1788–1803.

Phillips, D., Taylor, T., Hall, S., Carr, M., and Mossop, J. E. (**1997**). ''Detection of silent intervals between noises activating different perceptual channels: some properties of ''central'' auditory gap detection,'' J. Acoust. Soc. Am. **101**, 3694–3705.

Price, P., and Simon, H. (**1984**). ''Perception of temporal differences in speech by normal-hearing adults: effects of age and intensity,'' J. Acoust. Soc. Am. **76**, 405–410.

Schneider, B., and Hamstra, S. (**1999**). ''Gap detection thresholds as a function of tonal duration for younger and older listeners,'' J. Acoust. Soc. Am. **106**, 371–380.

Schneider, B., Pichora-Fuller, M., Kowalchuk, D., and Lamb, M. (**1994**). ''Gap detection and the precedence effect in young and old adults,'' J. Acoust. Soc. Am. **95**, 980–991.

Shannon, R., and Otto, S. (**1990**). ''Psychophysical measures from electrical stimulation of the human cochlear nucleus,'' Hear. Res. **47**, 159–168.

Snell, K. (**1997**). ''Age-related changes in temporal gap detection,'' J. Acoust. Soc. Am. **101**, 2214–2220.

Snell, K., and Frisina, D. (**2000**). ''Relationships among age-related differences in gap detection and word recognition,'' J. Acoust. Soc. Am. **107**, 1615–1626.

Snell, K., Ison, J., and Frisina, D. (**1994**). ''The effects of signal frequency and absolute bandwidth on gap detection in noise,'' J. Acoust. Soc. Am. **96**, 1458–1464.

Sommers, M., and Humes, L. (**1993**). ''Auditory filter shapes in normal-hearing, noise-masked normal, and elderly listeners,'' J. Acoust. Soc. Am. **93**, 2903–2449.

Strouse, A., Ashmead, D., Ohde, R., and Grantham, W. (**1998**). ''Temporal processing in the aging auditory system,'' J. Acoust. Soc. Am. **104**, 2385–2399.

Tyler, R., Summerfield, Q., Wood, E., and Fernandes, M. (**1982**). ''Psychoacoustic and phonetic temporal processing in normal and hearing impaired listeners,'' J. Acoust. Soc. Am. **72**, 740–752.

van Rooij, J., and Plomp, R. (**1990**). ''Auditive and cognitive factors in speech perception by elderly listeners II. Multivariate analyses,'' J. Acoust. Soc. Am. **88**, 2611–2624.

Williams, K., and Elfner, L. (**1976**). ''Gap detection with three auditory events: A single-channel process,'' J. Acoust. Soc. Am. **60**, 423–428.

Williams, K., and Perrott, D. (**1972**). ''Temporal resolution of tonal pulses,'' J. Acoust. Soc. Am. **51**, 644–647.

Working Group on Speech Understanding and Aging, National Research Council, Committee on Hearing, Bioacoustics, and Biomechanics (**1988**). ''Speech understanding and aging,'' J. Acoust. Soc. Am. **83**, 859–895.

Efficient adaptive procedures for threshold and concurrent slope estimates for psychophysics and speech intelligibility tests

Thomas Brand and Birger Kollmeier
Carl von Ossietzky Universität Oldenburg, Medizinische Physik, Fachbereich Physik, D-26111 Oldenburg, Germany

(Received 20 November 2000; revised 5 September 2001; accepted 20 March 2002)

The minimum standard deviations achievable for concurrent estimates of thresholds and psychometric function slopes as well as the optimal target values for adaptive procedures are calculated as functions of stimulus level and track length on the basis of the binomial theory. The optimum pair of targets for a concurrent estimate is found at the correct response probabilities $p_1 = 0.19$ and $p_2 = 0.81$ for the logistic psychometric function. An adaptive procedure that converges at these optimal targets is introduced and tested with Monte Carlo simulations. The efficiency increases rapidly when each subject's response consists of more than one statistically independent Bernoulli trial. Sentence intelligibility tests provide more than one Bernoulli trial per sentence when each word is scored separately. The number of within-sentence trials can be quantified by the *j* factor [Boothroyd and Nittrouer, J. Acoust. Soc. Am. **84**, 101–114 (1988)]. The adaptive procedure was evaluated with 10 normal-hearing and 11 hearing-impaired listeners using two German sentence tests that differ in *j* factors. The expected advantage of the sentence test with the higher *j* factor was not observed, possibly due to training effects. Hence, the number of sentences required for a reliable speech reception threshold (approximately 1 dB standard deviation) concurrently with a slope estimate (approximately 20%–30% relative standard deviation) is at least $N = 30$ if word scoring for short, meaningful sentences ($j \approx 2$) is performed. [DOI: 10.1121/1.1479152]

PACS numbers: 43.66.Yw, 43.71.Gv, 43.71.Ky [SPB]

I. INTRODUCTION

In many psychophysical tasks, the experimenter is interested not only in the threshold but also in the slope of the psychometric function. However, an accurate assessment of both threshold and slope requires much more measurement time than the assessment of the threshold alone. This study investigates how both parameters can be assessed concurrently and as efficiently as possible. The primary applications are sentence intelligibility tests, while some of the methods introduced here might also be applied to other psychophysical tasks.

Sentence intelligibility tests generally measure the speech-reception threshold (SRT), that is, the speech level that corresponds to 50% intelligibility in noise. The standard deviation of the SRT estimate should be less than 1 dB in order to differentiate between different acoustical situations [such as, e.g., spatial distributions of target speaker and interfering noise sources (Bronkhorst and Plomp, 1988; Peissig and Kollmeier, 1997)] and between different listeners (such as, normal-hearing listeners and hearing-impaired listeners with various impairments). On the other hand, high efficiency is necessary, because measurement procedures which take too much time before yielding reliable results are not practicable in clinical audiometry and hearing aid fitting.

The discrimination functions (i.e., the intelligibility as a function of speech level or signal-to-noise ratio, which is often referred to as the performance-intensity curve) of many sentence tests (e.g., Plomp and Mimpen, 1979; Hagerman, 1982; Nilsson *et al.*, 1994; Kollmeier and Wesselkamp, 1997; Wagener *et al.*, 1999a) show slopes of between 0.15 and 0.25 dB^{-1} which are considerably steeper than the values obtained with single-word tests. Since the standard deviation of SRT estimates is inversely proportional to the slope of the discrimination function, these sentence tests are better suited for efficient and reliable SRT measurements than, for example, single-word tests. An interfering effect, however, is that many hearing-impaired listeners show flatter discrimination functions than normal-hearing listeners. The audiological relevance of the discrimination function slope is based on the fact that the SRT is related to an intelligibility value of 50%, which is a value too low for a satisfying conversation. Much more relevant to the listener's communication in noise is the range of SNRs where intelligibility is beyond about 80%. This relevant level range increases with decreasing slope.

While it is known that efficient SRT measurements are possible with sentence tests, this study investigates whether an accurate concurrent estimate of SRT and slope is possible within a tolerable measuring time. The standard deviation of slope estimates is proportional to the slope of the underlying discrimination function. Typical slope values range from 0.2 dB^{-1} (20% increase in intelligibility for 1 dB increase in SNR) for normal-hearing listeners to 0.05 dB^{-1} for severely hearing-impaired listeners. In order, for example, to reliably differentiate between high, intermediate, and low slope values, a relative intraindividual standard deviation of below 25% of the actual slope value has to be reached.

The measurement time necessary to obtain sufficient precision in SRT and slope estimates is determined by the presentation levels, the speech material, and the number of sentences used in the measurement. The precision of the SRT and slope estimates can be calculated as a function of the

number of trials and of the placement of presentation levels based on the binomial theory. For this calculation, the predictability of the speech material is essential. This is characterized by the *j* factor, which denotes the effective number of statistically independently perceived elements per sentence (Boothroyd and Nittrouer, 1988). Since the precision of estimates is inversely proportional to the square root of the effective number of statistically independent elements tested during the track, a higher *j* factor yields a higher precision within the same number of sentences, thus providing a more efficient estimate.

Adaptive procedures can be used to concentrate presentation levels in the range which yields the smallest standard deviations in SRT and slope estimates. A variety of adaptive procedures have been described in the literature, such as PEST (parameter estimation by sequential testing) (Taylor and Creelman, 1967), BUDTIF (block-up-and-down, two-interval, forced-choice) (Campbell, 1974) and UDTR (up-down transformed response) (Levitt, 1971). All of these procedures are designed for conditions with only two possible results per trial, for example *true* and *false* in forced-choice tasks or *yes* and *no* in *yes–no* tasks. In sentence tests, however, each word can be scored independently, so that each trial has more than two possible outcomes. This additional information can be used to design adaptive procedures which might converge more efficiently than the procedures mentioned above. In this study, a generalization of the procedure of Hagerman and Kinnefors (1995) is investigated with respect to its efficiency of SRT and slope estimation.

Kollmeier *et al.* (1988) investigated different adaptive staircase procedures with the help of Markov chains. This approach permits one to derive variances and biases of psychometric function parameter estimates given a fixed number of trials analytically without any random sampling. In this study, however, Monte Carlo simulations are applied to investigate the accuracy and efficiency of the adaptive procedures.

To evaluate the results of the simulations, two different German sentence intelligibility tests, the Göttingen sentence test (Kollmeier and Wesselkamp, 1997) and the Oldenburg sentence test (Wagener *et al.*, 1999c, b, a), were applied to normal-hearing and hearing-impaired listeners. These two tests were recorded with the same talker and have nearly the same SRT and slope values for normal-hearing listeners, but differ in predictability of the words.

II. STATISTICAL METHOD

A. Discrimination function

The discrimination function describes the listener's speech intelligibility or discrimination as a function of speech level. Speech intelligibility is defined as the mean probability p that the words of a sentence are repeated correctly by the listener (so-called "*word scoring*"). It is also possible to define p as the probability of repeating whole sentences correctly (so-called "*sentence scoring*"). The speech level L may either refer to the sound pressure level of the speech signal in conditions without competitive noise or to the signal-to-noise ratio (SNR), if the test is performed under noise. Similar definitions hold for psychometric functions in different psychophysical experiments.

A logistic function (1) was chosen to represent the discrimination function:

$$p(L,L_{50},s_{50}) = \frac{1}{1+\exp(4\cdot s_{50}\cdot (L_{50}-L))}. \tag{1}$$

Here L_{50} denotes the speech reception threshold (SRT), which refers to a 50% probability of correct responses. The parameter s_{50} denotes the slope of the discrimination function at L_{50}.

B. Variability of estimates and optimal presentation levels

1. Efficient threshold estimation

Each trial (i.e., each stimulus with the subject's response) can be assumed to be a Bernoulli trial with the probability $p(L)$ of a correct outcome given by the psychometric or discrimination function. The standard deviation, σ_p, of an estimate based on n trials is

$$\sigma_p = \sqrt{\frac{p(1-p)}{n}}. \tag{2}$$

The 50% correct level is the level which can be estimated with the minimal standard deviation σ_{SRT} for the logistic discrimination function (Levitt, 1971; Laming and Marsh, 1988; Green, 1990). It is sometimes called the "*sweetpoint*." To a first approximation, the value of σ_{SRT} is equal to the standard deviation of the intelligibility estimate σ_p divided by the slope of the psychometric function at the SRT. If n trials are presented at the *sweetpoint*, the asymptotic minimum value of $\sigma_{L_{50}}$ for large values of n is

$$\sigma_{L_{50}}(\text{sweetpoint}) = \frac{0.5}{s_{50}\cdot\sqrt{n}}. \tag{3}$$

The efficiency of an adaptive procedure for SRT estimates can be quantified by the normalized standard deviation $\hat{\sigma}_{L_{50}} = \sigma_{L_{50}}/\sigma_{L_{50}}(\text{sweetpoint})$, with $\sigma_{L_{50}}$ denoting the empirical standard deviation in SRT estimates provided by the procedure. The normalized standard deviation is equal to the reciprocal square root of the *efficiency* as defined by Taylor and Creelman (1967).

The considerations above imply that all trials are presented at a constant presentation level. However, at least two different discrimination values p_1 and p_2 at two presentation levels L_1 and L_2 are required to estimate L_{50} and s_{50} concurrently. In this case, L_{50} and s_{50} can be calculated by solving a system of two logistic functions and two variables L_{50} and s_{50}. According to the Gaussian error law the standard deviation $\sigma_{L_{50}}$ of L_{50} can be calculated as

$$\sigma_{L_{50}} = \sqrt{\frac{1}{n_1}\left(\frac{\partial L_{50}}{\partial p_1}\right)^2\cdot p_1(1-p_1) + \frac{1}{n_2}\cdot\left(\frac{\partial L_{50}}{\partial p_2}\right)^2\cdot p_2(1-p_2)} \tag{4}$$

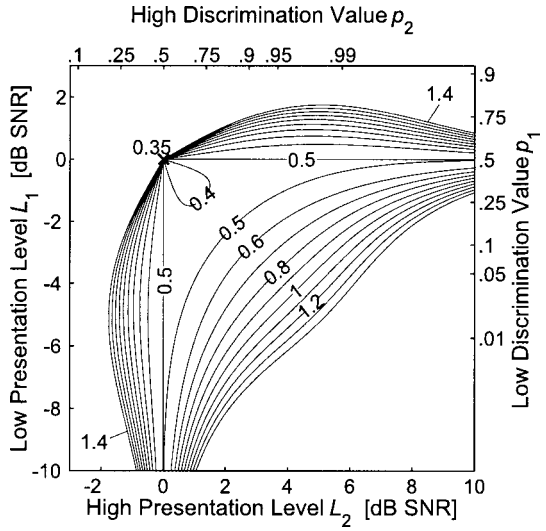

FIG. 1. Contour plot of the standard deviation $\sigma_{L_{50}}$ of the threshold estimate, when two different presentation levels are used. The contour lines show $\sigma_{L_{50}}$ in dB. The cross indicates the *sweetpoint* (i.e., the minimum of $\sigma_{L_{50}}$). The discrimination function is logistic with a midpoint of $L_{50}=0$ dB and a slope of $s_{50}=0.2$ dB^{-1}. $n_1=n_2=25$ trials were performed at each level. The axes are given both as presentation levels in dB units and as discrimination values.

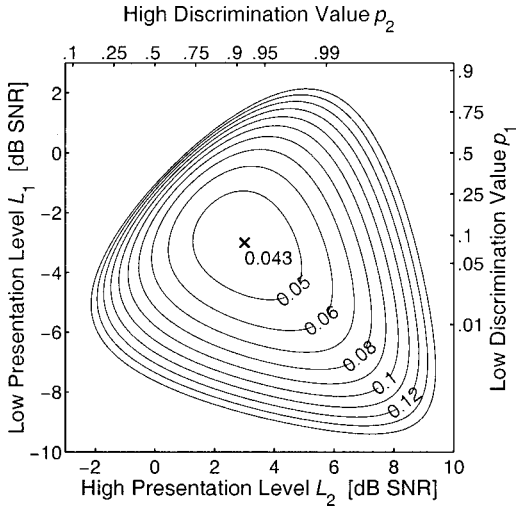

FIG. 2. Contour plot of the standard deviation $\sigma_{s_{50}}$ of the s_{50} estimate in the same condition and representation as given in Fig. 1. The contour lines show $\sigma_{s_{50}}$ in dB^{-1}. The cross indicates the *sweetpair* (i.e., the minimum of $\sigma_{s_{50}}$).

with n_1 and n_2 denoting the number of trials presented at the two levels. Figure 1 shows $\sigma_{L_{50}}$ as a function of (L_1,L_2) and $(p_1(L_1),p_2(L_2))$, respectively. The parameters n_1 and n_2 are set to 25. The L_{50} parameter is set to 0 dB and s_{50} is set to 0.2 dB^{-1}. These values refer to typical parameters of a test employing short, meaningful sentences (cf. Sec. II C for the settings of n_1 and n_2). The minimum of $\sigma_{L_{50}}$ for this condition is found to be 0.35 dB. This value is accomplished if both stimuli are presented exactly at the *sweetpoint* ($L_1=L_2=0$ dB and $p_1=p_2=0.5$). However, $\sigma_{L_{50}}(L_1,L_2)$ is not continuous at this point.

2. Efficient slope estimation

The standard deviation $\sigma_{s_{50}}$ of the s_{50} estimate can be derived by analogy to Eq. (4). Numerical minimization of $\sigma_{s_{50}}$ gives the pair of discrimination values ($p_1=0.083$, $p_2=0.917$) with the minimum standard deviation of slope estimation. By analogy to the *sweetpoint* we denote this pair of stimulus levels as the "*sweetpair*." The value of $\sigma_{s_{50}}$ at the *sweetpair* is proportional to s_{50}. Under the assumption that $n_1=n_2=n$ trials are performed at both levels of the *sweetpair*, the asymptotic minimum value of $\sigma_{s_{50}}$ can be derived numerically as

$$\sigma_{s_{50}}(\text{sweetpair})=\frac{1.07\cdot s_{50}}{\sqrt{n}}. \tag{5}$$

The efficiency of an adaptive procedure that estimates the slope of the discrimination function can be quantified by the normalized standard deviation $\hat{\sigma}_{s_{50}}=\sigma_{s_{50}}/\sigma_{s_{50}}(\text{sweetpair})$, with $\sigma_{s_{50}}$ denoting the standard deviation of slope estimates provided by the procedure.

Figure 2 shows $\sigma_{s_{50}}$ as a function of (L_1,L_2) and $(p_1(L_1),p_2(L_2))$. The conditions are the same as in Fig. 1. The minimal $\sigma_{s_{50}}$ is 0.043 dB^{-1}, which is reached at the *sweetpair* ($L_1=-3.00$ dB, $L_2=3.00$ dB and $p_1=0.083$, $p_2=0.917$). Wetherhill (1963) and O'Regan and Humbert (1989) calculated the same optimal values for p_1 and p_2 for the logistic function with the second derivatives of the likelihood function. Levitt (1971) calculated the optimal presentation levels for slope estimates for the cumulative normal psychometric function. He proposed placing observations at a distance of 1.57σ on either side of μ, that is, at $p=0.058$ and $p=0.942$. This shows that the form of the underlying discrimination function—whether logistic or normal—has only a small influence on the position of the *sweetpair*.

3. Concurrent threshold and slope estimation

Since the discrimination values of the *sweetpoint* ($p=0.5$) and of the *sweetpair* ($p_1=0.08$, $p_2=0.92$) differ considerably, an efficient concurrent SRT and slope estimate requires a compromise between the accuracies of L_{50} and s_{50} estimates. One approach quantifying the accuracy of a common L_{50} and s_{50} estimate is to calculate the quadratic mean of the standard deviations $\sigma_{L_{50}}$ and $\sigma_{s_{50}}$ normalized by their respective minima, $\min(\sigma_{L_{50}})$ and $\min(\sigma_{s_{50}})$:

$$\sigma_{\text{comp}}=\frac{1}{\sqrt{2}}\cdot\sqrt{\left(\frac{\sigma_{L_{50}}}{\min(\sigma_{L_{50}})}\right)^2+\left(\frac{\sigma_{s_{50}}}{\min(\sigma_{s_{50}})}\right)^2}. \tag{6}$$

The minimum of σ_{comp} is reached at $p_{1,\text{comp}}=0.19$, $p_{2,\text{comp}}=0.81$. Wetherhill (1963) and O'Regan and Humbert (1989) derived similar values ($p_{1,\text{comp}}=0.176$ and $p_{2,\text{comp}}=0.823$) from the second derivatives of the likelihood function. Levitt (1971) proposed similar values for a good compromise in estimating both σ and μ of the cumulative normal psychometric function. He proposed placing observations at distance σ on either side of μ, that is, at $p=0.159$ and $p=0.841$.

C. Predictability of speech

In Sec. II A each trial (i.e., each presentation of a stimulus and the subject's response) was assumed to be a Bernoulli trial. In the case of sentence tests, we have to extend this assumption, as each sentence consists of several words which can be scored separately. That is, several Bernoulli trials are performed per sentence. Because of context effects prevalent in the perception of speech, the effective number of statistically independent Bernoulli trials is smaller than the number of words. If one or more words of a sentence have been recognized, the probability of recognizing the remainder increases. According to Boothroyd and Nittrouer (1988) the effective number of statistically independent elements in a sentence can be quantified with the j factor, which is defined as:

$$j = \frac{\log\,(p_s)}{\log\,(p_w)}. \tag{7}$$

The value p_s denotes the probability of understanding a sentence completely (i.e., understanding all words in a sentence correctly) and p_w denotes the probability of correctly understanding each single word of the sentence separately. To take the context effect into account, the number of Bernoulli trials n in Eqs. (2)–(5) has to be set to jN, with N denoting the number of sentences tested. For example, the setting of $n_1 = n_2 = 25$ in Figs. 1 and 2 corresponds to 10 sentences with $j = 2.5$.

D. Maximum likelihood estimator

In order to fit the discrimination function to the data, a maximum-likelihood method is employed. If a test list with a total of m words is presented to the listener, the likelihood of a given discrimination function $p(L, L_{50}, s_{50})$ is

$$l(p(L,L_{50},s_{50})) = \prod_{k=1}^{m} p(L_k,L_{50},s_{50})^{c(k)} \times [1-p(L_k,L_{50},s_{50})],^{1-c(k)}, \tag{8}$$

with $c(k)=1$ if the word k was repeated correctly and $c(k)=0$ if the word k was not repeated correctly. The discrimination function with the maximum likelihood is determined by varying the parameters L_{50} and s_{50} until $\log\,(l(p(L,L_{50},s_{50})))$ is maximal.

E. Monte Carlo simulations

Monte Carlo simulations were performed for the logistic discrimination function. Two thousand Monte Carlo runs were performed in Sec. IV A. Ten thousand runs were performed in Sec. IV B. Without loss of generality, L_{50} was set to 0 dB in all simulations. The initial level of each simulation was chosen randomly from a normal distribution with a standard deviation of 15 dB. A number of j Bernoulli trials with a probability of success $p(L)$ were performed per sentence to account for the j factor. The discrimination value for each sentence was calculated by dividing the sum of the results of the Bernoulli trials by j. Thus, only integer values of j could be simulated, which is a simplification, because in real speech noninteger j factors occur as well.

III. ADAPTIVE PROCEDURE

A generalization of the procedure of Hagerman and Kinnefors (1995) is proposed which changes the presentation level of the subsequent sentence by

$$\Delta L = -\frac{f(i)\cdot(\text{prev}-\text{tar})}{\text{slope}}. \tag{9}$$

The parameter tar denotes the target discrimination value at which the procedure should converge, prev denotes the discrimination value obtained in the previous sentence which is used as input to the adaptive level setting. The slope parameter is set to 0.15 dB^{-1} in this study, which is a medium value for the sentence tests used in this study. The parameter $f(i)$ controls the rate of convergence. Its value depends on the number i of reversals of presentation level. The sequence $f(i)$ has to start at values above 1 to allow for large steps at the beginning of the adaptive procedure. With increasing number of reversals, $f(i)$ has to decrease to stabilize presentation levels near the target. The influence of $f(i)$ is investigated using Monte Carlo simulations in Sec. IV A. The sequence $f(i) = 1.5 \times 1.41^{-i}$ yielded the optimal efficiency in these simulations. With $f(i)=1$, tar$=0.4$, and slope$=0.2$, Eq. (9) is equal to the adaptive rule of Hagerman and Kinnefors (1995).

If only the SRT is to be measured, tar is set to 0.5 (*sweetpoint*) to yield an optimal SRT estimate. In this condition, the adaptive procedure is called A1. If L_{50} and s_{50} are to be measured concurrently, two randomly interleaved tracks are used which converge at $p_1 = 0.2$ and $p_2 = 0.8$ (*pair of compromise*). This condition of the adaptive procedure, using the targets 0.2 and 0.8 in a randomly interleaved order with random switching between two concurrent adaptive procedures, is called A2.

IV. SIMULATIONS

A. Rate of convergence

Since the discrimination function is fitted to the complete track, the efficiency of an adaptive procedure is optimal if all stimuli during the whole track are placed as close to the target as possible.

The rate of convergence is controlled by $f(i)$, with i denoting the index of the reversal. The exponential function $f(i) = a \cdot b^{-i}$ was chosen to parametrize the step size. It implements rules of halving step size after each reversal ($b = 2$) and of halving step size after every second ($b = 1.41$), third ($b = 1.26$), and fourth ($b = 1.189$) reversal. Mean values and standard deviations of the presentation level L were derived as functions of trial number n by Monte Carlo simulations. Simulations were carried out for all combinations of the parameters $a = 1, 1.5, 2, 2.5, 3, 4$ and $b = 1.189, 1.26, 1.41, 2$. The final value of $f(i)$ was limited to 0.1. This minimal value produced the best convergence for high trial numbers in a pilot study in which the final values 0.025, 0.05, 0.1, and 0.2 were tested. The parameters ($a = 1.5$, $b = 1.41$) yielded the best convergence for both procedures A1 and A2 over all of the tested slope values. Further details can be found in Brand (2000).

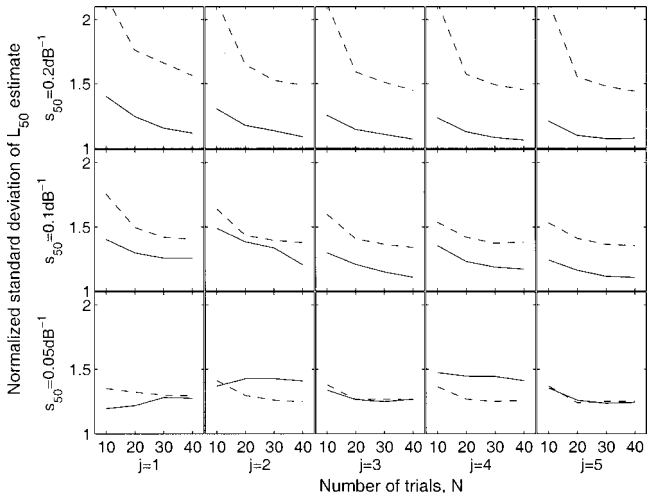

FIG. 3. Normalized standard deviations of L_{50} estimates as functions of N for different settings of s_{50} and j. The ordinate of each panel indicates $\hat{\sigma}_{L_{50}}$ [i.e., $\sigma_{L_{50}}$ divided by its minimum value at the sweetpoint according to Eq. (3)], the abscissa indicates N. Solid line: procedure A1 (i.e., target value set to 0.5), dashed line: procedure A2 (i.e., target values set to $p_1=0.2$ and $p_2=0.8$).

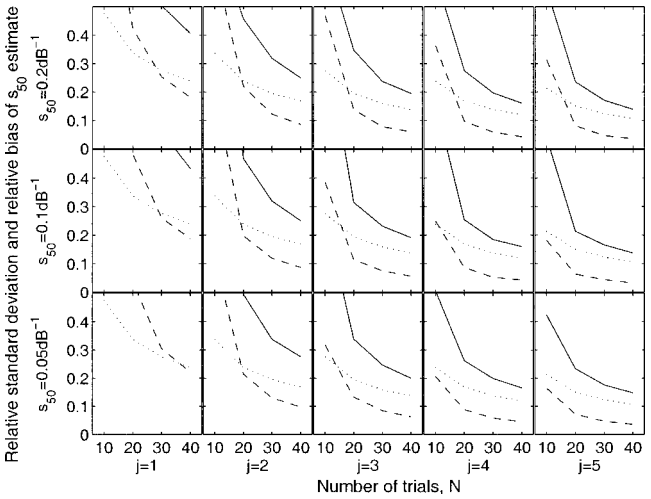

FIG. 4. Relative standard deviations and biases of s_{50} estimates yielded by procedure A2 as a function of N for different settings of s_{50} and j. The ordinate of each panel indicates the standard deviation (solid line) and the bias (dashed line) of the s_{50} estimate relative to the underlying s_{50} value; the abscissa indicates N. The dotted line indicates the minimum achievable standard deviation of s_{50} estimates at the *sweetpair* according to Eq. (5).

B. Accuracy of fit

For both algorithms the intraindividual standard deviations and biases in L_{50} and s_{50} estimates were predicted using Monte Carlo simulations. All combinations of $s_{50}=0.05$, 0.10, and 0.20 dB^{-1} and $j_1=j_2=1,2,3,4,5$ and $N=10,20,30,40$ were performed. In order to simplify the simulations, j was kept constant with level. In the interleaved tracks $N_1=N_2=N/2$ sentences were performed per target.

1. Threshold estimates

Figure 3 shows the normalized standard deviations $\hat{\sigma}_{L_{50}}$ of the L_{50} estimates, that is, $\sigma_{L_{50}}$ relative to its minimal value at the *sweetpoint* for the respective settings of $n=N\cdot j$ and s_{50} given by Eq. (3). Each panel shows $\hat{\sigma}_{L_{50}}$ as a function of N for both procedures and for different settings of s_{50} and j.

Except for $s_{50}=0.05$ dB^{-1}, the $\hat{\sigma}_{L_{50}}$ values of the respective procedures for constant settings of $N\geqslant 20$ and j scarcely vary with the underlying s_{50} value. In other words, the panels of a given column in Fig. 3 are similar. This means that the efficiency of the algorithms is scarcely influenced by the discrimination function slope. Under most conditions, $\hat{\sigma}_{L_{50}}$ decreases with increasing N, although $\hat{\sigma}_{L_{50}}$ is already normalized with $1/\sqrt{N}$. This is certainly due to the fact that the adaptive procedures converge at their specific targets during the track, which causes a larger portion of trials to be placed more efficiently.

For $s_{50}>0.05$ dB^{-1}, procedure A1, which is better suited for L_{50} estimates as it converges at the *sweetpoint*, yields better results than procedure A2.

The $\hat{\sigma}_{L_{50}}$ values decrease with increasing j. Since $\hat{\sigma}_{L_{50}}$ is already normalized with $1/\sqrt{j}$, this means that the estimates can use the additional amount of statistically independent elements per trial even more than predicted by Eq. (3).

Different results were derived for an underlying s_{50} value of 0.05 dB^{-1}. Due to the flat discrimination function, the initial distribution of levels corresponds to discrimination values which are already relatively close to $p=0.5$.

The Monte Carlo simulations showed no tendency towards systematic biases. This was expected, because all procedures generate symmetric level distributions around the L_{50}. The bias of L_{50} estimates was always smaller than 8% of the absolute standard deviation $\sigma_{L_{50}}$ and has no practical relevance.

2. Slope estimates

Figure 4 shows the relative standard deviations of the s_{50} estimates as functions of N for the different settings of s_{50} and j.

As expected, algorithm A1 fails completely in slope estimates. For the respective equal values of j, N, and s_{50} this procedure generates $\sigma_{s_{50}}$ values which are about ten times larger than the results obtained using A2. For that reason, the slope estimates of A1 are out of the range of the ordinate in Fig. 4, and they are not further discussed in this section.

The dotted lines in Fig. 4 show the minimal achievable standard deviations in s_{50} estimates according to Eq. (5). The relative standard deviations of slope estimates $\sigma_{s_{50}}/s_{50}$ decrease faster than with $1/\sqrt{N}$, that is, the ratios between solid and the dotted lines decrease with increasing N, because the stimuli are concentrated at the *pair of compromise* during the track.

The $\sigma_{s_{50}}/s_{50}$ values decrease faster than with $1/\sqrt{j}$ as well, that is, the ratios between solid and the dotted lines decrease with increasing j. This is probably due to the faster convergence at the target level, which is caused by the more reliable estimation of ΔL according to Eq. (9) at each trial.

Figure 4 also shows the relative biases in s_{50} estimates. All estimates are positively biased. The relative bias decreases with increasing j and increasing N. For $N=10$ the relative bias is unacceptably high. For $j\geqslant 2$ and $N\geqslant 30$ the relative bias of slope estimation is smaller than 0.14 for all

underlying slopes. Thus, at least 30 sentences should be used to obtain a reliable slope estimate.

V. EXPERIMENTAL METHOD

A. Apparatus

A computer-controlled audiometry workstation was used, which was developed within a German joint research project on speech audiometry (Kollmeier *et al.*, 1992). A personal computer with a coprocessor board (Ariel DSP 32C) with 16-bit stereo AD-DA converters was used to control the complete experiment as well as stimulus presentation and recording of the listener's responses. The stimulus levels were adjusted by a computer-controlled custom-designed audiometer comprising attenuators, anti-aliasing filters, and headphone amplifiers. Signals were presented monaurally to the listeners with Sennheiser HDA 200 headphones with free-field equalization. The listeners were situated in a sound-insulated booth. Their task was to repeat each sentence presented over headphones as closely as possible. The instructor, also situated in the booth in front of the listener, marked each incorrectly repeated word. For this purpose, an Epson EHT 10S handheld computer was used with a LCD touchscreen on which the target sentence was displayed. The handheld computer was connected to the personal computer via serial interface.

B. Speech material

Two similar sentence tests, the Göttingen and the Oldenburg sentence test, which differ mainly in predictability, were used in the measurements. For both tests, speech and noise were added digitally at a predefined signal-to-noise ratio and converted to analog (16 bits, 25-kHz sampling frequency).

The Göttingen sentence test (Kollmeier and Wesselkamp, 1997) consists of 20 lists with 10 sentences each, recorded with a male nonprofessional speaker. The average number of words per sentence is 5. The predictability of the speech material is high [$j=1.95$ at a SNR of -8 dB ($p=0.21$) and $j=2.38$ at a SNR of -4 dB ($p=0.84$) (Kollmeier and Wesselkamp, 1997)]. The different lists have equivalent discrimination functions in a speech-spectrum-shaped noise. Measurements with normal-hearing listeners with a noise level of 65 dB SPL gave an L_{50} of -6.23 dB SNR with a standard deviation of 0.27 dB between lists. The slope of the discrimination function at the SRT is 0.192 dB^{-1} with a standard deviation of 0.025 dB^{-1} between lists (Kollmeier and Wesselkamp, 1997). From the speech material a nonmodulated competitive noise was generated which provides the same long-time frequency spectrum as the sum of all sentences.

The Oldenburg sentence test (Wagener *et al.*, 1999a, c) consists of 120 lists with 30 sentences each recorded with the same speaker as the Göttingen sentence test. Each sentence consists of 5 words and has the same syntactical form: *Name verb number adjective object*. The predictability of the speech material is low [$j=3.18$ at a SNR of -9 dB ($p=0.22$) and $j=4.29$ at a SNR of -5 dB ($p=0.81$) (Wagener *et al.*, 1999a)]. The different lists have equivalent discrimination functions in a speech spectrum-shaped noise. Measurements with normal-hearing listeners with a noise level of 65 dB SPL gave an L_{50} of -7.11 dB SNR with a standard deviation of 0.16 dB between lists (Wagener *et al.*, 1999a). The slope of the discrimination function at the SRT is 0.171 dB^{-1} with a standard deviation of 0.0165 dB^{-1} between lists (Wagener *et al.*, 1999a). From the speech material a speech-spectrum-shaped noise was generated in the same manner as in the Göttingen sentences.

For both sentence tests nonmodulated competitive noises were used with the same long-time frequency spectra as the respective speech materials.

C. Subjects and measurement program

Ten normal-hearing (four males, six females; aged 22–32 years; median age 26 years) and 11 hearing-impaired (five males, six females; aged 37–80 years; median age 69 years) listeners participated in the experiment. The normal-hearing listeners had hearing thresholds better than 15 dB HL at the frequencies 0.125, 0.25, 0.5, 1, 1.5, 2, 3, 4, 6, and 8 kHz. The sentence tests were performed in their respective better ear. The hearing-impaired listeners showed different types and degrees of sensorineural hearing loss. Pure-tone hearing thresholds ranged from 5 dB HL up to more than 100 dB HL (one flat hearing loss at 60 dB HL, three pure high-frequency hearing losses, and seven sloping hearing losses). No listener had prior experience in psychoacoustical experiments. All listeners were paid for their participation on an hourly basis.

All listeners performed three tracks each with both procedures A1 and A2 and with both the Göttingen and the Oldenburg sentences. Each listener performed two sessions: At the beginning of the first session a pure-tone audiogram was measured. For the hearing-impaired listeners, a categorical loudness measurement using the noise signal also was performed. Subsequently, each listener performed three practice lists with 20 sentences which were not analyzed (two tracks using the Oldenburg sentences and procedures A1 and A2, and one track using the Göttingen sentences and procedure A2). Then four to six tracks were performed using the different procedures and speech materials in pseudo-random order. At the beginning of the second session, which was performed on another day, a practice track with 30 trials using the Oldenburg sentences and procedure A2 was performed. Then the remainder of the tracks were performed in pseudo-random order.

In the normal-hearing listeners, the interfering noise was presented at 65 dB SPL, which is the typical ''medium'' loudness level for this signal in normal-hearing listeners. In the hearing-impaired listeners, the interfering noise was presented at the individual medium-loudness level, which was determined by categorical loudness scaling (Hohmann and Kollmeier, 1995) using the noise signal as stimulus. The signal level varied according to the respective signal-to-noise ratio.

TABLE I. Mean individual L_{50} and s_{50} estimates as well as intraindividual standard deviations and biases for normal-hearing and hearing-impaired listeners using the Göttingen and the Oldenburg sentence tests. In order to make results comparable between listeners with different slope values, the intraindividual standard deviations and biases of the L_{50} estimates have been multiplied by the individual slope value of the respective listener before averaging across listeners. For the same reason, the standard deviations and biases of the c_{50} estimates are given relative to individual slope values. The corresponding predicted values from the Monte Carlo simulations are shown in parentheses below the observed values.

	Göttingen sentence test				Oldenburg sentence test			
	Normal hearing		Hearing impaired		Normal hearing		Hearing impaired	
	A1	A2	A1	A2	A1	A2	A1	A2
Mean individual L_{50}	−5.6 dB	−5.5 dB	−0.5 dB	−0.8 dB	−6.3 dB	−6.1 dB	−2.9 dB	−2.4 dB
$s_{50}\cdot \mathrm{STD}(L_{50})$	0.05	0.08	0.09	0.11	0.07	0.06	0.07	0.08
	(0.08)	(0.10)	(0.08)	(0.10)	(0.05–0.07)	(0.06–0.07)	(0.05–0.07)	(0.06–0.07)
$s_{50}\cdot \mathrm{Bias}(L_{50})$	−0.01	0.01	−0.02	0.03	−0.01	0.00	−0.03	0.03
	(0)	(0)	(0)	(0)	(0)	(0)	(0)	(0)
Mean individual s_{50}	0.20 dB^{-1}	0.16 dB^{-1}	0.12 dB^{-1}	0.13 dB^{-1}	0.14 dB^{-1}	0.16 dB^{-1}	0.14 dB^{-1}	0.14 dB^{-1}
Relative $\mathrm{STD}(s_{50})$	0.69	0.16	0.84	0.24	0.52	0.21	0.59	0.29
	(−)	(0.31–0.33)	(−)	(0.31–0.33)	(−)	(0.18–0.20)	(−)	(0.18–0.20)
Relative $\mathrm{bias}(s_{50})$	0.59	0.05	0.75	0.10	0.34	0.09	0.43	0.12
	(−)	(0.13)	(−)	(0.13)	(−)	(0.05)	(−)	(0.05)

VI. EXPERIMENTAL RESULTS

The individual L_{50} and s_{50} values for each listener were calculated by fitting the model function (1) to all trials which were performed with the specific listener, adaptive procedure, and speech material. Because of the large number of trials that entered this estimate ($N=90$ sentences), this s_{50} estimate can be assumed to be almost bias free. The resulting individual ''bias free'' L_{50} and s_{50} estimates were used to calculate the bias of the single-track fits. The individual ''bias free'' s_{50} estimates were also used to normalize the individual L_{50} and s_{50} estimates. The mean individual L_{50} and s_{50} estimates are shown in Table I.

Table I also shows the mean intraindividual standard deviations and biases of the L_{50} and s_{50} estimates for the normal-hearing and hearing-impaired listeners using the Göttingen and Oldenburg sentence tests. In order to make results comparable between listeners with different slope values, the intraindividual standard deviations and biases of the L_{50} estimates were multiplied by the slope value of the respective listener before averaging across listeners. For the same reason, the standard deviations and biases of the s_{50} estimates were divided by the slope value of the respective listener before averaging, that is, the standard deviations and biases are given relative to the individual slope value. The corresponding predicted values from the Monte Carlo simulations (cf. Sec. IV B 2) are shown in parentheses below the observed values.[1] In cases where the results of the Monte Carlo simulations depended on the slope of the discrimination function, the minimal and the maximal predicted values are shown in Table I.

The observed values of $s_{50}\cdot \mathrm{STD}(L_{50})$ shown in Table I are relatively consistent with the predicted values. There are only small differences between speech materials. The measurements show no tendency towards a significant bias of L_{50} estimates, as predicted by the Monte Carlo simulations. Since the mean slope values in all conditions are larger than 0.10 dB^{-1}, a conservative estimate in dB of the standard deviation of L_{50} estimates can easily be calculated by multiplying the $s_{50}\cdot \mathrm{STD}(L_{50})$ values in Table I by 10 dB.

In the predictions, procedure A1 failed completely in slope estimates. For that reason, no predictions for slope estimates are shown in Table I. The observed standard deviations and biases of s_{50} estimates using procedure A1 are unacceptably high as well. This means that procedure A1 is not suitable for slope estimates. For that reason, only the results of procedure A2 are discussed.

Using the Göttingen sentences the measured relative standard deviations of s_{50} are smaller than the predicted values. This effect is significant for the normal-hearing listeners. The predicted improvement of s_{50} estimates using the Oldenburg sentences does not occur, as the measured relative standard deviations of s_{50} have about the same size for both sentence tests. The relative standard deviations of s_{50} are smaller in the normal-hearing listeners than in the hearing-impaired listeners.

The relative bias of the s_{50} estimates is smaller than predicted for both normal-hearing and hearing-impaired listeners when the Göttingen sentences are used. This is not the case when the Oldenburg sentences are used. Here, the measured values are larger than predicted for the normal-hearing listeners. For the hearing-impaired listeners, the measured bias of s_{50} is clearly larger than predicted. The reasons for this unexpected discrepancy are discussed below.

VII. DISCUSSION

Different authors have proposed different procedures for level placement in order to estimate threshold and psychometric function slope concurrently: Hall (1981) used the PEST adaptive procedure with the midpoint of the psychometric function as target. Leek *et al.* (1992) used transformed up–down adaptive procedures either with the target $p=0.71$ or with the target $p=0.79$. Both approaches are based on the fact that the adaptive procedures do not converge immediately at their specific target, but tend to wander up and down the level axis. Indeed, the convergence has to be slow, because otherwise the presentation levels are placed too closely and the slope estimate is inaccurate. Lam *et al.* (1996) proposed presenting several trials at four different

levels which are guessed or estimated by the investigator prior to measurement, and which are newly estimated iteratively during the measurement until the estimates of threshold and slope stabilize.

In the current study the adaptive procedure converges at the *pair of compromise*, which are the target levels enabling the most efficient concurrent threshold and psychometric function slope estimates. In this way, the theoretically optimal level placement is achieved, provided that the adaptive procedure converges optimally.

The results of the present study can be compared to those of earlier studies in which the efficiencies of the procedures are specified. Hall's hybrid adaptive procedure (1981) yields an *efficiency* [as defined by Taylor and Creelman (1967)] of 68% in threshold estimates after 50 trials. The efficiency of slope estimates is not specified in Hall's study. In the current study, procedure A2 yields an *efficiency* of 75% in threshold estimates and of 39% in slope estimates after 30 trials, if the Göttingen sentence test is used. Leek *et al.* (1992) specify the efficiency of the slope estimates of their procedure as the standard deviation of the logarithm of slope estimates. Therefore, their results cannot be directly compared to this study. Lam *et al.* (1996) specified the standard deviations of their procedure, but did not state how many iterations they used. Therefore, it is not possible to calculate the efficiency of their procedure.

The adaptive procedure presented in this study exploits the fact that a sentence trial has more than one statistically independent element. This allows for a more efficient convergence and data collection. At least in Monte Carlo simulations, acceptable slope estimates can be obtained using at least 30 sentence trials. In usual forced-choice situations about 100 trials are necessary to obtain slope estimates with comparable accuracy (e.g., O'Regan and Humbert, 1989).[2]

Transformed up–down procedures (Levitt, 1971) can be modified in order to converge on the *pair of compromise* as well (Brand, 2000). However, procedures A1 and A2, which are generalizations of the adaptive procedure of Hagerman and Kinnefors (1995), yielded a higher efficiency and converged efficiently at their target values independently of the predictability of speech material. The modified transformed up–down procedures converged efficiently at their target values only if the number of statistically independent elements per sentence was approximately 2. For these reasons, the use of adaptive procedure A1 should be used for simple SRT measurements and procedure A2 for simultaneous SRT and slope measurements for all kinds of speech material.

The optimal final step size of the adaptive procedures found in this study is clearly smaller than those found by other authors (e.g., Green, 1989; Hagerman and Kinnefors, 1995). Note, however, that the slope of the discrimination function in sentence tests is much greater than in most other psychoacoustical tests. Consequently, smaller step sizes are required for sentence tests. The restriction of $f(i)$ to 0.1 in procedures A1 and A2 causes final step sizes which are only 13.3% of those used by Hagerman and Kinnefors (1995). This final value is reached after the eighth reversal, when the target level can be estimated very accurately and there is no reason for large changes in presentation level.

Significant biases of slope estimates have been reported several times, especially when the chance level (the probability to guess the right response) is nonzero and if small track lengths ($N<200$) are used (O'Regan and Humbert, 1989; Leek *et al.*, 1992). Fortunately, the chance level is nearly zero for sentence tests. Furthermore, for $j>1$, more than one Bernoulli trial is performed per sentence and thus much smaller track lengths ($N=30$) can be used. However, even in the Monte Carlo simulations of this study, the s_{50} estimate was positively biased in all conditions, but for $N\geqslant 20$ and $j \geqslant 3$ the relative bias in slope estimation was smaller than 10%, which is acceptable for diagnostics. Further, these biases do not depend on the SRT and the discrimination function slope. Therefore, they can be compensated for by the correction factors which were calculated by the Monte Carlo simulations.

Both simulations and measurements showed that slope estimates are much more sensitive to an inadequate level placement than are SRT estimates. This is very consistent with the standard deviations predicted on the basis of the binomial theory shown in Figs. 1 and 2. Figure 1 shows that the L_{50} estimate is relatively robust if stimuli are presented not very accurately at the sweetpoint. Figure 2, however, shows that the s_{50} estimate becomes very ineffective if stimuli are presented near the sweetpoint and not near the sweetpair. In fact, each trial which is presented near the sweetpoint does not contribute to the slope estimate at all.

The measurements using the Göttingen sentence test showed intraindividual standard deviations and biases in L_{50} and s_{50} estimates which were smaller than the predicted values. The measured relative standard deviation is even half of the predicted value for the normal-hearing listeners. This is very striking, because measurements with ''real'' listeners usually generate larger errors than do simulations, which is generally explained by ''human factors.'' One reason for the unexpected accurate measurements might be that the intelligibility is calculated using weighting factors for each word in the Göttingen sentence test (Kollmeier and Wesselkamp, 1997). These weighting factors have been introduced to reduce the inhomogeneities in the test material. However, they seem to cause an increase in efficiency as well.

The measurements with the Oldenburg sentence test, on the other hand, showed somewhat less efficiency for s_{50} estimates than predicted by the Monte Carlo simulations which might be caused by a training effect. Since all lists of the Oldenburg sentence test consist of the same vocabulary, the L_{50} estimates were observed to decrease by 2 dB within the first six tracks due to training (Wagener *et al.*, 1999a). The main portion of this training effect occurs within the first two lists. In the Göttingen sentences, no comparable training effect was observed. In order to reduce this training effect in the current study, each listener performed training consisting of two tracks employing the Oldenburg sentences before the actual measurements. This training, and the fact that Oldenburg and Göttingen sentence lists were measured in an interleaved order, aimed at reducing the training effect. Nevertheless, a small training effect occurred in this study anyway, as the L_{50} estimates of a specific listener decreased about 1 dB within the whole six tracks using the Oldenburg sentences in

both the normal-hearing and the hearing-impaired listeners. Using the Göttingen sentences, no training effect was observed.

A further possible reason for differences between predictions and measurements might be caused by the adaptive procedure. Procedure A2 generates relatively large steps of the presentation level which might disturb the attention of the subject and hence might produce a reduction of j. This effectively lower j value might then decrease the observed estimation accuracy. To test this hypothesis, we computed j for both the adaptive procedures and the fixed-level case for both sentence tests as a function of p. In this representation of the data, we found no systematic difference in j between the adaptive procedures and the fixed-level case. This excludes the hypothesis of a decreased j factor as a reason for the unexpected poor results of the Oldenburg sentences. The j factor in the data presented here was analyzed in more detail by Bronkhorst *et al.* (2002).

This study uses word scoring, that is, each word of a sentence is scored separately. Other sentence tests score whether or not the complete sentence is repeated correctly (e.g., Plomp and Mimpen, 1979; Nilsson *et al.*, 1994). The latter implies one statistically independent element per sentence ($j=1$). The simulations of this study, however, show that this scoring method is the worst condition for efficient L_{50} and s_{50} estimates, because the adaptive procedures cannot work properly and the fitting is based on too few samples. Although no measurements with sentence scoring have been performed in this study, we assume that sentence scoring is ineffective in measurements as well. Word scoring only takes a little more experimental effort than sentence scoring, but this effort seems to be justified by the gain in efficiency and accuracy.

Plomp and Mimpen (1979) proposed using 13 sentences to obtain a standard deviation in SRT estimates of approximately 1 dB with normal-hearing listeners in noise. Nilsson *et al.* (1994) proposed using ten sentences for SRT measurements and obtained a standard deviation of 1.52 dB in noise with normal-hearing listeners. However, if decreased slope values for hearing-impaired listeners are accounted for as well as the fact that differences of only a few dB in SRTs in noise can be very important for diagnostics and hearing aid fitting, it appears necessary to achieve smaller standard deviations in SRT measurements.

For single SRT measurements, we therefore propose to use procedure A1 with at least 20 sentences to get reliable results with a standard deviation of less than 1 dB for listeners with $s_{50} \geqslant 0.10\ \mathrm{dB}^{-1}$.

If the slope should also be measured, the use of procedure A2 with at least 30 sentences is recommended. In this case, a standard deviation of SRT estimate of less than 1 dB is achieved in combination with a relative standard deviation of slope estimate of 20% to 30%.

VIII. CONCLUSIONS

Both Monte Carlo simulations and measurements clearly indicate that the "*pair of compromise*" target levels should be used for a concurrent estimate of threshold and slope of the psychometric function. The adaptive procedures introduced in this study are based on this finding. They also utilize the fact that more than one statistically independent Bernoulli trials is sampled in each sentence, if word scoring is applied. This fact allows for more efficient SRT and slope estimates compared to usual forced-choice tasks. To obtain a reliable bias-free SRT estimate with a standard deviation of less than 1 dB, it is recommended to use at least 20 sentence trials and an adaptive procedure that converges at a discrimination value of $p=0.5$ with decreasing step size. A reliable concurrent estimate of discrimination function slopes using sentence tests is problematic, because clinical diagnostics requires measurement times much shorter than those typical of psychoacoustics. At least 30 sentences are necessary for a j value $\geqslant 2$ (more are recommended) as well as an adaptive procedure that converges at the discrimination values of $p_1=0.2$ and $p_2=0.8$ in randomly interleaved order. Using these settings, a relative standard deviation of slope estimates of 20% to 30% and a relative bias of about 10% within 30 sentence trials can be obtained concurrently with a standard deviation of 1 dB for the SRT estimate.

Theoretically, sentence tests with lowly predictable speech materials [such as the Oldenburg sentence test (Wagener *et al.*, 1999c)] should be more efficient in estimating SRTs and discrimination function slopes than sentence tests with highly predictable speech materials [such as the Göttingen sentence test (Kollmeier and Wesselkamp, 1997)]. In measurements with normal-hearing and hearing-impaired listeners, however, the expected advantage of the Oldenburg sentence test could not be observed. Possibly, this is due to a training effect. Hence, the number of sentences to obtain a reliable concurrent threshold and slope estimate cannot be further reduced if a more efficient sentence test with a higher j factor is employed.

ACKNOWLEDGMENTS

We would like to thank Anita Gorges, Kirsten Wagener, Müge Gökalan, and Birgitta Gabriel for performing the measurements. We would like to thank Adelbert Bronkhorst for valuable hints concerning the j factor. Thanks are also due to Karin Zimmer, Angelika Sievers, and Andrew J. Oxenham for helpful comments on the manuscript. The valuable hints of Sid P. Bacon and two anonymous reviewers are gratefully acknowledged. This study was supported by DFG KO 942/13-1 and by the CEC supporting action NATASHA.

[1]The predictions of the normalized standard deviations of L_{50} estimates were calculated as follows: Since 30 sentences were used per track, the minimal value of $s_{50}\cdot \mathrm{STD}(L_{50})$ at the *sweetpoint* is $0.5/\sqrt{30\cdot j}$, with $j=2$ for the Göttingen sentences and with $j=4$ for the Oldenburg sentences [cf. Eq. (3)]. These values have been multiplied with the normalized standard deviations of the L_{50} estimates $\hat{\sigma}_{L_{50}}$ for the specific procedure, j factor, and slope value s_{50} as displayed in Fig. 3 to obtain predictions of $s_{50}\cdot \mathrm{STD}(L_{50})$. Standard deviations and biases of the slope estimate were predicted using the results shown in Fig. 4 and assuming $j=2$ in the Göttingen sentences and $j=4$ in the Oldenburg sentences.

[2]O'Regan and Humbert (1989) tested different constant stimuli distributions with respect to their accuracy in threshold and slope estimates. In Monte Carlo simulations the best distributions produced relative standard deviation of slope estimates of about 0.14 using 100 trials. In this study, procedure A2 produced a relative standard deviation of slope estimates of about 0.16 in Monte Carlo simulations for $j=4$ using 30 trials.

Boothroyd, A., and Nittrouer, S. (**1988**). ''Mathematical treatment of context effects in phoneme and word recognition,'' J. Acoust. Soc. Am. **84**, 101–114.
Brand, T. (**2000**). ''Analysis and Optimization of Psychophysical Procedures in Audiology,'' Ph.D. thesis, BIS, University of Oldenburg, Germany.
Bronkhorst, A. W., and Plomp, R. (**1988**). ''The effect of head-induced interaural time and level differences on speech intelligibility in noise,'' J. Acoust. Soc. Am. **83**, 1508–1516.
Bronkhorst, A. W., Brand, T., and Wagener, K. (**2002**). ''Evaluation of context effects in sentence recognition,'' J. Acoust. Soc. Am. **111**, 2874–2886.
Campbell, R. A. (**1974**). ''Modifications to the BUDTIF procedure,'' J. Acoust. Soc. Am. Suppl. 1 **56**, S57.
Green, D. M. (**1989**). ''Stimulus step size and heterogeneous stimulus conditions in adaptive psychophysics,'' J. Acoust. Soc. Am. **86**, 629–636.
Green, D. M. (**1990**). ''Stimulus selection in adaptive psychophysical procedures,'' J. Acoust. Soc. Am. **87**, 2662–2674.
Hagerman, B. (**1982**). ''Sentences for testing speech intelligibility in noise,'' Scand. Audiol. **11**, 79–87.
Hagerman, B., and Kinnefors, C. (**1995**). ''Efficient adaptive methods for measuring speech reception thresholds in quiet and in noise,'' Scand. Audiol. **24**, 71–77.
Hall, J. L. (**1981**). ''Hybrid adaptive procedure for estimation of psychometric functions,'' J. Acoust. Soc. Am. **69**, 1763–1769.
Hohmann, V., and Kollmeier, B. (**1995**). ''Weiterentwicklung und klinischer Einsatz der Hörfeldskalierung (Further development and use of hearing field scaling in clinics),'' Audiol. Akust. **34**, 48–59.
Kollmeier, B., and Wesselkamp, M. (**1997**). ''Development and evaluation of a German sentence test for objective and subjective speech intelligibility assessment,'' J. Acoust. Soc. Am. **102**, 2412–2421.
Kollmeier, B., Gilkey, R. H., and Sieben, U. (**1988**). ''Adaptive staircase techniques in psychoacoustics: A comparison between theoretical results and empirical data,'' J. Acoust. Soc. Am. **83**, 1852–1862.
Kollmeier, B., Müller, C., Wesselkamp, M., and Kliem, K. (**1992**). ''Weiterentwicklung des Reimtests nach Sotscheck (Further development of the rhyme test according to Sotscheck),'' in *Moderne Verfahren der Sprachaudiometrie*, *Buchreihe Audiologische Akustik*, edited by B. Kollmeier (Median-Verlag, Heidelberg), pp. 216–237.
Lam, C. F., Mills, J. H., and Dubno, J. R. (**1996**). ''Placement of observations for the efficient estimation of a psychometric function,'' J. Acoust. Soc. Am. **99**, 3689–3693.
Laming, D., and Marsh, D. (**1988**). ''Some performance tests of QUEST on measurements of vibrotactile thresholds,'' Percept. Psychophys. **44**, 99–107.
Leek, M. R., Hanna, T. E., and Marshall, L. (**1992**). ''Estimation of psychometric functions from adaptive tracking procedures,'' Percept. Psychophys. **51**, 247–256.
Levitt, H. (**1971**). ''Transformed up-down methods in psychoacoustics,'' J. Acoust. Soc. Am. **49**, 467–477.
Nilsson, M., Soli, S. D., and Sullivan, J. A. (**1994**). ''Development of Hearing In Noise Test for measurement of speech reception thresholds in quiet and in noise,'' J. Acoust. Soc. Am. **95**, 1085–1099.
O'Regan, J. K., and Humbert, R. (**1989**). ''Estimating psychometric functions in forced-choice situations: Significant biases found in threshold and slope estimations when small samples are used,'' Percept. Psychophys. **46**, 434–442.
Peissig, J., and Kollmeier, B. (**1997**). ''Directivity of binaural noise reduction in spatial multiple noise-source arrangements for normal and impaired listeners,'' J. Acoust. Soc. Am. **101**, 1660–1670.
Plomp, R., and Mimpen, A. M. (**1979**). ''Improving the reliability of testing the speech reception threshold for sentences,'' Audiology **18**, 43–52.
Taylor, M. M., and Creelman, C. D. (**1967**). ''PEST: Efficient estimates on probability functions,'' J. Acoust. Soc. Am. **41**, 782–787.
Wagener, K., Brand, T., and Kollmeier, B. (**1999a**). ''Entwicklung und Evaluation eines Satztests für die deutsche Sprache III: Evaluation des Oldenburger Satztests (Development and evaluation of a German sentence test III: Evaluation of the Oldenburg sentence test),'' Z. Audiol. **38**, 86–95.
Wagener, K., Brand, T., and Kollmeier, B. (**1999b**). ''Entwicklung und Evaluation eines Satztests für die deutsche Sprache II: Optimierung des Oldenburger Satztests (Development and evaluation of a German sentence test II: Optimization of the Oldenburg sentence test),'' Z. Audiol. **38**, 44–56.
Wagener, K., Kühnel, V., and Kollmeier, B. (**1999c**). ''Entwicklung und Evaluation eines Satztests für die deutsche Sprache I: Design des Oldenburger Satztests (Development and evaluation of a German sentence test I: Design of the Oldenburg sentence test),'' Z. Audiol. **38**, 4–15.
Wetherhill, G. B. (**1963**). ''Sequential estimation of quantal response curves,'' J. R. Stat. Soc. Ser. B. Methodol. **25**, 1–48.

Control of oral closure in lingual stop consonant production

Anders Löfqvist[a)]
Haskins Laboratories, 270 Crown Street, New Haven, Connecticut 06511 and
Department of Logopedics & Phoniatrics, Lund University, Lund, Sweden

Vincent L. Gracco
Haskins Laboratories, 270 Crown Street, New Haven, Connecticut 06511 and
School of Communication Sciences and Disorders, McGill University, Montreal, Canada

(Received 30 May 2001; accepted for publication 27 February 2002)

Previous work has shown that the lips are moving at a high velocity when the oral closure occurs for bilabial stop consonants, resulting in tissue compression and mechanical interactions between the lips. The present experiment recorded tongue movements in four subjects during the production of velar and alveolar stop consonants to examine kinematic events before, during, and after the stop closure. The results show that, similar to the lips, the tongue is often moving at a high velocity at the onset of closure. The tongue movements were more complex, with both horizontal and vertical components. Movement velocity at closure and release were influenced by both the preceding and the following vowel. During the period of oral closure, the tongue moved through a trajectory of usually less than 1 cm; again, the magnitude of the movement was context dependent. Overall, the tongue moved in forward–backward curved paths. The results are compatible with the idea that the tongue is free to move during the closure as long as an airtight seal is maintained. A new interpretation of the curved movement paths of the tongue in speech is also proposed. This interpretation is based on the principle of cost minimization that has been successfully applied in the study of hand movements in reaching.
[DOI: 10.1121/1.1473636]

PACS numbers: 43.70.Aj, 43.70.Bk [KRK]

I. INTRODUCTION

Stop consonants are commonly produced with a complete closure in the vocal tract to allow the build-up of oral air pressure that drives the noise source at the release. The purpose of this study is to make a detailed examination of tongue tip and tongue body kinematics in the production of stop consonants with particular emphasis on events before, during, and after the oral closure. The influences of stop consonant voicing and vowel environment on movement kinematics are evaluated. In addition, we want to extend our previous work on bilabial stop consonant production (Löfqvist and Gracco, 1997; see also Westbury and Hashi, 1997), which has shown that the lips are moving at a high velocity at the onset of the oral closure, resulting in tissue compression and mechanical interactions between the lips, with the lower lip pushing the upper lip upward. These results for the lips suggested that a virtual target for the lips in making the stop closure is a region of negative lip aperture. That is, to reach their virtual targets, the lips would have to move beyond each other. The resulting tissue compression produces the airtight seal for the stop to allow the build-up of oral air pressure. Such a control strategy would ensure that the lips will form an airtight seal regardless of any contextual variability in the onset positions of their closing movements. In addition, this strategy appears to be used in controlling the duration of the closure for a bilabial stop (Löfqvist, 2000). By changing the virtual target for the lower lip, the lips will stay in contact for a longer or shorter period. More specifically, a stop with a longer closure duration is produced with the lower lip reaching a higher vertical position, reflecting a higher virtual target position. Given these findings for labial stop consonants, it is of interest to examine if a similar view of virtual targets is also viable for the tongue, i.e., a virtual target that would effectively require the tongue to move into the nasal cavity. Data on tongue movements and tongue–palate contact patterns presented by Fuchs *et al.* (2001) support such a view of a virtual target for the tongue. They noted that the magnitude of the deceleration of the tongue movement into the closure was highly correlated with the tongue–palate contact pattern, thus suggesting that the tongue is moving towards a virtual target at the onset of the oral closure. Also, the material presented by Mooshammer *et al.* (1995) clearly indicates that the tongue body is moving at the onset of the oral closure for a velar stop consonant, and that the velocity at closure is influenced by the quality of the preceding vowel. In addition, their results also showed that the tongue body is moving during the closure for a velar stop (see also Houde, 1968; Perkell, 1969). The amount of tongue movement during the closure varied with vowel context. Thus, the tongue-body movement during the closure was about 1 mm when the preceding vowel was /i/, and between 4 and 10 mm when the preceding vowel was /u/ or /a/.

Studies of tongue movements during velar stop consonant production have shown that the tongue tends to move in curved paths (Houde, 1968; Perkell, 1969; Kent and Moll, 1972; Schönle, 1988; Munhall *et al.*, 1991; Löfqvist and Gracco, 1994; Mooshammer *et al.*, 1995). In the production

a)Electronic mail: lofquist@haskins.yale.edu

of velar stops, the tongue movement trajectory into the stop closure is usually going forward, and the location of the point of contact between the tongue body and the palate at stop closure is influenced by the phonetic context of the stop (cf. Dembowski *et al.*, 1998). There are two properties of the tongue movement kinematics in speech that need to be addressed—the direction of the movement, i.e., forward or backward, and the nature of the path, i.e., straight or curved. Some of the proposed explanations to account for the tongue movement trajectories in velar stop consonants have been based on aerodynamic factors, such as an increase in cavity size to maintain voicing, or the increase in oral air pressure behind the closure (e.g., Coker, 1976; Hoole *et al.*, 1998). Alternatively, tongue movement kinematics has been explained in terms of the biomechanics of the tongue and the jaw (Perrier *et al.*, 1998). None of these explanations has been generally accepted, however. We should also note that in a vowel–consonant–vowel sequence with a bilabial stop, the tongue movement from the first to the second vowel tends to follow a curved path (Löfqvist and Gracco, 1999). Less information on movement kinematics (ignoring for the moment tongue–palate contact patterns obtained by electropalatography) is available for stops produced with the tongue tip and tongue blade, /t, d/, although the data published by Kent and Moll (1972) show that the location of the point of contact between the tongue tip and the palate, or alveolar ridge, is influenced by phonetic context.

In a recent study (Löfqvist and Gracco, 1999), we showed that in a vowel–bilabial stop-vowel sequence, more than 50% of the tongue movement trajectory from the first to the second vowel tends to occur during the stop closure for the consonant. The most likely explanation is that if a large part of the tongue movement trajectory occurred before or after the oral closure, an ''extra'' vowel sound might be perceived. In a vowel–consonant–vowel (VCV) sequence where the stop is alveolar or velar, one would expect a different pattern, however. The reason is that the tongue is not actively involved in making the labial closure in a VCV sequence with a bilabial stop consonant, but rather in making the vowel-to-vowel gesture. However, in the VCV sequences with the alveolar and velar stops, the tongue is actively involved both in making the stop closure and in the vowel-related gestures. One would thus expect that less than 50% of the tongue movement trajectory from the first to the second vowel occurs during the stop closure. The tongue is constrained in its freedom to move since it has to stay in contact with the palate to maintain the airtight seal.

Kinematic recordings of tongue movements were made in four subjects producing vowel–consonant–vowel sequences. To examine the specific hypothesis about virtual targets for the tongue in stop consonant production, measurements were made of the horizontal and vertical velocity at the onset of the oral closure for the stop. High movement velocities at the onset of the oral closure would be compatible with the notion of a virtual target for the tongue. In addition, the magnitude of tongue movement during the stop closure was evaluated. Finally, a calculation was made of the percentage of the tongue movement from the first to the second vowel that occurred during different intervals of the VCV sequence, such as during the first vowel, during the stop closure, and during the second vowel. We also present detailed analyses of tongue movement trajectories for a small number of tokens produced by two of the subjects. Our rationale for doing this is that such a presentation is useful for constraining the behavior of tongue models (e.g., Payan and Perrier, 1997; Sanguineti *et al.*, 1998).

II. METHOD

A. Subjects

Two female (LK, DR) and two male subjects (VG, AL) participated. All subjects had normal speech and hearing and no history of speech or hearing disorders. Three of the subjects (LK, DR, VG) are native speakers of American English. Subjects LK and DR grew up in the Midwest, while subject VG grew up in Florida; they all currently live in the Northeast. Speaker AL is a native speaker of Swedish who is also fluent in English. Subjects VG and AL are the two authors.

B. Linguistic material

The linguistic material consisted of 36 V_1CV_2 sequences, where the first vowel (V_1) was one of /i, a, u/, the consonant (C) one of /t, d, k, g/, and the second vowel (V_2) one of /i, a, u/. The sequences were placed in the carrier phrase ''Say ... again,'' with sentential stress occurring on the second vowel (V_2) of the sequence. Ten repetitions of each sequence were recorded.

C. Procedure

The movements of the tongue were recorded using a three-transmitter magnetometer system (Perkell *et al.*, 1992). Receivers were placed on four positions on the tongue; these positions will be referred to, from front to back, as tip, blade, body, and rear. Although an attempt was made to position the receivers equidistantly on the tongue, there was some variability in the positions of the tongue receivers between subjects (this can be seen in Figs. 6 and 9 below). Two additional receivers placed on the nose and the upper incisors were used for the correction of head movements. All tongue receivers were attached using Ketac-Bond (ESPE). Care was taken during each receiver placement to ensure that it was positioned at the midline with its long axis perpendicular to the sagittal plane. Two receivers attached to a plate were used to record the occlusal plane by having the subject bite on the plate during recording. All data were subsequently corrected for head movements and rotated to bring the occlusal plane into coincidence with the *x* axis. This rotation was performed to obtain a uniform coordinate system for all subjects (cf. Westbury, 1994).

The articulatory movement signals (induced voltages from the receiver coils) were sampled at 625 Hz after low-pass filtering at 200 Hz. The resolution for all signals was 12 bits. After voltage-to-distance conversion, the movement signals were low-pass filtered using a 25-point triangular window with a 3-dB cutoff at 17 Hz; this was done forwards and backwards to maintain phase. To obtain instantaneous velocity, the first derivative of the position signals was calculated

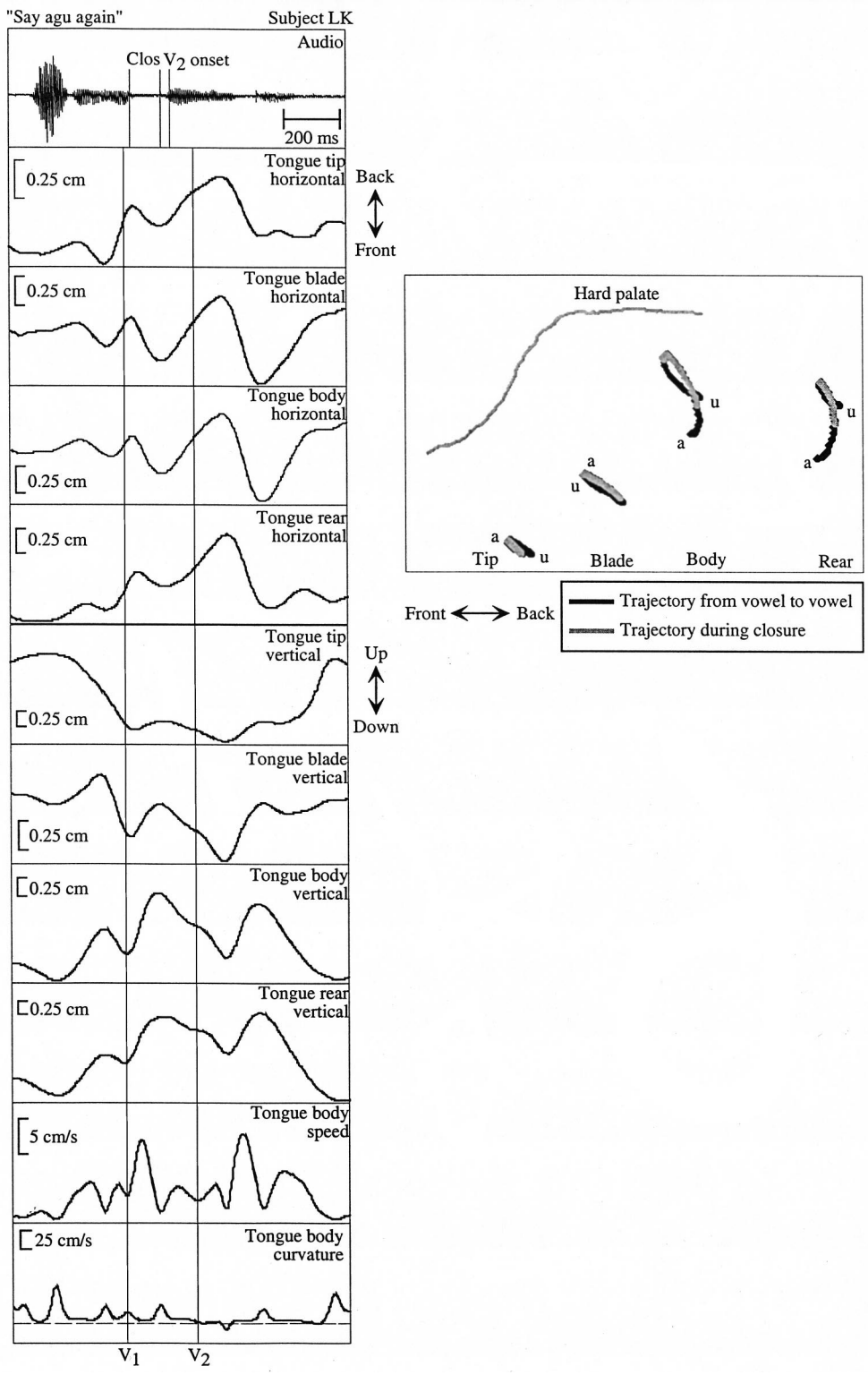

FIG. 1. Acoustic and movement signals recorded during the production of the utterance ''Say agu again'' by subject LK. The labels in the audio signal correspond to the onset and release of the oral closure for the consonant, and the onset of the second vowel in /agu/. The vertical lines labeled V1 and V2 were defined in the speed signal of the tongue body to identify the onset and offset of the tongue movement from the first to the second vowel in /agu/. The right panel shows the receiver trajectories from the first to the second vowel and also the part of the trajectory made during the oral closure for the consonant.

using a three-point central difference algorithm. The velocity signals were smoothed using the same triangular window. The speed $[v=\sqrt{(\dot{x}^2+\dot{y}^2)}]$ was calculated for each receiver. In addition, the curvature $[c=(\dot{x}\ddot{y}-\ddot{x}\dot{y})/v^3]$ was obtained. The sign of the curvature shows the direction of the movement, negative for clockwise movement and positive for counterclockwise movement (cf. Löfqvist *et al.*, 1993); in the coordinate system used in the present study, a positive sign of curvature indicates that the movement is going forward–backward; see Fig. 1. The magnitude of the curvature is a measure of how ''curved'' a movement trajectory is. Tongue movement onsets and offsets were defined algorithmically in the tongue body speed signal as minima during the first and second vowel. We should note that at these points in time, the horizontal and vertical velocity of the tongue is usually not zero. All the signal processing was made using the Haskins Analysis Display and Experiment System (HADES) (Rubin and Löfqvist, 1996).

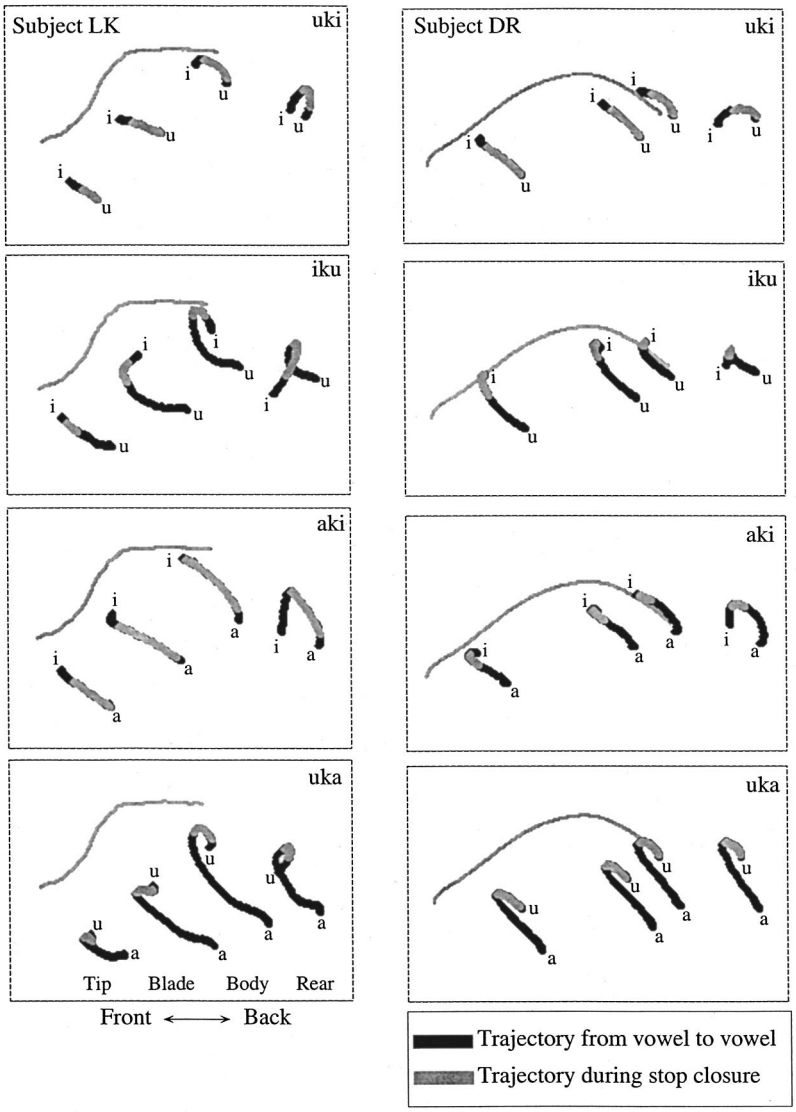

FIG. 2. Plots of receiver trajectories during single productions of sequences with a voiceless velar stop /k/ for subjects LK and DR. The trajectory from the first to the second vowel is shown and also the part of the trajectory that occurred during the oral closure for the consonant.

The acoustic signal was pre-emphasized, low-pass filtered at 9.5 kHz, and sampled at 20 kHz. The onset and release of the oral closure were identified in waveform and spectrogram displays of the acoustic signal. The onset of the closure was identified by the decrease in the amplitude of the acoustic waveform, and by the disappearance of spectral energy at higher frequencies. The release was identified by the burst and the onset of the second vowel in the VCV sequence by the beginning of regular glottal vibrations.

Figure 1 provides an example of tongue movements in one production of the sequence /agu/ by subject LK and also an overview of the labeling and measurement procedures. It presents the acoustic signal, the horizontal and vertical positions of each receiver, the tongue body speed, and the tongue body curvature signals. The following labels were placed in the acoustic and tongue body speed signals and used for measurements. In the acoustic signal, the labels from left to right correspond to the onset of the oral closure, the release of the oral closure, and the onset of the second vowel /u/. The first two of these labels were used for measuring the velocity of the tongue at the onset and release of the oral closure. They were also used to measure the movement of the tongue during the oral closure. The second and third of these acoustic labels, placed at the release and the acoustic onset of the second vowel, respectively, were used to examine the amount of movement between the release and the onset of the second vowel. In the tongue body speed signal, labels were placed at the speed minimum during the first and second vowels, respectively, and used to identify the onset and offset of the tongue movement in the first and second vowels. Thus, the two vertical lines running across the nine lower panels in Fig. 1 correspond to the onset of the closing movement from the first vowel /a/ and the offset of the opening movement into the second vowel /u/, defined in the tongue body speed signal. The first label in the tongue body speed signal was used together with the label at oral closure in the audio signal to measure the movement from the first vowel to the onset of the oral closure. The second label in the tongue body speed signal was used together with the label at the second vowel onset in the acoustic signal to measure the tongue movement during the second vowel. Note that these movement onset and offset in the two vowels were always defined in the tongue body speed signal. That is, they also served as onsets and offsets for the tongue tip movements in

sequences with an alveolar stop. The reason is that the tongue body is more directly associated with the production of the vowels than the tongue tip. An examination of the location of the left vertical line in the movement signals in Fig. 1, marking the onset of the movement towards consonant closure, shows that it corresponds to instances of very small vertical movement for all the tongue receivers. However, all the receivers move backwards at this point in time. At the second vertical line in Fig. 1, all the receivers are moving down and back.

The right panel in Fig. 1 shows an $x-y$ plot of the trajectories of the tongue receivers from the first to the second vowel and also the part of the trajectory that occurred during the oral closure for the consonant. The temporal extent of this plot corresponds to the interval between the two vertical lines in the left panel, i.e., between the two vowels.

The bottom panel in Fig. 1 shows the curvature of the tongue body receiver. It has a positive sign during the sequence /agu/ defined by the two vertical lines, thus indicating that the movement is counterclockwise. There is only one instance of clockwise movement of the tongue body during the whole utterance, immediately to the right of the label "V_2;" this instance is thus not included in the trajectories shown in the right panel. In order to maintain consistency in labeling the movement and acoustic signals, all the labeling was made by the first author. The labeling of the movement signals was made interactively using both the temporal and $x-y$ plots shown in Fig. 1. Once the proper interval in the signal had been identified, an algorithm was used to place the label at the minimum of speed.

Measurements were made of receiver positions and velocities at the onset and offset of the oral closure. In addition, the path of the receiver during the oral closure were measured. The following movement trajectories were also measured: from the first vowel to the consonant closure, during the closure, between consonant release and the onset of the second vowel, and during the second vowel. The movement magnitude was measured in two different ways, as the Euclidean distance between receiver onset and offset, and as the movement path by summing the Euclidean distances between successive samples from movement onset to movement offset. The ratio of the path length and the Euclidean distance provides a metric to assess how much the trajectory deviates from a straight line, with a ratio of 1 implying a straight line.

Analyses of variance were conducted to assess the influence of consonant type and vowel context on movement properties. Since many comparisons were made, a p value of $\leqslant 0.0001$ was adopted as significant. Given the large number of degrees of freedom, η^2 values showing the variation accounted for are also reported (cf. Young, 1993).

The kinematic signals represent the movements of receivers placed at the midline of the tongue. When presenting the results, we will use the terms "tongue tip receiver" and "tongue tip" interchangeably, while acknowledging that we are only examining the movements of a single point. Thus, we make no claims about asymmetrical movements of the left and right sides of the tongue during closure and release, although such asymmetries are known to exist (e.g., Hamlet *et al.*, 1986; Stone, 1990). Moreover, it is not possible to know the position of a given tongue receiver relative to the point, or region, of the tongue used for making the tongue–palate contact during the stop closure in a given subject. Finally, the tongue movements include the contribution of the jaw, which is proper when the focus is on the tongue as an end effector.

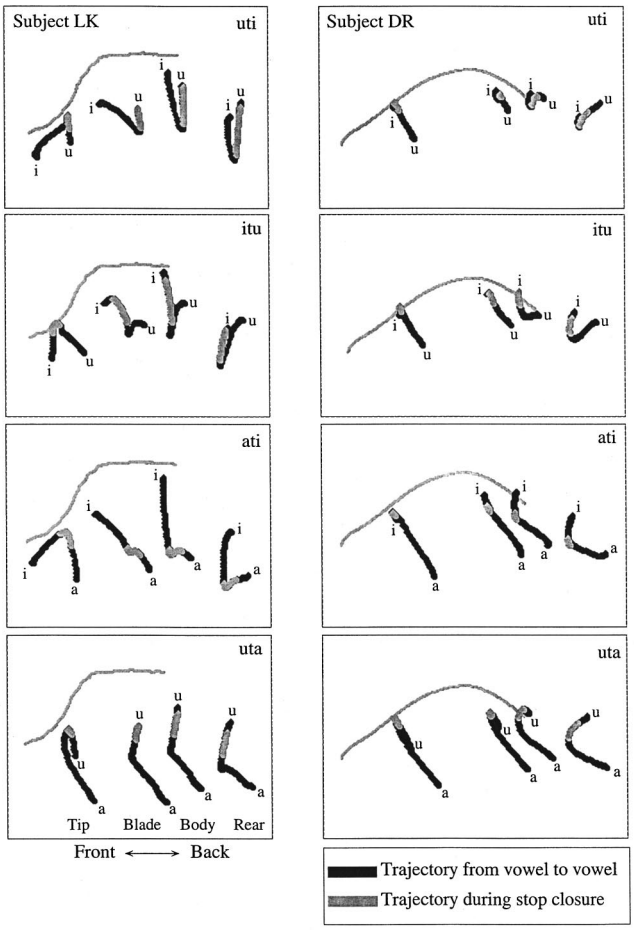

FIG. 3. Plots of receiver trajectories during single productions of sequences with a voiceless alveolar stop /t/ for subjects LK and DR. The trajectory from the first to the second vowel is shown and also the part of the trajectory that occurred during the oral closure for the consonant.

III. RESULTS

We shall first examine some characteristics of tongue movements in selected vowel contexts for two of the speakers. Figure 2 shows receiver movement trajectories from the first to the second vowel for selected sequences with a voiceless velar stop /k/ produced by subjects LK and DR. Figure 3 shows similar sequences with a voiceless alveolar stop /t/. The whole trajectory from vowel to vowel is shown, as well as the part of the trajectory that occurred during the oral closure for the consonant. The letters at the onset/offset of each trajectory identify the receiver positions for the respective vowels. A tracing of the outline of the hard palate is also shown for identification purposes. Since this outline was obtained by having the subject move the tongue tip receiver from the alveolar ridge and as far backwards as possible,

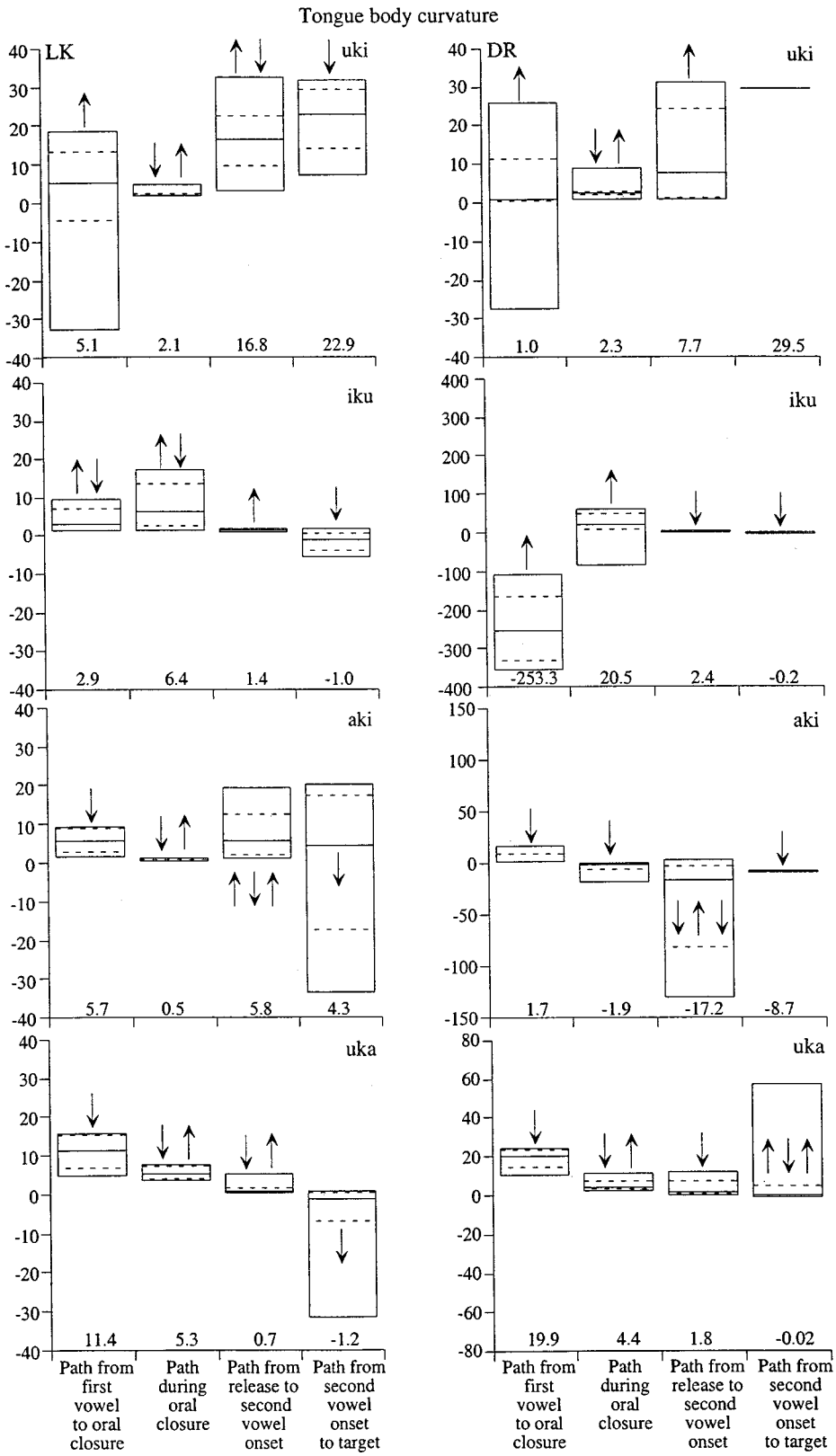

FIG. 4. Percentile plots of tongue body curvature for the productions with a velar stop consonant shown in Fig. 2. The box encloses 90% of the data with the bottom representing 5% and the top 95% of the data. The solid line inside the box is the median value, while the lower and upper two dashed lines in the box represent 25% and 75% of the data, respectively. The numbers below each box show the median curvature for the interval. The arrows above or in each box show the change in curvature for the interval. Two or more arrows indicate several changes occurring in the order from the left to the right arrows.

these tracings do not necessarily give the true outline of the palate in the posterior region (in some cases, a receiver crosses the outline of the palate).

In these figures, several aspects of tongue movements in speech are exemplified. The trajectories of the four tongue receivers show both similarities and differences. In the sequences with a velar stop, shown in Fig. 2, the tongue receivers mostly move in a curved trajectory with a counterclockwise, i.e., forward, movement. There are, however, several instances where this generalization does not hold and also where different receivers move in different directions. Figure 4 shows percentile plots of the curvature of the tongue body for the productions shown in Fig. 2. The box encloses 90% of the data with the bottom representing 5%

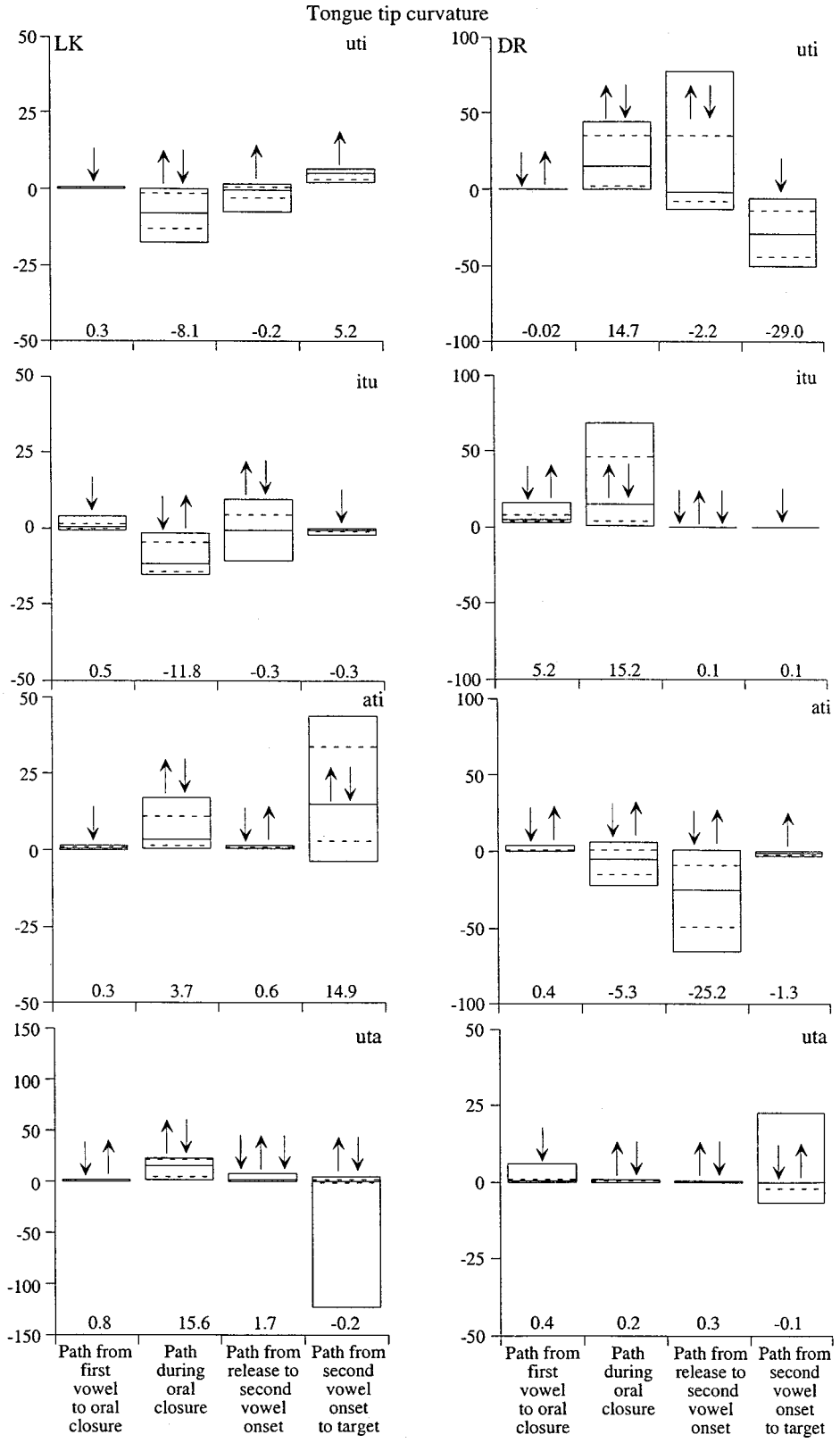

FIG. 5. Percentile plots of tongue tip curvature for the productions with an alveolar stop consonant shown in Fig. 3. The box encloses 90% of the data with the bottom representing 5% and the top 95% of the data. The solid line inside the box is the median value, while the lower and upper two dashed lines in the box represent 25% and 75% of the data, respectively. The numbers below each box show the median curvature for the interval. The arrows above or in each box show the change in curvature for the interval. Two or more arrows indicate several changes occurring in the order from the left to the right arrows.

and the top 95% of the data. The solid line inside the box is the median value, while the lower and upper two dashed lines in the box represent 25% and 75% of the data. Recall that a positive value of curvature indicates a clockwise forward–backward-going movement. The numbers below each box show the median curvature for the interval. The arrows above or in each box show the change in curvature for the interval. Two or more arrows indicate several changes occurring in the order from the left to the right arrows.

The median values for the curvature were always positive, with a few exceptions. These occurred in subject LK's productions of /iku/ and /uka/, and in subject DR's productions of /iku/, /aki/, and /uka/. Thus, the movement direction of the tongue body was going forward–backward. In many

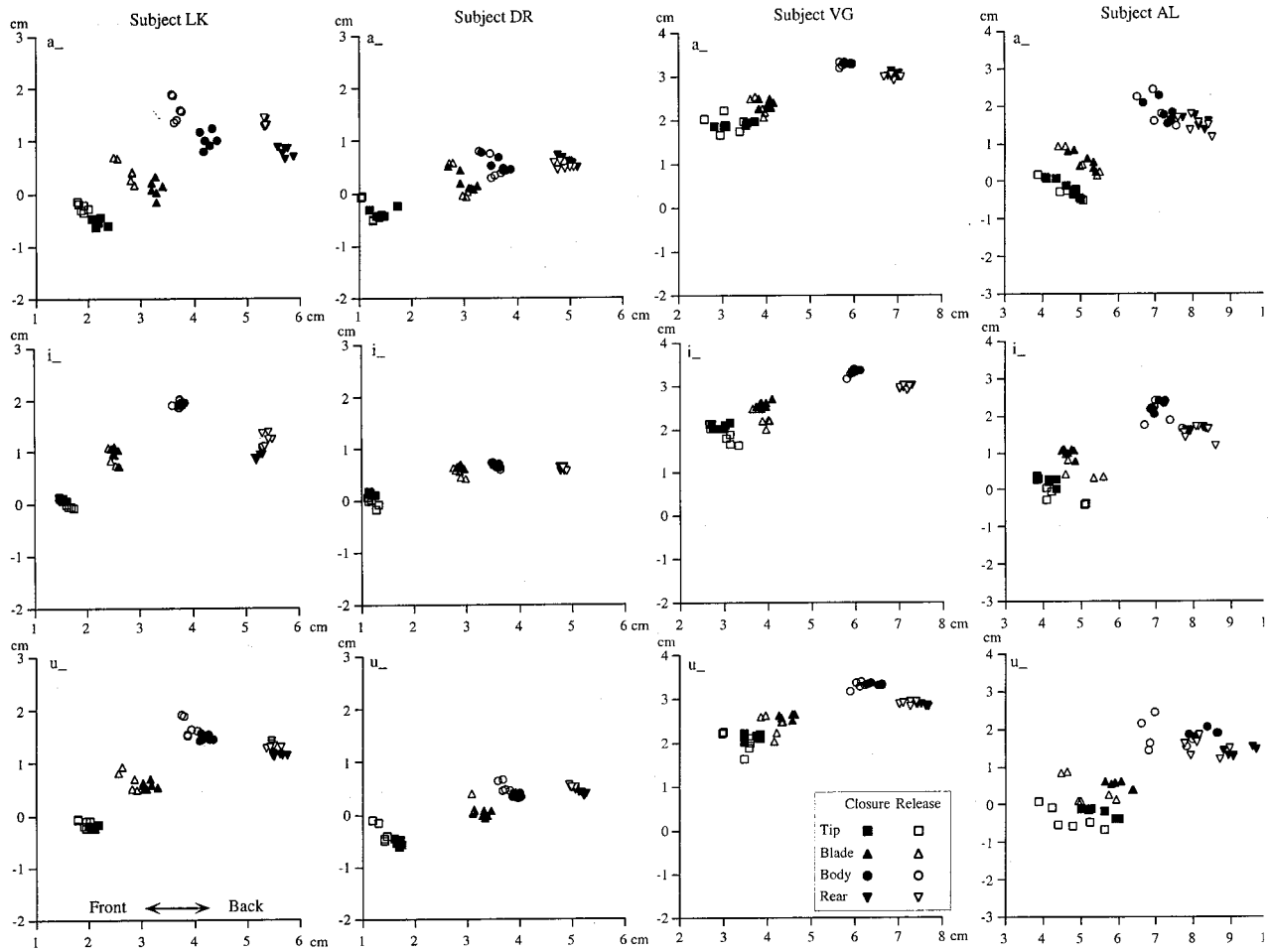

FIG. 6. Receiver positions at onset and release of oral closure for velar stops.

productions, the curvature of the tongue body was positive during all articulatory intervals. However, it is also apparent in Fig. 4 that the tongue body often changed its movement direction during the VCV sequence and sometimes even during an interval, e.g., during the movement during the closure in the sequence /uki/ for both subjects LK and DR.

During the closing movement, different tongue receivers sometimes moved in different directions. For example, in the sequence /aki/ of subject LK in Fig. 2, the tongue tip and tongue blade always moved clockwise while the tongue body and the tongue rear moved counterclockwise. On the other hand, in the closing movement of the sequence /iku/ of subject DR, the tongue tip and tongue blade always moved counterclockwise while the tongue body and tongue rear moved clockwise.

For the sequences with an alveolar stop consonant shown in Fig. 3, the most notable aspect is the difference in the tongue body and tongue rear receiver movements between the two subjects in the sequences /uti, itu/. In particular, during the oral closure the tongue body and tongue rear receivers of subject LK show an extensive lowering movement that is not found in the same sequences for subject DR. For subject LK, the vertical displacement of the tongue body during the closure is 0.7 and 0.8 cm for /uti/ and /itu/, respectively, while the same numbers for subject DR are 0.1 and 0.3 cm. For subject LK, the tongue tip vertical movement during the closure is 0.2 cm in both sequences. In the case of subject LK, this lowering of the tongue body during the oral closure in the sequences with the vowels /i, u/ is also followed by an upward movement after the release of the closure to the position for the second vowel. The path of the tongue body movement from the first to the second vowel is thus much longer for subject LK than for subject DR in the sequence /uti/, 2.0 and 0.7 cm respectively, and 2.2 and 0.9 cm for the sequence /itu/.

Figure 5 shows percentile plots of the curvature of the tongue tip for the productions shown in Fig. 3. Like the tongue body, the median tongue tip curvature was positive with the exception of five intervals for subject LK (/uti/, /itu/, /uta/) and five intervals for subject DR (/uti/, /ati/, /uta/). In general, the absolute curvature values were smaller for the tongue tip than the tongue body. It was also less common for the tongue tip to change its direction of movement during the individual articulatory intervals shown in Fig. 5.

The tongue receivers can move in both straight-line and curved paths. The ratio of the tongue movement measured as the Euclidean distance and as the length of the path provides a metric for how much the path deviates from a straight line.

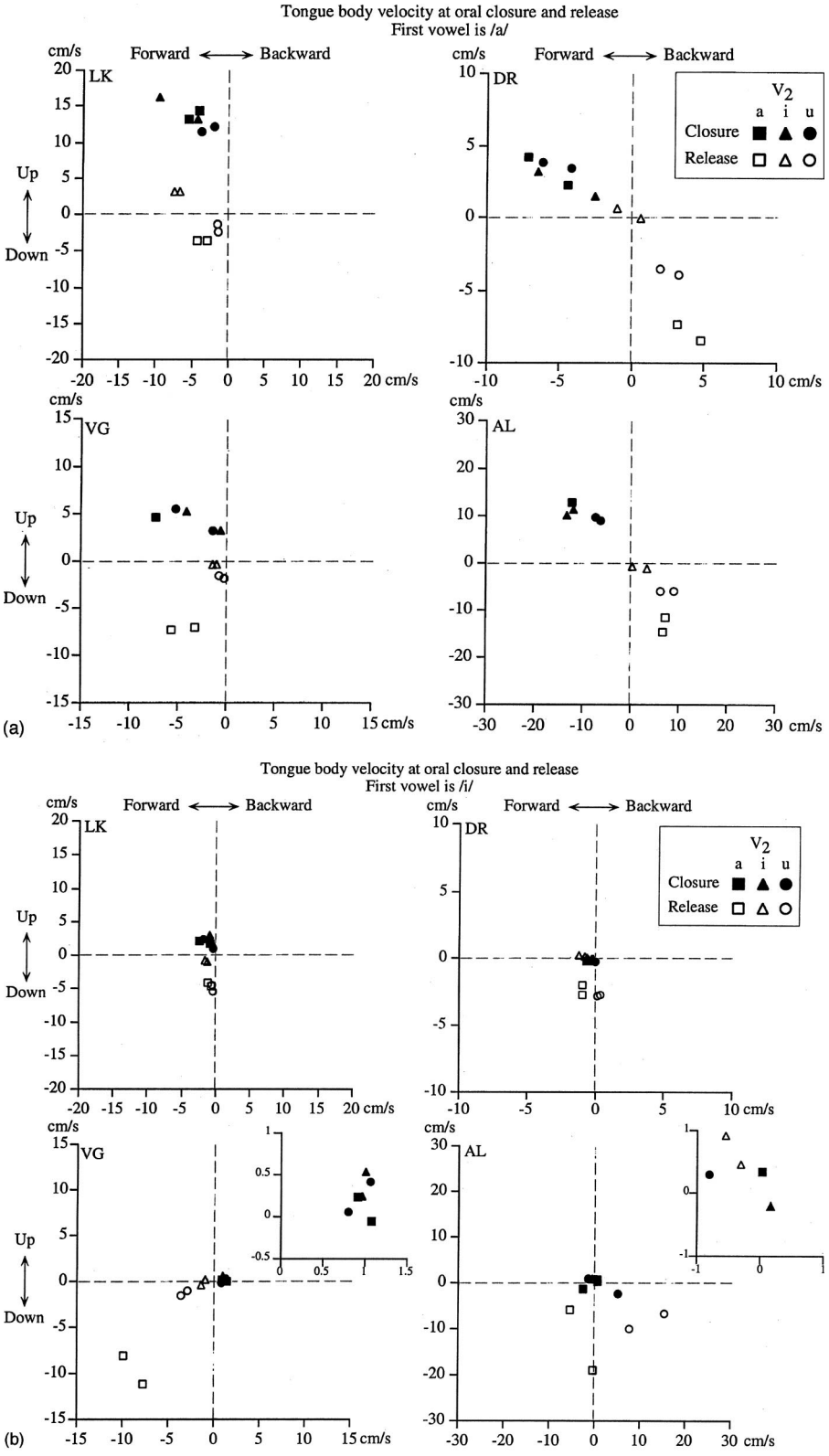

FIG. 7. Average tongue body velocity at the onset and offset of the oral closure in sequences where the first vowel is (a) /a/; (b) /i/; and (c) /u/.

Examination of such ratios for the tongue tip and tongue body movement during the stop closure for the utterances shown in Figs. 2 and 3 showed ratios higher than 2 for the tongue tip in /uti/ of subject LK and in /itu/ and /uta/ of subject DR. In these cases, the tongue tip was moving up and down during the closure, so that its position at the beginning and end of the closure was very similar. It is obvious from a qualitative analysis of the trajectories shown in Figs. 2 and 3 that in many cases the different parts of the tongue move in different paths during parts of the trajectory from the first to the second vowel.

The trajectory for a pair of VCV sequences with the same vowels but in different positions, such as /uki/ and /iku/ or /uti/ and /itu/, do not show paths that are mirror images of each other. This is due, in part, to the fact that the context for the first and second vowels differ due to the carrier phrase

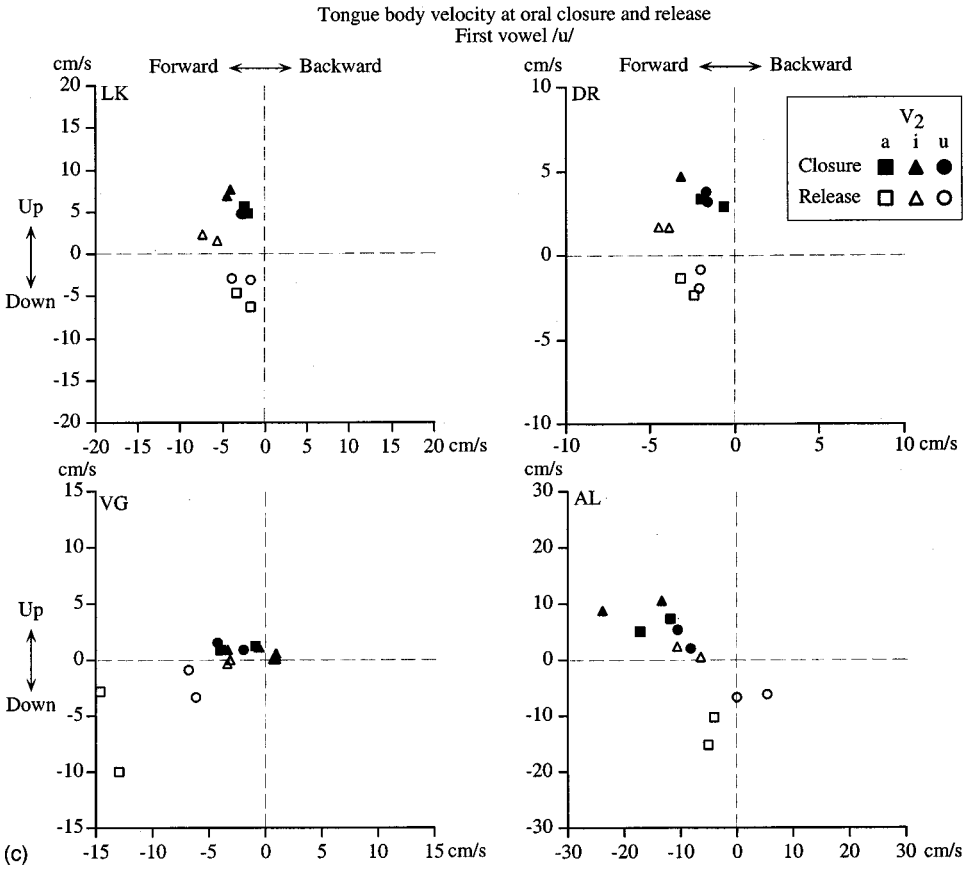

FIG. 7. (*Continued.*)

used, and also to the stress pattern (see Löfqvist and Gracco, 1999, for a detailed analysis of this issue).

A. Tongue body movements at stop closure

The first set of analyses focused on the tongue body and tongue tip before, during, and after the oral closure for the velar and alveolar stop consonants, respectively. An overview of all average receiver positions at onset and release of the oral closure for velar stops is shown in Fig. 6. In almost all cases, the positions of the open- and filled-circles representing the tongue body receiver differ, thus indicating tongue body movement during the closure. Generally, the tongue body is at a higher and more forward position at the release of the closure.

The average horizontal and vertical velocity of the tongue body receiver at the onset and offset of the oral closure for the velar stops are shown in Fig. 7 for all subjects. In this figure, there are two identical symbols for each subject, e.g., the filled triangles. They refer to the voiced and voiceless velar stops. As will be discussed in more detail below, the effect of stop consonant voicing was inconsistent. A first thing to note in this figure is that the tongue body is generally moving up and forward at the onset of the closure: The filled symbols cluster in the upper left quadrant of each panel. The only exceptions to this pattern are found when the first vowel is /i/ for subjects DR, VG, and AL [Fig. 7(b)], where the tongue body may be moving backward and down at closure. A second thing to note is that the velocity at closure is heavily influenced by the first vowel in the VCV sequence: The filled symbols in Figs. 7(a), (b), (c) tend to cluster in nonoverlapping regions of the plots. Conversely, within Figs. 7(a), (b), and (c), the filled squares, triangles, and circles, coding the quality of the second vowel, overlap. The filled symbols in Fig. 7(b) cluster around zero along both axes, indicating that the velocity at closure is very low when the first vowel is /i/. For the other two vowels /a, u/, the pattern shows some differences between speakers for the horizontal and vertical velocity. The results of the analysis of variance are summarized in Table I. (In this and the following section, the degrees of freedom in the analysis of variance were 1,162 for consonant voicing and 2,162 for vowels.)

The analysis of variance showed that the horizontal ve-

TABLE I. F and η^2 values for tongue body movements at the stop closure. Boldface indicates significant effect at $p<0.0001$.

Measure	LK	DR	VG	AL
Horizontal velocity at closure				
V1	**84.73**, 0.15	**501.01**, 0.36	**184.20**, 0.36	**449.79**, 0.28
V2	**20.91**, 0.04	1.98	**12.04**, 0.02	**85.92**, 0.05
Vertical velocity at closure				
V1	**1163.66**, 0.3	**556.61**, 0.32	**346.61**, 0.41	**832.37**, 0.38
V2	**29.85**, 0.02	4.83	1.51	**40.30**, 0.02
Horizontal velocity at release				
V1	**74.19**, 0.13	**434.92**, 0.62	**155.99**, 0.13	**123.21**, 0.26
V2	**71.89**, 0.13	**82.36**, 0.12	**561.71**, 0.22	**154.3**, 0.33
Vertical velocity at release				
V1	**22.44**, 0.07	**120.12**, 0.14	5.04	3.64
V2	**126.99**, 0.38	**264.79**, 0.32	**441.25**, 0.41	**757.47**, 0.36
Movement path during closure				
V1	**815.89**, 0.23	**391.03**, 0.21	**108.44**, 0.11	**551.33**, 0.16
V2	**45.47**, 0.01	**12.2**, 0.001	**98.32**, 0.1	**86.19**, 0.03

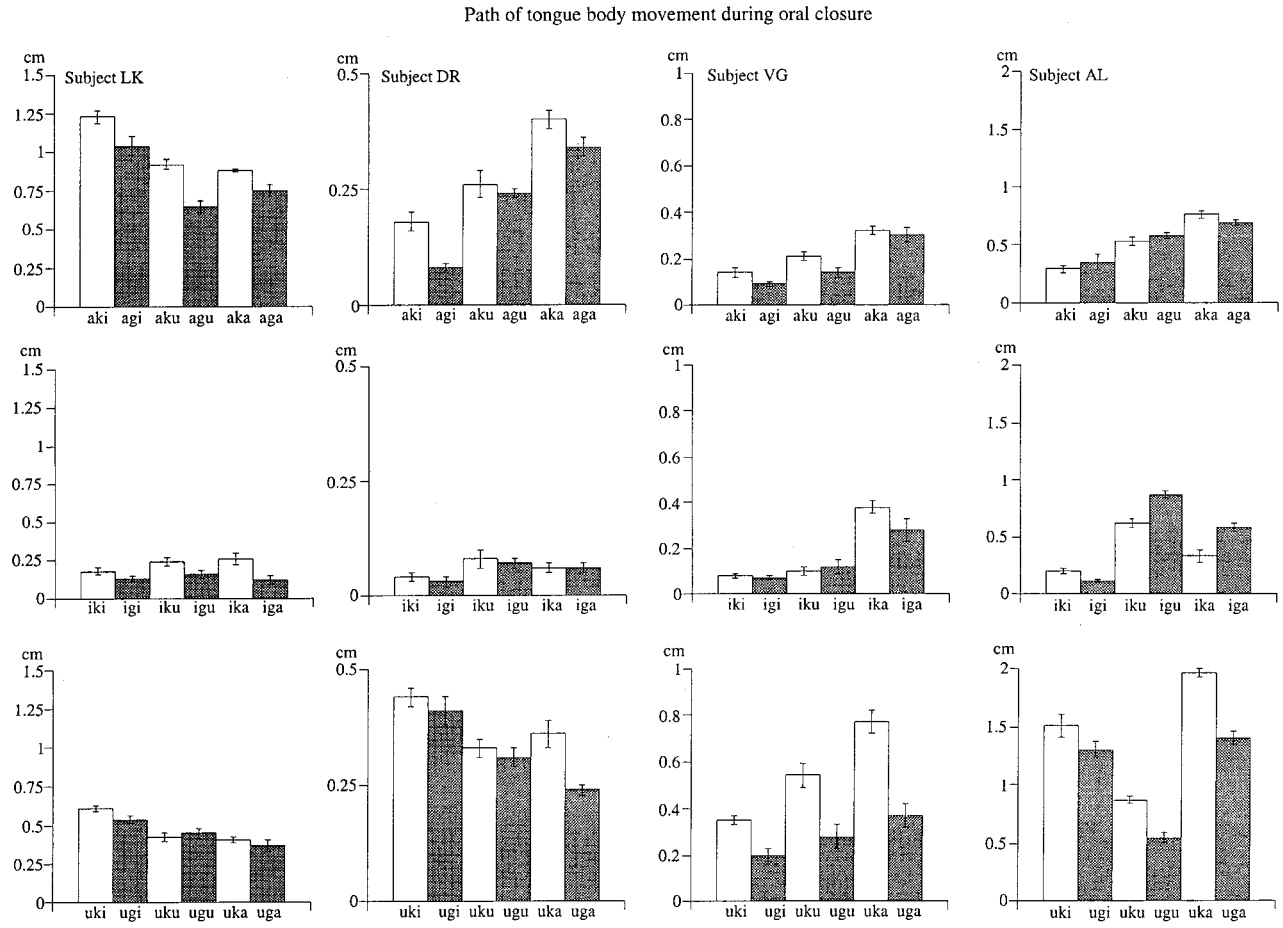

FIG. 8. Average movement path of the tongue body receiver during the period of oral closure; the error bars show the standard deviation.

locity at oral closure was reliably influenced by the quality of the first vowel. The same was true for the vertical velocity at closure. The effect of the second vowel on the horizontal velocity at closure was significant for subjects LK, VG, and AL, but not for subject DR. For the vertical velocity at closure, the second vowel effect was significant for subjects LK and AL. The η^2 values for the effect of the second vowel are very low compared to those of the first vowel. Stop consonant voicing did not show any consistent influences on the tongue body movement at oral closure across subjects.

At the release of the oral closure for the velar stops, the results presented in Fig. 7 show more variability between the subjects. In the majority of cases, the tongue body is moving downward at the release, but exceptions to this pattern are found for all subjects when the second vowel is /i/, the unfilled triangles. The vertical velocity at the release tends to be smaller when the second vowel is /i/ (unfilled triangles) than when it is /a/ or /u/ (unfilled squares and circles. For two subjects, LK and VG, the tongue body is always moving forward at the release, whereas for the other two subjects, DR and AL, a backward movement occurs in the vowel contexts /a_a/ [Fig. 7(a)], /a_u/ [Fig. 7(a)], and /i_u/ [Fig. 7(b)]. It is reasonable to assume that at the release of the velar closure, the tongue body movement is mostly influenced by the second vowel in the VCV sequence. Thus, the unfilled symbols should cluster by shape. This is generally the case for all subjects.

The horizontal velocity of the tongue body at the release was reliably influenced by the first vowel for all subjects. However, the first vowel only had a reliable influence on the vertical velocity at the release for subjects LK and DR. Also, the influence of the second vowel on the horizontal and vertical velocity at the release was reliable. Thus, to judge from the η^2 values, the horizontal velocity of the tongue body at the release of the velar closure is still influenced by the first vowel, whereas the vertical velocity is mostly influenced by the second vowel. Again, the influence of consonant voicing was inconsistent.

The tongue body receiver usually continued to move during the oral closure for the velar stops; the path of the movement was generally less than 1, as summarized in Fig. 8. The effect of the first vowel on the movement path was reliable for all subjects; see Table I. The second vowel also reliably influenced the movement path during the closure, although the η^2 values were lower. Consonant voicing had a reliable effect on tongue body movement during the closure for subjects LK, DR, and VG. As is evident in Fig. 8, the path was longer for the voiceless stops.

B. Tongue tip movements at stop closure

An overview of all average receiver positions at onset and release of the oral closure for alveolar stops is shown in Fig. 9. In almost all cases, the positions of open- and filled-

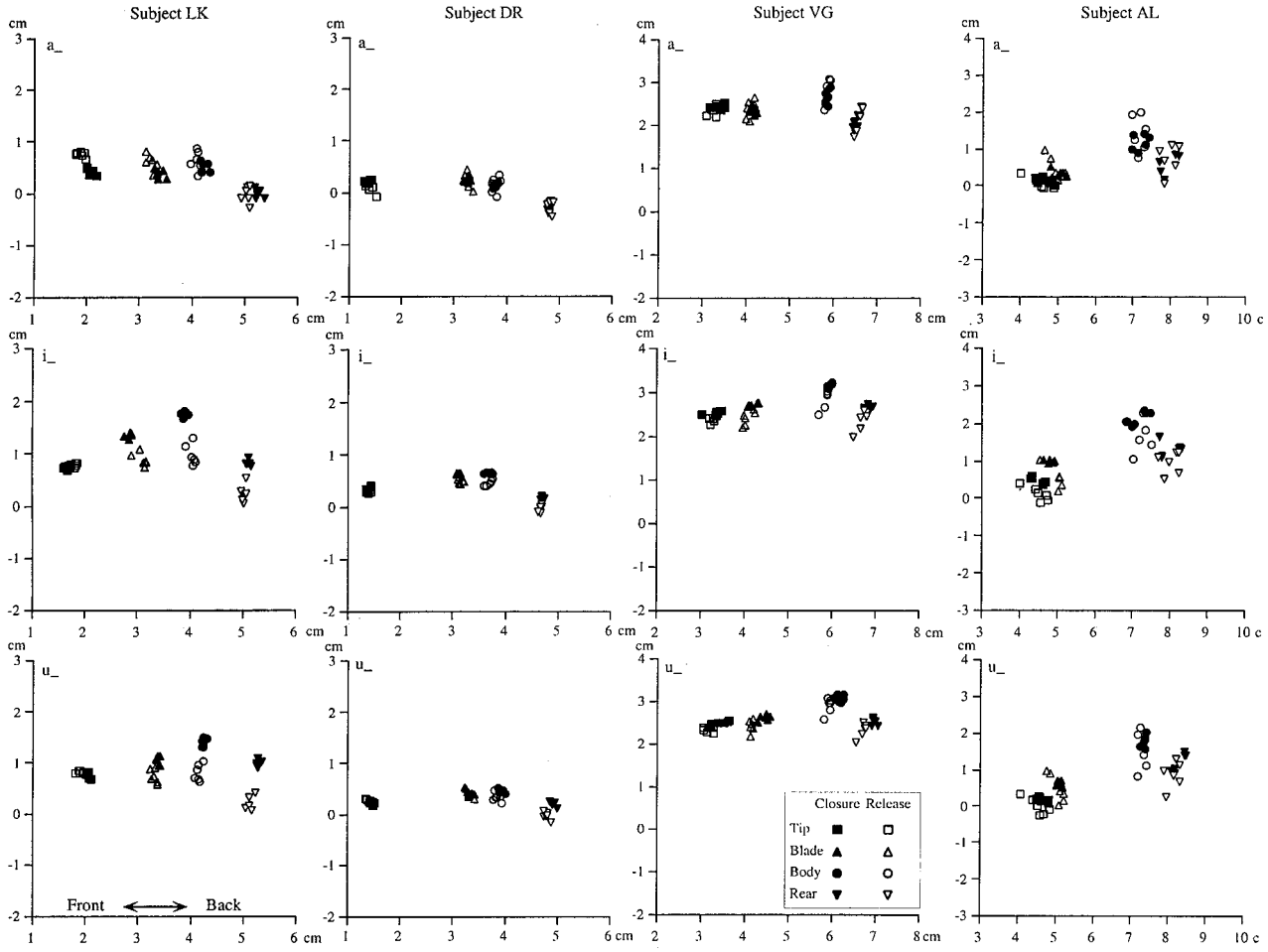

FIG. 9. Receiver positions at onset and release of oral closure for alveolar stops.

squares representing the tongue tip receiver differ, thus indicating tongue tip movement during the closure. Generally, the pattern of tongue tip movement during the closure is more variable across subjects that that of the tongue body shown in Fig. 6.

The average horizontal and vertical velocity of the tongue tip receiver at the onset and offset of the oral closure for the alveolar stops are shown in Fig. 10. In this figure, there are two identical symbols for each subject, e.g., the filled triangles. They refer to the voiced and voiceless alveolar stops. At the onset of the oral closure, the tongue tip is generally moving upward. A few exceptions to this pattern occur for subject AL. The pattern of horizontal movement differs between subjects. Subject DR always shows a forward movement, while subjects LK, and AL have a forward movement when the first vowel is /a/ and /u/ [Figs. 10(a) and (c)], but a backward movement when the first vowel is /i/ [Fig. 10(b)]. For subject VG, the movement is forward when the first vowel is /u/ and backward when the first vowel is /i/. Interestingly, when the first vowel is /a/, the movement is forward for the voiced stops but backward for the voiceless ones. The strong influence on the movement velocity at oral closure from the first vowel is evident from the fact that the filled symbols tend to cluster in nonoverlapping regions in Figs. 10(a)–(c). Note, however, that the filled symbols are higher in Fig. 10(a) for subjects LK, VG, and AL than in Figs. 10(b) and (c), whereas the filled symbols are higher for subject DR in Fig. 10(c) than in Figs. 10(a) and (b). This shows that the tongue tip is moving upwards at a faster speed when the preceding vowel is /a/ for subjects LK, VG, and AL, but when it is /u/ for subject DR.

The strong influence on the first vowel on the tongue tip velocity at the closure for the alveolar stops was also shown by the statistical analysis, summarized in Table II. For the horizontal velocity at closure, the effect of the first vowel was reliable. The influence of the second vowel was only significant for subjects DR and AL and accounted for a smaller proportion. Also, for the vertical velocity at closure there was a reliable influence of the first vowel. The effect of the second vowel was only significant for subject LK.

At the release of the oral closure, Fig. 10 shows that the tongue tip is moving downward; there are only two exceptions, one for subject DR, /a_i/ [Fig. 10(a)], where the velocity is very small, and one for subject AL, /u_i/ [Fig. 10(c)]. The horizontal movement at the release is mostly forward for subject VG, mostly backward for subjects DR and AL, and variable for subject LK. For subject AL, the tongue tip is moving forward at the release when the second vowel is /i/ [the open triangles in Figs. 10(a)–(c)]. At the release of the alveolar closure, the velocity of the tongue tip is mostly governed by the second vowel. This is shown by the fact that the unfilled symbols cluster by shape.

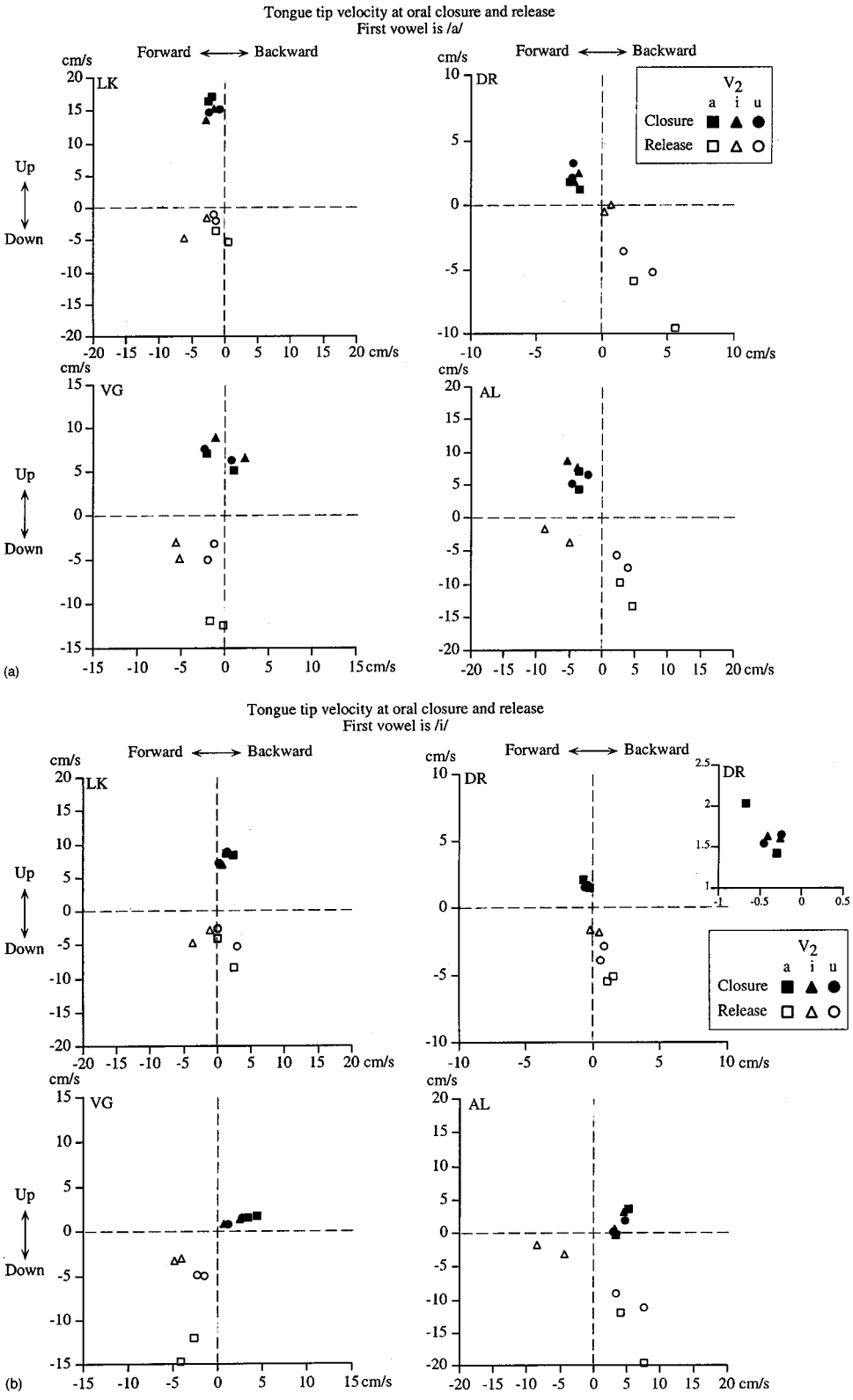

FIG. 10. Average tongue tip velocity at the onset and offset of the oral closure in sequences where the first vowel is (a) /a/; (b) /i/; and (c) /u/.

The effect of the first vowel on the horizontal velocity at the release was reliable for all subjects. The same was true for the second vowel. As for the vertical velocity, the first vowel had a significant effect for subjects LK, DR, and AL. The second vowel had a significant effect for all subjects.

Similar to the tongue body, the tongue tip moved during the closure for the alveolar stops but the length of its path was small and generally less than 0.5 cm; see Fig. 11. The effect of the first vowel on the tongue tip path during the closure was reliable for all subjects. The second vowel had a reliable effect for subjects DR, VG, and AL. Note, however that the η^2 values shown in Table II are quite small. Consonant voicing only had an effect of the tongue tip path during the closure for subject DR, who had a tendency for longer paths in the voiced stops.

The final analysis examined of the relative movement

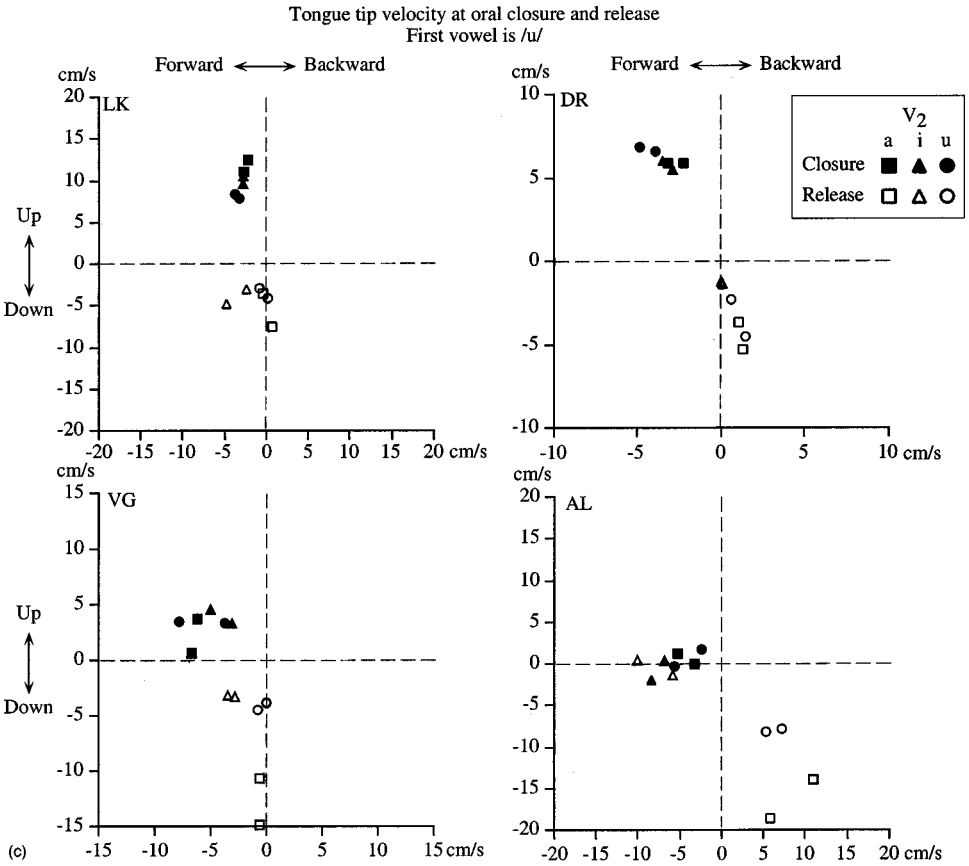

FIG. 10. (*Continued.*)

trajectories during the tongue movement from the first to the second vowel. The results are shown in Table III for the individual subjects and the sequences where the movement during a given interval exceed 50% of the whole trajectory. The first thing to note that during the oral closure, more than 50% of the whole trajectory only occurred for only five sequences (subjects LK and AL) and these sequences all had velar stops. The interval from the first vowel to the stop closure took more than 50% of the whole trajectory in a number of sequences for subjects DR, VG, and AL. In 82% of these sequences, the first vowel was /a/, while the first vowel was /u/ in the remaining sequences. In addition, 70% of these sequences had an alveolar stop. The interval between the stop release and the onset of the second vowel accounted for more than 50% of the whole trajectory in a few sequences for subjects LK, DR, and VG. In 86% of these sequences, the first vowel was /i/, and 86% of them had a velar stop. Finally, the movement during the second vowel took more than 50% of the whole trajectory in some sequences for all subjects. In 63% of them, the second vowel was /a/, while in the remaining 37% the second vowel was /u/ 58% of these sequences had a velar stop, while 42% had an alveolar stop.

TABLE II. F and η^2 values for tongue tip movements at the stop closure. Boldface indicates significant effect at $p<0.0001$.

Measure	LK	DR	VG	AL
Horizontal velocity at closure				
V1	**208.14**, 0.52	**299.46**, 0.25	**204.79**, 0.59	**696.81**, 0.72
V2	4.08	**13.45**, 0.01	2.73	**22.17**, 0.02
Vertical velocity at closure				
V1	**266.23**, 0.07	**457.62**, 0.25	**311.95**, 0.24	**319.12**, 0.4
V2	**20.6**, 0.01	8.16	7.23	1.89
Horizontal velocity at release				
V1	**65.61**, 0.13	**112.75**, 0.16	**12.51**, 0.04	**31.91**, 0.02
V2	**203.96**, 0.39	**123.29**, 0.16	**41.68**, 0.15	**1182.73**, 0.79
Vertical velocity at release				
V1	**37.04**, 0.02	**21.88**, 0.01	1.73	**43.02**, 0.01
V2	**50.59**, 0.03	**450.83**, 0.2	**597.80**, 0.25	**1091.13**, 0.26
Movement path during closure				
V1	**81.69**, 0.03	**70.33**, 0.05	**10.62**, 0.01	**76.88**, 0.02
V2	3.27	**47.71**, 0.03	**35.29**, 0.001	**97.15**, 0.03

IV. DISCUSSION

The present results are compatible with the idea of a virtual target for the tongue in making a stop closure. Similar to the lips for a bilabial stop (Löfqvist and Gracco, 1997), the tongue can move at a high velocity at the onset of the oral closure for the stop. The resulting tissue compression thus makes the airtight seal during the closure. Such a control strategy would also ensure that the tongue will form an airtight seal irrespective of any contextual variability in the onset positions of its closing movements. Together with the results presented by Mooshammer *et al.* (1995) and Fuchs *et al.* (2001), the present findings thus suggest a virtual target for the tongue that would make it move into the nasal cavity. The velocity of both the tongue tip and tongue body at oral closure was closely related to the quality of the preceding vowel. In particular, it was very low when the preceding vowel was /i/, compared to /a/ and /u/. This variation is related to the fact that movement velocity scales with movement amplitude. Hence, the tongue has a longer distance to

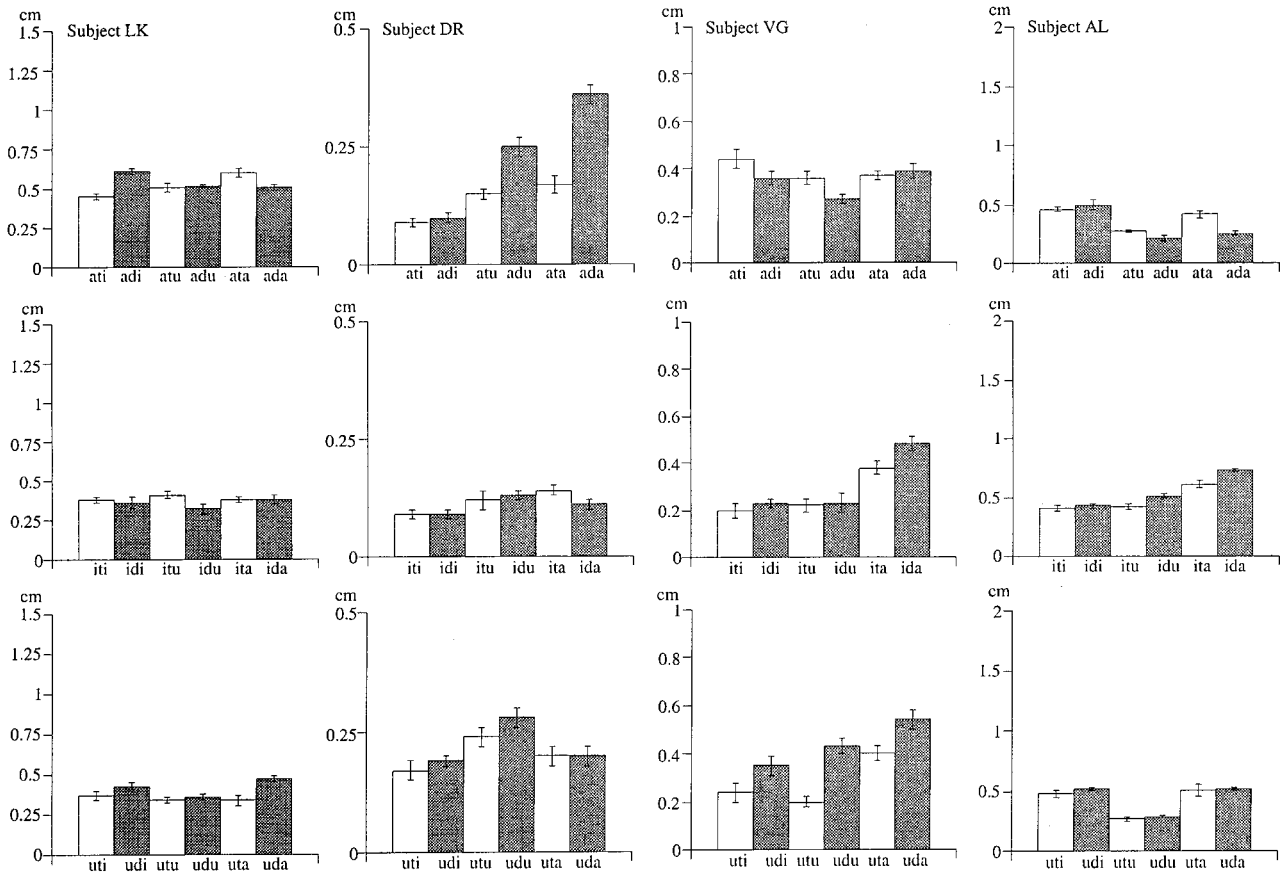

FIG. 11. Average movement path of the tongue tip receiver during the period of oral closure; the error bars show the standard deviation.

travel when the preceding vowel is /a/ or /u/. For the vowel /i/, the tongue is already raised in the oral cavity, however.

The tongue movement trajectories for subjects LK and DR shown in Fig. 3 illustrate a substantial individual difference in the trajectories for the alveolar stop occurring between the high vowels /i/ and /u/. Here, subject LK lowers the rear portion of the tongue for the production of the stop. No similar pattern was observed for the other subjects. In these productions of subject LK, the tongue seems to be pivoting around an imaginary axis located behind the tongue tip receiver. Similar pivoting patterns have been described by Stone (1990), who showed them to occur both in the longitudinal and transverse dimensions of the tongue. The nature of such individual differences is poorly understood at present. As we have argued before (Löfqvist and Gracco, 1997), if an articulatory pattern is to be maintained and transmitted across generations of speakers, the pattern would have to either be recoverable by auditory or audiovisual means, and/or follow from general principles of biomechanics and motor control. Since most differences in tongue movements between subjects LK and DR in Fig. 3 occur during the oral closure, the movements may not produce audible effects and hence the variability may be random.

In producing a stop consonant, one task of the speaker is to make a momentary closure in the vocal tract. This closure

TABLE III. VCV sequences and articulatory intervals where the tongue movement path occupied more than 50% of the whole path from the first to the second vowel. For sequences with the velar stop /g/, the movement is that of the tongue body receiver, while for the sequences with an alveolar stop /d/, the movement is that of the tongue tip receiver.

Interval	LK	DR	VG	AL
From first vowel to closure		aki, agi, ati, atu, uti, adi ada, udi	aki, agi, agu, ati, atu, adi adu	aki, agi, ati, uti, adi, ada, adu, udi
Oral closure	aki, agi			uki, uka, ugi
Release to onset of second vowel	ika, uka	iki, iku, itu	iki, iku	
During second vowel	iga, igu, aga, uga, ida, ada, uda	ika, iga, igu, uga, ugu, ita, ida, idu, uda	iga, igu	idu

allows for a build-up of oral air pressure that drives the transient noise source at the release of the oral closure. In the present study, all the stops were produced with an oral closure, based on acoustic analyses, which may not be the case in normal running speech (cf. Crystal and House, 1988). The present results are compatible with the assumption that as long as the closure is maintained, the articulators can move. In the bilabial stops studied by Löfqvist and Gracco (1997), the lower lip was moving vertically during the closure. The present results show that movements during the closure also occur for an articulator that is directly involved in making the oral closure such as the tongue tip and the tongue body. As long as the closure is maintained, the tongue can slide along the palate. The amount of tongue movement during the closure was heavily influenced by vowel context, in particular for the velar stops, cf. Figs. 8 and 11. The path of the tongue tip was generally shorter than that of the tongue body during the consonant closure. The velocity of the tongue tip and tongue body at the onset of the oral closure did not show any consistent pattern across or within subjects. Thus, it was not the case that the velocity of one of them was always greater than that of the other.

As expected, more than 50% of the whole tongue movement trajectory from the first to the second vowel only occurred during the closure in a few sequences with a velar stop, as shown in Table III. This is contrast to what happens in a VCV sequence with a bilabial stops where commonly more than 50% of the trajectory from vowel to vowel occurs during the bilabial closure (Löfqvist and Gracco, 1999).

The tongue movement observed during the stop closure suggests that it is appropriate to view the ''target'' in lingual stop production as making a vocal tract closure. Given the magnitude of the tongue movement during the closure, it would appear to be actively controlled and not only due to biomechanical and/or aerodynamic factors. The best way of describing the patterns of tongue movements observed in this and other studies is that of a curved trajectory between the two vowels. This is the case for both the tongue body and the tongue tip. The direction of this movement is predominantly forward–backward, with its speed and amplitude modulated by the vowel context. The results of the statistical analyses revealed strong influences from both the preceding and following vowels. We should add that the present data on tongue movements include the contribution of the jaw. It is unlikely, however, that representing the tongue movements in a mandible-based coordinate system would significantly alter the trajectories, as shown by the different coordinate systems used in the study by Munhall *et al.* (1991).

The present results show that at the instant of the acoustically defined oral closure for a velar stop the tongue body is moving forward in the majority of cases. Also for the alveolar stop, the tongue tip is moving forward at the oral closure. Such a forward tongue body movement for a velar stop consonant can also occur when the vowel preceding the stop is the front vowel /i/ and the vowel following the stop is a back vowel /a, u/, although this only consistently occurred for subject LK. One implication of this is that the tongue is not necessarily moving along a path that might be considered to be the most direct one. This is most likely related to the fact that the tongue movement for a sequence of a vowel, a velar stop consonant, and a vowel does not follow a straight path, but a curved one. That is, even in the case when the vowels before and after the consonant are identical, such as the back vowel /a/, the tongue does not stop during the closure and then return to the low back position for the second vowel. Such a looping pattern appears to be the most common one, but a generally accepted explanation for it has not been put forward. Mooshammer *et al.* (1995) present an extensive discussion of some of the proposed explanations. One of these suggests that the forward movement is made to help sustain voicing in voiced stops by expanding the cavity behind the closure. The problem with this suggestion is that the same movement pattern is also found for voiceless stops. Another explanation proposes that the build-up of air pressure behind the closure is a contributing factor. Hoole *et al.* (1998) specifically examined the role of aerodynamic factors in explaining tongue movement trajectories. They thus had speakers produce speech with the normal egressive air flow and also with an ingressive air flow. Their results showed that the magnitude of the tongue movement during the closure was reduced when speakers spoke on inhalation. However, there was no reversal in the commonly observed forward movement during the stop closure in the egressive condition. Hence, aerodynamic factors alone do not explain the movement patterns. In addition, a recent simulation experiment by Perrier *et al.* (2000) suggested that the influence of air pressure and flow on tongue movements is limited and may only play a role in a sequence like /ika/, where the tongue body is raised towards the palate for the vowel, cf. Fig. 6. Based on simulations using a tongue model, Perrier *et al.* (1998) argue that the movement pattern of the tongue is due, at least in part, to biomechanical factors. One problem with this suggestion is that in another very basic tongue function, i.e., swallowing, the movement pattern of the tongue is the opposite of the one observed in speech. In the oral part of swallowing, the tongue is moving backward in contact with the palate to move the bolus into the pharynx (e.g., Logeman, 1995). In addition, tongue movements during speech can go in the direction opposite to the one observed here for the VCV sequences with lingual consonants. That is, the case in VCV sequences with a labial consonant, where the tongue movement is made from the first to the second vowel in the sequence (e.g., Löfqvist and Gracco, 1999). It is thus not clear that the biomechanics of the tongue muscles can explain the commonly observed forward–backward curved path of the tongue in speech.

Since none of these explanations is entirely satisfactory in itself, we should perhaps view the movement pattern observed for the tongue in stop production as an example of a more general principle of motor control. Such principle could be based on a cost minimization, often expressed as a minimum jerk criterion (Flash, 1987; Flash and Hogan, 1985) or as a smoothness constraint (Uno *et al.*, 1989). The development of this principle has been based on studies of reaching movements of the hand. In a reaching task where the hand has to move through a sequence of target positions, the hand moves in a curved path between the targets. The observed hand trajectory could be accurately modeled based

on such a cost minimization function. In the case of tongue movements, a similar principle may thus explain why in a sequence such as /aka/ the tongue moves in a loop and not in a straight line from the first vowel to the consonant closure and then returns along a similar straight-line path. Such a movement pattern would involve successive accelerations and decelerations of the tongue that might involve a higher effort. In the production of /iku/ with a very high curvature value of subject DR, the velocity of the tongue body is very small, as shown in Fig. 7(b). This idea is also compatible with a continuous tongue movement during the stop closure, since the tongue maintains contact with the palate during its movement. In this view, the whole trajectory from the first to the second vowel is planned and there is no point target for the tongue during the stop. Biomechanical models of the tongue (e.g. Sanguineti *et al.*, 1998) could be used to explore this idea. The present results are also useful in constraining the movement trajectories that such models will have to generate. In addition, the development of speech motor control might provide further insights, since the subjects examined in this and other studies of speech movement kinematics have all been beyond childhood, and their speech movement patterns are thus well established.

ACKNOWLEDGMENTS

We are grateful to Pascal Perrier and Kenneth de Jong for comments on an earlier version of the paper. This work was supported by Grant Nos. DC-00865, DC-00594, and DC-03102 from the National Institute of Deafness and Other Communication Disorders, National Institutes of Health.

Coker, C. (**1976**). ''A model of articulatory dynamics and control,'' IEEE Trans. Acoust., Speech, Signal Process. **64**, 452–460.

Crystal, T., and House, A. (**1988**). ''The duration of American English stops: An overview,'' J. Phonetics **16**, 285–294.

Dembowski, J., Lindstrom, M. J., and Westbury, J. R. (**1998**). ''Articulator point variability in the production of stop consonants,'' in *Neuromotor Speech Disorders: Nature, Assessment, and Management*, edited by M. P. Cannito, K. M. Yorkston, and D. R. Beukelman (Brookes, Baltimore), pp. 27–46.

Flash, T. (**1987**). ''The control of hand equilibrium trajectories in multi-joint arm movements,'' Biol. Cybern. **57**, 257–274.

Flash, T., and Hogan, N. (**1985**). ''The coordination of arm movements: An experimentally confirmed mathematical model,'' J. Neurosci. **5**, 1688–1703.

Fuchs, S., Perrier, P., and Mooshammer, C. (**2001**). ''The role of the palate in tongue kinematics: An experimental assessment in VC sequences,'' *Eurospeech 2001*, Aalborg.

Hamlet, S., Bunnell, H. T., and Struntz, B. (**1986**). ''Articulatory asymmetries,'' J. Acoust. Soc. Am. **79**, 1164–1169.

Hoole, P., Munhall, K., and Mooshammer, C. (**1998**). ''Do airstream mechanisms influence tongue movement paths?,'' Phonetica **55**, 131–146.

Houde, R. (**1968**). *A Study of Tongue Body Motion during Selected Consonant Sounds* (Speech Communications Research Laboratory, Santa Barbara), SCRL Monograph 2.

Kent, R., and Moll, K. (**1972**). ''Cinefluorographic analyses of selected lingual consonants,'' J. Speech Hear. Res. **15**, 453–473.

Löfqvist, A. (**2000**). ''Control of closure duration in stop consonants,'' in *Proceedings of the 5th Seminar on Speech Production: Models and Data* (Institut für Phonetik und Sprachliche Kommunikation, Munich), pp. 29–32.

Löfqvist, A., and Gracco, V. L. (**1994**). ''Tongue body kinematics in velar stop production: Influences of consonant voicing and vowel context,'' Phonetica **51**, 52–67.

Löfqvist, A., and Gracco, V. L. (**1997**). ''Lip and jaw kinematics in bilabial stop consonant production,'' J. Speech Lang. Hear. Res. **40**, 877–893.

Löfqvist, A., and Gracco, V. (**1999**). ''Interarticulator programming in VCV sequences: Lip and tongue movements,'' J. Acoust. Soc. Am. **105**, 1864–1876.

Löfqvist, A., Gracco, V. G., and Nye, P. (**1993**). ''Recording speech movements using magnetometry: One laboratory's experience,'' ACCOR Workshop on Electromagnetic Articulography in Speech Research (München), pp. 143–162.

Logeman, E. (**1995**). ''Dysphagia: Evaluation and treatment,'' Folia Phoniatr. **47**, 140–164.

Mooshammer, C., Hoole, P., and Kühnert, B. (**1995**). ''On loops,'' J. Phonetics **23**, 3–21.

Munhall, K., Ostry, D., and Flanagan, R. (**1991**). ''Coordinate spaces in speech planning,'' J. Phonetics **19**, 293–307.

Payan, Y., and Perrier, P. (**1997**). ''Synthesis of V–V sequences with a 2D biomechanical tongue model controlled by the Equilibrium Point hypothesis,'' Speech Commun. **22**, 185–205.

Perkell, J. S. (**1969**). *Physiology of Speech Production: Results and Implications of a Quantitative Cineradiographic Study* (MIT Press, Cambridge, MA).

Perkell, J., Cohen, M., Svirsky, M., Matthies, M., Garabieta, I., and Jackson, M. (**1992**). ''Electromagnetic midsagittal articulometer (EMMA) systems for transducing speech articulatory movements,'' J. Acoust. Soc. Am. **92**, 3078–3096.

Perrier, P., Payan, Y., Perkell, J., Zandipour, M., and Matthies, M. (**1998**). ''On loops and articulatory biomechanics,'' in Proceedings of the 5th International Conference on Spoken Language Processing (Sydney), Vol. 2, 421–424.

Perrier, P., Payan, Y., Perkell, J., Zandipour, M., Pelorson, X., Coisy, V., and Matthies, M. (**2000**). ''An attempt to simulate the fluid–walls interaction during velar stops,'' in *5th Seminar on Speech Production: Models and Data* (Institut für Phonetik und Sprachliche Kommunikation, Munich), pp. 149–152.

Rubin, P. E. R., and Löfqvist, A. (**1996**). ''HADES (Haskins Analysis Display and Experiment System),'' Haskins Labs. Status Rep. Speech Res. (available at www.haskins.yale.edu/haskins/SR/SRweb/SRweb1.html).

Sanguineti, V., Laboissière, R., and Ostry, D. (**1998**). ''A dynamic biomechanical model for neural control of speech,'' J. Acoust. Soc. Am. **103**, 1615–1627.

Schönle, P. (**1988**). *Elektromagnetische Artikulographie* (Springer, Berlin).

Stone, M. (**1990**). ''A three-dimensional model of tongue movement based on ultrasound and x-ray microbeam data,'' J. Acoust. Soc. Am. **87**, 2207–2217.

Uno, Y., Kawato, M., and Suzuki, R. (**1989**). ''Formation and control of optimal trajectory in human multi-joint arm movement—Minimum torque change model,'' Biol. Cybern. **61**, 89–101.

Westbury, J. (**1994**). ''On coordinate systems and the representation of articulatory movements,'' J. Acoust. Soc. Am. **95**, 2271–2273.

Westbury, J., and Hashi, M. (**1997**). ''Lip-pellet positions during vowels and labial consonants,'' J. Phonetics **25**, 405–419.

Young, M. A. (**1993**). ''Supplementing tests of statistical significance: Variations accounted for,'' J. Speech Hear. Res. **36**, 644–656.

An EMA study of VCV coarticulatory direction

Daniel Recasens
Laboratori de Fonètica, Institut d'Estudis Catalans, c/Carme 47, Barcelona 08001, Spain and
Departament de Filologia Catalana, Universitat Autònoma de Barcelona, Bellaterra, Barcelona, Spain

(Received 27 November 2000; revised 25 October 2001; accepted 6 March 2002)

This study addresses three issues that are relevant to coarticulation theory in speech production: whether the degree of articulatory constraint model (DAC model) accounts for patterns of the directionality of tongue dorsum coarticulatory influences; the extent to which those patterns in tongue dorsum coarticulatory direction are similar to those for the tongue tip; and whether speech motor control and phonemic planning use a fixed or a context-dependent temporal window. Tongue dorsum and tongue tip movement data on vowel-to-vowel coarticulation are reported for Catalan VCV sequences with vowels /i/, /a/, and /u/, and consonants /p/, /n/, dark /l/, /s/, /ʃ/, alveolopalatal /ɲ/ and /k/. Electromidsagittal articulometry recordings were carried out for three speakers using the Carstens articulograph. Trajectory data are presented for the vertical dimension for the tongue dorsum, and for the horizontal dimension for tongue dorsum and tip. In agreement with predictions of the DAC model, results show that directionality patterns of tongue dorsum coarticulation can be accounted for to a large extent based on the articulatory requirements on consonantal production. While dorsals exhibit analogous trends in coarticulatory direction for all articulators and articulatory dimensions, this is mostly so for the tongue dorsum and tip along the horizontal dimension in the case of lingual fricatives and apicolaminal consonants. This finding results from different articulatory strategies: while dorsal consonants are implemented through homogeneous tongue body activation, the tongue tip and tongue dorsum act more independently for more anterior consonantal productions. Discontinuous coarticulatory effects reported in the present investigation suggest that phonemic planning is adaptative rather than context independent. [DOI: 10.1121/1.1479146]

PACS numbers: 43.70.Aj, 43.70.Bk [AL]

I. INTRODUCTION

A. The DAC model

A goal of this investigation is to verify the validity of the degree of articulatory constraint model (DAC model) for predicting patterns of coarticulatory direction in speech production. Data on dorsopalatal contact and F2 frequency presented in Recasens *et al.* (1997) suggest that this model may account satisfactorily for trends in coarticulation extent and direction in VCV sequences.

Within the framework of the coproduction theory of coarticulation (Fowler, 1977, 1980), the DAC model is based on the assumption that articulatory gestures associated with consecutive segments are coproduced and overlap to different degrees depending on their spatiotemporal properties as well as on prosodic factors and speech rate. According to this model, coarticulatory sensitivity for consonants to the influence of the adjacent vowels in VCV sequences (V-to-C effects) varies inversely with the strength of the consonantal effects (C-to-V effects) and with the degree of articulatory constraint for the intervocalic consonant. Regarding the dorsum of the tongue (which is the articulator about which the model can make theoretical predictions so far), consonants differ in DAC value according to the following order: dorsals (alveolopalatals, palatals, velars), lingual fricatives (/s/, /ʃ/), dark /l/, which can be assigned a maximum DAC value (DAC=3); dentals and alveolars such as /n/ and clear /l/ (DAC=2); and bilabials, with the lowest DAC value (DAC=1). Strictly speaking, /ʃ/ is both a lingual fricative and a dorsal consonant to the extent that it involves tongue dorsum activation.

Consonants are specified for a maximal DAC value based on demands on place and manner of articulation. It is hypothesized that dorsal consonants are highly constrained based on the observation that their primary contact or constriction location stays relatively fixed in line with the large contact size involved and perhaps the sluggishness of the tongue dorsum. The same observation may even apply to velars provided that at least two targets in front and back vowel contexts are accounted for. Maximal tongue body constraint is also associated with tongue dorsum grooving for lingual fricatives and with the formation of a secondary postdorsal constriction at the upper pharynx for dark /l/. Among the remaining consonants specified for a lower degree of tongue dorsum constraint, a higher DAC value for dentals and alveolars (2) than for bilabials (1) is related to coupling effects between the tongue dorsum and the primary tongue front articulator for the former consonantal group and to the absence of tongue body activation for the latter. Among the vowels, /i/ should be essentially more constrained (DAC=3) than /a/ and /u/ (DAC=2) at the tongue predorsum given the fact that this tongue region is actively raised for front vowels while staying low and inactive for back vowels. The lowest DAC value (1) corresponds to /ə/ which does not involve any obvious tongue body target configuration (see however Browman and Goldstein, 1992).

In our previous paper, the size and temporal extent of

 0001-4966/2002/111(6)/2828/14/$19.00

the C-to-V coarticulatory effects were found to depend not only on the articulatory characteristics of the consonant but on those of the vowel as well. Thus, as expected, C-to-V effects happen to be particularly salient as the DAC value for the consonant increases with respect to that for the vowel, e.g., effects from /ɲ/ (DAC=3) on /a/ (DAC=2). More interestingly, maximal consonantal effects on vowels are also obtained when the lingual gestures for the two consecutive segments are at the same time highly constrained and antagonistic, e.g., effects from dark /l/ on /i/ which are both specified for DAC=3 and are produced with tongue body lowering and retraction (dark /l/) and tongue dorsum raising and fronting (/i/).

Within this theoretical framework, patterns of C-to-V coarticulatory direction were characterized as anticipatory or carryover according to the requirements on consonantal production. Consonants with a maximal DAC value (3) favor a specific direction for the consonantal effects on vowels: on the one hand, dark /l/ favors C-to-V1 anticipation given that tongue dorsum lowering and retraction often start before tongue tip raising for the implementation of this consonantal realization; on the other hand, consonants produced with tongue dorsum raising such as alveolopalatals, palatals, and velars favor C-to-V2 carryover effects in line with the slow lowering motion of the primary dorsal articulator at consonantal release which may be due to inertia. Two basic C-to-V patterns are found for consonants produced with the tongue front and involving little tongue dorsum activation (DAC =2), e.g., dentals and alveolars (but for dark /l/): consonantal effects on /a/ happen to be more prominent at the anticipatory level presumably since this vowel permits free apical anticipation; effects on /i/, on the other hand, are especially salient at the carryover level for analogous reasons to (alveolo) palatals.

A major prediction of the DAC model is that these patterns of C-to-V coarticulatory direction in VCV sequences should account for the direction of the vocalic effects. According to the model, vocalic anticipation (i.e., V2-to-C and V2-to-V1 effects) ought to vary inversely with the prominence of the C-to-V2 carryover effects while vowel-dependent carryover effects (i.e., V1-to-C and V1-to-V2) are expected to decrease with the strength of the C-to-V1 anticipatory component. These inverse relationships occur because carryover effects associated with the vowel conflict with anticipatory effects associated with the consonant while vocalic anticipatory effects conflict with consonantal carryover effects. In agreement with this prediction our previous papers report robust patterns of V-to-C and V-to-V coarticulatory direction in VCV sequences with clear patterns of C-to-V direction: sequences with dark /l/ allow more vocalic anticipation than vocalic carryover while vocalic carryover exceeds vocalic anticipation in sequences with /ɲ/.

Patterns of vowel-dependent coarticulatory direction in other VCV cases were found to be less consistent, though in general agreement with our initial predictions. A specific situation applies to VCV sequences with velars: vocalic effects from /i/ versus /a/ show the expected carryover direction when the transconsonantal vowel is /i/ (i.e., in the sequence pair /aki/-/iki/), but not so in the transconsonantal /a/ condition where extensive vocalic anticipation appears to be facilitated by forward tongue dorsum motion during the velar closure period (i.e., sequence pair /aki/-/aka/). Regarding dentoalveolars and labials, vocalic effects appear to favor the carryover component when transconsonantal /i/ contributes to tongue dorsum raising during the consonant and thus causes much C-to-V2 carryover coarticulation to occur (e.g., /ati/-/iti/); on the other hand, the absence of substantial tongue dorsum raising for those consonants in the context of /a/ may explain why the anticipatory direction prevails (e.g., /ati/-/ata/).

The present study seeks to improve our understanding of the directionality patterns for the vocalic effects in VCV sequences using articulatory movement data collected with electromagnetic articulometry (EMA) instead of linguopalatal contact or acoustic data. In comparison to Recasens *et al.* (1997), more natural experimental conditions will be used. Temporal patterns of V-to-V coarticulation will be analyzed for the same consonants and vowels in long real sentences (instead of in isolated VCVs). Stress will be placed on V2 (instead of on V1), and the Catalan phonological rule reducing unstressed /a/ to [ə] will be avoided so that the sequences /aˈCa/ become fully symmetrical at the phonetic level. The same analysis method will be used: anticipatory V2-to-V1 effects associated with two different V2 will be measured during the consonant and preceding V1 (e.g., effects from /i/ versus /a/ on /ɲ/ and preceding /i/ in the pair /iɲa/-/iɲi/) and carryover effects for V1 pairs will be analyzed during the consonant and following V2 (e.g., effects in the pair /aɲi/-/iɲi/).

Within the DAC model framework, the present paper also investigates the extent to which V-to-V effects at the tongue tip conform to patterns of tongue dorsum coarticulatory direction. In a previous EMA study of V-to-C lingual coarticulation in German symmetrical VCV sequences, Hoole *et al.* (1990) found somewhat larger vocalic effects at the tongue front than at the tongue back, perhaps because the tongue tip has less inertia. VCVs with alveolars and velars yielded more carryover than anticipatory effects at the tongue front and dorsum while VCV sequences with bilabials happened to favor the opposite trend at the two lingual regions; also, anticipatory effects were greater than carryover effects at the tongue front in sequence pairs starting with /uk/. As expected, V-to-V coarticulation was blocked to a larger extent by /i/ than by /a/.

B. Temporal window and discontinuous coarticulatory effects

An interesting research topic regarding temporal coarticulation is the extent to which coarticulatory effects provide information about the execution of phonemes and may reflect phonemic planning as well. Differences in the temporal extent of coarticulation could be assigned two different interpretations, i.e., phonemes are executed at different times depending on the articulatory properties of the preceding contextual segments or else, while they are required to begin at a given time, their surface manifestation may vary according to the degree of coarticulation resistance for the contextual segmental units (Fowler, 1993; Fowler and Brancazio,

2000). According to Fowler and Saltzman (1993), the onset of anticipatory coarticulation for a given lingual, labial, or velar gesture is essentially fixed, and occurs about 200–250 ms before the target phoneme; moreover, the actual phonetic implementation of a given anticipatory effect may be discontinuous and thus momentarily interrupted by the ongoing requirements on segmental production. This view is consistent with the time-locked model of temporal coarticulation proposed by Bell-Berti and Harris (1981) in that the period of anticipation associated with the target phoneme is independent of preceding phone length; contrary to the model by Bell-Bert and Harris, it assumes that articulatory conflict does not delay anticipatory coarticulation. Discontinuties in vocalic coarticulation during a noncontiguous segment such as those referred to are not equivalent to troughs, namely, interruptions in the articulatory manifestation of a vocalic gesture in symmetrical VCV sequences caused by the intervocalic consonant (e.g., the trough associated with active lip retraction for /t/ in the sequence /utu/; Perkell, 1986).

In the present paper we will test the validity of Fowler and Saltzman's (1993) approach through an analysis of the temporal location, duration, and frequency of occurrence of discontinuous V-to-V effects in the VCV sequences under study. If their approach is correct, the onset of V2-dependent anticipatory activity should not vary much with changes in V1 and in the intervocalic consonant independently of whether those vocalic anticipatory effects are continuous or discontinuous. The opposite finding could be taken in support of the notion that phonemic planning is adaptative rather than context independent, i.e., phonemes are planned at different times depending on the articulatory requirements for the consonant and/or for the transconsonantal vowel.

This paper also explores the possibility that discontinuous anticipatory effects differ essentially from discontinuous carryover effects. While discontinuous anticipatory effects may reflect the implementation of an early planning strategy, momentary interruptions in long-lasting effects occurring after the target segment are probably related to other factors. A possible origin for discontinuous carryover effects is articulatory overshoot in strings of consecutive highly constrained segments sharing a specific articulatory property; thus, for example, differences in tongue height in V2 in the sequence pair /aʃi/-/iʃi/ could be associated with an intensification of the tongue dorsum raising gesture for /ʃ/ when the consonant is preceded by V1=/i/ rather than with tongue dorsum lowering for V1=/a/.

Even if the onset of V2-dependent anticipation turns out to be contextually conditioned rather than invariant, the present research allows testing whether the temporal span of the anticipatory effects is less variable than that of the carryover effects. This is the expected outcome if phonemic anticipation reflects preprogramming and carryover effects do not, while being strongly determined by inertia and by the gestural requirements for the contextual phonetic segments (Gay, 1977; Recasens, 1989).

II. METHOD

A. Recording procedure

Three Catalan speakers (DR, JP, JC) who also acted as subjects in Recasens *et al.* (1997) uttered all possible VCV combinations with the consonants /p,n,l,s,ʃ,ɲ,k/ and the vowels /i,a,u/. Those VCV sequences were repeated ten times before and after other phonetic segments unspecified for lingual activity ([p], [ə], [β]) in the Catalan sentence [ˈgɾaβəpVˈCVpəˈβans] ("He records pVCVp earlier"); the inclusion of contextual labial consonants and a schwa ensured that the temporal extent of tongue dorsum coarticulation could be expanded sufficiently along the time domain.

Articulatory movement and acoustic data were collected simultaneously using electromagnetic articulometry by means of a Carstens articulograph system AG-100. This system consists of a head mount with three magnetic transmitters that generate a magnetic field, and a set of small transducer coils that can be attached to different articulatory structures in the midsagittal plane. As the articulators move inside the vocal tract, the transducer coils induce a signal that is inversely proportional to the cube of the distance between transmitter and transducer. The output signal results in a set of voltages which can be converted to distance. In the present experiment coils were placed on the tongue tip (TT), tongue blade (TL), tongue dorsum (TD), incisors of the lower jaw (J), upper lip (UL), and lower lip (LL), as well as on the bridge of the nose and upper incisors for head movement correction. The three coils attached on the tongue surface were roughly equidistant both for TL-TT (DR =1.5 cm; JP=2.3 cm; JC=1.8 cm) and for TD-TL (DR =1.9 cm; JP=1.4 cm; JC=1.6 cm). Estimates for the subjects' occlusal planes were obtained as anatomical references to which the data could be rotated (correction angles in degrees were 0.8 for DR, 0.7 for JP and 0.4 for JC), as well as traces of their palates.

Movement and acoustic data were digitized using a real-time input system at a sampling rate of 250 Hz for movement and 10 kHz for speech; the time resolution of the EMA data was 4 ms. The kinematic data were converted from voltage to distance, corrected for head movement, rotated to the occlusal plane, and extracted into X and Y articulatory channels.

B. Data analysis

The temporal extent of V-to-V coarticulatory effects was analyzed from $[\beta]_1$ onset to $[\beta]_2$ offset in the sequence [βə##pVCVp##əβ]. For each VCV repetition, the onset and offset of the intervocalic consonant were identified from visual inspection of spectrographic and waveform displays. Consonantal boundaries were placed at closure onset and at V2 voicing onset following the stop burst for stops (/p/,/k/), and at the onset and offset of frication for the lingual fricatives (/s/,/ʃ/). The segmental boundaries for /l/, /n/, and /ɲ/ were located at the onset and offset times of the low-intensity formants for the two nasals and for the lateral, and often coincided with the endpoints of the vowel transitions. Occasionally these segmental boundaries could not be clearly detected on the spectrographic displays because of the low in-

tensity level of the acoustic signal; in this case consonantal onsets were identified with the onset of maximal TT displacement for /n/, /l/, and /s/, maximal TL displacement for /ʃ/ and /ɲ/, and maximal TD displacement for /k/.

Vocalic temporal effects were considered to occur as long as a significant vowel-dependent difference (referred to as ''changing'' vowel in this paper) extends into the consonant and the transconsonantal vowel (also ''fixed'' vowel from here forward). The changing vowel is V2 and the fixed vowel is V1 when measuring V-to-V anticipation, while V1 is the changing vowel and V2 is the fixed vowel when V-to-V carryover effects are analyzed. In order to single out these effects, significant differences in articulatory displacement were calculated as a function of each changing vowel condition (/i/ versus /a/, /i/ versus /u/, /a/ versus /u/) for each consonant and fixed vowel condition (/i/, /a/, /u/). X and Y movement data were analyzed for all six articulatory regions TT, TL, TD, J, UL, and LL though results will only be presented for TDX, TDY, and TTX.

Statistical evaluation was applied to differences in articulatory position associated with a given pair of vowels in the consonant and the transconsonantal vowel, e.g., effects from V2=/i/ on /ɲ/ and transconsonantal V1=/a/ were measured through a statistical comparison between mean articulatory trajectories across repetitions for /aɲi/ with those for /aɲa/. It was thus assumed that vowels affect each other in asymmetrical sequences and that the degree of vocalic coarticulation may be obtained when data for a given asymmetrical sequence are compared with those in symmetrical sequences composed of the same consonant and the same fixed transconsonantal vowel. There were 1134 sequence pairs submitted to statistical analysis, i.e., 3 changing vowel conditions×3 fixed vowels×7 consonants×3 trajectory types (TDX,TDY,TTX)×2 directions (anticipatory, carryover)×3 speakers. One-way ANOVAs Scheffé ($p<0.05$, df=1) were applied every 4 ms starting at consonantal offset back to $[\beta]_1$ onset in order to determine the extent of vocalic anticipation and from consonantal onset until $[\beta]_2$ offset in order to estimate the extent of vocalic carryover. $[\beta]_1$ onset and $[\beta]_2$ offset were identified with the shortest temporal values for a given pair of symmetrical and asymmetrical VCV sequences across repetitions. The last significant difference counting backwards during fixed V1 was taken to be the onset of a V2-dependent anticipatory effect and the last significant difference counting forwards during fixed V2 was taken to be the offset of a V1-dependent carryover effect. The following expected differences in amplitude of articulatory movement were submitted to statistical analysis: TDY differences in vowel height for /i/>/a/, /i/>/u/, and /u/>/a/; TTX and TDX differences in vowel fronting for /i/>/a/, /i/>/u/, and /a/>/u/.

Discontinuous effects, i.e., coarticulatory effects which cancel out and reappear earlier or later in time, were identified and the onset and offset times of the (nonsignificant) interruption periods associated with them were measured. These measurements were taken for TDX and TDY but not so for TTX since more than one interruption was found to hold for a considerable number of TTX coarticulatory comparisons. With regard to the tongue dorsum trajectories, two successive interruptions occurred only in five coarticulatory comparisons and were unified as a single discontinuity.

Figure 1 illustrates the analysis procedure for measuring V-to-V coarticulation. Movement data in the figure correspond to TTX, TLX, and TDX trajectories (top) and to TTY, TLY, and TDY trajectories (bottom) for the sequence pair /aɲa/-/iɲa/ (speaker JP). According to the top graph, the TTX, TLX, and TDX signals show a lower value for V1 =/i/ versus V1=/a/ before the 0 line up point at /ɲ/ closure onset which means that the tongue surface is positioned at a fronter location for the former vowel than for the latter; according to the bottom graph, /i/ exhibits higher TTY, TLY, and TDY values than /a/ during V1 meaning that the tongue body occupies a higher position for /i/ versus /a/. Carryover coarticulatory effects in the figure are judged to occur when the same X and Y differences, i.e., /a/>/i/ for X and /i/ >/a/ for Y, reach significance during the consonant (the acoustic period allocated to /ɲ/ closure ends up at +92 ms for /iɲa/ and at +63 ms for /aɲa), the fixed transconsonantal V2, and the following segments [p], [ə], and $[\beta]_2$ of the carrier sentence. Significant coarticulatory periods after the 0 line up point are indicated with horizontal bars at the base of each panel. Thus, small V1-dependent carryover effects for X last until $[\beta]_2$ offset for TTX and TLX, and end at +164 ms about V2 offset for TDX; on the other hand, Y effects end at +248 ms for TDY, at +144 ms for TLY, and presumably at $[\beta]_2$ offset (+364 ms) for TTY.

While we measured the longest possible extent of V-to-V coarticulation, coarticulatory effects could be discontinuous and, thus, cancel out and reappear. In Fig. 1, coarticulatory interruptions occur during the consonantal period for TLX (from closure onset until +68 ms), TDX (0/+84 ms), and TLY (0/+20 ms), or else after this period for TTX (between +164 ms and +200 ms) and TTY (+152/+200 ms and +264/+324 ms).

Significant coarticulation times obtained according to the procedure just described are shown in Tables I and II across speakers. Those values were submitted to further statistical analysis in view of the large speaker-dependent variability involved (see standard deviations in the tables). Repeated measures ANOVAs and *post-hoc* tests (Scheffé) were performed for TDX, TDY, and TTX with speaker as a factor and coarticulation time as the dependent variable ($p<0.05$, 2 df between groups). While only results with a probability of having been obtained by chance of 0.05 or less are reported, precise probabilities are provided. Two analyses were carried out. In test 1, main effects and interactions were computed for the independent variables ''direction'' (anticipatory, carryover), ''changing vowel'' (/i/ versus /a/, /i/ versus /u/, /a/ versus /u/ for TTX, TDX, and TDY) and ''consonant'' (/p, n, l, s, ʃ, ɲ, k/). In order to evaluate the role of the fixed vowel in the duration of the coarticulatory effects, test 2 was run for the variables ''direction,'' ''consonant,'' and ''fixed vowel'' separately for changing front /i/ versus back /a/, /u/ (thus pooling together the coarticulation times for the two back vowels) (test 2a) and for changing low back /a/ versus high back /u/ (test 2b). Significant effects for the mean values of interest are presented in Table III.

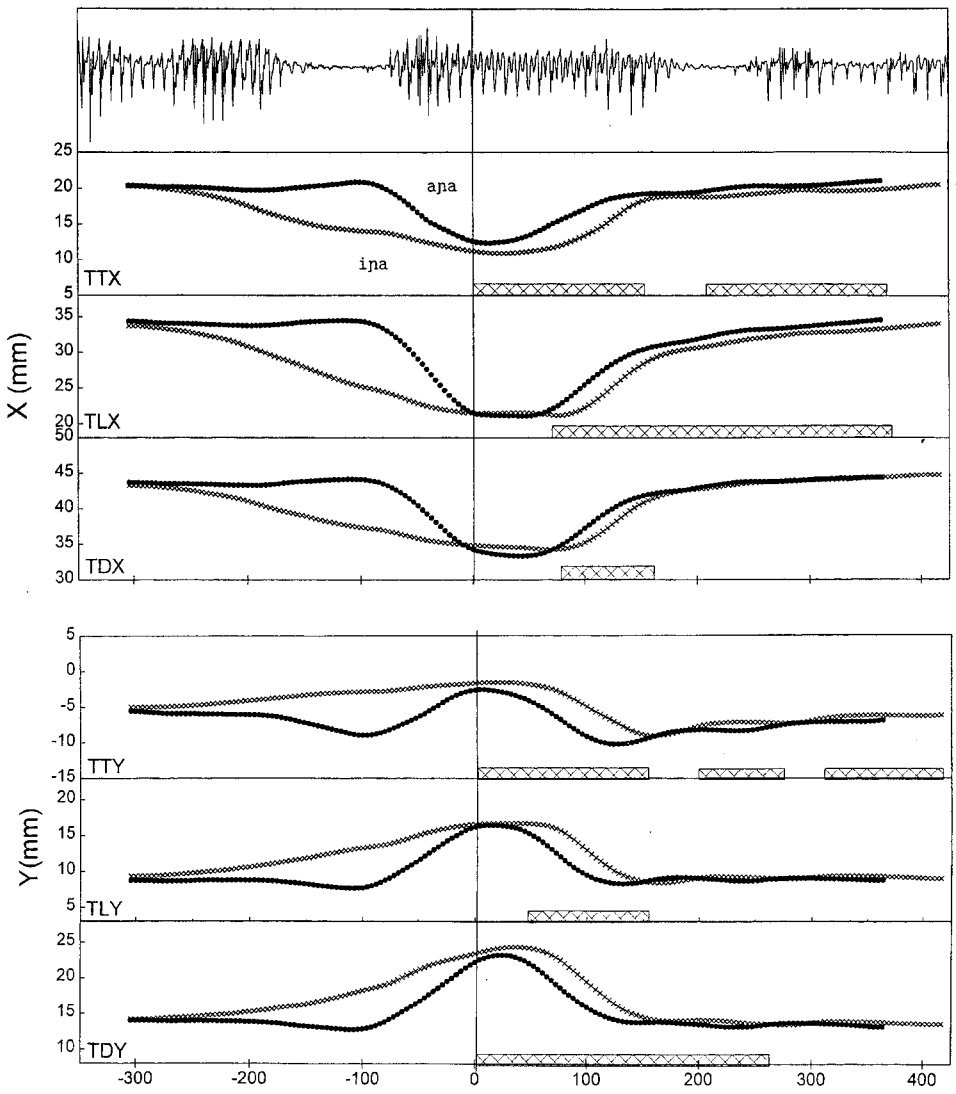

FIG. 1. Mean trajectories across repetitions for TTX, TLX, and TDX (top) and for TTY, TLY, and TDY (bottom) for the sequences /iɲa/ and /aɲa/ (speaker JP). Trajectories have been lined up at closure onset for /ɲ/ so as to measure carryover effects from changing V1 during the consonant, fixed V2 = /a/, and the following segments of the carrier sentence. Periods with significant differences after the 0 line up point are indicated with horizontal bars above the baseline. The acoustic waveform corresponds to one repetition of the symmetrical sequence /aɲa/ preceded and followed by the segments [βəp] and [pəβ] of the carrier sentence.

III. RESULTS

A. Tongue dorsum

1. Coarticulatory durations

Coarticulatory durations for TDX were significantly longer for the carryover direction than for the anticipatory direction according to results from test 1 [anticipation=147 ms, carryover=191 ms; $F(2,24)=5.837$, $p<0.020$] and from test 2a [anticipation=147 ms, carryover=208 ms; $F(2,2)=19.838$, $p<0.000$]. The latter test yielded a significant consonant×direction interaction [$F(2,12)=8.806$, $p<0.000$] which was associated with differences in the duration of the carryover effects for /n/, /ɲ/>/ʃ/ (see Table III, top central panel). The top panels in the table also reveal the existence of very short TDX anticipatory effects and very long TDX carryover effects for /n/, /l/, and /ɲ/ in the /i/ versus /a/, /u/ condition and for the two lingual fricatives /s/ and /ʃ/ in the /a/ versus /u/ condition.

TDY data also yielded a significant interaction consonant×direction both according to test 1 [$F(2,12)=4.291$, $p<0.002$] and to test 2a [$F(2,12)=9.035$, $p<0.000$]. Those interactions were related to differences in carryover coarticulation for /ɲ/>/l/, /k/ (test 1) and for /s/, /ɲ/>/l/ (test 2a). Data in Table III (top left and central panels) indicate the existence of an important difference between TDY anticipatory and carryover durations for dark /l/ and /k/ (long anticipation, short carryover) and those for alveolopalatal /ɲ/ (short anticipation, long carryover). On the other hand, the two fricatives resemble each other in exhibiting much TDY anticipation when the changing vowel condition is /a/ versus /u/, and differ from each other in that /s/ allows longer TDY carryover effects than /ʃ/ when the changing vowel is /i/ versus /a/, /u/.

A main significant effect of fixed vowel was obtained for TDY which was associated with longer coarticulation times for fixed back /a/, /u/ (207 ms) than for fixed front /i/ (154 ms) [test 2a; $F(2,2)=13.743$, $p<0.001$]. As shown in Table III (bottom left panel), this difference applies to six consonants taken independently in the case of the TDY coarticulation times, and to five consonants when the TDX coarticulatory durations are taken into consideration. Regarding the changing /a/ versus /u/ condition (Table III, bottom right panel), tongue dorsum coarticulatory durations for most consonants are longer in sequences with fixed /a/ than in those with fixed /u/ (TDY=187 versus 130 ms and TDX=175 versus 131 ms across consonants). In summary, V-to-V ef-

TABLE I. Temporal extent of significant V-to-V anticipatory and carryover effects at the tongue dorsum across speakers. Data (in ms) are listed as a function of consonant, and changing and fixed vowel condition, for the X dimension (a) and for the Y dimension (b). Each cell shows the mean value at the top and the standard deviation at the bottom.

	i vs a (*fixed i*)	i vs u (*fixed i*)	i vs a (*fixed a*)	i vs u (*fixed u*)	a vs u (*fixed a*)	a vs u (*fixed u*)
(a)						
p *(Ant-X)*	**150**	**171**	**299**	**188**	**49**	**231**
	134	*126*	*92*	*142*	*13*	*124*
p *(Car-X)*	**104**	**84**	**237**	**189**	**128**	**207**
	71	*31*	*152*	*104*	*34*	*76*
n *(Ant-X)*	**184**	**65**	**75**	**155**	**255**	**164**
	136	*20*	*20*	*112*	*131*	*148*
n *(Car-X)*	**263**	**268**	**321**	**337**	**231**	**23**
	131	*114*	*6*	*2*	*155*	*22*
l *(Ant-X)*	**120**	**71**	**156**	**79**	**112**	**116**
	139	*48*	*170*	*46*	*194*	*166*
l *(Car-X)*	**189**	**295**	**333**	**191**	**137**	**76**
	132	*65*	*13*	*142*	*173*	*72*
s *(Ant-X)*	**143**	**144**	**188**	**152**	**85**	**95**
	140	*100*	*138*	*53*	*51*	*82*
s *(Car-X)*	**60**	**129**	**260**	**219**	**175**	**209**
	7	*74*	*92*	*147*	*137*	*167*
ʃ *(Ant-X)*	**264**	**225**	**107**	**48**	**76**	**119**
	187	*184*	*98*	*46*	*132*	*206*
ʃ *(Car-X)*	**43**	**203**	**59**	**104**	**356**	**131**
	26	*152*	*53*	*100*	*8*	*199*
ɲ *(Ant-X)*	**8**	**8**	**171**	**137**	**116**	**225**
	11	*14*	*174*	*238*	*104*	*134*
ɲ *(Car-X)*	**264**	**307**	**220**	**292**	**245**	**45**
	37	*66*	*122*	*139*	*143*	*79*
k *(Ant-X)*	**248**	**237**	**204**	**125**	**309**	**120**
	146	*92*	*122*	*5*	*51*	*106*
k *(Car-X)*	**316**	**252**	**195**	**89**	**177**	**67**
	62	*177*	*149*	*18*	*12*	*36*
(b)						
p *(Ant-Y)*	**168**	**193**	**228**	**127**	**275**	**37**
	118	*110*	*108*	*67*	*134*	*36*
p *(Car-Y)*	**135**	**184**	**280**	**180**	**356**	**65**
	90	*135*	*116*	*135*	*17*	*25*
n *(Ant-Y)*	**215**	**104**	**239**	**177**	**228**	**127**
	141	*124*	*135*	*141*	*166*	*174*
n *(Car-Y)*	**120**	**149**	**239**	**145**	**220**	**153**
	110	*171*	*137*	*173*	*191*	*159*
l *(Ant-Y)*	**219**	**197**	**237**	**261**	**175**	**77**
	107	*122*	*131*	*52*	*140*	*45*
l *(Car-Y)*	**40**	**69**	**147**	**67**	**141**	**115**
	16	*110*	*154*	*34*	*139*	*98*
s *(Ant-Y)*	**149**	**88**	**160**	**208**	**87**	**368**
	120	*22*	*118*	*79*	*13*	*11*
s *(Car-Y)*	**204**	**312**	**196**	**331**	**75**	**164**
	152	*62*	*143*	*34*	*86*	*114*
ʃ *(Ant-Y)*	**84**	**29**	**203**	**293**	**233**	**203**
	14	*41*	*137*	*186*	*173*	*168*
ʃ *(Car-Y)*	**81**	**161**	**155**	**236**	**216**	**83**
	72	*175*	*99*	*204*	*172*	*45*
ɲ *(Ant-Y)*	**19**	**108**	**100**	**212**	**135**	**32**
	6	*187*	*94*	*206*	*206*	*14*
ɲ *(Car-Y)*	**317**	**311**	**321**	**248**	**227**	**163**
	64	*94*	*64*	*215*	*132*	*169*
k *(Ant-Y)*	**221**	**213**	**291**	**196**	**160**	**232**
	107	*82*	*96*	*167*	*153*	*198*
k *(Car-Y)*	**145**	**76**	**201**	**129**	**85**	**0**
	114	*52*	*147*	*129*	*74*	*0*

TABLE II. Temporal extent of significant V-to-V anticipatory and carryover effects at the tongue tip along the X dimension across speakers. See Table I for details.

	i vs a (*fixed i*)	i vs u (*fixed i*)	i vs a (*fixed a*)	i vs u (*fixed u*)	a vs u (*fixed a*)	a vs u (*fixed u*)
p *(Ant-X)*	**227**	**192**	**269**	**279**	**211**	**260**
	90	*108*	*143*	*149*	*115*	*146*
p *(Car-X)*	**217**	**264**	**181**	**197**	**275**	**228**
	136	*142*	*176*	*96*	*158*	*113*
n *(Ant-X)*	**179**	**65**	**75**	**255**	**275**	**131**
	145	*10*	*6*	*93*	*96*	*171*
n *(Car-X)*	**209**	**329**	**237**	**337**	**300**	**39**
	149	*8*	*140*	*2*	*35*	*33*
l *(Ant-X)*	**136**	**139**	**52**	**148**	**115**	**0**
	151	*158*	*28*	*110*	*113*	*0*
l *(Car-X)*	**237**	**327**	**244**	**191**	**219**	**52**
	161	*12*	*142*	*144*	*189*	*90*
s *(Ant-X)*	**240**	**112**	**247**	**239**	**159**	**41**
	161	*26*	*115*	*95*	*158*	*42*
s *(Car-X)*	**56**	**88**	**52**	**176**	**353**	**177**
	14	*33*	*52*	*107*	*20*	*108*
ʃ *(Ant-X)*	**253**	**83**	**139**	**40**	**71**	**119**
	188	*81*	*151*	*14*	*122*	*206*
ʃ *(Car-X)*	**131**	**276**	**149**	**207**	**316**	**367**
	213	*146*	*185*	*126*	*97*	*23*
ɲ *(Ant-X)*	**136**	**20**	**157**	**199**	**236**	**81**
	208	*18*	*164*	*198*	*123*	*70*
ɲ *(Car-X)*	**273**	**219**	**324**	**227**	**117**	**131**
	76	*192*	*66*	*138*	*203*	*159*
k *(Ant-X)*	**257**	**235**	**224**	**132**	**256**	**137**
	122	*56*	*149*	*11*	*156*	*115*
k *(Car-X)*	**271**	**281**	**259**	**96**	**292**	**93**
	141	*126*	*146*	*28*	*104*	*49*

fects are blocked to a larger extent by front /i/ than by back /a/ and /u/ and, less clearly so, by high /u/ than by /a/ among back vowels.

Consonant×fixed vowel interactions reached significance for TDX according to test 2a [$F(2,12)=5.656$, $p<0.001$] and for TDY according to test 2b [$F(2,12)=3.258$, $p<0.032$]. *Post-hoc* tests revealed that the former interaction is related to the difference /k/>/s/ when the fixed vowel is /i/, while the latter depends on /p/>/s/,/k/ when the fixed vowel is /a/. As shown in Table III, the former interaction reflects the existence of a more general trend towards long TDX effects in VCV sequences with dorsal consonants and fixed /i/ and in those with labial and dentoalveolar consonants and fixed /a/, /u/.

2. Coarticulatory direction

In order to estimate trends in coarticulatory direction, the vowel-dependent carryover effects (C) were subtracted from the vowel-dependent anticipatory effects (A) for each consonant and all pairs of changing vowels in each fixed vowel context condition. Bars in Fig. 2 show C-A differences in temporal extent of V-to-V tongue dorsum coarticulation across speakers for the X dimension (top) and for the Y dimension (bottom). For each consonant, bars plot C-A values for /i/ versus /a/ and for /i/ versus /u/ in the fixed /i/ condition (two black bars; left), for /i/ versus /a/ in sequences with fixed /a/ and for /i/ versus /u/ in sequences with fixed

TABLE III. Mean values across speakers (in ms) and significant effects (indicated by brackets) for V-to-V coarticulation times. Data for the consonant x direction condition (top) are plotted as a function of changing vowel and articulatory dimension (columns) and consonant and direction (rows). Data for the consonant x fixed vowel condition (bottom) are presented as a function of changing vowel and articulatory dimension (columns) and consonant and fixed vowel (rows).

Consonant x direction

	(i vs a; i vs u; a vs u)			(i vs a, u)			(a vs u)		
	TDX	TDY	TTX	TDX	TDY	TTX	TDX	TDY	TTX
p *(Ant)*	181	171	240	202	179	242	140	156	235
p *(Car)*	158	200	227	154	195	215	167	211	251
n *(Ant)*	150	182	163	120	184	144	209	177	203
n *(Car)*	240	171	242	297	163	278	127	187	169
l *(Ant)*	109	194	98	106	229	119	114	126	57
l *(Car)*	204	96	212	252	81	250	107	128	135
s *(Ant)*	134	177	173	157	151	209	90	227	100
s *(Car)*	175	214	150	167	261	93	192	119	265
ʃ *(Ant)*	140	174	117	161	152	129	97	218	95
ʃ *(Car)*	149	155	241	102	158	191	243	149	341
ɲ *(Ant)*	111	101	138	81	110	128	171	83	159
ɲ *(Car)*	229	264	215	271	299	261	145	195	124
k *(Ant)*	207	219	207	204	230	212	215	196	197
k *(Car)*	183	106	215	213	138	227	122	43	193

C x fixed V

	(i vs a, u)		
	TDX	TDY	TTX
p *(fixed i)*	127	170	225
p *(fixed a u)*	228	204	232
n *(fixed i)*	195	147	196
n *(fixed a u)*	222	200	226
l *(fixed i)*	169	131	210
l *(fixed a u)*	190	178	159
s *(fixed i)*	119	188	124
s *(fixed a u)*	205	224	178
ʃ *(fixed i)*	184	89	186
ʃ *(fixed a u)*	79	222	134
ɲ *(fixed i)*	147	189	162
ɲ *(fixed a u)*	205	220	227
k *(fixed i)*	263	204	261
k *(fixed a u)*	153	164	178

C x fixed V

	(a vs u)		
	TDX	TDY	TTX
p *(fixed a)*	89	315	243
p *(fixed u)*	219	51	244
n *(fixed a)*	243	224	287
n *(fixed u)*	93	140	85
l *(fixed a)*	125	158	167
l *(fixed u)*	96	96	26
s *(fixed a)*	130	81	256
s *(fixed u)*	152	266	109
ʃ *(fixed a)*	216	225	193
ʃ *(fixed u)*	125	143	243
ɲ *(fixed a)*	181	181	177
ɲ *(fixed u)*	135	97	106
k *(fixed a)*	243	123	274
k *(fixed u)*	93	116	115

/u/ (two hatched bars; middle), and for /a/ versus /u/ in the fixed /a/ and fixed /u/ conditions (two white bars; right).

X and Y effects for the alveolopalatal /ɲ/ favor the carryover over the anticipatory component mostly so in VCV sequences with fixed /i/. Vocalic anticipation overrides vocalic carryover in one case only, i.e., in /VɲV/ sequences with changing /a/ versus /u/ and fixed /u/ along the X dimension.

The velar /k/ favors the anticipatory direction for the TDY effects in all VCV pairs under analysis. Regarding the TDX effects, V-to-V anticipation exceeds V-to-V carryover in sequences without /i/. Sequences with changing or fixed /i/ exhibit smaller C-A differences and may assign more weight to the carryover direction. Overall, the strength of the anticipatory component increases as we proceed from VCV pairs with /i/ towards those without /i/.

Dark /l/ usually favors the carryover component along the X dimension and the anticipatory component along the Y dimension, mostly so in VCV pairs with /i/. Coarticulatory durations in VCV sequences made exclusively of back vowels exhibit unclear directionality patterns.

Regarding lingual fricatives, VCV pairs with fixed /i/ (black bars) favor the anticipatory direction along the X dimension and the carryover direction along the Y dimension. Sequences without fixed /i/ (hatched and white bars) often exhibit prevalent TDX carryover effects, and prevalent TDY anticipatory effects except for those /VsV/ sequences with /i/ and fixed /a/ and /u/ (hatched bars).

Analogously to the TDX data for /l/, VCV sequences with /n/ favor the carryover direction along the X dimension but for VCV pairs without /i/ where vocalic anticipation may prevail upon vocalic carryover. Regarding the TDY data, differences between the carryover and the anticipatory direction are small and show no clear pattern of coarticulatory direction.

The bilabial consonant /p/ also exhibits small temporal differences between the carryover and the anticipatory com-

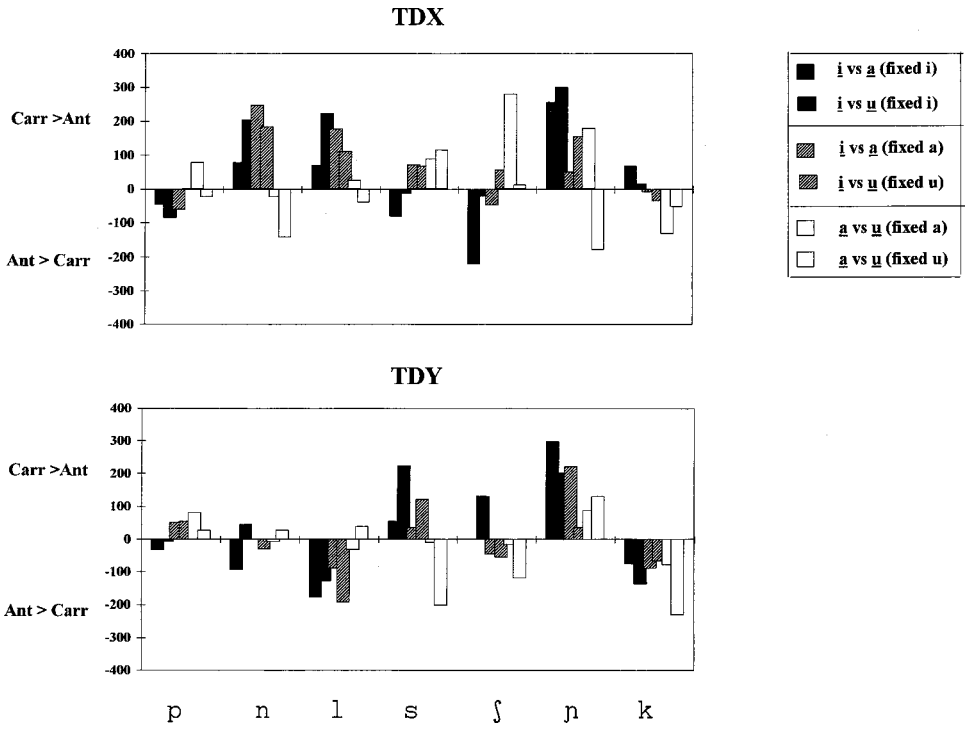

FIG. 2. C-A differences in temporal extent of V-to-V coarticulation for TDX (top) and TDY (bottom) across speakers. Data are displayed for all changing and fixed vowel conditions. Positive values indicate prevalence of the carryover over the anticipatory direction, and negative values the opposite relationship.

ponents. There appears to be a tendency to favor the anticipatory direction in sequences with fixed /i/ mostly along the X dimension, and the carryover direction in sequences with a fixed back vowel mostly along the Y dimension.

B. Tongue tip

1. Coarticulatory durations

Correlation analyses between TTX and TDX effects across changing vowel conditions yielded high *r* values for nonfricative alveolars (/n/ 0.87; /l/ 0.70), lower *r* values for dorsals (/ʃ/ 0.57; /ɲ/ 0.52; /k/ 0.40) and very low ones for /p/ and /s/.

TTX coarticulatory durations yielded a significant effect of direction according to tests 1 [$F(2,2)=10.148$, $p<0.003$] and 2a [$F(2,2)=6.979$, $p<0.013$], which reflects the existence of longer carryover than anticipatory coarticulation times (215, 216 ms versus 162, 169 ms). Test 1 also yielded a significant interaction changing vowel×consonant ×direction [$F(2,12)=2.165$, $p<0.033$], which turned out to be related to differences in carryover coarticulation for /p, n, l, ɲ, k/ (199, 223, 241, 299, and 265 ms)>/s/ (54 ms), /l,ɲ,k/>/ʃ/ (140 ms), and /ɲ/>/p/ in the changing /i/ versus /a/ condition. These consonant-dependent differences hold to a large extent for changing /i/ versus /a/, /u/ as well, as revealed by a consonant×direction interaction associated with /n/>/s/ in test 2a [$F(2,12)=4.094$, $p<0.005$] and by the existence of short carryover effects for the two lingual fricatives (see Table III, top central panel).

The TTX data resemble the TDX data in many respects. Regarding the changing /i/ versus /a/, /u/ condition, the two articulatory dimensions exhibit short anticipatory effects and long carryover effects for /n/, /l/, and /ɲ/, and short carryover effects for /s/ and /ʃ/. TTX and TDX coarticulation times for changing /a/ versus /u/ are short in the case of /l/, and short at the anticipatory level and long at the carryover level in the case of /s/ and /ʃ/.

TTX coarticulatory durations were also significantly longer for fixed /a/ (228 ms) versus fixed /u/ (133 ms) according to test 2b [$F(2,2)=7.928$, $p<0.014$]. As shown in Table III (bottom right panel), five consonants allow much longer coarticulation times in the former versus latter fixed vowel condition.

2. Coarticulatory direction

Differences in coarticulatory direction for TTX in Fig. 3 are similar to those for TDX in a good number of instances. Analogously to TDX, TTX shows more carryover than anticipation for /ɲ/ in most vocalic conditions, for /k/ in the context of fixed /i/, for /n/ and dark /l/ in VCV sequences with /i/, and for lingual fricatives and /p/ mostly in sequences without /i/. TTX and TDX effects also agree to a large extent in favoring the anticipatory direction for fricatives in sequences with fixed /i/, for /p/ in sequences with /i/, and for /n/ and /k/ in sequences without /i/.

In other cases, TTX and TDX exhibit different directionality patterns. Thus, vocalic carryover overrides vocalic anticipation for TTX but not so for TDX in several VCV pairs with /p/, /l/, /ʃ/, and /k/.

C. Discontinuous effects

Figures 4 and 5 display data on discontinuous V-to-V effects for the tongue dorsum. As pointed out in the Introduction, a discontinuous effect may be characterized as a long coarticulatory effect which becomes nonsignificant during a given temporal period.

For all the discontinuous effects in our coarticulation data, Fig. 4 plots differences between the onset time of each

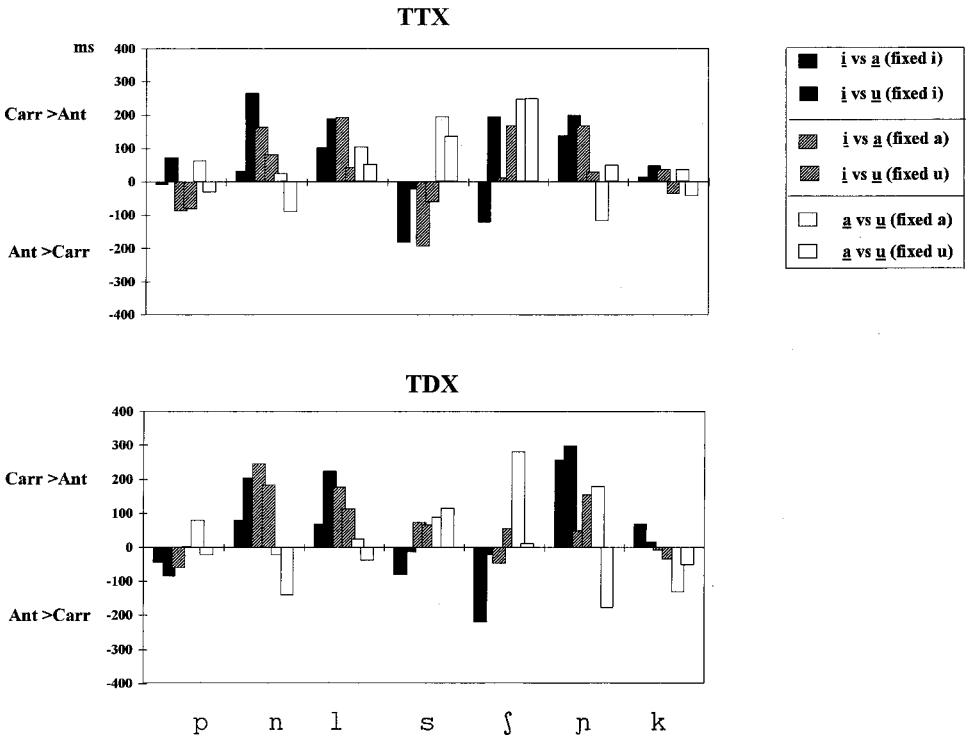

FIG. 3. C-A differences in temporal extent of V-to-V coarticulation for TTX (top) and TDX (bottom). See Fig. 2 for details.

interruption period and consonantal onset or consonantal offset depending on whether the coarticulatory interruptions occur during V1 or V2, respectively. In a few cases (nine) discontinuities did not extend beyond the closure period and, thus, started and ended during the consonant. These differences are given for each consonant and changing vowel condition, i.e., /i/ versus /a/ (upper graph), /i/ versus /u/ (middle graph), and /a/ versus /u/ (bottom graph); they are plotted separately for speakers DR, JP, and JC, the anticipatory and carryover directions, fixed /i/, /a/ and /u/, and the X and Y dimensions. Negative values indicate that a given interruption begins during the consonant (i.e., after consonantal onset for the anticipatory direction and before consonantal offset for the carryover direction) and positive values that it begins during V1 or V2. Figure 5 reports the absolute durations of all interruption periods.

Let us take, for example, the leftmost bottom panel in Fig. 4 which is displayed by itself in Fig. 4(a). The two unfilled triangles below the 0 baseline indicate two discontinuities in anticipatory coarticulation for /upa/ versus /upu/ starting 40 and 100 ms after /p/ closure onset and thus occurring during consonantal closure. (In the former case, i.e., TDX data for speaker JP, the interruption started about closure midpoint since closure was 88 ms long; in the latter, i.e., TDX data for speaker DR, the interruption lasted throughout the entire 100 ms closure period.) The filled triangle below the baseline corresponds to an interruption in carryover coarticulation for the sequence pair /apu/ versus /upu/ for speaker DR starting shortly (8 ms) before closure offset. The two symbols above the baseline refer to discontinuities starting during the vowel period for speaker JP, i.e., an interruption in the anticipatory effects for /apu/ versus /apa/ starting 85 ms before closure onset during V1 (unfilled square), and another interruption in the carryover effects for /upa/ versus /apa/ beginning 45 ms after closure offset during V2 (filled square).

A count of the number of interruptions for each consonant across all other factors yields a higher figure for /ɲ/ (26) than for all other consonants (12–18), and the lowest figure for the alveolar fricative /s/ (5). Figure 4 shows that these interruption events are often negative and therefore begin during the consonant in VCV sequences with dorsal /ʃ/, /ɲ/, and /k/. Moreover, they are usually positive and thus occur during the transconsonantal vowel in VCV sequences with alveolars and /p/. This scenario is most evident for changing /i/ versus /a/ in the upper graph.

The quality of the fixed vowel also plays a role in allowing more or less interruptions. Data for the VCV pairs with changing /i/ versus /a/ (top graph) reveal the existence of more interruptions during fixed /i/ (squares) than during fixed /a/ (triangles), and a trend for coarticulatory interruptions to occur mostly for the carryover effects in sequences with dorsal consonants (filled symbols) and for the anticipatory effects in sequences with alveolars (empty symbols). According to data for changing /i/ versus /u/ (middle graph), interruptions occur mostly at the carryover level during fixed /i/ in VCV pairs with /l/ and /ɲ/. Data for changing /a/ versus /u/ (bottom graph) show anticipatory interruptions during fixed /u/ and, less so, during fixed /a/, and many more carryover interruptions during fixed /a/ than during fixed /u/.

According to Fig. 5, coarticulatory interruptions tend to be longer in VCV sequences with dorsal consonants than in those with alveolar and labial consonants, clearly so when the fixed vowel is /i/ (top graph and, less so, middle graph). The same trend is also available in the fixed /a/ and /u/ conditions on the bottom graph.

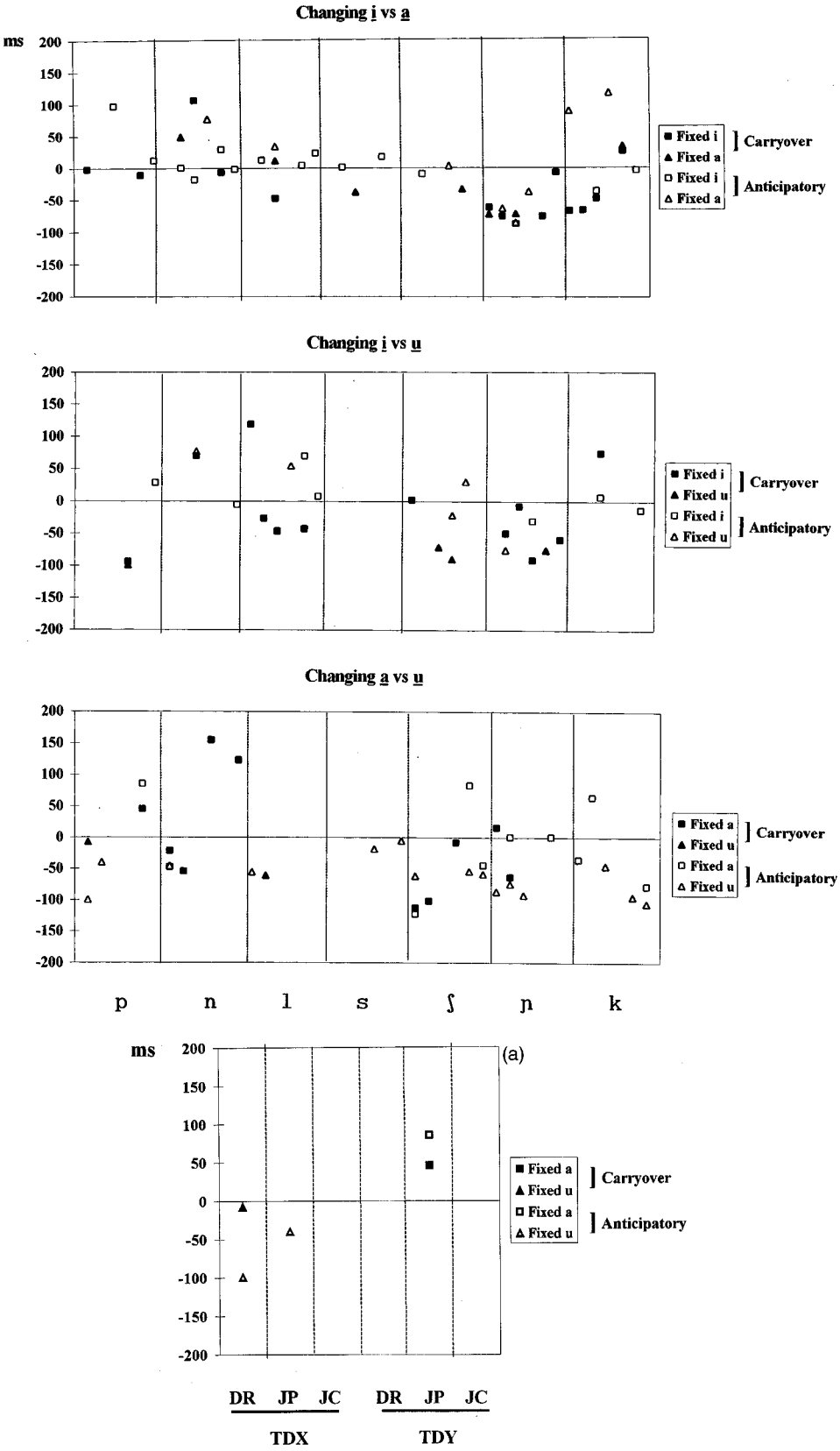

FIG. 4. Temporal differences between the onset time of all discontinuities in tongue dorsum coarticulation and the constriction onset or offset time for the intervocalic consonant. Negative values indicate that the interruption period begins during the consonant and positive values that it starts during the transconsonantal vowel. Data have been plotted as a function of consonant and changing vowel condition; values within each panel correspond to discontinuous effects for the two coarticulatory directions (carryover, anticipatory) and the three fixed vowel conditions (/i/, /a/, /u/); columns within each panel display data for a given articulatory dimension (TDX on the 3 left columns, TDY on the 3 right columns) and a given speaker (DR, JP, JC on columns 1, 2, and 3 for the TDX and TDY data sets). (a) Leftmost bottom panel of Fig. 5.

IV. DISCUSSION

A. General findings

In agreement with predictions from the DAC model, a major finding of this investigation is that V-to-V directionality patterns depend on specific articulatory requirements for the production of consonants (see following sections). The fact that all consonant×direction interactions reported in Sec. III occur for the carryover effects indicates that, as a general rule, the duration of these effects is far more variable

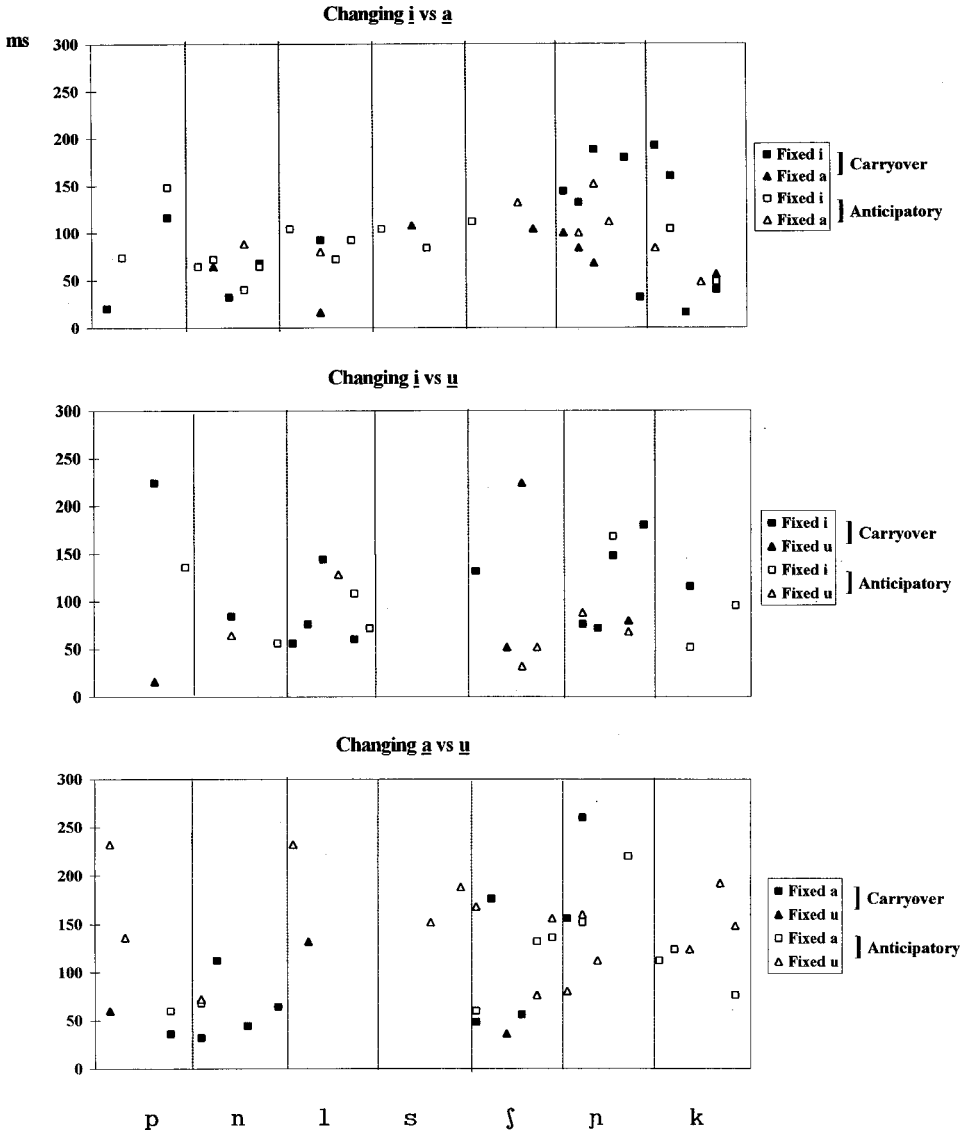

FIG. 5. Durations of the interruption periods for the discontinuous coarticulatory effects reported in Fig. 4.

than the temporal extent of the anticipatory effects. This finding confirms the hypothesis that, while anticipatory coar ticulation is associated with phonemic planning, carryover coarticulation is strongly dependent on the ongoing articulatory requirements for the production of the contextual segments (see the Introduction).

DAC specification for fixed vowels also plays a relevant role on the extent of V-to-V coarticulation. Vocalic effects were found to be generally longer in the context of fixed back /a/, /u/ versus front /i/ (TDX, TDY) and of fixed high back /u/ versus low back /a/ (TDX, TDY, TTX). However, dorsal consonants may cause long tongue dorsum effects to occur during fixed /i/ along the horizontal dimension.

B. Patterns of coarticulation

(a) The DAC model has been found to account satisfactorily for patterns of TDY coarticulatory direction in the case of VCV sequences with highly constrained consonants exerting either maximal C-to-V anticipation (dark /l/) or maximal C-to-V carryover (alveolopalatal/ɲ/). The C-to-V component blocks vowel-dependent effects along the crucial dimension (i.e., anticipation for /ɲ/ and carryover for /l/), which is why V-to-V coarticulation favors the opposite direction in each case (i.e., carryover across /ɲ/ and anticipation across dark-/l/). Accordingly, V-to-V effects for TDY were found to be quite short at the carryover level in /VlV/ sequences and at the anticipatory level in /VɲV/ sequences.

These two patterns of coarticulatory direction become most obvious in sequences with /i/. Prevalence of V-to-V anticipation for /l/ in the fixed /i/ condition is in agreement with a situation of gestural antagonism, i.e., C-to-V anticipation becomes especially prominent in this case so as to make sure that the velarization or pharyngealization gesture for the consonant will be successfully performed during a preceding antagonistic vowel which is also highly constrained. Vocalic carryover effects in VCV sequences with /ɲ/ and fixed /i/ appear to be caused by articulatory overshoot since they last until V2 offset most of the time.

(b) TDY data on vocalic coarticulation in VCV sequences with unconstrained /p/ and /n/ and the vowel /i/ presented in this paper were found to favor the carryover component to a lesser degree than dorsopalatal contact and acoustic data in Recasens *et al.* (1997). The fact that the present investigation deals with long sentences and more

natural speech conditions than our previous study could account for the finding that carryover effects exerted by /i/ do not play a very important role. Additional evidence is needed in order to validate this hypothesis as well as the possibility that VCV sequences with consonants which are specified for an unconstrained tongue dorsum favor vocalic carryover or vocalic anticipation depending on the presence of fixed /i/ or fixed /a/, respectively (see the introduction).

(c) Similar trends in coarticulatory direction were reported for TDX and TTX in VCV sequences with the alveolars /n/ and /l/ and the alveolopalatal /ɲ/, mostly so in the context of /i/. In these circumstances, a given direction may prevail depending on the consonant taken into account, e.g., carryover (for /ɲ/, and for /n/ and /l/ in sequences with /i/) or anticipatory (for /n/ in sequences without /i/). TDX and TTX coarticulatory durations were in agreement with these directionality trends to a large extent, i.e., short at the anticipatory level and long at the carryover level for /ɲ/, /n/, and /l/ in sequences with /i/.

Regarding dorsal consonants for the production of which the tongue tip is down, these data suggest that TTX coarticulatory activity may reflect TDX coarticulatory activity. Indeed, the finding that data for TDX, TDY, and TTX are highly correlated and favor the same V-to-V coarticulatory direction in /VɲV/ sequences may be related to the possibility that tongue dorsum raising and tongue dorsum fronting start being implemented simultaneously for alveolopalatal production. Moreover, coarticulatory effects at the tongue dorsum are essentially the same as those at the less active tongue front since the entire tongue body moves in a homogeneous fashion for the implementation of /ɲ/. In agreement with this finding, vertical and horizontal lingual movements for front vowels have been found to start simultaneously at /p/ closure onset in English /əpV/ sequences (Alfonso and Baer, 1982).

TDX and TTX temporal effects for apical consonants (/n/, /l/) yielded high correlation coefficient values which may be taken to show that the tongue tip and the tongue dorsum do not move independently of each other along the horizontal dimension and TTX activity governs TDX activity for the production of these alveolar consonants. Moreover, the tongue tip articulator (and the tongue dorsum) was subjected to a major carryover action from dorsal vowels along the horizontal dimension. This finding is compatible with the DAC model if we assume that the two alveolars exert little C-to-V apical anticipation under the present experimental conditions, thus allowing extensive V-to-V carryover effects to occur. Prominent V-to-C carryover effects at alveolar closure location have also been reported for /i/>/a/,/u/ in /VɾV/ sequences (Recasens, 1991).

(d) Patterns of V-to-V coarticulatory direction in VCV sequences with /k/ may also be related to patterns of C-to-V coarticulatory direction. In agreement with F2 data in Recasens *et al.* (1997), vocalic anticipation has been found to prevail upon vocalic carryover both for TDX and TDY in /VkV/ sequences with fixed /a/ and /u/. This trend may be related to continuous fronting of the entire tongue body during closure (Perkell, 1969; Mooshamer *et al.*, 1995). On the other hand, TTX anticipatory effects may be more salient than TTX carryover effects in sequences without /i/ presumably since the tongue tip for velars is left quite free to coarticulate with the surrounding vowels.

Regarding coarticulatory trends in /VkV/ sequences with fixed /i/, TDX and TTX data in the present study are also in agreement with Recasens *et al.* (1997) in assigning more weight to the carryover over the anticipatory component both for the consonantal and for the vocalic effects. This finding may be accounted for assuming that now the tongue body is not being pushed forward during closure and TTX coarticulatory activity conforms to TDX coarticulation. Contrary to previous results, TDY in this fixed /i/ condition has been found to favor the anticipatory over the carryover direction.

(e) Remarkable similarities in TDX and TTX coarticulatory direction for /s/ and /ʃ/ could be attributed to manner requirements and are in support of the notion that dorsal activity conforms to apicolaminal activity along the horizontal dimension during lingual fricative production. Regarding sequences with /i/, vocalic effects favor the anticipatory component for TTX and TDX in VCV pairs with fixed /i/ and for TTX in those with fixed /a/ presumably since these consonants need to be executed quite early, mostly so if preceded by an antagonistic high front vowel; accordingly, carryover effects were found to be short for TDX and TTX in the VCV sequences of interest. On the other hand, the existence of long carryover and short anticipatory effects for TDX and TTX in /VsV/ and /VʃV/ sequences without /i/ may be explained assuming that there is less need to anticipate the lingual gesture for the fricative consonant after an unconstrained vowel and perhaps that fricatives exert some blocking action on anticipatory lip protusion for /u/.

Regarding coarticulation along the Y dimension (TDY), carryover effects were found to exceed anticipatory effects in sequences with /i/ possibly because tongue dorsum raising for the fricative facilitates the carryover action associated with a preceding high front vowel. This finding is in agreement with coarticulation data for /VsV/ and /VʃV/ sequences with /i/ in the literature (Farnetani and Faber, 1991; Hoole *et al.*, 1993). TDY effects in VCV sequences with /i/ and a fixed back vowel exhibit this same pattern of coarticulatory direction for /s/ (also Recasens *et al.*, 1997) but not for /ʃ/, perhaps in view of the fact that the latter consonant exerts a particularly prominent anticipatory action at the predorsal constriction location. Moreover, TDY anticipation prevails upon TDY carryover in the absence of /i/ (long anticipatory effects occur in this case), presumably since the tongue dorsum does not have to be raised much for fricative production in this contextual condition.

C. Discontinuous coarticulatory effects

Coarticulation data in the present paper reveal that V-to-V effects may be interrupted during a consonant or vowel involving the tongue dorsum and reappear later or earlier on. Therefore, failure to find evidence for much tongue dorsum coarticulation during a dorsal segment in previous studies does not imply necessarily that coarticulatory effects were completely absent. As discussed by Fowler and Saltzman, if occurring at the anticipatory level, those inter-

ruption events could be taken in support of the existence of a fixed, long-term planning strategy of the upcoming V2 in a VCV string.

It should be pointed out, however, that such interruption periods occur mostly at one of both sides of the consonant (i.e., during V1 or during V2) depending on the VCV sequence. On the one hand, anticipatory interruptions show up mostly in VCV sequences made of an alveolar consonant preceded by /i/, and in VCV sequences with a dorsal consonant preceded by fixed /u/ in the V2=/a/ versus /u/ changing condition. On the other hand, discontinuous effects also occur at the carryover level in VCV sequences with dorsal consonants and fixed /i/, namely, in a contextual situation yielding articulatory overshoot. These carryover effects (and the interruption periods associated with them) were found to last for a very long time and could thus be attributed to some reinforcement of the dorsal gesture.

Our data do not confirm a strong version of Fowler and Saltzman's (1993) hypothesis but are rather consistent with the coarticulation model proposed by Bell-Berti and Harris (1981) (see the Introduction). Thus, e.g., the absence of discontinuous anticipatory effects in the /iɲV/ sequences and their presence in the /uɲV/ sequences suggests that speakers accommodate the occurrence of coarticulation to context and thus plan the upcoming phonemes according to the articulatory requirements for the ongoing phonetic segments. On the other hand, discontinuous effects during V2 cannot be related to phonemic anticipation but are caused by articulatory overshoot (e.g., only few effects occur in /VCi/ sequences with an alveolar consonant) and thus cannot reflect a phoneme-independent production mechanism.

Another piece of evidence for this accommodating strategy is provided by the existence of early anticipatory effects in the sequence pairs /uCa/-/uCu/. Prominent TDX anticipatory effects in these VCV pairs were found to hold for several consonants in our study, e.g., /n/, /l/, /ɲ/, /k/. An early onset of tongue dorsum activity for V2=/a/ in these circumstances may be explained assuming that the tongue predorsum for V1=/u/ stays inactive and allows substantial contextual modifications [also Hoole *et al.* (1990) for /ukV/; see the Introduction].

V. CONCLUSIONS

EMA data on temporal coarticulation of tongue dorsum vertical movement presented here are in accordance with several predictions formulated by the DAC model regarding highly constrained consonants, i.e., preference for anticipatory (for /l/) or carryover (for /ɲ/) V-to-V coarticulation, mostly so in situations of gestural antagonism, and long carryover effects in strings of dorsal segments due to articulatory overshoot. Other trends in vocalic coarticulatory direction have been attributed to the dynamical properties of the consonantal gesture, e.g., much vocalic anticipation through the frontwards sliding dorsal gesture for velars. In comparison to previous studies the present paper reports more vocalic anticipation relative to vocalic carryover in other cases (i.e., TDY data for /k/, /n/, and /p/ in VCV sequences with /i/) which could be related to differences in sentence length and stress placement. Our initial prediction on V-to-V coarticulation for front consonants and labials was found to be at work for the TDY data in VCV sequences with fricatives: indeed, /s/ and /ʃ/ turned out to allow more vocalic carryover in the context of /i/ and more vocalic anticipation in the absence of this vowel.

This study reports analogous patterns of coarticulatory direction for TDX, TDY, and TTX for /ɲ/ and /k/ in line with the fact that their production involves a homogeneous tongue body activity. Fronter lingual consonants exhibit analogous directionality trends for TDX and TTX (but not so TDY), i.e., vocalic carryover prevails upon vocalic anticipation presumably since apical anticipation is not too prominent; this finding is in support of the possibility that TTX activity governs TDX activity and that X and Y movements are relatively independent of each other in this case. Fricatives are exceptional in allowing much TDX and TTX anticipation on fixed /i/ in line with the manner constraints involved.

Overall, vowel coarticulation mechanisms have been found to be much the same at different articulatory structures in VCV sequences with /ɲ/ and /k/ (TDX, TDY, TTX). Coarticulatory interactions happen to be less robust for fricatives and even less so for other apical consonants, i.e., these consonants exhibit analogous TDX and TTX effects but different degrees of TDX-TDY coarticulatory coordination.

Our data also suggest that phonemic planning adapts to context or at least that context affects crucially the onset and offset times of gestural anticipation. This conclusion is supported by the absence of tongue dorsum discontinuous effects during V1 in /iɲV/ sequences vis-à-vis their presence in /uɲV/ sequences, and from an early onset of TDX activity for V2=/a/ during a preceding /uC/ string.

ACKNOWLEDGMENTS

This work was supported by Project Nos. DGES PB96-0103 and BFF2000-0075-C02-01 of the Ministry of Education and Science of Spain and by research group 1997SGR 00290 of the Government of Catalonia. I would like to thank Anders Löfqvist, Jonathan Harrington, and an anonymous reviewer for comments, and Maria Dolors Pallarès for help with the statistical analysis.

Alfonso, P. J., and Baer, T. (**1982**). ''Dynamics of vowel articulation,'' Lang. Speech **25**, 151–173.

Browman, C. P., and Goldstein, L. (**1992**). ''Targetless schwa: An articulatory analysis,'' in *Papers in Laboratory Phonology II, Gesture, Segment, Prosody*, edited by G. J. Docherty and R. Ladd (Cambridge U. P., Cambridge), pp. 26–56.

Bell-Berti, F., and Harris, K. S. H. (**1981**). ''A temporal model of speech production,'' Phonetica **38**, 9–20.

Farnetani, E., and Faber, A. (**1991**). ''Tongue-jaw coordination in vowel production: Isolated words versus connected speech,'' Speech Commun. **11**, 401–410.

Fowler, C. A. (**1977**). *Timing Control in Speech Production* (Indiana Univ. Linguistics Club, Bloomington).

Fowler, C. A. (**1980**). ''Coarticulation and theories of extrinsic timing,'' J. Phonetics **8**, 113–133.

Fowler, C. A. (**1993**). ''Phonological and articulatory characteristics of spoken language,'' in *Linguistic Disorders and Pathologies*, edited by G. Blanken, J. Dittmann, H. Grimm, J. C. Marshall, and C.-W. Wallesch (Walter de Guyter, Berlin), pp. 34–46.

Fowler, C. A., and Brancazio, L. (**2000**). ''Coarticulatory resistance of American English consonants and its effects on transconsonantal vowel-to-vowel coarticulation,'' Lang. Speech **43**, 1–41.

Fowler, C. A., and Saltzman, E. (**1993**). ''Coordination and coarticulation in speech production,'' Lang. Speech **36**, 171–195.
Gay, T. (**1977**). ''Cinefluorographic and electromyographic studies of articulatory organization,'' in *Dynamic Aspects of Speech Production*, edited by M. Sawashima and F. S. Cooper (Univ. of Tokyo, Tokyo), pp. 85–102.
Hoole, P., Gfroerer, S., and Tillmann, H. G. (**1990**). ''Electromagnetic articulography as a tool in the study of coarticulation,'' Forschungsberichte des Instituts für Phonetik, Munich, **28**, 107–122.
Hoole, P., Nguyen-Trong, N., and Hardcastle, W. J. (**1993**). ''A comparative investigation of coarticulation in fricatives: electropalatographic, electromagnetic and acoustic data,'' Lang. Speech **36**, 235–260.
Mooshammer, C., Hoole, P., and Kühnert, B. (**1995**). ''On loops,'' J. Phonetics **23**, 3–22.
Perkell, J. S. (**1969**). *Physiology of Speech Production: Results and Implications of a Quantitative Cineradiographic Study* (MIT, Cambridge).
Perkell, J. S. (**1986**). ''Coarticulation strategies: preliminary implications for a detailed analysis of lower lip protrusion movements,'' Speech Commun. **5**, 47–86.
Recasens, D. (**1989**). ''Long range coarticulatory effects in VCVCVC sequences,'' Speech Commun. **8**, 293–307.
Recasens, D. (**1991**). ''On the production characteristics of apical taps and trills,'' J. Phonetics **19**, 267–280.
Recasens, D., Pallarès, M. D., and Fontdevila, J. (**1997**). ''A model of lingual coarticulation based on articulatory constraints,'' J. Acoust. Soc. Am. **102**, 544–561.

Timing interference to speech in altered listening conditions

Peter Howell[a] and Stevie Sackin
Department of Psychology, University College London, Gower Street, London WC1E 6BT, England

(Received 20 August 2001; accepted for publication 27 February 2002)

A theory is outlined that explains the disruption that occurs when auditory feedback is altered. The key part of the theory is that the number of, and relationship between, inputs to a timekeeper, operative during speech control, affects speech performance. The effects of alteration to auditory feedback depend on the extra input provided to the timekeeper. Different disruption is predicted for auditory feedback that is out of synchrony with other speech activity (e.g., delayed auditory feedback, DAF) compared with synchronous forms of altered feedback (e.g., frequency shifted feedback, FSF). Stimulus manipulations that can be made synchronously with speech are predicted to cause equivalent disruption to the synchronous form of altered feedback. Three experiments are reported. In all of them, subjects repeated a syllable at a fixed rate (Wing and Kristofferson, 1973). Overall timing variance was decomposed into the variance of a timekeeper (C_v) and the variance of a motor process (M_v). Experiment 1 validated Wing and Kristofferson's method for estimating C_v in a speech task by showing that only this variance component increased when subjects repeated syllables at different rates. Experiment 2 showed DAF increased C_v compared with when no altered sound occurred (experiment 1) and compared with FSF. In experiment 3, sections of the subject's output sequence were increased in amplitude. Subjects just heard this sound in one condition and made a duration decision about it in a second condition. When no response was made, results were like those with FSF. When a response was made, C_v increased at longer repetition periods. The findings that the principal effect of DAF, a duration decision and repetition period is on C_v whereas synchronous alterations that do not require a decision (amplitude increased sections where no response was made and FSF) do not affect C_v, support the hypothesis that the timekeeping process is affected by synchronized and asynchronized inputs in different ways. [DOI: 10.1121/1.1474444]

PACS numbers: 43.70.Fq, 43.70.Gr [AL]

I. INTRODUCTION

Feedback control is one way of modeling on-line regulation of an action. Such models have been applied to speech control, for which several potential sources of feedback are available (Fairbanks, 1955; Lee, 1950; Postma, 2000). Early models proposed that information about the identity of speech segments is used as feedback and that speakers take corrective action when the phonetic content of the actual speech output is discrepant from that intended (Fairbanks, 1955). Evidence that was originally regarded as strong support for this view was the disruption to speech performance that occurs when auditory feedback is altered experimentally (Lee, 1950). One such alteration is delayed auditory feedback (DAF), where speech is electronically delayed for a short time before it is replayed to the speaker. When DAF is administered, a speaker's accuracy and timing are affected dramatically (Lee, 1950). A monitoring account maintains that these effects arise because the experimentally altered feedback signals to the speaker that the speech was in error. The corrective action that is then taken results in disruption to speech control (Lee, 1950; Fairbanks, 1955).

Borden (1979) pointed out two fundamental problems in assuming auditory feedback is used to control speech: The checking and correcting operation cannot start until speech has been output. As processing the speech sounds and determining what action is necessary also take a significant amount of time (for instance, Marslen-Wilson and Tyler, 1981 estimate recognition time for speech at about 200 ms), such feedback monitoring would lead to a slow speech output rate. Borden's second point was that speakers who are adventitiously deafened after they have learned a language do not lose the ability to speak immediately, but that usually there is long-term degradation to speech control. The ability to speak immediately after hearing loss suggests feedback is not necessary for on-line speech control (though the long-term effects may suggest feedback has a role in establishing and maintaining speech representations).

There are other problems, besides those raised by Borden, for this type of feedback view: The auditory system would need to supply the speaker with a veridical record of what was produced; otherwise, establishing if and what error has occurred with the intention of correcting it would not be possible. However, it is not clear that the representation of articulatory output provided by the auditory system is veridical of the intended message. This is because the auditory representation the speaker receives while speaking is affected by internal noise. The noise that is present then affects the information that can be recovered from the acoustic output. The main source of internal noise originates in vibrations of the articulatory structures that are transmitted to the cochlea through bone. This bone-conducted sound is delivered to the cochlea at about the same time as the acoustic

[a]Electronic mail: p.howell@ucl.ac.uk

 0001-4966/2002/111(6)/2842/11/$19.00

output from the vocal tract. Bone-conducted sound during vocalization is loud enough to make its effects significant. von Bekesy (1960), for instance, estimated that bone- and air-conducted components are at approximately the same level. The airborne sound contains sufficient information to decode a speaker's intention (other people listening to the speech understand the message). The bone-conducted sound, on the other hand, is dominated by the voice fundamental; formant structure is heavily attenuated and resonances of body structures extraneous to vocalization (such as the skull) affect this component (Howell and Powell, 1984). Consequently, the bone-conducted sound contains limited information about articulation. The degraded bone-conducted sound would also mask out the formant information in the air-conducted sound. Such masking would reduce the ability of a speaker to retrieve information about the articulation from the air-conducted feedback. This argument relies heavily on the evidence presented by Howell and Powell (1984). If future work confirms that the auditory feedback signal is restricted in the information it provides about articulation, models that assume feedback is used to compute a precise correction needed to obviate an error will need revision (Guenther, 2001; Neilson and Neilson, 1991; see the general discussion).

Another piece of evidence that the role of auditory feedback available over the short term may have a more limited role than previously thought was given by Howell and Archer (1984). They reported an experiment in which a nonspeech noise was substituted for the delayed signal under DAF conditions where the noise had the same intensity profile as the original speech. There was no difference in the time taken to read a list in this stimulus condition compared with that in a delayed speech condition. This suggests that any sound that stands in the same temporal relationship with the direct speech as does the DAF signal will cause equivalent disruption to the delayed speech sound. Alteration to auditory feedback may not, then, have an effect on a monitor to correct segmental control, though it could still have a role in establishing and maintaining long-term speech representations (Borden, 1979).

The final piece of evidence on the role of feedback in short-term regulation of speech is based on changes that occur in voice intensity when altered auditory feedback (AAF) is presented. When speaking in noise, voice level increases, whereas when concurrent speech level is increased, voice level decreases (Lane and Tranel, 1971). Howell (1990) reported that if DAF sounds are amplified, speakers increase vocal level. From this, it appears that delaying a person's speech creates a sound that is responded to as noise, rather than being processed as speech. A noise would be no use for indicating to a feedback mechanism whether adjustments to articulation are required (though, as noted earlier, auditory feedback could still have a role in establishing and maintaining long-term speech representations).

More recent models for the role of feedback have concentrated on (1) use of auditory feedback during development and recovery of speech control and (2) whether feedback can be used to check representations at suprasegmental (rather than segmental) levels. A representative example of each of these points of view is now described. The first approach can be illustrated in the work of Perkell and colleagues on normal speakers and speakers fitted with a cochlear implant. Perkell (1980) outlined a model in which feedback is used both for on-line control and monitoring overall speech output to make sure that it conforms with the norms of the language being spoken. The work reviewed earlier argues against auditory feedback having a role in on-line control, principally by questioning the interpretation of experiments that employ altered auditory feedback procedures. This would not necessarily undermine auditory feedback having a role in maintaining long-term representations. Also, a lot of this group's evidence is from patients fitted with cochlear implants and there are grounds, and evidence, for considering that cochlear implant patients may be able to use auditory feedback for segmental control, regardless of whether fluent speakers can use auditory feedback for this purpose.

Cochlear implant patients have no useful hearing before they receive an implant. The implanted electrode by-passes the peripheral auditory system and delivers sound direct to the auditory nerve. A limited amount of auditory input can be presented to these patients once the electrode is switched on and any improved speech abilities investigated in a controlled way. Perkell, Guenther, Lane *et al.* (2001) reviewed their work on the role of auditory feedback in cochlear implant patients. They reported that partial restoration of hearing results in improved perception of vowels and of fricatives, production of vowels improved, and this improvement occurred soon after patients received implants. Such findings support the view that these speakers may use feedback for control of speech. Note, though, that during vocal control, the information provided by the implanted electrode differs from that received by nonhearing impaired listeners. Bone-conducted sound is processed by the same peripheral mechanisms that transduce air-conducted sound (von Bekesy, 1960) and that have been destroyed in these patients. Thus, when vocalizing, these patients would hear neither air-nor bone-conducted sound. The electrode only restores a representation of the air-conducted sound. The loss of bone-conducted sound during vocalization would prevent this sound from masking the airborne sound. The airborne component would then be a more useful source of information about what was articulated compared with normally hearing individuals. The better information carried in the airborne source, relative to normally hearing speakers, would suggest that auditory feedback could be useful for control in these speakers (as Perkell's group has established).

An example of the view that auditory feedback is important for maintaining suprasegmental representations is reported by Natke and Kalveram (2001). They delivered frequency shifted feedback (FSF) shifted an octave down and measured any compensation speakers made. They found significant compensation on long, stressed vowels but not on short, unstressed ones. They argued that the compensatory response was based on a negative feedback mechanism. They also argued that the effects occur at a suprasegmental level since they were only observed on the long vowels. As voice pitch is available in both air and bone signals, long-

latency feedback mechanisms could extract it and it might then serve as a basis for suprasegmental control (i.e., in the way Natke and Kalveram, 2001, propose).

The aim of this article is to assess how AAF affects speech control in the short-term in normally hearing individuals. The work does not address the issue whether auditory feedback is used outside these experimental procedures directly, nor how an internal model is established, nor whether auditory feedback is used for monitoring prosodic aspects of speech. This has a different focus from the work with cochlear implantees, where the auditory feedback is different from that received by normally hearing/listening speakers and from work investigating whether auditory feedback mechanisms have a role in suprasegmental control. The review of work on the involvement of a feedback mechanism in segmental control, offered above, suggests that in hearing individuals, the immediate effects of AAF do not arise because of interference with a feedback monitoring mechanism. The basic assumption behind the current tests is that altering sounds spectrally or temporally creates conditions that lead to multiple sound sources (the altered sound itself and unaltered sounds such as that conducted through bone). Depending what type of alteration is made, the altered sources will be asynchronous or synchronous with unaltered auditory feedback. The temporal relation between the sound sources that arises when an alteration is made will determine the amount of disruption experienced.

Synchronous and asynchronous components that occur under different forms of AAF are considered first. Vocal output transmitted through bone will always remain in synchrony with articulation. With DAF, the delayed version of the speaker's voice is, then, asynchronous with this sound. In frequency shifted feedback (FSF), the voice is spectrally shifted with negligible delay (Howell, El-Yaniv, and Powell, 1987). Bregman's (1990) work shows that such spectral manipulations (and, indeed, temporal alterations like those under DAF) lead to perceptibly distinct sound streams. So, in the case of FSF, the shifted sound source would lead to a separate, but synchronous, component to that which arises from any bone-conducted sound. The air-conducted component can be amplified independent of the bone-conducted sound and replayed, again with negligible delay. The difference in amplitude of these sound components creates conditions that would again favor segregation of the air-conducted from the bone-conducted sound (Bregman, 1990). The segregated sources under amplification would remain in synchrony (as with FSF).

The next stage in the argument concerns reasons for thinking that speaking at the same time as synchronous sound sources will be less disruptive on voice control than when speaking at the same time as asynchronous sound sources. Howell, Powell, and Khan (1983) described several frequently encountered situations that show asynchronous sounds are far more disruptive on speech control than synchronous sounds. This is demonstrated by considering two forms of song. Canons can be described as singing one song at the same time as another synchronous rhythm is heard. This is simple to perform, as shown by the fact that children are taught this form of song. One possible reason why tasks like canon singing are simple is that speaking or singing along with synchronous sounds reinforces the timing of the singer's own attempt, giving the listener a clearer sense of the beat that has to be followed (see Howell and Sackin, 2000, for supporting evidence). The second type of singing, hoquetus, is a medieval form in which different singers produce notes at the offset of the notes of a previous singer. So, the singer hears an asynchronous rhythm as well as that he or she produces. This form of song is difficult to perform relative to canon singing because of the presence of the asynchronous rhythm. According to the current hypothesis, extraneous synchronous and asynchronous rhythms create parallel situations to FSF or amplified feedback, and DAF, respectively. The effect of synchronous and asynchronous concurrent signals on voice control appears to be general (it is shown in AAF tasks and different forms of song). As this disruption is general, it suggests that the influences do not arise via the operation of a feedback mechanism (it is unlikely that hoquetus singers treat other singers' notes as feedback about their own voice control that then gives rise to the observed disruption).

The next step is to consider what mechanism could explain differential disruption in situations where synchronous and asynchronous rhythms are heard, regardless of whether these rhythms derive from a speaker's own speech or from an external event. As argued earlier, AAF manipulations can be regarded as transforming the speech task into one with additional rhythmic inputs (synchronous or asynchronous depending on the form of AAF). As the activity is serial, they could constitute input to a general-purpose timekeeping mechanism and the nature (synchronous or not) and number of inputs could then produce disruption through the timekeeper. Other serial activity would input to this same mechanism and give equivalent disruption depending, again, on the nature (relative to current input) and the number of such inputs.

Arguments for a central timekeeper that functions separately from motor processing activity have often been put forward in motor control since Lashley's (1951) seminal report on serial order behavior. (see for example Ivry, 1997; Vorberg and Wing, 1996; Wing and Kristofferson, 1973). Lashley argued that successive elements in a serial activity may be timed without reference to the peripheral motor events they give rise to. In particular, the completion of a motor element is not necessary for the generation of the next element in a sequence (as in a feedback process). One advantage of having a timekeeper that is independent of the execution of a particular act is that it can be used in a variety of tasks where timing control is needed.

Wing and Kristofferson (1973) established the properties of such a general-purpose timekeeper with data from a tapping task. Subjects started by tapping along with an isochronous metronome click. Once responses were entrained to the metronome's rate, the click was switched off and subjects continued the response sequence on their own. Variance associated with timekeeping processes (clock variance, C_v) was estimated separately from that associated with motor (motor variance, M_v) components. Wing and Kristofferson (1973) assumed that when a motor response deviated from

its required position, two intervals were affected: If the response was ahead of its required position, the preceding interval would be short and the following interval would be long. Based on this, an estimate of 2 M_v was obtained from the negative covariance between adjacent response intervals (lag one autocovariance). C_v and other residual components were then obtained by subtracting 2 M_v from the total variance (T_v). The C_v estimate, unlike the M_v estimate, was not theoretically motivated. In further work, Wing (1980) validated that the residual provided an estimate of C_v by showing that as the length of the interval subjects were required to repeat (repetition interval) was increased, C_v also increased. This would be expected if keeping the time of long intervals is more difficult than keeping the time of short intervals and if difficulty is reflected in more variable responses. M_v, on the other hand, remained constant across repetition interval. Howell, Au-Yeung, and Rustin (1997) have reported a similar validation to Wing (1980) for a task involving repeated movement of the lower lip (see also Hulstijn *et al.*, 1992 for another application of the Wing–Kristofferson task to speech).

Work has also been conducted to establish the general properties of the timekeeper by examining whether C_v measures relate to other timekeeping operations. For instance, Ivry and Hazeltine (1995) examined production of specified intervals and, in separate tests with the same subjects, examined the relationship to subjects' perceptual time estimation ability. They reported a significant relationship. This relationship suggests that the mechanism has a general role in timing very different tasks.

The three experiments reported below test the hypothesis that AAF creates an ancillary sound that mainly affects the timekeeper (C_v) when speech is taking place concurrently. All the experiments use a speech version of the Wing–Kristofferson task and apply these authors' analysis procedure to estimate C_v and M_v. The speech version of the Wing–Kristofferson task involves repeating the syllable /bae/ at specified repetition intervals. The requirement to produce a single syllable with exact timing renders the task different to spontaneous speech. However, without these artificial task constraints, C_v cannot be estimated separately from M_v. Though there is this limitation, the same limitation applies whenever experimental techniques are used to study speech. Experiment 1 validates application of the Wing–Kristofferson method of obtaining C_v from residual variance after M_v has been extracted from T_v in the same way as in Wing's (1980) experiment discussed earlier. The second experiment tests whether synchronous and asynchronous forms of AAF reduce and increase C_v, respectively (Howell *et al.*, 1983; Howell and Sackin, 2000). The delayed sound during DAF procedures is asynchronous relative to direct speech, so should lead to large increases in C_v (by analogy with the observations about performance disruption that occurs when activities are asynchronous, Howell *et al.*, 1983). The second form of AAF tested is FSF in which the feedback is shifted in frequency with a negligible time delay. The psychoacoustic work described above shows two coincident spectrally-different streams of sound segregate (Bregman, 1990). Thus, in the case of FSF, the altered signal will separate from bone-conducted sound giving two synchronous inputs to the general-purpose timekeeper. In contrast to DAF, these should give a better beat so should not cause an increase in C_v. Experiment 3 investigates whether another way of changing synchronous input to the timekeeper (an intensity change) has similar effects to FSF. The effects of a secondary decision task on timekeeper operation were also examined in this experiment. Based on Ivry and Hazeltine (1995), a secondary task was chosen that involves a duration decision (i.e. time-based). It is assumed that the timekeeper is only sensitive to time-based decisions such as this (this is not tested explicitly). Consequently, C_v will only be affected when a duration decision is required.

II. EXPERIMENT 1

The Wing–Kristofferson analysis is applied to data from a speaking task that requires the syllable /bae/ to be repeated. Total variance is decomposed into C_v and M_v components. The principal question is whether C_v, but not M_v, increases with repetition period (Wing, 1980) as validation that the Wing–Kristofferson procedure to obtain C_v applies to a speech task.

A. Subjects

Eight adults (five males, three females) were employed. They had no history of speech or hearing disorder. They ranged in age from 26 to 34. The same subjects were used in experiments 2 and 3 with half the subjects doing the experiments in one order, and the other half in reverse order (with the exception mentioned in the procedure for experiment 3, below). Counterbalancing was done to avoid practice effects and to permit comparison across experiments (condition-specific practice for each type of trial was also given to avoid this problem). Subjects did each experiment on different days.

B. Procedure

Subjects were told that the aim of the experiments was to establish the accuracy of articulatory timing when speaking a single C_v syllable (/bae/) repeatedly at selected fixed rates. The syllable /bae/ was used because it is easy to say and its onset can be located reliably (the analyses are made from stop release). Subjects were instructed that on any trial the experimenter would play a recorded /bae/ at 70 dB SPL repeatedly at a particular rate. Subjects were told that when they were ready, they should take a deep, but not excessive, breath (as though preparing to say a long sentence). They should then start their own production in time with the recording. The subjects were monitored to ensure they did not take a breath within a sequence. When they were going at the requisite rate the /bae/ used for entraining the speaker was switched off manually by the experimenter after the subject had responded to a minimum of five consecutive recorded /bae/s. The subject continued until either the experimenter stopped them or they stopped themselves because they had run out of breath. They were told not to take a breath in the middle of a sequence. The experimenter required the subject to continue the sequence for a minimum of 11 /bae/s. Four

/bae/–/bae/ repetition periods were used (200, 400, 600, and 800 ms). The experiment started with practice at each repetition period until the experimenter judged that the subject was familiar with the task and could synchronize to the target at each rate. They then did the four different rates eight times each in a predetermined random order.

Subjects were tested individually in an Amplisilence sound-attenuated booth. The entrainment-/bae/s were played binaurally from a Toshiba laptop fitted with a Soundblaster 16 sound card. These sounds were relayed to Sennheiser HD480II headphones via a Fostex 6301B amplifier. Level of speech feedback after entrainment was set so that it was comfortable for listening (typically around 70 dB SPL). Level was periodically checked. Speech was transduced with a Sennheiser K6 microphone and recorded on a DAT recorder.

C. Analysis

The recordings were transferred to disk for analysis (48-kHz sampling rate, 16-bit samples). The recordings were downsampled to 10 kHz. /bae/ onsets were manually marked on 11 /bae/s in the phase after the entrainment sequence had been switched off starting at the onset of the first /bae/. Following Vorberg and Wing (1996), linear trends in the data were removed to ensure stationarity in the sequence. Interonset durations were calculated and M_v and C_v were computed from the algorithm given in Wing and Kristofferson (1973) on the ten intervals. The Wing–Kristofferson model only applies where the lag one autocorrelation, r, is bounded by $-0.5<r<0$ and some of the raw values lay outside these limits. So as not to bias the data by dropping these trials, intervals from each end of the series were dropped (a minimum of four intervals had to remain) from the original sequence; the truncated series was detrended and examined to see if it then fitted the Wing–Kristofferson model. The longest sequence that fitted was used in subsequent analyses. This allowed 98% of all trials to be included in the analysis. An analysis was also conducted to check that this procedure does not affect the results. The trials where only the whole sequences fitted the model were used in these analyses. Analyses of data prepared in this manner produced equivalent results to those reported below.

D. Results

C_v and M_v are plotted over repetition periods in Fig. 1. A two-way repeated measures analysis of variance (ANOVA) was conducted with factors source of variance (C_v or M_v) and repetition period (200, 400, 600, or 800-ms repetition periods). The main effect of repetition period ($F3,21=13.3$, $p<0.001$) was significant. The C_v/M_v by repetition period interaction ($F3,21=5.60$, $p<0.005$) was also significant. Separate ANOVAs using either C_v or M_v alone showed C_v increased significantly as repetition period increased ($F3,21=13.3$, $p<0.001$) but M_v did not. The only repetition period that showed a significant increase in C_v over other intervals is 800 ms. The fact that significant differences between C_v and M_v occurred at the longest interval is to be expected on the basis that C_v alone is affected when repetition period is lengthened.

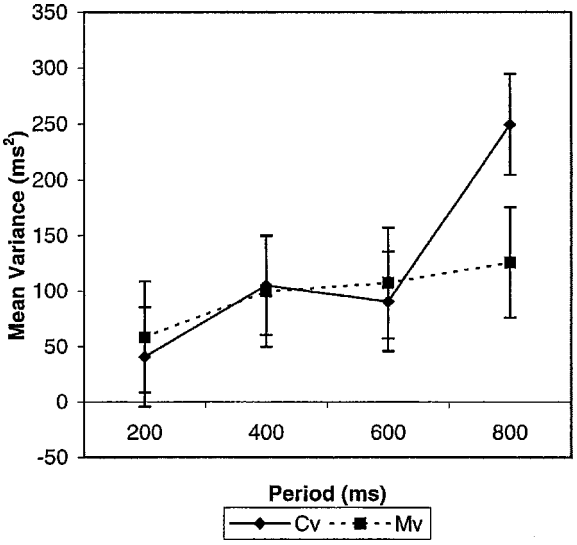

FIG. 1. Motor (dashed line) and clock (solid line) variances (ordinate) for repeating the syllable /bae/ at different periods (abscissa). Periods used were 200, 400, 600, and 800 ms.

E. Discussion

The pattern of variance estimates (C_v and M_v) with change in duration of the repetition period is similar to that reported by Wing (1980) for a manual tapping task and by Howell *et al.* (1997) in a lip-tracking task. There is no change in M_v over repetition periods, whereas C_v increases, with the increase most apparent at the longest repetition period (800 ms). Wing (1980) argued that the selective increase in C_v with repetition period arises because of the greater difficulty controlling the timing of longer intervals. If Wing's (1980) reasoning is correct, the present results show that C_v provides an estimate of timekeeping processes in a task involving the speech articulators. Repetition periods of 600 and 800 ms are used in experiments 2 and 3 to check whether feedback, intensity, and decision-task manipulations affect this pattern. The repetition periods chosen (600 and 800 ms) are in the region where C_v increases occur.

III. EXPERIMENT 2

Speakers performed the Wing–Kristofferson task while listening to one of two forms of AAF (FSF and DAF). According to the hypothesis, both these types of AAF create an additional sound source as input to the timekeeper. The extra sound source in the case of FSF is effectively synchronous with speech and arises due to the spectral difference between the direct speech and its altered form. The additional sound source under DAF arises because of the temporal disparity between the direct and altered forms and so is asynchronous relative to the speech. According to the current hypothesis, asynchronous inputs to the timekeeper (as with DAF) cause more difficulty in performance than synchronous events. Consequently, the effect on C_v should be greater when DAF is presented than when FSF is presented. As DAF delay in-

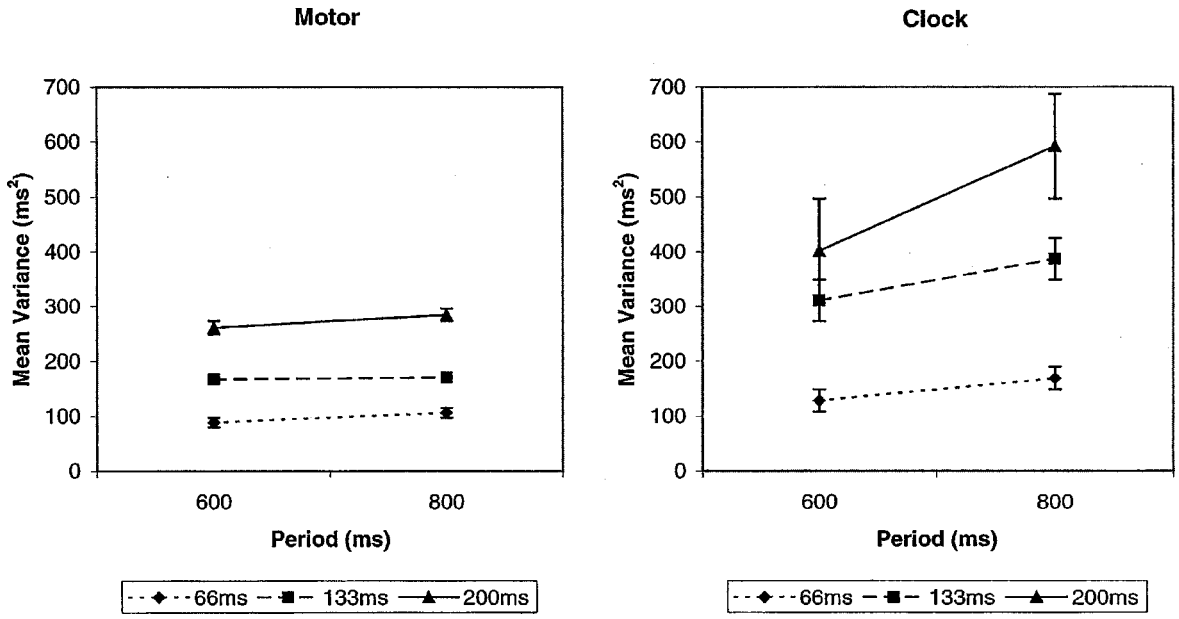

FIG. 2. Motor and clock variances against period (600 and 800 ms) for the delayed auditory feedback conditions of experiment 2. Motor variances are shown on the left and clock variances on the right. DAF delay of the points connected together was 66, 133, or 200 and the delay used for connected points can be identified from the symbol in the caption.

creases, the asynchrony between direct and delayed sources increases (in the experiment going from 66 through 133 to 200-ms DAF delay). More disruption should occur to the general purpose timekeeper as asynchrony increases. The effect on C_v and M_v while hearing each form of AAF is established, again, using the speech variant of the Wing–Kristofferson task.

A. Participants

The same eight subjects were used as in the other experiments.

B. Procedure

All conditions were performed as in experiment 1 with the addition that one of the different forms of AAF was also heard. Besides this, the basic task was the same as in experiment 1. The subjects were told to ignore the feedback and attempt to continue at the specified rate. On a trial involving a delayed sound, subjects heard standard DAF at one of three delays (66, 133, or 200 ms). (As argued in the Introduction, in this, and all DAF experiments, non-shifted sound also occurs through bone conduction.) Subjects were tested at each DAF delay at repetition periods of 600 and 800 ms. Subjects received eight practice trials at each repetition period and DAF delay and then performed eight test trials at the same repetition period and DAF delay. The DAF delay and repetition period conditions were received in random order. The procedure for FSF was the same except that a time-synchronous, half-octave, downward frequency shift was fed back rather than a delayed sound.

The entrainment /bae/ sequence was played over a Toshiba laptop and Fostex monitor at the required repetition period, as in experiment 1. Two Sennheiser K6 microphones were used to pick up the speech. One microphone supplied speech to a DAT recorder for use in the analyses. The other microphone output was relayed via a Quad microphone amplifier to the Digitech model studio 400 signal processor that produced the selected form of AAF. The Digitech output was played binaurally over Sennheiser HD480II headphones. The output (set at 70 dB SPL) is at approximately normal conversational level so, according to von Bekesy's (1960) calculation, the bone-conducted sound should also be roughly at this level too. The data were analyzed as in experiment 1.

C. Results

The results from the DAF conditions are shown in Fig. 2. M_v's are plotted on the left and C_v's on the right. The axes are repetition period (abscissa) and variance (ordinate), as for experiment 1, and the data points under the same DAF delay

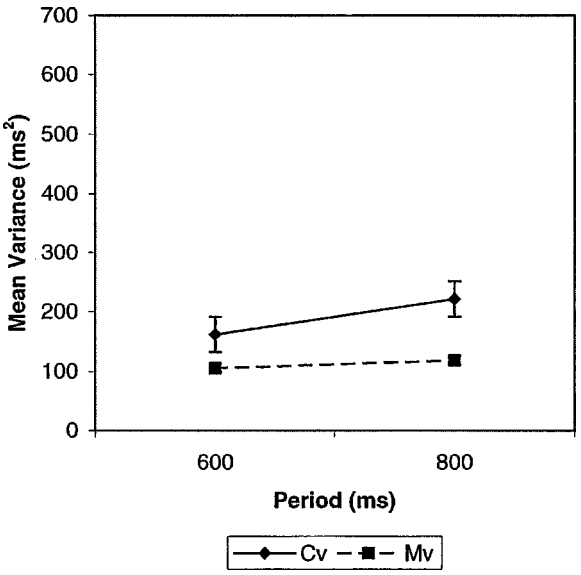

FIG. 3. Motor and clock variances against period (600 and 800 ms) for the frequency-shifted condition of experiment 2.

are connected together (identified by symbol). The results for the FSF condition are shown in Fig. 3 in an equivalent way to the results of experiment 1 (C_v and M_v estimates for each repetition period).

The M_v's in the DAF conditions were examined first with respect to whether DAF has a similar pattern to the results in normal listening conditions. Separate analyses were conducted for each DAF delay and for each variance component to assess how DAF affects M_v and C_v relative to results on the same repetition periods in experiment 1. For M_v, three two-way repeated measures ANOVAs were conducted. One factor was listening condition (the normal listening condition from experiment 1 was always included and was compared with the selected DAF-delay condition, 66, 133, or 200 ms, from the current experiment). The second factor was repetition period (600 or 800 ms). For the M_v measurement, no significant differences occurred between the normal listening condition and the 66- and 133-ms DAF delays. The difference between normal listening and DAF was significant at 200 ms ($F1,7=11.4$, $p<0.025$) DAF delay. These findings indicate that M_v increases under DAF over normal listening only at the longest delay. No interactions with listening condition were significant, so even with the most severe form of DAF, M_v appears to have the same pattern across repetition periods as in normal listening. Corresponding ANOVAs on C_v's showed normal listening differed from DAF at 133 ($F1,7=17.1$, $p<0.005$) and 200 ms ($F1,7=30.2$, $p<0.001$) delays. Differences across repetition periods were significant at all DAF delays as main effects (66 ms:$F1,7=11.50$, $p<0.025$;133 ms:$F1,7=8.5$, $p<0.025$;200 ms:$F1,7=29.00$, $p<0.001$). However, no interactions involving listening conditions were significant so there are only absolute differences between normal listening and DAF conditions.

A three-way repeated measures analysis with factors DAF-delay condition (66, 133, or 200-ms delay), variance source (C_v or M_v) and repetition period (600 or 800 ms) was next conducted to assess whether DAF delay differentially affects C_v's and M_v's. DAF delay was significant ($F2,14=16.5$, $p<0.001$) showing DAF increases variances. These was also a difference between variance sources ($F1,7=60.0$, $p<0.001$) due to C_v's being greater than M_v's. Repetition period was significant ($F1,7=7.6$, $p<0.05$) with higher variances at the longer repetition period. The interaction of the latter factor with source of variance component shows higher variance at the longer repetition period. This is due to C_v increasing more over repetition periods than M_v does ($F1,7=4.10$, $p<0.01$). This result would be expected from Wing (1980) and experiment 1. DAF-delay condition interacted with variance source ($F2,14=6.9$, $p<0.01$). This suggests that C_v and M_v increase at different rates with DAF delay. Inspection of Fig. 2 confirms this is most marked for C_v; M_v's exhibit less increase than C_v's (M_v's increase roughly threefold over delays while C_v's increase more than fivefold).

A two-way ANOVA in which normal listening was compared with FSF (factor one) and repetition period (factor two) failed to reveal any significant differences. The equivalent two-way analysis on C_v's with normal listening and FSF as one factor and repetition period as a second factor showed a significant effect of repetition period ($F1,7=10.6$, $p<0.025$) but no further effects. The lack of an effect of FSF/normal listening as main effect or in interaction shows that performance under FSF was not distinguishable from speech produced under normal listening conditions. As C_v increased in normal listening conditions over repetition period in experiment 1, this might suggest that this occurs with FSF too. If so, it is surprising as Fig. 3 appears to show little increase over repetition periods. This was investigated further in a two-way repeated measures ANOVA with factors variance source and repetition period on the data from the FSF condition alone. In this analysis, there was a main effect of C_v/M_v ($F1,7=11.9$, $p<0.025$) but the effect of repetition period was not significant. Interpretations based on effects that are not significant are problematic. Taking the two analyses together, the cautious conclusion would be that there is some attenuation of the increase in C_v over repetition periods (explaining why no C_v/M_v by repetition period interaction occurred when FSF alone was analyzed) but the attenuation is not detectable when C_v is compared across repetition periods between normal and FSF listening.

To summarize the findings, the pattern of C_v/M_v results over repetition periods shows that the global pattern of results under DAF is similar to what occurs under normal listening conditions (M_v is flat while C_v increases over repetition period). FSF also shows no increase in M_v over repetition periods but, more surprisingly, little evidence for an increase in C_v over repetition periods. The other major finding is that C_v increases more than M_v as DAF delay is increased.

D. Discussion

When DAF was given, M_v showed less increase over repetition periods than C_v for delays of 600 and 800 ms. Note that this general pattern, once again, validates the Wing–Kristofferson model for decomposing variance components (Wing, 1980). As well as the increase over repetition periods, C_v's increased more as DAF delay was increased from 66, through 133 to 200 ms. Thus the prediction that DAF should cause a marked increase in C_v with longer DAF delays was confirmed. FSF produced a pattern of results in which C_v did not markedly increase as repetition period lengthened. The lack of increase in C_v under FSF at long repetition periods could be because this form of AAF is in synchrony with activity associated with speech. As argued in the Introduction, the auditory feedback through bone and the FSF that is synchronous with speech reinforce the timing of the direct speech giving the listener a clearer sense of the speech beat. This would help maintain the rate of the entrainment sequence leading to more precise control by the timekeeper (lower C_v).

The hypothesis that C_v does not increase at long repetition periods when the timekeeper has an input with a dominant beat is tested further in experiment 3. In the Introduction, it was argued that amplification can be considered as a form of time synchronous manipulation (Lane and Tranel, 1971). A better beat should arise when speech feedback is amplified so it should reduce C_v too (in this case, the louder

the signal synchronized to speech activity the better sense of beat a speaker has available to maintain ongoing timing).

IV. EXPERIMENT 3

In experiment 2, FSF (synchronous feedback) led to less of an increase in C_v at the long repetition period compared with M_v in the same listening condition and compared with the increase in C_v observed under DAF and under normal listening conditions. Amplitude alterations on the produced sequence of sounds were made in the current experiment as another form of synchronous sound alteration that should combine with sound sources that arise during vocalization, produce a better beat and prevent any increase in C_v at the longest repetition period. The experiment also included two conditions that varied what the subject had to do with the altered amplitude sections. A duration decision expected to tax the timekeeper (based on Ivry and Hazeltine's 1995 work) was selected as most likely to elicit effects on C_v. In one condition, no response was made to the section where amplitude was altered (creating a condition similar to the FSF in experiment 2). In the second condition, a duration response was made about the amplitude-altered section after the sequence was produced. These conditions were included to establish whether attention to the altered sound (such as when a response is required) leads to a C_v increase whereas, when attention to the sound is not required (as with FSF in experiment 2), C_v does not increase. If a duration decision calls on the timekeeper's capacity, it would be revealed as increased C_v in conditions where timekeeping is most difficult (i.e., at long repetition periods).

A. Participants

The same eight subjects were used as in the previous experiments.

B. Procedure: Condition one (no response)

The basic experimental setup was the same for the two main conditions and was similar to that employed in experiment 1. In condition one, some syllables were selected manually and amplified by 6 dB by the experimenter as the speaker spoke. They heard the altered sound but did not make a judgment about it in this condition. The selection of syllables for amplification was made according to preset criteria (the remaining syllables were at the same level as in the previous experiments). Over all trials, the start of the first amplified section was either two or three /bae/s after the entrainment sequence stopped. This continued for two or three sounds. It was then presented at the standard level, again for two or three sounds. Finally, two or three more sounds were played at increased amplitude. This arrangement ensured that subjects did not know exactly when each of the two increased amplitude stretches in the sequences would start, or their duration. There were also equal numbers of trials that were the same (also with the same number of amplified sections containing two, or three amplified /bae/s) or different (same number of two/three and three/two amplified /bae/s). There were eight types of trial according to these criteria. These were presented eight times each in random order. Condition one was always received before condition two and condition three at the end to keep the subjects naive as to the purpose of the amplified /bae/s. Subjects were given practice trials at the start. Only the two longest repetition periods were used (600 and 800 ms) because of the difficulty of the task.

C. Procedure: Condition two (response)

The procedure for condition two was the same as for condition one, except that after they completed the interval production task, the subject was required to make a same or a different response about whether the two groups of amplified /bae/s had the same number of /bae/s or not. They were aware that they needed to make the decision before they started performing this condition. The experimenter gave feedback as to whether the subject was correct or incorrect after each trial (in actual fact, subjects were always correct).

D. Procedure: Condition three

Condition three was a control included to check that subjects were able to perform the perceptual judgment in condition two accurately and how performance in condition two compared with a perception-only judgment. It did not involve production of sequences, only listening to, and making judgment about, recordings of the sequences obtained in condition two. This was done to ensure speakers did not maintain interval production performance by allowing duration decisions to be less accurate in that task. As duration decisions in condition two were perfect, this is superfluous. This condition is, however, described for completeness. The subjects listened to recordings of the sequences they had produced and did the same–different perceptual task alone. Performance on this task was (as in condition two) always correct. These results are not discussed further.

In conditions one and two, the entrainment /bae/ sequence was played over the Toshiba laptop and Fostex monitor at the required rate as in experiment 1. Two Sennheiser K6 microphones were used to pick up the speaker's responses. One led directly to the DAT recorder to be used later in the analysis. The other was routed via a Quad microphone amplifier to a Digitech model studio 400 signal processor. The output from the processor was split. Low-amplitude white noise at about 60 dB SPL was added to the voice signal before the sound was fed back to the speaker to mask out the sounds of apparatus switching. This was played binaurally over a Sennheiser HD480II headset. The other output was recorded on a second channel of the DAT recorder (for use in the perceptual condition, condition three, and to check that the experimenter had made the alterations correctly).

E. Results

The results are shown on the left of Fig. 4 for the condition where the altered sound was heard but subjects did not judge the duration of the demarcated intervals and on the right for the condition where subjects did the duration judgment task after they completed the /bae/ synchronization task. Separate ANOVAs equivalent to those in experiment 1

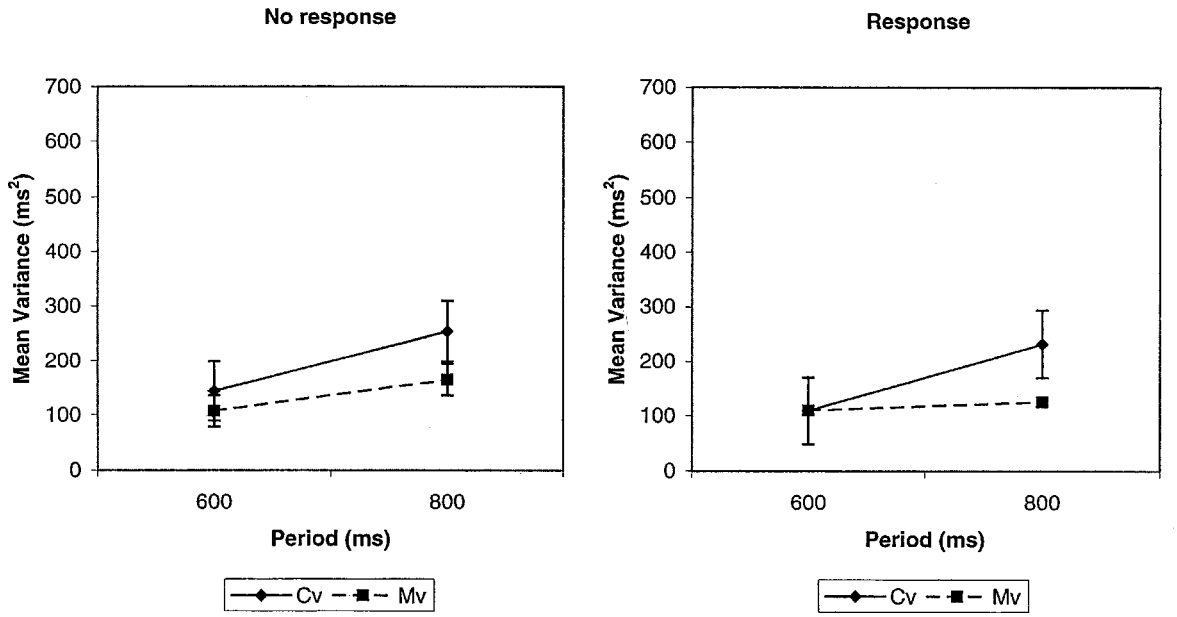

FIG. 4. Motor and clock variances against period for experiment 3. Periods used were 600 and 800 ms. The results for the no-response condition are on the left and the response condition on the right.

were conducted on each condition. In the condition where subjects made no response, there was a difference over repetition periods ($F1,7=17.2$, $p<0.005$). Unlike experiment 1, there was no interaction between C_v/M_v and repetition period. This suggests that the greater increase in C_v compared with M_v that occurred, particularly at 800-ms repetition period in experiments 1 and 2, did not occur here.

A somewhat different pattern of results was found when subjects made a response to the altered sound. C_v/M_v ($F1,7=5.6$, $p=0.05$), repetition period ($F1,7=7.3$, $p<0.05$), and C_v/M_v by repetition period interaction ($F1,7=24.1$, $p<0.005$) were all significant. The interaction shows C_v increased over repetition periods when a response was made (as expected from experiment 1 and Wing, 1980). There was an interaction between response condition, source of variance component (C_v/M_v), and repetition period ($F1,7=8.2$, $p<0.025$) when a three-way ANOVA was conducted with response condition as the extra factor. This shows that C_v increased at a different rate across repetition periods in the two response conditions (no increase in C_v over repetition periods when no response was made but an increase when a response was made).

F. Discussion

C_v only increased relative to M_v over repetition periods if a response to sections increased in amplitude was required. This shows that this secondary decision affects the operation of the timekeeper. As only one task was used here, general disruption by any secondary task (rather than one specifically involving timing) cannot be definitely ruled out. However, Ivry and Hazeltine (1995) found that performance on perceptual timing judgments correlates with variance in a tapping task. Given the very different nature of these tasks, it is difficult to see how there could be this relationship other than through a timing mechanism. The secondary task in the current experiment has similarities to that of Ivry and Hazeltine (1995) (insofar as a duration judgment is required). The main difference between Ivry and Hazeltine's work and the current is that in the latter the judgment is made concurrent with the interval production task rather than as a separate task. If it is accepted that Ivry and Hazeltine's (1995) result showing correlations between the perceptual and production tasks operates through the timekeeping process, the interference from the secondary judgment task on C_v here would also seem to operate at the level of the timekeeper.

The next question considered is why statistically there is no increase in C_v relative to M_v when subjects just listened to the sequences that had their amplitude altered. The results with FSF in experiment 2, where again no increase in C_v over repetition occurred (though the lack of significance needs to be treated cautiously), were explained by proposing that synchronized sound gives a better sense of beat to follow than occurs in normal listening conditions, leaving C_v less affected by repetition period. This explanation would apply in the condition where no response is given, as the amplified sound gives a better beat and response requirements are the same as in the FSF condition. The general pattern of the results when a response has to be made to the altered sound is similar to that in experiment 1 and as reported by Wing (1980) to validate the assumptions of the Wing–Kristofferson model. While the enhanced beat can remove the increase over repetition period, adding a duration decision adversely affects the timekeeper. The adverse effect of making a duration response is most evident in conditions where timekeeping is difficult (long repetition period). Note also that the effect of duration decisions on the timekeeper is consistent with the general role this mechanism is assumed to play (here, general to perception and production).

V. GENERAL DISCUSSION

Experiment 1 validated the application of the Wing–Kristofferson task to speech and provided benchmark data

against which to compare effects of AAF and additional response tasks. Experiment 2 showed that DAF has its principal effect on C_v, whereas FSF did not lead to an increase in C_v at long repetition periods (note that this needs to be treated cautiously as it is based on finding no significant increase). The DAF result was predicted from the hypothesis that the DAF signal is asynchronous with direct speech and asynchronous inputs markedly affect timekeeper operations. The FSF effect was predicted on the basis that the altered sound is in synchrony with the ongoing speech sound input to the timekeeper and two synchronized inputs give the timekeeper a better sense of beat that aids (or prevents degraded) performance. Experiment 3 tested the effect of enhancing the beat on timekeeper operation further by altering the amplitude of sections of speech output. This experiment also included conditions where subjects were, and were not, required to make a response about the sections with higher amplitude (enhanced beat). In the condition in which an amplitude alteration was heard but not responded to, C_v showed no increase at the long repetition period as occurred with FSF. However, C_v did increase when the same sounds were heard when a duration judgment was required about the amplified section. This suggests the C_v increase emerges when a duration decision is required because the difficulty faced by the timekeeper is enhanced.

The implications of the results are considered for the role of AAF experiments for speech control. The first topic considered is whether a case can be made that temporal alterations lead to temporal disruption of speech and nontemporal alterations lead to nontemporal changes in speech output. The evidence on FSF appears to speak against the second proposition. In conditions approximating closer-to-normal speaking conditions, at first sight there is evidence that the spectral alteration of FSF does not produce any noticeable change in timing (for instance, overall average speech rate appears normal). However, Howell and Sackin (2000) looked at FSF on sentence material and found that timing variability around specified segmentation points is affected by this manipulation. In particular, FSF reduced timing variability possibly by enhancing the direct beat. Thus, as spectral alterations during FSF lead to significant effects on timing control, the notion that only timing alterations cause speech-timing changes on vocal output cannot be sustained.

This leads to the second issue, whether AAF experiments provide support for feedback monitoring models. The current work does not necessarily rule out auditory feedback having a role in maintaining internal long-term models for the speaker's language (Perkell, 1980). Auditory feedback might also have a role in control of segmental aspects in speech produced outside AAF procedures, depending on the position taken about whether the auditory feedback is reflexive of the speaker's intention or not. Currently there is only one study that suggests auditory feedback is not reflexive of speech output (Howell and Powell, 1984). This suggests that the cautious approach would be to not definitely rule out auditory feedback having a role in maintaining gross segmental information. Having said this, a model that does not require reflexivity (Howell, in press) merits brief discussion. Examples of each of these two types of model are considered starting with two models that require reflexivity, Neilson and Neilson's (1991) adaptive model theory (AMT) and Guenther's (2001) DIVA model.

Neilson and Neilson's (1991) AMT theory has a controlled dynamic system driven by an adaptive controller. The adaptive controller transforms motor commands into sensory events. The adaptive controller has to have access to the speech-output ''solution'' that is obtained by an inverse dynamics process applied on sensory feedback. It would not be possible to determine whether and what correction is necessary if the sensory signal is nonreflexive of speech output. In Guenther's (2001) model, auditory targets are projected from premotor cortical areas to the posterior superior temporal gyrus, where they are compared to incoming auditory information via primary auditory cortex. Any difference represents an error signal that is mapped through the cerebellum and the auditory error signal indicates a change is required to the motor velocity signal that controls the articulators to zero out the error. Again, if the auditory feedback is not sufficiently reflexive of speech output, information about segment articulation would not be veridical and could potentially even lead to incorrect corrections.

Howell (in press) has offered a model where the altered sound inputs to the timekeeper and how this causes disruption rather than the feedback from the altered sound continues to be used by a monitor for feedback control. The principal advantage of this model is that it avoids the nonreflexivity problem. This interpretation suggests alteration to auditory feedback creates an artificial speaking situation. This does not necessarily rule out a role for auditory feedback in segmental control in normal speaking situations. Howell's (in press) model circumvents the reflexivity problem by proposing cerebellar mechanisms give an error signal that arises only when timing problems occur. This alert acts as an all or none signal given the sole role of slowing speech rather than segmental correction. Loss of hearing just leads to one less input to the timekeeper and the timekeeper is not adversely affected by removal of this source of input. Initiation of a subsequent sound once one sound has finished does not depend on the results of processing sound back through an auditory feedback loop. As this rate-limiting step in speech control is removed, there is no problem in accounting for the rapidity at which speech can be produced. It would not matter, then, whether auditory feedback of the voice presents a veridical representation of what was said; it will only depend on the timing of the altered sound in relation to other timekeeper inputs. Thus, an altered sound that has the same timing as DAF speech would offer the same serial input to the timekeeper and produce equivalent disruption (Howell and Archer, 1984). Finally, manipulations that transform speech into noise that has lost its association with the original speech by being delayed (Howell, 1990) would be effective because of the asynchronous input they provide, not because the sounds were originally derived from speech. The EXPLAN model has its limitations. For instance, it does not address the issue about how long-term representations are established. Establishing how degraded auditory feedback is of speech output is a topic that merits further attention as it features in many monitoring models.

ACKNOWLEDGMENTS

This research was supported by a grant from the Wellcome Trust. Thanks to Richard Ivry and Alan Wing for advising on how to treat the data so little is excluded from analysis.

Borden, G. J. (**1979**). ''An interpretation of research on feedback interruption in speech,'' Brain Lang **7**, 307–319.

Bregman, A. S. (**1990**). *Auditory Scene Analysis: The Perceptual Organization of Sound* (MIT Press, Cambridge, MA).

Fairbanks, G. (**1955**). ''Selective vocal effects of delayed auditory feedback,'' J. Speech Hear Disord. **20**, 335–348.

Guenther, F. H. (**2001**). ''Neural modeling of speech production,'' in *Speech Motor Control in Normal and Disordered Speech*, edited by B. Maassen, W. Hulstijn, R. Kent, H. F. M. Peters, and P. H. M. M. van Lieshout (Uttgeverij Vantilt, Nijmegen), pp. 12–15.

Howell, P. (**1990**). ''Changes in voice level caused by several forms of altered feedback in normal speakers and stutterers,'' Lang Speech **33**, 325–338.

Howell, P. (in press). ''The EXPLAN theory of fluency control applied to the Treatment of Stuttering by Altered Feedback and Operant Procedures,'' in *Current Issues in Linguistic Theory. Pathology and Therapy of Speech Disorders*, edited by E. Fava (Benjamins, Amsterdam).

Howell, P., and Archer, A. (**1984**). ''Susceptibility to the effects of delayed auditory feedback,'' Percept. Psychophys. **36**, 296–302.

Howell, P., Au-Yeung, J., and Rustin, L. (**1997**). ''Clock and motor variances in lip-tracking: A comparison between children who stutter and those who do not,'' in *Speech Production: Motor Control, Brain Research and Fluency Disorders*, edited by W. Hulstijn, H. F. M. Peters, and P. H. H. M. van Lieshout (Elsevier, Amsterdam), pp. 573–578.

Howell, P., El-Yaniv, N., and Powell, D. J. (**1987**). ''Factors affecting fluency in stutterers when speaking under altered auditory feedback,'' in *Speech Motor Dynamics in Stuttering*, edited by H. Peters and W. Hulstijn (Springer, New York), pp. 361–369.

Howell, P., and Powell, D. J. (**1984**). ''Hearing your voice through bone and air: Implications for explanations of stuttering behavior from studies of normal speakers,'' J. Fluency Dis. **9**, 247–264.

Howell, P., Powell, D. J., and Khan, I. (**1983**). ''Amplitude contour of the delayed signal and interference in delayed auditory feedback tasks,'' J. Exp. Psychol.: Hum. Percept. Perform. **9**, 772–784.

Howell, P., and Sackin, S. (**2000**). ''Speech rate manipulation and its effects on fluency reversal in children who stutter,'' J. Devel. Phys. Disab. **12**, 291–315.

Hulstijn, W., Summers, J. J., van Lieshout, P. H. M., and Peters, H. F. M. (**1992**). ''Timing in finger tapping and speech: A comparison between stutterers and fluent speakers,'' Hum. Movement Sci. **11**, 113–124.

Ivry, R. (**1997**). ''Cerebellar timing systems,'' in *The Cerebellum and Cognition*, edited by J. Schmahmann (Academic, San Diego), pp. 555–573.

Ivry, R. B., and Hazeltine, R. E. (**1995**). ''Perception and production of temporal intervals across a range of durations: Evidence for a common timing mechanism,'' J. Exp. Psychol.: Hum. Percept. Perform. **21**, 3–18.

Lane, H., and Tranel, B. (**1971**). ''The Lombard sign and the role of hearing in speech,'' J. Speech Hear. Res. **14**, 677–709.

Lashley, K. S. (**1951**). ''The problem of serial order in behavior,'' in *Cerebral Mechanisms in Behavior*, edited by L. A. Jeffress (Wiley, New York).

Lee, B. S. (**1950**). ''Effects of delayed speech feedback,'' J. Acoust. Soc. Am. **22**, 824–826.

Marslen-Wilson, W. D., and Tyler, L. K. (**1981**). ''Central processes in speech understanding,'' Philos. Trans. R. Soc. London, Ser. B **259**, 297–313.

Natke, U., and Kalveram, K. T. (**2001**). ''Effects of frequency-shifted auditory feedback on fundamental frequency of long and short stressed and unstressed syllables,'' J. Speech Lang. Hear. Res. **44**, 577–584.

Neilson, M. D., and Neilson, P. D. (**1991**). ''Adaptive model theory of speech motor control and stuttering,'' in *Speech Motor Control and Stuttering*, edited by H. G. M. Peters, W. Hulstijn, and C. W. Starkweather (Elsevier, Amsterdam), pp. 149–156.

Perkell, J. (**1980**). ''Phonetic features and the physiology of speech production,'' in *Language Production*, edited by B. Butterworth (Academic, London), Vol. 1, pp. 337–372.

Perkell, J., Guenther, F., Lane, H., Matthies, M., Vick, J., and Zandipur, M. (**2001**). ''Planning and auditory feedback in speech production,'' in *Speech Motor Control in Normal and Disordered Speech*, edited by B. Maassen, W. Hulstijn, R. Kent, H. F. M. Peters, and P. H. M. M. van Lieshout (Uttgeverij Vantilt, Nijmegen), pp. 5–11.

Postma, A. (**2000**). ''Detection of errors during speech production: A review of speech monitoring models,'' Cognition **77**, 97–131.

Vorberg, D., and Wing, A. (**1996**). ''Modeling variability and dependence in timing,'' in *Handbook of Perception and Action* (Academic, London), Vol. 2, pp. 181–262.

von Bekesy, G. (**1960**). *Experiments in Hearing* (McGraw-Hill, New York).

Wing, A. M. (**1980**). ''The long and the short of timing in response sequences,'' in *Tutorials in Motor Behavior*, edited by G. E. Stelmach and J. Requin (North-Holland, Amsterdam), pp. 469–486.

Wing, A. M., and Kristofferson, A. B. (**1973**). ''Response delays and the timing of discrete motor responses,'' Percept. Psychophys. **14**, 5–12.

Anchoring effects in audiovisual speech perception

Sumi Shigeno[a)]
Department of Psychology, College of Literature, Aoyama Gakuin University, 4-4-25 Shibuya, Shibuya-ku, Tokyo 150-8366, Japan

(Received 23 October 2000; accepted for publication 5 March 2002)

Two experiments were conducted to investigate whether or not anchoring and selective adaptation induce basically the same psychological effects. The purpose of the first experiment is to show how an audiovisual anchor modifies the perception of consonant–vowel (CV) syllables. The anchors were two purely acoustical, two purely optical, and three audiovisual CV syllables. The results were compared with those of audiovisual speech selective-adaptation experiments conducted by Roberts and Summerfield [Percept. Psychophys. **30**, 309–314 (1981)] and Saldaña and Rosenblum [J. Acoust. Soc. Am. **95**, 3658–3661 (1994)]. The audiovisual anchoring effects were found to be very similar to the audiovisual selective-adaptation effects, but the incompatible audiovisual anchor produced more auditory-based contrast than the purely acoustical anchor or the compatible audiovisual anchor. This difference in contrast had not been found in the previous selective-adaptation experiments. The second experiment was conducted to directly compare audiovisual anchoring and selective-adaptation effects under the same stimuli and with the same subjects. It was found that the compatible audiovisual syllable (AbVb) caused more contrast in selective adaptation than in anchoring, although the discrepant audiovisual syllable (AbVg) caused no difference between anchoring and selective adaptation. It was also found that the anchor AbVg caused more auditory-based contrast than the anchor AbVb. It is suggested that the mechanisms behind these results are different. © *2002 Acoustical Society of America.*
[DOI: 10.1121/1.1474446]

PACS numbers: 43.71.An, 43.71.Pc [CWT]

I. INTRODUCTION

Context effects caused by stimuli preceding and following a target stimulus are well known in speech perception. They are referred to in various ways, such as selective adaptation, anchoring effects, and range or frequency effects (Repp, 1982). In a typical selective-adaptation paradigm, subjects participate in two sessions and a stimulus continuum consists of syllables that vary in equal increments of one or more acoustic parameters and that span two phonetic categories. In the first ''baseline'' session, the target stimuli are presented in random order and the listeners are asked to classify them into two or more phonetic categories. In the second session, several repetitions of one of the endpoint syllables (called adaptors) are presented and listeners are asked to identify the same target stimuli used in the baseline sessions. For each subject, phoneme boundaries are derived from each of the sessions. The phoneme boundary from the baseline session moves towards the category defined by the adaptor because subjects identify the targets more often as belonging to the category of which the adaptor is not a member. This phenomenon is called the ''selective-adaptation effect,'' and the size of the boundary shift is a measure of the adaptation effect.

To clearly dissociate auditory and phonetic bases for adaptation, Roberts and Summerfield (1981) carried out an audiovisual test of speech-selective adaptation. Their experiment involved the presentation of an audiovisually discrepant adaptor consisting of an acoustic /bɛ/ in synchrony with an optical /gɛ/. Previous findings had suggested that subjects presented with a discrepant syllable such as an acoustic /ba/ with an optical /ga/ would be likely to believe that the speaker uttered a fused syllable such as /da/ (McGurk and MacDonald, 1976). Roberts and Summerfield (1981) thought that if perceptual adaptation can occur at the presumably central level at which visual and auditory information are combined, a subject's identification of acoustically presented test syllables might be affected by the visually presented adaptors. They contrasted two hypotheses. First, if the adaptation effect is predominantly auditory, subjects to whom the discrepant audiovisual adaptor had been presented would identify a greater proportion of the test syllables as /dɛ/, and the phoneme boundary would shift toward /bɛ/. Second, if the effect is predominantly phonetic, however, the subjects would identify a greater proportion of the test syllables as /bɛ/, and the phoneme boundary would shift toward /dɛ/. They reported that their discrepant audiovisual adaptor resulted in a consistent phoneme boundary shift towards /bɛ/. They thus concluded that the selective-adaptation effect is purely auditory.

Saldaña and Rosenblum (1994) questioned this interpretation, because in order for it to be valid, the discrepant audiovisual adaptor (acoustic /bɛ/ with optical /gɛ/) should actually induce a phonetic /dɛ/ percept in subjects. Roberts and Summerfield (1981), however, reported that this discrepant audiovisual syllable did not always result in the same percept within individual subjects or a group of subjects. Saldaña and Rosenblum (1994) used a more compelling audiovisual adaptor, which yielded a visually influenced percept 99% of

[a)]Electronic mail: sshigeno@cl.aoyama.ac.jp

the time, to replicate the study of Roberts and Summerfield (1981). Regarding the auditory component, they still reported that systematic adaptation occurred. And they concluded that the selective-adaptation effect in speech perception depends on the acoustic structure of the stimuli and not on the phonetic percept of the listener.

In a typical anchoring paradigm, subjects also participate in two sessions. In the first, the target stimuli are presented in random order and subjects classify them into one of the phonetic categories. In the second session, a particular endpoint stimulus (called an anchor) is presented more often than other stimuli. Either the anchor is repeatedly scattered randomly among the target stimuli and subjects are asked to classify all stimuli (anchor and target) into one of the phonetic categories (e.g., Simon and Studdert-Kennedy, 1978; Sawusch and Nusbaum, 1979) or the anchor is paired with one of the target stimuli and subjects are asked to classify only the target stimulus into one of the phonetic categories (e.g., Thompson and Hollien, 1970; Shigeno and Fujisaki, 1979). In both types of anchoring paradigms, the phoneme boundary from the baseline session moves toward the anchor.

There has been some controversy as to whether or not the anchoring and selective-adaptation paradigms are basically the same. Simon and Studdert-Kennedy (1978) compared the effects of anchoring on the identification of a synthetic stop-consonant continuum ranging from /bæ/ to /dæ/ with those on the identification of fundamental frequency. The two types of stimulus variation are perfectly correlated and are carried simultaneously on the same series of syllables. Between anchoring and selective adaptation they compared the extent of dissociation on phonetic and nonphonetic judgments. The anchoring experiments differed from the selective-adaptation experiments in that the repetitions of the anchor were distributed randomly among the test syllables of each block and that the anchor was presented less often than the adaptor. Simon and Studdert-Kennedy (1978) found the two types of judgments—phonetic and nonphonetic—were significantly dissociated under both anchoring and selective-adaptation paradigms and concluded that differences between results in the two types of experiment might well be of degree rather than of kind. They also concluded that ''there seem to be no grounds for distinguishing the paradigms in terms of the psychological processes that they activate'' (p. 1355).

Although many researchers have explored anchoring and selective-adaptation effects and have proposed various explanations for the perceptual or judgmental processes that induce these effects, either their auditory process or their phonetic process has been a question under discussion. It is very difficult to dissociate the individual contribution of the two processes because the auditory and phonetic structure of conventional acoustical stimuli is mutually predictive, as pointed out by Roberts and Summerfield (1981). If the above speculation by Simon and Studdert-Kennedy (1978) were true, anchoring in speech perception would also depend on the acoustic structure of the stimuli as seen in selective adaptation (Roberts and Summerfield, 1981). The results of both audiovisual anchoring and selective adaptation would also be very similar, although the magnitude of the effects of anchoring would be smaller than that of the effects of selective adaptation. On the other hand, if the anchoring effect is predominantly phonetic and results from the operation of processes such as response bias (Diehl *et al.*, 1980) or frequency analysis (Parducci, 1965, 1974), the effect of the discrepant audiovisual anchor (acoustic /ba/ with optical /ga/) would be different from that of selective adaptation, and the phoneme boundary would shift toward the opposite category to the anchor (in the above case, toward /da/). Audiovisual anchoring experiments would then be very useful for confirming the conclusion by Simon and Studdert-Kennedy (1978) and for finding out whether or not anchoring and selective adaptation induce basically the same psychological effect.

The present study therefore addresses the following questions. (1) How does an audiovisual anchor modify the perception of acoustically presented target stimuli? (2) Is anchoring in speech perception also purely auditory as seen in selective adaptation? (3) Are the effects and mechanisms of the two paradigms—anchoring and selective adaptation—in principle equivalent?

II. EXPERIMENT 1

The purpose of the first experiment is to show how an audiovisual anchor modifies the perception of target stimuli.

A. Method

1. Subjects

Fourteen undergraduate students at Tokyo University participated in the experiment. All were native speakers of Japanese with no reported histories of speech or hearing disorders.

2. Stimuli

The face of a Japanese female speaker was filmed with a video-recorder (SONY, ACP-80), and her voice was recorded on the PCM track of an 8-mm videotape. Several of the /ba/, /da/, and /ga/ syllables she pronounced were analyzed by computer, and the parameters for preparing synthetic CV-syllables were determined. Then seven synthetic syllables on the /ba/-/da/ continuum, a typical /ba/, a typical /da/, and a typical /ga/ were generated by computer (NEC, 9801RX2). Each syllable was 380 ms in duration: 70–90 ms of initial formant transitions followed by 290–310 ms of a steady-state vowel. The onset frequency of the first formant (F1) was fixed at 375 Hz. The onset frequencies of the second formant (F2) ranged in equal steps from 1200 to 1670 Hz and those of the third formant (F3) ranged from 2600 to 3060 Hz. The steady-state frequencies of these three formants were 875 (F1), 1400 (F2), and 2900 Hz (F3). The frequencies of the fourth (F4) and fifth formant (F5) were respectively fixed at 3800 and 4800 Hz. The amplitude contour rose to its maximum over the first 15 ms ([ba]) or 20 ms ([da]). The fundamental frequency was fixed at 220 Hz for the vowel /a/ over the duration of each syllable.

All tests were done with purely acoustical target stimuli, but five of the seven anchoring stimuli were visual or audio-

visual. The seven target stimuli were on the /ba/-/da/ continuum. The two purely acoustical anchors were a typical /ba/ and a typical /da/. They were used in conditions Ab (auditory /ba/-anchor) and Ad (auditory /da/-anchor). Two anchors were purely optical; that is, video recordings of the Japanese female speaker whose speech was used in the auditory conditions. The two purely optical anchors were used in conditions Vb (visual /ba/-anchor) and Vd (visual /da/-anchor). Three audiovisual anchors were generated, each by synchronizing a video recording of the same speaker uttering a CV syllable with either the typical /ba/ or typical /da/ sound. The three audiovisual combinations were an acoustical /ba/ with an optical /ba/ (condition AbVb), an acoustical /da/ with an optical /da/ (condition AdVd), and an acoustical /ba/ with an optical /ga/ (condition AbVg). The acoustical stimuli were dubbed to the visual stimuli at an accuracy of 33 ms.

Eight color videotapes were made. The first tape had no video signal and was simply an audio recording of the seven target syllables, each of which occurred ten times in random order with a 3-s interval between syllables. The tape was used to establish baseline phoneme boundaries prior to each anchoring experiment. The other seven tapes were for auditory (Ab, Ad), visual (Vb, Vd), and audiovisual (AbVb, AdVd, AbVg) anchoring experiments. The target stimuli in all experiments were acoustical. Each tape included 70 trials, and each trial consisted of an anchor–target stimulus pair. The stimulus onset asynchrony (SOA) between anchor and target was 2 s, and the intertrial interval was 3 s.

3. Procedure

Auditory stimuli were presented in a soundproof room, at about 75 dB (A), through loudspeakers (ONKYO, Scepter 1001) on both sides of a 24-in. TV monitor (Victor, AV-2553) at eye level. The viewing distance was 1.1 m, and the stimuli were played back on an 8-mm recorder (SONY, EVO-9850).

The subjects were divided into two groups; one required to participate under the auditory anchor conditions (Ab, Ad) and the other required to participate under the visual anchor conditions (Vb, Vd). The subjects in both groups participated under the audiovisual anchor conditions (AbVb, AdVd, and AbVg). All subjects thus took part in five sessions. Each session consisted of two consecutive parts: an initial baseline sequence and an anchoring sequence. In the baseline sequence a 70-trial baseline randomization was presented and the subjects were instructed to listen to each stimulus syllable and to identify its initial consonant as /b/ or /d/ by writing ''B'' or ''D'' on a response sheet. In the anchoring sequence, the subjects were instructed to pay attention to a pair of stimuli. Under the Ab and Ad conditions, the subjects were instructed to listen to both the anchor and the target very carefully. Under the Vb and Vd conditions, the subjects were instructed to gaze at the anchor (facial movements without sound) on the screen and then listen to the target very carefully. Under the AbVb, AdVd, and AbVg conditions, the subjects were instructed to gaze at the anchor and at the same time listen to the anchor and target carefully. Under all conditions, they were asked to identify the initial consonant of the target. Ten judgments per target stimulus were obtained under every condition. Before each session, the subjects were told whether to expect an acoustical, optical, or audiovisual anchor. At the end of each anchoring session the subjects were required to write down the syllable(s) that they perceived when the anchors were presented.

B. Results and discussion

For each subject, the percentage of responses indicating that the target was /d/ was approximated by a cumulative normal distribution whose mean and standard deviation were obtained by the least square method with Müller–Urban weight. The mean indicates the category boundary between /ba/ and /da/.

The difference between the means obtained from the baseline and the anchoring sequences can thus be regarded as a measure of the anchoring effect. In this paper a positive value indicates that the boundary shifted toward /ba/, while a negative value indicates that it shifted toward /da/.

The anchoring effects for individual subjects are listed in Table I. The identification of anchors was analyzed first to see whether the McGurk effect occurred when the anchor was AbVg. Four of the 14 subjects (nos. 2, 8, 10, and 13) identified AbVg as /ba/. The other subjects reported dental consonants: six (nos. 4, 5, 7, 9, 11, and 14) identified it as /da/, /ra/, or /la/ instead of /ba/, and the other four identified it as /da/, /za/, /gwa/, and /dra/ besides /ba/.

The averaged difference scores were examined first by using two-tailed *t*-tests to determine whether or not anchoring effects occurred. The two acoustic anchors produced significant contrast effects [Ab,$t(6)=2.87$, $p<0.0283$; Ad,$t(6)=4.33$, $p<0.0049$], and the two purely optical anchors did not. The audiovisual anchors with compatible acoustical and optical components produced significant contrast effects [AbVb:$t(13)=3.32$, $p<0.0055$; AdVd:$t(13)=2.33$, $p<0.0363$]. The discrepant audiovisual anchor produced a significant shift in subjects' phoneme boundaries toward the /ba/ end of the auditory continuum (the data of subject no. 11 were rejected, because he showed too much contrast) [$t(12)=4.56$, $p<0.0007$]. The sizes of the boundary shifts in the audiovisual anchoring experiments were very similar to those in the selective-adaptation experiments of Roberts and Summerfield (1981) and of Saldaña and Rosenblum (1994).

To determine whether the addition of compatible optical information to acoustical anchors modified anchoring effects systematically, we evaluated the data obtained under conditions Ab, Ad, AbVb, and AdVd by using a repeated-measures, three-way, within-subject analysis of variance (ANOVA)—presentation (acoustical versus audiovisual)×anchor (ba versus da)×sequence (baseline versus anchoring). The interaction between anchor and sequence was significant [$F(1,6)=3.85$, $p<0.0042$], showing that the directions of the boundary shifts for the /ba/ and /da/ anchors are opposite. The main effect of presentation was not significant, showing that the addition of compatible optical information did not affect the size of the anchoring effects. The simple main effect of the anchor in the anchoring sequence was significant [$F(1,6)=13.18$, $p<0.0110$]. The

TABLE I. Anchoring effects for individual subject. Phonetic transcriptions of subjects' description of the anchor used in condition AbVg are listed in the right-hand column. ''ra'' and ''la'' are not discriminated in Japanese.

	Condition							
Subject	Ab	Ad	Vb	Vd	AbVb	AdVd	AbVg	
1	2.23	−0.18			0.82	−1.14	1.65	[ba][da][za]
2	0.64	−0.25			0.41	0.50	0.18	[ba]
3	0.80	−0.25			0.50	0.56	2.18	[ba][gwa][dra]
4	0.10	−0.60			0.62	−0.22	3.14	[la]
5	0.85	−0.69			−0.03	−0.51	0.45	[da]
6	1.99	−0.12			0.33	−0.54	2.85	[ba][da]
7	−0.02	−0.58			0.92	−0.51	0.33	[da]
Mean	0.94	−0.38			0.51	−0.27	1.54	
8			−0.62	0.26	−0.21	−0.28	0.91	[ba]
9			−0.23	0.05	0.33	−1.57	2.35	[da][ra]
10			−0.61	0.00	0.05	−0.28	−0.40	[ba]
11			0.15	−0.73	−0.41	−0.42	[a]	[ra]
12			0.30	−0.07	0.64	−1.70	1.28	[ba][da]
13			0.68	0.23	0.21	0.32	1.09	[ba]
14			−0.91	−0.13	0.65	−0.15	1.68	[da]
Mean			−0.18	−0.06	0.18	−0.58	1.15	
Grand Mean	0.94	−0.38	−0.18	−0.06	0.35	−0.42	1.36[b]	

[a]The subject showed too many ''da'' responses for the anchoring condition.
[b]Represents the grand mean of 13 subjects.

results indicate that the /ba/ and /da/ anchors move the boundary toward the anchor, separately.

A 3×2 ANOVA—presentation (Ab versus AbVb versus AbVg)×sequence (baseline versus anchoring)—was conducted to determine whether the size of the anchoring effect under condition AbVg differed from that under the other acoustical or compatible audiovisual conditions. The main effects of presentation [$F(2,12)=6.40$, $p<0.0128$] and sequence [$F(1,6)=21.08$, $p<0.0037$] were significant but the interaction between presentation and sequence was not. Multiple comparisons by LSD indicated that the AbVg anchor induced more contrast than the Ab anchor ($p<0.0050$) and the AbVb anchor ($p<0.0233$).

Figure 1 compares the amount of anchoring effects under condition AbVg between those who showed the McGurk effect (nine subjects) and those who did not (four subjects). A *t*-test was conducted on those who showed the McGurk effect (ME) and those who did not (NME) to examine the shift of boundary toward /ba/. ME shows significant shift of boundary toward /ba/ [AbVb,$t(8)=5.53$, $p<0.0006$; AbVg,$t(8)=5.43$, $p<0.0006$], while NME shows no significant effects. In both groups, it was found that the AbVg anchor is stronger than the AbVb anchor. To confirm this finding, a three-way ANOVA—subjects (ME versus NME) ×anchor (AbVb versus AbVg)×sequence (baseline versus anchoring)—was conducted. The interaction of the three factors was not significant. The interactions between subjects and sequence and between anchor and sequence were significant [$F(1,11)=9.80$, $p<0.0096$; $F(1,11)=7.17$, $p<0.0215$]. The single effects of subjects indicated that ME showed more contrast than NME when the anchor was AbVg [$F(1,11)=7.67$, $p<0.0183$], but no significant effects were obtained when the anchor was AbVb.

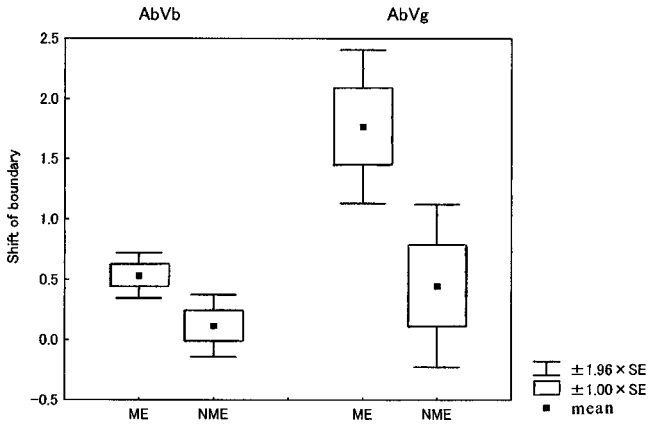

FIG. 1. The shifts of /ba/-/da/ boundary under the audiovisual compatible and incompatible anchoring conditions for the nine subjects who showed the McGurk effect (ME) and the four subjects who did not (NME).

Figure 2 shows the boundary shift produced by anchoring sequence under each of the seven anchoring conditions. Under conditions Ab, Ad, AbVb, and AdVd, the shift of category boundary was greater around the middle of the curves than around the ends. Under the AbVg condition, however, the shift of category boundary was great near to the /ba/ end of the continuum as well as around the middle of the continuum.

III. EXPERIMENT 2

Experiment 1 demonstrated that an audiovisual anchoring effect can be induced on a synthetic stop consonant continuum and that the AbVg anchor induced the greatest contrast among auditory and audiovisual anchors. Previous studies (Roberts and Summerfield, 1981; Saldaña and Rosenblum, 1994) did not find the strongest contrast effects when the adaptor was AbVg in the selective-adaptation experiment. There are, however, some differences between the cur-

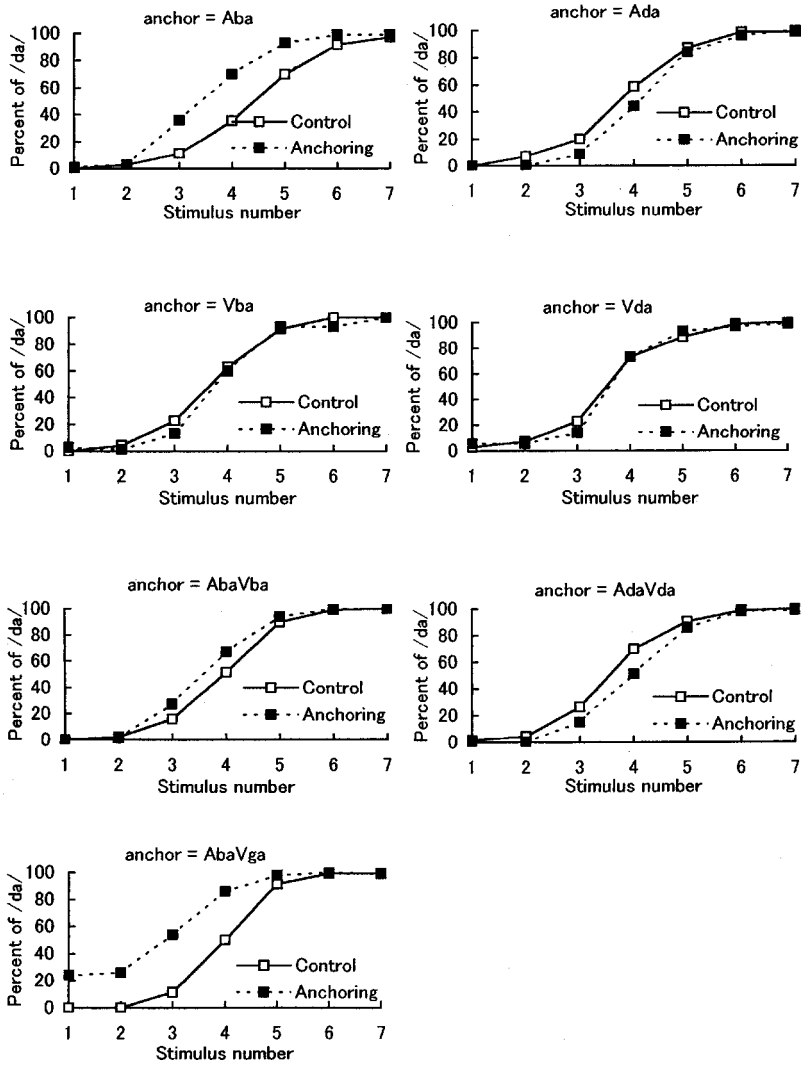

FIG. 2. The boundary shifts under the seven anchoring conditions.

rent and previous studies including specific stimuli and subjects. Some researchers reported that there are some differences between the McGurk effects experienced by Japanese and American subjects (Sekiyama and Tohkura, 1991). Sekiyama and Tohkura (1991) reported that the McGurk effect in the /a/-context is less easily induced in Japanese subjects when listening to very clear Japanese speech. The other studies on the Japanese McGurk effect in the /a/-context also reported fewer responses than that by McGurk and MacDonald (1976): about 25% of the responses for AbVg are fused response (Shigeno, 1999), about 35% (Shigeno, 2000), and about 57% (Burnham, 1998).

One might take the results in experiment 1 to be due to the linguistic-cultural differences. It thus would be necessary to conduct an adaptation experiment with the same stimuli and with the same subjects to confirm that there really is a difference between the anchoring and selective-adaptation effects. The aim of experiment 2 is to directly compare findings on the audiovisual anchoring and selective adaptation.

A. Method

1. Subjects

Eight graduate and undergraduate students of Aoyama Gakuin University participated in the experiment. All were native speakers of Japanese with no reported histories of speech or hearing disorders. None of them had participated in experiment 1.

2. Stimuli

The target stimuli were the seven synthetic syllables on the /ba/-/da/ continuum used in experiment 1. AbVb and AbVg were used as anchors in the anchoring paradigm and as adaptors in the selective-adaptation paradigm. Both of them had been used as anchors in experiment 1. In the anchoring paradigm, the other stimulus conditions were the same as experiment 1.

In the selective-adaptation paradigm, all testing was also done with purely acoustical target stimuli, although two adapting stimuli were audiovisual. Three color videotapes were prepared. The first one was the same tape that had been used in experiment 1 to establish baseline phoneme boundaries. It had no video signal and was simply an audio recording of seven target syllables, each of which occurred ten times in random order, with a 3-s intertrial interval. These sequences were used to establish baseline phoneme boundaries prior to each adaptation experiment. The second and the third tapes each consisted of 24 adaptation test trials. The first response of the first trial and the last response of the last

TABLE II. Comparison between anchoring and selective adaptation effects. Phonetic transcriptions of the subject's description of the anchor and adaptor used under condition AbVg are listed in the right-hand column, separately.

	Anchoring effects			Selective adaptation effects		
Subject	AbVb	AbVg		AbVb	AbVg	
KN	−0.34	2.27	[da][ra]	0.41	2.11	[da][ra][ba]
ST	1.97	1.91	[la][ga]	0.87	1.98	[la][da][ga][ba]
MT	0.15	1.59	[da][za]	1.02	1.19	[da][ba][la][sa]
MY	−0.11	[a]	[da]	0.70	0.28	[bara][sara]
YH	−0.77	2.25	[ra][da]	1.91	1.31	[za][ba][ra][da][wa][ga]
IM	0.01	1.00	[da][la]	1.56	1.25	[da][la]
SM	0.59	0.85	[da][ba]	2.65	−0.06	[da][ba][la][sa]
ME	0.79	[a]	[la][na]	0.86	−0.13	[la][da][ndha]
Mean	0.29	165[b]		1.25	0.99	

[a]The subjects showed too many ''da'' responses for the anchoring condition.
[b]Mean of six subjects.

trial were deleted from the data. The adapting stimulus on each tape was different but the format of each tape was the same. Each trial consisted of 50 repetitions of an audiovisual adapting stimulus. The SOA between each adaptor was 1 s. This sequence was followed after a 2-s pause by three purely acoustical test syllables drawn randomly from the test series with a SOA of 2.0 s. The first test trial on each tape included an additional 50 repetitions of the adapting stimulus (Roberts and Summerfield, 1981; Saldaña and Rosenblum, 1994).

3. Procedure

Stimuli were presented on a 29-in. TV monitor (SONY, KV-29DR1) at eye level in a quiet room. The viewing distance was 1.1 m, and the stimuli were played back on an 8-mm recorder (SONY, Video 8 PRO, CCD-V200). Auditory stimuli of about 75 dB (A) were emitted from the speakers attached to the monitor.

In the anchoring experiment, the procedure was identical to that of experiment 1. In the selective-adaptation experiment, each session consisted of a baseline sequence and a selective-adaptation sequence. Regarding the baseline sequence, subjects were instructed to listen to each stimulus syllable and to identify its initial consonant as /b/ or /d/ by writing ''B'' or ''D'' on a response sheet. Before the selective-adaptation sequence, subjects were instructed to watch the video monitor throughout the duration of each sequence of adaptors. Following the sequence of adaptors, they were required to listen to the three test syllables. They then had to record their responses and immediately return their gaze to the TV monitor. Ten judgments per target stimulus were obtained under every condition. At the end of each selective-adaptation session, the subjects were asked to write down the syllable(s) that they perceived when the adaptors were presented (Roberts and Summerfield, 1981).

Each subject took part in four separate experiments spread over two days with an interval of one week. On every day, subjects participated in the anchoring experiment first. After a break, they participated in the selective-adaptation experiment. Each experiment consisted of baseline and anchoring sessions or of baseline and selective-adaptation sessions.

Five subjects participated in the anchoring and selective-adaptation experiments of the AbVb condition on the first day and in those of the AbVg condition one week later. The other three subjects participated in the anchoring and selective-adaptation experiments of AbVg condition first and a week later in those of the AbVb condition.

B. Results and discussion

The mean and standard deviation of the results from each subject were obtained by the least square method with Müller–Urban weight. The difference between the means obtained from the baseline and the anchoring/adaptation sequences can be regarded as a measure of the anchoring/adaptation effect.

Table II lists the shift of boundary under anchoring and selective-adaptation effects. The identification of anchors/adaptors was analyzed first to see whether the McGurk effect occurred when the anchor or adaptor was AbVg. Subjects identified AbVg as various consonants, including the dental consonants /da/, /ra/, /la/, /sa/, /gwa/, /dra/, and so on instead of or besides /ba/. It shows that the /ba/-sound (the auditory component of AbVg) was influenced by the visual synchronized /ga/ presentation in the perception of all subjects.

The averaged-difference scores were examined first by using two-tailed *t*-tests to determine whether or not anchoring or selective-adaptation effect occurred. The audiovisual adaptor with compatible acoustical and optical components (AbVb) produced significant contrast effects [$t(7) = 4.76$, $p < 0.0021$], but the anchor AbVb did not. The discrepant audiovisual anchor/adaptor (AbVg) produced a significant shift in subjects' phoneme boundaries toward the /ba/ end of the auditory continuum (in anchoring the data of subjects MY and ME were dropped, because they showed too much contrast) [anchoring: $t(5) = 6.59$, $p < 0.0012$; selective adaptation: $t(7) = 3.22$, $p < 0.0146$]. The sizes of the boundary shifts caused by the audiovisual anchoring were very similar to those obtained in experiment 1, although AbVb did not produce the significant contrast in experiment 2.

Figure 3 shows the boundary shift under each of the two anchoring or the two selective-adaptation conditions. To determine how anchoring and selective adaptation modified the

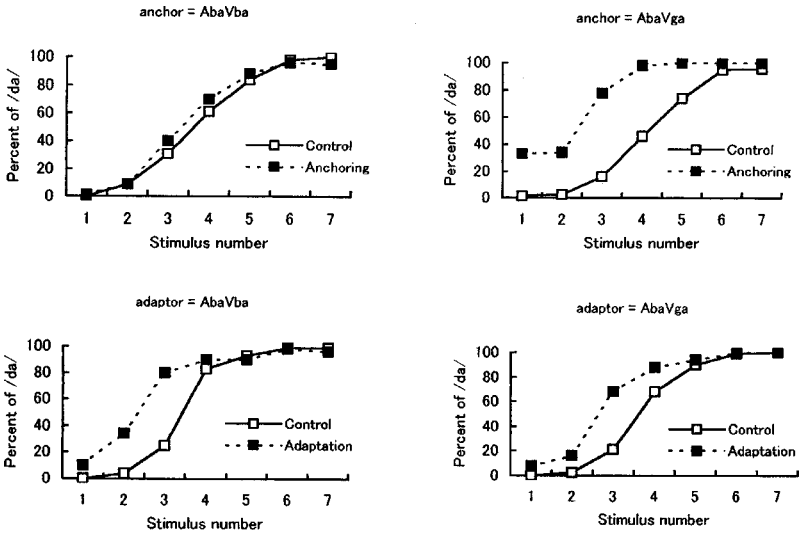

FIG. 3. The boundary shifts under the AbVb and AbVg anchoring/selective-adaptation conditions.

boundaries systematically, we evaluated the data obtained under anchoring and adaptation by using a repeated measures three-way within-subject ANOVA—context (AbVb versus AbVg)×paradigm (anchoring versus adaptation) ×sequence (baseline versus test). The interactions were not significant. The main effect of paradigm [$F(1,5)=16.28$, $p<0.0100$] and that of sequence [$F(1,5)=107.92$, $p<0.0001$] were significant but that of context was not.

To examine each of anchoring and selective adaptation more precisely, a 2×2 ANOVA—context (AbVb versus AbVg)×sequence (baseline versus test)—was conducted, separately. As for anchoring, the interaction between context and sequence was significant [$F(1,5)=7.42$, $p<0.0416$]. Then a single effect of context was calculated. The shift of boundary induced by the AbVg anchor was greater than that by the AbVb anchor [$F(1,5)=6.70$, $p<0.0489$]. Meanwhile, as for selective adaptation, the interaction between context and sequence was not significant. The main effect of context and that of sequence were significant [$F(1,7)=10.29$, $p<0.0149$; $F(1,7)=49.01$, $p<0.0002$], although there was no significant effect of context in the baseline or in the test sequence. The current results from the Japanese selective adaptation were very similar to those from the previous research (e.g., Roberts and Summerfield, 1981) and support the arguments that phonetic categorization follows audiovisual integration in speech perception.

To compare the size of effects when the anchor or the adaptor was AbVb, a 2×2 ANOVA—paradigm (anchoring versus selective adaptation)×sequence (baseline versus test) was conducted. The interaction between paradigm and sequence was not significant; the main effect of paradigm [$F(1,7)=11.91$, $p<0.007$] and that of sequence [$F(1,7)=16.58$, $p<0.0047$] were significant. The results mean that the category boundary was shifted toward /ba/ by the AbVb anchor and by the AbVb adaptor, but that this auditory-based contrast effect was stronger in selective adaptation than that in anchoring. A 2×2 ANOVA—paradigm (anchoring versus adaptation)×sequence (baseline versus test)—was conducted in the case of the discrepant audiovisual syllable (AbVg). The interaction was not significant. The main effect of sequence was significant [$F(1,5)=30.71$, $p<0.0026$] but that of paradigm was not. The results mean that the category boundary was shifted toward /ba/ by AbVg, and that the size of shift was not different between anchoring and selective adaptation.

IV. GENERAL DISCUSSION

A. Comparison between the results of anchoring and those of selective adaptation

The present results obtained from the anchoring and the selective-adaptation experiments indicate that the two effects have some differences as well as similarities. The similarities are the following points. (1) The category boundary of the target stimuli moved toward the anchor or the adaptor so as to produce contrast. (2) An auditory anchor or adaptor was very effective, while an optical one was not. (3) The discrepant audiovisual syllable (AbVg) moved the category boundary toward /ba/ and the size of the auditory-based contrast caused by AbVg was not different between anchoring and selective adaptation. The differences are the following points. (1) The compatible audiovisual syllable (AbVb) induced more contrast in selective adaptation than in anchoring. (2) In anchoring the discrepant audiovisual syllable AbVg induced more auditory-based contrast than auditory (Ab, Ad) and compatible audiovisual ones (AbVb, AdVd), although in selective adaptation AbVg did not induce more auditory-based contrast than AbVb. These differences between anchoring and selective-adaptation effects have not been found so far.

B. Are the effects and mechanisms of anchoring and selective adaptation equivalent?

The above results lead to the conclusion that the perceptual mechanisms of the two psychological effects are similar but not equivalent. Simon and Studdert-Kennedy (1978) conducted several auditory experiments on anchoring and selective adaptation and examined their perceptual processes in the light of various psychological hypotheses: adaptation level theory (Helson, 1964, 1971), frequency analysis (e.g.,

Parducci, 1965, 1974), response organization (Studdert-Kennedy, 1976), perceptual sharpening (Cole *et al.*, 1975), anchor contrast (e.g., Blumstein *et al.*, 1977), and fatigue (e.g., Warren and Gregory, 1958). They concluded that anchoring and selective adaptation are in principle equivalent and that the main factors in speech-adaptation effects are due to peripheral fatigue and central auditory contrast. They also argued that although the energy of anchor is different from that of adaptor, ''fatigue'' is more likely to occur under adaptation than under anchoring. It could be argued that the above hypothesis is right if one just looks at the results that Ab or AbVb caused a greater contrast effect in selective adaptation than in anchoring. The present results support the idea that selective-adaptation effect is due to peripheral fatigue, but do not support the idea that the effects and mechanisms of the two paradigms are in principle equivalent and that ''fatigue'' occurs in the anchoring experiments. In spite of the fact that the anchor AbVg was presented no less frequently than the anchor AbVb, the amount of auditory-based contrast caused by the anchor AbVg is greater than that caused by the anchor AbVb. Peripheral fatigue thus cannot explain the difference in the contrast.

Sawusch and Nusbaum (1979) conducted the acoustic anchoring experiments using synthetic vowels and found the shift of phoneme boundary very similar to that obtained from the previous acoustic selective-adaptation experiments. They suggested that neither feature-detector fatigue nor response-criterion changes could adequately account for the adaptation or anchoring effects in the perception of vowels. They argued that auditory contrast explanation involving auditory memory fit the experimental data on anchoring. They noted that ''any residual trace of previous stimuli, in auditory memory, is likely to contain more information about the anchoring stimulus than about other stimuli. If identification of each new stimulus is made with reference (contrast) to this memory trace, as well as to some long-term memory prototypes for the relevant categories, then the anchoring conditions should produce changes in identification, especially for otherwise ambiguous (boundary) stimuli'' (p. 301). If ''fatigue'' cannot explain the audiovisual anchoring, the concept of auditory memory might be very useful.

C. How does audiovisual anchoring occur?

The previous hypotheses on the mechanisms of anchoring were just derived from the results of the auditory anchoring and selective-adaptation experiments. We similarly found that the selective-adaptation effect was greater than the anchoring effect when the anchor or the adaptor was AbVb. However, the most important result obtained from the current experiments is the fact that the discrepant audiovisual anchor AbVg was more effective than the auditory or the compatible audiovisual anchor.

According to the present findings, the process of auditory and audiovisual anchoring can be explained as follows. When an auditory-alone anchor is presented, its position on the stimulus continuum is first mapped onto the sensation continuum. The output from the mapping is stored in an immediate memory (sensory memory) (Pisoni, 1975). The information stored in the sensory memory lasts for a very short time. And its output is mapped onto the auditory continuum and is stored in the precategorical short-term memory (auditory memory). Information stored in the auditory memory is liable to lapse but lasts longer than that in the sensory memory. Phonetic judgments are therefore made with reference to this memory trace as well as to some long-term memory prototypes for relevant categories (Sawusch and Nusbaum, 1979; Shigeno and Fujisaki, 1979). The new frame of reference (or auditory ground) including the anchor is established and the phoneme boundary moves toward the anchor. Then the target is presented. Its sensory memory and auditory memory are stored, separately. The target is identified as one of the categories in the new frame of reference, which includes the anchor and has been shifted by the anchor. As a result, the identification of target changes so as to show contrast. Thus, the /ba/ anchor, for example, causes many /da/ responses.

When a discrepant audiovisual anchor (AbVg) is presented, the position of the typical /ba/-sound (auditory component) of AbVg on the stimulus continuum is first mapped onto the sensation continuum. The output from the mapping is stored in the sensory memory. And its output is mapped onto the auditory continuum and is stored in the auditory memory. This mapping is influenced by the visual information (visual component) of AbVg. Then phonetic judgments are made with reference to this memory trace. Subjects are apt to identify AbVg as ''da'' as a result of the influence of its visual component (McGurk and MacDonald, 1976). Adding to the auditory contrast, the fact that AbVg has just been identified as /da/ makes the frame of reference move toward /ba/ considerably so that the anchor AbVg may belong to the /da/-category. Then the target is presented. The target is identified as one of the categories in the new frame of reference, which includes the anchor and has been shifted by the anchor considerably. The identification of the target thus changes so as to show auditory-based contrast. Even if the target near to a typical /ba/ sound is presented, the subjects easily judge it to be /da/, because the position on the stimulus continuum of any target stimulus is nearer /da/ than that of AbVg (its auditory component is a typical /ba/). This hypothesis is confirmed by the fact that the /da/ responses increased near the /ba/ end of the continuum as well as around its middle (Figs. 2 and 3).

According to Simon and Studdert-Kennedy (1978), the central assumption of all psychophysical accounts of anchoring or adaptation is that the frame of reference is established by the experiment itself, although this assumption may be valid for judgments of arbitrarily labeled dimensions such as pitch and does not hold for judgments of consonants. However, Shigeno (1999) reported that when a discrepant audiovisual anchor (AbVg) is presented, its timbre is judged to be different from the timbre of the original sound (the auditory component of AbVg: a typical /ba/ sound) because of the McGurk effect. Shigeno (1999) suggested that judgments of consonants under the visual influence do not have a firm perceptual structure.

Roberts and Summerfield (1981) noted, ''Rather than phonetic categorization occurring after the confluence of continuous and essentially analog information from vision

and audition, independent analyses would generate a phonetic feature description of the input to each modality. Summation rules would then determine which combination of feature should determine the percept'' (p. 313). Although the current results support the idea that phonetic categorization follows audio-visual integration, they also suggest that the mapping onto the auditory (or psychological) continuum is influenced by the visual information. Shigeno (1999) noted, ''A speaker's preparatory movements of articulation play an important role in helping subjects construct a perceptual set. This would help them perceive the audio-visual stimulus. In fact, a bilabial articulation is easily distinguished from alveolar or velar articulation by observing closed lips. Thus, in the case of the /b/-vowel syllable we can easily anticipate that a speaker is ready to utter a syllable starting with /b/ before seeing the actual utterance'' (p. 166). This suggestion might be also supported by the research, which indicated the robustness of the McGurk effect. For example, audiovisual integration appears to be able to resist temporal discrepancies (McGrath and Summerfield, 1985; Smeele *et al.*, 1992). It might be the most important role for the visual information to give a perceptual set to subjects.

Sawusch and Jusczyk (1981) suggested that contrast effects operate at a level of processing based on the ''perceptual similarity'' between the context and the test item. Roberts and Summerfield (1981) concluded that adaptation effects cannot be attributed to the perceived phonetic similarity between the adaptor and test syllables. The current study also reveals that it is not the phonetic similarity but the perceptual (auditory) similarity between the anchor and test syllables that is an essential factor in the anchoring effects.

V. CONCLUSIONS

The results of the current study suggest that effects of anchoring and of selective adaptation are caused by different mechanisms and that the anchoring effects are not produced by peripheral fatigue but by the shift of the frame of reference.

ACKNOWLEDGMENTS

This research was supported by Grant-in Aid for Scientific Research on Priority Areas (No. 08202212) and Research (c) (No. 08610093) from the Japanese Ministry of Education, Science, and Culture.

Blumstein, S. E., Stevens, K. N., and Nigro, G. N. (**1977**). ''Property detectors for bursts and transitions in speech perception,'' J. Acoust. Soc. Am. **61**, 1301–1313.

Burnham, D. (**1998**). ''Language specificity in the development of auditory-visual speech perception,'' in *Hearing by Eye II*, edited by R. Campbell, B. Dodd, and D. Burnham (Psychology, Hove, UK), pp. 27–60.

Cole, R. A., Cooper, W. E., Singer, J., and Allard, F. (**1975**). ''Selective adaptation of English consonants using real speech,'' Percept. Psychophys. **18**, 227–244.

Diehl, R. L., Lang, M., and Parker, E. M. (**1980**). ''A further parallel between selective adaptation and contrast,'' J. Exp. Psychol. Hum. Percept. Perform. **6**, 24–44.

Helson, H. (**1964**). *Adaptation-Level Theory: An Experimental and Systematic Approach to Behavior* (Harper, New York).

Helson, H. (**1971**). ''Adaptation-level theory: 1970 and after,'' in *Adaptation Level Theory*, edited by M. H. Appley (Academic, New York), pp. 5–17.

McGrath, M., and Summerfield, Q. (**1985**). ''Intermodal timing relations and audio-visual speech recognition by normal-hearing adults,'' J. Acoust. Soc. Am. **77**, 678–685.

McGurk, H., and MacDonald, J. (**1976**). ''Hearing lips and seeing voices,'' Nature (London) **264**, 746–748.

Parducci, A. (**1965**). ''Category judgment: A range-frequency model,'' Psychol. Rev. **72**, 407–418.

Parducci, A. (**1974**). ''Contextual effects: A range-frequency analysis,'' in *Handbook of Perception 2*, edited by E. C. Carterette and M. P. Friedman (Academic, New York), pp. 127–141.

Pisoni, D. B. (**1975**). ''Auditory short-term memory and vowel perception,'' Memory Cogn. **3**, 7–18.

Repp, B. H. (**1982**). ''Phonetic trading relations and context effects: New experimental evidence for a speech mode of perception,'' Psychol. Bull. **92**, 81–110.

Roberts, M., and Summerfield, Q. (**1981**). ''Audiovisual presentation demonstrates that selective adaptation in speech perception is purely auditory,'' Percept. Psychophys. **30**, 309–314.

Saldaña, H. M., and Rosenblum, L. D. (**1994**). ''Selective adaptation in speech perception using a compelling audiovisual adaptor,'' J. Acoust. Soc. Am. **95**, 3658–3661.

Sawusch, J. R., and Jusczyk, P. (**1981**). ''Adaptation and contrast in the perception of voicing,'' J. Exp. Psychol. Hum. Percept. Perform. **7**, 408–421.

Sawusch, J. R., and Nusbaum, H. C. (**1979**). ''Contextual effects in vowel perception I: Anchor-induced contrast effects,'' Percept. Psychophys. **25**, 292–302.

Sekiyama, K., and Tohkura, Y. (**1991**). ''McGurk effect in non-English listeners: Few visual effects for Japanese subjects hearing Japanese syllables of high auditory intelligibility,'' J. Acoust. Soc. Am. **90**, 1797–1805.

Shigeno, S. (**1999**). ''The use of short-term memory in the discrimination of visually-influenced CV-syllables,'' Jpn. J. Psychonom. Sci. **18**, 62–72.

Shigeno, S. (**2000**). ''Influence of vowel context on the audio-visual speech perception of voiced stop consonants,'' Jpn. Psychol. Res. **42**, 155–167.

Shigeno, S., and Fujisaki, H. (**1979**). ''Effect of a preceding anchor upon the categorical judgment of speech and nonspeech stimuli,'' Jpn. Psychol. Res. **21**, 165–173.

Simon, H., and Studdert-Kennedy, M. (**1978**). ''Selective anchoring and adaptation of phonetic and nonphonetic continua,'' J. Acoust. Soc. Am. **64**, 1338–1357.

Smeele, P. M. T., Sittig, A. C., and van Heuven, V. J. (**1992**). ''Intelligibility of audio-visually desynchronized speech: Asymmetrical effect of phoneme position,'' Proc. ICSLP, pp. 65–68.

Studdert-Kennedy, M. (**1976**). ''Stimulus range as a determinant of phoneme boundaries along synthetic continua,'' J. Acoust. Soc. Am. Suppl. 1 **60**, S92.

Thompson, C. L., and Hollien, H. (**1970**). ''Some contextual effects on the perception of synthetic vowels,'' Lang Speech **13**, 1–13.

Warren, R. M., and Gregory, R. L. (**1958**). ''An auditory analogue of the visual reversible figure,'' Am. J. Psychol. **71**, 612–613.

Quantitative assessment of second language learners' fluency: Comparisons between read and spontaneous speech

Catia Cucchiarini,[a] Helmer Strik, and Lou Boves
A²RT, Department of Language and Speech, University of Nijmegen, P.O. Box 9103, 6500 HD Nijmegen, The Netherlands

(Received 2 February 2001; revised 23 October 2001; accepted 15 February 2002)

This paper describes two experiments aimed at exploring the relationship between objective properties of speech and perceived fluency in read and spontaneous speech. The aim is to determine whether such quantitative measures can be used to develop objective fluency tests. Fragments of read speech (Experiment 1) of 60 non-native speakers of Dutch and of spontaneous speech (Experiment 2) of another group of 57 non-native speakers of Dutch were scored for fluency by human raters and were analyzed by means of a continuous speech recognizer to calculate a number of objective measures of speech quality known to be related to perceived fluency. The results show that the objective measures investigated in this study can be employed to predict fluency ratings, but the predictive power of such measures is stronger for read speech than for spontaneous speech. Moreover, the adequacy of the variables to be employed appears to be dependent on the specific type of speech material investigated and the specific task performed by the speaker. © *2002 Acoustical Society of America.* [DOI: 10.1121/1.1471894]

PACS numbers: 43.71.Es, 43.71.Gv, 43.71.Hw, 43.72.Ne [DOS]

I. INTRODUCTION

Oral fluency is viewed as an important characteristic of second language speech, which explains why it is often the object of evaluation in testing second language skills (Riggenbach, 1991; Freed, 1995). In spite of the wide use that is made of this notion with respect to second language speech, there is no generally agreed definition of fluency and this term has been used to indicate different constructs. In everyday language use, fluency is often considered as a synonym of ''overall language performance.'' In this interpretation native-like performance is viewed as the final goal. Brumfit (1984, p. 57), on the other hand, defines fluency as ''the maximally effective operation of the language system so far acquired by the student.'' In this definition of fluency, native-speaker-like performance does not constitute the target to be achieved (Brumfit, 1984, p. 56). A different, more restricted definition of fluency is the one that refers to the temporal aspect of speech (Nation, 1989; Lennon, 1990; Riggenbach, 1991; Schmidt, 1992; Freed, 1995; Towel *et al.*, 1996) and puts emphasis on ''native-like rapidity'' (Lennon, 1990, p. 390). According to this interpretation, the goal in second language learning would be to produce ''speech at the tempo of native speakers, unimpeded by silent pauses and hesitations, filled pauses...self-corrections, repetitions false starts and the like'' (Lennon, 1990, p. 390). However, various quantitative studies have revealed that even native speech, far from being always smooth and continuous, exhibits many hesitations and repairs (Raupach, 1983; Lennon, 1990; Riggenbach, 1991).

With a view to gaining more insight into the factors that contribute to perceived fluency, attempts have been made to try to define fluency in terms of objective properties of speech (Lennon, 1990; Riggenbach, 1991; Freed, 1995). These studies have adopted a dual approach in which listeners' evaluations of speech, in this case perceived fluency scores, are related to objective measures calculated for the same speech. This type of approach, which proved particularly useful to gain insight into the dimensions underlying the listeners' evaluations, has a long tradition in phonetic research and has been used previously in other domains such as the evaluation of voice (Laver, 1980), running speech (Boves, 1984), vocal expressions of emotions (Van Bezooijen, 1984), and non-native pronunciation (Neumeyer *et al.*, 1996). Another important aspect of fluency studies based on this method is that they may contribute to developing more objective and, possibly, less labor intensive tests of second language fluency (see, for instance, Townshend *et al.*, 1998). With the growing numbers of immigrants who have to learn other languages, the practical advantages of objective fluency measures are obvious.

In Cucchiarini *et al.* (2000) a study was described in which the dual approach was adopted to gain insight into the temporal definition of fluency. That study differed from previous ones in two important respects. First, the objective measures, which were calculated manually in previous studies (Lennon, 1990; Riggenbach, 1991; Freed, 1995), were calculated automatically with the help of a continuous speech recognizer (CSR), which has the advantage that huge amounts of data can be analyzed in relatively short time and in a very consistent manner. Second, instead of using spontaneous speech, read speech was used, so that the raters would not be distracted by differences in vocabulary and syntax-related parameters, which are known to affect fluency ratings (Riggenbach, 1991; Freed, 1995). However, our idea was to apply this approach to spontaneous speech too, if it turned out to be feasible for read speech.

The experiment reported in Cucchiarini *et al.* (2000)

[a]Electronic mail: c.cucchiarini@let.kun.nl

 0001-4966/2002/111(6)/2862/12/$19.00

produced interesting results in two respects. First, the results showed that the expert ratings of fluency in read speech were reliable (Cronbachs' α varied between 0.90 and 0.96), which contrasted with the much lower reliability coefficients reported in previous studies (Riggenbach, 1991; Freed, 1995), but seemed plausible given that those studies concerned spontaneous speech. Second, very high correlations were found between the expert fluency ratings and the objective measures of fluency: five objective measures showed correlations with the fluency scores with magnitudes between 0.77 and 0.91. Further analyses revealed that two factors are important for perceived fluency in read speech: the rate at which speakers articulate the sounds and the number of pauses they make. Rate of speech appears to be an excellent predictor of perceived fluency because it incorporates these two aspects.

The results of this previous study on read speech also raised some questions, the most important being: would these results hold for spontaneous speech too? In particular, it seemed interesting to determine whether the quantitative measures that were found to affect perceived fluency in read speech would be equally important for perceived fluency in spontaneous speech and/or, the other way round, whether there are measures that are suitable for spontaneous speech, but not for read speech. In an attempt to find answers to these questions, an experiment with spontaneous speech was carried out in which the dual approach was used to investigate the same temporal notion of fluency.

As explained previously, the importance of this type of research is not only related to the possibility of getting more insight into the relationship between perceived fluency and temporal characteristics of speech, but also to the potential that this kind of research might have for the development of objective testing instruments for fluency assessment, especially in the context of second language teaching and testing. Against this background it seemed more advantageous to use an existing test of second language proficiency rather than collecting speech material especially for this experiment. In this way the material under study would be less of the ''laboratory'' type and would be more similar to what is generally found in the ''field.'' On the one hand, this might have the disadvantage that the experimenter cannot control all aspects of the experiment. On the other hand, it has the considerable advantage that in this way external validity is guaranteed. Since it is clear that the importance of external validity cannot be overestimated in these kinds of studies and that the advantages of using a real test evaluated by real raters outweigh the disadvantages of using a less elegant experimental design, it was decided to use an already existing test of second language proficiency that would be suited for our purpose.

The test that was eventually selected for this experiment is the *Profieltoets*. This test was developed by the Dutch National Institute for Educational Measurement (Cito) and is normally administered to immigrants who, within the framework of the Newcomer Integration Act, are obliged to follow a Dutch language course upon arrival in The Netherlands. In general, newcomers take the *Profieltoets* after they have followed about 500–600 h of lessons in the Dutch language. In this test the four skills speaking, listening, reading, and writing are tested. For this experiment a subtest corresponding to the speaking test was used. This test is administered in a language lab to a group of several candidates simultaneously. The candidates have to answer questions which elicit unprepared answers. The speech can therefore be classified as extemporaneous, spontaneous speech. In other words, this experiment does not concern speech that was especially elicited for the purpose of the experiment, but speech that subjects produced while they were taking a real examination.

As in our previous study, the dual approach was adopted in which the speech material was evaluated by a group of raters and by an automatic speech recognizer which was used to calculate a number of objective measures that are known to be related to perceived fluency. The aim of the present paper is to explore the relationship between these objective properties of speech and perceived fluency in read and spontaneous speech, with a view to determining whether such quantitative measures can be used to develop objective fluency tests. To pursue this aim, the read speech data from our previous experiment were compared with the spontaneous speech data from the present one. In the read speech experiment the speech of 20 native and 60 non-native speakers of Dutch was scored for fluency by nine experts and was then analyzed by means of a CSR. Since in the spontaneous speech experiment only non-natives were involved (recall that these data stemmed from a real second language proficiency test), from the read speech experiment only the data pertaining to the 60 non-native speakers were used. These two experiments will be referred to as Experiment 1 (read speech) and Experiment 2 (spontaneous speech). Although Experiment 1 has already been presented in detail in Cucchiarini *et al.* (2000), the data concerning the non-native speakers were not presented as explicitly as they are in this paper. In any case, here we will limit ourselves to providing only the Experiment 1 data and details that are necessary to make comparisons between read speech (Experiment 1) and spontaneous speech (Experiment 2) of non-native speakers of Dutch.

II. METHOD

A. Speakers

1. Experiment 1

The data presented here stem from 60 non-native speakers (NNS) who all lived in The Netherlands and were attending or had attended courses in Dutch as a second language (DSL). They were selected to obtain a group that was sufficiently varied with respect to mother tongue, proficiency level, and gender. Three proficiency levels were distinguished: PL1: beginner, PL2: intermediate, and PL3: advanced. For more detailed information on the composition of this sample, see Cucchiarini *et al.* (2000).

2. Experiment 2

The speakers involved in this experiment constitute a subgroup of the candidates who took part in the test *Profieltoets* in June 1998. In this investigation the answers of 60 subjects of two different proficiency levels were analyzed: a

lower proficiency group at the beginner level (BL) and a higher proficiency group at the intermediate level (IL). These two proficiency levels roughly correspond to the first two levels (PL1 and PL2) in Experiment 1. Cito workers selected for us a subgroup of 30 speakers at the beginner level and a subgroup of 30 speakers at the intermediate level. In both groups the speakers varied with respect to gender and mother tongue.

B. Speech material

1. Experiment 1

Each speaker read two different sets of five phonetically rich sentences designated set 1 and set 2, respectively. The only difference between sets 1 and 2 is that they contain different sentences. However each group of five sentences contains all phonemes of Dutch at least once, while more common phonemes appear more than once. Since the average duration of each set was 30 s, almost 1 min of speech per speaker was available. The sentences were printed on paper together with the instructions and were read by the speakers over the telephone. The subjects had not explicitly been encouraged to rehearse before reading, but since they had received the material beforehand, they had this possibility. They also had the possibility of restarting the recording session if they felt something had gone wrong. However, this happened only in one case.

As the recording system was connected to an ISDN line, the input signals consisted of 8 kHz, 8 bit, A-law coded samples. Almost all subjects called from their homes, while two called from the first author's office. No provisions were made to control background noise; consequently, the acoustic quality of the recordings varied considerably.

2. Experiment 2

The speech material used in this experiment consisted of the answers given by the candidates mentioned in Sec. II A 2 to part of the items which constitute the *Profieltoets*. This test is administered to candidates at the beginner and intermediate proficiency levels and is therefore available in two different versions corresponding to the two groups, BL and IL. For this experiment eight items were selected for each version of the test. The items differed for the two proficiency groups, because in this case we have less influence on the selection of the material. This is a consequence of choosing an existing test. An important requirement in selecting the items was that they had to elicit relatively long answers, which is a necessary condition for calculating fluency measures.

For the IL group the so-called long tasks were chosen, in which the candidates have 30 s to answer each question. In these items the candidate has to answer questions by choosing from among various possibilities and has to explain why he/she made that choice. In other words, the candidate, when answering, has to reflect to find good motivations for his/her choice.

The BL version of the test contains only the short tasks, in which the subjects have 15 s at their disposal to answer each question. In general, in these items a given situation is presented and the candidate has to indicate what he/she would say in that context. From these tasks we chose those for which, given the nature of the questions, reasonably long answers of at least a few words can be expected. Effectively, the BL subjects talked for about 70 s on average, while for the IL subjects the average was 180 s.

The fact that the BL items elicit rather straightforward responses, whereas the IL items seem to require more cognitive effort could have an impact on the fluency scores, as has been reported by Grosjean (1980) and Bortfeld *et al.* (1999). In particular, Grosjean (1980, pp. 42–43) has shown that more cognitively demanding tasks will lead to a lower speech rate, which, in turn, is accounted for by a lower articulation rate, but especially by a lower phonation/time ratio, shorter runs, and longer pauses.

Finally, it should be observed that the speech samples thus obtained are different for the various speakers, an obvious implication of using extemporaneous speech, whereas in Experiment 1 all speakers produced the same sentences, which is easy to achieve with read speech.

The speech material of Experiment 2 was recorded in language laboratories on audio cassettes and was subsequently digitized. In this case the recording conditions were rather adverse: the subjects, who were taking an exam, were all sitting in one room and started to answer the questions almost at the same time, so that there was a lot of background speech.

C. Raters

1. Experiment 1

Since previous studies had revealed that expert fluency ratings displayed low reliability (Lennon, 1990; Riggenbach, 1991; Freed, 1995), in this experiment it was decided to ask multiple groups of experts to evaluate the speech material: a group of three phoneticians (PH) and two groups of three speech therapists (ST1 and ST2). The phoneticians were chosen for obvious reasons, whereas the speech therapists were chosen because their expertise is usually invoked when learners of Dutch exhibit pronunciation problems, including all fluency-related temporal phenomena. As reported in Cucchiarini *et al.* (2000), reliability appeared to be very high for all three groups of raters.

2. Experiment 2

In the present experiment ten teachers of Dutch as a second language were employed, because they are normally used as raters for this kind of examination by Cito. To be able to work as raters for Cito these teachers have to take a three-day course which they have to conclude with an examination. Furthermore, their performance as raters in different kinds of tests administered by Cito is regularly checked and Cito workers keep track of each rater's performance by calculating overall indices of reliability that can be made available if required.

The scoring sessions were organized by Cito according to the procedure that is usually followed for the *Profieltoets*. One group of five teachers, designated as raters for the beginning level (RBL), evaluated the BL speakers and another group of five teachers designated as raters for the intermedi-

ate level (RIL), evaluated the IL speakers. There was no overlap of speakers between the two rater groups, which means that there was no subgroup of speakers that was evaluated by both rater groups.

D. Fluency ratings

1. Experiment 1

The speech material was transferred from disk to DAT tape adopting different random orders for the different raters. All raters listened to the speech material and evaluated perceived fluency individually. This was done to enhance flexibility (each rater could thus carry out the task at the most suitable time) and to avoid raters influencing each other.

Each rater received two tapes which contained the set 1 and the set 2 sentences, respectively. The material was scored on a scale ranging from 1 to 10. The scores were not assigned to each individual sentence, but to each set of five phonetically rich sentences. No specific instructions were given as to how to assess fluency. However, before starting with the evaluation proper, each rater listened to five sets of sentences spoken by five different speakers, which were intended to familiarize the raters with the task they had to carry out and to help them anchor their ratings. As a matter of fact, the five speakers were chosen so as to give an indication of the range that the raters could possibly expect. Since it was not possible to have all raters score all speakers (it would cost too much time and it would be too tiring for the raters) the speakers were proportionally assigned to the three raters in each group. However, part of the material (overlap material) was scored by all three raters in one group so as to allow reliability checks. For further details on this point, see Cucchiarini *et al.* (2000).

The scores assigned to the two sets of sentences by each speaker were subsequently averaged to obtain one score for each speaker. The scores assigned by the three raters were then combined to compute correlations with the machine scores. This way 60 human-assigned fluency scores were obtained, which were subsequently compared with the various quantitative measures.

2. Experiment 2

All raters listened to the speech material on audio cassettes and assigned scores individually. The raters first scored each speaker on the *Profieltoets* as they normally do. Subsequently, they were asked to score the eight selected items on fluency. The raters could listen to the speech fragments as often as they wanted. They were asked to score fluency on a scale ranging from 1 to 10. Each rater assigned one fluency score per set of eight items so that for each speaker in this experiment five fluency scores assigned by five raters were obtained. As in the experiment in Cucchiarini *et al.* (2000), no specific instructions were given for fluency assessment, but, as mentioned previously, these raters had all received a three-day training before starting to work as raters for Cito.

3. Experiment 1 versus Experiment 2

Two important differences between the two experiments should be mentioned. First, in Experiment 2 the two groups of speakers, BL and IL, were assigned to two different groups of raters, RBL and RIL, whereas in Experiment 1 each group of three raters evaluated all 60 speakers. This point should be borne in mind because it has consequences for the analyses that can be carried out and for the results of these experiments.

Second, the phoneticians and speech therapists involved in Experiment 1 simply judged the speech of a number of speakers without having information on the proficiency level of each speaker, except the cues that they could derive from the speech itself. The language teachers in Experiment 2, on the other hand, were judging candidates in an examination and therefore knew whether a speaker was at the beginner or intermediate level. As a consequence, they may have judged fluency in relation to each speaker's assumed proficiency level, so that the same score, say eight, would not have the same meaning in the two groups, but would represent a higher fluency level in the IL group than in the BL group.

E. Objective assessment of fluency

This part of the analysis procedure was the same for Experiments 1 and 2. All speech material was orthographically transcribed by SPEX (http://www.spex.nl/), an expertise center that specializes in database construction and validation. The material was also checked on quality both by SPEX and the first author (C.C.) before being used for the experiment. The recordings of three speakers in Experiment 2 could not be used because their quality was so poor that they were not even scored by the raters. This way a total of 28 BL speakers and 29 IL speakers was obtained.

In transcribing the material, special symbols were used for four categories of nonspeech acoustic events (as is usually done at SPEX):

(1) filled pauses: uh, er, mm, etc.
(2) speaker noise: lip smack, throat clear, tongue click, etc.
(3) intermittent noise: noise that occurs incidentally during the call such as door slam and paper rustle.
(4) stationary noise: continuous background noise that has a rather stable amplitude spectrum such as road noise or channel noise.

Repetitions, restarts, and repairs were transcribed exactly as they were pronounced and were indicated by a special disfluency symbol so that they could be counted automatically.

1. The automatic speech recognizer

To calculate the quantitative measures, the continuous speech recognizer (CSR) described in Strik *et al.* (1997) was used. Feature extraction is done every 10 ms for frames with a width of 16 ms. The first step in feature analysis is a fast Fourier transform to calculate the spectrum. The energy in 14 mel-scaled filter bands between 350 and 3400 Hz is then calculated. Next, a discrete cosine transformation is applied to the log filter band coefficients. The final processing stage is a running cepstral mean subtraction. Besides 14 cepstral coefficients (c0–c13), 14 delta coefficients are also used. This makes for a total of 28 feature coefficients.

The CSR uses acoustic models [39 context-independent hidden Markov models (HMMs)], language models (unigram and bigram), and a lexicon. The lexicon contains orthographic and phonemic transcriptions of the words to be recognized. The continuous density HMMs consist of three parts of two identical states, one of which can be skipped. One HMM was trained for nonspeech sounds and one for silence. For each of the phonemes /l/ and /r/ two models were trained, since a distinction was made between prevocalic (/l/ and /r/) and postvocalic position (/L/ and /R/). For each of the other 33 phonemes of Dutch, one HMM was trained.

The HMMs were trained by using part of the Polyphone corpus (Den Os *et al.*, 1995). This corpus is recorded over the telephone and consists of read and (semi-) spontaneous speech of 5000 subjects with varying regional accents. For each speaker 50 items are available. Five of these 50 items are the so-called phonetically rich sentences; each set of five sentences contains all phonemes of Dutch at least once. Each speaker read a different set of sentences. In this experiment the phonetically rich sentences of 4019 speakers were used for training the CSR.

The CSR was subsequently used to analyze the utterances produced by the speakers. For each utterance a Viterbi alignment between the speech signal and the canonical phonemic transcription, which was generated automatically from the orthographic transcription, was obtained. For the purpose of the research in this paper only the boundaries between speech and nonspeech signals (silences, but also filled pauses) are relevant. The accuracy of forced alignment was checked manually for a representative sample of the material. In general, the segmentation appeared to be of sufficient quality for this purpose and was then used to calculate the quantitative measures which are described in detail in the following.

2. Quantitative measures of fluency

Previous studies of temporal phenomena in native and non-native speech have identified a number of quantitative variables that appear to be related to perceived fluency (Goldman-Eisler, 1968; Grosjean and Deschamps, 1975; Grosjean, 1980; Nation, 1989; Lennon, 1990; Riggenbach, 1991; Freed, 1995; Towell *et al.*, 1996). The clearest taxonomy is provided by Grosjean (1980, p. 40), who distinguishes between primary and secondary variables. Primary variables are ''variables that are always present in language output'' (Grosjean, 1980, p. 40). Secondary variables are related to hesitation phenomena such as filled pauses, repetitions, repairs, and restarts. These variables are not necessarily present in speech and seem to be infrequent in read speech (Grosjean, 1980, p. 42).

Before introducing the variables used, we first give some definitions:

(1) silence: every frame of silence detected by the CSR,
(2) silent pause: a stretch of silence with a duration of no less than 0.2 s,
(3) nph: number of phonemes,
(4) dur1: duration of speech without utterance internal silences,
(5) dur2: duration of speech including utterance internal silences.

TABLE I. Definition of quantitative fluency measures. dur1 = duration of speech without utterance internal silences, dur2 = duration of speech including utterance internal silences.

Name	Definition
Seven primary variables	
Articulation rate	Number of phonemes/dur1
Rate of speech	Number of phonemes/dur2
Phonation/time ratio	100% × dur1/dur2
Mean length of runs	Mean number of phonemes between silent pauses
Mean length of silent pauses	Mean length of all silent pauses
Duration of silent pauses per minute	Total duration of all silent pauses/(dur2/60)
Number of silent pauses per minute	Number of silent pauses/(dur2/60)
Two secondary variables	
Number of filled pauses per minute	Number of filled pauses/(dur2/60)
Number of disfluencies per minute	Number of disfluencies/(dur2/60)

dur1 and dur2 were measured from the beginning of the first word to the end of the last word for every utterance. Consequently, silences present at the beginning and end of every utterance were discarded.

These definitions were employed to calculate seven primary and two secondary variables, i.e., primary variables are further divided into complex variables and simple variables. Complex variables are speaking rate and phonation time ratio, while simple variables are articulation rate, length of silent pauses, and length of runs. As is clear from Table I, the Simple Variables are subcomponents of the Complex Variables. In our previous study (Cucchiarini *et al.*, 2000) as well as in the present one, measures similar to those proposed by Grosjean (1980) were adopted, albeit with slightly different definitions. These variables differ from those defined by Grosjean (1980) in three respects. First, phonemes were used as units instead of syllables. Second, a distinction was made between mean length, total length, and number of silent pauses (see also Towell *et al.*, 1996). Third, the variables *duration of silent pauses per minute, number of silent pauses per minute, number of filled pauses per minute, and number of disfluencies per minute* are all calculated relative to utterance length (i.e., dur2/60). This was not done in our previous paper (Cucchiarini *et al.*, 2000), because in that case all speakers read the same sentences, and thus the utterances of different subjects had almost the same length. In the present study, on the other hand, speech fragments of different length have to be compared and such absolute measures are not suitable for this purpose. As time unit the minute was chosen because it seemed most appropriate to express the frequency of phenomena such as filled and silent pauses and disfluencies. As indicated by Grosjean, disfluencies and filled pauses appeared to be infrequent in read speech (Cucchiarini *et al.*, 2000). However, it was decided to include them in the present investigation because they could be more frequent in spontaneous speech, especially that of non-natives.

TABLE II. Interrater reliability coefficients (Cronbach's α) for the five rater groups.

Rater group	Interrater reliability
Phoneticians	0.96
Speech therapists 1	0.88
Speech therapists 2	0.83
Raters beginner level	0.86
Raters intermediate level	0.82

For each speaker in Experiment 1 the above-mentioned objective fluency measures were calculated over the five sentences in each set, thus obtaining two values per objective measure for each speaker. These two values were then averaged so as to obtain one value per objective measure per speaker. With 60 speakers a total of 60 values was obtained for each objective measure. In Experiment 2 the objective fluency measures were calculated over the eight items of each speaker, thus obtaining a set of 57 values for each objective measure. In this manner two sets of 60 (Experiment 1) and 57 (Experiment 2) scores were obtained for each objective measure. Correlations between these values and the human-assigned fluency scores were then calculated.

III. RESULTS

In presenting the results of the two experiments, attention is first paid to the fluency ratings assigned by the various groups of raters. Subsequently, the results concerning the quantitative measures of fluency are examined. Finally, the relationship between the human-assigned fluency ratings and the quantitative measures is considered.

A. Fluency ratings

The fluency scores assigned by the various rater groups involved in the two experiments, PH, ST1, and ST2 for Experiment 1 and RBL and RIL for Experiment 2, were analyzed to determine interrater reliability. The results of these analyses are shown in Table II. As is clear from Table II, interrater reliability is reasonably high, which may be surprising in view of the low reliability coefficients reported by Lennon (1990), Riggenbach (1991), and Freed (1995).

Besides considering interrater reliability, we also checked the degree of interrater agreement. Close inspection of the data revealed that in both experiments the means and standard deviations varied between the various raters. In other words, in both experiments the raters differed from each other in degree of strictness. As a consequence, the degree of agreement was not very high. A low degree of agreement within a group of raters has the effect of lowering the correlation coefficient computed between the combined scores of the raters and another set of data (i.e., the ratings by another group or the machine scores). The same is true when several groups are compared: differences in correlation may be observed, which are a direct consequence of differences in the degree of agreement between the ratings.

Therefore, before calculating the correlation coefficients between the human-assigned fluency ratings and the objective measures it was necessary to normalize for the differences in the values by using standard scores instead of raw scores. In Experiment 1, the scores were normalized by using the means and standard deviations of each rater in the overlap material, because in this case all raters scored the same samples. For individual raters, these values hardly differed from the mean and standard deviations for the total material, as was illustrated in Cucchiarini *et al.* (2000). In Experiment 2 normalizing the scores was more straightforward, because all five raters in one group rated all speakers. For each rater his/her mean was then subtracted from each of his/her scores and the resulting scores were then divided by the standard deviation for that rater.

Table III shows the mean and standard deviations (raw scores) of the fluency ratings for the speakers in the two experiments. In Table III it can be clearly seen that the read speech fluency scores vary for the three proficiency levels PL1 (beginner), PL 2 (intermediate), and PL3 (advanced) and that they gradually increase from PL1 to PL3, which means that the more proficient speakers are also perceived as being more fluent than the less proficient speakers. In the spontaneous speech data this relationship between proficiency and fluency does not seem to obtain, as the scores for the IL speakers are lower than those for the BL speakers. Although one might argue that the scores for the two speaker groups are not really comparable because they were assigned by two different groups of raters, it seems that these results are probably related to the context within which the evaluation was carried out.

As explained previously, the raters in Experiment 1 had no information about the proficiency level of each speaker, except the cues contained in the speech, whereas the raters in Experiment 2 knew to which proficiency group the speaker belonged. As a consequence, they judged fluency in relation to each speaker's proficiency level, thus assigning higher scores to less proficient speakers if the desired fluency level was lower, i.e., in the BL group. Another possibility is that the failure to find the expected difference between the two proficiency groups in Experiment 2 is due to the difference between the tasks performed by the two groups. As explained previously, the IL group carried out cognitively more demanding tasks which might have induced lower fluency

TABLE III. Means and standard deviations for the raw fluency scores for read and spontaneous speech of speakers of different proficiency levels.

	Read speech (RS)								Spontaneous speech (SS)					
	PL1		PL2		PL3		all-RS		BL		IL		all-SS	
	$\bar{x}$	s.d.	$\bar{x}$	s.d.	$\bar{x}$	s.d.	$\bar{x}$	s.d.	$\bar{x}$	s.d.	$\bar{x}$	s.d.	$\bar{x}$	s.d.
Raw fluency scores	4.65	2.01	5.00	1.81	7.36	0.95	5.85	1.96	5.64	0.88	4.80	1.06	5.21	1.06

TABLE IV. Means and standard deviations (in parentheses) for the quantitative measures for read and spontaneous speech of speakers of different proficiency levels, PL1 (beginner), PL2 (intermediate), PL3 (advanced), BL (beginner level), and IL (intermediate level). For the various subgroups *N* is indicated in square brackets.

	Read speech (RS)				Spontaneous speech (SS)			9
Column 1	2 PL1 [10] $\overline{x}$ (s.d.)	3 PL2 [27] $\overline{x}$ (s.d.)	4 PL3 [23] $\overline{x}$ (s.d.)	5 all-RS [60] $\overline{x}$ (s.d.)	6 BL [28] $\overline{x}$ (s.d.)	7 IL [29] $\overline{x}$ (s.d.)	8 all-SS [57] $\overline{x}$ (s.d.)	SS/RS ratio col. 8 col. 5
nph	430.0 (7.0)	434.6 (16.7)	428.8 (7.5)	431.6 (12.6)	417.4 (115.1)	950.2 (246.9)	688.4 (330.3)	
dur1	44.5 (5.1)	43.9 (5.8)	38.3 (2.8)	41.9 (5.5)	34.6 (10.6)	80.3 (20.1)	57.9 (28.1)	
dur2	57.9 (10.3)	56.4 (12.7)	43.7 (5.2)	51.8 (11.8)	70.0 (16.0)	179.9 (29.8)	125.9 (60.3)	
Articulation rate	10.87 (1.41)	11.15 (1.38)	12.47 (0.82)	11.61 (1.37)	12.25 (1.25)	11.85 (0.81)	12.04 (1.06)	1.0
Rate of speech	8.54 (1.88)	8.95 (1.87)	11.03 (1.16)	9.68 (1.94)	5.99 (0.96)	5.31 (1.17)	5.65 (1.12)	0.6
Phonat./time ratio	77.97 (7.69)	79.62 (8.68)	88.28 (5.42)	82.66 (8.57)	49.33 (8.71)	44.92 (9.51)	47.09 (9.32)	0.6
$\overline{x}$ length of runs	16.51 (7.67)	18.10 (7.44)	27.73 (7.13)	21.5 (8.77)	9.50 (2.22)	9.33 (2.27)	9.41 (2.23)	0.4
$\overline{x}$ length sil. paus.	0.40 (0.08)	0.40 (0.12)	0.34 (0.16)	0.38 (0.13)	0.92 (0.20)	1.02 (0.28)	0.97 (0.25)	2.6
Dur. sil. paus. p/m	9.29 (4.48)	8.67 (5.15)	3.97 (2.96)	6.97 (4.87)	27.90 (5.52)	31.02 (6.04)	29.49 (5.95)	4.2
No. sil. paus. p/m	22.33 (8.45)	20.11 (9.45)	10.18 (6.45)	16.67 (9.65)	31.00 (5.56)	31.41 (4.77)	31.21 (5.13)	1.9
No. fil. paus. p/m	0.31 (0.50)	0.35 (0.94)	0.32 (0.77)	0.33 (0.81)	10.83 (8.24)	10.55 (7.84)	10.69 (7.97)	32.4
No. disf. p/m	1.82 (2.20)	1.78 (1.75)	1.04 (1.53)	1.50 (1.76)	2.39 (1.82)	2.19 (2.27)	2.29 (2.04)	1.5

scores. The analyses of the quantitative fluency measures will shed light on this point.

B. Quantitative measures of fluency

In this section the quantitative variables are analyzed in various respects. First, the mean and standard deviation are calculated for all variables for all groups. These results are given in Table IV.

The rows nph, dur1, and dur2 give an indication of the amount of material that was analyzed for the current study on read speech (RS) and spontaneous speech (SS).

Table IV also shows how the values for the different variables vary as a function of speech modality (read versus spontaneous) and proficiency level. In order to see how the measures vary as a function of speech modality the means for read speech (column 5) can be compared with those pertaining to spontaneous speech (column 8). In order to facilitate this comparison, the SS/RS ratio for the seven primary and the two secondary variables was calculated by dividing the averages in column 8 by the averages in column 5. The results are presented in column 9.

These comparisons indicate that for most of the variables the values drastically change as we go from read speech to spontaneous speech. For the primary variables, *rate of speech, phonation/time ratio, and mean length of runs* are roughly halved (SS/RS ratio: 0.6, 0.6, and 0.4, respectively), *number of silent pauses per minute* is almost doubled (1.9), while *mean length of silent pauses* and *duration of silent pauses per minute* are more than doubled (2.6 and 4.2, respectively). On the other hand, *articulation rate* hardly changes (1.0).

As to the secondary variables, disfluencies are somewhat more frequent in spontaneous speech as compared to read speech (1.5), whereas the frequency of filled pauses is more than 30 times higher in spontaneous speech (32.4). Furthermore, it is clear that for the secondary variables the value of the standard deviation is relatively high with respect to the mean. In some cases the standard deviation is even much higher than the mean. This means that, instead of being monomodal, the frequency distributions of disfluencies and filled pauses are mainly characterized by extremely low and extremely high values.

In order to see how the quantitative measures vary as a function of proficiency level, we can compare columns 2, 3, and 4 within read speech and columns 6 and 7 within spontaneous speech. The first thing to be observed is that the values change as a function of proficiency level. In the read speech material gradual changes can be observed for the primary variables from PL1 to PL3. The change is either an increase or a decrease, depending on the variable in question, but all changes indicate that the less proficient speakers also obtain lower fluency scores in terms of these quantitative measures. In the spontaneous speech material the opposite seems to hold: the values of the primary variables for the less proficient speakers indicate higher fluency than those of the more proficient speakers. This is all the more remarkable

because it holds for all seven measures. On the one hand, these results are in line with those presented in the previous section: in the human ratings the BL speakers were also perceived as being more fluent than the IL speakers. On the other hand, these findings are contrary to our expectations and to the results concerning read speech.

However, these findings are less surprising against the background of what was mentioned previously with respect to the speech material used in Experiment 2. In particular, it was suggested that the differences between the items used for the two proficiency groups in Experiment 2 might influence the fluency scores. As explained previously, the short and the long tasks differ not only with respect to length, but also with respect to the nature of the task. More precisely, the BL items contain questions that can be answered immediately by the candidate without much thinking, whereas the IL items contain questions that require more preparation to be answered. In other words, the IL items require more cognitive effort than the BL items, which, in turn, could explain the lower fluency scores, since more cognitively demanding tasks are associated with a lower articulation rate, a lower phonation/time ratio, shorter runs, and longer pauses (Goldman-Eisler, 1968; Grosjean, 1980, pp. 42–43). This is exactly what appears from the comparison of the data for BL and IL in Table IV. The fact that the objective measures also reveal lower fluency in the IL group indicates that the raters in Experiment 2 did a good job and managed to judge fluency independently of proficiency level. The absence of variation in the frequency of filled pauses between proficiency levels might indicate that this phenomenon is not a good indicator of fluency. However, more relevant data in this respect may be provided by the correlation analyses that are presented in the following section.

A final observation about disfluencies concerns the differences between read and spontaneous speech in the specific type of disfluencies produced. To gain more insight into the occurrence of these phenomena in read and spontaneous speech, a manual, more detailed analysis of disfluencies was carried out in which not only quantitative, but also qualitative properties were taken into consideration. Three categories of disfluencies were distinguished: repetitions (exact repetitions of words), repairs (corrections), and restarts (repetitions of initial parts of words). This analysis revealed that the frequency of occurrence of these phenomena varies in the two types of speech. In read speech disfluencies are divided as follows: 12% repetitions, 51% repairs, and 37% restarts. In spontaneous speech, on the other hand, the percentages are: 65% repetitions, 23% repairs, and 12% restarts. These differences between the two distributions appear plausible if one considers that in read speech speakers have to read the words they see on paper and not articulate those which they are planning in their minds. In other words, they are forced, as it were, to pronounce a number of words, some of which might be problematic for them. It is therefore more likely that they will stumble in pronouncing these words, than when they have to pronounce words which they have chosen themselves. It is indeed reasonable to assume that speakers will resort to specific strategies to avoid words that may be difficult to pronounce. However, since they have to formulate the sentences themselves, they will probably need some strategies to win time. This might explain their recourse to repetitions and filled pauses.

TABLE V. Pearson's *r* correlations between fluency ratings and quantitative measures for read and spontaneous speech. *N* is indicated in square brackets, while the significance level is indicated by asterisks: *=sign at 0.05 and **=sign at 0.01.

	Read speech all-RS [60]	Spontaneous speech RBL [28]	Spontaneous speech RIL [29]
Articulation rate	0.83**	0.07	0.05
Rate of speech	0.92**	0.57**	0.39*
Phonation/time ratio	0.86**	0.46**	0.39*
Mean length of runs	0.85**	0.49**	0.65**
Mean length of silent pauses	−0.53**	−0.08	−0.01
Duration of silent pauses p/m	−0.84**	−0.45**	−0.40*
Number of silent pauses p/m	−0.84**	−0.33*	−0.49**
Number of filled pauses p/m	−0.25	−0.21	−0.21
Number of disfluencies p/m	−0.15	−0.07	−0.27

C. Quantitative measures as indicators of perceived fluency

In this section the automatically calculated temporal measures of speech are compared with the fluency scores assigned by the raters, in order to determine how and to what extent objective measures of speech are related to perceived fluency in read and spontaneous speech. To this end the correlations (Pearson's *r*) between the two sets of scores in each experiment were calculated. For Experiment 1 the means over the scores assigned by the three rater groups were calculated, because the ratings of the three groups appeared to be very strongly correlated with each other (Cucchiarini *et al.*, 2000). For Experiment 2, on the other hand, the ratings assigned to the two groups of speakers are not directly comparable, because they were assigned by different raters and to different kinds of speech. Consequently, the correlations were calculated for each group of speakers separately. In this way the variation in proficiency level is reduced, which could have consequences for the correlations. All correlations are given in Table V.

The correlations for the read speech material are first considered. As is clear from Table V, all correlations are strong and highly significant (at the 0.01 level), except those for *number of filled pauses per minute* and *number of disfluencies per minute*, which appear not to be statistically significant. Furthermore, it can be observed that although the correlation between perceived fluency and *mean length of silent pauses* is also significant at the 0.01 level, its magnitude is clearly smaller than those of the other coefficients. These results indicate that, at least for read speech, all primary variables are relevant for perceived fluency, the length of silent pauses seems to play a minor role, whereas the secondary variables are not significant. The fact that the number of filled pauses and disfluencies appear not to be good indicators of fluency in read speech is not surprising as these phenomena appeared to be infrequent in read speech. The finding that *mean length of silent pauses* is less related to perceived fluency than the other measures concern-

TABLE VI. Pearson's *r* correlations between fluency ratings and primary variables for read speech at three proficiency levels: PL1 (beginner), PL2 (intermediate), PL3 (advanced). *N* is indicated in square brackets, while the significance level is indicated by asterisks: * = sign at 0.05 and ** = sign at 0.01.

	PL1 [10]	PL2 [27]	PL3 [23]
Articulation rate	0.85**	0.76**	0.66**
Rate of speech	0.92**	0.91**	0.73**
Phonation/time ratio	0.82**	0.86**	0.58**
Mean length of runs	0.91**	0.86**	0.57**
Mean length of silent pauses	−0.50	−0.68**	−0.50**
Duration of silent pauses per minute	−0.71*	−0.85**	−0.61**
Number of silent pauses per minute	−0.83**	−0.83**	−0.57**

ing pauses can be seen as an indication that less fluent speakers, in general, do not make longer pauses than more fluent speakers, but they do pause more often, as was explained in Cucchiarini *et al.* (2000).

When considering the correlations for spontaneous speech, it appears that the secondary variables are not relevant for perceived fluency. In the category of primary variables, on the other hand, there seem to be substantial differences between the various measures. While *rate of speech*, *phonation/time ratio*, *mean length of runs*, *number of silent pauses per minute*, and *duration of silent pauses per minute* exhibit statistically significant correlations with the fluency ratings, *articulation rate* and *mean length of silent pauses* seem to have almost no relation at all with perceived fluency. In particular, *rate of speech* turns out to be the best predictor of fluency for the BL group, while for the IL group *mean length of runs* exhibits the strongest relation with the fluency ratings.

The values in Table V also show that all correlations between the objective measures and the fluency ratings that appear to be statistically significant are systematically lower for spontaneous speech than for read speech. As a possible explanation for this finding one could invoke the lower range in proficiency levels in Experiment 2 as compared to Experiment 1. Recall that in Experiment 1 three proficiency levels were compared and in Experiment 2 only two. In addition, in Experiment 2 this already lower range was further reduced because the correlations were calculated for each proficiency level separately and, therefore, for a rather homogeneous group of speakers as far as proficiency is concerned. To test whether this explanation might be correct, the correlations between the primary variables and the fluency ratings for read speech were computed separately for the three proficiency levels. These correlations are shown in Table VI. As is clear from Table VI, these correlations are slightly lower than those pooled over the three groups, and the correlation concerning *mean length of silent pauses* does not even reach significance in the PL1 group. However, these correlations are still considerably higher than those for spontaneous speech. In other words, even if the range in proficiency is limited by taking a homogeneous group, the correlations for read speech are still higher. Actually, it is amazing that correlations between physical measures and subjective ratings computed on such limited numbers of observations as those in each proficiency level (10 for PL1, 23 for PL2, and 27 for PL3) turn out to be so significantly high. This suggests that the relationship between objective properties and perceived fluency in read speech is rather clearcut, whereas this holds to a lesser extent for spontaneous speech.

However, the most remarkable difference between read and spontaneous speech concerns the correlations between the fluency ratings on the one hand and *mean length of silent pauses* and *articulation rate* on the other. *mean length of silent pauses* already appeared to be less related to perceived fluency than the other variables in read speech, from which it could be concluded that the frequency of the pauses is more important for perceived fluency than their mean length (Cucchiarini *et al.*, 2000). So, in a sense, this finding is less surprising. The absence of a correlation between perceived fluency and *articulation rate*, on the other hand, is much more surprising, because this variable appears to have a strong correlation with perceived fluency in read speech, as is clear from column 2 in Table V. This seems to suggest that when the presence of pauses in speech increases dramatically, as is the case when we go from read speech to spontaneous speech, the contribution of *articulation rate* diminishes and can even become negligible. In other words, even though the dimension of *articulation rate* is perceptually available to the listeners, its effect is overwhelmed by the many pauses.

To determine whether a combination of variables allows one to make better predictions, we submitted these data to a multiple regression analysis in which the temporal variables are used as the predictors and the fluency ratings as the criterion. Both for read and spontaneous speech it was found that combining physical parameters does not lead to substantial improvements in predictive power. The results of this analysis show that for read speech the variable that explains the greatest amount of variance is *rate of speech*: R is 0.92; $F=308.8$; $df=1$. The second variable that is added in the stepwise procedure is *number of silent pauses per minute*. However, the increase in explained variance is marginal: R rises to 0.93 ($F=176.5$; $df=2$). In spontaneous speech the variable that explains the greatest amount of variance is *rate of speech* for the BL group ($R=0.57$; $F=12.5$; $df=1$) and *mean length of runs* for the IL group ($R=0.65$; $F=20.2$; $df=1$). The second variable added in the stepwise procedure is *number of silent pauses per minute* in both cases and in both cases the increase in explained variance is marginal: for the BL group R rises to 0.63 ($F=8.2$; $df=2$) while for the IL group R rises to 0.70 ($F=12.6$; $df=2$).

IV. DISCUSSION

In this paper the results of two experiments on perceived fluency in read and spontaneous speech have been presented. In these experiments a dual approach was adopted: fluency ratings assigned by experts to read and spontaneous speech produced by non-natives were compared with a number of objective measures that were calculated for the same speech fragments by means of a CSR.

The results of these experiments show that it is possible to obtain reliable ratings of fluency: reliability was high for

all rater groups in both experiments (Cronbach's α varied between 0.82 and 0.96). These results may be surprising in view of the much lower degrees of reliability (around 0.68) obtained in previous studies (Riggenbach, 1991; Freed, 1995) and require some explanation. Various factors may have led to such high reliability coefficients in our two experiments in comparison to those in previous studies, in particular, the type of speech analyzed and the raters' degree of experience. First, in Experiment 1 read speech was used while the studies by Riggenbach (1991) and Freed (1995) concerned spontaneous speech. With spontaneous speech, raters have to evaluate fragments that differ not only with respect to fluency in the temporal sense, but also with respect to grammar and vocabulary. As a matter of fact, Riggenbach (1991) and Freed (1995) found that the raters' judgments of fluency were confounded by these linguistic factors. With read speech, on the other hand, these factors can be kept constant so that the raters can concentrate on the temporal variables. In turn, this is likely to result in higher reliability coefficients. Second, a difference in amount of experience in rating speech between our raters and those in Riggenbach's and Freed's experiments may have played a part. The raters in Experiment 2 were professional raters who had received training before starting their activities as raters and had participated in various rating sessions at Cito. The raters in Riggenbach's experiment were ESL instructors and not professional raters. Although ESL instructors are familiar with non-native speech and know how to help learners improve their oral skills, they are probably less used to rating speech in an exam situation than the raters in our experiment. The raters in Freed's experiment were simply native speakers of the language to be rated.

With respect to the major goal of this study, to determine how and to what extent objective properties of speech are related to perceived fluency in read and spontaneous speech, the data analyzed here provide interesting results. First of all, the results obtained in this study have shown how fluency scores, both those assigned by human raters and those obtained on the basis of objective measures, can vary as a function of the type of speech under investigation. Although the human ratings are not readily comparable because they were assigned by different raters, the objective measures do indicate that speakers appear to be less fluent in spontaneous speech than in read speech.

Second, these findings also indicate how the nature of the task carried out by the speaker is related to the fluency scores obtained, both the human ratings and the objective measures. In particular, in presenting the speech material we suggested that the differences between the items used for the two proficiency groups in Experiment 2 might influence the fluency ratings. As explained previously, the short and the long tasks differ not only with respect to length, but also with respect to cognitive load, this being higher for the IL items than for the BL items. In turn, this difference could explain why the speakers in the IL group received lower fluency ratings and had a lower articulation rate, a lower phonation/time ratio, and made longer pauses and shorter runs.

Third, with respect to the role played by the various objective variables these results show that there are both similarities and differences between read and spontaneous speech. The similarities concern the weak relation between the secondary variables and perceived fluency in both types of speech. The differences concern the varying roles of the primary variables in the two speech modalities. As far as read speech is concerned, Table V reveals that the fluency ratings are strongly related to *rate of speech, articulation rate, phonation/time ratio, number of silent pauses per minute, duration of silent pauses per minute*, and *mean length of runs*, while *mean length of silent pauses* has a smaller effect. This suggests that for perceived fluency the frequency of pauses is more relevant than their length. In other words, the difference between more fluent and less fluent speakers lies in the number of the pauses they make, rather than in their length, and the longer *duration of silent pauses per minute* of less fluent speakers is caused by a greater number of pauses rather than by longer pauses. These findings are in line with those of previous investigations, see Chambers (1997, p. 543) and are corroborated by the data concerning the three proficiency levels: Table IV shows that the differences between the proficiency levels with respect to *mean length of silent pauses* are relatively smaller than those concerning *number of silent pauses per minute* and *duration of silent pauses per minute*. These results suggest that two factors are particularly important for perceived fluency in read speech: the rate at which speakers articulate the sounds and the frequency with which they pause.

With regard to spontaneous speech, Table V shows that the fluency ratings are more strongly related to *rate of speech, phonation/time ratio, number of silent pauses per minute, duration of silent pauses per minute*, and *mean length of runs*, while *articulation rate* and *mean length of silent pauses* have almost no relationship with perceived fluency. Since pauses are much more frequent in spontaneous speech than in read speech (see Table IV), it is possible that their prominence effaces the importance of *articulation rate*. In other words, in speech where pauses are very frequent it seems plausible that a variable that takes no account of pauses whatsoever, like *articulation rate*, shows no relation to perceived fluency. Furthermore, when one considers the nature of all these variables it appears that fluency ratings of spontaneous speech are particularly related to variables that contain information about the frequency of the pauses, and these are *rate of speech, phonation/time ratio, number of silent pauses per minute, duration of silent pauses per minute*, and *mean length of runs*, but not *articulation rate* and *mean length of silent pauses*. In turn, this suggests that of the two factors that are important for perceived fluency in read speech, namely the rate at which speakers articulate the sounds and the frequency with which they pause, the latter is most important for perceived fluency in spontaneous speech.

Another interesting finding in this study is that *mean length of runs* is a particularly good predictor of fluency in spontaneous speech and for the IL group it is better than all other measures that do take pause frequency into account. What distinguishes *mean length of runs* from the other measures is that *mean length of runs* takes account not only of the frequency of the pauses but, to a certain extent, also of their distribution. The importance of this variable seems to

suggest that pauses are tolerated, provided that sufficiently long uninterrupted stretches of speech are produced. The fact that the predictive power of *mean length of runs* is greater for the IL group, i.e., for speech material where the speaker has to present his/her arguments in a coherent and organized manner and where the distribution of pauses is of course more important, lends further support to this interpretation.

In our previous paper (Cucchiarini *et al.*, 2000) it was noted that a possible limitation of that study was that it only indicated a strong relationship between objective measures of temporal speech characteristics on the one hand and expert fluency ratings on the other, but it did not provide information as to how varying articulation rate and/or pause time would affect the fluency ratings. In other words, we admitted that we were not in a position to make strong claims about the causal relationships obtaining between the objective measures and the fluency ratings. By using speech where a different relationship between articulation rate and pause time obtains, such as the spontaneous speech used in the present study, we have attempted to get more insight into how variations in the objective properties of speech affect fluency ratings. As a matter of fact, it turned out that as pauses become more frequent, as in spontaneous speech, the importance of articulation rate is reduced.

At this point it is interesting to consider what implications the results of this study can have for the future of fluency assessment. In our previous paper (Cucchiarini *et al.*, 2000) we expressed our optimism with respect to the potential that our approach could have for objective fluency assessment in read speech by identifying quantitative speech variables that appear to be strongly related to perceived fluency. The extension to spontaneous speech analyzed in the present paper has shown that the predictive power of the various quantitative variables may differ for read and spontaneous speech and that, even within the same speech type, fluency ratings may vary depending on the specific task carried out by the speaker. In this respect the results of this study confirm those of previous investigations which indicated that cognitively more demanding tasks lead to lower fluency scores. For fluency assessment these findings imply that objective measures can be employed, but that the specific selection of variables and their interpretation should be related to the type of speech and the type of task.

V. CONCLUSIONS

On the basis of the results of the present study the following conclusions can be drawn. First, expert listeners are able to evaluate fluency with a high degree of reliability, both in read and in spontaneous speech. Second, fluency scores, both those assigned by human raters and those calculated on the basis of objective properties of speech, appear to vary with the type of speech under investigation: speakers turn out to be more fluent in read than in spontaneous speech. Third, fluency scores also vary with the type of task carried out by the speaker, with cognitively more demanding tasks being associated with lower fluency scores. Fourth, while expert fluency ratings of read speech are mainly related to speed of articulation and frequency of pauses, those of spontaneous speech appear to be more related to the frequency and distribution of pauses while speed of articulation shows almost no relation to perceived fluency. Fifth, expert fluency ratings can be more accurately predicted in read speech than in spontaneous speech on the basis of automatically calculated measures such as *rate of speech, articulation rate, phonation/time ratio, number*, and *total duration of pauses* and *mean length of runs*. Of all these measures *rate of speech* appears to be the best one in almost all cases. The only exceptions are the cognitively more demanding tasks in the spontaneous speech experiment for which *mean length of runs* turns out to be the best predictor of fluency.

To conclude, these findings indicate that temporal measures of fluency may be employed to develop objective testing instruments of fluency in read and spontaneous speech. However, the selection of the variables to be employed in such tests should be dependent on the specific type of speech material investigated and the specific task performed by the speaker.

ACKNOWLEDGMENTS

This research was supported by SENTER (an agency of the Dutch Ministry of Economic Affairs), the Dutch National Institute for Educational Measurement (CITO), Swets Test Services of Swets and Zeitlinger, and KPN. We are indebted to Uriël Schuurs and Ron Engelen of Cito, Arnhem, for making the scores of the Profieltoets available to us, and for their advice in the data processing.

Bortfeld, H., Leon, S. D., Bloom, J. E., Schober, M. F., and Brennan, S. E. (**1999**). ''Which speakers are most disfluent in conversation and when?,'' Proceedings ICPhS99 Satellite Meeting on Disfluency in Spontaneous Speech, pp. 7–10.

Boves, L. (**1984**). *The Phonetic Basis of Perceptual Ratings of Running Speech* (Foris, Dordrecht).

Brumfit, C. (**1984**). *Communicative Methodology in Language Teaching: The Roles of Fluency and Accuracy* (Cambridge University Press, Cambridge).

Chambers, F. (**1997**). ''What do we mean by fluency?,'' System **4**, 535–544.

Cucchiarini, C., Strik, H., and Boves, L. (**2000**). ''Quantitative assessment of second language learners' fluency by means of automatic speech recognition technology,'' J. Acoust. Soc. Am. **107**, 989–999.

Den Os, E. A., Boogaart, T. I., Boves, L., and Klabbers, E. (**1995**). ''The Dutch polyphone corpus,'' Proceedings Eurospeech95, pp. 825–828.

Freed, B. F. (**1995**). ''What makes us think that students who study abroad become fluent?,'' in *Second Language Acquisition in a Study-Abroad Context*, edited by B. F. Freed (Benjamin, Amsterdam), pp. 123–148.

Goldman-Eisler, F. (**1968**). *Psycholinguistics: Experiments in Spontaneous Speech* (Academic, New York).

Grosjean, F. (**1980**). ''Temporal variables within and between languages,'' in *Towards a Cross-Linguistic Assessment of Speech Production*, edited by H. W. Dechert and M. Raupach (Lang, Frankfurt), pp. 39–53.

Grosjean, F., and Deschamps, A. (**1975**). ''Analyse contrastive des variables temporelles de l'Anglais et du Francais: Vitesse de parole et variables composantes, phénomènes d'hésitation,'' Phonetica **31**, 144–184.

Laver, J. (**1980**). *The Phonetic Description of Voice Quality* (Cambridge University Press, Cambridge).

Leeson, R. (**1975**). *Fluency and Language Teaching* (Longman, London).

Lennon, P. (**1990**). ''Investigating fluency in EFL: A quantitative approach,'' Language Learning **3**, 387–417.

Nation, P. (**1989**). ''Improving speaking fluency,'' System **3**, 377–384.

Neumeyer, L., Franco, H., Weintraub, M. and Price, P. (**1996**). ''Automatic text-independent pronunciation scoring of foreign language student

speech,'' Proceedings of the International Conference on Spoken Language Processing (ICSLP) '96, pp. 1457–1460.
Raupach (**1983**).
Riggenbach, H. (**1991**). ''Toward an understanding of fluency: A microanalysis of non-native speaker conversations,'' Discourse Process. **14**, 423–441.
Schmidt, R. (**1992**). ''Psychological mechanisms underlying second language fluency,'' Stud. Second Language Acquisition **14**, 357–385.
SPEX http://lands.let.kun.nl/spex.
Strik, H., Russel, A., Van den Heuvel, H., Cucchiarini, C., and Boves, L. (**1997**). ''A spoken dialog system for the Dutch Public Transport Information Service,'' Int. J. Speech Technol. **2**, 121–131.
Towell, R., Hawkins, R., and Bazergui, N. (**1996**). ''The development of fluency in advanced learners of French,'' Appl. Linguist. **1**, 84–119.
Townshend, B., Bernstein, J., Todic, O. and Warren, E. (**1998**). ''Estimation of spoken language proficiency,'' Proceedings of the ESCA Workshop Speech Technology in Language Learning (STiLL 98), pp. 179–182.
Van Bezooijen, R. (**1984**). *Characteristics and Recognizability of Vocal Expressions of Emotions* (Foris, Dordrecht).

Evaluation of context effects in sentence recognition

Adelbert W. Bronkhorst
TNO Human Factors, POB 23, 3769 ZG Soesterberg, The Netherlands

Thomas Brand and Kirsten Wagener
Carl von Ossietzky Universität Oldenburg, AG Medizinische Physik, 26111 Oldenburg, Germany

(Received 11 April 2001; revised 17 October 2001; accepted 8 January 2002)

It was investigated whether the model for context effects, developed earlier by Bronkhorst *et al.* [J. Acoust. Soc. Am. **93**, 499–509 (1993)], can be applied to results of sentence tests, used for the evaluation of speech recognition. Data for two German sentence tests, that differed with respect to their semantic content, were analyzed. They had been obtained from normal-hearing listeners using adaptive paradigms in which the signal-to-noise ratio was varied. It appeared that the model can accurately reproduce the complete pattern of scores as a function of signal-to-noise ratio: both sentence recognition scores and proportions of incomplete responses. In addition, it is shown that the model can provide a better account of the relationship between average word recognition probability (p_e) and sentence recognition probability (p_w) than the relationship $p_w = p_e^j$, which has been used in previous studies. Analysis of the relationship between j and the model parameters shows that j is, nevertheless, a very useful parameter, especially when it is combined with the parameter j', which can be derived using the equivalent relationship $p_{w,0} = (1-p_e)^{j'}$, where $p_{w,0}$ is the probability of recognizing none of the words in the sentence. These parameters not only provide complementary information on context effects present in the speech material, but they also can be used to estimate the model parameters. Because the model can be applied to both speech and printed text, an experiment was conducted in which part of the sentences was presented orthographically with 1–3 missing words. The results revealed a large difference between the values of the model parameters for the two presentation modes. This is probably due to the fact that, with speech, subjects can reduce the number of alternatives for a certain word using partial information that they have perceived (i.e., not only using the sentence context). A method for mapping model parameters from one mode to the other is suggested, but the validity of this approach has to be confirmed with additional data.
[DOI: 10.1121/1.1458025]

PACS numbers: 43.71.Gv [DOS]

I. INTRODUCTION

In both clinical and experimental audiology, sentence tests are used extensively for the evaluation of speech perception abilities in normal and hearing-impaired listeners. An important advantage of sentence tests over word tests is that the performance-intensity function is steeper, so that thresholds (e.g., the speech reception threshold or SRT—the level corresponding to a score of 50%) can be determined more accurately (Plomp and Mimpen, 1979; Nilsson *et al.*, 1994; Kollmeier and Wesselkamp, 1997). Other practical advantages are that sentence recognition is a very easy task and that sentences are more representative of everyday conversation than isolated words. An obvious disadvantage of sentence tests is that they do not provide detailed information concerning phoneme perception and the occurrence of confusions.

One of the main features of a sentence is that it normally contains a wealth of contextual information. This information can be globally divided into two parts: syntactic information, concerning the structure of the sentence, and semantic information, relating to its meaning (see, e.g., Boothroyd and Nittrouer, 1988, for examples of speech materials with varying contextual information). In addition, there may be coarticulatory effects which enhance the probability of correct identification of words within a sentence because of the information contained in transitions from and to neighboring words. Furthermore, there can be context effects that are not mediated by the sentence itself, but that depend on *a priori* knowledge of the listener of, for example, sentence topic or of the set out of which the sentences are drawn. Data obtained with various types of sentence material show that the performance-intensity function depends to a considerable degree on the amount of contextual information (Kalikow *et al.*, 1977; Boothroyd and Nittrouer, 1988; Van Rooij and Plomp, 1991; Olsen *et al.*, 1996). This affects the applicability of sentence tests, because when the sentence recognition scores should quantify (peripheral) hearing capabilities, it must be assumed that the influence of the contextual information is constant across listeners. A simple example of a situation where this assumption is violated is the repeated presentation of a restricted set of sentences to the same listener. This allows the listener to learn the set and causes a significant increase of the recognition scores (cf. the effect of set size on word recognition demonstrated by Miller *et al.*, 1951).

In several early studies, methods were proposed for the quantitative analysis of context effects in the recognition of

printed text; these include the measure of linguistic entropy described by Shannon (1951) and the ''cloze'' procedure used by Taylor (1953) and Treisman (1965). Such measures are also useful when analyzing speech recognition performance because they capture a considerable part of the contextual information present in speech. Van Rooij and Plomp (1991), for example, found that the linguistic entropy can account for differences of up to 3 dB in the SRT in noise, obtained with the corpus of everyday Dutch sentences developed by Plomp and Mimpen (1979). In a recent study by van Wijngaarden *et al.* (2002), it was shown that linguistic entropy can also be used to explain differences in speech recognition performance between native and non-native listeners.

Methods based on printed text have, however, limited use in evaluating context effects in speech because of the fundamental differences between speech recognition and recognition of printed text. In the last decades, several alternative methods have been developed that do not suffer from this disadvantage because they can be directly applied to speech. The approach that is presently most widely used makes use of two equations, formulated by Boothroyd (1978) and Boothroyd and Nittrouer (1988). The first equation expresses the relationship between recognition probabilities p_e and p_w of elements and wholes (e.g., phonemes and words, or words and sentences)

$$p_w = p_e^j, \tag{1}$$

where j is a parameter that depends on the amount of contextual information. This parameter is equal to n (the number of elements) when there is no context and it decreases when the amount of context increases. The value of j indicates the effective number of independent elements in a whole. The second equation gives the relationship between recognition probabilities p_e and q_e of elements with and without context (e.g., words presented in sentences and in isolation)

$$p_e = 1 - (1 - q_e)^k. \tag{2}$$

The parameter k has a value of 1 when there is no context, and it increases when context is added. As explained by Boothroyd and Nittrouer (1988), k can be interpreted as the proportional increase of the number of channels with independent information, occurring when context is added to an element. For details concerning the derivation of Eqs. (1) and (2), the reader is referred to Boothroyd and Nittrouer (1988). The parameters j and k have been used to quantify differences between speech tests (Boothroyd and Nittrouer, 1988; Bosman, 1989; Bronkhorst *et al.*, 1993) and effects of hearing impairment on speech recognition (Olsen *et al.*, 1996; Grant and Seitz, 2000). Another application of the parameter j is in models that predict the statistics of speech recognition scores (Kollmeier and Wesselkamp, 1997; Brand, 2000). Advantages of these parameters are that they provide a convenient, single measure of contextual information and that they can be derived relatively easily from speech recognition data. However, there is a problem involved in applying j to results for meaningful sentences because it was found in several studies that j is then not constant but increases as a function of p_e (Boothroyd and Nittrouer, 1988; Kollmeier and Wesselkamp, 1997; Wagener *et al.*, 1999b). This would suggest that it is preferable to use k instead of j in that case. However, because data for speech material with and without context must be combined in order to calculate k, estimation of this parameter is not only more difficult, but also less reliable, than estimation of j.

A radically different method for modeling context effects was recently proposed by Müsch and Buus (2001a), as part of their model for predicting speech intelligibility that is based on statistical signal detection theory. In the model, it is assumed that the listener correlates the internal representation of the perceived speech with templates of a number of alternatives, and that these correlations can be mapped to distributions with nonzero mean for the target, and zero mean for the other alternatives. The mean of the target distribution depends on the parts of the frequency spectrum that are conveyed. The variances of the distributions are all the same, and they are determined by noise originating from three sources: nonideal production (articulation), audibility, and linguistic entropy (lack of context). An interesting aspect of this approach is that two sources of contextual information are treated separately. Information concerning set size (response alternatives) is dealt with directly in converting d' (the mean of the target distribution divided by the standard deviation of the distributions) to recognition probability [see Eq. (1) in Müsch and Buus, 2001a]. This part is based on earlier work by Green and Birdsall (1958), who used a similar approach to explain the effect of set size on word recognition, as measured by Miller *et al.* (1951). The remaining contextual information is modeled by choosing a certain level of ''cognitive'' noise. Müsch and Buus (2001a, 2001b) have successfully applied their model to predict effects of set size, speech material, and frequency-domain distortions on word recognition. However, because the predictions are based on multiple parameters, not only those related to context, it is difficult to determine how reliable the estimates of set size and cognitive noise power are. Furthermore, it is not clear whether the model is equally successful in predicting sentence recognition.

A third approach, which is somewhat similar to that of Boothroyd (1978) and Boothroyd and Nittrouer (1988), was developed by Bronkhorst *et al.* (1993). They presented a model that provides a single framework for the analysis of recognition probabilities of wholes and elements with or without context, and that can predict the probabilities $p_{w,m}$ that m elements of the whole ($m = 0,1,...,n$, where n is the number of elements) are correctly recognized. In the model, the recognition process is broken up into two parts: recognition of elements without context (in isolation) and guessing of missing elements using contextual information. It is assumed that the chance of correctly guessing a missing element (c_i) is independent of the position of the element in the whole, but depends only on the number of missing elements (i). The probability that m elements of the whole are recognized is obtained by summing over all permutations of combinations of k recognized elements ($k = 0,...,m$) and $m-k$ guessed elements. The parameters c_i, $i = 1,...,n$ (the c values) quantify the amount of contextual information; their value lies between 1 over the number of response alterna-

tives (when no context is present and a random choice has to be made) and 1. A more detailed explanation of the model can be found in Bronkhorst *et al.* (1993); the equations for calculating $p_{w,m}$ are also given in Appendix A of this paper.[1] Bronkhorst *et al.* (1993) have shown that their model can be applied to recognition of CVC words, presented either auditorily or orthographically. Using c values that were estimated from word counts in a CVC lexicon, they were able to predict effects of set size on CVC word recognition. Recently, the model has also been used to improve performance of multiband speech recognizers (Hagen and Boulard, 2001). Drawbacks of the model are, however, that the mathematical equations that are involved are relatively complex, especially for large numbers of elements, and that the number of parameters is large—it is, in principle, either n or $n-1$ (see Appendix A). As a result, the model cannot easily be applied to experimentally obtained scores, in particular when only average recognition scores of wholes and elements are determined. Furthermore, although application of the model to sentence recognition was added as an example in the paper by Bronkhorst *et al.* (1993), there has been no thorough evaluation of how well sentence recognition scores can be predicted by the model.

The purpose of the present paper is to address the abovementioned problems, associated with the model of Bronkhorst *et al.* (1993), and to investigate more closely the relationship between this model and the approach developed by Boothroyd (1978) and Boothroyd and Nittrouer (1988). The paper can be divided into two parts. In the first part, the model is applied to speech recognition data obtained with two German sentence tests, which differ with respect to semantic content, and a comparison is made between results for auditory and orthographic presentation. In the second part, the relationships between different context parameters (the c values, k, j, and j', a new parameter introduced in this paper) are investigated in detail. All parameters quantify the same thing and it is evident that they should be intimately related. The analysis of the relationship between the c values themselves is particularly relevant for application of the model because it is probable that they can be represented by a smaller number of truly independent parameters. One possible representation, based on a recursive relation, was already proposed by Bronkhorst *et al.* (1993) and verified for c values derived from a CVC lexicon (see footnote 5 of that paper).

II. PREDICTION OF RESULTS OF SENTENCE TESTS

A. Speech material

The data used in this study were obtained with two different German sentence tests: the so-called Göttingen and Oldenburg tests. For both tests, extensive validations have been carried out and great effort was taken to equalize the sentences and sentence lists with respect to word recognition score (Kollmeier and Wesselkamp, 1997; Wagener *et al.*, 1999a, 1999b). The Göttingen test comprises 200 simple, meaningful sentences with varying length (between three and seven words), pronounced by a male talker. The Oldenburg test is based on a test developed several years ago by Hagerman (1982) for the Swedish language. It consists of five-word sentences with a fixed syntactical structure that are constructed by randomly choosing one of ten alternatives for each of the five words. The structure of the sentences is: name—verb—number—adjective—object; e.g., *Peter gets three wet knives*. The sentences are syntactically correct, but the meaning can be somewhat strange. Of the 10^5 different sentences that can be constructed in this way, ten lists of ten sentences were selected for the test. The sentences were generated by combining recordings of pairs of words, pronounced by the same talker as used for the Göttingen test. In terms of contextual information, the sentences of the Göttingen and Oldenburg tests are comparable to the high- and low-predictability sentences developed by Boothroyd and Nittrouer (1988).

B. Collection of speech recognition data

The speech recognition data used in this study were obtained from normal-hearing listeners with hearing thresholds better then 15 dB HL at octave frequencies ranging from 125 to 8000 Hz. The listeners were between 16 and 42 years of age. Recognition performance was measured using a procedure in which the signal-to-noise (S/N) ratio was varied adaptively. The masker was speech-shaped noise with a fixed rms level of 65 dB. In both tests, word scoring was used and listeners could draw their responses from open sets.

The data for the Göttingen test were collected in a study aimed at optimizing adaptive procedures with respect to their efficiency in estimating the SRT and the slope of the performance-intensity function (Brand, 2000, 2002). Results for 12 listeners were analyzed. Each of the listeners was presented with 1 list of 20 sentences and 6 lists of 30 sentences. The data for the Oldenburg test originated from experiments in which the learning effects, that occur with this material, were investigated (Wagener *et al.*, 1999b). Results for two groups of normal-hearing listeners were used; one group (10 subjects) had previous experience with this test, the other (19 subjects) not. In order to minimize the effect of learning in the present analysis, only 4 of the 5 lists (of 30 sentences) completed by the first group, and 2 of the 6 lists (of 20 sentences) completed by the second group were included.

C. Application of the model to speech

As shown in Appendix A, the probabilities $p_{w,m}$ that m of the n elements in a whole are recognized correctly, can be expressed as functions of the variable q, the probability of recognizing elements without context, and the parameters c_i $(i=1,...,n)$, which quantify the amount of contextual information. When $p_{w,m}$ is known for all values of m larger than 0, the average element recognition probability p_e can be calculated as well. However, when working with sentence material, it is normally not feasible to measure q directly, and the only available experimental data are estimates of $p_{w,m}$ (and p_e) obtained as function of a certain independent variable, for example S/N ratio. In order to apply the model to these data, we have used an iterative procedure consisting of the following steps: (1) Initial estimates of c_i $(i=1,...,n$

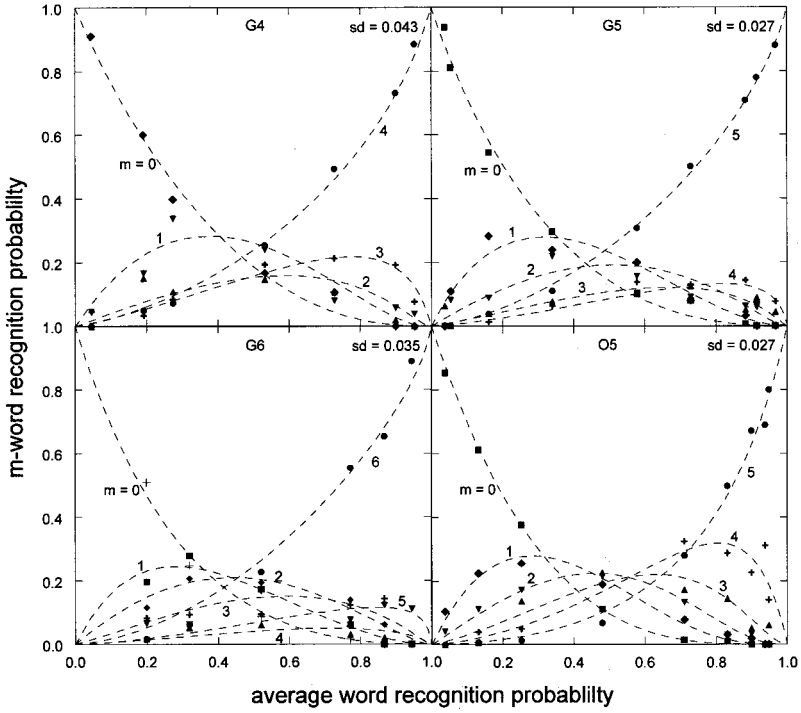

FIG. 1. Patterns of responses obtained for the four-, five- and six-word sentences of the Göttingen test (G4, G5, and G6) and the five-word sentences of the Oldenburg test (O5). The symbols indicate proportions of whole and partial sentences that are reproduced correctly, plotted as a function of the word recognition score. The dashed lines represent model predictions. The standard deviations between measured and predicted values are indicated in the upper right-hand corners of the panels.

-1) are chosen; (2) using Eqs. (A1) and (A2), the probabilities $p_{w,m}$ ($m=0,...,n$) and p_e are calculated for values of q between 0 and 1 with steps of 0.025; (3) the values of q that correspond to the measured values of p_e are determined by linear interpolation and the probabilities $p_{w,m}$ for those values are calculated; (4) the rms difference between measured and predicted values of $p_{w,m}$ is determined; (5) when the rms difference is not minimal, new estimates of c_i are chosen and the procedure is continued at step (2). The minimization was carried out using the MATLAB© routine *fmins*, which employs the Nelder–Mead simplex (direct search) method. The MATLAB© routine that was used to evaluate $p_{w,m}$ and p_e is listed in Appendix B.

In the adaptive procedure used for collecting speech recognition data, the step size for changing the S/N ratio was not fixed but determined by the performance of the listener. Consequently, data were available for continuum of S/N ratios. In order to obtain average values for fixed values of the S/N ratio, data within consecutive intervals with a width of 1.5 dB were pooled across sentence lists and listeners. When less than 15 sentences had S/N ratios falling within an interval, the results for that interval were discarded. For the Göttingen test, this resulted in data for 7, 9, and 6 S/N ratios, for sentences with 4, 5, and 6 words, respectively; the results for sentences with 3 and 7 words were discarded because insufficient data were available. For the Oldenburg test, which only consists of five-word sentences, data for eight S/N ratios were obtained. Application of the iterative fitting procedure to these data resulted in estimates of $c_1,\ldots,c_{n-1}$ ($n=4,5,6$) for the two types of material and for the three sentence lengths. It was assumed that c_n was equal to zero in all cases because no random guessing had been allowed during administration of the tests (see Appendix A). The data points and the optimal predictions are plotted in Fig. 1. Results for the Göttingen sentences with 4, 5, and 6 words, and for the Oldenburg sentences are shown in separate panels. Each (dashed) curve corresponds to a certain value of m, the number of correctly perceived words. It can be seen that there is, in general, a good correspondence between data and predictions, as indicated by the standard deviations of the differences, shown in the upper right-hand corners of the panels. The obtained values of c_i are listed in Table I and plotted in the left-hand panel of Fig. 2. Standard errors of these estimates were calculated using the residuals and partial derivatives of $p_{w,m}$ with respect to the c values (Snedecor and Cochran, 1978). For all types of material, estimates of j were also determined, using a one-dimensional iterative procedure similar to the one described above; the results are also listed in Table I. It should be noted that these represent average values of j because the dependence of j on p_e (discussed in Sec. III B below) was ignored in this analysis.

D. Orthographic presentation of sentences

An experiment was performed in which 150 of the 200 sentences of the Göttingen test were presented orthographically with 1–3 missing words. Fifty sentences, all with 3, 5, or 7 words, were left out. This was done in order to limit the number of words to 4–6, and to get a more even distribution of sentences with different lengths than in the original set. The four-word sentences were presented only with one or two missing words; the others also with three missing words. Each number of missing words occurred in the same proportion of sentences (i.e., 50% for the four-word sentences and 33.3% for the five- and six-word sentences). The missing words in the sentences were chosen randomly. The sentences were divided into five lists of 30 sentences. The order of presentation of the lists was balanced over subjects. Five native German subjects participated in the experiment; they all worked at the Hanse Wissenschaftskolleg in Delmenhorst.

TABLE I. Context parameters obtained by fitting the present model and Eqs. (1) and (3) to sentence recognition data obtained with the Göttingen and Oldenburg tests. The standard errors (s.e.) of the estimates are given as well. The values in the upper and lower parts of the table represent results for auditory and orthographic stimulus presentation, respectively.

	Göttingen test						Oldenburg test	
	4		5		6		5	
# words	Estimate	s.e.	Estimate	s.e.	Estimate	s.e.	Estimate	s.e.
Auditory								
c_1	0.72	0.03	0.87	0.01	0.92	0.01	0.53	0.03
c_2	0.55	0.04	0.75	0.02	0.89	0.02	0.43	0.03
c_3	0.19	0.03	0.44	0.03	0.71	0.04	0.28	0.03
c_4			0.13	0.02	0.36	0.04	0.12	0.01
c_5					0.13	0.02		
j	2.25	0.19	2.29	0.18	2.41	0.29	3.96	0.33
j'	2.50	0.26	3.02	0.28	3.32	0.18	3.43	0.08
Orthographic								
c_1	0.34	0.06	0.47	0.04	0.68	0.07	$\leqslant$0.1	
c_2	0.15	0.06	0.34	0.02	0.41	0.07	$\leqslant$0.1	
c_3			0.18	0.02	0.29	0.03	$\leqslant$0.1	

They were asked to complete the sentences, ensuring that the answers were meaningful and syntactically correct. It should be noted that we also obtained results for orthographic presentation of the Oldenburg test. However, for reasons explained below and in footnote 3, these results were discarded.

E. Application of the model to results for orthographic presentation

In analyzing results for orthographic presentation, the c values can be obtained directly, because the probabilities of perceiving individual words (without context) are then either 1 or 0, and at most one term remains when the probabilities $p_{w,m}$ are evaluated using Eq. (A1). Thus, when subjects complete sentences from which one word was removed, an estimate of c_1 can be obtained by dividing the number of times that this word was answered by the number of sentences. Similarly, the proportions of sentences with 2,3,... words missing that are ''correctly'' completed (i.e., the answer is equal to the target sentence) are estimates of c_1c_2, $c_1c_2c_3$, etc. Direct estimates of c_2,c_3,… are obtained by dividing the average number of ''correct'' words in sentences with 2, 3,... missing words by the number of those sentences.

In scoring the results, target words and answers were first converted to one type of notation, containing no diereses (i.e., ''*ä*'' was converted to ''ae,'' etc.) and using ''ss'' instead of ''ß.'' By counting both the average number of correct words and the number of correctly completed sentences, estimates of c_1, c_2, c_3, c_1c_2, and $c_1c_2c_3$ were obtained for the five- and six-word sentences, and estimates of c_1, c_2, and c_1c_2 for the four-word sentences. For each subject, the c values were determined iteratively, minimizing the squared deviations from the estimates.[2] Subsequently, results were averaged across subjects. The results are listed in Table I and presented graphically in Fig. 2 (right panel). It appears that, in all cases, the c values are much lower than those obtained for auditory presentation. The large discrepancy between the two sets of data is remarkable, and, although we were not able to obtain reliable estimates of the c values for orthographic presentation of the Oldenburg sentences,[3] it is clear that these cannot be larger than 1 over the number of alternatives for each word (i.e., 0.1). This is indicated graphically in the right-hand panel of Fig. 2 by symbols with error bars. A possible explanation for the large discrepancy between results for the two presentation modes is given in Sec. IV C.

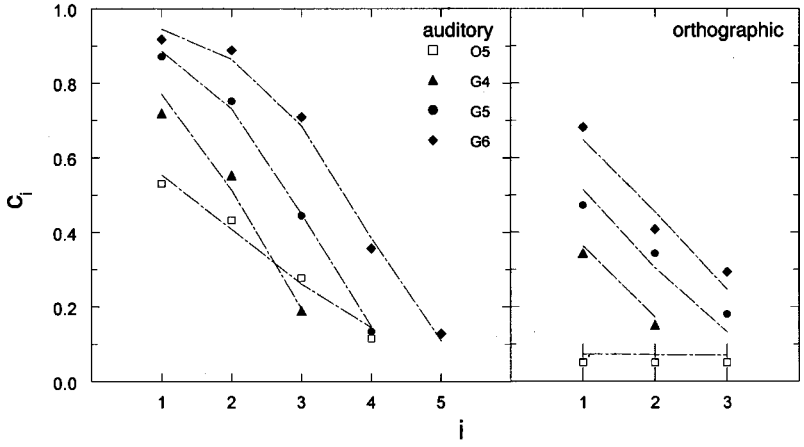

FIG. 2. Model parameters (c values) plotted as a function of the index i (representing the number of missing words), determined by fitting the model to data obtained with the Göttingen (G4, G5, G6) and Oldenburg (O5) sentence tests. The left-and right-hand panels show results for auditory and orthographic stimulus presentation, respectively. The curves in the left-hand panel were obtained by fitting Eq. (5) to the data points; those in the right-hand panel result from transforming the fitted values to equivalent values for orthographic presentation, using the procedure described in Sec. IV C.

III. RELATIONSHIP BETWEEN CONTEXT PARAMETERS

A. Definition of the parameter j'

As mentioned in the Introduction, the parameter j, introduced by Boothroyd and Nittrouer (1988), can be interpreted as the effective number of independent elements in a whole. Normally, j is defined using Eq. (1), but it can also be defined using the following, equivalent equation:

$$p_{w,0}=(1-p_e)^{j'}. \tag{3}$$

The parameter is called j' because j and j' are, in general, not equal to each other. This is illustrated in Table I, which lists estimates of j and j', obtained by fitting Eqs. (1) and (3), respectively, to the results of the Göttingen and Oldenburg speech tests. It appears that j' is larger than j, regardless of sentence length, for the Göttingen data, and smaller than j for the Oldenburg data. The values of j', thus, cover a smaller range than those of j, which suggests that j' depends less on the type of speech material than j does. As will be shown in Sec. III C, the parameter j' is of interest because it quantifies the influence of context at low values of p_e, whereas j is related to context effects at high values of p_e.

B. Using the model to evaluate other context parameters

Given that the model allows evaluation of $p_{w,n}$ $(=p_w)$, $p_{w,0}$ and p_e as a function of q and the c values, it is easy to express j, j' and k, defined in Eqs. (1), (3), and (2), respectively, as functions of the same variables. The resulting equations are given in Appendix A. Shown as well are expressions that can be used to evaluate the three parameters for values of q close to 0 or 1. Because p_e is equal to q for these values, the same limits apply when the parameters are evaluated as a function of p_e.

According to these expressions, and assuming that $c_n=0$ and $c_{n-1}>0$ (which will normally be the case), the limit of j for low values of p_e is 1, while j' has a higher limit, equal to $n/\{1+c_{n-1}(n-1)\}$. Both j and j' converge to a value of n for high values of p_e. The parameter k approaches $1+c_{n-1}(n-1)$ when p_e is small and is close to 1 when p_e is large. Numerical evaluations show that j typically increases as a function of p_e while j' remains relatively constant, with a minimum for high values of p_e; k either decreases as a function of p_e or increases to a maximum for values of p_e close to 1. This is illustrated in Fig. 3, which shows the dependence of j/n, j'/n, and k on p_e, calculated using the c values for auditory presentation of the Göttingen and Oldenburg sentences, listed in Table I. The curves were obtained by evaluating j, j', k, and p_e for values of q between 0 and 1 using Eqs. (A3)–(A6).

The predicted increase of j as a function of p_e is in agreement with results of earlier studies. Boothroyd and Nittrouer (1988), who assumed a linear relationship, found slopes of 0.87 and 2.23 for their high- and low-predictability sentence material, respectively. Results of listening tests with the German sentence material, performed at fixed S/N ratios, yield slopes of 0.68 and 1.88 for the Göttingen and Oldenburg material, respectively (Kollmeier and Wesselkamp, 1997; Wagener *et al.*, 1999b). As can be seen in the top panel of Fig. 3, the model also predicts that the slope is largest for the Oldenburg material, and the slopes of the curves (in the middle part) are about the same as those observed by Kollmeier and Wesselkamp (1997) and Wagener *et al.* (1999b). (Note that, because j/n is plotted in the figure, the slopes of the curves should be multiplied by the number of words.)

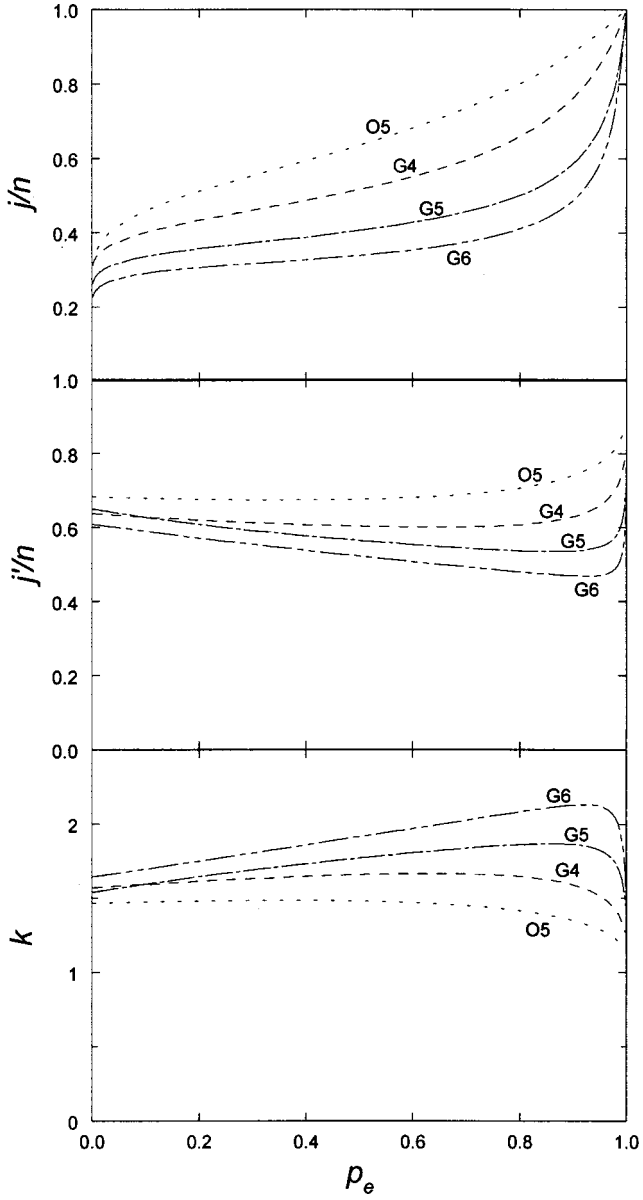

FIG. 3. Predicted dependence of j/n (upper panel), j'/n (middle panel), and k (lower panel) on the element recognition probability p_e for the c values obtained for the Göttingen (G4, G5, G6) and Oldenburg (O5) sentence tests. The variable n represents the number of words in the sentence.

C. Relationship between c values

A problem associated with the application of the present model is that the number of free parameters increases with the number of words in a sentence. Although it may be argued that the context effects in long sentences are, potentially, more complex than those in short sentences, it is questionable whether this increase in complexity should really require one parameter per extra word, especially when the

sentence only conveys one, simple, message (as is normally the case in sentence tests). It is therefore probable that there exists a relationship between the c values, which can be modeled using only a few independent parameters. When the c values are interpreted as chances of filling in missing words, it is intuitively clear that such a relationship should exist because, on the average, the number of possible sentences that fit to an incomplete set of words should increase in an orderly manner when the number of words in the set is reduced. The increase is, of course, related to syntax, vocabulary, and meaning, but it should not be too different for sentences of varying length that show similar redundancy. The c values for the Göttingen sentences, plotted in Fig. 2, provide support for this point because they, indeed, show a very regular dependence on the index i (which can be interpreted as the number of missing words) for all sentence lengths. A simple way of modeling this dependence was already proposed by Bronkhorst *et al.* (1993). They suggested that the number of competing alternatives $\nu_i=(1/c_i-1)$ is multiplied by a constant factor A_c when the number of perceived elements is reduced by one (i.e., it increases exponentially), while it is limited to a certain maximum value $\nu_{\max}$

$$\nu_{i+1}=\frac{1}{\frac{1}{A_c\nu_i}+\frac{1}{\nu_{\max}}}. \tag{4}$$

In this way, c values that were obtained by counting alternatives in a CVC lexicon (plotted in the left-hand panel of Fig. 3 of Bronkhorst *et al.*, 1993) could be predicted accurately. It appears that the same rule can be applied to predict the dependence of the c values on the size of the set of CVC words: $(1/c-1)$ can be multiplied by a constant factor A_s each time the set size is doubled. An excellent fit (s.d. $=0.016$) to all c values can then be obtained using only four independent parameters: c_1 for the smallest set, A_c, A_s, and $\nu_{\max}$.

However, Eq. (4) is less successful in predicting the c values for the Göttingen sentence test. In particular, it cannot account for the decrease of the (negative) slope that occurs as a function of i and it is only possible to obtain a reasonable fit when unrealistically large values of $\nu_{\max}$ are used. A better fit is obtained when the increase in the (total) number of alternatives is modeled with a power function

$$c_{i+1}=c_i^{\alpha}+(1-c_i^{\alpha})\left(\frac{c_{\min}}{1+c_{\min}^{\alpha-1}}\right). \tag{5}$$

This equation will converge to a certain minimum (equal or close to $c_{\min}$ for values of α greater than about 1.5) when i is large. With this relation, one is able to predict the dependence of the c values on both i and the number of words in the sentence, using different values for α (α_c and α_l), but only a single estimate of $c_{\min}$, and, as fourth parameter, c_1 for the six-word sentences. In fitting the data, α_l is first substituted in Eq. (5) to obtain estimates of c_1 for the other sentence lengths; subsequently, α_c is used to predict the dependence of c on i for each of the three sentence lengths. The best fit (s.d. $=0.026$) is obtained for $c_1=0.94$, $\alpha_c=2.69$, $\alpha_l=2.23$, and $c_{\min}=0.035$. Using the same value of $c_{\min}$, but different values of c_1 and α_c (0.55 and 1.60, respectively), the c values for the Oldenburg test can also be reproduced relatively accurately (s.d. $=0.024$). The results of the fits are shown in the left-hand panel of Fig. 2. Because one can also obtain a good four-parameter fit to the c values derived from the CVC lexicon with this equation, it probably represents a more generic description of the relationship between c values than Eq. (4).

Although the exact values of the parameters used in Eq. (5) will be different for each sentence test, it is not unreasonable to assume that the values found for the two German sentence tests, in particular α_c, α_l, and $c_{\min}$, are good first-order approximations of parameter values for other, similar sentence tests. This makes it possible to apply the present model to other data using only a minimum number of free parameters. For example, assuming that the high- and low-predictability sentences of Boothroyd and Nittrouer (1988) are similar to the Göttingen and Oldenburg sentences, respectively, we can use the two values of α_c and the single value of $c_{\min}$, given above, to fit the model to their data (listed in their Table III), while varying only one parameter: c_1. The optimal fits for the high- and low-predictability material were obtained for $c_1=0.79$ and 0.29, respectively. Standard deviations were 0.050 and 0.046, respectively. In comparison, Boothroyd and Nittrouer (1988) obtained standard deviations of 0.051 and 0.049, respectively, using a modified version of Eq. (1) in which j depends linearly on p_e.

D. Approximate relationships between j, j', and the c values

Both j and j' can be derived easily from the results of sentence tests, and the parameter j has been used in a number of previous studies (Boothroyd and Nittrouer, 1988; Bosman, 1989; Olsen *et al.*, 1996; Kollmeier and Wesselkamp, 1997). It therefore seems useful to look more carefully at the relationship between j and j' on the one hand, and the c values on the other hand, because, if estimates of the latter values can be derived from the former, it becomes possible to apply the present model when less data are available, and without the complex iterative determination of the c values. Given that the analytic relationships given in Appendix A are not very helpful for practical purposes, we carried out numerical evaluations in order to obtain more simple, approximate relationships.

It was assumed that the dependence of the c values on i $(i=1,...,n-1)$ can be modeled adequately with Eq. (5) and that c_n equals 0. For given values of c_i, estimates of j and j' were determined by first calculating p_w and $p_{w,0}$ as a function of p_e using Eqs. (A1) and (A3) (for values of q that increase in steps of 0.025 between 0 and 1), and by subsequently fitting p_w and $p_{w,0}$, evaluated using Eqs. (1) and (3), respectively, to these data. Because we wanted to obtain average values of j and j', the dependence of these parameters on p_e was not taken into account. In the calculations, we used values of n ranging from 4–7; c_1 had values between 0.2 and 0.9, increasing in steps of 0.1; α_c ranged from 1.5–5 (increment 0.5), and $1/c_{\min}$ was chosen between 10 and 30 (increment 5). This resulted in a total of 1280 combinations

of these four parameters. The values of j and j', obtained for these combinations, were divided by n and then submitted to a multiple linear regression analysis, using as independent variables both the four parameters above and the parameter c_{n-1}, multiplied by n. The latter combination (which is not truly independent because it is obtained from other parameters) was added because initial calculations showed that it accounts for most of the variance of j'.

The analysis revealed, rather surprisingly, that c_1 is very strongly correlated with j/n. More than 96% of the variance of j/n is explained by the following simple relationship:

$$\frac{j}{n} = 1.04 - 0.63c_1. \tag{6}$$

When only values of α_c greater than or equal to 2 are considered, the explained variance is even higher (99%). Because j does not depend on $c_{\min}$, and only slightly on α_c (when $\alpha_c > 1.5$), Eq. (6) will hold regardless of how exactly the dependence of c_i on i is modeled, as long as c_i does not decrease too slowly as a function of i. Equation (6) demonstrates that the parameters c_1 and j are essentially equivalent in most cases. Given that c_1 can be interpreted as the chance of completing a whole with only a single missing element, something which is most likely to occur when the element recognition probability p_e is high, it can be concluded that both c_1 and j quantify performance at high values of p_e.

As mentioned above, it was found that j' is highly correlated with nc_{n-1}. This relationship, however, turned out to be nonlinear and a better correspondence was obtained when $\log(j'/n)$ was used as the dependent variable in the regression analysis. It appeared that 93% of the variance of j'/n is captured by the following relationship:

$$\frac{j'}{n} = e^{-0.08-0.37nc_{n-1}}. \tag{7}$$

The explained variance can be increased slightly (to 95%) when c_1 is included as the second parameter, but, for simplicity, this was not done. Because j' mainly depends on n and c_{n-1}, and hardly on the other parameters, we can again conclude that the exact shape of the dependence of c_i on i does not matter. In addition, it can be deduced in a similar way as above that both c_{n-1} and j' quantify performance at low values of p_e.

IV. DISCUSSION

A. Validity of the model

As stated in the Introduction, one of the aims of this paper is to check whether the present model can be used to predict results of sentence tests. This was investigated by applying it to data obtained with two different types of sentences, with varying length. It appeared that the model can accurately reproduce the complete pattern of responses—scores for reproduction of both complete and partial sentences—in all cases. As stated earlier (see footnote 1), this does not mean that the scheme underlying the model (in particular the two-stage process of sensory perception and guessing of elements) is a valid representation of the actual speech perception. It only demonstrates that the model is able to extract all contextual information present in the scores. Interestingly, the results for the two sentence tests deviate in a way that reflects the fundamental differences between them: the c values for the Oldenburg test are not only smaller than those for the Göttingen test, indicating that there is less context, but they also decrease less as a function of the index i (interpreted as the number of missing elements), which means that the context depends less on the amount of perceived information. This can by explained by the fact that the context is mainly *a priori* information concerning syntax and the word set that is used.

The analysis of the relationship between j and the c values provides additional support for the model. In studies employing either the same sentence material as used here (Kollmeier and Wesselkamp, 1997; Wagener *et al.*, 1999b) or different material (Boothroyd and Nittrouer, 1988), it was found that j is not constant, but increases as a function of the word recognition probability p_e. This increase is predicted by the model, and it is shown that the data of Boothroyd and Nittrouer (1988) that were fitted using a modified version of Eq. (1), in which j depends linearly on p_e, can be predicted at least as accurately by the model. The fact that no increase was found for other types of material (e.g., the zero-predictability sentences and the CVC words used by Boothroyd and Nittrouer, 1988) is not in contradiction with the predictions. As shown in Fig. 3 (top panel), there are cases when j is virtually constant over a wide range of values of p_e. When there is no context and the c values are all zero, this is trivial, because the model then predicts that j is constant (equal to the number of elements).

A shortcoming of the model is that it uses many parameters—normally the number of elements minus 1, which implies that an extensive data set is required to obtain reliable estimates. It appears, however, that the experimentally obtained c values show a clear regularity: they decrease monotonically as a function of the index i and they converge to a certain minimum. It is shown that this dependence can be modeled using a recursive relation with three free parameters: c_1, α_c, determining the decrease as a function of i, and the minimum value $c_{\min}$. Although the particular relation proposed here [Eq. (5)] may not be accurate in all cases—it has only been verified with a limited amount of data—it nevertheless provides a useful extension of the model because, in practice, the c values can only be determined with limited accuracy.

B. Relationship between context parameters

Another aim of the present paper was to perform a detailed analysis of the relationships between the context parameters j, k, and the c values. Within the framework of the model, this is straightforward because j and k can be expressed as a function of the c values (and of q, the probability of recognizing elements without context). Such a relationship can also be formulated for a new parameter, j', defined in Eq. (3), which just as j itself can be interpreted as the effective number of elements in the whole. Although the relationships are useful for detailed evaluations, shown, for example, in Fig. 3, they are rather complex and not very helpful for practical purposes. We therefore carried out a

statistical analysis, using Eq. (5) to generate "realistic" sets of c values and concentrating on the parameters j and j' which, just as the c values, can be derived from the scores obtained with one type of material (evaluation of the parameter k requires comparison of results for speech with and without context). The outcome shows that in most cases (when $\alpha_c > 1.5$, which means that c_i should decrease not too slowly as a function of the index i), there are almost one-to-one relations between j and c_1, and between j' and c_{n-1}. From this, two conclusions can be drawn. First, it appears that both j and j' yield only partial information concerning the context: one can roughly say that j quantifies the effect of context when speech perception is good, and j' that when speech perception is poor. This is not too surprising because j is based on responses that are entirely correct, and j' on responses that are entirely incorrect. Second, using Eqs. (6) and (7) in combination with Eq. (5), one can easily map j (and j') to c values, requiring estimates of only two (or one) additional parameter(s). This facilitates application of the model when only minimal information is available.

C. Effect of presentation mode

One of the advantages of the model, which was also utilized in the study by Bronkhorst *et al.* (1993), is that it can be applied to both speech and text. However, because the c values capture all contextual information present in the material, differences can occur between results for the two presentation modes, even when the speech is the verbal equivalent of the text. Such differences were found by Bronkhorst *et al.* (1993)—only for presentation of words in noise—and they were ascribed to coarticulation. Given that coarticulation and other potential factors, such as intonation, probably have a small effect in sentences,[4] it is at first sight puzzling that the present results show such a large difference for both types of sentences. In order to understand this, we must look more closely at the way in which the stimuli are degraded in the two presentation modes. During orthographic presentation, elements have recognition probabilities of either 1 or zero, and no intermediate values. In fact, this corresponds most closely to the scheme underlying the model, because a clear distinction can be made between sensory perception of elements that are presented and pure guessing to fill in the missing elements. During auditory presentation, all elements are degraded to a certain extent and, except when the degradation is severe, they are never "missing," but there is always some sensory information present. The fact that the model does not take this information into account when a certain element is taken as missing (i.e., when it would not be correctly identified without sentence context) is the most probable explanation of the discrepancy between results for auditory and orthographic presentation.[5] Performance is better in the former case (the c values are higher) because, even when the sensory information is insufficient to identify the element without context, it can always be used to reduce the number of alternatives from which the response should be chosen. A simple example is when the listener has only heard one phoneme of a certain word in a sentence. Without context, identification of the word would be virtually impossible (i.e., q is essentially zero), but when the context reduces the number of candidates to, say, ten (which means that c would be 0.1 during orthographic presentation), the additional information might well narrow it down to only two or three alternatives (and c would lie between 0.33 and 0.5).[6]

It would evidently be very useful to be able to transform a set of c values obtained for one presentation mode to equivalent values for the other presentation mode. For example, one could then predict the performance-intensity function of sentences before actually recording them. The relationship between results for the two presentation modes can also be used to differentiate between processing skills for speech and text, e.g., when testing children or non-native subjects. A possible approach for obtaining this transformation is derived here. However, given that we can base it only on a limited amount of data, it is tentative and subject to validation with further data. The approach is based on the observation that Eq. (5) can accurately predict the results for orthographic presentation, using values of α_c (for the dependence on the index i) and α_l (for the dependence on sentence length) that are proportional to the values for auditory presentation (i.e., that are obtained from the latter values by multiplying them with a constant β, where $\beta < 1$). The finding that α_c and α_l are lower for orthographic than for auditory presentation is in line with the explanation given above because, in the former case, the c values represent "real" contextual information that is spread out over the sentence and thus less sensitive to reductions of the number of words that are available than the local sensory information that is presumably used to reduce the number of alternatives during auditory presentation.

Considering first the dependence of the c values on sentence length, and assuming that we can also apply Eq. (5) to map values of c_1 from auditory to orthographic mode (disregarding the second term), it can be derived that the value of α, to be entered in Eq. (5) is proportional to $\beta^{(6-n)}$, where $n (n = 4,5,6)$ is the number of words in the sentence. In order to limit the number of free parameters to only 1, we now make one additional assumption: that α reduces to a value of 1 when n is equal to 0. This implies that

$$\alpha = \beta^{-n}. \tag{8}$$

We have used this expression to obtain estimates of c_1 for orthographic presentation from the fitted values of c_1 for auditory presentation, and we have applied Eq. (5), with α_c equal to 2.69β (using the value of α_c for auditory presentation, given in Sec. III C), to predict the dependence of c on the index i. The c values were then fitted to the data for orthographic presentation; the best result (s.d. of fit 0.039) is obtained for $\beta = 0.71$. The predicted values are plotted as lines in the right-hand panel of Fig. 2. Given that only one free parameter is used in the transformation, the agreement between data and predictions is remarkably good. The figure also shows predictions of c values for orthographic presentation of the Oldenburg sentences. These were obtained in the same way as above, keeping β the same, but now multiplying it by 1.6 (the value of α_c for that material). Because the predictions fall within the expected range (between 0 and 0.1), we can conclude that, although further validation is

clearly warranted, the present, simple method appears to be quite effective.

ACKNOWLEDGMENTS

This research was made possible by a fellowship granted to the first author by the Hanse Wissenschaftskolleg in Delmenhorst, Germany. The authors wish to thank Birger Kollmeier for his support and three anonymous reviewers for their critical evaluation of an earlier version of the paper.

APPENDIX A: MODEL EQUATIONS

The model of Bronkhorst *et al.* (1993) yields predictions of the probabilities $p_{\mathrm{w,m}}$ that m ($m=0,...,n$) elements of wholes containing n elements are recognized. These are evaluated as a function of the probabilities that elements in position i of the whole ($i=1,...,n$) are recognized without context (i.e., in isolation). The latter are designated by the symbol q_i. For simplicity, it will be assumed here that q_i is independent of i. The probabilities $p_{\mathrm{w,m}}$ can then be calculated as follows:

$$
\begin{aligned}
p_{w,n} &= q^n + nc_1q^{n-1}(1-q) + \frac{n(n-1)}{2!}c_1c_2q^{n-2}(1-q)^2 + \cdots + c_1c_2\cdots c_n(1-q)^n \\
p_{w,n-1} &= (1-c_1)\left\{ nq^{n-1}(1-q) + 2\frac{n(n-1)}{2!}c_2q^{n-2}(1-q)^2 + \cdots + nc_2\cdots c_n(1-q)^n \right\} \\
p_{w,n-2} &= (1-2c_2+c_1c_2)\left\{ \frac{n(n-1)}{2!}q^{n-2}(1-q)^2 + 3\frac{n(n-1)(n-2)}{3!}c_3q^{n-3}(1-q)^3 + \cdots + nc_3\cdots c_n(1-q)^n \right\} \\
&\vdots \\
p_{w,0} &= \left(1 - nc_n + \frac{n(n-1)}{2!}c_nc_{n-1} - \frac{n(n-1)(n-2)}{2!}c_nc_{n-1}c_{n-2} + \cdots \right)(1-q)^n.
\end{aligned}
\tag{A1}
$$

The element recognition probability p_e can be derived simply from the probabilities $p_{\mathrm{w,m}}$ using

$$
p_e = p_{w,n} + \frac{(n-1)}{n}p_{w,n-1} + \frac{(n-2)}{n}p_{w,n-2} + \cdots + \frac{1}{n}p_{w,l}, \tag{A2}
$$

which can also be expressed as

$$
p_e = q + c_1q^{n-1}(1-q) + 2\frac{(n-1)}{2!}c_2q^{n-2}(1-q)^2 + 3\frac{(n-1)(n-2)}{3!}c_3q^{n-3}(1-q)^3 + \cdots + c_n(1-q)^n. \tag{A3}
$$

A MATLAB© procedure for the evaluation of these expressions is listed in Appendix B.

In the equations, the parameters c_i represent the chances of correctly guessing one missing element given that i of the n elements were missed. Because it is, in general, more difficult to fill in an element when fewer elements have been perceived, c_i will normally decrease as a function of i. The value of c_n, the chance of guessing one element when nothing has been heard, has a special significance: it quantifies the effect of random guessing when no sensory information is present. As can be derived easily from Eq. (A3), it also is the lower limit of p_e. In most cases, subjects are asked to refrain from this kind of guessing, which means that c_n should be taken equal to zero.

Using the above equations, one can easily express the context parameters j, j', and k, defined in Eqs. (1), (3), and (2), respectively, as functions of q and c_i, $i=1,...,n$

$$
j = \frac{\log\{q^n + nc_1q^{n-1}(1-q) + \cdots + c_1\cdots c_n(1-q)^n\}}{\log\{q + c_1q^{n-1}(1-q) + \cdots + c_n(1-q)^n\}}, \tag{A4}
$$

$$
j' = \frac{\log\left\{ \left(1 - nc_n + \frac{n(n-1)}{2!}c_nc_{n-1} - \frac{n(n-1)(n-2)}{3!}c_nc_{n-1}c_{n-2} + \cdots \right)(1-q)^n \right\}}{\log\{1 - q - c_1q^{n-1}(1-q) - \cdots - c_n(1-q)^n\}}, \tag{A5}
$$

$$
k = \frac{\log\{1 - q - c_1q^{n-1}(1-q) - \cdots - c_n(1-q)^n\}}{\log(1-q)}. \tag{A6}
$$

Unfortunately, these relationships cannot be simplified analytically, and numerical evaluation shows that the three context parameters depend in a complex manner on the c values. It is, however, relatively straightforward to calculate j, j', and k for values of q close to 0 and close to 1

$$\lim_{q\to 0} j=\frac{\log(c_1\cdots c_n)}{\log(c_n)},\quad c_n>0=m,\quad c_1,\ldots,c_{n-m}>0,\ c_{n-m+1},\ldots c_n=0 \tag{A7}$$

$$\lim_{q\to 1} j=n,$$

$$\lim_{q\to 0} j'=\frac{\log(1-nc_n+n(n-1)c_nc_{n-1}/2-\cdots)}{\log(1-c_n)},\ c_n>0=\frac{n}{1+c_{n-1}(n-1)},\qquad c_n=0 \tag{A8}$$

$$\lim_{q\to 1} j'=0,$$

$$\lim_{q\to 0} k=\infty,\quad c_n>0=1+c_{n-1}(n-1),\ c_n=0$$

$$\lim_{q\to 1} k=1. \tag{A9}$$

APPENDIX B: COMPUTER PROGRAM FOR EVALUATION OF THE MODEL EQUATIONS

MATLAB© program that evaluates Eqs. (A1) and (A2) when the *c* values and the number of elements are given. By default, calculations are performed for values of *q*—the recognition probabilities of elements without context—ranging from 0 to 1 in steps of 0.025. Optionally, a user-defined vector with *q* values can be specified.

```
function [pe,P] = context(c,Ne,q);
% function [pe,P] = context(c,Ne,q);
% Evaluate recognition probabilities using the model of Bronkhorst et al.
% [J. Acoust. Soc. Am. 93, 499-509, (1993)]
% c     : vector with context parameters
% Ne    : number of elements (>=length(c))
% q     : (optional) array with recognition probabilities of elements without
%         context; normally q = [0:0.025:1]
% pe    : vector with average element recognition probabilities
% P     : matrix with recognition probabilities; columns contain probabilities
%         that 0, 1, ..., Ne elements are correct for the average recognition
%         probabilities given in vector pe
% A.W. Bronkhorst, TNO Human Factors, The Netherlands, march 2001

if exist('q')~=1,
  q = [0:0.025:1].';                    % Standard resolution of q
else
   q = q(:);                            % Must be column
end
if length(c)<Ne,
   c = [c(:);zeros(Ne-length(c),1)];    % Add zeroes so that length is Ne
else,
   c = c(:);                            % Must be column
end
Q = q.^Ne;                              % First col of Q, only power of q
if Ne>1,
   for ii=1:Ne-1,                       % Add cols with powers of q and (1-q)
      Q = [Q,nk(Ne,ii)*((1-q).^ii).*(q.^(Ne-ii))];
   end
end
Q = [Q,(1-q).^Ne];                      % Last col, only power of (1-q)
P = Q*cumprod([1;c]);                   % First col of P, multiply by
                                        % 1,c(1),c(1)c(2),...
cq = ([1:Ne].').*cumprod([1;c(2:Ne)]); % cq = 1,2*c(2),3*c(2)*c(3),...
P = [P,(1-c(1))*Q(:,2:Ne+1)*cq];        % Second col
if Ne>2,
   for ii=2:Ne-1,                       % Cols 3..Ne-1
      cq = 1;
      for jj=ii:Ne-1,
         cq = [cq;nk(jj+1,ii)];         % Row with nrs of permutations
      end
      cq = cq.*cumprod([1;c(ii+1:Ne)]); % Multiply by 1,c(ii+1),c(ii+1)*c(ii+2),...
      cc = 1;
      for jj=1:ii,
         cc = [cc,nk(ii,jj)*Sn(jj)];    % Row with nrs of permutations times sign
      end
      cc = cc*cumprod([1;c(ii:-1:1)]); % Multiply by 1,c(ii),c(ii)*c(ii-1),...
      P = [P,cc*Q(:,ii+1:Ne+1)*cq];     % Calculate col
   end
end
cc = 1;
for jj=1:Ne,
```

```
   cc = [cc,nk(Ne,jj)*Sn(jj)];          % Row with nrs of permutations times sign
end
cc = cc*cumprod([1;c(Ne:-1:1)]);        % Multiply by 1,c(Ne),c(Ne)*c(Ne-1),...
P = [P,cc*Q(:,Ne+1)];                   % Calculate last col
pe = P*([Ne:-1:0].')/Ne;                % Average element recognition probabilities

function m = nk(n,k);                   % Calculate permutations
   if (n<=k) | (k==0),
      m = 1;
   else,
      m = prod(n:-1:n-k+1)/prod(1:k);
   end
return

function m = Sn(n);                     % Calculate sign
   if mod(n,2)==0,
      m = 1;
   else,
      m = -1;
   end
return
```

[1]It should be made clear that the present model is not designed to model the perception of speech or text; its only purpose is to provide a description of the pattern of the errors that is obtained when speech or text is perceived in nonoptimal conditions. In explaining the model, we refer to perceptual and cognitive aspects when we state that we use probabilities that elements are perceived and chances that elements are guessed, but this is only to illustrate how the mathematical relationships can be interpreted.

[2]In general, the stress in these fits was small. In other words, the product of c_1 and c_2 was always close to the observed value of c_1c_2, and the product of c_1, c_2, and c_3 was very close to the observed value of $c_1c_2c_3$. This indicates that the hypothesis used in deriving the model—that c_i depends (on average) only on *i*, and not on the position(s) of the missing word(s) in the sentence—is valid for the results obtained with orthographic presentation.

[3]The five subjects that participated in the experiment with the Göttingen sentences also completed 30 sentences from the Oldenburg test with one or two missing words. They were instructed to adhere to the fixed syntactical structure of these sentences. It appeared that c_1 and c_2 were essentially zero in this test. Subjects that have experience with the Oldenburg test can reach higher *c* values because they have learned part of the set of possible words. However, their performance could not be evaluated using orthographical presentation because a simple strategy (always filling in words of one sentence that they have remembered) already ensures that all the *c* values will be 0.1.

[4]Evidence for this is provided by the fact that Boothroyd and Nittrouer (1988) found no context effects (a *j* equal to the number of words) with their zero-predictability sentences.

[5]Our explanation thus suggests that the *c* values for auditory presentation overestimate the actual influence of context. It is important to note that this conclusion also applies to other context parameters, and in particular to *j* because of the direct relationship between the *c* values and the other context parameters.

[6]This explanation seems to be at odds with the fact that Bronkhorst *et al.* (1993) found virtually the same *c* values for CVC words presented orthographically and auditorily (in quiet). There are, however, two reasons why one would expect that the effect of presentation mode is less for CVC words than for sentences. First, there is a smaller difference between element recognition scores without and with context when the elements are phonemes than when they are words, for the simple reason that there are much fewer alternative phonemes than alternative words. As a result, a reduction of the number of potential alternatives based on partial sensory information has less effect. Second, it is more likely that useful partial information can be extracted from a word than from a single phoneme, because individual phonemes within a word can be recognized, in particular vowels with a relatively high level.

Boothroyd, A. (**1978**). ''Speech perception and sensorineural hearing loss,'' in *Auditory Management of Hearing-Impaired Children*, edited by M. Ross and T. G. Giolas (University Park, Baltimore).

Boothroyd, A., and Nittrouer, S. (**1988**). ''Mathematical treatment of context effects in phoneme and word recognition,'' J. Acoust. Soc. Am. **84**, 101–114.

Bosman, A. J. (**1989**). ''Speech perception by the hearing impaired,'' Doctoral thesis (University of Utrecht, The Netherlands).

Brand, T. (**2002**). ''Efficient adaptive procedures for threshold and concurrent slope estimates for psychophysics and speech intelligibility tests,'' J. Acoust. Soc. Am. **111**, 2801–2810.

Brand, T. (**2000**). ''Analysis and optimization of psychophysical procedures in audiology,'' Doctoral thesis (University of Oldenburg, Germany).

Bronkhorst, A. W., Bosman, A. J., and Smoorenburg, G. F. (**1993**). ''A model for context effects in speech recognition,'' J. Acoust. Soc. Am. **93**, 499–509.

Grant, K. W., and Seitz, P. F. (**2000**). ''The recognition of isolated words and words in sentences: Individual variability in the use of sentence context,'' J. Acoust. Soc. Am. **107**, 1000–1011.

Green, D. M., and Birdsall, T. G. (**1958**). ''The effect of vocabulary size on articulation score,'' Technical Memorandum, No. 81 and Technical Note AFCRC-TR-57-58, University of Michigan: Electronic Defense Group.

Hagen, A., and Boulard, H. (**2001**). ''Error correcting posterior combination for robust multiband speech recognition,'' Proceedings Eurospeech 2001, Scandinavia.

Hagerman, B. (**1982**). ''Sentences for testing speech intelligibility in noise,'' Scand. Audiol. **11**, 79–87.

Kalikov, D. N., Stevens, K. N., and Elliot, L. L. (**1977**). ''Development of a test of speech intelligibility in noise using sentence materials with controlled word predictability,'' J. Acoust. Soc. Am. **61**, 1337–1351.

Kollmeier, B., and Wesselkamp, M. (**1997**). ''Development and evaluation of a German sentence test for objective and subjective speech intelligibility assessment,'' J. Acoust. Soc. Am. **102**, 2412–2421.

Miller, G. A., Heise, G. A., and Lichten, W. (**1951**). ''The intelligibility of speech as a function of the context of the test materials,'' J. Exp. Psychol. **41**, 329–335.

Müsch, H., and Buus, S. (**2001a**). ''Using statistical decision theory to predict speech intelligibility. I. Model structure,'' J. Acoust. Soc. Am. **102**, 2896–2909.

Müsch, H., and Buus, S. (**2001b**). ''Using statistical decision theory to predict speech intelligibility. II. Measurement and prediction of consonant-discrimination performance,'' J. Acoust. Soc. Am. **102**, 2910–2920.

Nilsson, M., Soli, S. D., and Sullivan, J. A. (**1994**). ''Development of the Hearing In Noise Test for the measurement of speech reception thresholds in quiet and in noise,'' J. Acoust. Soc. Am. **95**, 1085–1099.

Olsen, W. O., van Tasell, D. J., and Speaks, C. E. (**1996**). ''Phoneme and word recognition for words in isolation and in sentences,'' Ear Hear. **18**, 175–188.

Plomp, R., and Mimpen, A. M. (**1979**). ''Improving the reliability of testing the speech reception threshold for sentences,'' Audiology **18**, 43–52.
Shannon, C. E. (**1951**). ''Prediction and entropy of printed English,'' Bell Syst. Tech. J. **30**, 50–64.
Snedecor, G. W., and Cochran, W. G. (**1978**). *Statistical Methods* (Iowa State Press, Ames, USA), pp. 465–467.
Taylor, W. L. (**1953**). ''Cloze procedure: A new tool for measuring readability,'' J. Quart. **30**, 415–433.
Treisman, A. M. (**1965**). ''Verbal responses and contextual constraint,'' J. Verbal Learn. Verbal Behav. **4**, 118–128.
Van Rooij, J. C. G. M., and Plomp, R. (**1991**). ''The effect of linguistic entropy on speech perception in noise in young and elderly listeners,'' J. Acoust. Soc. Am. **90**, 2985–2991.
Van Wijngaarden, S. J., Steeneken, H. J. M., and Houtgast, T. (**2002**). ''Quantifying the intelligibility of speech in noise for non-native listeners,'' J. Acoust. Soc. Am. **111**, 1906–1916.
Wagener, K., Brand, T., and Kollmeier, B. (**1999a**). ''Entwicklung und Evaluation eines Satztests für die deutsche Sprache. II. Optimierung des Oldenburger Satztests,'' Z. Audiol. **38**(2), 44–56.
Wagener, K., Brand, T., and Kollmeier, B. (**1999b**). ''Entwicklung und Evaluation eines Satztests für die deutsche Sprache. III. Evaluation des Oldenburger Satztests,'' Z. Audiol. **38**(3), 86–95.

The limits of training Japanese listeners to identify English /r/ and /l/: Eight case studies

Naoyuki Takagi[a)]
Tokyo University of Mercantile Marine, 2-1-6 Etchujima, Koto-ku, Tokyo, Japan

(Received 21 January 2000; accepted for publication 27 March 2002)

Eight monolingual Japanese listeners were trained to identify English /r/ and /l/ by using 560 training tokens produced by ten talkers in three positions (200 word initial, 200 consonant cluster, and 160 intervocalic tokens). Their baseline performance and transfer of learning were measured using 200 word initial and 200 consonant cluster tokens produced by additional ten talkers. Long-term training (15 days) with feedback indeed increased sensitivity to the nontraining tokens, but tremendous individual differences were found in terms of initial and final sensitivity and response bias. Even after training, however, there remained some tokens for each subject that were misidentified at a level significantly below chance, suggesting that truly nativelike identification of /r/ and /l/ may never be achieved by adult Japanese learners of English. © *2002 Acoustical Society of America.* [DOI: 10.1121/1.1480418]

PACS numbers: 43.71.Hw, 43.71.An, 43.71.Es [KRK]

I. INTRODUCTION

Most native speakers of Japanese without prepubescent exposure to natural spoken English find it difficult to identify English /r/ and /l/, and several researchers have tried to train adult Japanese listeners to identify them. Although laboratory training with a synthetic /r/-/l/ continuum did not lead to a successful result (Strange and Dittmann, 1984), use of naturally produced tokens proved to be highly effective (Bradlow *et al.*, 1997; Lively *et al.*, 1993, 1994; Logan *et al.*, 1991; Yamada, 1993). These studies revealed that training Japanese listeners with naturally produced tokens of /r/ and /l/ by multiple talkers that occur in different positions (i.e., word initial, consonant cluster, and intervocalic positions) led to improvement in the percentage of correct identification [henceforth P(c)] of a different set of tokens produced by a single talker that were used in the pretest and the posttest. The learning effect transferred to novel tokens produced by new talkers, and was retained even after a period of six months (Lively *et al.*, 1994).

Stimuli used in those studies for the pretest and the posttest were 16 minimally paired words produced by a single talker (/r/ and /l/ appeared in 4 word initial, 4 consonant cluster, 4 intervocalic and 4 word final, postvocalic positions), and each word was presented only a few times. This approach has the advantage of keeping listeners' familiarity with these tokens from increasing their identification rate, and thus can provide a good estimate of the average training effect across subjects. The small number of tokens and presentations, however, inevitably reduces the accuracy of each listener's identification performance estimation.

Furthermore, use of P(c) as a dependent variable does not allow independent estimation of sensitivity and response bias. Takagi (1995) applied signal detection theory (henceforth SDT) to Japanese listeners' identification of individual /r/-/l/ token pairs and found that it can be described by the following SDT model: each /r/ (or /l/) token produces a one-dimensional, normally distributed sensory random variable **R** (or **L**) on ''dimension R-L'' and listeners make their categorical judgment by establishing a response criterion on this dimension. The present study attempted to estimate the impact of identification training on an individual basis by using a large set of tokens in terms of SDT based parameters of sensitivity and bias.

The present study also focused on possible limits of training. In every training study cited above, the subjects' average performance after training was not truly native like. In the phonetic environments where Japanese listeners have difficulty (i.e., word initial, cluster, and intervocalic positions), their average P(c) was always below 100%. This suggests that native speakers of Japanese cannot fully master the contrast once they have established their Japanese sound system. There seems to remain some difference between Japanese and English speakers even after intensive training.

The nature of this difference can be further elucidated by observing the error rate for each token. If Japanese listeners' perceptual difficulty stems from some random psychological noise affecting all tokens uniformly, there will be no token whose identification rate goes below chance aside from extreme overall response bias. If this is the case, one can conclude that Japanese listeners have a random noise problem.

If, on the other hand, there exist some tokens that are consistently misidentified while the majority of other tokens are properly identified, one might say that Japanese listeners have a scaling problem. Some /r/ (or /l/) tokens are, under Japanese listeners' scaling scheme, judged to be very much /l/-like (or /r/-like). This will lead to what one might call ''token specific category reversal'' (henceforth TSCR). The present study tried to determine, on an individual basis, if TSCR occurs.

To summarize, the present experiment is complementary to the series of /r/ and /l/ training studies cited above. The focus has been shifted from effectiveness of training in terms of the average P(c), which these studies clearly demon-

a)Electronic mail: takagi@ipc.tosho-u.ac.jp

strated, to accurate estimation of training effect on an individual basis in terms of SDT parameters and to possible limitations of training viewed in the light of TSCR.

II. METHOD

A. Subjects

Subjects were eight monolingual speakers of Japanese (four male and four female) who had gone through typical grammar-translation-based English education in Japan, and they had had no previous intensive exposure to spoken English. They were all undergraduate students at Tokyo University of Mercantile Marine in their late teens to early 20's. None of them self-reported a hearing problem. Among these one female subject (subject 6) had to discontinue the experiment for a reason completely unrelated to the nature of the experiment after the first training stage.

B. Stimulus presentation and data collection

A software package developed at the University of Alabama at Birmingham (UAB) was used to present stimuli and collect responses from subjects. This software presents digitized speech files in prespecified order and observers respond to them by clicking on response buttons on a computer screen using a mouse. The interstimulus interval was set at 1 s throughout this study.

Two different types of hardware were used. During the stimulus verification conducted in the U.S., an IBM compatible computer with a Sound Blaster 16 sound card was used. When Japanese subjects were tested in Japan, one additional laptop computer (Dynabook SS 475 with a built-in sound card) was used so that two subjects could be tested at one time. Stimuli were presented binaurally to subjects through conventional headphones at a comfortable level set by each subject.

C. Stimuli

Stimuli were taken from the UAB corpus, which was created while the author was a post-doctoral fellow at UAB under the auspices of J. E. Flege. They were produced by 20 native speakers of non-southern dialects of English from 15 different states. The stimuli recorded were then digitized, peak normalized, and pretested by four native speakers of English to verify that the tokens were indeed identifiable by native English speakers. Then the stimuli were edited by removing the latter half of the vowel and coda to conceal lexical identity for the purpose of SDT application.

1. Stimulus words

Of possible environments in which /r/ and /l/ occur, word initial (IN), consonant cluster (CL) and intervocalic (IV) positions were chosen. Word final, postvocalic position was not included in this research, since /r/ and /l/ in this position go through ''opposing assimilation'' following the terminology of perceptual assimilation model (PAM, Best *et al.*, 1988). Takagi (1993) reported that /r/ tokens in this position were mostly assimilated to Japanese vowel /a/, and /l/ tokens are assimilated mostly to Japanese /ɾu/ or /o/. (The symbol /ɾ/ will be used to represent Japanese ''r.'')

Each of the 20 talkers contributed ten minimally paired tokens for IN and CL, and eight such pairs for IV. The talkers were divided into two groups of ten, each with five male and five female talkers. Group 1 talkers and Group 2 talkers read different sets of IN and CL words, whereas identical IV words were used for both talker groups. In choosing the minimally paired words, an effort was made to include a variety of vowels after the target consonants. For the words in the CL condition, an additional effort was made to include five different initial consonants (/p, b, k, g, f/) with equal frequency.

2. Recording procedures

The recordings were made in a sound treated chamber using a Shure SM10A head-mount microphone connected to a Symetrix sx202 Dual Mic Preamp. The output from the preamplifier was recorded using a Teac DA-P20 digital audio tape recorder. Each talker read each word three times, and of these three ''takes,'' the last token was chosen by default and digitized. Whenever there was a problem with the last token such as lip-noise, uneven loudness, etc., one of the other two ''takes'' was used. Digitization was done using a Sound Blaster 16 sound card on an IBM compatible PC with 16 bit resolution at the sampling frequency of 22 kHz.

3. Pretest

The 1120 tokens thus digitized (20 talkers$\times$56 words) were then peak-normalized and pretested by four additional native speakers of English. The tokens for each position were divided into four subsets produced by five talkers and were randomly presented twice to each of the four listeners binaurally through conventional headphones and the listeners clicked on an appropriate ''R'' or ''L'' button on the screen.

Of all the tokens tested, one token was misidentified twice by the very first listener. Later, she listened to the original tape and informed the author that the talker clearly mispronounced the target sound. Since the second ''take'' was pronounced properly, this was digitized and peak-normalized. The other three listeners tested this new token and they made no errors on it. This particular case aside, no token was misidentified more than once, and even in this case, the listener who made an error listened to the token and verified that it was indeed an intended sound.

4. Editing procedure

Several researchers (Flege *et al.*, 1996; Yamada *et al.*, 1992) studied the effect of lexical familiarity on native Japanese listeners' perception of English /r/ and /l/ and found that Japanese listeners tend to name the target consonant as the one that makes the stimulus a known or more familiar word. This effect of lexical familiarity is a nuisance factor in applying SDT, since the theory assumes that response criterion remains stable for a given mode of response. Thus, sizable fluctuation of response criterion due to lexical familiarity must be avoided.

Since only IN and CL tokens were to be used for baseline measurement, the latter half of each IN and CL token was edited out at a place where the vocalic portion immedi-

TABLE I. Default design of five baseline and transfer tests (B1, B2, M1, M2, and A), three training phases (TP1, TP2, and TP3), and three anomalous cases.

	Session days								
	1	2	3–8	9	10	11–16	17–19	20	21
Default	B1	B2	TP1	M1	M2	TP2	TP3	A	TSCR
S3	B1	B2	TP1	M1	M2	TP2	TP3[a]	A	TSCR
S5	B1	B2	TP1	M1	M2		TP3[a]	A	TSCR
S6	B1	B2	TP1	M1	M2				

[a]Subject 3's TP3 lasted only 1 day. Subject 5 skipped TP2 and did only special training during TP3, which lasted only 2 days. Subject 6 discontinued the experiment after test M2.

ately following the target sound is clearly heard yet the final consonant(s) if any cannot be heard. After the cut was made, the final 5 ms of each token was ramped off.

Two additional native speakers of English further tested the edited tokens. They listened to all of the 800 tokens once each, one using a desk top and the other using a laptop. The task given to them was identical to what Japanese subjects went through for sensitivity measurement except that they had only two response alternatives (L, R), whereas Japanese subjects had four (L2, L1, R1, R2) to report confidence ratings as well. One listener identified all 800 tokens correctly, and the other made four response errors, but these four tokens were verified as containing intended sounds later, indicating that the editing procedure did not affect the identifiability of the target consonants.

D. Procedure

1. Overview

The default design of the present study and deviations from it are summarized in Table I. Sensitivities and response biases to the baseline, edited tokens were measured twice (tests B1 and B2) before training phase 1 (TP1), and twice after TP1 (tests M1 and M2), and once after training phase 3 (test A). A test of token specific category reversal (TSCR) was administered at the very end.

Presentation of the unedited training tokens was blocked by position alone during TP1 and TP3, and additional talker blocking was introduced during TP2. TP3 also contained special sessions that contained tokens each subject misidentified frequently in the previous training phase. TP1 and TP2 lasted 6 days, and TP3 lasted 3 days. Thus, those who finished the entire study participated in 15 days of training sessions, 5 days of sensitivity and bias measurement, and 1 day of a TSCR test.

The tokens used for training sessions with feedback and those for baseline measurement were produced by different talkers. Half of the subjects (1, 2, 5, and 6) were tested on the edited tokens produced by group 1 talkers in the five baseline and transfer tests, and were trained on the unedited tokens produced by group 2 talkers. For the remaining subjects, this combination was reversed. Half of the subjects (1, 3, 5, and 7) used a laptop and the remaining subjects used a desktop.

Since no training was given between tests B1 and B2, nor between tests M1 and M2, any change in sensitivity or bias between B1 and B2 or M1 and M2 should be attributed to some factor(s) unrelated to training (e.g., familiarity with the stimuli and/or the task). Hence, in the complete absence of any incidental learning, one expects no difference between tests B1 and B2 and tests M1 and M2. If training increases sensitivity, there will be improvement between tests B2 and M1 and tests M2 and A.

The experimental sessions on each day took 1 to 1.5 h. In addition to the fixed ¥1500 payment for each day, the subjects were paid ¥1 for each correct identification trial above the chance level. Each subject proceeded at the pace of approximately 3 days per week and all the subjects, including those who completed the full 21 days of sessions, finished the experiment within 2 months.

2. Baseline and transfer tests

In order to obtain SDT-based sensitivity and bias measures, the rating method was used (see Macmillan and Creelman, 1991 for this method and general introduction to SDT). Subjects were given four response buttons of ''L2, L1, R1, R2,'' where the numbers correspond to confidence levels, ''2'' being more confident and ''1'' being less confident. Subjects were told to respond with ''L2'' or ''R2'' when they were relatively more confident and with ''L1'' or ''R1'' when they were relatively less confident.

For each position (IN or CL), subjects were first given practice trials, which consisted of 25 /l/ and 25 /r/ tokens sampled evenly from ten talkers. This practice block was followed by two main blocks, each of which consisted of 200 tokens presented once in random order. The randomization orders were different between the two main blocks, and they were fixed across all the tests. Subjects always listened to IN tokens first.

3. Training phase 1 (TP1:6 days)

The training paradigm in this study was designed after Logan *et al.* (1991) with some modifications. Before the presentation of each stimulus, possible response alternatives appeared on the response buttons, for example, ''light'' and ''right'' (/l/-words always appeared on the left button and /r/-words appeared on the right). If the response was correct, the next stimulus was presented. If incorrect, a message indicating the correct response appeared, and the same stimulus was played again.

The stimuli used for training were all unedited (200 IN, 200 CL, and 160 IV words), and training was blocked by position. For example, on one day subjects first listened to IN words, then CL words, and finally IV words. In each of the three training sessions (i.e., IN, CL, and IV), all the tokens were presented once in random order. The order of

these three position sessions was completely counterbalanced across the 6 days of training, which constituted training phase 1. For the sake of data presentation, the first 3 days of TP1 will be referred to as ''TP1A'' and the last 3 days as ''TP1B.''

4. Training phase 2 (TP2: 6 days)

During TP1, strong talker-dependent response biases were observed among subjects whose identification rate was moderate. Tokens produced by some talkers were more or less neutral (both /r/ and /l/ tokens had similar identification rates), yet tokens from some other talkers were /r/-biased or /l/-biased (i.e., the identification rate for /r/ tokens was much higher than that of /l/ tokens or vice versa). In the hope that talker blocking would diminish such talker-dependent response bias, the training in this phase proceeded by blocking both position and talker. On TD 7 (training day 7) and TD 10, the IN words were presented in such a way that all the tokens produced by one talker were presented three times in random order. There were 10 such talker blocks, each of which consisted of 60 trials (20 words$\times$3 repetitions), leading to a total of 600 trials. CL words were presented on TD 8 and TD 11, and IV words on TD 9 and TD 12. Since there were only 16 words for IV, TD 9 and TD 12 had only 480 trials. Data from the first three days (TD 7 to TD 9) will be referred to as ''TP2A,'' and data from the last three days (TD 10 to TD 12) as ''TP2B.'' Subject 5, since her identification rate was near perfect, did not participate in this phase.

5. Training phase 3 (TP3: 3 days)

The final 3 days of training sessions returned to the nontalker blocking version. In addition to the same training sessions as in TP1, each subject was given special training sessions composed of stimulus pairs that each had identified poorly during the previous training phase. To keep the training sessions on each day within 1.5 h, two different selection criteria were used. Minimally paired words from a given talker were selected (a) if at least one member of the pair was identified at the rate of 3/6 or less for subjects 1–4, and (b) if identification rate for the pair was 7/12 or less for subjects 7 and 8. For all the subjects except subjects 3 and 5, these sessions were blocked by position, and the special training for each position was given after the full session for the position.

Subject 3, whose identification performance on the first day of TP3 was near perfect (IN, 95.0%; CL, 96.0%; IV, 98.1%), had ten special training tokens left (4 IN, 4 CL, and 2 IV tokens). All of these ten tokens were presented in random order ten times, in two blocks of five repetitions each. In the final block, he identified all of them with 100% accuracy. At the completion of this session, this subject expressed his reluctance to continue further training sessions, since he felt that his performance had reached an asymptotic stage. Thus, he skipped the following 2 days of TP3, and took final test A.

Subject 5, who skipped TP2, did only the special training during TP3. She was trained on all the CL and IV tokens she had previously misidentified in TP1B and their minimally paired counterparts. (She had identified all the IN tokens correctly 3 days in a row in TP1. See below.) She had 18 such tokens (10 CL and 8 IV), and they were presented 30 times in six blocks of five repetitions on the day following her test M2. Of all these nine pairs, six pairs were perfectly identified in the last four blocks. On the next training session day, the remaining three pairs were presented 40 times in blocks of ten repetitions, and all of them were correctly identified in the last two blocks, which completed her special training. On the same day, immediately after the training, she went through her last test A.

TABLE II. Data from subject 5 in P(c) for three positions as a function of tests and training phases.

	B1	B2	TP1A	TP1B	M1	M2	A
IN	97.3	99.3	99.7	100.0	100.0	100.0	
CL	95.3	97.0	99.3	99.1	96.8	97.3	98.2
IV			98.1	99.4			

6. Test of token specific category reversal (TSCR)

Inspection of raw data from tests M1, M2, and A indicated that each subject had some tokens that were misidentified highly consistently (i.e., worse than chance). For each subject in both the IN and CL positions, the five /r/ tokens and five /l/ tokens that were misidentified most frequently were chosen and combined with the five /r/ and five /l/ tokens that enjoyed the highest identification accuracy. The subjects came back shortly after test A and identified each of these 20 tokens five times.

III. RESULTS

A. Subject 5

Since subject 5 exhibited exceptionally high identification performance prior to any training, her baseline sensitivity data are not compatible with SDT. Thus, it seems best to describe her data separately first (Table II).

Since subject 5 identified all of the IN tokens correctly during TP1 on 3 successive days (TD3 to TD5), only CL and IV words were presented twice on the last day. The final test (A) was not given for IN simply because she attained 100% accuracy in both tests M1 and M2.

This subject learned to identify all the IN tokens used in baseline measurement as well as those used for training. Some difficulty, however, remained for the CL tokens. Even though she had learned, in the final special training sessions, to identify all the CL and IV tokens she had misidentified during TP1B, her identification performance in test A fell short of 100%. Moreover, her errors in tests M1, M2, and A concentrated on a handful of tokens. These tokens were used in the final test of TSCR, and her data will be presented in the appropriate section below.

B. General trend

A succinct description of the overall trend in terms of familiar P(c) will be helpful before we go into detailed description of individual data in terms of SDT-based param-

TABLE III. Mean P(c) across six subjects (except subjects 5 and 6) for three positions as a function of tests and training phases.

	B1	B2	TP1A	TP1B	M1	M2	TP2A	TP2B	TP3[a]	A
IN	51.9	54.5	63.3	74.6	75.3	77.7	85.7	89.1	84.9	80.7
CL	54.2	51.8	62.2	72.1	73.6	74.3	82.0	85.2	77.8	78.1
IV			64.9	76.6			85.6	88.6	84.6	···

[a]The entries for TP3 do not include special training sessions.

eters of sensitivity and bias. Table III presents the average P(c) across six subjects (excluding subjects 5 and 6) as a function of tests and training phases.

There was little difference between tests B1 and B2, nor between tests M1 and M2 in terms of the average P(c). There was about 20% mean percentage increase between tests B2 and M1 for both IN and CL (for all six subjects M1>B2), indicating that the effect of training transferred to the new stimuli for which no feedback was provided. There was some increase between tests M2 and A, and for all six subjects except in one case (subject 3, CL), the scores for A were greater than those for M2. However, the overall amount of increase (about 3%) was much smaller than the 20% difference between tests B2 and M1, which indicates that the learning curve is almost asymptotic at this stage. As will be seen below, tremendous individual differences lurk behind these well-behaved average P(c) data.

Turning to training data, we find steady increases (about 10%) between TP1A and TP1B. Again this trend was found in all six subjects in all conditions. There also were some increases between TP2A and TP2B, and the scores for TP2B were larger than those of TP2A except in two cases (subject 2 IN, and subject 3 CL). Here again, however, the difference (about 4%) was smaller than the previous increments. Finally, average P(c) dropped from TP2B to TP3 by about 5% (in all cases except S2 IN, and S3 IV) when talker blocking was removed. [The average P(c)'s for TP3 were obtained excluding the special training data.] Nonetheless, the average P(c)'s at TP3 were always better than those at TP1B and they were better than those on the last day of TP1B for each of the six subjects in all positions. The average P(c)'s for the last day of TP1 were 78.4% for IN, 73.7% for CL, and 78.6% for IV.

C. Individual data analysis

In the following sections, individual data obtained in tests B1, B2, M1, M2, and A will be presented in terms of SDT-based measures of sensitivity and response bias. The parameter for sensitivity is d_a, and the one for bias is c_a, both of which can incorporate unequal variance (i.e., non-unit slope ROC) cases. (See Macmillan and Creelman, 1991 for further details of d_a and c_a.) Since the probability of correctly identifying an /l/ token as ''L'' is taken to be the hit rate, a positive c_a means an /r/ bias, that is, the percentage of correctly identifying /r/ tokens [P(R), henceforth] is higher than the percentage of correctly identifying /l/ tokens [P(L), henceforth].

Raw identification data with confidence ratings for each individual subject were analyzed using the maximum likelihood estimation technique (see Dorfman and Alf, 1969) by running the computer program by Dorfman that appeared in Swets and Pickett (1982, in Appendix D). This program provides, among other things, sensitivity parameter d_a, standard deviation of this parameter, and the corresponding chi-square value representing the goodness of fit to the underlying SDT model.

Based on the standard deviations of a given pair of d_a's (let these be σ_1 and σ_2), one can test the significance of the difference by dividing the d_a difference by the square root of $(\sigma_1^2+\sigma_2^2)$. In Table IV, which presents sensitivity parameters for each subject for each test, a star (*) attached to an entry indicates that the difference between this entry and the previous one is significant at 0.05 level.

The standard deviation of d_a was also used to test if a given d_a is significantly below zero, and, when this is the case, the corresponding entry in Table IV is underlined. (The test statistic here is d_a/σ.) This means that the subject has a general category reversal problem, and that one must take this category reversal into consideration in estimating the net sensitivity increase.

When a given data set does not fit the underlying model (i.e., its chi-square value exceeds 0.05 level critical value), some caution is necessary. Even in this case, however, one can go back to the original percent correct data for each

TABLE IV. Sensitivity changes in d_a as a function of tests for each subject. A star (*) indicates the difference between the entry and the previous one is significant at 0.05 level.

	IN					CL				
	B1	B2	M1	M2	A	B1	B2	M1	M2	A
S1	−0.18	0.09	1.25*	1.53	1.92*	0.10	−0.06	0.85*	0.66	1.37*
S2	0.36	0.61	1.47*	1.81	1.85	−0.08	−0.03	0.69*	1.03*	0.97
S3	0.73	1.37*	2.77*	3.21	3.04	1.38	1.05	2.83*	3.15	3.25
S4	0.47	0.41	0.68	0.95	1.18	0.63	0.63	1.46*	1.51	1.73
S6	1.26	1.66*	2.68*	2.52		0.89	1.11	2.58*	2.74	
S7	**−0.69**	**−0.51**	0.82	1.11	1.10	**−0.25**	**−0.25**	0.84*	0.81	0.93
S8	−0.18	**−0.42**	0.97*	0.98	1.21	−0.02	**−0.42***	1.03*	0.97	1.09

category (i.e., /r/ and /l/), and use the normal approximation technique of binomial distributions. Suppose that identification rate for /r/ increased from 50% to 70% from B2 to M1. Since each rate is estimated based on 200 observations, one can approximate each binomial distribution by a normal distribution that has a variance of $200*0.5*(1-0.5)=50$ and $200*0.7*(1-0.7)=42$, respectively. Since the test statistic $(200*0.7-200*0.5)/\mathrm{SQRT}(50+42)=4.17$ exceeds 1.96, one can conclude that the difference is significant at 0.05 level.

For all the significant differences that involved d_a values whose chi-square statistics exceeded the 0.05 critical value, this normal approximation test was applied. In all the cases except one (subject 1, IN at A), one of the following two conditions was met: (a) either P(R) or P(L) was significantly different, while the other was not, or (b) both P(R) and P(L) were significantly different. Even in the only exceptional case for subject 1, the fit to the model was not so poor [$\chi^2(1)$ was 7.59* for M2, 1.67 for A], and P(L) greatly increased from 52.5% to 74.0% whereas P(R) dropped only a little (97.0% to 91.0%), although this difference was significant.

D. Sensitivity changes

Table IV summarizes sensitivity parameters for each test for each subject. Subjects 7 and 8 had a general category reversal problem before training (B1 and B2), as is indicated by their negative sensitivity values that were significantly below zero. In order to concentrate on the net sensitivity increase, evaluation of sensitivity changes between tests B2 and M1 for these subjects was performed by reversing the signs of d_a values at B2. For example, instead of using $[0.82-(-0.51)=1.33]$ as a numerator in the significance test for subject 7's IN (this would have certainly led to a significant result), $[0.82-0.51=0.31]$ was used, which led to a nonsignificant result presented in the table.

Of all the 28 cases where incidental learning was at issue (7 subjects$\times$2 positions at B and M), there were three clear cases of increase in sensitivity without training between tests B1 and B2. Subject 3 showed a significant increase of 0.64 for IN, subject 6 showed 0.4 increase for IN and subject 8 showed the same amount of increase for CL. (Subject 8, due to her category reversal problem, decreased her negative sensitivity by 0.4.) There was one such case between M1 and M2, where subject 2 showed an increment of 0.34 for CL.

Thus, some Japanese listeners seem to be capable of increasing their sensitivity to a large set of English /r/ and /l/ tokens without training (but maybe not to English /r/ and /l/ in general, since no subject showed incidental increases for both IN and CL at the same time), simply by listening to these tokens repeatedly. For this reason, the overall increase in sensitivity found in this study cannot be attributed solely to the training sessions that utilized different sets of stimuli with feedback.

However, the impact of such incidental learning was much smaller in size compared to the massive improvement found between tests B2 and M1. The differences between B2 and M1 were all significant except in two cases (subject 4, IN, and subject 7, CL), and the average sensitivity increase between B2 and M1 across all subjects for both IN and CL was 0.89.

Compared to this massive increase after TP1, only one subject (subject 1 for both IN and CL) showed significant sensitivity increase after TP2 and TP3 (i.e., between tests M2 and A). This was the case in spite of the fact that for each subject for every position, the average P(c) during TP3 (except the special training) was always better than the P(c) on the final day of TP1B as was mentioned above.

The table also shows tremendous individual differences in terms of both initial and final sensitivities and the total amount of increase in d_a. Subject 1, for example, had almost no sensitivity before training (B1 and B2) for both IN and CL, whereas others had moderate sensitivity (S3 and S6). Subject 5's sensitivity was so high that it did not fit the SDT model at all. Thus, the eight subjects recruited, although small in number, represented almost the entire range of initial sensitivity. Final sensitivities achieved by these subjects also varied widely. Subject 3 exceeded 3.0 for both IN and CL, and subject 6 exceeded 2.5 at M2 for both IN and CL. This result is not surprising since these two subjects had the highest initial sensitivities.

However, the initial performance alone does not seem to predict the final performance. Subject 7, whose sensitivity for IN was 0.69, scored only 1.10 in the final test, the increment of 0.41 being the smallest among all the subjects. On the other hand, subject 1, whose sensitivity for IN was near zero before training, attained much higher sensitivity of 1.92.

Since two different combinations of training and baseline tokens and two different computers were used, some of the individual differences mentioned above could be attributed to these differences. But even when we restrict the comparison to those subjects who used the same combination of baseline and training tokens and hardware, differences still remain. Comparisons of subjects 3 and 7, and subjects 2 and 6, represent such cases. Subject 3 and subject 7's initial sensitivities to IN tokens were almost the same (0.73 and 0.69, respectively), whereas those to CL tokens were totally different (1.38 and 0.25, respectively). More marked were their final sensitivity differences. Subject 3 reached above 3.0 for both IN and CL, whereas subject 7's sensitivities remained around 1.0. Subject 6, who only underwent TP1, reached much higher sensitivities for both IN and CL than subject 2.

E. Response bias changes

Table V represents the response bias parameter c_a for each subject for each test. Here again, marked individual differences were found. Subjects 1 and 2 started out with almost no bias before training, but subject 1 suddenly developed a strong /r/ bias at M2, whereas subject 2 developed an opposite /l/ bias at M1. Subject 3 had a slight /l/ bias for his CL tokens initially, and the bias changed its direction at M2 (from -0.26 at M1 to 0.65 at M2). No such change was found for his IN tokens. All of this indicates that response bias can change drastically without training, and that biases for IN and CL tokens can be independent.

Subject 4 initially had a strong /r/ bias for both IN and CL, and the same /r/ bias remained even after training al-

TABLE V. Response bias changes in c_a as a function of tests for each subject.

	IN					CL				
	B1	B2	M1	M2	A	B1	B2	M1	M2	A
S1	−0.04	−0.06	0.15	0.88	0.35	0.00	0.01	0.18	0.72	0.46
S2	−0.01	0.08	−0.26	−0.22	−0.11	−0.01	0.10	−0.28	−0.33	−0.28
S3	−0.07	−0.02	0.10	0.08	0.04	−0.10	−0.22	−0.26	0.65	0.16
S4	0.60	0.53	0.17	0.28	0.25	0.63	0.70	0.13	0.25	0.19
S6	0.11	0.10	0.05	0.25		0.06	0.11	0.04	−0.02	
S7	−0.12	−0.07	0.09	0.07	0.09	−0.02	−0.01	0.07	0.10	0.11
S8	0.03	−0.18	−0.15	−0.05	0.02	−0.07	−0.28	−0.05	−0.11	−0.05

though its magnitude was reduced. The response biases of subjects 7 and 8 stayed around 0 with little fluctuation.

It is intriguing that only subject 4 showed a sizable improvement in terms of response bias, and that subjects 1 and 2 even developed strong response biases as training proceeded, since one would naturally expect that training should lead to more optimal (i.e., more neutral) response criterion location.

F. Effect of talker blocking

Table VI illustrates how overall P(c) and talker dependent response bias changed as a function of training for all subjects except subjects 5 and 6. Subject 5 had extremely high identification rates and had little room for response bias, and subject 6 discontinued the experiment after TP1.

The amount of talker dependent response bias is represented by the average absolute value of P(L)−P(R). Suppose, for a certain listener, P(L) and P(R) are 50% and 80% for tokens produced by talker X, and 80% and 50% for tokens by talker Y. The average P(L)−P(R) becomes 0%, whereas the average $|P(L)-P(R)|$ is 30%, the latter statistic truly reflecting the total amount of talker dependent response bias.

As the overall P(c) increased from TP1A to TP1B, the average $|P(L)-P(R)|$ also increased from 19.1% to 23.7%. The introduction of talker blocking at TP2 further increased the overall P(c) and decreased the talker dependent response bias from the previous 23.7% (TP1B) to 10.1% (TP2A). When talker blocking was discontinued at TP3, however, the overall P(c) decreased slightly from 87.6% (TP2B) to 82.4% (TP3), and the talker dependent response bias increased from 8.0% (TP2B) to 17.1% (TP3).

All of the above-mentioned changes in P(c) and $|P(L)-P(R)|$ between different phases of training were observed for almost all subjects and conditions. Even when this was not the case, the deviation was limited to either 1 or 2 cases out of the total 18 comparisons (6 listeners×3 positions). For example, the decrease in P(c) from TP2B to TP3, which was the smallest, was observed in all cases except 2 (subject 2, IN and subject 3, IV), and even these subjects showed decreases in the other positions.

The data clearly indicate that Japanese listeners with moderate sensitivities to the /r/-/l/ contrast find it difficult to adjust their response criterion optimally for each talker if tokens from multiple talkers are presented randomly. Given somewhat smaller $|P(L)-P(R)|$ during TP3 (17.1%) than during TP1B (23.7%), the training during TP2 with talker blocking seems to have had some impact. Nonetheless, the subjects failed to adjust their response criterion optimally for each talker's tokens during TP3 at the same level as they did during TP2.

TABLE VI. Mean P(c) and $|P(L)-P(R)|$ as a function of training phases for 6 subjects (except subjects 5 and 6).

	TP1A	TP1B	TP2A	TP2B	TP3
$P(c)$	63.5	74.4	84.5	87.6	82.4
$\|P(L)-P(R)\|$	19.1	23.7	10.1	8.0	17.1

G. Talker specific category reversal

Tables VII and VIII summarize each subject's average P(c)'s for the five tokens that he/she most frequently misidentified during tests M1, M2, and A (these entries are underlined), and other subjects' P(c)'s for these tokens. In computing P(c)'s, the confidence levels were ignored. The subjects are grouped together in terms of the stimulus set they used for these tests. (Subjects 1, 2, and 5 used tokens from Group 1 talkers, and the remaining subjects used those from Group 2 talkers.) Since Subject 5 made no response errors for IN, her IN rows are left empty. She also misidentified only four /l/ tokens for CL. Thus all the row entries for S5L are taken from 24 trials (4 tokens×6 repetitions), whereas all the remaining entries are summarized over 30.

Assuming that the identification rate for each of these frequently misidentified tokens is at pure chance (i.e., 0.5), the normal approximation technique for binomial distribu-

TABLE VII. P(c)'s for each subject's 5 most poorly identified tokens during tests M1, M2, and A (underlined) and other subjects' P(c)'s for these tokens for subjects 1, 2, and 5. The entries in the first row marked as "S1L," for example, represent the P(c)'s for subject 1's five most poorly identified L tokens from subjects 1, 2, and 5 (columns) for IN and CL. The starred entries are significantly below 50%.

	IN			CL		
	S1	S2	S5	S1	S2	S5
S1L	0.0*	90.0	100.0	0.0*	60.0	96.7
S1R	36.7	40.0	100.0	13.3*	40.0	83.3
S2L	53.3	33.3	100.0	40.0	16.7*	100.0
S2R	50.0	23.3*	100.0	63.3	0.0*	80.0
S5L				62.5	91.7	62.5
S5R				56.7	26.7*	60.0

TABLE VIII. P(c)'s for each subject's five most poorly identified tokens during tests M1, M2, and A (underlined) and other subjects' P(c)'s for these tokens for subjects 3, 4, 7, and 8. The entries in the first row marked as "S3L," for example, represent the P(c)'s for subject 3's five most poorly identified L tokens from subjects 3, 4, 7, and 8 (columns) for IN and CL. The starred entries are significantly below 50%.

	IN				CL			
	S3	S4	S7	S8	S3	S4	S7	S8
S3L	40.0	53.3	90.0	96.7	30.0*	60.0	60.0	43.3
S3R	40.0	60.0	53.3	26.7	66.7	76.7	76.7	73.3
S4L	93.3	0.0*	60.0	56.7	80.0	3.3*	60.0	50.0
S4R	90.0	16.6*	43.3	56.7	93.3	36.7	43.3	56.7
S7L	100.0	43.3	0.0*	33.3	83.3	60.0	0.0*	46.7
S7R	86.7	46.7	0.0*	20.0*	93.3	66.7	0.0*	40.0
S8L	96.7	60.0	6.7*	0.0*	76.7	23.3*	30.0*	0.0*
S8R	100.0	70.0	53.3	0.0*	93.3	70.0	30.0*	0.0*

tions reveals that any P(c) value 30% or below is significantly worse than chance at 0.05 level. For subject 5's entries that are taken from 24 observations, the same critical value is 29.2% (7/24 or below).

Notice that the majority of the underlined entries [i.e., each subject's P(c) for his/her most poorly identified tokens] are below 50%, except subject 3's /r/ and subject 5's /r/ and /l/ tokens for CL. In 18 cases out of 26, the underlined entries are significantly below chance. Viewed from the standpoint of SDT, these poorly identified tokens are located near the edge of each sensory distribution (one from /r/ and one from /l/ tokens) that is closer to the mean of the other distribution. That is why category reversal occurs for these tokens alone. When a given observer has a relatively high sensitivity, the two underlying distributions are further apart from each other and hence the number of TSCR cases will be considerably reduced. That is why the data from subjects 3 and 5 looked different with respect to TSCR.

The data also reveal that tokens that undergo TSCR are mostly different from subject to subject. There were certainly cases where a single token appeared in different sets of poorly identified tokens from multiple subjects. Of all the 129 poorly identified tokens (20 tokens from each subject except subject 5, who contributed only nine), 14 tokens were common to two subjects, and 2 tokens to three subjects. If we assume that the small number of these overlapping tokens is simply due to chance variability and that tokens located near the overlapping area of the two underlying sensory distributions are the same across all subjects, then we should expect similar P(c) values across all the row entries as well as column entries. But this was not the case. When the worst items for a particular subject were identified significantly below chance, other subjects' P(c)'s for these items were mostly not significantly below 50%. For the column entries for subjects 3 and 5, almost all the entries except the underlined ones were above 80%.

This indicates that tokens that lead to the highest probability of misidentification depend on observers. Even subjects 3 and 5, who had the highest overall sensitivity, were sometimes outperformed by other subjects on the identification of their poorly identified tokens. Subject 2 had a higher P(c) (91.7%) than subject 5 for subject 5's poorly identified /l/ tokens for CL. Subject 3's underlined entries are the lowest across each row except in one case (subject 8, row S3R).

To further verify that the poorly identified tokens for each subject do lead to TSCR, they were presented to each subject, five times each, together with five /l/ and five /r/ tokens that they identified with 100% accuracy during tests M1, M2, and A. These highly identifiable stimuli were included to reproduce the same stimulus range as before. The same four response buttons were provided as in tests M1, M2, and A. Since subject 5 had only four /l/ tokens, one of them, which showed perfect category reversal (i.e., 0%), was presented 20 times, and the remaining tokens were presented 10 times.

Table IX presents the results of this final test of TSCR. The entries in parentheses are average P(c)'s during tests M1, M2, and A. Subject 5's data will be described separately

TABLE IX. P(c) data for each subject's five most poorly identified tokens (reversal tokens) and five most accurately identified tokens (nonreversal tokens) in the final test of TSCR. The values in parentheses are P(c)'s from the previous tests M1, M2, and A. The starred entries are significantly below 50%.

	IN				CL			
	Reversal		Nonreversal		Reversal		Nonreversal	
	L	R	L	R	L	R	L	R
S1	8.0* (0.0)	28.0* (36.7)	100.0	100.0	0.0* (0.0)	32.0 (13.3)	100.0	100.0
S2	72.3 (33.3)	56.0 (23.3)	92.0	76.0	40.0 (16.7)	8.0* (0.0)	100.0	92.0
S3	68.0 (40.0)	88.0 (40.0)	96.0	96.0	32.0 (30.0)	96.0 (66.7)	92.0	100.0
S4	24.0* (0.0)	52.0 (16.0)	92.0	96.0	16.0* (3.3)	52.0 (36.7)	92.0	100.0
S7	20.0* (0.0)	16.0* (0.0)	100.0	96.0	3.0* (0.0)	1.0* (0.0)	92.0	92.0
S8	36.0 (0.0)	32.0 (0.0)	96.0	96.0	24.0* (0.0)	8.0* (0.0)	84.0	96.0

below. Since each entry is computed based on 25 trials, any value 28% (7/25) or below is significantly worse than chance.

Obviously, with several exceptions (subject 2, IN, L and R; subject 3, IN, L and R, CL, R; subject 4, R for both IN and CL), the tokens whose P(c)'s were below 50% led to P(c)'s lower than 50% in this new test, indicating that the results obtained during tests M1, M2, and A were not simply by random statistical fluctuation. High P(c)'s for the nonreversal tokens show that category reversal is indeed specific to particular sets of tokens.

Subject 3, whose sensitivity was high, had only one case of category reversal, i.e., for his /l/ tokens in CL. His P(c) (32%) was not significantly below 50% in this test, but when we take into consideration the result from the previous tests (30%), we have enough evidence to conclude that his P(c) for this particular set of tokens is below 50%.

Subject 5 correctly identified all of her nonreversal tokens with 100% accuracy. She also identified her /r/ tokens she had previously misidentified almost perfectly (1 error out of 50 trials). But the one /l/ token that had led to perfect category reversal remained so even here. In all of the 20 trials, her response was constantly /r/. Since she pushed the ''R1'' button 18 times, she was relatively less confident about her decision, but nonetheless her judgement was consistently /r/.

Interestingly, this particular token caused no problem for subjects 1 and 2, who correctly identified this token six and five times, respectively, in the six trials during tests M1, M2, and A. So for this particular token alone, subjects 1 and 2, whose overall sensitivity to /r/-/l/ contrast is much lower, can outperform subject 5.

For each subject, then, there existed at least one set of tokens (in case of subject 5, one token) that led to token specific category reversal. Since the tokens used here had been edited in such a way that their lexical identity was masked, response bias due to lexical familiarity cannot explain the TSCR phenomenon observed here. Just in case, one of the native speakers of English who tested the edited tokens was asked to identify all of the poorly identified tokens again, this time matching the hardware used by the learner who misidentified the tokens. Each stimulus was presented twice, and no error was made. Thus the tokens were all appropriate exemplars of /r/ or /l/ . The TSCR phenomenon seems, then, to depend on the position of each token in the range of sensory impressions which varied for individual Japanese listeners as they attempted to respond to various tokens of /r/ and /l/ .

IV. DISCUSSION

Although identification training increased each subject's sensitivity to /r/ and /l/ tokens that were not used during training, the final sensitivities attained by each subject varied widely, ranging from somewhat mediocre 70% ($d_a = 0.93$; subject 7 for CL) to perfect discrimination (100%, subject 5, IN). Even after intensive training, however, there remained, for each subject, some tokens that were misidentified at a rate significantly worse than chance. This token specific category reversal indicates that the perceptual difficulty experienced by Japanese listeners is due to an inherent limitation of the scaling or classification scheme developed after training, for it fails to assign a proper category to some tokens consistently.

This scaling scheme is likely to be mediated, at least partially, by the goodness of fit to Japanese /ɾ/. Takagi (1995) found that English /l/ tokens are judged to be closer to Japanese /ɾ/ than English /r/ tokens by Japanese listeners, and that the goodness of fit rating difference between pairs of /r/ and /l/ tokens is highly correlated with the discriminability of these pairs. When the subjects were asked to describe the difference between /r/ and /l/ verbally after the entire experiment, four subjects indeed mentioned that English /l/ sounded closer to Japanese /ɾ/, although one insisted that English /r/ was closer to /ɾ/. Either way, it seems that Japanese listeners identify /r/ and /l/ by using Japanese /ɾ/ as a reference point, or a perceptual anchor.

The subjects also described the target consonants using adjectives. Frequently used words for /l/ were ''karui'' (light, not heavy), ''akarui'' (light, not dark), and ''hakkiri-shita'' (clear), and /r/ was often described using opposite words: ''omotai'' (heavy), ''kurai'' (dark), and ''aimaina'' (unclear). Also used for /l/ was ''hajiku-yona oto'' (a flap like sound). The word ''makijita'' (a retroflex) was also used for /r/. No matter what kind of scaling scheme Japanese listeners may develop internally, however, it seems to be bound by Japanese phonology.

Not only intensive laboratory training but also prolonged naturalistic exposure to spoken English does not seem to lead to nativelike perceptual mastery of /r/ and /l/. Takagi and Mann (1995) tested 12 native speakers of Japanese who had come to the U.S. after puberty and had spent more than 12 years using English on a daily basis, and found that none of them were able to identify /r/ and /l/ at the same level of accuracy as native speakers of English (all below 85% for CL tokens).

There certainly exists a logical possibility that some adult Japanese speakers may attain nativelike perceptual mastery of /r/ and /l/, but the present author remains pessimistic about such a prospect because all 7 subjects who were tested for TSCR, including the one with exceptional sensitivity, had TSCR problems.

Random presentation of tokens from multiple talkers was found to increase talker dependent response biases and decrease the overall percentage of correct identification. The fact that the optimal response criterion location depends on talker may explain the finding that training with tokens produced by multiple talkers leads to better transfer to nontraining stimuli produced by a different talker (Logan *et al.*, 1991). During training in which subjects identify various tokens from multiple talkers with talker blocking, they learn to adjust their response criterion for the entire range of tokens produced by each talker. This optimal criterion shifting cannot be mastered if tokens from only one talker are used for training.

This unstable nature of Japanese listeners' response criterion suggests the lack of clear ''percepts'' comparable to L1 phonetic categories. When native speakers of Japanese are presented with English /r/ and /l/ tokens (except in word

final postvocalic position), what they hear is, in most cases, Japanese /ɾ/ (Takagi, 1993). They classify these tokens as /r/ or /l/ based on the within-category auditory impression that forms a continuum with no clear demarcation.

The reason we found strong token-observer interaction in this study may be related to the fact that most English /r/ and /l/ tokens go through this single assimilation process. The perceptual system of Japanese listeners is designed to categorize both /r/ and /l/ as Japanese /ɾ/, and it has nothing to do with further classifying them into two categories. It remains to be seen whether other single assimilation cases also lead to unpredictable token–observer interaction.

The fact that the tokens that led to TSCR depended on individual listeners suggests that every Japanese listener has his or her own unique way of perceiving /r/ and /l/, or computing sensory random variables **R** and **L** based on the multidimensional acoustic information contained in the tokens. Such individual differences may be a function of the number of such acoustic dimensions involved and different weighting schemes among them. Possible acoustic properties may include formant frequencies for the liquids, the duration of their steady formant states, burst characteristics for cluster tokens, etc. By carefully analyzing the tokens that led to TSCR and those that did not on an individual basis, one might be able to identify acoustic characteristics that caused TSCR for each subject.

The token–observer interaction also points to the importance of conducting a small-N study with tokens produced by multiple talkers in which each subject's performance with respect to each token is estimated accurately. Many studies in the field of L2 speech perception use what one might call a moderate-N ANOVA approach, where tokens produced by a few talkers are presented several times to a moderate number of subjects, and an ANOVA determines possible main effect(s) and their interactions. Although this approach has an advantage of finding central tendencies with reasonable resources, it has certain limitations.

When token–observer interaction exists, results obtained by this approach have limited generalizability, since one might find different results with new sets of tokens and/or subjects. Therefore, interpretation of significant main effects and interactions (or lack of them) must be done with caution, since the same effect or interaction may not be found in every member of a certain L1 population, or with every token of a certain L2 sound. We can guard against such overgeneralizations by conducting small-N studies with accurate estimation of each subject's performance on each token. The present author believes that complementary use of the small-N and conventional moderate-N ANOVA approaches in future experimentation will increase our knowledge of L2 speech perception in general.

ACKNOWLEDGMENTS

This research was supported by grant in aid for scientific research by the Japanese Ministry of Education, Science, Sports, and Culture. The author thanks J. E. Flege for providing the opportunity to record and test the tokens used in the present research. He is also grateful to T. Riney for his comments on an earlier version of the paper. He is indebted to the associate editor (K. R. Kluender) and two reviewers (J. Logan, and T. L. Gottfried) for their helpful suggestions and valuable comments, which greatly enhanced the quality of the present paper.

Bradlow, A. R., Pisoni, D. B., Akahane-Yamada, R. A., and Tohkura, Y. (**1997**). ''Training Japanese listeners to identify English /r/ and /l/: IV. Some effects of perceptual learning on speech production,'' J. Acoust. Soc. Am. **101**, 2299–2310.

Best, C. T., McRoberts, G. W., and Sithole, N. N. (**1988**). ''Examination of perceptual reorganization for nonnative speech contrasts: Zulu click discrimination by English-speaking adults and infants,'' J. Exp. Psychol. Hum. Percept. Perform., **14**, 345–360.

Dorfman, D. D., and Alf, Jr., E. (**1969**). ''Maximum likelihood estimation of parameters of signal detection theory and determination of confidence intervals—rating method data,'' J. Math. Psychol. **6**, 487–496.

Flege, J. E., Takagi, N., and Mann, V. (**1996**). ''Lexical familiarity and English-language experience affect Japanese adults' perception of /ɹ/ and /l/,'' J. Acoust. Soc. Am. **99**, 1161–1173.

Lively, S. E., Logan, J. S., and Pisoni, D. B. (**1993**). ''Training Japanese listeners to identify English /r/ and /l/. II. The role of phonetic environment and talker variability in learning new perceptual categories,'' J. Acoust. Soc. Am. **94**, 1242–1255.

Lively, S. E., Pisoni, D. B., Yamada, R. A., Tohkura, Y., and Yamada, T. (**1994**). ''Training Japanese listeners to identify English /r/ and /l/. III. Long-term retention of new phonetic categories,'' J. Acoust. Soc. Am. **96**, 2076–2087.

Logan, J. S., Lively, S. E., and Pisoni, D. B. (**1991**). ''Training Japanese listeners to identify English /r/ and /l/: A first report,'' J. Acoust. Soc. Am. **89**, 874–886.

Macmillan, N. A., and Creelman, D. C. (**1991**). *Detection Theory: A User's Guide* (Cambridge U.P., New York).

Strange, W., and Dittman, S. (**1984**). ''Effects of discrimination training on the perception of /r-l/ by Japanese adults learning English,'' Percept. Psychophys. **36**, 131–145.

Swets, J. A., and Pickett, R. M. (**1982**). *Evaluation of Diagnostic Systems: Methods from Signal Detection Theory* (Academic, New York).

Takagi, N. (**1993**). ''Perception of American English /r/ and /l/ by adult Japanese learners of English: A unified view,'' Unpubl. Ph.D dissertation, Univ. of California at Irvine.

Takagi, N. (**1995**). ''Signal detection modeling of Japanese listeners' /r/-/l/ labeling behavior in a one-interval identification task,'' J. Acoust. Soc. Am. **97**, 563–574.

Takagi, N., and Mann, V. (**1995**). ''The limits of extended naturalistic exposure on the perceptual mastery of English /r/ and /l/ by adult Japanese learners of English,'' Appl. Psycholing. **16**, 379–405.

Yamada, R. A. (**1993**). ''Effects of extended training on /r/ and /l/ identification by native speakers of Japanese,'' J. Acoust. Soc. Am. **93**, 2391(A).

Yamada, R. A., Tohkura, Y., and Kobayashi, N. (**1992**). ''Effect of word familiarity on non-native phoneme perception: Identification of English /r/, /l/, and /w/ by native speakers of Japanese,'' in Second Language Speech, edited by A. James and J. Leather (Mouton de Gruyter, The Hague).

Benefit of modulated maskers for speech recognition by younger and older adults with normal hearing

Judy R. Dubno,[a] Amy R. Horwitz, and Jayne B. Ahlstrom
Department of Otolaryngology-Head and Neck Surgery, Medical University of South Carolina, 39 Sabin Street, P.O. Box 250150, Charleston, South Carolina 29425

(Received 17 April 2001; accepted for publication 29 March 2002)

To assess age-related differences in benefit from masker modulation, younger and older adults with normal hearing but not identical audiograms listened to nonsense syllables in each of two maskers: (1) a steady-state noise shaped to match the long-term spectrum of the speech, and (2) this same noise modulated by a 10-Hz square wave, resulting in an interrupted noise. An additional low-level broadband noise was always present which was shaped to produce equivalent masked thresholds for all subjects. This minimized differences in speech audibility due to differences in quiet thresholds among subjects. An additional goal was to determine if age-related differences in benefit from modulation could be explained by differences in thresholds measured in simultaneous and forward maskers. Accordingly, thresholds for 350-ms pure tones were measured in quiet and in each masker; thresholds for 20-ms signals in forward and simultaneous masking were also measured at selected signal frequencies. To determine if benefit from modulated maskers varied with masker spectrum and to provide a comparison with previous studies, a subgroup of younger subjects also listened in steady-state and interrupted noise that was not spectrally shaped. Articulation index (AI) values were computed and speech-recognition scores were predicted for steady-state and interrupted noise; predicted benefit from modulation was also determined. Masked thresholds of older subjects were slightly higher than those of younger subjects; larger age-related threshold differences were observed for short-duration than for long-duration signals. In steady-state noise, speech recognition for older subjects was poorer than for younger subjects, which was partially attributable to older subjects' slightly higher thresholds in these maskers. In interrupted noise, although predicted benefit was larger for older than younger subjects, scores improved more for younger than for older subjects, particularly at the higher noise level. This may be related to age-related increases in thresholds in steady-state noise and in forward masking, especially at higher frequencies. Benefit of interrupted maskers was larger for unshaped than for speech-shaped noise, consistent with AI predictions. © *2002 Acoustical Society of America.* [DOI: 10.1121/1.1480421]

PACS numbers: 43.71.Lz, 43.66.Dc, 43.66.Sr, 43.66.Mk [CWT]

I. INTRODUCTION

Speech recognition by younger subjects with normal hearing improves substantially in modulated maskers relative to steady-state maskers, whereas performance of older subjects, especially those with hearing loss, improves less or not at all (Festen and Plomp, 1990; Takahashi and Bacon, 1992; Eisenberg *et al.*, 1995; Stuart and Phillips, 1996; Bacon *et al.*, 1998). That is, in time-varying maskers, older subjects benefit less from momentary improvements in signal-to-noise ratio (i.e., speech audibility) due to envelope fluctuations. These findings are noteworthy for several reasons. First, maskers with time-varying characteristics are temporally similar to maskers in the environment, i.e., single or multiple voices. Second, individuals with only mild hearing loss appear to benefit less from modulated maskers (Takahashi and Bacon, 1992; Dubno and Ahlstrom, 1997). Third, differences in performance between listeners with normal and impaired hearing decrease with the addition of multiple voices or a steady-state background, which has the effect of reducing the masker's envelope fluctuations (Bronkhorst and Plomp, 1992; Dubno and Ahlstrom, 1997).

Two explanations of these findings have been proposed. First, if thresholds are elevated, signal sensation levels are lower, which limits the improvement in signal-to-noise ratio that may be realized when the noise level momentarily decreases. This may also limit the increase in benefit expected with increasing overall noise level. Second, certain characteristics of temporal masking may render time-varying speech or noise a more effective masker. For example, the extent to which fluctuating improvements in signal-to-noise ratio benefit listeners may be related to recovery from forward masking (Feston and Plomp, 1990; Bronkhorst and Plomp, 1992; Festen, 1993; Gustafsson and Arlinger, 1994). Benefit from masker fluctuations may be reduced for subjects with elevated absolute thresholds, given that the decay of forward masking for pure tones is more gradual at lower sensation levels (e.g., Jesteadt *et al.*, 1982; Nelson and Freyman, 1987). For all subjects, benefit due to masker fluctuations should increase with increasing masker level, given that recovery is faster at higher masker levels (e.g., Jesteadt *et al.*, 1982). In addition to the effects of threshold differences among subjects, fluctuating noise may be a more effective masker for subjects with age-related changes in forward masking. Although it is possible that most of the deficit

[a]Electronic mail: dubnojr@musc.edu

for listeners with hearing loss is due simply to limited audibility, differences in performance in modulated maskers between younger and older subjects and between subjects with normal and impaired hearing have not been adequately explained (Eisenberg *et al.*, 1995; Bacon *et al.*, 1998).

The purpose of this experiment was to assess age-related differences in benefit from masker modulation while minimizing differences in signal audibility among subjects. An additional goal was to determine if age-related differences in speech recognition in steady-state and modulated noise could be explained by differences in thresholds measured in simultaneous and forward maskers. A secondary goal was to determine if benefit from modulated maskers varied with masker spectrum; this also permitted comparisons of benefit to previous studies. Here, thresholds and speech recognition of younger and older subjects with normal hearing were measured in a speech-shaped steady-state noise and in the same noise modulated by a 10-Hz square wave. The 10-Hz modulation rate was shown in previous studies to improve speech recognition relative to scores in steady-state noise (e.g., Miller and Licklider, 1950; Takahashi and Bacon, 1992; Bacon *et al.*, 1998) and was similar to the 12-Hz phoneme production rate occurring during speech (Plomp, 1983). Forward- and simultaneous-masked thresholds were also measured at several signal frequencies in two masker levels. An additional low-level noise was always present to minimize differences in speech audibility due to differences in quiet thresholds among subjects. Thresholds and speech recognition in steady-state and interrupted noise were also measured for younger subjects in a noise that was not spectrally shaped.

II. METHODS

A. Subjects

There were two subject groups: (1) eight younger subjects (mean age: 24.1 years; range: 20–27); and (2) eight older subjects (mean age: 67.3 years; range: 60–74). All subjects had ''normal hearing'' defined as thresholds $\leqslant$20 dB HL (ANSI, 1996) at octave frequencies from 0.25 to 4.0 kHz. Immitance measures were within normal limits. Subjects did not have experience with the psychophysical tasks used in this study and thus received approximately 2 h of practice with the various tasks. Data collection was completed in five to six 2-h sessions. Subjects were paid an hourly rate for their participation.

Mean thresholds (in dB SPL) for the two subject groups are shown in Fig. 1. Thresholds for frequencies in the audiometric range are in the left panel (see below for signals and procedures); thresholds for extended high frequencies are in the right panel (measured using a Demlar audiometer and Koss earphones). From 0.8 to 6.3 Hz, thresholds for the older subjects were higher than thresholds for the younger subjects, although all subjects met the criterion for ''normal hearing.'' Over this frequency range, thresholds averaged 10 dB higher for older than younger subjects. Although these older subjects would be considered to have ''normal hearing,'' they have substantial hearing loss in the extended high frequencies.

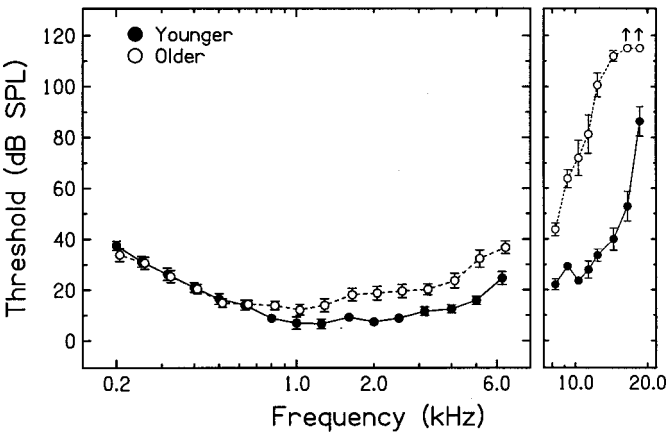

FIG. 1. Mean thresholds for 350-ms pure tones measured in quiet for younger subjects (filled) and older subjects (open). Error bars indicate ± 1 standard error of the mean (SE). Thresholds for frequencies in the audiometric range are in the left panel and thresholds for extended high frequencies are in the right panel. In the right panel, if subjects did not respond at the maximum intensity presented (110 dB SPL), thresholds were assigned a value of 115 dB SPL and the mean values are designated with an arrow (↑).

B. Apparatus and stimuli

1. Tonal signals

Tonal signals were digitally generated (TDT DA3-4) pure tones sampled at 50 kHz and low-pass filtered at 12 kHz (TDT FT6). Signals were either 350 ms, including 10-ms raised-cosine rise/fall ramps, or 20 ms, including 5-ms raised-cosine rise/fall ramps. Thresholds for the 350-ms signals were measured at 16 one-third-octave frequencies ranging from 0.2 to 6.3 kHz in quiet and in various noise maskers. Thresholds for the 20-ms signals were measured at 0.5, 1.0, 2.0, and 4.0 kHz in simultaneous and forward masking. Signal level was varied adaptively.

2. Noises

For simultaneous and forward masking (20-ms signals), the masker was a digitally generated (TDT DA3-4) broadband noise, 200 ms in duration with 5-ms rise/fall times. For forward masking, the duration between the masker and the signal was 0 ms (at the 0-voltage points). For simultaneous masking, the signal onset was 10 ms following the onset of the masker.

For simultaneous masking (350-ms signals) and for speech recognition, the masker was a steady-state broadband noise, digitally generated at a sampling rate of 28 kHz, and then spectrally shaped in one-third-octave intervals to match the long-term spectrum of the speech. For interrupted noise, this speech-shaped noise was modulated by a 10-Hz square wave at a modulation depth of 100% (Cool Edit Pro™ Version 1.2, Syntrillium Software Corp., Scottsdale, AZ). The noise was generated such that during the period when the interrupted noise was ''on,'' it was identical to the steady-state noise. Accordingly, the overall level of the interrupted noise was approximately 3–4 dB lower then the steady-state noise; no adjustments in level were made to compensate for this difference. Syllable durations ranged from 480 to 851 ms (for consonant-vowel syllables) and from 453 to 950 ms (for vowel-consonant syllables); of course, consonant durations

were shorter. Given the 50-ms ''off'' period of the interrupted noise, many silent periods occurred during each syllable presentation. The timing of each syllable presentation was random and independent of the noise, so that the location of the consonant portion of the syllable with respect to the ''on'' or ''off'' periods of the noise was also random. Noises were output through a 16-bit digital-to-analog converter (TDT DA3–4), low-pass filtered at 12 kHz (TDT FT6), and recorded onto digital audio tape (DAT) for playback.

Recall that quiet thresholds for older subjects were slightly higher than those of younger subjects (see Fig. 1); in addition, there were small differences in thresholds among subjects within each group. Accordingly, differences in speech audibility could arise during the ''off'' periods of the interrupted noise. To minimize these differences, a ''threshold matching noise'' (TMN) was present during threshold and speech-recognition measurements. This low-level broadband noise was generated and its spectrum adjusted at one-third-octave intervals (Cool Edit Pro™ Version 1.2) to produce equivalent masked thresholds for all subjects. Band levels of the TMN were set to shift thresholds to 20–25 dB HL from 0.2 to 3.15 kHz, 30 dB HL through 5.0 kHz, and 40 dB HL at 6.3 kHz (thresholds which were slightly higher than the highest thresholds of any subject). TMN was output through a 16-bit digital-to-analog converter (TDT DA3-4), low-pass filtered at 12 kHz (TDT FT6), and recorded onto digital audio tape (DAT) for playback. Spectral characteristics of all noises were verified on an acoustic coupler and a signal analyzer (Stanford Research SR780).

3. Speech

Speech signals were 66 consonant-vowel and 63 vowel-consonant syllables formed by combining 22 or 21 English consonants with /ɑ,i,u/ spoken by one male and one female talker (a total of 258 syllables). The stimulus set was divided into 12 subsets to provide for a more reasonable listening interval. A more detailed description of the speech stimuli can be found in Dubno and Schaefer (1992, 1995). Each syllable was presented two times in random order; thus, each speech-recognition score was the average of 516 responses. Digital speech waveforms (without a carrier phrase) were output at a sampling rate of 32.89 kHz and low-pass filtered at 12 kHz (TDT FT6). The level of the speech was fixed at 82 dB SPL. Speech recognition was measured in the steady-state and interrupted noises with noise presented at 77 or 85 dB SPL. Benefit was defined as the score in interrupted noise minus the score in steady-state noise.

A subset of five younger subjects also listened to speech in unshaped steady-state and interrupted noise. Speech recognition in both noises was measured with the speech and noise each presented at 85 dB SPL. Articulation index (AI) calculations predicted that this slightly higher speech level would result in similar scores in the steady-state speech-shaped and unshaped noise. Given that the benefit of interrupted maskers was known to be dependent on the score in the steady-state condition, it was important to equate scores in that condition to make appropriate comparisons of benefit in speech-shaped and unshaped maskers.

The amplitudes of all signals and maskers were controlled individually using programmable and manual attenuators (TDT PA4). The signal was added to the masker (TDT SM3), low-pass filtered (TDF PF1) at 7.0 kHz, and delivered through one of a pair of TDH-49 earphones mounted in a supra-aural cushion.

C. Procedures

For each subject, thresholds were measured in the following order: (1) thresholds in quiet for 350-ms pure tones; (2) masked thresholds for the 350-ms tones in the low-level TMN; (3) masked thresholds for 350-ms pure tones in the speech-shaped steady-state and interrupted noises at 77 and 85 dB SPL; and (4) thresholds for the 20-ms signals in forward and simultaneous masking. For a subset of five younger subjects, masked thresholds were also measured in the unshaped steady-state and interrupted noises at 85 dB SPL.

Thresholds were obtained using a single-interval (yes–no) maximum-likelihood psychophysical procedure, similar to that described by Green (1993) and discussed in detail in Leek *et al.* (2000). Each threshold was determined from 24 trials, four of which were catch trials. Listen and vote periods were displayed on the screen of a computer monitor. Subjects responded by clicking one of two mouse buttons corresponding to the responses ''yes, I heard the tone'' and ''no, I did not hear the tone.''

Following threshold measures, recognition of consonant-vowel and vowel-consonant syllables was measured in the steady-state and interrupted noises. Subjects were instructed to respond by clicking the mouse on the appropriate alphabetic symbol displayed on the computer monitor. All consonants contained in the subset were available alternatives; correct answer feedback was not provided. Differences in scores due to age, noise level, and noise type were assessed by repeated-measures ANOVA (effects were significant with $p<0.05$).

III. RESULTS AND DISCUSSION

A. Masked thresholds

1. Thresholds in steady-state and interrupted noise (350 ms)

Figure 2 shows thresholds for 350-ms tones for younger and older subjects in steady-state and interrupted noises at 77 dB (top) and 85 dB (bottom). TMN was present while these thresholds were measured; thresholds in TMN alone are also shown in both panels (circles). Note that masked thresholds in the interrupted noise (plus TMN) were nearly equivalent to those in the TMN alone. That is, the interrupted masker provided very little masking of tonal signals. This was likely due to the long duration of the signal (350 ms) in relation to the duration of the ''off'' time of the interrupted noise (50 ms). To obtain a single value with which to compare masked thresholds between groups, weighted average thresholds in steady-state noise, interrupted noise, and TMN were computed using weights from the frequency importance function for the speech stimuli used in this experiment (Dirks *et al.*, 1990a,b). Averaged across masker level, weighted average

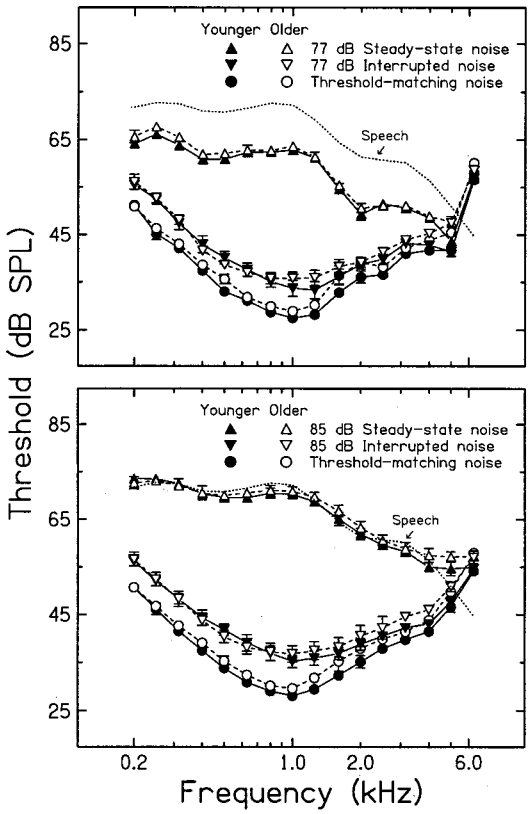

FIG. 2. Mean thresholds (±1 SE) for 350-ms pure tones for younger subjects (filled) and older subjects (open) in steady-state noise (triangles) and interrupted noise (inverted triangles). Thresholds in the 77-dB noise are in the top panel and thresholds in the 85-dB noise are in the bottom panel. Both panels include the spectrum of the speech at 82 dB SPL (dotted lines) and thresholds in the threshold-matching noise (circles).

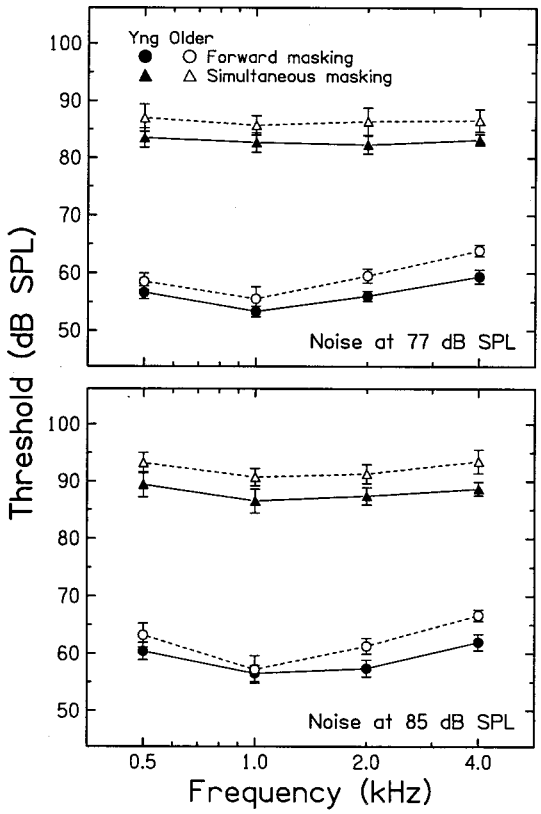

FIG. 3. Mean thresholds (±1 SE) for 20-ms pure tones at 0.5, 1.0, 2.0, and 4.0 kHz for younger subjects (filled) and older subjects (open), in forward masking (circles) and in simultaneous masking (triangles). Thresholds in the 77-dB masker are in the top panel and thresholds in the 85-dB masker are in the bottom panel.

thresholds were 1–2 dB higher for older than younger subjects in the steady-state and interrupted noises, and TMN, but differences were not statistically significant.

2. Thresholds in forward and simultaneous masking (20 ms)

Figure 3 includes thresholds for 20-ms tones at 0.5, 1.0, 2.0, and 4.0 kHz for younger and older subjects measured in forward and simultaneous masking, for the 77-dB masker (top) and the 85-dB masker (bottom). Averaged across frequency, thresholds were significantly higher by 3–4 dB for older than younger subjects in both forward and simultaneous masking. Thus, age-related differences in masked thresholds were larger for shorter-duration signals (Fig. 3) than for longer-duration signals (Fig. 2). However, differences between thresholds in forward and simultaneous masking were similar for younger and older subjects. That is, the size of the age-related threshold difference was similar in forward and in simultaneous masking.

B. Speech recognition

1. Steady-state and interrupted noise

Figure 4 plots speech-recognition scores for younger and older subjects in speech-shaped steady-state noise (top) and speech-shaped interrupted noise (bottom) as a function of noise level. In steady-state noise, scores declined with increasing noise level, as expected, and declined similarly for younger and older subjects. However, across level, scores averaged 11.7% higher for younger than for older subjects. This was an unexpected result given that (1) subjects had essentially equal audibility and (2) most of the variance in speech-recognition scores in steady-state noise has been attributed to differences in audibility (e.g., van Rooij and Plomp, 1992). In the interrupted noise, scores declined with increasing noise level, but declined less than in the steady-state noise, as listeners benefitted from the momentary improvements in signal-to-noise ratio during the ''off'' periods. However, scores declined significantly more for older than younger subjects with increasing level of interrupted noise, suggesting less benefit of interrupted maskers for older than younger subjects (this will be addressed again in later sections). Across level, scores in interrupted noise averaged 15.2% higher for younger than older subjects, an even larger age-related difference than was observed in steady-state noise.

2. Benefit of interrupted noise

Figure 5 contains the same data as Fig. 4 but shows differences in scores for steady-state and interrupted noise for younger and older subjects as a function of noise level. Scores were higher in interrupted noise than in steady-state noise for all subjects, especially at the higher noise level. However, scores of older subjects improved significantly less

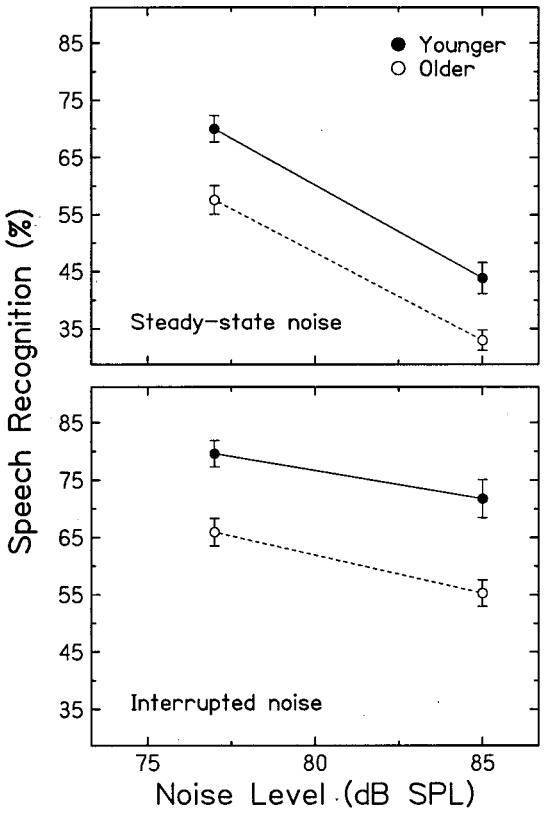

FIG. 4. Mean speech-recognition scores (±1 SE) in steady-state noise (top) and interrupted noise (bottom) as a function of noise level. The parameter is subject group.

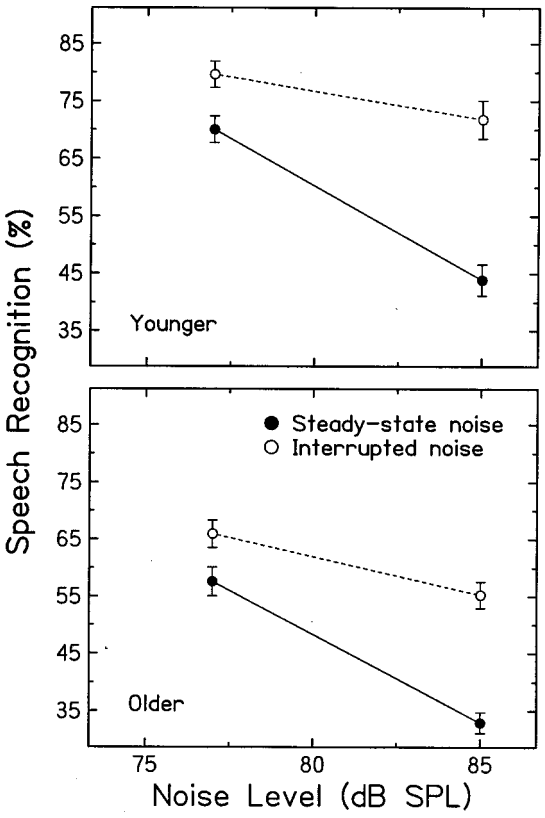

FIG. 5. Mean speech-recognition scores (±1 SE) for younger subjects (top) and older subjects (bottom). The parameter is noise type.

in interrupted noise than those of younger subjects, consistent with the conclusion from Fig. 4 that age-related differences in speech recognition were greater in interrupted noise than in steady-state noise. That is, older subjects did not benefit as much as younger subjects from the improvements in signal-to-noise ratio that occurred when the interrupted noise was ''off.''

The pattern of results shown in Fig. 5 suggested another estimate of the benefit of interrupted noise. Note that for younger subjects (top), the mean score in the 77-dB steady-state noise (70.0%) was nearly equivalent to the mean score in the 85-dB interrupted noise (71.8%). That is, with noise modulation, younger listeners maintained the same score achieved in steady-state noise despite an increase in noise level of 8 dB. Similar results were seen for older subjects (bottom), but the benefit of interrupted noise was smaller.

Benefit of interrupted noise and effect of noise level are seen in a different way in the left panel of Fig. 6 which plots benefit, i.e., score in interrupted noise minus score in steady-state noise, as a function of noise level for younger and older subjects (the right panel of Fig. 6 will be discussed later). Benefit increased significantly as noise level increased, suggesting that in higher noise levels, larger improvements in signal-to-noise ratio in the interrupted noise resulted in larger increases in scores. Given that scores for older subjects in steady-state noise were poorer than those of younger subjects, older subjects had the *potential* of greater benefit. Overall, however, older subjects derived significantly less benefit from improved signal-to-noise ratios than younger subjects.

3. Effect of audibility

a. Speech recognition in steady-state noise. Reduced speech recognition for older than younger subjects in steady-state noise was an unexpected result because of the assumption of equal audibility for all subjects. Although age-related differences in weighted average thresholds were not statistically significant, thresholds for older subjects were consistently higher than those for younger subjects by 1–2 dB. To determine if poorer scores in the steady-state noise for older subjects could be attributed to their slightly higher thresholds in the steady-state noise, AI values were computed and scores were predicted using each subject's masked thresholds in the steady-state noise (from Fig. 2). Figure 7 shows scores for younger and older subjects in steady-state noise at two levels plotted against AI. The solid line is the normal transfer function relating the AI to speech recognition established for the nonsense syllables used in this experiment (Dirks *et al.*, 1990a,b); the dashed lines encompass the 95% confidence interval.

At the lower noise level (77 dB, circles), the distribution of AI values computed for younger and older subjects generally overlapped, although the three highest AI values were for younger subjects. Scores for most older subjects fell slightly below the transfer function, suggesting that performance was somewhat poorer than predicted from the AI. In contrast, scores for most younger subjects clustered around the transfer function or were better than predicted. This pattern suggested that higher masked thresholds in the 77-dB

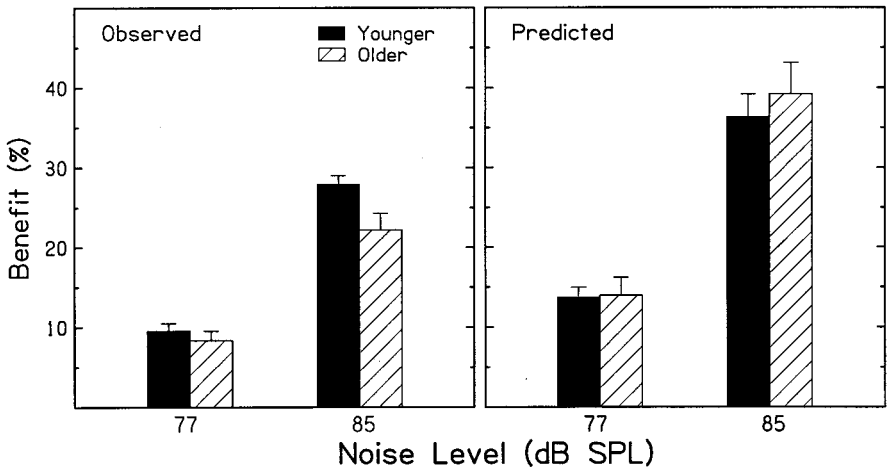

FIG. 6. Mean benefit (+1 SE) as a function of noise level for younger subjects (solid bars) and older subjects (striped bars). Benefit was defined as the score in interrupted noise minus the score in steady-state noise. Benefit computed from observed scores is in the left panel and benefit predicted from articulation index values for steady-state and interrupted noise is in the right panel (see text for details).

noise for older subjects and the subsequent decrease in audibility did not entirely account for their lower scores. Nevertheless, observed scores for nearly all subjects were within the 95% confidence interval of their predicted scores. In the higher noise level (85 dB, triangles), age-related differences in AI values were similar to those observed in the lower noise level. However, there was not as clear a differentiation between scores for younger and older subjects with respect to the transfer function; indeed, scores for most subjects in both groups were better than predicted by the AI. This suggested that threshold differences among subjects in the 85-dB noise accounted for the lower scores observed for older subjects in that noise.

To quantify the contribution of masked thresholds to age-related differences in scores in steady-state noise, differences were computed between individual observed scores and scores predicted by the AI (represented by the transfer function in Fig. 7). Here, the difference between the observed and predicted score (usually referred to as the ''residual'') was used as an estimate of speech recognition that was independent of threshold elevation. As such, comparison of observed–predicted differences for younger and older subjects provided an estimate of the age-related difference in scores that remained after accounting for differences in masked thresholds among subjects. If poorer scores of older subjects were entirely attributed to reduced audibility related to their elevated masked thresholds, differences between observed and predicted scores would be equivalent for younger and older subjects. When effects of masked thresholds were accounted for, the average difference in scores between younger and older subjects decreased from 11.7% to 7.4%; this group difference remained statistically significant ($p = 0.03$). However, the analysis also suggested that the portion of the age-related difference in scores attributable to masked thresholds varied with noise level. In the higher level noise, with audibility accounted for, score differences between younger and older subjects were no longer significant ($p = 0.348$). In the lower level noise, score differences remained significant even while accounting for audibility ($p = 0.004$). Thus, in this condition, age-related differences in speech recognition in steady-state noise could not be entirely explained by audibility.

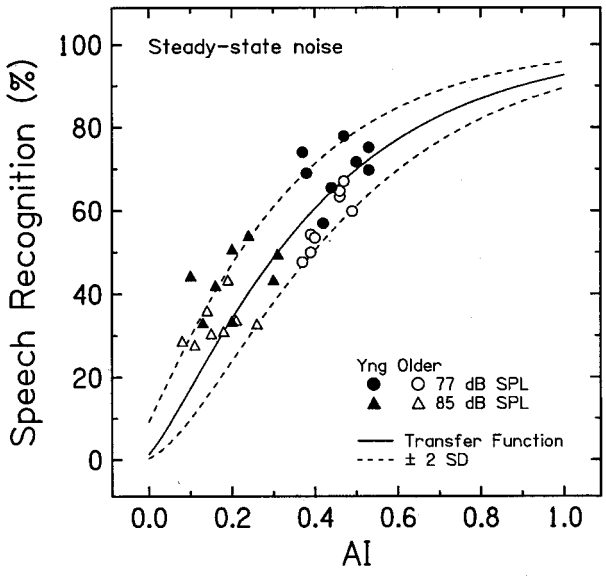

FIG. 7. Speech-recognition scores for individual younger subjects (filled) and older subjects (open) in steady-state noise at two levels plotted against articulation index (AI) values computed using each subject's thresholds in the steady-state noise. The solid line is the AI-recognition transfer function for the nonsense syllables and the dashed lines encompass the 95% confidence interval.

b. Speech recognition in interrupted noise and benefit. In the interrupted noise, the noise was ''on'' half the time; during the remaining time, thresholds were determined by the TMN. Given that thresholds were slightly higher for older than younger subjects in both steady-state noise and TMN, it was possible that poorer scores for older than younger subjects in interrupted noise could be attributed to reduced audibility both when the noise was ''on'' and ''off.'' Initially, AI values for interrupted noise were estimated using the corrections described in Sec. 5.1.2 (Masking by Non-Steady-State Noise) of the AI standard (ANSI, 1969) and given in Figs. 9 and 10 of the standard. However, using these corrections, AI values for younger subjects were all very high, resulting in scores that were nearly all substantially poorer than predicted. In addition, for the 77-dB noise, AI values were nearly identical for all subjects. These results called into question the suitability of AI values for interrupted noise computed using methods specified in the ANSI standard.

Several other procedures for computing AIs and predict-

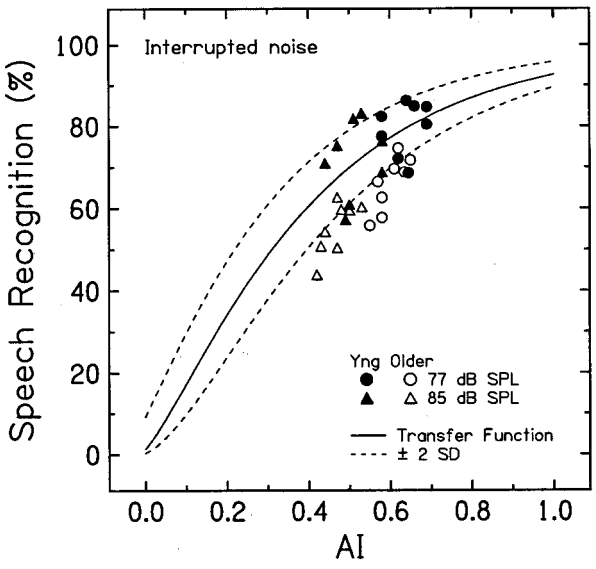

FIG. 8. Speech-recognition scores for individual younger subjects (filled) and older subjects (open) in interrupted noise at two levels plotted against articulation index (AI) values computed by taking the mean AI with and without steady-state noise. The solid line is the AI-recognition transfer function for the nonsense syllables and the dashed lines encompass the 95% confidence interval.

ing scores for interrupted noise were evaluated, each using a different method to estimate an effective noise level for the interrupted condition. The best results were obtained using the method described by Houtgast *et al.* (1992) wherein the AI for the interrupted noise was integrated over time by (in this case) taking the mean of the AI for TMN alone and the AI for steady-state noise. Predicted scores were obtained using the same AI-recognition transfer function used to predict scores in steady-state noise (Fig. 7). Figure 8 shows observed scores for younger and older subjects in interrupted noise at two levels plotted against AI. Here, observed scores in interrupted noise for nearly all of the younger subjects were within the 95% confidence interval of their predicted scores, supporting the validity of the method used to estimate the AI for interrupted noise. Further, observed scores in interrupted noise for nearly all of the older subjects were poorer than predicted.

As described above for steady-state noise, a comparison of observed–predicted differences for younger and older subjects provided an estimate of the age-related difference in scores in interrupted noise that remained after accounting for differences in masked thresholds among subjects. When effects of masked thresholds were accounted for, the average difference in scores in interrupted noise between younger and older subjects decreased only slightly, from 15.2% to 12.2%. This group difference remained statistically significant ($p = 0.0018$), with no significant age by noise-level interaction. Thus, consistent with the pattern of results in Fig. 8, age-related differences in speech recognition in interrupted noise could not be explained by audibility.

AI values for steady-state and interrupted noise were also used to predict benefit of masker modulation for younger and older subjects (i.e., predicted score in interrupted noise minus predicted score in steady-state noise).

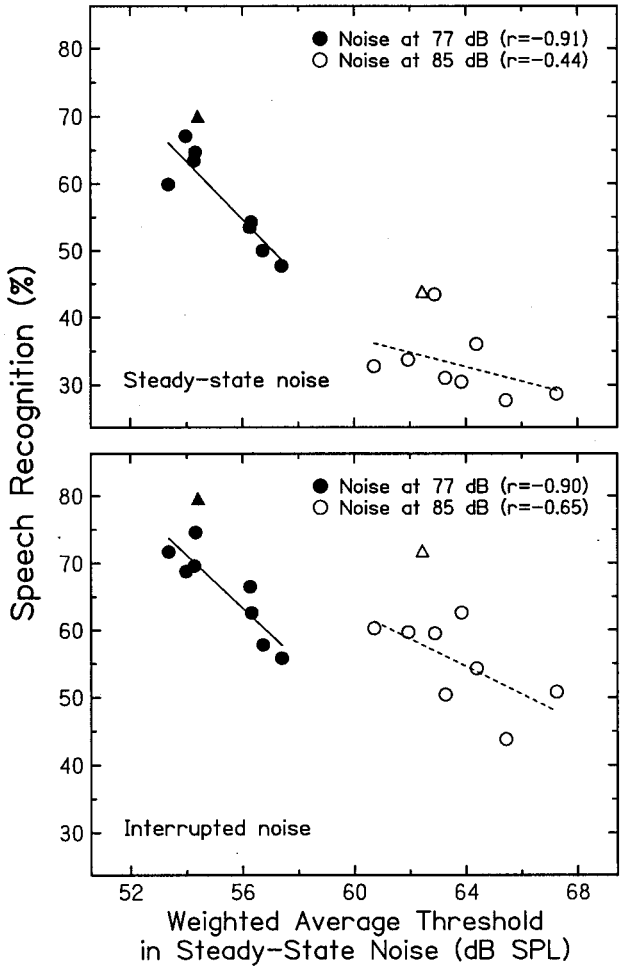

FIG. 9. Speech-recognition scores for older subjects (circles) in steady-state noise (top) and interrupted noise (bottom) plotted against weighted average thresholds measured in steady-state noise. The parameter is noise level. The lines are best fit linear regression functions; correlation coefficients are included in each panel. The triangles are mean weighted average thresholds and scores for the younger subjects.

Mean predicted benefit for the two noise levels is shown in the right panel of Fig. 6, along with mean observed benefit (left panel). Overall, observed benefit was less than predicted, but the source of this effect differed between groups. For younger subjects, on average, observed scores in interrupted noise were nearly equal to predicted scores whereas observed scores in steady-state noise were better than predicted, resulting in less observed benefit. For older subjects, on average, observed scores in interrupted noise were much worse than predicted whereas observed scores in steady-state noise were closer to or better than predicted, resulting in even less observed benefit (as much as 17% less). An interesting pattern was seen at the higher noise level. Here, older subjects were predicted to benefit *more* than younger subjects from modulation (as noted earlier), but actually derived *less* benefit. Greater predicted benefit for older subjects was based on their slightly higher thresholds in steady-state noise; these higher thresholds reduced both audibility and predicted score more in steady-state than in interrupted noise, resulting in greater predicted benefit. Overall, however, older subjects derived significantly less benefit than

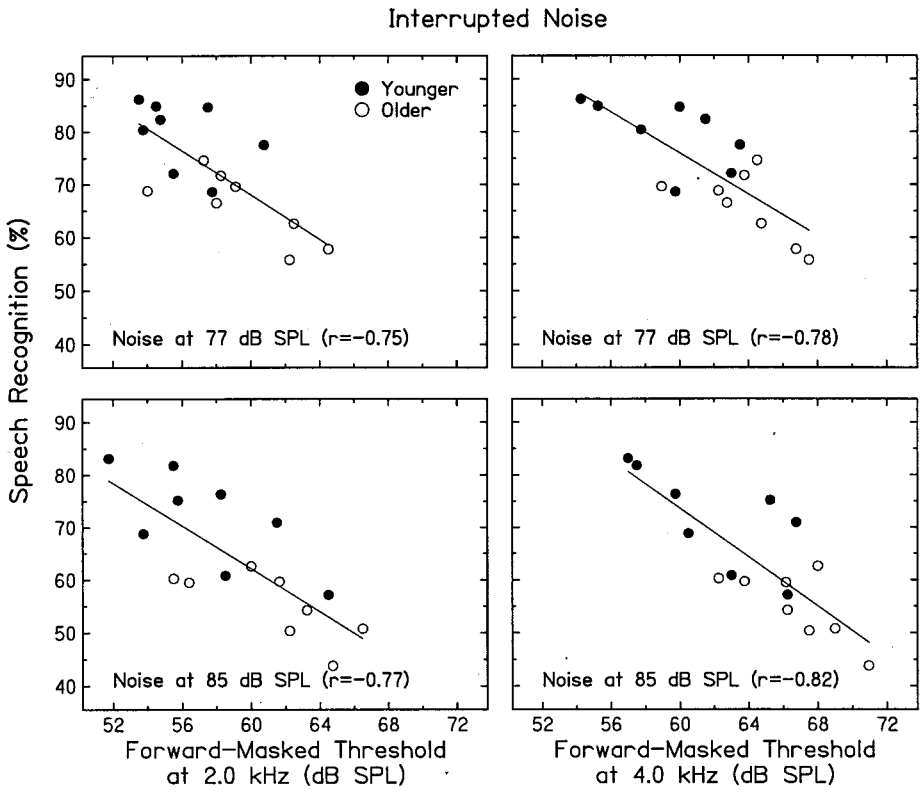

FIG. 10. Speech-recognition scores in interrupted noise plotted against forward-masked thresholds. Data for two noise levels (77 and 85 dB) are presented in the top and bottom panels and data for two signal frequencies (2.0 and 4.0 kHz) are presented in the left and right panels. Results for younger and older subjects are indicated by filled and open symbols, respectively. Linear regression functions were fitted to the pooled data. Correlation coefficients are given in each panel.

younger subjects, due to their poorer-than-predicted scores in interrupted noise.

c. Relationship between thresholds in steady-state noise and speech recognition in steady-state and interrupted noise. Linear regression analysis was used to assess the relationship between scores in steady-state and interrupted noise and weighted average thresholds in steady-state noise. Figure 9 includes scores in two levels of steady-state noise (top) and interrupted noise (bottom) for older subjects plotted against weighted average thresholds in steady-state noise. Correlation coefficients (r) are also given in the figure for each pair of variables. The negative correlations suggested that scores in both steady-state and interrupted noise decreased as masked thresholds in steady-state noise increased. Indeed, the correlations for the 77-dB noise indicated that 81%–83% of the variance in scores was accounted for by weighted average thresholds (but less was accounted for in the 85-dB noise). Because scores in interrupted noise and weighted average threshold were also significantly correlated with age, multiple correlations were computed and the R^2 partitioned to determine the portion of the variance attributable to each factor individually and that attributable to the joint contribution of these factors (the total explained variance was 97.7%). For scores in the 77-dB steady-state noise, 5.2% of the variance in score was accounted for by weighted average thresholds in the steady-state noise and 15.6% was contributed by subject age. However, most of the variance in score (76.9%) was explained by the joint contribution of age and weighted average threshold. Correlations between scores in the higher level steady-state noise and age and between scores and weighted average threshold were not statistically significant.

For comparison, also shown in Fig. 9 (triangles) are mean scores for each noise type plotted against mean weighted average thresholds in each noise level for the younger subjects. In contrast to results for older subjects, scores for younger subjects in steady-state and interrupted noise were not strongly correlated with weighted average thresholds in steady-state noise. As shown in Fig. 9, although mean thresholds for younger subjects were within the range of those for the older subjects, mean scores were higher, especially in interrupted noise.

4. Relationship between forward masking and speech recognition in interrupted noise

One goal of the current experiment was to determine if age-related differences in speech recognition in interrupted noise could be explained by differences in thresholds measured in forward maskers. Although weighted average thresholds in steady-state noise accounted for a large proportion of the variance in scores in the lower level interrupted noise for older subjects, only modest correlations were observed for the higher level noise and for younger subjects. One explanation is that thresholds in the steady-state masker (which determined audibility when the interrupted noise was ''on'') underlie scores in lower level interrupted noise, whereas recovery from forward masking (which determined audibility when the interrupted noise was ''off'') underlies scores for higher level interrupted noise with its larger improvement in signal-to-noise ratio when the noise was ''off.''

To test this hypothesis, linear regression analysis was used to assess the relationship between scores in interrupted noise at two levels and thresholds in forward maskers at two

levels. Negative correlations were observed between scores and thresholds at each of the four signal frequencies (0.5, 1.0, 2.0, and 4.0 kHz), suggesting that the benefit to speech recognition achieved in interrupted noise decreased as forward masking increased. At both noise levels, correlation coefficients increased with increasing frequency, reaching a peak at 4.0 kHz. Correlation coefficients at 0.5 and 1.0 kHz ranged from −0.38 to −0.45 and were not statistically significant. Correlation coefficients at 2.0 kHz for lower and higher noise levels were −0.75 and −0.77 ($p=0.0004$ and $p=0.0002$); the comparable values at 4.0 kHz were −0.78 and −0.82 (for each, $p=0.0002$). Figure 10 shows speech-recognition scores in two levels of interrupted noise (top and bottom panels) for younger and older subjects plotted against forward-masked thresholds at two signal frequencies (left and right panels). Each panel in Fig. 10 displays data, linear regression, and the correlation coefficient for a different pair of variables. Note that slightly stronger correlations were observed for the higher level than the lower level interrupted noise. Because scores in interrupted noise were also significantly correlated with age and weighted average threshold, multiple correlations were computed and the R^2 partitioned, as described above (the total explained variance ranged from 76.0% to 80.7%). For the four conditions (two noise levels and two forward-masked thresholds), the variance accounted for differed slightly but the general pattern was the same. That is, 9.9%–15.9% of the variance in scores in interrupted noise was accounted for by forward-masked thresholds and 12.7%–22.0% was contributed by subject age. However, most of the variance in score (42.8%–52.1%) was explained by the joint contribution of age and forward-masked threshold.

Finally, a stepwise regression was used to determine the relative importance of thresholds in steady-state noise and thresholds in forward masking to scores in interrupted noise. Consistent with our hypothesis, at the lower interrupted noise level, steady-state threshold and age accounted for the most variance, whereas at the higher noise level, forward-masked thresholds and age accounted for the most variance.

The frequency dependence observed in the relation between scores in interrupted noise and forward masking may be interpreted in at least three ways. First, the frequency dependence may be related to the relative importance of lower and higher frequencies to nonsense syllable recognition. The frequency importance function for the nonsense syllables used in this experiment increased with frequency and had a broad peak from 2.0 to 4.0 kHz. Information in these higher frequency bands contributed more to recognition of the nonsense syllables than information in the lower frequency bands at 0.5 and 1.0 kHz. Thus, speech recognition in interrupted noise may be more dependent on recovery from forward masking and the subsequent improvements in signal-to-noise ratio at higher frequencies than at lower frequencies. Second, the frequency dependence may be related to the spectral shape of the noise. The speech-shaped noise used in this experiment had more energy at lower than at higher frequencies (see Fig. 2). Thus, for a given overall noise level, the momentary improvement in signal-to-noise ratio during the ''off'' periods of the interrupted noise was substantially greater in the lower frequencies than in the higher frequencies. With less speech information available in the higher frequencies, small differences in recovery from forward masking and the subsequent effects on speech audibility may have been critical. Third, scores in interrupted noise may have depended more on recovery from forward masking at higher than at lower frequencies as a result of differences in the contribution of higher and lower frequency fibers to processing of speech in time-varying noise.

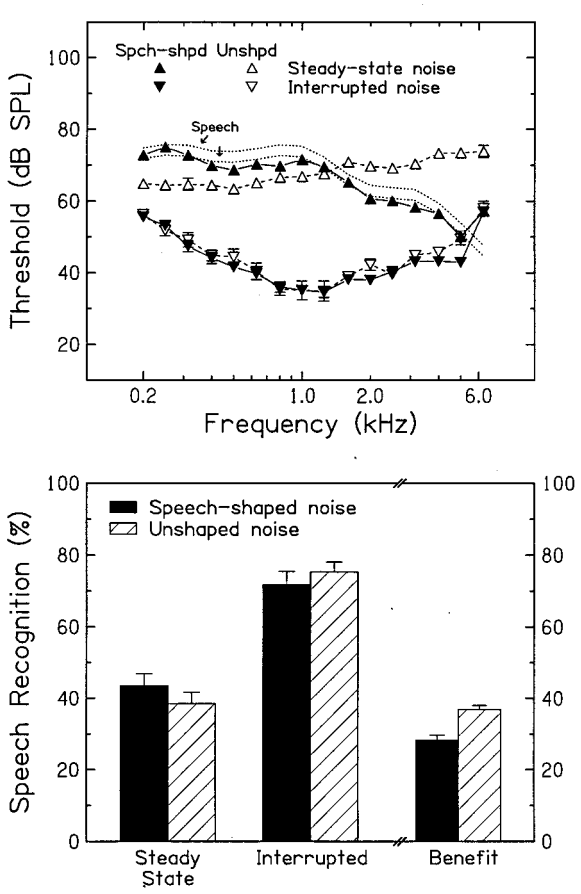

FIG. 11. *Top panel*: Mean thresholds (±1 SE) in speech-shaped noise (filled) and unshaped noise (open). Overall level of each noise was 85 dB SPL. Thresholds are shown for steady-state noise (triangles) and interrupted noise (inverted triangles). The spectra of the speech at 82 dB SPL (speech-shaped noise) and 85 dB SPL (unshaped noise) are also included as a reference (dotted lines). *Bottom panel*: Mean speech-recognition scores (+1 SE) for speech-shaped noise (filled bars) and unshaped noise (striped bars). Scores for steady-state and interrupted noise are the left and middle pairs of bars, respectively; benefit (interrupted score minus steady-state score) is the right pair of bars.

5. Effect of masker spectrum

Figure 11 plots thresholds (top) and speech-recognition scores (bottom) for younger subjects measured in unshaped and speech-shaped steady-state and interrupted noise. As expected, in the steady-state condition, thresholds in the unshaped noise were lower in the lower frequencies than in the speech-shaped noise, but higher in the higher frequencies. Very little masking of pure tones was observed due to either unshaped or speech-shaped interrupted noise. In the steady-state condition, speech-recognition scores were poorer for unshaped noise than for speech-shaped noise, but, in inter-

rupted noise, scores were better for unshaped than for speech-shaped noise; differences were not statistically significant.[1] Nevertheless, these opposing trends resulted in significantly more benefit for the unshaped noise than for the speech-shaped noise. This suggested that, in the unshaped noise, listeners benefitted from the larger improvements in signal-to-noise ratio in the higher frequencies that occurred during the periods when the interrupted noise was ''off.'' As mentioned earlier, given the importance of higher frequencies for these nonsense syllables, improved higher frequency audibility would be expected to contribute substantially to performance. Indeed, consistent with this assumption, benefit for unshaped noise predicted from AI values (39.4%) was larger than benefit predicted for speech-shaped noise (36.4%).

IV. SUMMARY AND CONCLUSIONS

Younger and older adults with normal but not identical audiograms listened to nonsense syllables at 82 dB SPL in each of two maskers presented at 77 and 85 dB SPL: (1) a steady-state noise shaped to match the long-term spectrum of the speech, and (2) this same noise modulated by a 10-Hz square wave, resulting in an interrupted noise. Speech recognition for younger subjects was also measured in unshaped steady-state and interrupted noise. An additional low-level broadband noise was always present which was shaped to produce equivalent masked thresholds for all subjects. Pure-tone thresholds at one-third-octave intervals were measured in quiet and in each masker; thresholds in forward and simultaneous masking were also measured at selected signal frequencies. Results may be summarized as follows:

(1) Masked thresholds of older subjects were slightly higher than those of younger subjects. Significant age-related threshold differences were observed for short-duration signals (3–4 dB) but not for long-duration signals (1–2 dB).
(2) In steady-state noise, speech recognition for older subjects was poorer than for younger subjects, which was partially attributable to older subjects' slightly higher thresholds in steady-state noise. For older subjects, scores in steady-state noise were strongly correlated with weighted average thresholds in steady-state noise, especially at the lower noise level.
(3) In interrupted noise, speech recognition for all subjects improved relative to steady-state noise, especially at the higher noise level, as subjects benefitted from momentary improvements in signal-to-noise ratio due to envelope fluctuations. However, although predicted benefit was larger for older than younger subjects, older subjects benefitted less from masker fluctuations than younger subjects. In the lower level interrupted noise, speech recognition was strongly correlated with age and thresholds in steady-state noise. In the higher level interrupted noise, speech recognition was strongly correlated with age and thresholds in forward masking at higher frequencies.
(4) Benefit of interrupted noise was larger for unshaped noise than for speech-shaped noise, which was probably attributable to spectral differences in the maskers at higher frequencies.
(5) Masked thresholds for shorter signals were higher for older than younger subjects. Further, speech-recognition deficits for older subjects were larger in fluctuating noise than in steady-state noise. Thus, age-related differences were largest for temporally-challenging listening tasks.

ACKNOWLEDGMENTS

This work was supported (in part) by Grant Nos. P50 DC00422 and R01 DC00184 from NIH/NIDCD, and the MUSC General Clinical Research Center (M01 RR 01070). The authors thank Chris Ahlstrom for computer and signal-processing support, Fu-Shing Lee for advice on data analysis, John H. Mills for editorial comments, and reviewer Adelbert Bronkhorst for valuable suggestions, including a reference for a method to compute AI values for interrupted noise.

[1]Observed scores for unshaped steady-state and interrupted noise were similar to scores predicted using the AI, as described in Sec. III B 3 for speech-shaped steady-state and interrupted noise. Except for one score for interrupted noise which was better than predicted, observed scores were within the 95% confidence interval of predicted scores.

ANSI (**1969**). ANSI S3.5-1969, ''Methods for the calculation of the articulation index'' (American National Standards Institute, New York).
ANSI (**1996**). ANSI S3.6-1996, ''Specification for audiometers'' (American National Standards Institute, New York).
Bacon, S. P., Opie, J. M., and Montoya, D. Y. (**1998**). ''The effects of hearing loss and noise masking on the masking release for speech in temporally complex backgrounds,'' J. Speech Lang. Hear. Res. **41**, 549–563.
Bronkhorst, A. W., and Plomp, R. (**1992**). ''Effect of multiple speechlike maskers on binaural speech recognition in normal and impaired hearing,'' J. Acoust. Soc. Am. **92**, 3132–3139.
Dirks, D. D., Dubno, J. R., and Bell, T. S. (**1990a**). ''Problems in the predictions of speech recognition among normal-hearing and hearing-impaired listeners,'' J. Acoust. Soc. Am. Supple. 1 **88**, S32.
Dirks, D. D., Dubno, J. R., Ahlstrom, J. B., and Schaefer, A. B. (**1990b**). ''Articulation index importance and transfer functions for several speech materials,'' Asha **32**, 91.
Dubno, J. R., and Ahlstrom, J. B. (**1997**). ''Additivity of multiple maskers of speech,'' in *Modeling Sensorineural Hearing Loss*, edited by W. Jesteadt (Erlbaum, Hillsdale, NJ), pp. 253–272.
Dubno, J. R., and Schaefer, A. B. (**1992**). ''Comparison of frequency selectivity and consonant recognition among hearing-impaired and masked-normal hearing listeners,'' J. Acoust. Soc. Am. **91**, 2110–2121.
Dubno, J. R., and Schaefer, A. B. (**1995**). ''Frequency selectivity and consonant recognition for hearing-impaired and normal-hearing listeners with equivalent masked thresholds,'' J. Acoust. Soc. Am. **97**, 1165–1174.
Eisenberg, L. S., Dirks, D. D., and Bell, T. S. (**1995**). ''Speech recognition in amplitude-modulated noise of listeners with normal and listeners with impaired hearing,'' J. Speech Hear. Res. **38**, 222–233.
Festen, J. M. (**1993**). ''Contributions of comodulation masking release and temporal resolution to the speech-reception threshold masked by an interfering voice,'' J. Acoust. Soc. Am. **94**, 1295–1300.
Festen, J. M., and Plomp, R. (**1990**). ''Effects of fluctuating noise and interfering speech on the speech-reception threshold for impaired and normal hearing,'' J. Acoust. Soc. Am. **88**, 1725–1736.
Green, D. M. (**1993**). ''A maximum-likelihood method for estimating thresholds in a yes-no task,'' J. Acoust. Soc. Am. **93**, 2096–2105.
Gustafsson, H. A., and Arlinger, S. A. (**1994**). ''Masking of speech by

amplitude-modulated noise,'' J. Acoust. Soc. Am. **95**, 518–529.
Houtgast, T., Steeneken, H. J. M., and Bronkhorst, A. W. (**1992**). ''Speech communication in noise with strong variations in the spectral or the temporal domain,'' Proceedings of the 14th International Congress on Acoustics, Vol. 3, pp. H2–6.
Jesteadt, W., Bacon, S. P., and Lehman, J. R. (**1982**). ''Forward masking as a function of frequency, masker level, and signal delay,'' J. Acoust. Soc. Am. **71**, 950–962.
Leek, M. R., Dubno, J. R., He, N.-j., and Ahlstrom, J. B. (**2000**). ''Experience with a yes-no single-interval maximum-likelihood procedure,'' J. Acoust. Soc. Am. **107**, 2674–2684.
Miller, G. A., and Licklider, J. C. R. (**1950**). ''The intelligibility of interrupted speech,'' J. Acoust. Soc. Am. **22**, 167–173.
Nelson, D. A., and Freyman, R. L. (**1987**). ''Temporal resolution in sensorineural hearing-impaired listeners,'' J. Acoust. Soc. Am. **81**, 709–720.
Plomp, R. (**1983**). ''Perception of speech as a modulated signal,'' in Proceedings of the 10th International Congress on Phonetic Science, Utrecht, pp. 29–40.
Stuart, A., and Phillips, D. P. (**1996**). ''Word recognition in continuous and interrupted broadband noise by young normal-hearing, older normal-hearing, and presbyacusic listeners,'' Ear Hear. **17**, 478–489.
Takahashi, G. A., and Bacon, S. P. (**1992**). ''Modulation detection, modulation masking, and speech understanding in noise in the elderly,'' J. Speech Hear. Res. **35**, 1410–1421.
van Rooij, J. C. G. M., and Plomp, R. (**1992**). ''Auditive and cognitive factors in speech perception by elderly listeners. III. Additive data and final discussion,'' J. Acoust. Soc. Am. **91**, 1028–1033.

Nonlinear analysis of irregular animal vocalizations

Isao Tokuda[a)]
Department of Computer Science and Systems Engineering, Muroran Institute of Technology, Muroran, Hokkaido 050-8585, Japan

Tobias Riede and Jürgen Neubauer
Institute for Theoretical Biology, Humboldt-University of Berlin, Invalidenstrasse 43, D-10115 Berlin, Germany

Michael J. Owren
Department of Psychology, 224 Uris Hall, Cornell University, Ithaca, New York 14853

Hanspeter Herzel
Institute for Theoretical Biology, Humboldt-University of Berlin, Invalidenstrasse 43, D-10115 Berlin, Germany

(Received 20 October 2001; revised 6 March 2002; accepted 8 March 2002)

Animal vocalizations range from almost periodic vocal-fold vibration to completely atonal turbulent noise. Between these two extremes, a variety of nonlinear dynamics such as limit cycles, subharmonics, biphonation, and chaotic episodes have been recently observed. These observations imply possible functional roles of nonlinear dynamics in animal acoustic communication. Nonlinear dynamics may also provide insight into the degree to which detailed features of vocalizations are under close neural control, as opposed to more directly reflecting biomechanical properties of the vibrating vocal folds themselves. So far, nonlinear dynamical structures of animal voices have been mainly studied with spectrograms. In this study, the deterministic versus stochastic (DVS) prediction technique was used to quantify the amount of nonlinearity in three animal vocalizations: macaque screams, piglet screams, and dog barks. Results showed that in vocalizations with pronounced harmonic components (adult macaque screams, certain piglet screams, and dog barks), deterministic nonlinear prediction was clearly more powerful than stochastic linear prediction. The difference, termed low-dimensional nonlinearity measure (LNM), indicates the presence of a low-dimensional attractor. In highly irregular signals such as juvenile macaque screams, piglet screams, and some dog barks, the detectable amount of nonlinearity was comparatively small. Analyzing 120 samples of dog barks, it was further shown that the harmonic-to-noise ratio (HNR) was positively correlated with LNM. It is concluded that nonlinear analysis is primarily useful in animal vocalizations with strong harmonic components (including subharmonics and biphonation) or low-dimensional chaos. [DOI: 10.1121/1.1474440]

PACS numbers: 43.80.Ka, 43.80.Lb, 43.25.Rq [WA]

I. INTRODUCTION

Animal vocalizations range from almost harmonic to completely noisy sounds (Tembrock, 1996; Hauser, 1996; Bradbury and Vehrencamp, 1998),[1] where calls containing noisy elements in various amounts are referred to as ''atonal'' (Tembrock, 1976; Hauser, 1993). Such sounds are characterized by broadband spectra with energy at many different frequencies and sometimes with traces of harmonic elements. A prototype of such vocal utterances is the ''scream,'' which is a vocalization described in the acoustic repertoires of many species (for instance, humans: Michelsson, 1980; macaques: Rowell, 1967; Grimm, 1967; Green, 1975; Hohmann, 1989; Gouzoules and Gouzoules, 2000; pigs: Schön *et al.*, 1999). Another typical atonal utterance is the ''bark'' which is present in the repertoire of several species, including primates (macaques: Struhsaker, 1967; Green, 1975; baboons: Hall and DeVore, 1965) as well as canids (Tembrock, 1976; Schassburger, 1993; Feddersen-Petersen, 2000). In those categories, various types of calls are often considered to be the same regardless of the difference in their functions or significances. For instance, in canids different functions have been ascribed to barks depending on the ratio of harmonic to nonharmonic energy in these vocalizations (Tembrock, 1976; Wilden, 1997; Feddersen-Petersen, 2000). Until now those differences have been rarely considered because of the difficulty of quantifying small variation between calls which are spectrally very similar (Owren and Linker, 1995). While statistical approaches like the multiparametric analysis (Schrader and Hammerschmidt, 1997) have been able to uncover statistical differences by using many acoustic parameters (Fischer *et al.*, 1995), the relationship between these parameters and the sound production mechanisms involved is not clear.

Understanding sound production mechanisms might help explain the communicative role of such atonal animal vocalizations by allowing spectral variability to be differentially ascribed to anatomical and motivational factors. Atonal

a)Author to whom correspondence should be addressed: electronic mail: tokuda@csse.muroran-it.ac.jp

 0001-4966/2002/111(6)/2908/12/$19.00

sounds are in general due to complex vocal production mechanisms such as regular and irregular vocal-fold vibrations as well as turbulent noise generated in the vocal tract (Davis and Fletcher, 1996). Vocal-fold vibration has been extensively studied in humans (reviewed in Titze, 1994), whereas few studies exist in nonhuman mammals (Paulsen, 1967; Brown and Cannito, 1995; Brown *et al.,* 2002).

The concept of ''nonlinear dynamics'' has been recently introduced to animal bioacoustics, where characteristics of vocalizations are classified using the terminology of dynamical systems (Wilden *et al.,* 1998). (i) Limit cycle: the spectrum is composed of a fundamental frequency with harmonics that are integer multiplies of that frequency. (ii) Subharmonics: additional spectral components appear in the harmonic stack, typically at multiples of 1/2 or 1/3 of the fundamental frequency. (iii) Biphonation: the simultaneous occurrence of two independent fundamental frequencies. (iv) Chaos: a broadband segment with no particular harmonics in the spectrum. (v) Bifurcations: transitions between different nonlinear dynamical states. Acoustic analyses of birds (Fee *et al.,* 1998) and mammals (Wilden *et al.,* 1998; Fitch *et al.,* 2002) have shown a variety of such nonlinear phenomena, including rapid transitions from harmonic to subharmonic and chaotic states without intervening silent intervals. These observations suggest that the transitions arise from intrinsic properties of the vibrating components of the larynx. The intrinsic dynamics of the vocal folds can thus produce complex temporal acoustic call patterns without complex nervous system control (Fitch *et al.,* 2002).

The theory of nonlinear dynamics shows that rather complex vocalizations can be generated from systems described by nonlinear equations of motion having very few dynamical variables. For example, the desynchronization of horizontal and vertical vibratory modes of the vocal folds (Berry *et al.,* 1994) or the desynchronization of the left and the right vocal folds (Steinecke and Herzel, 1995; Tigges *et al.,* 1997) can lead to subharmonics, biphonation, and low-dimensional deterministic chaos. Such observations imply that some of the noisy animal utterances which have been considered as turbulent noise or high-dimensional dynamics might be generated from low-dimensional nonlinear systems. In order to quantify the complexity of animal vocalizations, it therefore becomes quite important to clarify whether the underlying dynamics are low-dimensional or high-dimensional.

Dynamical systems are considered low-dimensional if they exhibit only a few (say, 3 to 10) dynamical components and high-dimensional if they have many more. Typical examples of low-dimensional dynamics in acoustics are certain pathological voices (Titze *et al.,* 1993) and musical instruments under certain conditions (Gibiat and Castellengo, 2000). An example of high-dimensional dynamics, on the other hand, is turbulent air flow. However, since broadband spectra do not always imply low-dimensional dynamics, special analysis techniques based on nonlinear dynamics should be applied to distinguish low-dimensional systems from high-dimensional ones.

From the point of view of animal voice production, detection of low-dimensionality in acoustic signals is of particular interest. In principle, acoustic signals are the result of the neural control of the vocal production system (respiratory system, larynx, and vocal tract), which has rich biomechanical properties. Nonetheless, it has been found in nonlinear studies of voice that even without complex nervous system control the vocal system can exhibit a variety of complex nonlinear phenomena such as chaos and bifurcations (Mende *et al.,* 1990; Titze *et al.,* 1993). Observations of low-dimensional dynamics therefore imply that a variety of complex features of animal vocalizations is traceable primarily to the biomechanical properties of the vocal production systems involved rather than close neural control *per se*.

Nonlinear analysis of animal vocalizations may have significant importance for animal communication research. For instance, in animal bioacoustics, sounds are often categorized as being either harmonic or atonal. Calls with mixed structural components (e.g., harmonic calls with noisy overlay or calls in which tonal and noisy components are interspersed) have been excluded from most analyses (e.g., Hauser, 1993) or considered as atonal. This poor dichotomy makes systematic studies of animal acoustic communication difficult (Ryan, 1988; Hauser, 1993). The harmonic-to-noise ratio has been recently introduced in order to improve differentiation among atonal calls (Riede *et al.,* 2001). The question of whether atonal calls are low dimensional or high dimensional, however, remains unresolved. This issue is important because we can differentiate three main sources of voice irregularities: (a) air turbulence generated in the vocal tract, (b) high-dimensional complex vocal-fold vibration, and (c) low-dimensional irregular vocal-fold vibration. Precise quantification of the degree of irregularity is therefore important for studies of animal communication.

For human speech signals, nonlinear analysis has been carried out rather extensively (Mende *et al.,* 1990; Townshend, 1991; Titze *et al.,* 1993; Herzel *et al.,* 1994; Narayanan and Alwan, 1995; Kubin, 1995; Kumar and Mullick, 1996; Behrman *et al.,* 1998; Behrman, 1999). For animal voice signals, however, nonlinear characteristics have not yet been thoroughly investigated. Narrow-band spectrographic analysis has been proven to be useful in interpreting nonlinear phenomena such as limit cycles, subharmonics, biphonation, chaotic episodes, and transitions among different nonlinear dynamical states (Wilden *et al.,* 1998; Fitch *et al.,* 2002). Simply counting the various phenomena has provided the first quantitative results (Riede *et al.,* 1997, 2000), but further application of more sophisticated techniques like Lyapunov exponents and fractal dimensions (Titze *et al.,* 1993; Fletcher, 2000) can be problematic as these measures are quite sensitive to nonstationarities that are common in animal signals.

In this paper, a new method is introduced to analyze nonlinear dynamics of animal voices. Some decades ago, any irregularity in signals was attributed to random noise and consequently, broadband signals have been modeled typically with linear stochastic models such as autoregressive (AR) models. With the advent of chaos theory (May, 1976), it became clear that irregularities may be due to deterministic chaos in low-dimensional nonlinear systems. In order to distinguish two sources of irregularities, Farmer and Sidorow-

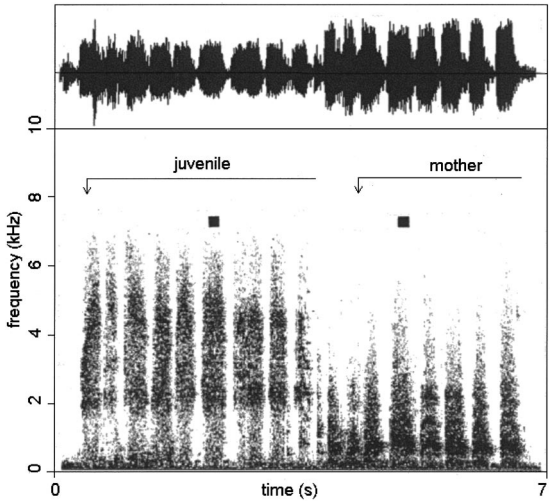

FIG. 1. Time series of the macaque screams (above) and its spectrogram (below). The first nine calls (marked with arrow as ''juvenile'') were from 1-year old juvenile, the tenth call was ambiguous, and the remaining calls (marked with arrow as ''mother'') were from the mother. The black markers above the spectrogram indicate the segments used for the DVS analysis. The juvenile's calls started when it became frightened due to the proximity of an alpha male. Then the mother came running over and began screaming, which drew the male's attention to her.

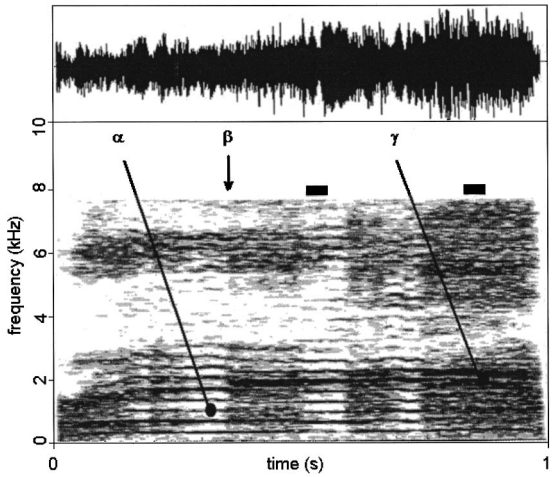

FIG. 2. Time series of a piglet scream (above) and its spectrogram (below). The black markers indicate the regions associated with harmonic and noisy spectral structures, which were analyzed using the DVS technique in Fig. 8. The arrows are directed to limit cycle with harmonic regime (α), bifurcation with a sudden transition between two different regimes (β), and complex dynamics with broadband spectral regime (γ).

ich (1987) suggested evaluating the predictive power of deterministic nonlinear models and stochastic linear models. By comparing the deterministic nonlinear predictability with the stochastic linear predictability, the strength of nonlinearity in the data can be measured. After this concept, the method is called the ''deterministic nonlinear versus stochastic linear (DVS)'' modeling technique (Farmer and Sidorowich, 1987; Casdagli, 1992). Here, we apply the DVS modeling technique to macaque screams, piglet screams, and dog barks as three examples of complex animal vocalizations. On the basis of further analysis of 120 samples of dog barks, we also examined the correlation between degree of nonlinearity and harmonic-to-noise ratios in the same signals.

II. MATERIAL

Voice data from Japanese macaques (*Macaca fuscata*), piglets (*Sus scrofa forma domestica*), and domestic dogs (*Canis lupus forma domestica*) were analyzed as representatives of atonal animal vocalizations.

The macaque screams were recorded from a 1-year-old juvenile and its adult-female mother, and digitized with a sampling frequency of 22 kHz. Figure 1 shows the time series of these screams, as well as a spectrogram computed with a 512-point FFT. The first nine calls are from the juvenile, the tenth sound is ambiguous, and the remaining screams are all from the mother. The broadband spectra apparent in the spectrogram show that neither the juvenile's scream nor the mother's call have a simple harmonic structure associated with fundamental frequencies.

As a next example, screams were recorded from six piglets (age: 16 days, body mass: 4.1 ± 0.9 kg) with a sampling frequency of 20 kHz. Figure 2 shows an example of the piglet scream and its corresponding spectrogram. The spectrogram shows that transitions among harmonic sounds with several peak frequencies and irregular sounds with broadband spectra occur in the series of the piglet scream.

As a final example, barks were recorded from 6 dogs (named as a, b, c, d, e, and f) with a sampling rate of 20 kHz. All dogs were from the breed dachshund, ranged in weight between 7.9 and 10.7 kg. The dogs a, b, e, and f belong to a clinic sample, where the barks were recorded while treated in a veterinary clinic for some disorders. The dogs c and d, on the other hand, are normal and healthy dachshunds whose barks were recorded at the owner's property. The barks were elicited by staring into dog's eyes (a mild threat to the animal), where only the dogs from which the barkings could be elicited in this way were used for the analysis. Samples of the dog barks used in the present study come from the samples used by Riede *et al.* (2001). Selection criterion was the dog's harmonic-to-noise-ratio (HNR) value averaged over its first 50 calls per recording session. The HNR is a measure that compares the acoustic energy of the harmonic components with that of the noise in time series. This measurement has been introduced to study hoarseness of human voice (Yumoto *et al.*, 1982; Awan and Frenkel, 1994). A voice with low HNR sounds quite hoarse, whereas a voice with high HNR is tense or pressed. According to the HNR analysis applied to 20 samples of dogs, the dogs a and b had the lowest average HNR (1st and 2nd rank), the dogs c and d had a medium HNR (14th and 16th rank), and the dogs e and f had the highest average HNR (19th and 20th rank). In the present study, 20 barks recorded from each dog were analyzed. Figure 3 shows three different dog barks and their corresponding spectrograms (bark A from dog a: HNR=9; bark B from dog c: HNR=13; bark C from dog f: HNR=17). The spectrograms show that several sharp peaks are observed in the frequency structure of the bark C, whereas the sharp frequency structure is flattened in the bark B, and is quite broad in bark A.

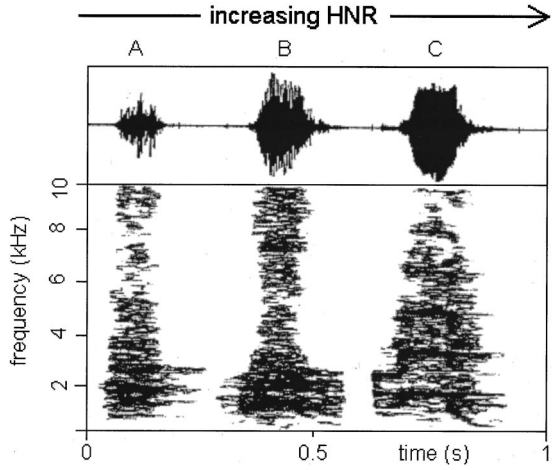

FIG. 3. Time series (above) of three dog barks with low (A); medium (B); and high (C) HNR and their corresponding spectrograms (below). The barks A, B, and C were recorded from the dogs a, c, and f, respectively.

III. METHODS

In the field of nonlinear dynamics, various techniques have been developed to estimate nonlinear dynamical quantities such as fractal dimensions and Lyapunov exponents from time series (for instance see reviews by Lauterborn and Parlitz, 1988; Abarbanel, 1996; Kantz and Schreiber, 1997). One must be careful in using such techniques, because reliable estimation of these quantities from short-term data requires delicate numerical computation (Theiler, 1986; Smith, 1988; Ruelle, 1990). The analysis of long-term voice data, on the other hand, suffers from nonstationarity. In addition, the contamination of the data with noise often gives rise to spurious results for dimension estimates (Ruelle, 1994; Rapp, 1993; Rapp *et al.*, 1993).

The DVS modeling technique introduced by Casdagli (1992) provides a more robust approach. In general, there are two major approaches to model irregular time series in nature: (A) deterministic nonlinear prediction model (Farmer and Sidorowich, 1987) and (B) stochastic linear prediction model (Markel and Gray, 1976). The main idea of DVS technique is to measure the strength of nonlinearity by comparing the prediction accuracy of the two models. If the data represent at least partially a low-dimensional attractor, its nonlinear dynamical components can be predicted by using nonlinear models. Linear prediction models, on the other hand, cannot accurately predict nonlinear dynamical components. The strength of the nonlinearity in the time series can therefore be measured as the gap between the nonlinear prediction error and the linear prediction error. The method is quite simple and effective for short-term noisy data, with applications to many real-world data such as coupled diodes, fluid turbulence, flame dynamics, human speech, EEG data, measles, and sunspots (Casdagli, 1992).

DVS analysis of the animal voice data was conducted as follows. First, we embedded the time series $\{x_t : t=1,2,...,N\}$ into delay coordinate space (Takens, 1981; Sauer *et al.*, 1991)

$$\mathbf{x}(t)=(x_t, x_{t-\tau}, x_{t-2\tau}, \ldots, x_{t-(d-1)\tau}) \tag{1}$$

(d: embedding dimension, τ: delay time). In this particular analysis, the delay time was always set to be $\tau=1$. By setting the embedding dimension d large enough, we get information of the basic waveform structure (in the case of periodic data, this corresponds to one period of the waveform) within the time length $d-1$ of the vector $\mathbf{x}(t)$. For a data point $\mathbf{x}(t)$, distances from other points $\mathbf{x}(s)$ were computed as $d_{t,s}=\|\mathbf{x}(t)-\mathbf{x}(s)\|=\sqrt{\Sigma_{i=0}^{d-1}(x_{t-i}-x_{s-i})^2}$ $(s=d,d+1,...,N)$. By ordering the distances as $d_{t,s(1)}\leqslant d_{t,s(2)}\leqslant\cdots\leqslant d_{t,s(N-d+1)}$, D neighbors $\{\mathbf{x}(s(i)):i=1,2,...,D\}$ of $\mathbf{x}(t)$ were found. Note that the data point itself and its temporally close points $\{\mathbf{x}(s):|s-t|\leqslant 15\}$ were not included in the neighbors (Theiler, 1986). Then, one step further state of x_t was predicted by using a local linear predictor as

$$\tilde{x}_{t+1}=\sum_{k=0}^{d-1} a_k(t)x_{t-k}, \tag{2}$$

where the prediction coefficients $\{a_0(t),a_1(t),\ldots,a_{d-1}(t)\}$ were determined by a least-square algorithm, minimizing the error function defined for the D neighbors as

$$E(a(t))=\sum_{i=1}^{D}\left\{x_{s(i)+1}-\sum_{k=0}^{d-1} a_k(t)x_{s(i)-k}\right\}^2. \tag{3}$$

This technique is called local linear prediction because the ''local'' dynamics of the data is approximated by ''linear'' models. Note that the ''local linear'' implies essentially a nonlinear model since the prediction model depends on the location of the data $\mathbf{x}(t)$ in coordinate space. Consequently, local linear models are also capable of generating deterministic chaos. The difference of the predicted signal $\tilde{x}_t$ and the true signal x_t measures the prediction accuracy. Using the residual signals: $r_t=x_t-\tilde{x}_t$, the signal-to-noise ratio (SNR) was computed as

$$\mathrm{SNR}=10\log\left(\frac{\Sigma_{t=d}^{N}\{x_t-\overline{x}\}^2}{\Sigma_{t=d}^{N}\{r_t-\overline{r}\}^2}\right)\mathrm{dB}, \tag{4}$$

where

$$\overline{x}=\frac{1}{N-d+1}\sum_{t=d}^{N} x_t,\quad \overline{r}=\frac{1}{N-d+1}\sum_{t=d}^{N} r_t.$$

Here, noise refers to unpredictable components within the signal.

This local linear prediction shows a remarkable dependence on the number of the neighbors [see Fig. 4, where $\#N=100\cdot D/(N-d+1)\%$ stands for a percentage of the number of the neighbors among all data points $\{\mathbf{x}(s):s=d,d+1,...,N\}$]. In the case of a small number of neighbors, prediction accuracy is sensitive to recording noise (meaning energy from a different source than the animal's vocal apparatus) contained in the data. This sensitivity results in a relatively low SNR. As the number of the neighbors is increased, the recording noise effect is suppressed, nonlinear structure of the data is well modeled by local linear predictor, and consequently the SNR is improved. With an intermediate number of the neighbors, the highest SNR with optimum nonlinear prediction is realized. As the number of the neighbors is further increased ($\#N\rightarrow 100\%$), the local linear pre-

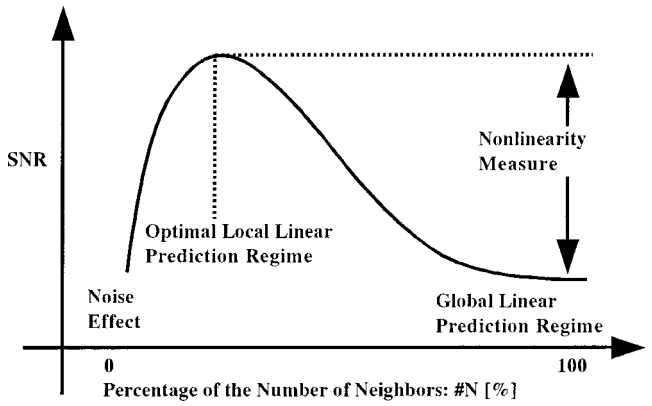

FIG. 4. Schematic illustration of the DVS plot. In the case of small $\#N$, the SNR is low due to noise contained in the data. As $\#N$ is increased, the SNR is improved and optimized at an intermediate value of $\#N$. As $\#N$ is further increased, the SNR is again lowered. The low-dimensional nonlinearity measure (LNM) is defined as an SNR gap between the optimal nonlinear prediction regime and the global linear prediction regime.

dictor eventually becomes close to a global linear predictor. This global linear model is almost identical to an AR model, except that in the parameter estimation it does not use temporally correlated data (AR modeling uses the complete data set). Nonlinear components cannot be well predicted by the global linear model and the SNR is again lowered. Depending on the strength of nonlinearity of the data, a gap should be observed between optimal nonlinear prediction and global linear prediction. If the nonlinearity of the data is strong (or weak), the gap should be large (or small). By using this property, the amount of nonlinearity included in the data can be measured.

Finally, we define the low-dimensional nonlinearity measure (LNM) as an SNR gap between the optimal nonlinear prediction and the linear prediction as

$$\mathrm{LNM} = \mathrm{SNR}_{\text{optimal nonlinear prediction}} - \mathrm{SNR}_{\text{global linear prediction}} \mathrm{dB}. \quad (5)$$

LNM can be interpreted as the amount of the signal that cannot be predicted by the linear model but is predicted by the nonlinear model. We note that in case of analyzing complex data generated from high-dimensional nonlinear systems, it is not easy for any modern technique (Lauterborn and Parlitz, 1988; Abarbanel, 1996; Kantz and Schreiber, 1997) to precisely detect nonlinearity in the data, because such data often cannot be distinguished from the ones generated from complex stochastic dynamics. We therefore emphasize that the LNM is to detect *low-dimensional* nonlinearity in data.

IV. ANALYSIS OF A PATHOLOGICAL VOICE

As a benchmark test for the DVS technique described in Sec. III, a pathological voice was first analyzed. Since nonlinear dynamics of pathological voices has been well analyzed (Titze *et al.*, 1993), such a voice sample provides good data for testing the DVS technique. Figure 5(a) shows the time series of a pathological voice recorded at the university hospital (Charité) of the Humboldt-University of Berlin from a female subject who had papillomas of the vocal folds. The

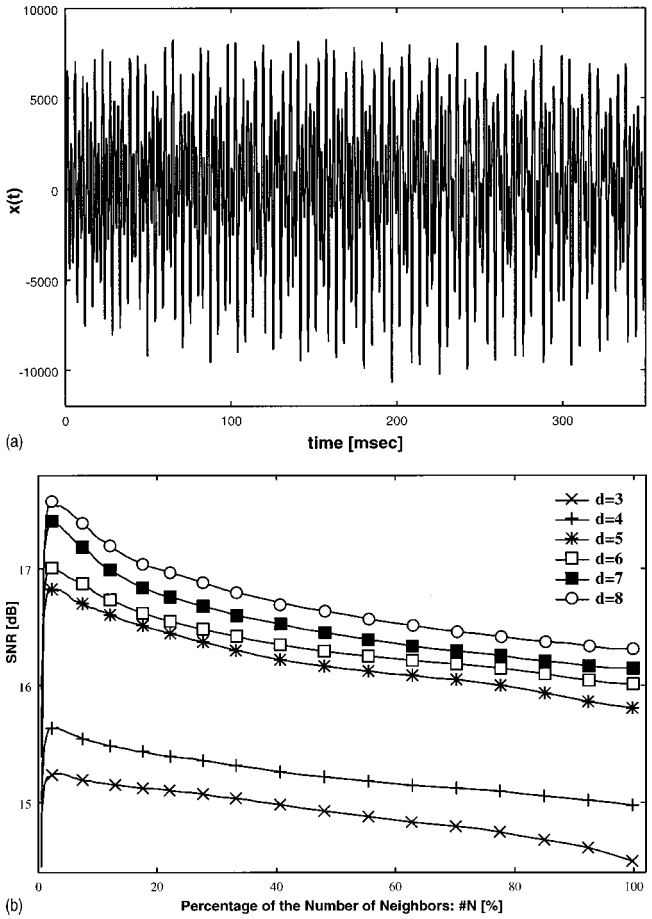

FIG. 5. (a) Waveform structure of the pathological voice. (b) DVS plot of the pathological voice.

data were digitized with a sampling frequency of 20 kHz and 12-bit resolution. By removing the initial transient phase and the final decay phase, the stationary part of the vowel /u/ composed of $N=7000$ data points was extracted. Nonlinear property of this voice sample was carefully investigated by Titze *et al.* (1993). By delay coordinate embedding technique, low-dimensional strange geometrical structure of the pathological voice was reconstructed. By fractal dimensional analysis, a noninteger dimension of $D_2=2.6$ was estimated. By Lyapunov spectrum analysis, positive first Lyapunov exponent of $\lambda_1 \approx 0.1\ \mathrm{ms}^{-1}$ indicating orbital instability of the data was estimated. These analysis results provided strong evidence for low-dimensional chaos in the pathological voice sample.

Figure 5(b) shows the result of the DVS analysis applied to the pathological voice data. The DVS plots were drawn for varying the embedding dimension $d=3,4,...,8$. For all DVS plots with different embedding dimensions, clear peak structures of the SNR at an intermediate number of neighbors were discernible. Namely, as the percentage of the number of the neighbors $\#N$ was increased from zero, the SNR increased with a peak at about $\#N=3\%$. As the number of neighbors was further increased from the peak, then the SNR decreased monotonically. This result implies that the pathological voice contains a certain amount of low-dimensional nonlinearity that gives rise to a clear gap between nonlinear prediction error and linear prediction error. For a variety of

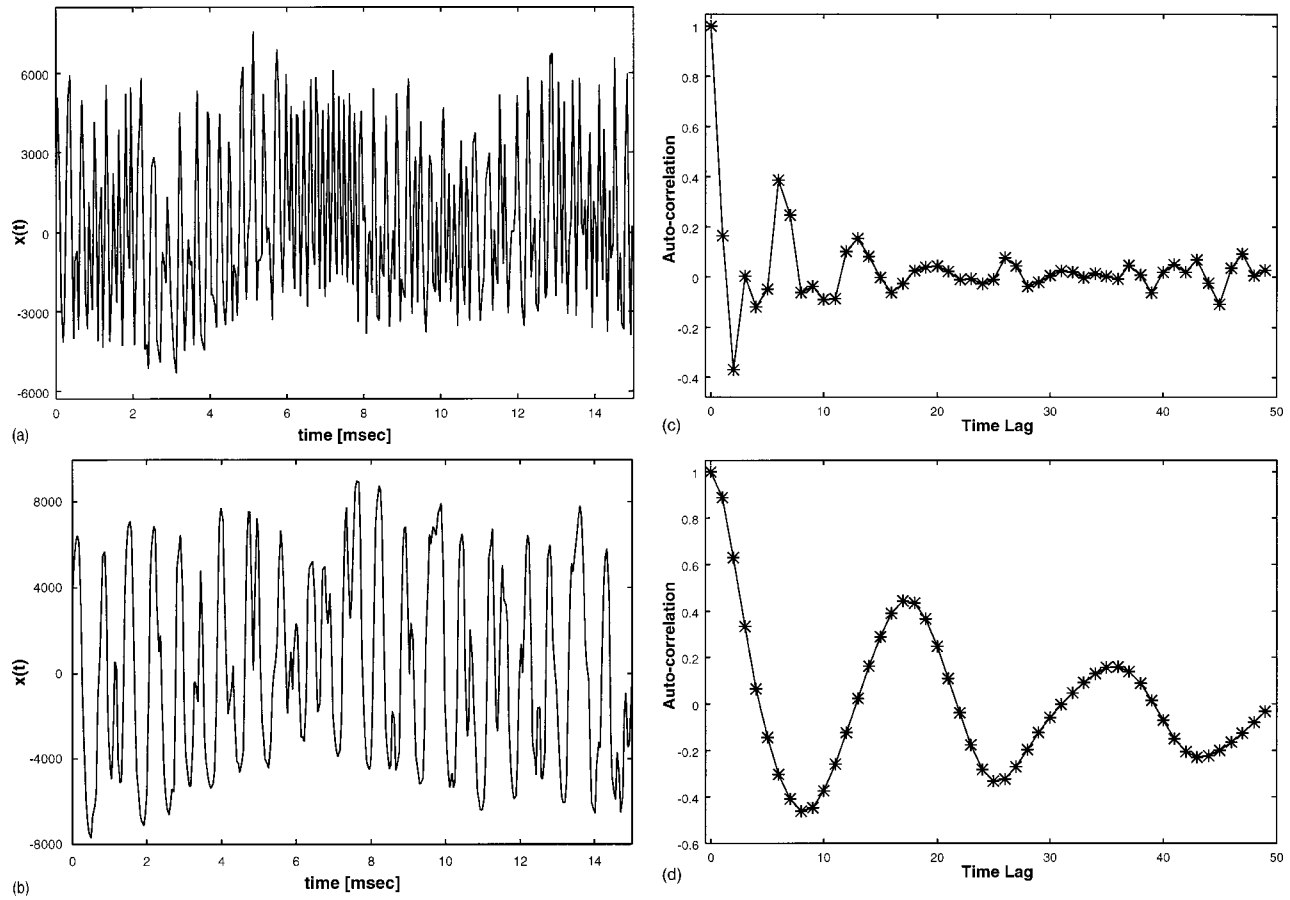

FIG. 6. (a) Enlarged waveform structure of the juvenile macaque's scream of Fig. 1. (b) Enlarged waveform structure of the mother macaque's call of Fig. 1. (c) Autocorrelation function of the juvenile macaque's scream. (b) Autocorrelation function of the mother macaque's call.

embedding dimensions, a nonlinearity measure LNM was in the order of 1 dB. Since this voice sample was shown to have low-dimensional chaotic property, we may say that the present DVS technique works for real acoustic data and the nonlinearity measure LNM of 0.5 dB implies existence of low-dimensional nonlinear dynamics in the data.

V. RESULTS

A. Macaque screams

Analyzing macaque screams as a first example of animal vocalization, Figs. 6(c) and (d) show autocorrelation functions for the calls from the juvenile and its mother, respectively. While the autocorrelation function for the juvenile's scream showed rapid decay, the mother's call gave rise to a function with a long tail. Strong correlation implies periodic structure, whereas weak correlation implies noisy structure. The long-term correlation of the mother's call reflected the waveform structure of Fig. 6(a), which showed relatively clear periodicity. The vanishing correlation of the juvenile's scream, on the other hand, might be due to the noisy waveform structure of Fig. 6(b). Figures 7(a) and (b) show results of the DVS analysis applied to screams of the juvenile and the mother. The DVS plots were drawn for varying embedding dimension $d=3,4,...,8$. In both figures, clear peak structures of the SNR at an intermediate number of neighbors were apparent. The peaks were observed at $\#N=3.33\%$ for the juvenile and $\#N=2.5\%$ for the mother. As the number of neighbors was increased from the peak point, SNR decreased monotonically. This result implies that both calls contain a certain amount of nonlinearity that gave rise to a gap between nonlinear prediction error and linear prediction error. Compared to the juvenile's scream, the mother's call showed a larger gap. In fact, in the case of $d=7$, the nonlinearity measure was LNM$=0.23$ dB for the juvenile and LNM $=0.50$ dB for the mother. As we have seen from the analysis of the pathological voice, LNM of more than 0.5 dB can point to low-dimensionality in acoustic signal. We may therefore say that the mother's call had low-dimensional nonlinear characteristic, whereas nonlinearity of the juvenile's scream was not so clear. This outcome might be due to the periodic components of the mother's call, as limit-cycle dynamics, which were well predicted by nonlinear models. The irregular dynamics of the juvenile macaque's calls seemed to reflect high-dimensional dynamics, since the nonlinear model with embedding dimension up to 8 allowed only a small improvement of the linear prediction.

B. Piglet screams

As a second example of an animal voice, piglet screams were analyzed. Figures 8(a) and (b) show results of the DVS analysis applied to the piglet scream of Fig. 2, where (a) corresponds to the harmonic sound region of Fig. 2 and (b) corresponds to the noisy scream region. The DVS plots were drawn by varying the embedding dimension as $d=3,...,8$.

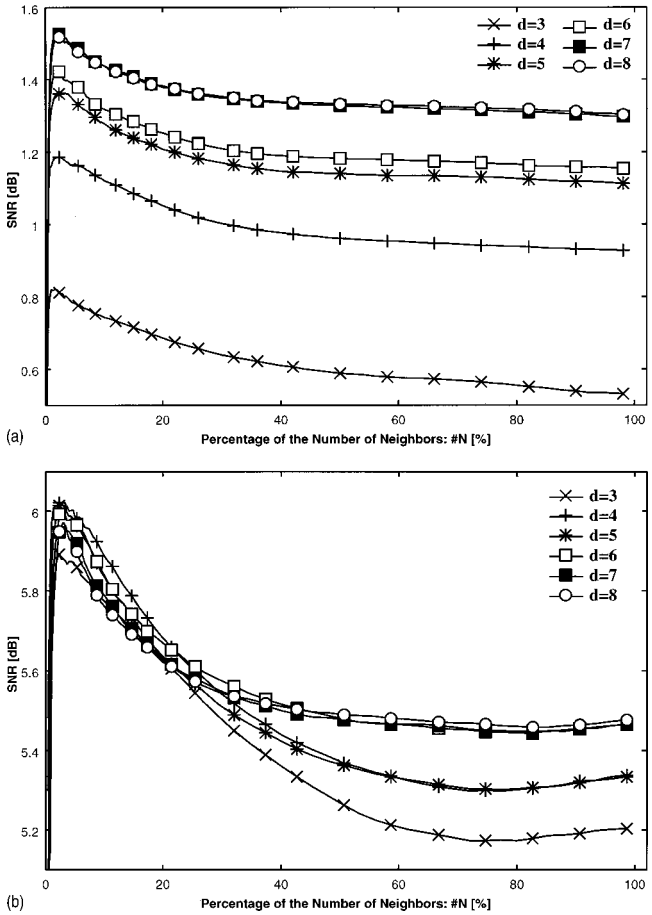

FIG. 7. (a) DVS plot of the juvenile macaque's scream of Fig. 6(a). (b) DVS plot of the mother macaque's scream of Fig. 6(b).

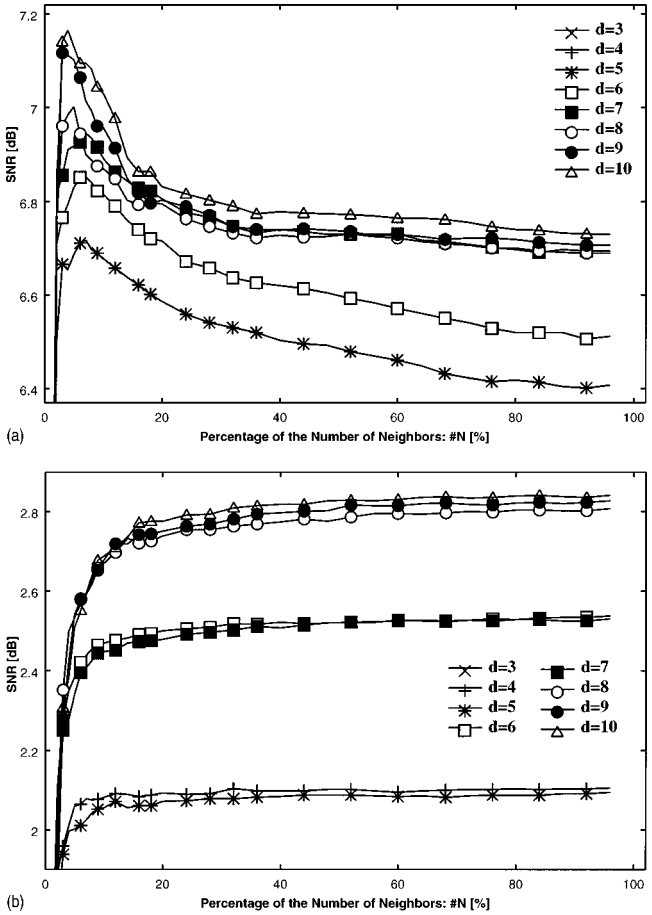

FIG. 8. (a) DVS analysis of the piglet scream extracted from the first marker in Fig. 2. (b) DVS analysis of the piglet scream extracted from the second marker in Fig. 2.

The harmonic part showed a large nonlinearity measure LNM, meaning a large gap between nonlinear prediction and linear prediction. The noisy part, on the other hand, did not exhibit such behavior. More specifically, in the case of $d=9$, the nonlinearity measure was LNM$=0.41$ dB for the harmonic part and LNM$=0$ dB for the noisy part. Conducting the same analyses with various screams from 5 other piglets produced similar results. Namely, strong nonlinearity was detected in harmonic screams, whereas no clear evidence for nonlinear dynamics was found in noisy screams. Hence, the harmonic parts of piglet screams can be considered to be due to low-dimensional nonlinear dynamics such as limit cycle, subharmonics, and biphonation (see the region indicated as α in Fig. 2 as an example of limit cycle regime). In contrast, the noisy parts may be due to turbulent noise or high-dimensional complex dynamics.

C. Dog barks

As the final example, we analyzed dog barks. First, three dog barks with low, medium, and high HNR (barks A, B, and C shown in Fig. 3) were tested. Figures 9(a), (b), and (c) show results of the DVS analysis applied to the three dog barks. As the HNR level increases from low to high (from bark A to B to C), the DVS plot gives rise to clearer peaks at an intermediate number of neighbors and the gap between nonlinear prediction regime and linear prediction regime becomes larger. In the case of $d=8$, the nonlinearity measure was LNM$=0.02$ dB for bark A with low HNR, LNM $=0.18$ dB for bark B with medium HNR, and LNM $=1.23$ dB for bark C with high HNR. These results imply that barks with high HNR exhibit low-dimensional dynamics. The irregular components included in the hoarse barking with low HNR may have been from turbulent noise or high-dimensional dynamics.

A further, more comprehensive analysis examined 120 barks recorded from the 6 dogs a, b, c, d, e, and f (20 barks from each). As shown in Fig. 10, the dog barks exhibit various waveform patterns [(a) and (b): two different barks of dog a, (c) and (d): two different barks of dog f]. Even in a single dog, the repeated barks exhibited different waveform structures. The relationship between the HNR and the nonlinearity measure LNM of the 120 barks is shown in Fig. 11(a), based on the computation of the LNM with fixed parameters of $d=5$ and $\#N=4.8\%$ for the nonlinear prediction. HNR and LNM were found to be correlated, with a correlation coefficient of $r=0.647$. In order to unfold the correlation curve, a ranked correlation plot is presented in Fig. 11(b), where the HNR (or the LNM) values are normalized between 0 and 1 in such a way that the ith-ranked HNR (or LNM) is given a value of $i/120$. A qualitatively similar structure to Fig. 11(a) is discernible with a ranked correlation coefficient of $r=0.646$. Hence, we may conclude that the

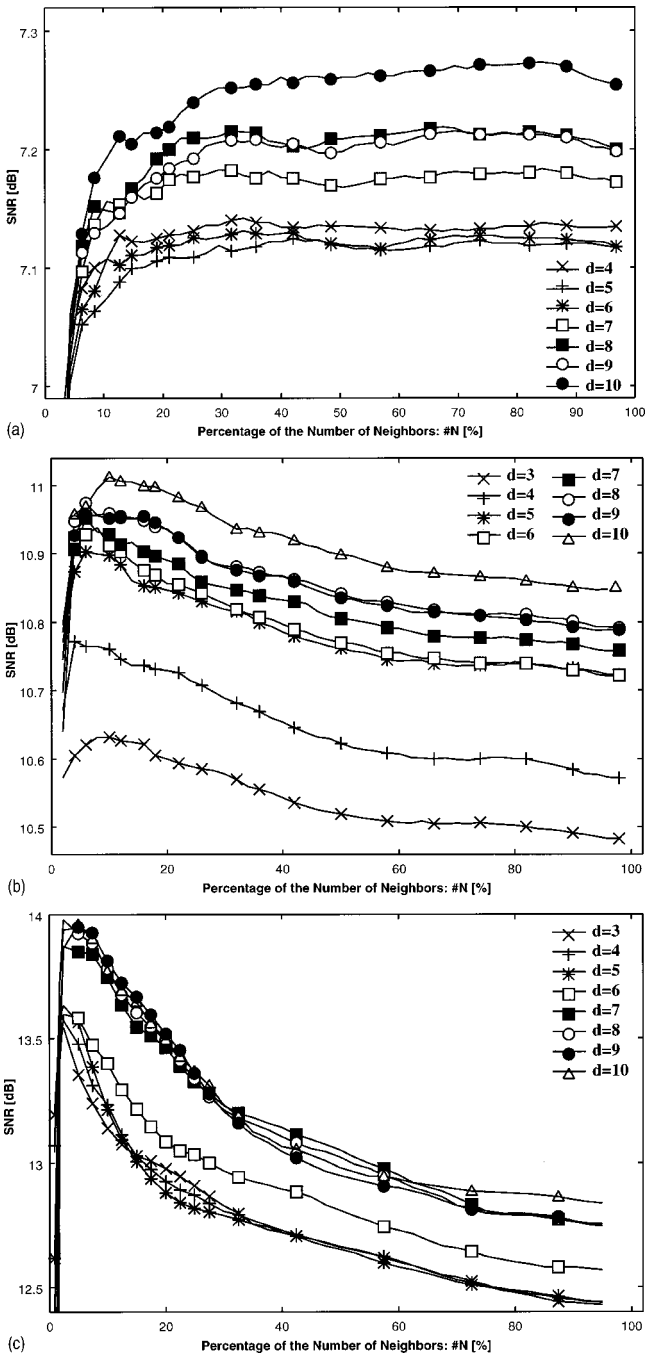

FIG. 9. (a) DVS plots of the dog bark with low HNR value (bark A of Fig. 3). (b) DVS plots of the dog bark with medium HNR value (bark B of Fig. 3). (c) DVS plots of the dog barks with high HNR value (bark C of Fig. 3).

nonlinearity measure LNM increased with the HNR. This result implies that nonlinearities are observed in dog barks mainly when they have clear harmonic dynamical components, such as limit cycles, subharmonics, and biphonation.

It should be noted that the correlation plots of Fig. 11 include several outliers which exhibit relatively strong nonlinearity measure LNM at intermediate HNR levels. There is a possibility that such relatively noisy barks are generated from low-dimensional nonlinear dynamics such as chaos. Careful investigation of these presumably chaotic data is thus an interesting research subject for future studies.

VI. SURROGATE ANALYSIS

In this section, we test the significance of nonlinearity observed in the animal vocalizations in Sec. V. In nonlinear data analysis, it is quite important to clarify the underlying dynamical process that has been detected by the nonlinear method. This clarification, however, is quite difficult, since there are a variety of stochastic processes that look similar to nonlinear dynamics. As a first approach to validate nonlinear analysis of irregular animal vocalizations, we carried out a surrogate analysis (Theiler *et al.*, 1992). The surrogate analysis is a kind of statistical hypothesis testing, which is to test a null hypothesis that the acoustic signal is generated from a particular class of stochastic dynamical process. In accordance with the null hypothesis, sets of artificial time series, called *surrogate data*, which preserve some of the statistical properties of the original signal are created. Then, a discriminating statistic is computed for the original and the surrogate data. If the discriminating statistic of the original signal is significantly different from those of the surrogate data, the null hypothesis can be rejected. The surrogate data have the property of ''constrained-realization'' (Theiler and Prichard, 1996), which is to randomize the original data by strictly preserving some of the original statistical quantities. It has been empirically known that the surrogate analysis is effective for statistical hypothesis testing when nonlinear dynamical quantity is utilized as a discriminating statistic.

In this study, as a standard surrogate analysis, we tested a null hypothesis that the macaque screams were generated from linear Gaussian dynamical process. Here, an iterative Fourier transformed algorithm (Schreiber and Schmitz, 1996) was utilized to shuffle the original signal and to generate surrogate data, which exactly preserved the original histogram and approximately preserved the original power spectrum. The local linear prediction error was then used as a nonlinear discriminating statistic.

Figures 12(a) and (b) show results of the surrogate analysis applied to the screaming data of the juvenile macaque [Fig. 6(a)] and its mother [Fig. 6(b)]. In each figure, local linear prediction errors for the original screaming data and its surrogate data are drawn by varying the embedding dimension $d=3,4,...,15$. Prediction errors of the surrogate data were averaged over 40 sets of different realizations of the surrogate data, where standard deviations are indicated by the error bars. For the local linear prediction, the number of the neighbors was fixed as $\#N=2.4\%$ for the juvenile's analysis and $\#N=2.9\%$ for the mother's analysis. For both juvenile's and mother's screams, it is clear that the original data had much higher SNRs than the surrogate data, where the differences were larger than several standard deviations of the surrogate statistics for all embedding dimensions $d=3,4,...,15$. This implies that the dynamical processes that generated the two macaque screams were not as simple as linear Gaussian. The original screams may have a certain amount of nonlinear dynamics which was well predicted by the nonlinear models. Such nonlinear dynamical structure had been destroyed by the surrogate data shuffling.

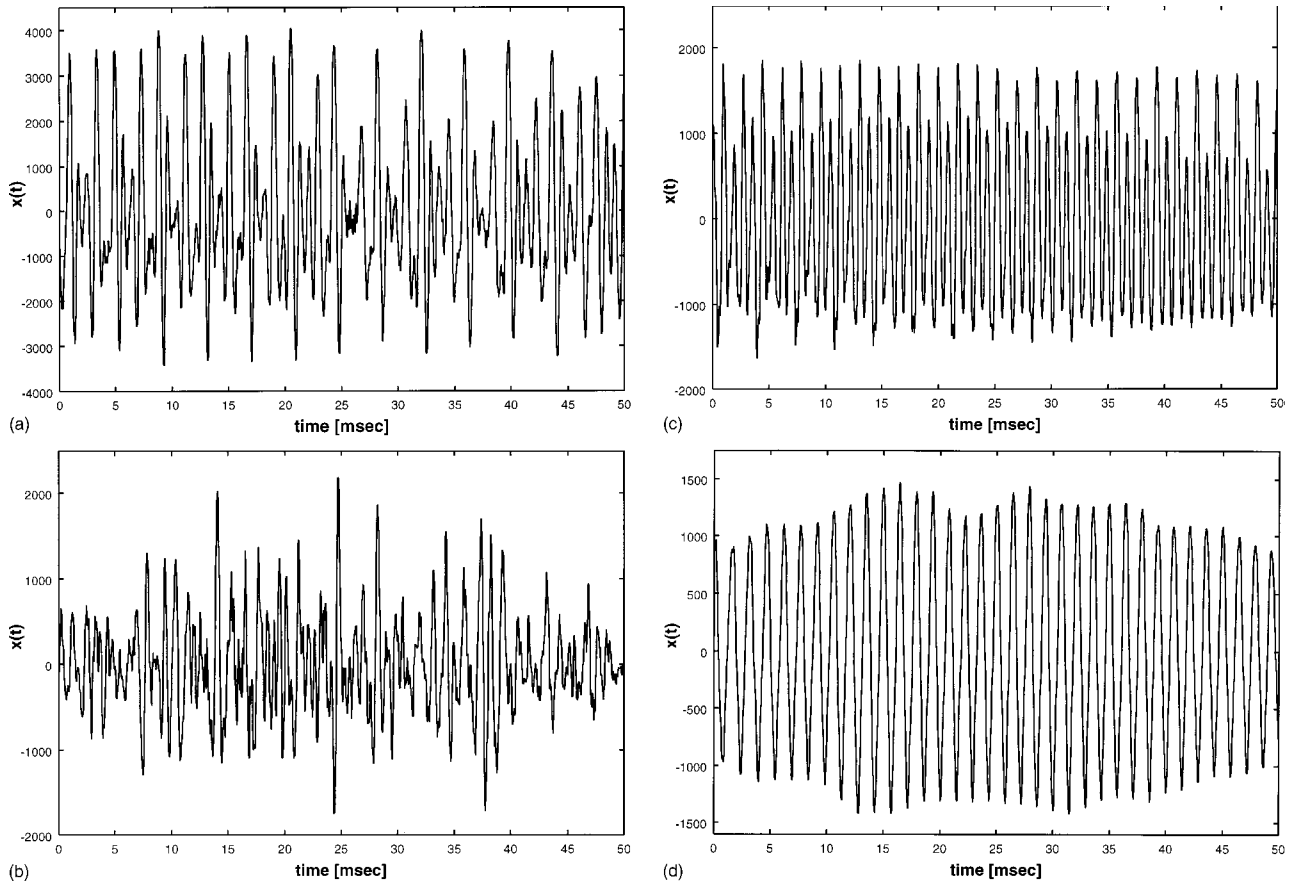

FIG. 10. Waveform structures of various dog barks. (a) and (b) show two different barks from dog a, whereas (c) and (d) show two different barks from dog f.

VII. SUMMARY AND DISCUSSION

Nonlinear analysis was carried out for complex animal vocalizations. As a measure to quantify the amount of nonlinearity in voice data, DVS analysis was applied to three types of animal vocalizations, namely macaque screams, piglet screams, and dog barks. Nonlinear components were detected in all three, particularly for vocalizations with strong harmonics such as limit cycles, subharmonics, and biphonation. In contrast, analysis of highly irregular vocalizations from the three species involved revealed no clear evidence of low-dimensional dynamics. Analyses of 120 dog barks showed good correspondence between the nonlinearity measure LNM and the HNR measure. This result implies that many irregular vocalizations observed in animals can be due to turbulent noise or high-dimensional complex dynamics. However, relatively large nonlinearity measure LNM was computed in some of the irregular vocalizations, such as the juvenile macaque's scream and some of the dog barks. Although careful future investigations are necessary to examine chaos in such real-world data, some of the irregular animal vocalizations seem to be generated from low-dimensional nonlinear dynamics. It is therefore well worth conducting further, detailed investigations of the possible occurrence of chaos in complex animal vocalizations with large nonlinearity measure.

A. Dimensionality of the macaque screams

In the analysis of macaque screams, evidence for low-dimensional nonlinear dynamics was more clearly recognized in the mother's scream than in the juvenile's one. Since the result is obtained from the analysis of only two samples of macaque screams, it is very difficult to judge whether this is a general property of adult and juvenile macaque screams. Nevertheless, it is interesting to consider a relationship between low-dimensional nonlinear dynamics and neural control of animal voice production, because low-dimensionality implies constrained laryngeal dynamics with strong nervous system control. If it is a general property that the dimensionality is lower in the mother's scream than in the juvenile's one, we may say that the mother's call production is more controlled than the juvenile's one. Such a new insight may be useful in understanding normative developmental processes of macaque vocal system. It is therefore a worthy investigation to increase the sample number of the macaque screams used for nonlinear analysis and compare the dimensionality of the adult macaque screams with that of the juvenile macaque screams.

B. Physical interpretation of the dog analysis

In the analysis of dog barks, a wide range of nonlinearity measure LNM was estimated. Let us consider the original causes of these differences. Since all six dogs analyzed by the nonlinear method were from the same breed (dachshund) and expressed similar body sizes, their laryngeal gross anatomy might be similar. We therefore speculate that differences in the acoustic product could come, for instance, from difference in fine (i.e., microscopic) anatomy (e.g., the vocal-

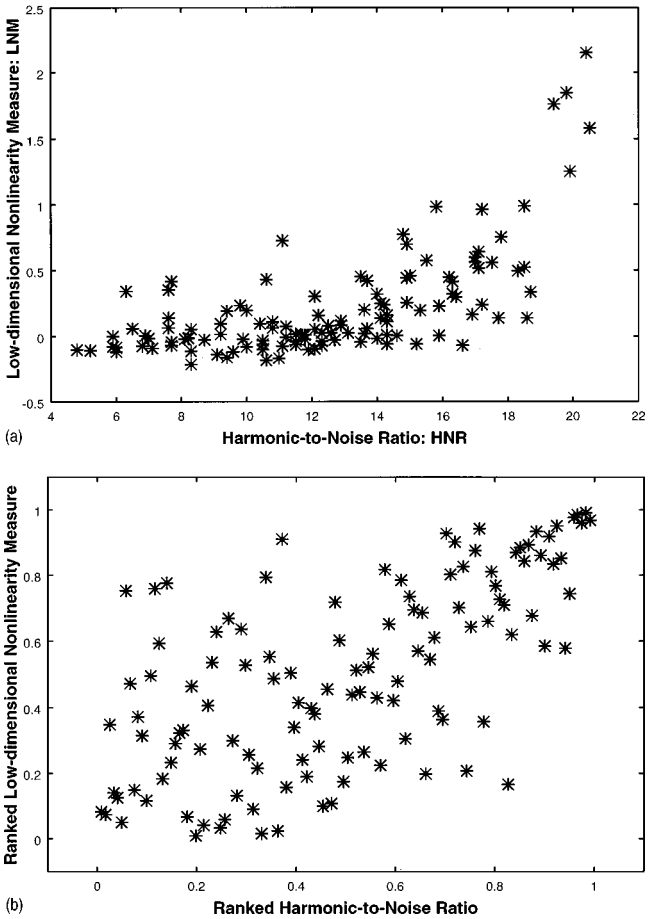

FIG. 11. (a) Correlation plot of the HNR and the nonlinearity measure LNM computed for 120 dog barks. (b) Ranked correlation plot of the HNR and the nonlinearity measure LNM.

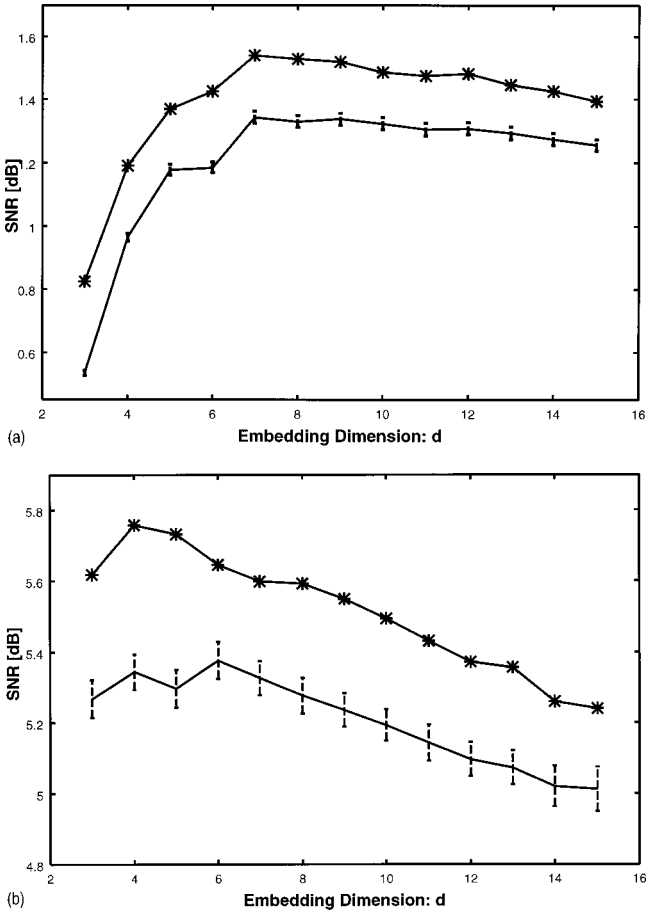

FIG. 12. (a) Nonlinear prediction of the juvenile's scream (solid line with crosses) and its surrogate data (solid line with error bars). (b) Nonlinear prediction of the mother's scream (solid line with crosses) and its surrogate data (solid line with error bars).

fold surface structure) or from differences in the nervous control of the voice production (e.g., vocal-fold parameter and subglottic pressure). In the HNR analysis of the dog barks (Riede *et al.*, 2001), we have earlier discussed that damage to the vocal folds (following hyperphonation) or functional hypertension of the vocal folds could be possible reasons for dog barks that exceeds a normative HNR range. Since the nonlinearity measure LNM was shown to strongly correlate with the HNR, these physical conditions may also give rise to nonlinearity measure that exceeds its normative range.

C. Other applications

In this study, significance of the nonlinear method was tested by using the method of surrogate. There are, however, other approaches to validate nonlinear analysis of animal vocalizations. For instance, there exist ongoing researches on biomechanical modeling of complex animal vocalizations (Mergell *et al.*, 1999; Fee *et al.*, 1998). Such models have been developed to understand the physical and physiological mechanism (e.g., laryngeal oscillations) that generates animal voices. Applying the present nonlinear method to synthetic voice produced from such biomechanical models and comparing the results with those of the real acoustic data might be of significant importance, because (1) such experiment may clarify the sources of nonlinearity which have been (or not have been) detected by the nonlinear method, and (2) plausibility of the biomechanical models can be judged by comparing the nonlinear structure of the model with that of the real acoustic data.

For applications of the present nonlinear analysis technique to other real data, excised larynx (Berry *et al.*, 1996) and EGG data may also provide important materials. Such data can be utilized to examine how the results of nonlinear analysis change as the source of nonlinear phenomena changes. Nonlinear analysis of these types of the measurement data will be carried out in a future work.

D. Usage of the nonlinearity measure

In the analyses of dog barks, there was a strong correlation between the nonlinearity measure LNM and the HNR measure. This is because, for analysis of nonlinear dynamics with strong harmonic components such as limit cycle, subharmonics, and biphonation, the HNR measure works in a similar way as the nonlinearity measure LNM. In the case of analyzing low-dimensional chaos, however, the nonlinearity measure LNM is capable of detecting low-dimensional dynamics, which cannot be detected by the HNR measure. We therefore stress that the nonlinearity measure LNM is useful in particular for analyzing low-dimensional chaos.

Finally, we note that there are limitations in applying the present nonlinear analysis technique to animal vocalizations. Nonstationarity, which is an inherent characteristic of vocalizations, always makes reliable nonlinear analysis quite difficult. Small signal amplitudes, recording noise, and nonlinear distortion in voice signals can also increase nonlinear modeling errors. Very high sampling rate, on the other hand, can sometimes enable linear models to predict nonlinear signals quite accurately, making the difference between nonlinear predictability and linear predictability difficult to interpret. Due to these limitations, some low-dimensional attractors in complex animal vocalizations may remain hidden. For a correct interpretation of complex vocalizations, accompanying simulations of biomechanical models (Mergell *et al.*, 1999; Fee *et al.*, 1998) and conventional spectrographic analysis will certainly be helpful.

[1]In this paper ''noise'' refers to any nonharmonic (irregular) energy within the acoustic utterance signal.

Abarbanel, H. D. I. (**1996**). *Analysis of Observed Chaotic Data* (Springer, New York).

Awan, S. N., and Frenkel, M. L. (**1994**). ''Improvements in estimating the harmonic-to-noise-ratio of the voice,'' J. Voice **8**, 255–262.

Behrman, A. (**1999**). ''Global and local dimensions of vocal dynamics,'' J. Acoust. Soc. Am. **105**, 432–443.

Behrman, A., Agresti, C. J., Blumstein, E., and Lee, N. (**1998**). ''Microphone and electroglottographic data from dysphonic patients: Type 1, 2, and 3 signals,'' J. Voice **12**, 249–260.

Berry, D. A., Herzel, H., Titze, I. R., and Krischer, K. (**1994**). ''Interpretations of biomechanical simulations of normal and chaotic vocal fold oscillations with empirical eigenfunctions,'' J. Acoust. Soc. Am. **95**, 3595–3604.

Berry, D. A., Herzel, H., Titze, I. R., and Story, B. H. (**1996**). ''Bifurcations in excised larynx experiments,'' J. Voice **10**, 129–138.

Bradbury, J. W., and Vehrencamp, S. L. (**1998**). *Principles of Animal Communication* (Sinauer, Sunderland).

Brown, C. H., and Cannito, M. P. (**1995**). ''Modes of vocal variation in Syke's monkey (*Cercopithecus albogularis*) squeals,'' J. Comp. Psych. **109**, 398–415.

Brown, C. H., Alipour, F., Berry, D. A., and Montequin, D. (**2002**). ''Laryngeal biomechanics and vocal communication in the squirrel monkey (*Saimiri boliviensis*),'' J. Acoust. Soc. Am. (submitted).

Casdagli, M. (**1992**). ''Chaos and deterministic versus stochastic nonlinear modeling,'' J. R. Stat. Soc. Ser. B. Methodol. **54**, 303–328.

Davis, P., and Fletcher, N. H., editors (**1996**). *Vocal Fold Physiology: Controlling Complexity and Chaos* (Singular, San Diego).

Farmer, J. D., and Sidorowich, J. J. (**1987**). ''Predicting chaotic time series,'' Phys. Rev. Lett. **59**, 845–848.

Feddersen-Petersen, D. U. (**2000**). ''Vocalization of European wolves (*Canis lupus lupus L.*) and various dog breeds (*Canis lupus f. fam.*),'' Arch. Tierz. Dummerstorf. **43**, 387–397.

Fee, M. S., Shraiman, B., Pesaran, B., and Mitra, P. P. (**1998**). ''The role of nonlinear dynamics of the syrinx in the vocalizations of a songbird,'' Nature (London) **395**, 67–71.

Fischer, J., Hammerschmidt, K., and Todt, D. (**1995**). ''Factors affecting acoustic variation in Barbary macaques (*Macaca sylvanus*) disturbance calls,'' Ethology **101**, 51–66.

Fitch, T., Herzel, H., Neubauer, J., and Hauser, M. (**2002**). ''Calls out of chaos: The adaptive significance of nonlinear phenomena in primate vocal production,'' Anim. Behav. (in press).

Fletcher, N. H. (**2000**). ''A class of chaotic bird calls?'' J. Acoust. Soc. Am. **108**, 821–826.

Gibiat, V., and Castellengo, M. (**2000**). ''Period doubling occurrences in wind instruments musical performance,'' Acust. Acta Acust. **86**, 746–754.

Gouzoules, H., and Gouzoules, S. (**2000**). ''Agonistic screams differ among four species of macaques: The significance of motivation-structural rules,'' Anim. Behav. **59**, 501–512.

Green, S. (**1975**). ''Variation of vocal pattern with social situation in the Japanese monkey (*Macaca fuscata*): A field study,'' in *Primate Behavior* (Academic, New York), pp. 1–102.

Grimm, R. J. (**1967**). ''Catalogue of sounds of the pigtailed macaque (*Macaca nemestrina*),'' J. Zool. Lond. **152**, 361–373.

Hall, K. R. L., and DeVore, I. (**1965**). ''Baboon social behavior,'' in *Primate Behavior: Field Studies of Monkeys and Apes*, edited by I. DeVore (Holt, Rinehart & Winston, New York), pp. 53–110.

Hauser, M. D. (**1993**). ''The evolution of nonhuman primate vocalizations: Effects of phylogeny, body weight, and social context,'' Am. Nat. **142**, 528–542.

Hauser, M. D. (**1996**). *The Evolution of Communication* (MIT Press, Cambridge).

Herzel, H., Berry, D., Titze, I. R., and Saleh, S. (**1994**). ''Analysis of vocal disorders with methods from nonlinear dynamics,'' J. Speech Hear. Res. **37**, 1008–1019.

Hohmann, G. (**1989**). ''Vocal communication of wild bonnet macaques (*Macaca radiata*),'' Primates **30**, 325–345.

Jürgens, U. (**1995**). ''Neuronal control of vocal production,'' in *Current Topics in Primate Vocal Communication*, edited by E. Zimmermann, J. D. Newman, and U. Jürgens (Plenum, New York), pp. 199–206.

Kantz, H., and Schreiber, T. (**1997**). *Nonlinear Time Series Analysis* (Cambridge U.P., Cambridge).

Kubin, G. (**1995**). ''Nonlinear processing of speech,'' in *Speech Coding and Synthesis*, edited by W. B. Kleijin and K. K. Paliwal (Elsevier Science, Amsterdam), pp. 557–610.

Kumar, A., and Mullick, S. K. (**1996**). ''Nonlinear dynamical analysis of speech,'' J. Acoust. Soc. Am. **100**, 615–629.

Lauterborn, W., and Parlitz, U. (**1988**). ''Methods of chaos physics and their application to acoustics,'' J. Acoust. Soc. Am. **84**, 1975–1993.

Markel, J. D., and Gray, A. H. (**1976**). *Linear Prediction of Speech* (Springer, Berlin).

May, R. M. (**1976**). ''Simple mathematical models with very complicated dynamics,'' Nature (London) **261**, 459–467.

Mende, W., Herzel, H., and Wermke, K. (**1990**). ''Bifurcations and chaos in newborn infant cries,'' Phys. Lett. A **145**, 418–424.

Mergell, P., Fitch, T., and Herzel, H. (**1999**). ''Modeling the role of nonhuman vocal membranes in phonation,'' J. Acoust. Soc. Am. **105**, 2020–2028.

Michelsson, K. (**1980**). ''Cry characteristics in sound spectrographic cry analysis,'' in *Infant Communication: Cry and Early Speech*, edited by T. Murry and J. Murry (College-Hill, Houston), pp. 85–105.

Narayanan, S. N., and Alwan, A. A. (**1995**). ''A nonlinear dynamical systems analysis of fricative consonants,'' J. Acoust. Soc. Am. **97**, 2511–2524.

Owren, M. J., and Linker, C. D. (**1995**). ''Some analysis methods that may be useful to acoustic primatologists,'' in *Current Topics in Primate Vocal Communication*, edited by E. Zimmermann, J. D. Newman, and U. Jürgens (Plenum, New York), pp. 1–27.

Paulsen, K. (**1967**). *Das Prinzip der Stimmbildung in der Wirbeltierreihe und beim Menschen* (Akademische, Frankfurt).

Rapp, P. E. (**1993**). ''Chaos in the neurosciences: Cautionary tales from the frontier,'' Biologist **40**, 89–94.

Rapp, P. E., Albano, A. M., Schmah, T. I., and Farwell, L. A. (**1993**). ''Filtered noise can mimic low-dimensional chaotic attractors,'' Phys. Rev. E **47**, 2289–2297.

Riede, T., Wilden, I., and Tembrock, G. (**1997**). ''Subharmonics, biphonations, and frequency jumps: Common components of mammalian vocalization or indicators for disorders,'' Z. Saugetierkunde **62**, Suppl. 2: 198–203.

Riede, T., Herzel, H., Mehwald, D., Seidner, W., Trumler, E., Tembrock, G., and Böhme, G. (**2000**). ''Nonlinear phenomena and their anatomical basis in the natural howling of a female dog–wolf breed,'' J. Acoust. Soc. Am. **108**, 1435–1442.

Riede, T., Herzel, H., Hammerschmidt, K., Brunnberg, L., and Tembrock, G. (**2001**). ''The harmonic-to-noise-ratio applied to dog barks,'' J. Acoust. Soc. Am. **110**, 2191–2197.

Rowell, T. E. (**1967**). ''Agonistic noises of the rhesus monkey (*Macaca mulatta*),'' Symp. Zool. Soc. Lond. **8**, 91–96.

Ruelle, D. (**1990**). ''Deterministic chaos: Science and fiction,'' Proc. R. Soc. London, Ser. A **427**, 244–248.

Ruelle, D. (**1994**). ''Where can one hope to profitably apply the ideas of chaos?'' Phys. Today **7**, 24–30.

Ryan, M. J. (**1988**). ''Constraints and patterns in the evolution of anuran

acoustic communication,'' in *The Evolution of the Amphibian Auditory System*, edited by B. Fritzsch, M. J. Ryan, W. Wilczynski, T. E. Hetherington, and W. Wlakowiak (Wiley, New York), pp. 637–677.
Sauer, T., York, J. A., and Casdagli, M. (**1991**). ''Embedology,'' J. Stat. Phys. **65**, 579–616.
Schassburger, R. M. (**1993**). *Vocal Communication in the Timber Wolf, Canis lupus, Linnaeus* (Paul Parey Sci., Berlin).
Schön, P. C., Puppe, B., Gromyko, T., and Manteuffel, G. (**1999**). ''Common features and individual differences in nurse grunting of domestic pigs (*Sus scrofa*): A multiparametric analysis,'' Behaviour **136**, 49–66.
Schrader, L., and Hammerschmidt, K. (**1997**). ''Computer-aided analysis of acoustic parameters in animal vocalizations: A multiparametric approach,'' Bioacoustics **7**, 247–265.
Schreiber, T., and Schmitz, A. (**1996**). ''Improved surrogate data for nonlinearity tests,'' Phys. Rev. Lett. **77**, 635–638.
Smith, L. A. (**1988**). ''Intrinsic limits of on dimension calculations,'' Phys. Lett. A **133**, 283–288.
Steinecke, I., and Herzel, H. (**1995**). ''Bifurcations in an asymmetric vocal fold model,'' J. Acoust. Soc. Am. **97**, 1571–1578.
Struhsaker, T. T. (**1967**). ''Auditory communication Among vervet monkeys (*Cercopithecus aethiops*),'' in *Social Communication Among Primates*, edited by S. A. Altmann (University of Chicago Press, Chicago), pp. 281–324.
Takens, F. (**1981**). ''Detecting strange attractors in turbulence,'' in *Lecture Notes in Math* (Springer, Berlin, 1981), Vol. 898, pp. 366–381.
Tembrock, G. (**1976**). ''Canid vocalizations,'' Behav. Processes **1**, 57–75.
Tembrock, G. (**1996**). *Akustische Kommunikation bei Saeugetieren* (Wissenschaftl. Buchgesell., Darmstadt).
Theiler, J. (**1986**). ''Spurious dimension from correlation algorithms applied to limited time-series data,'' Phys. Rev. A **34**, 2427–2432.
Theiler, J., Eubank, S., Longtin, A., Galdrikian, B., and Farmer, J. D. (**1992**). ''Testing for nonlinearity in time series: The method of surrogate data,'' Physica D **58**, 77–94.
Theiler, J., and Prichard, D. (**1996**). ''Constrained-realization Monte-Carlo method for hypothesis testing,'' Physica D **94**, 221–235.
Tigges, M., Mergell, P., Herzel, H., Wittenberg, T., and Eysholdt, U. (**1997**). ''Observation and modeling glottal biphonation,'' Acust. Acta Acust. **83**, 707–714.
Titze, I. R. (**1994**). *Principles of Voice Production* (Prentice-Hall, Englewood Cliffs, NJ).
Titze, I. R., Baken, R. J., and Herzel, H. (**1993**). ''Evidence of chaos in vocal fold vibration,'' in *Vocal Fold Physiology*, edited by I. R. Titze (Singular, San Diego), pp. 143–188.
Townshend, B. (**1991**). ''Nonlinear prediction of speech,'' in *Proceedings of the International Conference on Acoustics, Speech, and Signal Processing* (IEEE, New York, 1991), pp. 425–428.
Wilden, I. (**1997**). ''Phonetische variabillitaet in der lautgebung afrikanischer wildhunde (Lycaon pictus) und deren frühe ontogenes,'' Ph.D. thesis, Humboldt-University, Berlin.
Wilden, I., Herzel, H., Peters, G., and Tembrock, G. (**1998**). ''Subharmonics, biphonation, and deterministic chaos in mammal vocalization,'' Bioacoustics, **9**, 171–196.
Yumoto, E., Gould, W. J., and Baer, T. (**1982**). ''Harmonic-to-noise-ratio as an index of the degree of hoarseness,'' J. Acoust. Soc. Am. **71**, 1544–1550.

Acoustic identification of female Steller sea lions (*Eumetopias jubatus*)[a)]

Gregory S. Campbell[b)]
Cetacean Behavior Laboratory, College of Sciences, San Diego State University, 5500 Campanile Drive, San Diego, California 92182-4611

Robert C. Gisiner
Code 342, Office of Naval Research, 800 North Quincy Street, Arlington, Virginia 22217

David A. Helweg
Code D3501E, Space and Naval Warfare Systems Center San Diego, 53560 Hull Street, San Diego, California 92152-5000

Linda L. Milette
Marine Mammal Research Unit, Fisheries Center, University of British Columbia, 2204 Main Mall, Vancouver, British Columbia V6T 1Z4, Canada

(Received 30 May 2001; revised 28 January 2002; accepted 27 February 2002)

Steller sea lion (*Eumetopias jubatus*) mothers and pups establish and maintain contact with individually distinctive vocalizations. Our objective was to develop a robust neural network to classify females based on their mother-pup contact calls. We catalogued 573 contact calls from 25 females in 1998 and 1323 calls from 46 females in 1999. From this database, a subset of 26 females with sufficient samples of calls was selected for further study. Each female was identified visually by marking patterns, which provided the verification for acoustic identification. Average logarithmic spectra were extracted for each call, and standardized training and generalization datasets created for the neural network classifier. A family of backpropagation networks was generated to assess relative contribution of spectral input bandwidth, frequency resolution, and network architectural variables to classification accuracy. The network with best overall generalization accuracy (71%) used an input representation of 0–3 kHz of bandwidth at 10.77 Hz/bin frequency resolution, and a 2:1 hidden:output layer neural ratio. The network was analyzed to reveal which portions of the call spectra were most influential for identification of each female. Acoustical identification of distinctive female acoustic signatures has several potentially important conservation applications for this endangered species, such as rapid survey of females present on a rookery. © *2002 Acoustical Society of America.* [DOI: 10.1121/1.1474443]

PACS numbers: 43.80.Ka, 43.80.Lb, 43.64.Tk [WA]

I. INTRODUCTION

Steller sea lions were selected for this study because biological theory predicts that colonially breeding individuals will possess refined means of individual identification in order to invest finite resources in a manner most likely to enhance their reproductive success (Trivers, 1972). Individual identification is potentially possible for any individual of any species; however, evolutionary theory predicts that the need to reduce confusion over reproductive investment will result in more obvious and consistent communication of individual identity in colonially breeding species (Beecher, 1982). The task of developing a mathematical means of discriminating amongst individuals is thus more likely to succeed with a colonially breeding species than with a species where opportunities for mistaking identity and misplacing competitive, breeding, or parental resources are less frequent and therefore less consequential.

Sea lions and fur seals (Otariids) typically demonstrate a polygynous breeding system, with females gathering in dense congregations to give birth and to copulate (Riedman, 1990). Mothers alternate between nursing their pups on land and feeding at sea, sometimes leaving the pup unattended for several days (Riedman, 1990). Acoustic mother-pup call recognition appears to be the primary means of initiating contact and orienting searching behavior after a period of separation (Insley, 1989, 1992; Gisiner and Schusterman, 1991; Schusterman *et al.*, 1992a; Phillips and Stirling 2000, 2001). Playback experiments have provided additional evidence to support the existence of mother-pup acoustic recognition systems. Studies on both the subantarctic fur seal (*Arctocephalus tropicalis*) and Galapagos fur seal (*A. galapagoensis*) have suggested that mothers and pups react positively to recordings of each others' calls but not to those of strangers (Trillmich, 1981; Roux and Jouventin, 1987). While individual call recognition among Otariids appears to be common, few studies have used acoustical and statistical

[a)]Portions of this work were presented in "Acoustic identification of female Steller sea lions," Proceedings of the 140th meeting of the ASA/Noise Congress, Newport Beach, CA, November 2000, and "Neural network classification of individual female Steller sea lions (*Eumetopias jubatus*)," Proceedings of the 14th Biennial Conference on the Biology of Marine Mammals, Vancouver, BC, Canada, November 2001.

[b)]Electronic mail: gcampbel@sonofsun.sdsu.edu

 0001-4966/2002/111(6)/2920/9/$19.00

analysis techniques to evaluate call stereotypy. Only studies of the northern fur seal *Callorhinus ursinus* (Insley, 1989, 1992), South American sea lion (Fernández-Juricic *et al.*, 1999), and South American fur seal *Arctocephalus australis* (Phillips and Sterling, 2000) have classified known females based on the acoustic structure of their calls.

The Steller sea lion ranges along the North Pacific Rim from Japan to Central California, with centers of abundance and distribution in the Aleutian Islands and the Gulf of Alaska (Loughlin *et al.*, 1984; Riedman, 1990). In response to population declines in Alaska since the 1970s, the Steller sea lion was listed in 1990 as *threatened* under the U.S. Endangered Species Act (NMFS, 1992). Genetic and distribution information subsequently led to the classification of two separate breeding stocks of Steller sea lions: a ''western'' stock, which included sea lions in the Gulf of Alaska, Aleutian Islands, and Bering Sea, and an ''eastern'' stock which included sea lions from Southeast Alaska to California (NMFS, 1995; Bickham *et al.*, 1996; Loughlin, 1997). In 1997, the western stock of Steller sea lions was relisted as *endangered* under the U.S. Endangered Species Act. This reclassification was in response to a dramatic population decline during the past 30 years, estimated at over 80% (Braham *et al.*, 1980; Merrick *et al.*, 1987; Loughlin *et al.*, 1992; Trites and Larkin, 1996; Sease *et al.*, 2001). During this same time period, Steller sea lion numbers have remained stable or increased in Southeast Alaska and throughout most of the range of the eastern stock (Calkins *et al.*, 1999; Sease *et al.*, 2001).

The causes of the decline in the western stock of Steller sea lions are not known, though poor nutrition is currently a leading hypothesis. Undernutrition resulting from changes in the abundance or appropriateness of Steller sea lion prey items may lead to reduced birth rates and increased mortality through starvation, disease, or predation (Merrick and Loughlin, 1997; Calkins *et al.*, 1999). Considerable research on Steller sea lion population dynamics and energy requirements is currently being conducted in an effort to better understand the factors influencing the population decline in the western stock and the stability of the eastern stock.

Between May and July, Steller sea lions gather on offshore rookeries for reproductive activities. Females give birth to a single precocial pup, and for one week following parturition, mothers fast and suckle their pups on land. No allomaternal behavior has been reported. Following this perinatal period, mothers begin a cycle of feeding at sea for approximately 24 hours and then returning to the rookery for approximately 24 hours to suckle their young and to rest (Higgins, 1984; Riedman, 1990; Milette *et al.*, 1999). When Steller sea lion mothers return from foraging trips, they must repeatedly find their pups on the large crowded rookery. Acoustic mother-pup recognition appears to be the primary means by which female Steller sea lions achieve this essential task (Higgins, 1984; Milette *et al.*, 1999).

Monitoring the arrival and departure activities of individually identified mothers within and across breeding seasons is one method that can provide important information on maternal care, energy transfer, site fidelity, patterns of rookery usage, and philopatry or dispersion of matrilines. Currently, individual identification is done visually by comparison of photographs or drawings of distinctive markings (Gisiner, 1985; Milette *et al.*, 1999). However, the accuracy of this identification method depends on the observer's experience and can lead to misidentification. Markings may be small and inconspicuous and only visible from one side, animals in the water usually cannot be identified visually, and crowded conditions make it difficult to single out and maintain visual contact with an identified individual. As an alternative, call identification has the potential for reliable discrimination of individuals based on acoustical parameters. Since females call whenever they move and whenever they depart to and return from the sea on feeding trips, acoustic identification may be preferred in conditions where direct visual observations may be difficult.

Campbell *et al.* (2000) demonstrated that female Steller sea lions can be discriminated by call characteristics. They evaluated a set of classifiers including linear discriminant analysis and three artificial neural network architectures (backpropagation, learning vector quantization, and adaptive resonance) using standardized training and generalization datasets of calls from 14 females. The backpropagation architecture clearly provided the highest classification accuracy on the novel generalization data.

Here, we advance development of a robust neural network to classify females based on their mother-pup contact calls. Average logarithmic spectra were extracted for calls from 26 females, and standardized training and generalization datasets created. A family of backpropagation networks (BPNs) was generated to assess relative contribution of spectral and architectural variables to classification accuracy. The BPN with best overall generalization accuracy was analyzed to reveal which portions of the call spectra were most influential for identification of each female.

II. MATERIALS AND METHODS

A. Study site and data collection

Our study site was Sugarloaf Island (58°53^{m}.N; 152°02^{m}.W), one of numerous offshore locations in the Gulf of Alaska that serve as rookery/haul out sites for the western population of Steller sea lions (Fig. 1). Prior to the current study, 70 females were visually identified and photographed at Sugarloaf during the breeding seasons of 1994–1997 (Milette *et al.*, 1999).

During the breeding seasons of 1998 and 1999, acoustic recordings were conducted with a two-channel Sony TCD-D8 DAT recorder connected to a Sennheiser M-60 Directional Microphone. One channel was devoted to sea lion calls and the second channel was used for observer narration. A typical recording contained a repetitive series of female calls with the name of the vocalizing individual stated after each call. We catalogued 573 contact calls from 25 females in 1998 and 1323 calls from 46 females in 1999. Nine known females were recorded in both years, yielding a total of 62 identified individuals.

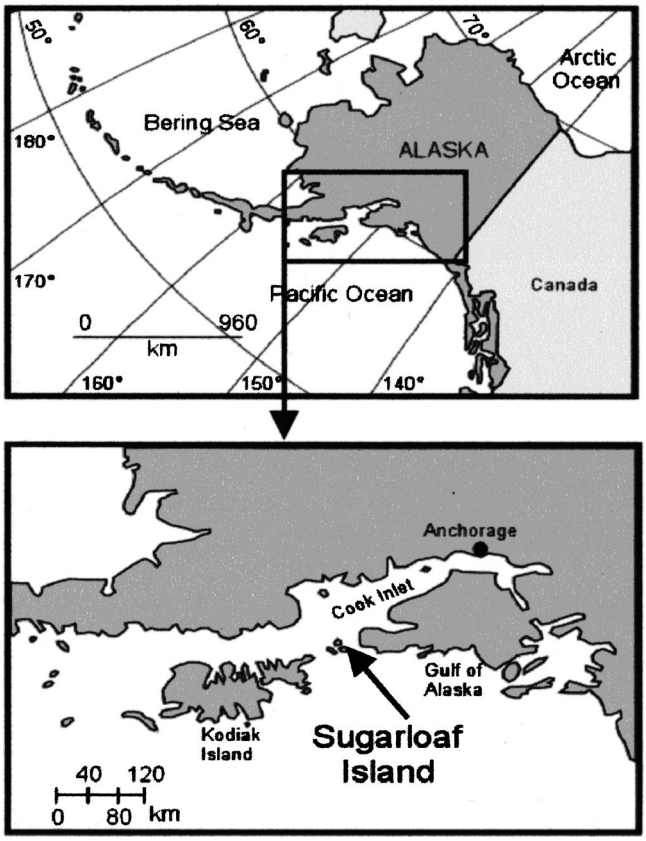

FIG. 1. The study site at Sugarloaf Island, Alaska. The top panel gives an overview of the western Gulf of Alaska region. The box and arrow indicate the location of study site, with a detail presented in the bottom panel.

B. Acoustical analyses

Acoustical analyses were limited to nonagonistic calls directed by mothers toward their pups while on the rookery. The digital data were transferred from DAT to PC with a Zefiro Acoustics ZA-2 digital sound card over a Sony POC-DA12P fiber optic cable. Transfer was managed via SoundForge 4.5 multimedia editing software. Raw data preserved the 44.1-kHz sampling rate and stereo format in PCM WAV files. The stereo WAV files were scanned using the narration channel, and each call was segmented using a SoundForge ''region.'' Each of the 1896 calls was labeled according to an individual female and one of four possible call quality ratings. Quality 1 (Q1) calls were vocalizations that had excellent signal to noise conditions with no little or no ambient noise. Quality 2 (Q2) calls were degraded by ambient noise (e.g., wind, rain or surf). Quality 3 (Q3) calls were degraded by other sea lion sounds and/or weather conditions, which made segmentation of the calls ambiguous. Quality 4 (Q4) calls were samples in which female identity was uncertain, and were not analyzed.

C. Backpropagation architectures

After all recordings were segmented, a batch process low-pass filtered (4 kHz) and decimated each call to an 11.025-kHz sampling rate, and extracted the call to an individual WAV file. The calls were cross-tabulated by female and call quality. Q1 and Q2 calls were pooled, which yielded a set of 26 females, each of which was represented by more than ten calls. Backpropagation is a supervised learning algorithm that requires a set of exemplars to be compiled into a learning set, and generalization ability can be tested using additional sets of novel exemplars. For this study, a standardized training set of calls was generated by drawing ten calls for each female at random ($n=260$), using Q1 calls and supplementing with Q2 calls where necessary. All remaining Q1–Q3 calls ($n=1281$) were placed into a generalization set. The data are summarized in Table I.

Each call was represented by an average logarithmic spectrum on the BPN input layer. We evaluated the effects of spectral and architectural variables on the generalization accuracy of the BPNs. Two spectral variables were manipulated. Frequency resolution was set at 5.38, 10.77, 21.53, or 43.07 Hz/bin, and bandwidth was set at 2 or 3 kHz. The BPN processing architecture was manipulated by modifying the ratio of hidden layer elements to output layer elements, using settings of 2:1, 4:1, and 6:1 hidden:output ratios. The output layer always had 26 elements, one for each female. Thus, for example, a BPN with a 3-kHz input bandwidth, a 10.77-Hz/bin frequency resolution, and a connectivity ratio of 4:1 would have 280 input elements (corresponding to the first 280 spectral bins, which span 0 to 3 kHz), 104 hidden layer elements, and 26 output layer elements.

The BPNs were fully interconnected and used standard cumulative-delta learning propagated across the bipolar tanh transfer function. Each BPN was trained to a rms error criterion of 0.05, which corresponds to approximately 95% correct across the training set. After training, the classification accuracy of each BPN for novel exemplars was tested using the generalization dataset. The overall generalization percent correct for each BPN was used to select the most accurate network. A detailed analysis of the relative importance of each frequency band in the input spectra was conducted. For every call in the generalization set that the BPN correctly classified, the value of each input bin was dithered by 20%, and the resulting percent change on the output neuron activation strength was measured. Dithering the values of input bins that had strong connection weights would result in large changes on the output neuron, thereby providing insight into the spectral characteristics that were most useful in classifying the females.

III. RESULTS

A. Female call characteristics

Female calls ranged in frequency from 30 to 3000 Hz with peak frequencies from 150 to 1000 Hz. Typical call duration was 1000 to 1500 ms. Call structure varied across females, illustrated in Fig. 2. Some individuals typically produced tonal calls, demonstrated by a call from Amatuli in the left column of Fig. 2, while others typically produced pulsed calls, demonstrated by a call from Ethel in the right column. Calls containing both mixed and pulsatile portions were also common in our data set. Note that the tonal call was characterized by clearly defined harmonic structure, which gives rise to the rippled spectra and harmonic lines in the spectrogram. In contrast, the pulsed call lacked strong harmonic structure and little spectral rippling.

TABLE I. The sample dataset. Data for each of the 26 females are broken out by quality factor within the training and generalization subsets. Each female was represented by ten calls in the training set, and by unequal *n*'s in the generalization set.

	Training		Generalization		
Female	Q1	Q2	Q1	Q2	Q3
763Girl	1	9	0	0	19
Amatuli	10	0	7	8	4
Bellow	6	4	0	9	6
Breeze	3	7	0	12	38
Bubbles	1	9	0	23	57
Chamille	10	0	7	45	82
Cher	10	0	1	82	96
Clover	1	9	0	1	3
Crunchie	2	8	0	25	40
Carcy	3	7	0	7	13
Demera	3	7	0	4	26
Dice	2	8	0	12	50
Ethel	4	6	0	9	53
Flo	9	1	0	12	28
Fungus Ear	0	10	0	0	65
GooGoo Doll	3	7	0	23	46
Jay	2	8	0	0	8
Jessica	7	3	0	9	5
Lucy	10	0	7	40	26
Moss	10	0	6	31	47
Pebbles	5	5	0	3	12
Pinky	4	6	0	1	5
Sasha	4	6	0	4	5
Scooby Doo	4	6	0	11	8
Snicker	9	1	0	16	25
Ziggy	0	10	0	33	66

B. Neural network evaluation

All BPNs learned to classify the set of 26 females with 100% accuracy on the training dataset. Overall generalization accuracy ranged from 58.5% on the BPN with 2-kHz bandwidth, 43.07-Hz/bin frequency resolution, and 2:1 hidden:output layer connectivity to 70.7% on the BPN with 3-kHz bandwidth, 10.77-Hz/bin frequency resolution, and 2:1 hidden:output layer connectivity. The results are summarized in Table II. The accuracy of BPNs with 2-kHz bandwidth was significantly lower than those with 3-kHz bandwidth [$t(22)=2.74$, $p=0.012$], with mean percent correct of 63.07 vs 66.99, respectively. Analysis of variance revealed that manipulating frequency resolution also resulted in significant differences in accuracy [$F(3,8)=148.16$, $p<0.01$]. Scheffe's *post hoc* comparison of means ($\alpha=0.01$) demonstrated that accuracy of networks using a 43.05-Hz/bin resolution was significantly lower than that of the networks using 21.53-, 10.77-, and 5.38-Hz/bin. No significant effect of manipulating hidden:output layer connectivity ratios was observed.

TABLE II. Comparison of the generalization accuracy of the backpropagation networks. The first column is the frequency resolution of the spectral input representation in Hz. The second column is the connectivity ratio between the number of elements in the hidden layer to the output layer. The third column is the average percent correct (APC) (with standard deviation, s.d.) computed over all 26 females, using a 2-kHz bandwidth spectral representation. The fourth column is average percent correct using a 3-kHz bandwidth.

Frequency resolution (Hz/bin)	H:O Ratio	APC (s.d.) 2 kHz BW	APC (s.d.) 3 kHz BW
5.38	2:1	61.77 (22.26)	68.81(19.50)
10.77	2:1	64.69 (20.23)	70.69(17.15)
21.53	2:1	62.58 (18.54)	69.19(18.99)
43.06	2:1	58.50 (19.03)	69.19(20.39)
5.38	4:1	64.54 (21.20)	69.19(17.88)
10.77	4:1	63.38 (20.85)	69.81(17.72)
21.53	4:1	64.54 (17.70)	68.38(17.37)
43.06	4:1	60.00 (20.22)	58.96(20.61)
5.38	6:1	64.19 (20.51)	68.46(17.8)
10.77	6:1	66.31 (20.06)	70.62(17.36)
21.53	6:1	65.73 (18.43)	68.92(18.93)
43.06	6:1	60.65 (18.93)	59.73(19.45)

On the basis of these evaluations, the BPN with 3 kHz of input bandwidth, 10.77-Hz/bin frequency resolution, and 2:1 hidden:output connectivity was selected for further study.

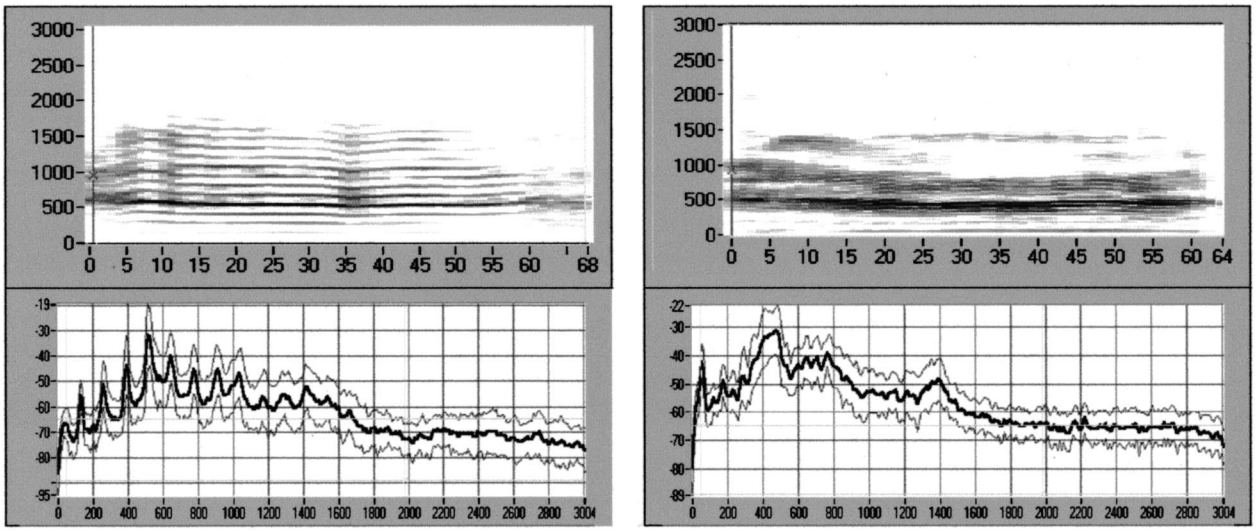

FIG. 2. Sample call types. A tonal call from Amatuli is presented on the left, and a pulsatile call from Ethel is presented on the right. The top panels are spectrograms and the bottom panels are average log power spectra. Duration of the calls were approximately X seconds. Frequency ranges from 0 to 3 kHz on both the spectrograms and power spectra; amplitude is in relative dB.

TABLE III. Confusion matrix for the optimal BPN on the generalization dataset. Actual female identity is in rows, and predicted identity is in columns. To facilitate comparison, values are percent classification, which normalizes across the unequal sampling. Percent correct is on the major diagonal.

	763GIRL	AMATULI	BELLOW	BREEZE	BUBBLES	CHAMILLE	CHER	CLOVER	CRUNCHIE	DARCY	DEMERA	DICE	ETHEL	FLO	FUNGUSEAR	GOOGOO	JAY	JESSICA	LUCY	MOSS	PEBBLES	PINKY	SASHA	SCOOBYDOO	SNICKER	ZIGGY
763GIRL	74	0	5	0	0	0	0	0	0	0	0	5	0	0	0	0	11	0	0	0	0	0	5	0	0	0
AMATULI	0	89	0	0	0	5	0	0	0	0	0	5	0	0	0	0	0	0	0	0	0	0	0	0	0	0
BELLOW	0	0	80	7	0	0	0	0	13	0	0	0	0	0	0	0	0	0	0	0	0	0	0	0	0	0
BREEZE	0	0	2	74	4	0	0	0	6	0	2	6	0	0	0	0	0	0	2	0	0	0	0	0	4	0
BUBBLES	0	0	0	0	76	0	0	0	1	0	1	19	0	0	0	0	0	2	0	0	0	0	0	0	0	0
CHAMILLE	13	3	1	1	1	51	0	1	0	1	1	1	0	0	9	0	5	1	1	1	0	4	2	1	0	1
CHER	1	0	7	1	0	0	63	1	7	0	0	1	1	0	0	0	0	3	0	8	1	0	1	1	0	5
CLOVER	0	0	0	0	0	0	0	75	0	0	0	0	0	0	0	0	0	0	0	0	25	0	0	0	0	0
CRUNCHIE	0	0	0	0	3	0	0	0	91	0	2	2	0	0	0	0	0	0	0	3	0	0	0	0	0	0
DARCY	0	0	0	0	5	0	0	5	0	65	0	5	5	0	0	0	0	5	0	0	5	0	0	0	0	5
DEMERA	0	0	0	0	0	0	0	0	0	0	90	7	0	0	0	0	0	3	0	0	0	0	0	0	0	0
DICE	2	0	0	3	16	2	0	0	0	0	3	68	2	0	0	0	0	3	0	0	0	0	2	0	0	0
ETHEL	0	0	0	2	6	0	6	0	0	0	0	2	53	0	0	0	0	0	0	16	0	8	2	2	0	3
FLO	0	0	0	0	2	0	2	5	2	8	0	2	5	40	0	0	0	0	0	0	0	0	0	0	30	2
FUNGUSEAR	2	0	0	0	0	2	0	0	2	0	0	0	0	0	51	2	2	3	0	18	0	17	0	2	0	2
GOOGOO	1	4	0	0	4	0	3	4	0	0	0	1	0	0	0	65	0	0	0	0	0	6	0	10	0	0
JAY	12	0	0	12	0	0	0	12	0	0	0	12	0	0	0	0	38	0	0	0	0	0	0	12	0	0
JESSICA	0	0	0	0	0	0	0	0	0	0	0	0	0	0	0	0	0	93	7	0	0	0	0	0	0	0
LUCY	0	1	0	1	8	7	0	0	1	0	0	8	0	0	0	0	3	5	56	0	0	3	3	3	0	0
MOSS	1	0	0	0	2	0	4	1	0	2	0	2	12	1	0	0	0	0	0	57	5	11	1	0	0	0
PEBBLES	0	0	0	0	0	0	0	13	0	13	0	0	0	0	0	0	0	0	0	7	60	0	0	7	0	0
PINKY	0	0	0	0	0	0	0	0	0	0	0	0	0	0	0	0	0	0	0	0	0	100	0	0	0	0
SASHA	0	0	0	0	0	0	0	0	0	0	0	0	0	0	0	0	0	0	0	0	0	0	78	0	0	22
SCOOBYDOO	0	0	0	0	0	0	0	0	0	0	0	0	0	0	0	0	0	0	0	0	0	0	0	100	0	0
SNICKER	2	0	0	0	2	2	2	0	0	2	0	0	2	2	0	0	0	0	0	2	2	0	2	2	73	0
ZIGGY	0	0	0	0	0	0	10	2	0	1	0	2	0	2	0	0	0	1	0	0	0	2	0	2	0	78

No difference was observed between the 2:1 and 6:1 architectures, so the simpler 2:1 network was chosen. The confusion matrix for this network is presented in Table III. Calls were correctly classified 70.69% of the time (± 17.15), with zero errors for some subjects. Interindividual variability in percent correct classification suggests that the BPN can distinguish some females more readily then others, though all individuals had scores that were well above what would be expected by chance (i.e., 26 females $= 1/26 = 3.8\%$). The most notable degradation in classification was observed for Flo (40%) and Jay (38%). The pattern of errors was not related to distribution of Q1 versus Q2 samples in the training set nor to the distribution of samples across quality levels in the generalization set. Also, the pattern of errors could not be attributed to the female call type (tonal versus pulsatile). Further analysis of errors would require a larger generalization set to justify more complex statistical treatment.

C. Representation of call features within the BPN

A detailed analysis of the relative importance of each frequency band in the input spectra was conducted. For every call in the generalization set that the BPN correctly classified, the value of each input bin was dithered by 20%, and the resulting percent change on the output neuron activation strength was measured. Dithering the values of input bins that had strong connection weights would result in large changes on the output neuron, thereby providing insight into the spectral characteristics that were most useful in classifying the females.

The results of this analysis are summarized in Fig. 3, one female per panel. The data are percent change in activation of the output neuron assigned to that female, ranging between $\pm 60\%$ change. The results can be interpreted as follows: The BPNs represented data on a -1 to $+1$ full-scale range (bipolar). An output neuron with activation of $+1$ indicates strong ''confidence'' of correct classification. An output neuron with activation of -1 indicates no confidence of correct classification. Therefore, strong positive-going changes in the activation levels indicate that those frequency bands made important contributions to confidence in correctly classifying the female. Strong negative-going changes in the activation levels indicate that those frequency bands made important contributions to confidence in classifying the call as *not* coming from that female. Small changes indicate weak areas of frequency differentiation.

The overall picture suggests that most of the highest frequency weightings lie below about 2 kHz, which is supported by an approximate 5–15-dB rolloff in sound energy above those frequencies. However, recall that the generalization accuracy of BPNs with 2-kHz bandwidth was significantly poorer than those with 3-kHz bandwidth. Thus, although the frequency weightings were attenuated in the 2–3-kHz range, they added about 10% improvement in classification accuracy. Visual comparison of the weightings indicates a diverse set of positive- and negative-going patterns that defy straightforward summary. However, note that the percent changes for Flo and Jay are attenuated (especially those for Jay)—these are the two females for which generalization accuracy was poorest. Dithering the input representation resulted in very little percent change in the output neuron, suggesting that the network could neither identify features for positive attribution nor features for positive rejection of these females.

IV. DISCUSSION

Acoustic signature recognition requires low intraindividual call variability and high interindividual call variability. Our analyses suggest that female Steller sea lions have

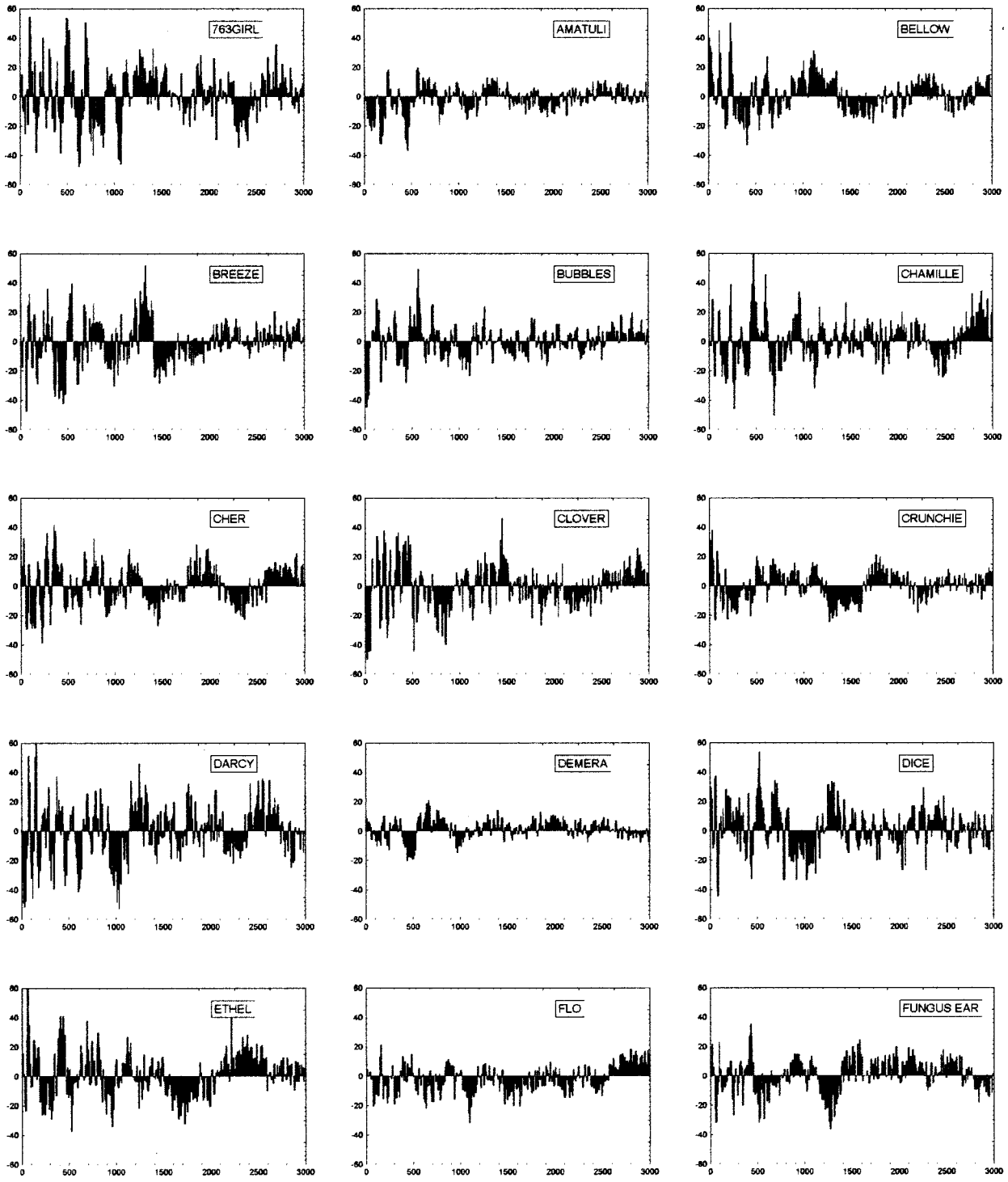

FIG. 3. Relative importance of spectral regions for neural network classification accuracy. Spectral frequency lies on the *x*-axis from 0 to 3000 Hz in 10.77 Hz bins. Percent change in output neuron activation lies on the *y*-axis from −60% to +60%. Large positive-going changes in the activation level indicate that those frequency bands made important contributions to confidence in classifying the calls as coming from that female. Large negative-going changes in the activation level indicate that those frequency bands made important contributions to confidence in rejecting the call as coming from that female. Small changes suggest that the network could identify features neither for confident attribution nor rejection of that female.

evolved sufficient vocal stereotypy to differentiate between individuals. The BPN was relatively accurate, and clearly able to consistently differentiate females based on their call parameters. The results of this research are consistent with other studies on colonially breeding pinniped species, which have suggested the existence of acoustic mother-pup recognition systems facilitated by individually distinctive vocal signatures (Bartolomew, 1959; Peterson and Bartholomew, 1969; Trillmich, 1981; Roux and Jouventin, 1987; Insley, 1989, 1992; Gisiner and Schusterman, 1991; Hanggi, 1992; Schusterman *et al.*, 1992b; Fernández-Jurisic *et al.*, 1999; Phillips and Stirling, 2000, 2001).

In this study, the best BPN yielded an overall percent correct classification of 71% on novel data (100% correct on the training data). In contrast, Phillips and Stirling (2000) reported that linear discriminant analysis resulted in 55%

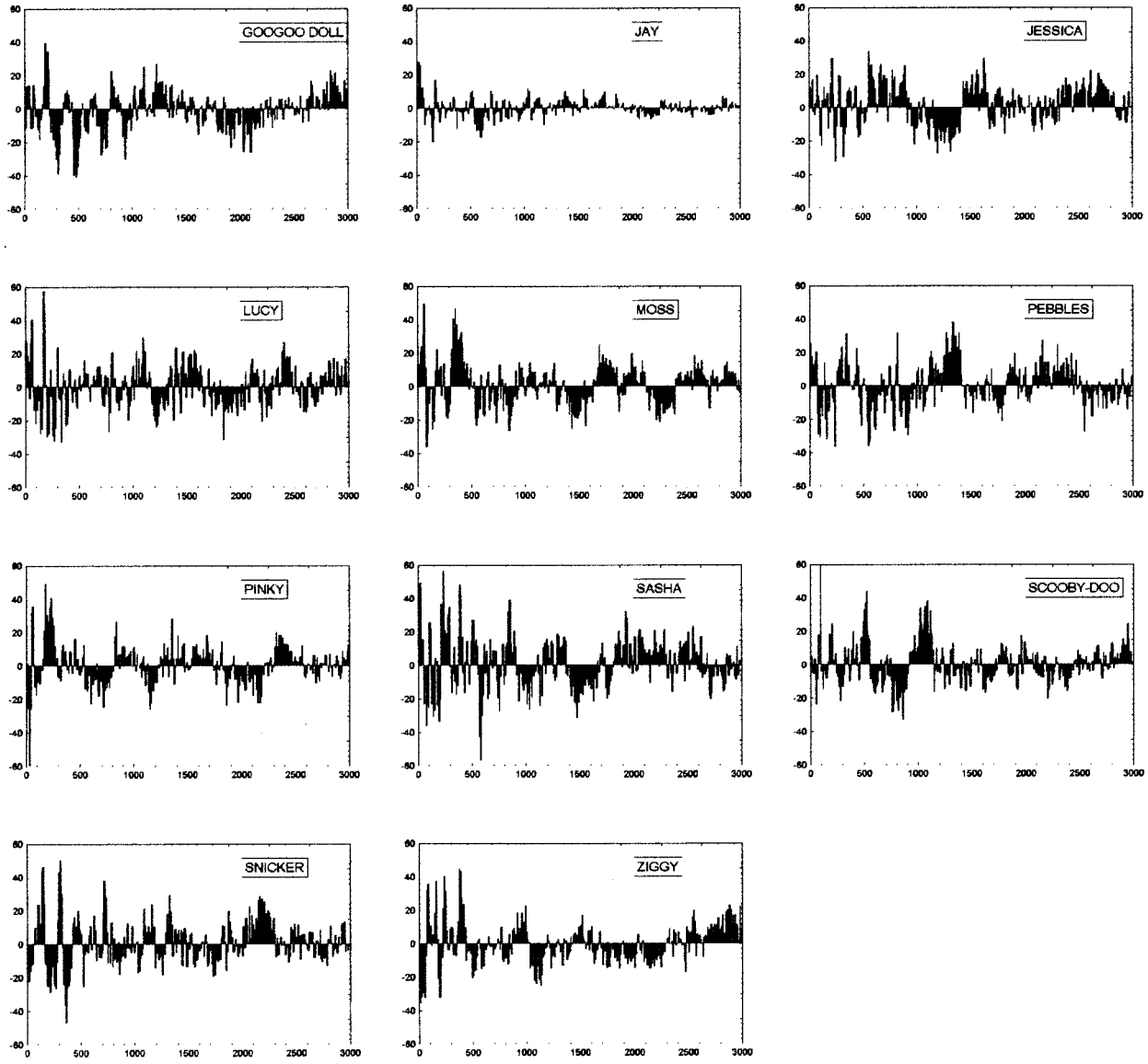

FIG. 3. (*Continued.*)

correct on novel data (70% on the training data) for a set of 15 female South American fur seals. Neural networks clearly outcompeted LDA on our Steller sea lion data as well (Campbell *et al.*, 2000). Though our BPN analyses of female Steller sea lion calls demonstrated the existence of individual acoustic signatures, the system was still prone to decision errors. The fact that classification rates were not higher overall may be explained by a number of factors. First, the specific acoustical parameters that pups use to identify mothers are not known and our inability to discern what variables are most important for identification may have limited the system's discriminatory power. In addition, recognition may occur in two ways, either by discrimination of only one individual (i.e., mother) but not of others, or discrimination among a number of related individuals (Beecher, 1982). Moreover, we do not understand the degree to which other factors may have contributed to variability in call structure. These factors include changes in motivational state within and between call bouts, effects of physiognamy (e.g., female size and condition), stability of female vocal tract characteristics across years, and varying signal-to-noise conditions in the recordings.

Implementing an autonomous acoustic recognition system in the real world faces several challenges. For example, the deployment of the acoustic sensor(s) needs to optimize the desire for maximal signal-to-noise ratio for female calls and the desire to survey as many females as possible. In the current study, calls were recorded by a field technician using a directional microphone, which provides both for intelligent survey of females, and best possible recording quality. An affordable autonomous system is not likely to be mobile (i.e., robotic), but an array of fixed microphones could be deployed which enclose the female haul-out site within their aperture. Beamforming would then substitute for the ability of a field technician to isolate a specific female and maximize signal strength by manually orienting the handheld directional microphone.

The recognition system must be robust with respect to signal quality and the presence of distractors such as male calls, pup calls, other types of female calls, and other discrete

ambient biotic sounds (e.g., songbirds). Moreover, the signal processing system must be able to extract female calls from the real-time acoustic data stream. Finally, the recognition system must be able to form new output categories for new females, ideally without supervision. We speculate that the signal processing issues might be solved as follows: The system would consist of several cascaded stages. In the first stage, the real-time data would be parsed into successive time slices. Each time slice would be presented to a filter in which mother-pup contact calls would be discriminated from other coarse classes of calls (e.g., male calls, pup calls, other female calls, and other biotic sounds). Once categorized as a female pup-contact call, the data segment would be passed to the second-stage classifier in which individual female recognition would occur. The second-stage classifier could utilize unsupervised learning algorithms, such as adaptive resonance. Theoretically, this type of architecture would permit formation of new categories for new females by detection of ''sufficiently novel'' calls. Testing the utility of this concept will require several years of field data from individually identified females.

These points illustrate the fact that development of an autonomous, real-time, adaptive recognition system is not trivial. Tradeoffs will exist inherently between the desire for real-time processing speed and the desire for accuracy. If the system is to be remotely deployed and the data are not required in real time, we suggest that real-time recognition be abandoned and that slower, more accurate signal processing methods be used. A haul-out site could be sampled for a segment of time, and the archived data processed between sampling epochs. Post-processing introduces the ability to apply tools such as adaptive ''whitening'' filters that increase signal-to-noise ratio by reduction of local ambient noise. In addition, post-processing could be used to scan multiple beams (from an array) to collect calls from multiple females, and to potentially allow the recognition system to reorganize as a result of novel incoming calls. Although an autonomous adaptive recognition system is technically exciting, it is important not to lose sight of the importance of verifying acoustic classification with visual recognition by an expert, such as reported in the current study.

Individually distinctive acoustic signatures in female Steller sea lions have several potentially important scientific applications. Statistically based voice identification may be a particularly important tool for studying the decline of this endangered species. First, because females usually call when they enter and leave the rookery but are not always visible, the classification system described here could be used in the field to document the precise female arrival and departure times at the rookery. This information could be used to document patterns of maternal care/energy transfer during the critical development stage of pups. Time devoted to foraging and feeding trips by different individuals in different age classes could be examined. Comparisons of these parameters between the western (endangered) and eastern (threatened) populations of Steller sea lions may be of particular interest due to the different conservation status of the two populations. In addition, data collected over multiple years could allow us to determine site fidelity of females, interannual patterns of rookery usage, and philopatry or dispersion of matrilines.

ACKNOWLEDGMENTS

We are grateful to R. H. Defran for providing advice and assistance with many aspects of this research. The Alaska Sea Life Center deserves recognition for its support of the field effort on Sugarloaf Island from 1994 to 1999. The SDSU Foundation provided essential administrative assistance. We thank two anonymous reviewers for their helpful comments. Funding was provided by an ONR Research Opportunities for Program Officers (ROPO) award to Dr. R. H. Defran at San Diego State University (ONR N00014-00-1-0114). This paper is dedicated to the loving memory of Olga and Woody Moore.

Bartholomew, G. A. (**1959**). ''Mother-young relations and the maturation of pup behavior in the Alaska fur seal,'' Behaviour **7**, 187–208.

Beecher, M. D. (**1982**). ''Signature systems and kin recognition,'' Am. Zool. **22**, 477–490.

Bickham, J. W., Patton, J. C., and Loughlin, T. R. (**1996**). ''High variability for control-region sequences in a marine mammal: Implications for conservation and biogeography of Steller sea lions (*Eumetopias jubatus*),'' J. Mammal. **77**, 95–108.

Braham, H. W., Everitt, R. D., and Rugh, D. J. (**1980**). ''Northern sea lion decline in the eastern Aleutian Islands,'' J. Wildl. Manage. **44**, 25–33.

Calkins, D. G., McAllister, D. C., Pitcher, K. W., and Pendleton, G. W. (**1999**). ''Steller sea lions status and trend in Southeast Alaska: 1979–1997,'' Marine Mammal Sci. **15**, 462–477.

Campbell, G. S., Gisiner, R., and Helweg, D. A. (**2000**). ''Acoustic identification of female Steller sea lions,'' Abstracts of the joint 140th meeting of the ASA/Noise Congress, Newport Beach, CA, November, p. 2541.

Fernández-Juricic, E., Campagna, C., Enriquez, V., and Ortiz, C. L. (**1999**). ''Vocal communication and individual variation in breeding South American sea lions,'' Behaviour **136**, 495–517.

Gisiner, R. (**1985**). ''Male territoriality and reproductive behavior in the Steller sea lion, *Eumetopias jubatas*,'' Ph.D. dissertation, Univ. of Calif. at Santa Cruz.

Gisiner, R., and Schusterman, R. J. (**1991**). ''California sea lion pups play an active role in reunions with their mothers,'' Anim. Behav. **41**, 364–366.

Hanggi, E. B. (**1992**). ''The importance of vocal cues in mother-pup recognition in a California sea lion,'' Marine Mammal Sci. **8**, 430–432.

Higgins, L. V. (**1984**). ''Maternal behavior and attendance patterns of the Steller sea lion in California,'' M.S. thesis, Univ. of Calif. at Santa Cruz.

Insley, S. J. (**1989**). ''Vocal recognition between mothers and pups in the northern elephant seal (*Mirounga angustirostris*) and northern fur seal *Callorhinus ursinus*,'' M.S. thesis, Univ. of Victoria.

Insley, S. J. (**1992**). ''Mother offspring separation and acoustic stereotypy: a comparison of call morphology in two species of pinnipeds,'' Behaviour **120**, 103–121.

Loughlin, T. R. (**1997**). ''Using the phylogeographic method to identify Steller sea lion stocks,'' in *Molecular Genetics of Marine Mammals*, edited by A. E. Dizon, S. J. Chivers, and W. F. Perrin (Soc. Marr. Mammal.), Spec. Publ. No. 3, pp. 329–341.

Loughlin, T. R., Perlov, A. S., and Vladimirov, V. A. (**1992**). ''Range-wide survey and estimation of total abundance of Steller sea lions in 1989,'' Marine Mammal Sci. **8**, 220–239.

Loughlin, T. R., Rugh, D. J., and Fiscus, C. H. (**1984**). ''Northern sea lion distribution and abundance: 1956–80,'' J. Wildl. Manage. **48**, 729–740.

Merrick, R. L., and Loughlin, T. R. (**1997**). ''Foraging behavior of adult female and young-of-the-year Steller sea lions in Alaskan waters,'' Can. J. Zool. **75**, 776–786.

Merrick, R. L., Loughlin, T. R., and Calkins, D. G. (**1987**). ''Decline in abundance of the northern sea lion, *Eumetopias jubatus*, in Alaska, 1956–1986,'' Fish. Bull. **85**, 351–365.

Milette, L. L., Trites, A. W., and Calkins, D. (**1999**). ''Behavior of lactating Steller sea lions: are they nutritionally stressed?,'' Abstracts of the 13th Biennial Conference on the Biology of Marine Mammals, Maui, HI, December, p. 125.

NMFS (National Marine Fisheries Service) (**1992**). ''Recovery plan for the Steller sea lion (*Eumetopias jubatus*)'' (NMFS, Silver Spring, MD).
NMFS (National Marine Fisheries Service) (**1995**). ''Status Review of the United States Steller sea lion (*Eumetopias jubatus*) population'' (NMFS, National Marine Mammal Laboratory, Seattle, WA).
Peterson, R. S., and Bartholomew, G. A. (**1969**). ''Airborne vocal communication in the California sea lion, *Zalophus californianus*,'' Anim. Behav. **17**, 17–24.
Phillips, A. V., and Stirling, I. (**2000**). ''Vocal individuality in mother and pup South American fur seals, *Arctocephalus australis*,'' Marine Mammal Sci. **16**, 592–616.
Phillips, A. V., and Stirling, I. (**2001**). ''Vocal repertoire of South American fur seals, Arctocephalus australis: structure, function, and context,'' Can. J. Zool. **79**, 420–437.
Riedman, M. (**1990**). *The Pinnipeds: Seals and Sea Lions* (Univ. of California, Berkeley).
Roux, J. P., and Jouventin, P. (**1987**). ''Behavioral cues to individual recognition in the Subantarctic fur seal, *Arctocephalus tropicalis*,'' NOAA Tech. Rep. NMFS No. 51.
Schusterman, R. J., Gisner, R., and Hanggi, E. B. (**1992a**). ''Imprinting and other aspects of pinniped/human interactions,'' in *The Inevitable Bond*, edited by H. Davis and D. Balfour (Cambridge U. P., New York), pp. 334–356.
Schusterman, R. J., Hanggi, E. B., and Gisiner, R. (**1992b**). ''Acoustic signalling in mother-pup reunions, interspecies bonding, and affiliation by kinship in California sea lions *Zalophus californianus*,'' in *Marine Mammal Sensory Systems*, edited by J. A. Thomas, R. A. Kastelein, and A. E. Supin (Plenum, New York), pp. 533–551.
Sease, J. L., Taylor, W. P., Loughlin, T. R., and Pitcher, K. W. (**2001**). ''Aerial and land-based surveys of Steller sea lions (*Eumetopias jubatus*) in Alaska, June and July 1999 and 2000,'' U.S. Dept. Commer., NOAA Tech. Memo. NMFS-AFSC-122.
Trillmich, F. (**1981**). ''Mutual mother-pup recognition in Galapagos fur seals and sea lions: Cues used and functional significance,'' Behaviour **78**, 21–42.
Trites, A. W., and Larkin, P. A. (**1996**). ''Changes in the abundance of Steller sea lions (*Eumetopias jubatus*) in Alaska from 1956 to 1992: how many were there?'' Aquatic Mamm. **22**, 153–166.
Trivers, R. L. (**1972**). ''Parental investment and sexual selection,'' in *Sexual Selection and the Descent of Man*, edited by B. Campbell (Aldine, Chicago), pp. 136–179.

Temporary shift in masked hearing thresholds in odontocetes after exposure to single underwater impulses from a seismic watergun

James J. Finneran
Space and Naval Warfare Systems Center, San Diego, Code 235, 53560 Hull Street, San Diego, California 92152-5000

Carolyn E. Schlundt and Randall Dear
Science Applications International Corporation, Maritime Services Division, 3990 Old Town Avenue, Suite 105A, San Diego, California 92110

Donald A. Carder and Sam H. Ridgway
Space and Naval Warfare Systems Center, San Diego, Code 235, 53560 Hull Street, San Diego, California 92152-5000

(Received 13 September 2001; revised 4 March 2002; accepted 18 March 2002)

A behavioral response paradigm was used to measure masked underwater hearing thresholds in a bottlenose dolphin (*Tursiops truncatus*) and a white whale (*Delphinapterus leucas*) before and after exposure to single underwater impulsive sounds produced from a seismic watergun. Pre- and postexposure thresholds were compared to determine if a temporary shift in masked hearing thresholds (MTTS), defined as a 6-dB or larger increase in postexposure thresholds, occurred. Hearing thresholds were measured at 0.4, 4, and 30 kHz. MTTSs of 7 and 6 dB were observed in the white whale at 0.4 and 30 kHz, respectively, approximately 2 min following exposure to single impulses with peak pressures of 160 kPa, peak-to-peak pressures of 226 dB *re* 1 μPa, and total energy fluxes of 186 dB *re* 1 μPa$^2\cdot$s. Thresholds returned to within 2 dB of the preexposure value approximately 4 min after exposure. No MTTS was observed in the dolphin at the highest exposure conditions: 207 kPa peak pressure, 228 dB *re* 1 μPa peak-to-peak pressure, and 188 dB *re* 1 μPa$^2\cdot$s total energy flux. © *2002 Acoustical Society of America.* [DOI: 10.1121/1.1479150]

PACS numbers: 43.80.Nd, 43.80.Lb [WA]

I. INTRODUCTION

Previous studies (e.g., Au *et al.*, 1999; Kastak *et al.*, 1999; Schlundt *et al.*, 2000) have demonstrated that a marine mammal exposed to a sufficiently intense sound may exhibit an increased hearing threshold, or threshold shift (TS), following cessation of the intense sound. If the hearing threshold returns to the preexposure value after a period of time, the TS is known as a temporary threshold shift (TTS); if the threshold does not return to the preexposure level, the TS is called a permanent threshold shift (PTS). PTS and TTS data were used to establish noise exposure limits in humans (e.g., Kryter *et al.*, 1966) and TTS data are often used to help predict the effects of anthropogenic noise on marine mammals in the wild (e.g., Department of the Navy, 1998, 2001).

There have been three previous studies of TTS in odontocetes: Au *et al.* (1999) and Nachtigall *et al.* (2001) measured TTS in a bottlenose dolphin exposed to 30–50 min of octave-band noise centered at 7.5 kHz; Schlundt *et al.* (2000) measured temporary shifts of masked hearing thresholds (MTTS) in bottlenose dolphins and white whales exposed to 1-s pure tones at frequencies of 0.4, 3, 10, 20, and 75 kHz. [These data included and expanded on the original pure-tone MTTS data for bottlenose dolphins described in a technical report by Ridgway *et al.* (1997).] Finneran *et al.* (2000) conducted a study designed to measure MTTS in bottlenose dolphins and white whales exposed to single underwater impulses (i.e., transient sounds with relatively high peak pressures and broad frequency content). The latter study used an ''explosion simulator'' (ES), consisting of an array of piezoelectric sound projectors with accompanying hardware and software, to generate impulsive sounds with pressure waveforms resembling those produced by distant underwater explosions. The pressure waveforms produced by the ES resembled those predicted by the Navy REFMS model (Britt, 1987; Britt *et al.*, 1991); however, the measured frequency spectra showed a lack of energy at frequencies below 1 kHz. No substantial (i.e., 6 dB or larger) threshold shifts were observed in any of the subjects (two bottlenose dolphins and one white whale) at the highest received level produced by the ES: approximately 70 kPa peak pressure, 221 dB *re* 1 μPa peak-to-peak pressure, and 179 dB *re* 1 μPa$^2\cdot$s total energy flux (Finneran *et al.*, 2000).

This paper presents the results of a study designed to measure TTSs in a dolphin and white whale exposed to single underwater impulses produced by a seismic watergun. The watergun was used because it was capable of producing impulses with higher peak pressures and total energy fluxes than the pressure waveforms produced using the ES. The watergun was selected over other seismic sources (e.g., airguns) because watergun impulses contain more energy at higher frequencies, where odontocete hearing thresholds are relatively low. The experimental approach was similar to that of Schlundt *et al.* (2000) and Finneran *et al.* (2000): a behavioral response paradigm was used to measure hearing thresh-

olds before and after exposure to single underwater impulses. The test site (in San Diego Bay) featured a relatively high and variable ambient noise background, thus band-limited white noise (masking noise) was introduced to create a floor effect and keep thresholds consistent despite fluctuations in the ambient noise level. The presence of masking noise has been shown to decrease the amount of TTS observed in humans (e.g., Parker *et al.*, 1976; Humes, 1980) and the amount of PTS in terrestrial mammals (Ades *et al.*, 1974). To indicate that the thresholds presented here were measured in the presence of masking noise, the term MTTS, rather than TTS, is used to identify these data. The potential effects of the masking noise on the measured thresholds are discussed in Sec. III.

II. METHODS

A. Experimental subjects

Experimental subjects consisted of one bottlenose dolphin (BEN, age 36 years, approximate weight 260 kg) and one white whale (MUK, 32 years, 600 kg). Subjects were housed in floating netted enclosures (9×9 to 12×24 m) located in San Diego Bay. The study followed a protocol approved by the Institutional Animal Care and Use Committee at SPAWAR Systems Center, San Diego, and operated under Department of Defense guidelines. All subjects were healthy during the course of the study.

B. Experimental apparatus

1. Underwater stations

Tests were conducted in a 9×9 m floating netted enclosure located approximately 50 m from the subjects' ''home'' enclosures [Fig. 1(a)]. Subjects swam to the test enclosure shortly before each test session and returned to their home enclosure afterward. The test apparatus consisted of two underwater listening stations, designated as the ''S1 station'' and the ''S2 station.'' Two stations were used to spatially separate the location of the impulsive sound exposure from the location of the hearing tests. The S1 station was the site for the presentation of the underwater impulse produced by the watergun and a ''start'' signal to begin the hearing test. The S2 station was the site for the hearing tests. Each station consisted of a polyvinylchloride (PVC) frame with a plastic biteplate on which the subjects were trained to station. The S1 and S2 biteplates were located at depths of approximately 4 and 2 m, respectively. Each station contained an underwater video camera; a third video camera was located in-air with a view of both stations.

The S1 station [Fig. 1(b)] contained a single sound projector (ITC 1001) that was used to emit a 1-s tone as the start signal for the subject to begin hearing tests. These start tones, or ''S1 tones,'' were at a frequency of 10 kHz and a sound pressure level (SPL) of approximately 120 dB *re* 1 μPa. The S1 start tones were produced using a programmable function generator (Wavetek 178) and amplified (BGW PS4) before being input to the S1 sound projector.

The S2 station [Fig. 1(c)] contained four sound projectors: an ITC 1032 and a USRD J13 were used to project hearing test tones, or ''S2 tones,'' and another ITC 1032 and a USRD J9 were used to project masking noise. Two projectors were required for both the hearing test tones and the masking noise to cover the frequency range of interest. Hearing tests were performed at three S2 frequencies: 0.4, 4, and 30 kHz; these frequencies were selected to strike a balance between the range of frequencies present in the watergun stimulus (see Sec. II B 2) and the audible frequency ranges of *Tursiops* and *Delphinapterus*. The S2 tones were 250 ms in duration including 5-ms rise and fall times. S2 tones were generated using a personal computer (PC) containing a multifunction board (National Instruments PCI-MIO-16E-1), attenuated (HP 350B), filtered (Ithaco 4302), and amplified (BGW PS2) before being input to the appropriate sound projector: the USRD J13 at 0.4 and 4 kHz or the ITC 1032 at 30 kHz.

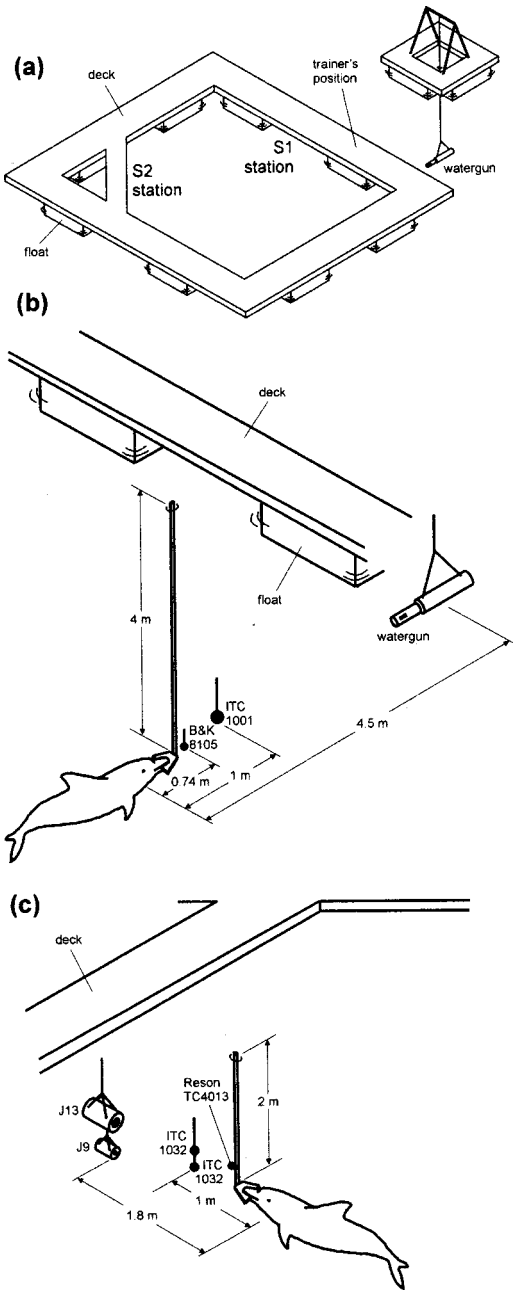

FIG. 1. (a) Test site showing locations of watergun and S1 and S2 underwater listening stations. (b) Detail of S1 station. (c) Detail of S2 station.

Masking noise was generated on a dedicated computer running custom software (Finneran *et al.*, 1999). This system allowed for the continuous generation of masking noise whose frequency spectrum was compensated to eliminate the effects of projector frequency-dependent transmission characteristics and acoustic standing waves. Masking noise was generated using a National Instruments PCI-MIO-16E-1, attenuated (HP 355D), filtered (SRS 560 and Ithaco 4302), and amplified (BGW PS2) before being input to the appropriate sound projector: the USRD J9 for testing at 0.4 and 4 kHz or the ITC 1032 at 30 kHz. The projected masking noise was centered at the appropriate S2 frequency and had a frequency bandwidth equal to the test frequency; e.g., for hearing thresholds measured at 0.4 kHz, the noise bandwidth was 0.2–0.6 kHz. The noise spectral density was 95, 90, and 80 dB *re* 1 μPa^2/Hz for S2 frequencies of 0.4, 4, and 30 kHz, respectively. The noise spectral density was flat within ± 3 dB over these ranges. Masking noise was continuously projected, from the time the subjects entered the test enclosure, to the cessation of testing.

The acoustic pressure during each S2 tone presentation was measured using a Reson TC4013 hydrophone (mounted to the S2 PVC frame) and a B&K 2635 charge amplifier, digitized using the PCI-MIO-16E-1 multifunction board, and stored on the PC. The pressure during the S1 start tone presentation was measured with a B&K 8105 hydrophone (mounted to the S1 PVC frame), amplified and filtered (B&K 2635), and digitized (PCI-MIO-16E-1). The PC was also used to record the time each S1 and S2 tone was produced.

2. Watergun stimuli

Seismic waterguns use compressed air to rapidly expel water from a water-filled chamber. The water leaving the chamber creates a void behind it; the collapse of water into this void creates an acoustic signal. In this study, underwater impulses were generated using a 1310 cm^3 (80 in^3) seismic watergun (Seismic Systems, Inc., Model S80). The watergun position was fixed relative to the subject; the amplitude of the sound produced by the watergun was varied by changing the pressure of the compressed air (the watergun static pressure charge). The watergun was located 4.5 m from the subject at the same depth, aligned with the subject's longitudinal axis. Water depth at this location was approximately 8 m.

Each exposure condition was assigned a nominal level, from M1 to M13 for MUK and B1 to B4 for BEN, in the order in which they were tested (MUK was tested first; the resulting data were used to guide the development of the abbreviated test matrix for BEN). The acoustic pressure amplitude produced by the watergun generally increased with the watergun static pressure charge but was highly variable. The actual received sound levels thus did not necessarily increase with each increase in watergun static pressure and the received level at a specific static pressure charge varied from day to day and from one impulse to the next. For MUK, the static charge at level M12 was intentionally reduced (as a control procedure) and level M13 was intended to replicate level M11.

The acoustic pressure produced by the watergun was measured during each subject exposure using a hydrophone (B&K 8105) mounted to the S1 PVC frame between the subject and the watergun; the hydrophone was located 0.74 m from the subject's ears. The hydrophone output was filtered from 2 Hz to 200 kHz and amplified (B&K 2635), then digitized at 500 kHz using the PCI-MIO-16E-1. The digitized waveforms were analyzed using custom software to calculate the peak pressure (p_p), peak-to-peak SPL ($\mathrm{SPL}_{p\text{-}p}$), total energy flux ($E_T$), and duration ($\tau$). A distance correction based on daily calibration measurements using a second hydrophone (B&K 8105 with a B&K 2635 amplifier) placed at the location of the subjects' ears (when on the S1 biteplate) was used to correct the sound levels measured during exposure (0.74 m from the subjects' ears) to the actual received sound levels at the ear position.

The peak pressure was determined from the absolute value of the measured waveform (i.e., the maximum negative or positive peak). The duration of each impulse was estimated using the "B-duration" (Hamernik and Hsueh, 1991; CHABA, 1992), defined using the first and last time values at which the absolute value of the waveform reached an amplitude of -20 dB relative to the maximum amplitude. [The B-duration was used, rather than the "A-duration," defined as the time from impulse start to the first zero-crossing (Hamernik and Hsueh, 1991; CHABA, 1992), because of the presence of multiple peaks in the received pressure waveforms.] The energy flux spectral density $E(m)$ was calculated as

$$E(m) = |P(m)|^2, \quad m = 0,1,...,N-1, \tag{1}$$

where

$$P(m) = \Delta t \sum_{n=0}^{N-1} p(n) e^{-j2\pi mn/N}, \quad m = 0,1,...,N-1, \tag{2}$$

$p(n)$ is the digitized pressure waveform, $P(m)$ is the discrete Fourier transform of $p(n)$, N is the number of samples in $p(n)$, Δt is the sampling interval, and $j = (-1)^{1/2}$. Fourier analysis of each signal used a 131-ms time window to produce the desired frequency resolution. Note that the medium characteristic impedance ρc has been eliminated from the definition of $E(m)$ described by Fricke *et al.* (1985) and Johnston *et al.* (1988); this was done to emphasize that the energy flux spectral density was based on individual pressure measurements rather than acoustic intensity measurements. The energy flux spectral density thus has units of μPa$^2\cdot$s/Hz, rather than J$\cdot$m$^{-2}\cdot$Hz^{-1} (0 dB *re* 1 J$\cdot$m$^{-2}\cdot$Hz$^{-1}\approx$182 dB *re* 1 μPa$^2\cdot$s/Hz, for seawater with nominal values of density $\rho = 1026$ kg/m^3 and sound speed $c = 1500$ m/s). The total energy flux E_T was calculated using

$$E_T = \Delta f \sum_{k=0}^{N-1} E(k), \tag{3}$$

where $\Delta f = 1/(N\Delta t)$. The total energy flux has units of μPa$^2\cdot$s (0 dB *re* 1 J/m^2 = 182 dB *re* 1 μPa$^2\cdot$s, for seawater with $\rho = 1026$ kg/m^3 and $c = 1500$ m/s).

Representative pressure waveforms and energy flux spectral densities measured for each of the impulse levels for MUK and BEN are shown in Figs. 2 and 3, respectively. Note that the pressure waveform axes scales are not uniform

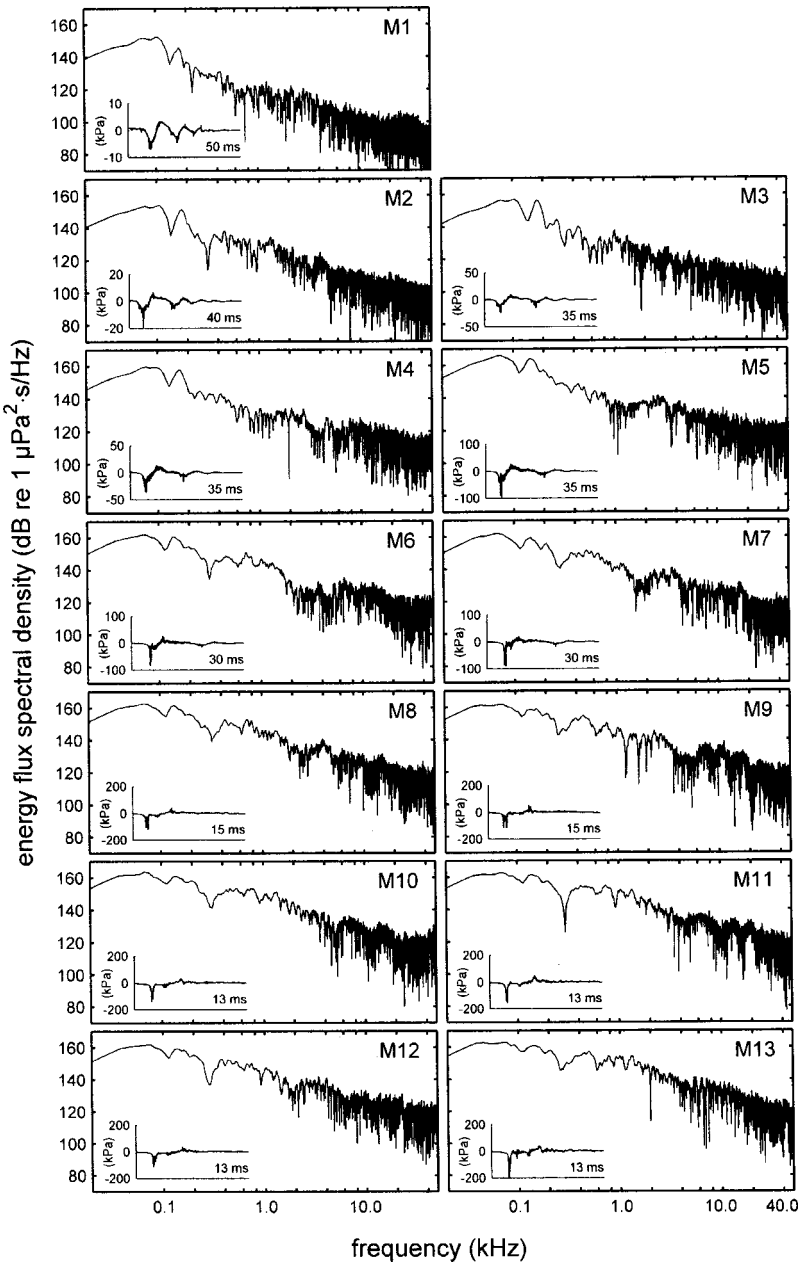

FIG. 2. Representative pressure signatures and energy flux spectral densities for impulse levels M1–M13. The analysis frequency bandwidth was 7.6 Hz.

throughout the panels. The pressure signatures exhibit features characteristic of watergun impulses: a low-amplitude, positive pressure precursor produced by the expulsion of water from the chamber, followed by a high amplitude negative pressure pulse created by the collapse of water into the void. The recorded pressure waveforms in Figs. 2 and 3 also show the effects of multipath propagation caused by reflections from the surface and bottom.

Tables I and II show the mean values for p_p, $\mathrm{SPL}_{p\text{-}p}$, E_T, and τ at each exposure condition for MUK and BEN, respectively. The $\pm$ values in Tables I and II indicate the standard deviation for linear quantities and the maximum $\pm$ excursion for decibel quantities. Waveform duration decreased with increasing watergun static pressure, making the frequency spectra more broadband at the higher exposure levels. Peak pressures were more variable than the $\mathrm{SPL}_{p\text{-}p}$ and E_T.

C. Procedure

1. Overview

Figure 4 illustrates the test sequence and data analysis techniques. Each test day consisted of two sessions: a morning session [Fig. 4(a)] and an afternoon session [Fig. 4(b)]. Each day one session (an ''exposure session'') featured an exposure to a watergun impulse. The other session was a control session and featured a ''mock'' exposure where the watergun firing procedures were simulated but no watergun impulse was produced. The choice of morning or afternoon for each exposure session was randomized.

Four hearing tests were conducted in each control and exposure session: Three hearing tests were performed before the exposure (or mock exposure); these tests yielded preexposure hearing thresholds at the three S2 test frequencies. The fourth hearing test was conducted after the exposure (or mock exposure) and yielded a postexposure hearing thresh-

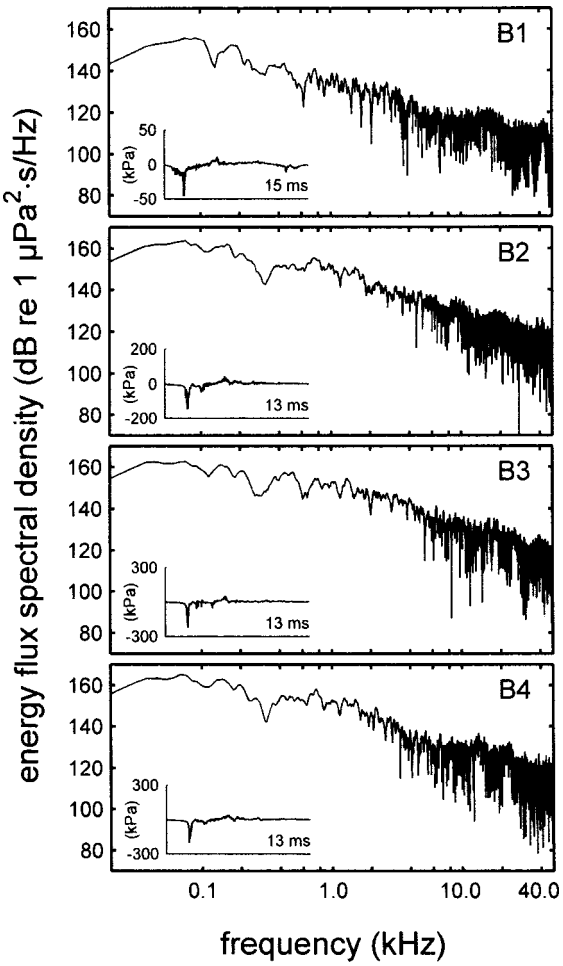

FIG. 3. Representative pressure signatures and energy flux spectral densities for impulse levels B1–B4. The analysis frequency bandwidth was 7.6 Hz.

old. The postexposure test frequency was the same as the last frequency tested preexposure. Three days of testing were required at each exposure condition to obtain a postexposure hearing threshold at each of the three S2 frequencies. The order in which the S2 frequencies were tested was varied to test all combinations over a number of days. The preexposure and postexposure hearing test procedures were nearly identical. The preexposure hearing test procedure is presented in detail next, followed by a discussion of the postexposure hearing test procedure which highlights the differences between the two.

2. Preexposure hearing tests

The hearing test procedure was based on the method of free response, or MFR (Egan *et al.*, 1961) and was very similar to that used by Schlundt *et al.* (2000) and Finneran *et al.* (2000). Each hearing test consisted of a number of relatively long observation periods, designated here as ''dives.'' During each dive the subject was presented with a number of S2 hearing test tones. Each dive began with the trainer directing the animal (with a hand signal) to the S1 station. The subject was trained to remain on the S1 station until presented with the S1 start tone, which signaled the subject to proceed to the S2 station. Once the subject was positioned at the S2 station, S2 hearing test tones were presented. The time interval between S2 tones (the interstimulus interval, or ISI) was randomized between 5 and 10 s and the subject (as well as the trainer) did not know when the next tone would occur. Subjects were trained to whistle if they heard a tone and to remain quiet otherwise (see Ridgway and Carder, 1997). The time period between 0.05 and 2.05 s immediately following each tone start was designated as a ''hit interval.'' A whistle response occurring within the hit interval following a tone was defined as a ''hit.'' No whistle response within the hit interval was a ''miss.'' The amplitudes of the S2 tones were adjusted using a modified up/down staircase procedure (e.g., Cornsweet, 1962): the amplitude was decreased 2 dB following each hit and increased 2 dB following each miss.

The trainer monitored the sound in the water (using the Reson TC4013 hydrophone mounted on the S2 frame) for any whistle responses by the subject. The trainer was also aware of the session type (control or exposure), the amplitude of each S2 tone, and was notified as each S2 tone was produced (but not before). After a variable number of tones, the trainer sounded an underwater buzzer to signal the subject to leave the S2 station and return to the surface for fish reward. The point at which reinforcement was delivered (i.e., the number of tones per dive) was randomly varied within the following guidelines: Subjects were reinforced only after

TABLE I. Exposure conditions for subject MUK. Mean values are listed. The ± values indicate the standard deviation for linear units (e.g., kPa) and the maximum± excursion for values in dBs.

Level	p_p (kPa)	p_p (psi)	$SPL_{p\text{-}p}$ (dB *re* 1 μPa)	E_T (dB *re* 1 μPa^2·s)	τ (ms)
M1	8.2±1.5	1.2±0.22	202±2	171±1	37±2.8
M2	20.2±2.1	2.9±0.30	208±1	174±1	24±4.0
M3	25.7±6.8	3.7±0.99	211±2	176±1	15±0.5
M4	38.6±3.3	5.6±0.48	215±1	178±1	15±1.8
M5	58.6±12.7	8.5±1.84	217±1	181±1	15±0.6
M6	87.2±17.5	12.7±2.54	221±1	182±1	14±1.9
M7	89.2±7.3	12.9±1.06	221±1	183±1	14±1.2
M8	116±28.6	16.8±4.15	224±2	184±1	13±1.9
M9	118±22.3	17.1±3.24	224±2	184±1	13±1.4
M10	143±8.4	20.8±1.22	225±1	185±1	11±1.3
M11	160±23.3	23.2±3.38	226±1	186±1	6.3±2.1
M12	107±11.8	15.5±1.71	223±1	183±1	13±2.1
M13	198±18.6	28.7±2.70	228±1	187±1	11±3.8

TABLE II. Exposure conditions for subject BEN. Mean values are listed. The ± values indicate the standard deviation for linear units (e.g., kPa) and the maximum± excursion for values in dBs.

Level	p_p (kPa)	p_p (psi)	$SPL_{p\text{-}p}$ (dB *re* 1 μPa)	E_T (dB *re* 1 $\mu Pa^2 \cdot s$)	τ (ms)
B1	43.5±7.3	6.3±1.06	215±1	177±1	14±0.9
B2	146±13.1	21.2±1.90	225±1	185±1	11±1.5
B3	220±27.9	31.9±4.05	229±1	187±1	10±1.4
B4	207±6.1	30.0±0.89	228±1	188±1	13±1.7

correct responses. An attempt was made to reinforce subjects after responding to low-level tones (i.e., at a lower level than any previously responded to). If the subject missed several tones in a row, reinforcement would generally not be given on the first subsequent hit. The dive times were normally kept to less than 3 min. The amount of reinforcement was scaled to the performance of the subject during the dive (e.g., more reinforcement was given for longer dives and/or responding to low-level tones).

After reinforcement, the next dive was begun and the procedure repeated until the hearing test was complete. Preexposure hearing tests were conducted until at least ten ''reversals,'' defined as a transition from a hit to a miss or from a miss to a hit, were obtained. The first five S2 tones at each frequency were presented at suprathreshold levels as warm-up tones, beginning approximately 10 dB above threshold; any reversals occurring in the first five tones were not counted as part of the required ten reversals. Each preexposure threshold could usually be estimated after one to four dives or 15 to 30 tones.

Figures 4(c)–(e) illustrate the threshold calculation method. The hearing test resulted in a record of the subject's performance (hit or miss) to each tone [Fig. 4(c)]. The performance data were then converted to a series of reversals, shown in Fig. 4(e). The time and amplitude for each reversal were defined as the mean time and mean SPL, respectively, of the hit/miss pair. Time values in Fig. 4(e) are referenced to the time of the exposure (or mock exposure), thus the preex-

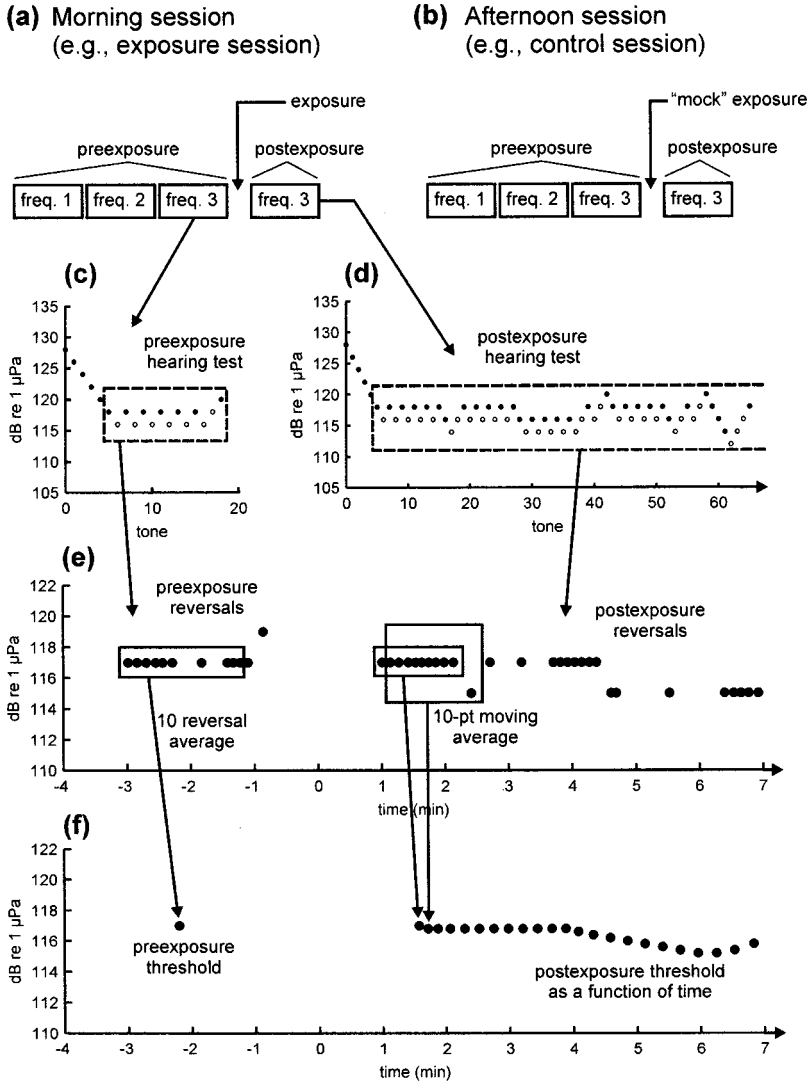

FIG. 4. Test sequence and data analysis technique. Each test day consisted of a (a) morning and (b) afternoon test session. Four hearing thresholds were measured during each session: three preexposure and one postexposure. (c) Preexposure and (d) postexposure hearing test results showing hits (filled symbols) and misses (open symbols) as functions of tone number. (e) and (f) Preexposure thresholds were calculated from the mean SPL of the first ten reversals. Postexposure thresholds were estimated by applying a 10-point moving average to the collection of postexposure reversals.

posure reversals occurred at negative times. Finally, preexposure hearing thresholds were calculated as the mean SPL of the first ten hit-miss/miss-hit reversal points [Fig. 4(f)]. The time at which the threshold occurred was defined as the mean time of the ten reversals.

3. Postexposure hearing tests

The postexposure hearing test procedure was identical to the preexposure procedure with three exceptions: (1) During exposure sessions, a single impulse was produced by the watergun 30 ms after the start of the first S1 start tone. During control sessions, a switch was used to disable the watergun triggering signal, preventing the watergun from firing. (2) An effort was made (during both control and exposure sessions) to get ten reversals within the first two dives after the exposure (or ''mock'' exposure), in order to test the hearing before any substantial recovery occurred. (3) The postexposure hearing tests were conducted for at least 20 min for MUK and at least 10 min for BEN (it was concluded after testing MUK that 10 min was a sufficient amount of time). The longer test durations were used to enable any TS and recovery to be tracked.

Figures 4(d)–(f) illustrate the postexposure threshold calculation. As with the preexposure tests, the postexposure hearing test resulted in a record of the subject's performance (hit or miss) to each tone [Fig. 4(d)], which was converted to a series of reversals, shown in Fig. 4(e). The time and amplitude for each reversal were defined as the mean time and mean SPL, respectively, of the hit/miss pair. Since the time values in Fig. 4(e) are referenced to the time of the exposure (or mock exposure), the postexposure reversals occurred at positive times. Postexposure hearing thresholds were calculated by applying a ten-point moving average to the postexposure reversals, which typically numbered many more than 10 [Figs. 4(e)–(f)]. Each output of the moving average consisted of two data points: the mean SPL over the ten reversals and the mean time over which the ten reversals occurred. The postexposure threshold as a function of time thus represented the mean time and mean SPLs of each group of ten postexposure reversals. Thresholds at specific postexposure times (e.g., 2 min, 4 min) were obtained by interpolating within the collection of thresholds from the moving average.

4. False alarm rate

Any whistle response by a subject not occurring within a hit interval was recorded as a false alarm. The ISI (defined from the start of one tone to the start of the next tone) was randomly varied between 5 and 10 s, thus the majority of time spent on the S2 station was outside any hit intervals and functioned as a ''catch trial'' period. The false alarm rate r was defined as the number of false alarms, N_{FA}, divided by the total amount of time that the subject was on the S2 station with no hit interval present. To obtain a dimensionless quantity, r was multiplied by the hit interval duration T_1:

$$rT_1 = \frac{N_{\mathrm{FA}}}{T - N_{\mathrm{S2}} T_1} T_1, \tag{4}$$

where T is the total amount of time the animal spent on the S2 station and N_{S2} is the number of S2 tones presented. For the MFR, rT_1 values calculated using Eq. (4) are analogous to false alarm rates obtained from a single interval experiment (Miller, 1969); however, this study employed a modified version of the MFR: the ISI was not open-ended but randomized between 5 and 10 s. The rT_1 values calculated here are therefore not precisely identical to those obtained with the MFR or to false alarm rates obtained from a single interval experiment; however, they do reliably assess a subject's response bias from session to session. The use of rT_1 is a method of normalizing the number of false alarms with respect to the number of tones presented and the total time that the subject was on the S2 station.

5. MTTS criterion

Postexposure hearing thresholds were compared to preexposure thresholds to determine if a subject experienced a MTTS, defined as a 6-dB or larger increase in threshold over the preexposure threshold at that frequency. This 6-dB criterion was derived from a substantial amount of threshold data for these animals obtained at several frequencies over a period of several years (e.g., Ridgway and Carder, 1997; Ridgway *et al.*, 1997; Schlundt *et al.*, 2000; Finneran *et al.*, 2000). This criterion was considered to be the minimum shift that was clearly larger than any day-to-day or session-to-session variations in the subjects' masked hearing thresholds. Studies of TTS in terrestrial mammals exposed to single impulses have shown that TTSs up to 40 dB may be fully recovered without a PTS or the loss of sensory hair cells (Ahroon *et al.*, 1996), thus the 6-dB criterion was considered well below levels resulting in a PTS.

In this report, the difference between a pre- and postexposure threshold is denoted as a TS. If the TS is larger than the 6-dB criterion and recovers after a period of time, it is referred to as a MTTS. MTTSs and TSs at specific times are denoted with subscripts: e.g., MTTS_2 indicates a temporary shift of 6-dB or more at 2 min postexposure.

III. RESULTS AND DISCUSSION

A. Preexposure thresholds and rT_1 values

Table III shows the mean preexposure thresholds and rT_1 values measured for MUK and BEN. Data from both control and exposure sessions are pooled. Preexposure hearing thresholds were consistent over the course of the study. Subjects rarely committed false alarms, thus the rT_1 values were generally low.

Table IV shows the mean rT_1 values measured during the postexposure sessions (control and exposure sessions are not pooled here). A repeated measures ANOVA was used to compare the postexposure rT_1 values from the control and exposure sessions to the appropriate preexposure rT_1 values and to each other. For MUK, there were no significant differences between rT_1 values. For BEN, there were no significant differences between rT_1 values at 0.4 and 30 kHz. At 4 kHz, rT_1 values measured during control sessions were significantly higher [$F(3,9)=5.26$, $p<0.05$]; however, this result may be somewhat misleading because of the low variability in the rT_1 values for the exposure condition (i.e., there were no false alarms during these sessions).

TABLE III. Mean values for preexposure masked hearing thresholds and rT_1 values for MUK and BEN. The ± values are standard deviations. Data from exposure and control sessions are pooled.

	MUK			BEN		
Frequency (kHz)	Threshold (dB *re* 1 μPa)	rT_1 (10^{-3})	*n*	Threshold (dB *re* 1 μPa)	rT_1 (10^{-3})	*n*
0.4	117±1.6	0±0	78	123±1.4	5.7±8.2	24
4	118±1.6	1.9±5.5	78	117±1.7	1.9±7.1	24
30	116±1.8	1.2±5.3	78	126±1.6	1.5±4.0	24

B. Threshold shifts and recovery

Figure 5 shows the postexposure thresholds measured for MUK at levels M10–M13. Each data series was normalized with respect to the appropriate preexposure threshold. Control sessions are displayed in the left set of panels; the right set shows the exposure sessions. Each panel row represents a control/exposure pair from the same test day. Inverted triangles, triangles, and circles indicate thresholds at 0.4, 4, and 30 kHz, respectively. Time zero indicates the time of the exposure (or mock exposure). The results for levels M10 and M12 are representative of the majority of the measured data: postexposure thresholds varied within the range of ±4 dB during the majority of the control and exposure sessions. No MTTS was observed in any exposure session from level M1 through M10 or in any control session.

At level M11, a 7-dB and a 6-dB $MTTS_2$ were observed at 0.4 and 30 kHz, respectively. At both frequencies, thresholds returned to within 2 dB of the preexposure value within 4 min postexposure. Received levels at M11 were approximately 160 kPa peak pressure, 226 dB *re* 1 μPa p-p pressure, and 186 dB *re* 1 $\mu Pa^2 \cdot s$ total energy flux. Figure 6 shows a detailed view of the recovery from MTTS at 0.4 kHz (inverted, filled triangles) and 30 kHz (open circles) for level M11. A linear regression was used to fit equations of the form

$$TTS_t = m \log_{10} t + b, \tag{5}$$

to these data, where m and b are constants, TTS_t is the threshold shift in dB at time t, and t is in minutes. The form of Eq. (5) was based on human TTS recovery functions for exposure to continuous-type sounds (Ward *et al.*, 1958, 1959). The curve fit was conducted over the time range up to 4 min, where both MTTSs returned to less than 2 dB. The fit to the 30 kHz data was good ($R^2 = 0.994$) and yielded $m = -14.5$ and $b = 9.93$; at 0.4 kHz the fit remained reasonable ($R^2 = 0.981$), yielding $m = -21.4$ and $b = 13.2$.

Received levels were reduced for exposure condition M12, to verify that the shifts observed at M11 were not a behavioral artifact; i.e., the subject did not simply stop responding to hearing test tones after exposures. Level M13 was an attempt to replicate level M11. No MTTSs of 6 dB or larger were observed at levels M12 and M13; however, at level M13 a maximum TS of 5 dB did occur at 1.7 min postexposure. Although lower than our predefined criterion for MTTS, this TS was larger than any of the TSs that occurred in any exposure session from levels M1–M10 and M12, or any control session.

The discrepancy between the TSs measured at level M11 and M13 (i.e., lower TS at the higher exposure level) was probably the result of day-to-day differences in the subject's susceptibility. The same exposure should not be expected to produce the same TTS in a given subject; standard deviations in repeated human TTS_2 measurements (the same ear exposed to repeated, widely spaced noise) have been reported to be around 4 dB for TTSs of approximately 20 dB (Lightfoot, 1955).

Figure 7 summarizes the postexposure thresholds measured for MUK. These plots show the TSs measured 2 min (upper), 4 min (middle), and 10 min (lower) postexposure for the control sessions (open symbols) and the exposure sessions (filled symbols). Inverted triangles, triangles, and circles indicate thresholds at 0.4, 4, and 30 kHz, respectively. The majority of TS_2, TS_4, and TS_{10} measurements (223/234) were within ±3 dB, there were 8/234 occurrences of ±4-dB TSs and one occurrence of a −5-dB TS_4. There were no systematic differences between control and exposure sessions, except for the MTTSs at level M11, which were the only TSs larger than 5 dB.

Figures 8 and 9 are analogous to Figs. 5 and 7, respectively, and show the results for BEN. Figure 8 shows the postexposure thresholds for levels B1–B4. Figure 9 shows the measured TS_2, TS_4, and TS_{10} for BEN at each exposure condition. As with MUK, postexposure thresholds varied over the course of testing. The majority of postexposure thresholds (65/72) were within ±3 dB of preexposure values. No MTTSs were observed in any control or exposure ses-

TABLE IV. Mean values for postexposure rT_1 values for MUK and BEN. The ± values are standard deviations.

	MUK			BEN		
Frequency (kHz)	Control rT_1 (10^{-3})	Exposure rT_1 (10^{-3})	*n*	Control rT_1 (10^{-3})	Exposure rT_1 (10^{-3})	*n*
0.4	0.3±0.9	0.5±1.2	13	15.8±7.6	16.1±29.4	4
4	1.4±4.1	2.9±4.2	13	10.1±3.6	0±0	4
30	1.4±2.7	0.6±1.4	13	1.6±3.2	8.5±7.2	4

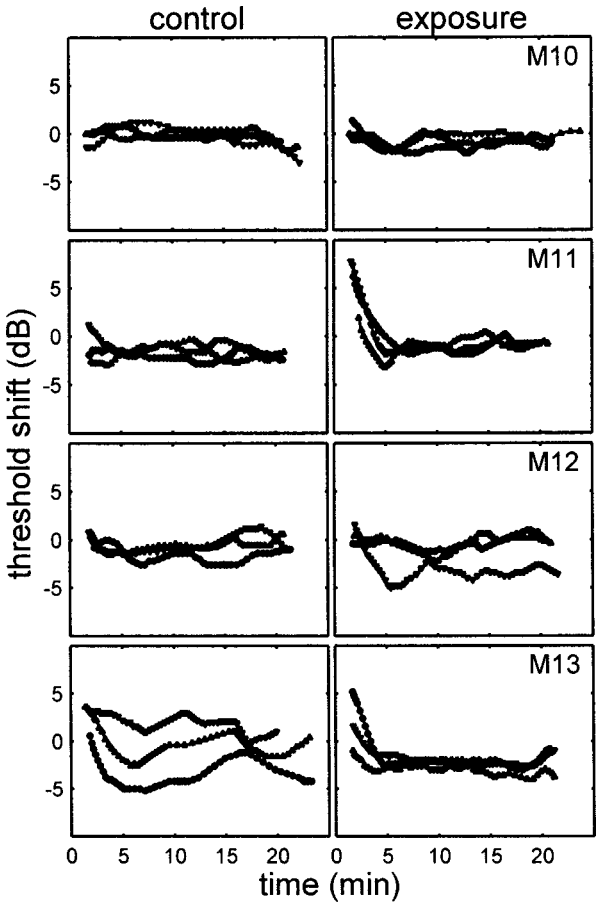

FIG. 5. Postexposure threshold shifts measured for MUK at levels M10–M13. Control sessions are displayed in the left set of panels; the right set shows the exposure sessions. Each panel row represents a control/exposure pair from the same test day. Inverted triangles, triangles, and circles indicate thresholds at 0.4, 4, and 30 kHz, respectively. Time-zero indicates the time of the exposure (or mock exposure for control sessions).

sions. The highest exposure conditions were 220 kPa (31.9 psi) peak pressure and 229 dB *re* 1 μPa p-p pressure (level B3) or 189 dB *re* 1 μPa^2·s total energy flux (level B4).

C. Behavioral observations

Previous studies of TTS in marine mammals have reported various behavioral reactions on the part of the test subjects during and/or after exposure to high levels of underwater sound (Kastak *et al.*, 1999; Schlundt *et al.*, 2000). These reactions mainly consisted of alterations in the subjects' trained behaviors that appeared to be deliberate attempts to avoid the sound exposure itself (for long duration exposures) or to avoid the spatial location of the exposure during subsequent tests. More severe reactions such as aggression toward the test apparatus (Schlundt *et al.*, 2000) or trainers (Kastak *et al.*, 1999) have also been observed. Although neither subject of the present study exhibited aggression towards the apparatus or trainers, the subjects' behavioral reactions were otherwise consistent with those of the earlier studies: both subjects were often reluctant to station at the S1 biteplate following exposure to the watergun impulse and sometimes vocalized after the exposure. For MUK, these behaviors began at the first exposure condition; this may have been a result of her prior experience with impulsive TTS testing (see Finneran *et al.*, 2000). For BEN, behavioral alterations began at level B3. The validity of extrapolating these types of behavioral observations of trained, experienced animals to wild and/or naive animals is questionable. The nature of the test sequence, where the exposures generally increased over time, also may have introduced order effects.

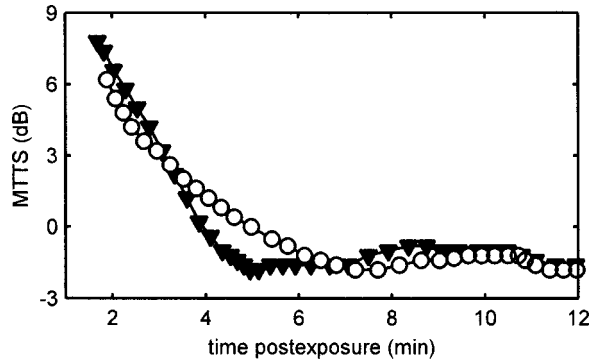

FIG. 6. Recovery of MTTS for MUK at level M11. Inverted, filled triangles, and open circles indicate threshold shifts measured at 0.4 and 30 kHz, respectively.

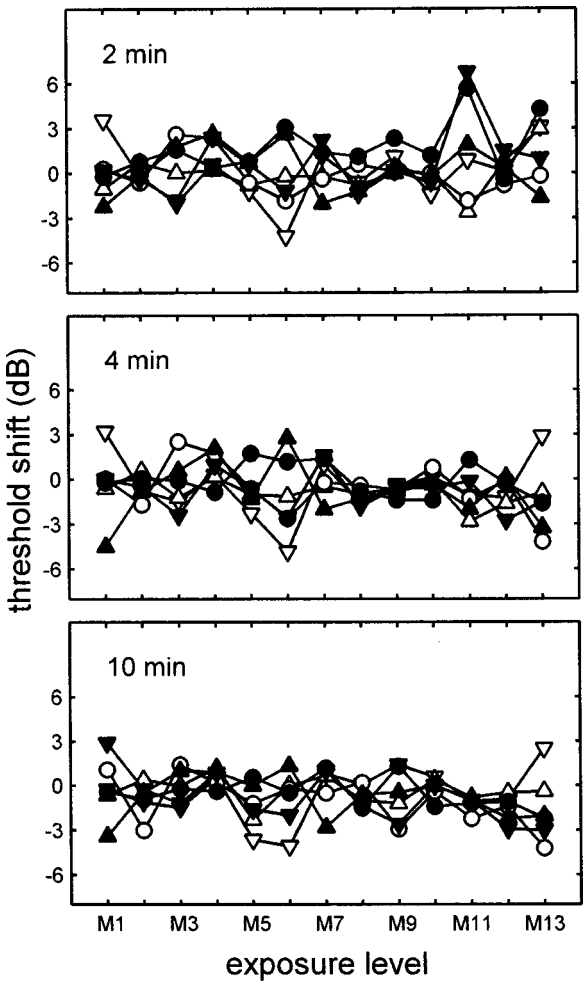

FIG. 7. Threshold shifts measured for MUK at 2 min (upper), 4 min (middle), and 10 min (lower) postexposure for the control sessions (open symbols) and the exposure sessions (filled symbols). Inverted triangles, triangles, and circles indicate thresholds at 0.4, 4, and 30 kHz, respectively.

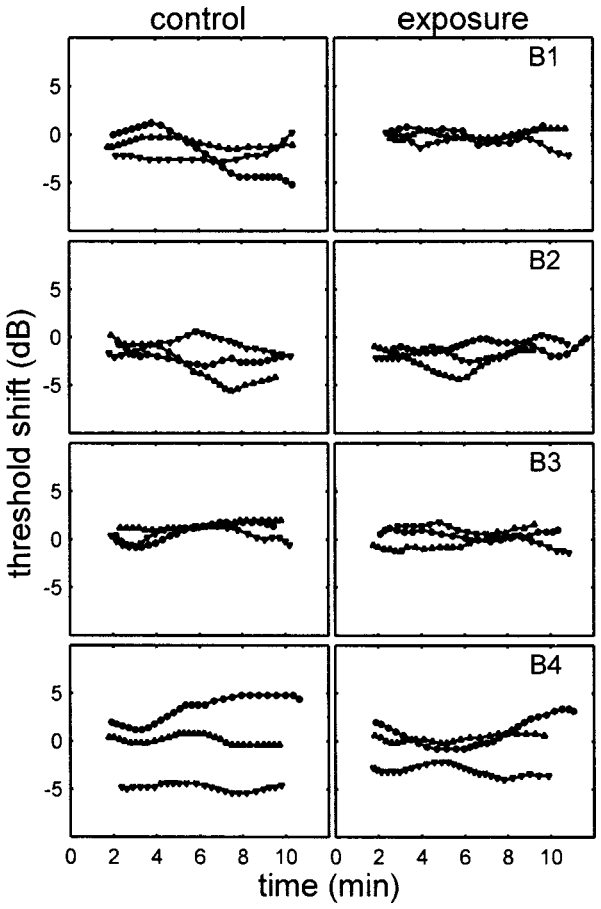

FIG. 8. Postexposure threshold shifts measured for BEN at levels B1–B4. Control sessions are displayed in the left set of panels; the right set shows the exposure sessions. Each panel row represents a control/exposure pair from the same test day. Inverted triangles, triangles, and circles indicate thresholds at 0.4, 4, and 30 kHz, respectively. Time-zero indicates the time of the exposure (or mock exposure for control sessions).

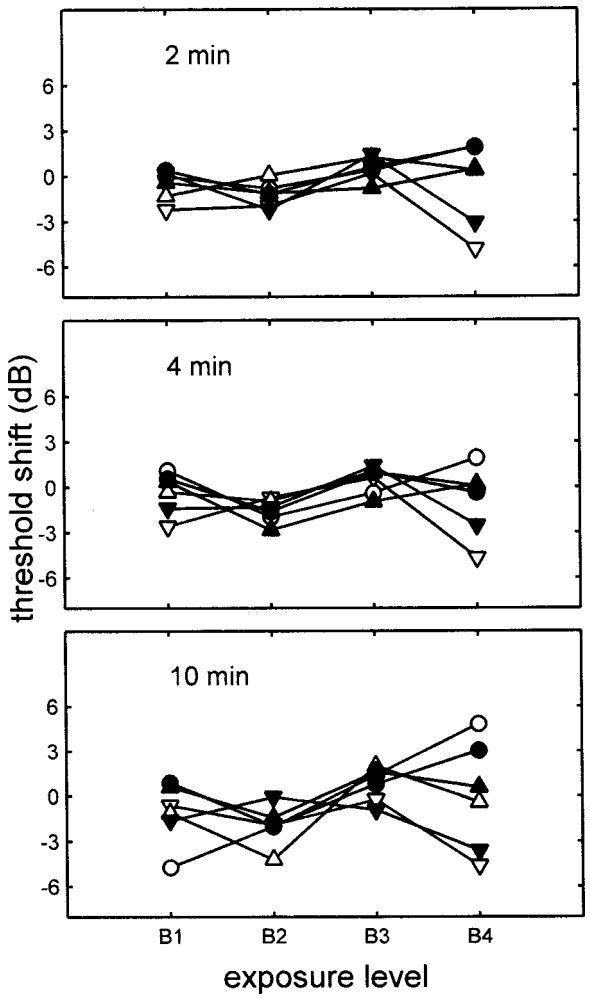

FIG. 9. Threshold shifts measured for BEN at 2 min (upper), 4 min (middle), and 10 min (lower) postexposure for the control sessions (open symbols) and the exposure sessions (filled symbols). Inverted triangles, triangles, and circles indicate thresholds at 0.4, 4, and 30 kHz, respectively.

D. Masking noise effects

Studies of TTS in humans (Parker *et al.*, 1976; Humes, 1980) have shown that the presence of masking noise results in elevated hearing thresholds (simulating a preexposure loss in hearing sensitivity) and decreases the amount of TTS measured. Ades *et al.* (1974) also measured smaller amounts of PTS in chinchillas when thresholds were obtained in the presence of masking noise compared to the amount of PTS measured when thresholds were determined in quiet. There are currently no conclusive data for the relationship between masking noise and TTS in odontocetes; it is possible that larger TSs may have been observed without the masking noise. Masking noise was employed out of necessity because the test site had a variable ambient noise level. The masking noise employed was at the lowest level (above ambient) at which uniform frequency content and stable hearing thresholds could be maintained. Subject preexposure hearing thresholds (Table III) ranged from approximately 10 dB (at 0.4 kHz) to 80 dB (at 30 kHz) above published ''absolute'' thresholds for *Tursiops* and *Delphinapterus* (Johnson, 1967; White *et al.*, 1978; Awbrey *et al.*, 1988); however, the masked thresholds at 30 kHz were only approximately 22 dB above thresholds measured in the presence of ambient noise in San Diego Bay (Schlundt *et al.*, 1999).

E. Comparison to existing data

In the absence of any cetacean TTS data, Ketten (1995) stated that, for exposure to single impulses, 34–103 kPa (5–15 psi) peak pressure was accepted as the value at which TTS was rare. This estimate, apparently based on anatomical studies and extrapolations from terrestrial mammal data, has been used to derive TTS impact zones for marine mammals exposed to underwater impulses (e.g., Department of the Navy, 2001). Ketten (1995) acknowledged that, in the absence of direct experimental evidence, her conclusions were ''highly speculative.'' The results of the present study may be summarized as follows: for the specific subjects and pressure waveforms employed, a peak pressure of 160 kPa (23 psi) caused a small MTTS in the white whale and a peak pressure of 207 kPa (30 psi) did not cause an MTTS in the dolphin. These data therefore suggest that, for single impulses with durations and waveforms comparable to those used in this study, peak pressures necessary to induce TTS may be higher than the previously predicted range of 34–103 kPa (5–15 psi).

Figure 10 compares the watergun results to the existing odontocete TTS data from Nachtigall *et al.* (2001) [TTS in a

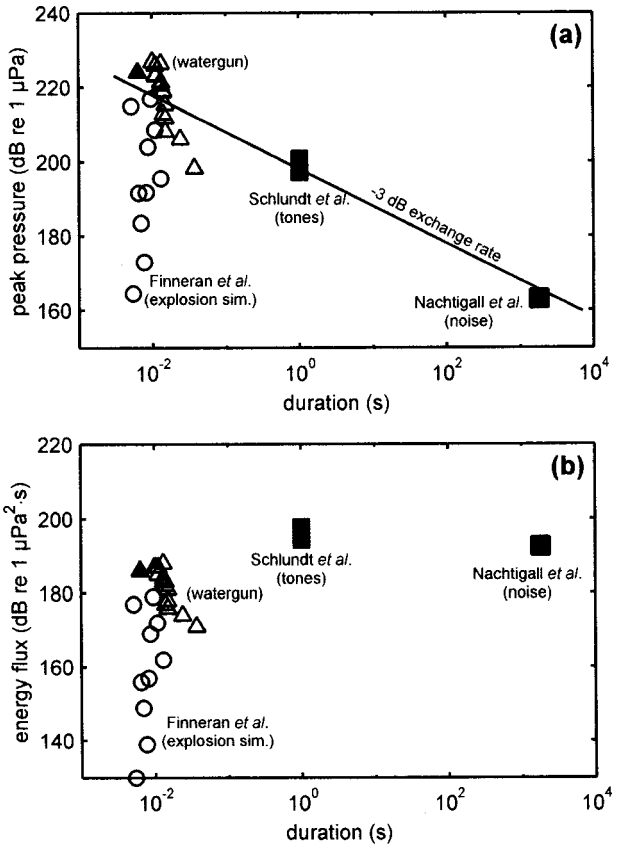

FIG. 10. Summary of existing TTS data for odontocetes. (a) Exposure peak pressure versus exposure duration. (b) Exposure energy flux versus exposure duration. Filled rectangles: TTS-inducing exposure conditions from Schlundt *et al.* (2000) and Nachtigall *et al.* (2001). Open circles: exposure conditions from Finneran *et al.* (2000). Open triangles: exposure conditions from the present study with no MTTS. Filled triangles: the condition M11, where MTTSs were observed.

bottlenose dolphin exposed to 30 min of octave-band noise centered at 7.5 kHz], Schlundt *et al.* (2000) [MTTS (6-dB or larger shifts) in dolphins and white whales exposed to 1-s pure tones at frequencies between 3 and 75 kHz], and Finneran *et al.* (2000) (no MTTS after exposure to single impulses). Figure 10(a) displays the peak SPL versus the exposure duration from each study; Fig. 10(b) displays the exposure energy flux versus the duration. The rectangles represent the TTS-inducing exposure conditions from Schlundt *et al.* (2000) and Nachtigall *et al.* (2001). Peak SPL values from Nachtigall *et al.* (2001) were approximated as the octave band (rms) level +3 dB. The open circles indicate exposure conditions from Finneran *et al.* (2000). The open triangles indicate the exposure conditions from the present study with no MTTS; the filled triangles indicate the condition M11, where MTTSs were observed. Figure 10(a) also includes a line with a slope of 3 dB per doubling of time fit to the mean value of the Schlundt *et al.* exposure levels. The 3 dB per doubling of time slope, or 3-dB exchange rate (NIOSH, 1998), is equivalent to an equal energy criterion relating the SPL and permissible exposure duration (for continuous-type sounds); that is, for continuous sounds, if the exposure duration is doubled, the SPL must be reduced by 3 dB for the energy flux to remain constant.

The large range of TTS-inducing peak pressures in Fig. 10(a) emphasizes that the use of a single SPL, without regard to exposure duration, is an inappropriate metric to predict TTS. For these species and stimuli, the −3-dB exchange rate appears to be a good fit to watergun, Schlundt *et al.*, and Nachtigall *et al.* TTS-inducing exposures presented in Fig. 10(a). A comparison of the TTS-inducing energy levels [Fig. 10(b)] shows good agreement between the Schlundt *et al.* and Nachtigall *et al.* data sets; the energy flux of the TTS-inducing watergun exposures was roughly 6-9 dB lower than that of the other studies. This range is reasonable considering the differences in methodology, exposure conditions, and subjects. From these limited data, it thus appears that the total energy may be a good predictor of onset-TTS levels in odontocetes, especially for continuous-type sounds. Of course, caution should be used in extrapolating these results to other impulsive pressure waveforms with much higher peak pressures and/or radically different waveforms or durations. Given the limited amount of data, it seems prudent to consider both the peak pressure and the energy flux when estimating the impact of impulsive sounds (e.g., Department of the Navy, 2001).

IV. CONCLUSIONS

A behavioral response paradigm was used to measure masked underwater hearing thresholds in a bottlenose dolphin and a white whale before and after exposure to single underwater impulsive sounds produced from a seismic watergun. MTTSs of 6–7 dB were observed in the white whale after exposure to single impulses with peak pressure of 160 kPa (23 psi) and total energy flux of 186 dB *re* 1 μPa^2·s. No MTTS was observed in the dolphin at the highest exposure conditions [207 kPa (30 psi) peak pressure and 188 dB *re* 1 μPa^2·s total energy flux].

ACKNOWLEDGMENTS

The watergun was supplied and maintained by Seth Mogk of Scripps Institution of Oceanography. Tricia Kamolnick, Steve Meck, and Kevin St. John trained the test subjects. Funding was provided by the Office of Naval Research (Dr. Robert Gisiner) and CNO (N45) (Dr. Frank Stone). Dr. David Helweg, Dr. John Sigurdson, and two anonymous reviewers provided helpful comments. James Finneran was supported by a National Research Council Research Associateship.

Ades, H. W., Trahiotis, C., Kokko-Cunningham, A., and Averbuch, A. (**1974**). ''Comparison of hearing thresholds and morphological changes in the chinchilla after exposure to 4 kHz tones,'' Acta Oto-Laryngol. **78**, 192–206.

Ahroon, W. A., Hamernik, R. P., and Lei, S.-F. (**1996**). ''The effects of reverberant blast waves on the auditory system,'' J. Acoust. Soc. Am. **100**, 2247–2257.

Au, W. W. L., Nachtigall, P. E., and Pawloski, J. L. (**1999**). ''Temporary threshold shift in hearing induced by an octave band of continuous noise in the bottlenose dolphin,'' J. Acoust. Soc. Am. **106**, 2251(A).

Awbrey, F. T., Thomas, J. A., and Kastelein, R. A. (**1988**). ''Low-frequency underwater hearing sensitivity in belugas, *Delphinapterus leucas*,'' J. Acoust. Soc. Am. **84**, 2273–2275.

Britt, J. R. (**1987**). ''Shock wave reflection and refraction in multi-layered ocean/ocean bottoms with shear wave effects. A user's manual for the REFMS code,'' NSWC TR 87-312, Naval Surface Warfare Center, November 1987.

Britt, J. R., Eubanks, R. J., and Lumsden, M. G. (**1991**). *Underwater Shock Wave Reflection and Refraction in Deep and Shallow Water: Volume I—A User's Manual for the REFMS Code (Version 4.0)* (Science Applications International Corporation, St. Joseph, LA).

CHABA (**1992**). ''Hazardous exposure to impulse noise,'' Rep. of Working Group on Hazardous Exposure to Exposure to Impulse Noise, NAS-NRC Committee on Hearing, Bioacoustics, and Biomechanics (National Academy of Sciences, Washington, DC).

Cornsweet, T. N. (**1962**). ''The staircase method in psychophysics,'' Am. J. Psychol. **75**, 485–491.

Department of the Navy (**1998**). *Final Environmental Impact Statement, Shock-testing the SEAWOLF submarine* (Department of the Navy, Washington, DC).

Department of the Navy (**2001**). *Final Environmental Impact Statement, Shock trial of the WINSTON S. CHURCHILL (DDG81)* (Department of the Navy, Washington, DC).

Egan, J. P., Greenberg, G. Z., and Schulman, A. I. (**1961**). ''Operating characteristics, signal detectability, and the method of free response,'' J. Acoust. Soc. Am. **33**, 993–1007.

Finneran, J. J., Carder, D. A., Ridgway, S. H., and Schlundt, C. E. (**1999**). ''Technique for the generation and frequency compensation of band-limited white noise and its application in studies of masked hearing thresholds,'' J. Acoust. Soc. Am. **106**, 2130(A).

Finneran, J. J., Schlundt, C. E., Carder, D. A., Clark, J. A., Young, J. A., Gaspin, J. B., and Ridgway, S. H. (**2000**). ''Auditory and behavioral responses of bottlenose dolphins (*Tursiops truncatus*) and white whales (*Delphinapterus leucas*) to impulsive sounds resembling distant signatures of underwater explosions,'' J. Acoust. Soc. Am. **108**, 417–431.

Fricke, J. R., Davis, J. M., and Reed, D. H. (**1985**). ''A standard quantitative calibration procedure for marine seismic sources,'' Geophysics **50**(10), 1525–1532.

Hamernik, R. P., and Hsueh, K. D. (**1991**). ''Impulse noise: some definitions, physical acoustics and other considerations,'' J. Acoust. Soc. Am. **90**, 189–196.

Humes, L. E. (**1980**). ''Temporary threshold shift for masked pure tones,'' Audiology **19**, 335–345.

Johnson, C. S. (**1967**). ''Sound detection thresholds in marine mammals,'' in *Marine BioAcoustics*, edited by W. N. Tavolga (Pergamon, New York), Vol. 2, pp. 247–260.

Johnston, R. C., Reed, D. H., and Desler, J. F. (**1988**). ''Special report of the SEG technical standards committee, SEG standards for specifying marine seismic energy sources,'' Geophysics **53**(4), 566–575.

Kastak, D., Schusterman, R. J., Southall, B. L., and Reichmuth, C. J. (**1999**). ''Underwater temporary threshold shift induced by octave-band noise in three species of pinniped,'' J. Acoust. Soc. Am. **106**, 1142–1148.

Ketten, D. R. (**1995**). ''Estimates of blast injury and acoustic trauma zones for marine mammals from underwater explosions,'' in *Sensory Systems of Aquatic Mammals*, edited by R. A. Kastelein, J. A. Thomas, and P. E. Nachtigall (De Spil, The Netherlands), pp. 391–407.

Kryter, K. D., Ward, W. D., Miller, J. D., and Eldredge, D. H. (**1966**). ''Hazardous exposure to intermittent and steady-state noise,'' J. Acoust. Soc. Am. **39**, 451–464.

Lightfoot, C. (**1955**). ''Contribution to the study of auditory fatigue,'' J. Acoust. Soc. Am. **27**, 356–364.

Miller, H. (**1969**). ''The FROC curve: A representation of the observer's performance for the method of free response,'' J. Acoust. Soc. Am. **46**, 1473–1476.

Nachtigall, P. E., Supin, A., Pawloski, J. L., and Au, W. W. L. (**2001**). ''Measuring recovery from temporary threshold shifts with evoked auditory potentials in the bottlenosed dolphin *Tursiops truncatus*,'' J. Acoust. Soc. Am. **110**, 2749(A).

NIOSH (**1998**). *Criteria for a Recommended Standard: Occupational Noise Exposure, Revised Criteria 1998*, DHHS (NIOSH) Publication No. 98-126 (NIOSH, Cincinnati, OH).

Parker, D. E., Tubbs, R. L., Johnston, P. A., and Johnston, L. S. (**1976**). ''Influence of auditory fatigue on masked pure-tone thresholds,'' J. Acoust. Soc. Am. **60**, 881–885.

Ridgway, S. H., and Carder, D. A. (**1997**). ''Hearing deficits measured in some *Tursiops truncatus*, and discovery of a deaf/mute dolphin,'' J. Acoust. Soc. Am. **101**, 590–594.

Ridgway, S. H., Carder, D. A., Smith, R. R., Kamolnick, T., Schlundt, C. E., and Elsberry, W. R. (**1997**). ''Behavioral responses and temporary shift in masked hearing thresholds of bottlenose dolphins, *Tursiops truncatus*, to 1-second tones of 141–201 dB *re* 1 μPa,'' Technical Report 1751, Naval Command, Control, and Ocean Surveillance Center, RDT&E Division, San Diego.

Schlundt, C. E., Finneran, J. J., Carder, D. A., and Ridgway, S. H. (**1999**). ''Masked hearing thresholds and critical bandwidths for dolphins and a white whale at 20 and 30 kHz,'' J. Acoust. Soc. Am. **106**, 2190(A).

Schlundt, C. E., Finneran, J. J., Carder, D. A., and Ridgway, S. H. (**2000**). ''Temporary shift in masked hearing thresholds (MTTS) of bottlenose dolphins, *Tursiops truncatus*, and white whales, *Delphinapterus leucas*, after exposure to intense tones,'' J. Acoust. Soc. Am. **107**, 3496–3508.

Ward, W. D., Glorig, A., and Sklar, D. L. (**1958**). ''Dependency of temporary threshold shift at 4 kc on intensity and time,'' J. Acoust. Soc. Am. **30**, 944–954.

Ward, W. D., Glorig, A., and Sklar, D. L. (**1959**). ''Temporary threshold shift from octave-band noise: applications to damage-risk criteria,'' J. Acoust. Soc. Am. **31**, 522–528.

White, M. J., Jr., Norris, J., Ljungblad, D., Baron, K., and di Sciara, G. (**1978**). ''Auditory thresholds of two beluga whales (*Delphinapterus leucas*),'' Hubbs/Sea World Research Institute Tech. Rep. 78-108.

Erratum: "Development of wide-band middle ear transmission in the Mongolian gerbil" [J. Acoust. Soc. Am. 111, 261–270 (2002)]

E. H. Overstreet and M. A. Ruggero
Institute for Neuroscience and Hugh Knowles Center, Department of Communication Sciences and Disorders, Northwestern University, 2299 North Campus Drive, Evanston, Illinois 60208-3550

(Received 17 February 2002; accepted for publication 17 February 2002)

[DOI: 10.1121/1.1473635]

PACS numbers: 43.64.Ha [BLM]

Panel B of Fig. 7 contains an error: the stapes-vibration phases from Fig. 4 of ''Measurements of middle-ear function in the Mongolian gerbil, a specialized mammalian ear,'' Audiol. Neurootol. **4**, 129–136 (1999), by J. J. Rosowski, M. E. Ravicz, S. W. Teoh, and D. Flandermeyer, were incorrectly plotted. The correct phase values are actually smaller by a factor of 2 than those shown in Fig. 7 (i.e., stapes phases should have varied between approximately +90 and −90 degrees).

 0001-4966/2002/111(6)/2941/1/$19.00